CODEN: JASI

The Journal of the Acoustical Society of America

0001-4966

Vol. 108, No. 4 October 2000

(Continued)

THE JOURNAL OF THE ACOUSTICAL SOCIETY OF AMERICA VOL. 108, NO. 4, OCTOBER 2000

CONTENTS—*Continued from preceding page*

(Continued)

THE JOURNAL OF THE ACOUSTICAL SOCIETY OF AMERICA VOL. 108, NO. 4, OCTOBER 2000

CONTENTS—*Continued from preceding page*

(Continued)

THE JOURNAL OF THE ACOUSTICAL SOCIETY OF AMERICA VOL. 108, NO. 4, OCTOBER 2000

CONTENTS—*Continued from preceding page*

ACOUSTICAL NEWS—USA

Elaine Moran
Acoustical Society of America, Suite 1NO1, 2 Huntington Quadrangle, Melville, NY 11747-4502

Editor's Note: *Readers of this Journal are encouraged to submit news items on awards, appointments, and other activities about themselves or their colleagues. Deadline dates for news items and notices are 2 months prior to publication.*

New Fellows of the Acoustical Society of America

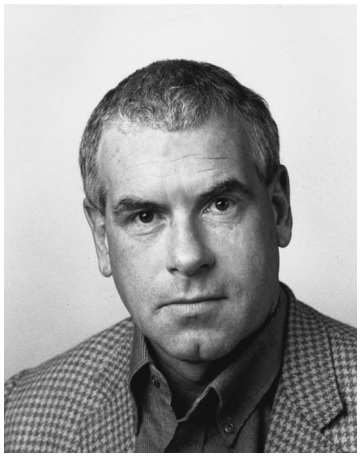

Laurent Demany—For contributions to the understanding of auditory processing.

Dennis F. Jones—For contributions to the development of flextensional transducers.

Hari S. Paul—For contributions to piezoelectric materials and international outreach.

Hans C. Strifors—For contributions to scattering of sound waves from submerged objects.

 0001-4966/2000/108(4)/1361/6/$17.00

Loyola Names Richard Fay as Faculty Scholar Award Winner

Loyola University Chicago has selected Richard Fay, professor of psychology, as one of six winners of the Loyola Faculty Scholars Award.

''These Faculty Scholars represent Loyola's commitment to reward faculty who have demonstrated excellence in both teaching and research and in their contributions to advance the mission of the university,'' said Lawrence Braskamp, senior vice president for academic affairs. ''They represent a small number of the faculty at Loyola who are worthy of such a designation.''

Fay's research focuses on the mechanisms of the nervous system that synthesize perceptions of sound sources. He works primarily with fish, which have simple and primitive vertebrate auditory systems.

Fay will receive an award of $5,000 annually for the next 3 academic years, and will retain the title ''Loyola Faculty Scholar'' for the remainder of his tenure at Loyola. He can use the funds for professional career development.

The faculty winners were selected from a list of 43 who were nominated by their peers and reviewed by a panel, all of whom hold endowed professorships at the university.

Lisa M. Zurk to be Fulbright Scholar

ASA member Lisa M. Zurk of the Massachusetts Institute of Technology (MIT) Lincoln Laboratory has been awarded a Fulbright program grant in mathematics to lecture and conduct research at the University of Helsinki, Finland. The Fulbright grant provides funding in the 2000–2001 academic year for Dr. Zurk to conduct research in the area of electromagnetic and acoustic wave propagation and scattering in stochastic media at the Rolf Nevanlinna Institute.

The Bureau of Educational and Cultural Affairs, U.S. Department of State sponsors the Fulbright Program, America's flagship international educational exchange program. The program was established in 1946 under legislation by former Senator J. William Fulbright of Arkansas. As part of the Fulbright program, the U.S. Scholar Program sends approximately 800 established American scholars and professionals a year to more than 125 countries for teaching and research. Recipients of a Fulbright grant are selected on the basis of their academic or professional achievement and their demonstrated leadership capabilities in their field.

Lisa Zurk received the BS in computer science from the University of Massachusetts in 1985, the MS in electrical and computer engineering from Northeastern University in 1990, and the Ph.D. in electrical engineering from the University of Washington in 1995. From 1985–1989 she worked at Nova Biomedical in Waltham, MA, and from 1990–1995 she was a research assistant at the Applied Physics Laboratory in Seattle, WA. Since 1996 she has been a technical staff member in the Advanced Array Technology Group at MIT Lincoln Laboratory. Her research at MIT is in the area of electromagnetic and acoustic propagation with application to airborne radar and sonar signal processing. Dr. Zurk also holds an adjunct faculty at Northeastern University teaching graduate courses in acoustics, electromagnetic theory, and applied mathematics. She has received previous awards and distinctions, including the Pew Teaching Leadership Award in 1995, the Young Scientist Award in 1995, and honorary induction into the Electromagnetic Academy in 1999. She is the author of more than 30 technical papers on electromagnetics and acoustics, and she is a member of the Women in Acoustics Committee (Acoustical Society of America) and the Women's Advisory Board at MIT.

ASA North Texas Chapter presents awards at 43rd Dallas Morning News–Toyota Regional Science and Engineering Fair

More than 1000 students from 82 North Texas schools competed in the 43rd Dallas Morning News–Toyota Regional Science and Engineering Fair. Brittany Boyer, under the guidance of Gretchen Gozu, Wilson Middle School, Plano ISD, entered the outstanding Junior Acoustics Project. Ms. Boyer used a clarinet and digital tuning meter to investigate effects of humidity, rigidity of wall surfacing, and room volume on musical pitch (see Fig. 1). Ms. Boyer subsequently won both the Junior Physics Division and the Junior Division Grand Prizes.

Travis Blakeley and Ben Siegelman, under the guidance of Richard Thieret, the Greenhill School, Dallas, entered the outstanding Senior Acoustic Project. Their presentation demonstrated that an ultrasonic laboratory glassware cleaner could also be used to sterilize. The technique worked with glass but not plastic containers. Optical measures, sample counts, and changes in cell replication/mutation rates were used to establish the extent of cultures killed (see Fig. 2). The work was intricate; Dr. Richard Cohen, a nationally known medical microbiologist, joined Chapter Officers Dr. Peter Assmann and Dr. Michael Daly in the review.

FIG. 1. Brittany Boyer, recipient of the outstanding Junior Acoustics Project award, with her entry titled ''For the Love of Music.''

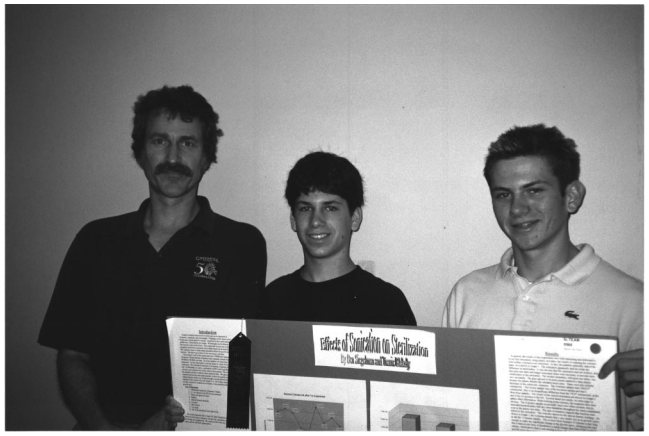

FIG. 2. Richard Thieret (l), Science Department Chair at Greenhill School with Ben Siegelman (c) and Travis Blakeley (r), recipients of the outstanding Senior Acoustic Project award for their entry titled ''Effects of Sonication on Sterilization.''

Report of the Auditor

Published herewith is a condensed version of our auditors' report for calendar year ended 31 December 1999.

Independent Auditors' Report

To the Executive Council
Acoustical Society of America

We have audited the accompanying statements of financial position of the Acoustical Society of America as of December 31, 1999 and the related statements of activity and cash flows for the year then ended. These financial statements are the responsibility of the Society's management. Our responsibility is to express an opinion on the financial statements based on our audit.

We conducted our audit in accordance with generally accepted auditing standards. Those standards require that we plan and perform the audit to obtain reasonable assurance about whether the financial statements are free of material misstatement. An audit includes examining, on a test basis, evidence supporting the amounts and disclosures in the financial statements. An audit also includes assessing the accounting principles used and significant estimates made by management, as well as evaluating the overall financial statement presentation. We believe that our audit provides a reasonable basis for our opinion.

In our opinion, the financial statements referred to above present fairly, in all material respects, the financial position of the Acoustical Society of America as of December 31, 1999 and the changes in its net assets and its cash flows for the year then ended in conformity with generally accepted accounting principles.

CONROY, SMITH & CO.
Certified Public Accountants
9 June 2000
New York, NY

ACOUSTICAL SOCIETY OF AMERICA
STATEMENT OF FINANCIAL POSITION
AS OF 31 DECEMBER 1999
(With Comparative Totals For 1998)

	1999	1998
Assets:		
Cash and cash equivalents	$ 489,533	$2,641,647
Accounts receivable	372,836	378,367
Marketable securities	7,398,853	3,914,155
Furniture, fixtures and equipment—net	118,078	102,218
Other assets	292,934	246,546
Total assets	$8,672,234	$7,282,933
Liabilities:		
Accounts payable and accrued expenses	$ 274,942	$ 205,838
Deferred revenue	1,524,755	1,146,724
Deferred rent liability	44,192	46,394
Total liabilities	$1,843,889	$1,398,956
Net assets:		
Unrestricted	$5,601,878	$4,758,932
Temporarily restricted	598,120	543,563
Permanently restricted	628,347	581,482
Total net assets	$6,828,345	$5,883,977
Total liabilities and net assets	$8,672,234	$7,282,933

ACOUSTICAL SOCIETY OF AMERICA
STATEMENT OF ACTIVITY
FOR THE YEAR ENDED 31 DECEMBER 1999
(With Comparative Totals For 1998)

	Unrestricted Net Assets	Temporarily Restricted Net Assets	Permanently Restricted Net Assets	Total	1998 Total
Support and revenue:					
Contributions	$ -	$ -	$ 1,310	$ 1,310	$ 1,309
Dues	628,110	-	-	628,110	693,123
Publishing	2,088,076	-	-	2,088,076	2,158,365
Standards	366,878	-	-	366,878	352,200
Meetings	239,591	-	-	239,591	786,311
Interest and dividends	271,870	26,933	28,812	327,615	261,216
Unrealized gain (loss)	326,017	35,846	39,683	401,546	124,411
Other	60,639	-	-	60,639	71,545
Realized gain (loss)	192,417	20,247	23,421	236,085	280,799
Net assets released from restrictions	28,469	(28,469)	-	-	-
Total support and revenue	$4,202,067	$ 54,557	$ 93,226	$4,349,850	$4,729,279
Expenses:					
Publishing	$1,783,477	$ -	$ -	$1,783,477	$1,682,237
Standards	461,999	-	-	461,999	448,058
Administrative and general	499,455	-	-	499,455	493,500
Meetings	250,613	-	-	250,613	690,157
Other	363,577	-	46,361	409,938	437,905
Total expenses	$3,359,121	$ -	$ 46,361	$3,405,482	$3,751,857
Increase in net assets	$ 842,946	$ 54,557	$ 46,865	$ 944,368	$ 977,422
Net assets, beginning of year	4,758,932	543,563	581,482	5,883,977	4,906,555
Net assets, end of year	$5,601,878	$ 598,120	$ 628,347	$6,828,345	$5,883,977

ACOUSTICAL SOCIETY OF AMERICA
STATEMENT OF CASH FLOWS
FOR THE YEAR ENDED 31 DECEMBER 1999
(With Comparative Totals For 1998)

	Total All Funds	
	1999	**1998**
Operating Activities		
Increase in net assets	$ 944,368	$ 977,422
Adjustments to reconcile net income to net cash provided by operating activities:		
Depreciation and amortization	31,355	28,964
Unrealized (gain) loss on marketable securities	(401,545)	(124,411)
Changes in operating assets and liabilities:		
(Increase) decrease in accounts receivable	5,531	(151,190)
Decrease (increase) in other assets	(46,388)	23,821
Increase (decrease) in accounts payable and accrued expenses	69,104	(28,646)
(Decrease) increase in deferred rent liability	(2,202)	166
Increase (decrease) in deferred revenue	378,031	309,819
Net cash flows provided by operating activities	$ 978,254	$1,035,945
Investing Activities		
Purchase of furniture, fixtures, equipment, and leasehold improvements	($ 47,336)	($ 30,017)
Proceeds from sale of securities	1,713,644	4,623,945
Purchase of securities	(4,796,676)	(3,279,609)
Net cash (used in) provided by investing activities	($3,130,368)	$1,314,319
Increase (decrease) in cash and cash equivalents	($2,152,114)	$2,350,264
Cash and cash equivalents, beginning of year	2,641,647	291,383
Cash and cash equivalents, end of year	$ 489,533	$2, 641,647

USA Meetings Calendar

Listed below is a summary of meetings related to acoustics to be held in the U.S. in the near future. The month/year notation refers to the issue in which a complete meeting announcement appeared.

2000

22–25 Oct. IEEE Ultrasonics Symposium, San Juan, Puerto Rico [R. Almar, 896 Buttonwood Ln., Altamonte Springs, FL 32714; Fax: 407-290-5181; WWW: www.uffcsymp2000.org].

4–8 Dec. Joint Meeting: 140th Meeting of the Acoustical Society of America/NOISE-CON 2000, Newport Beach, CA [Acoustical Society of America, Suite 1NO1, 2 Huntington Quadrangle, Melville, NY 11747-4502; Tel.: 516-576-2360; Fax: 516-576-2377; E-mail: asa@aip.org; WWW: asa.aip.org].

2001

4–8 Feb. Midwinter Meeting, Association for Research in Otolaryngology, St. Petersburg, FL [ARO Office, 19 Mantua Rd., Mt. Royal, NJ 08061; Tel.: 856-423-7222; Fax: 856-423-3420; E-mail: meetings@aro.org; WWW: www.aro.org/mwm/mwm.html].

22–25 March ''New Frontiers in the Amelioration of Hearing Loss,'' St. Louis, MO [Sarah Uffman, CID Department of Research, 4560 Clayton Ave., St. Louis, MO 63110; Tel.: 314-977-0278; Fax: 314-977-0030; E-mail: suffman@cid.wustl.edu].

30 April–3 May 2001 SAE Noise & Vibration Conference & Exposition, Traverse City, MI [Patti Kreh, SAE Int'l., 755 W. Big Beaver Rd., Suite 1600, Troy, MI 48084; Tel.: 248-273-2474; Fax: 248-273-2494; E-mail: pkreh@sae.org].

4–8 June 141st Meeting of the Acoustical Society of America, Chicago, IL [Acoustical Society of America, Suite 1NO1, 2 Huntington Quadrangle, Melville, NY 11747-4502; Tel.: 516-576-2360; Fax: 516-576-2377; E-mail: asa@aip.org; WWW: asa.aip.org].

15–19 Aug. ClarinetFest 2001, New Orleans, LA [Dr. Keith Koons, ICA Research Presentation Committee Chair, Music Dept., Univ. of Central Florida, P.O. Box 161354, Orlando, FL 32816-1354; Tel.: 407-823-5116; E-mail: kkoons@pegasus.cc.ucf.edu]. Deadline for receipt of abstracts: 15 January 2001

7–10 Oct. 2001 IEEE International Ultrasonics Symposium Joint with World Congress on Ultrasonics, Atlanta, GA [W. O'Brien, Electrical and Computer Engineering, Univ. of Illinois, 405 N. Mathews, Urbana, IL 61801; Fax: 217-244-0105; WWW: www.ieee-uffc.org/2001].

ACOUSTICAL NEWS—INTERNATIONAL

Walter G. Mayer
Physics Department, Georgetown University, Washington, DC 20057

Papers published in JASJ(E)

A listing of Invited Papers and Regular Papers appearing in the latest issue of the English language version of the *Journal of the Acoustical Society of Japan*, JASJ(E), was published for the first time in the January 1995 issue of the Journal. This listing is continued below.

The July 2000 issue of JASJ(E), Vol. 21, No. 4, contains the following contributions:

M. Ohta, A. Ikuta, K. Hatakeyama, and H. Ogawa, ''A practical determination of an optical order of state probability distribution expression with hierarchical expansion form observed in the actual sound and vibration environment''
T. Yoshimura, K. Tokuda, T. Masuko, T. Kobayashi, and T. Kitamura, ''Speaker interpolation for HMM-based speech synthesis system''
H. Habibzadeh Vaneghi and S. Kitazawa, ''An approach to auditory neural transduction reverse model''

International Meetings Calendar

Below are announcements of meetings to be held abroad. Entries preceded by an * are new or updated listings with full contact addresses given in parentheses. *Month/year* listings following other entries refer to meeting announcements, will full contact addresses, which were published in previous issues of the *Journal*.

October 2000

3–5 **WESTPRAC VII,** Kumamoto. (Web: cogni.eecs.kumamoto-u.ac.jp/others/westprac7) *6/98*

3–6 **EUROMECH Colloquium on Elastic Waves in NDT,** Prague. (Fax: +420 2 858 4695; e-mail: ok@bivoj.it.cas.cz) *10/99*

12–14 **International Conference on Newborn Hearing Screening,** Milan. (Fax: +39 2 23993367/.60; Web: www.biomed.polimi.it/nh2000) *2/00*

16–18 **2nd Iberoamerican Congress on Acoustics, 31st National Meeting of the Spanish Acoustical Society, and EAA Symposium,** Madrid. (Fax: +34 91 411 7651; e-mail: ssantiago@fresno.csic.es) *12/98*

16–20 **6th International Conference on Spoken Language Processing,** Beijing. (Fax: +86 10 6256 9079; Web: www.icslp2000.org) *10/98*

26–27 ***7th Mexican Congress on Acoustics,** Veracruz, Ver., Mexico. (S. Beristain, P.O. Box 75805, Col. Lindavista, 07300 Mexico D. F., Mexico; e-mail: sberista@maya.esimez.ipn.mx)

November 2000

10–12 **Institute of Acoustics Autumm Conference (Industrial Noise),** Stratford-upon-Avon, UK. (Fax: +44 1727 850553; Web: www.ioa.org.uk) *8/00*

15–16 ***Australian Acoustical Society Conference,** Perth—Joodalup Resort, Australia. (Conference Secretary, Australian Acoustical Society, WA Division, P.O. Box 1090, West Perth, WA 6872, Australia; e-mail: dlloyd@ermperth.erm.com.au)

17–19 **Reproduced Sound 16,** Stratford-upon-Avon, UK. (Fax: +44 1727 850553; Web: www.ioa.org.uk) *8/00*

24–27 **21st Tonmeistertagung (VDT International Audio Convention),** Hannover, Germany. (Fax: +49 2204 21584; Web: www.tonmeister.de) *6/00*

December 2000

4–7 ***8th Australian International Conference on Speech, Science, and Technology,** Canberra, Austrashlia. (S. Barlow, Secretary SST-2000, School of Computer Science, Australian Defence Academy, Northcott Drive, Canberra, ACT 2600, Australia; Web: www.cs.adfa.edu.au/ssst2000)

January 2001

14–17 ***4th European Conference on Noise Control (euronoise 2001),** Patras, Greece. (LFME, University of Patras, P.O. Box 1400, Patras 26500, Greece; e-mail: euronoise2001@upatras.gr)

March 2001

26–29 ***German Acoustical Society Meeting (DAGA 2001),** Hamburg-Harburg, Germany. (e-mail: dega@aku.physik.uni-oldenburg.de)

April 2001

9–11 **Acoustical Oceanography,** Southampton, UK. (Fax: +44 1727 850553; Web: www.ioa.org.uk) *8/00*

23–25 ***1st International Workshop on Thermoacoustics,** s'Hertogenbosch, The Netherlands. (C. Schmid, Acoustical Society of America, Suite 1NO1, 2 Huntington Quadrangle, Melville, NY 11747-4502, USA; Web: www.phys.tue.nl/index.html)

May 2001

21–25 ***5th International Conference on Theoretical and Computational Acoustics (ICTCA2001),** Beijing, China. (E. C. Shang, CIRES, University of Colorado, NOAA/ETL, Boulder, Colorado, USA; Fax: +1 303 497 3577; Web: www.etl.noaa.gov/ictca01)

28–31 ***3rd EAA International Symposium on Hydroacoustics,** Jurata, Poland. (G. Grelowska, Polish Naval Academy, Smidowkcza 69, 81-103 Gdynia, Poland; Fax: +48 58 625 4846; Web: www.amw.gdynia.pl/pta/sha2001.html)

July 2001

2–6 **8th International Congress on Sound and Vibration,** Kowloon, Hong Kong. (Fax: +852 2365 4703; Web: www.iiav.org) *8/00*

August 2001

28–30 **INTER-NOISE 2001,** The Hague. (Web: internoise 2001.tudelft.nl) *6/99*

September 2001

2–7 **17th International Congress on Acoustics (ICA),** Rome. (Fax: +39 6 4424 0183; Web: www.uniroma1.it/energ/ica.html) *10/98*

10–13 **International Symposium on Musical Acoustics (ISMA 2001),** Perugia. (Fax: +39 75 577 2255; e-mail: perusia@classico.it) *10/99*

October 2001

17–19 **32nd Meeting of the Spanish Acoustical Society,** La Rioja. (Fax: +34 91 411 76 51; Web: www.ia.csic.es/sea/index.html) *10/99*

March 2002

4–8 ***German Acoustical Society Meeting (DAGA 2002),** Bochum, Germany. (J. Blauert, Institute of Communi-

 0001-4966/2000/108(4)/1369/2/$17.00

cation Acoustics, Ruhr-Universität Bochum, 44780 Bochum, Germany; Fax: +49 234 321 4165; Web: www.ika.ruhr-uni-bochum.de)

September 2002

16–21 **Forum Acusticum 2002 (Joint EAA-SEA-ASJ Meeting),** Sevilla. (Fax: +34 91 411 7651; Web: www.cica.es/aliens/forum2002) *2/00*

December 2002

2–6 ***Joint Meeting: 9th Mexican Congress on Acoustics, 144th Meeting of the Acoustical Society of America, and 3rd Iberaoamerican Congress on Acoustics.** (Mexican Institute of Acoustics. P.O. Box 75805, Col Lindavista, 07300 Mexico D. F., Mexico; e-mail: sberista@maya.esimez.ipn.mx; Web: asa.aip.org)

TECHNICAL PROGRAM SUMMARY

Joint Meeting: 140th Meeting of the Acoustical Society of America and NOISE-CON 2000
Newport Beach Marriott Hotel and Tennis Club
Newport Beach, California

3–8 December 2000

TENTATIVE AGENDA—SUBJECT TO CHANGE

***Indicates Special Session**

Sunday Afternoon, 3 December

0pNSa	NOISE-CON and Noise: Theoretical and Experimental Noise Control
0pNSb	NOISE-CON and Noise: Active Noise and Vibration Control
0pNSc	NOISE-CON and Noise: Aircraft Noise
0pNSd	NOISE-CON and Noise: Community Noise
0pNSe	NOISE-CON and Noise: Plenary Session—Global Players in Acoustic Standardization

Monday Morning, 4 December

*1aAO	Acoustical Oceanography: Bioacoustics I
*1aBB	Biomedical Ultrasound/Bioresponse to Vibration Topical Meeting: Physics of Echo-Contrast Agents I
1aNSa	NOISE-CON and Noise: Plenary Session—Noise Control Engineering for the Airport Railway in Hong Kong
1aNSb	NOISE-CON, Noise and Architectural Acoustics: Heating Ventilating and Air Conditioning Noise
1aNSc	NOISE-CON and Noise: Classroom Acoustics
1aNSd	NOISE-CON, Noise and Engineering Acoustics: Noise Control Materials and Elements
1aSC	Speech Communication: All Things Prosodic (Poster Session)

Monday Afternoon, 4 December

*1pAA	Architectural Acoustics and Engineering Acoustics: Loudspeaker Student Design Competition
*1pAO	Acoustical Oceanography: Bioacoustics II
*1pBB	Biomedical Ultrasound/Bioresponse to Vibration Topical Meeting: Physics of Echo-Contrast Agents II
1pNSa	NOISE-CON and Noise: Plenary Session-Product Sound Quality—From Perception to Design
*1pNSb	NOISE-CON, Noise and Engineering Acoustics: Performance Assessment of Acoustical Test Rooms
*1pNSc	Noise and NOISE-CON: Noise Standards—Challenges to Quieter Products
1pNSd	NOISE-CON and Noise: Community Noise and Community-Noise Barriers
1pSA	Structural Acoustics and Vibration: Methods for Control of Vibration and Radiation
1pSC	Speech Communication: Learning and Cognitive Processing (Poster Session)
1pSP	Signal Processing in Acoustics: Signal Processing Techniques
1pUW	Underwater Acoustics: Scattering

Monday Evening, 4 December

*1eID	Tutorial Lecture on Virtual Musical Instruments

Tuesday Morning, 5 December

*2aAA	Architectural Acoustics and Engineering Acoustics: Loudspeaker Student Design Competition
*2aAO	Acoustical Oceanography: Bioacoustics III
*2aBB	Biomedical Ultrasound/Bioresponse to Vibration/ Physical Acoustics and Acoustical Oceanography: Detection and Characterization of Bubbles, Acoustic Cavitation, and Associated Physical Effects I
*2aEA	Engineering Acoustics: Ultrasonic Sensors and Motors
*2aNSa	Noise and NOISE-CON: Soundscapes
*2aNSb	Noise and NOISE-CON: Power Plant Noise Control and Prediction and Industrial Noise
*2aNSc	Noise, NOISE-CON and Architectural Acoustics: International Noise Standards
*2aSA	Structural Acoustics and Vibration: Signal Processing in Acoustics, and Physical Acoustics: Diagnostics of Vibration and Noise in Structures I
2aSC	Speech Communication: Articulation (Poster Session)
*2aUW	Underwater Acoustics and Acoustical Oceanography: High-Frequency Sediment Acoustics and Associated Sediment Properties and Processes I

Tuesday Afternoon, 5 December

2pAA	Architectural Acoustics: Building Renovation and Sound Scattering and Absorption
*2pABa	Animal Bioacoustics: Distinguished Lecture on Ultrasonic Eyeglasses for the Blind
*2pABb	Animal Bioacoustics and Noise: Standards and Animals: Where are We?
*2pBB	Biomedical Ultrasound/Bioresponse to Vibration, Physical Acoustics and Acoustical Oceanography: Detection and Characterization of Bubbles, Acoustic Cavitation, and Physical Effects II
2pEA	Engineering Acoustics: Acoustic Measurements and Materials Characterization
*2pED	Education in Acoustics: Informal Education in Acoustics
*2pNSa	Noise, NOISE-CON and Architectural Acoustics: Environmental Noise Focused on Combined Noise Sources
*2pNSb	Noise and NOISE-CON: Construction Machinery Noise Limits and Means of Compliance
2pNSc	Noise and NOISE-CON: Vehicle Noise and Vehicle Noise Tests
*2pNSd	Noise and NOISE-CON: Power Plant Acoustics Round Table
2pSA	Structural Acoustics and Vibration Signal Processing in Acoustics and Physical Acoustics: Diagnostics of Vibration and Noise in Structures II
2pSC	Speech Communication: Measuring and Modeling Speech and Voice (Poster Session)
*2pUW	Underwater Acoustics and Acoustical Oceanography: High-Frequency Sediment Acoustics and Associated Sediment Properties and Processes II

Wednesday Morning, 6 December

*3aAA	Architectural Acoustics: Integration of Synthesis Techniques and ''Acoustical'' Music

*3aABa	Animal Bioacoustics: Use of Acoustics for Wild Animal Surveys
3aABb	Animal Bioacoustics: General Topics in Bioacoustics
3aAO	Acoustical Oceanography: Special Topics
3aBB	Biomedical Ultrasound/Bioresponse to Vibration: Therapeutic and Diagnostic Ultrasound
*3aEA	Engineering Acoustics: International Comparison of Calibration and Measurements
*3aMU	Musical Acoustics: Asian Musical Instruments and Traditions I
3aPA	Physical Acoustics: Thermoacoustics I
3aSA	Structural Acoustics and Vibration: Vibrations of Structures
*3aSC	Speech Communication: Alvin M. Liberman and the Development of Scientists
3aSP	Signal Processing in Acoustics: Acoustical Imaging
3aUW	Underwater Acoustics: Modeling

Wednesday Afternoon, 6 December

*3pAA	Architectural Acoustics: Amphitheater Acoustic Design and Sound Control for Nearby Communities
*3pID	Interdisciplinary: Hot Topics in Acoustics
*3pMU	Musical Acoustics: Asian Musical Instruments and Traditions II
*3pNSa	Noise and Archives and History: Acoustical Society's Role in Noise Control
3pPA	Physical Acoustics: Thermoacoustics II
3pPP	Psychological and Physiological Acoustics: Potpourri (Poster Session)
3pSA	Structural Acoustics and Vibration: Acoustic Scattering from Elastic Structures
3pSC	Speech Communication: Signal Processing for Speech (Poster Session)
3pUW	Underwater Acoustics: Propagation

Thursday Morning, 7 December

*4aAA	Architectural Acoustics: Theme Park Acoustics
*4aAB	Animal Bioacoustics: Instrumentation for Animal Bioacoustics Monitoring and Measurements
*4aAO	Acoustical Oceanography: Acoustical Oceanography and Satellite Remote Sensing
4aEA	Engineering Acoustics: Acoustic Noise Characterization and Mitigation
*4aED	Education in Acoustics and Noise: Public Education in Noise
*4aMUa	Musical Acoustics: Model Analysis Techniques in Musical Acoustics
4aMUb	Musical Acoustics: General Topics in Musical Acoustics
4aPA	Physical Acoustics: Propagation and Mixed Physical Topics
4aPP	Psychological and Physiological Acoustics: Pitch, Loudness, and Localization
*4aSA	Structural Acoustics and Vibration: Acoustic Microsensors
4aSCa	Speech Communication: Auditory Function and Segmental Perception (Poster Session)
*4aSCb	Speech Communication and Archives and History: Speech Communication Within the Acoustical Society of America
4aUW	Underwater Acoustics and Signal Processing in Acoustics: Acoustic Time Reversal and Acoustic Communications

Thursday Afternoon, 7 December

*4pAAa	Architectural Acoustics: Technical Committee on Architectural Acoustics Vern O. Knudsen Distinguished Lecture
*4pAAb	Architectural Acoustics: Building Acoustics Test Standards
*4pAB	Animal Bioacoustics: William Cummings Session on the Acoustics of Whales and Dolphins I
*4pAO	Acoustical Oceanography: Acoustic Measurements of Sediment Transport
*4pMUa	Musical Acoustics: Historical Brasses and Related Instruments
*4pMUb	Musical Acoustics: Concert Performance by the Americus Brass Band
*4pNSa	Noise: Hearing Protection Standards
*4pPA	Physical Acoustics, Noise, S2, Signal Processing in Acoustics and Structural Acoustics and Vibration: Novel Optical Techniques for Measuring Surface Vibration
4pSA	Structural Acoustics and Vibration: Sound/Structure Interaction
*4pSC	Speech Communication: Kenneth Stevens' Contributions to Speech Research: Influences and Future Directions
*4pSP	Signal Processing in Acoustics, Underwater Acoustics, Speech Communication: Blind Deconvolution and Source Separation in Acoustics

Friday Morning, 8 December

*5aAA	Architectural Acoustics: Speech Privacy and Speech Intelligibility in the Built Environment
*5aAB	Animal Bioacoustics: William Cummings Session on the Acoustics of Whales and Dolphins II
5aEA	Engineering Acoustics: Special Purpose Acoustic Sources
5aPA	Physical Acoustics: Scattering—Periodic and Aperiodic
5aPP	Psychological and Physiological Acoustics: Complex Sounds: Physiology to Application
*5aSC	Speech Communication: Functional Neuroanatomy and Neurophysiology of Spoken Word Recognition and Speech Perception
5aUW	Underwater Acoustics: Matched Field Processing and Beamforming

Friday Afternoon, 8 December

5pAA	Architectural Acoustics: Measures of Auditorium Acoustics
5pPA	Physical Acoustics: Outdoor Sound, Mostly
5pSC	Speech Communication: Second Language Learning and Use (Poster Session)

BOOK REVIEWS

P. L. Marston
Physics Department, Washington State University, Pullman, Washington 99164

These reviews of books and other forms of information express the opinions of the individual reviewers and are not necessarily endorsed by the Editorial Board of this Journal.

Editorial Policy: *If there is a negative review, the author of the book will be given a chance to respond to the review in this section of the Journal and the reviewer will be allowed to respond to the author's comments. [See ''Book Reviews Editor's Note,'' J. Acoust. Soc. Am.* ***81****, 1651 (May 1987).]*

Fourier Acoustics: Sound Radiation and Nearfield Acoustical Holography

Earl G. Williams

Academic Press, London, 1999.
xi+306 pp. Price: $79.95 (hardcover), ISBN: 0-12-753960-3.

Dr. Earl Williams has made exceptional contributions to structural acoustics during his career. This book represents many of these accomplishments. Most importantly, this book provides an excellent self-contained reference for nearfield acoustical holography (NAH) and related wave number processing techniques. In addition to clear explanations of physical phenomena, Dr. Williams provides superb descriptions of the details needed to implement the processing on a computer. Figures are used expertly to make important points that are often hard to visualize with words alone.

The book does require a good background in acoustics and structural vibrations to understand all that is in it. However, as I am finding out with a new graduate student, it does provide good explanations on how to implement the NAH processing so that the student can develop the physical understanding while working with data.

I would recommend it very highly as a reference book for people using NAH in their work and as a text in a course on measurement techniques such as NAH. This could also serve as a supplemental book to a course on structural acoustics. The author provides problems at the end of each chapter.

The book begins with a review of Fourier transforms and special functions that will be used in the following chapters. The review includes a brief comparison of continuous and discrete Fourier transforms. The reference list is short, but the chapter is complete enough to provide the basic information.

Chapter 2 is a key chapter of the book and is packed with a wealth of information, showing how the plane wave can be used to study sound radiation from planar structures. The chapter begins with a basic discussion of wavenumbers, making a distinction between the wavenumber of a freely propagating plane wave and the wavenumbers in the wavenumber spectrum. The definitions of sound intensity are also presented along with a discussion of evanescent waves. Dr. Williams then presents a plane wave expansion as a means to introduce the wavenumber processing. This can help the reader understand the wavenumber spectrum, calculated from a spatial Fourier transform, in terms of a physically understandable plane wave. Finally, the expansion is applied to understanding the sound radiation from planar radiators as Rayleigh's integral is implemented with the Fourier transform. There is a good discussion of supersonic intensity. Sound radiation from baffled pistons and arrays is discussed along with edge and corner mode radiation from vibrating plates. This chapter is well done and provides a good basis to physically understand the wavenumber spectrum. A person could spend a long time working through this chapter alone.

Chapters 4 and 6 present similar material, but for cylindrical and spherical coordinates. While each is less extensive than Chap. 2, they provide excellent information on the wave functions in each coordinate. Both the interior and exterior problems are discussed. The characteristics of the sound radiation from cylindrical and spherical objects are emphasized in each respective chapter.

Chapters 3, 5, and 7 present the inverse problem in planar, cylindrical, and spherical coordinates: nearfield acoustical holography. Chapter 3 clearly describes the signal processing steps for NAH. Not only are the steps such as windowing, zeropadding, and filtering discussed, specific methods to implement each is given. The discussion of noise and filtering is especially well done. This chapter presents material that is not completely contained in the archival literature. Chapter 3 can be used as a manual for writing or understanding a NAH program.

Chapter 5 presents NAH in cylindrical coordinates. Several case studies that have been published in archival journals are presented. Chapter 7 presents NAH for spherical coordinates. While there are no examples given as in previous chapters, there is a brief discussion of the interior problem.

In the final chapter, Chap. 8, Green's functions and the Helmholtz integral are discussed for the purposes of presenting conformal NAH. This allows NAH to be extended to arbitrary geometries. While the discussion is good, no data is presented that effectively demonstrates applications. This leads to one common criticism of NAH and the Fourier transform techniques for structural radiation, that they can only be applied to nearly planar, cylindrical, or spherical shapes. This severely limits the applicability of this material to areas such as noise control where complex shapes are the norm.

This book is a valuable resource for anyone working in the area of NAH and structural acoustics. It is especially helpful to have a clear reference on NAH that combines all the material in archival journal articles into one place. Dr. Williams should be commended for clearly communicating his exceptional contributions and understanding of NAH and structural acoustics.

J. ADIN MANN III
[S0001-4966(00)01910-X]
Iowa State University
2271 Howe Hall
Ames, Iowa 50011

The Acoustics of Speech Communication: Fundamentals, Speech Perception Theory, and Technology

J. M. Pickett

Allyn and Bacon, Boston, Massachusetts, 1999.
404 pp. Price: $64.00 (hardcover), ISBN: 0-205-19887-2.

J. M. Pickett successfully accomplished the basic aim of his book, ''to teach the technical acoustics of speech and its perception to the nontechnical student.'' His 1999 text is divided into two sections and is an updated, enhanced, and well-expanded version of his 1980 text. The first ten chapters are written by Pickett and provide a general description of the acoustics of speech, speech analysis, and English speech sound distinctions. Chapters 11–16 deal with speech perception and include chapters by Winifred Strange, Sarah Hawkins, and Sally Revoile. Chapter 17 reviews speech technology.

Pickett begins Chap. 1 by describing the difference between a phoneme and an allophone and the importance of the syllable. He provides a cursory review of anatomy to aid in the understanding of the sound source and radiation characteristics. In ten chapters, he successfully moves the reader from the phonetic segment to conversational speech. Chapter titles are

 0001-4966/2000/108(4)/1373/2/$17.00

Language, Phonetics, and Speech Production
Sounds, Resonance, and Spectrum Analysis
Vowel Shaping and Vowel Formants
The Glottal Sound Source and the Spectra of Vowels
Prosodic and Tonal Features
Consonant Features, Glides, and Stops
Consonants: Nasal, Stop, and Fricative Manners of Articulation
Consonants: Features of Place of Articulation
The Flow of Speech

Chapter 10 does a very nice job tying everything together for the reader and presents the big picture of speech production. Pickett emphasizes the need to attend to conversational speech and not get lost in the segment. He shares his hope that future analyses will be able to use the movement flow instead of the segment as the fundamental starting point. Throughout the text, Pickett provides nice examples that keep the reader interested and allow the beginning student to grasp difficult concepts. Common scenarios that relate to specific physiological functions are frequently included. For example, the glottal source sound is compared to a New Year's noisemaker. When a vocal track or horn is added to the sound source, the resultant sound is altered. An additional helpful aspect of the text for the beginning student is the inclusion of specific rules. For example, to help understand the many variables related to formant changes, Pickett provides length and constriction rules and discusses why they affect specific formants. Moreover, the selection of diagrams and figures included in the text is excellent and greatly aids understanding.

An advantage of the text is the cross-linguistic, disordered, and developmental information interspersed throughout the book. Phonology note boxes in each chapter describe how the phonological patterns of different languages fit into the acoustic information just presented. These will be very useful to the instructor who is trying to facilitate student understanding of the differences between English phonemes and phones as well as cross-linguistic differences. Further, the inclusion of disordered speech examples makes this text an excellent choice for beginning speech-language pathology students. After reading the first section of the text and studying the helpful figures, one should have a stable understanding of the acoustic elements of English phonemes and comprehend important differences between specific manners and places of articulation.

Part two of the text discusses the perception of speech. Winifred Strange walks the reader through the perception of vowels and consonants in Chaps. 11 (Perception of Vowels) and 12 (Perception of Consonants). The acoustic differences between place of articulation and voicing and the resulting perceptual properties are carefully discussed. Categorical and continuous perception of speech and nonspeech acoustic signals are thoroughly explained. Further, the complexities in the perceptual processes that enable the listener to understand the phonetic message even when the acoustic patterns vary as speech speeds up and slows down is discussed. In Chap. 13 (Auditory Capacities and Phonological Development: Animal, Baby, and Foreign Listener), Sarah Hawkins presents information on general auditory capabilities, phonological development, and infant and animal perception. Specific speech perception research methodologies are described and selected results are presented. Hawkins carefully describes and evaluates the two classical speech perception theories: Lieberman's motor theory and Steven's quantal theory in Chap. 14 (Looking for Invariant Correlates of Linguistic Units: Two Classical Theories of Speech Perception). More recent theories such as direct realist theory of speech perception (Fowler, 1986), articulatory phonology (Browman and Goldstein, 1992), and Diehl and colleagues' auditory enhancement theory are presented in Chap. 15 (Reevaluating Assumptions about Speech Perception). In this chapter the strengths and weaknesses of each theory are defined and compared. Moreover, Hawkins provides an overview of models of developmental perception and a complete evaluation of the assumptions of speech perception and the presented theories.

Sally Revoile leads the reader through a hearing evaluation of an individual with a hearing loss in Chap. 16 (Hearing Loss and the Audibility of Phoneme Cues). She explains which acoustic characteristics present the greatest problems for a hypothetical individual with a hearing loss and helps the reader understand why specific sounds are problematic. Figures visually help the reader understand the acoustic properties that are audible to individuals with normal hearing and individuals with different levels of hearing loss.

The final chapter of the book, Speech Technology, discusses speech technology and includes segments by Pickett, Juergen Schroeter, Corine Bickley, Ann Syrdal, and Diane Kewley-Port. The reader is given a brief history of speech synthesis and speech recognition. Common problems and newer systems are described and evaluated. Additionally, clinical applications of synthesized speech are discussed.

A major benefit to the text is found in the appendices. Appendix A discusses the need to incorporate laboratory exercises into any course of speech and hearing science. Several acoustic software packages are named and references for more complete reviews are included. Pickett has developed a lab to go with each of the chapters in the text. He notes that the labs are not completely self-explanatory and students will need the guidance of their instructor. Notes to the instructor are included and should help avoid common trouble areas. Appendix B provides book reviews that will be of interest to phoneticians, linguistics, and speech-language pathologists.

Pickett's text is easy to read, enjoyable, and an excellent choice for the nontechnical student. This reviewer highly recommends this text for introductory speech and hearing science courses.

SHERRILL R. MORRIS
[S0001-4966(00)02010-5]
Department of Communication Sciences and Disorders
Rockhurst University
Kansas City, Missouri 64110-2561

REVIEWS OF ACOUSTICAL PATENTS

Lloyd Rice
11222 Flatiron Drive, Lafayette, Colorado 80026

The purpose of these acoustical patent reviews is to provide enough information for a Journal reader to decide whether to seek more information from the patent itself. Any opinions expressed here are those of reviewers as individuals and are not legal opinions. Printed copies of United States Patents may be ordered at $3.00 each from the Commissioner of Patents and Trademarks, Washington, DC 20231. [S0001-4966(00)05610-1]

Reviewers for this issue:

GEORGE L. AUGSPURGER, *Perception, Incorporated, Box 39536, Los Angeles, California 90039*
DAVID PREVES, *Songbird Medical, Inc., 5 Cedar Brook Drive, Cranbury, New Jersey 08512*
KEVIN P. SHEPHERD, *M.S., 463, NASA Langley Research Center, Hampton, Virginia 23681*
ERIC E. UNGAR, *Acentech, Incorporated, 33 Moulton Street, Cambridge, Massachusetts 02138*

5,986,224

43.35.Yb ACOUSTIC CONDITION SENSOR EMPLOYING A PLURALITY OF MUTUALLY NON-ORTHOGONAL WAVES

Joel Kent, assignor to Elo TouchSystems, Incorporated
16 November 1999 (Class 178/18.04); filed 19 April 1995

Some touchscreen systems generate acoustic surface waves and then detect disturbances in their transmission. The patent describes an improved version of this general method, using at least two distinct sets of waves which overlap temporally or physically. More than 30 illustrations clarify the concept. The text is well written and includes a thorough survey of the art of touchscreen design.—GLA

5,857,027

43.38.Ja LOUDSPEAKER

Alexandr Sergeevich Gaidarov and Alxei Vladimir Vinogradov, both of Moscow, Russian Federation
5 January 1999 (Class 381/182); filed in Russian Federation 6 August 1993

Two mid-range speakers face each other in a vertical array. Counter-radiating high-frequency transducers are located between them. This geometry attempts to ''reconstruct'' the main reverberation component by bouncing sound energy off the floor and ceiling, thus providing a feeling of presence while minimizing Doppler distortion.—GLA

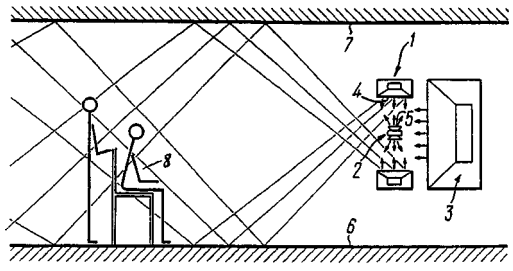

5,963,640

43.38.Ja RADIOTELEPHONE HAVING AN ACOUSTICAL WAVE GUIDE COUPLED TO A SPEAKER

Karl W. Rabe, assignor to Ericsson, Incorporated
5 October 1999 (Class 379/433); filed 7 November 1996

When using a standard telephone handset, the receiver is normally in contact with, or very close to, the user's ear. Flip-top portable telephones employ the same geometry. The inventor argues that the response of miniaturized transducers used for this application typically roll off at about 12 dB/oct below 1 kHz. This can be acoustically equalized by conducting

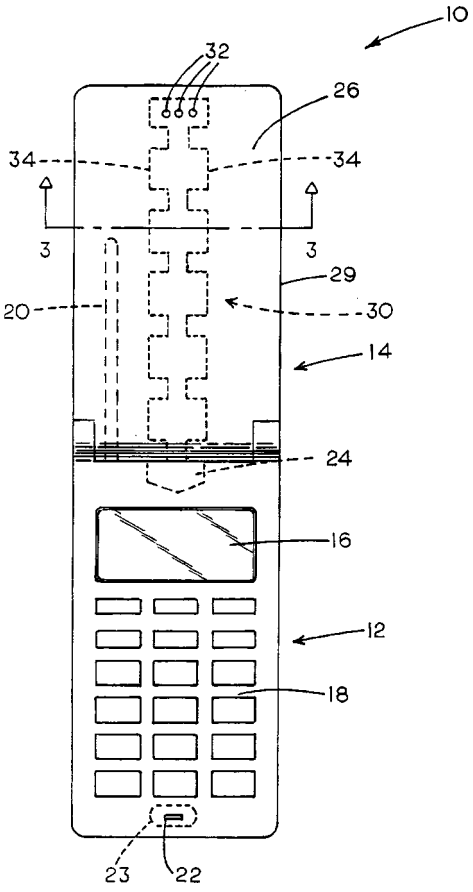

 0001-4966/2000/108(4)/1375/10/$17.00

sound from transducer **24** through an elongated waveguide **30** having a varying cross-sectional area. Presumably this arrangement allows greater freedom in product design than simply equalizing the amplifier that drives the receiver.—GLA

6,014,448

43.38.Ja FLUID COUPLED SUBWOOFER ACOUSTIC ENCLOSURE SYSTEM

Noyal J. Alton, Jr., assignor to Sound Related Technologies
11 January 2000 (Class 381/351); filed 5 November 1997

At one time or another, consumers have used water-filled radiators, hot water bottles, water skis, and water beds. At long last comes the announcement of a water-coupled loudspeaker. Twin woofers **150** are located in vented cavity **20**. Side walls **70** are flexible and may be segmented. Compression chambers **135** couple sound pressure to flexible support walls **130**

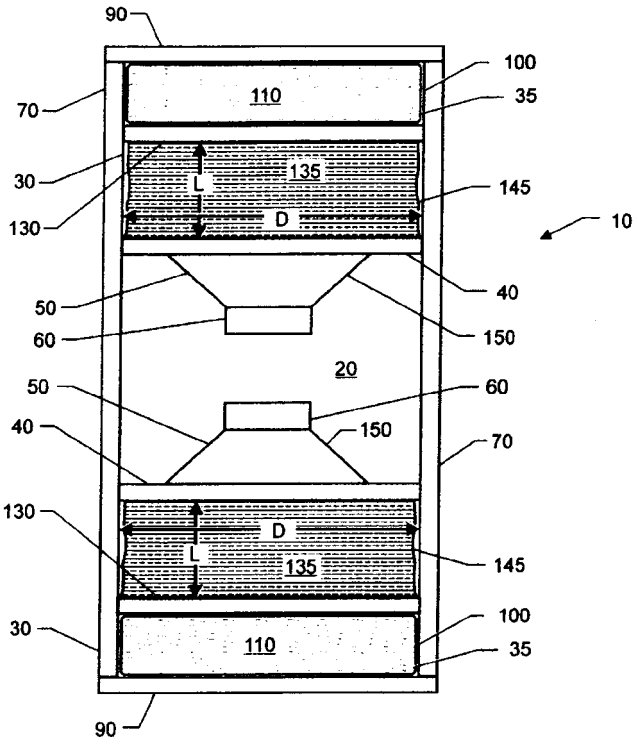

and then to bladders **100** filled with fluid **110**. For reasons not explained in the patent document, this arrangement is said to efficiently reproduce, ''...the vibrating sensations felt by audio signals below 20 Hz that are typically present during a live performance....''—GLA

6,014,239

43.38.Kb OPTICAL MICROPHONE

James T. Veligdan, assignor to Brookhaven Science Associates
11 January 2000 (Class 359/172); filed 12 December 1997

More than 50 years ago Philco marketed a ''beam of light'' phonograph pickup. The stylus wiggled a small mirror which deflected a beam of light across the aperture of a photocell. This diaphragmless microphone is considerably more sophisticated. It employs a laser and beamsplitter in an arrangement that measures changes in the local refractive index resulting from the passage of sound waves. In comparison with conventional microphones, advantages cited include greater sensitivity, unlimited bandwidth, and attenuation of popping ''P'' sounds.—GLA

5,933,769

43.38.Si PORTABLE TELEPHONE CAPABLE OF DECREASING NOISE

Yasuhiro Kaneko, assignor to NEC Corporation
3 August 1999 (Class 455/296); filed in Japan 11 July 1996

One would expect a major international corporation such as NEC to insist on the best possible English translation when filing for a patent in the United States. The patent at hand is a curiousity, a throwback to the time when brochures and owner's manuals were written in Pidgin English. The invention embodies improved noise suppression circuitry for use in portable telephones. Two switchable low-pass filters are selected in relation to rf field intensity by making use of a logic table.—GLA

6,009,178

43.38.Si METHOD AND APPARATUS FOR CROSSTALK CANCELLATION

Jonathan S. Abel and Stacy Lynn Welsh, assignors to Aureal Semiconductor, Incorporated
28 December 1999 (Class 381/1); filed 16 September 1996

A number of earlier schemes have been devised to allow accurate perception of binaural recordings when reproduced from loudspeakers rather than headphones. The patent describes circuitry which provides reasonably good reproduction even when the listener is not at the ideal location, or if the head-related transfer function of the listener does not correspond well with the function used to design the system.—GLA

6,010,216

43.38.Si ''HEAR SPEAK'' TWO-WAY VOICE RADIO COMMUNICATIONS EYEGLASSES

Daniel Stephen Jesiek, Flint, Michigan
4 January 2000 (Class 351/158); filed 19 January 1993

The invention is similar to a binaural, eyeglass-frame hearing aid except that it is really a hands-free walkie-talkie. At least one of the earbuds also serves as a microphone, picking up voice signals traveling up the Eustachian tube.—GLA

5,771,294

43.38.Vk ACOUSTIC IMAGE LOCALIZATION APPARATUS FOR DISTRIBUTING TONE COLOR GROUPS THROUGHOUT SOUND FIELD

Toshihiro Inoue and Hiroyuki Torimura, assignors to Yamaha Corporation
23 June 1998 (Class 381/17); filed in Japan 24 September 1993

In recent years, a great amount of effort has been dedicated to producing stable, well-localized, phantom sound sources at locations beyond the spacing of stereo loudspeakers. In most cases, this work has been targeted at computer games or reproducing surround sound channels without surround sound loudspeakers. However, numerous other applications come to mind. For example, an electronic keyboard instrument might have controls to set locations of individual voices. The patent describes a sophisticated method of doing just that. It is clearly written and should be of interest to anyone involved with electronic music.—GLA

5,953,067

43.38.Vk MULTICHANNEL TELEVISION SOUND STEREO AND SURROUND SOUND ENCODER

Sealtiel Avalos *et al.*, assignors to Cable Electronics, Incorporated
14 September 1999 (Class 348/485); filed 25 August 1997

The surround sound that is (occasionally) heard from present-day TV receivers is transmitted as part of the amplitude-modulated L-R stereo signal. According to the patent, most modulators have excessive rolloff at high frequencies, which effectively filters out some or all of the surround sound information. The patent describes a method of using preemphasis companding, and synchronizing circuitry to transmit stereo and surround sound in accordance with multichannel television sound protocol.—GLA

6,032,552

43.40.Tm VIBRATION CONTROL BY CONFINEMENT OF VIBRATION ENERGY

Daryoush Alleai, assignor to Quality Research Development & Consulting, Incorporated
7 March 2000 (Class 74/574); filed 7 August 1995

This patent addresses the confinement of vibration to one or more specified areas of a mechanical structure, in order to reduce the vibrations that reach other areas. This confinement is achieved by means of devices that do not permit vibrations to be transmitted past them. These devices effectively apply translational and torsional forces, and they may be active or passive. The patent reviews the underlying theory and illustrates numerous embodiments, largely applicable to beams, in which flexural wave propagation can be inhibited by preventing rotations and lateral translations.—EEU

6,035,980

43.40.Tm MAGNETIC SPRING HAVING DAMPING CHARACTERISTICS AND VIBRATION MECHANISM HAVING SAME

Etsunori Fujita *et al.*, assignors to Delta Tooling Company, Limited
14 March 2000 (Class 188/267); filed in Japan 8 April 1996

This patent basically relates to suspension seats as may be used in off-road vehicles, trucks, etc., for the purpose of isolating the seats' occupants from vibrations. It describes a series of configurations that employ opposing magnets and mechanical linkages to obtain nonlinear spring characteristics of various types. It presents some related theoretical analyses and the results of corresponding calculations, as well as some experimental data.—EEU

6,026,690

43.40.Yq VIBRATION SENSOR USING THE CAPACITANCE BETWEEN A SUBSTRATE AND A FLEXIBLE DIAPHRAGM

Yoshimori Nakagawa and Jun Kishigami, assignors to Sony Corporation
22 February 2000 (Class 73/654); filed in Japan 20 June 1944

The major components of this vibration sensor, which is intended for use in navigation systems for motor vehicles, are a backing plate with an electret film and a diaphragm. As in an electret microphone, the diaphragm is located near the electret film and displacement of the diaphragm relative to the backing plate is sensed via changes in the electrostatic capacity. In order to make the vibration sensor less responsive to airborne sound, a series of holes is provided in the diaphragm near its circumference, leaving only thin radial strips to support the diaphragm.—EEU

6,033,756

43.50.Gf APPARATUS FOR AND METHOD OF ATTENUATING ACOUSTIC ENERGY

Paul Handscomb, assignor to Pritex Limited
7 March 2000 (Class 428/138); filed in the United Kingdom 4 December 1996

The sound-absorbing surface arrangement described in this patent is intended for use in headliners of cars, for architectural applications, or the like. It consists of three layers, the middle one of which is of closed cell foam and has a series of holes through it. A layer of open-cell foam or of fibrous material is located between the aforementioned one and an essentially impermeable surface, such as the roof of a car or the wall of a room. The holes in the closed-cell foam layer and the air space in which the open-cell layer is located constitute an array of Helmholtz resonators; the open-cell material serves to broaden and reduce their absorption spectrum peaks. Another open-cell layer is placed atop the entire assembly for the purpose of increasing the high-frequency absorption.—EEU

6,035,965

43.50.Gf SOUND ABSORBING BODY, SOUND ABSORBING BOARD, AND SOUND ABSORBING UNIT

Kyoji Fujiwara *et al.*, assignors to Nitto Boseki Company, Limited
14 March 2000 (Class 181/293); filed in Japan 11 October 1994

This patent relates to sound absorption for ceilings and walls in buildings, tunnel walls, and outdoor installations. The primary element consists of a board of fibrous material with a larger number of through-holes, which may be placed against a rigid surface either directly or with some standoff. A major concern addressed by this patent is improvement of the visual appearance of this board, largely to avoid ''flicker.'' This improvement is achieved by various configurations in which the openings of the holes on the side that can be seen are widened, deepened, and partially covered with visually attractive elements. These elements, which may be in the form of strips or disks, etc., are configured so that they do not obstruct sound transmission into the holes significantly.—EEU

6,024,189

43.50.Gf NOISE ATTENUATING APPARATUS

Stephen G. Heuser, Lawrence, Michigan
15 February 2000 (Class 181/264); filed 20 August 1997

An engine muffler is described in which exhaust gases enter at **14**. A diverter **19** serves to direct the flow along the outside of the inner cone assembly **18**. ''Sound waves are repeatedly reflected against the inner cone

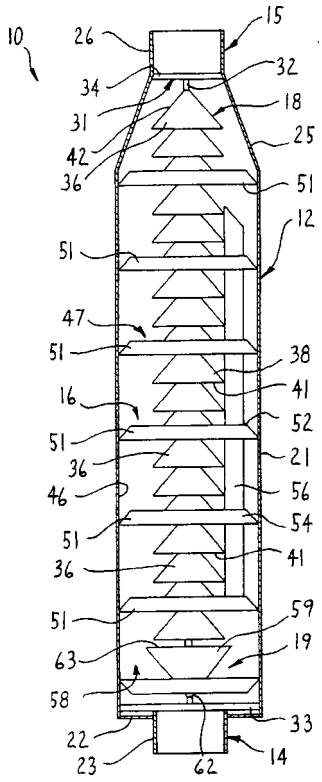

assembly **18**'' and ''destructively interfere with one another such that sound levels are reduced.''—KPS

6,024,617

43.50.Gf MARINE ENGINE SILENCING APPARATUS AND METHOD

Joseph I. Smullin and Matthew E. Denis, assignors to Smullin Corporation

15 February 2000 (Class 440/89); filed 6 August 1997

A marine engine muffler has inlet **22** into which enter a mixture of cooling water and engine exhaust gases. A means is provided to separate the gases from the water. Water is kept in the separation chamber, thus cooling

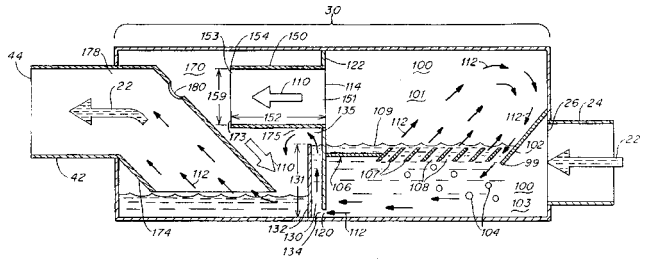

the gases, for operation at low engine speeds. The water level is designed to drop at higher speeds in order to minimize back pressure on the engine. Several alternative designs for the separation chamber are described.—KPS

6,036,212

43.50.Gf DAMPING SYSTEM HAVING SEPARATELY ADJUSTABLE DAMPING CIRCUITS

Ricardo R. Baldomero, assignor to Rockshox, Incorporated

14 March 2000 (Class 280/276); filed 17 March 1998

A shock absorber intended for use on bicycles is described which allows independent adjustment of compression and rebound damping. Fluid flow is restricted within two circuits using a single adjustment rod.—KPS

6,012,426

43.50.Lj AUTOMATED PSYCHOACOUSTIC BASED METHOD FOR DETECTING BORDERLINE SPARK KNOCK

Michael Alan Blommer, assignor to Ford Global Technologies, Incorporated

11 January 2000 (Class 123/406.38); filed 2 November 1998

Spark knock (''pinging'') in an internal combustion engine is detected using the signal from a microphone placed in the vicinity of the engine. In particular, this patent aims to determine a degree of knocking which is just below a human observer's ability to detect it. The method uses signal processing to represent the human auditory system and consists of one-third-octave band filters centered from 4 to 10 kHz and a temporal masking model to characterize the impulsive nature of the sound. The number of detectable spark knocks per unit time is thus used to determine the optimum spark timing.—KPS

6,014,899

43.50.Lj METHOD AND APPARATUS FOR MEASURING VIBRATION DAMPING OF BRAKE PARTS

Robert P. Uhlig and Cheryl A. Fry, assignors to Chrysler Corporation

18 January 2000 (Class 73/664); filed 16 September 1997

A brake rotor **12** is driven by an exciter coil **52** at its resonance frequency and the resultant vibration is detected by a microphone **54**. Damping of the rotor is determined from examination of the decay of the microphone signal when the signal to the exciter coil is terminated. The rotor is rotated to several positions and at each of these positions the resonance frequency is

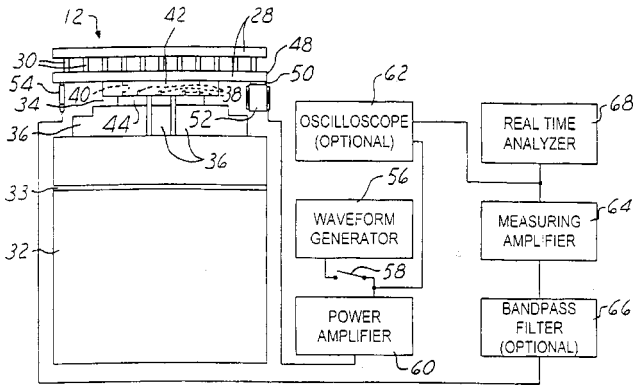

determined and a decay measurement is made. The resultant Q-factors are found to vary periodically around the circumference. This phenomena is explained by the presence of twin bending modes of the rotor. A sinusoidal curve-fit to the Q-factor data enables a more reliable estimate of damping to be made.—KPS

6,021,364

43.50.Lj ACOUSTIC HIGHWAY MONITOR

Edward Fredrick Berliner *et al.*, assignors to Lucent Technologies, Incorporated
1 February 2000 (Class 701/1); filed 28 May 1993

A method to acoustically monitor highway traffic is described in which a microphone array **111** is used to detect the presence of a vehicle in the zone **107**. In contrast to an inductive loop method, this approach does not

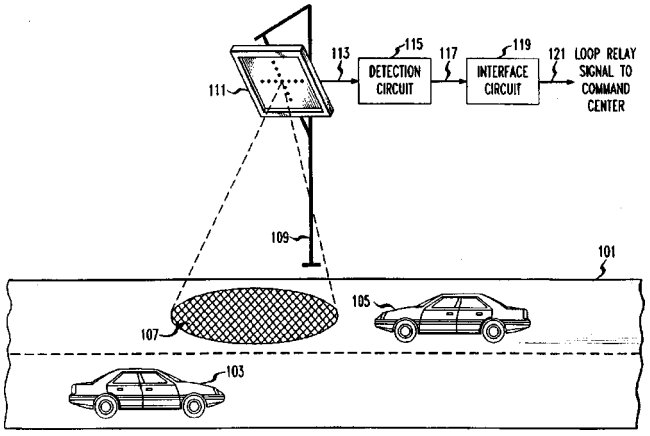

require that the roadway be dug up and will be effective for vehicles having high nonmetallic content.—KPS

6,026,338

43.50.Lj SYSTEM TO CONTROL A CHASSIS VIBRATION DAMPING DEVICE

Udo Borschert and Thomas Kutsche, assignors to Fichtel & Sachs AG
15 February 2000 (Class 701/37); filed in Germany 25 October 1995

A method is described which produces control signals for use in an adaptive or active vehicle suspension system. The required control signals are acceleration in three orthogonal directions (axes). A single accelerometer is oriented in a direction that is inclined to all three axes. This accelerometer signal, in combination with one other signal from either the speedometer, steering wheel, brake, or gas pedal, is filtered and somehow decomposed to yield acceleration values for all three axes.—KPS

6,026,776

43.50.Lj INTERNAL CRANKSHAFT VIBRATION DAMPER

Randy S. Winberg, Denver, Colorado
22 February 2000 (Class 123/192.1); filed 26 June 1997

A method to provide vibration damping of an engine crankshaft is described in which damping elements are mounted within the counterbalance weights adjacent to the connecting rod journal bearings. This approach is contrasted with conventional treatment applied at one end of the crankshaft.—KPS

6,023,513

43.66.Ts SYSTEM AND METHOD FOR IMPROVING CLARITY OF LOW BANDWIDTH AUDIO SYSTEMS

Eliot M. Case, assignor to U S West, Incorporated; MediaOne Group, Incorporated
8 February 2000 (Class 381/61); filed 11 January 1996

A method is described that is said to enhance the sound clarity of voice transmission in restricted bandwidth audio systems. Enhancement is provided by adding in even harmonic distortion at any point in the signal transmission path. The even harmonics are added into a frequency range

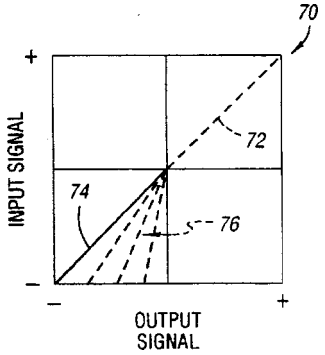

within the limited bandwidth of the system. Distortion is created deliberately by providing different amounts of gain to the positive and negative half-cycles of the voice signals.—DAP

6,031,923

43.66.Ts ELECTRONMAGNETICALLY SHIELDED HEARING AIDS

Louis Thomas Gnecco, Herdon, Virginia and Paula Sharyn Gnecco, Herdon, Virginia
29 February 2000 (Class 381/322); filed 13 November 1995

Several methods are described for shielding hearing aids against external electromagnetic interference. These include use of electrically conductive foil and conductive gaskets to shield the hearing aid case, making the hearing aid housing out of metal-impregnated plastic, and adding series inductors and/or ferrite beads and/or parallel capacitors to the circuitry.—DAP

6,035,050

43.66.Ts PROGRAMMABLE HEARING AID SYSTEM AND METHOD FOR DETERMINING OPTIMUM PARAMETER SETS IN A HEARING AID

Oliver Weinfurtner and Inga Holube, assignors to Siemens Audiologische Technik GmbH
7 March 2000 (Class 381/313); filed in European Patent Office 21 June 1996

Determining the optimum electroacoustic performance characteristics for hearing aid wearers for different listening situations is a difficult task that is normally performed by the hearing aid fitter. This patent describes a method and apparatus for having hearing aid wearers, rather than hearing aid fitters, determine indirectly the set(s) of programmable parameters that control the electroacoustic performance of their hearing aids. This determination is made automatically in a training session in which the wearer selects from a number of different parameter sets, stored in a first memory bank, to produce different electroacoustic performances for different listening situations. The software in the hearing aid keeps track in a second

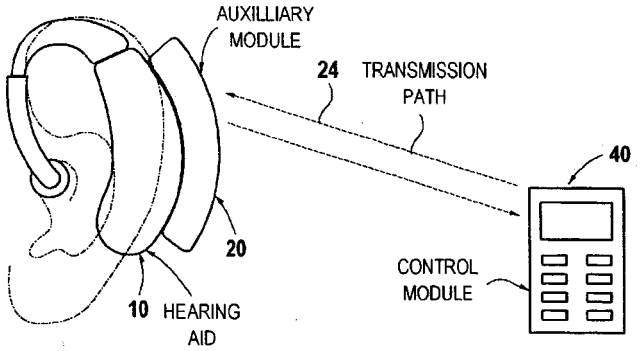

memory of the number of times the hearing aid wearer makes an allocation of a particular parameter set for a specific listening situation. The final programmable parameters selected are based on which parameter sets were used most frequently by the hearing aid wearer during the training phase. The programmed parameter set used for a particular listening situation is selected either by the user manually or by the hearing aid automatically using a neural net structure which learns over time when a particular listening situation is present. To facilitate the selection and storage of parameter sets, external control and mobile auxiliary modules are described which are coupled via hard wire or wireless connection.—DAP

6,049,617

43.66.Ts METHOD AND CIRCUIT FOR GAIN CONTROL IN DIGITAL HEARING AIDS

Ullrich Sigwanz and Fred Zoels, assignors to Siemens Audiologische Technik GmbH
11 April 2000 (Class 381/312); filed in European Patent Office 23 October 1996

The algorithm described is intended to reduce the harmonic distortion in digital hearing aids that is produced by smoothing the rectified sampled values of the signal during simulation of the charging and discharging of an AGC capacitor in an analog hearing aid. Large jumps in the amplified sampled values that cause harmonic distortion are minimized by smoothing relative to a mean gain value after, rather than before, applying stored gain values to determine the amount of amplification. The smoothed gain values are combined with the sampled values and then are converted back to analog form.—DAP

6,049,618

43.66.Ts HEARING AID HAVING INPUT AGC AND OUTPUT AGC

Oleg Saltykov, assignor to Siemens Hearing Instruments, Incorporated
11 April 2000 (Class 381/321); filed 30 June 1997

This patent describes a hearing circuit that saves components by providing both input AGC and output AGC using a single variable gain amplifier. Input and output signal levels are detected with separate rectifiers

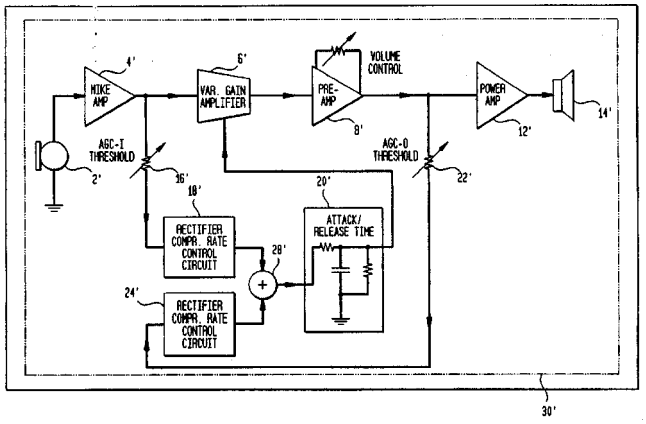

whose outputs are summed to drive a single attack/release time constant network. The variable gain amplifier is located in the circuit prior to the volume control.—DAP

6,019,607

43.70.Dn METHOD AND APPARATUS FOR TRAINING OF SENSORY AND PERCEPTUAL SYSTEMS IN LLI SYSTEMS

William M. Jenkins, Pacifica, California *et al.*
1 February 2000 (Class 434/116); filed 17 December 1997

The system described here is designed for a population having certain auditory deficiencies referred to as language learning impairment. The description of the target population includes children with certain hearing defects, stroke victims, and second language learners. The figure purportedly shows a difference in ''phoneme recognition'' by normal and impaired lis-

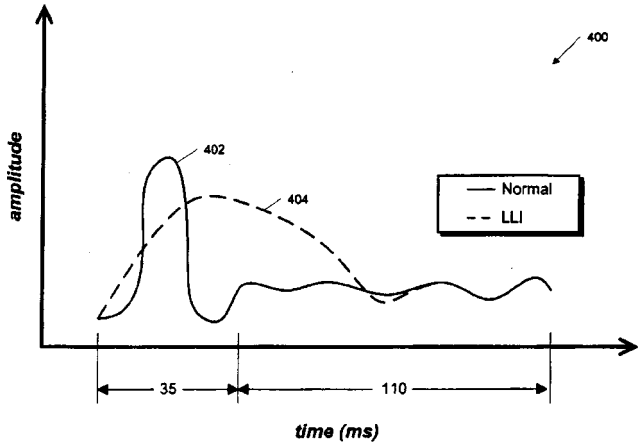

teners. The device provides repeated playback with variable time scales and testing of the perceived sounds. The playback stimuli include speech sounds, frequency sweeps, and other sounds with rapidly changing components.—DLR

6,006,187

43.72.Ar COMPUTER PROSODY USER INTERFACE

Michael Abraham Tanenblatt, assignor to Lucent Technologies, Incorporated
21 December 1999 (Class 704/260); filed 1 October 1996

This patent describes a computer interface used for manually entering prosodic parameters into a speech synthesis control data file. It is, in other words, a prosody editor. Both duration effects and syllable or word promi-

nence can be modified. Current parameter values are displayed in some sort of graphical presentation and the current speech data can be heard by means of a playback function.—DLR

6,006,188

43.72.Ar SPEECH SIGNAL PROCESSING FOR DETERMINING PSYCHOLOGICAL OR PHYSIOLOGICAL CHARACTERISTICS USING A KNOWLEDGE BASE

Rostislav Bogdashevsky *et al.*, assignors to Dendrite, Incorporated
21 December 1999 (Class 704/270); filed 19 March 1997

The patented device accepts a speech signal from a local or remote origin and analyzes that signal into the form of a parameter matrix of cepstral and delta cepstral coefficients. By collecting and storing such data from populations with known physiological or psychological conditions, the system may then be used to compare newly collected data with stored reference models representing selected classes or personality types. The system is said to be able to detect truth/falsity as well as a number of emotional states.—DLR

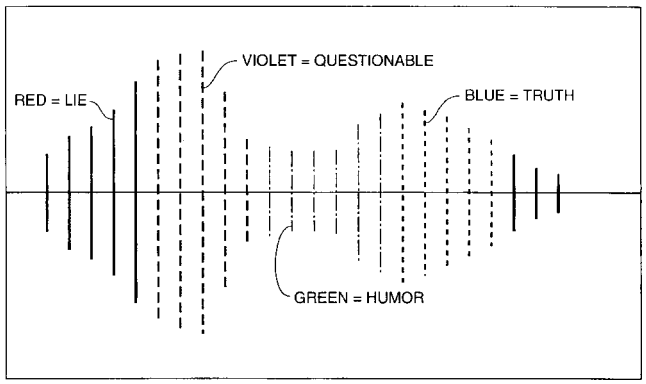

6,014,617

43.72.Ar METHOD AND APPARATUS FOR EXTRACTING A FUNDAMENTAL FREQUENCY BASED ON A LOGARITHMIC STABILITY INDEX

Hideki Kawahara, assignor to ATR Human Information Processing Research Laboratories
11 January 2000 (Class 704/207); filed in Japan 14 January 1997

This is a method for speech fundamental frequency analysis based on a comparison of the bands of a multi-channel filter bank analyzer. Each band of the filter bank has a gradual low-frequency skirt and a very sharp high-frequency cutoff. Amplitude and frequency modulation values are computed for each band, giving a signal stability index. Instantaneous frequency is computed for all bands, from which the fundamental is extracted.—DLR

6,018,706

43.72.Ar PITCH DETERMINER FOR A SPEECH ANALYZER

Jian-Cheng Huang *et al.*, assignors to Motorola, Incorporated
25 January 2000 (Class 704/207); filed 26 January 1995

As more and more computing power becomes available at a lower cost, the algorithms used become less and less clever. That is not necessarily bad, if it works. This vocoder pitch analyzer achieves a more accurate pitch estimate by running multiple analysis programs and then selects the most accurate estimate by resynthesizing the speech with each pitch method and comparing all outputs to the original speech signal.—DLR

6,023,671

43.72.Ar VOICED/UNVOICED DECISION USING A PLURALITY OF SIGMOID-TRANSFORMED PARAMETERS FOR SPEECH CODING

Kazuyuki Iijima *et al.*, assignors to Sony Corporation
8 February 2000 (Class 704/214); filed in Japan 15 April 1996

This voiced/unvoiced detector uses a weighted sum of speech frame parameters to reach the V/UV decision. The parameters include energy level, autocorrelation peak value, spectral similarity, zero crossings, and pitch lag. Each parameter is weighted by a sigmoid function with parameter-specific coefficients. This provides a diverse set of nonlinear weighting functions, some increasing, some decreasing, and some with higher weighted mid-range values.—DLR

6,023,674

43.72.Ar NON-PARAMETRIC VOICE ACTIVITY DETECTION

Fisseha Mekuria, assignor to Telefonaktiebolaget L M Ericsson
8 February 2000 (Class 704/233); filed 23 January 1998

This voice activity detector uses a combination of a nonlinear sample amplitude function and a periodicity measure to make a voice-presence decision. The amplitude function is a soft threshold, which ignores samples less than a minimum amplitude. The periodicity detector is a type of peak detector whose parameters change as a function of the signal-to-noise ratio. The figure shows a decision boundary in the two-parameter space.—DLR

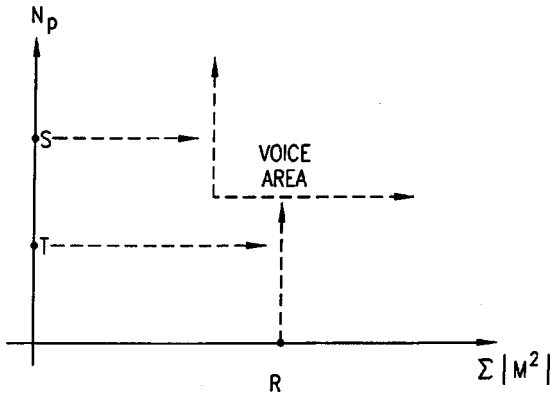

6,021,387

43.72.Bs SPEECH RECOGNITION APPARATUS FOR CONSUMER ELECTRONIC APPLICATIONS

Forrest S. Mozer *et al.*, assignors to Sensory Circuits, Incorporated
1 February 2000 (Class 704/232); filed 21 October 1994

This low-cost, small-vocabulary speech recognizer uses a five-band filter bank and a neural network to recognize the digits zero through nine. Filter bank coefficients are optimized, allowing filters from 7th to 13th order, energy, and zero crossing extraction to be performed using only shift and add operations. A five-layer network uses limited interconnections.

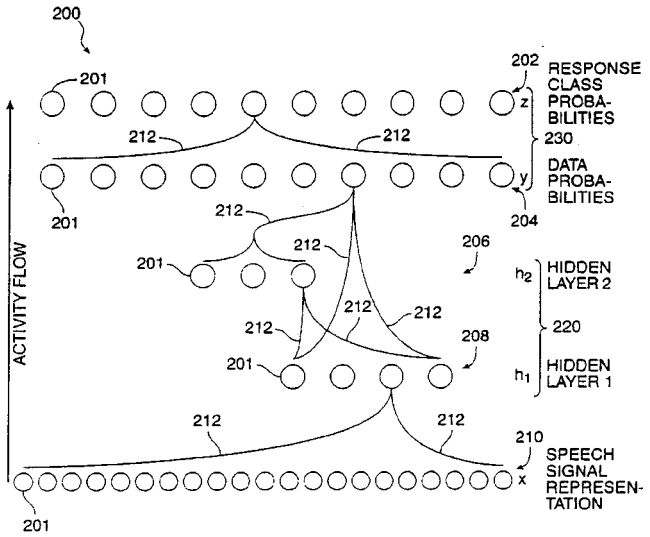

Within each layer, all unit inputs are connected as shown in the figure for one unit of that layer. The device is said to achieve 96% to 98% accuracy, with most errors flagged as low confidence, allowing a repetition to be requested.—DLR

6,014,623

43.72.Ja METHOD OF ENCODING SYNTHETIC SPEECH

Xingjun Wu and Yihe Sun, assignors to United Microelectronics Corporation
11 January 2000 (Class 704/230); filed 12 June 1997

This is a syllable-based speech synthesizer in which the speech frames within each syllable are coded as line spectral pairs. The first frame of each syllable includes the complete set of ten LSP coefficients and each following frame contains 4-bit differential coefficients.—DLR

6,016,471

43.72.Ja METHOD AND APPARATUS USING DECISION TREES TO GENERATE AND SCORE MULTIPLE PRONUNCIATIONS FOR A SPELLED WORD

Roland Kuhn *et al.*, assignors to Matsushita Electric Industrial Company, Limited
18 January 2000 (Class 704/266); filed 29 April 1998

The patent describes a decision tree technique for generating phonetic transcriptions from text. Referred to as a ''mixed tree'' method, the system uses decisions based on either letter or phonetic symbol sequences. These are said to provide more accurate transcriptions than prior techniques.—DLR

6,018,709

43.72.Ja SPEECH AND SOUND SYNTHESIZERS WITH CONNECTED MEMORIES AND OUTPUTS

Robert W. Jeffway, Jr., assignor to Hasbro, Incorporated
25 January 2000 (Class 704/258); filed 30 January 1997

This patent describes a control system which allows a LPC speech synthesizer chip, such as a Texas Instruments TSP series, and a typical ADPCM audio synthesis chip to be combined into a single synthesis system. The encoded sound data includes codes which identify whether each portion is to be synthesized with the speech chip or the audio chip. This allows use of the best coding technique for each type of data, speech versus nonspeech audio.—DLR

6,021,388

43.72.Ja SPEECH SYNTHESIS APPARATUS AND METHOD

Mitsuru Otsuka *et al.*, assignors to Canon Kabushiki Kaisha
1 February 2000 (Class 704/268); filed in Japan 26 December 1996

This patent describes the waveform synthesizer portion of a text-to-speech system. One or more spectral functions are stored for each phoneme to be synthesized. A sine wave is then sampled at multiple fractions of the

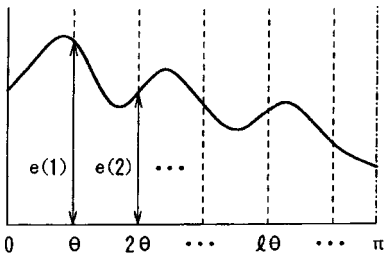

$$\theta = 2\pi / N_p(f)$$

fundamental period and multiplied by the spectral level for each harmonic. A number of different embodiments of the design use different strategies for the harmonic signal generation.—DLR

6,006,186

43.72.Ne METHOD AND APPARATUS FOR A PARAMETER SHARING SPEECH RECOGNITION SYSTEM

Ruxin Chen *et al.*, assignors to Sony Corporation; Sony Electronics, Incorporated
21 December 1999 (Class 704/254); filed 16 October 1997

This hidden Markov model (HMM)-based speech recognition system makes multiple use of the trained HMMs by sharing spectral density functions between the HMMs in various ways. Shared HMMs are generated for triphone-trained HMMs when they have common biphones, common pho-

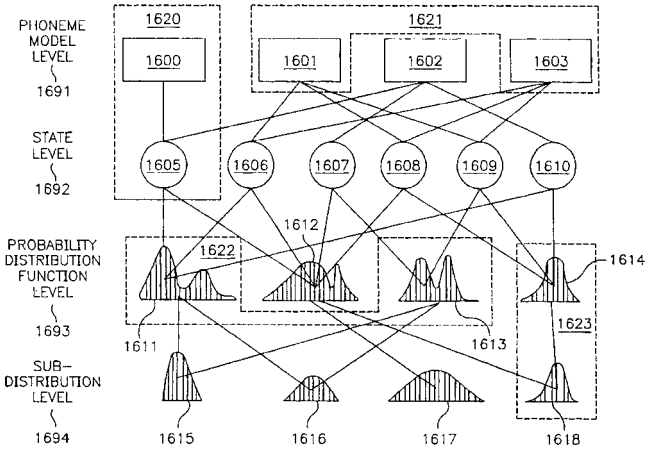

netic context, or common center phonemes, and when they are represented by at least a threshold number of training frames. The sharing occurs within and across levels of the recognition system.—DLR

6,009,392

43.72.Ne TRAINING SPEECH RECOGNITION BY MATCHING AUDIO SEGMENT FREQUENCY OF OCCURRENCE WITH FREQUENCY OF WORDS AND LETTER COMBINATIONS IN A CORPUS

Dimitri Kanevsky and Wlodek Wlodzimierz Zadrozny, assignors to International Business Machines Corporation
28 December 1999 (Class 704/245); filed 15 January 1998

This speech recognition training method is designed to eliminate the requirement for labeled training data. Instead of relying on user-supplied phonetic information, the system performs clustering of the input speech feature data, attempting to group the segments into phonetically related

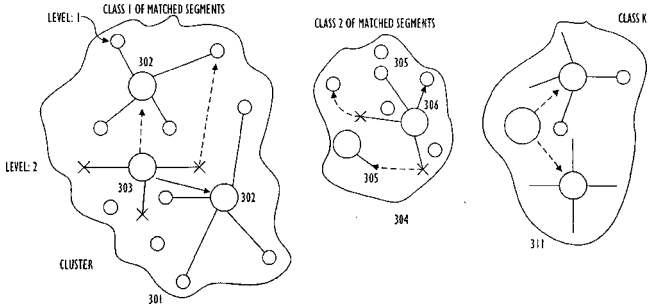

groups. Based on the spectral characteristics and the occurrence distribution of sounds and of words in the sample, the system makes a phonetic class assignment.—DLR

6,014,624

43.72.Ne METHOD AND APPARATUS FOR TRANSITIONING FROM ONE VOICE RECOGNITION SYSTEM TO ANOTHER

Vijay R. Raman, assignor to NYNEX Science and Technology, Incorporated
11 January 2000 (Class 704/243); filed 18 April 1997

This patent is primarily concerned with the conversion of speech or speaker information between database formats as would be used by speaker-dependent (SD) versus speaker-independent (SI) recognition systems. For example, a SD template may be useful in adding to the phonetic models of a SI system. Since such a conversion typically involves a loss of information, provision is made to include original speech data from compressed recordings, whenever possible.—DLR

6,016,470

43.72.Ne REJECTION GRAMMAR USING SELECTED PHONEMES FOR SPEECH RECOGNITION SYSTEM

Chang-Qing Shu, assignor to Gte Internetworking, Incorporated
18 January 2000 (Class 704/244); filed 12 November 1997

The grammar used with a speech recognition system typically specifies a finite list of words or phrases which are acceptable as possible utterances at the particular time. Whatever the actual input speech might be, a choice is forced to one of the expected ''target'' inputs. This system relaxes that requirement by maintaining a secondary (rejection) grammar. The rejection grammar scores individual phonemes, rather than complete words or phrases. Thus, an out-of-grammar input may score highly as an unknown phonetic sequence, beating the score for the best-fitting target word or phrase.—DLR

6,018,708

43.72.Ne METHOD AND APPARATUS FOR PERFORMING SPEECH RECOGNITION UTILIZING A SUPPLEMENTARY LEXICON OF FREQUENTLY USED ORTHOGRAPHIES

Jean-Guy Dahan and Vishwa Gupta, assignors to Nortel Networks Corporation
25 January 2000 (Class 704/244); filed 26 August 1997

A method is described for improving the second-pass best-choice selection from the *N* best results of a first speech recognition pass. The first pass is performed with a standard recognition dictionary. A new dictionary created for the second pass contains added items which tend to occur with a higher probability, increasing the chance of selecting those items. In this case, the phrases consist of phone numbers to be called and the high-probability items represent numbers that the user frequently calls.—DLR

6,021,278

43.72.Ne SPEECH RECOGNITION CAMERA UTILIZING A FLIPPABLE GRAPHICS DISPLAY

Bryan D. Bernardi *et al.*, assignors to Eastman Kodak Company
1 February 2000 (Class 396/57); filed 30 July 1998

This patent describes an application of speech recognition for controlling a still-image camera while looking through the viewfinder. Various camera adjustments can be made, such as zoom, exposure, and flash. A prior

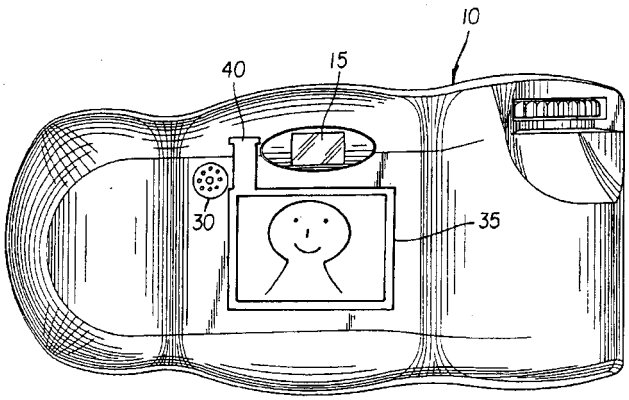

patent allowed camera control from a remote location, but not in the hand-held situation. The complete small-vocabulary recognizer is built on a single integrated circuit.—DLR

6,021,384

43.72.Ne AUTOMATIC GENERATION OF SUPERWORDS

Allen Louis Gorin and Giuseppe Riccardi, assignors to AT&T Corporation
1 February 2000 (Class 704/1); filed 29 October 1997

This is a low-cost method for obtaining some of the benefits of a word sequence probability model for speech recognition. It is well known that recognition results improve with the use of ''*N*-gram'' models, which specify the probability of occurrence of sequences of *N* words. However, as *N* increases, the memory requirements become very large. The method described here represents the most frequently occurring word sequences as single long words, referred to as ''super words.''—DLR

6,023,673

43.72.Ne HIERARCHICAL LABELER IN A SPEECH RECOGNITION SYSTEM

Raimo Bakis *et al.*, assignors to International Business Machines Corporation
8 February 2000 (Class 704/231); filed 4 June 1997

In this speech recognition system, the reference feature vector data is divided into subsets corresponding roughly to a coarse phonetic classification, followed by a finer classification. Additional levels may also be added such that each finer level would contain 10 to 20 times the number of reference vectors as the previous level. In this manner, total sets of tens of thousands of feature sets may be matched without greatly increasing the processing time.—DLR

6,023,676

43.72.Ne KEYWORD RECOGNITION SYSTEM AND METHOD

Adoram Erell, assignor to DSPC Israel, Limited
8 February 2000 (Class 704/241); filed 12 December 1996

This is a two-tier, isolated-word recognition system, using dynamic time warping in a speaker-dependent mode. An initial keyword match is performed in an open-microphone method. Apparently, this mode searches for a single ''trigger'' keyword. If that word is seen, then the system switches to a microphone ''window'' mode, during which any of a set of command words is expected. To improve the accuracy of detecting the initial trigger word, a possible candidate is matched against the full command set to determine a ''false match'' reference level.—DLR

6,023,677

43.72.Ne SPEECH RECOGNITION METHOD

Fritz Class *et al.*, assignors to Daimler Benz AG
8 February 2000 (Class 704/254); filed in Germany 20 January 1995

The connected-word recognition method described here is a ''rediscovery'' of the well-known method of branching word graphs. Word transition probabilities are accumulated to provide a sentence match probability.

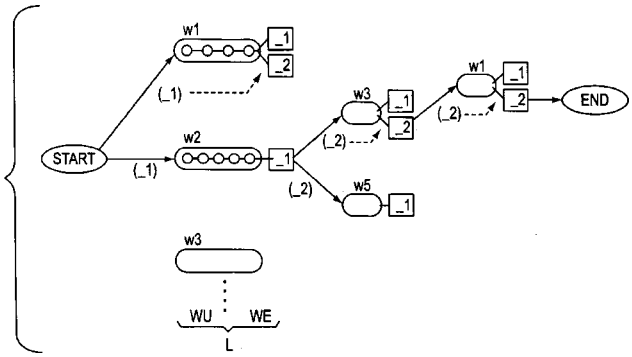

Seemingly in consideration of branching factor concerns, the system is to be limited to relatively small numbers of sentences.—DLR

Localization of a pontine vocalization-controlling area

Uwe Jürgens
German Primate Center, Kellnerweg 4, 37077 Göttingen, Germany

(Received 24 May 1999; accepted for publication 20 June 2000)

To find out whether there exist additional regions in the pontine brainstem, apart from the phonatory motoneuron pools involved in vocal motor control, the effects of a localized blockade of excitatory neurotransmission in the pons were studied on squirrel monkey vocalization. Vocalization was elicited by electrical stimulation of the periaqueductal gray of the midbrain. Blockade was carried out by stereotaxic injections of kynurenic acid, a nonspecific glutamate antagonist. It was found that injections made into the ventrolateral pons around the ventral nucleus of the lateral lemniscus and superior olive could block periaqueductally elicited vocalization. Injections were only effective ipsilaterally, not contralaterally to the stimulation site. The blockade was limited to one particular class of calls, all of which had in common a characteristic stereotyped frequency modulation over several kHz. It is concluded that critical processing steps of vocal motor control take place in the periolivary region. © *2000 Acoustical Society of America.* [S0001-4966(00)00110-7]

PACS numbers: 43.70.Aj, 43.70.Bk [AL]

I. INTRODUCTION

Phonation consists of a complex interaction of laryngeal, respiratory, and articulatory activity. While there is good knowledge about the muscles involved in phonation and the location of the laryngeal, respiratory, and articulatory motoneurons, very little is known about the way these motoneurons are coordinated in their activity to accomplish a specific vocal pattern. Neurological studies in human patients revealed that destruction of several structures causes speech and singing disturbances. Such structures are the face area of the motor cortex, the ventrolateral thalamus projecting into the motor cortex, the cerebellum (more specifically, the paravermal lobulae VI & VII) projecting into the ventrolateral thalamus, the putamen, an output structure of the motor cortex, and the corticobulbar and corticospinal tracts connecting the motor cortex with the lower brainstem and spinal cord, respectively (Alajouanine and Thurel, 1933; Bauer *et al.*, 1980; Bell, 1968; Groswasser *et al.*, 1988; Kent *et al.*, 1979; Lechtenberg and Gilman, 1978; Lee *et al.*, 1996; Metter *et al.*, 1986; Samra *et al.*, 1969). As patients with damage to the above areas and with speech and singing disturbances are often still able to produce normal nonverbal emotional vocal utterances, such as crying, moaning, and laughing, it is unlikely that the integration of laryngeal, respiratory, and supralaryngeal activity is generally carried out in the aforementioned structures. This assumption is further supported by the fact that anencephalic children, that is, infants born without forebrain and cerebellum, are able to cry loudly when exposed to painful stimuli (Monnier and Willi, 1953). The persistence of vocalization in anencephalic children suggests that the integration of laryngeal, respiratory, and supralaryngeal activity necessary for the production of, at least, nonverbal vocal utterances, is carried out in subcortical structures. Animal experiments point to the same direction. Lesioning studies in the squirrel monkey have revealed that bilateral destruction of the facial motor cortex, ventrolateral thalamus, cerebellum, putamen, or corticobulbar/corticospinal tracts does not abolish the ability to produce different species-specific calls (Jürgens *et al.*, 1982; Kirzinger, 1985; Kirzinger and Jürgens, 1985). In the cat, transection experiments have shown that cutting all connections between brainstem and forebrain does not prevent the production of mewing, purring, growling, and spitting (Bazett and Penfield, 1922). This suggests that the brainstem does not only integrate the laryngeal, respiratory, and supralaryngeal activities, but that it also contains the pattern generators for different vocal utterances.

The present study is an attempt to localize brainstem areas that, apart from the phonatory motoneuron pools, are involved in vocal motor coordination. The study was carried out in such a way that vocalization-eliciting electrodes were implanted into the periaqueductal gray of the midbrain. Then, injections of kynurenic acid, a glutamate antagonist capable of blocking excitatory neurotransmission at glutamatergic synapses, were placed at sites caudal to the periaqueductal gray, but rostral to the phonatory motoneuron pools. The effect of these injections on the elicitability of vocalization from the periaqueductal gray was tested. It was hypothesized that injection of kynurenic acid into sites that form part of a vocal motor coordination mechanism will block or deteriorate vocalization elicited by periaqueductal stimulation.

II. METHODS

In five squirrel monkeys (*Saimiri sciureus*), under deep narcosis (40-mg/kg pentobarbital sodium), a platform with electrode and injection cannulae guide tubes was stereotaxically fixed to the skull with four stainless steel screws, nuts, and dental cement. Then small holes (0.5 mm diam) were drilled into the bone at sites for insertion of stimulation electrodes and injection cannulae.

Stimulation electrodes consisted of a stainless steel tube (0.47 mm outer diam) and a Teflon-insulated stainless steel wire (0.15 mm diam) protruding 2 mm from the tube. The wire was uninsulated at the tip for 1 mm. Stimulation current consisted of a biphasic rectangular pulse pair with a repeti-

tion rate of 20–70 Hz, pulse duration of 1 ms, intensity of 50–300 μA, and a train duration of 10 s. Vocalization was elicited by electrical stimulation through electrodes lowered into the periaqueductal gray through the guide tubes. Depending on the electrode site and stimulation parameters, various call types were obtained. Injection guide tubes (0.47 mm outer diam, 0.2 mm internal diam) were used to insert the cannula of a Hamilton microsyringe (0.2 mm outer diam). Normally, two pairs of injection guiding tubes and two to three stimulation electrodes were implanted per animal. Tests were carried out in the awake animal, sitting in a restraining chair. First, the threshold was determined for all electrodes yielding vocalization. Then, 0.25–0.5 μl of 2% kynurenic acid in sterile water was injected into the site to be tested. Each site was tested ipsilateral, contralateral, and bilateral with respect to the vocalization-eliciting electrode. Ten min after the injection, electrodes were stimulated again and checked for changes in threshold for elicitation of vocalization. If, after injection, vocalization could not be obtained with intensities at least 100% above the pre-injection threshold, the effect was considered as blockade. Only those effects were counted that showed complete recovery within 24 h.

After the tests, the animals were sacrificed with an overdose of pentobarbital sodium, perfused with physiological saline and 4% paraformaldehyde. The brains were removed, sectioned at 33 μm on a freezing microtome, and mounted on slides. Alternate sections were stained with cresylviolet and luxol fast blue combined with nuclear fast red, respectively. Determination of the stimulation and injection sites was carried out with the aid of the stereotaxic brain atlas of Emmers and Akert (1963).

All procedures were approved by the governmental ethical committee for animal experimentation (Bezirksregierung Braunschweig).

III. RESULTS

Altogether 125 injections sites were tested for their effect on periaqueductally elicited vocalization. The sites extended from the rostrodorsal midbrain down into the caudal pons. Their locations are indicated in Figs. 1(a)–(c). Out of the 125 sites, injections in 20 were able to block periaqueductally elicited vocalization. These sites were all located in the ventrolateral pons in a region comprising the ventral nucleus of the lateral lemniscus, the periolivary nuclei, and bordering parvocellular reticular formation. Blockade was obtained with injections ipsilateral to the stimulation electrode, never with injections contralateral to the stimulation site. In all cases in which bilateral injections were effective, ipsilateral injections were effective as well. Blockade was limited to one particular class of call types, the so-called twitter/chatter/cackling calls (Fig. 2). At stimulation sites at which calls of this class were the only calls elicitable, there was complete blockade of vocalization after kynurenic acid injections into the ventrolateral pons. At stimulation sites at which calls of the twitter/chatter/cackling class were intermixed with calls of other classes, such as cawing, purring, growling, spitting, shrieking, squealing, or peeping, pontine injections abolished only calls of the twitter/chatter/cackling class; other calls remained unaffected. Twitter, chatter, and cackling calls differ from other calls by their characteristic frequency modulation of 150–270 Hz/ms over a range of 2–8 kHz.

IV. DISCUSSION

The study shows that by blocking excitatory neurotransmission in the ventrolateral pons, it is possible to abolish specific call types electrically elicitable from the periaqueductal gray. This makes clear that there is a group of neurons in the pons that is involved in vocal production. According to Holstege (1989), the vocal motor control pathway consists of a direct connection from the periaqueductal gray to the nucl. retroambiguus in the medulla oblongata, and from there to the phonatory motoneuron pools in the pons, medulla oblongata, and spinal cord. The present results do not support this hypothesis. Obviously, the periaqueductal gray, nucl. retroambiguus, and phonatory motoneuron pools are not the only brainstem areas involved in vocal motor control.

The present results fit with several other observations. Electrical stimulation of a region similar to that from which vocalization could be blocked in the present study has been reported to produce vocalization in the cat (Magoun *et al.*, 1937; Kanai and Wang, 1962), bat (Schuller, 1998), and squirrel monkey (Jürgens and Ploog, 1970). As vocalization could not only be obtained with electrical stimulation but also with glutamate stimulation, a method that activates neuronal cell bodies and dendrites, but not axons, it may be concluded that the blockade observed in the present study was due to the blockade of a vocal relay station, rather than of by-passing fibers. As, furthermore, the vocalizations elicitable from the periolivary region usually have an artificial acoustic structure (i.e., a structure not found in spontaneously produced vocalizations), it may be assumed that this region is part of the vocal motor coordination mechanism (Jürgens and Ploog, 1988). The artificial character of the elicited vocalizations probably results from the abnormal activity pattern forced upon vocalization-coordinating neurons by the electrical or glutamate stimulation.

Further, support for a role of the periolivary region in vocal control comes from single-unit recording and *c-fos* expression studies. As Fos is a nuclear protein known to be produced by a variety of stimuli capable of neuronal excitation, it is generally accepted as a marker of neuronal activation. In the saddleback tamarin (*Saguinus fuscicollis*), a New World primate, it was found that extensive vocalizing results in an increased Fos production in neurons dorsal and lateral to the superior olive (Jürgens *et al.*, 1996). In the squirrel monkey, another New World primate, a systematic exploration of the brainstem with microelectrodes revealed vocalization-correlated neuronal activity in an area between the superior olive and the ventral nucleus of the lateral lemniscus (Kirzinger and Jürgens, 1991). Neuroanatomically, the periolivary region receives a direct input from the periaqueductal gray (Jürgens and Pratt, 1979). On the output side, it is connected with all cranial motor nuclei involved in phonation, that is, the nucl. ambiguus, responsible for vocal fold movements; the trigeminal motor nucleus, responsible

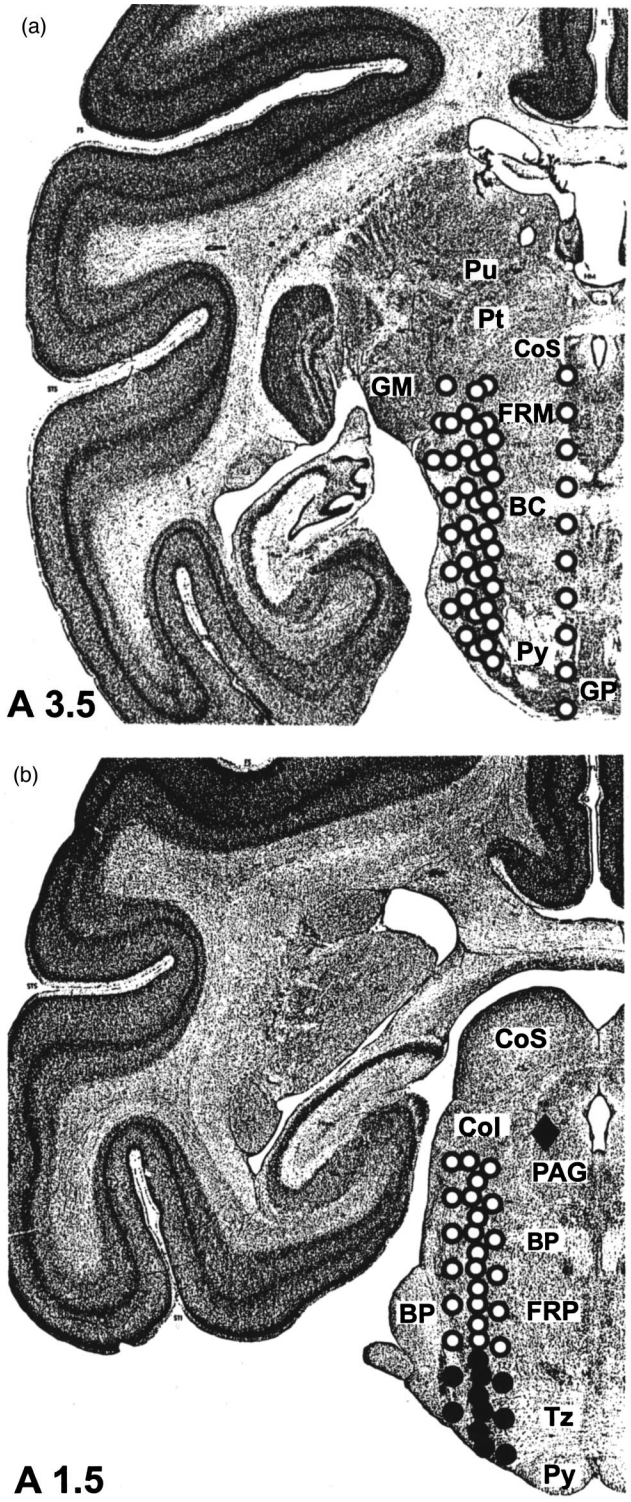

FIG. 1. (a)–(c) Frontal sections through the squirrel monkey's brainstem showing all injection sites tested in the present study. Black circles indicate sites at which injection of kynurenic acid blocked periaqueductally elicited vocalization. White circles indicate sites without effect. Black diamond indicates periaqueductal vocalization site. Abbreviations: BC brachium conjunctivum, BP brachium pontis, CoI colliculus inferior, CoS colliculus superior, FRM formatio reticularis mesencephali, FRP formatio reticularis pontis, GM corpus geniculatum mediale, GP griseum pontis, PAG periaqueductal gray, Pt praetectum, Pu nucl. pulvinaris, Py tractus pyramidalis, Tz corpus trapezoideum.

for jaw movements; the facial nucleus controlling lip movements, and the hypoglossal nucleus controlling tongue movements (Thoms and Jürgens, 1987).

Vocalization involves bilateral activation of the vocal folds and other phonatory muscles. Normal vocalization, nevertheless, can be obtained with unilateral periaqueductal stimulation. This means that there must be a bifurcation of the vocal control pathway on the way from the periaqueductal gray to the phonatory motoneurons. The fact that in the present study periaqueductally elicited vocalizations were only affected by ipsilateral, not by contralateral injections indicates that this bifurcation is ''downstream'' from the periolivary area. An unexpected finding of the present study was the observation that not all call types elicitable from the periaqueductal gray were abolished by periolivary injections of kynurenic acid. Among the unaffected calls, there were high-pitched calls (e.g., squealing) as well as low-pitched calls (e.g., cawing), harmonic calls (e.g., peeping) as well as noiselike calls (e.g., spitting), rhythmic calls (e.g., purring) as well as continuous calls (e.g., shrieking). While no com-

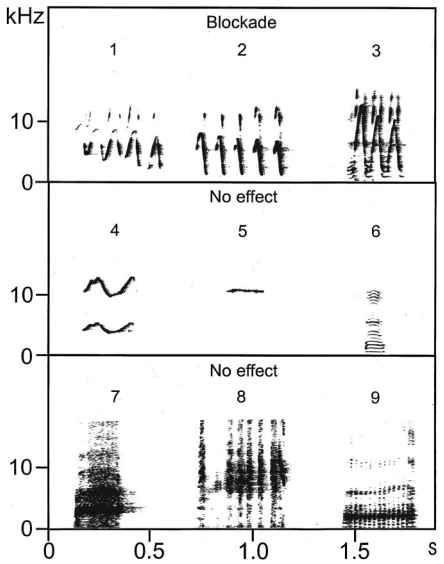

FIG. 2. Sonagrams of periaqueductally elicited normal (i.e., naturally sounding) squirrel monkey calls. 1 trill, 2 chatter, 3 cackle, 4 squeal, 5 peep, 6 caw, 7 shriek, 8 spit, 9 purr. Blockade was effective for call types 1 to 3, but there was no effect for call types 4 to 9.

mon features could be detected among the unaffected calls, the calls abolished by injections all shared a characteristic, highly stereotyped frequency modulation over several kHz. This finding suggests that different vocal patterns are processed in different brainstem regions. Vocalizations requiring well-controlled frequency modulation seem to depend on the intactness of the periolivary region; other features seem to be processed in regions caudal to the presently explored pontine brainstem section.

Alajouanine, T., and Thurel, R. (**1933**). ''La Diplégie Faciale Cérébrale Forme Corticale de la Paralysie Pseudobulbaire,'' Revue Neurologique **60**, 441–458.

Bauer, G., Gerstenbrand, F., and Heugl, W. (**1980**). ''Involuntary motor phenomena in the locked-in-syndrome,'' J. Neurology **223**, 191–198.

Bazett, H. C., and Penfield, W. G. (**1922**). ''A study of the Sherrington decerebrate animal in the chronic as well as the acute condition,'' Brain **45**, 185–265.

Bell, D. S. (**1968**). ''Speech functions of the thalamus inferred from the effects of thalamotomy,'' Brain **91**, 619–638.

Emmers, R., and Akert, K. (**1963**). *A Stereotaxic Atlas of the Brain of the Squirrel Monkey (Saimiri sciureus)* (University of Wisconsin Press, Madison).

Groswasser, Z., Korn, C., Groswasser-Reider, J., and Solzi, P. (**1988**). ''Mutism associated with buccofacial apraxia and bihemispheric lesions,'' Brain Lang. **34**, 157–168.

Holstege, G. (**1989**). ''Anatomical study of the final common pathway for vocalization in the cat,'' J. Comp. Neurol. **284**, 242–252.

Jürgens, U., and Ploog, D. (**1970**). ''Cerebral representation of vocalization in the squirrel monkey,'' Exp. Brain Res. **10**, 532–554.

Jürgens, U., and Ploog, D. (**1988**). ''On the motor coordination of monkey calls'' in *The Physiological Control of Mammalian Vocalizations*, edited by J. D. Newman (Plenum, New York), pp. 7–19.

Jürgens, U., and Pratt, R. (**1979**). ''Role of the periaqueductal gray in vocal expression of emotion,'' Brain Res. **167**, 367–378.

Jürgens, U., Kirzinger, A., and von Cramon, D. (**1982**). ''The effects of deep-reaching lesions in the cortical face area on phonation. A combined case report and experimental monkey study,'' Cortex **18**, 125–140.

Jürgens, U., Lu, C.-L., and Quondamatteo, F. (**1996**). ''C-fos expression during vocal mobbing in the New World monkey *Saguinus fuscicollis*,'' Eur. J. Neurosci. **8**, 2–10.

Kanai, T., and Wang, S. C. (**1962**). ''Localization of the central vocalization mechanism in the brainstem of the cat,'' Exp. Neurol. **6**, 426–434.

Kent, R. D., Netsell, R., and Abbs, J. H. (**1979**). ''Acoustic characteristics of dysarthria associated with cerebellar disease,'' J. Speech Hear. Res. **22**, 627–648.

Kirzinger, A. (**1985**). ''Cerebellar lesion effects on vocalization of the Squirrel Monkey,'' Behav. Brain Res. **16**, 177–181.

Kirzinger, A., and Jürgens, U. (**1985**). ''The effects of brain stem lesions on vocalization in the Squirrel Monkey,'' Brain Res. **358**, 150–162.

Kirzinger, A., and Jürgens, U. (**1991**). ''Vocalization-correlated single-unit activity in the brain stem of the Squirrel Monkey,'' Exp. Brain Res. **84**, 545–560.

Lechtenberg, R., and Gilman, S. (**1978**). ''Speech disorders in cerebellar disease,'' Ann. Neurol. **3**, 285–290.

Lee, M. S., Lee, S. B., and Kim, W. C. (**1996**). ''Spasmodic dysphonia associated with a left ventrolateral putaminal lesion,'' Neurology **47**, 827–828.

Magoun, H. W., Atlas, D., Ingersoll, E. H., and Ranson, S. W. (**1937**). ''Associated facial, vocal and respiratory components of emotional expression: An experimental study,'' J. Neurol. Psychopath. **17**, 241–255.

Metter, E. J., Jackson, C., Kempler, D., Riege, W. H., Hanson, W. R., Mazziotta, J. C., and Phelps, M. E. (**1986**). ''Left hemisphere intracerebral hemorrhages studied by (F-18)-fluorodeoxyglucose PET,'' Neurology **36**, 1155–1162.

Monnier, M., and Willi, H. (**1953**). ''Die integrative Tätigkeit des Nervensystems beim meso-rhombo-spinalen Anencephalus (Mittelhirnwesen),'' Monatsschr. Psychiat. Neurol. **126**, 239–273.

Samra, K., Riklan, M., Levita, E., Zimmerman, J., Waltz, J. M., Bergmann, L., and Cooper, J. S. (**1969**). ''Language and speech correlates of anatomically verified lesions in thalamic surgery for Parkinsonism,'' J. Speech Hear. Res. **12**, 510–540.

Schuller, G. (**1998**). *Neural Mechanisms of Vocal Control in Bats*, 5th Internet World Congress on Biomedical Sciences at McMaster University, Canada, Dec. 7–16.

Thoms, G., and Jürgens, U. (**1987**). ''Common input of the cranial motor nuclei involved in phonation in Squirrel Monkey,'' Exp. Neurol. **95**, 85–99.

Resonance properties of the vocal folds: *In vivo* laryngoscopic investigation of the externally excited laryngeal vibrations

Jan G. Švec[a)]
Center for Communication Disorders, Medical Healthcom, Ltd., Řešovská 10/491, 181 00 Prague 8, the Czech Republic

Jaromír Horáček
Institute of Thermomechanics Academy of Sciences of the Czech Republic, Dolejškova 5, 182 00 Prague 8, the Czech Republic

František Šram
Center for Communication Disorders, Medical Healthcom, Ltd., Řešovská 10/491, 181 00 Prague 8, the Czech Republic

Jan Veselý
Institute of Thermomechanics Academy of Sciences of the Czech Republic, Dolejškova 5, 182 00 Prague 8, the Czech Republic

(Received 26 July 1999; accepted for publication 20 June 2000)

The study presents the first attempt to investigate resonance properties of the living vocal folds by means of laryngoscopy. Laryngeal vibrations were excited via a shaker placed on the neck of a male subject and observed by means of videostroboscopy and videokymography (VKG). When the vocal folds were tuned to the phonation frequency of 110 Hz and sinusoidal vibration with sweeping frequency (in the range 50–400 Hz) was delivered to the larynx, three clearly pronounced resonance peaks at frequencies around 110, 170, and 240 Hz were identified in the vocal fold tissues. Different modes of vibration of the vocal folds, observed as distinct lateral-medial oscillations with one, two, and three half-wavelengths along the glottal length, respectively, were associated with these resonance frequencies. At the external excitation frequencies below 100 Hz, vibrations of the ventricular folds, aryepiglottic folds and arytenoid cartilages were dominant in the larynx. © *2000 Acoustical Society of America.* [S0001-4966(00)00210-1]

PACS numbers: 43.70.Aj, 43.40.At [AL]

I. INTRODUCTION

From the theory of vibration it is known that vibration of a structure can generally be decomposed into a set of independent characteristic vibration patterns, called *eigenmodes*. Like any other vibrating structure, vocal folds have inherent eigenmodes which are crucial in determining their possible vibration behavior. Each of the eigenmodes is associated with a specific *eigenfrequency* and exhibits certain *damping*. The eigenmodes, eigenfrequencies, and damping are called the ''*dynamic characteristics*'' of the vibrating system and are independent of the excitation mechanism of the vibration. These characteristics can be used to describe inherent vibration properties of the vocal folds. Information on the dynamic characteristics of the true vocal folds has been rather limited, however, mostly due to difficulties related to measurement of these characteristics in the delicate and hardly accessible vocal fold tissues.

Titze and Strong (1975) were the first who theoretically studied the eigenmodes of the vocal folds. The theory predicts generally infinite number of eigenmodes in the vocal fold tissues (e.g., Titze and Strong, 1975; Titze, 1994). Only a few dominant (lowest) modes, however, are assumed to play a substantial role in the actual vibration of the vocal folds. In a study with a finite-element model of the vocal folds, Berry *et al.* (1994) have found that combination of only two eigenmodes captures more than 95% of the variance of the vocal fold vibration in normal phonation and more than 70% of irregular vocal fold vibration. Prevalence of two dominant eigenmodes has also been recently found experimentally in vibration of the vocal folds in excised canine larynges (Berry, in press).

The two dominant eigenmodes have been theoretically known and designated as x-10 and x-11.[1] The x-10 mode presents a lateral-medial oscillation which is responsible for opening and closing of the vocal folds in a vibratory cycle. The x-11 mode presents an out-of-phase motion of the upper and lower margins of the vocal folds, which plays an important role in the transfer of the aerodynamic energy into the motion of the vocal fold tissues (Stevens, 1977; Ishizaka, 1988; Titze, 1988). Higher-order modes, such as, e.g., x-20, x-21 or x-30, x-31 (lateral-medial oscillations encompassing two or three half-wavelengths along the glottal length) are assumed to partially contribute to production of more complex vocal fold vibration patterns, especially those related to pathologic voice quality (Titze and Strong, 1975; Titze, 1994; Berry *et al.*, 1994).

During phonation, the oscillation of the vocal folds is significantly influenced by phonatory airflow. Aerodynamic coupling leads, along with inherent nonlinearity of the vocal

a)Electronic mail: svecjan@mbox.vol.cz

folds, to phenomena such as entrainment of the eigenmodes (also known as ''mode locking''), which cause rearrangement of the eigenfrequencies of the vocal folds (Berry *et al.*, 1994; Fletcher, 1996; Berry, in press). A well known example can be found in the behavior of a simple two-mass model of the vocal folds (Ishizaka and Flanagan, 1972): under typical conditions the eigenmodes of the model, which correspond to the modes x-10 and x-11, are tuned to 120 and 201 Hz (e.g., Titze, 1976; Ishizaka, 1988). Under the influence of the airflow these two eigenmodes are entrained to vibrate at identical frequency around 130–150 Hz (depending on the subglottal pressure; see Ishizaka and Flanagan, 1972). This effect illustrates a need for studies of vocal fold behavior not influenced by the phonatory airflow revealing the dynamic characteristics more accurately.

Only a few experimental studies have been devoted to the vibrations of the vocal folds without the airflow. In a study with excised human larynges, Tanabe *et al.* (1979) displaced a vocal fold via a metal plate attached to a stretched elastic rod. When the rod was cut, the vocal fold was released and exhibited a damped oscillation which was monitored using a high-speed (cinematographic) camera. These experiments were performed for obtaining information on the damping properties of the vocal folds. The results could, in principle, have been used also for studying the eigenfrequencies of the vocal folds, but these authors did no determine these values.

The only studies to date, which provide information on eigenfrequencies as well as damping characteristics of the true vocal folds, were published by Kaneko *et al.* (1981, 1983, 1987). Here, the vibration of the vocal folds was excited externally using a shaker placed on the thyroid cartilage. The response of the vocal folds was registered by means of modified ultrasonic equipment. Kaneko designed a special phonatory maneuver in order to investigate the eigenfrequencies of the vocal folds in living subjects: the subject phonated at a given pitch and stopped delivering the air from the lungs while keeping the vocal folds in the phonatory position (the so-called ''*neutral phonatory position*''). At that moment the shaker was switched on and the response measurement was done. Kaneko identified two distinct eigenfrequencies of the vocal folds, which changed with the phonation frequency. The lower of the eigenfrequencies was found to be close to the frequency of phonation. Similar results were obtained by Kaneko *et al.* in a number of living subjects as well as in excised human larynges.

The eigenfrequencies of the true vocal folds measured by Kaneko *et al.* correspond well to the eigenfrequencies of the two-mass model of the vocal folds designed by Ishizaka and Flanagan (1972). On the basis of this correlation it has been hypothesized (Ishizaka, 1988) that these two eigenfrequencies are related to the eigenmodes x-10 and x-11. Recently, however, this hypothesis has been challenged by Berry and Titze (1996) who have, on the basis of a theoretical analysis of a continuum model of the vocal folds, predicted the eigenfrequencies of the x-10 and x-11 modes to be nearly identical. A much smaller difference (0–25 Hz) than that measured by Kaneko *et al.* (ca. 50–100 Hz) was also found between the eigenfrequencies of the x-10 and x-11 modes in the finite-element model of the vocal folds by Dedouch *et al.* (1999). The eigenfrequencies of eigenmodes found in the finite-element model of Jiang *et al.* (1998) were, on the other hand, quite far apart ($>$100 Hz). Unfortunately, Kaneko's experiments did not bring any information on mode shapes of vibration of the vocal folds and thus it has not been clear whether, indeed, the measured eigenfrequencies belong to x-10 and x-11, or to some other eigenmodes. This uncertainty has called for new, more specific measurements of the dynamic characteristics of the true vocal folds.

This study presents the first attempt to investigate the dynamic characteristics of the vocal folds *in vivo* laryngoscopically. The basic question of the present study is the following one: Is it possible to externally induce the vibration of the vocal folds to such extent that they can be monitored laryngoscopically?

Certain positive evidence can be found in the studies of Fukuda *et al.* (1987) and Fukuda (1993). Here, a laryngeal shaker, principally similar to the one used by Kaneko, was used to excite the vocal fold vibrations in patients undergoing surgery under general anesthesia. The vibration of the vocal fold mucosa could be observed laryngoscopically under stroboscopic light. The studies of Fukuda were, however, clinically oriented and did not pay attention to the dynamic characteristics of the vocal folds.

The aim of the present study is to employ the laryngoscopical observation (1) to identify the eigenfrequencies of the vocal folds and (2) to relate these eigenfrequencies to the specific mode shapes of vibration.

II. MATERIALS AND METHODS

A resonance approach, well known from technical practice (e.g., Anderson, 1967; Richardson, 1997) and previously adapted by Kaneko *et al.* (1981), was modified for the measurement of the dynamic characteristics of the vocal folds. Laryngeal vibrations were excited externally via a shaker placed anteriorly on the thyroid cartilage. The vibration response of the vocal folds was monitored laryngoscopically. *Resonance frequencies* (i.e., frequencies at which the vocal folds exhibit maximal amplitudes of vibration) and *resonance modes of vibration* (i.e., vibration patterns of the vocal folds at the resonance frequencies) were examined. The resonance frequencies and resonance modes can be seen as practical approximations of the eigenfrequencies and eigenmodes of the vocal folds. (More detailed information on the relationship between the eigenfrequencies/modes and resonance frequencies/modes can be found in literature on dynamics of vibrating systems, e.g., Anderson, 1967.)

A. Experimental setup

The experimental setup, shown in detail in Fig. 1, consisted of three parts: (1) generation and monitoring of the vibration of the external shaker; (2) monitoring the force by which the shaker is pressed against the neck; and (3) laryngoscopic observation of the excited vocal fold vibrations.

1. Excitation of the laryngeal vibrations

Signal (sinusoidal and impulse, see Sec. II B for details) from a generator (HP type 3324A Synthesized Function

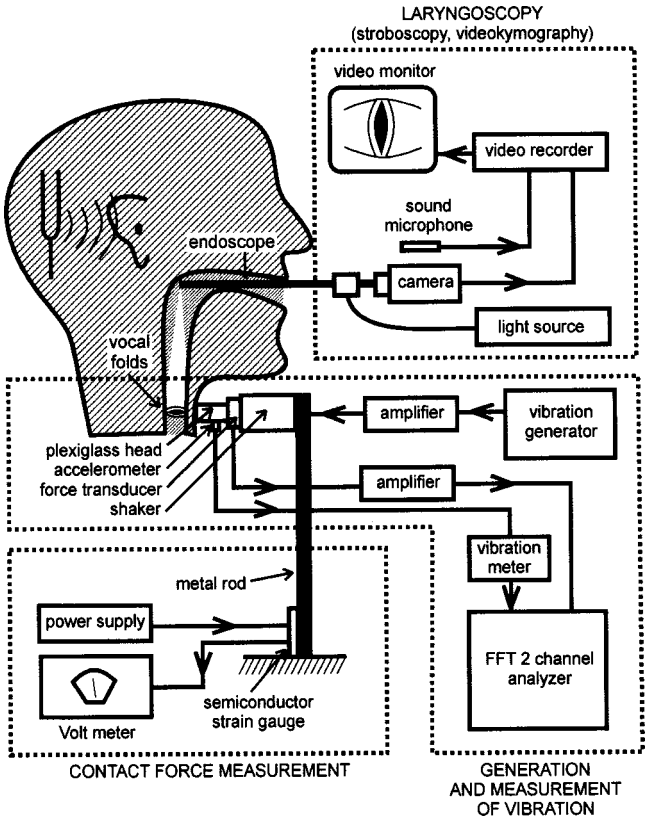

FIG. 1. Experimental setup for the laryngoscopic examination of externally excited laryngeal vibrations.

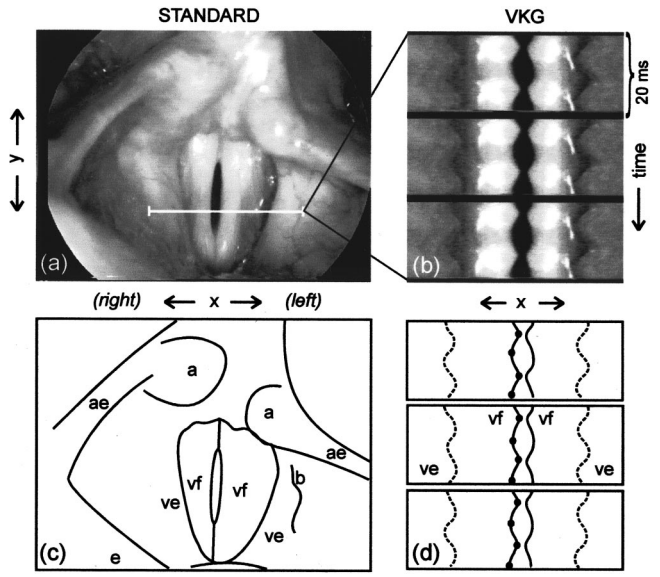

FIG. 2. Standard and videokymographic (VKG) images of the larynx. (a) Standard, laryngostroboscopic image of the vocal folds in neutral phonatory position. (b) High-speed VKG image at the position marked in (a). Chain of three successive VKG fields, each of 20-ms duration, is presented. Each field depicts ca. 18 ms of time, ca. 2-ms interruption between each two successive fields corresponds to a vertical blanking interval which is reserved for synchronization purposes and does don contain any image data (CCIR/PAL video standard). (c) Sketch of the laryngeal image (a): vf—vocal fold; ve—ventricular fold; b—blood vessel on left ventricular fold, a—arytenoid cartilage; ae—aryepiglottic folds; e—epiglottis. (d) Sketch of the videokymographic image (b). Vibrating borders of the ventricular folds (dashed) and vocal folds (solid) are outlined. Dots on the right vocal fold indicate the points used for measuring the amplitude and frequency of the externally excited vibrations. Note that the left and right sides are reversed in all the images (it reflects the situation seen by the examiner when facing the examined subject).

Sweep Generator) was amplified by a VEB Metra Verstärker (type LV 103) and fed into a shaker (Brüel & Kjaer, type 4810). A specially designed plexiglass cylindrical head was firmly attached (screwed) to a vibrating element of the shaker. This plexiglass head served as an electrically isolated contact element which was placed on the neck of the subject. Acceleration of the cylindrical head was registered via an attached accelerometer (Brüel & Kjaer, type 4344). Signal from the accelerometer was amplified by means of a vibration meter (Brüel & Kjaer, type 4511) and recorded on the first channel of an FFT analyzer (Brüel & Kjaer, type 2034 Dual Channel Signal Analyzer). The vibration force was registered by means of a force transducer (Brüel & Kjaer, type 8200) which was placed between the plexiglass cylinder and the vibrating element of the shaker. Signal from the force transducer was amplified by a Brüel & Kjaer (type 2626) amplifier and recorded on second channel of the FFT analyzer.

Signals from the generator, accelerometer, and force transducer were used to obtain transfer functions of the excitation system. The transfer functions (force/generator as well as acceleration/generator) were found to be essentially flat in the frequency range 100–400 Hz. Below 100 Hz, in the relevant range 50–100 Hz, the transfer functions monotonically decreased with descending frequency. Maximum displacement amplitude of the shaker was observed at 50 Hz and measured to be ca. 3 mm.

2. Contact force measurement

The body of the shaker was firmly attached onto a metal rod (Fig. 1). The rod bent when the shaker was pressed against the neck. The amount of bending was measured by means of a semiconductor strain gauge designed at the Institute of Thermomechanics of the Academy of Sciences of the Czech Republic (Vaněk and Cibulka, 1994). The strain gauge was powered from a stabilized power supply of 10 V (TESLA, type BS 525). Change of voltage in the sensory circuit of the semiconductor strain gauge caused by the bending was monitored by means of a voltmeter (TESLA, type DU 20). The system was calibrated, making it possible to convert the measured voltage to the force applied to the shaker.

3. Laryngoscopic observation of the excited laryngeal vibrations

Two methods of monitoring the vocal fold vibration were used: laryngostroboscopy and high-speed videokymography. Laryngostroboscopy is a well-known technique routinely used in laryngology and a more detailed description can be found elsewhere (e.g., Hirano and Bless, 1993). Videokymography is a newly developed method for high-speed optical investigation of vibrations (Švec and Schutte, 1996; Švec *et al.*, 1997, 1999; Schutte *et al.*, 1998).

In *Videokymography* (VKG) a modified video camera is used. The camera can function in two different modes, standard and high speed. In the standard mode, it works as a standard commercial video camera, monitoring the vibration

of the vocal folds with a speed of 25 frames (respectively, 50 interlaced fields) per second (CCIR/PAL standard was used here). An example of a standard laryngoscopic image is shown in Fig. 2(a). In the high-speed mode the camera delivers images from a single selected line with a speed of 7812.5 line images per second. These line images are put below each other and together create a new, videokymographic image monitoring vibration of the selected part of the vocal folds in time [Fig. 2(b)]. A mechanical switch enables to change between the standard and high-speed modes instantly. Both the normal as well as the high-speed images are transmitted in a standard TV format and can be recorded and monitored using a standard video recorder and a TV-compatible monitor. More detailed information on videokymography can be found elsewhere (Švec and Schutte, 1996; Švec *et al.*, 1997, 1999).

The laryngoscopic setup is shown in Fig. 1. For stroboscopy, the following equipment was used: Light source (Rhino-Laryngeal Stroboscope Kay Elemetrics, model 9100), rigid endoscope (70° Kay Elemetrics, type 9106), and 3CCD color camera (Panasonic GP-US502 with a Control Unit) with a C-mount 35mm lens/adapter (Kay Elemetrics, model 9116). Xenon light source (Richard Wolf Auto LP/FLASH 5135), Lupenlaryngoskop (90° Richard Wolf, model 4450.47), and videokymographic CCD black and white camera (Lambert Instruments) with a C-mount objective/adapter (ATMOS) were employed for videokymography. The laryngeal image, registered by (either standard or videokymographic) video camera attached to the endoscope, was presented simultaneously on two video monitors (in Fig. 1, only one monitor is depicted, for simplicity). The examiner used the first monitor; the second monitor provided feedback to the examined subject. The images were recorded using an s-VHS video tape recorder (Panasonic, model AG 7355). An audio signal was registered by means of an electret microphone (Kay Elemetrics lapel microphone, type 7175-6000) and recorded on audio track of the videotape.

B. Experimental procedure

One of the authors (JGS, male, age 32, an amateur jazz-singer) served as a subject for the study. The phonation frequency of 110 Hz was chosen as a reference for the investigation. During the experiment the subject placed the plexiglass cylindrical head of the shaker anteriorly on the prominence of the thyroid cartilage and pushed the neck against the shaker with a force of ca. 3–5 Newton (higher forces were subjectively judged as uncomfortable). The shaker was not firmly fixed to the neck, for safety reasons. The subject at comfortable intensity in chest register reproduced the reference frequency, given by means of a tuning fork. Next, the endoscope was inserted into the oral cavity and the subject repeated the phonation. After this, the subject took a breath and produced the Kaneko maneuver: a short phonation which was interrupted while keeping the vocal folds in the neutral phonatory position. Attempt was made to avoid any movement of the larynx during the Kaneko maneuver (see also the Appendix). At this time, the external vibrations were delivered to the larynx. Three different approaches were used for investigating the externally excited laryngeal vibrations:

1. Videostroboscopy

Sinusoidal excitation signal with a constant frequency (50, 75, 100, 110, 125, 150, 175, 200, 225, 250, 275, 300, 325, 350, 375, and 400 Hz) was used and the laryngeal vibrations were monitored videostroboscopically.

2. Frequency sweep

A sinusoidal signal of constant input power was delivered to the shaker and the frequency was linearly increased. The vibration amplitude of the shaker was dependent on the frequency of oscillation (see the Appendix). Two frequency sweeps in the frequency range of 100–400 Hz and 50–200 Hz were used, each sweep 5 s in duration. The measurement position was aimed at the middle of the membranous part of the vocal folds, transversally to the glottis [Fig. 2(a)], using a standard mode of the VKG camera. The measurement position was adjusted manually by moving the endoscope to the desirable position during the phonation preceding the Kaneko maneuver. Before the start of the frequency sweep, the camera was switched into the high-speed mode and the position of the endoscope was held still during the sweep. After the end of the sweep, the VKG camera was switched back into the standard mode in order to confirm that the measurement position had not changed during the VKG measurement. The measurement was repeated several times for each sweep.

3. Impulse excitation

A periodic rectangular impulse excitation signal of 1-ms duration was delivered from the generator to the shaker. The vibration response of the laryngeal tissues was observed by means of videokymography. Vocal folds responded with damped oscillations; their amplitude was found rather small, however, which appeared problematic for a detailed analysis. The VKG data from this particular condition were thus not analyzed in detail and are not treated in this study. The signals from the force transducer and accelerometer were used to obtain transfer functions of the excitation system (discussed in Sec. II A 1).

C. Analysis of the video data

1. Frequency sweep

The best VKG samples were selected from the videotape. The basic selection criteria were: (a) correctly produced Kaneko maneuver (see the Appendix); (b) well focused image; (c) clearly visible externally induced vibrations of the vocal folds with highest possible amplitude; (d) VKG examination covering the whole frequency sweep (no interruptions of the VKG image by the standard image); (e) approximately constant VKG measurement position during the sweep. A single sample for each frequency sweep was chosen for analysis. That sample was digitized and fed into a PC using a videoboard (Miro PCTV) and saved as an AVI file. A CorelScript program under CorelPhotoPaint 8 software was

written in order to extract successive video fields from the AVI files and save them into a sequence of bitmaps (250 bitmap images per 1 sweep of 5 s in duration). Each 20 successive bitmaps then were concatenated (concatenating more than 20 bitmaps into a single image appeared unpractical for the software used), forming a ''train'' of video fields representing altogether the vocal fold vibration pattern within the time sequence of 400 ms, and saved as a new image [a section of such an image with three concatenated video fields is given in Fig. 2(b)]. From these images, after an adjustment of an optimal contrast, amplitudes of the externally induced vocal fold vibration were extracted.

Extremes of the displacements of the vocal folds and ventricular folds were read manually for every period [Fig. 2(d)] using a cursor in SigmaScan (Jandel Scientific) software. Each value was represented by a pair of pixel values x,y (x pixel corresponding to the position of the vocal folds, y pixel corresponding to a specific time). The data were processed in SigmaPlot (Jandel Scientific) software. Here, the y pixel values were converted to time values in milliseconds, amplitudes were calculated as a half of the difference between the displacement extremes for each vibration period, duration of periods was calculated and converted to frequency values in Hz, best fit of the measured frequency values was done using the known parameters of the sweep (accuracy better than ± 1 Hz), and a graph of the frequency response was plotted. Further on, the data were interpolated, smoothed via the Kernel smoothing algorithm, and plotted.

Resonance frequencies (F_r) and half-power (3-dB) bandwidths (ΔF_r) were measured from the smoothed response curves. F_r were found as frequencies at which the amplitude reached maximal value ($A_{\max}$), ΔF_r was measured as difference of two frequencies around F_r at which the amplitude was equal to $A_{\max}/\sqrt{2}$ (Anderson, 1967; Herlufsen, 1984).

2. Videostroboscopy

Videostroboscopic records representative of selected discrete frequencies were digitized and saved as AVI files. Four phases of a vibration cycle were selected (maximal and minimal displacements of the vocal folds, or other laryngeal structures, and two intermediate states) and composed into an image using Corel PhotoPaint 8 software. Sketches outlining borders of the laryngeal structures in their extreme positions were drawn carefully by hand using CorelDraw 8 software. No quantitative analysis of the stroboscopic images was done.

III. RESULTS

A. 100–400 Hz frequency sweep

Frequency response function of the left vocal fold for the 100–400 Hz sweep is shown in Fig. 3(a). Three resonance peaks with maxima at 114, 171, and 241 Hz are clearly pronounced here. The first resonance maximum is 4 Hz higher than the intended phonation frequency 110 Hz. The bandwidth of the first resonance peak was impossible to measure since the maximum was too close to the lower limit

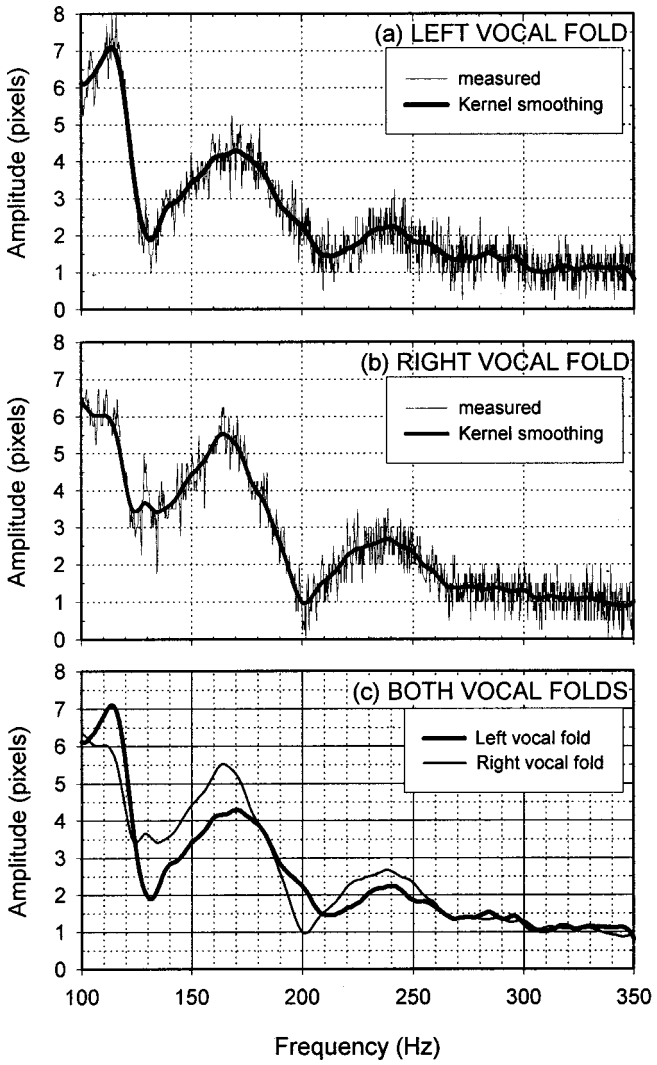

FIG. 3. Frequency response functions of the vocal folds extracted from 250 successive VKG fields representing one 100–400 Hz sweep. Adjustment of the vocal folds corresponds to the phonation frequency of ca. 110 Hz (this reference frequency remains the same for the whole study). (a) Left vocal fold; (b) right vocal fold; (c) smoothed curves for both vocal folds. Three resonance peaks centered near the frequencies of 110, 170, and 240 Hz are visible in the responses. Values above 350 Hz are not plotted since the amplitude of vibration was below the detection level.

frequency of the sweep. The second and third resonance maxima were identified at 171 and 241 Hz with bandwidths of 44 and 45 Hz, respectively.

The response of the right vocal fold is given in Fig. 3(b). It reveals two resonance peaks with central frequencies of 164 and 238 Hz and bandwidths of 37 and 41 Hz, respectively. An increase in the vibration amplitude is evident also around 100 Hz; this resonance falls, however, partially below the low frequency limit of 100 Hz and therefore its central frequency and bandwidth cannot be identified. Smoothed frequency response functions of the vocal folds are set side by side in Fig. 3(c). The measured resonance frequencies (F_r) and bandwidths (ΔF_r) of both the vocal folds are summarized in Table I.

B. 50–200 Hz frequency sweep

In order to find out the dynamic characteristics of the vocal folds below 100 Hz, the data from the 50–200 Hz

TABLE I. Resonance frequencies and half-power (3-dB) bandwidths of the vocal folds evaluated from 250 successive VKG fields representing one 100–400 Hz sweep.

Intended phonation frequency $F_0 = 110$ Hz	Resonance frequency F_r (Hz)	Bandwidth ΔF_r (Hz)
Left vocal fold		
1st resonance	114	unidentifiable
2nd resonance	171	44
3rd resonance	241	45
Right vocal fold		
1st resonance	<100	unidentifiable
2nd resonance	164	37
3rd resonance	238	41

frequency sweep were analyzed. Smoothed frequency response functions of both the vocal folds for this sweep are shown in Fig. 4. Large left–right asymmetry is evident in the graph. The left vocal fold exhibits two distinct resonance peaks around the central frequencies of 77 and 104 Hz. The right vocal fold shows a weak maximum at 58 Hz and a strong resonance peak with two local maxima at 92 and 100 Hz. Bandwidths of these resonance peaks were not measured due to their nontrivial shape. A local minimum, suggesting an antiresonance, is found in the right vocal fold at the frequency of 75 Hz.

The second resonance peak in both the vocal folds observed in Fig. 4 corresponds to the first resonance peak found in Fig. 3 in the previously described 100–400 Hz sweep. The resonance frequencies from these two measurements are close, but not identical (the observed difference in the left vocal fold is 10 Hz), which may suggest that the vocal folds were adjusted slightly differently during the two measurements.

Besides the vocal folds also ventricular folds clearly responded to the external excitation (Fig. 5). Maximal vibration amplitudes of the ventricular folds were more than twice as large as those of the vocal folds within this frequency range. Maxima were identified at 67 and 72 Hz for the left

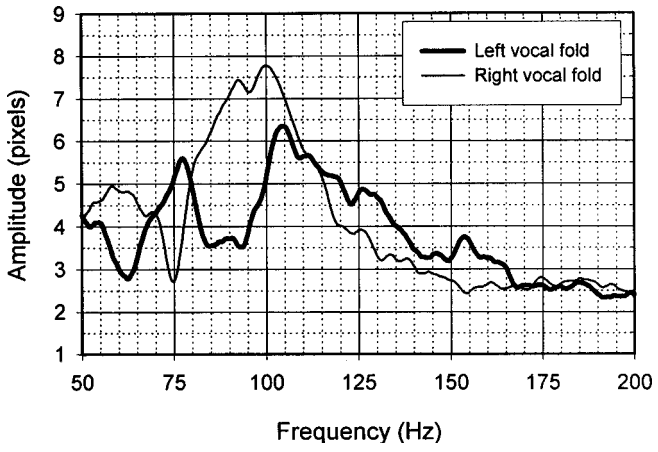

FIG. 4. Frequency response functions of the vocal folds extracted from 250 successive VKG fields representing one 50–200 Hz sweep (after Kernel smoothing). Maximum response of the vocal folds is located around 100 Hz; below this frequency there are large left–right differences. Amplitude of the shaker was reduced here with respect to the measurement shown in Fig. 3.

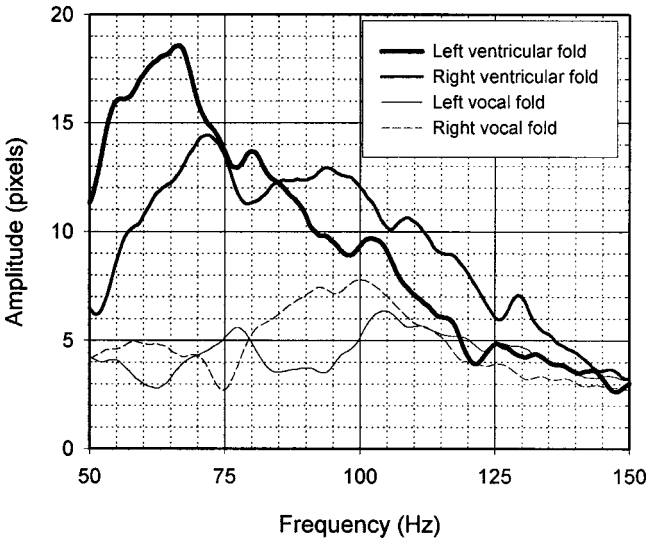

FIG. 5. Frequency response functions of the ventricular folds extracted from the same images as used in Fig. 4 (after Kernel smoothing). Maximal responses of the ventricular folds appear around 70 Hz. Responses of the vocal folds (identical to those in Fig. 4) are also shown, for comparison.

and right ventricular fold, respectively. Figure 5 reveals local maxima also at 80, 105, and 125 Hz (left) and 94, 108, and 129 Hz (right); these resonance peaks are relatively weak, however. The resonance frequencies of the vocal folds and ventricular folds identified from the 50–200 sweep are summarized in Table II.

C. Laryngostroboscopy

Laryngostroboscopic investigation was used to find out the vibration shapes of the vocal folds during the external excitation at distinct frequencies in order to distinguish the resonance modes of vibration. A laryngostroboscopic image of the studied vocal folds in the neutral phonatory position is presented in Fig. 2(a); its sketch is given in Fig. 2(c). The larynx appeared generally normal, it differed slightly from an ideal laryngeal outlook in two features: (1) there was a slight left–right asymmetry, especially in the position of the arytenoid cartilages [this finding may not be considered unusual, however, since some degree of asymmetry is observed practically in all larynges (Hirano *et al.*, 1989; Lind-

TABLE II. Resonance frequencies of the vocal folds and ventricular folds evaluated from 250 successive VKG fields representing one 50–200 Hz sweep.

Intended phonation frequency $F_0 = 110$ Hz Resonance frequency F_r (Hz)		Note
Left vocal fold		–
lower resonance	77	–
higher resonance	104	asymmetric peak
Right vocal fold		
lower resonance	62	weak
higher resonance	92, 100	double peak
Left ventricular fold	67	asymmetric peak
Right ventricular fold	72	asymmetric peak

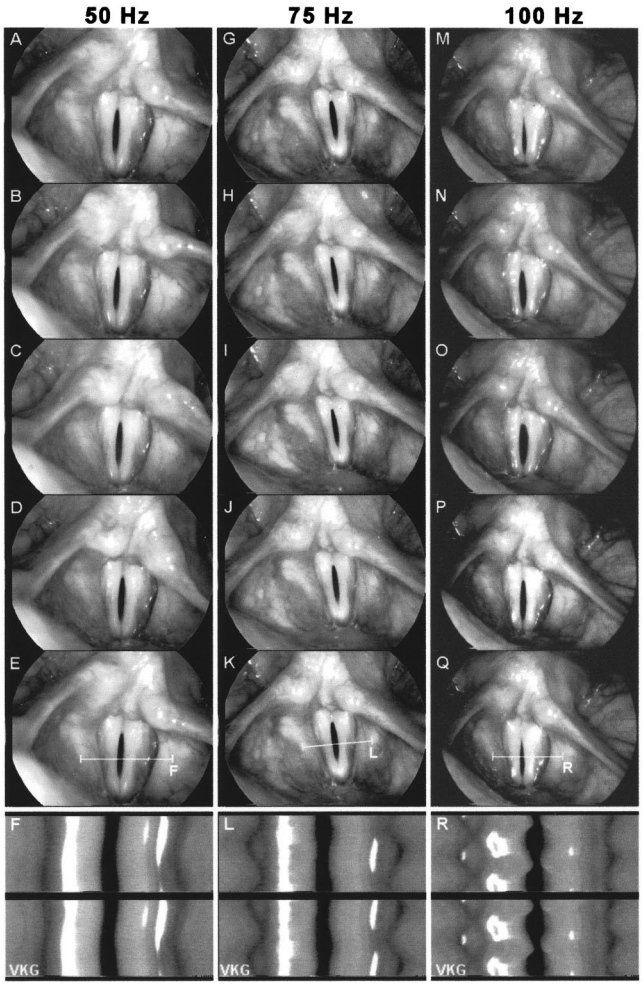

FIG. 6. Series of laryngostroboscopic images of the externally excited laryngeal vibrations at the frequencies of 50, 75, and 100 Hz. Five successive phases of the vibration cycle are shown; images A and E, G and K, and M and Q represent the same phase at the beginning and the end of the stroboscopic cycle. Videokymographic images at the bottom (F,L,R) show vibration of the laryngeal structures at the positions marked in the images E, K, and Q. Oscillations of the aryepiglottic folds and arytenoid cartillages are dominant at 50 (A–E) and 75 Hz (G–K), the VKG image L reveals also large oscillations of the ventricular folds at 75 Hz. Opening–closing response of the vocal folds is apparent at 100 Hz (M–O). (See the sketches in Fig. 7.)

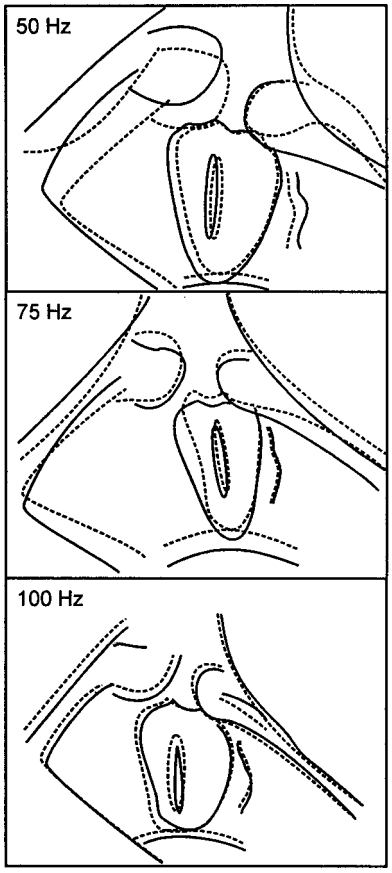

FIG. 7. Sketches showing positions of the laryngeal structures at two opposite phases of the vibratory cycle at 50, 75, and 100 Hz (solid versus dashed lines, extracted from images A and C, G and I, M and O in Fig. 6, respectively). Large amplitudes of vibration of the aryepiglottic folds and arytenoid cartilages are evident at 50 Hz (top), these amplitudes successively decrease with increasing the external driving frequency to 75 (middle) and 100 Hz (bottom). Large amplitude of the left ventricular fold can be observed at 75 Hz. An evident response of the vocal folds—the opening–closing motion—can be seen at 100 Hz.

estad, 1997)]; (2) the vocal folds were slightly bowed, thus the glottis remained slightly open in the neutral phonatory position. For the purpose of this study, the bowing was not considered as an impediment but rather an advantage since it eliminated the collision between the vocal folds that would otherwise perturb their oscillations. Sequences of laryngostroboscopic images at frequencies 50, 75, 100, 110, 175, and 250 Hz are presented in Figs. 6 and 8, sketches extracting the oscillation of the laryngeal tissues from these images are given in Figs. 7 and 9.

Excitation at 50 Hz: At this frequency, large oscillations of the laryngeal collar, especially the aryepiglottic folds and arytenoid cartilages, were visually dominant in the stroboscopic view [Figs. 6(A)–(F), Fig. 7 top]. Vocal folds oscillated as a unit with other laryngeal structures. Left–right and anterior–posterior phase differences in oscillation were visible among the laryngeal structures; no analysis of these phase shifts was done, however.

Excitation at 75 Hz: Oscillations of the arytenoid and aryepiglottic folds were dominant at this frequency, their amplitudes were, however, smaller compared to the frequency of 50 Hz [Figs. 6(G)–(L), Fig. 7 middle]. Ventricular folds (or, more accurately, the spatial distance between the medial borders of the ventricular folds) exhibited large vibrations [this is partially obscured in the stroboscopic images; VKG image in Fig. 6(L) reveals the large amplitude of the ventricular folds more clearly]. Oscillation of the left vocal fold was noticed in VKG; its vibration amplitude was small with respect to the amplitudes of the ventricular folds [Fig. 6(L)], arytenoid cartilages, and aryepiglottic folds. In the stroboscopic view [Figs. 6(G)–(K)], the right anterior part of the larynx appeared slightly squeezed, presumably due to slightly asymmetrical placement of the shaker on the neck.

Excitation at 100 Hz: At this frequency (only 10 Hz lower than the reference phonation frequency) the vocal folds responded by a clear opening–closing movement [Figs. 6(M)–(R), Fig. 7 bottom]. Amplitudes of vibration of the arytenoid cartilages, aryepiglottic folds, and ventricular folds were smaller compared to the excitation at 75 Hz.

Excitation at 110 Hz: Excitation frequency matched the reference phonation frequency here. A clear opening–closing

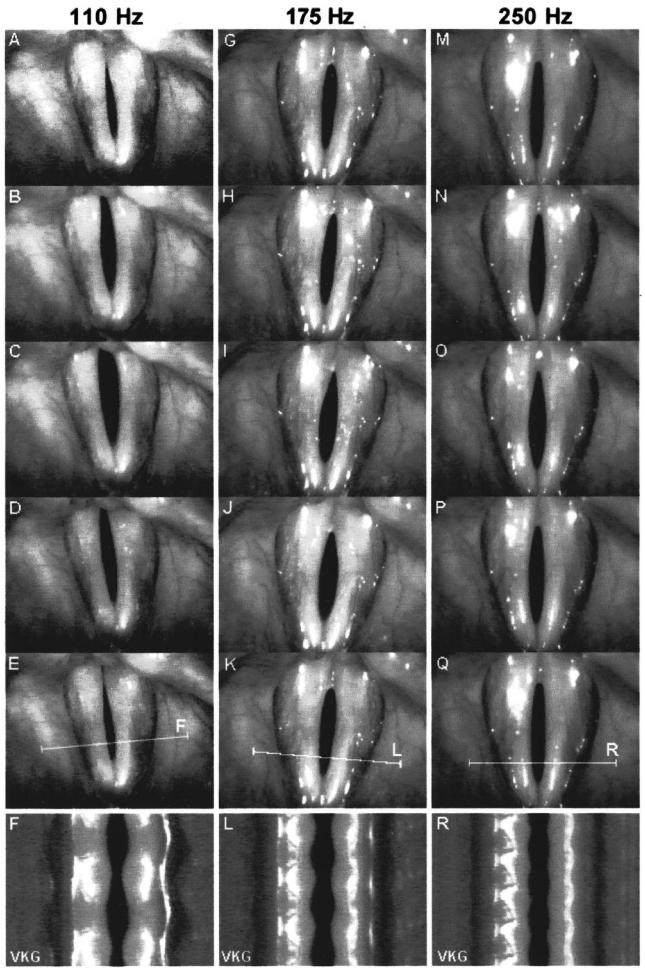

FIG. 8. Series of laryngostroboscopic images of the externally excited vocal fold vibrations at the frequencies of 110, 175, and 250 Hz. The stroboscopic and VKG images are selected and organized analogously to Fig. 6. (See the sketches in Fig. 9 for more details.)

movement of the vocal folds was dominant in the larynx [Figs. 8(A)–(F), Fig. 9 left]. Oscillations of the laryngeal collar were of relatively small amplitude and are not shown here.

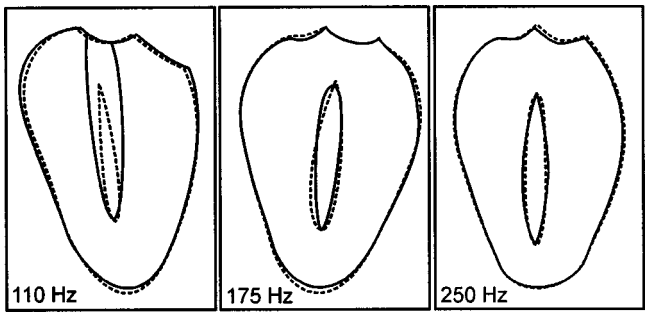

FIG. 9. Sketches illustrating the vibration shapes of the vocal folds at two opposite phases of the vibratory cycle at 110, 175, and 250 Hz (solid versus dashed lines, extracted from images A and C, G and I, and M and O in Fig. 8, respectively). These vibration shapes represent the resonance mode shapes associated with the first three resonance frequencies of the vocal folds. 110 Hz: opening–closing (x-1) mode; 175 Hz: anterior and posterior halves of the glottis oscillate with opposite phases (x-2 mode); 250 Hz: middle third of the glottis oscillates at an opposite phase to the anterior and posterior thirds (x-3 mode).

Excitation at 175 Hz: Here, the external frequency was very close to the second resonance frequency of the vocal folds (in accordance with Fig. 3). The vocal folds responded with lateral-medial oscillations encompassing two half-wavelengths along the glottal length–anterior and posterior parts of the glottis oscillated with opposite phases [Figs. 8(G)–(L), Fig. 9 middle].

Excitation at 250 Hz: Here, the external frequency was close to the third resonance frequency of the vocal folds (in accordance with Fig. 3). Despite the small amplitude of the vibration it was possible to identify response in the vocal folds showing lateral-medial oscillations encompassing three half-wavelengths along the glottal length–middle part of the glottis oscillated in an opposite phase to the anterior and posterior parts [Figs. 8(M)–(Q), Fig. 9 right].

IV. DISCUSSION

The results bring an encouraging message: principally, it is possible to use laryngoscopy for obtaining more detailed information on dynamic characteristics of the vocal folds. Three distinct resonance frequencies of the vocal folds were found around 110, 170, and 240 Hz. The first resonance frequency around 110 Hz corresponded to the frequency of phonation. The resonance frequencies were found to be associated with different modes of vibration of the vocal folds. Figure 9 reveals the associated resonance mode shapes as seen in the laryngoscopic view; these three mode shapes can be designated as modes x-1, x-2, and x-3, respectively (1, 2, 3 meaning the number of the half-wavelengths along the longitudinal axis of the vocal folds).

The resonance frequencies show an interesting relationship: it can be seen from the results in Table I, particularly in the case of the left vocal fold, that the relationship of the resonance frequencies F_{r1}:F_{r2} (114:171 Hz) is exactly 2:3, the relationship F_{r1}:F_{r2}:F_{r3} (114:171:241 Hz) is close to 2:3:4. Theoretically, if all the modes associated with these resonance frequencies would be excited simultaneously during phonation, a complex vocal fold vibration with a resulting subharmonic frequency of $F_{r1}/2$ (57 Hz) would be produced. This finding might be related to an $F_0/2$ subharmonic phonation which was found in the same subject when phonating with slightly abducted vocal folds at high airflow volume velocities. The complex vibration pattern of the vocal folds typical for this phonation was described in detail in our previous study (Švec *et al.*, 1996). The 2:3:4 relationship is, however, suspected to be not a general but rather specific feature of the vocal folds investigated here, since the phonatory maneuver of Švec *et al.* (1996) was found to lead to the $F_0/2$ subharmonic phonation not in every subject.

The laryngoscopic findings do not support the hypothesis of Ishizaka (1988) that the x-11 mode is related to the second resonance frequency of the vocal folds; it was rather the x-2 mode which was found to play the role here. The out-of-phase oscillations of the upper and lower margins of the vocal folds, typical of the x-11 mode, were not distinguished in the present study since the lower margin remained hidden in the laryngoscopic view and it was impossible to detect its movement. For the same reason, it was impossible to clearly specify whether the x-10 or the x-11 mode (or

their combination) is responsible for the first resonance peak. The recent analysis of Berry (in press) suggests that all the modes from the x-1 class (x-10, x-11, x-12, etc.) cluster into a joint resonance peak which makes them practically undistinguishable in the laryngoscopic view. This result would correspond with our difficulties with distinguishing these modes.

Certain discrepancies were found in our data between the 50–200 Hz and 100–400 Hz sweeps. The responses of the vocal folds were expected to be similar in the overlapping range 100–200 Hz. Comparison of Fig. 3(c) and Fig. 4 reveals clear differences in this range, however: the first resonance frequency F_{r1} in the 100–400 Hz sweep is slightly higher than the corresponding resonance frequency measured in the 50–200 Hz sweep (114 vs. 104 Hz, respectively, was measured on the left focal fold). This suggests that the vocal folds might have been tuned slightly differently in these two measurements.

Another and more serious discrepancy is that the resonance peak around 170 Hz, which is clearly pronounced in both the vocal folds in the 100–400 Hz response curve [Fig. 3(c)], is not present in the 50–200 Hz response of the vocal folds (Fig. 4). This discrepancy might be attributed to at least two factors. First, the amplitude of the vibrations of the shaker, which was reduced in the 50–200 Hz sweep, might have been too small to excite the vibration of the vocal folds at this resonance frequency to a laryngoscopically detectable level. Second, an even more plausible origin of this discrepancy might be due to slightly different measurement position used for the two VKG investigations. Whereas in the 50–200 Hz sweep the VKG measurement position was close to the middle of the glottis (Fig. 6, images E, K, Q), which is the nodal point of the x-2 mode at which the amplitude is minimal, in the 100–400 Hz sweep the measurement line was placed in a more anterior part of the glottis (Fig. 8, images E,K,Q) where the amplitude of the x-2 mode is maximal. Such sensitivity of the results to the VKG measurement position is one of the pitfalls of the VKG method used here. A more complete list of the potential complications and pitfalls is given in the Appendix.

Not only the vocal folds but also other laryngeal structures apparently responded to the vibrations applied externally on the neck. Below 100 Hz, the amplitude of vibration of the vocal folds was much smaller than that of the ventricular folds (their resonance frequency was identified to be close to 70 Hz; see Table II) as well as the aryepiglottic folds and arytenoid cartilages (their resonance frequency is suspected to be close to 50 Hz in this experiment). Different parts of the larynx thus appear to be tuned to different resonance frequencies. The resonance and antiresonance peaks of the vocal folds found below 100 Hz (Fig. 4) are suspected to have the origin in an interaction of the vocal-fold vibration with the vibration of the adjacent laryngeal structures. The large left–right asymmetry in the vocal fold response below 100 Hz (Fig. 4) is assumed to be related to the clear asymmetry of the laryngeal structures shown in Fig. 2(a).

In future studies it is important to investigate the dynamic characteristics of the vocal folds at various frequencies of phonation and in more subjects. More detailed information on dynamic characteristics of the other laryngeal structures, like, e.g., the ventricular folds, could also be helpful since these structures contribute to phonation in certain singing styles (Fuks *et al.*, 1998; Lindestad and Södersten, 1999) or in patients with voice disorders (Kruse, 1981; von Doersten *et al.*, 1992; Schutte *et al.*, 1998; Švec *et al.*, 1997, 1999). For a more extensive analysis, however, it is desirable to employ automated or semi-automated image detection (Wittenberg, 1997, 1998; Saadah *et al.*, 1998; Larsson *et al.*, 1999) instead of manual analysis of the images which is exceedingly time consuming. Certain other questions remain to be answered, e.g., whether the direction of the frequency sweep does not influence the observed resonance properties. In general, however, the method presented here appears useful and promising for studying the dynamic characteristics of the larynx.

ACKNOWLEDGMENTS

The paper was presented to the 2nd International Conference on Voice Physiology and Biomechanics, March 12–14, 1999, Berlin, Germany. The authors are grateful to the Sound Studio of the Academy of Performing Arts in Prague for providing us with a part of the equipment needed for the experiment. The research has been supported by the Grant Agency of the Czech Republic (GA ČR), project no. 109/98/K019.

APPENDIX: GENERAL COMPLICATIONS AND PITFALLS OF THE METHOD PRESENTED

A. Vocal folds and the Kaneko maneuver

(1) Vocal fold tuning: There is no control of the vocal fold tuning in the neutral phonatory position, thus it is not certain that the tension of the vocal folds remains the same as compared to the actual phonation. The difference in the tension may result in a change of the dynamic characteristics. The accuracy of the Kaneko maneuver in living subjects remains to be specified in this respect.

(2) Degree of adduction: Investigated subject might tend either to abduct (open) or to hyperadduct (press together) the vocal folds during the neutral phonatory position while holding the breath. In order to avoid this tendency, laryngoscopic view was monitored and provided as a feedback to the experimental subject as well as to the examiner. The Kaneko maneuver and the neutral phonatory position were judged correct if the vocal folds were kept essentially in the same position as they were during the preceding phonation.

(3) Airflow: Even a small amount of glottal flow might influence behavior of the vocal folds, thus the glottal flow shall be avoided when the vocal folds are in the neutral phonatory position. Small airflow velocities are, however, difficult to perceive by the examined subject when the shaker vibrations are applied onto the neck. In our case, the far-from-sinusoidal vibration pattern of the vocal folds seen in the videokymogram R in Fig. 6 with an indication of a shear movement of the vocal folds and the occurrence of mucosal waves leads us to suspect that some glottal flow might have

distorted the externally (sinusoidally) excited vibrations at that particular moment during the VKG examination.

B. Laryngoscopy

An important aspect is the constant measurement position during VKG examination. The difference in the VKG measurement position is suspected to be the main origin of the discrepancies found between the two sweeps. A full-image high-speed video recording system would be an alternative which would allow to select the proper measurement position after the examination as well as to correct the measuring position in case of some unpredictable motion (of the endoscope or of the examined subject) during the examination (Wittenberg *et al.*, 1995; Wittenberg, 1998; Larsson *et al.*, 1999).

Another problem is that the laryngoscopic view does not allow to reliably identify vertical movements of the vocal folds and distinguish, e.g., the x-10 versus x-11 mode, or the theoretically described z-modes of the vocal folds (Berry *et al.*, 1994; Berry and Titze, 1996). Also, a good laryngoscopic view of the larynx and tolerance of the endoscope might be problematic in some subjects.

C. Shaker

For safety reasons, it is not recommended to fix the shaker to the living larynx. Due to this, the contact force as well as the position of the shaker on the neck may vary slightly (laterally or vertically) which could alter the excitation force acting on the vocal folds. The variation of the contact force was suppressed here by monitoring its value and using it as a feedback. The shaker placement is assumed not critical for investigating the dynamic characteristics of the vocal folds: Kaneko *et al.* (1981) reported no significant differences in the resonance properties of the vocal folds when the position of the shaker on the larynx was varied.

At constant excitation force, the amplitude of vibrations of the shaker is inversely proportional to the second power of frequency. This leads to excessive vibration amplitudes at low frequencies and small displacement amplitudes at high frequencies. Therefore two different sweeps were used in the present study. The highest possible excitation force was used for the 100–400 Hz sweep in order to achieve maximal oscillatory response in the laryngeal tissues. For the 50–200 Hz sweep, the input power of the shaker was reduced otherwise the excessive shaker amplitudes at low frequencies (excursions of ca. ± 3 mm at 50 Hz) caused uncomfortable sensations in the subject. It appears desirable to compensate for this phenomenon in future studies.

[1]In the x-ij notation, ''x'' designates oscillations in the lateral-medial direction and the i,j indices give number of oscillatory half-wavelengths occurring along the horizontal and vertical dimensions of the vocal folds (i.e., length and thickness), respectively. For a more detailed description and examples see, e.g., Titze and Strong (1975); Titze (1994); Berry *et al.* (1994); Berry and Titze (1996); Berry (in press).

Anderson, R. A. (**1967**). *Fundamentals of Vibrations* (Macmillan, New York).

Berry, D. A. (**in press**). ''Toward mechanisms of non-modal phonation,'' J. Phonetics.

Berry, D. A., and Titze, I. R. (**1996**). ''Normal modes in a continuum model of vocal fold tissues,'' J. Acoust. Soc. Am. **100**, 3345–3354.

Berry, D. A., Herzel, H., Titze, I. R., and Krischer, K. (**1994**). ''Interpretation of biomechanical simulations of normal and chaotic vocal fold oscillation with empirical eigenfunctions,'' J. Acoust. Soc. Am. **95**, 3595–3604.

Dedouch, K., Vampola, T., and Švec, J. (**1999**). ''Analýza vlivu délky kmitající části hlasivky na změnu modálnich vlastností hlasivky [Influence of the length change on modal properties of the vocal fold tissues],'' in *15th Conference COMPUTATIONAL MECHANICS '99, October 18–20, 1999, Nečtiny, Czech Republic*, edited by J. Křen (University of West Bohemia, Pilsen), pp. 39–46.

von Doersten, P. G., Izdebski, K., Ross, J. C., and Cruz, R. M. (**1992**). ''Ventricular dysphonia: a profile of 40 cases,'' Laryngoscope **102**, 1296–301.

Fletcher, N. H. (**1996**). ''Nonlinearity, complexity, and control in vocal systems,'' in *Vocal Fold Physiology: Controlling Complexity and Chaos*, edited by P. J. Davis and N. H. Fletcher (Singular Publishing Group, San Diego, CA), pp. 3–16.

Fuks, L., Hammarberg, B., and Sundberg, J. (**1998**). ''A self-sustained vocal-ventricular phonation mode: Acoustical, aerodynamic and glottographic evidences,'' TMH-QPSR **3/1998**, 49–59.

Fukuda, H. (**1993**). ''Fundamental study on vocal fold vibration and its clinical application,'' Ann. Bull. Res. Inst. of Logopedics and Phoniatrics, University of Tokyo **27**, 89–102.

Fukuda, H., Muta, H., Kanou, S., Takayama, E., Fujioka, T., Kawaida, M., Tatehara, T., and Saito, S. (**1987**). ''Response of vocal folds to externally induced vibrations: basic study and its clinical application,'' in *Laryngeal Function in Phonation and Respiration*, edited by T. Baer, C. Sasaki, and K. S. Harris (College-Hill/Little, Brown, Boston), pp. 366–377.

Herlufsen, H. (**1984**). ''Dual channel FFT analysis (Part II),'' Brüel & Kjaer Technical Review No. 2.

Hirano, M., and Bless, D. M. (**1993**). *Videostroboscopic Examination of the Larynx* (Singular Publishing Group, San Diego, CA).

Hirano, M., Yukizano, K., Kurita, S., and Hibi, S. (**1989**). ''Asymmetry of the laryngeal framework: a morphologic study of the cadaver larynges,'' Ann. Otol. Rhinol. Laryngol. **98**, 135–140.

Ishizaka, K. (**1988**). ''Significance of Kaneko's measurement of natural frequencies of the vocal folds,'' in *Vocal Folds Physiology, Vol. 2: Voice Production Mechanisms and Functions*, edited by O. Fujimura (Raven, New York), pp. 181–190.

Ishizaka, K., and Flanagan, J. L. (**1972**). ''Synthesis of voiced sounds from a two-mass model of the vocal cords,'' Bell Syst. Tech. J. **51**, 1233–1268.

Jiang, J. J., Diaz, C. E., and Hanson, D. G. (**1998**). ''Finite element modeling of vocal fold vibration in normal phonation and hyperfunctional dysphonia—Implications for the pathogenesis of vocal nodules,'' Ann. Otol. Rhinol. Laryngol. **107**, 603–610.

Kaneko, T., Masuda, T., Shimada, A., Suzuki, H., Hayasaki, K., and Komatsu, K. (**1987**). ''Resonance characteristics of the human vocal fold in vivo and in vitro by an impulse excitation,'' in *Laryngeal Function in Phonation and Respiration*, edited by T. Baer, C. Sasaki, and K. S. Harris (College-Hill/Little, Brown, Boston), pp. 349–365.

Kaneko, T., Komatsu, K., Suzuki, H., Kanesaka, T., Masuda, T., Numata, T., and Naito, J. (**1983**). ''Mechanical properties of the human vocal fold—Resonance characteristics in living humans and in excised larynges,'' in *Vocal Fold Physiology: Biomechanics, Acoustics and Phonatory Control*, edited by I. R. Titze and R. C. Scherer (The Denver Center for the Performing Arts, Denver, CO), pp. 304–317.

Kaneko, T., Uchida, K., Suzuki, H., Komatsu, K., Kanesaka, T., Kobayashi, N., and Naito, J. (**1981**). ''Mechanical properties of the vocal fold: measurement *in vivo*,'' in *Vocal Fold Physiology*, edited by K. N. Stevens and M. Hirano (University of Tokyo Press, Tokyo), pp. 365–376.

Kruse, E. (**1981**). ''Der Mechanismus der Taschenfaltenstimme. Eine kritische alternative Erwiderung auf die Vorstellungen Réthis,'' Folia Phoniatr. **33**, 294–313.

Larsson, H., Hertegård, S., Lindestad, P.-Å., and Hammarberg, B. (**1999**). ''Vocal fold vibrations: High-speed video imaging, kymography and acoustic analysis,'' Karolinska Institute, Huddinge University Hospital Phoniatric and Logopedic Progress Report **11**, 7–16.

Lindestad, P.-Å. (**1997**). *Laryngeal Asymmetries in Normals, Preliminary Results*, Poster presented at the Pan European Voice Conference PEVOC II, Regensburg, Germany, August 29–31, 1997.

Lindestad, P.-Å., and Södersten, M. (**1999**). ''Voice source characteristics in Mongolian ''throat singing'' studied with high speed imaging technique,

acoustic spectra and inverse filtering,'' Karolinska Institute, Huddinge University Hospital Phoniatric and Logopedic Progress Report **11**, 17–26.
Richardson, M. H. (**1997**). ''Is it a mode shape, or an operating deflection shape?'' Sound Vib. **31**, 54–61.
Saadah, A. K., Galatsanos, N. P., Bless, D., and Ramos, C. A. (**1998**). ''Deformation analysis of the vocal folds from videostroboscopic image sequences of the larynx,'' J. Acoust. Soc. Am. **103**, 3627–3641.
Schutte, H. K., Švec, J. G., and Šram, F. (**1998**). ''First results of clinical application of videokymography,'' Laryngoscope **108**, 1206–1210.
Stevens, K. N. (**1977**). ''Physics of laryngeal behaviour and larynx modes,'' Phonetica **34**, 264–279.
Švec, J. G., and Schutte, H. K. (**1996**). ''Videokymography: High-speed line scanning of vocal fold vibration,'' J. Voice **10**, 201–205.
Švec, J. G., Schutte, H. K., and Miller, D. G. (**1996**). ''A subharmonic vibratory pattern in normal vocal folds,'' J. Speech Hear. Res. **39**, 135–143.
Švec, J. G., Schutte, H. K., and Šram, F. (**1997**). *Introduction to Videokymography (Video tape)* (Medical Healthcom, Prague).
Švec, J. G., Šram, F., and Schutte, H. K. (**1999**). ''Videokymografie: nová vysokofrekvenční metoda vyšetřování kmitů hlasivek [Videokymography: A new high-speed method for the examination of vocal-fold vibrations],'' Otorinolaryngol (Prague) **48**, 155–162.
Tanabe, M., Isshiki, N., and Sawada, M. (**1979**). ''Damping ratio of the vocal cord,'' Folia Phoniatr. **31**, 27–34.
Titze, I. R. (**1976**). ''On the mechanics of vocal-fold vibration,'' J. Acoust. Soc. Am. **60**, 1366–1380.
Titze, I. R. (**1988**). ''The physics of small-amplitude oscillation of the vocal folds,'' J. Acoust. Soc. Am. **83**, 1536–1552.
Titze, I. R. (**1994**). *Principles of Voice Production* (Prentice-Hall, Englewood Cliffs, NJ).
Titze, I. R., and Strong, W. (**1975**). ''Normal modes in vocal fold tissues,'' J. Acoust. Soc. Am. **57**, 736–744.
Vaněk, F., and Cibulka, J. (**1994**). ''Křemíkové tenzometrické čidlo síly [Silicon force sensor],'' in *Proceedings of the Colloquium Dynamics of Machines '94, Prague, April 11–13, 1994* (Institute of Thermomechanics of the Academy of Sciences of the Czech Republic, Prague), pp. 97–100.
Wittenberg, T. (**1997**). ''Automatic motion extraction from laryngeal kymograms,'' in *Advances in Quantitative Laryngoscopy. Proceedings of the 2nd 'Round Table' Advances in Quantitative Laryngoscopy using Motion-, Image- and Signal Analysis, Erlangen, 1997*, edited by T. Wittenberg, P. Mergell, M. Tigges, and U. Eysholdt (Abteilung Phoniatrie, Universitäts-HNO-Klinik Göttingen, Germany), pp. 21–28.
Wittenberg, T. (**1998**). ''Wissenbasierte Bewegungsanalyse von Stimmlippenschwingungen anhand digitaler Hochgeschwindigkeitsaufnahmen,'' Doctoral dissertation (Shaker Verlag, Aachen, Germany).
Wittenberg, T., Moser, M., Tigges, M., and Eysholdt, U. (**1995**). ''Recording, processing, and analysis of digital high-speed sequences in glottography,'' Mach. Vision Appl. **8**, 399–404.

Time normalization of voice signals using functional data analysis

Jorge C. Lucero[a)]
Department of Mathematics, University of Brasilia, Brasilia DF 70910-900, Brazil

Laura L. Koenig[b)]
Haskins Laboratories, 270 Crown Street, New Haven, Connecticut 06511 and Long Island University, Brooklyn, New York 11201-8423

(Received 6 October 1999; accepted for publication 28 March 2000)

The harmonics-to-noise ratio (HNR) has been used to quantify the waveform irregularity of voice signals [Yumoto *et al.*, J. Acoust. Soc. Am. **71**, 1544–1550 (1982)]. This measure assumes that the signal consists of two components: a harmonic component, which is the common pattern that repeats from cycle-to-cycle, and an additive noise component, which produces the cycle-to-cycle irregularity. It has been shown [J. Qi, J. Acoust. Soc. Am. **92**, 2569–2576 (1992)] that a valid computation of the HNR requires a nonlinear time normalization of the cycle wavelets to remove phase differences between them. This paper shows the application of functional data analysis to perform an optimal nonlinear normalization and compute the HNR of voice signals. Results obtained for the same signals using zero-padding, linear normalization, and dynamic programming algorithms are presented for comparison. Functional data analysis offers certain advantages over other approaches: it preserves meaningful features of signal shape, produces differentiable results, and allows flexibility in selecting the optimization criteria for the wavelet alignment. An extension of the technique for the time normalization of simultaneous voice signals (such as acoustic, EGG, and airflow signals) is also shown. The general purpose of this article is to illustrate the potential of functional data analysis as a powerful analytical tool for studying aspects of the voice production process. © *2000 Acoustical Society of America.* [S0001-4966(00)00310-6]

PACS numbers: 43.70.Aj, 43.70.Dn, 43.70.Gr, 43.72.Lc [AL]

I. INTRODUCTION

This paper deals with the problem of quantifying the irregularity in the waveform of a voice signal. It has long been known that measures of irregularity in the time and/or amplitude domain may differentiate normal from abnormal voice qualities, with the pathological samples showing more extreme measures of irregularity than the normal samples (Lieberman, 1962; Titze, 1994a). Thus accurate measures of waveform irregularity could be used as a noninvasive technique for voice evaluation and diagnosis.

As pointed out by Qi (1992), computing such measures of waveform irregularity presents the difficulty that an infinite amount of information is involved, in contrast to, e.g., measures of fundamental frequency irregularity (jitter) which deal with a single parameter. The simplest approach is to compute the variability on the maximum amplitude of each period (wavelet) of the signal. However, this measure has limitations since it misses information at other points of the wavelets. It is easy to see that wavelets of different shapes but the same maximum amplitude would produce a zero measure of irregularity by such an approach.

As an improved measure, the harmonics-to-noise ratio (HNR; Yumoto *et al.*, 1982) was proposed, in which the whole wavelet is used in the computation. The HNR assumes that the signal consists of two components: a harmonic component which is the periodic pattern that repeats through all the wavelets, and an additive noise component which produces wavelet irregularity. In the cited work, the harmonic component was computed as the average of the wavelets, and the noise component as the difference of the wavelets to their average. Since the wavelets have different lengths due to jitter, they were normalized in time by zero padding (i.e., filling with zeroes) each wavelet to the longest period, so that they could be compared on a point-by-point basis.

Qi (1992) showed the limitations of the zero-padding normalization: since the wavelets differ in length, a large portion of the computed noise will be caused by the length irregularity. Thus voices with high values of jitter will necessarily produce low values of the HNR, so that the HNR in such cases does not provide an accurate indication of general waveform irregularity. A first solution to this problem would be a linear expansion or compression of all wavelets to a common length. However, phase differences between wavelets would remain, which would also contaminate the computed HNR. To illustrate this problem, a simple case of two wavelets is shown in Fig. 1. In each plot, the broken line is the computed average. In the case of zero-padding normalization (Fig. 1, top), the average clearly does not resemble either of the wavelets. It also has a point of discontinuity at the start of the zero-padding region. With linear normalization (Fig. 1, middle), a better continuous average is obtained, although its shape is still different from those of the wavelets. To obtain a better average, phase differences between the wavelets should be removed. A more accurate computa-

[a)]Electronic mail: lucero@mat.unb.br
[b)]Electronic mail: koenig@haskins.yale.edu

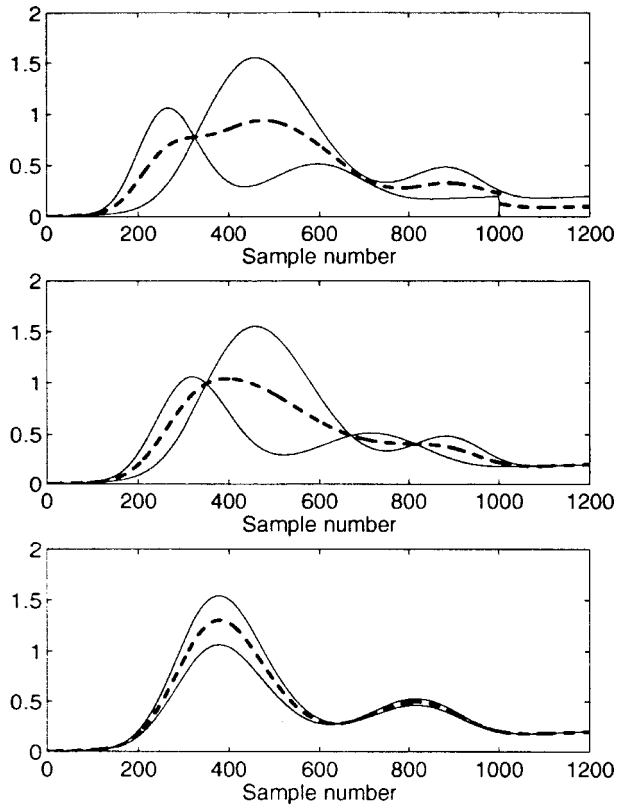

FIG. 1. Methods of temporal normalization applied to the extraction of the average (dashed line) of two wavelets. Top: zero padding. Middle: linear normalization. Bottom: nonlinear normalization.

tion of the wavelet average and the HNR requires a nonlinear expansion or compression of the wavelets in time, so that their shapes become aligned (Fig. 1, bottom). Only in this case may the average be considered as the common pattern of the wavelets. To accomplish an optimal wavelet alignment, Qi (1992) applied a dynamic programming algorithm. In later works (Qi *et al.*, 1995; Qi and Hillman, 1997), unconstrained dynamic programming and zero phase transformation were used for the alignment. The zero phase transformation simply removes all phase-related information from the wavelets prior to computation of the HNR; however, this approach produced in general poorer measures of waveform irregularity than nonlinear normalization, according to tests using synthetic signals (Qi *et al.*, 1995).

A similar issue has been recently discussed in the case of speech movement signals (Lucero *et al.*, 1997). In that work, three techniques for extracting the average of a set of speech wavelets were considered, namely: un-normalized averaging (equivalent to zero padding, Fig. 1, top), linearly normalized averaging (as in Fig. 1, middle), and nonlinearly normalized averaging (as in Fig. 1, bottom). To achieve the nonlinearly normalized average, a new algorithm based on functional data analysis (FDA; Ramsay, 1998; Ramsay *et al.*, 1996; Ramsay and Li, 1998; Ramsay and Silverman, 1997) was introduced. It was argued that this algorithm has advantages over previous dynamic programming because the results are smooth and differentiable (thus allowing for further processing), it does not require users to select one of the wavelets as a reference or template for the alignment, and different optimization criteria may be adopted according to the application.

This work will show the application of the FDA nonlinear normalization technique to extract averages and compute the HNR of voice signals. Results obtained for the same signals using zero-padding, linear normalization, and dynamic programming algorithms will also be presented for comparison. Our general purpose is to illustrate the potential of FDA as a powerful analytical tool for studying aspects of the voice production process.

II. MEASUREMENT OF VOICE SIGNAL IRREGULARITY USING FDA

A. Nonlinear time normalization

FDA has emerged in recent years as a set of analytical tools to explore patterns and variability in sets of data that may be regarded as functional observations (Ramsay and Silverman, 1997). The term functional here means that, although the data may be observed and recorded discretely, they may be described by some function of time. A single functional observation z consists of a finite set of pairs (t_j, z_j), where z_j is the measured jth sample of z at time t_j. In FDA, the existence of an underlying function $y(t)$ is postulated, such that

$$z_j = y(t_j) + \epsilon_j, \tag{1}$$

where ϵ_j represents an observational error or noise term. A variety of analytical tools may be applied to extract the main characteristics of the functional data set. Such tools may require evaluating such a function $y(t)$ at any particular instant of time, and all its derivatives that exist at such an instant. Two approaches may then be followed: (1) extracting $y(t)$ from the raw data by filtering out the noise (i.e., by smoothing the data), or (2) leaving the noise in the data and requiring smoothness of the results of the analysis. In the present case, smoothing the raw data would eliminate or attenuate the same irregularity we want to assess, so the second approach will be followed. We will align the raw voice wavelets by requiring a smooth expansion or compression of the time scale. We describe briefly the FDA algorithm for nonlinear time normalization. For more details, we refer the reader to the cited references (Lucero *et al.*, 1997; Ramsay, 1998; Ramsay and Li, 1998; Ramsay and Silverman, 1997).

Let us denote the set of wavelets to normalize as $x_i(t)$, where $i=1,...,N$, and N is the number of wavelets. For simplicity, let us assume that all the wavelets have the same length, from $t=0$ to $t=1$. For each wavelet, a strictly increasing and smooth transformation of time $h_i(t)$ (warping function) is determined, such that each normalized wavelet

$$x_i^*(t) = x_i[h_i(t)] \tag{2}$$

is close in some measure to their average

$$\overline{x^*}(t) = \frac{1}{N}\sum_{i=1}^{N} x_i^*(t). \tag{3}$$

Such a transformation is defined as

$$h_i(t) = A \int_0^t e^{\int_0^u w_i(v)dv}\, du, \tag{4}$$

where $w_i(t)$ is the relative curvature of $h_i(t)$ (to be determined optimally), v is an integration variable, and coefficient A is selected so that $h_i(t) = 1$. Given any function $w_i(t)$ such that the integrals in Eq. (4) exist, this equation will produce a strictly increasing and twice differentiable function $h_i(t)$.

Different measures may be used to evaluate the closeness of the normalized records to their average, according to the particular application. Here, the measure

$$F(x_i, w_i, \alpha, \lambda) = \int_0^1 \alpha(t)[x_i^*(t) - \overline{x^*}(t)]^2\, dt + \lambda \int_0^1 w_i^2(t)dt \tag{5}$$

is adopted, where $\alpha(t)$ is a weighting function and λ is a positive constant. The first integral is the classic squared error measure used in dynamic programming algorithms (Qi, 1992; Qi *et al.*, 1995; Qi and Hillman, 1997). The weighting function $\alpha(t)$ may be used to emphasize alignment in particular regions of the wavelets [by setting a larger value of $\alpha(t)$ at those regions]. The second integral incorporates a penalty for the roughness of the warping function, controlled by parameter λ (the larger the value of λ, the smaller the curvature of h_i).

Hence, the problem consists of estimating the curvature functions $w_i(t)$ in Eq. (4) that will minimize the total measure (cost function)

$$C(x_1, \ldots, x_N, w_1, \ldots, w_N, \alpha, \lambda) = \sum_{i=1}^{N} F(x_i, w_i, \alpha, \lambda). \tag{6}$$

This minimization problem may be solved by using an expansion of $\int_0^1 w_i(t)dt$ into a basis of B-spline functions, as described by Ramsay and Silverman (1997) and Lucero *et al.* (1997).

The algorithm assumes that all the wavelets have the same length from 0 to 1. It is possible to modify it to accommodate wavelets of different lengths and time spans. However, it is computationally much simpler to interpolate all wavelets to a common length and attribute to this length an artificial [0, 1] time span before applying the nonlinear normalization. The results should be the same in either case.

After the wavelets have been optimally aligned in time, we extract the normalized average $\overline{x^*}(t)$ and the normalized noise components $x_i^*(t) - \overline{x^*}(t)$, $i = 1, \ldots, N$. We also compute the expression $\Delta h_i(t) = h_i(t) - t$, $i = 1, \ldots, N$, which represents the amount of nonlinear warping or phase shift for each wavelet [if no warping is required, then $h_i(t) = t$ and $\Delta h_i(t) = 0$]. The irregularity of the set of wavelets may then be seen in the above functions or related ones. For example, one may compute the standard deviation of both $x_i^*(t)$ and $h_i(t)$ across the N wavelets, to visualize how the waveform irregularity and phase irregularity are distributed along the wavelet period [0, 1].

B. Extension to simultaneous signals

The above algorithm may be easily extended for simultaneous normalization of sets of signals. When various signals are recorded simultaneously (e.g., acoustic, EGG, oral airflow, and other voice signals), it might be desirable also to normalize them simultaneously, to keep their synchrony in time. Also, simultaneous normalization may be applied to reveal phase relations between the signal sets.

For this case, instead of scalar-valued wavelets, one may consider vector-valued wavelets such as

$$\mathbf{x}_i(t) = [\text{Acoustics}_i(t), \text{EGG}_i(t), \text{Airflow}_i(t), \ldots]^T. \tag{7}$$

The warping functions are still scalar functions, which simultaneously align all the components of the wavelets.

The cost function has now the general expression

$$F(\mathbf{x}_i, w_i, \mathbf{A}, \lambda) = \int_0^1 [\mathbf{x}_i^*(t) - \overline{\mathbf{x}}^*(t)]^T \mathbf{A}(t)[\mathbf{x}_i^*(t) - \overline{\mathbf{x}}^*(t)]dt + \lambda \int_0^1 w_i^2(t)dt, \tag{8}$$

where $\mathbf{A}(t)$ is a matrix of weight functions.

C. Indices of irregularity

We consider here two indices of irregularity. The HNR (Yumoto *et al.*, 1982),

$$\text{HNR} = \frac{N \int_0^1 \overline{x^*}^2(t)dt}{\sum_{i=1}^N \int_0^1 [x_i^*(t) - x^*(t)]^2\, dt} \tag{9}$$

and an index of nonlinear warping (INW), defined as the mean of the root-mean-squared values of warping functions $\Delta h_i(t)$:

$$\text{INW} = \frac{1}{N} \sum_{i=1}^{N} \sqrt{\int_0^1 \Delta h_i(t)dt}. \tag{10}$$

III. EXAMPLES WITH SYNTHETIC SIGNALS

A. Signals

We first applied the above techniques to synthetic signals, in order to determine the relative accuracy of the different approaches. To allow comparison with previous work, we synthesized signals following the equations given by Titze and Liang (1993).

We set the instantaneous frequency of the signals to

$$f_c(t) = f_0(1 + K_f \sin(2\pi f_0 t/10)), \tag{11}$$

where f_0 is the center frequency, and K_f is a parameter for frequency variability. For simplicity, we adopted a sinusoidal frequency modulation instead of a random modulation. The instantaneous phase is

$$\theta(t) = \int_0^t 2\pi f_c(t)dt. \tag{12}$$

The signal is then synthesized as

$$x(t) = y[\theta(t)] + K_a\, \text{Randn}(t), \tag{13}$$

where $y(\theta)$ is a periodic function, K_a is a parameter for amplitude variability of the signal noise, and Randn(t) is a function that generates a random value from a normal distri-

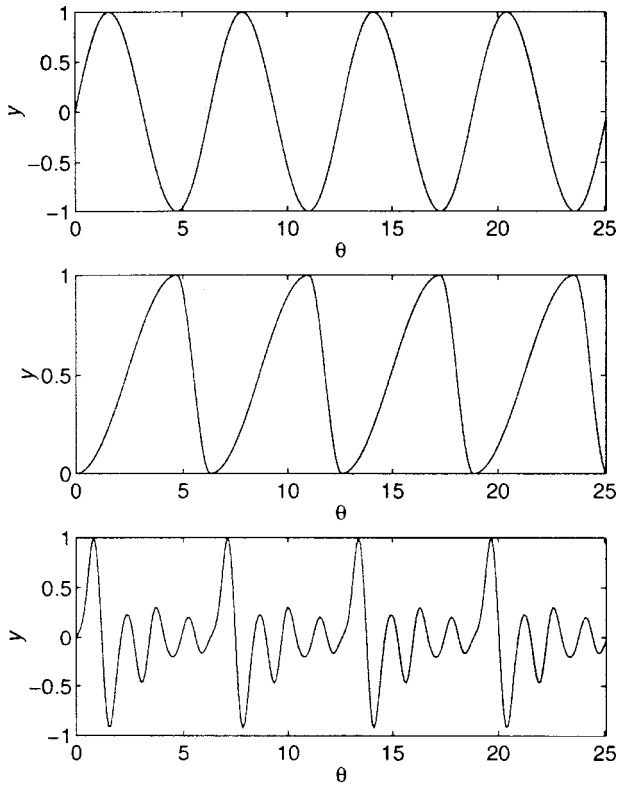

FIG. 2. Synthetic signals used to test the algorithms. Top: sine wave. Middle: EGG analog. Bottom: mouth pressure analog.

bution. We considered various functions for $y(\theta)$: (a) plain sine wave (Fig. 2, top)

$$y(\theta)=\cos(\theta), \tag{14}$$

(b) EGG analog (Fig. 2, middle), using the expression (Titze and Liang, 1993)

$$y(\theta)=\begin{cases} 0.5[1-\cos(2\theta)], & 0\leqslant\theta<\pi/2 \\ 0.5[1-\cos(2\theta/3+2\pi/3)], & \pi/2\leqslant\theta\leqslant 2\pi \end{cases}, \tag{15}$$

and (c) mouth pressure analog (Fig. 2, bottom), using the expression

$$y(\theta)=2.18\sum_{n=0}^{10}\mathrm{Real}(C_n)\cos(n\theta)+\mathrm{Imag}(C_n)\sin(n\theta), \tag{16}$$

where C_n are the coefficients in Table I. These values were obtained by first synthesizing a mouth pressure analog signal using the technique described by Titze and Liang (1993), and then extracting its first 11 Fourier coefficients. Coefficient 2.18 sets its peak amplitude to 1.

B. Processing and results

All the algorithms were implemented in Matlab, and run on a personal computer. Trains of cycles of the three signals were synthesized using a sampling frequency of 10 kHz and center frequency $f_0=150$ Hz. Wide ranges of values for K_a and K_f were considered, from 0 (no irregularity) to $K_a=0.1$ and $K_f=0.6$ (large irregularity, as assessed visually). Twenty individual cycles were then identified as the portions with $2\pi(n-1)\leqslant\theta<2\pi n$, $n=1,...,20$, and arranged as a set of 20 wavelets (this number of wavelets was used to insure statistical validity of the results yet to keep the processing task manageable). Each set of wavelets was then normalized in time applying zero-padding, linear normalization (using cubic spline interpolation; Press *et al.*, 1992), and nonlinear normalization using the above FDA algorithm. For comparison, we also applied the Dynamic Programming algorithm given by Qi (1992). Let us briefly recall that this algorithm computes a warping function by minimizing the total square error (cost) between the aligned wavelet and a template, with higher and lower limits imposed to the warping as constraints. The template is chosen as the wavelet with the minimum total cost compared to all the other wavelets. After aligning all wavelets, the mean total cost is the noise energy [denominator in Eq. (8)] divided by a factor of N.

For FDA normalization, we we set function $\alpha(t)$ in Eq. (5), to a constant value of 1000 (i.e., giving the same weight to alignment along all the wavelet length). The constant value was selected so as to have cost function values in the range 1–100, to facilitate the application of the optimization Matlab routine (BFGS quasi-Newton algorithm; Press *et al.*, 1992) available in its standard toolboxes. The roughness penalty parameter was set at $\lambda=1$. This value was selected by visual inspection of the results, so as to allow alignment of the wavelets without significant waveform distortion.

After the normalizations, we computed the HNR and, in the case of nonlinear normalization with FDA, the index of nonlinear warping (INW). Also, we computed the signal-to-noise ratio of the train of cycles

$$\mathrm{SNR}=\frac{\int_0^T y^2[\theta(t)]dt}{\int_0^T\{x(t)-y[\theta(t)]\}^2\,dt}, \tag{17}$$

where $x(t)$ and $y(t)$ are the signals before and after the addition of noise (amplitude variability), respectively [see Eq. (13)], and T is the train's length. Since the SNR measures the ratio of the energy of the signal without noise to the noise energy, it may be regarded as the ''true'' HNR value. Hence, we consider computed HNRs that are closer to the SNR to be more accurate. Let us remark here that the objective of nonlinear normalization is to obtain an HNR value that is close to the SNR [as defined in Eq. (17)] by aligning the wavelets while keeping their general shape.

TABLE I. Fourier coefficients for Eq. (16).

n	C_n
0	$-0.000\,10+i0$
1	$0.068\,83+i0.011\,02$
2	$0.049\,44-i0.078\,75$
3	$-0.031\,22-i0.095\,82$
4	$-0.170\,36-i0.049\,38$
5	$0.029\,29+i0.073\,95$
6	$0.022\,15+i0.020\,59$
7	$0.034\,19-i0.000\,90$
8	$-0.001\,43-i0.005\,95$
9	$-0.000\,56-i0.001\,16$
10	$-0.000\,24-i0.000\,29$

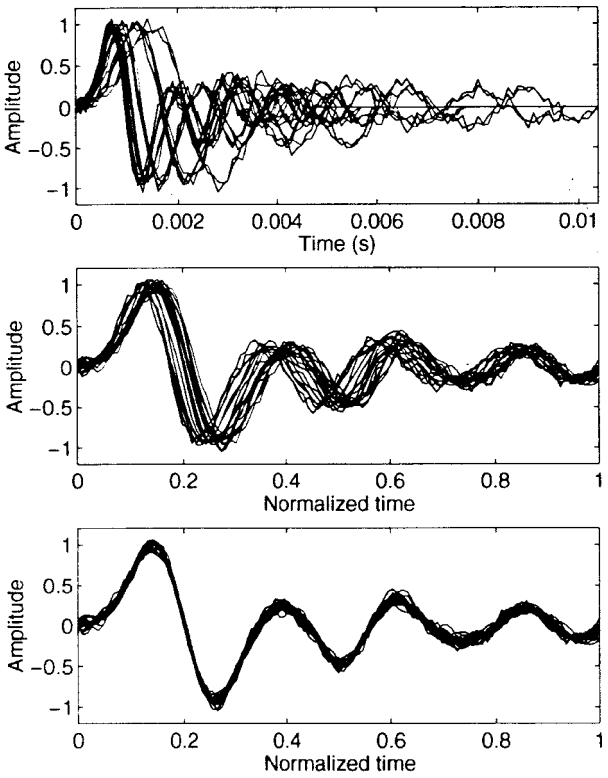

FIG. 3. Mouth pressure wavelets for $K_a=0.05$ and $K_f=0.4$, after zero-padding normalization (top), linear normalization (middle), and nonlinear normalization (bottom).

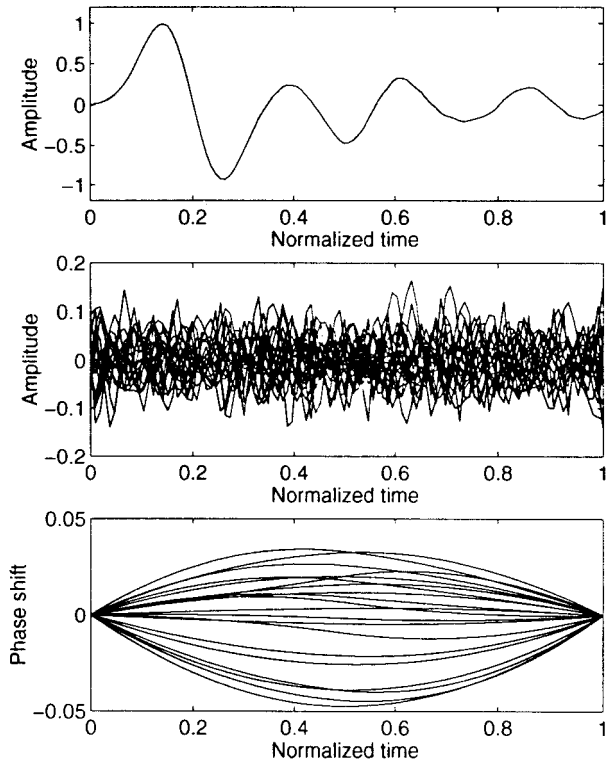

FIG. 4. Average component (top), noise components (middle), and warping functions (bottom) of wavelets in Fig. 3, with nonlinear normalization.

Figure 3 shows an example of the mouth pressure wavelets [Eq. (16)] for $K_a=0.05$ and $K_f=0.4$, after zero-padding normalization (top), linear normalization (middle), and nonlinear normalization with FDA (bottom). We can see that nonlinear normalization aligns the wavelets by removing all phase variability. Figure 4 shows the extracted average $\overline{x}^*(t)$ after nonlinear normalization (top), the noise components of the normalized signals $x_i(t)-\overline{x}^*(t)$ (middle), and the phase shift functions $\Delta h_i(t)$ (bottom). The average matches the common pattern of the wavelets, and the noise is uniformly distributed along the wavelets. The HNR is -2.76 dB with zero padding, 6.69 dB with linear normalization, 15.0 dB with nonlinear normalization using Dynamic Programming, and 18.54 dB with nonlinear normalization using FDA. The SNR is 17.82 dB. Clearly, the HNR with nonlinear normalization using FDA produces the best approximation to the SNR of the four methods.

It is instructive to compare the resultant waveforms produced by the two nonlinear normalization methods. Figure 5 shows one of the wavelets after nonlinear normalization by both methods, and the phase shift functions $\Delta h_i(t)$. We can see that the normalized wavelet with FDA maintains the same original shape with a smooth phase shift. On the other hand, the normalized wavelet with Dynamic Programming has noticeable distortions (e.g., compare the shapes of peaks and valleys). These distortions are the consequence of an irregular (nonsmooth) phase shift function.

Figure 6 shows results when the frequency variability of the signal is fixed to $K_f=0.4$, and the amplitude variability is

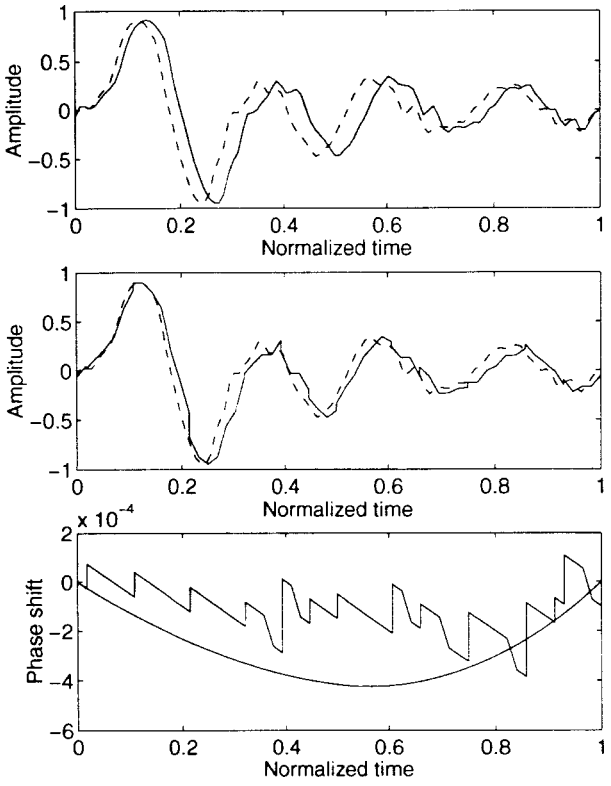

FIG. 5. Comparison of nonlinear normalization results using FDA and Dynamic Programming. Top: linearly normalized wavelet (dashed line) and normalized wavelet using FDA (solid line). Middle: linearly normalized wavelet (dashed line) and normalized wavelet using Dynamic Programming (solid line). Bottom: phase shift functions produced by FDA (smooth curve) and Dynamic Programming (discontinuous curve).

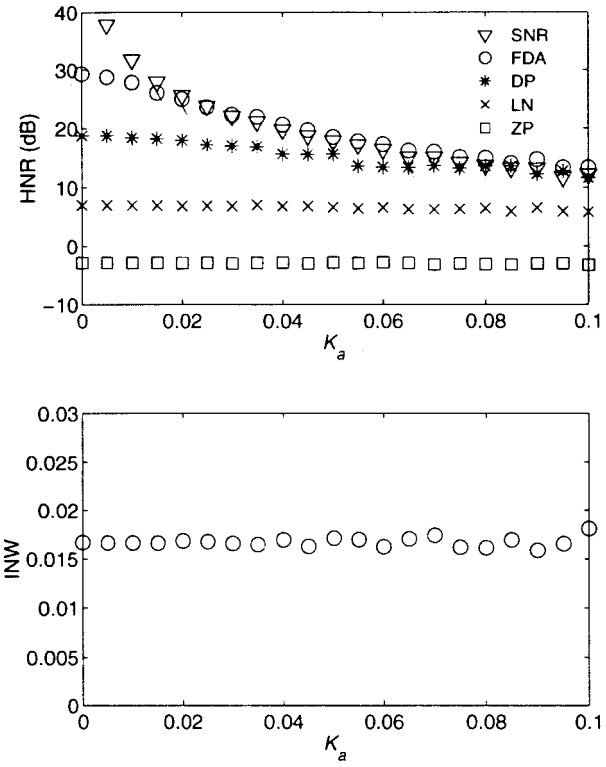

FIG. 6. HNR (top) and INW (bottom) versus amplitude variability K_a, for $K_f=0.4$. Circles: nonlinear normalization using FDA. Stars: nonlinear normalization using Dynamic Programming. Crosses: linear normalization. Squares: zero padding. Triangles: SNR.

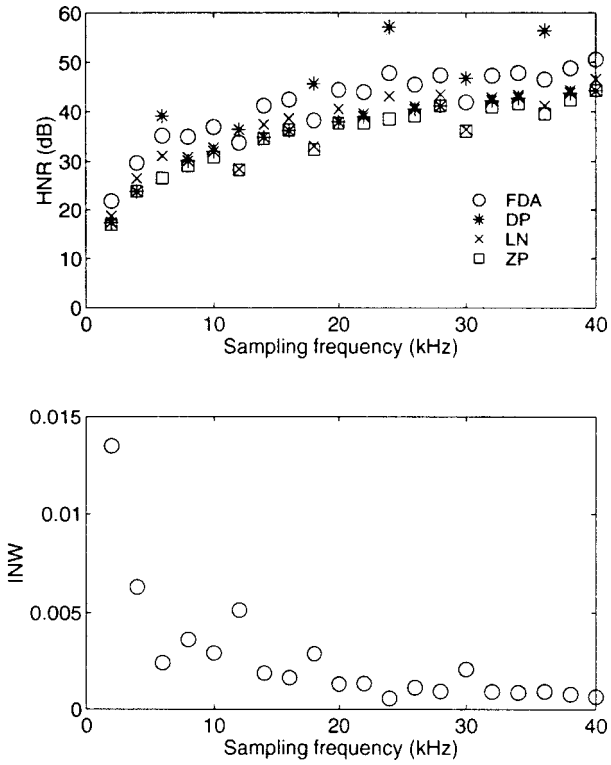

FIG. 7. HNR (top) and INW (bottom) versus sampling frequency, for $K_a=K_f=0$. Circles: nonlinear normalization using FDA. Stars: nonlinear normalization using Dynamic Programming. Crosses: linear normalization. Squares: zero padding. The ideal values of the HNR and INW should be HNR=SNR=∞ and INW=0.

in the range $K_a=0$ to 0.1. The nonlinearly normalized HNR using FDA measures the SNR with good accuracy. The HNR using Dynamic Programming produces results similar to FDA at large values of K_a, but the results worsen as K_a decreases. Both the zero-padded HNR and the linearly normalized HNR are almost constant, since they measure mostly the frequency and phase variability of the wavelets, which is also constant. The lower plot shows the index of nonlinear warping versus the amplitude variability. It is approximately constant in the whole range, reflecting the constant frequency variability.

Figure 6 (top) also shows that, as the amplitude variability tends to 0, the SNR tends to infinity. However, the HNR with both methods of nonlinear normalization reaches a maximum finite value at $K_a=0$. This is a consequence of errors introduced by discretization at the sampling frequency, and numerical errors produced by the algorithms. To assess the degree of precision of the algorithms and test the effect of the sampling frequency, we set both K_a and K_f to zero, and varied the sampling frequency. Figure 7 shows the computed HNR for the four methods and the index of nonlinear warping. In general, as the sampling frequency increases, the HNR increases and INW decreases (ideally, they should be infinite and zero, respectively). The dips and peaks of the HNR and peaks of INW correspond to integer relations between the sampling frequency and central frequency of the signal. In general, the nonlinear normalization with FDA produces more accurate values of the HNR than the other methods. The only exceptions occur at integer relations between sampling frequency and signal central frequency, where nonlinear normalization using Dynamic Programming produces higher values.

Figure 8 shows results when the amplitude variability of the signal is fixed to $K_a=0.05$, and the frequency variability is in the range $K_f=0-0.6$. Both nonlinear normalization methods yield an HNR that is a good approximation to the almost constant SNR, and in general, nonlinear normalization with FDA is more accurate than Dynamic Programming. Both the zero-padded and linearly normalized HNR decrease as the frequency and phase variability increase. We also observe that the index of nonlinear warping increases with the frequency variability, as required.

The results with sine waves and EGG analogs are similar to the ones shown for the mouth pressure analog. According to these results, the nonlinearly normalized HNR using FDA predicts the SNR of the signals with good accuracy. Further, results using FDA are better than results using Dynamic Programming, in the sense that the HNR is usually more accurate and the resultant normalized wavelets and phase shift functions are smoother with FDA, whereas Dynamic Programming introduces significant shape distortions in the wavelets. The results also show that nonlinear normalization is less sensitive to frequency variability than linear normalization or zero padding, thus reducing the effect of jitter on the HNR.

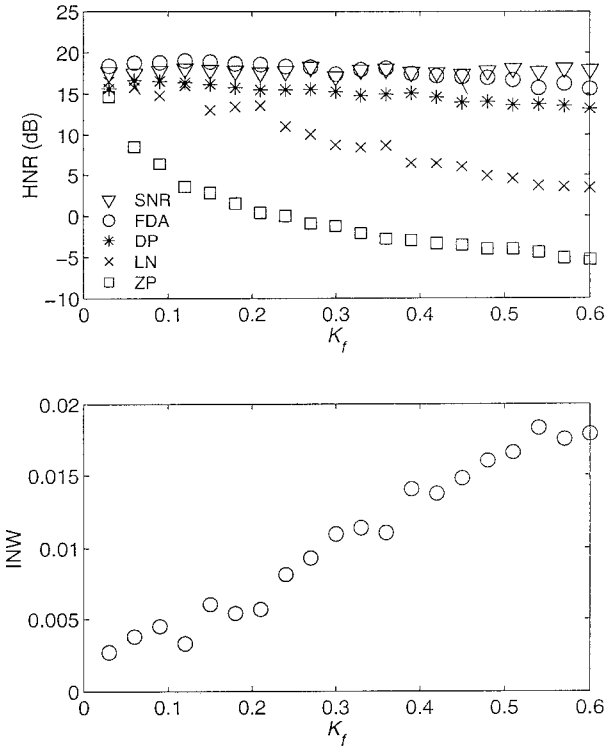

FIG. 8. HNR (top) and INW (bottom) versus frequency variability K_f, for $K_a=0.05$. Circles: nonlinear normalization using FDA. Stars: nonlinear normalization using Dynamic Programming. Crosses: linear normalization. Squares: zero padding. Triangles: SNR.

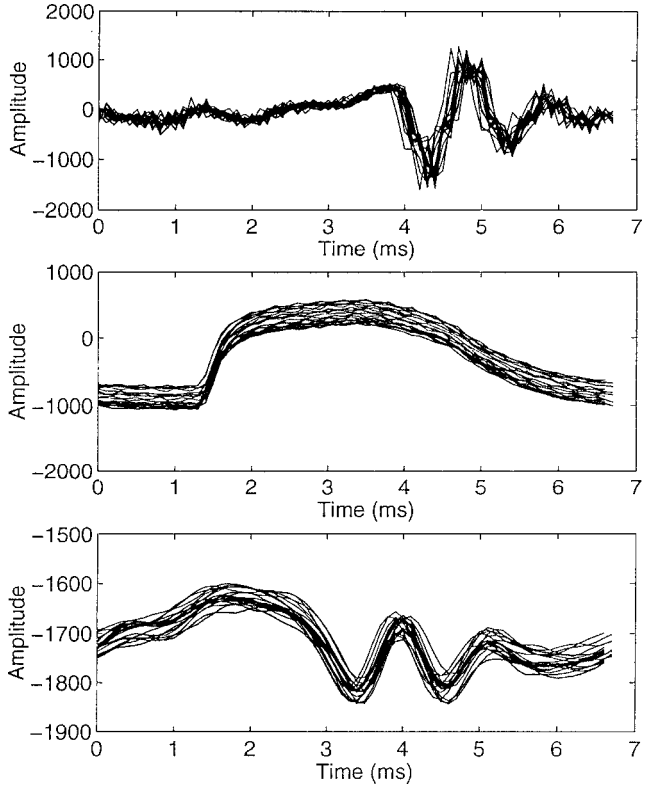

FIG. 9. Recorded acoustic (top), EGG (middle), and airflow (bottom) wavelets for normal speaker A.

IV. EXAMPLES WITH RECORDED VOICE SIGNALS FROM NORMAL SPEAKERS

A. Signals

We next tested the FDA normalization with recorded voice signals. We collected simultaneous acoustics, EGG, and oral airflow from two normal adult subjects producing a sustained /a/. One of the subjects (A) was female, age 33, and the other (B) was male, age 28. The airflow was recorded using an undivided (oral–nasal) Rothenberg mask, and a Glottal Enterprises MSIF-2 filter. The acoustics was recorded with a Seimheiser MKH 816T directional microphone placed outside the mask. The EGG was recorded with a Synchrovoice Research Electroglottograph and Glottal Enterprises Linear Phase Filter and Digital Delay LPHP-2, with settings at 3-kHz frequency limit, no delay, no coupling, and high-pass filter at 5 Hz. All signals were low-pass filtered at 4.8 kHz and digitized at 10 kHz with 12-bit precision. Using the same sampling rate for all signals facilitated the application of the normalization algorithms.

For each subject, the signals were inspected using a signal visualization program, and a stable segment (one which showed the smallest level of amplitude and pattern variability through all cycles, as assessed by visual inspection) was identified, from which 20 consecutive wavelets were extracted from all the three signals. That is, we extracted 3 simultaneous sets (acoustics, EGG, and airflow) of 20 wavelets each. The wavelet boundaries were determined on the EGG using the method of zero crossings with low-pass filtering (Titze and Liang, 1993). Nonlinear normalization was next applied using weights $\alpha=0.001$, 0.01, and 0.01, for the acoustic, EGG, and airflow wavelets, respectively, and $\lambda=0.1$. These values were selected following the same criteria as in the case of the synthetic signals. The lower value of α for the acoustic wavelets is a consequence of their larger amplitude values. Selecting a proper value of α might be facilitated by normalizing all wavelets in amplitude prior to the nonlinear normalization, e.g., by dividing the wavelet amplitudes by their peak amplitudes (Wang and Gasser, 1997).

Figure 9 shows the three sets of wavelets for subject A. The three sets have some phase variability, apparently larger in the acoustic and airflow wavelets. We can also note a large dc component in the EGG wavelets, probably produced by vertical movements of the larynx during the recording.

Prior to the FDA normalization, the wavelets were aligned vertically by removing their mean. An alternative for performing a vertical alignment may be to use the first or second derivative of the wavelets (Ramsay and Silverman, 1997). After the derivatives have been normalized in time, then the computed warping functions may be used to normalize the original wavelets. We adopted the first alternative as being computationally simpler, and because the alignment is done directly on the signals whose irregularity is analyzed. The effects of different methods of alignment is a topic that requires further study.

B. Results

Figure 10 shows all normalized wavelets for subject A. The computed indices for all wavelets are listed in Table II. In all cases (except the airflow HNR for subject A), the HNR

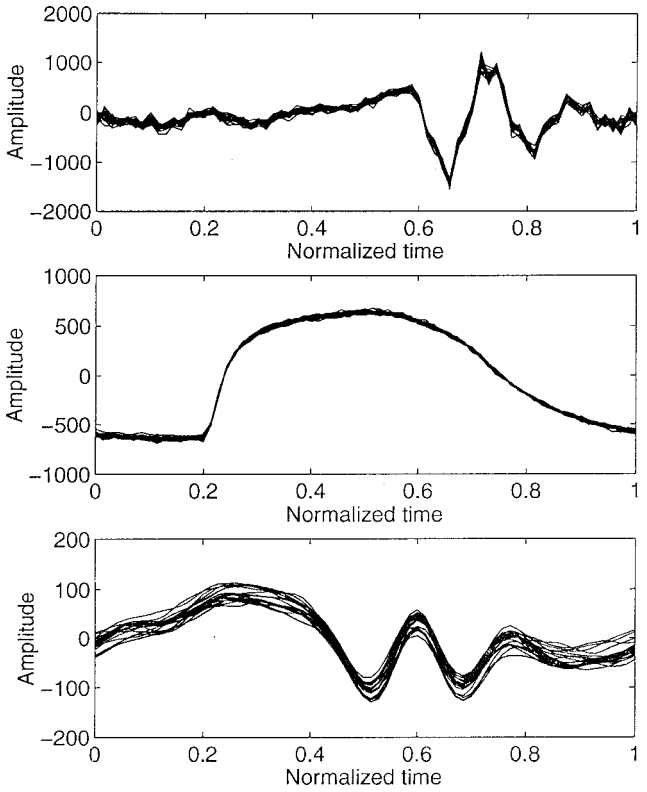

FIG. 10. Normalized acoustic (top), EGG (middle), and airflow (bottom) wavelets for subject A.

values are the highest for nonlinear normalization using FDA, since all phase and frequency variability have been removed by the normalization. We note that the acoustics and oral airflow have similar values of the HNR after nonlinear normalization with FDA, even when the values of HNR using zero padding are a bit different, as in the case of subject B. They also require similar amounts of time warping. A possible interpretation for these results might be that, since the airflow and acoustics are signals produced at the same level (oral output), then one might expect similar indices of amplitude and phase irregularity in both of them. The difference between the acoustic and airflow indices prior to nonlinear normalization would then be an artifact produced by phase shifts between wavelets.

We note also that, in both subjects, the EGG signals have the highest HNR, and require the least warping. The lower values of INW on the EGG suggest that a large phase variability is introduced into the voice above the level of the larynx. This phase variability is produced as a consequence of the vocal tract filtering of the voice source, since different harmonies of the glottal signal are filtered at different gain and timeshift, according to their frequency.

The HNR values with Dynamic Programming are in general a bit lower than values with FDA, except in the case of the airflow for subject A. In the case of EGG for subject A, the HNR results using Dynamic Programming are lower than the value computed with linear normalization. The resultant waveforms show a similar degree of distortion to the example with synthetic signals shown in Fig. 5, which also leads us to question the validity of the HNR measures for the Dynamic Programming normalization. Recall that the objective of nonlinear normalization with FDA is to obtain an HNR value that is close to the SNR [as defined in Eq. (17)] by aligning the wavelets while keeping their general shape. FDA preserves the wavelets' shapes by introducing a roughness penalty constraint in the algorithm [second integral in Eq. (5)]. Dynamic Programming, on the other hand, minimizes the square error measure [first integral in Eq. (5)] only. Since this measure appears in the denominator of the HNR's definition [Eq. (9)], we may then state that Dynamic Programming uses the maximization of the HNR as the criterion for alignment (see also Qi, 1992). However, a higher value of the HNR does not necessarily mean that the value is more accurate. Higher values of the HNR may also be produced by FDA nonlinear normalization, if lower values of the roughness penalty coefficient λ are adopted, at the cost of distorting the wavelets' shapes.

C. Simultaneous normalization

In the previous results, each set of wavelets (acoustics, EGG, and airflow) was normalized separately. As a result, the normalized wavelets are no longer synchronized in normalized time. To keep their synchrony in normalized time, one must perform a simultaneous normalization.

For this, we used vector-valued wavelets, as explained in Sec. II B. Each wavelet was considered three-dimensional, where the three dimensions correspond to the acoustic, EGG, and airflow components. The simultaneous normalization

TABLE II. Computed HNR values for recorded voice signals in normal speakers. ZP: zero-padded HNR; LN: linearly normalized HNR; DP: nonlinearly normalized HNR using Dynamic Programming; FDA: nonlinearly normalized HNR using FDA; INW: index of nonlinear warping.

Signal	ZP (dB)	LN (dB)	DP (dB)	FDA (dB)	INW
Subject A, female, age 33, $F_0=148.5$ Hz,[a] Jitter=1.1 Hz[b]					
Acoustics	6.7	7.5	10.8	15.9	0.0063
EGG	21.3	27.2	26.8	30.9	0.0030
Airflow	10.6	10.8	13.4	12.4	0.0062
Subject B, male, age 28, $F_0=109.8$ Hz,[a] Jitter=0.9 Hz[b]					
Acoustics	−1.7	−0.6	9.2	13.7	0.015
EGG	19.6	24.3	27.1	28.6	0.0054
Airflow	8.6	9.1	15.7	15.9	0.017

[a]Mean of $1/T_i$, $i=1,...,20$, where T_i are the wavelet lengths.
[b]Standard deviation of $1/T_i$.

TABLE III. Characteristics of signals from Kay Elemetrics Voice Disorders Database (Kay Elemetrics, 1994).

Speaker	Filename	Age	Sex	Diagnosis	Characteristics	Jitter[a]	Shimmer[a]	NHR[a]	DSH[a,b]
SLM	SLM27AN.NSP	20	M	hyperfunction; anterior–posterior squeezing and ventricular squeezing: head trauma; unilateral paralysis; 7 days post-intubation	moderate shimmer	2.525	14.26	0.233	0
TPS	TPS1GAN.NSP	39	M	unilateral paralysis	moderate shimmer	2.241	14.941	0.25	0
JJD	JJD29AN.NSP	23	M	gastric reflux; bilateral pachydermia and edema; unilateral suleus vocalis	moderate jitter, shimmer, subhar monic components	5.528	12.253	0.411	18.75
VMS	VMS04AN.NSP	27	F	hyperfunction; ventricular compression; bilateral laryngeal web; post-laser removal of subglottic web; scarring	moderate jitter, shimmer, subhar monic components	6.354	15.04	0.495	26.316

[a]Values from the Kay Multidimensional Voice Program.
[b]Degree of subharmonics: estimated relative evaluation of subharmonic to f_0 components in the voice sample.

was performed using the same weights for each component as in the separate normalization.

With simultaneous normalization, the acoustic, EGG, and airflow HNRs for subject A become 11.8 dB, 30.3 dB, and 11.6 dB, respectively, and INW is 0.0039. For subject B, the HNRs are 6.9 dB, 25.9 dB, 11.1 dB, and INW is 0.0087. Comparison with Table II shows that the HNR values are now lower than those for independent normalization, especially for the acoustic wavelets. The lower values of HNR result because the EGG requires a much smaller nonlinear warping than the other two sets (if the EGG required the same amount of warping, both in magnitude and time distribution, as the other two signals, then the results would be similar to the separate normalization). The resultant warping is then a compromise for the three sets. The differences in the results obtained using simultaneous and separate normalization confirm the conclusion obtained from separate normalization, i.e., that a large phase variability is introduced above the larynx.

When only the acoustic and airflow wavelets are simultaneously normalized, their HNRs for subject A are 15.8 dB and 12.1 dB, respectively, with an INW of 0.0061. For subject B we obtain 11.4 dB, 15.7 dB, with an INW of 0.0016. All of these HNR values are now close to those in Table II. This fact shows that the irregularity of the acoustic and airflow wavelets is not only similar (because in Table II the HNR and INW values of the acoustic and airflow signals are similar), but it is also equally distributed in time for both sets (because separate and simultaneous normalization produce similar results).

V. EXAMPLES WITH PATHOLOGICAL VOICE SIGNALS

A. Signals

Finally, we tested the algorithms with voice signals from the Voice Disorders Database of the Voice and Speech Laboratory of the Massachusetts Eye and Ear Infirmary (Kay Elemetrics, 1994). The recording procedure used in the database was as follows: each subject was asked to produced a sustained /a/ at comfortable fundamental frequency and intensity levels. The signals were recorded in a soundproof booth, using a condenser microphone and a DAT-recorder set to a sampling rate of 44.1 kHz. From the DAT-tape the recordings were converted into an analog signal and digitized into a computer at a sampling rate of 25 kHz, with 12-kHz anti-aliasing filtering, and 16-bit resolution.

We selected two signals with high amplitude irregularity but relatively low frequency irregularity (subjects SLM and TPS) and two with high values of jitter and high subharmonic content (subjects JJD and VMS). Table III provides information on the speakers and the main characteristics of their voice signals. The signals were inspected as before using a signal visualization program, and a stable segment was identified, from which 20 consecutive wavelets were extracted. The wavelet boundaries were determined by identifying an easily recognizable event in the signals. We selected the negative zero crossing immediately before the main negative peak in subjects SLM, TPS, and VMS, and the positive zero crossing immediately before the main positive peak in JJD. Other techniques for wavelet extraction were also applied, as discussed in the next section. Nonlinear normalization was applied using a weight $\alpha = 10^{-5}$ and $\lambda = 0.1$.

B. Results

The computed indices for all signals are listed in Table IV. In general, the FDA nonlinear normalization algorithm achieved a good alignment of all signals, in spite of their high degree of irregularity (see results for subject SLM in Fig. 11) We note that Dynamic Programming produces higher values of HNR than FDA in all cases. One could interpret this result as an indication of better alignment of the wavelets, but a closer look at the resultant waveforms shows a large distortion (see Fig. 12). In this figure, the distortion can be seen at the first positive and negative peaks, and in the flat portion near the end of the wavelet. Looking at the phase shift functions, we see that Dynamic Programming tends to align the wavelet in its finer details, without constraints for smoothness, whereas FDA tends to align its general shape with a smooth phase shift function [the degree of smoothness of the phase shift function can be manipulated by varying

TABLE IV. Computed HNR values for voice signals from the Voice Disorders Database of the Voice and Speech Laboratory, Massachusetts Eye and Ear Infirmary (Kay Elemetrics, 1994). Wavelet boundaries at zero crossing before main positive or negative peak. ZP: zero-padded HNR; LN: linearly normalized HNR; DP: nonlinearly normalized HNR using Dynamic Programming; FDA: nonlinearly normalized HNR using FDA; INW: index of nonlinear warping.

Subject	F_0 (Hz)[a]	Jitter (Hz)[b]	ZP (dB)	LN (dB)	DP (dB)	FDA (dB)	INW
SLM	80.4	2.3	9.1	8.6	13.5	10.6	0.0072
TPS	112.5	1.3	14.8	14.0	19.7	16.5	0.0041
JJD	135.4	5.2	2.7	2.9	7.6	4.7	0.0084
VMS	294.0	8.4	2.1	2.9	7.3	4.4	0.0135

[a]Mean of $1/T_i$, $i=1,...,20$, where T_i are the wavelet lengths.
[b]Standard deviation of $1/T_i$.

coefficient λ in Eq. (5)]. Thus we believe that the higher HNR values of Dynamic Programming are an artifact of the distortion and they do not reflect the actual wavelet irregularity.

Signals of subjects JJD and VMS presented some difficulty due to their content of subharmonies. The frequency spectrum of JJD (computed on the raw signal prior to wavelet extraction) revealed a main peak at 136.4 Hz, with a low frequency component at 68.2 Hz (period-2 phonation; Titze, 1994b). VMS had a main peak at 293.7 Hz, with a lowest frequency component at 59.5 Hz (period-5 phonation; Titze, 1994b). The FDA time normalization performed well when the wavelets were extracted at the higher frequency values (i.e., 136.4 Hz and 293.7 Hz for JJD and VMS, respectively). The indices reported in Table IV correspond to this case. Figure 13 shows results for VMS. On the other hand, at the lower frequency values (i.e., 68.2 Hz and 59.5 Hz for JJD and VMS, respectively), the extracted wavelets presented complex waveform patterns with several peaks and valleys, and the nonlinear normalization algorithm failed to extract a good average. This difficulty might be worst in cases of phonation at two or more incommensurate frequencies (e.g., biphonation) since there is not a consistent waveform pattern repeating at regular intervals, and even identifying the wavelet boundaries would not be trivial. For these cases, voice irregularity may be better evaluated using other techniques, such as those developed by Herzel *et al.* (1994) applying

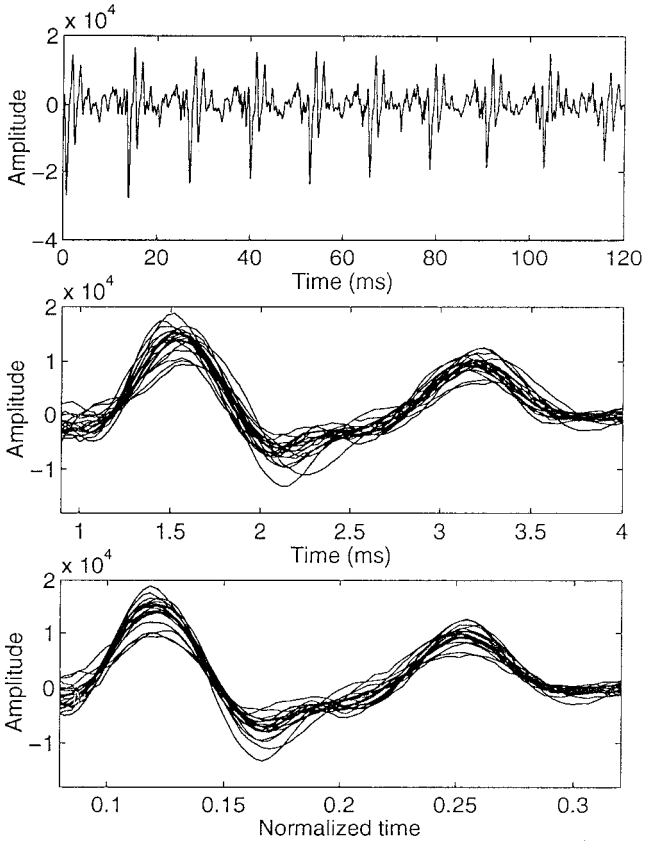

FIG. 11. Original signal (top), extracted unnormalized wavelets (middle), and normalized wavelets using FDA (bottom) for subject SLM. Only a portion of the wavelets is shown, for better visualization of the alignment.

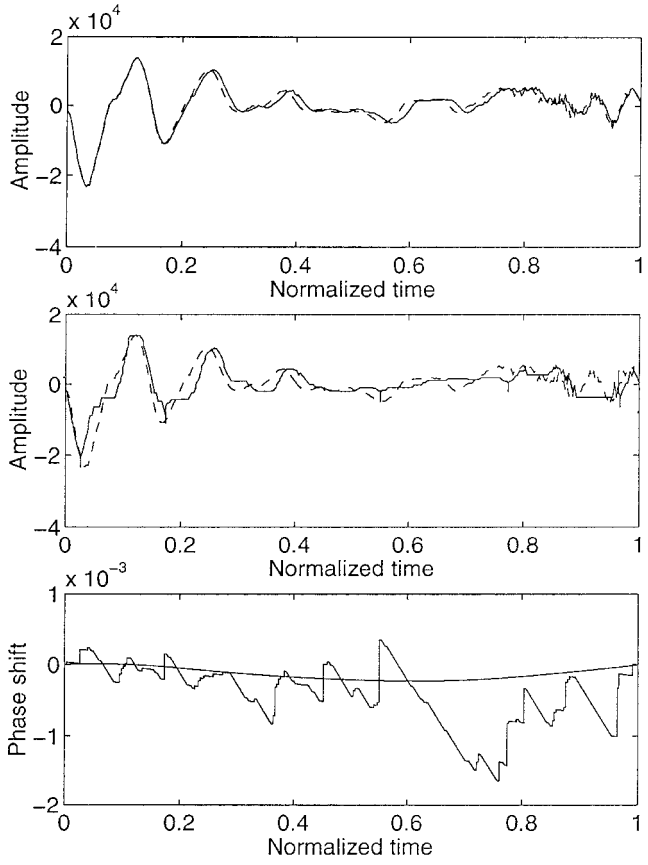

FIG. 12. Comparison of nonlinear normalization results using FDA and Dynamic Programming for subject SLM. Top: linearly normalized wavelet (dashed line) and normalized wavelet using FDA (solid line). Middle: linearly normalized wavelet (dashed line) and normalized wavelet using Dynamic Programming (solid line). Bottom: phase shift functions produced by FDA (smooth curve) and Dynamic Programming (discontinuous curve).

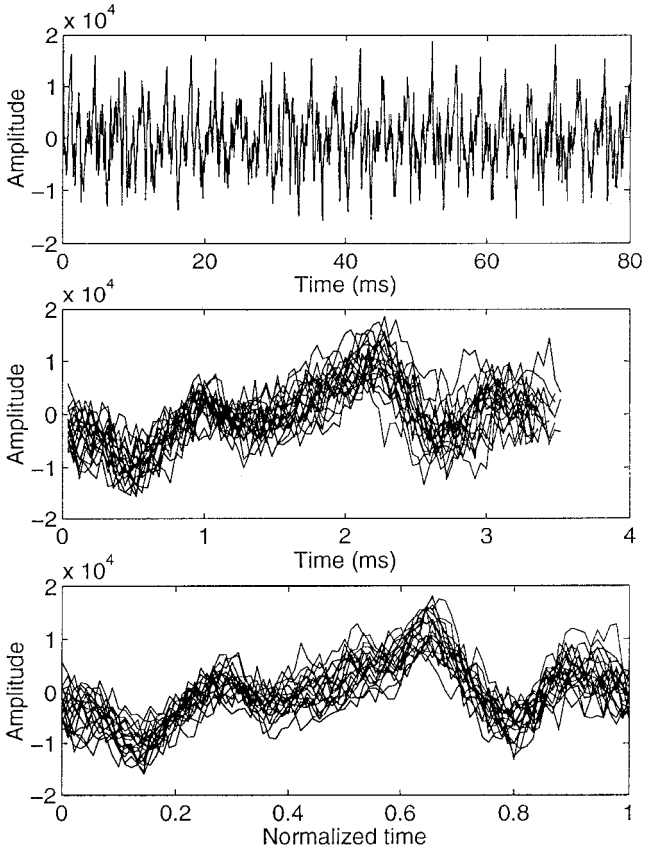

FIG. 13. Original signal (top), extracted unnormalized wavelets (middle), and normalized wavelets (bottom) for subject VMS (wavelet extraction at 293.7 Hz).

nonlinear dynamic theory (bifurcation models, F_0 and amplitude contours, phase portraits, next amplitude and next period maps).

The difficulty encountered with the pathological voices led us to experiment with different techniques to extract the wavelets from the signals. As an example, Table V shows results for negative peak-picking on SLM, TPS, and VMS; and positive peak-picking for JJD. Comparing these values with those in Table IV, there is a mean variation of 2.65 dB, 0.48 dB, 0.35 dB, and 0.15 dB for the zero-padded HNR, linearly normalized HNR, nonlinearly normalized HNR using Dynamic Programming, and nonlinearly normalized HNR using FDA. Wavelet extraction at negative zero crossings of a low-pass filtered signal, and using waveform matching (Titze and Liang, 1993) produced similar results for signals SLM and TPS, and much lower values of HNR for JJD and VMS. In all cases also the variation for both methods of nonlinearly normalized HNR was smaller than for the zero-padded and linearly normalized HNR. These results show that nonlinear normalization is in general less sensitive to the wavelet extraction technique applied in that differences in extraction method yield less HNR variation for nonlinear normalization than for zero-padding or linear normalization. The choice of a wavelet extraction technique seems to be more critical when dealing with highly irregular signals. However, we believe that this is an issue that needs further consideration. For example, it might be possible to combine a waveform matching method of wavelet extraction (which is based on comparing shapes of adjacent cycles) with a wavelet time normalization to improve the selection of the optimal wavelet boundaries. Also, the method used here fixes both ends of wavelets and does not allow any phase shift there. It might be possible to remove the constraints on alignment at the wavelet ends by including additional signal samples before and after the extracted cycles. In this way, errors in detecting the exact cycle boundaries would have less effect on the results.

VI. CONCLUSIONS

We have presented an application of FDA to the time normalization of voice signals and assessment of signal irregularity, which offers certain possible advantages over previous approaches. FDA normalizes the signals while preserving meaningful features of their shapes. Although normalization is done by removing phase differences from the signals, those differences are kept as separate measures in the warping functions. The underlying pattern and irregularity of the signals may then be extracted as separate functions, and the irregularity may be evaluated in terms of irregularity in the waveform (as measured by the HNR), and in phase (as measured by the index of nonlinear warping). We believe that the two indices permit a better assessment of the signal irregularity than a single general index combining phase and waveform irregularity (as the HNR with zero-padding or linear normalization). Two sets of wavelets with different shapes may have the same waveform and phase irregularity, but produce very different values of HNR with zero-padding or linear normalization (as in the examples with the recorded

TABLE V. Computed HNR values for voice signals from the Voice Disorders Database of the Voice and Speech Laboratory, Massachusetts Eye and Ear Infirmary (Kay Elemetrics, 1994). Wavelet boundaries at main positive or negative peak. ZP: zero-padded HNR; LN: linearly normalized HNR; DP: nonlinearly normalized HNR using Dynamic Programming; FDA: nonlinearly normalized HNR using FDA; INW: index of nonlinear warping.

Subject	F_0 (Hz)[a]	Jitter (Hz)[b]	ZP (dB)	LN (dB)	DP (dB)	FDA (dB)	INW
SLM	81.3	2.0	5.3	9.1	13.7	10.9	0.0055
TPS	112.4	1.2	8.9	14.9	19.5	16.4	0.0033
JJD	135.3	3.4	2.0	2.8	7.4	4.7	0.0096
VMS	293.2	9.2	1.9	3.3	8.1	4.2	0.0090

[a]Mean of $1/T_i$, $i=1,...,20$, where T_i are the wavelet lengths.
[b]Standard deviation of $1/T_i$.

airflow and acoustic signals). The similarities in their irregularity would only be revealed after separating them into waveform and phase irregularity.

The possibility of partitioning signal variability into phasing and waveform components also holds promise for research into the nature and significance of variability in speech production. In particular, we plan to extend this method to study of children's speech. Increased variability in children's speech relative to adults has frequently been found (e.g., Chermak and Schneiderman, 1986; Eguchi and Hirsh, 1969; Kent and Forner, 1980; Ohde, 1985; Sharkey and Folkins, 1985; Smith, 1994, 1995; Smith *et al.*, 1983; Tingley and Allen, 1975; Watkin and Fromm, 1984), but the significance and nature of adult–child differences remain matters of debate (see, e.g., Chermak and Schneiderman, 1986; Sharkey and Folkins, 1985; Smith, 1994; Stathopoulos, 1995). More detailed information about how variability is distributed within child and adult data may provide greater insight into the processes by which speech production skill develops.

As shown with synthetic signals, the waveform irregularity measured by nonlinear normalization is less sensitive to jitter, and to errors introduced by sampling frequency discretization than zero-padding or linear normalization techniques. The results from recorded signals show that the irregularity measure is also less sensitive to the wavelet extraction technique used.

We have also shown the limitations of nonlinear normalization using Dynamic Programming. The algorithm tested (Qi, 1992) produced significant distortion in the wavelets, as a consequence of nonsmooth warping functions. Some techniques have been proposed in the literature to reduce wavelet distortion (e.g., Parsons, 1987; Strik and Boves, 1991) by constraining excessive expansion or contraction of the time scale. However, the results (wavelets, warping functions, averages) are in general nonsmooth (i.e., nondifferentiable). Differentiability may be a desirable property, for further processing of the results. One may differentiate the warping functions (which represent phase differences between wavelets) to analyze instantaneous frequency irregularity. For vocal fold oscillation, instantaneous frequency is mainly related to tissue stiffness (Titze, 1994a), so that frequency irregularity (e.g., in the EGG signals) may reveal aspects of the tissue biomechanies and voice motor control. The ability to differentiate a signal one or two times also has great potential applications in work on speech kinematics and aerodynamics. Zero crossings in the first time derivative of a signal may be used as a means of determining the timing of articulatory or aerodynamic events (e.g., Gracco and Löfqvist, 1994; Koenig, in press; Kollia *et al.*, 1995; Löfqvist and Gracco, 1997, 1999). The second time derivative has similarly been used to define articulatery events; for example, Koenig (in press) used the second time derivative in an oral airflow signal to define release and closure for oral stop consonants, and Löfqvist and Gracco (1997) used the second time derivative of a lip opening measure to define the onset of labial closing for a stop consonant. Other potentially interesting FDA techniques also require differentiability of wavelets, such as principal differential analysis, in which a linear differential operator is fitted to the wavelets and irregularity is assessed on a resultant empirical forcing function (see details in Ramsay and Silverman, 1997).

An additional advantage of FDA over Dynamic Programming is that FDA does not require selecting one of the wavelets as a template for the alignment. Further, it allows for considerable flexibility in selecting the alignment criteria, with roughness penalty terms, derivatives, and weighting functions, and one may process simultaneous sets of signals. Simultaneous normalization of signals may be useful for analyzing sets of signals in which one signal is considered to result from variation in other recorded signals. This is the case, for example, with intraoral pressure signals, which vary as a function of both glottal area and supraglottal articulation (e.g., Koenig *et al.*, 1995; Müller and Brown, 1980). Although the warping functions represent a compromise among the various signals, it is possible to vary the influence of various signals so as to achieve an optimal normalization for the particular application.

However, several technical details of the FDA algorithm remain to be further considered, such as how best to select the weighting functions and roughness penalty coefficient, based on the characteristics of the signals. It might also be possible to achieve a better alignment of wavelets by using a weighted combination of the wavelets and their derivatives in the squared error integral in Eq. (5) (Wang and Gasser, 1997), but further study is needed on determining the most appropriate methods for selecting alignment criteria.

In this paper we have used the HNR of the normalized signals as one criterion for selecting among various methods. A noted above, however, obtaining a higher HNR does not always necessarily mean that a method is superior. For example, in the examples with pathological voice signals, time normalization by Dynamic Programming produced higher values of HNR, but at the expense of a large distortion of the wavelets. We do claim that nonlinear normalization using FDA produces a good prediction of the signal SNR [defined as in Eq. (17)], typically higher than the other methods tested, while preserving the shape and smoothness of the resultant wavelets.

In our analyses, we attributed an artificial length of 1 to the normalized wavelet time scale. This is a common technique in FDA, since one is usually interested in analyzing shape characteristics of wavelets. However, it is also possible to interpret the results in absolute time, e.g., by attributing the mean length of the original wavelets to the normalized time length.

The technique is based on the assumption that there is a common pattern to all the wavelets. For regular voices, this assumption is reasonable, and amounts simply to claiming that the laryngeal signal represents the output of a pattern of vocal fold vibration that is essentially periodic, albeit with some minor irregularity due to jitter and shimmer, among other things. The oral signals then represent the periodic laryngeal signal combined with the vocal tract transfer function. Highly disordered voices, on the other hand, present a difficulty for FDA in that the laryngeal signal may not have a consistent pattern repeating at periodic intervals. Cases of signals with subharmonics may still be handled reasonably

well by extracting the wavelets at the frequency with the highest energy, but the technique becomes less appropriate as it becomes more difficult to define a single base frequency for the signal.

ACKNOWLEDGMENTS

These results were presented in partial form at the Second International Conference on Voice Physiology and Biomechanics in Berlin, Germany, 12–14 March 1999. We thank Dr. Jean Schoentgen and Dr. Yingyong Qi for helpful discussions; and Dr. Anders Löfqvist, Dr. Helmer Strik, and an anonymous reviewer for comments on a previous version of this paper. This research was supported by CNPq, FEMAT, and CAPES of Brazil, and grants of the US National Institutes of Health (NIH) to Haskins Laboratories.

Chermak, G. D., and Schneiderman, C. R. (**1986**). ''Speech timing variability of children and adults,'' J. Phonetics **13**, 477–480.

Eguchi, S., and Hirsh, I. J. (**1969**). ''Development of speech sounds in children,'' Acta Oto-Laryngol. Suppl. **257**, 1–51.

Gracco, V. L., and Löfqvist, A. (**1994**). ''Speech motor coordination and control: Evidence from lip, jaw, and laryngeal movements,'' J. Neurosci. **14**, 6585–6597.

Herzel, H., Berry, D., Titze, I. R., and Salch, M. (**1994**). ''Analysis of vocal disorders with methods from nonlinear dynamics,'' J. Speech Hear. Res. **37**, 1008–1019.

Kay Elemetrics (**1994**). *Voice Disorders Database, Voice and Speech Laboratory, Massachusetts Eye and Ear Infirmary* (Kay Elemetrics, Lincoln Park, NJ).

Kent, R. D., and Forner, L. L. (**1980**). ''Speech segment durations in sentence recitations by children and adults,'' J. Phonetics **8**, 157–168.

Koenig, L. L. (in press). ''Laryngeal factors in voiceless consonant production in men, women, and 5-year-olds,'' J. Speech Lang. Hear. Res.

Koenig, L., Löfqvist, A., Gracco, V., and McGowan, R. (**1995**). ''Articulatory activity and aerodynamic variation during voiceless consonant production,'' J. Acoust. Soc. Am. **97**, S3401.

Kollia, H. B., Gracco, V. L., and Harris, K. S. (**1995**). ''Articulatory organization of mandibular, labial, and velar movements during speech,'' J. Acoust. Soc. Am. **98**, 1313–1324.

Lieberman, P. (**1962**). ''Some acoustic measures of the fundamental periodicity of normal and pathological larynges,'' J. Acoust. Soc. Am. **35**, 344–353.

Löfqvist, A., and Gracco, V. L. (**1997**). ''Lip and jaw kinematics in bilabial stop consonant production,'' J. Speech Lang. Hear. Res. **40**, 877–893.

Löfqvist, A., and Gracco, V. L. (**1999**). ''Interarticulator programming in VCV sequences: Lip and tongue movements,'' J. Acoust. Soc. Am. **105**, 1864–1876.

Lucero, J. C., Munhall, K. G., Gracco, V. L., and Ramsay, J. O. (**1997**). ''On the registration of time and the patterning of speech movements,'' J. Speech Lang. Hear. Res. **40**, 1111–1117.

Müller, E. M., and Brown, W. S. (**1980**). ''Variations in the supraglottal air pressure waveform and their articulatory interpretation,'' in *Speech and Language: Advances in Basic Research and Practice*, edited by N. Lass (Academic, New York), pp. 317–389.

Ohde, R. N. (**1985**). ''Fundamental frequency correlates of stop consonant voicing and vowel quality in the speech of preadolescent children,'' J. Acoust. Soc. Am. **78**, 1554–1561.

Parsons, T. W. (**1987**). *Voice and Speech Processing* (McGraw-Hill, New York).

Press, W. H., Teukolsky, S. A., Vetterling, W. T., and Flannery, B. P. (**1992**). *Numerical Recipes in C—The Art of Scientific Computing*, 2nd ed. (Cambridge University Press, Cambridge).

Qi, Y. (**1992**). ''Time normalization in voice analysis,'' J. Acoust. Soc. Am. **92**, 2569–2576.

Qi, Y., and Hillman, R. E. (**1997**). ''Temporal and spectral estimations of harmonics-to-noise ratio in human voice signals,'' J. Acoust. Soc. Am. **102**, 537–543.

Qi, Y., Weinberg, B., Bi, N., and Hess, W. J. (**1995**). ''Minimizing the effect of period determination on the computation of amplitude perturbation in voice,'' J. Acoust. Soc. Am. **97**, 2525–2532.

Ramsay, J. O. (**1998**). ''Estimating smooth monotone functions,'' J. Royal Stat. Soc., Ser. B **60**, 365–375.

Ramsay, J. O., and Li, X. (**1998**). ''Curve registration,'' J. Royal Stat. Soc. B **60**, 351–363.

Ramsay, J. O., Munhall, K. G., Gracco, V. L., and Ostry, D. J. (**1996**). ''Functional data analyses of lip motion,'' J. Acoust. Soc. Am. **99**, 3718–3727.

Ramsay, J. O., and Silverman, B. W. (**1997**). *Functional Data Analysis* (Springer-Verlag, New York).

Sharkey, S. G., and Folkins, J. W. (**1985**). ''Variability of lip and jaw movements in children and adults: Implications for the development of speech motor control,'' J. Speech Hear. Res. **28**, 8–15.

Smith, B. L. (**1994**). ''Effects of experimental manipulations and intrinsic contrasts on relationships between duration and temporal variability in children's and adults' speech,'' J. Phonetics **22**, 155–175.

Smith, B. L. (**1995**). ''Variability of lip and jaw movements in the speech of children and adults,'' Phonetica **52**, 307–316.

Smith, B. L., Sugerman, M. D., and Long, S. H. (**1983**). ''Experimental manipulation of speaking rate for studying temporal variability in children's speech,'' J. Acoust. Soc. Am. **74**, 744–749.

Stathopoulos, E. T. (**1995**). ''Variability revisited: An acoustic, aerodynamic, and respiratory kinematic comparison of children and adults during speech,'' J. Phonetics **23**, 67–80.

Strik, H., and Boves, L. (**1991**). ''A dynamic programming algorithm for time-aligning and averaging physiological signals related to speech,'' J. Phonetics **19**, 367–378.

Tingley, B. M., and Allen, G. D. (**1975**). ''Development of speech control in children,'' Child Dev. **46**, 186–194.

Titze, I. R. (**1994a**). *Principles of Voice Production* (Prentice-Hall, Englewood Cliffs).

Titze, I. R. (**1994b**). *Workshop on Acoustic Voice Analysis—Summary Statement* (National Center for Voice and Speech, Iowa City).

Titze, I. R., and Liang, H. (**1993**). ''Comparison of F_0 extraction methods for high-precision voice perturbation measurements,'' J. Speech Hear. Res. **36**, 1120–1133.

Wang, K., and Gasser, T. (**1997**). ''Alignment of curves by dynamic time warping,'' Annals of Statistics **25**, 1251–1276.

Watkin, K., and Fromm, D. (**1984**). ''Labial coordination in children: Preliminary considerations,'' J. Acoust. Soc. Am. **75**, 629–632.

Yumoto, E., Gould, W. J., and Baer, T. (**1982**). ''Harmonies-to-noise ratio as an index of degree of hoarseness,'' J. Acoust. Soc. Am. **71**, 1544–1550.

Frication noise modulated by voicing, as revealed by pitch-scaled decomposition

Philip J. B. Jackson[a] and Christine H. Shadle[b]
Department of Electronics and Computer Science, University of Southampton, Southampton SO17 1BJ, United Kingdom

(Received 28 December 1999; accepted for publication 18 April 2000)

A decomposition algorithm that uses a pitch-scaled harmonic filter was evaluated using synthetic signals and applied to mixed-source speech, spoken by three subjects, to separate the voiced and unvoiced parts. Pulsing of the noise component was observed in voiced frication, which was analyzed by complex demodulation of the signal envelope. The timing of the pulsation, represented by the phase of the anharmonic modulation coefficient, showed a step change during a vowel-fricative transition corresponding to the change in location of the noise source within the vocal tract. Analysis of fricatives /β, v, ð, z, ʒ, ɣ, ʕ/ demonstrated a relationship between steady-state phase and place, and f_0 glides confirmed that the main cause was a place-dependent delay. © *2000 Acoustical Society of America.* [S0001-4966(00)00410-0]

PACS numbers: 43.70.Bk, 43.72.Ar [AL]

I. INTRODUCTION

The production of voiced fricatives involves two predominant sources of sound exciting the vocal-tract resonances: the phonation source, produced by vocal-fold oscillation, and the noise source, produced downstream of a supraglottal constriction. Thus if we wish to determine source characteristics from the speech signal, the analysis problem is more complicated than for single-source speech sounds and, as some authors have noted, the two sources are not entirely independent. In particular, the voicing source appears to modulate the noise source (Fant, 1960; Flanagan, 1972). Others have found that modulating the aspiration source during a vowel-to-voiced fricative transition leads to better quality synthesis (Klatt and Klatt, 1990; Scully, 1990; Scully *et al.*, 1992). While such interaction of sources inevitably complicates the model used for synthesis, and the analysis problem, it may also be the key to a more accurate model of the production mechanism itself. Closer study of the source interaction could lead directly to better quality synthesis of voiced fricatives and, potentially, of other mixed-source signals, such as breathy vowels.

In simple models of voiced fricatives, the voicing and frication sources are inserted into the system and the output is formed from the sum of their individual contributions: voicing as a volume velocity source at the glottis; frication as a pressure source at the supraglottal constriction. Although Fant (1960) noted that source–source interaction occurred as ''periodic and synchronous'' modulation of the frication source by phonation, Flanagan's electrical analog model was one of the first to incorporate modulation of the fricative source amplitude (Flanagan and Cherry, 1969). Band-passed Gaussian noise (0.5–4 kHz) was multiplied by the square of the volume velocity at the constriction exit U_n, which included the dc component, to give the pressure (voltage) source P_n in series with a variable source resistance R_n. Sondhi and Schroeter (1987) employed a similar model for a practical implementation of an aspiration source at the glottis, gated by a threshold Reynolds number; for frication they placed a volume velocity source P_n/R_n one section (0.5 cm) downstream of the constriction exit (or at the lips for /f, v, θ, ð/), because of poor subjective results with pressure sources.

Scully (1990; Scully *et al.*, 1992) based her source generation on Stevens' (1971) result from static experiments: the strength of the pressure source $p_s \propto \Delta P^{3/2}$, where ΔP is the pressure across the constriction. This source, depending on slowly varying articulatory and aerodynamic parameters, was applied equally to aspiration and frication sources. Since ΔP across the supraglottal constriction is lower for voiced than voiceless fricatives, this equation partially accounts for the weaker frication source. These parameters do not encode any modulation, or allow for the flow separation lag in jet formation (Pelorson *et al.*, 1997). However, motivated by the results of perceptual tests, the aspiration source was modulated using the rapidly varying glottal area. Klatt, treating aspiration and frication identically, modulated the noise source with a square wave (50% burst duration) that was switched on during voicing, remarking that it is ''not necessary to vary the degree of amplitude modulation..., but only to ensure that it is present'' (Klatt, 1980). In an analysis-by-synthesis procedure, Narayanan and Alwan (1996) used a combination of pressure (dipole) and volume-velocity (monopole) sources to match measured fricative spectra, and concluded that the monopoles should be placed at the constriction exit and the dipoles at one or more obstacles: at the lips for /f, v, θ, ð/, at the teeth for /s, z/ and at the teeth and vocal-tract wall for /ʃ, ʒ/.

None of the above models considers any nonacoustic fluid motion, yet in a flow duct experiment (Coker *et al.*, 1996), the arrival time of a pulse of radiated noise, depending strongly on the constriction-obstacle distance, suggested a convection velocity of less than half the flow velocity at the

[a]Present address: School of Electronics and Electrical Engineering, University of Birmingham, Birmingham B15 2TT, United Kingdom. Electronic mail: p.jackson@bham.ac.uk
[b]Electronic mail: chs@ecs.soton.ac.uk

jet exit (8 m/s). In his recent Ph.D. thesis, Sinder (1999) presents a model for fricative production that is based on aeroacoustic theory. Once the necessary flow-separation conditions have been met, vortices are shed, which convect along the tract, generating sound as they go, particularly when encountering an obstacle. Therefore, we want to consider both acoustic and aerodynamic mechanisms.

We have previously described an algorithm, the pitch-scaled harmonic filter (PSHF), that decomposes speech into harmonic and anharmonic signals (Jackson and Shadle, 1998), which are estimates of the voiced and unvoiced components, respectively. The PSHF was developed from a measure of harmonics-to-noise ratio (HNR; Muta *et al.*, 1988) to provide full reconstruction of harmonic (voiced) and anharmonic (unvoiced) time series, on which subsequent analyses can be performed independently. This method is especially suited to acoustic analysis of sustained sounds with regular voicing (i.e., low values of jitter and shimmer), because of the underlying harmonic model of the voiced part, which is based on optimal (maximum likelihood) estimation. Other than the choice of the number of pitch periods (which is typical for adaptive filtering techniques), the PSHF is without any arbitrary features for heuristic adjustments, such as cutoff frequency (Laroche *et al.*, 1993) and number of cepstral coefficients (Qi and Hillman, 1997; Yegnanarayana *et al.*, 1998), and does not suffer the bias, harmonic interference and variable performance problems of asynchronous harmonic techniques (Hardwick *et al.*, 1993; Laroche *et al.*, 1993; Qi and Hillman, 1997; Serra and Smith, 1990; Silva and Almeida, 1990; Yegnanarayana *et al.*, 1998).

In this paper, we employ the PSHF to study the interaction between sources in voiced fricatives, to arrive at better source models, and to obtain clues to the production mechanism that governs the interaction. Section II describes the PSHF method and tests of it using synthetic signals. Section III describes the recording method, subjects, and corpus, and presents preliminary results of the decomposition. Section IV presents further analysis by considering the modulation of the aperiodic component in voiced fricatives, for which results are given in Sec. V. These results are discussed in light of possible aeroacoustic mechanisms in Sec. VI and Sec. VII gives conclusions.

II. DECOMPOSITION METHOD

A. Pitch-scaled harmonic filter

The pitch-scaled harmonic filter (PSHF) was designed to separate harmonic and anharmonic components, $v(n)$ and $u(n)$, of a recorded speech signal $s(n)$. It assumes that these components will be representative of the acoustic consequences of the voiced and unvoiced sound sources, respectively, i.e., the vocal-tract filtered excitations. A detailed description of the PSHF, including pitch estimation, windowing sequence, and algorithm, can be found elsewhere (Muta *et al.*, 1998; Jackson and Shadle, 2000; Jackson, 2000). Here we present a schematic summary of the central process, illustrating it with some spectra, followed by a description of tests using synthetic speechlike signals.

In the PSHF, the original speech signal $s(n)$ is decomposed primarily into the harmonic and anharmonic estimates, $\hat{v}(n)$ and $\hat{u}(n)$, respectively. Further harmonic and anharmonic estimates, $\tilde{v}(n)$ and $\tilde{u}(n)$, are computed based on a power interpolation (PI) of the anharmonic spectrum, which improves the spectral composition of the signals when considering features over a time-frame longer than two pitch periods. Figure 1 describes the PSHF algorithm, which takes a four-pitch period windowed section of the signal $s_w(n)$, transforms it into $S_w(k)$ by discrete Fourier transform (DFT), and decomposes it in the frequency domain by a harmonic filter (HF).[1] The output signals are then constructed by transforming the spectra $\hat{V}(k)$ and $\hat{U}(k)$ back into the time domain (by inverse DFT or IDFT) and windowing.

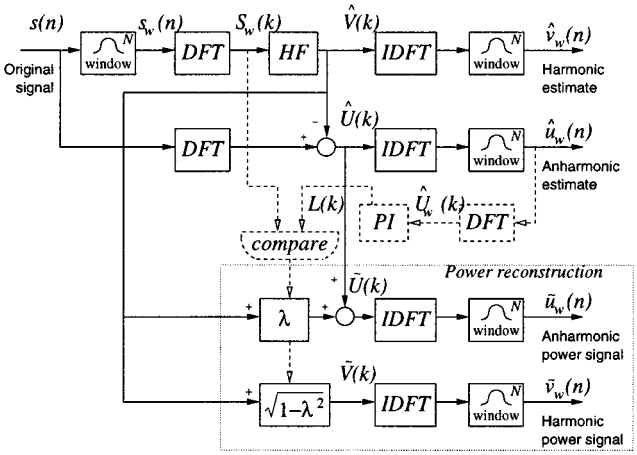

FIG. 1. Flow diagram of the pitch-scaled harmonic filter (PSHF) algorithm. See text for explanation of the harmonic filton (HF), power interpolation, and factor λ.

Figure 2 illustrates the operation of the harmonic filter using a mid-vowel recording of [ɑ] by an adult male (from example #1 by PJ; see Sec. III for details). It shows the original spectrum $S_w(k)$ after windowing, the spectrum of the harmonic estimate $\hat{V}_w(k)$, and the remainder $\hat{U}_w(k)$, the anharmonic spectrum. The essence of this technique is that, by scaling the window size to exactly four-pitch periods N

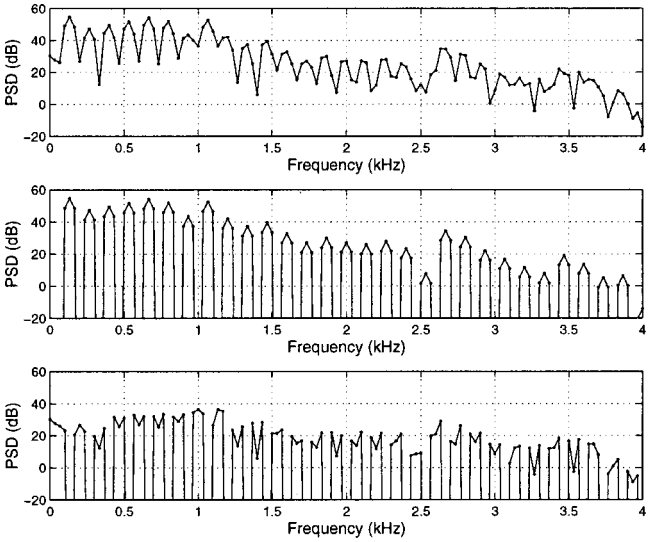

FIG. 2. Spectra of (top) windowed speech signal $S_w(k)$, (middle) the harmonic estimate $\hat{V}_w(k)$, and (bottom) the anharmonic estimate $\hat{U}_w(k)$.

$=4T_0$, the voiced (quasi-periodic) part is concentrated into every fourth bin of the spectrum. The pitch estimation process finds the value of T_0 that optimizes the concentration. Thus a harmonic comb filter that passes these harmonic bins (and doubles them) yields an estimate of the voiced component $\hat{V}(k)$ which, after applying an IDFT, results in a periodic signal of length $N=4T_0$. Finally, the envelope of the estimate $\hat{v}_w(n)$ is matched to that of the input signal $s_w(n)$ by applying the same window function. The spectral consequences can be seen in Fig. 2, which shows how, for each harmonic, the Fourier coefficient (middle) maintains the same value as that of the original spectrum (top), but has spread to the adjacent bins (at -6 dB). The residue is the anharmonic component $\hat{u}_w(n)$, whose spectrum (Fig. 2, bottom) accordingly contains gaps at the harmonics. For a periodic signal in Gaussian white noise, the harmonic Fourier coefficients provide the optimal (maximum likelihood) estimate of the signal (Rife and Boorstyn, 1974; Bretthorst, 1988) and the residue is thus the best estimate of the noise. However, if one is interested in the anharmonic power spectrum, particularly at a fine frequency resolution ($\leqslant f_0/2$), intuitively one would consider filling the gaps by some form of interpolation, assuming that the noise is the result of a stochastic process with a smoothly varying frequency response. So, the PI stage computes the mean power of the bins either side of each harmonic $L(k)$. Then, by comparing $L(k)$ with the original coefficients $S_w(k)$, the factor $\lambda(k)$ is used to share the power from the harmonic bins between the harmonic and anharmonic spectra, $\tilde{V}(k)$ and $\tilde{U}(k)$, giving new power-based estimates $\tilde{v}_w(n)$ and $\tilde{u}_w(n)$, respectively. An entire section of voiced speech can be processed by sliding the window along, and by overlapping and adding the outputs $\hat{v}_w$, $\hat{u}_w$, $\tilde{v}_w$, and $\tilde{u}_w$ to obtain complete signals $\hat{v}$, $\hat{u}$, $\tilde{v}$, and $\tilde{u}$.

B. Synthetic test signals

To use the PSHF for studying modulation of noise sources in detail, we need to ascertain the performance of the PSHF for such signals. Twelve speechlike test signals $s(n)$ were composed of a deterministic part $v(n)$ and a noise part $u(n)$:

$$s(n)=v(n)+u(n), \tag{1}$$

at sampling rate $f_s=48$ kHz. The deterministic part was synthesized by convolving a pulse train $g(n)$, which was periodic at $f_0=120.0$ Hz, with an appropriate impulse-response filter h:

$$v=g*h, \tag{2}$$

where $*$ denotes convolution. The filter h was built using the linear prediction coefficients (LPC, autocorrelation, 50-pole) obtained from the same adult male mid-vowel [ɑ] recording used in Fig. 2 (#1 by PJ). The noise signal was similarly created by convolving Gaussian white noise $d(n)$ (zero mean, unit variance) with the LPC filter. However, the noise was combined in two ways: with constant-variance noise, and with its amplitude modulated at the fundamental frequency, f_0:

TABLE I. PSHF performance versus HNR for synthetic signals with constant and modulated noise ($\beta=\pi$); results are η_u (η_v) in dB.

HNR	Constant		Modulated	
∞	72.6	$(-\infty)$	72.6	$(-\infty)$
20 dB	25.2	(5.3)	25.4	(5.6)
10 dB	15.1	(5.2)	15.4	(5.5)
5 dB	10.1	(5.2)	10.2	(5.4)
0 dB	4.9	(5.1)	5.0	(5.2)
-5 dB	-0.0	(5.1)	-1.0	(4.2)

$$u=\begin{cases} G(d*h) \\ G(d*h)\sqrt{\dfrac{2}{3}}\left[1+\cos\left(\dfrac{2\pi f_0 n}{f_s}+\beta\right)\right]. \end{cases} \tag{3}$$

The modulation was set at phase $\beta\in\{0,\pi/4,...,7\pi/4\}$ in relation to the glottal excitation; the factor of $\sqrt{2/3}$ equalized the noise to give the same mean signal power. The gain G was adjusted to give harmonics-to-noise ratios (HNRs) at one of six specified levels: ∞, 20, 10, 5, 0, or -5 dB.[2]

Using the specified pitch as an initial estimate, the local minimum in the pitch-estimating cost function was found at a series of points throughout each test signal. For high HNRs, the estimated period was identical to the true T_0 but, as the noise level was increased, so did the deviation of the estimates. These values were given as the pitch input to the PSHF, which then processed each signal in the usual way: incrementing the analysis frame, decomposing the signal, and accumulating the outputs.[3] Thus using the PSHF signal estimates $\hat{v}$ and $\hat{u}$, the changes in signal-to-error ratio (SER), η_v and η_u, were calculated as a measure of performance of the decomposition algorithm. For the harmonic component, the change in SER η_v is defined as the ratio of the initial noise to the residual error; conversely, the anharmonic performance η_u is the ratio of the deterministic part to the error. Both are expressed in decibels:

$$\eta_v=10\log_{10}\left(\frac{\langle v^2\rangle/\langle e^2\rangle}{\langle v^2\rangle/\langle u^2\rangle}\right)=10\log_{10}\left(\frac{\langle u^2\rangle}{\langle e^2\rangle}\right), \tag{4}$$

$$\eta_u=10\log_{10}\left(\frac{\langle v^2\rangle}{\langle e^2\rangle}\right), \tag{5}$$

where the residual error is $e=(\hat{v}-v)=-(\hat{u}-u)$. Although these two expressions are clearly related by the HNR σ_N (i.e., $\eta_u=\sigma_N+\eta_v$), it is useful to describe the performance of both components separately.

Table I lists the harmonic (in parentheses) and anharmonic performance over the range of specified noise conditions. Except for the anharmonic performance at the -5 dB condition, all the performance values are positive, which implies that the quality of the separated component is better than the input signal, i.e., the remaining errors are always smaller than the original corruption from the interfering source. The anharmonic performance is strongly correlated with HNR, and is approximately 5 dB greater than the initial HNR, so that any residual errors in the extracted anharmonic signal are about half as large as the true noise component. Meanwhile, the harmonic component is cleaned up to a similar degree by the PSHF, which reduces the errors to about

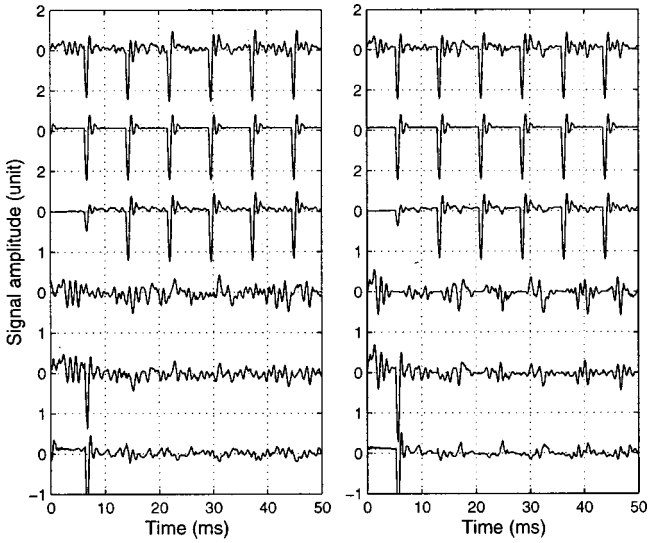

FIG. 3. Time series of the synthetic signal $s(n)$ with its constituent harmonic and anharmonic parts $v(n)$ and $u(n)$, the PSHF signal estimates $\hat{v}(n)$ and $\hat{u}(n)$, and the error $e(n)$, at HNR=10 dB for (left) constant-variance noise, and (right) modulated noise with $\beta=\pi$. They are arranged, from top to bottom, as s, v, $\hat{v}$, u, $\hat{u}$, and e (anharmonic and error signals are double amplitude scale).

half of their original amplitude, on average. Note that the results of the constant-variance and modulated noise cases are almost identical for $\beta=180°$, which implies that the performance is not significantly affected by the envelope of the noise. Tests at other phase settings produced similar results ± 0.2 dB. Overall, the results indicate the extent to which we can have confidence in the output signals that the PSHF produces.

Although there are transient errors for the first two pitch periods, as the tail of the first window ramps up toward its center, the decomposed components shown in Fig. 3 soon approach the true components. Looking at the time series more closely, it is apparent that the modulation of the noise envelope is retained. Indeed, the error signal also exhibits some modulation, suggesting that the error is proportionally related to the noise, for a given mean HNR. The amplitude of the envelope of $\hat{u}$ is slightly reduced with respect to the input component u, but *its phase remains unaltered*. This finding, which is crucial to the results presented in this article, will be further justified in Sec. IV D. These simulations, therefore, support the assertion that any modulation exhibited by the anharmonic component is not a processing artifact, but a property of the source component from which it is derived.

III. APPLICATION OF PSHF

A. Recording details

A series of recordings was made by three adult subjects who had no known speech pathologies: two native British English speakers, one male (PJ) and one female (SB), and a Portuguese male (LJ). The speech corpus contained sustained fricatives (all subjects) and some additional items: sustained vowels /ɑ, i, u/ (PJ, LJ, SB), nonsense words /pɑFɑ/ (PJ, LJ, SB), and fricatives with f_0 glides /v, ð, z, ʒ/ (PJ). One subject, PJ, also recorded nonmodal sustained

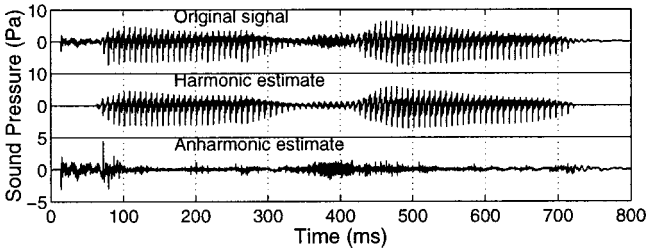

FIG. 4. Time series, from #1 by subject PJ, of (top) the original singal $s(n)$, (middle) the harmonic component $\hat{v}(n)$, and (bottom, double amplitude scale) the anharmonic component $\hat{u}(n)$.

vowels (viz., pressed, breathy, and whispered). The sustained fricatives were placed in a vowel context /VF:/ and sustained for 5 s. The fricatives F:, given here in unvoiced–voiced pairs, were: /Φ, β/ (bilabial), /f, v/ (labiodental), /θ, ð/ (dental), /s, z/ (alveolar), /ʃ, ʒ/ (palatoalveolar), /x, ɣ/ (velar), /ħ, ʕ/ (pharyngeal). None of the subjects was a trained phonetician, and none has all of the fricatives natively; the recordings nevertheless exhibit a range of place variation. The /pɑFɑ/ nonsense words were repeated to give ten tokens using a single breath.

The sound pressure at 1 m was measured in a sound-treated room using a microphone (B&K 4165/4133), a preamplifier (B&K 2639), and amplifier (B&K 2636, 22 Hz–22 kHz band-pass, linear filter). An electroglottograph (EGG, Laryngograph PCLX) with large (adult) electrodes was used to measure the transglottal impedance. Both signals were recorded on DAT (Sony TCD-D7, $f_s=48$ kHz), from which they were later digitally transfered to computer as 16-bit stereo data. A calibration tone and background noise were recorded with the microphone channel to give an absolute reference to pressure and to assess the measurement-error (noise) floor, respectively.

B. Decomposition of [p^hɑzɑ]

The utterance that we refer to as example #1 consisted of the nonsense word [p^hɑzɑ] spoken by subject PJ. To illustrate the effect of the PSHF, it was decomposed into its harmonic and anharmonic parts, as shown in Fig. 4. The original signal (top) shows the initial burst (20 ms) followed by voice onset (70 ms), the first vowel (100–320 ms), the voiced fricative (320–420 ms) and the second vowel (420–720 ms). The harmonic component shows the voicing with reduced noise, as expected; the anharmonic component contains the burst transient and initial noise (20–70 ms), a small amount of noise during the vowels and a larger amount during the fricative.

The PSHF algorithm tended to provide the most faithful decomposition during steady spells of voicing, when the amplitude and fundamental frequency varied little. The presence of jitter, shimmer, and abrupt changes causes perturbation errors, which can be seen in the anharmonic component (70–100 ms, 200 ms, 270 ms, and 450 ms in Fig. 4).

Figure 5 shows spectrograms of the signals, which contain the following features: vertical stripes at the glottal pulse instants, slowly varying horizontal bands (the formant resonances), a generally mottled appearance of the anharmonic

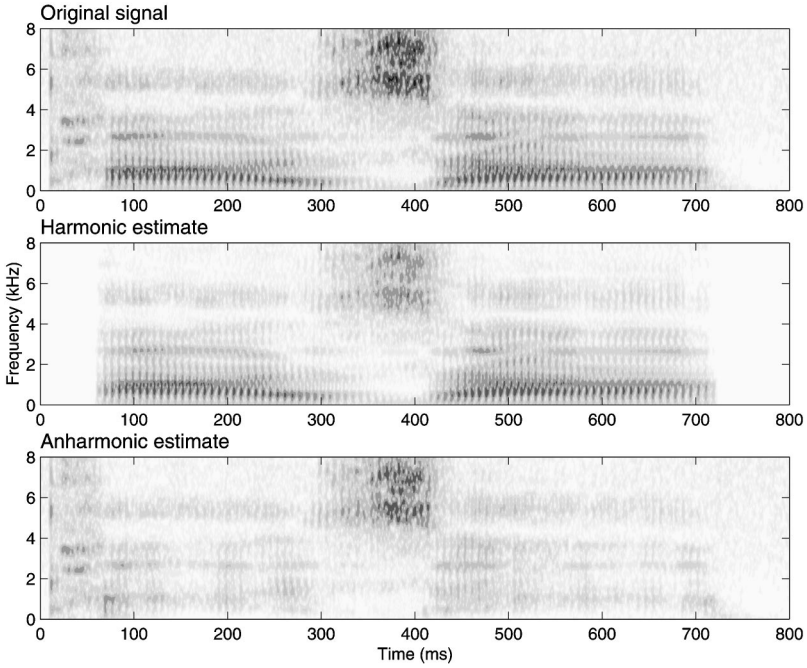

FIG. 5. Spectrograms (5 ms, Hanning window, ×4 zero-padded, fixed gray-scale) computed from the decomposition of #1 by subject PJ: (top) the original signal $s(n)$, (middle) the harmonic estimate $\hat{v}(n)$, and (bottom) the anharmonic estimate $\hat{v}(n)$.

component indicative of a noisy signal, and the separation of voicing and frication during the voiced fricative. Note that, without the aid of any heuristic filtering, the majority of the high-frequency turbulence noise has been passed to the anharmonic component, while the low-frequency voiced part has been successfully allocated to the harmonic component. It is also possible to see vertical striations during the frication onset in the high-frequency turbulence noise, which become less noticeable mid-fricative.

Looking at the vowel-fricative transition in more detail (see Fig. 6), we see the growth of the anharmonic component while the voicing dies down. Compared with the original signal, the harmonic component is much cleaner in appearance, and the regularity of the continuing vocal-fold oscillation is obvious, even in the middle of the fricative (ca. 380 ms), despite much weaker phonation. Although devoicing sometimes occurs in voiced fricatives, it is clear that that is not the case here. The anharmonic component $\hat{u}$, which is plotted with double the amplitude scale, is very small at the end of the vowel, commensurate with a typically high HNR

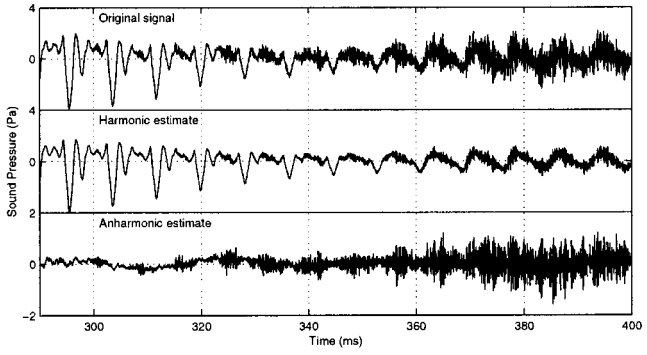

FIG. 6. A detailed view of the time series, from the vowel-fricative transition [–ɑz–] in #1 by subject PJ, of (top) the original signal $s(n)$, (middle) the harmonic component $\hat{v}(n)$, and (bottom, double amplitude scale) the anharmonic component $\hat{u}(n)$.

for modal voice (+17 dB). The HNR drops dramatically by 20 dB, to about −3 dB, as $\hat{u}$ grows during the transition. We also see pulsing of the noise, which becomes less noticeable as the fricative develops; the noise initially comes in bursts with each glottal pulse, then disperses into continuous noise in the fully developed fricative. Despite the inevitable degradation in PSHF performance, the disappearance of the modulation probably owes more to the decreased amplitude of phonation than to processing artifacts.

IV. MODULATION

A. Short-time power (STP)

By seeing how the envelopes of the harmonic and anharmonic signals vary over time, we can investigate not only the ratio of the two, the short-time HNR, but also their individual trajectories. Averaging over a frame comparable with a pitch period, we can see finer variations such as those of the anharmonic component caused by the modulation of the noise. The use of these derived measures is best demonstrated at the transition between a vowel and a mixed-source sound that has a strong anharmonic component, as illustrated by the vowel-fricative transition [–ɑz–] in Fig. 6.

The short-time power (STP) is a moving, weighted average of the squared signal, centered at time p. It is defined, for any signal $y(n)$, as

$$P_y(p) = \frac{\Sigma_{m=0}^{M-1} x^2(m) y^2(p+m-M/2)}{\Sigma_{m=0}^{M-1} x^2(m)}, \tag{6}$$

using the smoothing window $x(m)$ of length M. Thus P_v is the STP of the harmonic component and P_u that of the anharmonic component. The window x acts as a low-pass filter on the squared signals, whose roll-off frequency is governed by the window length M, which reduces the interference from higher harmonics. As such, periodic variations in STP are eliminated with the larger window, yet remain, albeit at a

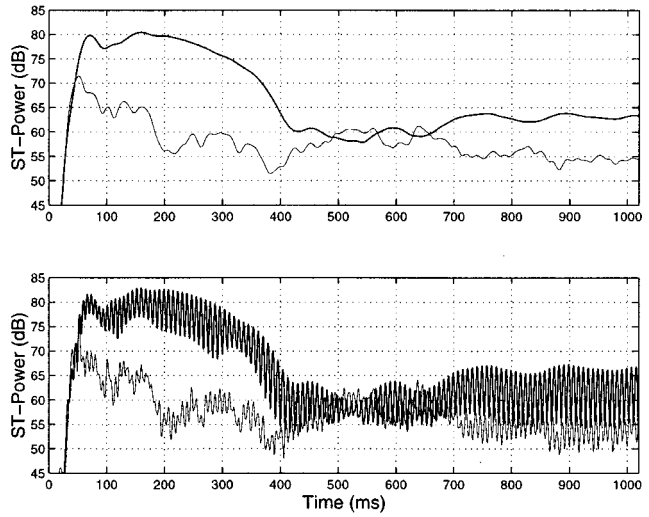

FIG. 7. The short-time power (STP) calculated over the medium term (top, $M \approx 32$ ms) and the short term (bottom, $M \approx 8$ ms) for the decomposed components from #2 by subject PJ: (thick) harmonic P_v, and (thin) anharmonic P_u.

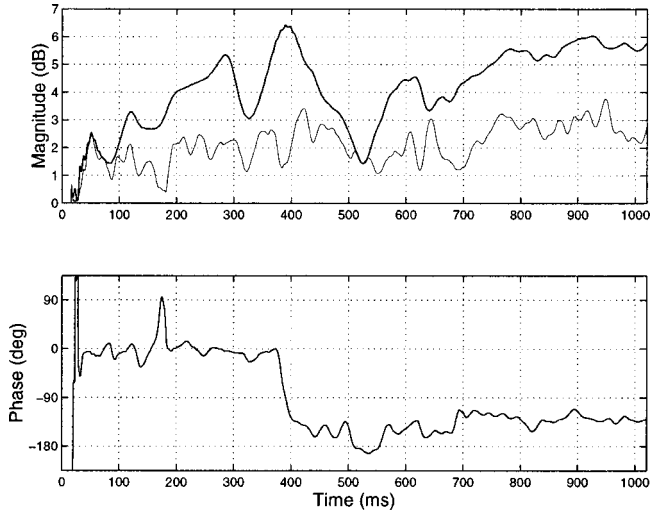

FIG. 8. Modulation of the short-term STPs at f_0 using token #2 by subject PJ, plotted as magnitudes (top: harmonic, thick; anharmonic, thin) and the phase difference (bottom).

reduced amplitude (-6 dB), with the shorter window.[4] For each computation of the STP, we set M to a constant and used a Hanning window: $x(m) = \frac{1}{2}(1 - \cos(2\pi m/M))$ for $m \in \{0,1,...,M-1\}$. In the present study, we were interested in features visible only at high time resolution (of order less than two pitch periods) so, although we were computing the (short-time) power from the signals to calculate P_v and P_u, $\hat{v}(n)$ and $\hat{u}(n)$ were used rather than the power-estimated $\tilde{v}(n)$ and $\tilde{u}(n)$, which are designed for narrow-band spectral analysis. In doing so, we were exploiting the PSHF's signal reconstruction in order to generate features from subsequent (asynchronous) analysis.

B. Observations of [ɑz:]

Speech example #2, the vowel-fricative transition [ɑz:] produced by subject PJ, was decomposed by the PSHF and the STPs were calculated. To observe short-term variations, the window length was set to the mean period, $M = \langle T_0 \rangle$; for medium-term variations over the length of the utterance, the window length was set to four times the mean period, $M = 4\langle T_0 \rangle$.

The resultant STPs are plotted in dB in Fig. 7. The difference between the harmonic and anharmonic medium-term STP trajectories (top) is the short-term HNR which, besides voice onset, shows a noticeable change at about 400 ms at the transition from vowel to fricative. Indeed, after voicing has peaked toward the beginning of the vowel (at about 160 ms), the harmonic amplitude dies away, reaching a maximum decay at the transition (ca. 400 ms). After some overshoot and subsequent fluctuations it returns to a steady value (ca. 700 ms). The anharmonic component grows during the development of the fricative (380–500 ms), undergoes a period of oscillation (500–660 ms), and finally settles down to a reasonably steady value. Note that the fluctuations of the two components at the start of the fricative are roughly equal and opposite. The initial period fluctuations at voice onset cause errors in the harmonic estimate, which get replicated, in negative, in the anharmonic estimate. Otherwise, the HNR is at least $+10$ dB in the vowel, rising to more than $+20$ dB at the steadiest point (around 200 ms). In the fricative, values range from -3 dB to $+10$ dB, settling to about $+8$ dB in the fully established part. The short-term STP curves (Fig. 7, bottom), which were computed using the single-period smoothing window, exhibit the same general trends, but have an oscillating element superimposed, which is caused by the modulations in signal power within individual pitch periods.

C. Pitch-scaled demodulation

In order to quantify the oscillations in STP, we calculated their magnitude and phase by complex demodulation of the logarithmic signals $10 \log_{10} P_v$ and $10 \log_{10} P_u$ [defined in Eq. (6)]. We took pitch-scaled frames of the signal, as for the PSHF ($N = 4T_0$, Hanning window w), and extracted the first harmonic, f_0:

$$\dot{P}_y(p) = \frac{10 \sum_{n=0}^{N-1} w(n) \exp\left(\frac{-j8\pi n}{N}\right) \log_{10} P_y\left(p + n - \frac{N}{2}\right)}{\Sigma_{n=0}^{N-1} w(n)}, \tag{7}$$

which provided the outputs $\dot{P}_v(p)$ and $\dot{P}_u(p)$ as complex Fourier coefficients, rather than as reconstructed single-harmonic signals. Implicit in the demodulation analysis is the assumption that the turbulence-noise source is multiplied by some signal that is related to the vibration of the vocal folds. Thus by rejecting the higher harmonics, we can take this model as a first order approximation, and extract reliably the phase of the principal mode, that at the fundamental frequency.

The modulation amplitudes are shown in Fig. 8 (top) and the relative phase (bottom). The modulation phases, which continually rotate at approximately the fundamental frequency f_0, are unwrapped and then subtracted from each other to form the phase difference between the modulation of the harmonic component and the modulation of the anhar-

monic component, as plotted (bottom). The degree of modulation of the harmonic part (Fig. 8, top, thick line) varies considerably during the vowel and the transition, but is more consistent during steady frication. The modulation amplitude is proportionately similar in the vowel and the fricative, and reaches its maximum value right at the transition into the fricative (~400 ms). It has minima at the points of weak voicing (around 520 ms and 640 ms), but otherwise grows in the fricative toward a steady value of approximately 6 dB. In contrast, modulation of the anharmonic component is relatively constant throughout, although it is slightly higher at about 3 dB in the steady fricative. There are no clear trends in the vowel; in the fricative, it is arguable whether or not the dips following the points of weak voicing (550 ms and 690 ms) are significant, although quieter phonation might be expected to cause a reduction in the subsequent modulation.

The phase difference (see Fig. 8, bottom), however, gives a more clearcut picture. During the vowel, the phase difference between the two sets of modulation coefficients is approximately zero, but it changes abruptly at the transition toward a markedly different equilibrium ca. $-130°$. We can calulate the mean phase more precisely by considering a series of unit vectors, each with its argument set equal to the instantaneous phase difference, θ:

$$\theta(n) = \arg\left(\frac{\dot{P}_u(n)}{|\dot{P}_u(n)|} \frac{\dot{P}_v^*(n)}{|\dot{P}_v(n)|} \right), \tag{8}$$

where $\dot{P}_v^*$ is the complex conjugate of $\dot{P}_v$, and $\dot{P}_y/|\dot{P}_y| = \exp(j \arg(\dot{P}_y))$ is the unit vector with the same phase as the modulation coefficient $\dot{P}_y$, for any y. To avoid phase wrapping errors, unit vectors were used to average the phase in a mathematically consistent circular algebra. Thus the (unweighted) time-averaged phase, with its standard deviation, is

$$\langle \theta \rangle = \arg(\mathbf{e}_\theta) \pm \sqrt{\frac{\Sigma_{n=1}^{S} |\exp(j\theta(n)) - \mathbf{e}_\theta|^2}{S-1}}, \tag{9}$$

in radians, where S is the number of sample points, and the mean unit vector $\mathbf{e}_\theta$ is

$$\mathbf{e}_\theta = \frac{\Sigma_{n=1}^{S} \exp(j\theta(n))}{S}. \tag{10}$$

For token #2 in Fig. 8 (bottom), $\langle \theta \rangle = -2° \pm 20°$ during the vowel (40–370 ms), and $-128° \pm 8°$ (700–1000 ms) during the fricative. This marked difference suggests that more than one voiceless source is in action. The finding is not news in itself yet, as a positive result, it can be used to explore variations in the source interaction quantitatively.

D. Using EGG as a reference signal

In order to tell which component is causing the change in the phase difference, we sought to relate the phases to some independent measurement of the glottis. An ideal reference signal would be the glottal waveform itself, but for practical purposes the glottal area or its electrical impedance,

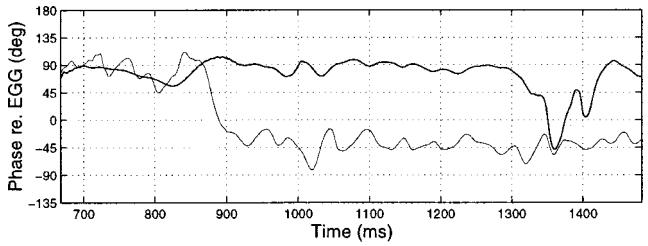

FIG. 9. Phase of the harmonic (thick) and anharmonic (thin) modulation components for #3 by subject PJ, related to that of the simultaneously recorded EGG signal.

which can be obtained using an EGG, may be used. Using the coefficient of the EGG signal at f_0, $\dot{L}_x(n)$, we compute the phases of the components:

$$\phi_v(n) = \arg\left(\frac{\dot{P}_v(n)}{|\dot{P}_v(n)|} \frac{\dot{L}_x^*(n)}{|\dot{L}_x(n)|} \right), \tag{11}$$

$$\phi_u(n) = \arg\left(\frac{\dot{P}_u(n)}{|\dot{P}_u(n)|} \frac{\dot{L}_x^*(n)}{|\dot{L}_x(n)|} \right). \tag{12}$$

Ignoring the effect of phase wrapping, the phases can be subtracted to give Eq. (8): $\theta = \phi_u - \phi_v$.

Using the above method on the synthetic signals from Sec. II B, we estimated the phase offset β for each of its eight specified values (0°, 45°, 90°, etc.) at three HNRs (20, 10, and 5 dB). All modulation phases measured from the decomposed synthetic signals were within 5° of their specified values. The mean error was less than 1° and the intermeasurement standard deviation was 2°. There were no noticeable differences across the different HNR levels, except perhaps a slight trend in the (much higher) intrameasurement deviations, which were 15°, 13°, and 13°, respectively.

Figure 9 contains the phase trajectories of the two components for another [ɑz:] token, #3, spoken by subject PJ, which do not exhibit the overshoot phenomenon that we saw earlier (Fig. 7, top). Both phases hover close to $+90°$ initially. The harmonic component is perturbed near the transition, returning to approximately the same value for the fricative, except when it strays as voicing momentarily falters (between 1300 ms and 1430 ms).

The anharmonic component shows greater variability, but approaches an equilibrium value after the transition that is distinctly offset from the average during the vowel. The change noted in $\langle \theta \rangle$ thus appears to be due primarily to changes in ϕ_u, signaling a change in source mechanism for the unvoiced component. We expect that the anharmonic component during the vowel is due to a slight breathiness, i.e., turbulence noise generated in the vicinity of the glottis, and that during the following [z:], the anharmonic component is primarily due to turbulence noise generated downstream of the tongue-tip constriction. The step change in ϕ_u at the vowel-fricative transition therefore corresponds to a change in source location. This effect would predict that the amount of phase change should depend on the fricative's place, which we will investigate in Sec. V. It should be noted

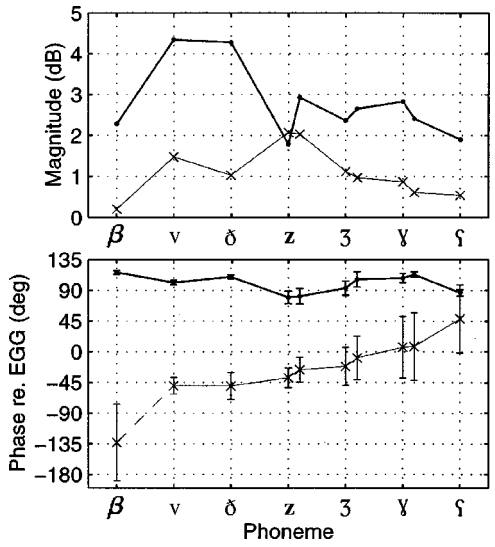

FIG. 10. Magnitude (top) and phase (bottom) of modulation coefficients, referred to the EGG signal, versus place of articulation for sustained fricatives [β, v, ð, z, ʒ, ɣ, ʕ] by subject PJ. Harmonic (•, thick line) and anharmonic (×, thin line) components were plotted with ($\pm 1\sigma$) error bars. Those measurements on vertical grid lines are for normal voicing; those adjacent (to the right), where a pair of measurements are shown, were taken from a section interrupted by devoicing.

that a phase difference of approximately zero could as easily be the product of perturbation errors (e.g., from jitter and shimmer) in the processing as of an in-phase modulated noise source. Nevertheless, examination of the time-series signals for the harmonic and anharmonic components for over 20 examples gives us confidence that the STP, as a summary of signal amplitude (or envelope), contains useful information about the sources.

V. RESULTS

A. Sustained fricatives

The magnitude and phase of the modulation coefficients were determined for ten fricative tokens that included seven different places of articulation. All of the tokens were similarly pitched at $f_0 = 120 \pm 5$ Hz, and sustained by subject PJ for at least 4 s, of which a steady section of approximately 1 s duration was analyzed. For some cases, the section analyzed included a part of the contextualizing vowel; for others, only the fricative was included. The PSHF was used to decompose each example, and modulation coefficients of the harmonic and anharmonic components were calculated, as described in Sec. IV. Finally, the coefficients were averaged over the fricative, excluding periods of devoicing, vowel-fricative transitions and two pitch periods from either end of the section. The time-averaged magnitudes and phases are plotted in Fig. 10. The points plotted on the vertical grid lines were all from steady regions of voicing, whereas those adjacent suffered an interruption in voicing.

As mentioned in Sec. IV C, the magnitudes (Fig. 10, top) were all halved by the low-pass effect on signal power of the windowing, which was adjusted accordingly for each measurement to allow comparisons between harmonic and anharmonic STP, and across different phonemes. The magnitude of the modulation of the harmonic components (thick) is 3 ± 1 dB and, in all but one case, is greater than that of the anharmonic components (thin). The anharmonic modulation magnitudes were equally variable, but ranged from almost zero in the bilabial fricative [β] to 2 dB in [z] (the same as that of the harmonic modulation).

The phase of the modulation coefficients was referred to the EGG signal by subtracting the phase of its f_0 component, as before. Care had to be taken in aligning pitch, power (STP), and phase vectors in the analysis, but the difference between using the pitch extracted from the acoustic signal versus that from the EGG was found to be negligible. The unweighted-mean values are plotted in Fig. 10 (bottom) with error bars indicating one standard deviation (± 1 s.d.), time-averaged over the appropriate portion of the token. Of the two components, the harmonic's results showed greater consistency within each phase measurement; across measurements, these values were all in the vicinity of $+100° \pm 20°$. The anharmonic phases, although more variable, were all distinct from their harmonic phases, except for [ʕ]. Moreover, where the transition from the vowel was included in the analysis segment, a clear step was seen in the time series of the anharmonic modulation phase.

The phase of the modulation of [β]'s anharmonic component had the largest variance, which was related to the unusually small amount of modulation and rendered it most susceptible to interference from disturbances. Since the anharmonic modulation in [β] was therefore poorly correlated with the EGG, we shall ignore this phoneme in subsequent evaluation. For the remaining anharmonic phase data, there were two notable trends: (i) the mean phase increased as the place of constriction moved in a posterior direction, and (ii) so did the variance. The systematic change of phase with place seems worth further investigation, although we might well expect the phase to depend also on f_0. Any delay in the speech production system, such as the propagation time from the lips to the microphone, would add a phase term that increased linearly with f_0, its gradient dependent on the amount of delay. In the following section we investigate the relationship between the pitch and anharmonic phase during sustained fricatives that contain changes in f_0, and attempt to identify the cause of any delays.

B. Pitch glides

When using spot measurements of phase for determining delay times, the main concern is that phase wrapping may occur, e.g., a phase reading of 420° might be misinterpreted as only 60°, or vice versa. The number of cycles is important because long delays, i.e., greater than a period, inherently entail phase-wrapping. A simple test for phase wrapping can be carried out by altering the fundamental frequency f_0 and by noting the phase changes. A few spot measurements can be made or, more dependably, a continuous measurement during a pitch glide. For a constant delay τ_u, the phase is simply a linear function of frequency:

$$\phi_u = 2\pi\tau_u f_0 + \beta, \tag{13}$$

where β is the phase offset between the actual modulating signal, whatever it may be, and the EGG signal. The phases

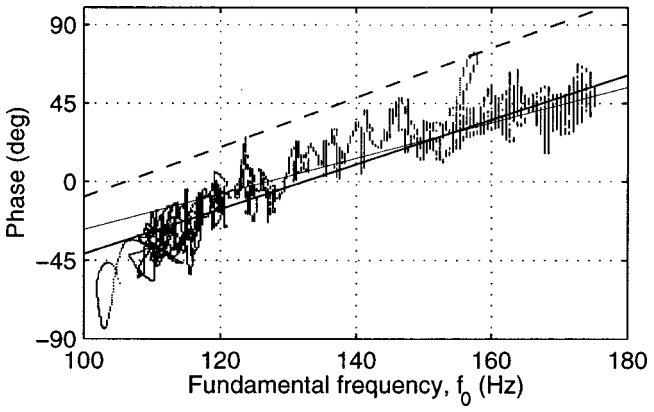

FIG. 11. Scatter plot of the anharmonic modulation phase vs fundamental frequency for the sustained fricative [z:] by PJ during a descending pitch glide, with its regression (thick solid line), and those of an ascending [z:] (thin solid line), and a descending [ʒ:] (thick dashed line).

ϕ_u and β can take any real value, although in our initial measurements they lie in the range $\pm 180°$. Hence, provided other independent variables remain unaltered, the gradient of the phase with respect to frequency provides an absolute estimate of τ_u, the delay duration for a given phoneme.

Subject PJ was asked to sustain a fricative during a smooth pitch glide sandwiched between two notes about a perfect fifth apart. That is, a constant-f_0 fricative was held for at least 1 s, then f_0 was increased steadily to approximately $1.5 f_0$ over a similar period, and finally the fricative was held at the higher note of about $1.5 f_0$ for at least another second, taking about 5 s in total. Recordings were also made of descending pitch glides.

For all of the tokens analyzed, the time series of the anharmonic modulation phase showed a definite correlation with the extracted f_0, and both parameters exhibited distinct equilibria at the end conditions, which were connected by a gradual transition. The relationship between f_0 and the phase ϕ_u can be seen more clearly by plotting them against each other, independently of time. Thus Fig. 11 is a scatter diagram of the anharmonic STP modulation phase versus fundamental frequency for the sustained fricative [z:], during a descending pitch glide.[5] In this example, the points lie roughly along a diagonal line, in the range $\pm 45°$, except for a few stray excursions that occured at transitions or near a singularity, where the modulation amplitude was almost zero. There is a higher density of points at either end of the trajectory line due to the period of constant pitch before and after the frequency ramp. The deviation from this line, $\sigma \approx 10°$, is of the same order as the deviation of the (constant-f_0) sustained fricatives considered earlier. Owing to the integer quantization of the extracted pitch period (in sample points), the fundamental frequency values also exhibit quantization, which explains why the data points lie on a set of vertical lines.

TABLE II. The anharmonic delay τ_u, the offset phase β and the standard deviation σ about the corresponding regression line, for three f_0 glides by subject PJ.

Phoneme	f_0 (Hz)	τ_u (ms)	β (°)	σ (°)
[z:] ascending	125→175	2.8	−129	10
[z:] descending	111←172	3.8	−169	11
[ʒ:] descending	121←178	4.0	−154	22

The best-fit line (thick solid line in Fig. 11) was calculated for the plotted data points by a least-mean-squares regression and provides good general agreement. The line's gradient provides an estimated delay time of $\tau_u \approx 3.8$ ms, and the intercept with the y-axis at $f_0 = 0$, was $\beta \approx -170°$. Regression lines were also calculated for two other examples: [z:] ascending and [ʒ:] descending. The lines for [z:] are within 10° of each other for the ranges of f_0 measured, although their gradients differ, which suggests that some other factor may have influenced these results. The line for a descending [ʒ:] is set apart from those for [z:], but has a similar gradient, particularly to that of the descending [z:].

The values of β and τ_u for all three cases are listed in Table II, with the mean values of the f_0-glide endpoints. The difference between the two descending fricatives [z:] and [ʒ:] was as expected in both direction and scale, yet there was a considerable discrepancy between the values calculated for the ascending and descending [z:], which was exacerbated by the extrapolation to $f_0 = 0$. Given that the propagation time for an acoustic wave from the lips to the microphone is 2.9 ms ($r = 1$ m, $c_0 = 343$ m/s, room temperature, dry air) and acoustic propagation in the tract would take about 0.5 ms ($l = 16.5$ cm, $c_0 = 359$ m/s, body temperature, saturated air), the times derived from the gradient are of an appropriate order of magnitude. The zero-frequency phase offset β, despite these errors, corresponds to a point between one-half and three-fourths of the way through the open portion of the glottal cycle. We shall speculate about potential interpretations of the coincidence of this timing relationship with the maximum glottal flow in the following section. For fricatives showing a higher variance, the scatter plots are less informative. Critically, no phase wrapping of the modal trajectories took place for any of the fricatives examined, which validates the order of our earlier phase measurements.

VI. DISCUSSION

A. From phase to delay

We would like to be able to convert the reported phase values into delay times in order to relate a peak in the acoustic response to the event that caused it. The glottal closure is commonly assumed to give the principal acoustic excitation of the vocal tract. The harmonic component $v(n)$ should then consist primarily of the vocal-tract response to that excitation. The smoothed STP of $v(n)$ has a peak every cycle that is slightly delayed with respect to the instant of excitation, and further delayed due to the acoustic propagation time from the glottis to the microphone in the far field. We computed its phase ϕ_v with respect to the peak of the fundamental component of the EGG signal. To refer it instead to the moment of closure of the vocal folds, we subtract $\alpha = \arg(\dot{L}_x)_{\mathrm{cl}}$; to convert this phase to a time delay, we divide by the instantaneous fundamental frequency:

$$\tau_v = \frac{\phi_v - \alpha}{2\pi f_0}, \tag{14}$$

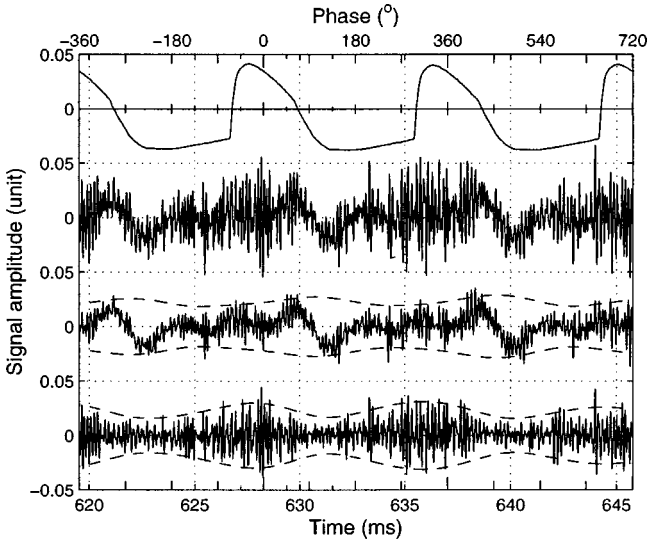

FIG. 12. Time series during a sustained [z:] by PJ: (from top) EGG signal L_x, sound pressure s, harmonic part v, and anharmonic part u.

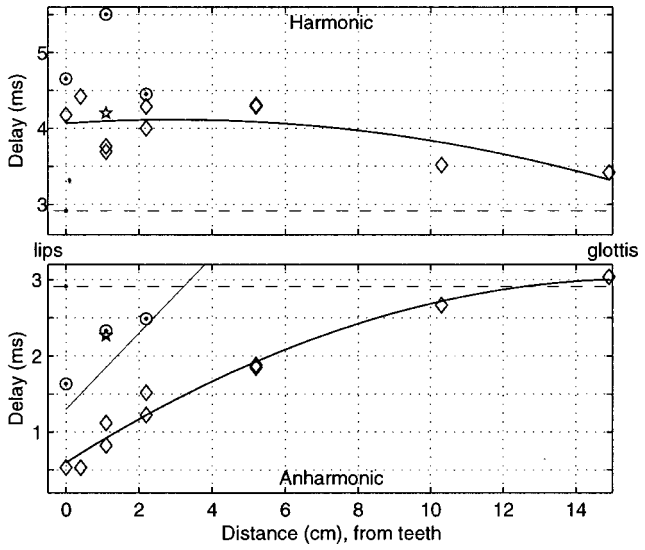

FIG. 13. Harmonic and anharmonic delay times, τ_v [top, Eq. (14)] and τ_u [bottom, Eq. (15)] respectively, versus distance of constriction from teeth, for subjects PJ (◇), LJ (⊙), and SB (☆). The dashed line is the predicted lip-mic propagation delay τ_R, the thin solid line is the predicted total delay, and the thick solid line is the quadratic line of best fit.

where ϕ_v is defined by Eq. (11). The anharmonic component $u(n)$ consists primarily of the vocal-tract response to the noise excitation. We wish to convert ϕ_u to a time delay also, but it is not clear whether we should refer ϕ_u to the same instant of closure of the EGG signal. If we use the same angle α as in Eq. (14), we are effectively assuming a model of the modulation mechanism, namely that the peak amplitude of the turbulence noise source is evoked by the excitation originating from the instant of glottal closure. We wish instead to deduce the mechanism controlling the modulation, by using the phase difference expressed as a time delay. Therefore, to refer the phase to an unknown point in the EGG signal, we subtract the angle β:

$$\tau_u = \frac{\phi_u - \beta}{2\pi f_0}, \tag{15}$$

where ϕ_u is defined by Eq. (12). For our initial discussions, we set $\beta = \alpha$.

Figure 12 shows a set of four synchronous time-series signals during the fricative [z:] sustained by subject PJ, which are (from top) recorded EGG $L_x(n)$, recorded sound pressure $s(n)$, and the decomposition into the harmonic and anharmonic signals, $v(n)$ and $u(n)$. The dashed lines around the harmonic and anharmonic components represent their envelopes (i.e., $\pm 2\sqrt{P_v}$ and $\pm 2\sqrt{P_u}$). The EGG measures the time-varying (high-pass filtered) part of the trans-glottal conductance, which is at a maximum when the glottis is closed. It shows a sharp rise at the instant of closure, occurring at around -0.4π ($-72°$), with respect to the EGG signal's fundamental component, whose phase is indicated by the upper abscissa in Fig. 12. This phase offset is slightly less than a quarter of a cycle, because of the long open portion and the abruptness of the closure. Although the phase may change slightly throughout the recorded corpus and for subjects other than PJ, the value of $\alpha = -0.4\pi$ shown here is used in all cases to refer the harmonic component to the same instant of the EGG signal.

TABLE III. Estimated distance from the constriction to the teeth for sustained voiced fricatives by subject PJ, in cm.

Phoneme	v	ð	z	ʒ	ɣ	ʕ	ɑʰ
Distance	0.0	0.4	1.1	2.2	5.2	10.3	14.9

Through a separate study (Shadle *et al.*, 1999), we obtained magnetic resonance imaging (MRI) data for subject PJ, saying [pʰɑsi]. Combining these with articulatory phonetics, we were able to estimate the constriction location for each phoneme. Distances along the vocal tract were measured from the glottis, and the position of the teeth was estimated in relation to the lips and the hard palate (upper) or tongue body (lower). Table III lists all the constriction-teeth distances, which agree closely with Table I in Narayanan *et al.* (1995). For the breathy vowel [ɑʰ], the place of greatest constriction was assumed to be the glottis.

Ideally, we would like to characterize each phoneme by two distances: from glottis to place of constriction, and from constriction place to the location of turbulence noise generation. Different aspects of sound generation take place over these two ''paths.'' However, while for some fricatives it is well known that noise generation is highly localized at the teeth (e.g., [s, ʃ, z, ʒ]), for others the noise source appears to be distributed, for instance, along the hard palate for [ç] (Shadle, 1991). The distance from the constriction to the source location is thus less precisely known for some fricatives. All delays are therefore calculated using the constriction-teeth distances given in Table III. These values were used for all three subjects, regardless of minor intersubject variation in physical dimensions. Although women's vocal tracts are generally shorter than those of men, most of the difference is in the pharynx. Since for LJ and SB we are dealing with distances from within the oral cavity to the teeth, the variation is considered negligible. Although this part of the procedure is crude compared with the signal processing, it enables us to visualize our results in a way that

TABLE IV. Estimated travel times (ms) for /z/ ($l_1=14.6$ cm, $l_2=1.1$ cm), /ʒ/ ($l_1=13.5$ cm, $l_2=2.2$ cm) and /ɤ/ ($l_2=10.2$ cm, $l_1=5.2$ cm), by acoustic propagation ac or by convection co, using $U_1=200$ cm^3/s and $U_2=600$ cm^3/s for co_1 and co_2, respectively. The column under t_1 gives the travel times over path 1, and the first row under t_2 those for path 2. The nine values inside each sub-table are t_1+t_2, rounded to two significant figures; those in bold face best match the measured data (see text).

/z/		t_2 (ms)		
		ac	co_1	co_2
t_1 (ms)		0.06	1.90	0.63
ac	0.38	0.44	**2.3**	**1.0**
co_1	690	690	690	690
co_2	230	230	230	230

/ʒ/		t_2 (ms)		
		ac	co_1	co_2
t_1 (ms)		0.08	3.0	1.0
ac	0.35	0.44	**3.4**	**1.4**
co_1	640	640	640	640
co_2	210	210	220	210

/ɤ/		t_2 (ms)		
		ac	co_1	co_2
t_1 (ms)		0.17	6.0	2.0
ac	0.27	0.44	**6.3**	**2.3**
co_1	490	490	490	490
co_2	160	160	170	160

has greater physical meaning. Bearing in mind that the teeth will not necessarily be the source location in all cases, we can nevertheless interpret trends and make order of magnitude calculations to help indicate the aero-acoustic processes that are likely to be operating.

The delays calculated for the voiced fricatives of three subjects are plotted against place of articulation in Fig. 13, including one breathy [ɑ] vowel (PJ). For reference, the lip-microphone propagation time is shown as a dashed horizontal line, $\tau_R=2.9$ ms for a microphone at 1 m (speed of sound $c_0=343$ m/s). In Fig. 13 (top), the delay times τ_v are all greater than the acoustic propagation delay, as expected. The additional delay, the reverberation lag, is reasonably consistent across phonemes, showing a mean value of 1.3 ms and no significant trend. In contrast, τ_u (Fig. 13, bottom) is generally below τ_R. Since the largest portion of these delays is, in fact, the wave propagation time from the lips to the microphone (which is obviously identical for both components), any variations in the delay are attributable to other causes. Such causes include jitter/shimmer effects, changes in glottal waveform, changes in vocal-tract configuration, the measurement noise on the data, processing errors, and actual changes in the source characteristics. However, before we attempt to interpret the anharmonic τ_u results, let us consider the physical mechanisms that could lead to modulation of the frication source, as has been observed.

B. Travel times

For all voiced fricatives, the path that the flow perturbation must take from glottis to far-field microphone can be divided into three sections: from glottis to constriction exit; from constriction exit to the principal location of turbulence noise generation; thence to the microphone. The first two paths are the most important with regard to the mechanism of noise modulation.

During phonation, the pulsing jet of air exiting from the glottis generates sound and sets up vortical motion. The sound wave travels downstream at the speed of sound; the vortices convect at the order of the mean flow velocity, which is much slower than the speed of sound c_0 (Barney *et al.*, 1999). The effects of phonation therefore traverse the first section of the path in two different ways, with two different travel times. The longer that section is, i.e., the more anterior the constriction, the bigger the discrepancy in time will be.

The travel time for a sound wave over this first glottis-to-constriction path of length l_1 can be estimated as $\tau_1|_{ac}=l_1/c_0$. Values are shown in Table IV computed for three different l_1 values ($c_0=359$ m/s). The convective travel time is estimated as $\tau_1|_{co}=l_1/(V/2)$. A minimum and maximum convective velocity are computed using volume velocities of 200 and 600 cm^3/s, and an average cross-sectional area through the back cavity of 5 cm^2. It is clear from the values shown in the table that even the lower of the convective delay estimates (co_2) is two orders of magnitude higher than the measured delays. Such delays would be easily observable at any transition, and would in particular lead to extensive phase wrapping on the pitch glides. Further, we observe longer delays (longer by approximately 1 ms) for a more posterior place, whereas a convective mechanism for path 1 would mean that delays would shorten by 50–150 ms. Therefore we conclude that the aspect of phonation that modulates the noise travels at the speed of sound over path 1.

The second path extends from the constriction to the principal location of turbulence noise generation. The flow velocity increases in the constriction; at the exit, a turbulent jet forms. The self-noise (from mixing) of the jet is relatively weak for vocal-tract dimensions and flow rates but, whatever obstacle the jet encounters (whether the palate or the teeth), additional turbulence noise is generated that is louder (and can be much more localized). If the jet emerging from the constriction is pulsing, the turbulence noise generated by it will likewise fluctuate, but an acoustic field can also influence the formation of turbulence (Crow and Champagne, 1971). We could further consider whether an acoustic field could influence not only the jet structure, but the sound generation where it impinges on the obstacle.

For path 2, we can again make order-of-magnitude estimates of the travel time at acoustic and convective velocities. We estimate l_2 to be the constriction-teeth distance, although we expect that the teeth do not act as the obstacle in all these cases. Again, two values of l_2 are chosen that correspond to the two values of l_1, that is, result in the same vocal tract length in both cases. The acoustic delay is then computed as $\tau_2|_{ac}=l_2/c_0$, as shown in the table. For the convective delay, V is recomputed using a typical constriction area of 0.1 cm^2 rather than the 5 cm^2 used earlier. The same minimum and maximum volume velocities are used, giving much higher values of V.

From Fig. 13 (bottom), lengthening l_2 from 2 to 5 cm actually increases the delay by approximately 0.7 ms. This is

consistent with the convective delay computed using the maximum convective velocity (column co_2 in Table IV). If travel times were at speed of sound in both paths, there would be virtually no difference in the delay with place. Therefore, the second path must involve some mechanism that convects.

C. Source modulation mechanisms

What theoretical models exist that describe the modulation mechanism itself? Most of the methods in the literature, summarized in the Introduction, incorporate modulation by a parameter related to glottal flow, such as the instantaneous component of the volume velocity at the constriction exit, but do not allow for a nonacoustic mechanism, i.e., for propagation velocities other than the speed of sound. The differences with place that we observe in the phase of the anharmonic component are not consistent with models depending only on acoustic propagation.

We have not so far discussed the extensive literature examining interaction of the glottal waveform with the vocal-tract driving-point impedance. Rothenberg (1981) showed, theoretically and by inverse-filtering speech, that the first formant frequency F_1 affects the degree of skewing of the glottal waveform U_G: the vowel [ɑ], with its high F_1, has a more skewed U_G (peak U_G occurring later in the glottal cycle) than does [i], with low F_1. Since all of the English voiced fricatives have lower F_1 than [ɑ], the peak U_G is predicted to shift earlier in the cycle during [ɑF], which was borne out by Bickley and Stevens' results (1986) for consonantal constrictions at the lips. Nevertheless, though such a mechanism could perhaps explain why the phase difference changes during the vowel-fricative transition, it does not explain the amount of change we observe (ranging from 40° to 150°) nor the difference with place, which should affect F_2 and higher formants rather than F_1.

Crow and Champagne (1971) showed that acoustic excitation applied to air in a duct upstream of the jet nozzle could induce an orderly structure in the jet wake, with a preference for $St=fD/V=0.30$. Such a structure appears when the acoustic velocity is greater than 1% of the mean flow speed V at the nozzle exit (nozzle diameter D). The turbulence noise spectra show that the forcing has the effect of suppressing background noise and enhancing noise at frequencies near the forcing fundamental and its harmonics.

We cannot compare all aspects of Crow and Champagne's results to ours because the relevant vocal-tract parameters cannot be measured accurately enough. However, we estimate that Strouhal numbers for voiced fricatives range from 0.3 to 0.9, based on $f=f_0$, a typical constriction diameter D, and the volume velocities U used in Table IV. The forcing takes some (unspecified) time to alter the shape of the jet; any change in the jet travels downstream at its convection velocity. We conjecture that the sound generation mechanism with which we are chiefly concerned, that of the jet impinging on an obstacle, would, in the presence of the ''forcing function'' of phonation at f_0, exhibit nonlinear emphasis of f_0 and its harmonics, similar to the free jet spectra shown by Crow and Champagne. Any change in f_0 would affect the noise generated after a delay, related to the convection velocity and the distance from constriction to obstacle. Their results provide a plausible mechanism for the modulation of voiced fricatives, but do not help us to estimate β, the angle that determines the phase of the glottal cycle to which we should refer the modulation of the anharmonic component. Nevertheless, we can place some bounds on β's range of variation.

D. Interpretation

Up to this point, we have set $\beta=\alpha=-72°$. However, this produced delays shorter than the acoustic propagation time from lips to microphone, i.e., $\tau_u<\tau_R$. This is not possible since if any part of the path is traveled at convection velocity, the delay will be increased. Therefore $\beta<\alpha$, i.e., β is more negative than α. Yet β has a lower bound, since otherwise we would observe phase wrapping during the pitch glides. (For the interval of a perfect fifth used here, the lower bound is -6π.) We thus have strong bounds on β: $-(3\times360)°<\beta<-72°$. In addition, we can compute the angle that would make the minimum τ_u just equal to the acoustic propagation of 2.9 ms: $\beta\lesssim-175°$.

The pitch glide data produced estimates of β that ranged from -120 to $-180°$, as presented in Table II. The estimates so derived must be treated with caution for two reasons: they are based on one subject and only three glides, and the fitted lines are used to extrapolate an intercept value. Thus any variation in the glide itself will be magnified in the intercept estimate. By modifying the best fit lines to the pitch glide results, using one standard deviation to give the worst case gradients, we get a range of $-200°<\beta<-100°$. These weak bounds for the range of β, together with the stronger bounds given above, predict that β in Eq. (15) should lie within the range: $-200°\lesssim\beta\lesssim-175°$. Taking $\beta=-175°$ would effectively add 2.4 ms to the delays shown in the lower half of Fig. 13.

While it is clear that modulation of the anharmonic component varies with place, we can do no more than speculate that the acoustic-convective theory of sound production for the fricative component in voiced fricatives is the most likely, whose mechanism can be described as follows. A pulsed flow is emitted from the glottis into the vocal tract. Sound waves propagate down the vocal tract towards the constriction; at the constriction, the flow forms a jet, developing turbulence as it travels downstream. The temporal and spatial characteristics of the mixing flow are strongly influenced by the intersecting sound waves, inducing synchronous pulses of turbulence; the pulsed turbulence and entrained vortices convect downstream. When the jet encounters an obstacle (such as the teeth), a new source is generated that is pulsed at f_0 and efficiently radiates sound. The sound source at the obstacle excites the vocal tract; sound radiated from the lips propagates into the far field.

Assuming this to be the case, the increasing variance in Sec. V A might be explained by three possible causes. First, the exact shape and location of the constriction may vary more for more posterior places, as the articulators become larger and are less finely controlled (e.g., tongue dorsum relative to tongue apex). Second, variations in convection velocity would make a larger contribution for the more pos-

terior fricatives where the vorticity has further to travel before reaching the obstacle. Third, the obstacle upon which the turbulence impinges is likely to extend further in the direction of flow, producing a more distributed source for constrictions nearer to the glottis.

VII. CONCLUSION

In this paper, we have used the pitch-scaled harmonic filter (PSHF) on voiced fricatives to decompose them into harmonic and anharmonic components. The amplitude of the components was represented by their short-time power, which exhibited modulation at the fundamental frequency f_0. The relative phase of the modulation of the two components changes rapidly at a vowel-fricative transition, settling near an equilibrium that depends on the fricative's place of articulation. The subjects were recorded uttering fricatives at a range of places. The findings of this article support the suggestion that the aero-acoustic mechanism of fricative sound production is modified by voicing, due to the powerful effect of upstream acoustic disturbances as they intersect the jet (Crow and Champagne, 1971).

Tests of our PSHF algorithm on synthetic signals confirmed that modulation was not a signal processing artifact. They showed improvements to the harmonic SER of greater than 5 dB, and to the anharmonic SER, of the HNR plus 5 db. The algorithm was then applied to give a plausible decomposition of the recorded utterance [pʰɑzɑ], successfully separating simultaneous parts of voiced and unvoiced speech. Inspecting the reconstructed time series, we observed the time-varying interaction of sources in the voiced fricative [z:], manifested as pulsing of the unvoiced component. Using the STP to approximate the signal envelopes, we derived an objective and quantitative method for measuring the magnitude and phase of the pulsation by complex demodulation. The phase difference between the modulation of the harmonic and anharmonic parts revealed two distinct states in the vowel-fricative transition [ɑz:]. Referring the phase values to the EGG provided better fidelity in the modulation analysis and allowed us to attribute the change in state to the anharmonic component, which corresponded to a change in the unvoiced source location. The phase change decreased as the place of the constriction moved posteriorly, which was verified on a second subject (LJ).

A set of f_0 glide experiments showed that the phase, as a function of f_0, behaves almost entirely like a constant place-dependent delay. It is tempting to speculate further about the role of the observed phase differences in the categorical perception of voiced fricatives, particularly in opposition to aspiration noise, but we have found scant empirical evidence in the literature to support these claims. In perceptual tests on synthetic signals, Hermes (1991) found that the perception of noise bursts is affected by their phase relative to voicing; out-of-phase noise is distinguished from the voicing component, whereas synchronous bursts are assimilated.

In summary, we have used a pitch-scaled harmonic filter to decompose voiced fricatives into harmonic and anharmonic components. The different phase of the envelopes of these components led us to vary place and f_0 systematically in order to determine the mechanism controlling the modulation. We have shown that a plausible explanation is that the acoustic signal generated at the glottis induces a structure in the jet emerging from the constriction, and thus alters the noise generated by the jet as it impinges on an obstacle. Further practical experiments using dynamic physical models should be conducted to establish whether this explanation is correct. The second non-acoustic path that accounts for the variation of phase with place has not been incorporated into speech synthesis models until recently (Sinder, 1999). It would be instructive to ascertain whether Sinder's model predicts the phase changes we observed. It would also be useful to explore inter-subject variations and the robustness of phase changes to changes in f_0, effort and speaking style. Finally, the phase difference between harmonic and anharmonic components, which changes suddenly in the vowel-fricative transition, may well be perceptually important and should be investigated.[6]

ACKNOWLEDGMENTS

This paper is based on a talk presented at the 2nd International Conference on Voice Physiology and Biomechanics, Berlin, Germany, 12–14 March 1999. The authors would like to thank Phil Nelson and Anna Barney, both at ISVR, University of Southampton, and Celia Scully, formerly at University of Leeds, for helpful discussions. The authors would also like to thank Dirk Michaelis, Drittes Physikalisches Institut, Göttingen, and Dan Sinder, Lincoln Laboratory, MIT, for their helpful comments on an earlier version of this manuscript.

[1]There is no reason why, in theory, a number of periods other than four may not be used, but we have not tested any alternatives. However, we believe that the current value, which has a time-frame comparable to others (e.g., Frazier *et al.*, 1976), offers a reasonable compromise between adaptability and ideal PSHF performance for speech signals.

[2]In a similar study, the PSHF performance was evaluated with three kinds of perturbation: jitter, shimmer and constant-variance additive noise. Although those tests were at a different pitch ($f_0 = 130.8$ Hz), the performance at matching conditions was unaffected.

[3]Incidentally, repeating the process with the prescribed pitch values showed that our using the noisy values had little effect on the anharmonic performance, which was degraded by 0.4 dB in the worst case. The observed decline in the harmonic performance with increasing noise, though, was entirely due to the effect of noise on the estimated pitch, which would otherwise have kept η_v pinned at 5.4 dB and 5.6 dB for all constant and modulated noise tests, respectively.

[4]Note that the STP can also be computed in a pitch-scaled way, but there is little advantage from this minor adjustment to the roll-off frequency, for the range of f_0 values within each token.

[5]Every one in ten points has been plotted, so the values have been effectively sampled at 4.8 kHz.

[6]Further information can be found on the internet, including Matlab script (.m) files of the algorithm, a data (.dat) file containing the LPC coefficients used in Sec. II B and sound (.wav) files of examples used in this paper: http://www.isis.ecs.soton.ac.uk/research/projects/nephthys/.

Barney, A., Shadle, C. H., and Davies, P. O. A. L. (**1999**). ''Fluid flow in a dynamic mechanical model of the vocal folds and tract. I. Measurements and theory,'' J. Acoust. Soc. Am. **105**, 444–455.

Bickley, C., and Stevens, K. N. (**1986**). ''Effects of a vocal-tract constriction on the glottal source: Experimental and modeling studies,'' J. Phonetics **14**, 373–382.

Bretthorst, G. L. **(1988)**. *Bayesian Spectrum Analysis and Parameter Estimation*, Lecture Notes in Statistics (Springer-Verlag, Berlin).

Coker, C. M., Krane, M. H., Reis, B. Y., and Kubli, R. A. (**1996**). ''Search for unexplored effects in speech production,'' Proc. ICSLP '96, Philadelphia, PA 14(6), pp. 415–422.
Crow, S. C., and Champagne, F. H. (**1971**). ''Orderly structure in jet turbulence,'' J. Fluid Mech. **48**, 547–591.
Fant, G. (**1960**). *Acoustic Theory of Speech Production* (Mouton, The Hague, The Netherlands).
Flanagan, J. L. (**1972**). *Speech Analysis Synthesis and Perception*, 2nd ed. (Springer-Verlag, Berlin).
Flanagan, J. L., and Cherry, L. (**1969**). ''Excitation of vocal-tract synthesizers,'' J. Acoust. Soc. Am. **45**, 764–769.
Frazier, R. H., Samsam, S., Braida, L., and Oppenheim, A. V. (**1976**). ''Enhancement of speech by adaptive filtering,'' Proc. IEEE-ICASSP, 251–253.
Hardwick, J., Yoo, C. D., and Lim, J. S. (**1993**). ''Speech enhancement using the dual excitation speech model,'' Proc. IEEE-ICASSP 2, 367–370.
Hermes, D. J. (**1991**). ''Synthesis of breathy vowels: Some research methods,'' Speech Commun. **10**, 497–502.
Jackson, J. B, and Shadle, C. H. (**1998**). ''Pitch-synchronous decomposition of mixed-source speech signals,'' J. Acoust. Soc. Am. **103**, 2776(A).
Jackson, P. J. B. (**2000**). ''Characterisation of plosive, fricative and aspiration components in speech production,'' Ph.D. thesis, University of Southampton, U.K.
Jackson, P. J. B., and Shadle, C. H. (**2000**). ''Performance of the pitch-scaled harmonic filter and applications in speech analysis,'' Proc. IEEE-ICASSP **3**, 1311–1314.
Klatt, D. H. (**1980**). ''Software for a cascade/parallel format synthesizer,'' J. Acoust. Soc. Am. **67**, 971–995.
Klatt, D. H., and Klatt, L. C. (**1990**). ''Analysis, synthesis, and perception of voice quality variations among female and male talkers,'' J. Acoust. Soc. Am. **87**, 820–857.
Laroche, J., Stylianou, Y., and Moulines, E. (**1993**). ''HNS: Speech modification based on a harmonic+noise model,'' Proc. IEEE-ICASSP 93(2), 550–553.
Muta, H., Baer, T., Wagatsuma, K., Muraoka, T., and Fukuda, H. (**1988**). ''A pitch-synchronous analysis of hoarseness in running speech,'' J. Acoust. Soc. Am. **84**, 1292–1301.
Narayanan, S. S., and Alwan, A. (**1996**). ''Parametric hybrid source models for voiced and voiceless fricative consonants,'' Proc. IEEE-ICASSP 1, 377–380.
Narayanan, S. S., Alwan, A., and Haker, K. (**1995**). ''An articulatory study of fricative consonants using magnetic resonance imaging,'' J. Acoust. Soc. Am. **98**, 1325–1347.
Pelorson, X., Hofmans, G. C. J., Ranucci, M., and Bosch, R. C. M. (**1997**). ''On the fluid mechanics of bilabial plosives,'' Speech Commun. **22**, 155–172.
Qi, Y., and Hillman, R. E. (**1997**). ''Temporal and spectral estimations of harmonics-to-noise ratio in human voice signals,'' J. Acoust. Soc. Am. **102**, 537–543.
Rife, D. C., and Boorstyn, R. R. (**1974**). ''Single-tone parameter estimation from discrete-time observations,'' IEEE Trans. Inf. Theory **20**, 591–598.
Rothenberg, M. R. (**1981**). ''Acoustic interaction between the glottal source and the vocal tract,'' *Vocal Fold Physiology*, edited by K. N. Stevens and M. Hirano (University of Tokyo Press, Tokyo), pp. 305–328.
Scully, C. (**1990**). ''Articulatory synthesis,'' in *Speech Production and Speech Modelling*, edited by W. Hardcastle and A. Marchal (Kluwer Academic), pp. 151–186.
Scully, C., Castelli, E., Brearley, E., and Shirt, M. (**1992**). ''Analysis and simulation of a speaker's aerodynamic and acoustic patterns for fricatives,'' J. Phonetics **20**, 39–51.
Serra, X., and Smith, J. (**1990**). ''Spectral modeling synthesis: A sound analysis/synthesis system based on deterministic plus stochastic decomposition,'' Comput. Music J. **14**, 12–24.
Shadle, C. H. (**1991**). ''The effect of geometry on source mechanisms of fricative consonants,'' J. Phonetics **19**, 409–424.
Shadle, C. H., Mohammad, M. A. S., Carter, J. N., and Jackson, P. J. B. (**1999**). ''Multi-planar dynamic Magnetic Resonance Imaging: New tools for speech research,'' Proc. ICPhS, San Francisco, CA 1, 623–626.
Silva, F. M., and Almeida, L. B. (**1990**). ''Speech separation by means of stationary least-squares harmonic estimation,'' Proc. IEEE-ICASSP 2, 809–812.
Sinder, D. J. (**1999**). ''Speech synthesis using an aeroacoustic fricative model,'' Ph.D. thesis, Rutgers University, New Brunswick, NJ.
Sondhi, M. M., and Schroeter, J. (**1987**). ''A hybrid time-frequency domain articulatory speech synthesiser,'' IEEE Trans. Acoust., Speech, Signal Process. **35**, 955–967.
Stevens, K. N. (**1971**). ''Airflow and turbulence noise for fricative and stop consonants: Static considerations,'' J. Acoust. Soc. Am. **50**, 1180–1192.
Yegnanarayana, B., d'Alessandro, C. R. A., and Darsinos, V. (**1998**). ''An iterative algorithm for decomposition of speech signals into periodic and aperiodic components,'' IEEE Trans. Speech Audio Process. **6**, 1–11.

Nonlinear phenomena in the natural howling of a dog–wolf mix[a)]

Tobias Riede[b)]
Institut für Biologie, Humboldt-Universität zu Berlin, Invalidenstrasse 43, 10115 Berlin, Germany

Hanspeter Herzel
Innovationskolleg für Theoretische Biologie, Humboldt-Universität zu Berlin, Invalidenstrasse 43, 10115 Berlin, Germany

Doreen Mehwald
Institut für Biologie, Humboldt-Universität zu Berlin, Invalidenstrasse 43, 10115 Berlin, Germany

Wolfram Seidner
Universitätsklinikum Charité, Abt. Phoniatrie, Pädaudiologie, Humboldt-Universität zu Berlin, Schumannstrasse 20/21, 10098 Berlin, Germany

Erika Trumler
Eberhard-Trumler-Station, Wolfswinkel 1, 57587 Birken-Honigsessen, Germany

Gerhard Böhme
Institut für Veterinär-Anatomie, Freie Universität Berlin, Koserstrasse 20, 14195 Berlin, Germany

Günter Tembrock
Institut für Biologie, Humboldt-Universität zu Berlin, Invalidenstrasse 43, 10115 Berlin, Germany

(Received 1 July 1999; accepted for publication 13 June 2000)

It was reported to the first author that a female dog–wolf mix showed anomalously rough-sounding vocalization. Spectral analysis of recordings of the vocalization revealed frequency occurrences of subharmonics, biphonation (two independent pitches) and chaos. Since these nonlinear phenomena are currently widely discussed as integral to mammalian vocalization [Wilden *et al.*, Bioacoustics **9**, 171–196 (1988)] or as indicators of vocal pathologies [Herzel *et al.*, J. Speech Hearing Res. **37**, 1008–1019 (1994); Riede *et al.*, Z. Sgtkde 62 Suppl: 198–203 (1997)], we sought to understand the production mechanism of the observed vocal instabilities. First the frequency of nonlinear phenomena in the calls was determined for the female and four additional individuals. It turned out that these phenomena appear, but much less frequently in the repertoire of the four other animals. The larynges of the female and two other individuals were dissected post mortem. There was no apparent asymmetry of the vocal folds but a slight asymmetry of the arytenoid cartilages. The most pronounced difference, however, was an upward extension of both vocal folds of the female. This feature is reminiscent of ''vocal lips'' (syn. ''vocal membranes'') in some primates and bats. Spectral analysis of the female's voice showed clear similarities with an intensively studied voice of a human who produces biphonation intentionally. Finally, the possible communicative relevance of nonlinear phenomena is discussed.
[S0001-4966(00)00510-5]

PACS numbers: 43.80.Lb, 43.80.Ka [WA]

I. INTRODUCTION

Harmonic phonation is characterized by periodic vibration of the vocal folds. This oscillation is due to a repetitive sequence of the same vibration pattern, the duration of which is called the period. According to van den Berg's myoelastic-aerodynamic theory (1958) vocal fold vibration is based on a dynamic equilibrium between viscoelastic forces depending on mass, damping, length, and tension of the vocal folds, and aerodynamic forces related to the Bernoulli effect. The effective length, mass, and tension of the vocal folds are determined by muscle action, which allows the fundamental frequency and the waveform of the pulses to be controlled. The vocal tract then acts as a filter which transforms the primary signals (Fant, 1960; Fitch and Hauser, 1995, 1997).

The vocal folds constitute a highly nonlinear self-oscillating system (Herzel *et al.*, 1995). Nonlinearity means that the factors (vocal fold amplitudes, glottal air flow, intraglottal pressure) vary in ways that are not linearly proportional to each other. This results in a complex relationship between pressure and flow. Nonlinear systems display a number of typical phenomena which we briefly describe here. Aperiodic (or chaotic) oscillations are characterized by irregularity, and in extreme cases there are no repeating periods at all. Period doubling is another characteristic of nonlinear dynamical systems. It is characterized by a sudden change in the frequency of the oscillations, such that the

[a)]Originally presented at the Second International Conference on Voice Physiology and Biomechanics, Berlin, 12–14 March 1999.
[b)]Electronic mail: tobiasriede@web.de

spacing between spectral components is halved.

As a first approximation, the vocal folds can be considered as two coupled oscillators. Each oscillator (left and right vocal fold) has an eigenfrequency depending on mass and muscle stiffness. In special cases such as vocal fold paralysis or anatomical asymmetry of the larynx, these frequencies can be detuned, causing desynchronized vocal fold vibrations. Subharmonics in the oscillation spectrum often correspond to integer ratios of the frequencies of the left and right vocal fold (e.g., 1:2 or 2:3) (Steineckel and Herzel, 1995). This phenomenon is termed frequency locking or entrainment and results in a vibration pattern characterized by more than one oscillation maximum. If the ratio of two frequencies is not a rational number, the dynamics corresponds to a torus, i.e., a superposition of two independent frequencies. The coexistence of two audible frequencies has been termed biphonation. Subharmonic regimes and biphonation often show sudden transitions to irregularity. Such chaotic oscillations show no repeating pattern over the duration of the vocal segment. A more detailed introduction into nonlinear dynamics of vocalization can be found in Herzel *et al.* (1994) and Wilden *et al.* (1998). By the phrase ''nonlinear phenomena'' we hereafter mean to refer collectively to subharmonics, biphonation, deterministic chaos, or any subset of these.

Nonlinearities are found in normal phonation of humans (e.g., Robb and Saxman, 1988; Titze *et al.*, 1993) and they have been characterized as an integral part of mammalian vocalization (Wilden *et al.*, 1998). Moreover, they are relevant as indicators of pathologies (e.g., in humans: Herzel *et al.*, 1994; Omori *et al.*, 1997; in animals: Riede *et al.*, 1997; Riede and Stolle-Malorny, 1998, 1999). That is, the occurrence of nonlinear phenomena increases during disorders of the vocal apparatus or some kinds of systematic diseases with impacts on phonation.

Since it is difficult to obtain reliable data about sound production mechanisms in living animals, Case studies are also useful instruments to understand the basic physiology and generation of nonlinear phenomena. We observed conspicuous rough vocalization of a female dog–wolf mix living in a pack of eight individuals. Spectral analyses allowed us to relate the conspicuous audible roughness to the occurrence of biphonation, subharmonics, and chaos.

The observed nonlinearities occurred in the female's vocalization during chorus howling of the pack. The howl is the best studied form of acoustic communication in wolves. It is a frequency modulated harmonic vocalization and plays a major role in territory maintenance, pack integration, and individual recognition (Harrington and Mech, 1979; Harrington, 1989). It is a form of communication that is effective over long distances (e.g., 1–2 km). A single wolf usually begins howling and is followed after some time by other pack members (Joslin, 1967). Three or more animals can be involved in the chorus (Klinghammer and Laidlaw, 1979) which can start spontaneously, i.e., without an obvious release, or may follow a special trigger (Theberge and Falls, 1967; Klinghammer and Laidlaw, 1979).

Our aim is to understand the underlying physiological mechanisms of the nonlinear phenomena observed in this animal. It is known from human vocalization studies that a variety of mechanisms can induce nonlinear phenomena. For example, left–right asymmetries and strong source-tract coupling can desynchronize vocal fold vibrations (Mergell *et al.*, 1997).

Unlike in humans, no systematic direct investigation of the *in vivo* vocal fold vibrations with stroboscopy or high-speed glottography is possible in animals. Consequently, we have to rely on indirect data to discuss the mechanisms of the instabilities. First, we compare the animal vocalizations with a surprisingly similar voice of a young woman, in whose case the underlying mechanism of the voice instabilities is well understood. Second, we perform a post mortem investigation of the animal's larynx to look for anatomical peculiarities.

II. MATERIALS AND METHODS

A. Studied animals

The observed animals lived in a group. All were derivatives from a male hybrid (Persian wolf, New Guinea singing dog, Australian dingo) and a female mixed-breed (Golden shakal, Elk dog, Siberian husky). Since 1981 this pack (in 1997 it consisted of eight animals: five males and three females) had lived without any further genetic influence on a 5000 m^2 area of the Eberhard–Trumler–Station (Birken–Honigsessen, Germany).

The female with the conspicuous voice (named ''Schaka'') died in December 1997 at the age of 7.9 years and with 18-kg body weight after a severe undetermined disease. A male (4 years) and an additional female (5 years) provided larynges for anatomical comparison. These two animals died after aggressive interactions with another dog group. All three animals were deep frozen until dissection. Unfortunately a detailed pathological investigation of the carcasses was not possible for technical reasons.

B. Acoustical analysis

Video and audio recording was done with two cameras (Video-Hi 8, Blaupunkt, CR 8700 H and CCD-V200E Video 8 PRO). Recordings were made in two observation periods, first period: June 1994, 15 choruses recorded, second period: April to June 1997, 64 choruses recorded. Three (from 1994) and twelve (from 1997) choruses respectively were available in which one, two or three of the anatomically investigated animals were clearly recognized. Additional recordings served for comparative purposes.

Spectral analyses were made with HYPERSIGNAL™-MACRO software. The calls were analyzed using the Fast Fourier Transformation (FFT), with 8-kHz sampling frequency and 512 points FFT order, i.e., narrow band analysis. Hanning windows and a 75% overlapping of the successive windows were applied.

For safe identification of an individual's calls during the howling chorus, the spectral analysis was compared with the simultaneous video recordings. This procedure was repeated by a second investigator and only those calls identically identified by both investigators were used for analysis.

For the description of the nonlinear phenomena in the calls we used the nomenclature as suggested by Wilden *et al.*

(1998) for the mammal vocal repertoire. Periodic signals exhibit the well-known harmonic structure in the spectrogram. Transitions to subharmonic regime induce parallel bands between the pre-existing harmonics (''period-doubling'') or at multiples of one third of the original pitch (''period-tripling''). Chaos is associated with the abrupt transitions to noiselike segments. Periodic windows often appear within these chaotic segments. Biphonation is characterized by a series of nonparallel bands related to two independent fundamental frequencies and their overtones.

For quantification we used a method used in humans (Robb and Saxman, 1988) and once in macaques (Riede *et al.*, 1997) and cats (Riede and Stolle-Malorny, 1998, 1999). For each individual a number of clearly identified calls were extracted from the choruses. We obtained a sample of 291 calls from 5 animals. The spectrogram of each call was then categorized according to the occurrence of nonlinear phenomena, and the relative duration of the nonlinear phenomena to the total call duration was calculated. For that purpose the duration of all 291 calls was measured and summed for each individual. Then the duration of all nonlinear phenomena was measured, summed up for each individual and divided by total call duration.

To ensure that the selected spectrograms were free of artifacts such as aliasing, clipping or reverberation, the samples were subjected to perceptual review by a second investigator (D.M.).

C. Anatomical investigation

The larynges (fix in formaline, 7%) were dissected in the dorso-ventral midline and macroscopically inspected. For microscopic investigation the vocal folds were excised in toto and embedded in paraffin. Six-mm sections were done at three levels (ventral, middle part, dorsal) and colored with Haemalaun–Erythrosine for a global inspection.

III. RESULTS

A. Acoustical analysis

Figure 1 shows the spectrogram of a howling chorus (60-s total duration). Five animals are involved in this chorus. For reason of clarity only the calls of ''Schaka'' are marked with arrows. The first call of Schaka exhibits a harmonic structure whereas her subsequent calls show a variety of complicated patterns.

1. Nonlinear phenomena in Schaka's vocalization

Figures 2 to 4 show spectrograms of Schaka's calls displaying a variety of transitions between harmonic vocalization, subharmonics, biphonation, and chaos. Relevant points in the spectrograms are indicated by arrows. The calls were extracted from choruses, therefore they are sometimes overlaid by calls of other animals.

A transition from harmonics to chaos can be seen for instance at arrow 5 in Fig. 2. A transition from chaos to biphonation occurs in the second call of Fig. 2 (arrow 6), and between arrow 1 and 4 in Fig. 3. In Fig. 4 chaotic elements (arrows 4 and 10) are followed by transitions to harmonic elements (at arrow 5 and 11) and the chaos is interrupted by

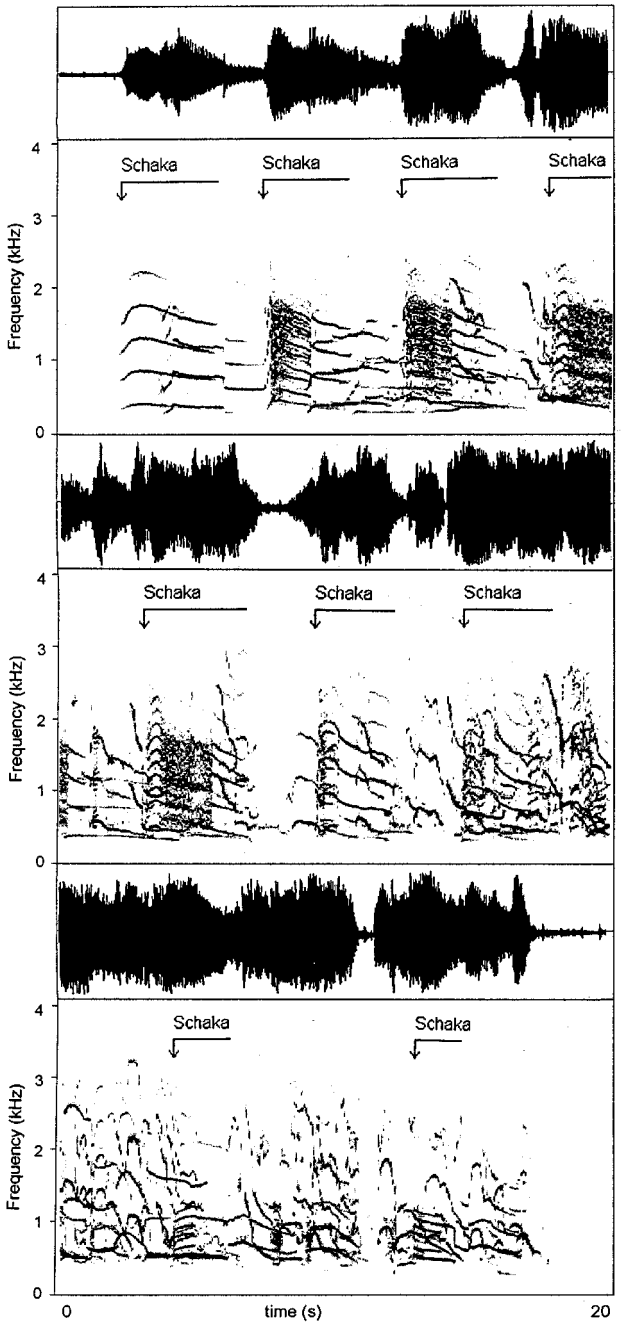

FIG. 1. Time series and the spectrogram of a chorus. The upper graphs represent the first 20 s, the middle ones the next 20 s, and below, the final 20 s of the chorus are shown. The calls uttered by ''Schaka'' are marked over the total call duration by arrows.

a harmonic window (arrows 2 and 8). These transitions are always abrupt. Chaos can occur at the beginning of a call, as in Fig. 3 (arrow 2) and in both calls of Fig. 4 (very short chaotic segments prior the harmonic window). A call never ended with chaotic elements.

The percentage of calls containing nonlinear phenomena is presented in Table I. Nonlinear phenomena can be found in the calls of four out of five animals. Schaka shows the highest amount with 32%, the other animals range between 0 and 24%.

Table I also presents the relative duration of the nonlin-

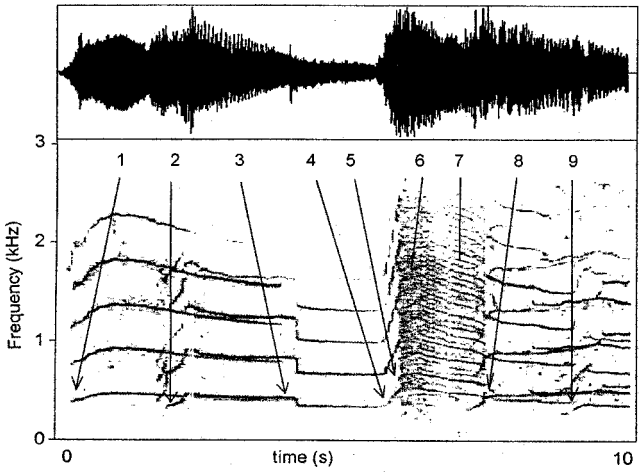

FIG. 2. Time series and spectrograms of a 10-s chorus cut-out with calls uttered by ''Schaka'': The first call (between arrows 1 and 3) was harmonical. Arrow 1 points to the fundamental frequency at the beginning of the call, which starts with 390 Hz rises to 470 Hz and ends with 410 Hz; call duration 3.7 s. This call was overlaid by the call of another animal (arrow 2) with very similar fundamental frequency. Schaka's second call started at arrow 4. It started harmonically with increasing fundamental frequency. There was an abrupt change (arrow 5) to a nonperiodic element with chaos at the beginning (arrow 6) which continues to biphonic structures (arrow 7). The biphonation ended suddenly (arrow 8) and passed on to a harmonic element with decreasing fundamental frequency from 430 Hz to 380 Hz (end of the call at arrow 9). This last call element was overlaid by the howling call of another animal with increasing fundamental frequency. Note that the time series displays a high amplitude during the chaotic and biphonic episode.

ear phenomena. Schaka again showed the highest value of 18%, the other animals range between 0 and 5%.

2. A human is able to produce similar acoustic features

The mammalian larynx is quite similar in gross anatomy between species (Negus, 1949; Harrison, 1995) suggesting similarities in the physiology, for instance, in the vibration pattern of the vocal folds. For that reason we compared Schaka's vocalization with that of a 24 year old woman who

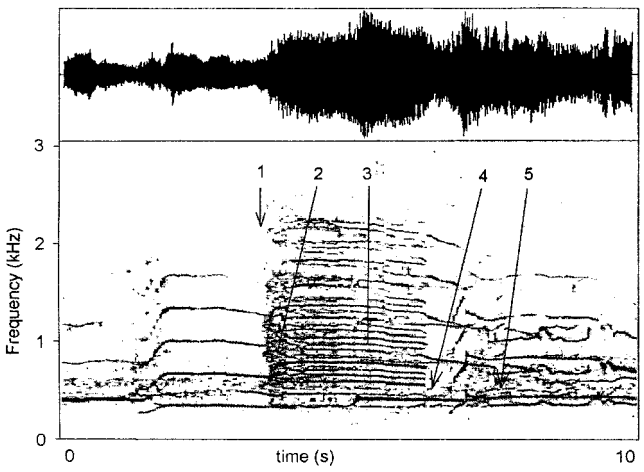

FIG. 3. The call starts (arrow 1) with a chaotic element (arrow 2) which passed on to biphonation (arrow 3). This part shows an abrupt transition (arrow 4) to a harmonic part with a fundamental frequency of 430 Hz, which decreases to 390 Hz (arrow 5). The total call duration is 4.4 s.

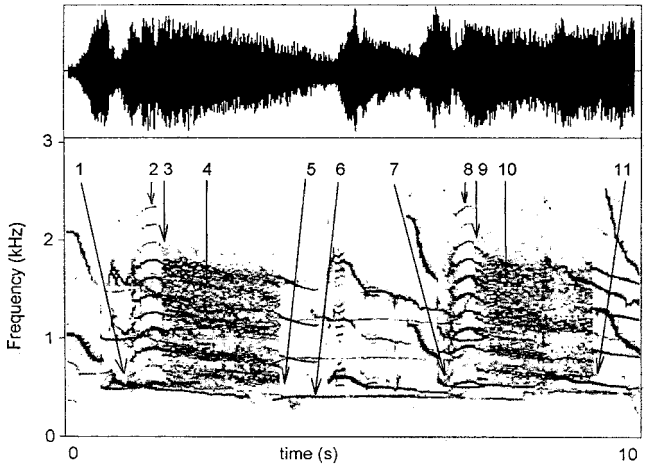

FIG. 4. Two calls of ''Schaka'' from the middle of a howling ceremony are shown. The first call is between arrows 1 and 6, the second call is between arrow 7 and the end of the window. Both calls are overlaid by calls of other animals. Both calls start with a short chaotic element (arrows 1 and 7, respectively) followed by a harmonic window (arrows 2 and 8, respectively) and a second, much longer chaotic element (arrows 4 and 10, respectively). The chaos ends at arrows 5 and 11, respectively. Both calls end with a harmonic element with a fundamental frequency decreasing from 410 Hz to 390 Hz and 430 Hz to 380 Hz. Arrows 3 and 9 indicate the transition from the harmonic window to chaos.

was able to produce biphonation intentionally and whose production mechanism is well understood [see Mergell and Herzel (1997) for details regarding high-speed glottography and modeling]. This woman is able to phonate simultaneously at two different fundamental frequencies (i.e., biphonation) during forceful expiration. The woman was asked to imitate Schaka's howl. From a subjective viewpoint, she was able to simulate Schaka's vocalization very closely. Figure 5 spectrograms of the woman's voice (left) and Schaka's original howling call (right). Spectral analysis of the woman's voice signal showed that during biphonic vocalization the fundamental frequency is of the same order as the first resonance frequency of the vocal tract (i.e., the first formant). When the fundamental frequency falls toward considerably lower values or reaches sufficiently higher values than the first formant frequency, the biphonic spectral pattern disappears.

3. ''Source-tract interaction'' in Schaka's vocalization—Comparison with the woman's voice

Now we discuss in detail a representative call of Schaka with biphonation. In the power-spectrum in Fig. 6 the peaks of two fundamental frequencies (termed f_0 and g_0) are visible at $f_0 = 515$ Hz and $g_0 = 875$ Hz. The major ratio of the two fundamental frequencies (f_0/g_0) in the call from Fig. 6 is about 0.59 which is significantly different from 1/2 or 2/3 as expected for subharmonic vocalization. Consequently we term this occurrence of two independent frequencies biphonation.

The major peaks in the power-spectrum are harmonics or linear combinations of these two fundamental frequencies. For example (Fig. 6), the spectrum demonstrates that all significant peaks can be expressed as linear combinations of two frequencies f_0 and g_0. As expected by Mergell and

TABLE I. Total number and percentage of calls containing nonlinear phenomena and relative duration of nonlinear phenomena. The calls come from different choruses.

Animal's name	Age (years)	Sex	Number of calls (number of choruses)	Calls containing nonlinear phenomena	Calls containing nonlinear phenomena (%)	Relative duration of nonlinear phenomena (%)
Schaka	7.3	f	72(10)	23	32	17.9
Chinuk	4.2	m	21(4)	5	24	4.9
Weisspitz	6.2	m	107(9)	11	10	2.7
Graue	6.2	f	29(5)	1	3	1.4
Koja	6.2	f	62(5)	0	0	0

Herzel (1997), and Reuter, Herzel and Orgelmeister (1999) for the human voice, and by Nowicki and Capranica (1986) and Fletcher (1992) for bird vocalization, the appearance of linear combinations indicates a nonlinear interaction of two frequencies. In humans direct observation of the vibrating vocal folds revealed that these biphonations represent a glottal or source-generated mechanism caused by asynchronous vibration pattern of the left and right vocal fold (Kiritani *et al.*, 1991, 1993; Mergell and Herzel, 1997).

As discussed in Mergell and Herzel (1997), slight asymmetry in the laryngeal framework is not sufficient to generate biphonation. Only together with source-tract interactions biphonation was sustained. This interaction is enhanced if the fundamental frequency coincides with the first formant. Moreover, high intensities due to large subglottal pressure support biphonation.

In Schaka's case we observed that during biphonic vocalization the fundamental frequency seems to be near to the first formant. The overlaid LPC curve showed a first formant peak at about 550 Hz. From post mortem measurements we know that Schaka's vocal tract length (from glottis to lips) is 16 cm, predicting a first formant frequency of 550 Hz, according to the equation for formant frequency calculation from the vocal tract length (VTL) and speed of sound in warm moist air ($c = 350$ m/s): $F1 = c/4^*(\mathrm{VTL})$ (for humans: Titze, 1994; for animals: Fitch, 1997; Owren and Bernacki, 1998). Thus the fundamental frequency of the source signal prior to the biphonation comes into resonance with the first resonance frequency of the vocal tract, enhancing the interaction between the glottal source and vocal tract. The biphonic pattern does not appear if the fundamental frequency falls toward lower values. For example, Schaka's first call in Fig. 2 reaches a maximum fundamental frequency of 470 Hz which is below the first formant frequency of about 550 Hz. This call is purely harmonic.

Access to subglottal pressure information is possible indirectly via examination of the time series and the amplitude envelope estimation. Subglottal pressure is the air pressure caudal from the glottis maintained by contraction of the in-

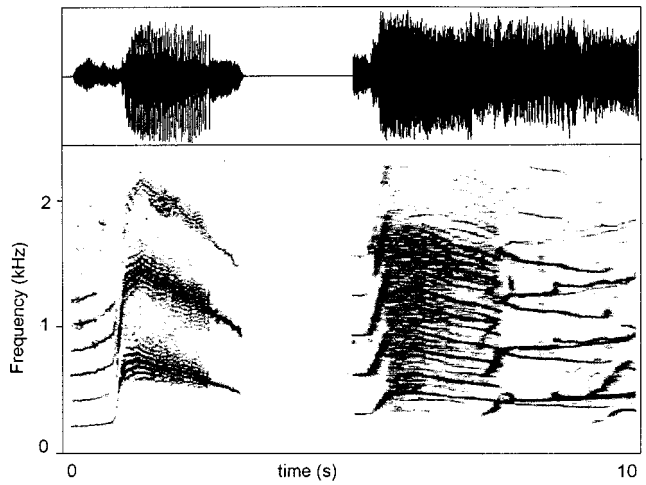

FIG. 5. Time series and spectrogram of two vocalizations. The left one is from a 24 years old woman who was asked to imitate Schaka's vocalization which is on the right side. The woman is able to produce biphonation intentionally.

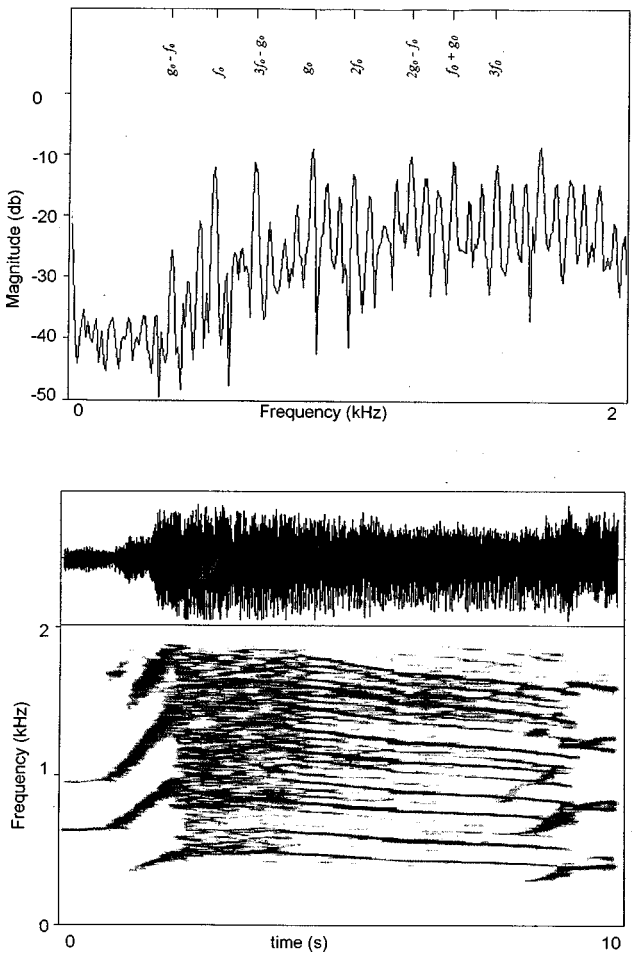

FIG. 6. Time series, spectrogram, and spectrum of the biphonic call from Fig. 2. The spectrum represents only a short term segment (50 ms) around 8 s in the spectrogram. Indications of vocal tract resonances are found with LPC analysis around 550 Hz and 1800 Hz.

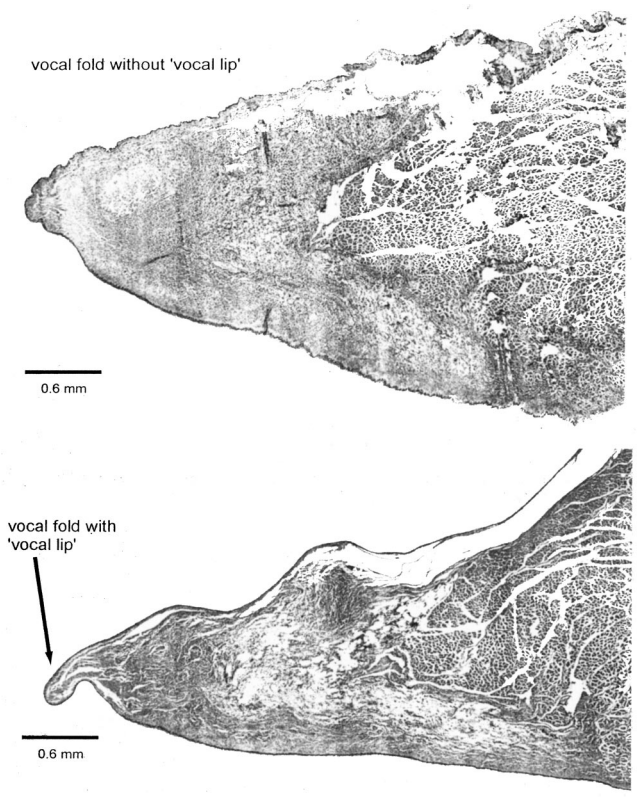

FIG. 7. Cross sections of the middle part of the vocal fold of Schaka (with vocal lip) and of a normal sounding animal (without vocal lip).

tercostal muscles and the abdominal muscle. The time series in Fig. 5 shows an increase in amplitude (indicating an increase of the subglottal pressure) during the woman's biphonic phonation. In Schaka's biphonic calls, the amplitude is about one-third higher than during harmonic phonation (Fig. 2).

B. Anatomical investigation

Macroscopic investigation of Schaka's larynx showed no obvious peculiarities of the vocal folds. The lengths of the left and right vocal folds were 16 mm and 18 mm, respectively. The Processus cuneiformes on the left side was larger than on the right side. The other wolves' larynges showed no macroscopic peculiarities. The vocal folds of the male were 18 mm on the left and 17 mm long on the right, and those of the female 16 mm on the left and right side.

The main result of the microscopic inspection was an upward extension of both vocal folds of ''Schaka'' but not of those of the two other investigated individuals (Fig. 7). These structures were about 400 μm high, 200 μm broad, and 8 mm long, situated on the edge of the vocal folds. This feature is reminiscent of ''vocal lips'' (syn. vocal membranes) in some primates and bats (Brown and Cannito, 1995; Mergell *et al.*, 1999). It also resembles oedema and *Sulcus vocalis* in pathological human voices.

IV. DISCUSSION

A female dog–wolf mix displayed an unusually high amount of nonlinear phenomena in its howling vocalization. Four other animals also showed nonlinear phenomena in their calls, but at a much lower rate. Further, they never produced biphonation, but only subharmonics and deterministic chaos.

A. The generation mechanism of nonlinear phenomena in Schaka's howling

The anatomical investigation of ''Schaka's'' larynx showed a slight asymmetry in the Processus cuneiformes (a part of the arytenoid cartilage). Hirano *et al.* (1989) showed in humans that the laryngeal framework is typically asymmetric, and that the degree of asymmetry did not differ among age groups or between sexes. They concluded that there must be some mechanism compensating for the asymmetric framework to keep the vocal fold edges relatively symmetric. Assuming that a similar compensatory mechanism exists in wolves, this slight asymmetry in Schaka's larynx is probably not solely responsible for the high amount of nonlinear phenomena in her voice.

Investigations of human voices have shown that asymmetries in vocal fold anatomy, as well as asymmetries in the vibration pattern, can be the basis for nonlinear phenomena (e.g., Ptok *et al.*, 1993; Moore *et al.*, 1987). These findings received further support from computer models of the vibrating vocal folds (Steinecke and Herzel, 1995; Tigges *et al.*, 1997; Mergell and Herzel, 1997). These models showed that slight asymmetries are able to produce nonlinear phenomena (Herzel and Reuter, 1997; Mergell and Herzel, 1997) if parameters such as the subglottal pressure or vocal tract shape are appropriately adjusted. The coincidence of vocal tract resonance frequencies and fundamental frequency of the vocal fold vibration support interactions and reciprocal reinforcement.

Studies with anaesthetized and centrally electrical stimulated dogs (Solomon *et al.*, 1994) showed that macroscopically normal looking vocal folds produced normal sounding dog vocalizations, but a subject with nodules produced rough sounding utterances (not analyzed in more detail).

In Schaka, we found a slight asymmetry of the laryngeal framework. Second, in biphonic calls we observed a coincidence of the fundamental frequency of the source with the first formant frequency of the vocal tract, suggesting the possibility of source-tract interaction. Third, the relative amplitude in biphonic call parts was about one-third higher than in harmonic call parts. All three points together may be responsible for biphonic, chaotic, and subharmonic regimes.

The microscopic investigation delivered a further aspect to be considered—an upward extensions of the mucous on the edges of the vocal folds. In two other animals we did not find such structures. These structures are well known as ''vocal lips'' (syn. vocal membranes) in bats and some primate species (Harrison, 1995). In canids there is no consensus about the frequency of vocal lip occurrence. Harrison (1995) did not describe vocal lips in the wolf. Jiang *et al.* (1994) described no vocal lip-like structures in the vocal folds of 13 mongrel dogs. Two other references showed histologic pictures of dog vocal folds which obviously had vocal lip like structures but the authors did not explicitly mention them in the text (Duckworth, 1912; Negus, 1929).

There are two main suggestions about the function of vocal lips in voice production. First, they might be responsible for the production of very high fundamental frequencies (Schön-Ybarra, 1995) as seen in some small primate species. Second, a computer simulation showed that vocal lips can lower the subglottal pressure at which phonation is supported, thus increasing vocal efficiency (Mergell *et al.*, 1999). Moreover, vocal lips induce vocal instabilities in the model, suggesting that the ''upward extension'' in Schaka's vocal folds may support the production of nonlinear phenomena. Also Brown and Cannito (1995) discussed vocal lips as being responsible for biphonation (they called it ''polyphonic vocalization''), hypothesizing that vocal lips represent a separately vibrating structure inducing a second fundamental frequency.

B. Communicative relevance of nonlinear phenomena

From video recordings we know that Schaka's conspicuous voice was present for at least the last three years. In the social rank order Schaka was in the alpha-position during the last four years and she reproduced three times during that period. Whether or not there is a relationship/coincidence between the occurrence of a high amount of nonlinear phenomena and any event in Schaka's life (for instance a disease) is unknown. The increased amount of nonlinear phenomena can be explained in two ways. On the one hand, Schaka might have produced the high amount of nonlinear phenomena involuntarily without communicative effect due to her special laryngeal anatomy (vocal lips, slight asymmetry), just displaying an idiosyncratic voice disorder. On the other hand, Schaka might have produced the high amount of nonlinear phenomena voluntarily, aided by her special laryngeal anatomy, and reinforced by auditory feedback, with unknown communicative effect.

Generally, the problem whether or not nonlinear phenomena are pathological or integral part of the repertoire remains an open question. There are examples pointing in both directions. Riede *et al.* (1997) showed in a Japanese macaque (*Macaca fuscata*) infant with an assumed metabolic disease an increased amount of nonlinear phenomena in the vocal repertoire, but unfortunately sufficient behavioral observations were lacking. East and Hofer (1991) showed spectrograms of spotted hyenas (*Crocuta crocuta*) whoops which indicated that nonlinear phenomena seem to be rather common in this type of vocalization. In the painted hunting dog (*Lycaon pictus*) Wilden (1997) showed nonlinear phenomena in the vocalization of all age classes. Wilden *et al.* (1998) screened the literature on mammalian acoustic signals and found nonlinear phenomena in many published spectrograms. The widespread occurrence of such phenomena suggests that they are integral parts of the vocal repertoire in many mammals.

In humans, rough sounding voices are primarily studied in connection with voice pathologies. There are, however, examples of nonlinear phenomena in normal voices which are well-known from modern pop singers and infant cries (Mende *et al.*, 1990). In these cases, rough sounding voices elicit strong attention from listeners. Hecker and Kreul (1970) showed that slightly rough sounding voices (i.e., voices with a higher amount of nonlinear phenomena) do not indicate an unhealthy voice to human listeners suggesting that nonlinear phenomena are common to a certain degree in the normal human voice. Hecker and Kreul (1970) found also that a higher degree of roughness affects the listener's ability to guess the speaker's age: listeners evaluated the speaker older than he/she was.

Together, these observations suggest that nonlinear phenomena in the otherwise primarily harmonic vocalization exhibit communicative relevance in humans. Further studies, including behavioral observations, are necessary to substantiate the communicative role of nonlinear phenomena in nonhuman mammal vocalization.

ACKNOWLEDGMENTS

We thank Patrick and Ariane Mergell for their support regarding biphonation of the human voice and valuable criticism. We thank Elke Zimmermann, Tecumseh Fitch, and Nick Nicastro for helpful comments on an earlier version of the manuscript and Mrs. Rückauer for her essential help with the histological work. This work was supported by a grant from the Land Berlin (NaFöG) to TR and by the Deutsche Forschungsgemeinschaft.

Brown, C. H., and Cannito, M. P. (**1995**). ''Modes of vocal variation in Sykes's Monkey (*Cercopithecus albogularis*) squeals,'' J. Comp. Psych. **109**, 398–415.

Duckworth, W. L. H. (**1912**). ''On some points in the anatomy of the plica vocalis,'' J. Anat. Physiol. **67**, 80–115.

East, M. L., and Hofer, H. (**1991**). ''Loud calling in a female-dominated mammalian society: I. Structure and composition of whooping bouts of spotted hyaenas, Crocuta crocuta,'' Anim. Behav. **42**, 637–649.

Fant, G. (**1960**). *Acoustic Theory of Speech Production* (Mouton, The Hague).

Fitch, W. T. (**1997**). ''Vocal tract length and formant frequency dispersion correlate with body size in *rhesus macaques*,'' J. Acoust. Soc. Am. **102**, 1213–1222.

Fitch, W. T., and Hauser, M. D. (**1995**). ''Vocal production in nonhuman primates: Acoustics, physiology, and functional constrains on 'honest' advertisement,'' Am. J. Primatol. **37**, 191–219.

Fletcher, N. H. (**1992**). *Acoustic Systems in Biology* (Oxford University Press, Oxford).

Harrington, N. H., and Mech, L. D. (**1979**). ''Wolf howling and ist role in territory maintenance,'' Behaviour **68**, 207–249.

Harrington, F. H. (**1989**). ''Chorus howling by wolves: Acoustic structure, pack size and the beau geste effect,'' Bioacoustics **2**, 117–136.

Harrison, D. F. N. (**1995**). *The Anatomy and Physiology of the Mammalian Larynx* (Cambridge University Press, Cambridge).

Hecker, M. H. L., and Kreul, E. J. (**1970**). ''Description of the speech of patients with cancer of the vocal folds. Part II: Judgements of age and voice quality,'' J. Acoust. Soc. Am. **49**, 1283–1287.

Herzel, H., Berry, D., Titze, I. R., and Saleh, S. (**1994**). ''Analysis of vocal disorders with methods from nonlinear dynamics,'' J. Speech Hear. Res. **37**, 1008–1019.

Herzel, H., Berry, D., Titze, I. R., and Steinecke, I. R. (**1995**). ''Nonlinear dynamics of the voice: Signal analysis and biomechanical modeling,'' Chaos **5**, 30–34.

Herzel, H., and Reuter, R. (**1997**). ''Whistle register and biphonation in a child's voice,'' Folia Phoniatr. **49**, 216–224.

Hirano, M., Kurita, S., Yukizane, K., and Hibi, S. (**1989**). ''Asymmetry of the laryngeal framework: a morphometric study of cadaver larynges,'' Ann. Otol. Rhinol. Laryngol. **98**, 135–140.

Jiang, J. J., Titze, I. R., Wexler, D. B., and Gray, S. D. (**1994**). ''Fundamental frequency and amplitude perturbation in reconstructed canine vocal folds,'' Ann. Otol. Rhinol. Laryngol. **103**, 145–148.

Joslin, P. W. B. (**1967**). ''Movements and homesites of timber wolfs in Algonquin Park,'' Am. Nat. **107**, 775–785.

Kiritani, S., Hirose, H., and Imagawa, H. (**1991**). ''Vocal fold vibration and the speech waveform in diplophonia,'' Ann. Bull. Res. Inst. Logopedics and Phoniatrics, Univ. Tokyo, pp. 55–62.

Kiritani, S., Hirose, H., and Imagawa, H. (**1993**). ''High-speed digital image analysis of the vocal fold vibration in diplophonia,'' Speech Commun. **13**, 23–32.

Klinghammer and Laidlaw (**1979**). ''Analysis of 23 months of daily howl records in a captive grey wolf pack (Canis lupus),'' *The Behavior and Ecology of Wolves*, edited by E. Klinghammer (New York), pp. 153–182.

Mende, W., Herzel, H., and Wermke, K. (**1990**). ''Bifurcations and chaos in newborn infant cries,'' Phys. Lett. A **145**, 418–424.

Mergell, P., and Herzel, H. (**1997**). ''Modeling biphonation—The role of the vocal tract,'' Speech Commun. **22**, 141–154.

Mergell, P., Fitch, W. T., and Herzel, H. (**1999**). ''Modeling the role of non-human vocal membranes in phonation,'' J. Acoust. Soc. Am. **105**, 2020–2028.

Moore, D. M., Berke, G. S., Hanson, D. G., and Ward, P. H. (**1987**). ''Videostroboscopy of the canine larynx: The effect of asymmetric laryngeal tension,'' Laryngoscope **97**, 543–553.

Negus, V. E. (**1929**). *The Mechanism of the Larynx* (Heinemann LTD, London).

Nowicki, S., and Capranica, R. R. (**1986**). ''Bilateral syringeal interaction in vocal production of an oscine bird sound,'' Science **231**, 1297–1299.

Omori, K., Kojima, H., Kakani, R., Slavit, D. H., and Blaugrund, S. M. (**1997**). ''Acoustic characteristics of rough voice: Subharmonics,'' J. Voice **11**, 40–47.

Owren, M. J., and Bernacki, R. H. (**1998**). ''Applying Linear Predictive Coding (LPC) to frequency-spectrum analysis of animal acoustic signals,'' in *Animals Acoustic Communication*, edited by S. L. Hopp, M. J. Owren, and C. S. Evans (Springer, Berlin).

Ptok, M., Sesterhenn, G., and Arold, R. (**1993**). ''Bewertung der laryngealen Klanggeneration mit der FFT—Analyse der glottischen Impedanz bei Patienten mit Rekurrenzparese,'' Folia Phoniatr. **45**, 182–197.

Reuter, R., Herzel, H., and Orgelmeister, R. (**1999**). ''Simulation of vocal fold vibrations with an analog circuit,'' Int. J. Bifurcation Chaos **9**, 1075–1088.

Riede, T., Wilden, I., and Tembrock, G. (**1997**). ''Subharmonics, biphonations, and frequency jumps—Common components of mammalian vocalization or indicators for disorders,'' Z. Säugetierkunde 62, Suppl. **2**, 198–203.

Riede, T., and Stolle-Malorny, A. (**1998**). ''Spektrale Analyse der Stimmveränderung bei einem Kater mit Schädel-Hirn-Trauma,'' Kleintierpraxis **43**, 773–780.

Riede, T., and Stolle-Malorny, A. (**1999**). ''The vocal change of a kitten with cranio-cerebellar trauma—A case study,'' Bioacoustics **10**, 131–141.

Robb, M. P., and Saxman, S. H. (**1988**). ''Acoustic observations in young children's noncry vocalizations,'' J. Acoust. Soc. Am. **83**, 1876–1882.

Schön-Ybarra, M. A. (**1995**). ''A comparative approach to the nonhuman primate vocal tract: Implications for sound production,'' in *Current Topics in Primate Vocal Communication*, edited by E. Zimmermann, J. Newman, and U. Jürgens (Plenum, New York).

Solomon, N. P., Luschei, E., and Kang, L. (**1994**). ''Fundamental frequency and tracheal pressure during three types of vocalizations elicited from anaesthetized dogs,'' J. Voice **9**, 403–412.

Steinecke, I., and Herzel, H. (**1995**). ''Bifurcations in an asymmetric vocal fold model,'' J. Acoust. Soc. Am. **97**, 1874–1884.

Theberge, J. B., and Falls, J. B. (**1967**). ''Howling as a means of communication in Timber wolves,'' Am. Zool. **7**, 331–338.

Tigges, M., Mergell, P., Herzel, H., Wittenberg, T., and Eysholdt, U. (**1997**). ''Observation and modeling of glottal biphonation,'' Acoustica **83**, 707–714.

Titze, I. R., Baken, R., and Hezel, H. (**1993**). ''Evidence of chaos in vocal fold vibration,'' in *Vocal Fold Physiology. New Frontiers in Basic Science*, edited by I. R. Titze (Singular Publishing Group, San Diego), pp. 143–188.

van den Berg, J. (**1958**). ''Myoelastic-aerodynamic theory of voice production,'' J. Speech Hear. Res. **1**, 227–244.

Wilden, I. (**1997**). ''Phonetische Variabillität in der Lautgebung Afrikanischer Wildhunde (Lycaon pictus) und deren frühe Ontogenese,'' Ph.D. thesis, Humboldt-University, Berlin.

Wilden, I., Herzel, H., Peters, G., and Tembrock, G. (**1998**). ''Subharmonic, biphonation, and deterministic chaos in mammal vocalization,'' Bioacoustics **9**, 171–196.

Vocalization-correlated respiratory movements in the squirrel monkey[a)]

Udo Häusler[b)]
German Primate Center, Kellnerweg 4, 37077 Göttingen, Germany

(Received 4 August 1999; accepted for publication 23 June 2000)

Respiratory abdominal movements associated with vocalization were recorded in awake squirrel monkeys. Several call types, such as peeping, trilling, cackling, and err-chucks, were accompanied by large vocalization-correlated respiratory movements (VCRM) that started before vocalization. During purring, in contrast, only small VCRM were recorded that started later after vocal onset. VCRM during trill calls, a vocalization type with repetitive frequency modulation, showed a modulation in the rhythm of the frequency changes. A correlation with amplitude modulation was also present, but more variable. As high frequencies need a higher lung pressure for production than low frequencies, the modulation of VCRM seems to serve to optimize the lung pressure in relation to the vocalization frequency. The modulation, furthermore, may act as a mechanism to produce different trill variants. During err-chucks and staccato peeps, which show a large amplitude modulation, a nonmodulated VCRM occurred. This indicates the existence of a laryngeal amplitude-controlling mechanism that is independent from respiration. © *2000 Acoustical Society of America.* [S0001-4966(00)00610-X]

PACS numbers: 43.80.Ka, 43.64.Tk [WA]

I. INTRODUCTION

Respiration is a necessary prerequisite for vocalization. Respiratory muscles show a different activity during vocalization and speech than during quiet breathing in man (Floyd and Silver, 1950; Draper *et al.*, 1959; Hoshiko, 1962; Hoshiko and Berger, 1965; McFarland and Smith, 1989; Estenne *et al.*, 1990) and primates (Jürgens and Schriever, 1991). It is generally believed that ''respiratory muscles act to generate and maintain lung pressures necessary for vocalization, while laryngeal and supralaryngeal structures help regulate subglottic pressure and modify the airflow to produce the appropriate sound'' (West and Larson, 1993). Accordingly, the influence of laryngeal and supralaryngeal structures on vocal parameters, like amplitude, frequency, and spectral content, has been extensively investigated, while the influence of respiratory temporal patterns on vocal parameters is largely neglected. A detailed electromyographic (EMG) study of respiratory muscle activity during vocalization in squirrel monkeys was made by Jürgens and Schriever (1991). They used electrical brain stimulation under general anesthesia to elicit peeping or sequences of chuck calls. In contrast to quiet breathing, inspiratory and expiratory intercostal muscles are coactivated and abdominal accessory muscles are additionally recruited during vocalization. The authors showed that the amplitude of the uttered vocalization is most closely related to the envelope of the abdominal obliquus internus EMG activity, which, accordingly, seems to be involved in the production and modulation of subglottic air pressure during vocalization. Furthermore, Hsiao *et al.* (1994) have shown that vocal frequency is influenced to some degrees by subglottic pressure and, therefore, also by lung pressure.

The aim of this study is to further investigate abdominal respiratory movements related to the production of subglottic pressure during vocal activity. The main question will be: Are respiratory movements during vocalization related to acoustic parameters other than sound intensity? Clarification of this question is regarded as an important step toward a better understanding of the central control of vocalization.

II. MATERIALS AND METHODS

A. Procedures

Five adult squirrel monkeys (*Saimiri sciureus*; 1 ''roman'' type, 4 ''gothic'' type) were trained to sit in a restraining chair inside a sound-attenuated chamber (Siemens + Matsushita Systems) for single sessions of about 1–2 h once a day. The chair was specially adapted to the monkeys' body shape and upholstered by soft cloth. Animals were able to move head, arms, and feet. To comfort the animal, meal worms, raisins, or nuts were given during training sessions. After getting used to the situation, animals started to vocalize either as response to playback calls or spontaneously.

B. Data recording

Respiratory movements were recorded with a magnetometric method. Two coils were mounted in the midline of the animal, one over the abdomen 20 mm below the lower end of the ribcage, the other on the back in an approximately aligned position. The coils had a diameter of 1 cm and a distance of 65–75 mm. The back coil was connected to a sine wave generator (Hameg HM8030) set to 15 kHz and was used as transmitting coil. The sense coil was connected directly to the input stage of a Tectronix 5110 oscilloscope

[a)]Originally presented at the Second International Conference on Voice Physiology and Biomechanics, Berlin, 12–14 March 1999.
[b)]Electronic mail: uhausl@t-online.de

with 5A22N type preamplifier. The signal was filtered with low cutoff at 10 kHz and high cutoff at 30 kHz. Amplitude of the sine wave generator and gain of the preamplifier was set to give a low noise 1.5 V (peak-to-peak) signal, the amplitude modulation of which reflected abdominal diameter changes. These diameter changes are related to respiratory movements in the way that inspiration is accompanied by an increase of abdominal diameter and a decrease of the measured signal. Conversely, expiratory movements are related to a decrease in diameter and an increase in the signal. Diameter changes were in the range of 3–6 mm.

Vocal utterances were recorded with a Sennheiser MKH directional microphone 1 m in front of the animal. The signal was filtered with a passband from 170 Hz to 30 kHz and amplifier to a level of 1.5 V. Playback vocalizations were presented with 65–70 dB SPL at the ear of the animal, depending on the actual stimulus. Calibration of the system was carried out with a B&K Type 2231 sound level meter. The recording system was linear within 1.5 dB between 200 Hz and 20 kHz. Recording of vocalizations as well as recording of the movement signal was made online with a microprocessor system (Macintosh Quadra 950 and an NI A2100 analog i/o board) at a rate of 48 kHz. In addition to online recording, the whole session was recorded on videotape (Panasonic, AG-5700) together with the vocal and movement signals.

Analysis was carried out offline with the program ''Signalyse.'' Sonagrams and amplitude plots were calculated for the animals' vocalizations. The ''movement'' signal was analyzed by calculating an amplitude plot which represents a plot of the distance between the abdominal coils.

Recorded vocalizations were classified according to Newman (1985) into peep calls, trilling, purring, cackling, and err-chucks. The following measures were taken for each vocal utterance: (1) Cycle time of frequency and amplitude modulation as well as respiratory modulation in trill calls. An amplitude envelope was determined by calculating the moving average of the squared signal within a 15-ms time window. Cycle time of amplitude modulation was measured if neighboring maxima and minima differed by more than 9 dB. (2) Amplitude of the vocalization-related respiratory movement relative to the movement during the nonvocal respiratory cycle. (3) Time between onset of expiratory movement and vocal activity. For all measures, only those recordings were accepted that were free of artifacts due to gross body movements. Results were transferred to a statistics program (Statview) for basic statistics and ANOVA. For each animal, data from 4 to 6 sessions were included in the analysis.

III. RESULTS

A. General characteristics of breathing

Breathing movements were recorded from the abdomen, as here the movements of the body wall were largest in amplitude and gave the most consistent results. Preliminary recordings of thoracic respiratory movements showed that in the dorso-ventral direction thoracic movements were very small in amplitude and difficult to record. Breathing movements showed the typical time course illustrated in Fig. 1. Inspiratory and expiratory phases could be clearly differentiated. The change from expiration to inspiration was characterized by an abrupt change in movement direction, while the transition from inspiration to expiration is gradual and slow. Even though the time course differed between individuals, the abrupt change during expiratory–inspiratory transition was present in all animals.

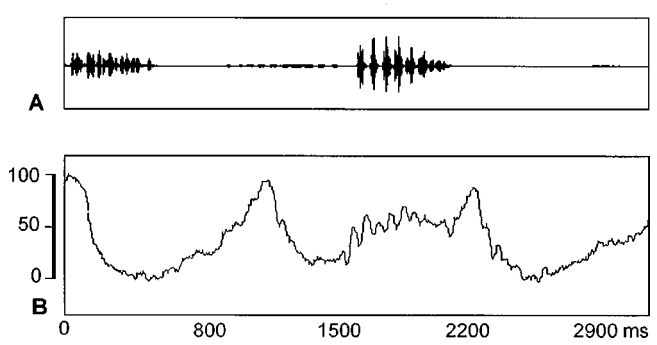

FIG. 1. Respiratory movements before and during vocal activity induced by a playback stimulus. The upper trace shows the oscillogram of the signal picked up by the microphone. The lower trace shows the corresponding respiratory movement. High values correspond to a small dorso-ventral abdominal diameter, low values to a large diameter. During normal respiration, an increase of the signal indicates expiration, while a decrease corresponds to inspiration. The scale bar indicates the range of abdominal movements in percentage of normal breathing.

B. Vocalization-correlated respiratory movements (VRCM)

Respiratory movements were recorded during a total of 342 vocalizations. Compared to normal breathing, vocalization is accompanied by an additional expiratory movement which will be called vocalization-correlated respiratory movement (VCRM). Depending on the type of vocalization, this expiratory movement was modulated in a characteristic way. The following types were recorded: isolation peeps and short peeps ($n=22$) [Figs. 2(A), (C)], trills ($n=286$) (Fig. 3), purring ($n=8$) (Fig. 6), cackling ($n=22$) and err-chucks ($n=6$) (Fig. 7). Peep calls.

A very simple relationship between call structure and VCRM is found in isolation peeps. Isolation peeps are long-distance contact calls showing only minor frequency and amplitude modulations. The expiratory movement in this case started with a median latency of 35 ms before vocalization. It gradually increased in amplitude until the onset of vocalization and remains constant throughout the call [Fig. 2(A)]. This indicates a rather constant expiratory effort during the course of vocalization. During 5 of the 22 cases, the VCRM showed some irregular modulations making up about 6% of the total respiratory movement. In a few cases, peep calls were preceded by distinct frequency-modulated elements [Fig. 2(B)]. In these cases, the VCRM showed a strong modulation that followed the time course of the frequency modulation.

Single short peeps were either observed at the very end of the expiratory phase or they were accompanied by a single short expiratory movement of high amplitude. Sequences of short peeps [staccato peeps, Fig. 2(C)] were characterized by

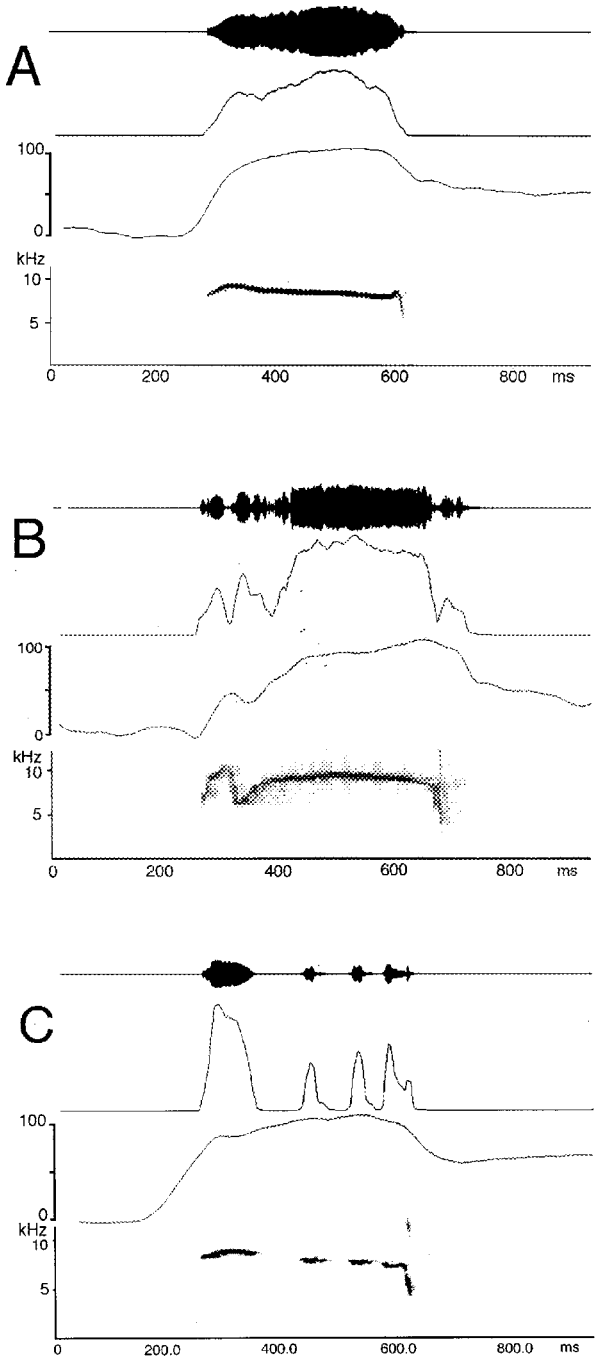

FIG. 2. Respiratory movements during different peep calls. In each subfigure the upmost trace shows the oscillogram of the vocalization, the second trace is an amplitude plot (mean power envelope within a 15-ms time window) of the vocalization, the third displays the respiratory movement (i.e., abdominal diameter). (High values correspond to a small dorso-ventral abdominal diameter, low values to a large diameter.) The lowest trace shows the spectrogram of the call. The scale bar of the respiratory trace indicates the range of abdominal movements during normal respiration, in percent. (A) Isolation peep. (B) Peep with preceding frequency-modulated element. (C) Series of short peep.

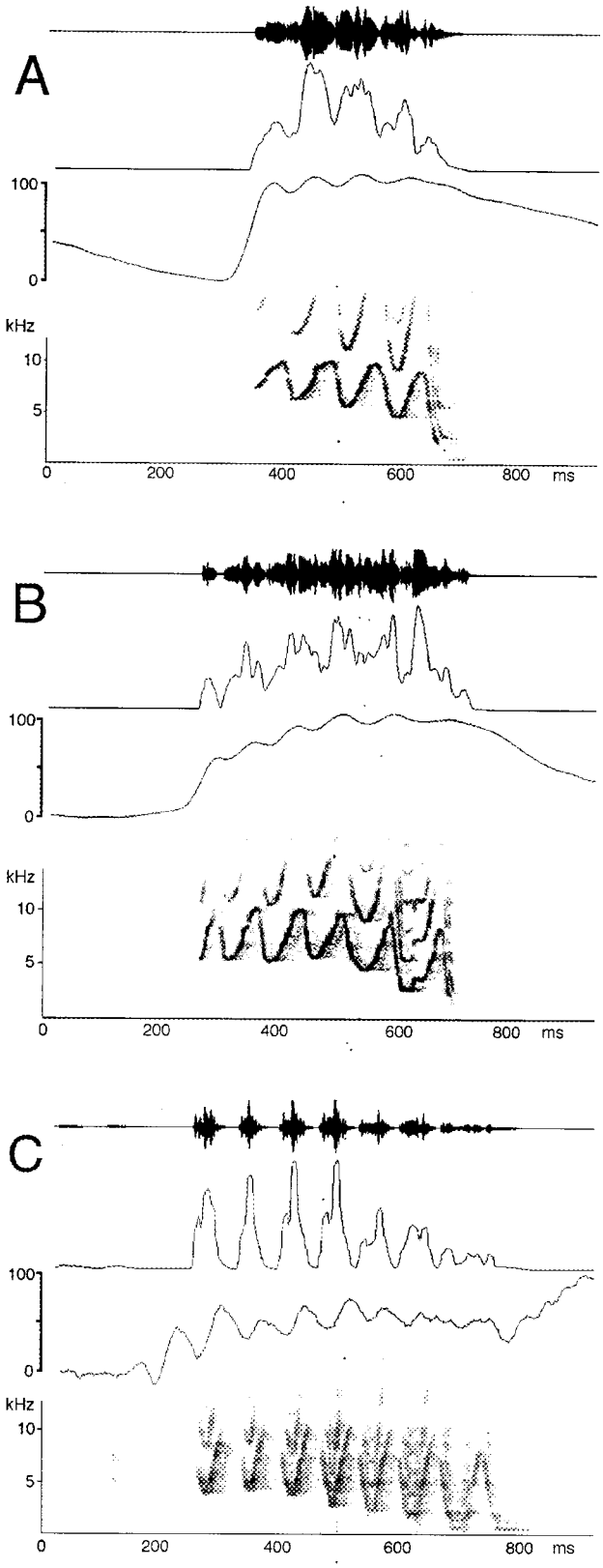

FIG. 3. Respiratory movements during different trill calls. Further explanations see Fig. 2. (A) Short trill. (B) Long trill with amplitude modulation largely in phase with respiratory movement modulation. (C) Trill with amplitude modulation out of phase with VCRM.

a continuous expiratory movement throughout the sequence that was nearly identical to the VCRM during isolation peeps.

C. Trill calls

Trills are tonal calls exhibiting a marked rhythmic frequency modulation with a repetition rate between 9 and 16 Hz. This frequency will be referred to as frequency modulation rate. The frequency modulation is often accompanied by an amplitude modulation of approximately the same rate, but with a phase relationship to the frequency modulation that can vary between animals as well as between vocalizations.

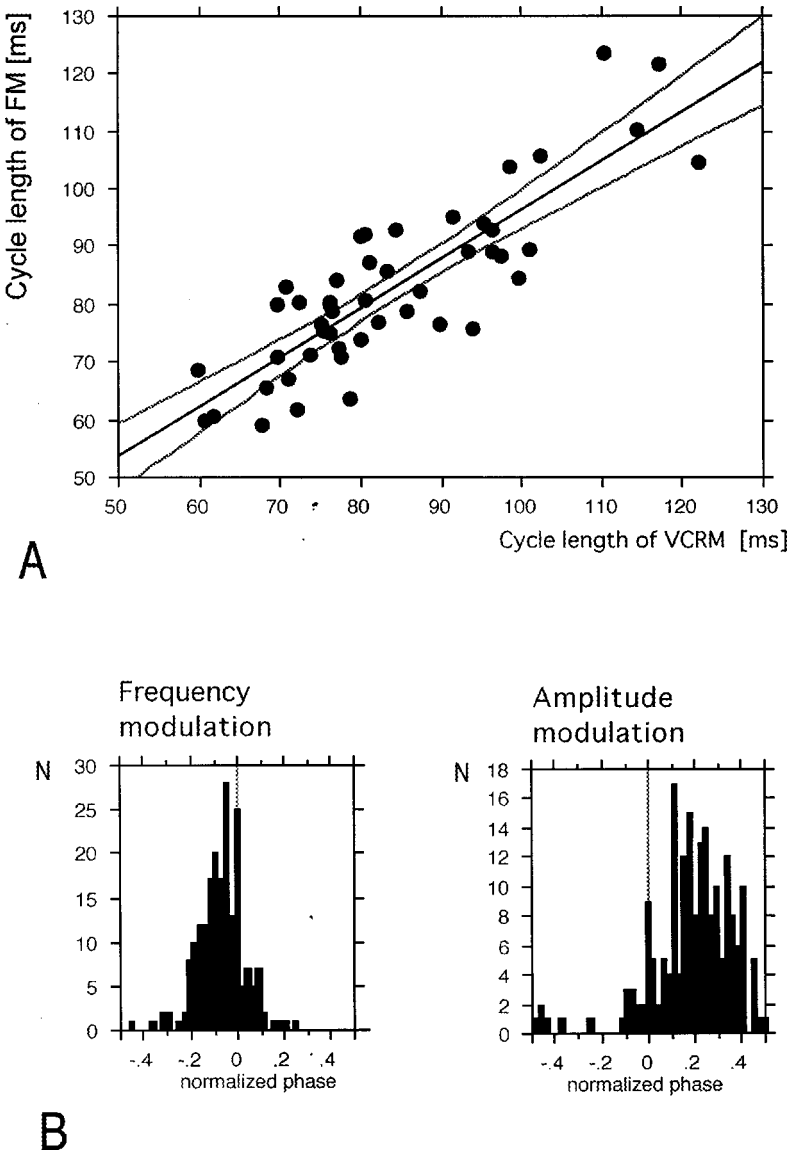

FIG. 4. (A) Relationship between cycle length of frequency modulation (FM) and corresponding respiratory movement (VCRM) modulation during trill calls ($r^2 = 0.721$). (B) Phase relationships between the VCRM modulation and frequency or amplitude modulation, respectively. (The normalized phase was calculated with the VCRM taken as reference. Time of small abdominal diameter is 0, the time of large abdominal diameter before this is +0.5 and the point of large diameter after 0 is −0.5. The time whether either frequency or amplitude reaches it maximum within the cycle was then taken as measure. Note that points of high amplitude were less well definable in a lot of cases so that the number of measures is smaller for amplitude modulation.)

A clearly rhythmic modulation of the VCRM is found in almost all trill calls. Out of the 286 recorded trills, only 3 lacked a rhythmic VCRM modulation. The modulation consists of either a stepwise decrease of the abdominal diameter [Fig. 3(B)], or large oscillations superimposed on the expiratory movement associated with the vocal activity [Fig. 3(C)]. The amplitude of the modulation in the latter case was above 25% of the total respiratory movement for most calls. In trills, VCRM starts with a median of 30 ms before vocal onset. In some cases, however, rhythmic modulation of VCRM was observed several hundred ms before audible vocalization.

The modulation of VCRM is related to both the amplitude and the frequency modulation of the call. Analysis of the cycle lengths of VCRM modulation and frequency modulation showed an approximately linear relationship between both [Fig. 4(A)]. In addition, there was a preferred phase relationship between them. The high-frequency phase of the fundamental corresponds to the large-amplitude phase of the respiratory movement. The phase-histogram distributions [Fig. 4(B)] indicate that there is some variation in phase relationship. In most cases, this variation was observed between different calls; several cases, however, were also observed in which the phase relationship changed within single calls. Such a phase shift correlated with changes in the cycle length of VCRM modulation or frequency modulation. These changes were always accompanied by a change in the character of the call elements (Fig. 5).

Measurement of large scale amplitude modulation during trill calls showed that these are correlated with the VCRM modulation. The phase distribution of the amplitude modulation peaks is significantly different from an equal distribution ($p < 0.01$). As can be seen from Fig. 4(B), however, the correlation was not as good as that between VCRM modulation and fundamental frequency modulation. The distribution of normalized phases was significantly broader for the amplitude modulation ($p < 0.005$, F-test). The mean preferred position of the amplitude peak was also different ($p < 0.001$, t-test), with the amplitude peak preceding the peak of the VCRM.

D. Purring, Cackling, Err-chucks

Purring is a low-intensity vocalization that consists of long pulse sequences with a rate of about 30 Hz. Animals

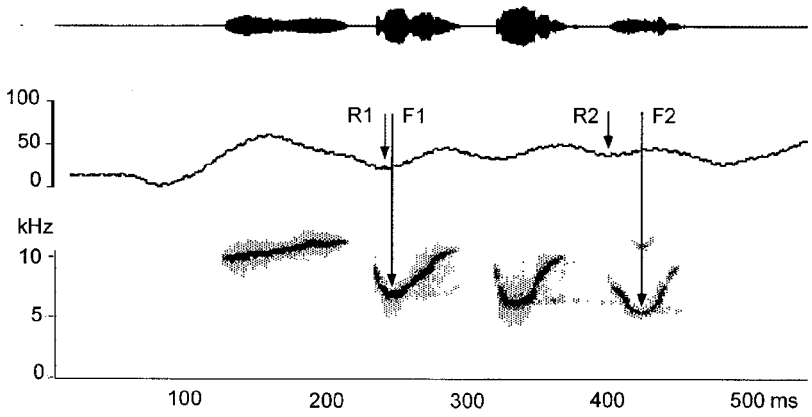

FIG. 5. Respiratory movements during short trill call with marked change in element shape. Upper trace: oscillogram of the vocalization. Middle trace: respiratory movement (i.e., abdominal diameter. High values correspond to a small dorso-ventral abdominal diameter, low values to a large diameter). Lower trace: spectrogram. The phase duration of frequency modulation is larger than the phase duration of VCRM modulation. Therefore a change in phase relationship between minima of respiratory signal ($R1$,$R2$) and minima of the fundamental frequency ($F1$,$F2$) is observed during the call. The change in accompanied by a change of acoustic structure from a predominantly upward sweep to a U-shaped form.

produce these vocalizations preferably during affiliative interactions (Newman, 1985). During purring, the VCRM is extremely small. Figure 6 shows a typical example. There is not extra expiratory movement detectable at the beginning of purring; only after about 250 ms, there is a small and constant expiratory movement. Mean latency of VCRM is 80 ms after vocalization onset.

Cackle calls consist of short wide-band calls with low fundamental frequency and high-to-moderate amplitude. They may be uttered as single calls or in a sequence. These calls are accompanied by distinct expiratory pulses. These pulses start with a very short latency of about 6–10 ms before vocalization onset. In 3 out of the 22 cases, the expiratory movement showed an oscillatory modulation consisting of two peaks which were not related to the vocal parameters.

Err-chucks consist of a relatively loud growling like element (''err'') followed by an ascending and descending or only descending high pitched element (''chuck'') within 100 ms (Fig. 7). The calls show a marked amplitude modulation. VCRM starts with a median of about 35 ms before the call and continues throughout all elements without interruption. Some modulation is present but has an irregular time course. Its amplitude was below 6% of the total respiratory movement and close to the spontaneously observed fluctuations. No obvious correlation of the modulation with the acoustic parameters of the call could be detected.

IV. DISCUSSION

The aim of the present study was to investigate if and how respiratory movements are differentially modulated during vocal activity. The study demonstrates such a modulation; its degree and character, however, depends upon the type of vocalization. The main finding of this study is that during frequency modulated trill calls and those peep vocalizations that contained a frequency modulated segment, a strong relationship between frequency modulation and VCRM is present a less strong relationship is also present between VCRM and sound amplitude.

CRM measured in this study generally consists of a decrease in abdominal diameter during vocal activity. The decrease of abdominal diameter is due to the activity of expiratory abdominal muscles that have been shown to be active during vocalization. Jürgens and Schriever (1991) demonstrated that during vocal activity in the squirrel monkey, the EMG of the musculi obliquus internus and externus were

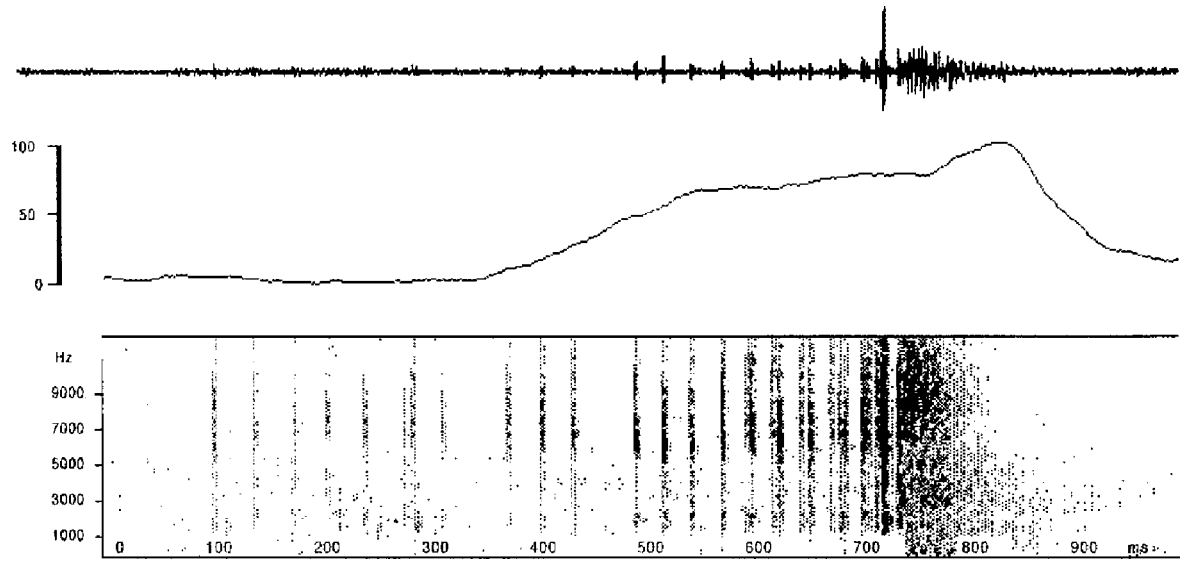

FIG. 6. Respiratory movement during purring. Upper trace: oscillogram of the vocalization; middle trace: respiratory movement; lower trace: spectrogram.

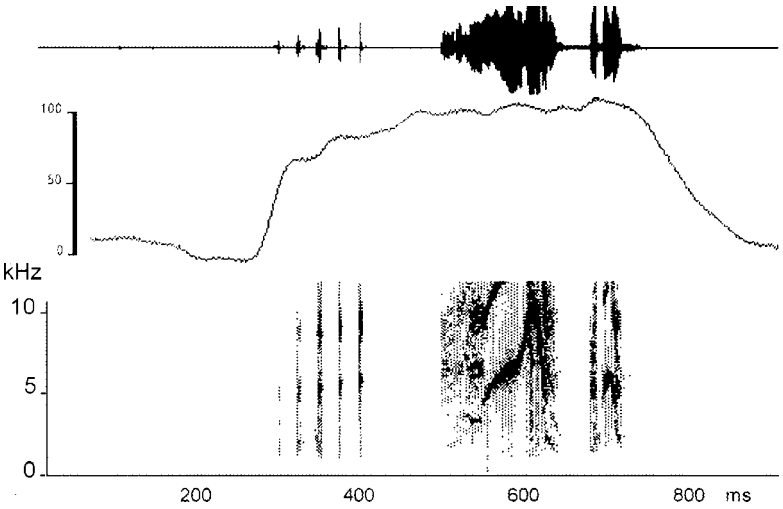

FIG. 7. Respiratory movement during err-chuck. Upper trace: oscillogram of the vocalization; middle trace: respiratory movement; lower trace: spectrogram.

closely related to the amplitude of peep calls and rhythmic cackling. For echolocating bats, Lancester *et al.* (1995) similarly have shown a close correlation of lateral abdominal wall EMG cavity with high-frequency ultrasonic pulses. A close relation of VCRM to expiratory abdominal muscle activity in the squirrel monkey is also indicated by the latency of EMG activity in the obliquus internus and externus muscles which started between 32 and 104 ms before vocal onset (Jürgens and Schriever, 1991). This corresponds to the latencies found for VCRM for peep and trill calls in the present study.

The VCRMs demonstrated during peep, trill, and cackle calls clearly differ from those characterizing respiratory movements during speech in humans (Estenne *et al.*, 1990; Draper *et al.*, 1959). In humans, a constant linear decrease of abdominal and thoracal diameter has been observed during speaking. This has been related to the production of a moderate but relatively constant subglottic pressure during speaking (Estenne *et al.*, 1990). Expiratory abdominal muscles, in this case, are only recruited after several seconds near the end of a speech period, while at the beginning, passive relaxation of the abdominal and thoracic wall is observed (Draper *et al.*, 1959; Hoshiko and Berger, 1965).

A situation partially similar to speech-related respiratory movements is observed during purring. Here, we also do not find an abrupt decrease of abdominal diameter, but a slow linear one starting sometime after vocal onset. Like speech, purring is a low-frequency vocalization that has low-or-moderate intensity and does not need such a high pressure for its production as high-intensity peep or trill calls. Therefore, as in human speech a relaxation of the respiratory muscles maybe sufficient to support the necessary subglottic pressure.

Jürgens and Schriever (1991) showed that in the squirrel monkey thoracic expiratory as well as inspiratory muscles are co-activated to stabilize the thorax, against which abdominal expiratory muscles can act to produce the appropriate subglottic pressure. As the decrease of abdominal diameter measured in this study is closely related to expiratory abdominal muscle activity, it should also be related to lung pressure as well as subglottic pressure. It may be assumed that VCRMs during vocalization are correlated with lung pressure in such a way that a short distance between spine and abdominal surface (upward position in our plots) relates to high lung pressure, which a large distance relates to low pressure. Therefore it is not surprising that large amplitude calls like peep calls exhibit a rather large VCRM and purring which is a low amplitude call has only a small VCRM.

As already stated sound intensity is not the only parameter with which respiratory movements are correlated. In the case of trill calls, there is a modulation of VCRM that is much better correlated with the time course of the fundamental frequency than with that of the amplitude. This is most clearly expressed by the fact that modulation of VCRM takes place only during the periods in which frequency modulation is present.

The phase relationships indicate that small abdominal diameter which, as stated above relates to high lung pressure, is normally correlated with high frequency. Surprisingly, there is not a strict relationship between the amplitude modulation present in the trill call and the breathing movement. This makes clear that expiratory effort bears a complex relationship to frequency and amplitude, depending upon the specific call type.

In order to explain this relationship, a model proposed by Titze (1989, 1993) for humans may be used. According to this model, higher fundamental frequencies need higher lung pressures for their production than lower ones. According to Titze, there is not only a lower limit of lung pressure but also an upper one. This is most relevant at low frequencies where the vocal folds have low tension. In this case, high pressure can either prevent glottal closure or result in a chaotic movement, so that tonality is lost. High pressure at low frequency, furthermore, will result in a high airflow which may be incompatible with prolonged phonation. The upper pressure limit also increases with frequency [Fig. 8(A)]. Data from Titze (1993) indicate that the upper pressure limit for low frequencies is below the threshold for high frequencies. This means that in order to produce a continuous vocalization with marked frequency modulation (above 50% of the vocal range) an active modulation of lung pressure is necessary. Furthermore, a specific phase relationship between frequency modulation and breathing modulation is necessary. High frequency has to be in phase with high pressure to produce a

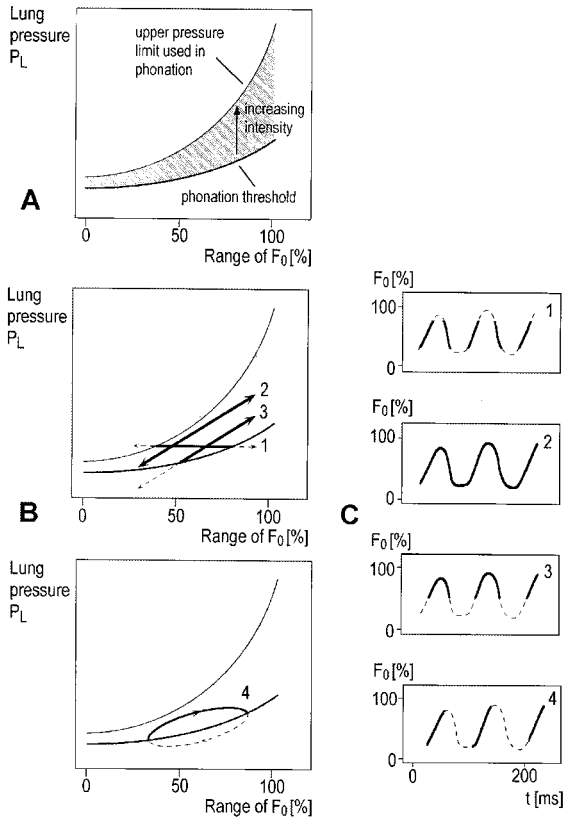

FIG. 8. (A) The shaded area represents the range of lung pressure (PL) which is compatible with the production of a specific fundamental frequency (F_0). Only within the shaded area, phonation is possible. Within the range, intensity increases with lung pressure (uppointing arrow). In (B) the shading is omitted in both diagrams; only upper and lower pressure limit is indicated. The numbered lines with double arrows represent tracks along which lung pressure and fundamental frequency can be modulated during trill calls. As phonation is only possible within the area shaded in (A), it is only along the marked sections of the tracks that vocalization will occur; the thin dashed sections of the tracks will not. The differential tracks represent different types of modulation: 1. No pressure modulation. 2. Optimal pressure modulation. 3. Pressure modulation with reduced overall pressure. 4. Frequency modulation and pressure modulation are shifted in phase. (C) The figures on the right side show schematic spectrograms that will result from three cycles along the corresponding modulation tracks of (B). Dashed lines in (C) correspond to the dashed parts in (B) and indicate fictitious frequency course during silent periods.

continuous trill call; this is exactly what has been observed during trill calls. Figure 8(B) shows a well adapted (curve 2) and a maladapted (curves 1, 3) lung pressure-frequency relationship.

By varying the phase relationship between frequency (frequency is assumed to be directly related to vocal fold tension) and VCRM, the model generates either pure upward or downward sweeps [Figs. 8(B), (C) curve 4]. Additional trill types can be generated by either changing the overall lung pressure [Figs. 8(B), (C) curves 2, 3] or the steepness and amplitude of frequency or lung pressure modulation. In fact, all the trill variants shown in Fig. 8(C) have been observed in spontaneously vocalizing animals (Winter *et al.*, 1966; Winter, 1969; Newman, 1985). One might therefore speculate that the above-described mechanism is used by the animals to produce different kinds of trill calls. It is further suggested that a similar mechanism underlies rhythmically frequency-modulated calls of other primates, like *Callithrix jacchus* or *Microcebus murinus* (Zimmermann *et al.*, 1995), and perhaps mammals in general as well.

With regard to the neuronal mechanisms underlying the above-described model, the question arises of how the respiratory and laryngeal components are appropriately synchronized. Is there a common generator for rhythmic vocal activity or are there separate laryngeal and respiratory rhythm generators? In the case of separate generators, one would expect that under certain conditions respiratory modulation and frequency modulation can run out of phase. It also might be expected that the modulation of either frequency or respiration could disappear independently from each other. In the above-described experiments, phase shifts were observed during some calls but the cycle length differences between frequency modulation and respiratory modulation always remained small. This indicates that the rhythm generation depends on separate but closely coupled generators for respiratory and laryngeal components.

The large amplitude modulations observed during peep sequences and err-chucks, neither of which is accompanied by a corresponding modulation of the VCRM, cannot be explained by the mechanism described above. Here, it must be assumed that the amplitude minima are due to laryngeal mechanisms alone, either a complete opening or closure of the glottis. As a complete opening of the glottis together with the high pressure during peep calls would result in a fast exhaustion of the respiratory airflow, it is likely that a transient glottal closure rather than an opening is the cause for the amplitude minima in these cases. A clarification of this question has to be left to further investigations directly observing the glottis during vocalization.

V. CONCLUSION

With regard to our initial questions, the most important finding of this study is that respiratory movements during trill calls are closely related to the frequency modulation of the trill fundamental frequency. Furthermore, the model proposed by Titze (1993) for the human is also applicable to the squirrel monkey. It provides an explanation for the production of a large group of different frequency-modulated squirrel monkey calls by only two basic mechanisms. It is proposed that the animals are able to control and utilize these mechanisms for the production of different types of trill calls.

ACKNOWLEDGMENTS

The author wants to thank Professor Uwe Jürgens for his help and discussion during the preparation of the manuscript and Professor Elke Zimmerman for her comments on an earlier version of the manuscript.

Draper, M. H., Ladefogedand, P., and Whitteridge, D. (**1959**). ''Respiratory muscles in speech,'' J. Speech Hear. Res. **2**, 16–27.

Estenne, M., Zocchi, L., Ward, M., and Macklem, P. T. (**1990**). ''Chest wall motion and expiratory muscle use during phonation in normal humans,'' J. Appl. Physiol. **68**, 2075–2082.

Floyd, W. F., and Silver, P. H. S. (**1950**). ''Electromyographic study of patterns of activity of the anterior abdominal wall muscles in man,'' J. Anat. **84**, 132–145.

Hirano, M., Vennard, W., and Ohala, J. (**1970**). ''Regulation of register, pitch and intensity of voice,'' Folia Phoniatr. **22**, 1–20.
Hoshiko, M. (**1962**). ''Electromyographic investigation of the intercostal muscles during speech,'' Arch. Phys. Med. Rehabil. **43**, 115–119.
Hoshiko, M., and Berger, K. W. (**1965**). ''Sequence of respiratory muscle activity during varied vocal attack,'' Speech Monographs **32**, 185–191.
Hsiao, T. Y., Solomon, N. P., Luschei, E. S., Titze, I. R., Liu, K., Fu, T. C. and Hsu, M. M. (**1994**). ''Effect of subglottic pressure on fundamental frequency of the canine larynx with active muscle tensions,'' Ann. Otol. Rhinol. Laryngol. **103**, 817–821.
Jürgens, U., and Schriever, S. (**1991**). ''Respiratory muscle activity during vocalization in the squirrel monkey,'' Folia Primatol. **56**, 121–132.
Lancester, W. C., Henson, O. W., and Keating, A. W. (**1995**). ''Respiratory muscle activity in relation to vocalization in flying bats,'' J. Exp. Biol. **198**, 175–191.
McFarland, D., and Smith, A. (**1989**). ''Surface recordings of respiratory muscle activity during speech: Some preliminary findings,'' J. Speech Hear. Res. **32**, 657–667.
Newman, J. D. (**1985**). ''Squirrel monkey communication,'' in *Handbook of Squirrel Monkey Research*, edited by L. A. Rosenblum and C. L. Coe (Plenum, New York), pp. 99–126.
Titze, I. R. (**1989**). ''On the relation between subglottal pressure and fundamental frequency in phonation,'' J. Acoust. Soc. Am. **85**, 901–906.
Titze, I. R. (**1993**). ''Current topics in voice production mechanisms,'' Acta Oto-Laryngol. **113**, 421–427.
West, R., and Larson, C. R. (**1993**). ''Laryngeal and respiratory activity during vocalization in macaque monkeys,'' J. Voice **7**, 54–68.
Winter, P. (**1969**). ''The variability of peep and twit calls in captive squirrel monkeys (*Saimiri sciureus*),'' Folia Primatol. **10**, 204–215.
Winter, P., Ploog, D., and Latta, J. (**1966**). ''Vocal repertoire of the squirrel monkey, its analysis and significance,'' Exp. Brain Res. **1** 359–384.
Zimmermann, E., Newman, J. D., and Jürgens, U. (**1995**). *Current Topics in Primate Vocal Communication* (Plenum, New York).

Interior near-field acoustical holography in flight[a)]

Earl G. Williams[b)] and Brian H. Houston
Code 7130, Naval Research Laboratory, Washington D.C. 20375

Peter C. Herdic
SFA, Inc., Landover, Maryland

S. T. Raveendra and Bryce Gardner
Automated Analysis Corp., Ann Arbor, Michigan

(Received 6 January 2000; revised 5 May 2000; accepted 7 July 2000)

In this paper boundary element methods (BEM) are mated with near-field acoustical holography (NAH) in order to determine the normal velocity over a large area of a fuselage of a turboprop airplane from a measurement of the pressure (hologram) on a concentric surface in the interior of the aircraft. This work represents the first time NAH has been applied *in situ*, in-flight. The normal fuselage velocity was successfully reconstructed at the blade passage frequency (BPF) of the propeller and its first two harmonics. This reconstructed velocity reveals structure-borne and airborne sound-transmission paths from the engine to the interior space. © *2000 Acoustical Society of America.* [S0001-4966(00)03310-5]

PACS numbers: 43.20.Ye, 43.40.At, 43.50.Yw, 43.60.Pt [ANN]

I. INTRODUCTION

Near-field acoustical holography (NAH) has had tremendous success analyzing sources with geometries which conform closely to one of the separable geometries of the acoustic wave equation; for example, planar, cylindrical, and spherical geometries.[1] In these analyses, the pressure field radiated or scattered from an object is measured on an imaginary surface outside (for exterior problems) or inside (for interior problems) the source. NAH uses this pressure hologram to reconstruct (an inverse problem) the pressure and normal velocity on the body of the source. The solution of the inverse problem in these geometries relies on expansion of the pressure field in terms of a complete set of eigenfunctions corresponding to the geometry. The reconstructions are very efficient, requiring only seconds of computation time per frequency. Sources with boundaries which vary appreciably in shape from one of these separable geometries can be attacked using boundary element methods (BEM), with a considerable sacrifice in computation time, however. Inversion is carried out using the singular value decomposition (SVD), the latter providing the eigenfunctions for the solution to the inverse problem. Original work on this approach was by Veronessi and Maynard in the early 1980s.[2] Extension to axisymmetric geometries[3,4] dealt with the vibration of point-driven submerged shells. General formulations using BEM began appearing in the 1990s.[5–7] This area is becoming increasingly attractive in commercial industries for both interior and exterior applications. For example, in the automotive industry it is applied to interior noise[8,9] and tire noise;[10,11] in musical acoustics to study vibrations of violin-family bodies;[12,13] and in the aircraft industry for interior noise.[14] In the latter case, the Neumann Green function for a cylindrical cavity was employed[15] instead of the free-space Green function normally used in the BEM formulations.

In the present work BEM and NAH are mated together and applied to a propeller-driven aircraft to study, in-flight, the fuselage vibration at the blade passage frequency (BPF) and its harmonics. This project was intended to demonstrate the feasibility of NAH in-flight and represents a cornerstone in efforts to expand NAH to a broad range of industrial noise-control problems. Similar to rotating tire noise investigations, interior noise in a propeller-driven aircraft represents a nonstationary source; that is, one which changes position with respect to time. Using a scanning microphone system, a pressure hologram can be acquired if measurements are taken at time increments which correspond to a fixed position in space of the rotating source. For the aircraft this fixed position can be obtained from a synchro-phaser signal from the propeller shaft, and thus data acquisition can be triggered off of it. This trigger corresponds to $t=0$ for each acquisition of time-series data and the BPF and harmonics are extracted from the discrete Fourier transform of this data. This simulates a stationary source and a coherent hologram can be acquired. One benefit of this is the ability to use signal averaging at each microphone position to increase the signal-to-noise ratio (SNR) of the pressure measurement. The analysis was done on a Beech 1900D airplane.

II. MATHEMATICAL FORMULATION

We consider two surfaces, the reconstruction surface S_v (upon which the normal velocity is to be determined) which consists of the fuselage and endcap surfaces, and the measurement surface S_p, which represents an imaginary surface where the microphone measurements are made (ideally located conformal to S_v) but does not include the bordering, planar endcaps. The surface S_v is shown in the upper mosaic of Fig. 1, and shown partially in the lower mosaic, cut out so that the inner surface S_p is displayed. The color coding will

[a)]Paper presented at the 6th International Congress on Sound and Vibration, Copenhagen, July 1999.
[b)]Electronic mail: williams@genah.nrl.navy.mil

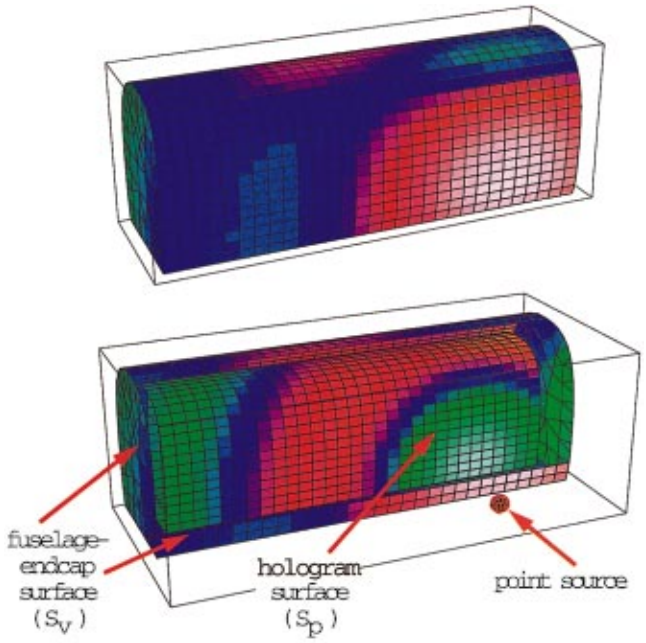

FIG. 1. Upper mosaic shows the complete fuselage (outer) surface S_v. In the lower mosaic the fuselage surface is cut out so that the pressure measurement surface S_p can be seen. S_p includes the two endcaps which are coincident with the endcaps of S_v. The colors on S_p represent the hologram pressure field due to a point source. Red is positive; green is negative; blue is zero. The colors on S_v represent the normal velocity field of the point source.

be explained later. The mathematical formulation arises from the interior form of the Helmholtz integral equation with S_v as the integration surface with interior points (field points denoted by P) specified on S_p

$$\alpha p(P) = \int \int_{S_v} \left(G(P|Q) \frac{\partial p(Q)}{\partial n} - p(Q) \frac{\partial G(P|Q)}{\partial n} \right) dS_v, \tag{1}$$

where the point $Q \in S_v$, $G \equiv e^{-ik|P-Q|}/4\pi|P-Q|$ (the free-space Green function with time dependence $e^{i\omega t}$), $\alpha=1$ if $P \in S_p$, and $\alpha=1/2$ if $P \in S_v$ and the surface is smooth. Note that S_p is contained completely within surface S_v. The surface S_v in Eq. (1) is discretized using the boundary elements[16] shown in Fig. 1. It includes the endcaps as well as the ''fuselage'' surface, the latter corresponding to the inner surface of the insulation blankets attached to the skin of the real fuselage, not the actual fuselage surface. The boundary element discretization of Eq. (1) and ensuing integrations converts this equation to a matrix equation. As is standard practice in these problems, when $P \in S_v$ one can eliminate $p(Q)$ through matrix manipulations,[8] resulting in a final linear equation between the measured pressure, $p(P \in S_p) \equiv p_h$ and the unknown normal velocity, $v = (i/\omega\rho)\partial p(Q \in S_v)/\partial n$

$$p_h = Hv, \tag{2}$$

where H is the complex transfer function obtained from the elimination process. The COMET acoustics code from Automated Analysis Corporation was used for the BEM computations. Quadrilateral elements were used over most of the structure with some triangular elements on the endcaps, as can be seen in Fig. 1. All the elements were linear. p_h is a column vector of length M made up of 30 axial rings of 43 points each ($M=1290$ field points total). These correspond to the measurement positions of the microphone array (Sec. VI).

Additional pressure measurements were obtained on two closely spaced vertical planes parallel to and bordering each endcap so that Euler's equation ($\partial p/\partial z = -i\omega\rho v_e$) could be used to approximate the endcap axial velocity distribution, v_e, using a finite difference approximation for $\partial p/\partial z$. v_e is discretized with 65 elements per endcap (see Fig. 1). If we partition the velocity vector as

$$v = \begin{bmatrix} v_f \\ v_e \end{bmatrix},$$

where v_f is the fuselage velocity (does not include endcaps), and partition

$$H = [H_f \;\; H_e]$$

to match the velocity partitioning, the discretized Helmholtz equation, Eq. (2), now becomes

$$p_h - H_e v_e = H_f v_f, \tag{3}$$

where the quantities on the left-hand side are all known.

This technique differs slightly from the normal procedure in which the endcap velocity is not specified. In this case the pressure hologram would include the outer endcaps, and the conformal axial velocity would be obtained through the reconstruction. However, this reconstruction requires inversion of a larger transfer function, increasing the computation times. Thus, with the objective of speeding up the inversion time the procedure leading to Eq. (3) was adopted.

As will be seen in Sec. VI, the microphone locations on the endcaps do not line up with the 65 endcap elements. Thus, the endcap data were interpolated using a two-dimensional curve fit to generate v_e at the center of the given elements. Since the endcap data are quite smooth, the interpolation is easily done.

The transfer function H is normalized by division by the element areas so that v_e and v_f are actually volume velocities (m^3/s); that is, velocity multiplied by the corresponding element area. Since the left-hand side of Eq. (3) is known, we define $p_m \equiv p_h - H_e v_e$ and Eq. (3) becomes

$$p_m = H_f v_f. \tag{4}$$

At this point we have assumed that p_m is noise-free so that this equation holds exactly, that is, to within the precision of the BEM. If we assume that the noise encountered during the experiment is Gaussian and spatially uncorrelated then, using a tilde over the symbol to represent a quantity with noise,

$$\tilde{p}_m \equiv p_m + n = H_f v_f + n, \tag{5}$$

where $\tilde{p}_m (\tilde{p}_m = \tilde{p}_h - H_e \tilde{v}_e)$ are the in-flight measured data with noise n.

It should be noted that the elements on the fuselage surface (see Fig. 1), which includes the floor, represent 30 axial rings of 45 points each, centered at the locations of the pressure measurements but offset normally from them by a distance of 8.58 cm. These rings include extra elements at the

floor–sidewall junction so that the pressure-measurement point on the corner is close to two adjacent velocity elements, one on the floor and one on the sidewall joined at the corner. If we denote the length of the column vector v_f as N, then $N=1350$ and H_f is a rectangular matrix, 1290×1350. Because of these added elements our transfer function is not square, and we have fewer equations than unknowns.

III. INVERSION

The solution for the (volume) velocity v_f on the fuselage can now be obtained by inversion of Eq. (5). This is carried out using the singular value decomposition (SVD) of the matrix H_f. Note that, even though Eq. (5) represents an underdetermined system of equations, the SVD is ideally suited to handle this condition; it is not necessary, as is sometimes claimed, that the number of measurement points equal or exceed the number of reconstruction points. Applying the SVD to H_f, given $U\in\mathcal{C}^{M\times M}$, $\Sigma\in\mathcal{C}^{M\times M}$, and $V\in\mathcal{C}^{N\times N}$ ($M=1290$ and $N=1350$), yields

$$H_f=U[\Sigma \quad 0]^{M\times N}V^H, \tag{6}$$

where $\Sigma\equiv\mathrm{diag}(\sigma_1,\sigma_2,...,\sigma_M)$ and $\sigma_1>\sigma_2>\sigma_3,\ldots$. Thus, Eq. (5) becomes

$$p_m=U[\Sigma \quad 0]V^H v_f. \tag{7}$$

U and V are unitary matrices defined by

$$U^HU=I_M \tag{8}$$

$$V^HV=I_N, \tag{9}$$

where I_M and I_N are $(M\times M)$ and $(N\times N)$ identity matrices, respectively, and the H superscript represents the conjugate transpose of the matrix. Thus, U^H is the inverse of U. The singular values σ are ranked from highest to lowest along the matrix diagonal. The rows of U^H and V^H contain the orthonormal eigenfunctions or ''modes'' of the SVD decomposition. We use the term ''modes'' loosely here, since it does not refer to the modes of the cavity, but instead refers to the two-dimensional pressure or velocity modes of the sidewall/floor surfaces shown in Fig. 1. Each mode u_i represents a row of U^H

$$U^H=\begin{bmatrix} u_1 \\ u_2 \\ \vdots \\ u_M \end{bmatrix}.$$

Since each mode spans a two-dimensional surface, we can visualize u_i spatially in matrix form by segmenting over the two coordinate dimensions (circumferential×axial)

$$u_i\rightarrow\overline{U^{(i)}}\equiv\begin{bmatrix} u_{i1} & u_{i2} & u_{i3} & \cdots & u_{i30} \\ u_{i31} & u_{i32} & u_{i33} & \cdots & u_{i60} \\ \vdots & & \vdots & & \vdots \\ \cdots & & \vdots & & u_{iM} \end{bmatrix}^{m_1\times m_2}, \tag{10}$$

with rows following the axial direction of the fuselage, and columns following the circumferential direction (including floor); $m_1=43$ (circumferential) and $m_2=30$ (axial) with $m_1\times m_2=M$. Color coding the real (and dominant) part of $\overline{U^{(i)}}$ for the first 36 modes ($i=1,...,36$), we arrive at the display shown in Fig. 2. Note that these modes are used for the decomposition of the pressure vector $\tilde{p}_m$. Although not displayed, the modes of V^H, used for the decomposition of the fuselage velocity v_f, are nearly identical to U^H due to the fact that the hologram and reconstruction surfaces are located close together and are nearly conformal. We will discuss the ''*k*-space'' nature of these modes in the next section.

A. ''*k*-space'' interpretation of the modes

To study these modes in more detail, we attempt to represent the modes of Fig. 2 in ''*k*-space.'' This representation results from Fourier transforming the data in the axial (wave number $k_z=2\pi m/L_z$) and ''circumferential'' (wave number $k_\phi=n/a$) directions, the latter approximating the sidewall and floor measurement contour as a simple circle of radius a. L_z is the axial scan length. For an extensive discussion of k space, see Ref. 1. A two-dimensional discrete Fourier transform (DFT) can be carried out on $\overline{U^{(i)}}$ [see Eq. (10)] by the following. Define the elements of the Fourier transform matrix W^n as

$$[W^n]_{kq}\equiv\frac{1}{\sqrt{n}}e^{2\pi i(k-1)(q-1)/n}, \quad k,q=1,2,...,n. \tag{11}$$

Then, the operation

$$\overline{U_F^{(i)}}\equiv W^{m_2}\overline{U^{(i)}}W^{m_1\dagger}, \tag{12}$$

where † represents the transpose, represents a spatial, two-dimensional discrete Fourier transform of the ith mode shape, $\overline{U^{(i)}}$. We show the result in Fig. 3 corresponding to the 36 modes in Fig. 2. We plot the magnitude of $\overline{U_F^{(i)}}$ with white representing the largest values. Since the spacing in the axial direction is uniform, the axial DFT provides an exact k-space representation. The spacing in the circumferential direction is only nearly uniform, the DFT in this direction is an approximate k-space representation. We still expect, however, that a sinusoidal ''mode'' would be represented by four white dots on the plot (four exponentials) along with sidelobes due to spectral leakage and nonuniform spacing as well as a noncircular fuselage contour. This is, indeed, the dominant characteristic seen in the figure. The red circle in each plot is the radiation circle, with radius equal to the acoustic wave number. When the modal wave number is closest to this circle, the mode is the most efficient due to the trace matching to interior resonances. As the dominant modal wave number moves outside the radiation circle the mode becomes evanescent, decaying exponentially from S_v to S_p, and is associated with smaller singular values as a result.

IV. REGULARIZATION

We use a truncated regularization for the inversion of Eq. (5). Given the properties of U and V,

$$\tilde{v}_f^c=V\begin{bmatrix}\Sigma_c^{-1} \\ 0\end{bmatrix}U^Hp_m, \tag{13}$$

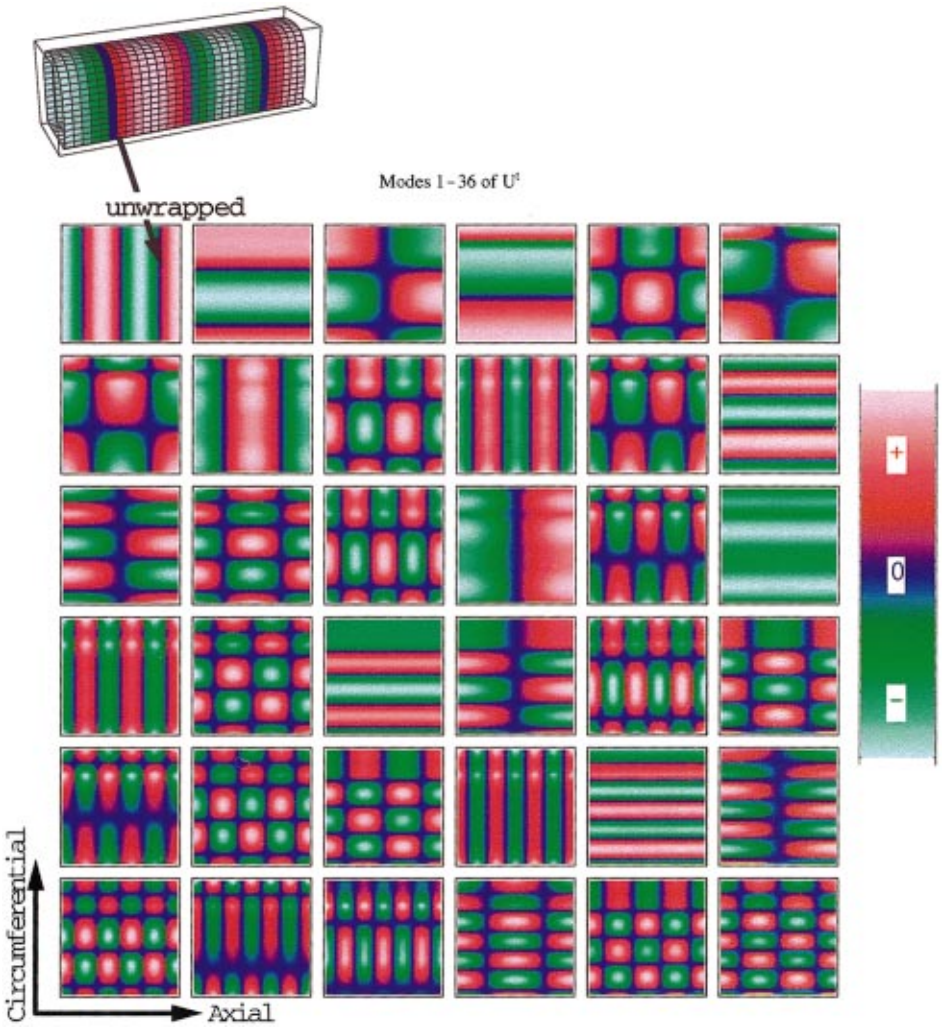

FIG. 2. The first 36 modes (36 rows of U^H) obtained from the SVD of H_f. The modes are ordered by decreasing singular value from the top left to the bottom right. The frequency was 103.7 Hz. Red is positive, green negative, and blue is zero. The mode shapes are remarkably simple. Modal excitation coefficients (the participation factor of each mode) are found from $U^H p_m$. This operation is perfectly analogous to a two-dimensional, spatial Fourier transform of the pressure data, the latter using a product in each dimension of $e^{2\pi inm/N}$ $(m=0,1,...,N-1)$ for the normal modes, $n=0,...,N-1$.

where

$$\Sigma_c^{-1} \equiv \mathrm{diag}\left(\frac{1}{\sigma_1}, \frac{1}{\sigma_2}, \ldots, \frac{1}{\sigma_c}, 0, 0, \ldots\right), \tag{14}$$

$c \leqslant M$ and the reconstructed normal velocity $\tilde{v}_f^c$ depends on the noise and the cutoff. The truncated regularization limits the number of singular values used in the inversion by zeroing out the remaining elements ($1/\sigma_i = 0$, where $i > c$). There are many other approaches to regularization,[17,18] which is an extremely important subject, but we will not discuss them here and reserve analysis for a future paper. The truncation method simulates a rectangular spatial wave number filter, eliminating modes with increasingly smaller spatial frequencies (increasing in evanescence), as can be seen in Fig. 3. Due to the ordering of the singular values, the modes are ordered essentially by radiation efficiency. The most efficient modes are due to cavity resonances (or amplifications when off resonance) of the surface S_v, in which case the dominant wavelength of the mode tends to trace match the acoustic wavelength. As the modal wavelength increases or decreases beyond the acoustic wavelength the efficiency decreases, as can be seen by the ordering of modes in Fig. 3. It is not surprising then that the ''dc'' modal wavelength corresponds to the 18th singular value.

A. Determination of the cutoff

Crucial to the success of the inversion is the correct choice of the cutoff singular value, σ_c in Eq. (13). Although there is no unique or best way (at this time) of accomplishing this, we use a method here which has proven successful in the point-source simulations described below. This method requires a knowledge of the signal-to-noise ratio (SNR) of the data. Once known, we create a simulated data set (v_f given) with the same SNR and determine the minimum error solution $\|v_f - \tilde{v}_f^c\|$ with respect to the cutoff singular value. The cutoff singular value determined in this fashion is then used for the regularization of the in-flight data set.

Of course, we must know the SNR of the experimental data. Since it is not known *a priori*, then we estimate it in the following fashion. First, assume that the noise is Gaussian with a variance of σ, spatially uncorrelated. Out of the M singular vectors of U^H we select the last q of these, corresponding to the smallest q singular values. That is, we partition U^H as

$$U^H = \begin{bmatrix} U_1^H \\ U_2^H \end{bmatrix}, \tag{15}$$

where $U_1^H \in C^{M-q \times M}$ and $U_2^H \in C^{q \times M}$. We determine the last q modal coefficients of the pressure by multiplication of Eq.

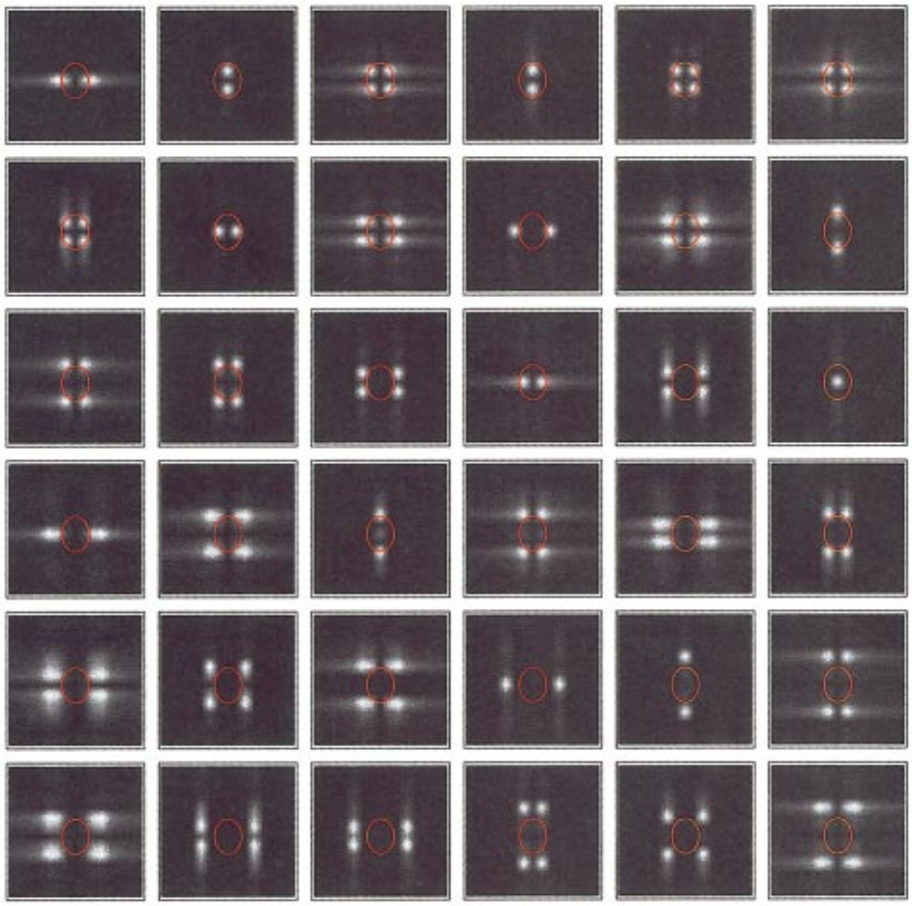

FIG. 3. Modes transformed into ''k space.'' The magnitude of $\overline{U_F^i}$ for the first 36 modes ($i=1,...,36$) ordered as in Fig. 2. The largest value is represented by white, and the smallest by black. The red circle represents the location of the radiation circle/ellipse (radius is the acoustic wave number).

(5) by U_2^H, then computing the 2-norm and the expectation E of the result

$$E[\|U_2^H n\|^2]=E[\|U_2^H\tilde{p}_m-U_2^H H_f v_f\|^2]. \tag{16}$$

Since the noise is spatially uncorrelated,

$$E[\|U_2^H n\|^2]=\sigma^2\,\mathrm{Tr}[U_2U_2^H]=q\sigma^2,$$

where Tr represents the trace of a matrix. Evaluating the right-hand side of Eq. (16) we obtain, using Eq. (6),

$$q\sigma^2=E[\|U_2^H\tilde{p}_m\|^2]+\|\Sigma_2 V_2^H v_f\|^2, \tag{17}$$

where the matrix V_2 and diagonal matrix Σ_2 arise from the following definitions:

$$V^H=\begin{bmatrix} V_1^H \\ V_2^H \\ V_3^H \end{bmatrix} \quad \text{and} \quad \Sigma=\begin{bmatrix} \Sigma_1 & 0 \\ 0 & \Sigma_2 \end{bmatrix}, \tag{18}$$

given $V_1^H\in\mathcal{C}^{M-q\times N}$, $V_2^H\in\mathcal{C}^{q\times N}$, $V_3^H\in\mathcal{C}^{N-M\times N}$, $\Sigma_1\in\mathcal{C}^{M-q\times M-q}$, and $\Sigma_2\in\mathcal{C}^{q\times q}$ which define the partitionings. Note that

$$\Sigma_2=\begin{bmatrix} \sigma_{M-q+1} & 0 & \cdots & 0 \\ 0 & \sigma_{M-q+2} & \cdots & 0 \\ \vdots & \vdots & \ddots & 0 \\ 0 & 0 & 0 & \sigma_M \end{bmatrix},$$

a diagonal matrix containing the last q singular values.

Although it may not be obvious at first glance, the second term in Eq. (17) is much less than the first and can be ignored as long as q is not too large. Physically there is a simple interpretation. The modal excitation coefficients $V_2^H v_f$ of the last q modes of the surface vibration are highly attenuated in amplitude when propagated to the hologram surface due to the multiplication with the small singular values. The modal excitation coefficients $U_2^H\tilde{p}_m$ of the noisy pressure signal are excessively large due to the presence of noise, and thus dominate the former.

Returning to Eq. (17), we now have an estimate of the noise given that the second term is negligible

$$\sigma^2\approx E[\|U_2^H\tilde{p}_m\|^2]/q. \tag{19}$$

For any particular experiment we have only one point in the ensemble with which to determine the expectation E. However, if we view each eigenvector as an independent estimate of $\sigma^2\approx|u_i\tilde{p}_m|^2$ where $M-q+1\leqslant i\leqslant M$, then $\|U_2^H\tilde{p}_m\|^2/q$ in Eq. (19) approximates an ensemble average of q events. Thus, we have for sufficiently small q

$$\sigma^2\approx\|U_2^H\tilde{p}_m\|^2/q. \tag{20}$$

This result is not new. Hansen[19] indicates that $|u_i\tilde{p}_m|$ ''levels off at'' σ and for the overdetermined system ($M>N$) Ih[20] has proven that Eq. (19) is true exactly. In his proof he uses the fact that the $q=M-N$ eigenvectors of U form a null space and thus the surface velocity associated with them is null, that is, zero. [The second term in Eq. (17) does not appear.]

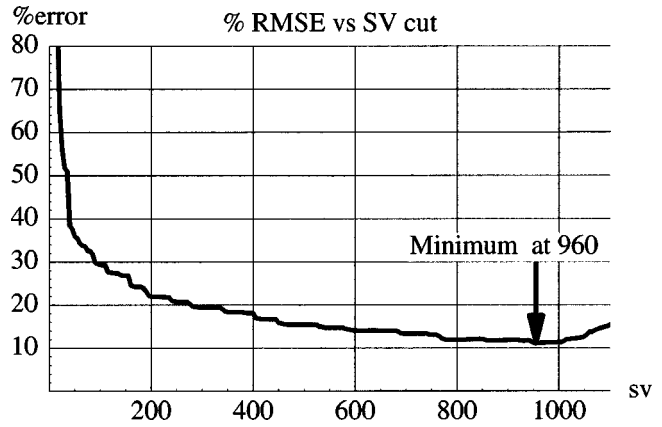

FIG. 4. RMSE (rms error) versus number of singular values used in the reconstruction for the normal velocity on the fuselage surface for an exterior point source with no noise.

Using Eq. (20), the SNR of the data can be estimated. If we define the SNR, S_n, as

$$S_n = \frac{\|\tilde{p}_m\|}{\sigma}, \tag{21}$$

then

$$S_n \approx \sqrt{q}\,\frac{\|\tilde{p}_m\|}{\|U_2^H \tilde{p}_m\|}. \tag{22}$$

Now, we can return to the issue of finding the cutoff singular value σ_c for the inversion of Eq. (13).

To determine σ_c we replace the in-flight data with synthetic hologram data, generated by placing a point source at the location of one of the aircraft engines, and treating the structure as completely transparent. That is, the surfaces S_v and S_p of Fig. 1 are placed in a free field, a homogeneous space with only the point source present. A synthetic hologram ($\tilde{p}_m$) is generated with the same SNR [computed from Eq. (22)] as the in-flight data. Using Eq. (13), the regularized reconstruction $\tilde{v}_f^c$ is determined for a given c. This is repeated for different values of c until the minimum error is found. The percent error is defined using the vector 2-norm as

$$E^c = 100\,\frac{\|\tilde{v}_f^c - v_f\|}{\|v_f\|}, \tag{23}$$

where v_f is the known normal velocity field from the point source. With c determined from Eq. (23) by the minimum error solution, this value is used for the in-flight data regularization. We will show some examples in the next section.

In general, any exterior source configuration can be used for generation of the synthetic hologram data, since H_f in Eq. (5) is completely independent of the source structure, as long as we do not place any sources *within* S_v. We found that moving the point source to different positions above the fuselage/floor showed very little change in c for the minimum error solution. However, it was found that if the source was placed too close (a distance equal to the length of two axial elements) to S_v, the minimum solution of Eq. (23) for a given SNR overestimated the value of c, with a corresponding larger E^c. Thus, it is important to select an exterior source configuration consistent with the actual experiment.

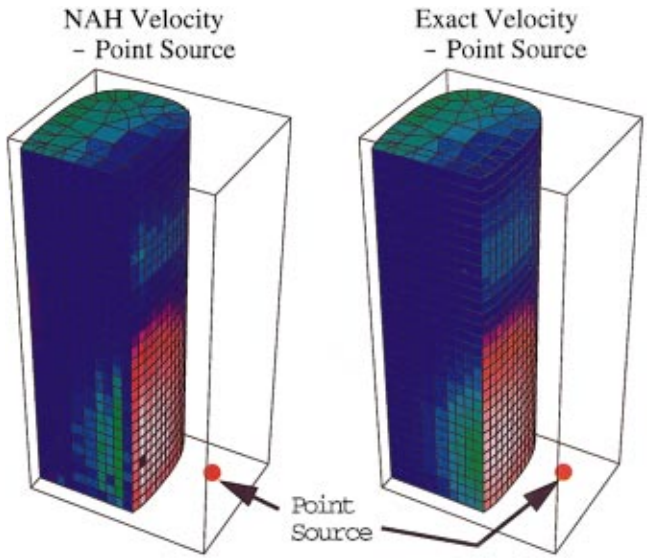

FIG. 5. The real part of the reconstructed normal velocity field due to an exterior point source compared with the exact solution (on the right). Red is positive, green negative. The location of the point source is shown.

V. SYNTHETIC HOLOGRAM DATA TESTS

The synthetic hologram data are also used to gain some experience with the inversion process and to check the computer programs used for the data inversion. This check proved invaluable in the debugging phase of this research.

Two cases were studied for the point-source simulations: one with no noise, and a second with random Gaussian noise added to the pressure hologram at same level as the in-flight experiment. Using Eq. (13), the fuselage normal velocity was reconstructed for the number of singular values which led to minimum error compared with the exact result through Eq. (23). Figure 4 shows the error as a function of the number of singular values kept in the reconstruction for the no-noise case. The minimum error occurred with 960 singular values (the maximum number of singular values was 1290). Figure 1 shows the pressure field due to the point source on the hologram surface located within the fuselage reconstruction surface.

The reconstructed normal velocity field (using 960 singular values) is shown in Fig. 5 compared with the exact

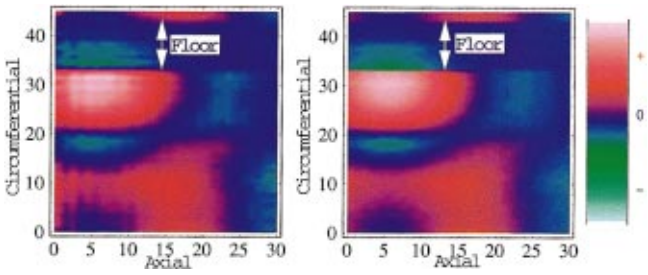

FIG. 6. The real part of the reconstructed normal velocity field due to an exterior point source compared with the exact solution (on the right). Red is positive, green negative. The total error [Eq. (23)] was 11.7%. This minimum error occurred with 960 singular values.

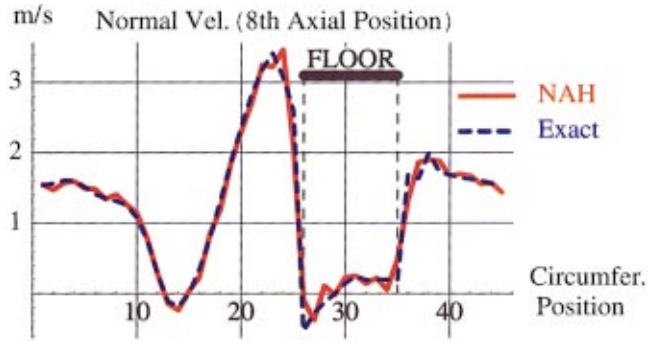

FIG. 7. The real part of the reconstructed normal velocity (solid curve) field compared with the exact solution (dashed curve) for the eighth axial station. The horizontal axis is the circumferential position with the floor located between 26 and 35 (shifted from location in Fig. 6).

field on the right. The normal velocity on the endcap v_e was specified as input in the reconstruction [see Eq. (3)]. Notice the slight differences near the junction of the floor and the sidewall, where the normal velocity is discontinuous due to the discontinuity in the normal to the surface. We will see below that this is due to the Gibbs phenomenon, perfectly analogous to that which arises from the Fourier transform of a discontinuous function. The total error, as defined by Eq. (23) with $c=960$, was 11.7%.

Figure 6 is another display of the reconstruction compared to the exact answer, unwrapping the surface shown in Fig. 5. The endcaps are not shown, however. The agreement is not perfect. One can understand the comparison better in the line plot shown in Fig. 7, which plots the reconstruction compared to the exact result (dashed curve) for the eighth axial station. Agreement is excellent except near the sidewall–floor junction, where the reconstruction tends to overshoot the exact result. Furthermore, the oscillations are reminiscent of the Gibbs effect from Fourier transform theory. This effect will become much more obvious below in the reconstruction of the hologram with noise. The rms error between the two curves is 10.8%. If one excludes the regions of discontinuity in the error calculation, the total error is reduced by approximately a factor of 2. It is unlikely that the error can ever be much lower than this, a fact of life when

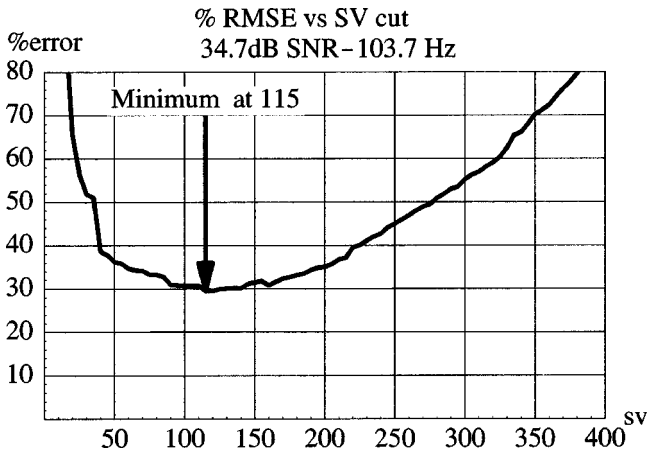

FIG. 8. rms error versus the number of singular values used in the inversion of the transfer function. The best solution occurred using 115 singular values.

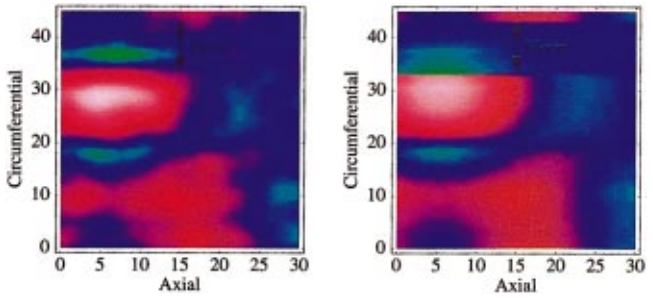

FIG. 9. Fuselage normal velocity reconstruction (real part) versus exact solution (on the right) using 115 singular values in the inversion (minimum error solution). Comparison with Fig. 6 shows that the reconstruction has degraded somewhat. The rms error has increased to 30%.

dealing with inverse problems and the discretizations inherent in the BEM model.

It is perhaps surprising that some regularization was required with no noise in the pressure data. This is due to the fact that p_m is derived exactly from the point-source model, not through Eq. (4). Thus, in the reconstruction of v_f slight inaccuracies in H_f from the BEM model appear as ''noise'' in the inversion.

A. Synthetic hologram data tests with noise added

To simulate the noise level expected in the in-flight hologram, random Gaussian noise was added to the point-source hologram with a 35-dB SNR and the reconstructions were carried out as before. To find the optimum solution, the singular value cutoff was varied from 10 to 500 in increments of 5. Figure 8 shows the result indicating that the best solution (with minimum rms error) was found using 115 singular values in the inversion. In order to determine the fuselage velocity from Eq. (13), the singular values above 115 were all set to zero, corresponding to using only 115 modes of the pressure and velocity basis functions. (The first 36 modes of the pressure basis function were shown in Fig. 2.)

The reconstruction of the normal velocity is shown in Fig. 9 compared to the exact result (on the right). Comparison to Fig. 6 indicates that the reconstruction has degraded a bit. The details of this degradation become clear in Fig. 10, which shows a comparison of the reconstruction with truth for the eighth axial position (as in Fig. 7). Now the disagreement clearly looks like a Gibbs effect, especially in the floor region.

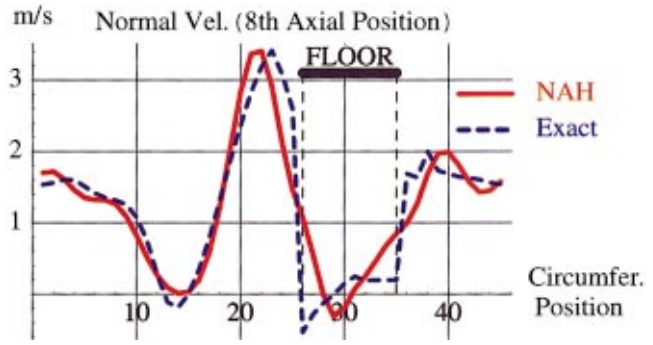

FIG. 10. Reconstruction versus exact solution again for the eighth axial position, as was done for Fig. 7. The Gibbs effect is very evident.

FIG. 11. The Beech 1900D experimental aircraft (UE1).

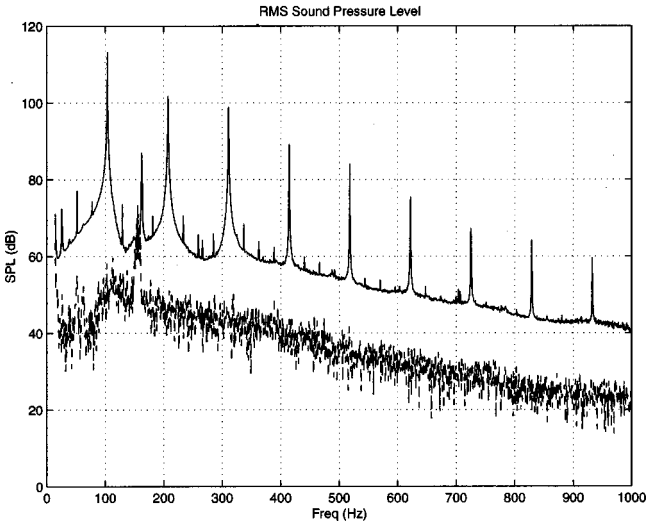

FIG. 13. The rms spatial average over the interior passenger cabin of the Beech 1900D displayed in units of sound-pressure level (SPL). Also shown is the nominal noise floor as measured in the prop plane (dropped by 20 dB to allow for detail of rms curve to be seen).

An important conclusion from the reconstructions of the point source with and without noise is that a large part of the error in the reconstruction is due to the overshoot caused by the Gibbs effect. This results from using modes which must represent the normal velocity on the sidewall and at the same time the floor. Since the modes are continuous from the sidewall to the floor, they do a poor job at representing the discontinuity in normal velocity. In the next section we will discuss the in-flight hologram acquision and its reconstruction.

VI. THE IN-FLIGHT MEASUREMENT AND RECONSTRUCTION

The experimental exercise involved a highly spatially sampled pressure measurement on the interior of a Beech 1900D (UE1) shown in Fig. 11. The experiment was conducted at a speed of 218 kn and at an altitude of 16 000 ft. This is a standard operating condition of the aircraft with a propeller shaft speed of 1550 rpm and an engine torque of

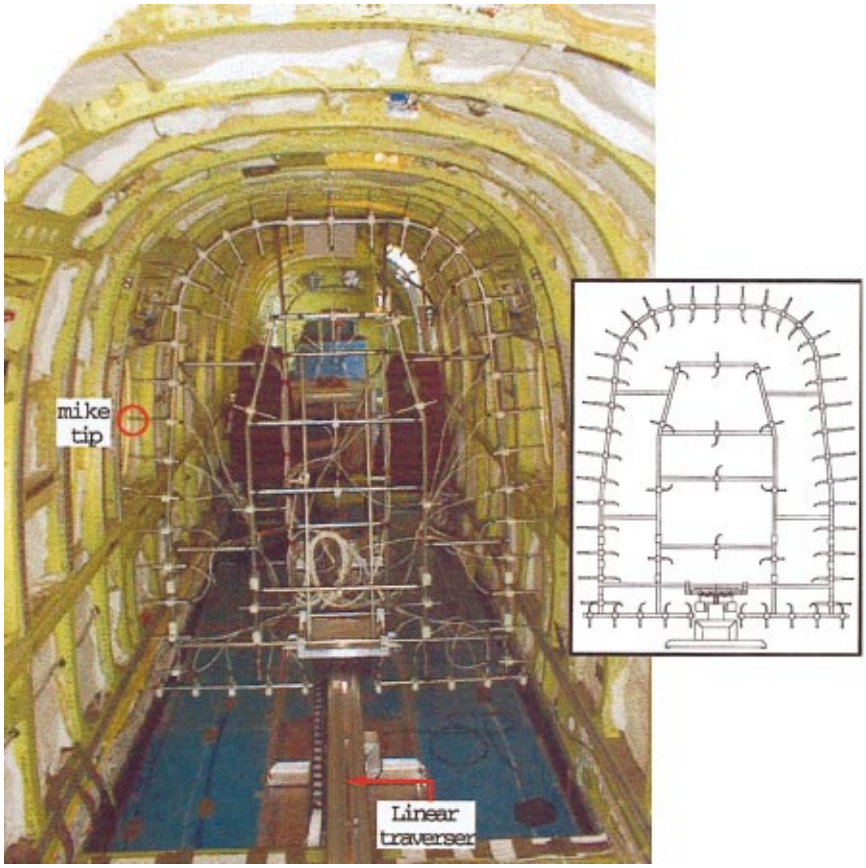

FIG. 12. Microphone boom consisting of a planar array of 55 microphones, 43 microphones on the outer ring and 12 in the internal region spaced to cover the internal area efficiently. The boom was moved on a linear traverser to 32 different axial locations during the experiment (5.12 m total scan length, maximum width and height were 1.36 and 1.68 m, respectively). Time-domain data were acquired with a sample rate of 5 kHz and were processed at the BPF and its harmonics. The total acquisition time for the data scan was 66 min. The pressure data at axial stations 1, 2 and 31, 32 were used to compute the axial velocity on the endcaps, in Eq. (2) using a finite difference approximation to Euler's equation.

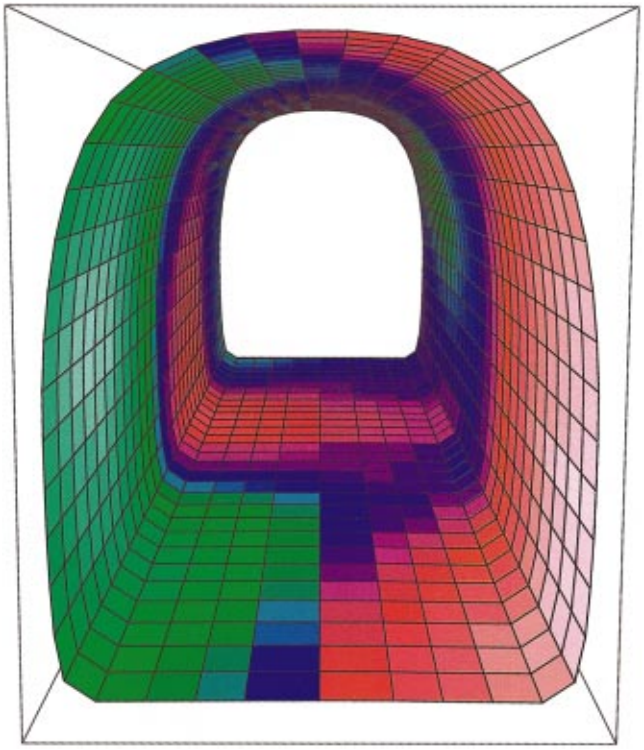

FIG. 14. The hologram pressure, looking aft, measured at 103.7 Hz using the outer 43 microphones of the array, acquired during the in-flight experiment. The real part of the field is plotted after the phase of all the data in the hologram was shifted by a fixed amount so that the maximum pressure level has zero phase (was only real). One can see that the pressure is 180 deg out of phase on either side of the aircraft. The quality of the data is outstanding. The smoothness of the pressure is proof that the synchro-phaser was an excellent time reference for the triggering of the data acquisition system.

3400 ft lb. The cabin was internally pressurized to a pressure differential of 5 psi and the flight occurred on a clear day with relatively smooth conditions.

A scanning boom with 55 microphones (Modal Shop ICP 130A10), mounted in the vertical plane, traversed the interior space of the Beech 1900D passenger cabin to acquire the pressure data which constitute the hologram. Before the flight, each microphone was calibrated with a specially designed benchtop calibrator and the calibration curves for amplitude and phase were stored in a computer so that they could be applied to the in-flight data. The insert in Fig. 12 shows a drawing of the array and to the left the photograph shows this array mounted in the aircraft interior, looking aft. The caption describes some of the details of the experiment. Also note that in the scan area the seats and trim panels are removed. The aircraft's insulation material is intact, and the internal structural complexity (frames, stringers, windows, and flooring) of the plane are left unmodified.

A number of steps were necessary in order to acquire a stable, coherent pressure field over the length of the scan during the in-flight measurement. First, the acquisition trigger was synchronized with the propeller shaft position by using the syncro-phaser signal which is part of the aircraft's standard instrumentation for controlling the phase between the dual turboprops. Thus, the $t=0$ starting point for the time-domain data always occurs at a an identical blade position. This allows for signal averaging. The averaged time-domain data are Fourier transformed and the corresponding frequency bins for the BPF and harmonics are selected to create the holograms. The second important step involved normalizing the pressure hologram with the fuselage wall acceleration in order to increase coherence of the data. This acceleration was measured, simultaneously with the pressure data, at a location near the intersection of the vertical and horizontal prop planes at the center of the thin-walled panel area. The stationary of this transfer function (Pa/g) amplitude improved nominally by a factor of 2 to 3 and the phase by a factor of 6 to 8 over the first three harmonics of the BPF as compared to the unnormalized pressure data in the prop plane. Finally, to further reduce fluctuations caused by minor turbulence of the flight, data were acquired with 28 time-domain averages for each microphone position.

The rms spatially averaged interior response is shown in

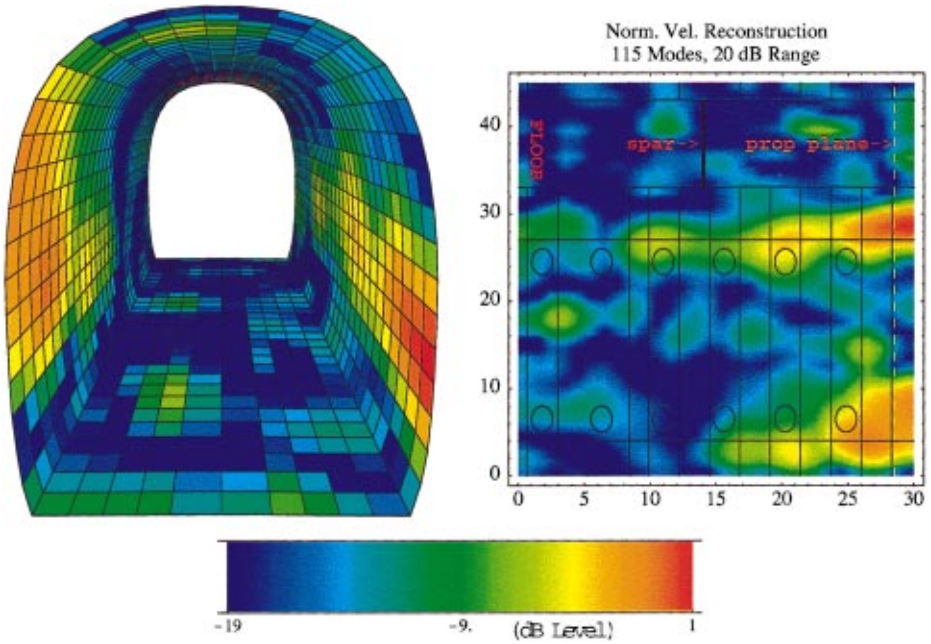

FIG. 15. Magnitude on a decibel scale of the reconstructed normal velocity at 103.7 Hz looking aft. Only the top 20 dB of data is shown as indicated by the color bar. The velocity is normalized by the velocity of an accelerometer located on a fuselage panel in the prop plane. The unwrapped display on the right indicates the positions of the windows and some of the major frames as well as the location of the floor and spar (support between the wings).

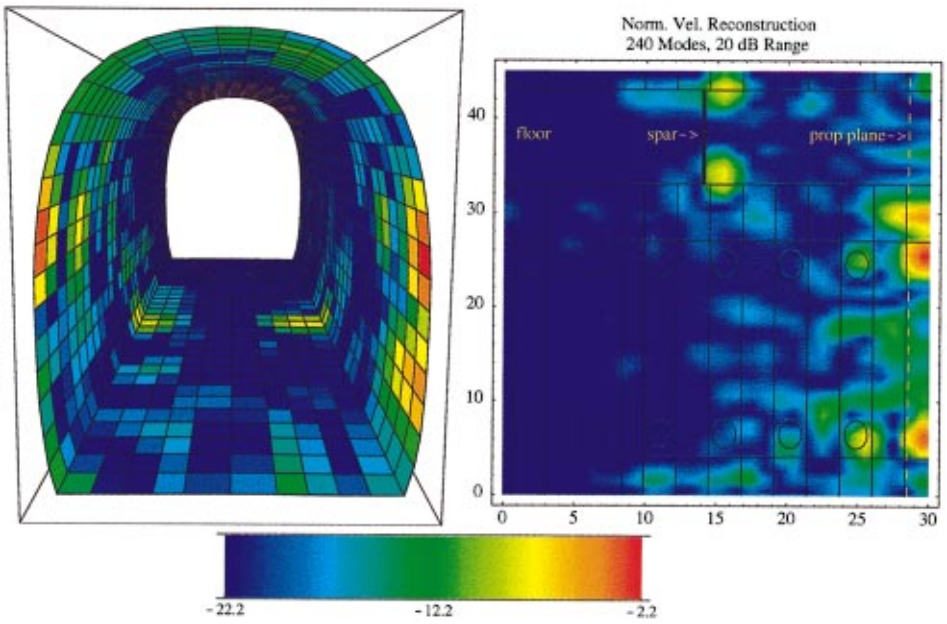

FIG. 16. Magnitude in dB of the normal velocity reconstruction for the first overtone of the BPF, at 207 Hz. The top 20 dB of data is displayed. The highest vibration levels are just in front of the propeller plane (latter indicated by vertical dashed line). The floor just in front of the spar also appears to be vibrating at a high level.

Fig. 13. This average was taken over 55 locations in the vertical plane and 32 axial positions for a total of 1760 data points. The fundamental BPF can be seen at 103.7 Hz along with its higher harmonics. The smaller spikes (40 dB down) seen at quarter intervals between the blade passage harmonics are due to slight differences in the dual, four-blade turboprops. The background (flow-dominated) noise was measured by setting the engine to idle and feathering the props. (In order to maintain a constant speed, the aircraft was placed in a moderate dive.) The noise curve is offset (lowered) by 20 dB to allow for the detail of the rms curve to be seen. Also note that the noise is averaged over the 55 positions in the prop plane and not the entire scan. Signal-to-noise ratios of around 40 dB can be seen at the fundamental harmonic, decreasing slightly for the next two harmonics. These ratios are sufficient for interior holographic projections, as we will see in the next section.

A. Reconstruction of the fuselage normal velocity

The pressure hologram was generated from a Fourier transform of the time-domain data acquired during the experiment, choosing the frequency bins corresponding to the BPF signal and its harmonics. The resulting pressure hologram for the first frequency (103.7 Hz) is shown in Fig. 14.

For the experiment, the actual solution to the inverse problem is not known. We estimate the cutoff for the singular values in Eq. (13) as described in Sec. IV above. As described, this technique is based on an estimate of the SNR in the in-flight hologram, then using the same SNR for a point-source synthetic hologram, and finally determination of the cutoff for the minimum error solution of the latter case.

We first present the reconstruction of the normal velocity for the BPF at 103.7 Hz. The reconstruction boundary is the exposed surface of the fuselage insulation (the white areas between the frames in Fig. 12), located 8.59 cm from the hologram surface. The actual skin of the fuselage was 12.4 cm from the hologram surface. Figure 15 shows the magnitude of normal velocity reconstruction resulting from the inversion. Equation (13) was used and 115 singular values ($c = 115$) were taken for the inversion as determined from the point-source simulation (result shown in Fig. 8). This corresponded to cutting off the singular values at 34.7 dB below the rms hologram pressure.

In Fig. 15 the propeller plane is indicated by a dashed, vertical yellow line in the unwrapped mosaic at the right of the figure, which corresponds to the front of the reconstruction in the left mosaic. Also, some of the major structural components are indicated in black in the mosaic including windows and major frames. Note that the floor is horizontal near the top of the mosaic. The highest vibration levels (red) are seen in the prop plane, with large vibration levels located physically higher on the sidewall on the copilot side of the aircraft than on the pilot side. The asymmetry of the panel vibrations in the prop plane is consistent with other measurements made on the exterior of this aircraft in previous experiments.[21] On the floor there appears to be an axial line of vibration coinciding with the seating track supports.

The reconstruction of the normal velocity at the first overtone (207.5 Hz) of the BPF is shown in Fig. 16, where the magnitude in dB is plotted. Using Eq. (20) the SNR was determined to be 29.3 dB. The point-source simulations pre-

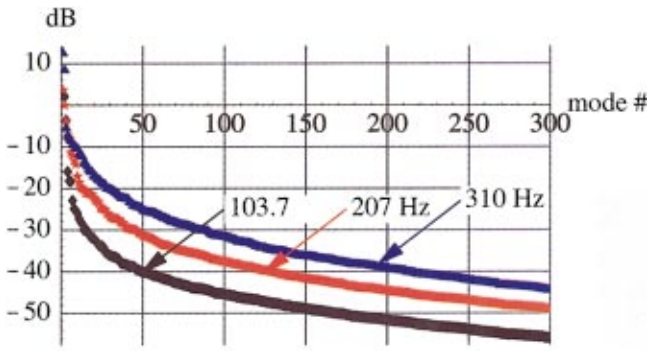

FIG. 17. The first 300 singular values for each frequency. The vertical scale is $20 \log_{10} \sigma/\rho c$.

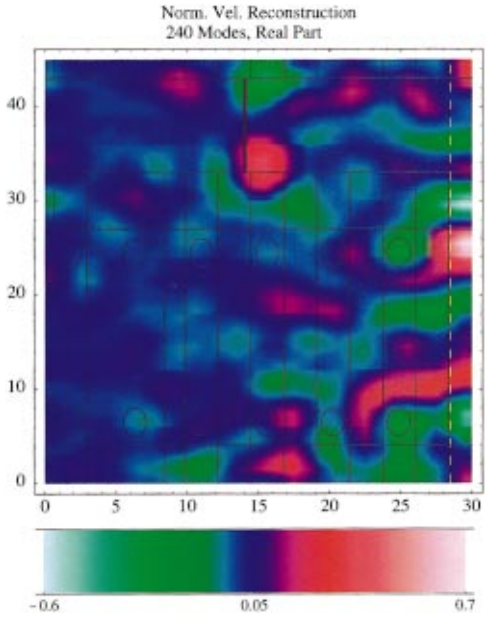

FIG. 18. Same as Fig. 16 except the real part of the reconstruction is displayed instead of the logarithmic magnitudes.

dicted the minimum error solution (26.0%) at $c=240$ singular values. Thus, 240 modes were used in the reconstruction of the in-flight data. Consideration of Fig. 17, which plots $20\log_{10}\sigma_i/\rho c$ for each of the three frequencies, indicates that as the frequency increases more modes participate at a given SNR. This is similar in concept to a plate radiator, in which case the number of modes participating in radiation increases with frequency. Examining the reconstruction in Fig. 16, compared with the BPF reconstruction in Fig. 15, the vibration levels are more confined to the front of the aircraft, with the highest levels in front of the propeller plane, as indicated. The floor in front of the spar (wing support) can be seen vibrating in a rocking fashion (as will become clear in the next figure).

The real part of the normal velocity which provides the phase of the vibration is shown in Fig. 18. Now it is clear that the floor vibration in front of the spar (15 on the horizontal axis in the figure) is out of phase (as in a rocking motion), whereas the vibration in front of the spar represents a structure-borne path from the propeller (since the engines are mounted on the wings), the vibration in the prop plane is caused by the airborne path directly from the blades. The uncovering of the structure-borne transmission path is perhaps the strongest tribute to the accuracy of the NAH–BEM effort. Unfortunately, without surface-mounted accelerometers, one must look to the correlation with structural details to provide confidence in the NAH reconstructions. Also, it can be seen that the fuselage panels in the propeller plane are vibrating in opposite phase across the horizontal stringer (location 27 on the vertical axis).

The last two figures provide the normal velocity reconstructions at the second overtone of the BPF (310.7 Hz). Figure 19 provides the magnitude in dB of the reconstruction, and Fig. 20 the real and imaginary parts of the normal velocity reconstruction. The SNR was determined to be 32.0 dB using Eq. (20). The minimum error for the point-source simulation matching this SNR gave $c=300$ singular values. Thus, 300 modes (singular values) were used in the reconstruction of the in-flight hologram.

The reconstruction of the normal velocity field, shown in Fig. 20, shows much more concentration in the regions around the propeller plane than at the two lower frequencies. This is not surprising since one expects that as the frequency increases the individual fuselage panels will be excited instead of the structure as a whole.

In general, we found that the reconstructions shown in Figs. 15, 16, and 19 were quite insensitive to moderate changes in the number of singular values below the cutoff. For example, reconstruction using 150 singular values instead of 115 for the BPF produces only small changes in the reconstruction, with the maximum levels in each remaining

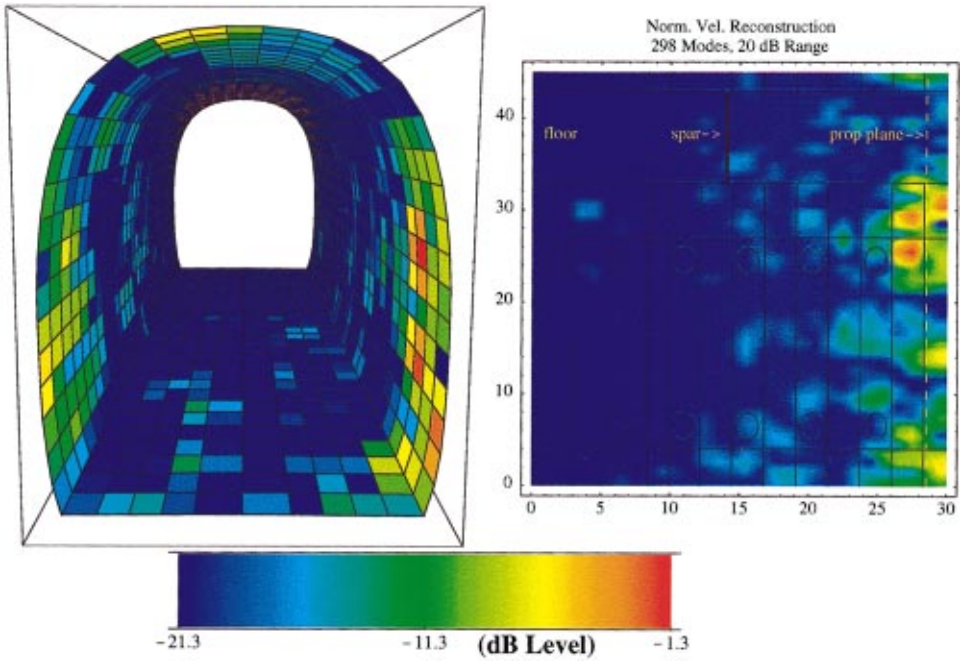

FIG. 19. Normal velocity reconstruction at 310.7 Hz, the second overtone of the BPF. 20 dB of data is shown.

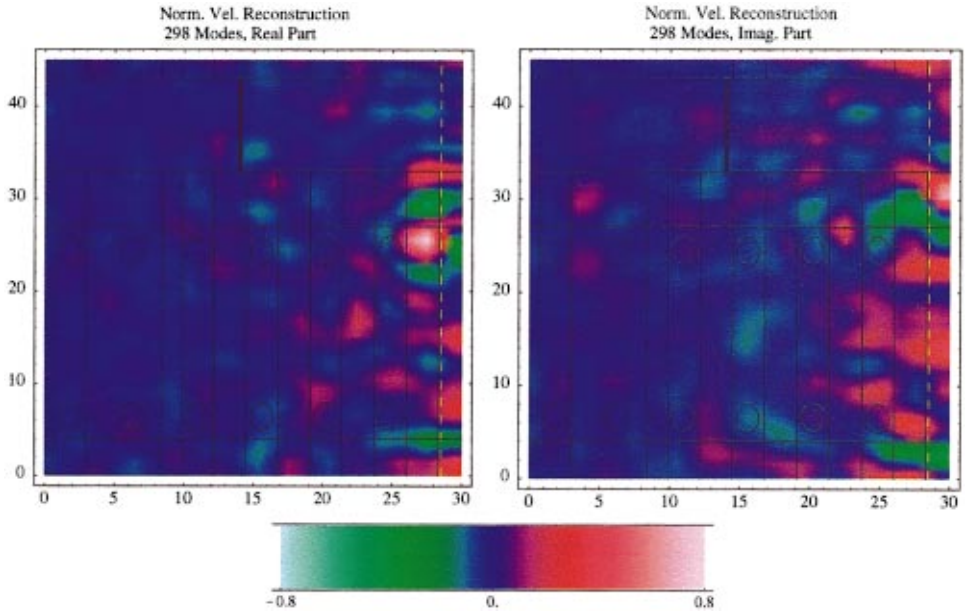

FIG. 20. Same as Fig. 19 except the real and imaginary parts of the reconstruction are displayed instead of the logarithmic magnitude.

nearly the same. This is an important and reassuring result, forgiving of small errors in the estimation of the cutoff, σ_c.

VII. CONCLUSIONS

The in-flight hologram and reconstruction were very successful. The correlation of reconstructed high-velocity regions to actual structural details of the fuselage provides a great deal of credibility to the success of the NAH–BEM effort. It was shown, however, in the simulations that due to the continuity of the modes a spatial Gibbs effect occurs which limits the accuracy of the reconstruction of the normal velocity. The reconstruction of pressure instead of normal velocity would provide a more accurate approach, avoiding the reconstruction of a discontinuous function. Clearly the marriage of BEM and NAH provides a powerful tool for the study of interior noise in propeller-driven aircraft, as well as in more general structures, locating sources of excess vibration and providing a means to evaluate the effectiveness of noise-control procedures. Although not demonstrated in this paper, once the velocity is computed one can use it to determine, through the forward solution of the Helmholtz-integral equation, the pressure, velocity, energy densities, and acoustic intensity throughout in the interior of the reconstruction surface.

Unfortunately, our approach to the regularization problem, although logical, is somewhat *ad hoc*. There is no doubt that better methods exist and intense research is now underway to find a better method. It is believed that regularization was especially difficult in this research due to (1) the Gibbs effect, and (2) the need to specify the endcap velocity v_e in Eq. (3). Although not discussed, the reconstructions appear more sensitive to errors in v_e than to errors in the hologram pressure on S_p. Due to the rather coarse discretization of the endcaps, this sensitivity is disconcerting. For future efforts we recommend keeping the pressure unknown on the endcaps and inverting the slightly larger problem. Furthermore, to avoid the Gibbs effect it would be advisable to reformulate the problem, eliminating the first term in the integrand of Eq. (1) instead of the second, in the BEM approach. With the resulting pressure reconstruction taken on two close concentric surfaces, the normal velocity can then be obtained through Euler's equation. This approach then will avoid any Gibbs problems, although it requires the computation of a second transfer function.

ACKNOWLEDGMENTS

Work supported under contract with Automated Analysis Corporation. Additional support provided by the Office of Naval Research and NASA, Langley. We want to acknowledge Ron Hund and Raytheon Aircraft for their excellence in providing the aircraft, crew, and related support for these experiments.

[1] Earl G. Williams, *Fourier Acoustics: Sound Radiation and Nearfield Acoustical Holography* (Academic, London, 1999).
[2] W. A. Veronesi and J. D. Maynard, ''Digital holographic reconstruction of sources with arbitrarily shaped surfaces,'' J. Acoust. Soc. Am. **85**, 588–598 (1989).
[3] G. Borgiotti, A. Sarkissian, E. G. Williams, and L. Schuetz, ''Generalized nearfield acoustic holography for axisymmetric geometries,'' J. Acoust. Soc. Am. **88**, 199–209 (1990).
[4] A. Sarkissian, ''Near-field acoustic holography for an axisymmetric geometry: A new formulation,'' J. Acoust. Soc. Am. **88**, 961–966 (1990).
[5] G.-T. Kim and B.-H. Lee, ''3-D sound source reconstruction and field reprediction using the Helmholtz integral equation,'' J. Sound Vib. **136**, 245–261 (1990).
[6] M. R. Bai, ''Application of BEM (boundary element method)-based acoustic holography to radiation analysis of sound sources with arbitrarily shaped geometries,'' J. Acoust. Soc. Am. **92**, 533–549 (1992).
[7] A. Tekatlian, P. Filippi, and D. Habault, ''Determination of vibration characteristics of noise sources solving an inverse radiation problem,'' Acustica **82**, 91–101 (1996).
[8] B.-K. Kim and J.-G. Ih, ''On the reconstruction of the vibro-acoustic field over the surface enclosing an interior space using the boundary element method,'' J. Acoust. Soc. Am. **100**, 3003–3016 (1996).
[9] Z. Wang and S. F. Wu, ''Helmholtz equation–least-squares method for reconstructing the acoustic pressure field,'' J. Acoust. Soc. Am. **102**, 2020–2032 (1997).
[10] F. Augusztinovicz, J. Gransst, F. Mssrki, W. Hendricx, and H. Van der Auweraer, ''Application and extension of acoustic holography techniques for tire noise investigations,'' J. Acoust. Soc. Am. **105**, 1373–1374 (1999).

[11] U.-U. Saemann, J. Hald, and A. Schuhmacher, ''Sound field studies of truck tires,'' J. Acoust. Soc. Am. **105**, 1336 (1999).
[12] C. Langrenne and A. Garcia, ''Integral formulations for the vibroacoustic characterization of a cello,'' J. Acoust. Soc. Am. **105**, 1088 (1999).
[13] L. Wang, ''Characterization and Analysis of the Acoustic Radiation from Violins, Using Near-field Acoustic Holography,'' Ph.D. thesis, The Penn State University, May 1999.
[14] E. G. Williams, B. H. Houston, and P. C. Herdic, ''Reconstruction of the surface velocity and interior acoustic intensity from an aircraft fuselage using NAH,'' NOISE-CON96, Seattle, October 1996.
[15] E. G. Williams, ''On Green functions for a cylindrical cavity,'' J. Acoust. Soc. Am. **102**, 3300–3307 (1997).
[16] A. F. Seybert, B. Soenarko, F. J. Rizzo, and D. J. Shippy, ''An advanced computational method for radiation and scattering of acoustic waves in three dimensions,'' J. Acoust. Soc. Am. **77**, 362–368 (1985).
[17] A. Kirsch, *An Introduction to the Mathematical Theory of Inverse Problems* (Springer, New York, 1996).
[18] P. A. Nelson, ''Some inverse problems in acoustics,'' Proceedings of the 6th International Congress on Sound and Vibration, Copenhagen, Denmark, July 1999, pp. 7–32 (unpublished).
[19] P. C. Hansen, *Rank-deficient and Discrete Ill-posed Problems* (SIAM, Philadelphia, 1998), p. 70.
[20] B.-K. Kim and J.-G. Ih, ''Design of an optimal wave-vector filter for enhancing the resolution of reconstructed source field by NAH,'' J. Acoust. Soc. Am. (in press).
[21] Mark Ewing, Personal communication, Dept. of Aerospace Engineering, Univ. of Kansas (1999).

A conjugated infinite element method for half-space acoustic problems

Jean-Pierre Coyette[a)]
Civil Engineering Department, Université catholique de Louvain, 1 Place du Levant, B1348 Louvain-la-Neuve, Belgium and Free Field Technologies S.A., 5 Rue Charlemagne, B1348 Louvain-la-Neuve, Belgium

Benoît Van den Nieuwenhof[b)]
Civil Engineering Department, Université catholique de Louvain, 1 Place du Levant, B1348 Louvain-la-Neuve, Belgium

(Received 25 April 2000; revised 1 July 2000; accepted 5 July 2000)

Many acoustic problems (especially in environmental acoustics) involve half-space domains bounded by a plane subjected to normal admittance boundary conditions. In the ''low'' frequency domain, the numerical treatment of such problems usually relies on boundary element methods based on a particular Green's function suited for the half-(admittance) plane. In the present paper, an alternative hybrid finite/infinite element scheme is proposed. The method relies on a direct treatment of nonhomogeneous boundary conditions along infinite element edges (or faces). The procedure is validated through comparisons with an available reference solution. © *2000 Acoustical Society of America.* [S0001-4966(00)03210-0]

PACS numbers: 43.20.El, 43.20.Fn, 43.20.Rz, 43.50.Gf [ANN]

I. INTRODUCTION

Exterior acoustic problems are frequently referring to propagation of sources in half-spaces. Such problems are, for instance, encountered in environmental acoustics (design of noise barriers) and require the handling of particular boundary conditions along the related half-plane. If this plane is either a ''rigid'' boundary (which enforces a zero normal velocity) or a ''soft'' boundary (which enforces a zero pressure), the problem can easily be solved using symmetry or antisymmetry considerations, respectively. Most practical applications, however, involve finite normal admittance values along the half-plane (which coincides with a road or grass surface for example). In such circumstances, the solution of the acoustic problem cannot fully rely on symmetry or antisymmetry considerations.

A boundary element solution scheme which avoids discretization of the half-plane can be built starting from a suitable boundary integral representation.[1–7] This requirement enforces the use of the specific Green's function[8,9] which corresponds to the solution of the Helmholtz equation for a point source radiating in a half-space. The selection of such a Green's function allows setting up a boundary integral representation which does not involve the half-plane boundary anymore. After discretization, this leads to a further reduction of the problem's size. The implementation of such a boundary element solution is penalized, however, by the additional complexity of the specific Green's function. As key ingredients in a boundary element context, appropriate numerical integration techniques have to be selected for handling related singularities.[7]

On the other hand, much effort has been spent during the last decade in order to apply domain-based techniques (like finite element methods) to exterior acoustic problems.[10] This includes the development of mixed finite element/boundary element formulations, the use of various absorbing boundary conditions, and, more recently, the development of higher-order methods (like Dirichlet-to-Neuman formulations (DtN),[11] for example). In this ''domain- based'' context, infinite element methods[12] appear as a natural extension of finite element methods: instead of truncating the acoustic domain and enforcing an appropriate boundary condition at a finite distance, infinite element methods rely on the full spatial discretization of the original problem and the selection of appropriate interpolation schemes for the outer region. Various infinite element schemes[13] are currently available for that purpose. Their convergence properties have been investigated systematically during the last few years.[14,15] Numerical studies[15,16] have shown the computational efficiency of infinite element formulations vs boundary element solutions. This efficiency results mainly from the fact that related matrices, although of larger size, have an attractive sparse structure which leads to superior computational performances for a wide class of direct and iterative solvers.

The present paper shows how to extend a conjugated infinite element formulation[12,17] in order to handle acoustic propagation above an admittance plane. The basis of this development is the multipole expansion of the solution of the Helmholtz equation outside a regular (spherical, prolate/oblate spheroidal, ellipsoidal) surface in a *free* space. This expansion is selected as a basis for the half-space problem. The weak variational form of the half-space problem refers to a boundary integral along the unbounded half-plane. This integral involves prescribed normal admittance values and/or incident pressures and their normal gradients. The handling of this integral in a finite/(conjugated) infinite element method is described. An example involving a single source is

a)Electronic mail: jean-pierre.coyette@fft.be
b)Electronic mail: vandennieuwenhof@gc.ucl.ac.be

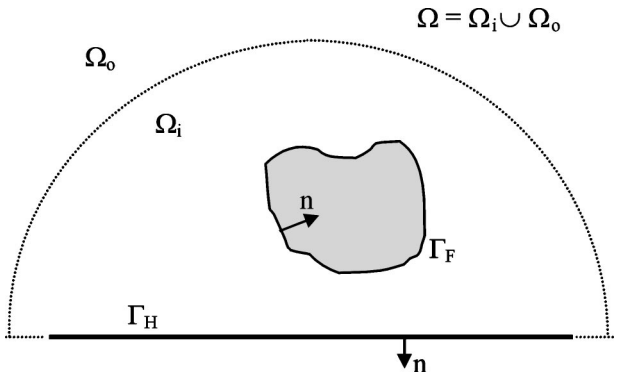

FIG. 1. Acoustic radiation problem in a half-space.

selected in order to show the efficiency of the proposed approach and to illustrate the convergence process. Reference is made to an available analytical solution. A very good agreement between numerical and analytical solutions is obtained.

II. PROBLEM STATEMENT

The exterior acoustic problem related to a half-space can be formulated in a radiation context or in a scattering context. These two problems are (obviously) closely related but lead to slight differences for half-plane boundary terms involved in the weak variational form and, therefore, in the related infinite element model. For these reasons, we state separately the radiation and the scattering problem. Both problems are formulated assuming a time-harmonic dependence ($e^{+i\omega t}$).

A. Radiation problem

The problem is to solve the (homogeneous) Helmholtz equation in a 3D half-space domain Ω bounded by a plane Γ_H and a finite boundary Γ_F (Fig. 1)

$$\Delta p + k^2 p = 0 \quad \text{in} \quad \Omega, \tag{1}$$

where p is the acoustic pressure and k is the acoustic wave number ($k=\omega/c$ with ω=circular frequency and c=speed of sound).

In the present case, the boundary conditions are

$$\partial p/\partial n = -ik\beta p \quad \text{along} \quad \Gamma_H, \tag{2}$$

$$\partial p/\partial n = \alpha \quad \text{along} \quad \Gamma_F, \tag{3}$$

where β is the specific normal admittance ($\beta \equiv A_n \rho c$) along Γ_H, α is a prescribed normal pressure gradient (as induced by a normal acceleration along the vibrating boundary Γ_F), and n is the unit outward normal along $\Gamma = \Gamma_H \cup \Gamma_F$.

These boundary conditions are supplemented by the so-called ''Sommerfeld'' radiation condition in order to allow only outgoing waves at infinity

$$r(\partial p/\partial r + ikp) \to 0 \quad \text{as} \quad r \to \infty. \tag{4}$$

B. Scattering problem

The scattering problem is formulated by referring to acoustic sources that create an incident field p_i in a *free* space. The total acoustic pressure field can be presented as the sum of this incident field p_i and a scattered field p_s

$$p = p_i + p_s. \tag{5}$$

Since p_i is assumed to satisfy the Helmholtz equation in a *free* space, the scattered component p_s is also a solution of the following Helmholtz equation:

$$\Delta p_s + k^2 p_s = 0 \ \text{in} \ \Omega, \tag{6}$$

with boundary conditions resulting from the substitution of Eq. (5) into Eqs. (2) and (3) (where α is assumed to be zero without any loss of generality)

$$\partial p_s/\partial n = -ik\beta p_s + \gamma \ \text{ along } \ \Gamma_H, \tag{7}$$

$$\partial p_s/\partial n = \eta \ \text{ along } \ \Gamma_F, \tag{8}$$

where

$$\gamma \equiv -ik\beta p_i - \partial p_i/\partial n, \tag{9}$$

$$\eta \equiv -\partial p_i/\partial n. \tag{10}$$

The Sommerfeld radiation condition also applies to the scattering problem

$$r(\partial p_s/\partial r + ikp_s) \to 0 \quad \text{as} \quad r \to \infty. \tag{11}$$

III. VARIATIONAL STATEMENT

Variational formulations of exterior radiation and scattering problems can be obtained following a formal procedure given by Gerdes[13,14] for both conjugated and unconjugated methods. Basically, the procedure refers initially to a truncated exterior domain Ω_γ whose ''radial'' extension can be controlled. In the present conjugated infinite element context, the Helmholtz equation is multiplied by the conjugate of a test function q and integrated over the truncated domain. After integration by parts, this results in a sesquilinear form. Introduction of the Sommerfeld radiation condition along the outer boundary of the truncated domain and investigation of the limit case when $\Omega_\gamma \to \Omega$ shows that L^2 integrability requirements for p and ∇p needs some caution.[13] This aspect is usually examined through a suitable partition of the acoustic domain Ω into an inner region Ω_i and an outer region Ω_o (Fig. 1)

$$\Omega = \Omega_i \cup \Omega_o. \tag{12}$$

In the present case, test functions q of order $O(r^{-3})$ are selected for the outer region Ω_o. This particular choice doesn't allow the explicit retention of the Sommerfeld radiation condition in the weak formulation. The condition is therefore directly incorporated in the definition of the following weighted Sobolev space $H^1_w(\Omega) = \{p : \|p\|^1_w < \infty\}$ with the norm $\|p\|^1_w$ corresponding to the inner product

$$(p,q)^1_w = \int_\Omega (wp\overline{q} + w\nabla p \cdot \nabla \overline{q}) d\Omega + \int_\Omega \left(\frac{\partial p}{\partial r} + ikp\right) \times \left(\overline{\frac{\partial q}{\partial r} + ikq}\right) d\Omega, \tag{13}$$

where the weight $w(x)$ is defined as $1/r^2$ in the outer domain and 1 in the inner domain. A dual weight $w^*(x)$ (equal to r^2

in the outer domain and 1 in the inner domain) is also defined. With these functional settings, the weak form of the exterior problem reads as

Find $p \in H_w^1(\Omega)$ such that

$$\int_\Omega \nabla p \cdot \nabla \overline{q}\, d\Omega - k^2 \int_\Omega p \overline{q}\, d\Omega = \int_\Gamma \frac{\partial p}{\partial n} \overline{q} d\Gamma \quad \forall \overline{q} \in H_{w*}^1(\Omega). \tag{14}$$

The variational form is now elaborated for the half-space radiation and scattering problems.

A. Variational form of the radiation problem

The weak variational form of Eq. (1) subjected to Eqs. (2) and (3) reads as

$$\int_\Omega \nabla p \cdot \nabla \overline{q}\, d\Omega - k^2 \int_\Omega p \overline{q}\, d\Omega + ik \int_{\Gamma_H} \beta p \overline{q}\, d\Gamma = \int_{\Gamma_F} \alpha \overline{q}\, d\Gamma \quad \forall \overline{q} \in H_{w*}^1(\Omega). \tag{15}$$

The last integral of the left-hand side refers to the boundary (half-) plane with the prescribed normal admittance boundary condition, while the right-hand side integral is related to the Neumann condition along the finite boundary Γ_F. The previous functional space settings ensures the integrability of $p\overline{q}$ along Γ_H if β has a finite value.

B. Variational form of the scattering problem

The weak variational form of Eq. (6) subjected to Eqs. (7) and (8) reads as

$$\int_\Omega \nabla p_s \cdot \nabla \overline{q}\, d\Omega - k^2 \int_\Omega p_s \overline{q}\, d\Omega + ik \int_{\Gamma_H} \beta p_s \overline{q}\, d\Gamma = \int_{\Gamma_F} \eta \overline{q}\, d\Gamma + \int_{\Gamma_H} \gamma \overline{q}\, d\Gamma \quad \forall \overline{q} \in H_{w*}^1(\Omega). \tag{16}$$

The same conclusion hold for this form: all boundary integrals are well posed if one refers to the related weighted Sobolev spaces.

IV. FINITE/INFINITE ELEMENT MODEL

A. Selection of trial functions

The discrete model is based on a finite/infinite element scheme. Finite elements are selected for the inner domain Ω_i while infinite elements are used for the outer domain Ω_o. Conventional polynomial trial functions support the derivation of finite elements. Serendipity elements have been used in the present study. The selection of trial functions for infinite elements requires some caution since these functions have to fulfill the above integrability requirements along the unbounded exterior domain. The selection of a suitable interpolation scheme for infinite elements results from the examination of the exact solution of the Helmholtz problem outside a regular (spherical, spheroidal, or ellipsoidal) surface enclosing the active ''sources.'' Such a solution can be expressed as an infinite sum in any suitable coordinate system (spherical, spheroidal, or ellipsoidal coordinates can conveniently be used)

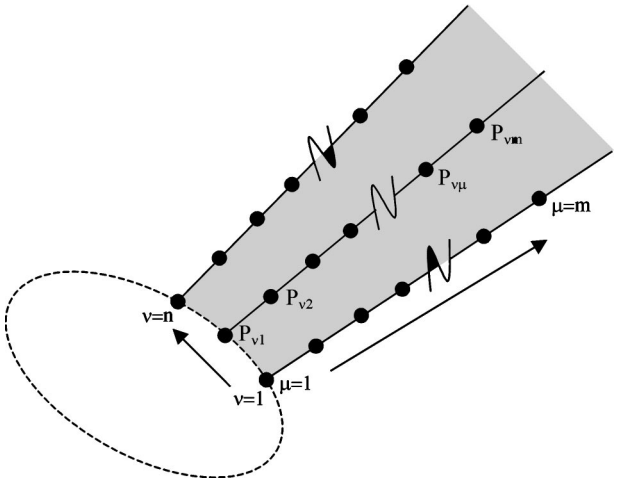

FIG. 2. Numbering of pressure DOFS within an infinite element.

$$p(r,\theta,\phi) = e^{-ikr} \sum_{n=1}^{\infty} \frac{F_n(\theta,\phi)}{r^n}, \tag{17}$$

where r is a radial coordinate and (θ,ϕ) are angular coordinates.

It is clear that such an expansion satisfies *a priori* the Sommerfeld radiation condition. Moreover, this series converges absolutely and uniformly outside the canonical surface.[16] The infinite interpolation scheme can rely on a truncated version of Eq. (17) (including all terms up to order m)

$$p(r,\xi,\eta) \approx e^{-ikr} \sum_{n=1}^{m} \frac{\tilde{F}_n(\xi,\eta)}{r^n}. \tag{18}$$

The above relation supports a particular interpolation scheme where angular variations are described by a set of conventional (''finite'') polynomial functions N_ν^a (expressed in terms of two local coordinates ξ and η) while radial variations (supported by functions N_μ^r) require an expansion in terms of $(1/r)$ weighted by the complex exponential (e^{-ikr}) which acts as a phase factor.

In a concise form, trial infinite functions can be expressed as

$$p(r,\xi,\eta) = \sum_{j=1}^{N} N_j(r,\xi,\eta;k) P_j, \tag{19}$$

where P_j are the nodal parameters (which reduce to the nodal pressures along the interface with the inner domain only) given by

$$P_j = P_{\mu\nu}, \tag{20}$$

and

$$N_j(r,\xi,\eta;k) = N_\mu^r(r;k) N_\nu^a(\xi,\eta), \tag{21}$$

with $j=(\nu-1)m+\mu$, $\mu=1,2,3\ldots,m$, $\nu=1,2,3\ldots,n$ and $N=n\times m$.

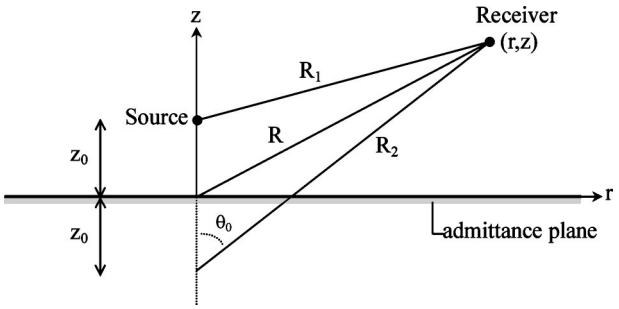

FIG. 3. Spherical source and receiver positions in a half-space bounded by a plane with a specific admittance.

The numbering of pressure degrees of freedom (DOFS) within an infinite element is illustrated in Fig. 2.

Functions $N_\nu^a(\xi,\eta)$ are conventional serendipity interpolation functions along the finite directions, while $N_\mu^r(r;k)$ are radial interpolation functions related to the truncated form of the multipole expansion

$$N_\mu^r(r;k)=e^{-ik(r-r_\mu)}\tilde{N}_\mu^r(r), \tag{22}$$

where $\tilde{N}_\mu^r(r)$ is a polynomial of order m in (1/r) and r_μ is the radial distance at element base (which is introduced in order to preserve continuity with adjacent finite elements).

B. Selection of test functions

Test functions can be presented in a similar way. Within finite elements, test functions are identical to trial functions while they are given by the following relation within infinite elements:

$$Q_j(r,\xi,\eta;k)=Q_\mu^r(r;k)Q_\nu^a(\xi,\eta), \tag{23}$$

where

$$Q_\nu^a(\xi,\eta)=N_\nu^a(\xi,\eta), \tag{24}$$

and

$$Q_\mu^r(r;k)=(1/r^2)N_\mu^r(r;k). \tag{25}$$

C. Discrete system

The discrete system of equations then appears in the form

$$\mathbf{A}(k)\mathbf{P}=\mathbf{b}, \tag{26}$$

where coefficient $A_{st}(k)$ of the matrix $\mathbf{A}$(k) is given by

$$A_{st}(k)=\int_\Omega \nabla\overline{Q}_s\cdot\nabla N_t\,d\Omega-k^2\int_\Omega \overline{Q}_s N_t\,d\Omega + ik\int_{\Gamma_H}\beta\overline{Q}_s N_t\,d\Gamma, \tag{27}$$

and b_s has the following form for radiation and scattering problems:

$$\text{Radiation problem:}\quad b_s=\int_{\Gamma_F}\overline{Q}_s\alpha d\Gamma, \tag{28}$$

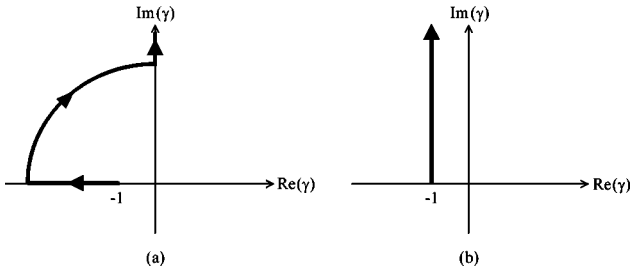

FIG. 4. Integration paths in the γ plane: (a) L contour; (b) steepest descent contour.

$$\text{Scattering problem:}\quad b_s=\int_{\Gamma_F}\overline{Q}_s\eta\,d\Gamma+\int_{\Gamma_H}\overline{Q}_s\gamma\,d\Gamma. \tag{29}$$

It can easily be shown by substitution of the above expressions of test and trial functions within Eq. (27) that matrix $\mathbf{A}$ can be split into the following form:

$$\mathbf{A}(k)=\mathbf{A_0}+ik\mathbf{A_1}(k)-k^2\mathbf{A_2}, \tag{30}$$

where matrices $\mathbf{A_0}$ and $\mathbf{A_2}$ are frequency independent while $\mathbf{A_1}$ is frequency dependent if the boundary admittance β varies with k. This particular feature of the selected conjugated infinite element formulation offers several advantages (see Refs. 18 and 19 for more details). It leads to a straightforward extension to time-domain analysis[19] through the formal application of an inverse Fourier transform to Eq. (26), at least if matrix $\mathbf{A_1}$ is not frequency dependent.

D. Evaluation of boundary integrals

As can be seen from inspection of Eqs. (27) and (29), normal admittance boundary conditions along the half-plane Γ_H influence both the matrix operator (for radiation and scattering problems) and the right-hand-side vector (at least for scattering problems). The evaluation of related boundary integrals could proceed as follows. First, the contribution to matrix $\mathbf{A}$ can be rewritten as

$$ik\int_{\Gamma_H}\beta\overline{Q}_s N_t\,d\Gamma=ik\int_{\Gamma_H}\beta Q_\nu^a(\theta,\phi)\overline{Q}_\mu^r(r;k)\times N_{\nu'}^a(\theta,\phi)N_{\mu'}^r(r;k)d\Gamma, \tag{31}$$

where $s=(\nu-1)m+\mu$ and $t=(\nu'-1)m+\mu'$.

Using Eqs. (22) and (25), one can easily rewrite $N_\mu^r(r;k)$ and $\overline{Q}_\mu^r(r;k)$ as

$$N_\mu^r(r;k)=(1/r^\mu)e^{-ikr}e^{+ikr_\mu}, \tag{32}$$

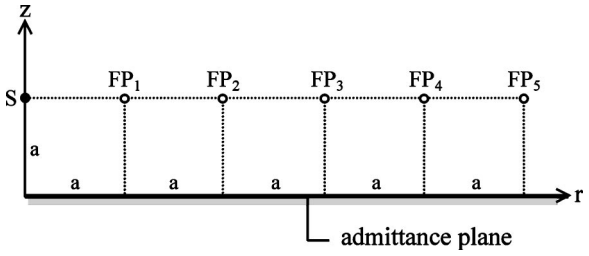

FIG. 5. Spherical source S above a half-plane with a specific admittance.

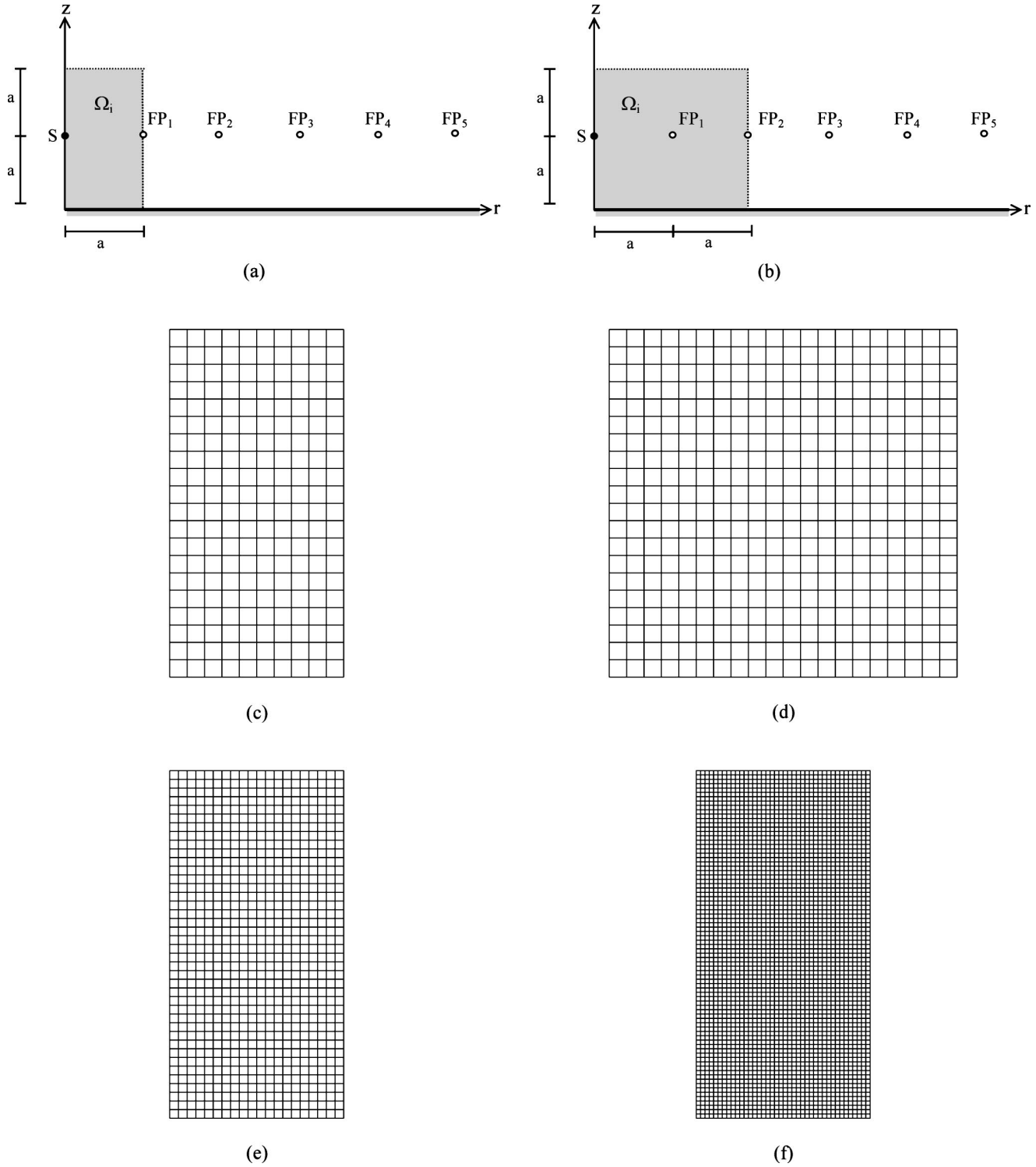

FIG. 6. Finite element meshes: (a) Inner domain Ω_i for meshes M_1, M_3, and M_4; (b) inner domain Ω_i for mesh M_2; (c) mesh M_1; (d) mesh M_2; (e) mesh M_3; (f) mesh M_4.

$$\overline{Q}^r_\mu(r;k) = (1/r^{\mu+2}) e^{+ikr} e^{-ikr_\mu}, \tag{33}$$

so that Eq. (31) can be expressed in the following form:

$$ik \int_{\Gamma_H} \beta \overline{Q}_s N_t d\Gamma = ik \int_{\Gamma_H} \beta Q^a_\nu(\theta,\phi) N^a_{\nu'}(\theta,\phi)(1/r^{\mu+2}) \times (1/r^{\mu'}) d\Gamma. \tag{34}$$

This integral does not contain oscillating terms and can be integrated readily using a Gauss–Legendre quadrature since the $(1/r)$ variable (where $r_\mu \leqslant r \leqslant \infty$) involved in Eq. (34) can easily be converted to a normalized coordinate ζ $(-1 \leqslant \zeta \leqslant +1)$ using

$$r = \frac{2r_\mu}{1-\zeta}. \tag{35}$$

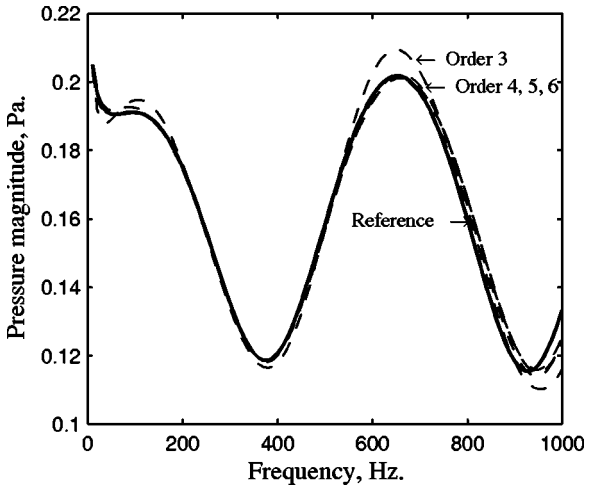

FIG. 7. Frequency response of the acoustic pressure magnitude at field point FP_1: comparison of exact solution and numerical solutions using mesh M_1 and infinite elements of radial order 3, 4, 5, and 6.

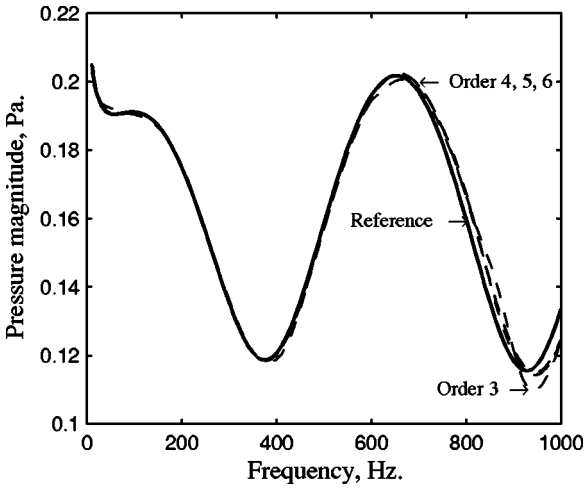

FIG. 8. Frequency response of the acoustic pressure magnitude at field point FP_1: comparison of exact solution and numerical solutions using mesh M_2 and infinite elements of radial order 3, 4, 5, and 6.

The second part of Eq. (29) requires more caution. It can be rewritten as

$$\int_{\Gamma_H} \overline{Q}_s \gamma \, d\Gamma = \int_{\Gamma_H} Q_\nu^a(\theta,\phi)\overline{Q}_\mu^r(r;k)(-ik\beta p_i(r,\theta,\varphi) - \partial p_i(r,\theta,\varphi)/\partial n) d\Gamma. \tag{36}$$

If one considers a set of monopole (or spherical) sources located in the inner region Ω_i and radiating in a free field, the description of the incident pressure p_i complies with the multipole expansion given by Eq. (17) so that integrability is ensured. It should be highlighted that the current representation excludes incident plane waves since such asymptotic representation of a spherical wave does not comply with the expected far-field behavior and therefore does not ensure the finiteness of Eq. (36).

Except for particular cases, the function to be integrated is no longer polynomial in parent coordinates, though. Since both $\overline{Q}_\mu^r(r;k)$ and $p_i(r,\theta,\varphi)$ are decreasing with the radial distance r, one can observe a fast radial decay and evaluate with good accuracy the boundary integral using higher-order Gauss–Legendre quadratures.

V. REFERENCE SOLUTION FOR HALF-SPACE ACOUSTIC PROBLEMS

In this section, a reference solution is given for the propagation of an acoustic source above an infinite admittance plane. The problem can be stated in the following way (Fig. 3): a point source located at a distance z_0 above an infinite plane of specific admittance β ($\mathrm{Re}(\beta)\geqslant 0$), radiates throughout the half-space $z\geqslant 0$. The medium is characterized by a density ρ and a sound speed c. The axial symmetry of the problem justifies the choice of cylindrical coordinates (r,z). We focus our interest on the pressure field and, more precisely, the pressure $p(r,z)$ at a receiver point. The solution of this problem satisfies the following Helmholtz equation in $z\geqslant 0$:

$$\Delta p + k^2 p = \delta(r)\,\delta(z-z_0). \tag{37}$$

Appropriate boundary conditions have to be added to this equation in order to ensure the uniqueness of the solution

(i) local admittance condition along the whole infinite plane:
$$\partial p/\partial z - ik\beta p = 0 \quad \text{for } z=0^+; \tag{38}$$
(ii) Sommerfeld condition, given by Eq. (4).

This problem has been fully treated by Wenzel[20] and Thomasson,[21,22] assuming another time dependence $[\exp(-i\omega t)]$, but will be briefly explained here for the sake of completeness.

The usual treatment relies on the following generalized problem in $z\geqslant 0$:

$$\Delta p + \kappa_0^2 p = \delta(r)\,\delta(z-z_0), \tag{39}$$

where $\kappa_0 = k - is$ (with $k,s>0$), subjected to $\partial p/\partial z - i\kappa_0\beta p = 0$ for $z=0^+$ and the Sommerfeld condition at an infinite distance. Referring to the source/image configuration of Fig. 3, it can be shown that its solution can be expressed as

$$p(r,z) = p_{\mathrm{So}}(r,z) + p_{\mathrm{Im}}(r,z) + p_{\mathrm{Co}}(r,z) = -\frac{1}{4\pi R_1} e^{-i\kappa_0 R_1} - \frac{1}{4\pi R_2} e^{-i\kappa_0 R_2} + \int_0^{+\infty} A(\lambda) e^{-\sqrt{\lambda^2-\kappa_0^2}\,z} J_0(\lambda r)\, d\lambda. \tag{40}$$

The solution appears as the superposition of a direct field p_{So} radiated by the source, a contribution p_{Im} due to the image source, and a correction term p_{Co} taking into account the absorption characteristics of the boundary.

The correction term p_{Co} has to be rewritten properly for practical implementation. First, considering the fact that the solution p satisfies Eq. (39), p_{Co} can be rewritten as

$$p_{\mathrm{Co}} = \frac{i\kappa_0\beta}{2\pi} \int_0^{+\infty} \frac{\lambda}{m(m+i\kappa_0\beta)} e^{-mh} J_0(\lambda r)\, d\lambda, \tag{41}$$

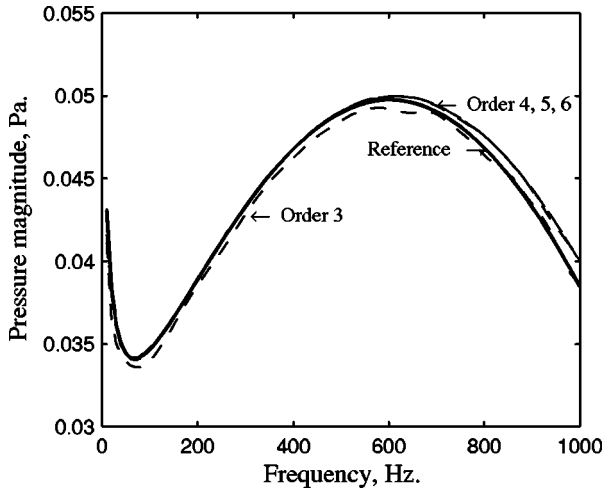

FIG. 9. Frequency response of the acoustic pressure magnitude at field point FP_5: comparison of exact solution and numerical solutions using mesh M_2 and infinite elements of radial order 3, 4, 5, and 6.

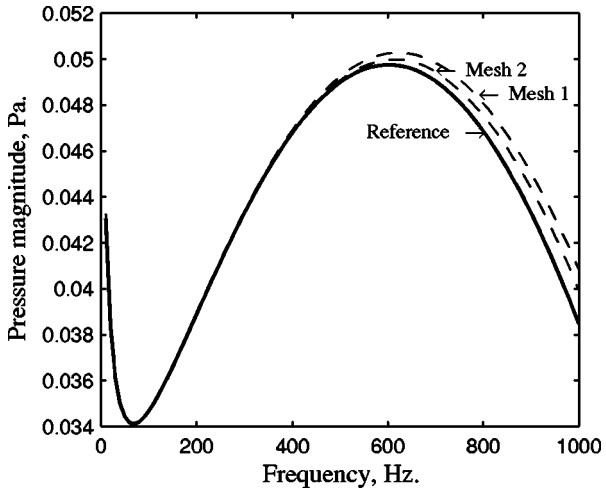

FIG. 10. Frequency response of the acoustic pressure magnitude at field point FP_5: comparison of exact solution and numerical solutions using meshes M_1 and M_2 and infinite elements of radial order 7.

where $h=z+z_0$ and $m=(\lambda^2-\kappa_0^2)^{1/2}$. Substituting the new variable $\gamma=im/\kappa_0$ and letting s in κ_0 tend to 0^+, p_{Co} can be expressed in the following integral form:

$$p_{\mathrm{Co}}=\frac{ik\beta}{2\pi}\int_L \frac{\exp(ikR_2\gamma)}{\sqrt{(\gamma\cos(\theta_0)-\beta)^2+(\sqrt{1-\gamma^2}\sin(\theta_0))^2}}d\gamma, \tag{42}$$

where L is the path shown in Fig. 4(a). One should note that the square root with a negative real part should be selected in the evaluation of Eq. (42). The radius of the circular part of the path L should be large enough so that the path includes all the poles of the integrand. Transforming the path L into the steepest-descent path SD shown in Fig. 4(b), and taking care of the singularities of the inverse of the square root, it can finally be shown that

$$p_{\mathrm{Co}}=\begin{cases} p_{\mathrm{SD}}+p_B & \text{if } \mathrm{Re}(\gamma_1)<-1 \quad \text{and } \mathrm{Im}(\beta)>0 \\ p_{\mathrm{SD}} & \text{for other cases} \end{cases}, \tag{43}$$

with

$$p_{\mathrm{SD}}=\frac{-k\beta}{2\pi}\exp(-ikR_2) \times\int_{t=0}^{+\infty}\frac{\exp(-kR_2t)}{\sqrt{(-1+it-\gamma_0)(-1+it-\gamma_1)}}dt, \tag{44}$$

$$p_B=\frac{k\beta}{2}H_0^{(2)}(kr\sqrt{1-\beta^2})\exp(ikh\beta), \tag{45}$$

and

$$\gamma_0=\beta\cos(\theta_0)+\sqrt{1-\beta^2}\sin(\theta_0), \tag{46}$$

$$\gamma_1=\beta\cos(\theta_0)-\sqrt{1-\beta^2}\sin(\theta_0), \tag{47}$$

$$t_1=\frac{\mathrm{Im}((\gamma_0+1)(\gamma_1+1))}{\mathrm{Re}((\gamma_0+1)+(\gamma_1+1))}. \tag{48}$$

The square root in the expression of p_{SD} should be taken with a positive real part when the following three conditions are fulfilled: (1) $\mathrm{Re}(\gamma_1)<-1$, (2) $\mathrm{Im}(\nu)>0$, and (3) $t>t_1$, and with a negative real part in all other cases.

As can be seen from the relations presented in this section, the total pressure field radiated by the source point is the sum of a direct field (p_{So}) and a reflected field ($p_{\mathrm{Im}}+p_{\mathrm{Co}}$). In some specific cases, a so-called ''surface wave'' contribution p_B has to be included in the reflected field.

Chien *et al.*,[23] Thomasson,[21,22,24] and Kawai *et al.*[25] have proposed some asymptotic relations that enable a faster evaluation of the pressure field. However, the computational efficiency of up-to-date computers no longer requires such approximations, and we have used the previous relations to compute the exact pressure field directly.

TABLE I. Global convergence of the numerical solution at frequency $f=100$ Hz ($ka=0.924$), taking into account different mesh resolutions and radial interpolation orders in infinite elements.

Radial order (IE)	Mesh M_1 10×20		Mesh M_3 20×40		Mesh M_4 40×80	
	e_Γ	Problem size	e_Γ	Problem size	e_Γ	Problem size
1	3.07E-2	231	3.07E-2	861	3.07E-2	3321
2	1.85E-2	262	1.86E-2	922	1.86E-2	3442
3	7.86E-3	293	7.96E-3	983	7.98E-3	3563
4	3.07E-3	324	3.10E-3	1044	3.11E-3	3684
5	1.45E-3	355	1.36E-3	1105	1.33E-3	3805
6	8.13E-4	386	6.93E-4	1166	6.66E-4	3926
7	4.29E-4	417	3.62E-4	1227	3.55E-4	4047

TABLE II. Global convergence of the numerical solution at frequency $f=500$ Hz ($ka=4.620$), taking into account different mesh resolutions and radial interpolation orders in infinite elements.

Radial order (IE)	Mesh M_1 10×20		Mesh M_3 20×40		Mesh M_4 40×80	
	e_Γ	Problem size	e_Γ	Problem size	e_Γ	Problem size
1	4.83E-2	231	4.65E-2	861	4.61E-2	3321
2	2.59E-2	262	2.52E-2	922	2.50E-2	3442
3	9.73E-3	293	1.04E-2	983	1.07E-2	3563
4	4.25E-3	324	3.69E-3	1044	3.89E-3	3684
5	4.35E-3	355	1.83E-3	1105	1.41E-3	3805
6	4.09E-3	386	1.24E-3	1166	5.92E-4	3926
7	3.88E-3	417	9.94E-4	1227	2.95E-4	4047

VI. NUMERICAL EXAMPLE

The simple scattering problem addressed in this section involves a spherical source of constant amplitude located at a distance a from a half-plane with a specific admittance β. The objective is to evaluate the acoustic pressure at different locations FP_i $(i=1,\ldots,5)$ as shown in Fig. 5. For the calculation, the following numerical values have been selected: specific admittance $\beta=0.2691-0.5625i$ (–) and distance $a=0.5$ (m). Four different meshes M_1 to M_4 have been considered. Finite element meshes M_1, M_3, and M_4 are referring to the inner domain Ω_i shown in Fig. 6(a), while finite element mesh M_2 is related to the inner domain Ω_i shown in Fig. 6(b). Meshes M_1, M_2, M_3, and M_4 are shown in Figs. 6(c)–(f). All meshes are uniform, involving square QUA04 elements (element size $= a/10$ for meshes M_1 and M_2, $a/20$ for mesh M_3, and $a/40$ for mesh M_4). The magnitude of the pressure field at locations FP_i has been calculated in the frequency range 10–1000 Hz ($ka=0.924-9.24$) using the foregoing exact solution and the numerical model, and are presented in Figs. 7 to 10. It should be emphasized that field pressure is produced by direct interpolation within related infinite elements. Numerical calculations have been performed using the axisymmetry capabilities of ACTRAN software.[26]

The convergence of the numerical solution at field point FP_1 is illustrated in Figs. 7 (mesh M_1) and 8 (mesh M_2) as the radial order along infinite elements is increased from 3 to 7. FP_1 is located at a nodal point in both finite element meshes. A good agreement between exact and numerical solutions is already obtained at a radial interpolation order = 4. The slight difference between exact and numerical solutions in the upper frequency range is due to the low resolution of both meshes. Comparing Figs. 7 and 8, it can be seen that an increased geometrical extension of the finite element mesh gives a better accuracy when the radial interpolation order of the infinite elements is 3, but this higher accuracy can also be reached by selecting a radial interpolation order greater than 3 along infinite elements.

If one selects a point located in the outer domain (like FP_5), an accurate evaluation of the acoustic pressure is obtained, especially in the low-frequency range (10–500 Hz), for infinite elements of radial order higher than 3, as shown in Fig. 9. Figure 10 shows, however, that an increased accuracy can be obtained when the inner domain is extended (i.e., using mesh M_2 rather than mesh M_1).

To get a better understanding of the global convergence of the numerical solution when the radial interpolation order along infinite elements is increased and the finite element (FE) mesh is refined, a global error norm is evaluated along the interface Γ_{FI} between finite and infinite domains (i.e., defined by the cylinder $r=a$ and the plane $z=2a$, for meshes M_1, M_3, and M_4)

$$e^2_{\Gamma_{FI}}=\int_{\Gamma_{FI}}|p_{\text{exact}}-p_{\text{num}}|^2 d\Gamma. \tag{49}$$

Tables I, II, and III show the values of this error norm for three characteristic frequencies: 100 Hz ($ka=0.924$), 500 Hz ($ka=4.620$), and 1000 Hz ($ka=9.240$). Inspection of these tables shows the convergence of the numerical solution when the radial interpolation order is increased along infinite elements and/or the FE mesh is refined. However, and this is especially apparent at higher frequencies, the error norm quickly converges to a nonzero value and the only way to further refine the solution accuracy is to increase the transversal mesh resolution. Tables I, II, and III also contain the

TABLE III. Global convergence of the numerical solution at frequency $f=1000$ Hz ($ka=9.240$), taking into account different mesh resolutions and radial interpolation orders in infinite elements.

Radial order (IE)	Mesh M_1 10×20		Mesh M_3 20×40		Mesh M_4 40×80	
	e_Γ	Problem size	e_Γ	Problem size	e_Γ	Problem size
1	7.39E-2	231	5.85E-2	861	5.61E-2	3321
2	5.49E-2	262	4.44E-2	922	4.27E-2	3442
3	3.40E-2	293	2.39E-2	983	2.42E-2	3563
4	2.52E-2	324	1.06E-2	1044	1.05E-2	3684
5	2.82E-2	355	9.22E-3	1105	5.12E-3	3805
6	2.84E-2	386	8.36E-3	1166	3.03E-3	3926
7	2.79E-2	417	7.57E-3	1227	2.03E-3	4047

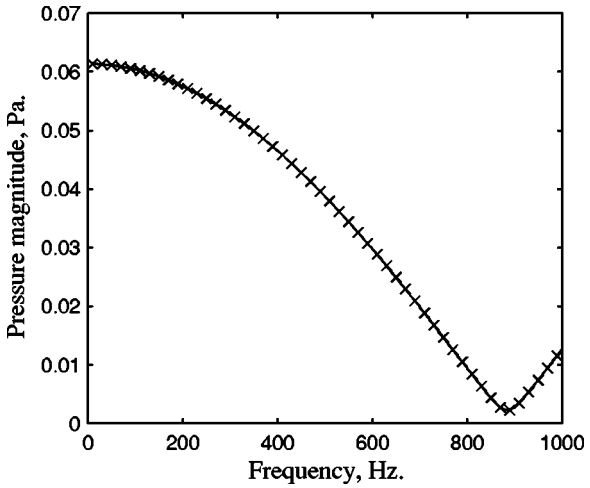

FIG. 11. Frequency response of the acoustic pressure magnitude at field point FP_5 in the case of a rigid half-plane (mesh M_4, radial order 7).

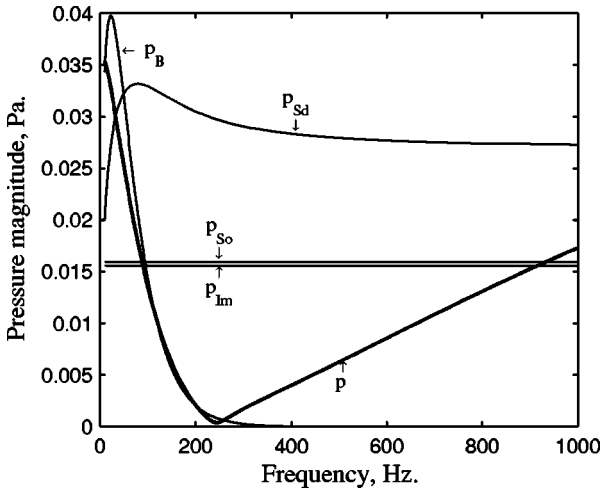

FIG. 13. Magnitudes of the different contributions to the total acoustic pressure at field point FP_{10}.

size of the discrete problem (number of degrees of freedom of the linear system to be solved).

Figure 11 presents the comparison between the exact solution and the numerical solution at FP_5 in the case of a rigid half-plane (zero valued admittance). The numerical solution, obtained with mesh M_4 and a radial interpolation order of 7 along infinite elements, shows an excellent agreement with the exact solution, in the whole frequency range. Clearly, the reference solution in this case can be easily obtained by the technique of image sources. One should, however, note that the numerical solution does not rely on such considerations but rather on the direct handling of nonhomogeneous boundary conditions [Eq. (7)] along Γ_H (with $\beta \equiv 0$ in this case).

Figures 12(a) and (b) compare field pressures at points FP_1 and FP_5, respectively, for the following three cases: rigid case ($\beta=0$), absorbing case ($\beta=0.2691-0.5625i$), and mixed case, where the specific admittance is constrained along the finite boundary and is kept to zero along the infinite boundary. These figures clearly demonstrate the need to take into account the nonzero value of the specific admittance on the whole half-plane, even if the observation point is close to the source and within the finite element domain.

Finally, the capability to handle the so-called ''surface wave'' component p_B [Eq. (43)] is illustrated by running the same problem with a modified specific admittance $\beta = 0.2691 + 0.5625i$ along the boundary plane. In such circumstances, it can be shown that the condition $\mathrm{Re}(\gamma_1) < -1$ leading to the activation of p_B component is fulfilled for a field point (denoted FP_{10}) located in ($r = 5.0$ m, $z = 0.5$ m).

Figure 13 shows the magnitudes of the complex contributions [Eqs. (40) and (43)] to the total acoustic pressure at point FP_{10}. The surface wave contribution p_B is shown to contribute significantly to the total response. The ability of the numerical model to capture this particular contribution for field point FP_{10} is shown in Fig. 14, where mesh M_3 has been selected with infinite elements of radial interpolation orders 5, 10, and 15.

VII. CONCLUSIONS

A conjugated infinite element method has been successfully extended and applied to the solution of acoustic prob-

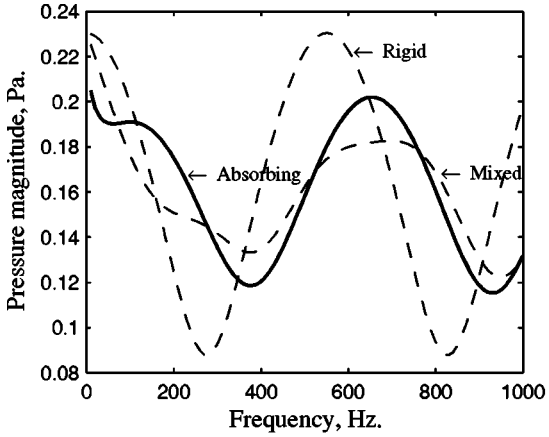

(a)

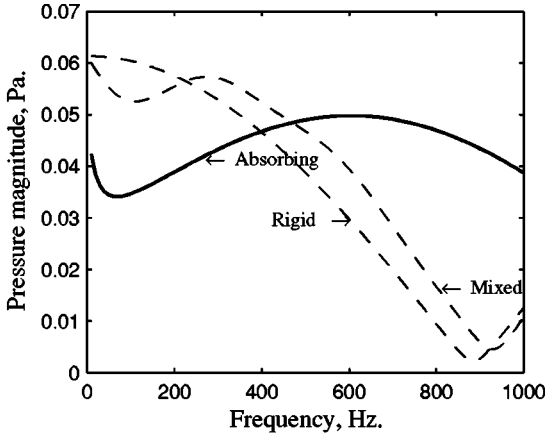

(b)

FIG. 12. Comparison of the frequency responses of the acoustic pressure magnitude at field points FP_1 (a) and FP_5 (b) in the case of rigid, mixed rigid/absorbing and absorbing boundaries (mesh M_4, radial order 7).

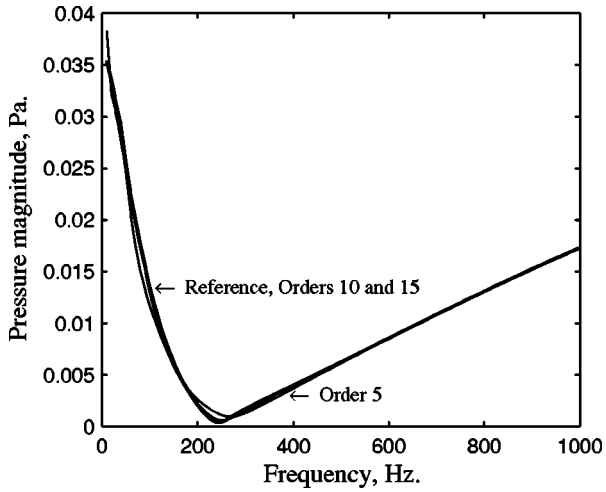

FIG. 14. Frequency response of the acoustic pressure magnitude at field point FP_{10}: comparison of exact solution and numerical solutions using mesh M_3 and infinite elements of radial interpolation orders 5, 10, and 15.

lems in a half-space with normal admittance conditions along the boundary plane. The procedure implicitly assumes the validity of the multipole expansion [Eq. (17)] for the half-space problem. Functional settings related to the full-space problem are kept for the half-space problem and ensure the integrability of boundary contributions along the half-plane Γ_H for both radiation and scattering problems. It has been shown that the contribution of the admittance condition to the matrix operator basically involves the integration of polynomial integrands (and is therefore trivial) while the right-hand-side contribution requires the handling of an oscillating function.

The procedure has been validated by using the reference solution for the problem of a single source above a plane with a specific admittance. Comparisons of numerical results with available reference results allow us to show the performances of the proposed model. Convergence is shown to rely basically on radial interpolation order up to a threshold value. Further convergence requires, as expected, finite element mesh refinement along the ''transverse'' (i.e., not radial) direction. The handling of admittance boundary condition along infinite edges (or faces) is also shown to have a strong influence on field results. It is expected that the present finite/infinite element method will constitute a basis for further extensions (handling of convective flow effects, transient acoustics) that are usually accounted for more easily in a domain-based context.

ACKNOWLEDGMENTS

The support of this work by the Belgian National Fund for Scientific Research (F.N.R.S.) is gratefully acknowledged.

[1] A. F. Seybert and T. W. Wu, ''Modified Helmholtz integral equation for bodies sitting on an infinite plane,'' J. Acoust. Soc. Am. **85**, 19–23 (1989).
[2] A. T. Peplow and S. N. Chandler-Wilde, ''Three-dimensional numerical modeling of sound propagation over noise barriers of arbitrary uniform cross section,'' Proc. IOA **14**, 667–672 (1992).
[3] W. L. Li, T. W. Wu, and A. F. Seybert, ''A half-space boundary element method for acoustic problems with a reflecting plane of arbitrary impedance,'' J. Sound Vib. **171**, 173–184 (1994).
[4] J. M. Park and W. Eversman, ''A boundary element method for propagation over absorbing boundaries,'' J. Sound Vib. **175**, 197–218 (1994).
[5] L. A. de Lacerda, L. C. Wrobel, and W. J. Mansur, ''A dual boundary element formulation for sound propagation around barriers over an impedance plane,'' J. Sound Vib. **202**, 235–247 (1997).
[6] D. Duhamel and P. Sergent, ''Sound propagation over noise barriers with absorbing ground,'' J. Sound Vib. **218**, 799–823 (1998).
[7] L. A. de Lacerda, L. C. Wrobel, H. Power, and W. J. Mansur, ''A novel boundary integral formulation for three-dimensional analysis of thin acoustic barriers over an impedance plane,'' J. Acoust. Soc. Am. **104**, 671–678 (1998).
[8] Y. L. Li, M. J. White, and M. H. Hwang, ''Green's functions for wave propagation above an impedance ground,'' J. Acoust. Soc. Am. **96**, 2485–2490 (1994).
[9] S. N. Chandler-Wilde and D. C. Hothersall, ''Efficient calculation of the Green function for acoustic propagation above a homogeneous impedance plane,'' J. Sound Vib. **180**, 705–724 (1995).
[10] I. Harari and T. J. R. Hughes, ''A cost comparison of boundary element and finite element methods for problems of time-harmonic acoustics,'' Comput. Methods Appl. Mech. Eng. **97**, 77–102 (1992).
[11] D. Givoli, *Numerical Methods for Problems in Infinite Domains* (Elsevier, New York, 1992).
[12] R. J. Astley, J. P. Coyette, and G. J. Macaulay, ''Mapped wave envelope elements for acoustical radiation and scattering,'' J. Sound Vib. **170**, 97–118 (1994).
[13] K. Gerdes, ''A summary of infinite element formulations for exterior Helmholtz problems,'' Comput. Methods. Appl. Mech. Eng. **164**, 95–105 (1998).
[14] K. Gerdes, ''The conjugated vs the unconjugated infinite element method for the Helmholtz equation in exterior domain,'' Comput. Methods Appl. Mech. Eng. **152**, 125–145 (1998).
[15] J. J. Shiron and I. Babuska, ''A comparison of approximate boundary conditions and infinite element methods for exterior Helmholtz problems,'' Comput. Methods Appl. Mech. Eng. **164**, 121–139 (1998).
[16] D. S. Burnett, ''A three-dimensional acoustic infinite element based on a prolate spheroidal multipole expansion,'' J. Acoust. Soc. Am. **96**, 2798–2816 (1994).
[17] L. Cremers, K. R. Fyfe, and J. P. Coyette, ''A variable order infinite acoustic wave envelope element,'' J. Sound Vib. **171**, 483–508 (1994).
[18] R. J. Astley, J. P. Coyette, and L. Cremers, ''Three-dimensional wave-envelope elements of variable order for acoustic radiation and scattering. I. Formulation in the frequency domain,'' J. Acoust. Soc. Am. **103**, 49–63 (1998).
[19] R. J. Astley, J. P. Coyette, and L. Cremers, ''Three-dimensional wave-envelope elements of variable order for acoustic radiation and scattering. II. Formulation in the time domain,'' J. Acoust. Soc. Am. **103**, 64–72 (1998).
[20] A. R. Wenzel, ''Propagation of waves along an impedance boundary,'' J. Acoust. Soc. Am. **55**, 956–963 (1974).
[21] S. I. Thomasson, ''Reflection of waves from a point source by an impedance boundary,'' J. Acoust. Soc. Am. **59**, 780–785 (1976).
[22] S. I. Thomasson, ''Sound propagation above a layer with a large refraction index,'' J. Acoust. Soc. Am. **61**, 659–674 (1977).
[23] C. F. Chien and W. W. Soroka, ''Sound propagation along an impedance plane,'' J. Sound Vib. **43**, 9–20 (1975).
[24] S. I. Thomasson, ''A powerful asymptotic solution for sound propagation above an impedance boundary,'' Acustica **45**, 122–125 (1980).
[25] T. Kawai, T. Hidaka, and T. Nakajima, ''Sound propagation above an impedance plane,'' J. Sound Vib. **83**, 125–138 (1982).
[26] J. P Coyette, J. L. Migeot, G. Lielens, and T. Leclercq, *ACTRAN User's Manual* (Free Field Technologies S.A., Louvain-la-Neuve, 2000).

Backscattering cross section of a rigid biconic reflector

Thomas J. Eisler[a)]
Coast Survey Development Laboratory, NOAA N/CS11, 1315 East–West Highway, Silver Spring, Maryland 20910

(Received 9 August 1999; revised 13 July 2000; accepted 18 July 2000)

Plane wave incidence on a rigid biconic target is considered. A biconic reflector consists of two cones truncated by planes perpendicular to their axes and joined at their smaller flat faces. The cone angles are allowed to be variable, provided their sum is equal to 90°. The backscattering cross section is expressed in terms of a surface integral of the geometrical acoustics field, which results from incident singly and doubly reflected rays. A saddle-point calculation gives a first-order high-frequency approximation in which the backscattering cross section is proportional to the incident wave number and a function of the angle of incidence, cone angles, and inner and outer radii of the truncated cones. This expression is algebraically complex but easy to implement numerically. Results are presented that exercise the parameters of the problem. An interesting result of the solution is that for fixed outer radii there is a nonzero optimum inner radius for backscattering strength. For broadside incidence on 45° cones with equal outer radii, this optimum value is approximately equal to 11% of the outer radius. [S0001-4966(00)04910-9]

PACS numbers: 43.20.Fn, 43.30.Gv [DLB]

I. INTRODUCTION

Reference targets are often needed during sonar operations. The present study was motivated by a need of the National Ocean Service to verify system operation when surveying in regions such as the Gulf of Mexico, where bottoms are so smooth and featureless that they may return only a barely detectable signal. The weak signal problem affects both the field hydrographer during data acquisition and processors who must later verify the side-scan sensor data. The presence of a reference target can verify that the system is operating properly. The biconic target has desirable properties for this purpose: strong backscattering strength, due to its corner reflector geometry, and azimuthal symmetry, which allows it to be easily identified and tracked by a vessel underway. The target used in survey operations is not the idealized one presented here but rather a shell filled with foam to provide positive buoyancy and tethered to an anchor to hold it in position approximately 1 m above the bottom. The survey vessel is at a sufficient distance so that the direction of insonification is within the corner reflector geometry of the target.

A biconic reflector consists of two cones truncated by planes perpendicular to their axes and joined at their smaller flat faces. Usually the cones are 45° right circular so that in any axial plane their surfaces are at right angles to form a corner reflector. In our development we will assume the cones to be circular but will allow the cone angles to be general, provided their sum is 90°. We will therefore continue to have a corner reflector with azimuthal symmetry.

a)Electronic mail: thomas.eisler@noaa.gov

II. ANALYSIS

We now consider a plane wave incident on a rigid reflector at an angle θ with its axis. Cylindrical coordinates ρ, z are used to express the equations of the upper and lower cones as follows:

$$\rho = z \tan \alpha_0 + b \quad (z \geqslant 0), \qquad \rho = -z \tan \alpha_1 + b \quad (z \leqslant 0), \tag{1}$$

where b is the smaller (inner) radius of the cones and, with reference to the angle between axis and surface, α_0 and α_1 are the upper and lower cone angles, respectively, assumed to satisfy

$$\alpha_0 + \alpha_1 = \frac{\pi}{2}. \tag{2}$$

In the Kirchhoff approximation the backscattering cross section, σ_b, is expressed in terms of a surface integral of the geometrical acoustics field over the insonified portion of the surface[1]

$$\sigma_b = 4\pi |f|^2, \tag{3}$$

where

$$f = -\frac{ik}{2\pi} \int dS_0 \, \hat{\mathbf{n}}_0 \cdot \hat{\mathbf{r}} p_{\mathrm{GA}} e^{-ik\hat{\mathbf{r}} \cdot \mathbf{r}_0}, \tag{4}$$

k is the wave number, p_{GA} the (dimensionless) surface geometrical acoustics pressure of the unit amplitude incident wave, $\hat{\mathbf{n}}_0$ the outward normal at the point $\mathbf{r}_0$ on the surface, and $\hat{\mathbf{r}}$ the backscattering direction (the negative of the direction of incidence). Carets are used to indicate unit vectors.

On a given cone the geometrical acoustics field consists of the incident plane wave plus the reflected wave from the other cone. However, only the latter contributes significantly to backscattering. Primakoff and Keller[2] give a general expression for the field along a reflected ray from a penetrable

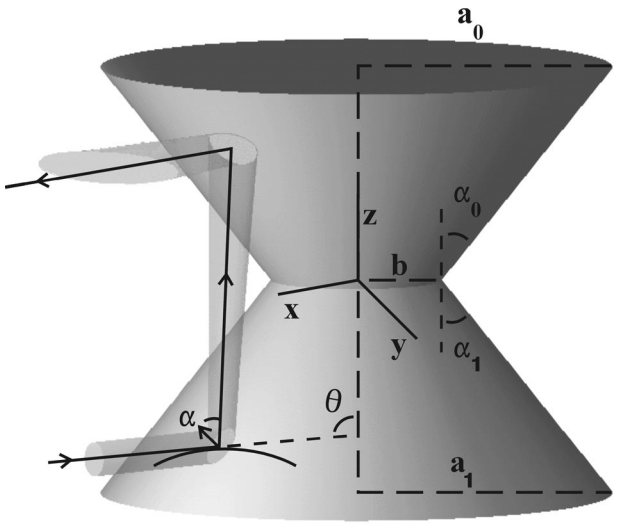

FIG. 1. Reflection and spreading of an incident ray bundle showing parameters used in the paper. Also shown is the surface curve in the normal plane perpendicular to a generator of the lower cone, which defines the curvature G_1.

surface in terms of local surface geometry at the point of reflection. This result can be specialized to the case of a rigid surface and expressed as follows:

$$p_{\mathrm{GA}}=p_{\mathrm{inc}}(0)\sqrt{\frac{d\sigma(0)}{d\sigma(l)}}e^{ikl}, \tag{5}$$

where $p_{\mathrm{inc}}(0)$ is the incident field at the point of reflection, l is the distance from that point along the reflected ray, and $d\sigma(l)$ is the cross-sectional area of an infinitesimal ray bundle about the ray. This area gives the effect of ray spreading, as shown in Fig. 1, and is expressible in terms of surface curvature. The latter is defined in terms of the curvature at a given point of curves formed by the intersection of the surface with various planes normal to it. The expression below follows from a further result of Primakoff and Keller[2]

$$\frac{d\sigma(0)}{d\sigma(l)}=[1-2l(G_1\cos\alpha+G_i\sin\alpha\tan\alpha)]^{-1}, \tag{6}$$

where α is the angle of reflection, G_1 is the surface curvature in the plane perpendicular to the generator of the cone through the point of reflection, which gives the maximum curvature at that point (see Fig. 1), and G_i is the surface curvature in the plane of incidence.

Without loss of generality we can assume that the incident rays are parallel to the $y=0$ plane. Therefore, let

$$\hat{\mathbf{r}}=(\sin\theta,0,\cos\theta), \tag{7}$$

where θ is the angle the incident direction makes with the z axis.

We consider rays incident on the lower cone and reflected to the upper cone. The unit amplitude pressure of the incident wave at the point of reflection, $\mathbf{r}_1$ say, on the lower cone is then given by

$$p_{\mathrm{inc}}(0)=e^{-ik\hat{\mathbf{r}}\cdot\mathbf{r}_1}, \tag{8}$$

and we have

$$f=-\frac{ik}{2\pi}\int dS_0\,\hat{\mathbf{n}}_0\cdot\hat{\mathbf{r}}\sqrt{\frac{d\sigma(0)}{d\sigma(l)}}e^{ik(-\hat{\mathbf{r}}\cdot\mathbf{r}_1+l-\hat{\mathbf{r}}\cdot\mathbf{r}_0)}. \tag{9}$$

We express the integral in terms of z_0 and the azimuthal angle, φ_0,

$$dS_0=\frac{z_0\tan\alpha_0+b}{\cos\alpha_0}dz_0\,d\varphi_0, \tag{10}$$

and perform a saddle-point (stationary phase) approximation of the φ_0 (inner) integral assuming k to be large. Integration is along the real axis with a saddle point at $\varphi_0=0$. It is from this point that the doubly reflected ray is exactly opposite in direction to the incident ray, thus giving the strongest contribution to backscattering. Following the standard stationary phase procedure[3] we set all quantities not in the argument of the exponential equal to their values at the saddle point. Thus,

$$\hat{\mathbf{n}}_0\cdot\hat{\mathbf{r}}=\sin(\theta-\alpha_0), \tag{11}$$

and

$$\frac{d\sigma(0)}{d\sigma(l)}=\left[1+\frac{2z_0\tan\alpha_0}{z_0\tan(\theta-\alpha_0)+b}\right]^{-1}. \tag{12}$$

In obtaining the latter result from Eq. (6), we have made use of the following. Surface curvature G_i in the plane of incidence vanishes at the saddle point because this plane intersects the cone in a straight line. For the curvature G_1 we derive

$$G_1=\frac{-\sin\alpha_0}{z_0\tan(\theta-\alpha_0)+b}, \tag{13}$$

where the minus sign appears in Primakoff and Keller's convention because the normal to the surface and the center of curvature are on opposite sides of the surface. We have also used l_0, the saddle point value of l,

$$l_0=\frac{z_0}{\cos\alpha_0\cos(\theta-\alpha_0)}, \tag{14}$$

and the relation

$$\alpha=\theta-\alpha_0. \tag{15}$$

We have thus arrived at

$$f=-\frac{ik}{2\pi}\sin(\theta-\alpha_0)\int dz_0\,G(z_0)\int d\varphi_0\,e^{ikF(z_0,\varphi_0)}, \tag{16}$$

where

$$G(z_0)=\frac{z_0\tan\alpha_0+b}{\cos\alpha_0}\sqrt{\frac{z_0\tan(\theta-\alpha_0)+b}{z_0(\tan(\theta-\alpha_0)+2\tan\alpha_0)+b}}, \tag{17}$$

and

$$F(z_0,\phi_0)=-\hat{\mathbf{r}}\cdot\mathbf{r}_1+l-\hat{\mathbf{r}}\cdot\mathbf{r}_0. \tag{18}$$

To continue with the saddle-point procedure, we must approximate the function $F(z_0,\phi_0)$ as follows:

$$F(z_0,\phi_0)\approx F(z_0,0)+H(z_0)\varphi_0^2. \tag{19}$$

For a saddle-point evaluation ($\phi_0=0$), incident and reflected rays lie in the $x-z$ plane and

$$z_1=-z_0\tan(\theta-\alpha_0)\tan\alpha_0. \tag{20}$$

From this relation, together with Eq. (1) and Eq. (14), it follows that

$$F(z_0,0)=-2b\sin\theta. \tag{21}$$

Since the z_0 dependence has dropped out, this factor will not enter the expression for the backscattering cross section as given by Eq. (3). Saddle-point estimation of the inner integral gives

$$f=-\frac{ik}{2\pi}\sin(\theta-\alpha_0)\int dz_0\,G(z_0)\sqrt{\frac{\pi}{kH(z_0)}}\,e^{-2ikb\sin\theta}. \tag{22}$$

Our remaining problem is to derive an expression for the function $H(z_0)$. We can write the following equation relating the point $\mathbf{r}_1$ at which a ray is incident on the lower cone to the point $\mathbf{r}_0$ where the reflected ray intersects the upper cone:

$$\mathbf{r}_1=\mathbf{r}_0-(2\hat{\mathbf{n}}_1\hat{\mathbf{n}}_1\cdot\hat{\mathbf{r}}-\hat{\mathbf{r}})l, \tag{23}$$

where $\hat{\mathbf{n}}_1$, the surface normal at $\mathbf{r}_1$, is given by

$$\hat{\mathbf{n}}_1=(\cos\alpha_1\cos\varphi_1,\cos\alpha_1\sin\varphi_1,\sin\alpha_1). \tag{24}$$

For a given value of z_0 the three equations given by Eq. (23) allow us to solve for z_1, φ_1, and l in terms of φ_0. We perturb the equations about $\varphi_0=0$

$$l=l_0+\delta l, \tag{25}$$

$$z_1=z_1^0+\delta z_1. \tag{26}$$

We assume that φ_1 is of order φ_0 and δl, δz_1 of order φ_0^2, to be verified *a posteriori*. Therefore, let

$$\phi_1=\tilde{\varphi}_1\varphi_0+\cdots, \tag{27}$$

$$\delta l=\tilde{\delta}l\,\varphi_0^2+\cdots, \tag{28}$$

$$\delta z_1=\tilde{\delta}z\,\varphi_0^2+\cdots. \tag{29}$$

The algebra is straightforward but tedious. We obtain

$$\tilde{\varphi}_1=\frac{z_0\tan\alpha_0+b}{z_0(\tan(\theta-\alpha_0)+2\tan\alpha_0)+b}, \tag{30}$$

$$\tilde{\delta}z_1=\tilde{\varphi}_1^2 l_0\sin\alpha_0\cos\alpha_0\sin\theta - \tilde{\delta}l(2\cos\alpha_0\cos(\theta-\alpha_0)-\cos\theta), \tag{31}$$

and

$$\tilde{\delta}l=\frac{\sin\alpha_0}{\cos(\theta-\alpha_0)}\left\{\tilde{\varphi}_1^2\left[z_0\left(\frac{\sin\theta}{\cos\alpha_0\cos(\theta-\alpha_0)}+\tan\alpha_0\right)+\frac{1}{2}(z_0\tan\alpha_0+b)\right]-\frac{1}{2}(z_0\tan\alpha_0+b)\right\}. \tag{32}$$

From Eq. (18) we finally obtain

$$H(z_0)=\tilde{\delta}z_1(\sin\theta\tan\alpha_1-\cos\theta)+\tfrac{1}{2}\tilde{\varphi}_1^2(-z_1^0\tan\alpha_1+b)\times\sin\theta+\tfrac{1}{2}(z_0\tan\alpha_0+b)\sin\theta+\tilde{\delta}l. \tag{33}$$

We can now evaluate numerically the integral that appears in Eq. (22). However, we still need to take into account scattering from both cones. To do so we now recognize explicitly the dependence of quantities on the upper cone angle α_0 and angle of incidence θ. Therefore, we now write

$$f(\theta,\alpha_0,z)=\sin(\theta-\alpha_0)\int_0^z dz_0\frac{G(\theta,\alpha_0,z_0)}{\sqrt{H(\theta,\alpha_0,z_0)}}. \tag{34}$$

We can now make use of the solution derived for scattering from the lower to the upper cone also to describe scattering from the upper to the lower cone. We may then express the backscattering cross section as follows:

$$\sigma_b(\theta,\alpha_0)=k\left|f(\theta,\alpha_0,\min\{(a_1-b)\cot(\theta-\alpha_0),(a_0-b)\cot\alpha_0\})+f\left(\pi-\theta,\frac{\pi}{2}-\alpha_0,\min\{(a_0-b_1)\tan(\theta-\alpha_0),(a_1-b)\tan\alpha_0\}\right)\right|^2, \tag{35}$$

where a_0, a_1 are the larger radii of the upper and lower cones, respectively.

III. BROADSIDE INCIDENCE

When we consider the special case of two equal 45° cones with incidence perpendicular to the axis of the target ($a_0=a_1\equiv a$, $\alpha_0=\alpha_1=45°$, $\theta=90°$), the above results undergo considerable simplification. We obtain

$$G(\pi/2,\pi/4,z_0)=\sqrt{2}\,\frac{(z_0+b)^{3/2}}{\sqrt{3z_0+b}}, \tag{36}$$

and

$$H(\pi/2,\pi/4,z_0)=\frac{(z_0+b)(2z_0+b)}{3z_0+b}. \tag{37}$$

From Eq. (3) and Eq. (22) we obtain

$$\sigma_b=4k\left[\int_0^a dz_0\frac{z_0+b}{\sqrt{2z_0+b}}\right]^2, \tag{38}$$

where a factor of 2 has been introduced to account for scattering from both surfaces. Finally, the above integral can be performed to give

$$\sigma_b=\frac{16k}{9}\left[\frac{a+b}{2}\sqrt{2a-b}-b^{3/2}\right]^2. \tag{39}$$

An interesting consequence of the above formula is that for fixed outer radius a slightly larger target scatters less than one of optimum dimensions. The optimum value for the smaller radius (i.e., one that maximizes σ_b) is not zero but approximately 11% of the outer radius. Specifically, its value is

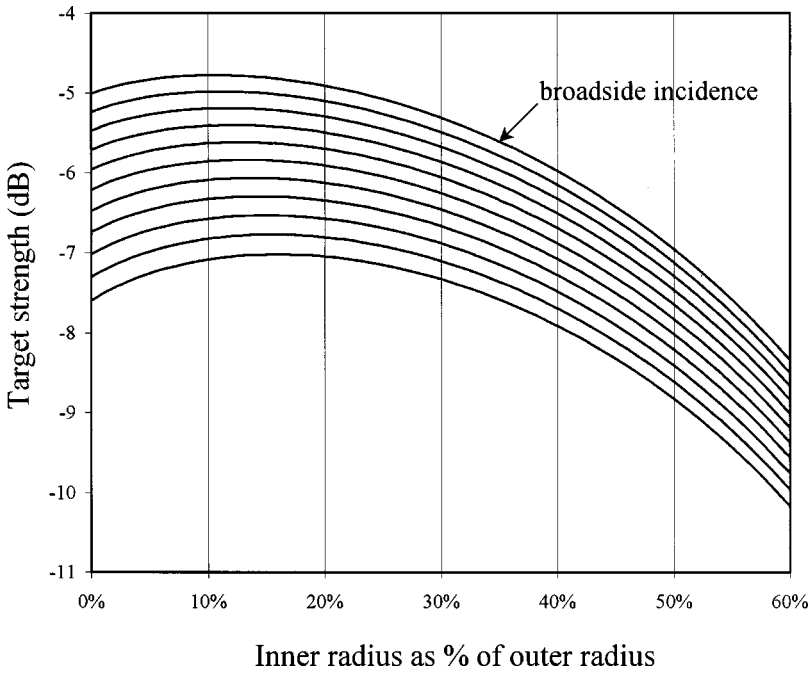

FIG. 2. Target strength versus inner radius. Incidence at 0°, 1°,...,10° from broadside (top to bottom). Frequency 100 kHz; cone angles 45°; outer radii 22 cm.

$$b = \frac{10 - \sqrt{80}}{10} a \approx 0.106a. \tag{40}$$

This value represents a compromise between two opposing effects. Surface curvature is larger nearer the tip, making these regions poorer scatterers. Areas farther from the tip scatter more strongly but the longer path length to the other cone causes higher attenuation due to geometrical spreading. By increasing the inner radius we lose relatively poor scattering areas but also reduce spreading loss from relatively strong scattering regions. This tradeoff determines the optimum inner radius.

An incorrect expression has previously appeared in the literature, for example in Ref. 4. Assuming $b/a \ll 1$, it can be shown that the incorrect result overestimates the target strength by approximately 6 dB.

IV. NUMERICAL EXAMPLES

The solution given by Eq. (17) and Eqs. (30)–(35) is algebraically complex but easy to evaluate numerically. Some examples will be given in this section to illustrate and exercise some of the parameters of the problem. Results will be expressed in terms of target strength, expressed in decibels. This quantity can be defined as follows:

$$\mathrm{TS} = 10 \log_{10} \left| \frac{\sigma_b}{4\pi} \right|, \tag{41}$$

where by convention the backscattering cross section is expressed in meters squared.

In all examples the frequency is 100 kHz, the sound speed 1500 m/s, and the outer radii are both equal to 22 cm. Figure 2 shows target strength as a function of inner radius, expressed as a fraction of outer radius, for various angles of incidence. For broadside incidence (0° elevation from horizontal) maximum backscattering can be observed at about 11%, the value given by Eq. (40). This value for the maximum does not hold as incidence is changed from horizontal, but shifts to somewhat larger values.

Target strength versus aspect is again shown in Fig. 3, in this example with the inner radius set equal to 0%, 11%, and 24% of the outer radius. As expected, at broadside incidence the optimal (11%) dimension outperforms both the larger and smaller dimensions. However, as the elevation angle is increased eventually there is a crossover after which the largest dimension performs best.

The effect of changing the cone angles is shown in Fig. 4. The elevation angle of the maximum return shifts from 0° as the cone angles are perturbed from 45°, maintaining a value equal to $\alpha_1 - \alpha_0$ as might be expected from the laws of reflection. This property has potential applications for vessels insonifying a target from above. It will also be seen that the maximum target strength increases as the cone angles vary away from 45°. However, it should be noted that the overall target area increases as well.

V. DISCUSSION AND CONCLUSIONS

High-frequency scattering strength of targets can be rank ordered in terms of powers of the wave number, k. For normal incidence on a flat plate the backscattering cross section is proportional to k^2, for normal incidence on a singly curved surface such as a cylinder it is proportional to k^1, and for normal incidence on a doubly curved surface such as an ellipsoid it is proportional to k^0. The influence of surface curvature on scattering strength can be associated with properties of the near (geometrical acoustics) portion of the field. Surfaces with no and single curvature produce collimated reflected rays. The latter are strictly parallel for the flat plate, a collimated pencil of rays. For a cylinder they are collimated within a layer, but for a doubly curved surface they exhibit three-dimensional spreading from the outset. Eventually, of course, three-dimensional spreading must occur in all

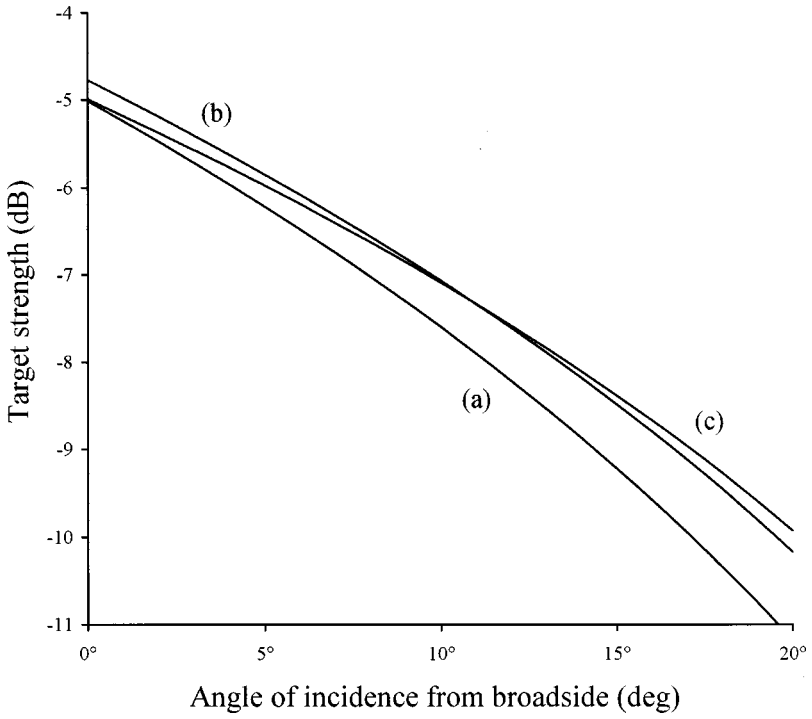

FIG. 3. Target strength versus angle of incidence from broadside. Inner radius=(a) 0 cm; (b) 2.32 cm (broadside optimum); (c) 5 cm. Frequency 100 kHz; cone angles 45°; outer radii 22 cm.

cases. For collimated rays this does not occur immediately but at a later distance, the Rayleigh length, that increases with frequency, thus explaining the dependence of target strength on frequency. It is well-known that the Kirchhoff method lacks a rigorous foundation. However, this method, which essentially treats the geometrical acoustics field as the source of the scattered wave, has proved to be accurate in cases where collimation is present, i.e., cases in which the geometrical acoustics field has special prominence. As the leading term of an asymptotic expansion, the saddle-point contribution to the Kirchhoff integral increases in accuracy as the frequency increases. Unfortunately, however, it is not possible to state *a priori* error bounds, for example, with respect to the minimum frequency required, since higher-order terms associated with edge diffraction, as we would have in the present case, are known to be incorrect.[5]

The present treatment has derived a backscattering cross section proportional to k, suggesting collimation of rays within a layer. This does not hold strictly (see Fig. 1) but is approximately correct in a neighborhood of the specular point. The principles of geometrical acoustics (the laws of reflection and energy conservation within ray bundles) were used to calculate the pressure field on the biconic due to an incident plane wave. The scattered wave could then be expressed as a surface integral iterated in terms of axial and azimuthal coordinates. The inner (azimuthal) integral has a saddle point at the specular point, the point at which incident and reflected rays form a perfect corner reflector. It could

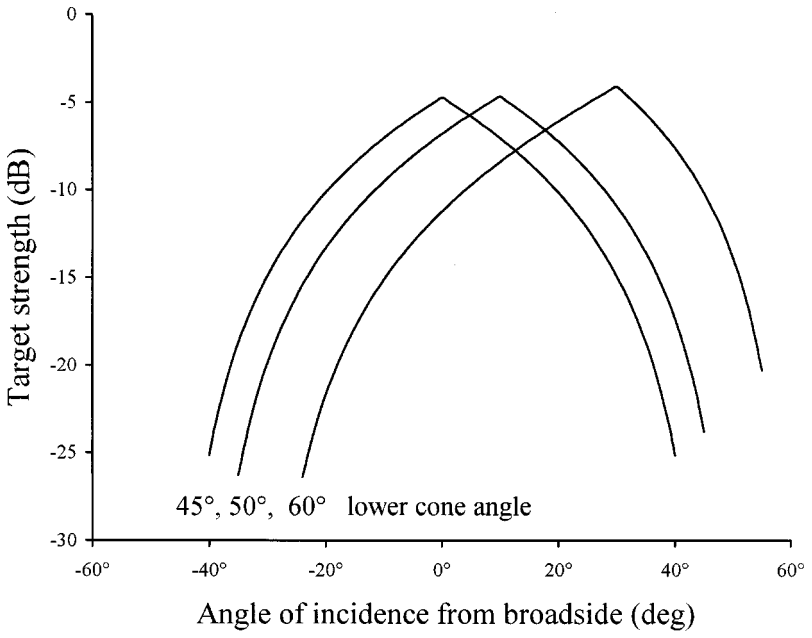

FIG. 4. Target strength versus angle of incidence from broadside. Cone angles (upper, lower): (45°,45°); (40°,50°); (30°,60°) (left to right). Frequency 100 kHz; inner radius 2.32 cm (broadside optimum); outer radii 22 cm.

therefore be evaluated, allowing the backscattering cross section to be expressed in terms of a single integration. The integrand is algebraically complicated but the integral can easily be evaluated numerically. An interesting result of the analysis has been the identification of an optimum inner radius of the biconic, the result of a tradeoff between surface curvature effects and attenuation by ray spreading. The treatment has allowed for arbitrary directions of incidence and variable cone angles, provided their sum is 90°. These parameters were exercised in numerical examples. It is hoped that this will show the value of results both for predictive purposes and as a design tool for special purpose targets, such as a bottom-tethered target insonified from above by a survey vessel.

ACKNOWLEDGMENTS

The author is grateful to Barry Gallagher, Gary Guenther, Lloyd Huff, and H. H. Shih for many helpful discussions and suggestions.

[1] B. B. Baker and E. T. Copson, *The Mathematical Theory of Huygens' Principle* (Oxford University Press, London, 1950).
[2] H. Primakoff and J. B. Keller, ''Reflection and transmission of sound by thin curved shells,'' J. Acoust. Soc. Am. **19**, 820–832 (1947).
[3] L. B. Felson and N. Marcuvitz, *Radiation and Scattering of Waves* (Prentice-Hall, Englewood Cliffs, NJ, 1973).
[4] J. W. Crispin and K. M. Siegel, *Methods of Radar Cross-Section Analysis* (Academic, New York, 1968).
[5] J. J. Bowman, T. B. A. Senior, and P. L. E. Uslenghi, *Electromagnetic and Acoustic Scattering by Simple Shapes* (American Elsevier, New York, 1969), pp. 29–31.

Complex modal statistics in a reverberant dissipative body

O. I. Lobkis and R. L. Weaver[a)]
Department of Theoretical and Applied Mechanics, University of Illinois, Urbana, Illinois 61808-2935

(Received 18 February 2000; revised 1 July 2000; accepted 5 July 2000)

The statistics of the ultrasonic resonance peaks of a finite elastic body are investigated. The distribution of peak phases, and the normalized variance of peak amplitudes, are shown to be consistent with a hypothesis that the modes themselves are complex Gaussian random numbers. A value $q=0.33$ for the ratio of the standard deviations of the imaginary and real parts of the modes is found to fit the data, and to bring recent theory of power variances into better accord with measurements. © *2000 Acoustical Society of America.* [S0001-4966(00)03110-6]

PACS numbers: 43.20.Ks, 43.40.At, 43.55.Cs [ANN]

I. INTRODUCTION

In the statistical description of vibrational and acoustic energy flow in complex structures, mean responses are sometimes predicted with a degree of success. This is most true for those structures with a kind of statistical homogeneity—in which properties are approximately constant over frequency bands that encompass many modes. Reverberation rooms, reverberant ultrasonic bodies, and reverberant elastic plates are the pre-eminent examples. Even for such simple structures, though, in which mean energy flow is well described by theory, fluctuations away from the mean are consistently overpredicted by theory.[1]

A recent study of ultrasonic reverberation ''rooms'' (small aluminum blocks at frequencies of hundreds of kHz such that wavelengths are small compared to block size) has come to the same conclusion. Observed power variances were less than predicted, sometimes by nearly a factor of 2. Theory for this variance has advanced considerably over the last couple of decades.[1–5] Level repulsion,[1,2] spectral rigidity,[4,5] Gaussian modal amplitude statistics,[4] and resonance width variations[5] have all been incorporated. The disagreements between theory and measurements have been reduced by some of these considerations, but the disagreement remains significant.

In the most recent study[5] it was speculated that a key assumption—one that has underlain all the theory to date—is in fact in error. This communication is addressed towards confirming that speculation and demonstrating the potential consequences of the error.

Almost universally in the structural vibrations literature, at least that which considers dissipation, it is implicitly or explicitly assumed that the modes $\{u_m\}$ of the structure have dissipation rates γ_m that depend on m, if at all, only very slowly, perhaps by means of a smooth dependence on the frequency $\gamma(\omega_m)$. This result follows, for example, from the common convenience of assuming that the damping matrix is a linear combination of the stiffness and mass matrices, ''proportional damping''

$$[C]=\alpha[M]+\beta[K], \tag{1}$$

in which case it is easy to show that the modal dissipation rates are given, for small loss tangent $\gamma/\omega \ll 1$, by

$$\gamma_m=(\alpha+\beta\omega_m^2)/2. \tag{2}$$

Lord Rayleigh,[6] wryly commenting on the ubiquity of the even simpler case $\beta=0$, said that this occurs frequently, ''in books at any rate.''

It is a simple matter to see that the γ can be random, with no smooth dependence on m. Perturbation theory indicates, for small $[C]$, that

$$\gamma_m=\{v_m\}^T[C]\{v_m\}/2, \tag{3}$$

where the v_m are the mode shapes of the undamped structure. Thus, the dissipation rate is given by the amplitude of the mode at the places where the loss mechanisms are concentrated. If C is distributed arbitrarily, we expect the γ to fluctuate depending on the precise spatial distribution of the mode amplitude. It is apparent that a more realistic model of damping can lead to a wide distribution of modal dissipation rates γ, even amongst neighboring modes. While much of the theory quoted above[1–4] has assumed that all dissipation rates γ in a narrow band are identical, this assumption was relaxed in the most recent work.[5]

A further consequence of assuming proportional damping is that the modes will be real, that they are in fact unmodified from the shapes they have in the undamped case at $\alpha=\beta=0$. Perturbation theory can also be applied to show that the modes $\{u\}$ are actually in general complex. They are given in terms of the modes $\{v\}$ of the undamped system, to leading order in C, by

$$\{u_m\}=\{v_m\}+i\omega_m\sum_{l\neq m}\frac{(\{v_l\}^T[C]\{v_m\})}{\omega_m^2-\omega_l^2}\{v_l\}, \tag{4}$$

where the ω_m are the undamped natural frequencies. The analytic simplifications that ensue from it notwithstanding, this clearly incorrect assumption requires scrutiny. This is particularly true when the assumption is implicated in chronic failures of theory to match experiment.

The previous work[5] did assume that the modes of a generic dissipative structure are real—as they would be if the structure were proportionally damped. This apparently incorrect assumption, it transpires, is crucial to the theory. Critical

a)Electronic mail: r-weaver@uiuc.edu

to theory is an understanding of the statistics of the mode amplitudes. The key quantity is the ratio of the mean fourth power of a mode amplitude to the square of the mean square

$$K=\langle u_m^4\rangle/\langle u_m^2\rangle^2, \tag{5}$$

all quantities being evaluated at the same position. Some of the literature has guessed that K is best estimated by the value it takes for oblique modes in a rectangular enclosure: (3/2) to the power of the dimensionality. More realistic modeling shows, for a generic elastic structure that lacks symmetries and lacks stable closed-ray paths, that the mode amplitudes are distributed as a real Gaussian random process. This yields a value $K=3$. It was this value that was used in the most recent work. Theory predicts power variances that scale essentially with the square of K. If one could justify, and predict, a K between 2 and 3, then theory could be brought into accord with measurements. This can be done if the modes are complex Gaussian processes. [Systems lacking time-reversal invariance (e.g., gyroscopic systems) have complex modes even in the absence of dissipation. We emphasize that the complexity considered here is entirely due to nonproportional damping.] They are, as discussed above, certainly complex. It is eminently reasonable to think that they should be distributed in a Gaussian manner, at least in generic structures. A complex Gaussian process with equal variances for real and imaginary parts will have a K (now defined as $\langle|u_m|^4\rangle/\langle|u_m|^2\rangle^2$) of 2.0. If the variance of the real part exceeds that of the imaginary part, then K will be closer to 3. As $K\approx 2.5$ was found in Ref. 5 to fit the observed variances, there is some reason to be optimistic that this approach will explain the chronic disagreements.[1,5]

In the next section the theory behind the response variance is modified for complex modes and the above argument is given quantitative detail. Then, we examine the multipeaked resonant response of one of the small aluminum blocks considered previously, and evaluate the phases and amplitudes of the resonance peaks. It is found that they are distributed in a manner consistent with our assumption about the complex Gaussian nature of the eigenfunctions and that their K takes a value that brings theory into accord with the previous measurements.

II. THEORY

The theory described previously[5] for relative power variance needs modification for the case of complex modes. Let two point transducers (receiver at position **x** and transmitter at position **y**) be located on the surface of an elastic object. Then, the Fourier transform of the output signal is

$$G(\mathbf{x},\mathbf{y},\omega)=R(\omega)\sum_m \frac{u_m(\mathbf{x})\,u_m(\mathbf{y})}{\omega^2-\omega_m^2-2i\omega\gamma_m}, \tag{6}$$

where u_m, ω_m, and γ_m are normal displacement component, angular frequency, and dissipation rate of the mth complex eigenmode, respectively. The complex factor $R(\omega)$ represents the transfer function of the transducers; it depends on their properties and their acoustical contacts with the object. The modes, even at neighboring frequencies, have different γ's. The γ's have been found to be distributed in accord with a chi-square distribution as[7,5]

$$p_\gamma(\gamma)d\gamma \propto \gamma^{n-1}\exp(-n\gamma/\overline{\gamma})\,d\gamma, \tag{7}$$

where $\overline{\gamma}$ is the average γ and the parameter n describes the width of the distribution.

In the previous paper's theoretical analysis[5] we presumed that the system is diagonally damped and the eigenfunctions are real. As discussed above, and will be demonstrated below, this presumption is far from reality. It is therefore necessary to consider the general case of complex eigenfunctions.

We use the simplification $\omega_m+\omega\approx 2\omega$[1,5] in Eq. (6) and then omit the unimportant prefactor $1/2\omega$ as irrelevant to our calculations. The power transmission function T can then be presented in the form

$$T=|G|^2=|R(\omega)|^2\sum_{m,l}\frac{u_m(\mathbf{x})u_m(\mathbf{y})}{\omega-\omega_m-i\gamma_m}\frac{u_l^*(\mathbf{x})u_l^*(\mathbf{y})}{\omega-\omega_l+i\gamma_l}, \tag{8}$$

where we have allowed the mode shapes to be complex. The different mode shapes are assumed uncorrelated with each other, and with themselves at points **x** far from **y**. Thus, after averaging, only the term with $m=l$ is left in the sum (8). The average value of T across the ensemble is equal to

$$\langle T\rangle=|R(\omega)|^2\sum_m\frac{\langle|u_m(\mathbf{x})|^2|u_m(\mathbf{y})|^2\rangle\equiv\langle|u|^2\rangle^2}{(\omega-\omega_m-i\gamma_m)(\omega-\omega_m+i\gamma_m)}, \tag{9}$$

where $\langle|u|^2\rangle$ is the ensemble average of the absolute value square of an eigenfunction.

The variance of T is determined in terms of $\langle T^2\rangle$, where

$$T^2=|R(\omega)|^4\sum_{m,l,i,j}\frac{u_m(\mathbf{x})u_m(\mathbf{y})}{\omega-\omega_m-i\gamma_m}\frac{u_l^*(\mathbf{x})u_l^*(\mathbf{y})}{\omega-\omega_l+i\gamma_l}\times\frac{u_i(\mathbf{x})u_i(\mathbf{y})}{\omega-\omega_i-i\gamma_i}\frac{u_j^*(\mathbf{x})u_j^*(\mathbf{y})}{\omega-\omega_j+i\gamma_j}. \tag{10}$$

Again assuming uncorrelated mode shapes,

$$\langle T^2\rangle=|R(\omega)|^4\left\{\sum_m\frac{\langle|u_m(\mathbf{x})|^4\rangle\langle|u_m(\mathbf{y})|^4\rangle\equiv\langle|u|^4\rangle^2}{(\omega-\omega_m-i\gamma_m)^2(\omega-\omega_m+i\gamma_m)^2}+2\sum_{m\neq l}\frac{\langle|u_m(\mathbf{x})|^2\rangle\langle|u_m(\mathbf{y})|^2\rangle\langle|u_l(\mathbf{x})|^2\rangle\langle|u_l(\mathbf{y})|^2\rangle\equiv\langle|u|^2\rangle^4}{(\omega-\omega_m-i\gamma_m)(\omega-\omega_m+i\gamma_m)(\omega-\omega_l-i\gamma_l)(\omega-\omega_l+i\gamma_l)}\right.$$
$$\left.+\sum_{m\neq l}\frac{\langle u_m^2(\mathbf{x})\rangle\langle u_m^2(\mathbf{y})\rangle\langle(u_l^*(\mathbf{x}))^2\rangle\langle(u_l^*(\mathbf{y}))^2\rangle\equiv|\langle u^2\rangle|^4}{(\omega-\omega_m-i\gamma_m)^2(\omega-\omega_l+i\gamma_l)^2}\right\}. \tag{11}$$

The calculation of the relative variance can now be performed as previously[5] by averaging over ω_m, ω_l and γ's.

$$relvar = \frac{\langle T^2\rangle - \langle T\rangle^2}{\langle T\rangle^2} = 1 + \frac{K^2}{M}\frac{n(n-1)}{(n-2)(n-3)} - \frac{f_1(M,n) + L^2 f_2(M,n)}{M}, \tag{12}$$

where the modal amplitude statistics K^2 and L^2 are defined below, and

$$f_1(M,n) = 4M\int_0^\infty \frac{b(t)dt}{(1+Mt/n)^{2n-2}}; \qquad f_2(M,n) = 4M^3\frac{(n-1)^2}{n^2}\int_0^\infty \frac{b(t)\,t^2\,dt}{(1+Mt/n)^{2n}}. \tag{13}$$

The modal overlap is $M = 2\pi\overline{\gamma}D$, where D is the modal density (modes per unit frequency $d\omega$). The function $b(t)$ is the Fourier transform of the Dyson two-level correlation function;[8] $b(t) = 1 - 2t + t\ln(1+2t)$ for $t<1$, and $b(t) = -1 + t\ln[(2t+1)/(2t-1)]$ for $t>1$. The detailed properties of the functions $f_1(M,n)$ and $f_2(M,n)$ have been considered in Ref. 5. In the limit of no decay curvature (i.e., a narrow distribution of γ's, $n=\infty$), and after approximating the function $b(t)\approx\exp(-2t)$, the functions f_1 and f_2 simplify: $f_1(M,\infty)\approx 2M/(M+1)$ and $f_2(M,\infty)\approx M^3/(M+1)^3$.

This result differs in two ways from that obtained previously when the modes were assumed real.[5] The factor $K = \langle|u|^4\rangle/\langle|u|^2\rangle^2$ depends now on the mean absolute values of eigenfunctions, and there is now an additional parameter $L = |\langle u^2\rangle|^2/\langle|u|^2\rangle^2$ equal to the ratio of the absolute mean square to the mean absolute square. In the case of real Gaussian-distributed eigenfunctions, K and L are 3 and 1, respectively.

We suggest further that the real and imaginary parts of u ($u = u_r + iu_i$) are independent centered Gaussian random numbers[9] with distribution

$$p_u(u_{r,i})du_{r,i} \propto \exp(-u_{r,i}^2/2\langle u_{r,i}^2\rangle)du_{r,i}, \tag{14}$$

where the $\langle u_{r,i}^2\rangle$ are the mean squares of the real and imaginary parts. The values K and L can be calculated as

$$K = \frac{\langle(u_r^2+u_i^2)^2\rangle}{\langle u_r^2+u_i^2\rangle^2} = \frac{\langle u_r^4\rangle + 2\langle u_r^2u_i^2\rangle + \langle u_i^4\rangle}{(\langle u_r^2\rangle + \langle u_i^2\rangle)^2} = \frac{3\langle u_r^2\rangle^2 + 2\langle u_r^2\rangle\langle u_i^2\rangle + 3\langle u_i^2\rangle^2}{(\langle u_r^2\rangle + \langle u_i^2\rangle)^2}, \tag{15}$$

and

$$L = \frac{|\langle u_r^2 + 2iu_ru_i - u_i^2\rangle|^2}{\langle u_r^2+u_i^2\rangle^2} = \frac{|\langle u_r^2\rangle + 2i\langle u_ru_i\rangle - \langle u_i^2\rangle|^2}{(\langle u_r^2\rangle + \langle u_i^2\rangle)^2} = \frac{(\langle u_r^2\rangle - \langle u_i^2\rangle)^2}{(\langle u_r^2\rangle + \langle u_i^2\rangle)^2}. \tag{16}$$

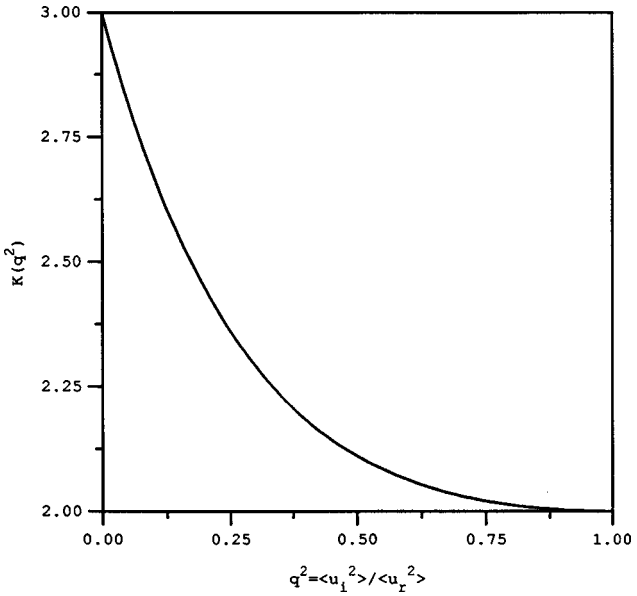

FIG. 1. The modal amplitude statistics $K = \langle|u|^4\rangle/\langle|u|^2\rangle^2$ as a function of modal complexity, Eq. (17).

It is convenient to introduce the parameter $q^2 = \langle u_i^2\rangle/\langle u_r^2\rangle$ equal to the ratio of the variances of imaginary and real parts. We then rewrite K and L in the form

$$K = 3 - \frac{4q^2}{(1+q^2)^2}; \quad L = 1 - \frac{4q^2}{(1+q^2)^2} = K - 2. \tag{17}$$

K varies from 3 for real modes ($q=0$) to 2 if the distributions of the real and imaginary parts are equivalent ($q=1$). $L = K-2$ changes from 1 to 0 over the same interval of q. A graph of the function $K(q^2)$ is presented in Fig. 1. It is apparent that the new theoretical prediction Eq. (12) for *relvar* can be significantly less than that given in Ref. 5, depending on the value of q. Experimental determination of the value K will be done in the next section.

We also consider consequences of the distribution (14) on the phases of the modes. For Gaussian distributed real and imaginary parts of eigenfunctions (14), the modal phase distribution $p_\varphi(\varphi)$ can be expressed as

$$p_\varphi(\varphi) = \int_{-\infty}^{\infty}\int_{-\infty}^{\infty}\delta(\varphi - \arctan(u_i/u_r)) \times \exp(-u_r^2/2\langle u_r^2\rangle - u_i^2/2\langle u_i^2\rangle)du_r\,du_i, \tag{18}$$

where δ is the Dirac delta function. Calculation of the integrals (18) in polar coordinates gives the normalized function $p_\varphi(\varphi)$,

$$p_\varphi(\varphi) = \frac{q}{2\pi}\frac{1}{q^2\cos^2\varphi + \sin^2\varphi}. \tag{19}$$

The function is a maximum at $\varphi = \pi k$ ($k = 0, \pm 1, \ldots$ corresponding to a real mode amplitude at the position of interest) with a value $1/2\pi q$. At the minima [$\varphi = \pi(k+1/2)$, corresponding to an imaginary mode amplitude at the position of interest] the value of p_φ is $q/2\pi$ (see the solid line in Fig. 2). For real modes ($q=0$) the function $p_\varphi(\varphi)$ tends to a delta function. For equivalently distributed real and imaginary

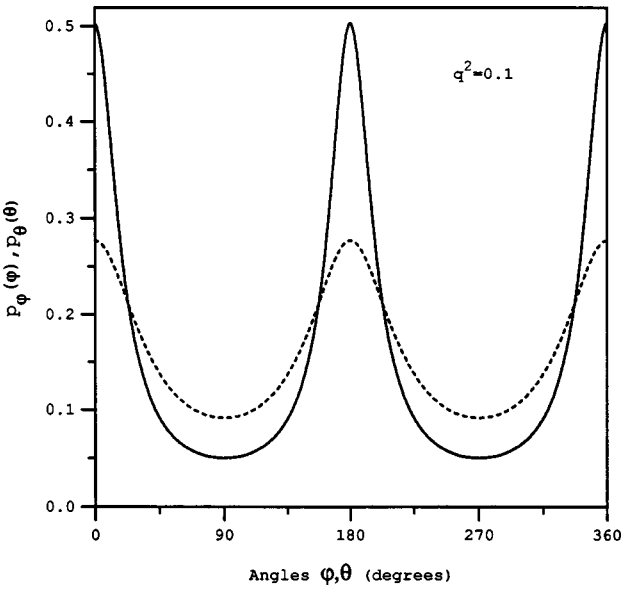

FIG. 2. The theoretical distribution for the phase of a mode [solid line, Eq. (19)] and of a peak [dashed line, Eq. (21)] for the case of modal complexity $q^2=0.1$.

parts ($q=1$), the modal phases are uniformly distributed; $p_\varphi(\varphi)=\text{const}=1/2\pi$.

The phase distribution of the eigenfunctions $p_\varphi(\varphi)$ cannot be measured directly because the received signal (6) depends on the product of the eigenfunctions at the points **x** and **y** by means of the complex peak amplitude $A=u(\mathbf{x})\,u(\mathbf{y})$. The phase θ of the peak amplitude A is equal to $\varphi_x+\varphi_y$ ($u_{x,y}=|u_{x,y}|\exp(i\varphi_{x,y})$). Therefore, the phase distribution $p_\theta(\theta)$ of the complex amplitudes A can be expressed through the phase distribution (19) as

$$p_\theta(\theta)=\left(\frac{q}{2\pi}\right)^2\int_0^{2\pi}\int_0^{2\pi}\times\frac{[\delta(\theta-\varphi_x-\varphi_y)+\delta(\theta-\varphi_x-\varphi_y+2\pi)]d\varphi_x\,d\varphi_y}{(q^2\cos^2\varphi_x+\sin^2\varphi_x)(q^2\cos^2\varphi_y+\sin^2\varphi_y)}. \tag{20}$$

After calculation of the integrals (20) over φ_x and φ_y,[10] the resulting phase distribution is found to be

$$p_\theta(\theta)=\frac{q}{\pi}\,\frac{(1+q^2)}{4q^2+(1-q^2)^2\sin^2\theta}. \tag{21}$$

A graph of the distribution $p_\theta(\theta)$ (dashed line) is presented in Fig. 2. The function has maxima and minima at the points $\theta_k=\pi k$ and $\theta_k=\pi(k+1/2)$ with $\max p_\theta=(1+q^2)/4\pi q$ and $\min p_\theta=q/\pi(1+q^2)$. The width of the $p_\theta(\theta)$ distribution is approximately $\sqrt{2}$ times larger than that of $p_\varphi(\varphi)$.

III. EXPERIMENTAL RESULTS

We study a small aluminum block with nominal dimensions $25\times25\times50$ mm. Several saw cuts on block edges and four defocusing surfaces in its corners serve to break reflection symmetry and provide sources of diffuse scattering. Two thin, dry-coupled pin transducers are used to transmit and receive transient wideband ultrasonic signals (diameter 1.5 mm each, piezoelectric element diameter 1.0 mm). The signal contains useful components in the frequency range between 50 and 2000 kHz. Signal are captured with a 32 000-word 8-bit waveform digitizer at a sampling rate of 5 MS/s, and 20 times repetition averaged to improve signal-to-noise ratios. The resulting transient decaying signals had a useful duration of about 90 ms. This wave capture was repeated with various trigger delays in order to access the full record, with a length of the order of 400 000 words. Repetition averaging and variable voltage scales resulted in a dynamic range considerably greater than 8 bits. The signal acquisitions were repeated for four different positions (**x**,**y**) of the transmitter and receiver.

The signals were then Fourier transformed and investigated in the frequency range between 110 and 195 kHz where about one hundred modes were located. In this frequency interval the modes are well separated (average modal overlap is 0.04) and their parameters [the peak positions $f_m=\omega_m/2\pi$, the widths γ_m, and the amplitudes $A_m=u_m(\mathbf{x})\,u_m(\mathbf{y})$] can be measured independently for each mode by fitting the local behavior to a single term of Eq. (6). The values f_m, γ_m, and $|A_m|$ were extracted from a fit of the local behavior of $|G|^2$ to a Lorentzian. Then, the phases θ_m of the complex quantities $R\,A_m$ were determined from $\mathrm{Re}\,G$ and $\mathrm{Im}\,G$ curves. It should be noted that phases θ_m will in general not vanish even if the modes are real, because the phase θ_R of the transducers' transfer function $R(f)$ is part of the $R\,A_m$. Thus, the phases of the modes cannot be extracted unambiguously. However, under the assumption that the transducer function $R(f)$ is smooth (effectively constant over short frequency intervals), we can extract the variation of modal phases.

The measurements show that experimental curves for the real and imaginary parts of the Fourier transform cannot be fitted on the assumption of real values for the peak amplitudes A_m. For example, Fig. 3 presents the real (solid curve) and imaginary (dashed curve) parts of the Fourier transform for two closely spaced modes. The plot shows a phase difference of nearly $\pi/2$ between these neighboring peaks. The transducer function $R(f)$ cannot change much over a frequency interval of 0.1 kHz (the transducer rings for at most about 10 μs; its R cannot vary significantly, except on a scale of 100 kHz). Thus, the only explanation for these data is that one or both of the peaks amplitudes A_m are complex.

A quantitative estimation of the complexity (i.e., a determination of the parameter q) can be done either from the statistics of the mode amplitude or the mode phases. First, the amplitudes $|A_m|$ of all the peaks have been measured and summarized for four transducer positions in the frequency interval between 110 and 195 kHz, a total of 420 peaks. The received signal (6) depends on the transducers' acoustical contact (notoriously nonreproducible) with the object, by means of the function R. To remove this random influence, the mode amplitudes for different positions were normalized (by dividing by the rms amplitude over the entire frequency interval) before assembly. The value of K^2 was then calculated as $K^2=\langle|A_m|^4\rangle/\langle|A_m|^2\rangle^2$; a value of $K\approx2.6$ was obtained. This corresponds to a value of the parameter q^2

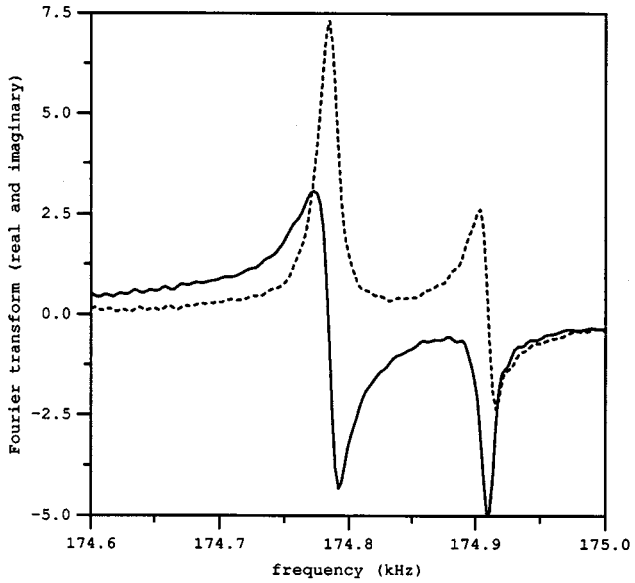

FIG. 3. A short interval of the spectrum (solid line real part and dashed line imaginary part) of the transform function for one position of the transducer pair. The very different phases of the two resonances illustrate the complex character of the modes.

≈ 0.12, based on Eq. (17). This implies a ratio of mean squares for the real and imaginary parts approximately equal to 8, $\langle u_r^2 \rangle \approx 8 \langle u_i^2 \rangle$.

Second, the phases θ_m of all the peaks in the frequency interval were measured; a histogram is presented in Fig. 4. The lowest-amplitude peaks, for which phase was not reliably determined, were excluded from this histogram. Most of the phases are located in two narrow angular intervals, near the angles $\theta_m = 60$ and 240 deg. This suggests that the transducer transfer function phase is $\theta_R \approx 60°$ and most of the modes are almost real with the phases near $\theta_m = 0$ and 180 deg (positive and negative amplitudes A_m) with small imaginary parts related to the distribution's width. There are only a few modes with phases very different from these values, with peak amplitudes having imaginary parts greater than real parts. The parameter q can be roughly estimated from the histogram. The renormalized theoretical phase distribution $p_\theta(\theta - \theta_R)$ is presented in the same figure for three different values of q ($q^2 = 0.05, 0.10, 0.15$). The phase distribution near $q^2 = 0.1$ has the best fit with experimental data. This result is in fair agreement with the value $q^2 = 0.12$ obtained from the peak amplitude statistics.

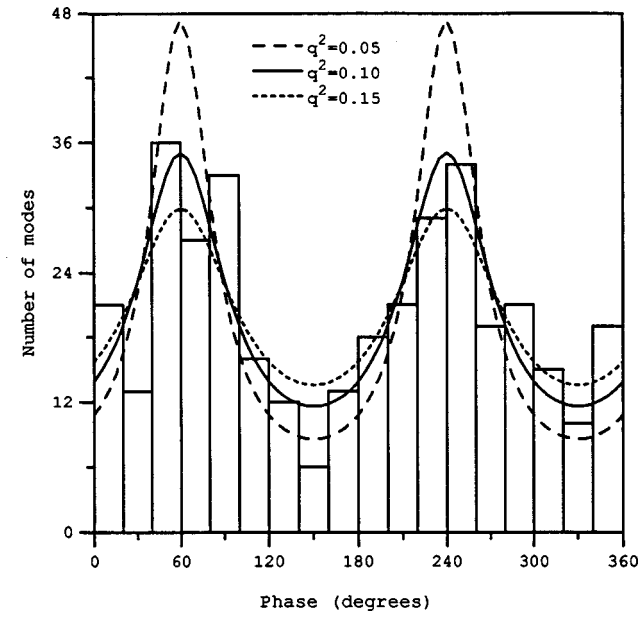

FIG. 4. A histogram of the resonance phases is superposed on the theoretical distribution [Eq. (21)] consequent to three choices for modal complexity. The best fit is at $q^2 = 0.1$.

The transducer function R can in principle vary over the frequency interval we investigate, thereby artificially enhancing the apparent fluctuations in peak amplitudes and peak phases. In practice, however, we observe very little variation. Our neglect of that effect may be responsible for the minor discrepancy between these two measures of q.

IV. CONCLUSIONS

We have advanced a hypothesis that the modes of a suitably generic reverberant, but dissipative, elastic body are distributed as complex Gaussian random numbers. A parameter q, being the ratio of the standard deviations of imaginary and real parts of the modes, is introduced with which to quantify the degree to which the modes are complex. We show, in a single specimen, and in a limited frequency interval in which the resonance peaks are distinct enough to allow our analysis of single modes, that a single value of q appears to account for both the peak amplitude statistics and the distribution of peak phases. This supports our hypothesis of Gaussian complex modes.

It is shown that this modification, when applied to extant theory for power variances, may serve to reconcile chronic disagreements between theory and measurements. The measured peak amplitude statistics were such that $K \approx 2.6$, a value that would bring a modified theory for power variances into accord with our previous measurements. All this is suggestive that a final resolution of the chronic problems with *relvar* may be at hand. Before that resolution can take place, however, it will be necessary to craft predictive theory, or at least independent measurements, for the quantitative measure of modal complexity q.

ACKNOWLEDGMENTS

This work was supported by Grant No. 9701142 from the National Science Foundation.

[1] J. L. Davy, ''The relative variance of the transmission function of a reverberation room,'' J. Sound Vib. **77**, 455–479 (1981); ''The ensemble variance of random noise in a reverberation room,'' *ibid.* **107**, 361–373 (1986); ''Improvements on formulae for the ensemble relative variance of random noise in a reverberation room,'' *ibid.* **115**, 145–161 (1987).

[2] R. H. Lyon, ''Statistical analysis of power injection and response in structures and rooms,'' J. Acoust. Soc. Am. **45**, 545–565 (1969).

[3] R. V. Waterhouse, ''Estimation of monopole power radiated in a reverberation chamber,'' J. Acoust. Soc. Am. **64**, 1443–46 (1978).

[4] R. L. Weaver, ''On the ensemble variance of reverberation room transfer functions, the effect of spectral rigidity,'' J. Sound Vib. **130**, 487–491 (1989).

[5] O. I. Lobkis, R. L. Weaver, and I. Rozhkov, ''Power variances and decay curvature in a reverberant system,'' J. Sound. Vib. (in press).

[6] J. W. S. Rayleigh, *Theory of Sound* (Dover, New York, 1945), Chap. 5, Sec. 97.
[7] J. Burkhardt and R. L. Weaver, ''Spectral statistics in damped systems. I. Modal decay rate statistics,'' J. Acoust. Soc. Am. **100**, 320–326 (1996); J. Burkhardt, ''Damage assessment using reverberant decays,'' Ultrasonics **36**, 471–475 (1998).
[8] M. L. Mehta, *Random Matrices* (Academic, Boston, 1990); T. A. Brody, J. Flores, J. B. French, P. A. Mello, A. Pandey, and S. S. M. Wong, ''Random matrix physics: Spectrum and strength fluctuations,'' Rev. Mod. Phys. **53**, 385 (1981). Our use of the GOE two level function $b(t)$ is an approximation. Weak dissipation surely affects it, weakly. The result (12) depends on $b(t)$, but not critically.
[9] Our hypothesis is predicated upon the plausibility of the Gaussian nature of the modes. It is also based on a notion that the real and imaginary parts should be uncorrelated, i.e., that the average phase is zero, or sufficiently smoothly varying that the average phase may be absorbed into a transducer function. This latter assumption follows in part from our inability to imagine what a nonzero average phase might depend on. Similar notions are present in a recent study of reverberant microwaves [P. Seba, F Haake, M. Kus, M. Barth, U. Kuhl, and H.-J. Stockmann, Phys. Rev. E **56**, 2680–2686 (1997)]. Our hypothesis is confirmed by the results presented in Sec. III.
[10] A. P. Prudnikov, Yu A. Brychkov, and O. I. Marychev, *Integrals and Series. Elementary Functions* (Nauka, Moscow, 1981), p. 183.

Experimental study of sound propagation in a chain of spherical beads

M. de Billy[a)]
Groupe de Physique des Solides, Universités Paris 6 et 7, Tour 23, 2, place Jussieu 75251 Paris cedex 05, France

(Received 3 August 1999; accepted for publication 20 June 2000)

In this paper are described experimental observations which are concerned by the propagation of pulsed ultrasonic waves transmitted through a limited one dimensional periodic granular medium submitted to a static force. This study—which is limited to a time domain analysis—exhibits experimental results which depend on the polarization of the acoustic excitation. In the case of compressional excitation, spherical Rayleigh type surface waves propagate around the beads. In the case of shear excitation, the experimental recordings point out the existence of a very low signal, the frequency of which is equal to the cut-off frequency of the chain. Moreover it is established that the frequency value varies with the radius of the bead, the normal force applied to the beads, and the mechanical properties of the material. © *2000 Acoustical Society of America.* [S0001-4966(00)01610-6]

PACS numbers: 43.20.Mv [DEC]

I. INTRODUCTION

For many years, the granular media were widely investigated in various domains.[1–6] The propagation of compressional sound wave in linear and nonlinear approximations was studied in details.[7–10] It was demonstrated that the interaction between two adjacent elastic spherical beads is described by the Hertz' law.[11] In the linear limit and in the case of a chain of identical beads submitted to a static force applied in the direction of the contact points, this law predicts the existence of a cut-off frequency. These results which are well known at the present time were experimentally tested and confirmed recently.[8,9] To our knowledge, the propagation of elastic shear waves in a one dimensional granular medium was theoretically studied[12–16] but not yet experimentally explored. In this paper our main objective is concerned by studying how a compressional or a shear periodic excitation is transmitted through a chain of few identical spherical beads in contact and loaded by a static force along the direction of the contact points. The acoustic excitation is realized with contact transducers and the analysis is limited to the temporal domain. The experiments realized in the transmission mode show that the detected acoustic signals are very different according to the polarization of the acoustic excitation and detection. Spherical surface acoustic waves (Rayleigh wave type) are generated when the transmitter is longitudinally excited. In case of a transversal excitation, the transmitted signals point out the existence of a very low frequency signal at the beginning of the wave form whose value varies with the applied static force, the radius of the beads and the material.

[a)]Permanent address: LUAP/LED, University Paris 7, Tour 33, boite postale 70/87, 2 place Jussieu 75251 Paris Cedex 05, France. Electronic mail: mdebilly@ccr.jussieu.fr

II. EXPERIMENTS

A. Experimental conditions

Our experimental analysis is limited to the propagation of a sound wave in a discrete one dimensional periodic medium. The experimental set-up is sketched in Fig. 1(a). The excitation and the detection of the acoustic signals are different from those used by Coste *et al.*[7–9] who used a vibration exciter for the generation of the compressional deformation. The experiments are realized with a chain of identical spherical elastic beads (1) aligned in a cardboard tube (2). The two furthest spheres of the chain are in contact with acoustic transmitters (3) the central frequency of which is 2.2 MHz. Two kinds of transmitters are used: compressional and shear contact transducers (Type Panametrics V106 and V156). In case of transversal experiments, the emitter and the receiver have the same direction of polarization. The short acoustic signals transmitted through the chain are recorded and visualized on the screen of a digital oscilloscope (Type Lecroy 9400) before being plotted on a graphic printer [Fig. 1(b)]. Steel, brass, glass and nylon beads were used because they showed various mechanical and acoustical properties (cf. Table I). The diameter of the spheres varied from 2 to 9 mm. A static force (F_0) was applied in the direction determined by the contact points; the loading is measured with a static force sensor (5) [Kistler SY2712] located between the screw (4) and the acoustic emitter (3). It is supposed that the static load is transmitted to the adjacent beads through the contact area without any loss and the friction with the cardboard tube is supposed to be negligible.

B. Experimental observations

In Fig. 2 are given two typical acoustic signals recorded in different conditions of excitation and reception: in Fig. 2(a) the excitation and the detection are longitudinal; in Fig. 2(b) the excitation and the detection are transversal. The static force is the same for the two records ($F_0 = 30$ N) and

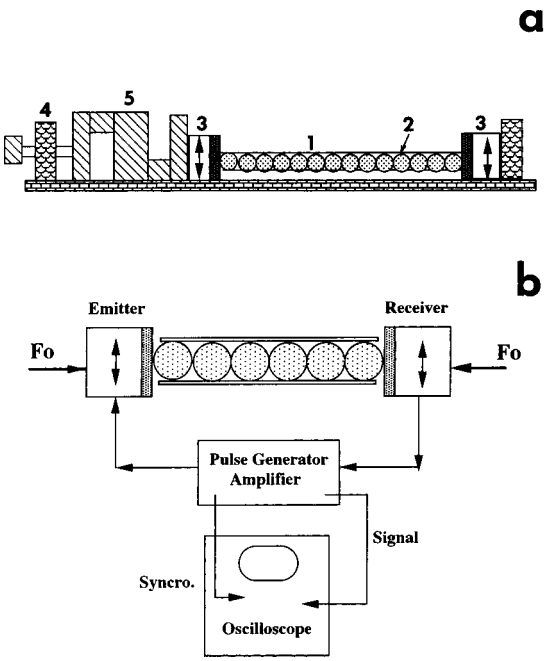

FIG. 1. Experimental set-up. (a) Mechanical apparatus. (b) Electronic device.

the chain is formed with five steel beads of 8 mm in diameter. We may note that the first signal [Fig. 2(a)] is characterized by the presence of a high frequency time response whereas the second one [Fig. 2(b)] is characterized by the existence of a very low frequency signal on which a high frequency component is superimposed.

III. LONGITUDINAL EXCITATION AND DETECTION

In Fig. 3(a) is plotted the transmitted echographic structure observed by transmission through a chain which consists of five steel beads of 8 mm in diameter in case of longitudinal excitation and reception. The acoustic wave form points out a periodic structure showing extrema regularly spaced in time. The structure between two adjacent echoes is very similar [see Figs. 3(b) and (c)] and we observe that the frequency of the transmitted signals is equal to the frequency of the excitation of the emitter (2.2 MHz) [see Fig. 3(d)]. In order to interpret the acoustic response obtained with a chain, a brief analysis of the signal obtained with one bead was first undertaken.

A. Case of a spherical bead

The propagation of a spherical surface acoustic wave (SSAW) on one bead was studied in a recent past with laser technique.[17,18] It was shown that the detected signal presents

TABLE I. Acoustic and mechanical parameters of the different beads used in the experiments.

Material	C_L (m/s)	C_T (m/s)	C_R (m/s)	ρ (kg/m^3)	E (10^{10} N/m^2)	ν
Steel	5960	3235	3005	7.85	21.6	0.276
Glass	5968	3764	3350	2.2	7.3	0.172
Brass	4347	2127	1986	8.2	10.4	0.374
Nylon	2620	1070	1007	1.1	0.35	0.40

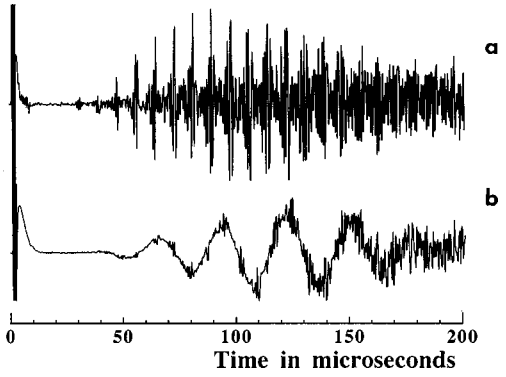

FIG. 2. Influence of the polarization of the transmitters on the detected acoustic waveform. (The chain is formed with five beads of 8 mm in diameter.) (a) Longitudinal excitation and reception (20 mv/div). (b) Transversal excitation and reception (50 mv/div).

characteristic features that we verified with our technique in case of individual spherical beads submitted to a longitudinal excitation.

(a) First it is verified that the amplitude of the echographic structure [Fig. 4(a)] diminishes when the sphere is surrounded by glue stuck on the surface [Fig. 4(b)]. This is a very characteristic behavior of a Rayleigh type surface acoustic wave.

(b) When the transmitters are facing each other, the spherical surface wave converges and diverges from the poles, which undergoes a $\pi/2$ phase shift. This is experimentally verified with a steel sphere of 6 mm in diameter [Fig. 4(c)].

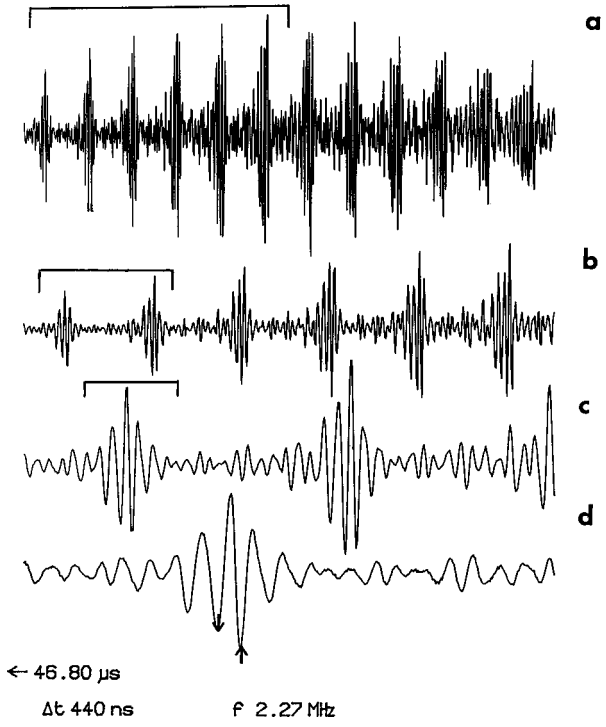

FIG. 3. Illustration of the periodicity observed in the transmitted signal through a steel bead of 8 mm. The excitation and reception are longitudinally polarized: (a) 10 μs; 10 mV/div; (b) 5 μs; 10 mv/div; (c) 2 μs; 5 mv/div; and (d) 1 μs; 5 mv/div.

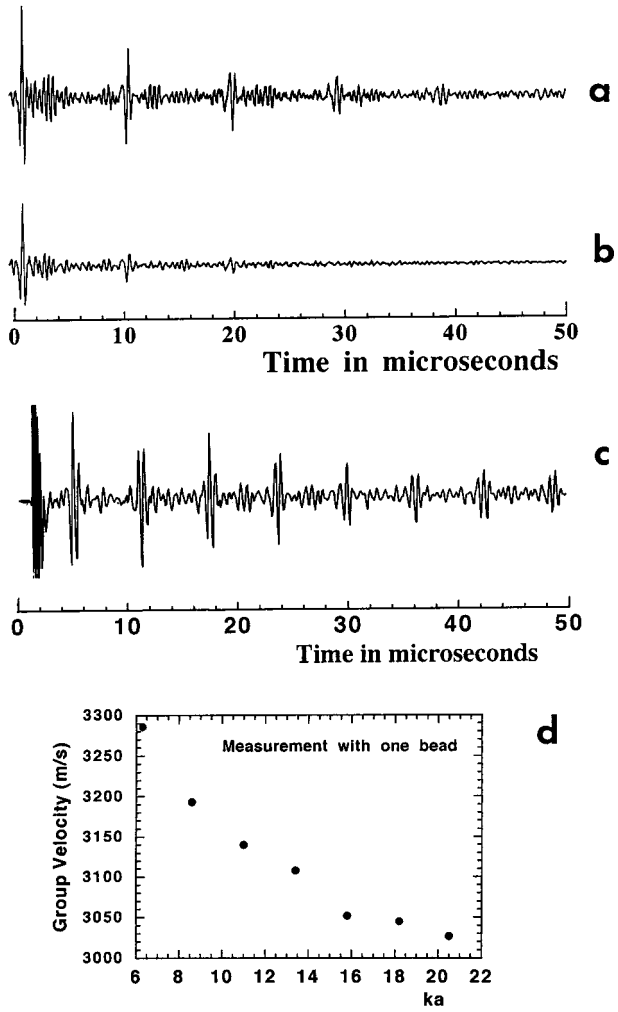

FIG. 4. Typical recordings illustrating the SSAW properties (case of one steel bead of 8 mm in diameter). (a) The sphere is free (without glue on the surface). (b) Glue is stuck on the surface of the sphere. (c) Confirmation of the $\pi/2$ phase shift at the contact points. (d) Group velocity dispersion curve as a function of ka.

(3) Such investigated spherical samples are dispersive[19] and the group velocity of the SSAW varies with the dimensionless quantity ka where k represents the wave vector and a the radius of the sphere. This is confirmed in Fig. 4(d) where the variations of the group velocity are plotted as a function of ka.

(4) If the transmitters are moved away from the poles, or if the beads are not well calibrated, or if the front faces of the transmitters are not well parallel, the recorded wave forms carry out the superposition of two slightly shifted signals, which gives rise to a structure whose shape looks characteristic of a frequency dispersion [Fig. 5(a)]. Still, under certain conditions two signals may be clearly observed [Fig. 5(b)].

From these experimental observations, it may be clearly concluded that, with our simple experimental technique, spherical Rayleigh type acoustic surface waves are generated on the surface of a bead when it is submitted to a longitudinal excitation via contact transmitters.

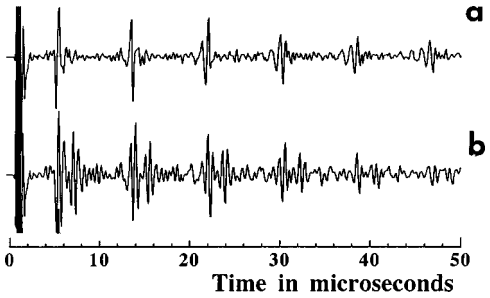

FIG. 5. Influence of the defect of alignment on the wave observed with a steel bead of 8 mm in diameter (vertical scale: 0.1 V/div).

B. Case of an array of spherical elastic beads

The train waves detected in the case of two identical spherical beads have shown the four behaviors described in the previous section as it is illustrated by the echographic structures presented in Figs. 6 and 7(a). Besides the confirmation of the existence of the echo regularly spaced in the time domain, the comparison between the two wave trains in the figures confirms that when glue is applied on the surface of the two spheres in contact, the amplitude of the signals decreases [Fig. 6(b)]. In Fig. 7(a), the π phase shift is observed whereas the group velocity measured with two beads of different radius reveals a ka dependence [Fig. 7(b)] similar to the one observed with one bead. In addition, as it was verified in the case of one bead, the limit value of the group velocity (=3020 m/s) for large values of ka coincides with the velocity of propagation of the Rayleigh surface wave on an infinite plane (=3005 m/s).

Because of all these observations, we concluded that the regular peaks observed on the transmitted acoustic records [Figs. 6(a) and 7(a)] are resulting from the superposition of SSAW which propagate around the two spherical beads. In the following we pertinently extended this conclusion to the case of a chain including several identical spheres. In that case, the contact area between two adjacent spheres behaves as a point source.

C. Amplitude analysis of the echographic structure obtained with a chain of identical beads

With an array of spherical balls, the most surprising effect is concerned by the observation—under certain

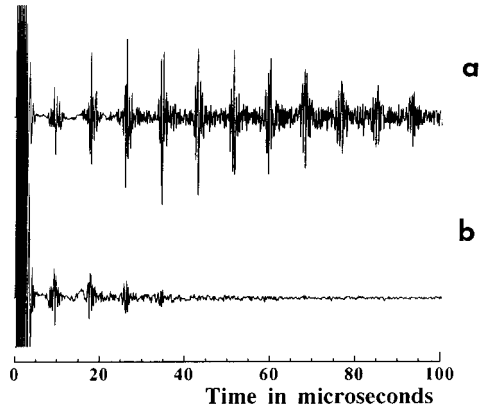

FIG. 6. Typical recordings showing the SSAW properties (case of two steel beads of 8 mm in diameter). (a) The spheres are free. (b) Glue is stuck on the spheres (the vertical scale is the same for both records.)

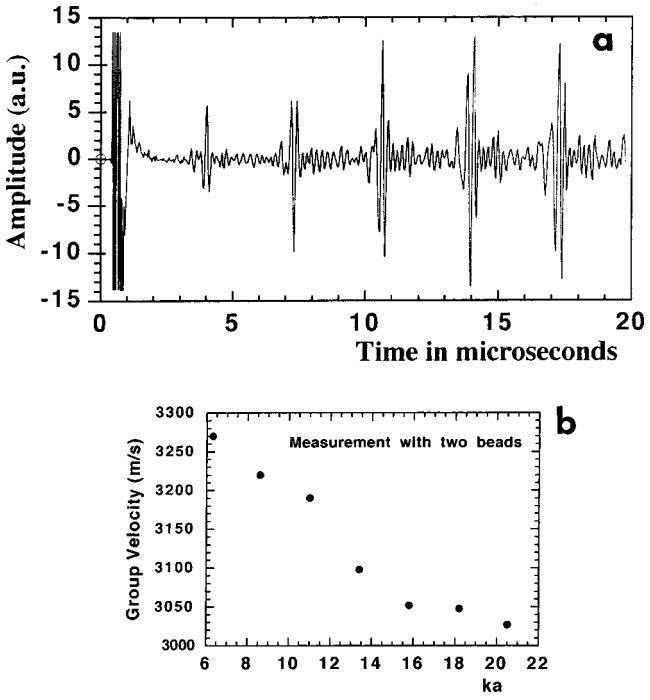

FIG. 7. (a) Experimental record showing the π phase shift at the contact points in case of two steel balls ($d=8$ mm). (b) Group velocity dispersive curve as a function of ka (case of two steel balls; $d=8$ mm).

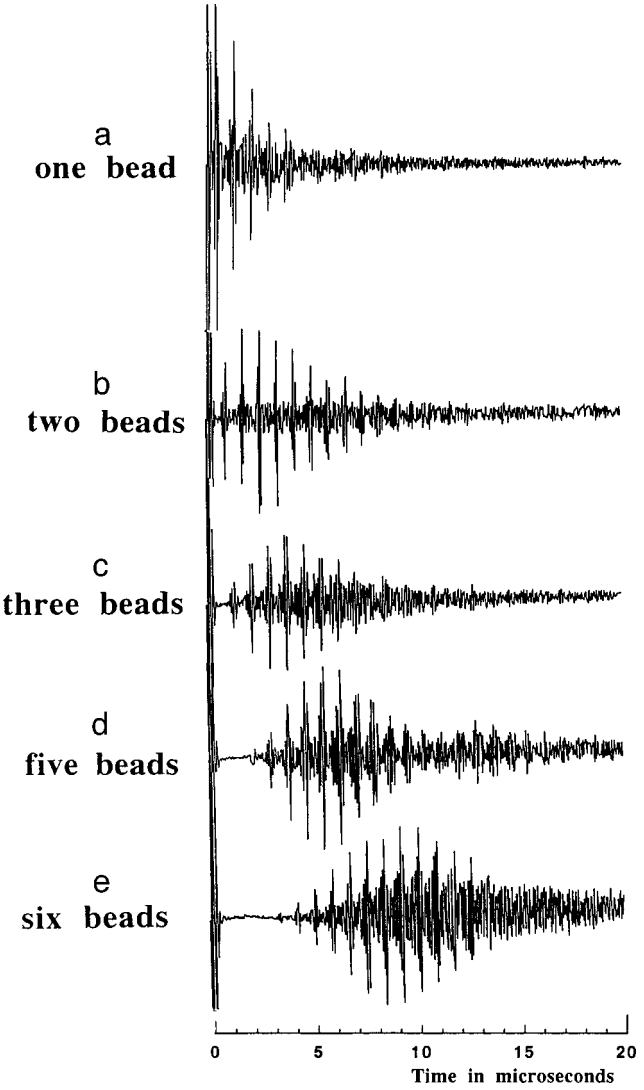

FIG. 8. Evolution of the transmitted wave form as a function of the number of beads in the chain (steel spheres of 8 mm in diameter). Vertical scale: (a) 50 mv/div; (b), (c) and (d) 20 mv/div, and (e) 10 mv/div.

conditions—of the increase of the amplitude of the echoes as the distance traveled by the surface acoustic wave increases; this is in contradiction with the fact that the SSAW attenuates as it propagates. The experimental data reveal that the amplitude variations of the echoes depend on the number of the spheres, on the material and also on the radius. The wave forms redrawn in Figs. 8–10 illustrate these observations. Figure 8 shows the evolution of the transmitted acoustical wave form as a function of the number of the beads in the chain made up of steel spheres of 8 mm in diameter. The data plotted in Figs. 9(a) and (b) were obtained, respectively, with two spheres of 8 mm in diameter and of different material: steel and glass, respectively. The wave trains represented in Fig. 10 were recorded, respectively, with four steel and glass spheres of 5 mm in diameter.

In these figures, we may notice the regular time spaced position of the echoes and also the increasing amplitude of the echoes, except in the Figs. 8(a) and 9(b) in which the amplitude of the successive signals decreases continuously.

In the following, in order to justify the amplitude variations of the echoes we suggest an elementary interpretation based on the attenuation of the SSAW as they propagate around the spheres. Let us call N_i the number of realizations that the SSAW may execute in order to travel a given distance $L_i=2\pi a p_i$ where p_i represents the circumferences around the spheres before being detected. This number N_i increases drastically with the number of the beads. In a first approximation, we have considered that the amplitude A_i of the echo E_i (which corresponds to a given time t_i) may be evaluated as the product of N_i times the amplitude a_i of the acoustic wave which traveled the distance L_i. The evaluation of the amplitude a_i as a function of the distance L_i, was obtained from the amplitude measurements of the echoes detected after one, two,...,p_i paths around one sphere. Experimental wave forms are given in Figs. 11(a)–(d); these plots are obtained with one sphere of different materials: steel, glass, brass and nylon, respectively. The experimental attenuation curves, deduced from the previous records, are reported in Fig. 12 for steel, glass and brass spheres. A comparison between the three plots confirms that the brass material attenuates the SSAW much more than the glass and steel beads which is in agreement with the results published in the literature.[19–21]

The values of the amplitude $A_i(=N_i a_i)$ obtained from the attenuation measurements should be compared with the amplitude (A_1') directly measured on the acoustic signals recorded after the SSAW have traveled the whole chain. Numerical comparisons between these two determinations are given in Tables II and III for different chains made up, respectively, with two steels beads of 8 mm in diameter and with four steel spheres of 5 mm in diameter. In Figs. 13(a) and (b) are compared the normalized amplitudes A_i and A_i' as a function of the echo number (E_i) for the two investigated chains. Although these two determinations do not

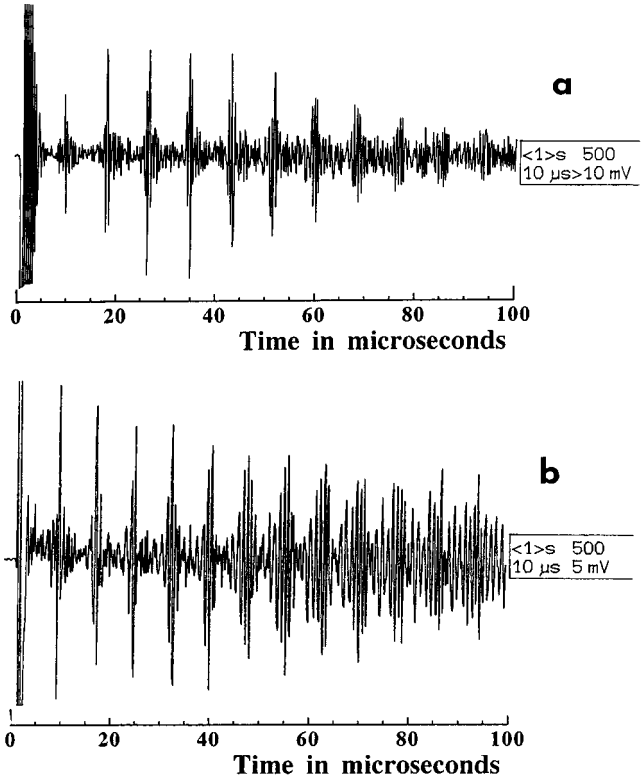

FIG. 9. Acoustic wave forms obtained with two steel beads (a) and glass beads (b); $d=8$ mm.

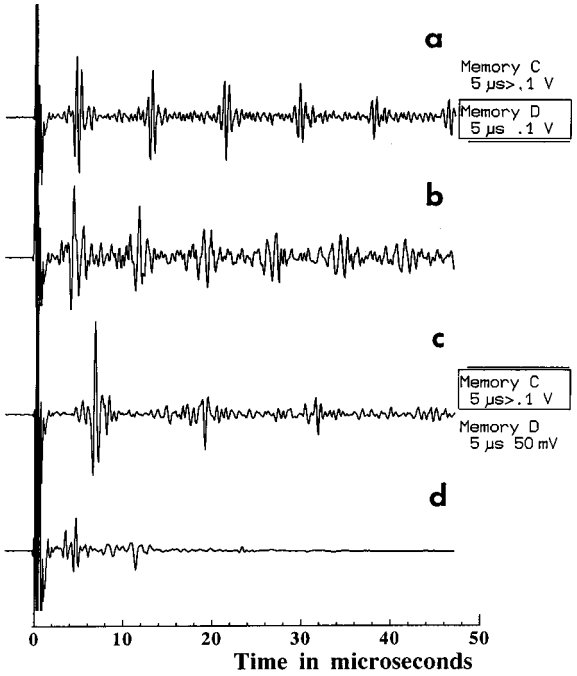

FIG. 11. Acoustic wave forms obtained with different materials for the attenuation measurements ($F_0=20$ N and $d=8$ mm). (a) Case of a steel bead (b) Case of a brass bead (c) Case of a glass bead (d) Case of a nylon bead.

agree very well, the existence of a maximum of the amplitude is clearly demonstrated in both cases which justifies the shape of the wave form which is experimentally observed in case of an acoustic pulse transmitted through a chain of identical spherical beads. This elementary explanation does not take into account the reflection and the transmission coefficients at the contact points. This problem which is directly related to the friction effects should be developed to get a better realistic behavior at the poles and a better agreement between the two determinations of the amplitude of the echoes.

IV. TRANSVERSAL EXCITATION AND DETECTION

In this section, we analyze the acoustic signal transmitted through an array of beads submitted to a sinusoidal and transversal excitation and we discuss the origin of the low frequency component observed in the wave form.

A. Experimental observations

The generation of shear waves with contact transducers of 2.2 MHz in central frequency yields transmitted signals the wave form of which are very different from the one observed with longitudinal excitation. This is illustrated in Fig. 14 which shows the influence of the polarization of the transmitters on the detected acoustic signal. The static force ($F_0=30$ N) is constant for the two recordings and the chain is made up with 15 steel beads of 5 mm in diameter. In Fig. 14(a), the emitters are both transversally polarized and longitudinally polarized in Fig. 14(b). The first plot carries out a very low frequency signal (typically few tenths of kHz) the structure of which shows a large Gaussian type shape pulse

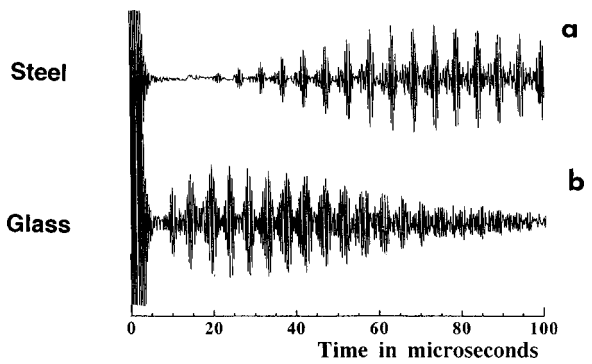

FIG. 10. Acoustic wave forms obtained with four steel beads (a) and four glass beads (b); $d=5$ mm. (a) 10 mv/div and (b) 5 mv/div.

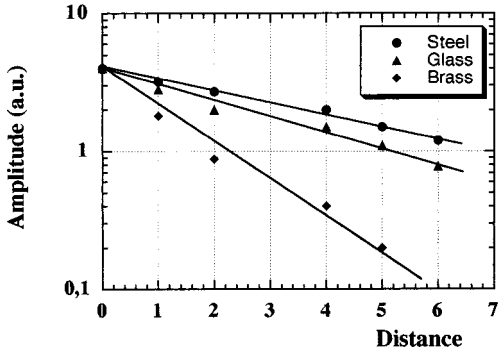

FIG. 12. Experimental attenuation measurements of the signal detected after one, two, three,... travels around one sphere.

TABLE II. A comparison between the amplitudes (A_i) of the echoes E_i obtained from the attenuation measurements and the amplitudes (A_i') of the echoes E_i measured directly on the acoustic signal. p_i represents the number of circumferences traveled by the SSAW around the spheres (the case of two steel beads of 8 mm in diameter).

Echo number (E_i)	Number of circumferences (p_1)	Realization number (N_i)	Normalized amplitude $A_i = N_i a_i$	Normalized amplitude A_i'
1	1	1	54	52
2	2	2	87	79
3	3	3	98	100
4	4	4	100	98
5	5	5	95	84
6	6	6	86	71
7	7	7	78	53
8	8	8	65	42

followed by oscillations, the amplitude of which decreases with time. The second wave form [Fig. 14(b)] reveals the presence of high frequency signals.

1. Influence of the frequency of excitation

The experimental data confirm that the value of the frequency of the low frequency wave form (described above) is the same whatever is the excitation frequency as long as the other experimental conditions are identical.

2. Influence of the number of the beads in the array

With our experimental device, the amplitude of the detected signals is very small and the shape of the wave form is directly related to the number of the beads in the chain as it is confirmed in Figs. 15, which represent the evolution of the acoustic wave form as a function of the length (L) of the chain ($L = 8$ N in mm, with $n = 1$ to 7, respectively, in Fig. 15). In these experiments, the steel spheres are submitted to a constant normal static force ($F_0 = 30$ N). We notice that the superimposed high frequency component is shifted and decreases as the number of beads increases, giving rise to a perfectly smooth low frequency signal.

TABLE III. A comparison between the amplitudes (A_i) of the echoes E_i obtained from the attenuation measurements and the amplitudes (A_i') of the echoes E_i measured directly on the acoustic signal. p_i represents the number of circumferences traveled by the SSAW around the spheres (the case of four steel beads of 5 mm in diameter).

Echo number (E_i)	Number of circumferences (p_i)	Realization number (N_i)	Normalized amplitude $A_i = N_i a_i$	Normalized amplitude A_i'
1	2	1	3	⋯
2	3	4	10	5
3	4	10	21	10
4	5	21	33	20
5	6	35	49	28
6	7	56	63	43
7	8	84	76	64
8	9	120	87	74
9	10	165	93	92
10	11	210	95	97
11	12	276	100	100
12	13	354	99	97
13	14	445	100	89
14	15	550	100	89
15	16	670	97	82
16	17	806	91	77

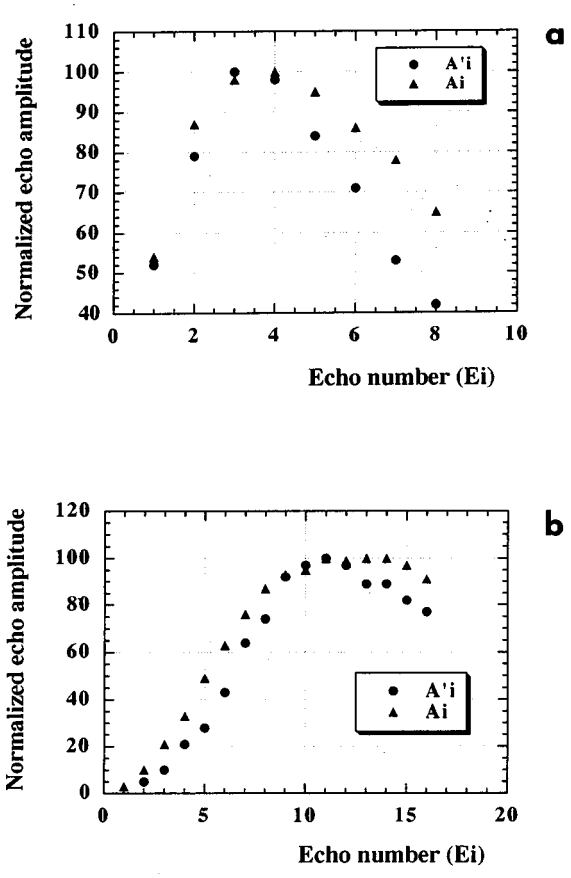

FIG. 13. A comparison between the two determinations of the amplitude A_i and A_1' of the echoes E_i.

3. Influence of the radius of the beads

In Fig. 16 are plotted the signals recorded for different values of the radius of the steel beads which make up the chain submitted to investigation. The normal force is con-

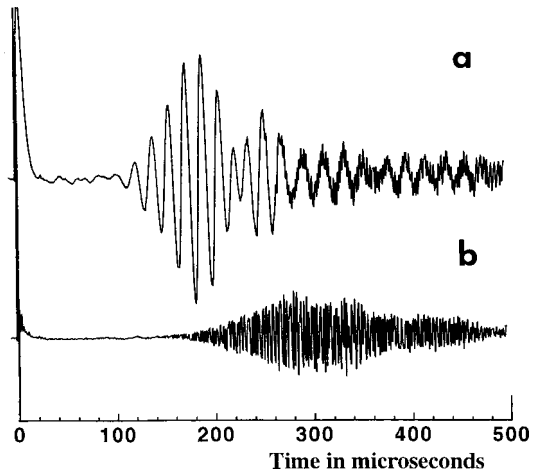

FIG. 14. Typical wave forms observed with identical transmitters (case of 15 beads of 5 mm in diameter; 10 mv/div): (a) Transversal excitation and detection. (b) Longitudinal excitation and detection.

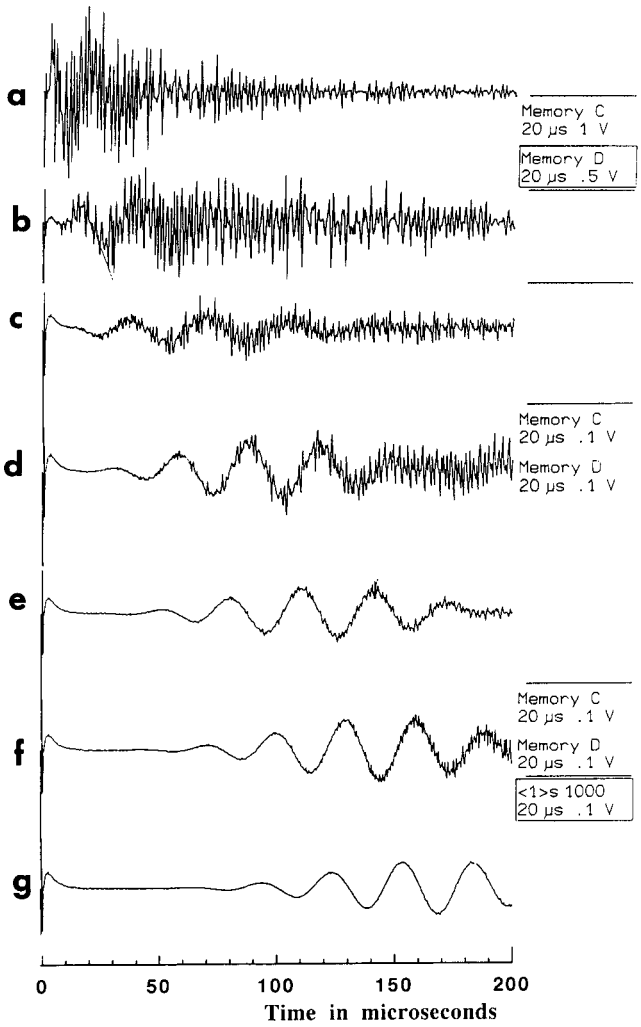

FIG. 15. Evolution of the acoustic signal as a function of the length (L) of the chain (steel beads of 8 mm in diameter and $F_0=20$ N): (a) $L=8$ mm; (b) $L=16$ mm; (c) $L=24$ mm; (d) $L=32$ mm; (e) $L=40$ mm; (f) $L=48$ mm; (g) $L=56$ mm.

stant ($F_0=30$ N) and the value of the length of the chain is roughly the same as it is indicated in Table IV. From these recordings, it may be concluded that the cut-off frequency of the chain decreases as the radius of the spherical beads increases.

4. Influence of the material

The experimental variations of the cut-off frequency (f_c) as a function of the normal static force F_0 (in Newtons) are plotted in Fig. 17(a) for two different kinds of spheres (brass and steel). The diameter of the beads is 8 mm and the common length of the chains is 48 mm. Similar data are obtained with glass and steel balls of 5 mm in diameter [Fig. 17(b)] and the length of the chain is 40 mm. We notice that ordinates scaling is changed in Fig. 17(b) which is justified by the changing of the diameter of the spheres between the two series of experiments. Referring to these experimental data, it is verified that the variations of f_c as a function of F_0 are the same whatever the medium of propagation and the value of the radius of the beads.

B. Analysis of the experimental results

Taking into account the experimental observations reported in the previous section, two origins may be suggested for the interpretation of the low frequency component: a possible mechanism socalled ''second (or Brillouin) precursor'' and a dynamic approach in which the chain is considered as a linear array of masses coupled by springs of stiffness constant C_T.

1. Second or "Brillouin precursor"

The treatment of electromagnetic wave in a dispersive medium was originally examined by Brillouin,[22] the results that he obtained are sufficiently general so that they can be used for elastic waves. It was demonstrated that the evaluation of the amplitude of the field can be achieved by calculating integrals with the stationary phase technique.[23,24] In these references it is shown that the dominant contributions to the integrals exist when the phase is stationary. Then evaluating and summing the contributions of the integrals in the neighborhood of each point of stationary phase, a good approximation of the amplitude of the field is obtained. In fact the calculations pointed out that the integrals are dominated by two regimes of frequency which correspond to the existence of two signals or ''precursors'' (cf. Fig. 7.16 in Ref. 23) the properties of which are briefly reminded. The amplitude of the first (or Sommerfeld) precursor is very small and its frequency is high. The second (or Brillouin) precursor of larger amplitude appears when the frequency goes to zero; its frequency depends on the properties of the medium and increases with time. Moreover, it can be mathematically justified that this precursor decays as the time increases.

By considering the experimental recorded wave trains (for example, see Figs. 15 and 16), it appeared interesting to consider these precursors as a possible mechanism for the interpretation of the wave forms. However, the low frequency components of these experimental records do not verify the properties of a second precursor: the frequency does not increase and the amplitude does not exponentially decreases as soon as the precursor is created as it is illustrated in Fig. 7.18 of Ref. 23. For these reasons, we considered that the precursors could not be held for the interpretation of the investigated echo wave forms.

2. Study of the dynamics of the chain

The other possibility for the identification of the signal is to consider that it is a ''chain mode'' due to the one-dimensional periodicity of the medium.[8,9,25,26] In the following we give a sketch of the theoretical approach which is concerned by this problem.

Consider two identical perfectly elastic spherical beads in contact and submitted to a constant static force F_0 which is applied along their axis. Assuming that a tangential force (F_T) is superimposed to the static loading and that there is no slip between the bodies, it was demonstrated[8,13,14] that the compliance of the two identical beads is written as

$$C_T=\frac{\delta_T}{F_T}=\frac{2-\nu}{4\mu R}, \tag{1}$$

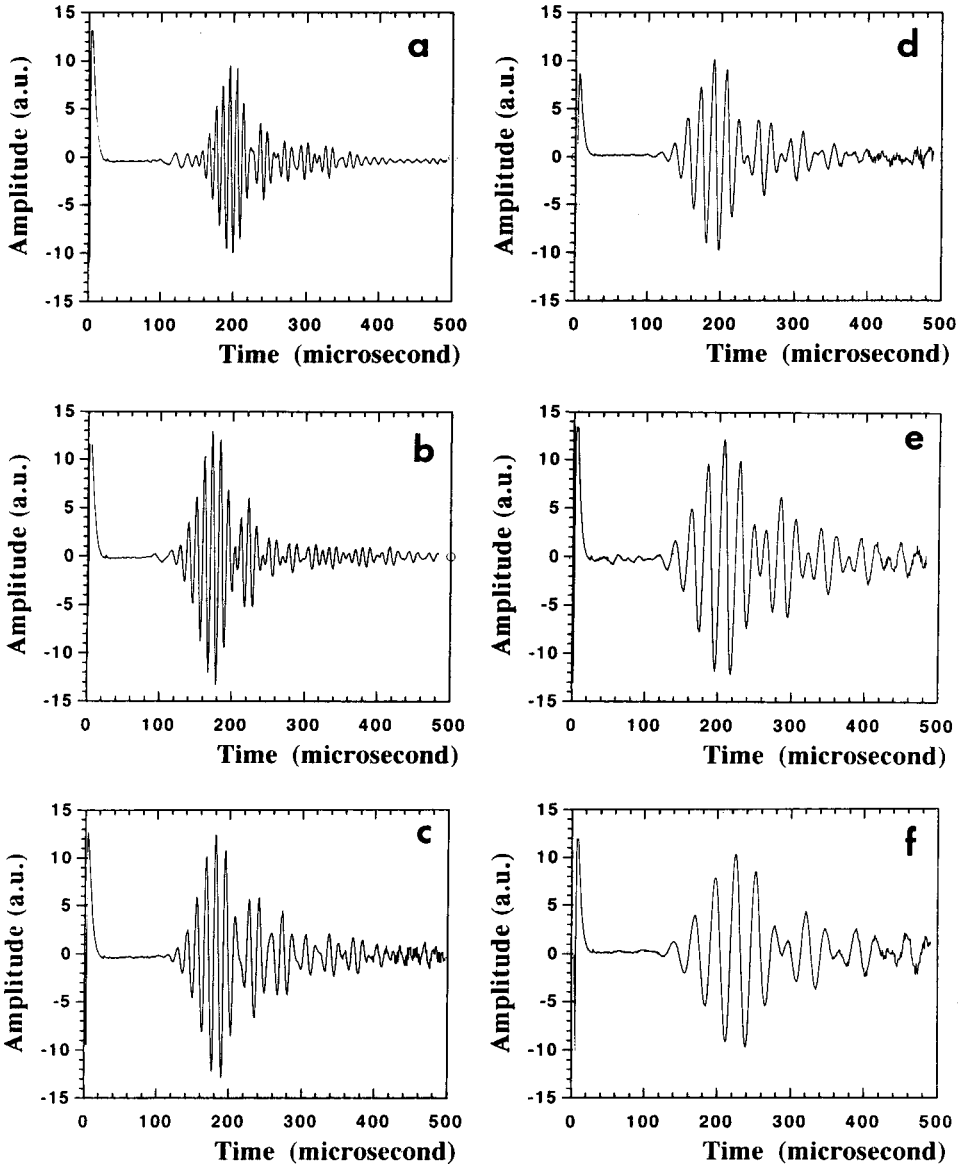

FIG. 16. Influence of the radius of the beads on the low frequency signals (see Table IV); $F_0=30$ N.

where μ is the modulus of rigidity, ν is the Poisson's ratio, R is the radius of the contact circle $=(\theta F_0 a)^{1/3}$, with $\theta=3(1-\nu^2)/4E$ (E designates the Young's modulus of the material).

In Table V are given orders of magnitude of the contact radius for different materials of the beads ($a=4$ mm and $F_0=30$ N).

In a linear approximation, the dynamics of the chain may be described by an array of identical masses coupled with linear springs of constant C_T. The well known theory developed for this kind of periodic structure confirms the existence of a cut-off frequency (f_c) of the chain. The angular frequency ω_c above which no wave propagates is given by

$$\omega_c=2\pi f_c=2\sqrt{1/\mathbf{C}_T\mathbf{m}}, \tag{2}$$

where $m=\frac{4}{3}\pi a^3\rho$ is the mass of the spheres and ρ the density of the material.

Carrying out the expressions of C_T [Eq. (1)] and m in Eq. (2), we get the following expression for the cut-off frequency:

$$f_c=\frac{1}{\pi}\left[\frac{3}{2\pi(1+\nu)(2-\nu)}\right]^{1/2} \times[\tfrac{3}{4}(1-\nu^2)]^{1/6}\rho^{-1/2}E^{1/3}a^{-4/3}F_0^{1/6}. \tag{3}$$

This theoretical relationship based on the Hertz' theory of contact predicts proportionality of the cut-off frequency to the sixth root of the compressional loading and to the minus four-third root of the radius of the sphere. The medium de-

TABLE IV. A description of the arrays used for the study of the variations of the cut-off frequency versus the radius of the beads.

Figure 16	Diameter in mm	Number of beads	Length in mm
a	3	29	87
b	3.5	22	77
c	4	19	76
d	5	15	75
e	6	13	78
f	7	11	77

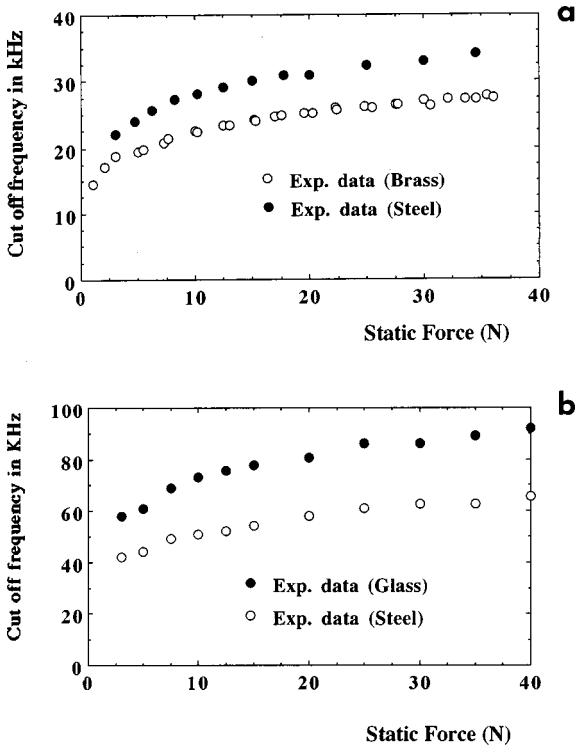

FIG. 17. Experimental curves showing the variations of $f_c(F_0)$ for two different materials: (a) Brass and steel beads ($d=8$ mm and $L=48$ mm); (b) glass and steel beads ($d=5$ mm and $L=40$ mm).

pendence is more complicated because it takes into account simultaneously the E, ρ and ν dependencies.

C. Comparison between theory and experiments

In Fig. 18 are compared the theoretical and the experimental dependencies of f_c as a function of the radius (a) of the spheres. The data indicate a reasonably good agreement with the theoretical variations which confirms the $-4/3$ power dependence of the frequency of the LF signal as a function of the radius of the beads.

In Figs. 19 are plotted the curves $f_c(F_0)$ obtained experimentally for steel [Fig. 19(a)] and brass [Fig. 19(b)], respectively. For comparison, we have indicated the corresponding theoretical values for two different power law dependences of the static loading F_0, $F_0^{1/6}$ and $F_0^{1/4}$. Some authors[6,8,27,28] mentioned that the experimental results indicated that the 1/6 power law changes for a lower static force and that the experimental measurements of the sound velocity (which is proportional to the frequency) scales as $F^{1/4}$. This observation which gave rise to different theoretical models (the modified Hertz' law[8] and the ''soft shell'' model[27]) is clearly verified in Fig. 19. In these pictures we observe that the agreement between the power law $F_0^{1/4}$ and the experimental data is better than with the power law $F_0^{1/6}$

TABLE V. Order of magnitude of the contact radius for the materials used in the experiments ($a=4$ mm and $F_0=30$ N).

Material	Steel	Brass	Glass	Nylon
Contact radius in mm	0.07	0.09	0.10	0.28

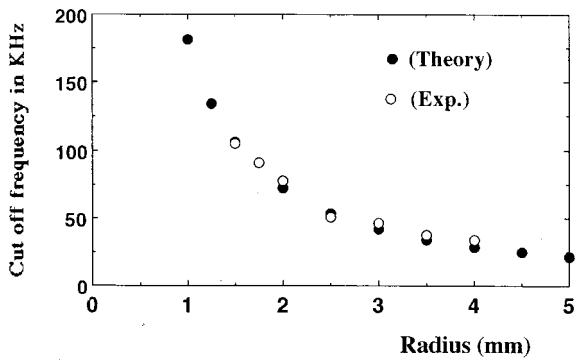

FIG. 18. A comparison between the experimental and the theoretical variations of the cut-off frequency as a function of the radius of the beads [f_c (a)]; case of steel beads. ($F_0=30$ N).

for both samples which is probably due to the fact that the applied static force is small.

V. CONCLUSION

In conclusion, it was shown that the response of a limited chain of elastic spherical beads submitted to a normal static loading is strongly dependent on the polarization of the acoustic transmitters which generates and receives the signals. In case of a compressional excitation and detection, the main feature of the results is the generation of SSAW which propagate around the spheres and the amplitude of which depends on the traveled path and on the attenuation of the

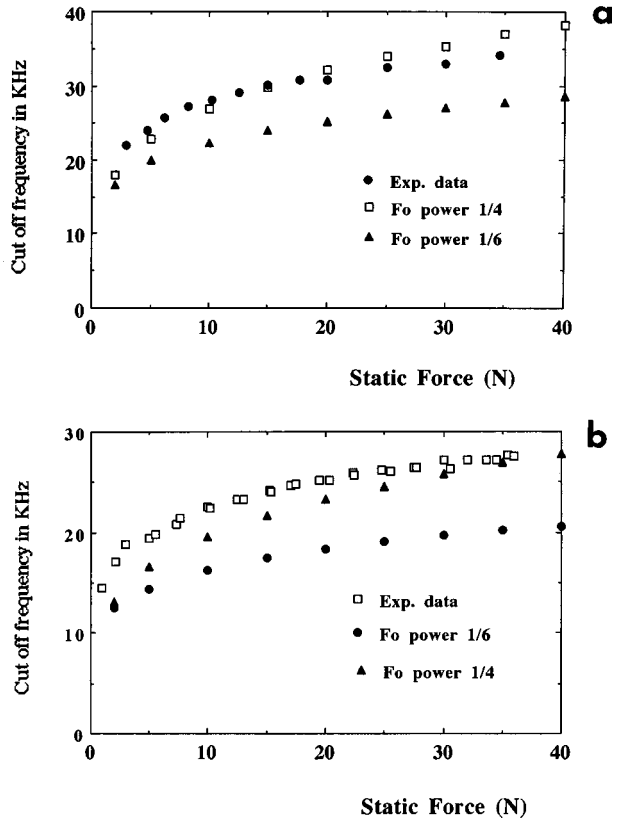

FIG. 19. A comparison between the experimental and the theoretical variations of the cut-off frequency as a function of the static force [$f_c(F_0)$]: (a) Case of steel spheres. (b) Case of brass spheres.

spherical surface acoustic waves. When the oscillating excitation is tangential, the acoustic signals carry out a wave form the frequency of which corresponds to the cut-off frequency of the chain. The use of the Hertz' contact theory yields a satisfactory interpretation of the generation of this ''chain mode.'' In addition the experimental measurements confirm that, in the range of the applied static loading, the frequency dependence as a function of the normal force varies better as $F_0^{1/4}$ than $F_0^{1/6}$.

[1] N. M. Jaeger and S. R. Nagel, ''Physics of the granular state,'' Science **255**, 1521–1531 (1992).
[2] C. Liu and S. A. Nagel, ''Sound in sand,'' Phys. Rev. Lett. **68**, 2301–2304 (1992).
[3] F. Radjai, D. E. Wolf, M. Jean, and J. J. Moreau, ''Bimodal character of stress transmission in granular packings,'' Phys. Rev. Lett. **80**, 61–64 (1997).
[4] A. N. Bogdanov and A. T. Skvortsov, ''Nonlinear process in granular medium,'' *Research Trends in Physics Nonlinear Acoustics*, edited by K. A. Nangol'nykn and L. A. Ostrovsky, La Jolla International School of Physics, The Institute for Advanced Physics Studies, La Jolla, California, 1994.
[5] M. Peyrard, ''Introduction to solitons and their applications in physics and biology,'' *Nonlinear Excitation in Biomolecules*, edited by M. Peyrard, Les Editions de Physique (Springer-Verlag, Berlin, 1995).
[6] X. Jia, C. Caroli, and B. Velicky, ''Ultrasound propagation in externally stressed granular media,'' Phys. Rev. Lett. **82**, 1863–1866 (1999).
[7] C. Coste, E. Falcon, and S. Fauve, ''Solitary waves in a chain of beads under Hertz contact,'' Phys. Rev. B **56**, 6104–6117 (1997).
[8] C. Coste and B. Gilles, ''On the validity of Hertz contact law of granular material acoustics,'' Eur. Phys. J. B **7**, 155–168 (1999).
[9] C. Coste, E. Falcon, and S. Fauve, ''Propagation d'ondes non linéaires dans une chaine de billes en contact de Hertz,'' in *Des Géomatériaux aux Ouvrages*, edited by C. Petit, G. Pijaudier-Cabot, and J. M. Reynouard (Hermès, Paris, 1995), pp. 33–52.
[10] A. N. Lazaridi and V. F. Nesterenko, ''Observation of a new type of solitary waves in a one-dimensional granular medium,'' J. Appl. Mech. Tech. Phys. **26**, 405–408 (1985).
[11] L. D. Landau and E. M. Lifshitz, *Theory of Elasticity* (Pergamon, Oxford, 1986).
[12] A. N. Bogdanov and A. T. Skvortsov, ''Nonlinear elastic waves in a granular medium,'' J. Phys. IV **C1**, 779–782 (1992).
[13] X. Duffy and R. D. Mindlin, ''Stress–strain relation and vibrations of granular medium,'' J. Appl. Mech. **X**, 585–593 (1957).
[14] R. D. Mindlin, ''Compliance of elastic bodies in contact,'' J. Appl. Mech. **X**, 259–260 (1949).
[15] A. N. Bogdanov and A. T. Skvortsov, ''Nonlinear shear waves in granular medium,'' Sov. Phys. Acoust. **38**, 224–226 (1992).
[16] K. L. Johnson, ''Surface interaction between elastically loaded bodies under tangential forces,'' Proc. R. Soc. London, Ser. A **320**, 531–549 (1955).
[17] D. Royer, E. Dieulesaint, and X. Jia, ''Optical generation and detection of surface acoustic waves on a sphere,'' Appl. Phys. Lett. **52**, 706–708 (1988).
[18] D. Royer, Y. Shui, X. Jia, and E. Dieulesaint, ''Surface waves on spheres,'' the 3rd Western Pacific Regional Acoustic Conference, 2–4 November 1988, Shanghai, China.
[19] I. A. Viktorov, *Rayleigh and Lamb Waves* (Plenum, New York, 1967).
[20] I. A. Viktorov, ''Damping of surface and spatial ultrasonic waves,'' Sov. Phys. Acoust. **10**, 91–92 (1964).
[21] K. N. Vinogradov and G. K. Ul'Yanov, ''Measurement of the velocity and attenuation of ultrasonic surface waves in hard materials,'' Sov. Phys. Acoust. **5**, 296–299 (1959).
[22] X. Brillouin, *Wave Propagation and Group Velocity* (Academic, New York, 1960).
[23] J. D. Jackson, *Classical Electrodynamics*, 2nd ed. (Wiley, New York, 1975), Sec. 7.11.
[24] P. M. Morse and K. U. Ingard, *Theoretical Acoustics* (McGraw Hill, New York, 1968), pp. 477–479.
[25] P. Plesko and I. Palocz, Phys. Rev. Lett. **22**, 1201–1204 (1969).
[26] J. M. Bretell, ''Elastic wave propagation in powders,'' Acustica **65**, 49–51 (1987).
[27] P. G. de Gennes, ''Static compression of a granular medium: the soft shell model,'' Europhys. Lett. **35**, 145–149 (1996).
[28] J. D. Goddard, ''Nonlinear elasticity and pressure dependent wave speeds in granular media,'' Proc. R. Soc. London, Ser. A **430**, 105–131 (1991).

Analyses of axisymmetric waves in layered piezoelectric rods and their composites

Adnan H. Nayfeh,[a] Wael G. Abdelrahman,[b] and Peter B. Nagy[c]
Department of Aerospace Engineering and Engineering Mechanics, University of Cincinnati, Cincinnati, Ohio 45221-0070

(Received 25 November 1999; accepted for publication 22 June 2000)

An exact treatment of the propagation of axisymmetric waves in coaxial anisotropic assembly of piezoelectric rod systems is presented. The rod system consists of an arbitrary number of coaxial layers, each possessing transversely isotropic symmetry properties. The treatment, which is based on the transfer matrix technique, is capable of deriving the dispersion relations for a variety of situations. These include the case of a single rod system that is either embedded in an infinitely extended solid or fluid host or kept free. The procedure is also adapted to derive approximate solutions for the cases of a periodic fiber distribution in a matrix material, which model unidirectional fiber-reinforced composites. The results are numerically illustrated for a widely used piezoelectric-polymer composite. It is seen that piezoelectric coupling can significantly change the morphology of the dispersive behavior of the composite. © *2000 Acoustical Society of America.* [S0001-4966(00)02410-3]

PACS numbers: 43.25.Cg [HEB]

I. INTRODUCTION

In a recent paper,[1] Nayfeh and Nagy presented a unified study of the propagation of axisymmetric longitudinal waves in coaxial anisotropic elastic fibers with application to a variety of their composites. The fiber bundle system consisted of an arbitrary number of coaxial layers, each possessing transverse isotropic symmetry and bonded at their interfaces in accordance with specified fashions. In the form of applications, the bundle was either embedded in an infinitely extended elastic solid or fluid host or kept free. Uniformly distributed bundles in a matrix material which model unidirectional bundle fiber-reinforced composites were also studied.

The solutions in Ref. 1 were obtained using the matrix transfer technique, originally introduced by Thomson[2] and later on enhanced by Haskell,[3] both for the study of wave interaction with layered isotropic flat media. Recently, this technique has been extensively used by a large number of investigators in a variety of wave propagation applications in layered media, often including cases of anisotropy. Most of this recent literature deals with flat layers. It is not the intent of the present work to review this vast literature. However, for the interested reader on this subject, we refer to Nayfeh.[4]

Up to quite recently, much fewer applications of the matrix transfer method to cylindrical layered media have been reported. In its application to the cylindrical systems of Ref. 1, the specific steps taken in constructing the model are summarized as follows: formal solutions in terms of Bessel functions are first obtained for each layer in terms of its displacement amplitudes. By specializing these solutions to the outer and inner faces (radii) of the layer, followed by eliminating the common displacement amplitudes, the local transfer matrix for the layer is constructed. This matrix relates the field variables (the displacements and stress components) of one face of the layer to its other one. Such a matrix relation can be used, in conjunction with satisfying appropriate interface conditions across neighboring layers, to directly relate the field variables at the inner face of one layer to the outer face of its outer neighbor. When this procedure is carried out consecutively for all layers in the bundle, a global transfer matrix, the product of the individual transfer matrices, results, which relates the field variables at the outer face of the bundle to those at its inner face or vice versa.

The global matrix is then used for all of the specific applications outlined above. For cases involving infinite solid or fluid hosts, the formal solution for the host has to be specialized to insure satisfying the radiation conditions far away from the bundle–host interface; this requires the field variables to stay bounded deep in the host. If the inner component of the bundle is solid with no concentric hole, its local transfer matrix has to be adjusted such that its field variables will not encounter the usual singularities. Finally, in simulating the bundle fiber-reinforced composite, the repeating hexagonal unit cell of the composite is isolated, approximated by a concentric cylindrical system and, due to its inherent symmetry, the vanishing of the radial displacement and shear stress components are imposed on its outer boundary.

The aim of the present article is to extend the results of Ref. 1 and present a parallel treatment for rod-bundle systems including piezoelectric effects. This problem has diverse applications in fields such as medical composite transducer design, fiber optics, signal processing, and nondestructive testing. Up to quite recently, it was believed that cylindrical geometry, together with piezoelectric coupling (which is inherently anisotropic), lead to algebraic complications in the attempt of obtaining exact solutions. That is perhaps why exact treatments of problems dealing

[a]Electronic mail: anayfeh@uceng.uc.edu
[b]Electronic mail: abdelrwl@email.uc.edu
[c]Electronic mail: pnagy@uceng.uc.edu

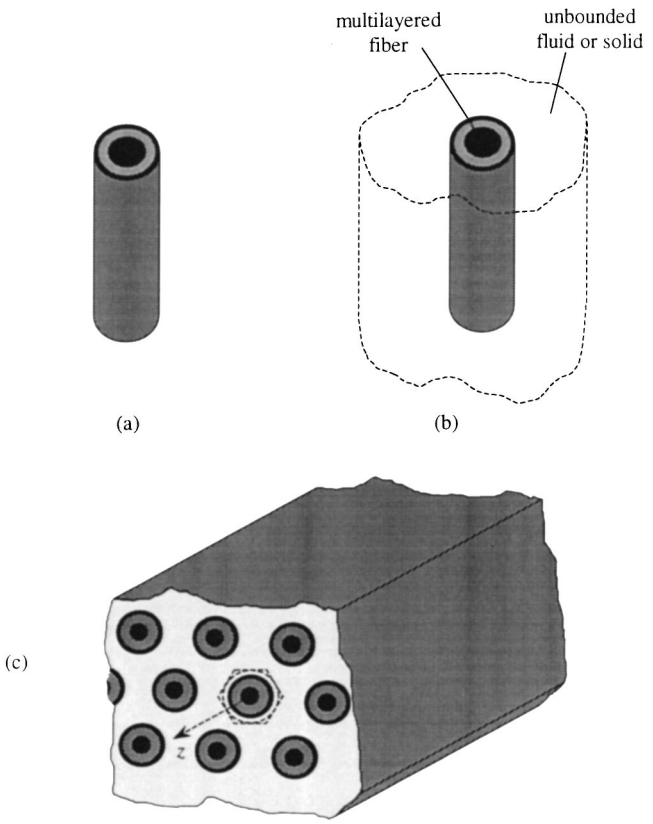

FIG. 1. Schematic diagram of (a) a single free multilayered rod, (b) a single multilayered rod embedded in a solid host or immersed in a fluid, and (c) an infinite unidirectional fibrous reinforced composite with periodically distributed multilayered fibers.

with piezoelectric rods are relatively rare. Nevertheless, our literature search revealed some limited, but relevant, publications that deal with exact analyses of piezoelectric rods.[5,6] Reference 5 treats vibrations of circular cylindrical shells and Ref. 6 develops exact solutions for waves in a single infinitely clad rod. For the interested reader, there is, however, a relatively larger body of literature that exists for the treatment of wave interaction with flat layered piezoelectric systems. Once again, while it is not the intent of the present work to give a complete account of this literature, we draw attention to some recent samples.[4,7–10]

II. FORMULATION OF THE PROBLEM

A. Field equations

Consider the multilayered rod systems of Fig. 1. Schematic 1(a) represents a single free multilayered rod, whereas Fig. 1(b) shows the case of a single multilayered rod embedded in an unbounded solid host or immersed in an unbounded fluid. Figure 1(c) shows the case of a periodic distribution of multilayered fibers in a fibrous-reinforced composite. Each of the rods of Fig. 1 consists of an arbitrary number p of transversely isotropic layers rigidly bonded at their interfaces and lined up such that their axes of symmetry coincide with each other and also with the reference coordinate axis z. The layers are consequently numbered 1,2,...,p from the host solid as shown in Fig. 2. In our subsequent

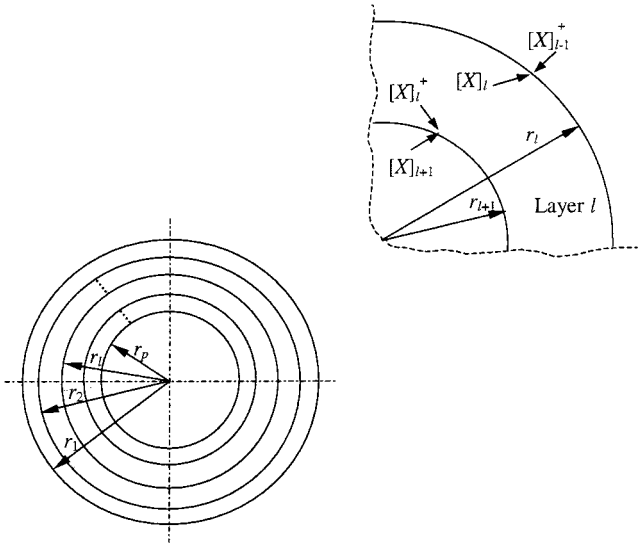

FIG. 2. Geometry of the multilayered system.

discussions, we reserve the subscripts ''h'' and ''f'' to designate the solid host material and fluid, respectively.

The outer surface of a typical layer l is located at the location $r=r_l$ measured from the center of the cylinder. It follows that the thickness of layer l will be r_l-r_{l+1} and hence the total radius of the cylinder will be r_1, i.e., the distance to the location of the host–rod interface.

With these restrictions on the geometry and the propagation directions for longitudinal waves, the motion is reduced to an axisymmetric one. Here, the displacement component u_θ vanishes and the remaining field variables are independent of θ. The relevant piezoelectric field equations which hold for each layer and also for the solid host consist of the following:

(i) the momentum equations

$$\frac{\partial \sigma_r}{\partial r}+\frac{\partial \sigma_{rz}}{\partial z}+\frac{1}{r}(\sigma_r-\sigma_\theta)=\rho\frac{\partial^2 u_r}{\partial t^2}, \tag{1a}$$

$$\frac{\partial \sigma_z}{\partial z}+\frac{1}{r}\frac{\partial}{\partial r}(r\sigma_{rz})=\rho\frac{\partial^2 u_z}{\partial t^2}, \tag{1b}$$

and the charge equation of electrostatics

$$\frac{\partial D_z}{\partial z}+\frac{1}{r}\frac{\partial}{\partial r}(rD_r)=0; \tag{2}$$

(ii) the coupled constitutive relations

$$\sigma_{ij}=c_{ijkl}^{E}S_{kl}-e_{kij}E_k, \tag{3a}$$

$$D_i=e_{ikl}S_{kl}+\varepsilon_{ik}^{S}E_k; \tag{3b}$$

(iii) the strain-mechanical displacement relations

$$S_r=\frac{\partial u_r}{\partial r},\quad S_\theta=\frac{u_r}{r},$$
$$S_z=\frac{\partial u_z}{\partial z},\quad S_{rz}=\frac{1}{2}\left(\frac{\partial u_z}{\partial r}+\frac{\partial u_r}{\partial z}\right), \tag{4}$$

and the electric field-electric potential relations

$$E_r=-\frac{\partial\phi}{\partial r},\quad E_z=-\frac{\partial\phi}{\partial z}. \tag{5}$$

In our subsequent analysis, we shall allow the subscripts r, θ, z to be synonymous with 1, 2, 3, respectively. We also recognize that σ_r, σ_z, S_r, and S_z are conveniently constructed and stand for σ_{rr}, σ_{zz}, S_{rr}, and S_{zz}, respectively. In Eqs. (1)–(5) we then have $i,j,k,l=1,2,3$; σ_{ij}, u_i, D_i, S_{ij}, E_i are the components of stress, mechanical displacement, electric displacement, mechanical strain, and electric field, respectively; ρ and ϕ are the mass density and the electric potential; c^E_{ijkl} are the elastic moduli for a constant electric field; ε^S_{ik} are the dielectric coefficients for a constant strain field, and e_{kij} are the piezoelectric constants.

The elastic, piezoelectric, and dielectric constants for the transversely isotropic piezoelectric system are given in the expanded matrix forms

$$C^E_{pq}=\begin{bmatrix} C^E_{11} & C^E_{12} & C^E_{13} & 0 & 0 & 0\\ C^E_{12} & C^E_{11} & C^E_{13} & 0 & 0 & 0\\ C^E_{13} & C^E_{13} & C^E_{33} & 0 & 0 & 0\\ 0 & 0 & 0 & C^E_{44} & 0 & 0\\ 0 & 0 & 0 & 0 & C^E_{44} & 0\\ 0 & 0 & 0 & 0 & 0 & C^E_{66} \end{bmatrix}, \tag{6}$$

where

$$2C^E_{66}=(C^E_{11}-C^E_{12}),$$

$$e_{ip}=\begin{bmatrix} 0 & 0 & 0 & 0 & e_{15}\\ 0 & 0 & 0 & e_{15} & 0\\ e_{31} & e_{31} & e_{33} & 0 & 0 \end{bmatrix}, \tag{7}$$

$$\varepsilon^S_{ij}=\begin{bmatrix} \varepsilon^S_{11} & 0 & 0\\ 0 & \varepsilon^S_{11} & 0\\ 0 & 0 & \varepsilon^S_{33} \end{bmatrix}, \tag{8}$$

which reflects the usual renaming of c_{ijkl}, $i,j,k,l=1,2,3$, as C_{pq}, $p,q=1,2,...,6$. For simplicity of notation, we shall thereafter suppress the superscripts E and S in the equations (6) and (8). According to the above relations, the constitutive equations (3) take the expanded forms

$$\sigma_r=C_{11}\frac{\partial u_r}{\partial r}+C_{12}\frac{u_r}{r}+C_{13}\frac{\partial u_z}{\partial z}+e_{31}\frac{\partial\phi}{\partial z}, \tag{9a}$$

$$\sigma_z=C_{13}\frac{1}{r}\frac{\partial}{\partial r}(ru_r)+C_{33}\frac{\partial u_z}{\partial z}+e_{33}\frac{\partial\phi}{\partial z}, \tag{9b}$$

$$\sigma_{rz}=C_{44}\left(\frac{\partial u_z}{\partial r}+\frac{\partial u_r}{\partial z}\right)+e_{15}\frac{\partial\phi}{\partial r}, \tag{9c}$$

$$D_r=\frac{e_{15}}{2}\left(\frac{\partial u_z}{\partial r}+\frac{\partial u_r}{\partial z}\right)-\varepsilon_{11}\frac{\partial\phi}{\partial r}. \tag{9d}$$

$$D_z=e_{31}\frac{1}{r}\frac{\partial}{\partial r}(ru_r)+e_{33}\frac{\partial u_z}{\partial z}-\varepsilon_{33}\frac{\partial\phi}{\partial z}, \tag{9e}$$

which, once again, hold for all layers.

B. Solution of the equations

Details of the procedure used here are readily available in Ref. 1. For the present system, the field equations (1) and (2) are combined with the constitutive relations (9) to yield the three coupled equations

$$\begin{aligned} &C_{11}\frac{\partial^2 u_r}{\partial r^2}+\frac{C_{11}}{r}\left(\frac{\partial u_r}{\partial r}-\frac{u_r}{r}\right)+C_{44}\frac{\partial^2 u_r}{\partial z^2}\\ &\quad+(C_{13}+C_{44})\frac{\partial^2 u_z}{\partial r\partial z}+(e_{31}+e_{15})\frac{\partial^2\phi}{\partial r\partial z}=\rho\frac{\partial^2 u_r}{\partial t^2},\\ &C_{33}\frac{\partial^2 u_z}{\partial z^2}+C_{44}\left(\frac{\partial^2 u_z}{\partial r^2}+\frac{1}{r}\frac{\partial u_z}{\partial r}\right)+(C_{13}+C_{44})\\ &\quad\times\left(\frac{\partial^2 u_r}{\partial r\partial z}+\frac{1}{r}\frac{\partial u_r}{\partial z}\right)+e_{33}\frac{\partial^2\phi}{\partial z^2}+e_{15}\left(\frac{\partial^2\phi}{\partial r^2}+\frac{1}{r}\frac{\partial\phi}{\partial r}\right)\\ &\quad=\rho\frac{\partial^2 u_z}{\partial t^2},\\ &(e_{31}+e_{15})\left(\frac{\partial^2 u_r}{\partial r\partial z}+\frac{1}{r}\frac{\partial u_r}{\partial z}\right)+e_{33}\frac{\partial^2 u_z}{\partial z^2}+e_{15}\left(\frac{\partial^2 u_z}{\partial r^2}+\frac{1}{r}\frac{\partial u_z}{\partial r}\right)\\ &\quad-\varepsilon_{33}\frac{\partial^2\phi}{\partial z^2}-\varepsilon_{11}\left(\frac{\partial^2\phi}{\partial r^2}+\frac{1}{r}\frac{\partial\phi}{\partial r}\right)=0. \end{aligned} \tag{10}$$

For a wave propagating along the z direction, the formal solution for u_r, u_z, and ϕ are given, parallel to the analysis in Ref. 1, as

$$(u_r,u_z,\phi)=[U_1\beta_1(\gamma r),U_2\beta_0(\gamma r),U_3\beta_0(\gamma r)]e^{i(kz-\omega t)}, \tag{11}$$

where γ is an unknown parameter, k is the longitudinal wave number related to the frequency and phase velocity as $k=\omega/c$, and β_0 and β_1 are zeroth- and first-order Bessel functions of the first or the second kind.

Substituting this solution into Eqs. (10) yields a set of three linear homogeneous equations in the amplitudes. In matrix form, these are

$$\begin{bmatrix} \rho\omega^2-C_{11}\gamma^2-C_{44}k^2 & -ik\gamma(C_{13}+C_{44}) & -ik\gamma(e_{31}+e_{15})\\ ik\gamma(C_{13}+C_{44}) & \rho\omega^2-C_{33}k^2-C_{44}\gamma^2 & -(e_{33}k^2+e_{15}\gamma^2)\\ ik\gamma(e_{31}+e_{15}) & -(e_{33}k^2+e_{15}\gamma^2) & \varepsilon_{33}k^2+\varepsilon_{11}\gamma^2 \end{bmatrix}\begin{Bmatrix} U_1\\ U_2\\ U_3 \end{Bmatrix}=\underline{0}. \tag{12}$$

For nonzero solution of the amplitudes, the determinant of this equation must vanish. This yields a sixth-order polynomial in γ (cubic in γ^2), relating it to the radial frequency ω. It admits six solutions which we number as $\gamma_1(\omega,k)$, $\gamma_2(\omega,k)$, $\gamma_3(\omega,k)$, $\gamma_4(\omega,k)$, $\gamma_5(\omega,k)$, and $\gamma_6(\omega,k)$, where $\gamma_4=-\gamma_1$, $\gamma_5=-\gamma_2$, and $\gamma_6=-\gamma_3$. For each γ_q, $q=1,2,...,6$, Eq. (12) yields the amplitude ratios $V_q=U_{2q}/U_{1q}$ and $W_q=U_{3q}/U_{1q}$, $q=1,2,...,6$, as

$$V_q=\frac{k^2\gamma_q^2(C_{13}+C_{44})(e_{31}+e_{15})+(\rho\omega^2-C_{11}\gamma_q^2-C_{44}k^2)(e_{33}k^2+e_{15}\gamma_q^2)}{ik\gamma_q[(C_{13}+C_{44})(e_{33}k^2+e_{15}\gamma_q^2)+(\rho\omega^2-C_{33}k^2-C_{44}\gamma_q^2)(e_{31}+e_{15})]},$$
$$W_q=\frac{(\rho\omega^2-C_{11}\gamma_q^2-C_{44}k^2)(\rho\omega^2-C_{33}k^2-C_{44}\gamma_q^2)-k^2\gamma_q^2(C_{13}+C_{44})^2}{ik\gamma_q[(C_{13}+C_{44})(e_{33}k^2+e_{15}\gamma_q^2)+(\rho\omega^2-C_{33}k^2-C_{44}\gamma_q^2)(e_{31}+e_{15})]}. \tag{13a}$$

Inspecting Eq. (13a) reveals the interesting and important relations

$$V_4=-V_1,\quad V_5=-V_2,\quad V_6=-V_3. \tag{13b}$$

The same relations also hold for W_q.

Using the principle of superposition, together with the constitutive relations (9), the formal solution for the relevant displacements, stresses, electric potential, and electric displacement in each layer l are combinations of Bessel functions of the first and second kind. These formal solutions can be written in the expanded matrix form

$$\begin{Bmatrix} u_r \\ u_z \\ \phi \\ \sigma_r \\ \sigma_{rz} \\ D_r \end{Bmatrix}_l = \begin{bmatrix} J_1(\gamma_1 r) & Y_1(\gamma_1 r) & J_1(\gamma_2 r) & Y_1(\gamma_2 r) & J_1(\gamma_3 r) & Y_1(\gamma_3 r) \\ V_1 J_0(\gamma_1 r) & V_1 Y_0(\gamma_1 r) & V_2 J_0(\gamma_2 r) & V_2 Y_0(\gamma_2 r) & V_3 J_0(\gamma_3 r) & V_3 Y_0(\gamma_3 r) \\ W_1 J_0(\gamma_1 r) & W_1 Y_0(\gamma_1 r) & W_2 J_0(\gamma_2 r) & W_2 Y_0(\gamma_2 r) & W_3 J_0(\gamma_3 r) & W_3 Y_0(\gamma_3 r) \\ D_{11} & \bar{D}_{11} & D_{12} & \bar{D}_{12} & D_{13} & \bar{D}_{13} \\ D_{21} & \bar{D}_{21} & D_{22} & \bar{D}_{22} & D_{23} & \bar{D}_{23} \\ D_{31} & \bar{D}_{31} & D_{32} & \bar{D}_{32} & D_{33} & \bar{D}_{33} \end{bmatrix}_l \begin{Bmatrix} A_1 \\ \bar{A}_1 \\ A_2 \\ \bar{A}_2 \\ A_3 \\ \bar{A}_3 \end{Bmatrix}_l, \tag{14}$$

where

$$D_{1q}=(C_{11}\gamma_q+ikC_{13}V_q+ike_{31}W_q)J_0(\gamma_q r)-(C_{11}-C_{12})\frac{J_1(\gamma_q r)}{r},$$
$$\bar{D}_{1q}=(C_{11}\gamma_q+ikC_{13}V_q+ike_{31}W_q)Y_0(\gamma_q r)-(C_{11}-C_{12})\frac{Y_1(\gamma_q r)}{r},$$
$$D_{2q}=(ikC_{44}-C_{44}V_q\gamma_q-e_{15}W_q\gamma_q)J_1(\gamma_q r),$$
$$\bar{D}_{2q}=(ikC_{44}-C_{44}V_q\gamma_q-e_{15}W_q\gamma_q)Y_1(\gamma_q r), \tag{15}$$
$$D_{3q}=(ike_{15}-e_{15}V_q\gamma_q+\varepsilon_{11}W_q\gamma_q)J_1(\gamma_q r),$$
$$\bar{D}_{3q}=(ike_{15}-e_{15}V_q\gamma_q+\varepsilon_{11}W_q\gamma_q)Y_1(\gamma_q r).$$

To facilitate our subsequent analysis, this equation is rewritten in the compact form

$$U_l=X_lA_l, \tag{16}$$

where U_l is the column matrix of the field variable components, X_l is the 6×6 square matrix in Eq. (14), and A_l is the column matrix of the wave amplitudes. This equation is supplemented with the continuity conditions

$$\begin{Bmatrix} u_r \\ u_z \\ \phi \\ \sigma_r \\ \sigma_{rz} \\ D_r \end{Bmatrix}_l = \begin{Bmatrix} u_r \\ u_z \\ \phi \\ \sigma_r \\ \sigma_{rz} \\ D_r \end{Bmatrix}_{l+1} \quad \text{at } r=r_{l+1}. \tag{17}$$

C. Local transfer matrix

Equation (14) can be specialized to the inner and outer radii $r=r_{l+1}$ and $r=r_l$ of layer l, respectively, as

$$U_l^-=X_l^-A_l \quad \text{at } r=r_l, \tag{18}$$

$$U_l^+=X_l^+A_l \quad \text{at } r=r_{l+1}. \tag{19}$$

Eliminating the common amplitude vector A_l, we relate U_l^- to U_l^+ as

$$U_l^-=M_lU_l^+, \tag{20}$$

where

$$M_l=X_l^-(X_l^+)^{-1} \tag{21}$$

is the 6×6 local individual transfer matrix for layer l, which relates the displacements, stresses, electric potential, and electric displacement at its outer surface to those at the inner surface. The superscripts $\pm$ are used here to label the inner and outer boundaries, respectively.

D. Global transfer matrix

By invoking the continuity conditions (17), we relate the stresses, displacements, electric potential, and electric displacement at the outer radius of the total system, $r=r_1$, to those at the inner radius, $r=r_p$, via the global transfer matrix M as

$$U_1^- = M U_{p-1}^+, \tag{22}$$

where

$$M = M_1 M_2 \cdots M_{p-1}. \tag{23}$$

Invoking the continuity at the interface between layer $p-1$ and the core p leads to

$$U_{p-1}^+ = U_p^-. \tag{24}$$

According to Eq. (18), for the core material we have

$$U_p^- = X_p^- A_p. \tag{25}$$

Then Eq. (22) takes the form

$$U_1^- = Q A_p, \tag{26}$$

where

$$Q = M X_p^-. \tag{27}$$

To avoid singularities at the origin in the core, the amplitudes A_1, A_2, A_3 should vanish, leading to

$$\begin{Bmatrix} u_r \\ u_z \\ \phi \\ \sigma_{rr} \\ \sigma_{rz} \\ D_r \end{Bmatrix}_l = \begin{bmatrix} Q_{11} & Q_{12} & Q_{13} & Q_{14} & Q_{15} & Q_{16} \\ Q_{21} & Q_{22} & Q_{23} & Q_{24} & Q_{25} & Q_{26} \\ Q_{31} & Q_{32} & Q_{33} & Q_{34} & Q_{35} & Q_{36} \\ Q_{41} & Q_{42} & Q_{43} & Q_{44} & Q_{45} & Q_{46} \\ Q_{51} & Q_{52} & Q_{53} & Q_{54} & Q_{55} & Q_{56} \\ Q_{61} & Q_{62} & Q_{63} & Q_{64} & Q_{65} & Q_{66} \end{bmatrix}_{sys} \begin{Bmatrix} A_1 \\ 0 \\ A_2 \\ 0 \\ A_3 \\ 0 \end{Bmatrix}_p. \tag{28}$$

For the interested reader, some interesting properties of both the local and global transfer matrices are listed in Ref. 1.

III. APPLICATIONS

A. Free multilayered rod system

We start by deriving the dispersion relation for cases involving free rods. A ''free'' rod is meant to be mechanically free, i.e., both normal σ_r and tangential σ_{rz} stresses must vanish at the surface, but it is still immersed in a dielectric medium, namely vacuum. Theoretically, the guided modes of a free piezoelectric rod become leaky at the cutoff frequencies where the phase velocity becomes infinitely high. However, the electromagnetic wavelength is so high relative to the acoustic one that electromagnetic radiation cannot occur except at these singularities and the modes are true guided waves with real wave numbers. Of course the velocity of the guided modes still could be perceivably affected by the pure imaginary electromagnetic radiation load of the surrounding vacuum, but the relative permittivity of the piezoelectric material is typically so high that the normal component of the dielectric displacement D_r can be also assumed to vanish at the ''free'' surface, which significantly simplifies the calculations. If we identify the rod outer radius r_1 with a, and invoke the free boundary conditions, namely $\sigma_r=\sigma_{rz}=D_r=0$ at $r=a$, then Eq. (28) reduces to the characteristic equation

$$\begin{vmatrix} Q_{41} & Q_{43} & Q_{45} \\ Q_{51} & Q_{53} & Q_{55} \\ Q_{61} & Q_{63} & Q_{65} \end{vmatrix}_p = 0, \tag{29}$$

relating phase velocity c to the wave number k.

B. Multilayered rod system embedded in a solid host

For cases involving a multilayered rod embedded in an infinitely extended solid host, it was shown in Ref. 1 that formal solutions in the host material are expressed in terms of Hankel functions of the first kind, namely,

$$H_n = J_n + iY_n, \tag{30}$$

since only outgoing waves are allowed physically in an unbounded medium. The formal solutions for the field variables in the host take the form

$$\begin{aligned} u_{rh} &= A_1 H_1(\gamma_{1h} a) + A_2 H_1(\gamma_{2h} a) + A_3 H_1(\gamma_{3h} a), \\ u_{zh} &= A_1 V_{1h} H_1(\gamma_{1h} a) + A_2 V_{2h} H_1(\gamma_{2h} a) \\ &\quad + A_3 V_{3h} H_1(\gamma_{3h} a), \\ \phi_h &= A_1 W_{1h} H_1(\gamma_{1h} a) + A_2 W_{2h} H_1(\gamma_{2h} a) \\ &\quad + A_3 W_{3h} H_1(\gamma_{3h} a), \end{aligned} \tag{31}$$

where a subscript h means ''specialized to the host material.'' The rest of the field variables σ_r, σ_{rz}, and D_r are calculated from Eqs. (9a), (9c), and (9d), when specialized for the host material. Applying the continuity conditions at the host–rod interface, namely

$$\begin{Bmatrix} u_r \\ u_z \\ \phi \\ \sigma_r \\ \sigma_{rz} \\ D_r \end{Bmatrix}_0 = \begin{Bmatrix} u_r \\ u_z \\ \phi \\ \sigma_r \\ \sigma_{rz} \\ D_r \end{Bmatrix}_1^- \quad \text{at } r=r_1=a, \tag{32}$$

yields the characteristic equation

$$\begin{vmatrix} Q_{11} & Q_{13} & Q_{15} & -H_1(\gamma_{1h}a) & -H_1(\gamma_{2h}a) & -H_1(\gamma_{3h}a) \\ Q_{21} & Q_{23} & Q_{25} & -V_{1h}H_0(\gamma_{1h}a) & -V_{2h}H_0(\gamma_{2h}a) & -V_{3h}H_0(\gamma_{3h}a) \\ Q_{31} & Q_{33} & Q_{35} & -W_{1h}H_0(\gamma_{1h}a) & -W_{2h}H_0(\gamma_{2h}a) & -W_{3h}H_0(\gamma_{3h}a) \\ Q_{41} & Q_{43} & Q_{45} & -D_{11h} & -D_{12h} & -D_{13h} \\ Q_{51} & Q_{53} & Q_{55} & -D_{21h} & -D_{22h} & -D_{23h} \\ Q_{61} & Q_{63} & Q_{65} & -D_{31h} & -D_{32h} & -D_{33h} \end{vmatrix} = 0, \tag{33}$$

where

$$D_{1qh} = (C_{11}\gamma_{qh} + ikC_{13}V_{qh} + ike_{31}W_{qh})H_0(\gamma_{qh}r) - (C_{11} - C_{12})\frac{H_1(\gamma_{qh}r)}{r},$$

$$D_{2qh} = (ikC_{44} - C_{44}V_{qh}\gamma_{qh} - e_{15}W_{qh}\gamma_{qh})H_1(\gamma_{qh}r),$$

$$D_{3qh} = (ike_{15} - e_{15}V_{qh}\gamma_{qh} + \varepsilon_{11}W_{qh}\gamma_{qh})H_1(\gamma_{qh}r).$$

C. Multilayered rod system immersed in fluid

The formal solutions in an unbounded fluid host can be obtained directly from those of a solid host, noting that no shear deformations exist in fluids. These solutions are

$$u_{rf} = CH_1(\gamma_f r),$$
$$u_{zf} = -(ik/\gamma_f)CH_1(\gamma_f r), \tag{34}$$
$$\sigma_{rf} = (\rho_f\omega^2/\gamma_f)CH_0(\gamma_f r),$$

where the radial wave number in the fluid γ_f is calculated for the isotropic fluid from

$$\gamma_f^2 = \omega^2/c_f^2 - k^2, \tag{35}$$

and where c_f is the sound velocity in the fluid. As in the case of free rods, a similar problem arises for rods immersed in a dielectric fluid. The relatively high permittivity of polar fluids like water ($\varepsilon \approx 80\varepsilon_0$) could possibly affect the electrical boundary conditions so much that the guided mode velocities change perceivably. This effect will be further investigated in a separate paper and in the following we will assume that the normal component of the dielectric displacement D_r vanishes at the surface of an immersed rod.

Satisfying the interface conditions between the fluid and the rod, namely $u_r^- = u_{rf}$, $\sigma_r^- = \sigma_{rf}$, $\sigma_{rz}^- = 0$, and $D_r^- = 0$ at $r = r_1 = a$, leads to the required characteristic equation

$$\begin{vmatrix} Q_{11} & Q_{13} & Q_{15} & -H_1(\gamma_f a) \\ Q_{41} & Q_{43} & Q_{45} & -(\rho_f\omega^2/\gamma_f)H_0(\gamma_f a) \\ Q_{51} & Q_{53} & Q_{55} & 0 \\ Q_{61} & Q_{63} & Q_{65} & 0 \end{vmatrix} = 0. \tag{36}$$

D. Periodic fibrous systems

For the case of infinitely extended medium consisting of a periodic array of unidirectional fibrous composites [see Fig. 1(c)], the symmetry of the problem allows isolating the repeating hexagonal cell and approximating it by a concentric cylindrical layered fiber surrounded by a coaxial matrix layer. With regard to Fig. 2, this matrix layer is called layer 1, and the fiber layers are layers 2,3,...,*p*. As pointed out in Ref. 1, the inherent periodicity and symmetry of the unbounded composite imply the vanishing of the lateral displacement u_r, the shear stress σ_{rz}, and the lateral electric displacement D_r at the outer radius of the fiber-matrix system. These boundary conditions should be contrasted with those appropriate for the free and clad systems where stress-free conditions are invoked at the outer boundaries. Furthermore, we recognize that the hexagonal-cylinder approximations do not accurately account for the structural details of the composite. At low frequencies, the error caused by this approximation can be essentially eliminated by adjusting the diameter of the matrix cladding so that the fiber volume fraction is accurately represented. In this case, the distance between neighboring fibers in the real hexagonal composite is slightly less than the diameter chosen for the clad fiber in the cylindrical model. For example, in the case of 25% fiber volume fraction, the distance between neighboring fibers in the real hexagonal composite is only ≈ 1.905 times the fiber diameter while the outer diameter of the clad fiber in the cylindrical model is exactly twice the fiber diameter. At high frequencies, when the acoustic wavelength becomes smaller than the fiber diameter, some error will inevitably arise as the wave velocity becomes more and more sensitive to the matrix geometry, too, rather than just the relative amount of matrix material in the composite. The shape difference between the approximate and real matrix geometry becomes more significant at high fiber volume fractions, therefore it is expected that the approximation breaks down above approximately 50% reinforcement. Although exact solutions are currently not available for comparison, it is clear that the above-described cylindrical model is more accurate at relatively low fiber volume fractions and at low normalized frequencies.

In the cylindrical approximation of infinite media, Eq. (29) can be translated into the following characteristic dispersion equation:

$$\begin{vmatrix} Q_{11} & Q_{13} & Q_{15} \\ Q_{51} & Q_{53} & Q_{55} \\ Q_{61} & Q_{63} & Q_{65} \end{vmatrix}_p = 0. \tag{37}$$

IV. NUMERICAL RESULTS

The material properties used in the following calculations are listed in Table I. In addition, we can introduce effective coupling coefficients to quantify the strength of pi-

TABLE I. The dimensions and material properties of illustration materials. Units of C_{pq} and e_{ip} are 10^9 N/m^2 and Co/m^2, respectively. ε_{ij} is given nondimensional as $\varepsilon^s/\varepsilon_0^S$, where $\varepsilon_0^S = 8.854\,10\times10^{-12}$ F/m.

Material	PZT 65/35	Spurr
Radius (mm)	0.707	1.0
ρ(g/cm^3)	7.500	1.100
C_{11}	159.4	5.3
C_{12}	73.9	3.1
C_{13}	73.9	3.1
C_{22}	159.4	5.3
C_{23}	73.9	3.1
C_{33}	126.1	5.3
C_{44}	38.9	1.1
C_{55}	38.9	1.1
C_{66}	42.8	1.1
e_{33}	10.7	0
e_{32}	−6.13	0
e_{31}	−6.13	0
e_{15}	8.39	0
e_{24}	8.39	0
ε_{11}	639.3	1
ε_{22}	639.3	1
ε_{33}	153.3	1

ezoelectric coupling in different situations. In the following, we are going to use an asterisk to indicate effective parameters of the piezoelectric material. For example, in the plane of isotropy of an infinite transversely isotropic material (radial direction), only the vertically polarized shear wave velocity, $c_{s1}^* = \sqrt{C_{44}^*/\rho} = \sqrt{C_{44}(1+\kappa_1^2)/\rho} = c_{s1}\sqrt{1+\kappa_1^2}$, is affected by the piezoelectric coupling while the longitudinal velocity is not, $c_{d1}^* = c_{d1} = \sqrt{C_{11}/\rho}$. In contrast, normal to the plane of isotropy (axial direction), only the longitudinal wave velocity, $c_{d2}^* = \sqrt{C_{33}^*/\rho} = \sqrt{C_{33}(1+\kappa_2^2)/\rho} = c_{d2}\sqrt{1+\kappa_2^2}$, is affected by the piezoelectric coupling while the vertically polarized shear velocity is not, $c_{s2}^* = c_{s2} = \sqrt{C_{44}/\rho}$. These coupling coefficients can be calculated from $\kappa_1^2 = e_{15}^2/(C_{44}\varepsilon_{11})$ and $\kappa_2^2 = e_{33}^2/(C_{33}\varepsilon_{33})$ as $\kappa_1 \approx 0.56$ and $\kappa_2 \approx 0.82$ in the case of PZT 65/35.

Figure 3 shows the dispersion curves for the six lowest-order axisymmetric guided modes in a free transversely isotropic PZT 65/35 rod of $a = 0.707$-mm radius. The solid lines represent the actual piezoelectric material while the dashed lines represent a similar material with identical elastic constants and density but no piezoelectricity. The substantial overall difference between the two sets of dispersion curves clearly indicates the very strong effect of piezoelectric coupling on the axisymmetric modes. These differences can be summarized as follows. First, there is a surprisingly large drop in the phase velocity of the lowest-order mode at low frequencies. We calculated Young's modulus of a transversely isotropic piezoelectric rod in the axial direction from the static limit of the field equations as

$$E_3^* = C_{33}\frac{2C_{13}^2\varepsilon_{33} + 4C_{13}e_{31}e_{33} - (C_{11}+C_{12})e_{33}^2}{(C_{11}+C_{12})\varepsilon_{33} + 2e_{31}^2}. \quad (38)$$

In comparison, Young's modulus of a transversely isotropic nonpiezoelectric rod is

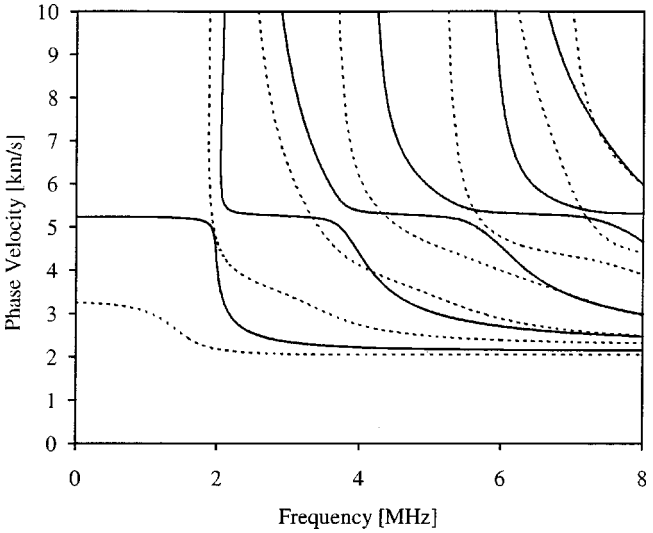

FIG. 3. Dispersion curves for the six lowest-order axisymmetric guided modes in a free transversely isotropic PZT 65/35 rod of $a = 0.707$-mm radius (solid lines—piezoelectric material, dashed lines—without piezoelectricity).

$$E_3 = C_{33} - 2C_{13}^2/(C_{11}+C_{12}). \quad (39)$$

We can write Young's modulus in terms of a characteristic coupling coefficient as $E_3^* = E(1+\kappa_E^2)$, where $\kappa_E \approx 1.26$ calculated for the PZT rod, indicating that it is larger than those of the bulk wave, i.e., $\kappa_1 < \kappa_2 < \kappa_E$.

Second, there is also a significant upward shift in the cutoff frequencies of the higher-order modes. Generally, each mode is a combination of coupled quasi-shear and quasi-longitudinal waves. However, at the cutoff frequencies, the phase velocity becomes infinitely high and the partial waves propagate strictly in the plane of isotropy where they decouple into either pure shear or pure longitudinal modes. The shear-type (e.g., the first-order mode) cutoff frequencies can be simply calculated from

$$f_n^* = \frac{j_n c_{s1}^*}{2\pi a} = f_n\sqrt{1+\kappa_1^2}, \quad (40)$$

where j_n is the nth zero of the first-order Bessel function of the first kind (J_1). Accordingly, these cutoff frequencies are approximately 15% higher in a piezoelectric rod than in an otherwise identical but nonpiezoelectric one. Although it is not obvious from Fig. 3, which is limited to relatively low phase velocities, the longitudinal-type (e.g., the second-order mode) cutoff frequencies are not affected by piezoelectric coupling since the longitudinal mode propagating in the plane of isotropy is not affected, i.e., $c_{d1}^* = c_{d1} = \sqrt{C_{11}/\rho}$. The longitudinal-type cutoff frequencies can be calculated from

$$f_m^* = \frac{g_m c_{d1}}{2\pi a} = f_m, \quad (41)$$

where g_m is the mth zero of the $G(\xi) = J_1(\xi)/[\xi J_0(\xi)] - C_{11}/(C_{11}-C_{12})$ function.

Third, the strong piezoelectric coupling also manifests itself through the appearance of a relatively flat ''plateau'' region around 5200 m/s. All modes crossing this region ex-

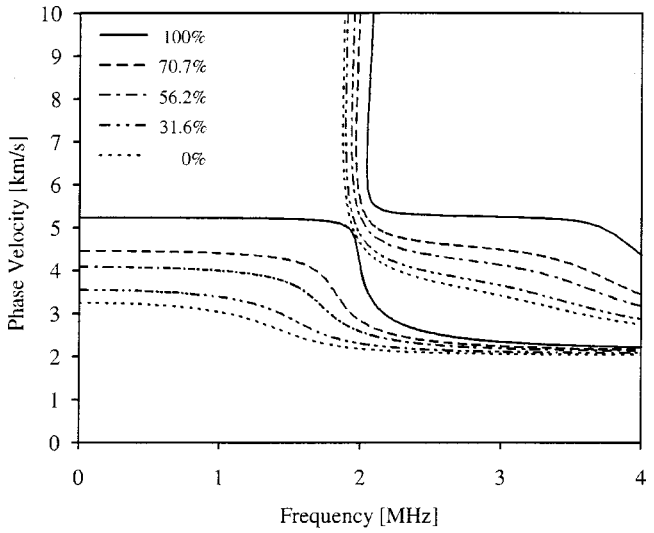

FIG. 4. Dispersion curves for the two lowest-order axisymmetric guided modes in a free transversely isotropic PZT 65/35 rod of $a=0.707$-mm radius with varying piezoelectric coupling. The piezoelectric coupling was decreased by proportionally increasing both ε_{11} and ε_{33} by the same amount with respect to their nominal values listed in Table I.

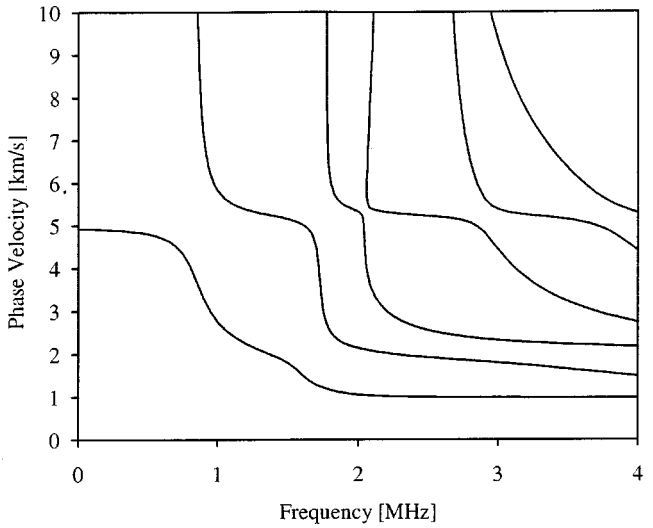

FIG. 5. Dispersion curves for the six lowest-order axisymmetric guided modes in a transversely isotropic piezoelectric PZT 65/35 rod of 0.707-mm radius covered with a spurr coating of 1-mm outer radius.

hibit an essentially flat dispersion curve over a fairly wide frequency range and these regions form a more or less continuous nondispersive branch.

The effect of piezoelectric coupling can be further investigated in more detail through the examples of the first two modes in the case of gradually increasing piezoelectric coupling. Figure 4 shows the dispersion curves for the two lowest-order axisymmetric guided modes in a free transversely isotropic PZT 65/35 rod of $a=0.707$-mm radius with varying piezoelectric coupling. The piezoelectric coupling was decreased by proportionally increasing both ε_{11} and ε_{33} by the same amount with respect to their nominal values listed in Table I. For example, a factor of 2 increase in the permittivities corresponds to 70.7% reduced piezoelectric coupling. Because of numerical difficulties, the nonpiezoelectric case was calculated by the numerical technique described in Ref. 1. These results well illustrate how the stiffening of the material caused by the gradual increase of the piezoelectric coupling modifies the dispersion curves by pushing them up towards higher phase velocities and to the right towards higher frequencies while the transitions between regions of low and high dispersion become sharper.

As an example of a multi-layered rod, Fig. 5 shows the dispersion curves for the six lowest-order axisymmetric guided modes in a transversely isotropic piezoelectric PZT 65/35 rod of 0.707-mm radius covered with a spurr coating of 1-mm outer radius. The main difference with respect to the previously shown case of the uncoated rod is that the cutoff frequencies become much lower, partly because of the increased radius and partly because of the lower sound velocity in the coating. In addition, at high frequencies the guided modes drop to a much lower phase velocity than in the uncoated rod, which is also due to the lower sound velocity in the coating.

Figure 6 shows the dispersion curves for the three lowest-order axisymmetric bulk modes in a composite containing 25% volume fraction of reinforcement. The matrix is isotropic nonpiezoelectric spurr while the periodic reinforcement is made from transversely isotropic piezoelectric PZT 65/35 fibers of 0.707-mm radius.

V. CONCLUSION

A unified general treatment of elastic guided wave propagation in anisotropic multilayered piezoelectric rod systems was presented. Dispersion relations were derived for either free, immersed, or embedded multilayered rod systems. Individual coaxial layers were assumed to be transversely isotropic and the system global transfer matrix was constructed by applying suitable continuity conditions at the interfaces. By invoking appropriate boundary conditions for multilayered fiber systems having an additional coaxial ma-

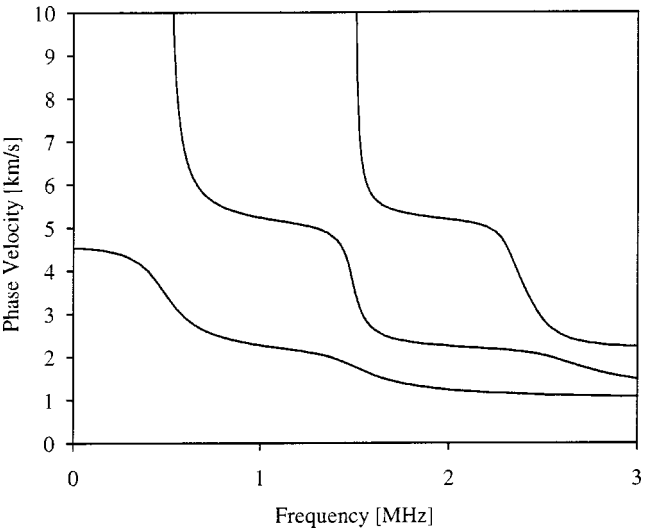

FIG. 6. Dispersion curves for the three lowest-order axisymmetric bulk modes in a composite containing 25% volume fraction of reinforcement. The matrix is isotropic nonpiezoelectric spurr while the periodic reinforcement is made from transversely isotropic piezoelectric PZT 65/35 fibers of 0.707-mm radius.

trix cladding, the same formal solutions were applied to approximate elastic wave propagation along the fibers in infinite composite media containing a periodic distribution of multilayered piezoelectric fiber systems. The analytical results were numerically illustrated through the example of a typical piezoelectric fiber-polymer coating (matrix) arrangement.

[1] A. H. Nayfeh and P. B. Nagy, ''General study of axisymmetric waves in layered anisotropic fibers and their composites,'' J. Acoust. Soc. Am. **99**, 931–941 (1996).

[2] W. T. Thomson, ''Transmission of Elastic Waves Through a Stratified Solid Medium,'' J. Appl. Phys. **21**, 89–93 (1950).

[3] N. A. Haskell, ''Dispersion of Surface Waves on Multilayered Media,'' Bull. Seismol. Soc. Am. **43**, 17–34 (1953).

[4] A. H. Nayfeh, *Wave Propagation in Layered Anisotropic Media with Applications to Composites* (North-Holland, Amsterdam, 1995).

[5] H. S. Paul, ''Vibration of circular cylindrical shells of piezoelectric silver iodide crystals,'' J. Acoust. Soc. Am. **40**, 1077–1080 (1966).

[6] V. Winkel, J. E. B. Oliviera, J. D. Dai, and C. K. Jen, ''Acoustic Wave Propagation in Piezoelectric Fibers of Hexagonal Crystal Symmetry,'' IEEE Trans. Ultrason. Ferroelectr. Freq. Control **42**, 949–955 (1995).

[7] S. Minagawa, ''Propagation of Harmonic Waves in a Layered Elasto-Piezoelectric Composite,'' Mech. Mater. **19**, 165–170 (1995).

[8] J. T. Stewart and Y. K. Yong, ''Exact Analyses of the Propagation of Acoustic Waves in Multilayered Anisotropic Piezoelectric Plates,'' IEEE Trans. Ultrason. Ferroelectr. Freq. Control **41**, 375–390 (1994).

[9] A. H. Nayfeh and H. Chien, ''The influence of piezoelectricity on reflected waves from fluid-loaded anisotropic plates,'' J. Acoust. Soc. Am. **91**, 1250–1261 (1992).

[10] L. Adler, ''Matrix Methods Applied to Acoustic Waves in Multilayers,'' IEEE Trans. Ultrason. Ferroelectr. Freq. Control **37**, 485–490 (1990).

Second-harmonic generation in a sound beam reflected and transmitted at a curved interface

Inder Raj S. Makin,[a] Michalakis A. Averkiou,[b] and Mark F. Hamilton
Department of Mechanical Engineering, The University of Texas at Austin, Austin, Texas 78712-1063

(Received 27 May 1999; accepted for publication 22 June 2000)

This article presents a model for second-harmonic generation in a sound beam that is reflected from or transmitted through a curved interface. Propagation in homogeneous fluids is assumed. Simple analytic solutions are derived for the case of focused Gaussian beams. The solutions are used to illustrate the effects of focusing or defocusing due to curvature of the interface, in combination with impedance change at the interface, on energy transfer from the fundamental to the second harmonic.
 [S0001-4966(00)02310-9]

PACS numbers: 43.25.Jh [HEB]

I. INTRODUCTION

Acoustic signals used in biomedical applications such as diagnostic and therapeutic ultrasound frequently exhibit nonlinear behavior in their propagation through tissue.[1] A recent development in the area of medical ultrasound imaging is based upon detection of second-harmonic components generated nonlinearly in a sound beam.[2–4] The sidelobes of the second-harmonic component are lower than those at the source excitation frequency, and therefore the image clutter is substantially reduced from its normal level in conventional imaging based on the source frequency alone.[5] In addition, the nonlinearly generated higher-harmonic beams are narrower than at the source frequency, and therefore spatial resolution is improved. Similar enhancement of spatial resolution has been reported in acoustical microscopy.[6,7] For both transmission through tissue and reflection from objects, second-harmonic generation is affected by curvature of the interface or surface under consideration, which is the subject of the present article.

Our work presents a theoretical model of second-harmonic generation in a sound beam that is reflected from or transmitted through a curved interface. The incident, reflected, and transmitted beams are assumed to propagate in homogeneous, fluid-like media. The analysis is based on the KZK equation, and it is therefore similar to the theory described by Garrett *et al.*[8] These authors investigated difference-frequency generation in a sound beam reflected from a planar target, with theory and experiment compared for reflection from a pressure release surface in water. Attention was devoted to the manner in which the difference-frequency component generated before reflection combines with the component generated after reflection. Previous investigations of harmonic generation in reflected sound beams were reviewed by these authors (see also Refs. 9 and 10).

In the present article, field integrals are developed for the fundamental and second-harmonic components in both the reflected and transmitted beams. Interface curvature is taken into account explicitly. Simple analytic solutions are obtained for the acoustic pressure fields and power associated with second-harmonic generation in reflected and transmitted beams produced by focused Gaussian sources. The solutions are used to illustrate focusing or defocusing due to curvature of the interface, and energy transfer from the fundamental to the second harmonic as a function of impedance at the interface. The analysis is based on work reported in portions of the dissertations by two of the authors.[9,10]

II. BASIC EQUATIONS

The geometric configuration for the source and interface is provided in Fig. 1. The source has characteristic dimension a and it radiates sound in the z direction at angular frequency ω. We assume $ka \gg 1$, where $k=\omega/c_0$ is the wave number at the source frequency and c_0 is the local sound speed.

The axis of the incident beam (designated by sound pressure p_i) intersects the interface at $z=z_s$. The interface separates two homogeneous fluid media I and II characterized by their ambient density ρ_0, small signal sound speed c_0, absorption coefficient α, and coefficient of nonlinearity β. Although a specific geometry is not prescribed for the interface, the following assumptions are made. The radius of curvature of the interface in the vicinity of the z axis (labeled b in Fig. 1) is assumed to be large in comparison with the local beamwidth, and the normal to the interface in that region is assumed to form a small angle with respect to the z axis (labeled θ in Fig. 1). These restrictions are imposed in order that the reflected beam in medium I and the transmitted beam in medium II (designated by p_r and p_t, respectively) remain well collimated and propagate in directions close to the z axis.

For the conditions outlined above, the KZK equation provides an accurate model of the incident, reflected, and transmitted beams:

$$\frac{\partial^2 p}{\partial z \partial \tau} - \frac{c_0}{2}\nabla_\perp^2 p - \frac{\delta}{2c_0^3}\frac{\partial^3 p}{\partial \tau^3} = \frac{\beta}{2\rho_0 c_0^3}\frac{\partial^2 p^2}{\partial \tau^2}, \tag{1}$$

where p is the sound pressure, z is the axis of the incident beam, $\nabla_\perp^2 = \partial^2/\partial x^2 + \partial^2/\partial y^2$ is the transverse Laplacian operator, $\tau = t - z/c_0$ is retarded time, and δ is the diffusivity of sound for a thermoviscous fluid. The second term on the

[a]Present address: Ethicon Endo-Surgery, 4545 Creek Road, Cincinnati, OH 45242.
[b]Present address: ATL Ultrasound, P.O. Box 30003, Bothell, WA 98041.

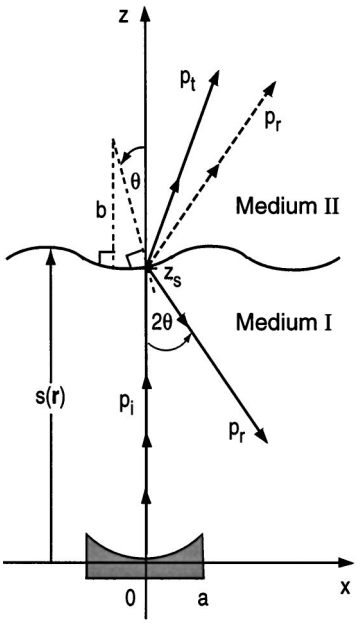

FIG. 1. Geometry of the interface separating media I and II. The dashed line for the reflected beam axis indicates the unfolded geometry in which solutions for that beam are expressed.

left-hand side in Eq. (1) accounts for diffraction, the third for thermoviscous absorption, and the right-hand side accounts for nonlinearity. Comparisons of solutions obtained from Eq. (1) with experiment are reviewed in Ref. 11.

For weak nonlinearity, such that shock formation does not occur, Eq. (1) may be solved for the fundamental and second-harmonic components by the method of successive approximations. The sound pressure at the source frequency ω is designated p_1, and the nonlinearly generated sound pressure at frequency 2ω is designated p_2. The sound fields are separated into their space- and time-dependent parts as follows:

$$p_n = \mathrm{Re}[iq_n(\mathbf{r},z)e^{-in\omega\tau}], \quad n=1,2, \tag{2}$$

where q_n is the complex pressure amplitude at frequency $n\omega$, and $\mathbf{r}=(x,y)$. The method of solution is based on the assumption that the second-harmonic pressure is small in comparison with the pressure in the primary beam, $|q_2| \ll |q_1|$. A homogeneous equation for q_1 is obtained by substituting Eq. (2) in (1) and setting the right side to zero:

$$\frac{\partial q_1}{\partial z} + \frac{1}{i2k}\nabla_\perp^2 q_1 + \alpha_1 q_1 = 0, \tag{3}$$

where $\alpha_1 = \delta\omega^2/2\rho_0 c_0^3$ is the thermoviscous absorption coefficient at the source frequency. An inhomogeneous equation for q_2 is obtained by substituting the solution for p_1 into the right-hand side of Eq. (1), and p_2 into the left-hand side:

$$\frac{\partial q_2}{\partial z} + \frac{1}{i4k}\nabla_\perp^2 q_2 + \alpha_2 q_2 = \frac{\beta k q_1^2}{2\rho_0 c_0^2}. \tag{4}$$

Here, α_2 is the absorption coefficient at frequency 2ω, and for a thermoviscous fluid, $\alpha_2 = 4\alpha_1$. However, the absorption coefficients are permitted hereafter to have arbitrary dependence on frequency. Effects of dispersion may be included by considering α_1 and α_2 to be complex quantities.

Equations (3) and (4) are solved sequentially for q_1 and q_2. The source function $q_{1i}(\mathbf{r},0)$ for the primary beam is arbitrary in terms of amplitude and phase shading. The phase shading may be introduced to account for focusing, which is considered explicitly in Sec. VI. There is no source radiation at the second harmonic, and therefore $q_{2i}(\mathbf{r},0)=0$. It is convenient to write the solutions in terms of integrals over the Green's function

$$g_n(\mathbf{r},z|\mathbf{r}',z') = \frac{nk}{i2\pi(z-z')} \times \exp\left[-\alpha_n(z-z') + \frac{ink|\mathbf{r}-\mathbf{r}'|^2}{2(z-z')}\right], \tag{5}$$

in terms of which the expressions for the incident fields q_{1i} and q_{2i} at the fundamental and second-harmonic frequencies, respectively, are

$$q_{1i}(\mathbf{r},z) = \int q_{1i}(\mathbf{r}',0) g_1(\mathbf{r},z|\mathbf{r}',0)\, d\mathbf{r}', \tag{6}$$

$$q_{2i}(\mathbf{r},z) = \frac{\beta k}{2\rho_0 c_0^2}\int_0^z dz' \int q_{1i}^2(\mathbf{r}',z') g_2(\mathbf{r},z|\mathbf{r}',z')\, d\mathbf{r}'. \tag{7}$$

An extensive literature is devoted to these integral solutions.[11]

III. REFLECTED BEAM

For application of the KZK equation to the reflected beam, an unfolded geometry is used whereby the beam is considered to propagate in the $+z$ direction even after reflection from the interface at $z=z_s$. We designate the axis of the reflected beam in the unfolded geometry by the dashed line for p_r in Fig. 1. The dashed line is the mirror image, with respect to the plane $z=z_s$, of the axis of the true reflected beam. The latter is designated by the solid line for p_r in Fig. 1. To obtain the solution at the true reflected field locations $z<z_s$, one employs the coordinate transformation $z\rightarrow(2z_s - z)$ in the solutions presented below for the reflected field in the region $z>z_s$. The unfolded geometry provides a convenient means of representing analytically, and later graphically, the properties of the reflected beam.

The reflected beam (in the region $z\geqslant z_s$) is described by

$$q_{1r}(\mathbf{r},z) = \int q_{1r}(\mathbf{r}',z_s) g_1(\mathbf{r},z|\mathbf{r}',z_s)\, d\mathbf{r}', \tag{8}$$

$$q_{2r}(\mathbf{r},z) = \int q_{2r}(\mathbf{r}',z_s) g_2(\mathbf{r},z|\mathbf{r}',z_s)\, d\mathbf{r}' + \frac{\beta k}{2\rho_0 c_0^2}\int_{z_s}^z dz' \int q_{1r}^2(\mathbf{r}',z') g_2(\mathbf{r},z|\mathbf{r}',z')\, d\mathbf{r}'. \tag{9}$$

The reflected field components depend on their values $q_{nr}(\mathbf{r},z_s)$ at the interface, which are determined in turn by the solutions $q_{ni}(\mathbf{r},z_s)$ for the incident field components at the interface, multiplied by appropriate reflection coefficients $\mathcal{R}_n(\mathbf{r})$:

$$q_{nr}(\mathbf{r},z_s)=\mathcal{R}_n(\mathbf{r})q_{ni}(\mathbf{r},z_s). \tag{10}$$

Note that the solution for the second harmonic in the reflected beam consists of two separate contributions. The first term in Eq. (9) is a surface integral over $q_{2r}(\mathbf{r},z_s)$, the second-harmonic pressure in the reflected beam at the interface. This is the homogeneous solution of Eq. (4), and it accounts for the second harmonic generated by the primary beam before reflection. The second term is a volume intergal over $q_{1r}^2(\mathbf{r},z)$. This is the particular solution of Eq. (4), and it accounts for the second harmonic generated by the primary beam after reflection. The reflection itself is described by linear theory, Eq. (10). In general, the contribution due to harmonic generation at the interface, e.g., due to the finite motion of the interface associated with the particle displacement in the fluid, is a local effect that is significant only at distances on the order of one wavelength away from the interface. This local effect has been discussed in detail by Blackstock[12] in connection with the finite displacement of piston sources.

We now develop an explicit expression for $\mathcal{R}_n(\mathbf{r})$. First, recognize that the geometry of the interface affects the phase of the reflected beam. Let the coordinates of the interface be $(\mathbf{r},s)$, where $s(\mathbf{r})$ is the distance between the interface and the source plane (see Fig. 1). With z_s defined to be the point along the z axis where the incident beam intersects the interface, the position of the interface relative to the plane $z=z_s$ is defined by

$$\zeta(\mathbf{r})=s(\mathbf{r})-z_s, \tag{11}$$

such that ζ vanishes where the surface intersects the z axis, $\zeta(\mathbf{0})=0$. Second, $\zeta(\mathbf{r})$ is assumed to vary slowly across the incident beam, in which case the amplitude of the reflection coefficient may be taken as independent of $\mathbf{r}$ and dependent only on frequency. We thus introduce the plane-wave reflection coefficient R_n and write

$$\mathcal{R}_n(\mathbf{r})=R_n\exp[i2nk\zeta(\mathbf{r})], \tag{12}$$

where 2ζ is the distance from the plane $z=z_s$ to and from the interface, and $2nk\zeta$ is the corresponding phase change at frequency $n\omega$. Because we have assumed that θ in Fig. 1 is small, R_n may be taken to be the plane-wave reflection coefficient evaluated for normal incidence.

The two principal effects of the interface geometry are focusing or defocusing due to curvature (i.e., for $b\neq\infty$ in Fig. 1), and deflection of the reflected beam away from the z axis when the normal to the interface does not coincide with the z axis (i.e., for $\theta\neq0$). These features are taken into account by the expression for ζ given by Eq. (A8) in the Appendix, substitution of which into Eq. (12) gives

$$\mathcal{R}_n(x,y)=R_n\exp\left\{ink\left[\left(\frac{x^2}{b_x}+\frac{y^2}{b_y}\right)+2(\theta_x x+\theta_y y)\right]\right\}. \tag{13}$$

The phase terms that are quadratic in x and y are associated with focusing and defocusing, the linear terms with beam deflection. As defined in the Appendix, b_x and b_y are the local radii of curvature where the z axis intersects the interface, in the (x,z) and (y,z) planes, respectively. A positive radius defines a curve that is convex as seen from the source plane, and a negative radius defines a curve that is seen as concave. Defocusing thus occurs when both b_x and b_y are positive, focusing when they are both negative. The angles θ_x and θ_y determine, in the (x,z) and (y,z) planes, respectively, the angles formed by the normal to the surface and the z axis (defined positive counterclockwise with respect to the $+z$ direction). In the Appendix, explicit relations for the curvature radii and deflection angles are provided for spherical, cylindrical, and ellipsoidal surfaces.

Because the KZK equation, and therefore our model, are based on the assumption that the incident and reflected sound beams are quasiplane waves that propagate in directions close to the z axis, a simple transformation may be obtained to describe the deflection of the reflected beam. The position of the reflected beam axis (the dashed line in Fig. 1), based on specular reflection and for small angles, is

$$\mathbf{r}_r=2\boldsymbol{\theta}(z-z_s), \quad \boldsymbol{\theta}=(\theta_x,\theta_y). \tag{14}$$

Substitution of Eqs. (10) and (13) in Eqs. (8) and (9) permits the latter to be manipulated into a form that yields

$$q_{nr}(\mathbf{r},z|\boldsymbol{\theta})=q_{nr}(\mathbf{r}-\mathbf{r}_r,z|\mathbf{0})e^{in\psi_r(\mathbf{r},z)}, \tag{15}$$

where

$$\psi_r(\mathbf{r},z)=2k[\boldsymbol{\theta}\cdot\mathbf{r}-\theta^2(z-z_s)] \tag{16}$$

and $\theta^2=\theta_x^2+\theta_y^2$. Since ψ_r is a real quantity, we also have

$$|q_{nr}(\mathbf{r},z|\boldsymbol{\theta})|=|q_{nr}(\mathbf{r}-\mathbf{r}_r,z|\mathbf{0})|. \tag{17}$$

Solutions for $\boldsymbol{\theta}\neq\mathbf{0}$, which involve beam deflection, may thus be obtained via transformation of the solutions for $\boldsymbol{\theta}=\mathbf{0}$, which involve no beam deflection. The transformation introduces a lateral shift $\mathbf{r}-\mathbf{r}_r$ and a phase $n\psi_r$ that account for rotation of the wave field to coincide with the new beam axis.

IV. TRANSMITTED BEAM

Analysis of the transmitted beam follows the framework used to model the reflected beam. For the transmitted beam we have, in place of Eqs. (8) and (9),

$$q_{1t}(\mathbf{r},z)=\int q_{1t}(\mathbf{r}',z_s)g_1^{\mathrm{II}}(\mathbf{r},z|\mathbf{r}',z_s)\,d\mathbf{r}', \tag{18}$$

$$q_{2t}(\mathbf{r},z)=\int q_{2t}(\mathbf{r}',z_s)g_2^{\mathrm{II}}(\mathbf{r},z|\mathbf{r}',z_s)\,d\mathbf{r}' + \frac{\beta^{\mathrm{II}}k^{\mathrm{II}}}{2\rho_0^{\mathrm{II}}(c_0^{\mathrm{II}})^2}\int_{z_s}^{z}dz'\int q_{1t}^2(\mathbf{r}',z') \times g_2^{\mathrm{II}}(\mathbf{r},z|\mathbf{r}',z')\,d\mathbf{r}'. \tag{19}$$

All parameters with superscript II are evaluated according to the physical properties of medium II. For brevity, the superscripts I and II are suppressed on the quantities q_{ni} and q_{nt}, respectively, because the existing notation is unambiguous. In place of Eqs. (10) and (12) we have the interface condition

$$q_{nt}(\mathbf{r},z_s)=\mathcal{T}_n(\mathbf{r})q_{ni}(\mathbf{r},z_s), \tag{20}$$

where

$$\mathcal{T}_n(\mathbf{r})=T_n\exp[in(k^{\mathrm{I}}-k^{\mathrm{II}})\zeta(\mathbf{r})], \tag{21}$$

and T_n is the plane-wave transmission coefficient. As with R_n, it is appropriate to use the value of T_n for normal incidence. The quantity $(k^{\mathrm{I}}-k^{\mathrm{II}})\zeta$ accounts for changes in the propagation distances in media I and II associated with the geometry of the interface. Substitution of Eq. (A8) into (21) yields

$$\mathcal{T}_n(x,y)=T_n\exp\left\{i(1-\eta)nk^{\mathrm{I}}\left[\frac{1}{2}\left(\frac{x^2}{b_x}+\frac{y^2}{b_y}\right)+(\theta_x x+\theta_y y)\right]\right\}, \tag{22}$$

where we have introduced the index of refraction

$$\eta=c_0^{\mathrm{I}}/c_0^{\mathrm{II}}=k^{\mathrm{II}}/k^{\mathrm{I}}. \tag{23}$$

When the sound speeds in the two fluids are equal ($\eta=1$), there is no refraction and, therefore, $\mathcal{T}_n=T_n$.

A transformation similar to Eq. (15) may be derived for the transmitted beam. On the basis of geometrical acoustics (i.e., according to Snell's law), the position of the transmitted beam axis in Fig. 1 is given for small angles by

$$\mathbf{r}_t=\boldsymbol{\theta}(z-z_s)(1-\eta)/\eta. \tag{24}$$

The corresponding transformation is

$$q_{nt}(\mathbf{r},z|\boldsymbol{\theta})=q_{nt}(\mathbf{r}-\mathbf{r}_t,z|\mathbf{0})e^{in\psi_t(\mathbf{r},z)}, \tag{25}$$

where

$$\psi_t(\mathbf{r},z)=(1-\eta)k^{\mathrm{I}}[\boldsymbol{\theta}\cdot\mathbf{r}-\theta^2(z-z_s)(1-\eta)/2\eta], \tag{26}$$

and therefore

$$|q_{nt}(\mathbf{r},z|\boldsymbol{\theta})|=|q_{nt}(\mathbf{r}-\mathbf{r}_t,z|\mathbf{0})|. \tag{27}$$

We conclude this section by presenting a transformation that relates the solutions for the reflected and transmitted beams when there is no absorption. Letting $f(\mathbf{r},z)$ be any function related to the reflected beam, we define $\hat{f}(\mathbf{r},z)$ to be the transformation that results from making the following substitutions in $f(\mathbf{r},z)$:

$$\begin{aligned}&R_n\rightarrow T_n,\quad b_{x,y}\rightarrow 2b_{x,y}/(1-\eta),\\&\theta_{x,y}\rightarrow\tfrac{1}{2}(1-\eta)\theta_{x,y},\quad z\rightarrow z_s+(z-z_s)/\eta.\end{aligned} \tag{28}$$

The first three substitutions yield $\hat{\mathcal{R}}_n(\mathbf{r})=\mathcal{T}_n(\mathbf{r})$, and for $\alpha_n=0$ the last gives $\hat{g}_n^{\mathrm{I}}(\mathbf{r},z|\mathbf{r}',z_s)=g_n^{\mathrm{II}}(\mathbf{r},z|\mathbf{r}',z_s)$. From Eqs. (8) and (18) one thus obtains

$$q_{1t}(\mathbf{r},z)=\hat{q}_{1r}(\mathbf{r},z). \tag{29}$$

The corresponding transformation for the second harmonic involves separate consideration of the homogeneous and particular solutions in Eqs. (9) and (19) (i.e., the first and second terms in each equation, respectively). Using the subscripts h and p to designate the homogeneous and particular solutions, respectively, one obtains

$$q_{2t}(\mathbf{r},z)=\hat{q}_{2r,h}(\mathbf{r},z)+\eta^4(\beta^{\mathrm{II}}\rho_0^{\mathrm{I}}/\beta^{\mathrm{I}}\rho_0^{\mathrm{II}})\hat{q}_{2r,p}(\mathbf{r},z). \tag{30}$$

V. AXISYMMETRIC BEAMS

In view of Eqs. (17) and (27) it is unnecessary to consider further the effect of beam deflection by the interface, and we let $\boldsymbol{\theta}=\mathbf{0}$. To examine the remaining effects of transmission and reflection at the interface, namely, focusing and defocusing due to curvature, and amplitude and phase changes due to the coefficients R_n and T_n, it is sufficient to consider axisymmetric geometries. Specifically, the source function $q_{1i}(r,0)$ for the primary beam, and the interface position $\zeta(r)$, are now assumed to vary only as functions of distance $r=|\mathbf{r}|$ from the z axis. The interface is considered to be a spherical surface of radius b, for which Eqs. (13) and (22) become

$$\mathcal{R}_n(r)=R_n\exp[ink^{\mathrm{I}}r^2/b], \tag{31}$$

$$\mathcal{T}_n(r)=T_n\exp[i(1-\eta)nk^{\mathrm{I}}r^2/2b]. \tag{32}$$

The surface is convex as viewed from the source for $b>0$, and concave for $b<0$. In the case of reflection, the interface thus introduces defocusing for $b>0$ and focusing for $b<0$. In the case of transmission, it is the sign of the quantity $(1-\eta)b$ that determines whether the interface causes focusing or defocusing:

$$\begin{aligned}&(1-\eta)b<0\leftrightarrow\text{focusing},\\&(1-\eta)b>0\leftrightarrow\text{defocusing}.\end{aligned} \tag{33}$$

The interface introduces no focusing or defocusing of the transmitted beam when the sound speeds in the two media match, and $\eta=1$.

For axisymmetric fields we use the following form of the Green's function in place of Eq. (5):[11]

$$g_n(r,z|r',z')=\frac{nk}{i(z-z')}J_0\left(\frac{krr'}{z-z'}\right)\times\exp\left[-\alpha_n(z-z')+\frac{ink(r^2+r'^2)}{2(z-z')}\right], \tag{34}$$

where J_0 is the zeroth-order Bessel function of the first kind. Equations (6) and (7) for the incident beam become

$$q_{1i}(r,z)=\int_0^\infty q_{1i}(r',0)g_1(r,z|r',0)r'\,dr', \tag{35}$$

$$q_{2i}(r,z)=\frac{\beta k}{2\rho_0c_0^2}\int_0^z dz'\int_0^\infty q_{1i}^2(r',z')\times g_2(r,z|r',z')r'\,dr', \tag{36}$$

and in place of Eqs. (8) and (9) for the reflected beam we have, following substitution of Eq. (10),

$$q_{1r}(r,z)=\int_0^\infty\mathcal{R}_1(r')q_{1i}(r',z_s)g_1(r,z|r',z_s)r'\,dr', \tag{37}$$

$$q_{2r}(r,z)=\int_0^\infty\mathcal{R}_2(r')q_{2i}(r',z_s)g_2(r,z|r',z_s)r'\,dr'+\frac{\beta k}{2\rho_0c_0^2}\int_{z_s}^z dz'\int_0^\infty q_{1r}^2(r',z')\times g_2(r,z|r',z')r'\,dr'. \tag{38}$$

As before, since only medium I is involved for the incident and reflected beams, the superscript I is suppressed in these relations because the context is clear. Following substitution of Eq. (20), Eqs. (18) and (19) for the transmitted beam become

$$q_{1t}(r,z)=\int_0^\infty \mathcal{T}_1(r')q_{1i}(r',z_s)g_1^{\mathrm{II}}(r,z|r',z_s)r'\,dr', \tag{39}$$

$$q_{2t}(r,z)=\int_0^\infty \mathcal{T}_2(r')q_{2i}(r',z_s)g_2^{\mathrm{II}}(r,z|r',z_s)r'\,dr' + \frac{\beta^{\mathrm{II}}k^{\mathrm{II}}}{2\rho_0^{\mathrm{II}}(c_0^{\mathrm{II}})^2}\int_{z_s}^z dz'\int_0^\infty q_{1t}^2(r',z') \times g_2^{\mathrm{II}}(r,z|r',z')r'\,dr'. \tag{40}$$

In the absence of absorption, the transformation in Eq. (28) may also be used here to relate the solutions for the reflected and transmitted beams. The required transformation is

$$R_n\rightarrow T_n,\quad b\rightarrow 2b/(1-\eta),\quad z\rightarrow z_s+(z-z_s)/\eta, \tag{41}$$

which yields, as before,

$$q_{1t}(r,z)=\hat{q}_{1r}(r,z), \tag{42}$$

$$q_{2t}(r,z)=\hat{q}_{2r,h}(r,z)+\eta^4(\beta^{\mathrm{II}}\rho_0^{\mathrm{I}}/\beta^{\mathrm{I}}\rho_0^{\mathrm{II}})\hat{q}_{2r,p}(r,z). \tag{43}$$

VI. FOCUSED GAUSSIAN BEAMS

The field integrals may be evaluated in closed form for a focused primary beam whose amplitude and phase profile at the source are determined by a Gaussian distribution. We thus let

$$q_{1i}(r,0)=p_0\exp[-r^2/a^2-ikr^2/2d], \tag{44}$$

where p_0 is the peak source pressure, a is the effective source radius, and d is the geometric focal length. Solutions and graphical results shall be presented in terms of the following dimensionless quantities:

$$P_n=q_n/p_0,\quad \sigma=z/d,\quad \rho=r/a,$$
$$G=ka^2/2d,\quad C=d/b,\quad N=\beta kdp_0/\rho_0c_0^2. \tag{45}$$

We continue to follow the convention used earlier whereby in the absence of any superscript I or II, physical parameters are evaluated according to the properties of medium I. As shown below, the parameter G is the small-signal focusing gain. The parameter C defines the curvature of the interface. It is positive for a convex surface, negative for a concave surface, and zero for a planar surface. The parameter N is the ratio of the focal length d to the shock formation distance $\bar{z}=\rho_0c_0^2/\beta kp_0$ for a plane wave in a lossless fluid, and it therefore determines the nonlinearity of the system. We shall evaluate the field integrals for the case of lossless media. Expressions similar to those developed below, but including absorption, are presented elsewhere.[10]

With $\alpha_1=0$, Eqs. (35), (37), and (42) for the incident, reflected, and transmitted primary beams yield, respectively,

$$P_{1i}(\rho,\sigma)=\frac{D_0(\rho,\sigma)}{f(\sigma)}, \tag{46}$$

$$P_{1r}(\rho,\sigma)=R_1\frac{D_C(\rho,\sigma)}{g(\sigma)}, \tag{47}$$

$$P_{1t}(\rho,\sigma)=T_1\frac{\hat{D}_C(\rho,\sigma)}{\hat{g}(\sigma)}, \tag{48}$$

where

$$D_C(\rho,\sigma)=\exp[-\Gamma_C\rho^2/g(\sigma)], \tag{49}$$

$$f(\sigma)=1-\sigma+i\sigma/G, \tag{50}$$

$$g(\sigma)=f(\sigma)+2C(\sigma-\sigma_s)f(\sigma_s), \tag{51}$$

$$\Gamma_C=1+iG[1-2Cf(\sigma_s)], \tag{52}$$

and $\sigma_s=z_s/d$. The quantities $D_0(\rho,\sigma)$ and Γ_0 are given by $D_C(\rho,\sigma)$ and Γ_C, respectively, evaluated with $C=0$. The transformation indicated on the right side of Eq. (48) is, from Eq. (41),

$$C\rightarrow\tfrac{1}{2}(1-\eta)C,\quad \sigma\rightarrow\sigma_s+(\sigma-\sigma_s)/\eta. \tag{53}$$

Keeping the unfolded geometry in mind for the reflected field (recall Fig. 1), we have $P_n=P_{ni}$ for $0\leqslant\sigma<\sigma_s$ and $P_n=P_{nr}$ for $\sigma>\sigma_s$. For the transmitted beam we have $P_n=P_{nt}$ for $\sigma>\sigma_s$. The quantity G is identified as the linear focusing gain because $|P_{1i}(0,1)|=G$, where $(\rho,\sigma)=(0,1)$ is the geometric focus of the source.

For the second harmonic with $\alpha_1=\alpha_2=0$, Eqs. (36), (38), and (43) yield

$$P_{2i}(\rho,\sigma)=GD_0^2(\rho,\sigma)\frac{N\ln f(\sigma)}{i2\Gamma_0 f(\sigma)}, \tag{54}$$

$$P_{2r}(\rho,\sigma)=GD_C^2(\rho,\sigma)\frac{F_r(\sigma)}{i2g(\sigma)}, \tag{55}$$

$$P_{2t}(\rho,\sigma)=G\hat{D}_C^2(\rho,\sigma)\frac{F_t(\sigma)}{i2\hat{g}(\sigma)}, \tag{56}$$

where

$$F_r(\sigma)=R_2\frac{N}{\Gamma_0}\ln f(\sigma_s)+R_1^2\frac{N}{\Gamma_C}\ln\frac{g(\sigma)}{f(\sigma_s)}, \tag{57}$$

$$F_t(\sigma)=T_2\frac{N^{\mathrm{I}}}{\Gamma_0}\ln f(\sigma_s)+T_1^2\frac{\eta N^{\mathrm{II}}}{\hat{\Gamma}_C}\ln\frac{\hat{g}(\sigma)}{f(\sigma_s)}. \tag{58}$$

The first terms in Eqs. (57) and (58) are associated with the homogeneous solutions [the first terms in Eqs. (38) and (40), respectively], the second terms with the particular solutions. The first terms thus account for second-harmonic generation in the incident beam, the second terms for second-harmonic generation in the reflected or transmitted beam. Recall that since the reflection and transmission coefficients are obtained from linear theory, the model does not account for the possibility of second-harmonic generation at the interface itself.

The dependence of both the fundamental and second-harmonic beams on ρ is determined entirely by $D_C(\rho,\sigma)$, and therefore Gaussian beam profiles are maintained even

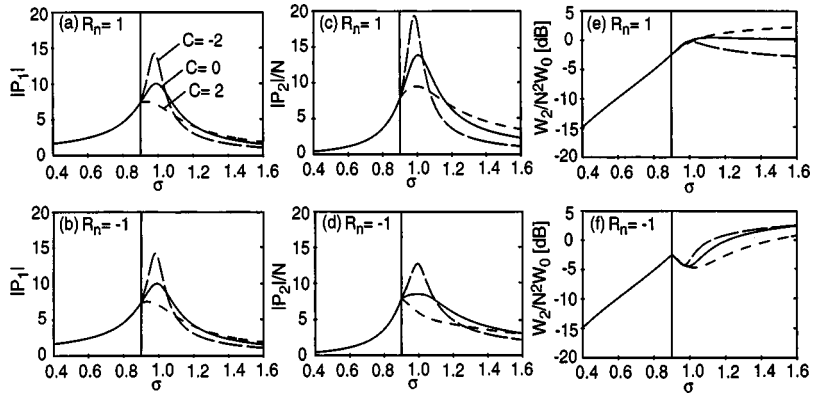

FIG. 2. Axial propagation curves for the fundamental (a,b) and second-harmonic (c,d) pressure, and power of the second harmonic (e,f), for a focused Gaussian beam with gain $G=10$. The parameters are curvature $C=d/b$ (positive for convex surface, negative for concave surface, zero for plane) and R_n ($R_n=1$ for rigid surface in upper row, $R_n=-1$ for free surface in lower row). Vertical lines at $\sigma=0.9$ designate the position of the reflecting surface. The solid curves in the upper row are identical to the free-field solutions for P_{ni} evaluated for $\sigma>\sigma_s$.

after reflection and transmission. The transverse amplitude distributions are given by (where $n=1$ for the fundamental, $n=2$ for the second harmonic)

$$|D_C^n(\rho,\sigma)|=\exp[-n\rho^2/|g(\sigma)|^2], \tag{59}$$

from which the following local beam radius may be defined:

$$r_n(\sigma)=\frac{a}{\sqrt{n}}|g(\sigma)|, \tag{60}$$

such that $r_1(0)=a$ for the primary beam at the source. For the incident beams replace $g(\sigma)$ by $f(\sigma)$ in Eq. (60) (i.e., set $C=0$ in the expression for g), and for the transmitted beams replace $g(\sigma)$ by $\hat{g}(\sigma)$.

Solutions for the acoustic power provide additional insight into the transfer of energy from the fundamental to the second-harmonic component. Within the framework of our theoretical model, the time-averaged intensity of the nth-harmonic component is

$$I_n(\rho,\sigma)=\frac{|q_n(\rho,\sigma)|^2}{2\rho_0 c_0}. \tag{61}$$

The time-averaged power as a function of σ is obtained by integrating the intensity across the beam:

$$W_n(\sigma)=4W_0\int_0^\infty |P_n(\rho,\sigma)|^2\rho\, d\rho, \tag{62}$$

where

$$W_0=\pi a^2 p_0^2/4\rho_0^{\mathrm{I}}c_0^{\mathrm{I}} \tag{63}$$

is the power radiated by the source, obtained with Eq. (44) substituted in Eq. (62).

With Eq. (59) taken into account, substitution of Eqs. (46)–(48) in Eq. (62) yields the following expressions for the power in the primary beam:

$$W_{1i}/W_0=1, \tag{64}$$

$$W_{1r}/W_0=|R_1|^2, \tag{65}$$

$$W_{1t}/W_0=(\rho_0^{\mathrm{I}}c_0^{\mathrm{I}}/\rho_0^{\mathrm{II}}c_0^{\mathrm{II}})|T_1|^2. \tag{66}$$

These results are equivalent to those for plane waves in lossless fluids. Equations (54)–(56) yield, for the second harmonic,

$$\frac{W_{2i}(\sigma)}{W_0}=\frac{G^2N^2}{8|\Gamma_0|^2}|\ln f(\sigma)|^2, \tag{67}$$

$$\frac{W_{2r}(\sigma)}{W_0}=\frac{G^2}{8}|F_r(\sigma)|^2, \tag{68}$$

$$\frac{W_{2t}(\sigma)}{W_0}=\frac{\rho_0^{\mathrm{I}}c_0^{\mathrm{I}}}{\rho_0^{\mathrm{II}}c_0^{\mathrm{II}}}\frac{G^2}{8}|F_t(\sigma)|^2. \tag{69}$$

The range dependence of the second-harmonic power in the reflected and transmitted beams is determined by the functions $F_r(\sigma)$ and $F_t(\sigma)$, respectively. Examination of Eqs. (57) and (58) reveals that the dependence is affected strongly by the relation of R_2 to R_1^2 for the reflected beam, and of T_2 to T_1^2 for the transmitted beam. One may anticipate, for example, that significant differences may be observed in beams reflected from rigid surfaces ($R_1=R_2=1$) and from free surfaces ($R_1=R_2=-1$), because in the first case $R_2/R_1^2=1$ and the coefficients are in phase, whereas in the second $R_2/R_1^2=-1$ and they are in opposite phase.

Given the functional similarities of $F_r(\sigma)$ and $F_t(\sigma)$, we illustrate here only the case of reflection. For our examples we choose $G=10$ for the focusing gain, $\sigma_s=0.9$ for the location of the interface (i.e., just before the geometric focus), and local curvatures $C=-2$ (concave), $C=0$ (plane), and $C=2$ (convex). From Eq. (60) we find that the radius of the primary beam at the interface is $r_1\simeq 0.13a$. For the maximum curvatures considered, $|C|=2$, the normal to the surface varies only slightly from its value of $\theta=0$ at $r=0$ to a value of $\theta_1\simeq 1.3/ka$ at $r=r_1$ (recall that an underlying assumption in the theory is $ka\gg 1$). The deviation in angle for the second harmonic is smaller by a factor of $\sqrt{2}$. Accordingly, the assumption of small surface variation across the beam is satisfied for both the fundamental and second harmonics.

To emphasize differences in surface impedance, we consider in Fig. 2 the two cases $R_n=1$ (rigid surface, upper row) and $R_n=-1$ (free surface, lower row) for $n=1,2$. The first column shows axial propagation curves for the pressure in the primary beam, the second column shows the corresponding propagation curves for the second harmonic, and the third shows the power at the second harmonic. The vertical lines at $\sigma=0.9$ separate the incident and reflected fields. For $R_n=1$ and $C=0$ (the solid curves in the upper row, for a rigid, planar surface), the solutions for the reflected beam in the region $\sigma>\sigma_s$ are identical to the solutions for the incident beam in the same region, with the reflector removed.

These solutions therefore serve as references against which the effect of the reflector may be assessed, and we shall refer to them as the free-field solutions.

We begin by considering the primary beam. The axial propagation curves are identical for $R_n=1$ [Fig. 2(a)] and $R_n=-1$ [Fig. 2(b)] because the reflection coefficients are equal in magnitude, and the influence of the second harmonic on the fundamental is not taken into account in the quasilinear approximation. The free-field solution reaches its peak amplitude at the geometric focus, $\sigma=1$. In comparison with the free-field solution, the concave surface ($C=-2$) is observed to enhance focusing, as expected, and the convex surface ($C=2$) is seen to offset focusing.

Consider now the axial propagation curves for the second harmonic, first for the rigid surface, Fig. 2(c). The same general trend is observed as for the primary beam, with the concave target producing higher peak pressure than the free-field result, the convex surface producing lower peak pressure. Now compare Fig. 2(c) with the results for a free surface, Fig. 2(d). Substantial reduction in the peak amplitude of the reflected beam is observed in Fig. 2(d) for all three curvatures. The explanation is that for $R_n=-1$, the second harmonic generated before reflection is, just after it is reflected, in antiphase with the second harmonic generated by the primary beam immediately after reflection. Therefore, the second harmonic generated after reflection tends initially to offset the reflected second harmonic that was generated in the incident beam. Garrett *et al.*[8] describe similar behavior for difference-frequency generation involving reflection from a free surface.

We turn now to the power in the second-harmonic beam. Consider first the free-field result in Fig. 2(e). The second-harmonic power increases steadily only up until the focus at $\sigma=1$, after which it levels off. In fact, on a linear rather than dB scale, the power is observed to dip very sightly after the focus. The reason for less efficient second-harmonic generation beyond the focus is that the fundamental and second-harmonic components experience different phase shifts due to propagation through the focal region. Coherent generation of the second-harmonic component in a plane wave (in which the amplitude of the second harmonic increases linearly with distance) results from the fact that the fundamental and second-harmonic components are always in phase. Diffraction interferes with this phase coherence, especially in focal regions. Whereas the fundamental experiences a phase shift of approximately π radians through the focus, the second harmonic experiences a phase shift of more nearly $3\pi/2$ [see Fig. 3, where the phase angles arg(P_n) are shown along the axis of the beam]. Surface curvature further complicates the phase relations. The convex surface ($C=2$), which defocuses the reflected beam, is seen in Fig. 2(e) to increase second-harmonic power beyond the focus. The concave target ($C=-2$), which enhances focusing, results in lower power. For the free surface ($R_n=-1$), a pronounced dip in the second-harmonic power is observed in Fig. 2(f) just beyond the focus for all three surface curvatures. In contrast to the rigid surface, the free surface results in higher power in the reflected beam at the second-harmonic frequency when far from the interface.

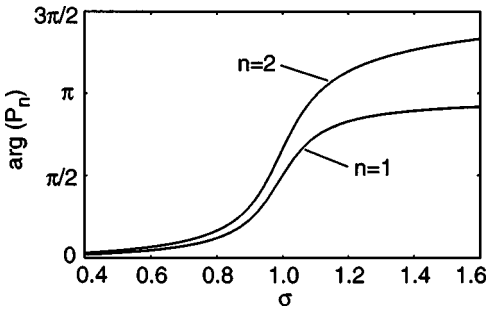

FIG. 3. Axial phases of fundamental and second-harmonic components for a focused Gaussian beam with $G=10$.

Sensitivity to the phase of the reflection coefficient is examined by allowing R_n to be a complex quantity and writing it as

$$R_n=|R_n|e^{i\phi_n}. \tag{70}$$

The expression is appropriate for describing reflection from targets with arbitrary complex impedance, and it may be substituted directly in Eq. (57). Solutions for the axial second-harmonic pressure are presented in Fig. 4 for $|R_n|=1$ and with $\phi_n=0$, $\pi/2$, π, $3\pi/2$ for $n=1,2$. The solutions for $\phi_n=0$ and $\phi_n=\pi$ are thus equivalent to the solutions for $R_n=1$ and $R_n=-1$, respectively, in Fig. 2.

We begin by discussing Fig. 4(b), for the planar surface ($C=0$), and recall that the result for $\phi_n=0$ is identical to

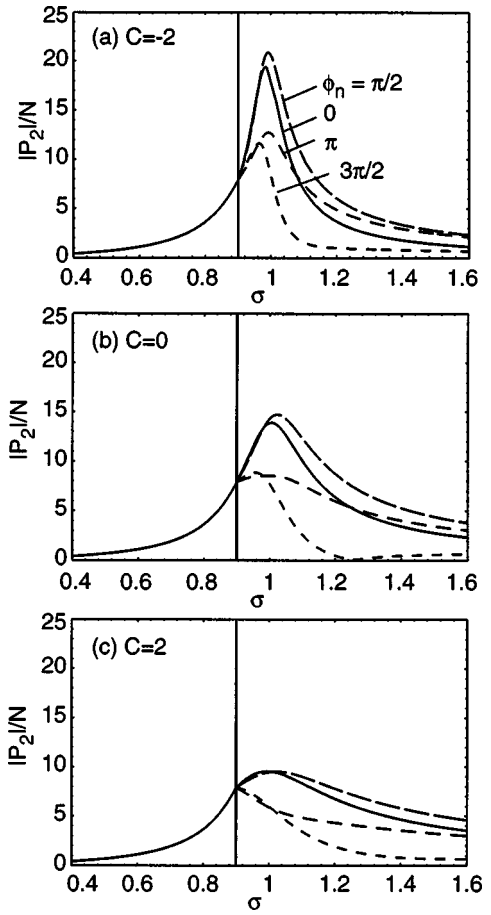

FIG. 4. Axial propagation curves for the second-harmonic pressure showing dependence on phase of the reflection coefficient.

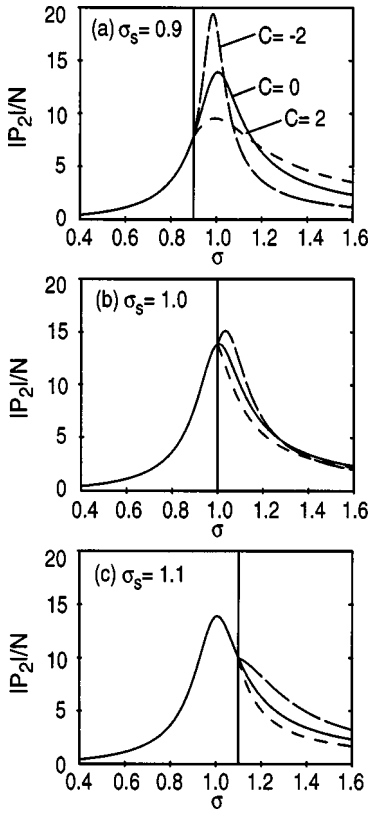

FIG. 5. Axial propagation curves for the second-harmonic pressure showing dependence on position of the reflecting surface.

the free-field solution in the absence of a reflecting surface. Note that the highest peak pressure is attained not for $\phi_n=0$, but for $\phi_n=\pi/2$, and the least efficient second-harmonic generation is attained for $\phi_n=3\pi/2$. Interpretation is facilitated by introducing the phase

$$\Phi=\arg(R_2/R_1^2)=\phi_2-2\phi_1, \tag{71}$$

which yields $\Phi=-\phi_n$ for the condition $\phi_1=\phi_2$ assumed here. For reflection of a plane wave, most efficient second-harmonic generation occurs for $\Phi=0$, because the phase coherence that existed between the fundamental and second harmonic before reflection is maintained just after reflection. The least efficient case for a plane wave is therefore $\Phi=\pi$. However, in a focused sound beam, the fundamental and second harmonic exit from the focal region with a net phase difference given by $\arg(P_2/P_1)\simeq\pi/2$ (recall Fig. 3). Diffraction thus introduces phase incoherence that is partially offset by a planar reflector for which $\Phi=-\pi/2$, and this is achieved in the present example with $\phi_n=\pi/2$. The least efficient second-harmonic generation observed in Fig. 4(b), for $\phi_n=3\pi/2$ and therefore $\Phi=-3\pi/2$, is consistent with this interpretation. Note that the second harmonic nearly vanishes on axis at $\sigma\simeq1.25$ as a result of phase incoherence. For the nonplanar surfaces represented in Figs. 4(a) and (c) the overall dependence on ϕ_n is similar.

We conclude by showing in Fig. 5 the effect of placing a rigid surface ($R_n=1$) at different positions relative to the focus ($\sigma_s=0.9,1.0,1.1$). The influence of surface curvature is least for the surface located at the focus, $\sigma_s=1$, where the radius of the incident beam is smallest. Observe the reversal in the order of the curves at $\sigma=1.6$ when comparing results for the surface positioned at $\sigma_s=0.9$ with those for $\sigma_s=1.1$.

VII. CONCLUSION

A theoretical model is presented for second-harmonic generation associated with reflection and transmission of a sound beam at a curved interface. For the case of reflection, the surface may have an arbitrary complex impedance. For the case of transmission it is assumed that both media are homogeneous fluids. Field integrals are presented for arbitrary incident sound beams, and they are evaluated in closed form for the case of focused Gaussian beams. The latter illustrates clearly the effects of curvature, impedance, and position of the interface on the reflected and transmitted second-harmonic beams.

ACKNOWLEDGMENTS

This work was supported by the Office of Naval Research, the National Science Foundation, and the David and Lucile Packard Foundation.

APPENDIX: INTERFACE POSITION ζ

Here we derive an expression for the position ζ that describes the geometry of the interface in the reflection and transmission coefficients. A general approach for arbitrary surfaces is provided by Marston.[13] For the case at hand, it proves convenient to instead consider first the specific case of an ellipsoidal surface defined by

$$\left(\frac{x-x_0}{l_x}\right)^2+\left(\frac{y-y_0}{l_y}\right)^2+\left(\frac{\zeta-\zeta_0}{l_z}\right)^2=1, \tag{A1}$$

where ζ is distance from the plane $z=z_s$ [recall Fig. 1 and Eq. (11)], (x_0,y_0) is the position of the ellipsoid center with respect to the axis of the incident sound beam (i.e., the z axis), the constant ζ_0 is defined below, and l_x, l_y, and l_z determine the relevant axis lengths.[9] Inversion of Eq. (A1) gives

$$\zeta(x,y)=\zeta_0-l_z[1-(x-x_0)^2/l_x^2-(y-y_0)^2/l_y^2]^{1/2}, \tag{A2}$$

where the negative root was selected to describe the lower half of the ellipsoidal surface, $\zeta<\zeta_0$. We define ζ_0 such that $\zeta(0,0)=0$ and expand Eq. (A2) about the point $(x,y)=(0,0)$, where the axis of the incident sound beam intersects the surface:

$$\zeta(x,y)=x\zeta_x(0,0)+y\zeta_y(0,0)+\tfrac{1}{2}x^2\zeta_{xx}(0,0)+\tfrac{1}{2}y^2\zeta_{yy}(0,0)+xy\zeta_{xy}(0,0)+O(r^3). \tag{A3}$$

Here $r=(x^2+y^2)^{1/2}$ is distance from the z axis and, for brevity, partial derivatives of ζ are indicated by subscripts.

We now let $r_0=(x_0^2+y_0^2)^{1/2}$ denote distance from the z axis to the center of the ellipsoid, l characterize the lengths $l_{x,y,z}$, and obtain approximations of the derivatives in Eq. (A3) for $r_0/l\ll1$. At leading order in r_0/l the results are

$$\zeta_x(0,0)=-x_0l_z/l_x^2,\quad \zeta_y(0,0)=-y_0l_z/l_y^2,$$
$$\zeta_{xx}(0,0)=l_z/l_x^2,\quad \zeta_{yy}(0,0)=l_z/l_y^2, \tag{A4}$$

$$\zeta_{xy}(0,0)=x_0y_0l_z/l_x^2l_y^2.$$

Since $\zeta_{xy}(0,0)$ is of order r_0/l in relation to both $\zeta_{xx}(0,0)$ and $\zeta_{yy}(0,0)$ it may be discarded, and therefore the leading-order terms in Eq. (A3) give

$$\zeta(x,y)=(l_z/l_x^2)(\tfrac{1}{2}x^2-x_0x)+(l_z/l_y^2)(\tfrac{1}{2}y^2-y_0y). \quad \text{(A5)}$$

For $r_0/l \ll 1$ one may identify

$$b_x=l_x^2/l_z, \quad b_y=l_y^2/l_z, \quad \text{(A6)}$$

as the local radii of curvature at $(x,y,z)=(0,0,z_s)$, in the (x,z) and (y,z) planes, respectively, and

$$\theta_x=-x_0/b_x, \quad \theta_y=-y_0/b_y, \quad \text{(A7)}$$

as the corresponding angles of the normal to the interface with respect to the z axis (recall Fig. 1, where $b\equiv b_x$ and $\theta \equiv \theta_x$). In terms of these quantities Eq. (A5) may be written in the more general form

$$\zeta(x,y)=\frac{1}{2}\left(\frac{x^2}{b_x}+\frac{y^2}{b_y}\right)+(\theta_x x+\theta_y y). \quad \text{(A8)}$$

The first term in parentheses accounts for focusing or defocusing due to curvature of the interface, and the second accounts for deflection of the reflected or transmitted beam away from the z axis due to inclination of the interface.

Two special cases are worth noting. For a spherical surface set $l_x=l_y=l_z\equiv b$, where $b=b_x=b_y$ is the radius of the sphere. If its center is displaced a distance x_0 from the z axis such that it lies on the line that passes through $(x,y)=(x_0,0)$ parallel to the z axis, Eq. (A5) reduces to

$$\zeta(x,y)=(x^2+y^2)/2b-x_0x/b. \quad \text{(A9)}$$

Now consider a cylindrical surface whose central axis passes through $(x,y)=(x_0,0)$ parallel to the y axis. In this case set $l_x=l_z\equiv b$, where $b=b_x$ is the radius of the cylinder, with $l_y=\infty$ and therefore $b_y=\infty$, such that Eq. (A5) reduces to

$$\zeta(x,y)=x^2/2b-x_0x/b. \quad \text{(A10)}$$

[1] E. L. Carstensen and D. R. Bacon, ''Biomedical applications,'' in *Nonlinear Acoustics*, edited by M. F. Hamilton and D. T. Blackstock (Academic, Boston, 1998), Chap. 15.

[2] M. A. Averkiou, D. N. Roundhill, and J. E. Powers, ''A new imaging technique based on the nonlinear properties of tissues,'' Proc. IEEE Ultrason. Symp. **2**, 1561–1566 (1997).

[3] B. Ward, A. C. Baker, and V. F. Humphrey, ''Nonlinear propagation applied to the improvement of resolution in diagnostic medical ultrasound,'' J. Acoust. Soc. Am. **101**, 143–154 (1997).

[4] P. T. Christopher, ''Finite amplitude distortion-based inhomogeneous pulse echo ultrasonic imaging,'' IEEE Trans. Ultrason. Ferroelectr. Freq. Control **44**, 125–139 (1997).

[5] H. Becher, K. Tiemann, C. Pohl, N. C. Nanda, M. A. Averkiou, J. E. Powers, and B. Lüderitz, ''Improvement in endocardial border delineation using tissue harmonic imaging,'' Echocardiography **15**, 511–517 (1998).

[6] D. Rugar, ''Resolution beyond the diffraction limit in the acoustic microscope,'' J. Appl. Phys. **56**, 1338–1346 (1984).

[7] L. Germain and J. D. N. Cheeke, ''Generation and detection of high-order harmonics in liquids using a scanning acoustic microscope,'' J. Acoust. Soc. Am. **83**, 942–949 (1988).

[8] G. S. Garrett, J. Naze Tjøtta, R. L. Rolleigh, and S. Tjøtta, ''Reflection of parametric radiation from a finite planar target,'' J. Acoust. Soc. Am. **75**, 1462–1472 (1984).

[9] M. A. Averkiou, ''Experimental investigation of propagation and reflection phenomena in finite amplitude sound beams,'' Ph.D. dissertation, The University of Texas at Austin, 1994.

[10] I. R. S. Makin, ''Reflection and transmission of a focused finite amplitude sound beam incident on a curved interface,'' Ph.D. dissertation, The University of Texas at Austin, 1994.

[11] M. F. Hamilton, ''Sound beams,'' in *Nonlinear Acoustics*, edited by M. F. Hamilton and D. T. Blackstock (Academic, Boston, 1998), Chap. 8.

[12] D. T. Blackstock, ''Propagation of plane sound waves of finite amplitude in nondissipative fluids,'' J. Acoust. Soc. Am. **34**, 9–30 (1962).

[13] P. L. Marston, ''Quantitative ray methods for scattering,'' in *Encyclopedia of Acoustics*, edited by M. J. Crocker (Wiley, New York, 1997), Chap. 43.

Compressibility effects on steady streaming from a noncompact rigid sphere

Ashok Gopinath[a)]
Department of Mechanical Engineering, Naval Postgraduate School, Code ME/Gk, Monterey, California 93943

Eugene H. Trinh[b)]
Jet Propulsion Laboratory, 4800 Oak Grove Drive, Pasadena, California 91109

(Received 21 November 1999; accepted for publication 25 June 2000)

The problem of steady streaming around a rigid isolated sphere in a plane standing acoustic field is considered. Existing results in the literature have been generalized to allow for noncompactness of the sphere, and the influence of fluid compressibility on the streaming behavior has been included. It is found that in the high-frequency limit of interest for which the streaming is strongest, the effective steady slip velocity at the edge of the inner boundary layer region that is responsible for driving the steady streaming in the bulk of the fluid in the outer region, has a complex variation over the surface of the sphere that depends on (i) the sphere position (with respect to the node/antinode of the acoustic field), (ii) the extent of sphere compactness, and (iii) on a well-defined function (representing compressibility effects) of the fluid Prandtl number and its ratio of specific heats. Not surprisingly, the contribution from this function is negligible when the host fluid is a liquid. The steady streaming behavior around the sphere is demonstrated with the help of flow streamlines for various cases in the diffusive limit of weak outer flow for low streaming Reynolds numbers. [S0001-4966(00)01810-5]

PACS numbers: 43.25.Nm, 43.25.Uv [MFH]

I. INTRODUCTION

Acoustic streaming is a well-known steady flow phenomenon induced by the time-averaged nonlinear interactions in a time-harmonic flow field, such as an acoustic field. A full review is beyond the scope of this paper and will not be attempted here; instead the interested reader is referred to recent comprehensive surveys by Riley[1] and Nyborg.[2]

In this paper we deal with the type of streaming that has its origins in the time-averaged effects in oscillatory boundary layers on an object in an acoustic field, as described, for instance, in an early paper by Nyborg.[3] The earlier history of the problem and the considerable body of literature on this topic that has developed since is described elsewhere.[1,2] The emphasis in the current paper is on the corrections to the main results in the literature that arise due to (i) noncompactness of the object that is important in ultrasonic fields, and (ii) compressibility effects, which can be quite significant if the host fluid is a gas, but has received little attention so far, as, for example, in the work of Qi.[4] The model problem being considered here is the streaming external to an isolated rigid sphere (of radius a) in a standing acoustic field (of wavelength $\lambda = 2\pi/k$), for which $ka \ll 1$, although as noted later the series solution being developed in powers of ka could be extended to desired accuracy for finite values of $ka < 1$. Early contributions to *this particular problem* were made by Lane[5] and Wang[6] (with probable omissions in the work of Lane,[5] as noted in recent comments by Nyborg[7]). Riley[8] provided the first complete treatment of this problem, although his leading-order solution is strictly valid only for the sphere located at the *velocity antinode*, and only in the limit of $ka \to 0$ for which fluid compressibility is unimportant. His primary solution was subsequently complemented by the work of Lee and Wang,[9] who (based on the formulation by Nyborg[3]) have provided $O(ka)$ corrections for arbitrary sphere location based on an adiabatic or *barotropic* treatment (i.e. density dependent only on pressure in the equation of state) of fluid compressibility effects. More recently, Zhao *et al.*[10] have developed further $O(ka)^2$ corrections to this flow, once again based on the barotropic assumption, but only for the case of the sphere located at the *velocity node*. In the current study, a complete solution to the above problem has been provided to $O(ka)^2$ accuracy that takes into account the above limitations, and includes a *baroclinic* treatment of the fluid compressibility (i.e., includes density dependence on both pressure *and* temperature). The associated thermoacoustic streaming behavior that gives rise to novel heating effects has been reported elsewhere.[11]

II. GOVERNING EQUATIONS

In the following development, a superscript $*$ always denotes dimensional quantities, a subscript m denotes the mean (initially) quiescent state of the fluid, while variables in **boldface** represent vector quantities. Consider the initial quiescent state of the fluid, at rest, characterized by a mean pressure, p_m, density, ρ_m, and temperature, T_m. The standing acoustic wave in the fluid is assumed to have a velocity distribution of the form

[a)]Author to whom correspondence should be addressed. Electronic mail: gopinath@nps.navy.mil
[b)]Currently at Microgravity Research Division, Code UG, NASA Headquarters, Washington, DC 20546.

$$u_z^* = U_0 \cos(kz^*)\cos(\varpi t^*), \tag{1}$$

where $U_0 = A\varpi$ is the velocity amplitude, A the displacement amplitude, $k = 2\pi/\lambda$ the wave number, $\varpi = 2\pi f$ the radian frequency, t^* the time, and z^* the axial coordinate measured from the velocity antinode of the standing wave. Now consider the presence of an isolated rigid sphere of radius, a, located in the standing wave at position $z^* = z_0^*$. To develop the series solution methodology it is assumed that the sphere radius is small compared to the acoustic radian wavelength ($ka \ll 1$), but large on the scale of the displacement amplitude of fluid oscillations in the acoustic field ($\epsilon \equiv A/a \ll 1$). However, the series solution being developed can be extended to desired accuracy (as demonstrated, for instance, by Van Dyke[12] in a different context), and it is expected that the results will be applicable to larger finite values of $ka < 1$, and $\epsilon < 1$, as has also been verified in an associated experimental study by Gopinath and Harder[13] on heat transfer due to acoustic streaming. Furthermore, interest here will only be in the high-frequency cases $M^2 \equiv 2a^2/\delta_\nu^2 \gg 1$ (where $\delta_\nu = \sqrt{2\nu/\varpi}$) for which the time-averaged effects in the shear layers are most pronounced.

Consider a fixed axisymmetric spherical coordinate system $(r^*, \vartheta, \varphi)$, with an origin at the center of the sphere, and the $\vartheta = 0$, π axis aligned with the direction of fluid oscillation. In the presence of the acoustic field, the fluid velocity $\mathbf{u}^* \equiv (u_r^*, u_\vartheta^*, 0)$ and other flow variables are defined as disturbance quantities from the quiescent mean and nondimensionalized as follows:

$$\tau = \varpi t^*, \quad z = kz^*, \quad r = \frac{r^*}{a}, \quad \mathbf{u} = \frac{\mathbf{u}^*}{U_0},$$

$$\psi = \frac{\psi^*}{U_0 a^2}, \quad \boldsymbol{\nabla} \equiv a\boldsymbol{\nabla}^*, \tag{2a}$$

$$\rho = \frac{(\rho^* - \rho_m)}{\Delta\rho_{\text{ref}}}, \quad p = \frac{(p^* - p_m)}{\Delta p_{\text{ref}}}, \quad \theta = \frac{(T^* - T_m)}{\Delta T_{\text{ref}}}, \tag{2b}$$

where

$$\Delta\rho_{\text{ref}} = \alpha\rho_m, \quad \Delta p_{\text{ref}} = \alpha\rho_m c_m^2,$$
$$\Delta T_{\text{ref}} = \alpha T_m (c_m^2/c_p T_m) \tag{2c}$$

with $c_m = \varpi/k$ being the *adiabatic* speed of sound in the quiescent state, γ the ratio of specific heats, and $\alpha = U_0/c_m = Ak$ the Mach number.

The governing equations of mass, momentum, and energy to be solved are

$$ka\frac{\partial\rho}{\partial\tau} + \epsilon ka(\boldsymbol{\nabla}\cdot\rho\mathbf{u}) + \nabla\cdot\mathbf{u} = 0, \tag{3}$$

$$(1+\epsilon ka\rho)\left[\frac{\partial\mathbf{u}}{\partial\tau} + \epsilon(\mathbf{u}\cdot\boldsymbol{\nabla})\mathbf{u}\right] = -\frac{1}{ka}\boldsymbol{\nabla}p + \frac{1}{M^2}\left[\nabla^2 u + \left(\frac{1}{3} + \frac{K}{\mu_v}\right)\boldsymbol{\nabla}(\boldsymbol{\nabla}\cdot\mathbf{u})\right], \tag{4}$$

$$(1+\epsilon ka\rho)\left[\frac{\partial\theta}{\partial\tau} + \epsilon(\mathbf{u}\cdot\boldsymbol{\nabla})\theta\right] = \frac{1}{\sigma M^2}\nabla^2\theta + \beta T^*\left[\frac{\partial p}{\partial\tau} + \epsilon(\mathbf{u}\cdot\boldsymbol{\nabla})p\right] + \frac{\epsilon ka}{M^2}\chi, \tag{5}$$

and need to be combined with the complete equation of state expressed as follows:

$$\Delta\rho^* = \left(\frac{\partial\rho^*}{\partial p^*}\right)_{T^*}\Delta p^* + \left(\frac{\partial\rho^*}{\partial T^*}\right)_{p^*}\Delta T^*, \tag{6}$$

which, in general, accounts for density variations with both pressure and temperature, as discussed, for example, by Morse and Ingard.[14] In (5), σ represents the Prandtl number, and the last term χ represents the viscous dissipation terms, while the other symbols in the above equations have their usual meanings. It maybe noted that the Mach number, α in (2c), can be expressed as $\alpha = \epsilon ka$ whereby the theoretical ordering of the different parameters in this study may be summarized as follows:

$$\alpha \ll \epsilon \ll 1 \ll M^2 \quad \text{and} \quad ka \ll 1. \tag{7}$$

The boundary conditions associated with the above equations are

$$\mathbf{u} = 0, \quad \theta = 0, \quad \text{on} \quad r = 1, \tag{8}$$

$$\mathbf{u}_z = \cos z e^{i\tau}, \quad \theta = 0, \quad \text{as} \quad r \to \infty, \tag{9}$$

where in (9) the real part is of course understood. The temperature boundary condition in (8) at $r = 1$ is a simplifying assumption made to thermally decouple the solid sphere from the host fluid so as to concentrate solely on the time-averaged streaming mechanics in the fluid. This restriction may be relaxed in a straightforward manner to treat the corresponding conjugate problem, as has been considered elsewhere by Gopinath *et al.*,[15] although in a different context.

The solution for $(\mathbf{u}, \theta, p, \rho)$ is sought in a perturbation series of the form

$$\mathbf{u} = \mathbf{u}_0 + \epsilon\mathbf{u}_1 + \cdots, \tag{10}$$

where a typical velocity term $\mathbf{u}_n$ in (10) can be further decomposed as follows:

$$\mathbf{u}_n = \mathbf{u}_n^{(\psi)} + ka\mathbf{u}_n^{(\phi)}, \quad \text{with} \quad \mathbf{u}_n^{(\phi)} = \mathbf{u}_n^{(\phi 1)} + ka\mathbf{u}_n^{(\phi 2)} + O(ka)^2, \tag{11}$$

where $\mathbf{u}_n^{(\psi)}$ represents the incompressible contribution, while $\mathbf{u}_n^{(\phi)}$ comprises the higher-order compressibility corrections. In anticipation of the importance of the flow mechanics in the narrow Stokes layer region, suitable boundary layer variables for this region are also defined as follows:

$$\boldsymbol{\mathcal{U}} \equiv (\mathcal{U}_\eta, \mathcal{U}_\vartheta, 0),$$
$$\text{where} \quad \boldsymbol{\mathcal{U}}_n = \boldsymbol{\mathcal{U}}_n^{(\psi)} + ka\boldsymbol{\mathcal{U}}_n^{(\phi)},$$
$$\text{with} \quad \boldsymbol{\mathcal{U}}_n^{(\phi)} = \boldsymbol{\mathcal{U}}_n^{(\phi 1)} + ka\boldsymbol{\mathcal{U}}_n^{(\phi 2)} + O(ka)^2, \tag{12a}$$

$$\eta = \frac{M}{\sqrt{2}}(r-1), \quad \mathcal{U}_\eta(\eta, \vartheta, \tau) = \frac{M}{\sqrt{2}}u_r(r, \vartheta, \tau),$$
$$[\mathcal{U}_\vartheta, \wp, \varrho, \Theta](\eta, \vartheta, \tau) \equiv [u_\vartheta, p, \rho, \theta](r, \vartheta, \tau). \tag{12b}$$

III. THE OSCILLATORY BOUNDARY LAYER

A. Leading-order terms

In the notation of (10)–(12), the results of Riley[8] can be used to obtain the components of the leading-order $O(\epsilon^0)$ first harmonic boundary layer velocity $\mathcal{U}_0$ as

$$\mathcal{U}_{\vartheta,0}^{(\psi)} = -\tfrac{3}{2}[1-e^{-\eta(1+i)}]\sin\vartheta\cos z_0 e^{i\tau}, \tag{13a}$$

$$\mathcal{U}_{\eta,0}^{(\psi)} = 3[\eta - \tfrac{1}{2}(1-i)(1-e^{-\eta(1+i)})]\cos\vartheta\cos z_0 e^{i\tau}. \tag{13b}$$

For the temperature, an $O(\epsilon^0)$ balance of the energy equation (5) in terms of (12) yields

$$\frac{\partial\Theta_0}{\partial\tau} = \frac{1}{2\sigma}\frac{\partial^2\Theta_0}{\partial\eta^2} + \beta_m T_m \frac{\partial\wp_0}{\partial\tau}, \tag{14}$$

where the leading-order pressure, $\wp_0$, in the inner region is uniform across the boundary layer. Setting $\Theta_0 = \overline{\Theta}_0 e^{i\tau}$, and $\wp_0 = \overline{\wp}_0 e^{i\tau}$, the solution of (14) subject to (8) is

$$\overline{\Theta}_0 = \beta_m T_m \overline{\wp}_0[1-e^{-\eta\sqrt{\sigma}(1+i)}], \tag{15}$$

The leading-order density term $\varrho_0 = \overline{\varrho}_0 e^{i\tau}$ can now be obtained in terms of $\wp_0$ and Θ_0 from the equation of state in (6), which, after some manipulation, yields

$$\overline{\varrho}_0 = \gamma\overline{\wp}_0 - \beta_m T_m \frac{c_m^2}{c_p T_m}\overline{\Theta}_0$$

$$= \overline{\wp}_0[\gamma - B'(1-e^{-\eta\sqrt{\sigma}(1+i)})], \tag{16}$$

where it can be shown[14] from Maxwell's generalized thermodynamic relations that the parameter B' in (16) is $(\beta_m T_m)^2(c_m^2/c_p T_m) \equiv (\gamma-1)$. It is the behavior of this density fluctuation term in (16) that is crucial in determining the extent of the influence of fluid compressibility on the nature of the streaming motion.

The pressure $\wp_0$ in the inner boundary layer region for use in (15) and (16) is obtained from the limiting form of the acoustic field in the outer region as shown, for instance, by Wang and Lee[16] as

$$\overline{\wp}_0 \equiv \overline{\wp}_0^{(c)} + ka[\overline{\wp}_0^{(\psi)} + ka\overline{\wp}_0^{(\phi)}],$$

$$\text{with } \wp_0^{(\phi)} = \wp_0^{(\phi 1)} + ka\wp_0^{(\phi 2)} + O(ka)^2, \tag{17a}$$

$$= -i\sin z_0 P_0(\mu) + ka[-\tfrac{3}{2}iP_1(\mu)\cos z_0 + kai\sin z_0$$

$$\times(\tfrac{1}{2}P_0(\mu) + \tfrac{5}{9}P_2(\mu)) + \cdots], \tag{17b}$$

where the $P_n(\mu)$ represent Legendre polynomials of order n with argument $\mu = \cos\vartheta$. Noting the direct dependence of ϱ_0 on $\wp_0$ in (16), for convenience in what follows ϱ_0 can also be decomposed according to (17) as

$$\varrho_0 = \varrho_0^{(c)} + ka[\varrho_0^{(\psi)} + ka\varrho_0^{(\phi)}], \tag{18}$$

wherein each term above in (18) corresponds to the associated term in (17) through (16).

B. Higher-order velocity terms

The higher $O(ka)$ correction terms to the leading order velocity in (13), as represented by the general form in (11), are now determined in a manner similar to that adopted by Zhao *et al.*[10]

An $O(\epsilon^0)$ balance of the ϑ component of the momentum equation (4) in the inner region gives

$$\frac{\partial\mathcal{U}_{\vartheta,0}}{\partial\tau} = -\frac{1}{ka}\frac{\partial\wp_0}{\partial\vartheta} + \frac{1}{2}\frac{\partial^2\mathcal{U}_{\vartheta,0}}{\partial\eta^2}, \tag{19}$$

from which the solution of $\overline{\mathcal{U}}_{\vartheta,0}$ subject to $\overline{\mathcal{U}}_{\vartheta,0} = 0$ at $\eta = 0$ in (8) is

$$\overline{\mathcal{U}}_{\vartheta,0} = \frac{i}{ka}\frac{\partial\overline{\wp}_0}{\partial\vartheta}(1-e^{-\eta(1+i)}), \tag{20}$$

which can be expressed in terms of the handy representation for $\wp_0$ in (17) as

$$\overline{\mathcal{U}}_{\vartheta,0} = i\left[\frac{\partial\overline{\wp}_0^{(\psi)}}{\partial\vartheta} + ka\frac{\partial\overline{\wp}_0^{(\phi)}}{\partial\vartheta}\right](1-e^{-\eta(1+i)})$$

$$\equiv \overline{\mathcal{U}}_{\vartheta,0}^{(\psi)} + ka\overline{\mathcal{U}}_{\vartheta,0}^{(\phi)}, \tag{21a}$$

$$= [-\tfrac{3}{2}\sin\vartheta\cos z_0 + kaC_0(\vartheta;ka,z_0)](1-e^{-\eta(1+i)}), \tag{21b}$$

where

$$C_0(\vartheta;ka,z_0) = \tfrac{5}{3}\cos\vartheta\sin\vartheta\sin z_0$$

$$+ \tfrac{1}{40}ka(3+35\cos^2\vartheta)\sin\vartheta\cos z_0. \tag{21c}$$

For the associated radial velocity component $\mathcal{U}_{\eta,0}$ in the boundary layer, the $O(\epsilon^0)$ solenoidal part $\mathcal{U}_{\eta,0}^{(\psi)}$ is known from (13b), whereas the desired compressibility correction $\mathcal{U}_{\eta,0}^{(\phi)}$ as defined in (12) may be determined from an $O(\epsilon^0)$ balance of the continuity equation (3), and is found to satisfy

$$i\overline{\varrho}_0 + \frac{\partial\overline{\mathcal{U}}_{\eta,0}^{(\phi)}}{\partial\eta} + \frac{1}{\sin\vartheta}\frac{\partial}{\partial\vartheta}(\overline{\mathcal{U}}_{\vartheta,0}^{(\phi)}\sin\vartheta) = 0, \tag{22}$$

which can be integrated once subject to the condition $\overline{\mathcal{U}}_{\eta,0}^{(\phi)} = 0$ at $\eta = 0$ in (8) to get

$$\overline{\mathcal{U}}_{\eta,0}^{(\phi)} = -C_1(\mu)\left[\eta - \frac{(1-i)}{2}(1-e^{-\eta(1+i)})\right]$$

$$-i\wp_0\left[\eta + \frac{(\gamma-1)(1-i)}{2\sqrt{\sigma}}(1-e^{-\eta\sqrt{\sigma}(1+i)})\right], \tag{23}$$

where

$$C_1(\mu) = \frac{1}{\sin\vartheta}\frac{\partial}{\partial\vartheta}[C_0(\vartheta)\sin\vartheta]$$

$$= \tfrac{5}{3}(3\mu^2-1)\sin z_0 + \tfrac{1}{2}ka\mu(7\mu^2 - \tfrac{16}{5})\cos z_0. \tag{24}$$

IV. THE STEADY STREAMING EQUATIONS

Having established the form of the leading-order first-harmonic boundary layer quantities in Sec. III, attention is

now turned to the $O(\epsilon^1)$ velocity term $\boldsymbol{\mathcal{U}}_1$ in the inner region, which as is well known contains a steady time-averaged component ($\boldsymbol{\mathcal{U}}_{1s}$), in addition to the second harmonic ($\boldsymbol{\mathcal{U}}_{1u}$). The governing equations for the driving ϑ component, $\boldsymbol{\mathcal{U}}_{\vartheta,1s}$, of $\mathcal{U}_{1s}$ is obtained from a time average of an $O(\epsilon^1)$ balance of the momentum equation in (4), and is sought as

$$\mathcal{U}_{\vartheta,1s}(\eta,\vartheta)=\mathcal{U}^{(0)}_{\vartheta,1s}+(ka)\mathcal{U}^{(1)}_{\vartheta,1s}+(ka)^2\mathcal{U}^{(2)}_{\vartheta,1s}+O(ka)^3, \quad (25)$$

where the governing equation for each of the components in (25) is

$$\frac{1}{2}\frac{\partial^2\mathcal{U}^{(0)}_{\vartheta,1s}}{\partial\eta^2}=\left\langle \mathcal{U}^{(\psi)}_{\eta,0}\frac{\partial\mathcal{U}^{(\psi)}_{\vartheta,0}}{\partial\eta}+\mathcal{U}^{(\psi)}_{\vartheta,0}\frac{\partial\mathcal{U}^{(\psi)}_{\vartheta,0}}{\partial\vartheta}\right\rangle+\frac{\partial\wp^{(\psi)}_{1s}}{\partial\vartheta}, \quad (26a)$$

$$\begin{aligned}\frac{1}{2}\frac{\partial^2\mathcal{U}^{(1)}_{\vartheta,1s}}{\partial\eta^2}=&\left\langle \underline{\varrho^{(c)}_0}\frac{\partial\mathcal{U}^{(\psi)}_{\vartheta,0}}{\partial\tau}\right\rangle\\&+\left\langle \mathcal{U}^{(\psi)}_{\eta,0}\frac{\partial\mathcal{U}^{(\phi1)}_{\vartheta,0}}{\partial\eta}+\mathcal{U}^{(\psi)}_{\vartheta,0}\frac{\partial\mathcal{U}^{(\phi1)}_{\vartheta,0}}{\partial\vartheta}\right\rangle\\&+\left\langle \underline{\mathcal{U}^{(\phi1)}_{\eta,0}}\frac{\partial\mathcal{U}^{(\psi)}_{\vartheta,0}}{\partial\eta}+\mathcal{U}^{(\phi1)}_{\vartheta,0}\frac{\partial\mathcal{U}^{(\psi)}_{\vartheta,0}}{\partial\vartheta}\right\rangle+\frac{\partial\wp^{(\phi1)}_{1s}}{\partial\vartheta}, \quad (26b)\end{aligned}$$

$$\begin{aligned}\frac{1}{2}\frac{\partial^2\mathcal{U}^{(2)}_{\vartheta,1s}}{\partial\eta^2}=&\left\langle \underline{\varrho^{(c)}_0}\frac{\partial\mathcal{U}^{(\phi1)}_{\vartheta,0}}{\partial\tau}+\underline{\varrho^{(\psi)}_0}\frac{\partial\mathcal{U}^{(\psi)}_{\vartheta,0}}{\partial\tau}\right\rangle\\&+\left\langle \underline{\mathcal{U}^{(\phi1)}_{\eta,0}}\frac{\partial\mathcal{U}^{(\phi1)}_{\vartheta,0}}{\partial\eta}+\mathcal{U}^{(\phi1)}_{\vartheta,0}\frac{\partial\mathcal{U}^{(\phi1)}_{\vartheta,0}}{\partial\vartheta}\right\rangle\\&+\left\langle \underline{\mathcal{U}^{(\phi2)}_{\eta,0}}\frac{\partial\mathcal{U}^{(\psi)}_{\vartheta,0}}{\partial\eta}+\mathcal{U}^{(\phi2)}_{\vartheta,0}\frac{\partial\mathcal{U}^{(\psi)}_{\vartheta,0}}{\partial\vartheta}\right\rangle\\&+\left\langle \mathcal{U}^{(\psi)}_{\eta,0}\frac{\partial\mathcal{U}^{(\phi2)}_{\vartheta,0}}{\partial\eta}+\mathcal{U}^{(\psi)}_{\vartheta,0}\frac{\partial\mathcal{U}^{(\phi2)}_{\vartheta,0}}{\partial\vartheta}\right\rangle+\frac{\partial\wp^{(\phi2)}_{1s}}{\partial\vartheta}, \quad (26c)\end{aligned}$$

where the angle brackets $\langle\cdots\rangle$ denote a time average of the enclosed quantities. These equations may now be integrated using the first-harmonic results from Sec. III, subject to the no-slip condition in (8), and boundedness as $\eta\to\infty$, to obtain the streaming velocity behavior, as discussed below. A close inspection of Eq. (26) reveals that the terms underlined in the forcing function on the RHS of each of (26b), and (26c), are the crucial terms that are responsible for introducing compressibility corrections through a time average of their phased interactions with the first-harmonic flow velocity. These terms were based on an adiabatic treatment of density in earlier studies,[9,10] whereas here they derive directly from the complete baroclinic equation of state in (6) that gives rise to the density fluctuation term in (16).

V. RESULTS AND DISCUSSION

In carrying out the time averaging of the RHS of (26), it must be noted that any nondecaying constant terms that arise are ignored in the integration process since they give rise to physically unrealistic growing velocities. In fact, such terms serve to balance the steady $O(\epsilon^1)$ pressure, $\wp_{1s}$, in the inner region as seen in (26), which, however, being peripheral to the current study is not treated here. Furthermore, in the interests of brevity, the complete distribution of the streaming velocity component, $\mathcal{U}_{\vartheta,1s}$, in the inner region is not provided either; instead only its limiting form as $\eta\to\infty$ is provided, which is important in that it serves as the ''slip velocity'' in driving the steady flow in the outer region that is the bulk of the flow domain. The results are presented below in terms of a new velocity term $\mathcal{W}_{\vartheta,1s}$, and a function $P^*_n(\mu)$, which have been introduced for convenience and are defined as

$$\mathcal{W}_{\vartheta,1s}=\mathcal{U}_{\vartheta,1s}\sin\vartheta \quad \text{and} \quad P^*_n(\mu)=\int_{-1}^{\mu}P_n(\mu')d\mu'. \quad (27)$$

A. The slip velocity

Integration of (26a) gives the leading-order streaming solution obtained by Riley,[8] with its limiting form at the edge of the inner region given in terms of (27) by

$$\mathcal{W}^{(0)}_{\vartheta,1s}|_{\eta\to\infty}=\tfrac{45}{8}P^*_2(\mu)\cos^2 z_0. \quad (28)$$

Similarly, integrating (26b), and determining its limiting form gives

$$\mathcal{W}^{(1)}_{\vartheta,1s}|_{\eta\to\infty}=\tfrac{1}{4}\sin 2z_0\{[1+3f(\sigma,\gamma)]P^*_1(\mu)-26P^*_3(\mu)\},$$

$$\text{where}\quad f(\sigma,\gamma)=\frac{\sqrt{\sigma}(\gamma-1)}{(1+\sigma)}, \quad (29)$$

where the function $f(\sigma,\gamma)$ representing compressibility effects is the new result here, and has the same functional dependence on σ and γ as in the simplified equations (B3), (B4) of Qi[4] for streaming due to a plane standing wave at grazing incidence to a plane rigid boundary. It may also be noted that the magnitude of the $O(1)$ slip velocity $\mathcal{W}^{(0)}_{\vartheta,1s}$ from (28) is a maximum for the sphere located at the velocity antinode ($z_0=0$), where, however, the $O(ka)$ term $\mathcal{W}^{(1)}_{\vartheta,1s}$ from (29) makes no contribution, its own maximum being for the sphere halfway between that node and antinode at $z_0=\pi/4$, as also noted by Lee and Wang.[9]

Finally, the $O(ka)^2$ correction term can be obtained by integrating (26c) to get

$$\begin{aligned}\mathcal{W}^{(2)}_{\vartheta,1s}|_{\eta\to\infty}=&\sin^2 z_0\left[\frac{25}{42}P^*_2(\mu)+\frac{400}{63}P^*_4(\mu)\right]\\&-\cos^2 z_0[\tfrac{9}{8}P^*_2(\mu)+6P^*_4(\mu)]+f(\sigma,\gamma)\\&\times[\tfrac{9}{4}\cos^2 z_0-\tfrac{5}{3}\sin^2 z_0]P^*_2(\mu), \quad (30)\end{aligned}$$

where the first term in $[\cdots]$ above with coefficient $\sin^2 z_0$ was obtained by Zhao *et al.*[10] in their recent study of streaming for the sphere at the velocity node, $z_0=\pi/2$. The second term in $[\cdots]$ in (30) with coefficient $\cos^2 z_0$ is a new term and represents $O(ka)^2$ corrections to the leading-order slip in (28), while the last term in $[\cdots]$ with coefficient $f(\sigma,\gamma)$ once again represents compressibility corrections, and makes contributions at both the node and antinode, and has not been included in any of the studies so far. As noted at the end of Sec. IV, the origin of this effect in $f(\sigma,\gamma)$ maybe traced directly to particular terms in the RHS of (26b) and (26c). However, since $f(\sigma,\gamma)\propto(\gamma-1)$, these compressibility cor-

rections in both (29) and (30) are negligibly small when the host fluid is a liquid.

B. The outer flow

The leading-order slip velocity in (28) has a dimensional magnitude of $O(\epsilon U_0 = U_0^2/a\varpi)$, and gives rise to a streaming Reynolds number defined by Stuart[17] as $R_s \equiv U_0^2/\varpi\nu$, which governs the behavior of the steady flow in the rest of the fluid domain. It can be shown that this outer steady flow is incompressible, and for $R_s \gg 1$ gives rise to a double boundary layer structure proposed by Stuart.[18] Here the simpler yet illustrative case of $R_s \ll 1$ is considered to determine the variations in the predominantly diffusive streaming flow patterns that arise as observed in many experimental studies on acoustic levitation.

In this creeping flow limit of $R_s \ll 1$, the incompressible flow can be conveniently represented in terms of a steady axisymmetric Stokes streamfunction ψ_{1s} of scale $O(\epsilon U_0 a^2)$, governed by

$$D^4\psi_{1s} = 0, \quad \text{where } D^2 \equiv \frac{\partial^2}{\partial r^2} + \frac{(1-\mu^2)}{r^2}\frac{\partial^2}{\partial \mu^2}, \tag{31}$$

subject to the boundary conditions

$$\begin{aligned} &\psi_{1s} = 0 \quad \text{and} \quad \frac{\partial \psi_{1s}}{\partial r} = -\mathcal{W}_{\vartheta,1s}\big|_{\eta\to\infty}, \quad \text{as } r \to 1, \\ &\text{and } \psi_{1s} = o(r^2), \quad \text{as } r \to \infty, \end{aligned} \tag{32}$$

where the slip velocity condition at $r=1$ above is obtained by matching with the results from the inner region in (28)–(30). In keeping with the notation in (25), ψ_{1s} can also be represented as

$$\psi_{1s}(r,\vartheta) = \psi_{1s}^{(0)} + (ka)\psi_{1s}^{(1)} + (ka)^2\psi_{1s}^{(2)} + O(ka)^3. \tag{33}$$

The leading-order solution in (33), $\psi_{1s}^{(0)}$, was obtained by Riley[8] as

$$\psi_{1s}^{(0)} = -\frac{45}{16}\left(1 - \frac{1}{r^2}\right)P_2^*(\mu)\cos^2 z_0, \tag{34}$$

while the $O(ka)$ term $\psi_{1s}^{(1)}$ can be determined to be

$$\begin{aligned} \psi_{1s}^{(1)} = &-\frac{1}{8}\sin 2z_0\left(1 - \frac{1}{r^2}\right) \\ &\times\left\{r[1+3f(\sigma,\gamma)]P_1^*(\mu) - \frac{26}{r}P_3^*(\mu)\right\}, \end{aligned} \tag{35}$$

and the $O(ka)^2$ correction $\psi_{1s}^{(2)}$ is

$$\begin{aligned} \psi_{1s}^{(2)} = &-\frac{1}{2}\left(1 - \frac{1}{r^2}\right)\left\{\sin^2 z_0\left[\frac{25}{42}P_2^*(\mu) + \frac{400}{63r^2}P_4^*(\mu)\right]\right. \\ &-\cos^2 z_0\left[\frac{9}{8}P_2^*(\mu) + \frac{6}{r^2}P_4^*(\mu)\right] + f(\sigma,\gamma) \\ &\left.\times\left[\frac{9}{4}\cos^2 z_0 - \frac{5}{3}\sin^2 z_0\right]P_2^*(\mu)\right\}. \end{aligned} \tag{36}$$

The slow outer streaming flow pattern represented by the series for ψ_{1s} in (33)–(36) depends on the parameters z_0, ka, σ, and γ [on the last two through $f(\sigma,\gamma)$]. As is typical in such Stokes flows, the series has terms that decay algebraically faster in r with increasing order of the contribution, and can be extended to desired accuracy as demonstrated by Van Dyke[12] for similar low Reynolds number flows. For a liquid of course, with $\gamma \approx 1$, it follows that $f(\sigma,\gamma) \approx 0$, and z_0 and ka are the only remaining governing parameters. Interestingly, at large distances from the sphere $r \gg 1$, considering that $ka < 1$, the dominant contribution to ψ_{1s} goes as

$$\begin{aligned} \psi_{1s} \to &-\frac{45}{16}P_2^*(\mu)\cos^2 z_0 - ka\frac{r}{8}\sin 2z_0 \\ &\times[1+3f(\sigma,\gamma)]P_1^*(\mu) + O(ka)^2, \quad \text{for } r \gg 1. \end{aligned} \tag{37}$$

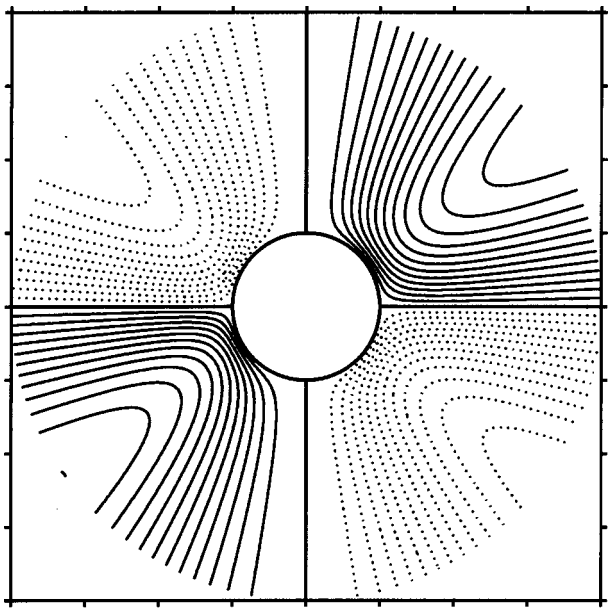

FIG. 1. Streamline plot in air for the sphere at $z_0 = 0$. The right half is for $ka = 0$; the left half is for $ka = 0.7$. Streamline spacing $\Delta\psi_{1s} = 0.04$. Solid lines represent CW flow; dotted lines are for CCW flow. The axis of fluid oscillation in the acoustic field is vertical ($\vartheta = 0, \pi$).

The results above are now discussed with the help of streamline plots for the case of air with $(\sigma,\gamma) = (0.71, 1.4)$ at STP. The behavior in liquids is discussed later. For comparison purposes two representative values of $ka = 0.4$ and 0.7 have been chosen which provide a marked contrast in the flow behavior. Although these values of ka strictly do not satisfy the ordering in (7), the progressively rapidly decaying nature with r in going from $\psi_{1s}^{(0)}$ in (34), to $\psi_{1s}^{(1)}$ in (35), to $\psi_{1s}^{(2)}$ in (36), combined with the cubic order of the error term in (33), make the total incurred error negligible even at these finite values of ka as further illustrated in Fig. 1 below. Figure 1 is a plot of the streamlines for the sphere located at the velocity antinode, $z_0 = 0$. The right half of Fig. 1 is from the leading-order solution $\psi_{1s}^{(0)}$ in (34) due to Riley,[8] while the left half is for $ka = 0.7$ with all the higher-order corrections of $O(ka)^2$ in (33) included. It is clear that qualitatively there is little noticeable difference in the streamline pattern for the two cases, indicating the negligible influence of these higher-order corrections at this location. Figure 2 is a plot of the streamlines for the sphere located midway between node

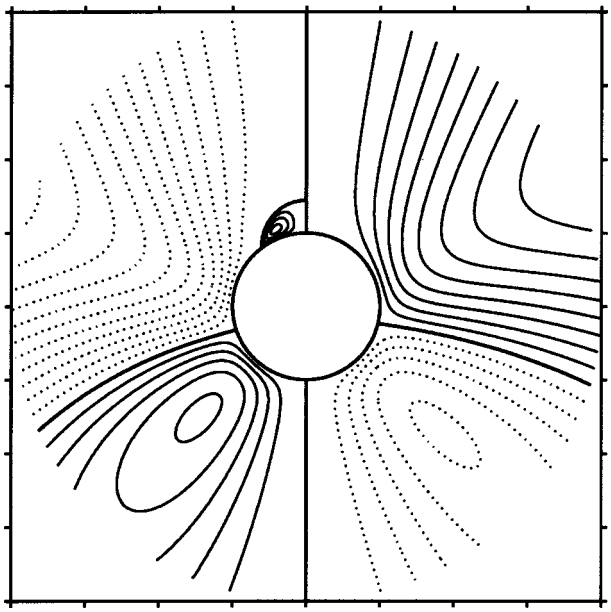

FIG. 2. Streamline plot in air for the sphere at $z_0=\pi/4$. The right half is for $ka=0.4$, while the left half is for $ka=0.7$. Streamline spacing $\Delta\psi_{1s}=0.04$, except in the ''bubble,'' where $\Delta\psi_{1s}=0.001$. Solid lines represent CW flow; dotted lines are for CCW flow. The axis of fluid oscillation in the acoustic field is vertical ($\vartheta=0,\pi$).

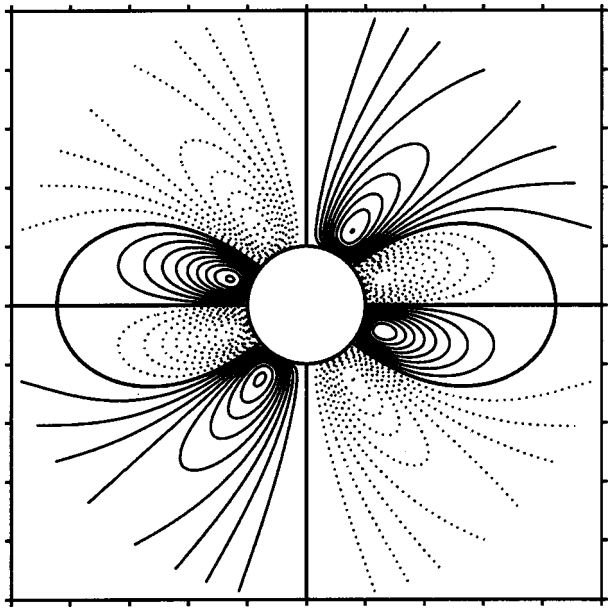

FIG. 4. Streamline plot in air for the sphere at $z_0=\pi/2$. The right half is for $ka=0.4$ with $\Delta\psi_{1s}=0.002$, while the left half is for $ka=0.7$ with $\Delta\psi_{1s}=0.004$. Solid lines represent CW flow; dotted lines are for CCW flow. The axis of fluid oscillation in the acoustic field is vertical ($\vartheta=0,\pi$).

and antinode at $z_0=\pi/4$, and shows the formation of a so far unreported incipient recirculatory ''bubble'' at a pole for the larger value of ka. Figure 3 is for the same values of ka as in Fig. 2, but with the sphere located at $z_0=1.5$ close to the velocity node ($z_0=\pi/2$). And finally Fig. 4 is for the sphere located exactly *at* the velocity node $z_0=\pi/2$, for the same values of ka as in Figs. 2 and 3.

Figures 1–4 suggest a clear trend in the streaming flow pattern to the order of accuracy being considered. For the sphere displaced from the velocity antinode, $z_0=0$, the streaming pattern is no longer symmetric about the equatorial plane, as also noted in Fig. 3 of Lee and Wang.[9] This is particularly true for the sphere at $z_0=\pi/4$ as in Fig. 2 here, for which the contribution from $\psi_{1s}^{(1)}$ in (35) is maximized, especially at larger distances from the sphere owing to the limiting behavior noted in (37). In addition, the new finding in this study that can be inferred from these figures is that in general for a large enough value of ka, and/or sphere location close enough to the velocity node ($z_0=\pi/2$), a ''bubble'' of recirculatory flow forms at the pole closer to the velocity node, and moves toward the equator as the sphere position approaches the velocity node. However, for z_0 sufficiently close to $\pi/2$, the ''bubble'' size and position become largely independent of ka and z_0 as is borne out in Fig. 3. Finally, at $z_0=\pi/2$ the ''bubble'' is now its largest, as underscored by the dramatic change in its characteristics for a small change in z_0 from a value of 1.5 in Fig. 3, to $\pi/2$ in Fig. 4, and has a shape and size that does not depend on ka anymore (although of course the strength of the fluid motion in it obviously does). The closed streamlines in the ''bubble'' for this case form a belt around the sphere and the flow is once again symmetric about the equatorial plane. Equations (33)–(36) indicate that the radial extent of the ''bubble,'' $r_b(\mu)$, at the equator ($\mu=0$) in this case is given by

$$r_b(\mu=0)=\sqrt{\frac{8}{1-\frac{14}{5}f(\sigma,\gamma)}}$$

$$[=4.224 \text{ for air with } f(\sigma,\gamma)=0.197], \quad (38)$$

as is clearly borne out in Fig. 4 here. It is probably at this sphere location $z_0=\pi/2$ that the influence of compressibility

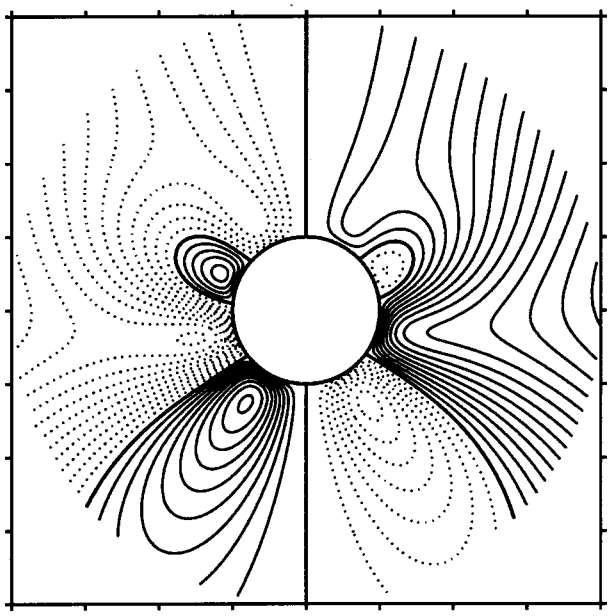

FIG. 3. Streamline plot in air for the sphere at $z_0=1.5$. The right half is for $ka=0.4$ with $\Delta\psi_{1s}=0.002$, while the left half is for $ka=0.7$ with $\Delta\psi_{1s}=0.004$. Solid lines represent CW flow; dotted lines are for CCW flow. The axis of fluid oscillation in the acoustic field is vertical ($\vartheta=0,\pi$).

in a gas is most distinguishable in comparison with a liquid for which $f(\sigma,\gamma)\approx 0$ gives $r_b(\mu=0)=\sqrt{8}$ in (38), resulting in a smaller ''bubble'' as shown in Fig. 2 of Zhao *et al.*[10]

It is noted that the decreasing trend in $\Delta\psi_{1s}$ in Figs. 1–4 clearly indicates that the streaming flow gets progressively weaker as the sphere position changes from $z_0=0$ to $z_0=\pi/2$. This suggests that the streaming flow becomes more susceptible to disruptions by external fields and disturbances, which probably explains the intermittent and fleeting flow patterns of the type in Figs. 2–4 that have been observed in various experimental studies on acoustic levitation in which the levitated object is significantly displaced from the $z_0=0$ location.

In closing, it is observed that it would be useful to extend this study on the role of noncompactness to the ''cavitation microstreaming'' problem involving streaming around a gas/vapor bubble in a liquid, originally treated analytically by Davidson and Riley,[19] and extended recently by Longuet-Higgins,[20] as well as the effects of compressibility on the associated problem of streaming *inside* the bubble in such a setting as treated by Nyborg[21] and Wu and Du.[22]

ACKNOWLEDGMENTS

The referees' comments are much appreciated. Support from the NASA Microgravity Program is gratefully acknowledged.

[1] N. Riley, ''Acoustic streaming,'' in *Encyclopedia of Acoustics*, edited by M. J. Crocker (Wiley, New York, 1997), Chap. 30, pp. 321–327; ''Steady streaming,'' Annu. Rev. Fluid Mech. (in press).

[2] W. L. Nyborg, ''Acoustic streaming,'' in *Nonlinear Acoustics*, edited by M. F. Hamilton and D. T. Blackstock (Academic Press, San Diego, CA, 1998), Chap. 7, pp. 207–231.

[3] W. L. Nyborg, ''Acoustic streaming near a boundary,'' J. Acoust. Soc. Am. **30**, 329–339 (1958).

[4] Q. Qi, ''The effect of compressibility on acoustic streaming near a rigid boundary for a plane travelling wave,'' J. Acoust. Soc. Am. **94**, 1090–1098 (1993).

[5] C. A. Lane, ''Acoustical streaming in the vicinity of a sphere,'' J. Acoust. Soc. Am. **27**, 1082–1086 (1955).

[6] C. Y. Wang, ''The flow induced by an oscillating sphere,'' J. Sound Vib. **2**, 257–269 (1965).

[7] W. L. Nyborg, ''Acoustic streaming near a rigid sphere,'' J. Acoust. Soc. Am. **95**, 556 (1994).

[8] N. Riley, ''On a sphere oscillating in a viscous fluid,'' Q. J. Mech. Appl. Math. **19**, 461–472 (1966).

[9] C. P. Lee and T. G. Wang, ''Outer acoustic streaming,'' J. Acoust. Soc. Am. **88**, 2367–2375 (1990).

[10] H. Zhao, S. S. Sadhal, and E. H. Trinh, ''Singular perturbation analysis of anacoustically levitated sphere: Flow about the velocity node,'' J. Acoust. Soc. Am. **106**, 589–595 (1999).

[11] A. Gopinath, ''Thermoacoustic streaming on a sphere,'' Proc. R. Soc. London, Ser. A **456**, 1–21 (2000).

[12] M. Van Dyke, ''Extension of Goldstein's series for the Oseen drag of a sphere,'' J. Fluid Mech. **44**, 365–372 (1970); M. Van Dyke, ''Extended Stokes series: laminar flow through a loosely coiled pipe,'' *ibid.* **86**, 129–145 (1978).

[13] A. Gopinath and D. R. Harder, ''An experimental study of heat transfer from a cylinder in low-amplitude zero-mean oscillatory flows,'' Int. J. Heat Mass Transf. **43**, 505–520 (2000).

[14] P. M. Morse and K. U. Ingard, *Theoretical Acoustics* (McGraw-Hill, New York, 1968), Chap. 6, pp. 270–300.

[15] A. Gopinath, N. L. Tait, and S. L. Garrett, ''Thermoacoustic streaming in a resonant channel: the time-averaged temperature distribution,'' J. Acoust. Soc. Am. **103**, 1388–1405 (1998).

[16] T. G. Wang and C. P. Lee, ''Radiation pressure and acoustic levitation,'' in *Nonlinear Acoustics*, edited by M. F. Hamilton and D. T. Blackstock (Academic, San Diego, CA, 1998), Chap. 6, pp. 177–205.

[17] J. T. Stuart, ''Unsteady boundary layers,'' in *Laminar Boundary Layers*, edited by L. Rosenhead (Clarendon, Oxford, 1963), Chap. VII, pp. 349–408.

[18] J. T. Stuart, ''Double boundary layers in oscillatory viscous flows,'' J. Fluid Mech. **24**, 673–687 (1966).

[19] B. J. Davidson and N. Riley, ''Cavitation microstreaming,'' J. Sound Vib. **15**, 217–233 (1971).

[20] M. S. Longuet-Higgins, ''Viscous streaming from an oscillating spherical bubble,'' Proc. R. Soc. London, Ser. A **454**, 725–742 (1998).

[21] W. Nyborg, ''Acoustic microstreaming within a gas-filled bubble,'' J. Acoust. Soc. Am. **96**, 3279(A) (1994).

[22] J. Wu and G. Du, ''Streaming generated by a bubble in an ultrasound field,'' J. Acoust. Soc. Am. **101**, 1899–1907 (1997).

Condensation in a steady-flow thermoacoustic refrigerator

R. A. Hiller[a] and G. W. Swift
Condensed Matter and Thermal Physics Group, Los Alamos National Laboratory, Los Alamos, New Mexico 87545

(Received 29 May 1999; accepted for publication 22 June 2000)

Condensation may occur in an open-flow thermoacoustic cooler with stack temperatures below the saturation temperature of the flowing gas. In the experimental device described here the flowing gas, which is also the acoustic medium, is humid air, so the device acts as a flow-through dehumidifier. The humid air stream flows through an acoustic resonator. Sound energy generated by electrodynamic drivers produces a high-amplitude standing wave inside of the resonator, which causes cooling on a thermoacoustic stack. Condensation of water occurs as the humid air passes through the stack and is cooled below its dew point, with the condensate appearing on the walls of the stack. The dry, cool air passes out of the resonator, while the condensate is wicked away from the end of the stack. Thermoacoustic heat pumping is strongly affected by the form of the condensate inside of the stack, whether condensed mostly on the stack plates, or largely in the form of droplets in the gas stream. Two simple models of the effect of the condensate are matched to a measured stack temperature profile; the results suggest that the thermoacoustic effect of droplets inside the stack is small. © *2000 Acoustical Society of America.* [S0001-4966(00)02210-4]

PACS numbers: 43.25.Ud [HEB]

I. INTRODUCTION

Superimposing steady flow with oscillating, or acoustic, flow in thermoacoustic engines and refrigerators promises to simplify the construction of these machines, and can lead to higher efficiency than conventional thermoacoustic designs.[1] In this arrangement the working fluid of the acoustic system is also the process fluid, which enters and exits the acoustic resonator at pressure nodes. If the working fluid is humid air and the stack temperature reaches the incoming dew point, condensation will occur in the stack. The condensed water flows along the stack plates, and may be collected and removed from the resonator. The flowing air stream exits the stack, and then the resonator, with a dew point equal to the temperature of the cold end of the stack. The result is dehumidification of the stream.[2]

Such a dehumidifier may have application in compressed-air drying, and in the drying of agricultural and industrial products. For example, it is possible to drive a thermoacoustic dehumidifier with a thermoacoustic prime mover to allow dehumidification powered by a flame or other heat source in remote locations.

To explore some of the issues involved in flow-through thermoacoustic dehumidification we have made measurements with humid air flowing through a loudspeaker-driven thermoacoustic cooler. The air stream is indeed dehumidified, simply and reliably, by this thermoacoustic apparatus. However, thus far the efficiency is much lower than that of commercial dehumidifiers based on vapor-compression refrigeration.

The steady flow velocity is small compared to acoustic velocities. The typical flow rate used is about 0.002 kg/s (each stack) at a static pressure of 300 kPa, which corresponds to a volume flow rate of about 10^{-3} m^3/s, or a velocity in a 15-cm-diam duct of 0.06 m/s, far smaller than the peak acoustic velocity of about 7 m/s. The steady flow may be viewed as a small drift of the fluid on top of the much larger acoustic oscillations. The steady flow does not directly affect the acoustics or thermoacoustics, but imposes an additional enthalpy flow.

For order-of-magnitude calculations a simple model of thermoacoustic heat pumping can be used to understand the heat flows and temperature gradient in a dehumidifying stack.[3] While quantitatively inaccurate, this model allows qualitative understanding of the effect of thermodynamic derivatives on the heat flows in the system, and (later in this article) why different models of the details of the condensation should make a large change in the estimated thermoacoustic heat pumping rates.

Reckoning distance z from the cold end of the stack towards the warm end, the boundary-layer approximation for thermoacoustic heat pumping in the stack is[3]

$$\dot{Q}_2 = \frac{1}{4}\Pi\,\delta_k T_m \beta p_1^s u_1^s \left(1 - \frac{dT_m/dz}{\nabla T_{\text{crit}}}\right) \tag{1}$$

if viscosity is neglected and the stack length is assumed to be so short that all relevant variables are essentially independent of z. Here Π is the total perimeter of the stack plates,

$$\delta_k = \sqrt{2K/\omega\rho_m c_p} \tag{2}$$

is the thermal penetration depth (the spacing between stack plates being typically a few δ_k), T_m is the mean, that is, time-averaged, temperature of the stack and fluid, β is the fluid's thermal expansivity, p_1^s and u_1^s are the (standing wave) acoustic pressure and velocity amplitudes, K is the fluid's thermal conductivity, ω is the acoustic radian frequency, ρ_m is the mean fluid density, and c_p is the heat

[a]Present address: Department of Physics and Astronomy, and National Center for Physical Acoustics, University of Mississippi, University, MS 38677.

capacity per unit mass at constant pressure. The critical temperature gradient is

$$\nabla T_{\rm crit} = \omega T_m \beta p_1^s / \rho_m c_p u_1^s . \tag{3}$$

For this apparatus $\nabla T_{\rm crit} \approx 150$ K/m, and $\dot{Q}_2$ at $dT_m/dz = 0$ is about 50 W.

With no steady flow the enthalpy flux down the stack is assumed to be equal to the thermoacoustic heat pumping $\dot{Q}_2$ (plus thermal conduction in the solid and the fluid). When there is a superimposed steady flow, there is an additional component of the enthalpy flux due to this steady flow, $\dot{H}_{\rm flow} = \dot{m} h$, where $\dot{m}$ is the mass flow rate and h is the specific enthalpy of the fluid. Ignoring thermal conduction, conservation of energy has $\dot{Q}_2 + \dot{H}_{\rm flow} = {\rm const}$. If the acoustic fluid may be modeled as an ideal gas inside the stack, $h(T,p) = c_p T$, and the conservation-of-energy equation leads to an exponential mean temperature profile in the stack.[1]

More accurate calculations are done using the full one-dimensional linearized Navier–Stokes, continuity, and entropy equations using the numerical computation program DeltaE.[4] Extensions were made to the code to model fluids in multiple phases, in particular condensing humid air, and to compute enthalpy flows including the effect of steady flow.[5]

Above and below the stack, where there is no condensation, the humid air stream is modeled as a mixture of dry air and water vapor, taken as ideal gases. Complications arise inside the stack where the water is condensing, since the gas will be in close contact with liquid water, either as a film on the stack-channel walls, or as droplets in the gas. This can result in different (non-ideal-gas) values for thermodynamic derivatives such as the effective specific heat and thermal expansivity, which in turn can affect the rate of thermoacoustic heat pumping.

The exact computation of the various thermodynamic derivatives would in general require a knowledge of the distribution and dynamics of entrained water inside the stack. Here, to perform calculations in the acoustic approximation, two simplified models of possible behavior of the fluid inside the stack are used. In the ''fog'' model all the condensate is assumed to be in the form of droplets sufficiently small, and sufficiently finely and uniformly dispersed relative to the thermal penetration depth, as to be in instantaneous thermal equilibrium with the surrounding gas. In the ''wet-wall'' model all the condensate is assumed to be on the stack-channel walls, and the gas between these wet walls is assumed to have a saturation concentration of water vapor, at the local mean temperature.

II. FOG THERMOACOUSTICS

In the ''fog'' model the condensate is assumed to be in the form of tiny droplets, so that the foggy air can be treated as a single fluid. The droplets must be so small that they are perfectly entrained in the gas motion, and they must be so finely and uniformly dispersed in the gas that the properties of the gas do not vary appreciably in the spaces between neighboring droplets. In other words, the droplet-to-droplet spacing must be much smaller than the thermal diffusion length δ_k and the corresponding mass-diffusion length $\delta_D = \sqrt{2D_{12}/\omega}$, where D_{12} is the water–air binary diffusion coefficient. In this model, evaporation and condensation of these dispersed droplets contribute significantly to the effective thermal expansivity, specific heat, etc. of the composite fluid.

The instantaneous pressure, $p = p_m + {\rm Re}\,[p_1 e^{i\omega t}]$, with p_1 complex to account for time phasing, is the sum of the partial pressures of air and water vapor. The water vapor is in equilibrium with the droplets, so its pressure is the saturation pressure at the instantaneous local temperature. (The liquid water droplets, however, are compressed above atmospheric pressure, having a pressure equal to the total local pressure, plus surface pressure $\Delta p = \alpha/2r$, where $\alpha = 0.0075$ J/m^2 is the surface tension for an air–water interface and r is the radius of the droplet. This elevated pressure does not significantly affect the thermodynamics or energy flows.)

Given p, T, and the mole fraction of water $\overline{x_w}$, other thermodynamic variables are computed:

the mole fraction of air:

$$\overline{x_a} = 1 - \overline{x_w}, \tag{4}$$

the mole fraction of water vapor:

$$\overline{x_g} = \overline{x_a}\,\frac{p_{\rm sat}(T)}{p - p_{\rm sat}(T)}, \tag{5}$$

the mole fraction of liquid water:

$$\overline{x_f} = \overline{x_w} - \overline{x_g}, \tag{6}$$

and the molar mass of the mixture:

$$M = \overline{x_a} M_a + (\overline{x_a} + \overline{x_f}) M_w . \tag{7}$$

Here $p_{\rm sat}(T)$ is the saturation, or vapor, pressure of water at temperature T, and M_a and M_w are the molar masses of air and water.

The specific enthalpy h of the fluid is the sum of the enthalpies of the components,

$$h = \frac{\overline{x_a}\,\overline{h_a} + \overline{x_g}\,\overline{h_g} + \overline{x_f}\,\overline{h_f}}{M}, \tag{8}$$

where $\overline{h_a} = (291\ {\rm J/mol\cdot K})T$ is the molar enthalpy of dry air near room temperature, $\overline{h_g}$ is taken as its saturation value, and $\overline{h_f}$ contains a first-order correction for compression,

$$\overline{h_f}(T,p) = \overline{h}_{f,{\rm sat}}(T) + \overline{v_f}(p - p_{\rm sat}(T)), \tag{9}$$

where $\overline{v_f}$ is the molar volume of liquid water. (This correction is small, $\lesssim 100$ ppm for temperatures and pressures in this apparatus.) The heat capacity is computed from this enthalpy as

$$c_p = \left(\frac{\partial h}{\partial T}\right)_{p,\overline{x_w}}. \tag{10}$$

The molar volume of the fluid is

$$\overline{v} = (\overline{x_a} + \overline{x_g})\frac{\overline{R}T}{p} + \overline{x_f}\,\overline{v_f}, \tag{11}$$

where $\overline{R}=8.314$ J/mol·K is the gas constant. The thermodynamic response functions (derivatives) may be calculated from the molar volume:

$$\kappa_T=\frac{-1}{\overline{v}}\left(\frac{\partial\overline{v}}{\partial p}\right)_{T,\overline{x}_w} \tag{12}$$

and

$$\beta=\frac{1}{\overline{v}}\left(\frac{\partial\overline{v}}{\partial T}\right)_{p,\overline{x}_w}. \tag{13}$$

The adiabatic index is computed as

$$\gamma=\left(1-\frac{T\beta^2\overline{v}}{M\kappa_T c_p}\right)^{-1}, \tag{14}$$

and the speed of sound is

$$a=\sqrt{\frac{\gamma\overline{v}}{M\kappa_T}}. \tag{15}$$

The thermal conductivity K of the fluid is taken as that of air, and is used to compute the thermal diffusivity,

$$\chi=K\overline{v}/Mc_p, \tag{16}$$

and the viscosity is taken as the viscosity of air, corrected for a suspension of water droplets with the Einstein equation,[6]

$$\eta=\eta_{\text{air}}(T)\left(1+\frac{5}{2}\frac{\overline{x}_f\overline{v}_f}{\overline{v}}\right). \tag{17}$$

No correction is made for the effect of water vapor on the viscosity, since this is much less than 1% at the temperatures in this apparatus.[7] Traditional studies of sound propagation in fog describe the extra attenuation[8] due to oscillating evaporation/condensation of the droplets, but here the ordinary viscous and thermal dissipation at the stack-channel walls is dominant.

For example, this model predicts that cooling humid air at 3 bar with a dew point of 300 K below its dew point results in an increase in c_p of 80%, an increase in $T\beta$ of 15%, and smaller changes in other properties. The large change in c_p occurs because a change in temperature (in the fog region) results in a large change in the fraction of water condensed, and thus a large change in enthalpy because of the latent heat of water. Such changes could have a dramatic effect on the stack's heat-pumping rate through δ_k, β, and ∇T_{crit} in Eq. (1).

The binary diffusion coefficient D_{12} for air and water is about 2.2×10^{-5} m^2/s at 1 atm and 300 K.[9,10] The coefficient varies inversely with the pressure,[10] so at the operating pressure of 3 bar, and at 300 K, the diffusion coefficient is approximately $D_{12}(3\text{ bar, }300\text{ K})=0.7\times10^{-5}$ m^2/s. The diffusive penetration depth at 40 Hz is $\delta_D=\sqrt{2D_{12}/\omega}=0.23$ mm, which is about the same as the viscous and thermal penetrations depths for this system $\delta_\nu=\sqrt{2\eta/\rho_m\omega}=0.21$ mm and $\delta_k=\sqrt{2K\rho_m c_p\omega}=0.24$ mm, compared with the stack plate half-spacing of 0.41 mm. The fog model would be applicable here only if the droplet density were at least ~10 droplets/$\delta_\kappa^3\sim10^{12}$ droplets/m^3. For $\overline{x}_f\sim0.01$, the droplet size would then be $\sim3\mu$m, comparable to typical sizes in atmospheric clouds.[11]

III. WET-WALL THERMOACOUSTICS

In the ''wet-wall'' model all of the condensate is assumed to be on the stack walls, and the gas between these wet walls is assumed to be saturated with water vapor at the local stack wall temperature.[9] As pressure and temperature oscillate in the gas, droplets do not form, even though the minima in the gas's temperature oscillations are slightly below the dew point. In this model (after a transient period during which water first builds up on the walls), the water that condenses in the stack must flow out of the cold end of the stack as liquid. We assume that this liquid flow is steady, driven by gravity and capillary forces, so that large droplets never occlude the stack channels.

In this model, we neglect any effects of *oscillating* diffusion of water vapor, even though the oscillating thermoacoustic temperature gradients must drive such diffusion, because the extra acoustic-power dissipation and time-averaged vapor pumping associated with the oscillating diffusion should be small at these small vapor mole fractions.[9,12] Nevertheless, we rely on *time-averaged* diffusion of water vapor from the center of the channels to the walls where it condenses. The gradient in water-vapor density that drives this diffusion can be estimated from the laminar steady-state velocity

$$u=\frac{3}{2}\frac{U}{A}\left(1-\frac{y^2}{y_0^2}\right) \tag{18}$$

between parallel plates of separation $2y_0$, with coordinate y measured from midway between the plates and A the cross-sectional area through which volume flow rate U passes. In this situation, the largest terms in the mass diffusion equation give

$$u\frac{d\overline{x}_g}{dz}=D_{12}\frac{d^2\overline{x}_g}{dy^2}, \tag{19}$$

where z is the direction of steady flow. The concentration gradient in the flow direction is related to the temperature gradient along the wet-wall channel by

$$\frac{d\overline{x}_g}{dz}\approx\frac{1}{p}\frac{dp_{\text{sat}}}{dT}\frac{dT}{dz}. \tag{20}$$

With boundary conditions $\overline{x}_g(\pm y_0)=\overline{x}_{g,\text{wall}}$, the solution to Eq. (19) using Eq. (18) for u is a quartic polynomial in y, which easily gives the water-vapor concentration difference between mid-channel and wall:

$$\overline{x}_g(0)-\overline{x}_{g,\text{wall}}=\frac{5}{8}\frac{y_0^2}{D_{12}}\frac{U}{A}\frac{1}{p}\frac{dp_{\text{sat}}}{dT}\frac{dT}{dz}. \tag{21}$$

For the conditions of the typical experiment described below, this concentration difference is only 10% of the concentration itself, and diffusion in the z direction carries 10^5 times less water than this diffusion in the y direction.

The effective thermal expansivity, specific heat, etc. used in calculations of thermoacoustic dynamics are simply those of an ideal gas mixture of air and water vapor, while only the enthalpy of the fluid used for computing the open-flow energy balance includes the effect of the condensate. The mole fractions of air and water vapor are computed from the mean temperature of the fluid:

$$\overline{x}_g = \frac{p_{\mathrm{sat}}(T_m)}{p_m} \tag{22}$$

and

$$\overline{x}_a = 1 - \overline{x}_g . \tag{23}$$

For calculations of oscillating variables these gases are assumed to act as an ideal gas, with a molar volume

$$\overline{v} = \frac{\overline{R}\overline{T}}{p}, \tag{24}$$

so

$$\beta = \frac{1}{\overline{T}} \tag{25}$$

and

$$\kappa_T = \frac{1}{p}. \tag{26}$$

The molar mass and heat capacity used for calculations of oscillating variables are weighted by the mole fractions:

$$M = \overline{x}_w M_w + \overline{x}_a M_a , \tag{27}$$

$$c_p = \frac{\overline{x}_a \overline{c}_{p,a} + \overline{x}_g \overline{c}_{p,g}}{M}, \tag{28}$$

where $\overline{c}_p$ is the heat capacity per mole at constant pressure. The adiabatic index and sound speed are computed from these variables as in the fog case.

While Eq. (28) is used for the calculation of oscillating quantities in the ''wet-wall'' model, the total enthalpy of the fluid is used for steady-flow energy balance to determine $T_m(z)$, and hence includes the effect of the condensate, most importantly the latent heat. Thus the steady-flow enthalpy is the same as in the fog case, above.

The thermal conductivity and viscosity are taken to be that of air at the same temperature and pressure.

A given parcel of gas is assumed to exist at constant mole fractions of air and water vapor at the fast (acoustic) time scale. The mole fractions vary slowly as this parcel of gas travels with the mean flow to regions of different mean temperature. This implies that during the rarefaction part of the cycle the water vapor becomes supersaturated, but does not condense. Practically, this means that the rate of nucleation of droplets is small.

IV. EXPERIMENT

A modification of the apparatus built by Reid is used to dehumidify air.[1] This thermoacoustic cooler is an annular resonator constructed of PVC piping with a circumference of 4.6 m along the wave-propagation direction, with an inner diameter ranging from 10 to 15 cm. A schematic drawing of the resonator is shown in Fig. 1. The working pressure of the air in the resonator is 3 atm.

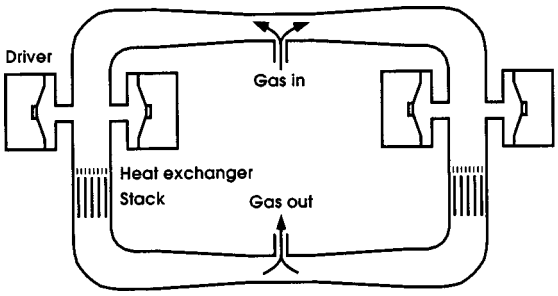

FIG. 1. Schematic diagram of the resonator. The sound field is left-right symmetric, with pressure nodes at the top and bottom centers, where the steady flow of gas may be introduced into or removed from the resonator. The duct is PVC piping, 150 mm ID, except near pressure nodes where it tapers to 100 mm ID. Acoustic energy is introduced with four 300-mm-diam woofers, driving the system near its resonance of 42 Hz. The stacks are parallel fiberglass sheets, 150 mm long, and spaced 0.81 mm apart. The ambient-temperature heat exchanger is water-cooled finned copper tubing.

Acoustic power is generated by four 300-mm-diam woofers operating near 42 Hz. The frequency is chosen to maximize the ratio of the stack temperature gradient at constant heat load to the acoustic work input to the resonator, which occurs close to the acoustic resonance frequency measured at very low power. The two woofers on each side are driven in phase, and the pairs of woofers on the two sides are driven out of phase to produce a standing wave with pressure nodes at the top and bottom, to allow the introduction and removal of the flowing gas without leakage of acoustic energy. At maximum drive without distortion the woofers produce a pressure amplitude $|p_1|/p_m = 0.025$, as measured by a pressure sensor placed between a pair of woofers. In this circumstance each woofer generates 12 W of acoustic power, with an electrical-to-acoustic efficiency of 20%. The overall second-law efficiency[13] of the heat pump is only about 1%—in other words, the electric power supplied to the woofers in order to cool the air is about 100 times larger than the minimum power required according to the first and second laws of thermodynamics.

Static and dynamic (acoustic) pressure are measured with piezoresistive pressure sensors placed in several locations around the resonator. By adjusting the voltage to the four woofers, the sound pressure amplitude may be made approximately equal in the two sides (to about 1%), and nulled at the pressure nodes at top and bottom (to about 0.01% of the maximum pressure amplitude in the resonator). The ''length'' of each half of the resonator from top pressure node to bottom pressure node is significantly less than $\frac{1}{2}$ wavelength, because the woofers are a substantial source of volume flow rate in quadrature with the oscillating pressure (roughly 30 times the in-phase volume flow rate that delivers acoustic power from the woofers to the resonator).

On each side of the resonator is a thermoacoustic stack, positioned about $\frac{1}{8}$ wavelength from the pressure node at the bottom. The stack is constructed of parallel plates of smooth fiberglass, with a length of 150 mm and a plate-to-plate separation of 0.81 mm maintained by axial spacers creating rectangular channels 0.81 mm by 12.7 mm in cross section. Just

above the stack is a copper fin-and-tube heat exchanger which is cooled to ambient temperature with a water stream. In the presence of the sound field, the stack produces a temperature gradient, with the colder end below.[3] Since the top of the stack is held at ambient temperature, the bottom of the stack is refrigerated. Humid air enters the resonator at the pressure node at the top, flows through the stack while transferring heat to the stack as it becomes colder, and exits the resonator at the pressure node at the bottom. Heat removed from the gas stream is pumped up the stack temperature gradient at the expense of acoustic energy, and is removed at the ambient-temperature heat exchanger.

The stack temperature profile is measured with ten thermocouple temperature sensors spaced along the (blocked) central channel of one stack. Additional temperature sensors are placed in the ambient heat exchanger metal, and in the gas space above and below the stack. Since the fluid is in close thermal contact with the stack, the local time-averaged temperature of the fluid inside the stack is assumed to be the same as that of the stack.

Humidity is measured with an Ohmic Instruments DPSC-35-XR Dew Point Meter, placed at the lower (outlet) port of the resonator. This detector uses a thin-film polymer capacitor exposed to the air stream, and reads relative humidity directly. The incoming humidity can be measured at the outlet with the acoustic drive off. In practice the hygrometer has limited utility because the PVC resonator material adsorbs or releases water, requiring many hours to equilibrate with the humid air stream.

All the runs are done with air, at varying humidity. House compressed air is used as the source of dry air, regulated down to the working pressure of the resonator and filtered through a plastic mesh having 8-μm square pores (not fine enough to remove typical condensation nuclei[11]). This source is well dehumidified, with a dew point at 3 bar of less than $-45\,^{\circ}\mathrm{C}$, the minimum detectable with the available hygrometer, for a specific humidity of less than 15 ppm. To obtain a desired humidity, this air stream is bubbled through liquid water of known, thermostat-controlled temperature. It is assumed that the exiting gas stream has a dew point equal to the temperature of the water, at a pressure equal to the pressure in the space above the liquid. The latent heat of the evaporated water is supplied by an electric heater.

Flow rates are measured using a laminar flow meter upstream of the humidifier. Since the incoming air stream is dry, this flow meter measures the (dry) air flow rate through the humidifier and resonator. The pressure drop across the element is proportional to the volume flow rate U and the viscosity of the gas, so

$$U = A\frac{\Delta p}{\eta/\eta_{70\,^{\circ}\mathrm{F}}}, \tag{29}$$

where A is a constant which depends on the geometry of the element, η is the dynamic viscosity, and $\eta_{70\,^{\circ}\mathrm{F}} = 182$ μ poise is the viscosity of air at 70 °F. The mass flow rate is computed from the density as an ideal gas,

$$\dot{m}_{\mathrm{air}} = U\rho_a = U\frac{p_{\mathrm{flow}} M_a}{\overline{R} T_{\mathrm{flow}}}, \tag{30}$$

where p_{flow} and T_{flow} are the pressure and temperature of the flowing air. After the humidifier, the mass flow rate of the fluid is

$$\dot{m} = \dot{m}_{\mathrm{air}} + \dot{m}_w = \dot{m}_{\mathrm{air}}(1+\Omega), \tag{31}$$

where $\Omega = \dot{m}_w/\dot{m}_{\mathrm{air}}$ is the specific humidity of the air downstream of the humidifier. This gas flow is assumed to split evenly through the two sides of the resonator, so the mass flow rate through each side is one-half of that calculated by Eq. (31).

When the flowing gas stream is humid air and the temperature anywhere inside the stack is below its dew point, liquid water will condense inside the stack. Since the flow is in close thermal contact with the stack plates, the gas stream will exit with a dew point equal to the temperature of the cold end of the stack. The condensate drains to the bottom of the stack. Water condensing in the stack is probably drawn into the corners of the stack's rectangular channels by capillary forces, so that most of the steady flow of liquid water down through the stack occurs in these corners. With a radius of curvature 0.4 mm typical of the channel corners, the surface tension of water reduces the pressure in the liquid by 200 Pa, in principle able to hold a 2-cm height of water against gravity.

In practice the cooler is started using flowing dry air, and it operates as an ordinary thermoacoustic flow-through cooler, with the air leaving the stack at the temperature of the cold end; the heat removed is pumped up the stack to be removed at the ambient-temperature heat exchanger. To operate the device as a dehumidifier the humidity of the incoming air may then be increased to reach an incoming dew point warmer than the coldest part of the stack. The temperature difference across the stack is observed to decrease because of the latent heat of the liquid condensing in the stack. Initially the dew point of the exiting air is measured to be the same as the cold-end stack temperature. Running this way for an hour will condense several grams of water in the stack. Eventually, the dew point of the exiting gas slowly rises, due to condensate appearing in the warmer sections of the resonator past the stack, signaling what we believe is the beginning of steady-state liquid holdup in the stack.

To determine the fate of this condensate, a 15-cm section of the resonator below the stack was replaced with transparent acrylic so the bottom (cold end) of the stack and the region below it could be seen. In addition, windows were installed in the resonator elbows above and below the stack to allow illumination or observation along the stack channels. The best view was obtained with a strong light above the stack (shining through the channels), observing through the acrylic resonator section.

Liquid water begins to appear as droplets on the bottom of the stack. The liquid water condensate at the bottom of the stack continues to accumulate, blocking some of the stack channels, and eventually falls away in a rain of millimeter-size or smaller drops. Cotton string, held against the bottom of the stack with a loose screen, was added to wick away the condensate, thereby eliminating the rain and preventing significant occlusion of the stack channels. The water drips off the ends of the dangling strings, and can be directed in this

way to a reservoir, from which it might be removed from the resonator. With this wick installed, viewing along the stack axis using the elbow windows shows no channels blocked by drops.

Under certain conditions, namely a very high incoming dew point (~35 °C, or around 10 °C higher than the temperature of the warmest part of the stack) and high air flow rate (~0.005 kg/s), a thin fog is seen exiting from the bottom of the stack. This fog can be seen best through the transparent duct below the stack, with strong illumination from above through the stack channels. The fog is visible in a region extending about 5 cm below the bottom of the stack, after which it presumably evaporates into the outgoing air stream. The fog appears about 30 min after introducing humidity into the operating resonator, and disappears after another 30 to 60 min, when significant amounts of liquid water (enough to occlude some stack pores) have appeared at the bottom of the stack. We suspect that this fog is created in the region roughly a peak-to-peak gas displacement amplitude (~2 cm) below the cold end of the stack, because the gas there is cooled some 6 °C below the temperature of the cold end of the stack by adiabatic pressure-displacement oscillations.

V. RESULTS AND DISCUSSION

To investigate the behavior of the air cooler/dehumidifier, the temperature profile along the stack is observed during operation. Of particular interest is the shape of the temperature profile in regions of the stack where water is, and is not, condensing. Figure 2 shows a temperature profile typical of those having the condensation line near the center of the stack, to show both dry and damp operation at the same time. Above this location the temperature of the stack is above the dew point of the incoming air so no condensation occurs. Below it condensation onto the stack keeps the local dew point equal to the local temperature of the stack.

Also shown are two calculations of the temperature profile using DeltaE.[4] These models use the actual geometry of the resonator around the stack, matching acoustic pressure amplitude and phase above and below the stack. The only free parameter is the additional parasitic heat load on the bottom of the stack due to convective streaming in the duct below. This parasitic heat load is fairly constant at about 20 W per side.

The two model curves represent DeltaE simulations using the ''fog'' and ''wet-wall'' computations for the enthalpy and thermodynamic derivatives of the air and liquid and gaseous water inside the stack. The kink in the fog-model curve is largely due to the large increase in c_p which occurs with the introduction of fog droplets. In the ''fog'' model, this abruptly lowers the critical temperature gradient according to the c_p dependence in Eq. (3), causing a corresponding abrupt change in dT_m/dz in Eq. (1) in order to keep the heat pumped continuous. In the ''wet-wall'' model, all variables in Eq. (1) are continuous at the dew point, so there is no discontinuity in dT_m/dz. The lack of this kink in the measured temperature profile suggests that the influence of droplets in this condensing thermoacoustic system is small

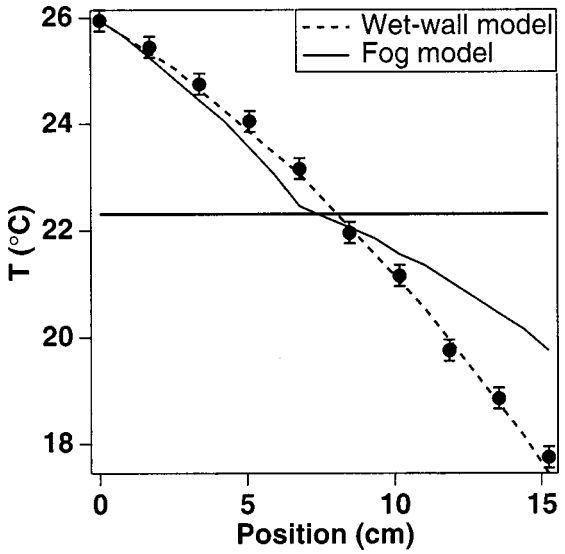

FIG. 2. Measured (markers) and simulated (lines) temperature distribution on one stack, with $|p_1|=7660$ Pa midway between the drivers above the stack and 0.001 kg/s of humid air flowing down through the stack, and with cotton string wick to prevent blockage of channels by drops. The curves are calculated using DeltaE: the solid curve represents the calculation assuming that the condensate is in the form of droplets (''fog''), and the dashed curve represents that with the condensate completely on the walls of the stack (''wet-wall''). The parasitic heat leak at the cold end (24 W) is the same for both curves, and is adjusted so the ''wet-wall'' curve matches the measured temperatures at the endpoints. For comparison, the calculation for dry air is hardly distinguishable from the ''wet-wall'' calculation, falling only 0.2 °C below it at the midpoint. The horizontal line is the dew point of the incoming air.

enough that the ''wet-wall'' model accurately describes this apparatus.

There are several reasons to expect that the ''wet-wall'' model is more applicable here than the ''fog'' model. In order to enforce the conditions of fog thermoacoustics, the distribution of water droplets must be sufficiently dense, so that most of the air in the thermoacoustically active region is close to a water droplet (much closer than a thermal or diffusive penetration depth). This would require that there be sufficient condensation nuclei to produce this density of droplets. Urban atmospheric air typically has 10^{11} nucleation-site impurities per cubic meter (mostly ionic ''Aitken nuclei,'' $r<200$ nm), and rural air is typically only an order of magnitude lower.[11] For the conditions of Fig. 2, 10^{11} droplets/m^3 results in only about 1 droplet/δ_k^3. This density would be too low to enforce ''fog'' behavior.

Moreover, any condensate that might form in droplets could tend to move to the stack walls, whether via streaming,[14] Stefan flow,[8,15] or diffusion. Continued condensation on droplets, and agglomeration due to collisions, would also tend to increase the size of the droplets, reducing their number so that the fog model would be invalid. (These effects might not, however, be important until several acoustic displacements below the condensation line, so that dense fog at the condensation line might still cause a kink in the temperature profile at the condensation line, even if the condensate were mostly on the walls below.)

If the observation of ''wet-wall'' thermoacoustics is indeed due to insufficient condensation nuclei, some predic-

tions may be made about the behavior of other condensing thermoacoustic systems. A small compressed air dryer, for example, would operate at the compressor pressure of 10–15 bar, and at a higher frequency than this device. Because of the higher pressure and frequency the penetration depths δ_k and δ_D would be smaller. If the same density of condensation nuclei were present, there would be even fewer droplets per δ_k^3, so ''wet-wall'' thermoacoustics would be even more strongly enforced. Other possible applications, such as lumber or grain drying, would probably use very large resonators operating at atmospheric pressure. In these systems low frequency and pressure lead to larger penetration depths, so that there could be enough condensation nuclei to produce many fog droplets per δ_k^3, and ''fog'' thermoacoustic behavior might occur.

The form of condensation in a particular thermoacoustic dehumidifier will have a strong influence on design. Condensate accumulating mostly on the stack plates is easier to remove, as in this experiment with wicks attached to the bottom of the stack. If the water were largely in the form of fog, some manner of capturing the small droplets would be required downstream of the stack to prevent the liquid entrained in the air stream from evaporating back into the dry air. In addition, the thermoacoustic heat pumping [Eq. (1)] and critical temperature gradient [Eq. (3)] may vary by 20% to 50% depending on the nature of the condensate, which may require substantial changes in stack length, spacing, and placement.

VI. CONCLUSION

We have demonstrated dehumidification of a humid air stream using a flow-through thermoacoustic cooler. While the efficiency is lower than commercial compressed air dehumidifiers using vapor-compression refrigeration, this approach promises the greater simplicity and reliability of thermoacoustic systems. The liquid condensate does not appear to affect the oscillating thermoacoustic variables, which can be described by ideal-gas equations, but the condensing water is a large thermal load on the refrigerator. The measured temperature profile is well fit by a model which assumes that all of the condensate is on the walls of the stack.

ACKNOWLEDGMENTS

We thank Bob Reid for the use of his thermoacoustic refrigerator, David Gardner for technical support, Rich Raspet for stimulating discussions, and Bill Ward for DeltaE support and modifications. This work was supported by the Office of Basic Energy Sciences in the U.S. Department of Energy.

[1] R. S. Reid, W. C. Ward, and G. W. Swift, ''Cyclic thermodynamics with open flow,'' Phys. Rev. Lett. **80**, 4617–4620 (1998); R. S. Reid and G. W. Swift, ''Experiments with a flow-through thermoacoustic refrigerator,'' submitted to J. Acoust. Soc. Am.

[2] O. T. Zimmerman and Irvin Lavine, *Psychrometric Tables and Charts* (Industrial Research Service, Dover, 1964).

[3] G. W. Swift, ''Thermoacoustic engines,'' J. Acoust. Soc. Am. **84**, 1145–1180 (1988).

[4] W. C. Ward and G. S. Swift, ''Design environment for low-amplitude thermoacoustic engines,'' J. Acoust. Soc. Am. **95**, 3671–3672 (1994). To review DeltaE's capabilities, visit http://www.lanl.gov/thermoacoustics/. For a beta-test version, contact ww@lanl.gov (Bill Ward) or swift@lanl.gov (Greg Swift). Fully tested software available from ESTSC, US DOE, Oak Ridge, TN.

[5] W. C. Ward (unpublished).

[6] L. D. Landau and E. M. Lifshitz, *Fluid Mechanics* (Pergamon, Oxford, 1987).

[7] J. Kestin and J. H. Whitelaw, ''The viscosity of dry and humid air,'' Int. J. Heat Mass Transf. **7**, 1245–1255 (1964).

[8] N. A. Fuchs, *The Mechanics of Aerosols* (Pergamon, Oxford, 1964).

[9] R. Raspet, C. J. Hickey, and J. M. Sabatier, ''The effect of evaporation-condensation on sound propagation in cylindrical tubes using the low reduced frequency approximation,'' J. Acoust. Soc. Am. **105**, 65–73 (1999).

[10] J. O. Hirschfelder, C. F. Curtiss, and R. B. Bird, *Molecular Theory of Gases and Liquids* (Wiley, New York, 1954).

[11] B. J. Mason, *The Physics of Clouds* (Oxford U. P., Oxford, 1957).

[12] G. W. Swift and P. S. Spoor, ''Thermal diffusion and mixture separation in the acoustic boundary layer,'' J. Acoust. Soc. Am. **106**, 1794–1800 (1999).

[13] A. Bejan, *Advanced Engineering Thermodynamics*, 2nd ed. (Wiley, New York, 1997).

[14] W. L. M. Nyborg, ''Acoustic Streaming,'' in *Physical Acoustics*, edited by W. P. Mason (Academic, New York, 1965), Vol. IIB, pp. 265–331.

[15] D. Camuffo, *Microclimate for Cultural Heritage* (Elsevier, Amsterdam, 1998).

Fluctuations of spherical waves in a turbulent atmosphere: effect of the axisymmetric approximation in computational methods

Erik M. Salomons
TNO Institute of Applied Physics, P.O. Box 155, 2600 AD Delft, The Netherlands

(Received 3 February 1998; revised 19 June 2000; accepted 3 July 2000)

The validity of the axisymmetric parabolic-equation (PE) method for line-of-sight sound propagation in a turbulent atmosphere is investigated. The axisymmetric PE method is a finite-difference method for solving a 2D parabolic wave equation, which follows from the 3D wave equation by the assumption of axial symmetry around the vertical axis through the source. It is found that this axisymmetric approximation has a considerable spurious effect on the fluctuations of the sound field. This is concluded from analytical expressions for the log-amplitude and phase variances, derived both for isotropic turbulence and for axisymmetric turbulence. The expressions for axisymmetric turbulence are compared with the results of numerical computations with the PE method. © *2000 Acoustical Society of America.* [S0001-4966(00)02810-1]

PACS numbers: 43.28.Fp [LCS]

I. INTRODUCTION

Atmospheric turbulence plays a major role in outdoor sound propagation. Two important effects that are due to turbulence are (i) scattering into refractive shadow zones and shadow zones behind noise barriers and (ii) sound level fluctuations in line-of-sight propagation. The term line-of-sight propagation is used for situations where the receiver is not in an acoustic shadow region, so that both direct waves and scattered waves are received. In this article, log-amplitude and phase fluctuations are studied, which are the origin of sound level fluctuations in line-of-sight propagation.

Theories of wave propagation in a turbulent atmosphere have been developed by Tatarskii,[1,2] Chernov,[3] Ishimaru,[4] and Ostashev.[5] These authors derive analytical expressions for the log-amplitude and phase fluctuations of plane and spherical waves in a turbulent atmosphere. These expressions are restricted to free-field propagation, i.e., the situation without a ground surface and with a (mean) atmosphere that is non-refracting.

Gilbert *et al.*[6] have developed a computational parabolic-equation method (PE method) for propagation of spherical sound waves in a turbulent atmosphere. This method takes into account a finite-impedance ground surface and atmospheric refraction. The effects of turbulence are taken into account by averaging over a number of ''frozen'' realizations of the turbulent atmosphere, generated with a random number generator. The PE method of Gilbert *et al.* is based on the axisymmetric approximation. This means that it is assumed that all system parameters are independent of the azimuthal angle α around the vertical axis through the source (see Fig. 1). For a non-turbulent atmosphere, this is a good approximation if all variations with the angle α are small. For a turbulent atmosphere, however, the axisymmetric approximation causes deviations of the log-amplitude and phase fluctuations, as will be shown in this article. These deviations originate from the fact that horizontal fluctuating gradients of the sound speed are absent in an axisymmetric system. In an axisymmetric system, wave fluctuations originate from vertical fluctuating gradients only, whereas in a real system, say with isotropic turbulence, wave fluctuations originate both from horizontal and from vertical fluctuating gradients.

This implies that results of the PE method for sound propagation in a turbulent atmosphere cannot be compared directly to experimental data for sound level fluctuations in outdoor situations. The results of this article, however, may be considered as a basis for constructing a correction to PE results to make them comparable to experimental data.

It should be noted that the reason for making the axisymmetric approximation is computational efficiency. By the axisymmetric approximation, the 3D wave equation reduces to a 2D wave equation, and the corresponding 2D parabolic equation is easily solved numerically, with a finite-difference method. In principle, the 3D parabolic equation can also be solved numerically, but this approach is limited by current computational possibilities.

This article is organized as follows. In Sec. II, analytical expressions for the log-amplitude and phase fluctuations of spherical waves are derived for isotropic turbulence and for axisymmetric turbulence. In Sec. III, it will be shown that PE results for axisymmetric turbulence agree with the analytical results for axisymmetric turbulence, and deviate considerably from the analytical results for isotropic turbulence (this comparison is for a non-refracting atmosphere, as the analytical expressions are valid for a non-refracting atmosphere only).

II. LOG-AMPLITUDE AND PHASE VARIANCES

A system is considered with a monopole source and a receiver in a homogeneous turbulent atmosphere. A rectangular xyz coordinate system is used, with the source at the origin $(0,0,0)$ and the receiver at position $(L,0,0)$. Analytical

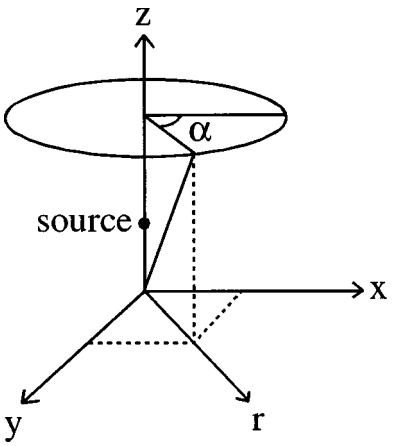

FIG. 1. Rectangular xyz coordinate system and cylindrical $rz\alpha$ coordinate system. In an axisymmetric system, all parameters are independent of the azimuthal angle α, and the field can be described in a single rz plane.

expressions will be given for the log-amplitude and phase variances of the field at the receiver, both for isotropic and for axisymmetric turbulence.

To define the log-amplitude and phase variances, the sound pressure field is written as $p=A\exp(iS)$, with A a fluctuating amplitude and S a fluctuating phase. The fluctuating amplitude is written as $A=A_0+\delta A$, with A_0 the average amplitude and δA the fluctuation. The log-amplitude fluctuation is $\chi=\ln A/A_0\approx\delta A/A_0$, and the corresponding variance is $V_1=\langle\chi^2\rangle$. In the same way, the variance of the phase fluctuation is $V_2=\langle(S-S_0)^2\rangle$, where S_0 is the average phase.

The turbulent atmosphere is modeled as a random medium, with an effective sound speed that represents both wind speed and temperature fluctuations[5] (this approach ignores the vector character of wind, which is justified for small fluctuations). The effective sound speed is a function of the position in the atmosphere only; averaging over the time is performed by ensemble averaging over different random realizations of the turbulent atmosphere. It is assumed that the mean atmosphere is non-refracting, so that the acoustic index of refraction $n=c_0/c_{\text{eff}}$ (c_{eff} is the effective sound speed and c_0 an average sound speed) can be written as $n(x,y,z)=1+\mu(x,y,z)$, where the fluctuation μ has zero average, $\langle\mu\rangle=0$.

A. General expression for the variances

A general analytical expression for the variances V_j of the log-amplitude fluctuations ($j=1$) and the phase fluctuations ($j=2$) of spherical waves can be derived by applying Rytov's perturbation method to the constant-frequency wave equation for a homogeneous turbulent atmosphere.[1,2,4,5,7] In Chap. 17 of Ref. 4, a derivation for plane waves is presented; in Chap. 18 of Ref. 4, the derivation is generalized for spherical waves. In the case of plane waves, the initial condition is an undisturbed plane wave incident upon a turbulent medium in the region $x>0$. In the case of spherical waves, the incident field is generated by a monopole source at $x=0$. The derivation starts from the wave equation for the turbulent atmosphere, which is converted to an integral equation for the fluctuation of the complex phase of the field; the integral equation is solved by a first-order perturbation method (the Rytov method). The resulting expression for the variances for spherical waves is

$$V_j=2\pi\int_0^L d\eta\int_{-\infty}^{\infty}\int_{-\infty}^{\infty}H_j^2\left(\eta-\frac{\eta^2}{L},\kappa\right)\times\Phi(0,\kappa_y,\kappa_z)\,d\kappa_y\,d\kappa_z, \tag{1}$$

with η an integration variable, $\kappa=\sqrt{\kappa_y^2+\kappa_z^2}$,

$$H_j(x,\kappa)=\begin{cases} k\sin\left(\dfrac{x\kappa^2}{2k}\right) & \text{for } j=1,\\ k\cos\left(\dfrac{x\kappa^2}{2k}\right) & \text{for } j=2,\end{cases} \tag{2}$$

where $k=\omega/c_0$ is the wave number (ω is the angular frequency), and $\Phi(\boldsymbol{\kappa})$ is the spectral density of the fluctuating index of refraction μ. The spectral density is related to the correlation function $B(\mathbf{r})=\langle\mu(\mathbf{r}_1)\mu(\mathbf{r}_1+\mathbf{r})\rangle$ by

$$\Phi(\boldsymbol{\kappa})=\frac{1}{(2\pi)^3}\int_{-\infty}^{\infty}\int_{-\infty}^{\infty}\int_{-\infty}^{\infty}\exp(-i\boldsymbol{\kappa}\cdot\mathbf{r})B(\mathbf{r})\,d\mathbf{r}, \tag{3}$$

i.e., a three-dimensional Fourier transformation.

B. Isotropic turbulence

For isotropic turbulence, we have $B(\mathbf{r})=B(r)$ and $\Phi(\boldsymbol{\kappa})=\Phi(\kappa)$. Transformation to polar coordinates in Eq. (1) yields the following expression for the variances:

$$V_j=(2\pi)^2\int_0^{\infty}\kappa\,d\kappa\left[\int_0^L H_j^2\left(\eta-\frac{\eta^2}{L},\kappa\right)d\eta\right]\Phi(\kappa) \tag{4}$$

or

$$V_j=2\pi^2k^2L\int_0^{\infty}\kappa\,d\kappa[1+(-1)^jU(\kappa)]\Phi(\kappa), \tag{5}$$

with

$$U(\kappa)=\sqrt{\frac{2\pi k}{\kappa^2L}}\left[\cos\left(\frac{\kappa^2L}{4k}\right)C\left(\sqrt{\frac{\kappa^2L}{2\pi k}}\right)+\sin\left(\frac{\kappa^2L}{4k}\right)S\left(\sqrt{\frac{\kappa^2L}{2\pi k}}\right)\right], \tag{6}$$

where C and S are the Fresnel integral functions, $C(x)=\int_0^x\cos(\frac{1}{2}\pi t^2)\,dt$ and $S(x)=\int_0^x\sin(\frac{1}{2}\pi t^2)\,dt$.

As an example, we consider the Gaussian correlation function

$$B(r)=\mu_0^2\exp\left(-\frac{r^2}{a^2}\right) \tag{7}$$

with μ_0 the standard deviation of μ and a the correlation length. This expression is a simple approximation for an atmosphere with temperature fluctuations only.[5] In this case, the spectral density defined by Eq. (3) is

$$\Phi(\kappa)=\mu_0^2\frac{a^3}{8\pi^{3/2}}\exp\left(-\frac{\kappa^2a^2}{4}\right), \tag{8}$$

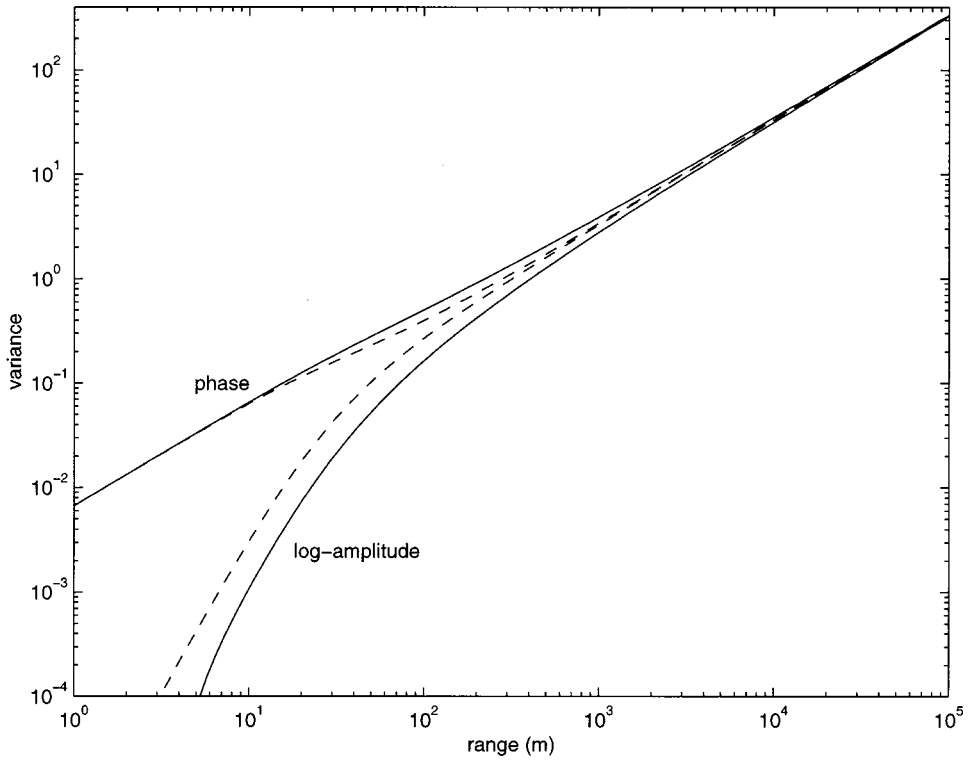

FIG. 2. Log-amplitude variance V_1 and phase variance V_2 as a function of range L, for isotropic turbulence (dashed curves) and axisymmetric turbulence (solid curves), at frequency 1000 Hz.

and we obtain

$$V_j=\frac{1}{2}\sqrt{\pi}\mu_0^2k^2La\left[1+(-1)^j\frac{a^2}{2}\int_0^\infty U(\kappa)\times\exp\left(-\frac{\kappa^2a^2}{4}\right)\kappa\,d\kappa\right]. \tag{9}$$

C. Axisymmetric turbulence

For axisymmetric turbulence, we set $B(\mathbf{r})=B(\sqrt{x^2+z^2})$ so that $B(\mathbf{r})=1$ for vectors $\mathbf{r}$ perpendicular to the propagation plane $y=0$. In this case, Eq. (3) gives

$$\Phi(\boldsymbol{\kappa})=\frac{1}{(2\pi)^2}\int_{-\infty}^{\infty}\int_{-\infty}^{\infty}\exp(-i[\kappa_x x+\kappa_z z])\times B(\sqrt{x^2+z^2})\,dx\,dz\,\frac{1}{2\pi}\int_{-\infty}^{\infty}\exp(-i\kappa_y y)\,dy \tag{10}$$

or

$$\Phi(\boldsymbol{\kappa})=F(\kappa_x,\kappa_z)\,\delta(\kappa_y), \tag{11}$$

with F the two-dimensional spectral density of the fluctuating index of refraction, and δ the Dirac delta function. In this case, Eq. (1) for the variances becomes (denoting κ_z as κ)

$$V_j=2\pi k^2L\int_0^\infty d\kappa\,[1+(-1)^jU(\kappa)]F(\kappa). \tag{12}$$

For the Gaussian correlation function (7) we have

$$F(\kappa)=\mu_0^2\frac{a^2}{4\pi}\exp\left(-\frac{\kappa^2a^2}{4}\right), \tag{13}$$

and we obtain

$$V_j=\frac{1}{2}\sqrt{\pi}\mu_0^2k^2La\left[1+(-1)^j\frac{a}{\sqrt{\pi}}\int_0^\infty U(\kappa)\times\exp\left(-\frac{\kappa^2a^2}{4}\right)d\kappa\right]. \tag{14}$$

D. Numerical examples

Figure 2 shows the log-amplitude and phase variances as a function of range L (source-receiver distance), at frequency 1000 Hz, both for isotropic turbulence and for axisymmetric turbulence. The Gaussian correlation function (7) was assumed for the fluctuating index of refraction, with $a=1.1$ m and $\mu_0^2=10^{-5}$ (see Ref. 8). The dashed curves represent Eq. (9) for isotropic turbulence, and the solid curves represent Eq. (14) for axisymmetric turbulence. For axisymmetric turbulence, the phase fluctuations are larger and the log-amplitude fluctuations are smaller than for isotropic turbulence. For $L\to\infty$, all curves in the figure approach the asymptotic relation $V_j=\frac{1}{2}\sqrt{\pi}\mu_0^2k^2La$, which follows from Eqs. (9) and (14). It should be noted that the validity of the relations (9) and (14) is limited to variances that do not exceed about 0.1 to 1. The origin of this limitation is the fact that Rytov's perturbation method is limited to small fluctuations. The curves in the figure are extended to large variances merely to show the approach to the asymptotic behavior.

Figure 3 shows the variances as a function of range up to $L=40$ m, for frequencies 125, 250, 500, and 1000 Hz. Again, the phase fluctuations are larger and the log-amplitude fluctuations are smaller for axisymmetric turbulence than for isotropic turbulence. Thus, the effect of the axisymmetric approximation is that phase fluctuations are enhanced and log-amplitude fluctuations are reduced.

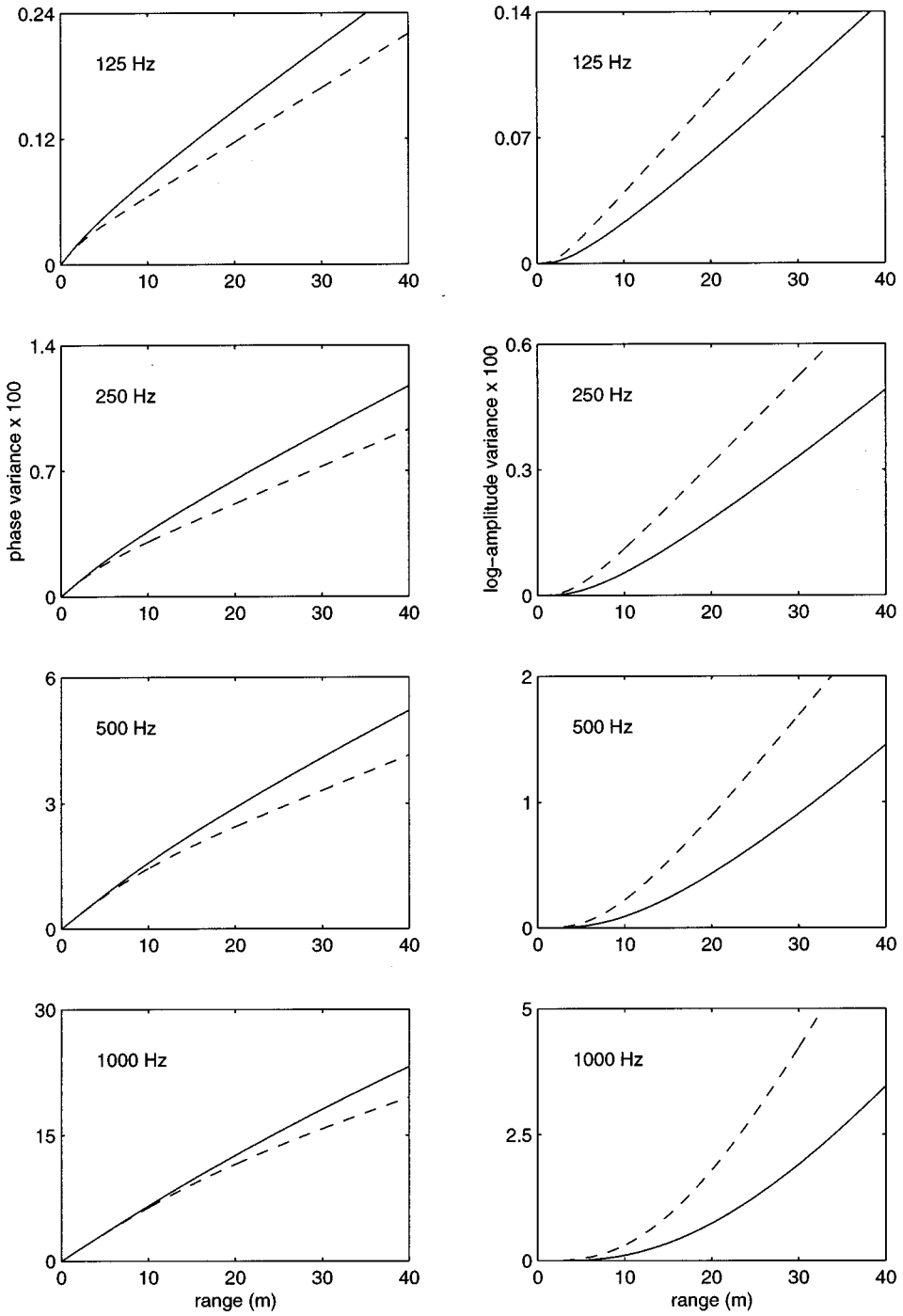

FIG. 3. Log-amplitude variance V_1 and phase variance V_2 as a function of range L, for isotropic turbulence (dashed curves) and axisymmetric turbulence (solid curves), at four frequencies.

This is a significant result. Phase and log-amplitude fluctuations play an important role in outdoor sound propagation. In situations in which the source and the receiver are near a ground surface, the fluctuations affect the interference between direct waves and waves reflected by the ground surface. In general, the fluctuations reduce the depth of the interference minima in the spectra of the received sound pressure level. If the fluctuations are calculated incorrectly, e.g., by the use of the axisymmetric PE method, errors occur in these spectra.

It should be noted that the results in Fig. 3 are examples. In practice, a wide range of turbulent scales and strengths occurs. In the examples in Fig. 3, the variances reach significant values at a propagation distance of 40 m; under different turbulent conditions, this may happen at smaller or larger distances.

III. COMPARISON WITH PE RESULTS

Figure 4 compares the curves from Fig. 3 for axisymmetric turbulence with PE results. Filled circles were computed with the Crank–Nicholson PE method[9] (CNPE method). Open circles were computed with the Green's function PE method[10] (GFPE method).

The CNPE computations were performed for a system with a ground surface (a CNPE code was used that always takes into account a ground surface), but the source height was chosen equal to half the system height, so that the

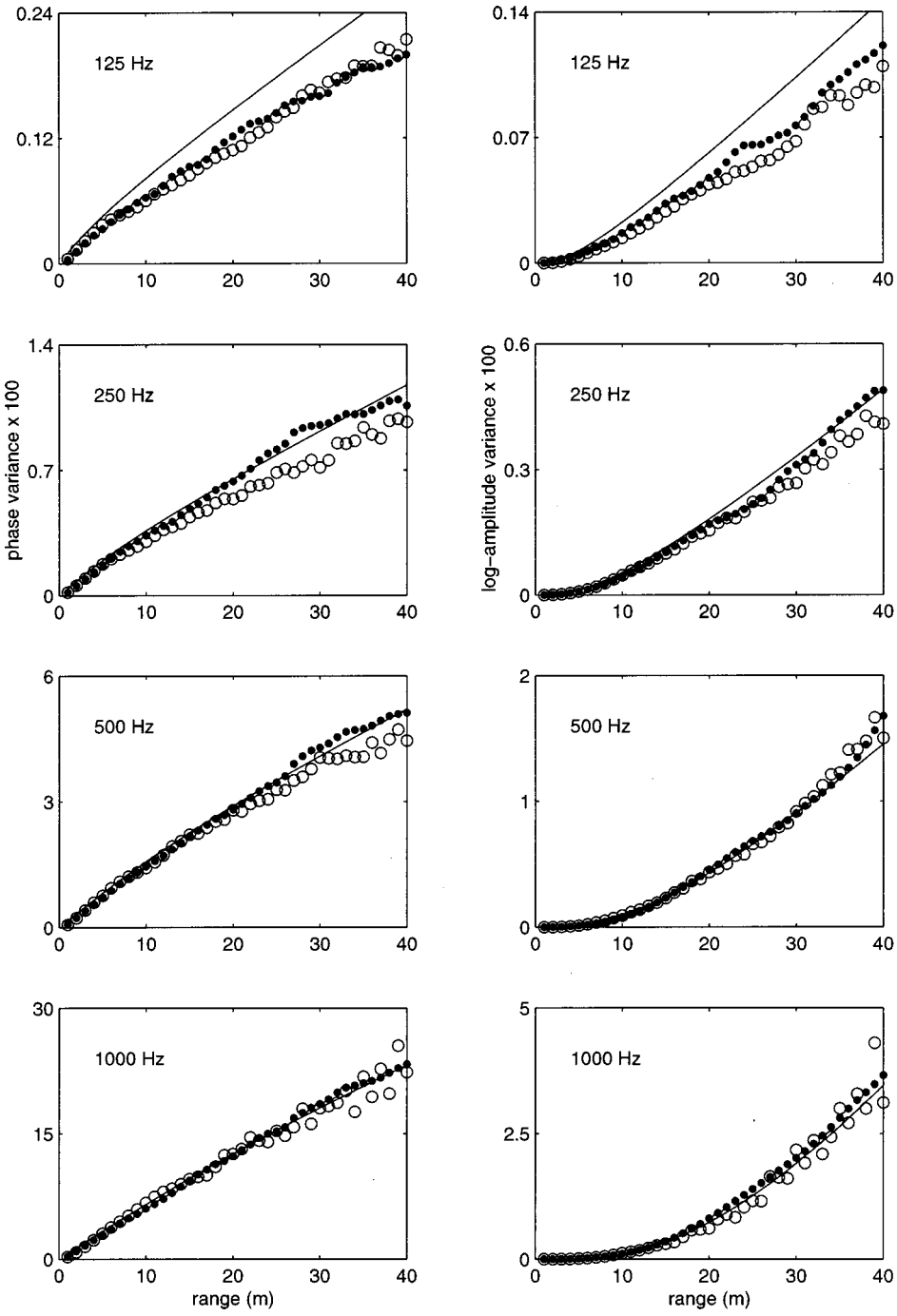

FIG. 4. Log-amplitude variance V_1 and phase variance V_2 as a function of range L, for axisymmetric turbulence, computed with Eq. (14) (solid curves), CNPE (filled circles), and GFPE (open circles).

ground and top surfaces have no effect on the results. Grid spacings of 0.25, 0.125, 0.067, and 0.033 m were used at the frequencies 125, 250, 500, and 1000 Hz, respectively. The numbers of grid points in the vertical direction were 2000, 2500, 4000, and 8000, respectively. Atmospheric turbulence was taken into account by the method described by Gilbert *et al.*[6]

The GFPE computations were performed for a system without a ground surface (due to the periodicity of the Fourier transform, the system is an infinite series of periodic images on top of each other). The vertical grid spacings were 0.25, 0.125, 0.067, and 0.033 m at the frequencies 125, 250, 500, and 1000 Hz, respectively. A horizontal range step size of 1 m was used for all frequencies. The numbers of grid points in vertical direction were 4096, 4096, 8192, and 8192, respectively. Atmospheric turbulence was taken into account by the phase-screen method described by Di and Gilbert[11] (see also Ref. 12).

All computations were repeated for 500 random realizations of the turbulent atmosphere. The Appendix describes the method that was used for the construction of a turbulent atmosphere, i.e., a random field of the fluctuating index of refraction. This method is similar to the method described by Chevret *et al.*[13] The variances shown in Fig. 4 were computed from the sets of 500 complex sound pressures, using the definitions $V_1=\langle(\ln A/A_0)^2\rangle$ and $V_2=\langle(S-S_0)^2\rangle$. The undisturbed amplitudes A_0 and S_0 were determined by separate PE computations for a non-turbulent atmosphere.

The figure shows that the PE results are in agreement with the analytical solutions for the frequencies 250, 500,

and 1000 Hz, although some statistical scatter is present, as a consequence of the finite number of random realizations. For frequency 125 Hz, however, the PE results are systematically lower than the analytical solutions. The origin of this deviation is not clear. The origin may be one of the approximations that are used in the derivation of the analytical solution for the variances. These approximations include the initial Rytov approximation (i.e., the approximation corresponding with the first-order perturbation solution mentioned in Sec. II A) and several subsequent approximations. To estimate the errors introduced by these approximations, some numerical computations were performed. The results of these computations suggest that the deviations introduced by these approximations are too small to explain the deviations observed in Fig. 4 for frequency 125 Hz. On the other hand, the PE method is based on two approximations: (i) the small elevation angle approximation and (ii) the one-way wave propagation approximation. The first approximation is probably not responsible for the deviations, because the CNPE and GFPE methods are based on different small-angle approximations, while both methods show similar deviations. Also the second approximation is probably not responsible for the deviations, because the analytical solutions are also based on the one-way wave propagation approximation (backscatter is neglected).

IV. CONCLUSIONS

It has been found that the axisymmetric approximation in the PE method has a considerable spurious effect on the fluctuations of spherical waves in a turbulent atmosphere, in the case of line-of-sight propagation. This effect originates from the fact that horizontal fluctuating sound speed gradients are ignored in an axisymmetric system. The axisymmetric approximation causes an increase of the phase fluctuations and a decrease of the log-amplitude fluctuations. This effect has been confirmed by numerical PE computations. At frequencies 250, 500, and 1000 Hz, good agreement was obtained between PE results and an analytical expression for axisymmetric turbulence. At frequency 125 Hz, a small deviation was observed between the PE results and the analytical expression.

Finally, it should be noted that similar spurious effects of the axisymmetric approximation are *not* expected for scattering of sound waves into a refractive shadow, in an upward refracting atmosphere. Scattering into a refractive shadow originates predominantly from vertical fluctuating gradients. Horizontal fluctuating gradients, which are ignored in an axisymmetric system, are of minor importance in this case.

APPENDIX: CONSTRUCTION OF REALIZATIONS OF A RANDOM FIELD

Using a random number generator, two-dimensional realizations of a homogeneous random field with given correlation function can be constructed as follows (cf. Chevret *et al.*[13]). The spectral decomposition of the correlation function $B(s)$ of a homogeneous, isotropic random field is[1,2,4]

$$\begin{aligned} B(s) &= \int_{-\infty}^{\infty}\int_{-\infty}^{\infty} \cos(\mathbf{k}\cdot\mathbf{s})F(k)\,d\mathbf{k} \\ &= \int_{0}^{2\pi}\int_{0}^{\infty} \cos(\mathbf{k}\cdot\mathbf{s})F(k)k\,dk\,d\theta \\ &= \left\langle 2\pi\int_{0}^{\infty} \cos(\mathbf{k}\cdot\mathbf{s})F(k)k\,dk \right\rangle, \end{aligned} \tag{A1}$$

where θ is the polar angle of the vector $\mathbf{k}$, $F(k)$ is the two-dimensional spectral density, and angular brackets denote averaging over the angle θ. For the Gaussian correlation function $B(s)=\mu_0^2\exp(-s^2/a^2)$ we have a Gaussian spectral density $F(k)=\mu_0^2a^2\exp(-k^2a^2/4)/4\pi$. The integral is approximated by a finite sum

$$B(s)\approx\left\langle 2\pi\Delta k\sum_n \cos(\mathbf{k}_n\cdot\mathbf{s})F(k_n)k_n \right\rangle. \tag{A2}$$

Random realizations of the corresponding random field $\mu(\mathbf{r})$ can be computed with the following relation:

$$\mu(\mathbf{r})=\sqrt{4\pi\Delta k}\sum_n \cos(\mathbf{k}_n\cdot\mathbf{r}+\phi_n)\sqrt{F(k_n)k_n}, \tag{A3}$$

where $\mathbf{k}_n=(k_n\cos\theta_n, k_n\sin\theta_n)$ with θ_n a random angle between 0 and 2π and $k_n=n\Delta k$ $(n=1,2,...,N)$, and ϕ_n a random phase angle between 0 and 2π (for the Gaussian spectral density, $\Delta k=0.1/a$ and $N=60$ are used). This can be proved as follows. Different fields $\mu(\mathbf{r})$ have different vectors $\mathbf{k}_n$ and angles ϕ_n. The correlation function is

$$B(s)=\langle\mu(\mathbf{r}+\mathbf{s})\mu(\mathbf{r})\rangle, \tag{A4}$$

where the average is over the fields $\mu(\mathbf{r})$. Substitution of Eq. (A3) gives

$$\begin{aligned} B(s)=\Bigg\langle & 4\pi\Delta k\sum_n \cos(\mathbf{k}_n\cdot\mathbf{r}+\phi_n+\mathbf{k}_n\cdot\mathbf{s})\sqrt{F(k_n)k_n} \\ & \times\sum_m \cos(\mathbf{k}_m\cdot\mathbf{r}+\phi_m)\sqrt{F(k_m)k_m}\Bigg\rangle. \end{aligned} \tag{A5}$$

Now the averaged products $\cos(\mathbf{k}_n\cdot\mathbf{r}+\phi_n+\mathbf{k}_n\cdot\mathbf{s})\cos(\mathbf{k}_m\cdot\mathbf{r}+\phi_m)$ vanish unless $n=m$. We have, using $\cos^2x=\frac{1}{2}+\frac{1}{2}\cos 2x$ and $\sin x\cos x=\frac{1}{2}\sin 2x$,

$$\begin{aligned} &\langle\cos(\mathbf{k}_n\cdot\mathbf{r}+\phi_n+\mathbf{k}_n\cdot\mathbf{s})\cos(\mathbf{k}_n\cdot\mathbf{r}+\phi_n)\rangle \\ &\quad=\langle\cos^2(\mathbf{k}_n\cdot\mathbf{r}+\phi_n)\cos(\mathbf{k}_n\cdot\mathbf{s})\rangle-\langle\sin(\mathbf{k}_n\cdot\mathbf{r}+\phi_n) \\ &\qquad\times\cos(\mathbf{k}_n\cdot\mathbf{r}+\phi_n)\sin(\mathbf{k}_n\cdot\mathbf{s})\rangle \\ &\quad=\tfrac{1}{2}\cos(\mathbf{k}_n\cdot\mathbf{s}). \end{aligned} \tag{A6}$$

This gives Eq. (A2), which completes the proof.

[1] V. I. Tatarski, *Wave Propagation in a Turbulent Medium* (McGraw-Hill, New York, 1961), pp. 3–26, 122–156, 173–188.

[2] V. I. Tatarskii, *The Effects of the Turbulent Atmosphere on Wave Propagation* (Israel Program for Scientific Translations, Jerusalem, 1971), pp. 1–33, 218–258.

[3] L. A. Chernov, *Wave Propagation in a Random Medium* (McGraw-Hill, New York, 1960), pp. 5–11, 58–83.

[4] A. Ishimaru, *Wave Propagation and Scattering in Random Media* (Academic, New York, 1978), pp. 347–387, 513–519.

[5] V. E. Ostashev, *Acoustics in Moving Inhomogeneous Media* (E&FN Spon, London, 1997), pp. 16, 67, 193–218.
[6] K. E. Gilbert, R. Raspet, and X. Di, ''Calculation of turbulence effects in an upward-refracting atmosphere,'' J. Acoust. Soc. Am. **87**, 2428–2437 (1990).
[7] V. E. Ostashev, F. Gerdes, V. Mellert, and R. Wandelt, ''Propagation of sound in a turbulent medium. II. Spherical waves,'' J. Acoust. Soc. Am. **102**, 2571–2578 (1997). (Note: the e.m. convention $\epsilon=2\mu$ is used for the refractive index fluctuation in this article and in Ref. 5, which introduces a difference of a factor of 4 in the variances.)
[8] G. A. Daigle, J. E. Piercy, and T. F. W. Embleton, ''Line-of-sight propagation through atmospheric turbulence near the ground,'' J. Acoust. Soc. Am. **74**, 1505–1513 (1983).
[9] K. E. Gilbert and M. J. White, ''Application of the parabolic equation to sound propagation in a refracting atmosphere,'' J. Acoust. Soc. Am. **85**, 630–637 (1989).
[10] K. E. Gilbert and X. Di, ''A fast Green's function method for one-way sound propagation in the atmosphere,'' J. Acoust. Soc. Am. **94**, 2343–2352 (1993).
[11] X. Di and K. E. Gilbert, ''The effect of turbulence and irregular terrain on outdoor sound propagation,'' in Proceedings Sixth International Symposium on Long Range Sound Propagation, Ottawa, Canada (1994), pp. 315–333.
[12] J. Martin, ''Simulation of wave propagation in random media: theory and applications,'' in *Wave Propagation in Random Media (Scintillation)* (The Society of Photo-Optical Instrumentation Engineers, Bellingham, WA, and The Institute of Physics Publishing, Bristol, 1993), pp. 463–486.
[13] P. Chevret, P. Blanc-Benon, and D. Juvé, ''A numerical model for sound propagation through a turbulent atmosphere near the ground,'' J. Acoust. Soc. Am. **100**, 3587–3599 (1996).

Variability in the passive ranging of acoustic sources in air using a wavefront curvature technique

Brian G. Ferguson
Maritime Operations Division, Defence Science and Technology Organisation, PO Box 44, Pyrmont NSW 2009, Australia

(Received 15 August 1998; revised 10 April 2000; accepted 12 May 2000)

Simultaneous time delay measurements from two adjacent pairs of sensors are used to estimate the ''instantaneous'' range and bearing of both stationary and moving broadband sources of continuous sound in air. The random fluctuations in the estimated source position are due to random errors in the time delay measurements. The variances of both the short time-scale and long time-scale random errors in the time delay estimates are quantified for different sensor separation distances and for different source positions. After normalization, the observed variances of the short time-scale random errors in the bearing and range estimates are found to agree with the theoretical results predicted for various sensor-source configurations where the independent variable is the length of the effective intersensor baseline. Increasing the intersensor separation distance by an order of magnitude reduces the bearing error variance by two orders of magnitude and the range error variance by four orders of magnitude. © *2000 Acoustical Society of America.*
[S0001-4966(00)03708-1]

PACS numbers: 43.28.Tc, 43.60.Cg [LCS]

INTRODUCTION

Passive ranging techniques are used in sonar systems to localize sources that radiate acoustic energy in the underwater environment.[1] In the passive sonar problem, the acoustic energy radiated by the source constitutes the signal, which is received at two or more hydrophones. Correlation of the emitted and received signal waveforms yields an absolute travel time, while correlation of the acoustic signals from spatially separated receivers yields a travel time difference (or relative travel time) which is commonly referred to as the differential time of arrival (or relative time delay).[2] The relative time delays can be used to estimate the position and velocity of a detected acoustic source.[3]

Passive ranging by wavefront curvature relies on spherical spreading of the acoustic energy emanating from a sound source. The curvature of the acoustic wavefront is sensed at the receiving array by estimating the interelement time delays, which are in turn processed to extract the range of the source.[4]

This paper applies a wavefront curvature technique to estimate the polar coordinates of both stationary and moving acoustic sources in air. The acoustic energy from a source is received by a linear array of three equally spaced sensors, then the outputs of each pair of adjacent sensors are cross-correlated. The time displacement at which the cross-correlation function attains its maximum value provides an estimate of the differential time-of-arrival (or time delay) of the acoustic wavefront at a pair of sensors. Simultaneous time delay estimates (one for each pair of adjacent sensors) are required to calculate the ''instantaneous'' range of the source; the range is equivalent to the wavefront's radius of curvature.

The more complicated problem of time delay estimation for atmospheric sound propagating in a multipath environment has been considered elsewhere where the signal peaks in the auto- and cross-correlation functions can have either high,[5] or low,[6] signal-to-noise ratios.

The propagation of sound in the atmosphere is influenced by the prevailing meteorological conditions.[7] Atmospheric turbulence in the form of eddies causes fluctuations in the amplitude and phase of an acoustic wavefront. As the radiated sound from a point source propagates through the atmosphere, an initially spherical wavefront (or surface of constant phase) encounters a superposition of turbulent eddies of many different sizes, which have fluctuating velocities and temperatures that differ from the overall average values. The turbulence results in the local sound speed varying in space and differing from its mean value randomly with time.[8] Turbulence leads to perturbations in the curvature of the wavefront which produces fluctuations in the measurements of the time delays resulting in source position errors.

I. THEORY

A. Passive wavefront curvature technique

It is necessary to know three points on a wavefront to measure its curvature. The simplest sensor configuration for wavefront curvature measurements is a linear array of three equally spaced sensors. The geometry of the source and three sensors (which all lie on the same plane) is shown in Fig. 1. The range R and bearing β are given by[1,3,9]

$$R=\frac{2d^2-c^2(\tau_{12}^2+\tau_{23}^2)}{2c(\tau_{12}-\tau_{23})}, \tag{1}$$

$$\beta=\cos^{-1}\left[\frac{c}{2d}(\tau_{12}+\tau_{23})+\frac{c^2}{4Rd}(\tau_{12}^2-\tau_{23}^2)\right], \tag{2}$$

where d is the separation distance between adjacent sensors, c is the speed of sound propagation, and τ_{ij} is the travel time difference (time delay) between sensors i and j (that is, τ_{ij}

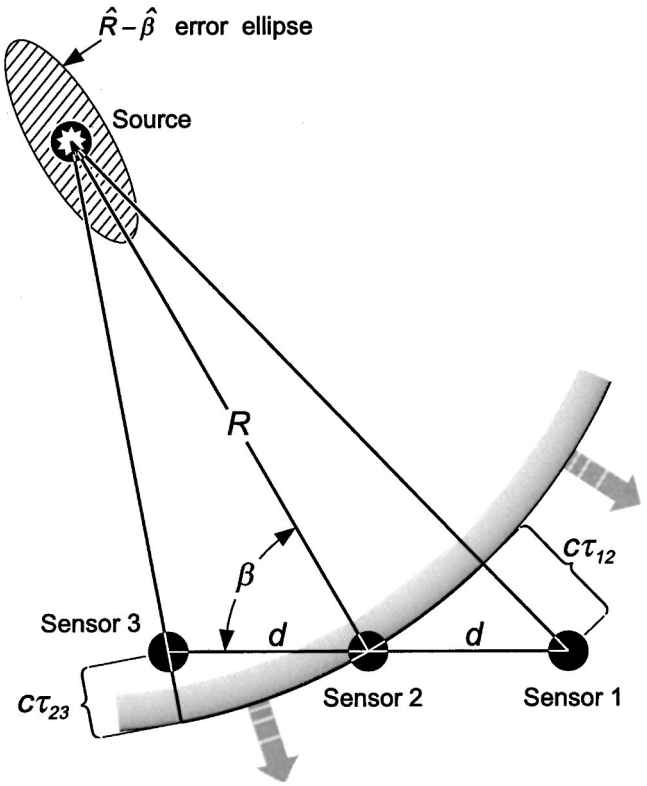

FIG. 1. Three spatially separated linear sensors are used to estimate the bearing and range of an acoustic source. The uncertainty in the estimated position of the source is represented by an ellipse. The ellipticity (or axial ratio) indicates that the along-range estimate errors are much larger than the cross-range estimate errors.

$=\tau_i-\tau_j$, where τ_i is the travel time between the source and sensor i). By estimating the relative delays and knowing the sensor positions, the position of the source can be estimated.

When $R \gg d$, the wavefronts are planar and the source of the plane wave arrivals is considered to be in the far field. The bearing of the source is then given by

$$\beta=\cos^{-1}\left(\frac{c\tau_{12}}{d}\right) \quad \text{for one sensor pair,}$$
$$\beta=\cos^{-1}\left[\frac{c(\tau_{12}+\tau_{23})}{2d}\right] \quad \text{for both sensor pairs.} \tag{3}$$

When the relative time delay is zero, the source bearing is broadside ($\beta=90°$) to the array axis and when the time delay reaches its maximum value, the source bearing coincides with endfire ($\beta=0$ or 180°, depending on the sign of the time delay).

B. Variance of random errors

The time delay estimation problem of a Gaussian signal embedded in additive uncorrelated Gaussian noise at each sensor has been studied extensively in the literature.[10] The performance of the range and bearing estimators based on the time delay estimates and the geometry of the problem have been analyzed in terms of bias and variance in the source localization parameters. The time delay can be estimated from the generalized cross-correlation function of the sensor outputs;[11] the cross-correlator has a zero mean output in the signal absent, noise present case.

Consider the model where the source signal received at sensor j is a time-delayed replica of the source signal received at sensor i, and where the noises at sensors i and j are uncorrelated with each other and also with the signal. Further, if the signal and noises are modeled as stationary Gaussian random processes and the observation time is large when compared with the time delay, then the Cramer-Rao lower bound for the variance of the time delay errors is given by[1]

$$\sigma^2_{\mathrm{CR}}(\hat{\tau}_{ij}-\hat{\tau}_{ij})=2\pi\left[2T\int_0^{\omega_H}\frac{\gamma_{ij}(\omega)}{1-\gamma_{ij}(\omega)}\omega^2 d\omega\right]^{-1}, \tag{4}$$

where $\hat{\tau}_{ij}$ is the estimated value of the true time delay τ_{ij}, ω_H is the highest source frequency after propagation to the receiver, T is the observation time, and $\gamma_{ij}(\omega)$ is the magnitude-squared coherence, which is given by

$$\gamma_{ij}(\omega)=\frac{|G_{ij}(\omega)|^2}{G_{ii}(\omega)G_{jj}(\omega)}, \tag{5}$$

where $G_{ij}(\omega)$ is the cross-power spectral density at frequency ω, and $G_{ii}(\omega)$ and $G_{jj}(\omega)$ denote the respective auto-power spectral densities of the two sensor outputs. Random uncertainty is an inherent feature of the time delay estimation method where the variance of the random errors depends on the signal-to-noise ratio, the signal bandwidth and the integration time.[12]

With one sensor pair, the variance of the bearing errors (for a source in the far field) is given by[1]

$$\sigma^2(\hat{\beta}-\beta)=\frac{c^2\sigma^2(\hat{\tau}_{ij}-\tau_{ij})}{(d\ \sin\beta)^2}, \tag{6}$$

where $\hat{\beta}$ is the estimated value of the true bearing β. Note that $d\ \sin\beta$ is the length of the effective intersensor baseline as ''seen'' by the source, that is, the projected intersensor separation distance orthogonal to the source direction. Although the bearing error variance depends linearly on the time delay error variance, it follows an inverse square law as the length of the effective intersensor baseline is increased. Thus the bearing error variance can be reduced by increasing the separation distance between the sensors and orientating the alignment of the sensors so that the source is at broadside rather than near endfire.

The variance of the range errors is given by[1]

$$\sigma^2(\hat{R}-R)=c^2\sigma^2[(\hat{\tau}_{12}-\tau_{12})-(\hat{\tau}_{23}-\tau_{23})]\left[\frac{R}{d\ \sin\beta}\right]^4, \tag{7}$$

where $\hat{R}$ is the estimated value of the true range R.

Unlike the bearing error variance, the range error variance depends on the *fourth* power of the ratio of the true source range to the length of the effective intersensor baseline. Hence, the area of uncertainty in the source position is bounded by an ellipse where the major (along-range) axis is elongated with respect to the minor (cross-range) axis because, for a given error in the time delay estimates, the error

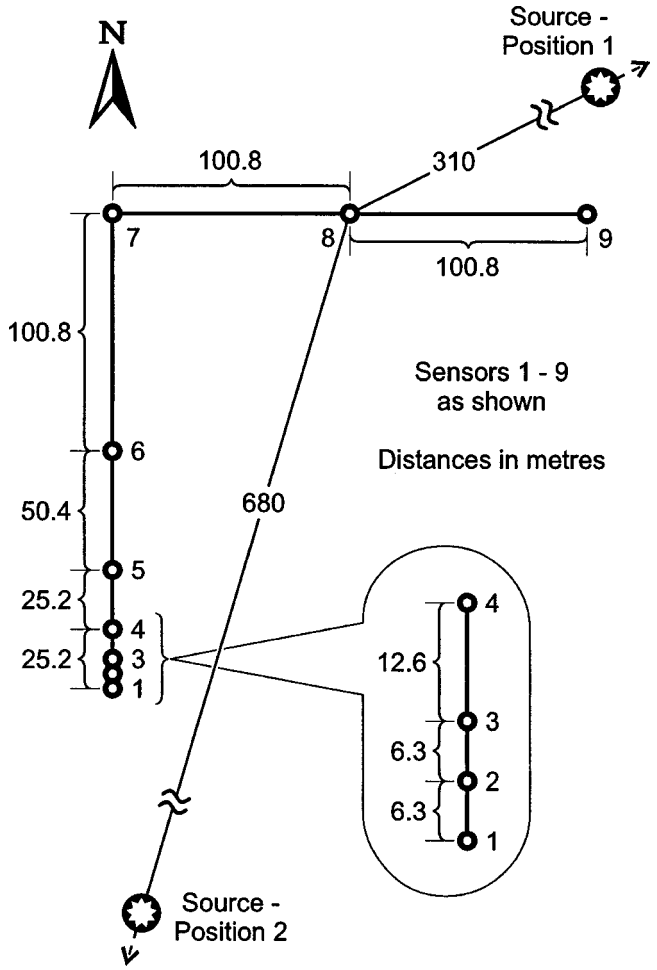

FIG. 2. Source-sensor geometry. The source is initially at position 1, then the experiment is repeated with the source at position 2.

in the (along-) range estimates is larger than the error in the bearing (and hence cross-range) estimates—see Fig. 1.

There is an inherent bias in the range estimate with the wavefront curvature technique, even if the errors in the time delay measurements are zero-mean.[4] The bias is due to the nonlinear relationship between the range R and the time delays τ_{ij} [Eq. (1)]; however, the bias will be negligible if the time delay estimation errors are small enough. Similarly, the bearing estimate is also biased due to the nonlinear relationship with the time delays[13] [Eq. (2)].

II. EXPERIMENTAL RESULTS—STATIONARY SOURCE

A. Experimental method

Figure 2 shows the geometrical configuration of the sensors and their orientation relative to the stationary source (positions 1 and 2 are the two alternative positions of the source). The sound source is a jet engine undergoing a thrust test on the ground. The intersensor separation distances are 6.3 m (sensors 1-2-3), 12.6 m (sensors 1–3–4), 25.2 m (sensors 1–4–5), 50.4 m (sensors 1–5–6), 100.8 m (sensors 1–6–7 and sensors 7–8–9).

Each sensor output is digitally sampled at a rate of 7111 times per second. The output waveforms from adjacent sensors are cross-correlated using a frequency-domain implementation of a standard wideband cross-correlator to process the acoustic data in the frequency range: 50–400 Hz. The time delay estimate corresponds to the time lag at which the cross-correlation function attains its maximum value. The time lag increment ($\Delta\tau$) is equal to the reciprocal of the sampling rate (that is, $\Delta\tau=0.14$ ms). The acoustic sensor data are partitioned into blocks of 512 samples so that the observation time interval $T=512/7111=0.072$ s. Sample cross-correlograms using the acoustic data have been published previously.[14]

Figure 3 shows the variation with time of the time delay estimates (denoted by circles) for various sensor separation distances when the source is at position 1. In the present experiment, the temporal variability in the time delay measurements is observed to occur on two different time scales: the *short* time-scale (subsecond) variability where the estimated values fluctuate randomly about a smooth curve (solid line) representing the *long* time-scale variability which appears also to be the result of a random process. (Methods for smoothing the data are considered below.) The long time-scale component of the temporal variability is slowly varying and has a time period that varies from seconds to tens of seconds.

The short time-scale variability is characterized by random fluctuations which arise because the random errors in the time delay measurements reflect the statistical uncertainty of the time delay estimation process, that is, the random errors can only be predicted on a statistical basis. The random errors (also commonly referred to as random uncertainties) are intrinsic to the time delay estimation method with the variance of the random errors being determined by the signal-to-noise ratio, the signal bandwidth and the integration time.[12]

Atmospheric turbulence leads to a sound propagation medium that is spatially inhomogeneous and temporally nonstationary with the acoustical refractive index varying in space and time along the sound propagation path, the effect of which is to produce fluctuations in the phase and amplitude of the sound pressure field at the receiver.[15] The underlying long time-scale component of the temporal variability in the time delay estimation data can be identified by applying either a data smoothing method or a low-pass filtering method to the sequence of time delay estimates. Thus, computing the running mean of a data window that progressively slides through the sequence (or time series) of the time delay estimates (or else, low-pass filtering the time series) extracts the long time-scale component of the temporal variability in the observations. The long time-scale variability (which is observed as a variation *in* the running mean) introduces a dynamic short-term bias, or *local* systematic error, into the time delay estimates. This is because the time periods that characterize the long time-scale variability are two or three orders of magnitude greater than the time period of the short time-scale variability. In the present experiment, the lower limit for the period of the short time-scale variability is set by the observation time interval for a single time delay estimate ($T=0.072$ s). In summary, the short time-scale variability (which is an inherent feature of the measurement

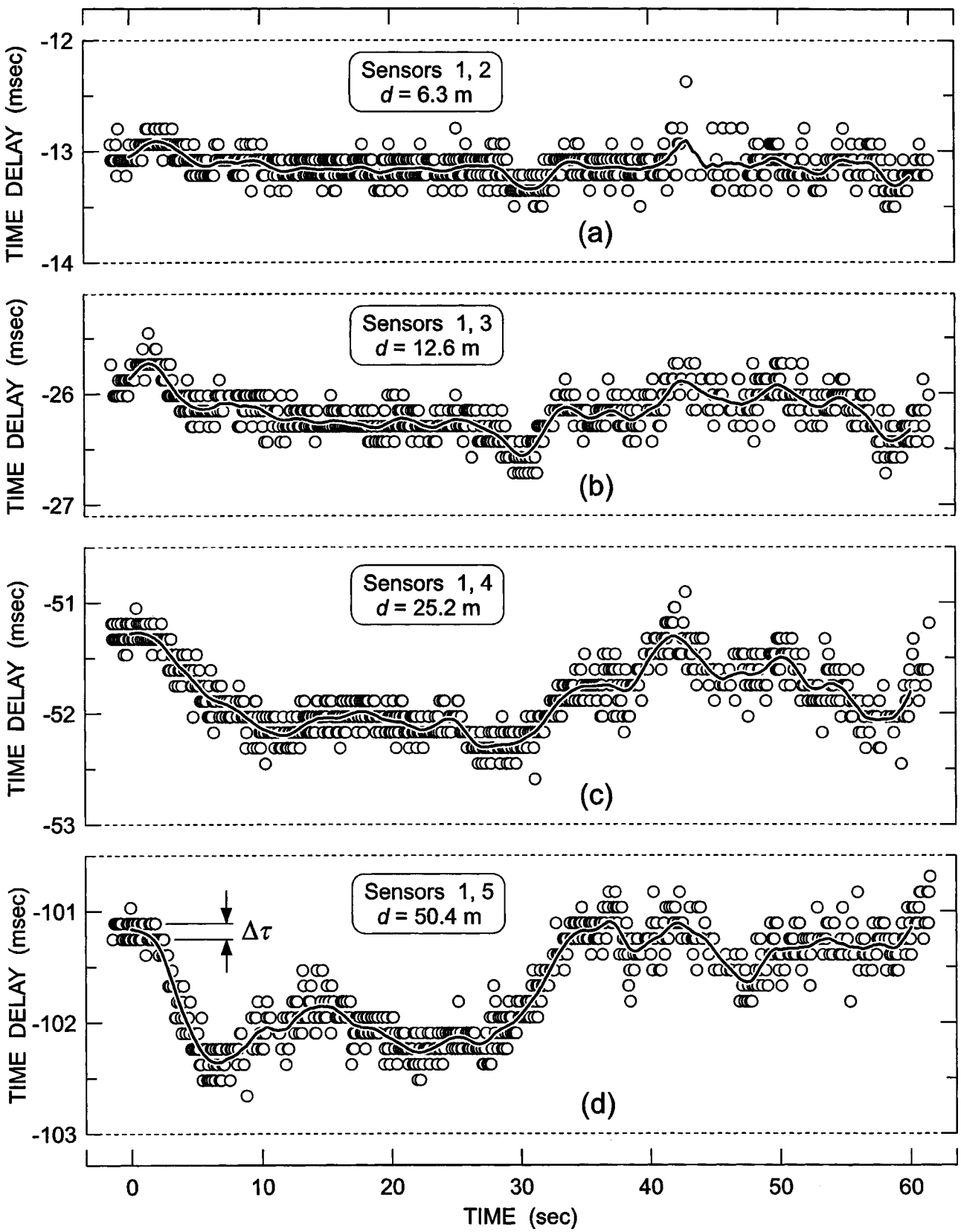

FIG. 3. Temporal variation of the time delay estimates for a geometric progression of the sensor-separation distance: (a) 6.3; (b) 12.6; (c) 25.2; (d) 50.4 m. The source is at position 1. Also shown is the magnitude of the time delay increment ($\Delta\tau = 0.14$ ms) which is equal to the reciprocal of the sampling frequency.

technique) manifests itself as short-term fluctuations of the time delay estimates *about* the running mean. The short time-scale variability is superimposed on the underlying long time-scale variability, which manifests itself as a variation *in* the running mean.

The solid line in Fig. 3 represents the running mean; fluctuations *in* the running mean are due to the long time-scale variability in the time delay estimates. The magnitude of the long time-scale variability increases significantly as the sensor separation distance increases. This observation is quantified by calculating the standard deviation $\sigma(\tau_{ij})$ of the running mean for each sensor separation distance (for the north-south arm of the sensor array). The results are plotted in Figs. 4(a) and 4(b) for the source at position 1 and position 2 (respectively). In comparison, the magnitude of the short time-scale variability tends to be independent of the sensor separation distance. Calculating the standard deviation of the short-term fluctuation *about* the running mean requires removal of the dynamic bias in the time delay estimates due to the variability in the long time-scale component. Note that the magnitude of the long time-scale variability only exceeds that of the short time-scale variability when the sensor separation distance exceeds 10 m for the source at position 1 [see Fig. 4(a)] and 25 m for the source at position 2 [see Fig. 4(b)]. Thus the long-time scale variability in the time delay estimates, which is caused by physical processes occurring in the atmosphere, can be observed only when the magnitude of the random errors in the time delay estimation process (or equilvalently, the time delay measurement precision) is sufficiently small.

The long time-scale variability in the time delay estimates is larger when the source is at position 1 [compare Fig. 4(a)—source position 1 and Fig. 4(b)—source position 2]. The measurement periods for the two source positions are about three hours apart (1000 and 1300 local time) so the sound propagation conditions (and strength of the atmospheric turbulence) may be different or else the signal arriving at the sensors is more variable after traveling along sound propagation paths that are transverse (source at position 1), rather than longitudinal (source at position 2), to the sensor array axis. [Further explanation of the differences between Figs. 4(a) and 4(b) requires knowledge of the meteorological parameters that would have affected the propagation of sound at the time of the experiment. Unfortunately, time series data of the atmospheric temperature and the ground wind vector are unavailable.] On the other hand, the *short* time-scale variability in the time delay estimates (due to the measurement method) tends to be independent of the sensor separation distance and the source position.

The long time-scale temporal variability in the time delay estimates, which is observed to increase with the sensor separation distance, is ascribed to fluctuations in the acoustical refractive index caused, for example, by atmospheric turbulence. When the atmosphere is turbulent, the sound propagation medium becomes spatially inhomogeneous and temporally nonstationary. Models of atmospheric turbulence indicate a statistical distribution of eddies of various sizes is present in the atmosphere at all times.[15] Large eddies are formed by atmospheric instabilities in the thermal and viscous boundary layers near the ground. Further instability progressively breaks down the size of the eddies according to a cascade process until the energy of the turbulence is finally dissipated by viscosity in very small eddies.[15] Theory predicts that the signal phase and amplitude fluctuations increase with increasing distance of propagation, source frequency, and strength of turbulence.[15]

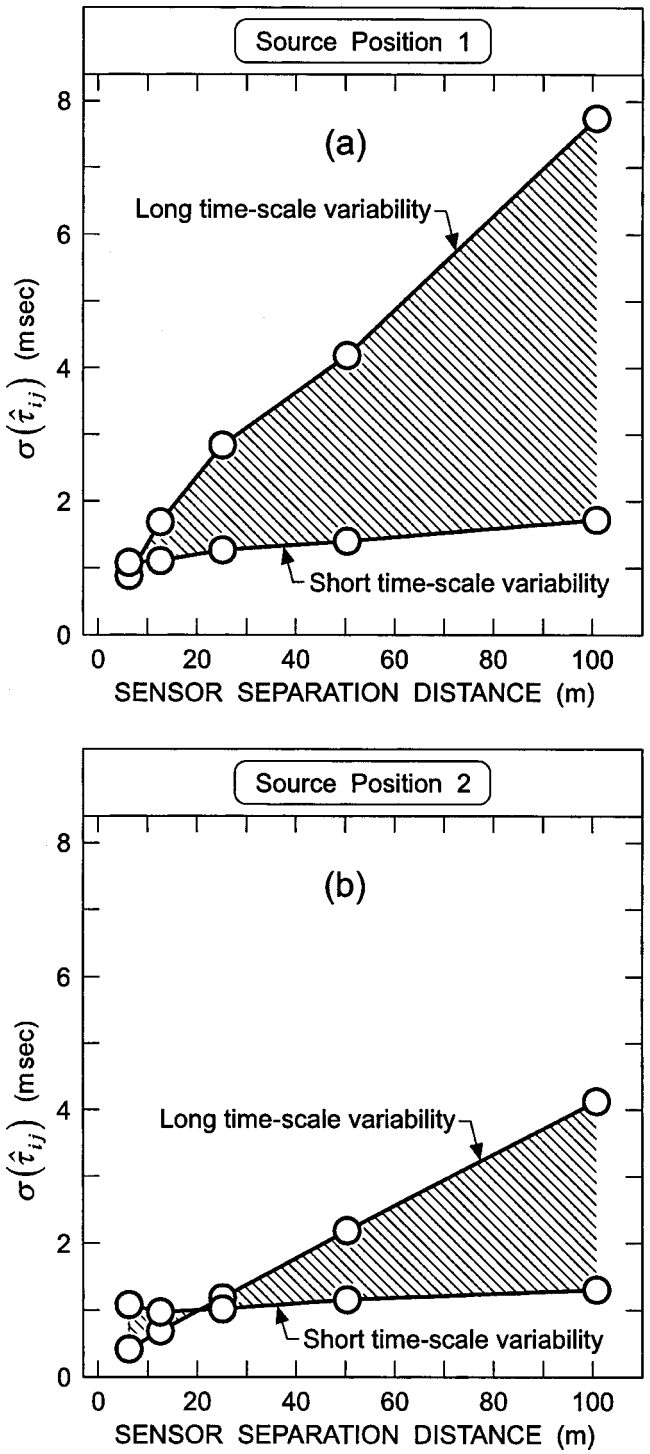

FIG. 4. Variation with sensor separation distance of the standard deviation in the time delay estimates for the short time-scale and long time-scale temporal components of the variability in the time delay estimates when the source is at: (a) position 1; and (b) position 2.

B. Result comparison—Theory and experiment

1. Bearing error variance

With the wavefront curvature passive ranging technique, the ''instantaneous'' bearing and range estimates are calculated using simultaneous time delay estimates from adjacent pairs of spatially separated sensors. Hence temporal variability in the time delay estimates translates to temporal variability in the bearing and range estimates. This variability occurs on the same short and long time-scales that characterize the variability in a time series of time delay measurements. The theoretical error variance formulas for the bearing and range estimators [Eqs. (6) and (7), respectively] are only relevant to the *short* time-scale variability in the ''instantaneous'' bearing and range estimates. The *long* time-scale variability in the time delay estimates cannot be modeled in the same way and so it is excluded from further consideration. (The theoretical performance bounds for acoustic direction-of-arrival arrays operating in atmospheric turbulence has been published recently[16] in which the degradation in system performance due to turbulence, rather than noise at the sensor, is studied using several atmospheric turbulence models.)

Note that the remainder of this paper addresses the *short-term variability* in the various parameter estimates due to random noise at each of the sensors. Also, it is the *precision* rather than the *accuracy* of the measurements[17] that is of interest here.

Figure 5 compares the theoretical and measured variances of the (far field) bearing as a function of the length of the effective intersensor baseline ($d \sin \beta$) for the source at positions 1 and 2. Both the abscissae and ordinates are plotted on logarithmic scales to reflect the predicted inverse square relationship between the variance of the bearing errors and $d \sin \beta$—see Eq. (6). The white-filled circles denote the observed bearing error variances of the short-term fluctuations in the bearing estimates calculated for the north-south sensor pairs: 1–2, 1–3, 1–4, 1–5 and 1–6, with the white-filled diamond representing the result for the east-west pair: 7–8. Each of the corresponding black-filled symbols represents the adjustment of the observed bearing error variance (for the short time-scale variability in the bearing estimates) so that the variance of the time delay estimates is the same for all sensor separation distances. (The time delay error variance of each sensor pair is normalized so that it matches the time delay error variance of the reference sensor pair: 1–6.) The dashed line represents the theoretical prediction of Eq. (6) for the variation of the bearing error variance with the length of the effective intersensor baseline. There is close agreement between theory and experiment (normalized observations) for both source positions. Hence, increasing the length of the effective intersensor baseline by one order of magnitude reduces the bearing variance by two orders of magnitude.

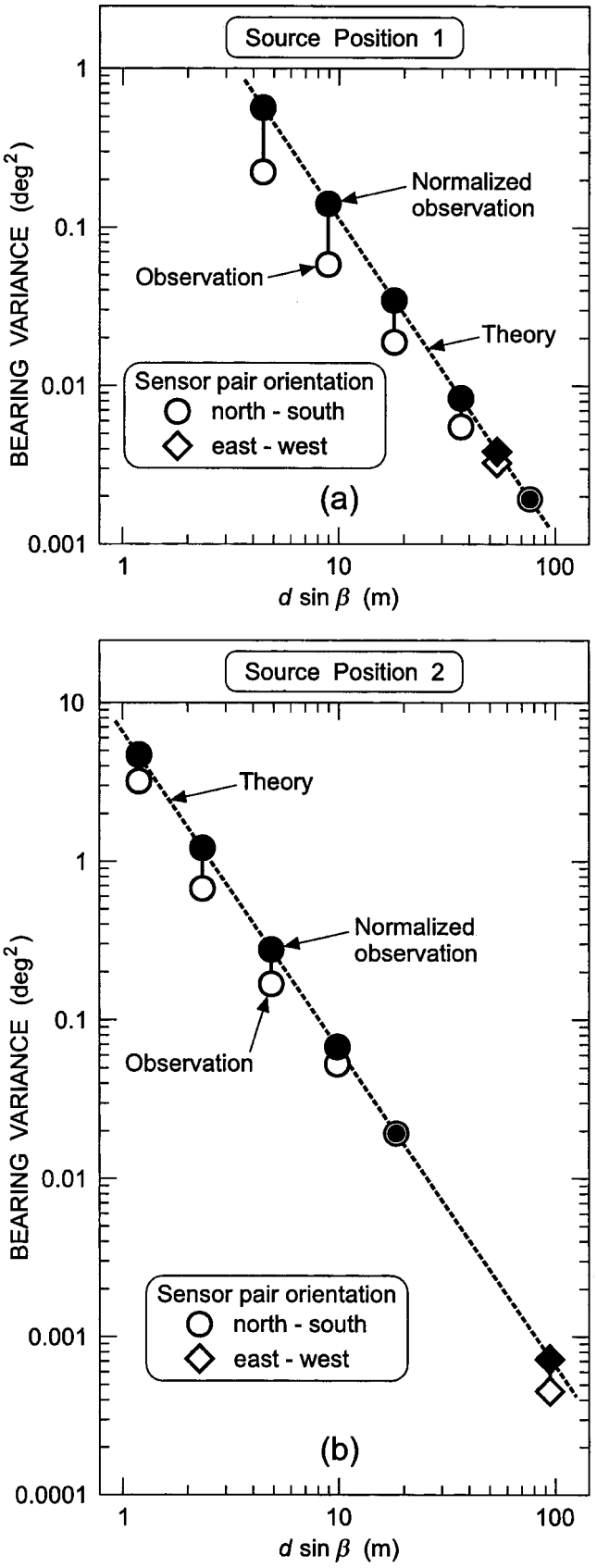

FIG. 5. Variation with the length of the effective intersensor baseline ($d \sin \beta$) of the observed and theoretical bearing error variance [$\sigma^2(\hat{\beta}-\beta)$] for the source at: (a) position 1; and (b) position 2. The experimental results pertain to the short time-scale variability in the bearing estimates.

2. Range error variance

Figure 6 shows the variation with time of the time delay estimates for two adjacent pairs of sensors [Figs. 6(a) and 6(b)] that comprise the east-west arm of the array (sensors

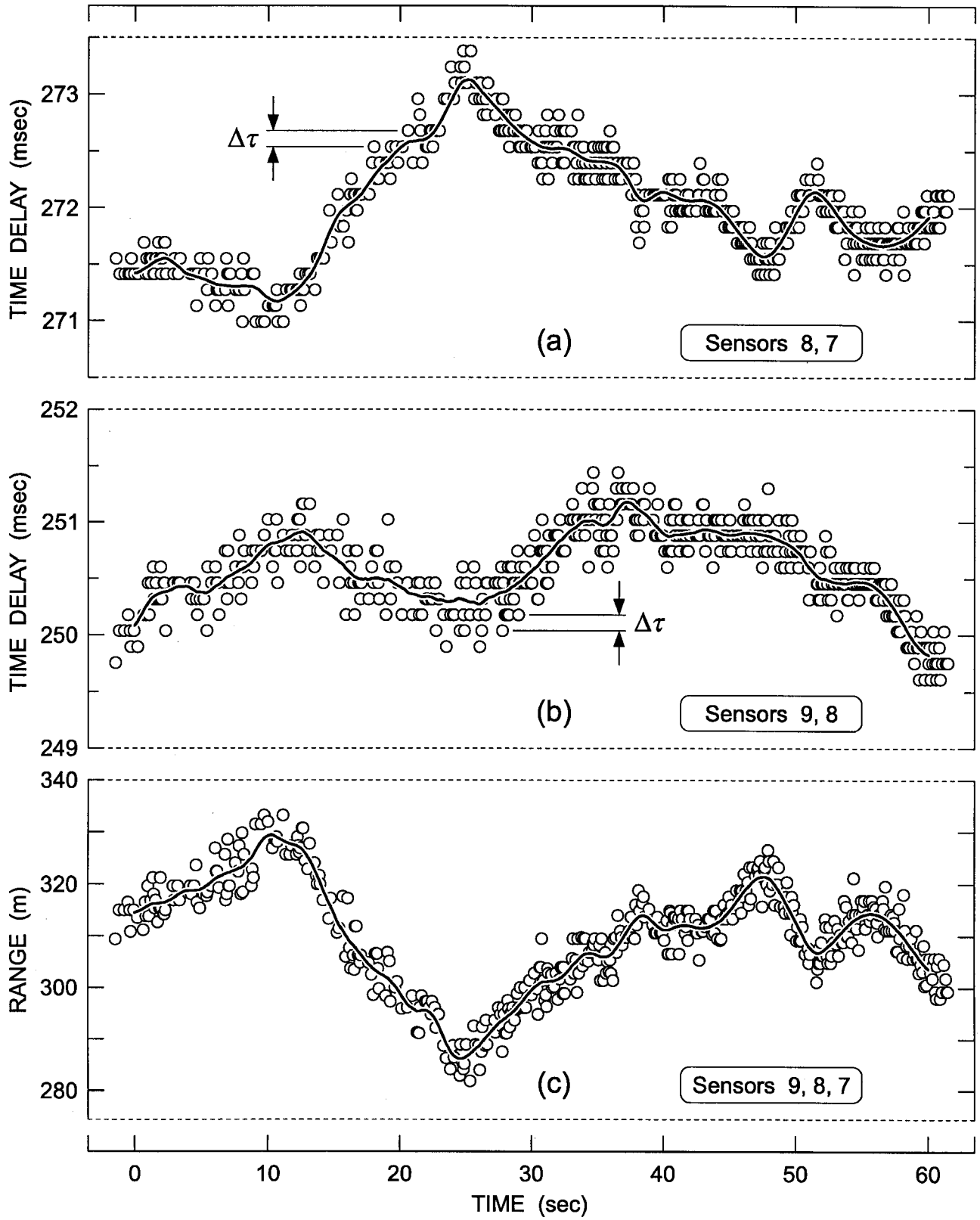

FIG. 6. Variation with time of the time delay estimates from the pair of sensors: (a) 7–8; and (b) 8–9. A pair of simultaneous time delay estimates, one from each pair of sensors, is used to provide an estimate of the ''instantaneous'' range using the wavefront curvature passive ranging formula. Diagram (c) shows the variation with time of the ''instantaneous'' range estimates.

7–8–9) and the resulting ''instantaneous'' range estimates [Fig. 6(c)] for the source at position 1. The intersensor separation distance is 100.8 m. Like the time delay estimates, the range estimates have temporally variable components occurring on both short and long time-scales. Both the short time-scale variability and the long time-scale variability can be observed in the range estimates (and in the time delay estimates on which they depend). As with the analysis of the

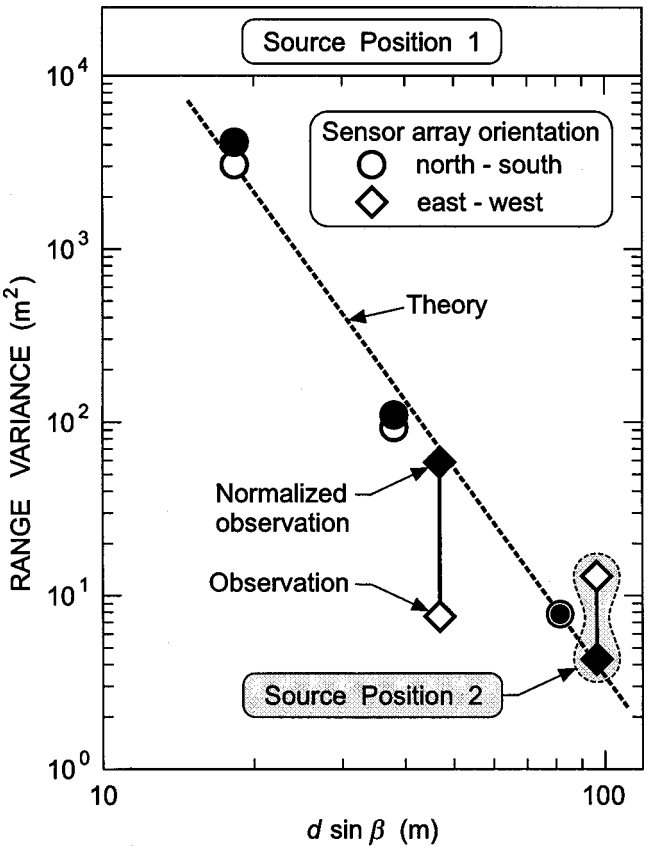

FIG. 7. Variation of the observed and theoretical range error variance $[\sigma^2(\hat{R}-R)]$ with the length of the effective intersensor baseline ($d \sin\beta$) for each of the sensor pairs. The experimental results pertain to the short time-scale variability in the range estimates.

bearing estimates, only the *short* time-scale random fluctuations in the range estimates are considered further.

Figure 7 shows the short time-scale random (error) variance of the range estimates for both source positions as a function of the length of the effective intersensor baseline. Both the abscissae and ordinates of the data points are plotted on logarithmic scales because of the predicted inverse fourth power relationship between the variance of the range errors and $d \sin\beta$—see Eq. (7). Only the sensor combinations for which the wavefront curvature technique produces meaningful range estimates are presented, that is, where the intersensor separation distance is large and the source is not near endfire. The circles represent the results when the source is at position 1 for the north-south sensor combinations: 1–4–5 ($d=25.2$ m), 1–5–6 ($d=50.4$ m), 1–6–7 ($d=100.8$ m) and the diamonds denote the results for the east-west sensor combination: 7–8–9 ($d=100.8$ m). Only the results for the east-west arm of the sensor array are presented when the source is at position 2 because of the proximity of the source to the endfire direction of the north-south arm. The black-filled symbols represent the normalized observations so that the differences in the observations (white-filled symbols) caused by differences in the time delay error variances and in the actual range of the source are removed by scaling. The range error variances are normalized so that the time delay error variance and source range are the same for all the sensor combinations. The dashed line represents the theoretical prediction of Eq. (7) for the variation of the range error variance with the length of the effective intersensor baseline. There is close agreement between the theoretical prediction and the normalized observations for both source positions. Hence, increasing the length of the effective baseline by one order of magnitude reduces the range error variance by four orders of magnitude.

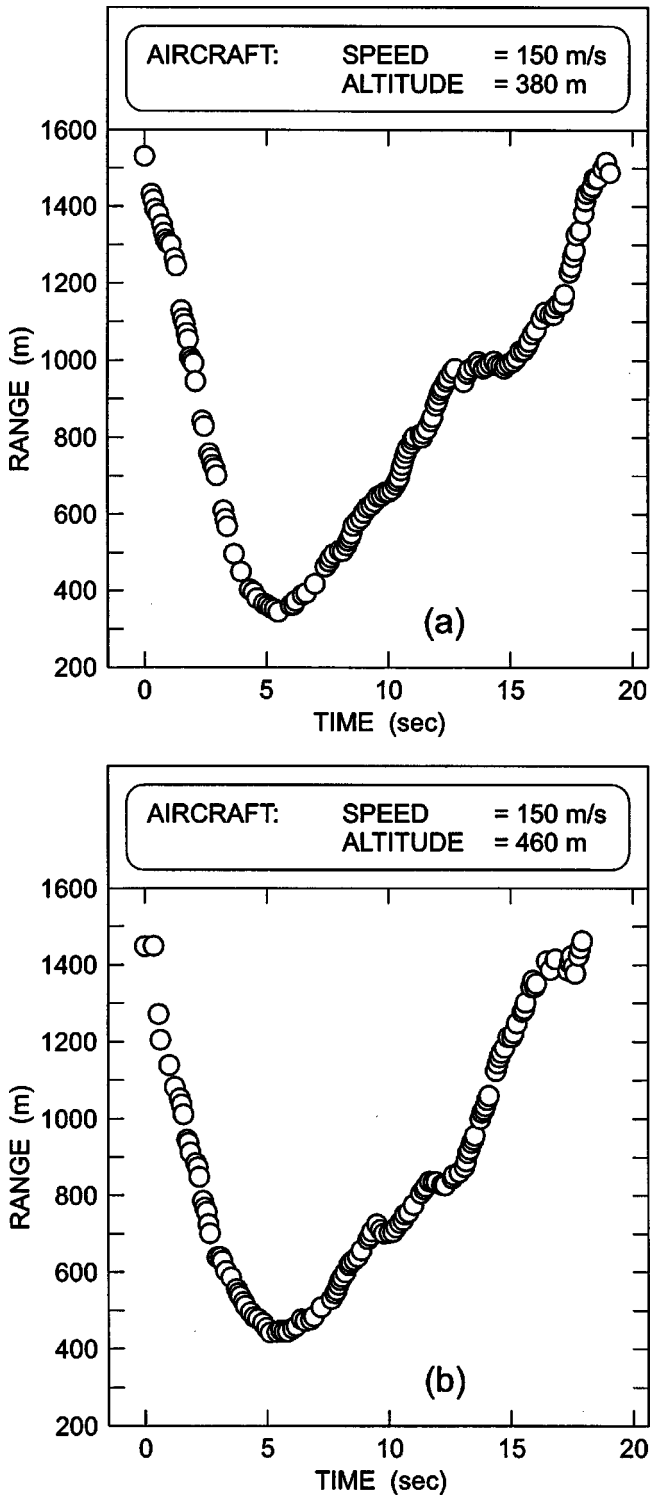

FIG. 8. Variation with sensor time of the range to the jet during its transit over the sensor array for an aircraft altitude of: (a) 380; and (b) 460 m.

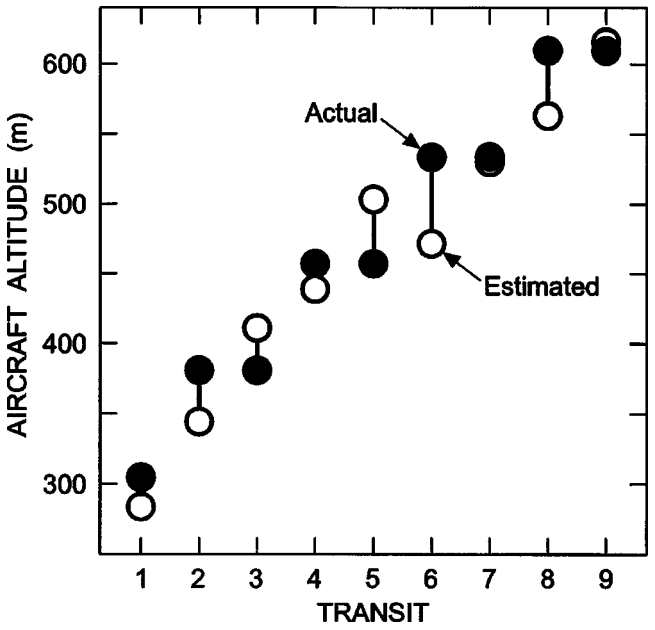

FIG. 9. Comparison of actual and estimated values of the aircraft altitude for a number of transits by the jet over the sensor array.

III. EXPERIMENTAL RESULTS—MOVING SOURCE

Next, a jet aircraft traveling at constant speed and in level flight made a number of transits over the array along a north-south flight path. The wavefront curvature passive ranging technique is used to observe the variation with time of the aircraft's range during each transit. Simultaneous time delay estimates from the adjacent sensor pairs that comprise the east-west arm of the array (that is, the sensor pairs: 7–8 and 8–9) are used to calculate the ''instantaneous'' range. Figure 8 shows the variation with time of the ''instantaneous'' range as a function of sensor time during transit 2 [Fig. 8(a)] and transit 4 [Fig. 8(b)]. The temporal asymmetry in the variation of the acoustic range with sensor time is due to the finite travel time for the sound to propagate from the source to the sensor and the high speed (Mach ≈ 0.5) of the aircraft; the relationship between source time and sensor time is considered elsewhere.[18] This temporal asymmetry is referred to as the *retardation effect*.[19]

If the aircraft flies directly over the middle sensor of the east-west arm of the array, then the range of the source at the closest point of approach is a minimum and coincides with the altitude of the aircraft. Figure 9 shows the actual and estimated values of the aircraft altitude for each of nine transits. The wavefront curvature technique provides a reliable estimate of the aircraft's altitude since the root-mean-square error between the estimated and actual altitudes is only 35 m for the nine transits. Hence, the wavefront curvature technique can be used to observe the variation with time of the ''instantaneous'' range of a moving airborne source and to estimate its altitude when it flies directly over the sensor array.

The east-west sensor configuration: 7–8–9 (rather than a north-south configuration) is chosen for the passive ranging of the aircraft during its transit so as to have a large effective baseline for the sensor array and to minimize the effect of differential Doppler on the performance of the wideband

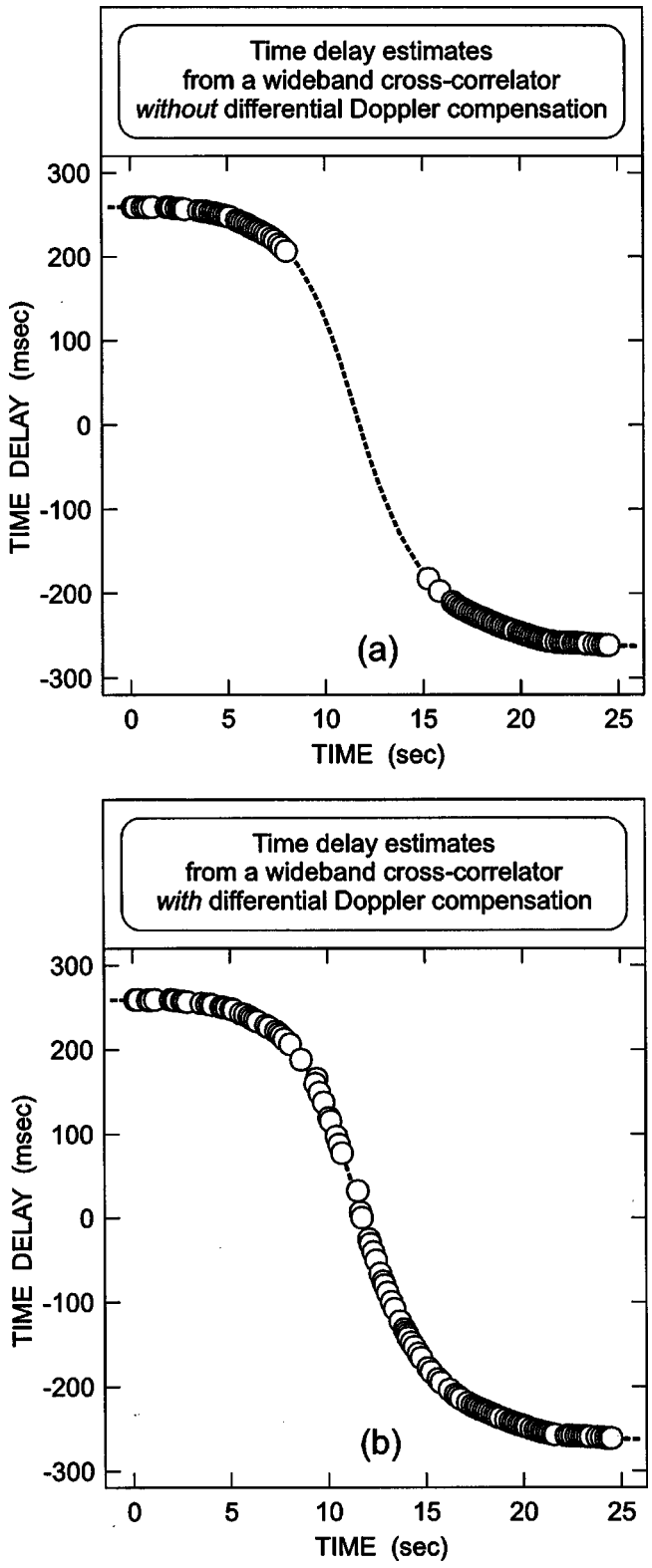

FIG. 10. Variation with time of the time delay estimates for the signal (radiated noise from a transiting jet aircraft) using a wideband cross-correlator: (a) *without* differential Doppler compensation; and (b) *with* differential Doppler compensation.

cross-correlation processor.[14,18] Figure 10 shows the effect of differential Doppler on the time delay estimates for the north-south sensor configuration: 1–6–7. The time delay is estimated for each observation period using (a) the standard cross-correlation method and (b) the wideband cross-

ambiguity function (or wavelet transform) which compensates for the differential Doppler effect.[14,18] The standard cross-correlator produces noisy estimates of the time delays (not shown in the figure) only during the overhead portion of the aircraft transit when the differential Doppler of the received signals is significant. At other times (when the aircraft is far from the closest point of approach), the differential Doppler effect is negligible and the time delay estimates are reliable—see Fig. 10(a) 0–8 and 15–24 s. The wideband cross-ambiguity function (or wavelet transform) compensates for the differential Doppler effect allowing reliable time delay estimates to be extracted from the wideband cross-correlation of the acoustic data throughout the aircraft transit—see Fig 10(b).

IV. CONCLUSIONS

Passive ranging of acoustic sources in air by the wavefront curvature technique has been demonstrated for a long sensor baseline using accurate time delay estimates with the source in the near field and in a direction away from endfire.

The wavefront curvature technique can be applied to the passive localization of a stationary sound source in air, but the bearing and range estimates are observed to fluctuate, although the source-sensor geometry is fixed. The temporal variability in the estimated position of a stationary source is observed to occur on two time scales: the *short* time-scale (subsecond) variability where the estimated values of the source localization parameters fluctuate randomly about an underlying slowly varying smooth curve that represents the *long* time-scale variability for which the time period varies from seconds to tens of seconds.

The short time-scale variability in the time delay estimates is responsible for short-term random errors in the bearing and range estimates. The variance of these random errors are quantified for various sensor separation distances, sensor orientations and source positions. The theoretical variation of the bearing error variance and the range error variance with the length of the effective intersensor baseline closely matches the experimental results provided they are normalized so that the time delay error variance is independent of the sensor separation distance and the range of the source.

The long time-scale component of the temporal variability is ascribed to fluctuations in the acoustical refractive index caused, for example, by atmospheric turbulence.

The wavefront curvature technique can be used to estimate the altitude of an aircraft when it flies over the middle sensor of three widely spaced elements of a line array from a broadside direction (so that the differential Doppler effect is small and the length of the effective baseline of the array is large).

ACKNOWLEDGMENTS

The author gratefully acknowledges the contributions made to this scientific paper by his colleagues Lionel Criswick and Gary Speechley of the Maritime Operations Division (Sydney).

[1] G. C. Carter, ''Time delay estimation for passive sonar signal processing,'' IEEE Trans. Acoust., Speech, Signal Process. **ASSP-29**, 463–470 (1981).

[2] E. B. Lunde, ''Wave front stability in the ocean,'' in *Signal Processing*, edited by J. W. R. Griffiths, P. L. Stocklin, and C. Van Schooneveld (Academic, New York, 1973), pp. 271–279.

[3] J. C. Hassab, B. W. Guimond, and S. C. Nardone, ''Estimation of location and motion parameters of a moving source observed from a linear array,'' J. Acoust. Soc. Am. **70**, 1054–1061 (1981).

[4] K. B. Theriault and R. M. Zeskind, ''Inherent bias in wavefront curvature ranging,'' IEEE Trans. Acoust., Speech, Signal Process. **ASSP-29**, 524–527 (1981).

[5] J. L. Spiesberger, ''Identifying cross-correlation peaks due to multipaths with application to optimal passive localization of transient signals and tomographic mapping of the environment,'' J. Acoust. Soc. Am. **100**, 910–917 (1996).

[6] J. L. Spiesberger, ''Linking auto- and cross-correlation functions with correlation equations: Application to estimating the relative travel times and amplitudes of multipath,'' J. Acoust. Soc. Am. **104**, 300–312 (1998).

[7] U. Ingard, ''A review of the influence of meteorological conditions on sound propagation,'' J. Acoust. Soc. Am. **25**, 405–411 (1953).

[8] T. F. W. Embleton, ''Tutorial on sound propagation outdoors,'' J. Acoust. Soc. Am. **100**, 31–48 (1996).

[9] P. Heimdal and F. Bryn, ''Passive ranging techniques,'' in *Signal Processing*, edited by J. W. R. Griffiths, P. L. Stocklin, and C. Van Schooneveld (Academic, New York, 1973), pp. 261–269.

[10] G. C. Carter, *Coherence and Time Delay Estimation* (IEEE, New York, 1993).

[11] C. H. Knapp and G. C. Carter, ''The generalized correlation method for estimation of time delay,'' IEEE Trans. Acoust., Speech, Signal Process. **ASSP-24**, 320–327 (1976).

[12] A. H. Quazi, ''An overview on the time delay estimate in active and passive systems for target localization,'' IEEE Trans. Acoust., Speech, Signal Process. **ASSP-29**, 527–533 (1981).

[13] J. C. Hassab, ''Passive bearing estimation of a broad-band source,'' IEEE Trans. Acoust., Speech, Signal Process. **ASSP-32**, 426–431 (1984).

[14] B. G. Ferguson, ''Time delay estimation techniques applied to the acoustic detection of jet aircraft transits,'' J. Acoust. Soc. Am. **106**, 255–264 (1999).

[15] G. A. Daigle, J. E. Piercy, and T. F. Embleton, ''Line of sight propagation through atmospheric turbulence near the ground,'' J. Acoust. Soc. Am. **74**, 1505–1513 (1983).

[16] D. K. Wilson, ''Performance bounds for acoustic direction-of-arrival arrays operating in atmospheric turbulence,'' J. Acoust. Soc. Am. **103**, 1306–1319 (1998).

[17] J. Topping, *Errors of Observation and their Treatment*, 3rd ed. (Chapman and Hall, London, 1962).

[18] B. G. Ferguson and Kam W. Lo, ''Passive wideband cross-correlation with differential Doppler compensation using the continuous wavelet transform,'' J. Acoust. Soc. Am. **106**, 3434–3444 (1999).

[19] F. Dommermuth and J. Schiller, ''Estimating the trajectory of an accelerationless aircraft by means of a stationary acoustic sensor,'' J. Acoust. Soc. Am. **76**, 1114–1122 (1984).

The effect of temperature on sound wave absorption in a sediment layer

Rafael Carbó[a] and Adriana C. Molero
Instituto de Acústica (C.S.I.C.), Serrano 144, 28006 Madrid, Spain

(Received 28 June 1999; revised 16 June 2000; accepted 20 June 2000)

The effect of temperature on sound velocity, absorption, and reflection coefficient in the seabed sediment layer is investigated. Experimental measurements of sound speed, absorption, and the reflection coefficient in a sandy sediment layer have been carried out at several temperatures. An absorption reduction of 75 dB/m and a velocity increase of 65 m/s have been measured at a frequency of 1 MHz when the temperature increases from 5 to 25 °C. Because of the absorption temperature dependence the amplitude of the reflected wave from the back surface of the sub-bottom layer after going back and forth across the layer increases with the temperature.
 [S0001-4966(00)01110-3]

PACS numbers: 43.30.Ma [DLB]

I. INTRODUCTION

The seabed classification based on inversion processing of echo-sounding signals requires accurate acoustic measures of the speed and absorption of sound waves into the sediments.[1] Experimental data in an interim U.S. Navy Oceanographic Office Technical Report[2] show a wide range in the seabed temperature values, depending on the location, depth, and season of the year.

A recent paper by Richards[3] concerning the effect of temperature, pressure, and salinity on sound attenuation in turbid sea water provides a theoretical model based on Urick's[4] expression for the viscous absorption coefficient and Sheng and Hay's[5] expression for the absorption coefficient by scattering in a suspension of spheres at high frequency. Accurate expressions for water density, viscosity, sound speed, and the absorption coefficient have been defined in this paper and used to compute the absorption coefficient variation of water suspensions with temperature, salinity, and pressure. Theoretical values obtained for temperature $0\,°\text{C} \leqslant t \leqslant 30\,°\text{C}$, salinity $0 \leqslant S \leqslant 36$, and pressure $1\ \text{dbar} \leqslant p \leqslant 1000\ \text{dbar}$ show only significant variations with the temperature. The acoustical response of sediment with the same solid material and porosity, therefore, may be different depending on the location, depth, and season of the year because of different temperatures. No experimental values are indicated in this study. Finally, several papers concerning the sound absorption in marine sediments[6–8] show experimental values of the absorption coefficient as a function of frequency, but the temperature effect on sound absorption is not considered.

The aim of this letter is to apply Richards' idea to unconsolidated sediments with high porosity. Experimental devices to measure temperature dependence of sound velocity, absorption, and the reflection coefficient in unconsolidated sediments have been developed.

II. DESCRIPTION OF THE MEASUREMENTS

Laboratory methods were employed to measure the physical parameters of a sediment sample collected by divers at the Biscay Gulf (43°35′N; 2°08′W) at the depth of 11 m. Porosity was obtained by heating the sediment sample during 24 h at 105 °C. The sample weighed before and after the heat determined a porosity of 42% and a wet density of 1973 kg/m^3. The grain size has been measured with a Microtrac-X100 laser system. The grain size distribution curve (Fig. 1) shows two peaks at 160 and 600 μm. All these physical parameter values are in accord with Hamilton's[8] fine sand measures in the continental terrace environment.

Compressional wave speed and the absorption coefficient were determined by using a pair of Panametrix ultrasonic transducers as an emitter and receiver of acoustic pulses. A Tektronix FG501A pulse generator and a National Instruments NIDaq card acquisition A/D converter were used with Virtual Bench™ software. This system allows accurate measurements of received voltages required for velocity and absorption measurements.

One transducer was driven with a 1-MHz, 30-V peak-to-peak sine wave triggered for 1-μs duration every 1 ms. The transmission pulse technique was used in a sample 40-mm thick. The signal received by the other transducer was amplified and digitized before making the time delay and receiving voltage measurements. Compressional wave

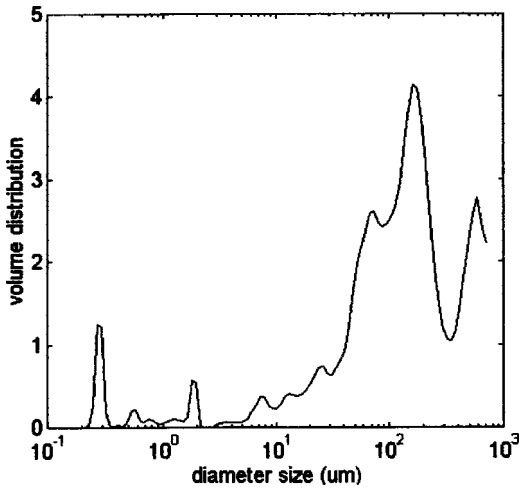

FIG. 1. Sediment sample grain size distribution.

[a]Electronic mail: iaccf31@fresno.csic.es

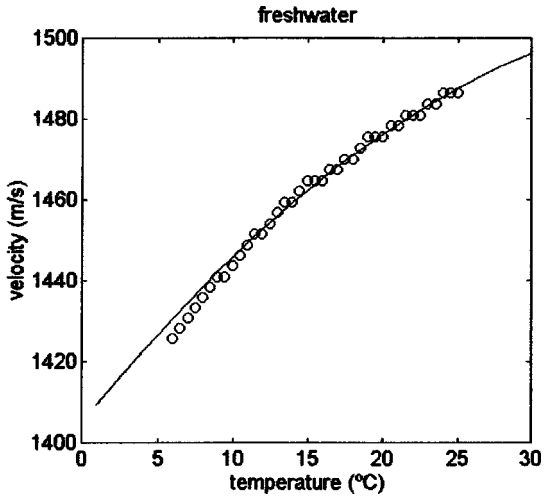

FIG. 2. Measured experimental values of freshwater sound velocity as a function of temperature (circles) compared with the theoretical curve (solid line).

velocity was calculated by the difference between the time delay measurements made on a vessel sample filled with freshwater and the time delay measurements made on the same vessel filled with a sediment sample. The accuracy of time measurements was 50 ns. The absorption coefficient was calculated as $20\log_{10}$ of the ratio of fast Fourier transform (FFT) receiving voltage pulse through the freshwater to the FFT receiving voltage pulse through the sediment referenced to 1 m of sample thickness (dB/m). The measurements were conducted at the same temperature in both water and sediment.

The temperature of the sample was measured with accuracy at 0.1 °C, varying from 6 to 25 °C. The freshwater absorption is neglected in comparison to the sediment absorption, because according to Fisher and Simmons[9] the sound absorption in freshwater at 1 MHz is lower than 0.02 dB/m, and the sediment absorption at this frequency is higher than 10 dB/m.

While testing the measurement method, theoretical[10] and experimental values of freshwater sound velocity in a temperature range from 6 to 30 °C (Fig. 2) were compared, with acceptable accuracy.

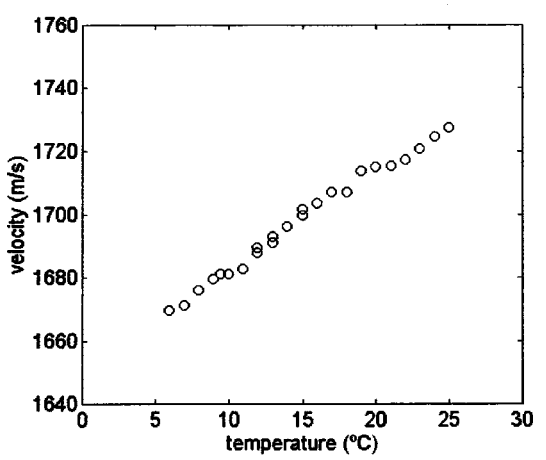

FIG. 3. Measured experimental values of sediment sound velocity as a function of temperature.

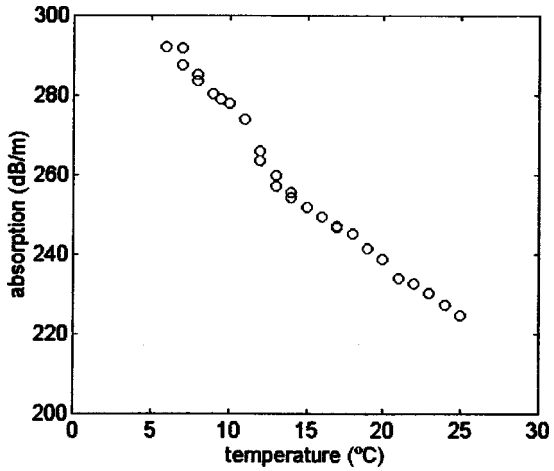

FIG. 4. Measured experimental values of sediment absorption coefficient as a function of temperature.

Figures 3 and 4 show the experimental values obtained for the sound velocity and sound absorption measured at 1 MHz in a sample of sediment with physical parameters quoted above (grain size of 160 μm and porosity of 42%). An absorption reduction of 75 dB/m and a velocity increase of 65 m/s have been measured when the temperature increases from 5 to 25 °C. Values of velocity and absorption agree with those reported by other authors (Hamilton,[11] Stoll[7]). They refer to samples of continental terrace sediment, with the same grain size and porosity as for our sample, giving velocities ranging between 1660 and 1820 m/s and, for a frequency of 1 MHz, absorption values between 200 and 300 dB/m.

A common shallow water geoacoustic model is a top layer of soft mud, or fine sand overlying a rock basement.[11] Figure 5 illustrates this seabed model.

The reflection coefficient of a layer can be obtained by considering the multiple reflections at the boundaries of the layer. The expression for the reflection coefficient from Brekhovskikh[12] is used and limited to the case of normal incidence. From Figure 5, the resultant wave reflected from

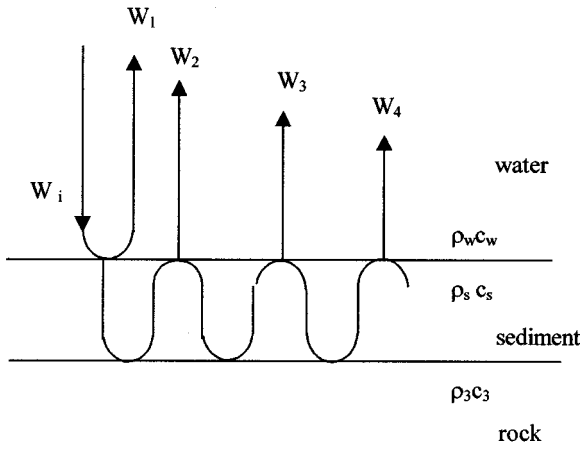

FIG. 5. Components of the reflected wave caused by a shallow water geoacoustic model (a thick layer of fine sand over rock).

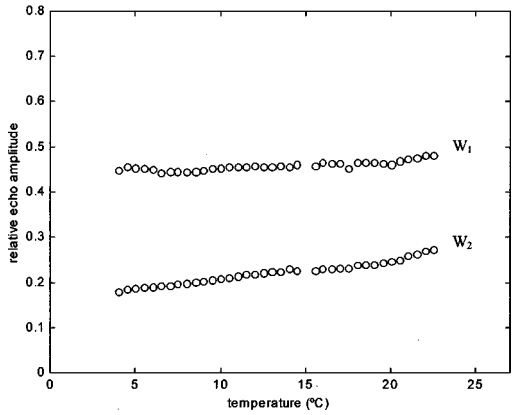

FIG. 6. Experimental values of reflected wave amplitude W_1 and W_2.

the layer may be regarded as a superposition of the following: W_1, the wave reflected from the front surface of the layer; W_2, the wave penetrating the front surface of the layer, passing through the layer, reflected from the back surface of the layer, and passing through the layer again and leaving through its front surface; W_3, the wave penetrating the layer, undergoing two reflections at the back surface and one at the front surface and then leaving the layer; W_4 etc.

Summing up all the waves which form the resultant reflected wave, and considering an incident wave of unit amplitude, the reflection coefficient from the layer is obtained.

Laboratory measurements of the reflection wave amplitudes' W_1 and W_2 variation with temperature have been obtained. A fine sand layer 2.5-cm thick with the same porosity density and grain size as the naturally occurring material discussed above and covering an aluminum base ($\rho_3 = 2700\,\mathrm{kg/m^3}$, $c_3 = 6200\,\mathrm{m/s}$), has been constructed. A Panametrix 1-MHz transducer emits and receives very short pulses in the water column at normal incidence to the fine sand layer. The experimental device is cooled and heated in a stable manner and the temperature is measured in both the water column and the sediment layer.

Figure 6 shows the results of these measurements. The amplitude of the reflected wave W_1 is approximately constant while the wave W_2 increases from 0.18 to 0.27 when the temperature increases from 5 to 25 °C.

III. CONCLUSION

The experimental results presented here have shown that over the range of values found in the environment, the temperature has a significant impact on the sound velocity and absorption coefficient of seabed sediments. The temperature effect observed may be summarized as follows: the absorption coefficient decreases and the sound velocity increases when the temperature increases. Various loss mechanisms could be at work in the granular sediment. Viscosity of the pore fluid is a possibility but another possible mechanism is enhanced lubrication of the grain-to-grain contacts as the pore fluid becomes warmer and hence less viscous.

As a further indication of the effect of temperature on the sediment, the amplitude of a reflected wave from the laboratory ''basement'' of aluminum after traveling across the sediment layer is strongly dependent upon the temperature, caused by the absorption variation in the layer with the temperature.

[1] M. I. Taroudakis, ''Inverse problems in underwater acoustics,'' *Proc. 2nd EAA International Symposium on Hydroacoustics*, Gdansk, Poland, edited by A. Stepnoski, R. Salomon, and E. Kozaczka, 1999, pp. 281–290.
[2] ''Interim report on the sound velocity distribution in the North Atlantic Ocean,'' U.S. Navy Oceanogr. Office Tech. Rep. 171 (1965).
[3] S. D. Richards, ''The effect of temperature, pressure and salinity on sound attenuation in turbid seawater,'' J. Acoust. Soc. Am. **103**, 205–211 (1998).
[4] R. J. Urick, ''The absorption of sound in suspensions of irregular particles,'' J. Acoust. Soc. Am. **20**, 283–289 (1948).
[5] J. Sheng and E. A. Hay, ''An examination of the spherical scatterer approximation in aqueous suspensions of sand,'' J. Acoust. Soc. Am. **83**, 598–610 (1988).
[6] N. R. Brown, T. G. Leighton, S. D. Richards, and A. D. Heathershaw, ''Measurement of viscous sound absorption at 50–150 kHz in a model turbid environment,'' J. Acoust. Soc. Am. **104**, 2114–2120 (1998).
[7] R. D. Stoll, ''Acoustic waves in marine sediments,'' in *Ocean Seismo-Acoustics*, edited by T. Akal and J. M. Berkson (Plenum, New York, 1986), pp. 417–434.
[8] E. L. Hamilton, ''Acoustic properties of sediments,'' in *Acoustics and Ocean Bottom*, edited by A. Lara, C. Ranz, and R. Carbó (CSIC, Madrid, 1987), pp. 3–58.
[9] F. Fisher and V. Simmons, ''Sound absorption in sea water,'' J. Acoust. Soc. Am. **62**, 558–564 (1977).
[10] H. Medwin, J. Fitzgerald, and G. Rautmann, ''Acoustic miniprobing for ocean microstructure and bubbles,'' J. Geophys. Res. **80**, 405–413 (1975).
[11] E. L. Hamilton, ''Geoacoustic models of the sea floor,'' in *Physics of Sound in Marine Sediments*, edited by L. Hampton (Plenum, New York, 1974), pp. 181–221.
[12] L. M. Brekhovskikh, *Waves in Layered Media* (Academic, New York, 1960), pp. 45–54.

An optimization approach to multi-dimensional time domain acoustic inverse problems

Mats Gustafsson
Department of Electromagnetic Theory, Lund Institute of Technology, P.O. Box 118, S-221 00 Lund, Sweden

Sailing He
Department of Electromagnetic Theory, Royal Institute of Technology, S-100 44 Stockholm, Sweden and Centre for Optical and Electromagnetic Research, State Key Laboratory for Modern Optical Instrumentation, Zhejiang University, Yu-Quan, 310027 Hangzhou, People's Republic of China

(Received 22 December 1997; revised 22 November 1999; accepted 13 June 2000)

An optimization approach to a multi-dimensional acoustic inverse problem in the time domain is considered. The density and/or the sound speed are reconstructed by minimizing an objective functional. By introducing dual functions and using the Gauss divergence theorem, the gradient of the objective functional is found as an explicit expression. The parameters are then reconstructed by an iterative algorithm (the conjugate gradient method). The reconstruction algorithm is tested with noisy data, and these tests indicate that the algorithm is stable and robust. The computation time for the reconstruction is greatly improved when the analytic gradient is used. © *2000 Acoustical Society of America.* [S0001-4966(00)00710-4]

PACS numbers: 43.30.Pc, 43.20.Fn [DLB]

I. INTRODUCTION

Acoustic inverse problems have been studied with various methods (see, e.g., Refs. 1–7). Recent developments and applications of various optimization methods have provided efficient tools for obtaining numerical solutions to various types of inverse problems (see, e.g., Refs. 8–11). Optimization methods can be grouped into two types, namely, global search methods and gradient search methods. A global search method is usually based on a stochastic algorithm, and its convergence can be very slow. A gradient search method is based on a deterministic algorithm, and it converges rapidly (though it may converge to a local minimum). In order to apply a gradient search method to an inverse problem, one first introduces a suitable objective functional, and then computes the gradient of this functional. Once the gradient of the objective functional has been computed, one can use a conventional steepest descent method or conjugate gradient method to minimize the objective functional in an iterative way.

Most of the literature in this field concerning multi-dimensional inverse problems deals with frequency domain problems. For a time domain multi-dimensional inverse problem, the computation is usually more memory- and time-consuming. Therefore, it is of great importance to find a reconstruction algorithm which can complete the reconstruction within a reasonable time (say, e.g., a few hours on a modern workstation).

In the present article, we use an optimization algorithm with an analytic gradient, which improves greatly the speed of the reconstruction. Wave-splitting is used to formulate a direct problem which can be solved easily by a finite difference method. Wave-splitting means the decomposition of the total field into two components which propagate in opposite directions.[12] Dual functions are introduced to derive an explicit expression for the gradient. It is shown that by using wave-splitting one obtains a simple expression for the gradient and a robust algorithm. Wave-splitting is integrated in the present optimization algorithm. An analysis based on energy estimates has been given in Ref. 13 to show that the wave-splitting provides the best linear combination of the fields for use in this type of inverse problem. The present work is useful for (or relevant to) many practical applications such as the oceanography,[14] tomography in underwater acoustics,[15] identification of seamounts,[16] and localization of sound sources,[17] etc.

The article is organized as follows. A multi-dimensional time domain acoustic inverse problem is formulated in Sec. II. In Sec. III, a simple explicit expression for the gradient of the objective functional is derived by introducing some dual functions and using the Gauss divergence theorem. A numerical reconstruction algorithm based on a conjugate gradient method is described in Sec. IV.

II. PROBLEM FORMULATION

The formulation presented in this section and in Sec. III is valid in two or three spatial dimensions. The numerical implementation in Sec. IV, however, is only made in two spatial dimensions.

Consider wave propagation in an inhomogeneous acoustic region $\Omega \in \mathbb{R}^3$ (or $\mathbb{R}^2$), which is described by the following stress-strain equations for fluids:[18]

$$\frac{1}{\rho c^2}\partial_t p + \nabla \cdot \mathbf{v} = 0, \tag{1}$$

$$\rho \partial_t \mathbf{v} + \nabla p = 0, \tag{2}$$

where p is the pressure, $\mathbf{v}$ is the sound speed (the time derivative of the displacement), ρ is the fluid density, and c is the sound speed in the medium. Outside the region Ω, the

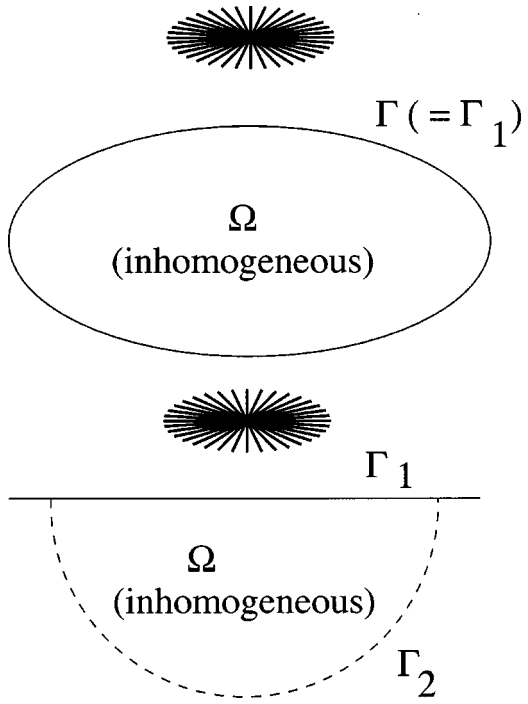

FIG. 1. Scattering configurations. (a) The case of a finite object; (b) the half-space case.

medium is homogeneous with the sound speed c_0 and the density ρ_0.

It is assumed that the source has compact spatial support and is located outside the surface Γ of the inhomogeneous region Ω. It is also assumed that the incident wave will not reach the surface Γ until the time $t=0$. This leads to the following initial conditions:

$$p(x,0)=0, \quad \mathbf{v}(x,0)=0, \quad x\in\Omega. \tag{3}$$

In the inverse problem, it is assumed that the pressure p and the normal component of the sound speed, v_n, are known for $t\in[0,T]$ on Γ_1, which is a part of the surface Γ, i.e.,

$$p(x,t)=p^{(m)}(x,t), \quad v_n(x,t)\equiv\mathbf{v}\cdot\hat{\mathbf{n}}=v_n^{(m)}(x,t), \quad x\in\Gamma_1, \quad t\in[0,T], \tag{4}$$

where $\hat{\mathbf{n}}$ is the unit normal vector of the surface Γ, and $p^{(m)}(x,t)$ and $v_n^{(m)}(x,t)$ are known functions on surface Γ_1 and for the period $t\in[0,T]$. The inverse problem is to determine the density $\rho(x)$ and/or the sound speed $c(x)$ in the inhomogeneous region Ω (the parameters at the surface Γ_1 are assumed to be known). Furthermore, we assume that the incident wave has not reached the surface $\Gamma_2=\Gamma\backslash\Gamma_1$ at the time $t=T$, i.e.,

$$p(x,t)=0, \quad \mathbf{v}(x,t)=0, \quad x\in\Gamma_2, \quad t\in[0,T]. \tag{5}$$

In the case when the inhomogeneity is confined in a bounded region Ω, one can measure p and v_n on the whole surface Γ, and thus set $\Gamma_2=\varnothing$ [see Fig. 1(a)]. In another case when the inhomogeneity exists in a half-space (the medium above the inhomogeneous half-space is homogeneous with sound speed c_0 and density ρ_0), one can choose Γ_1 on the surface of the half-space large enough so that there exists a surface Γ_2 (in the inhomogeneous half-space) on which the condition (5) holds [see Fig. 1(b)].

Introduce the following split pressures $p_\pm$ at the boundary Γ:

$$p_\pm=\tfrac{1}{2}[p\mp\rho_0 c_0 v_n], \quad x\in\Gamma. \tag{6}$$

Note that p_+ and p_- have a physical meaning as incident (in-coming) and scattered (out-going) pressures, respectively, only in a homogeneous region (characterized by c_0 and ρ_0) and in a local sense, in the case of an incident wave that is locally a normally incident plane wave. One of the main advantages of using such a splitting is that a simple expression for the gradient can be obtained in a strict sense with energy estimate methods [cf. Eq. (14)]. Numerically it has advantages for the direct solver, as it is, e.g., simpler to implement the boundary condition (cf. Sec. IV A). From the above definition, one has

$$p=p_+ + p_-, \tag{7}$$

$$v_n=\frac{1}{\rho_0 c_0}[p_- - p_+]. \tag{8}$$

Define an objective functional $J(\rho,c)$ as follows,

$$J(\rho,c)=\int_0^T\int_{\Gamma_1}\Phi\{[p-p^{(m)}]^2+\rho_0^2c_0^2[v_n-v_n^{(m)}]^2\}dS\,dt \tag{9}$$

$$=2\int_0^T\int_{\Gamma_1}\Phi\{[p_+-p_+^{(m)}]^2+[p_--p_-^{(m)}]^2\}dS\,dt, \tag{10}$$

where $\Phi=\Phi(x,t)$ is a weight function, dS is a surface area element, and

$$p_\pm^{(m)}=\tfrac{1}{2}[p^{(m)}\mp\rho_0 c_0 v_n^{(m)}], \quad x\in\Gamma. \tag{11}$$

The inverse problem is to find a function $\rho(x)$ and/or $c(x)$ which minimizes $J(\rho,c)$. The minimum of $J(\rho,c)$ is zero if the data is clean and the inverse problem has a solution. However, for noisy data we take a distribution of ρ or c which fits the data to an acceptable (nonzero) level as the solution to the inverse problem. In the present article we will treat $p_+(x,t)$ as the input to the optimization algorithm and $p_-(x,t)$ as the corresponding output, i.e.,

$$p_+=p_+^{(m)}, \quad x\in\Gamma_1, \quad t\in[0,T]. \tag{12}$$

III. EXPLICIT EXPRESSION FOR THE GRADIENT

Let $\tilde{p}$, $\tilde{\mathbf{v}}$ be the solution to the system of equations (1), (2), (3), (5), and (12) with perturbed parameters $\rho+\delta\rho$, $c+\delta c$. Then $\delta p\equiv\tilde{p}-p$ and $\delta\mathbf{v}\equiv\tilde{\mathbf{v}}-\mathbf{v}$ satisfy the following system of equations (obtained by taking the first-order approximation):

$$\begin{aligned}
&\frac{1}{\rho c^2}\partial_t(\delta p)+\nabla\cdot\delta\mathbf{v}=-\left(\frac{\delta\rho}{\rho}+\frac{2\,\delta c}{c}\right)\nabla\cdot\mathbf{v},\\
&\rho\partial_t\delta\mathbf{v}+\nabla\delta p=\frac{\delta\rho}{\rho}\nabla p,\\
&\delta p(x,t)=0, \quad \delta\mathbf{v}(x,t)=0, \quad x\in\Gamma_2, \quad t\in[0,T],\\
&\delta p_+=0, \quad x\in\Gamma_1, \quad t\in[0,T],\\
&\delta p(x,0)=0, \quad \delta\mathbf{v}(x,0)=0, \quad x\in\Omega.
\end{aligned} \tag{13}$$

The corresponding increment of the objective functional $J(\rho,c)$ can then be written as follows:

$$\begin{aligned}
\delta J(\rho,c) &\equiv J(\rho+\delta\rho, c+\delta c) - J(\rho,c) \\
&= 2\int_0^T \int_{\Gamma_1} \Phi[(p_+ + \delta p_+ - p_+^{(m)})^2 + (p_- + \delta p_- \\
&\quad - p_-^{(m)})^2 - (p_+ - p_+^{(m)})^2 - (p_- - p_-^{(m)})^2]\, dS\, dt \\
&= 2\int_0^T \int_{\Gamma_1} \Phi[\,\delta p_+ (2p_+ - 2p_+^{(m)} + \delta p_+) \\
&\quad + \delta p_- (2p_- - 2p_-^{(m)} + \delta p_-)]\, dS\, dt \\
&= 4\int_0^T \int_{\Gamma_1} \Phi[\,\delta p_+ (p_+ - p_+^{(m)}) + \delta p_- (p_- - p_-^{(m)}) \\
&\quad + (\delta p_+)^2 + (\delta p_-)^2]\, dS\, dt \\
&= 4\int_0^T \int_{\Gamma_1} \delta p_- [\Phi(p_- - p_-^{(m)})]\, dS\, dt \\
&\quad + O(\|\delta\rho\|^2 + \|\delta c\|^2), \qquad (14)
\end{aligned}$$

where $O(x)/x$ is bounded as x approaches 0, and $\|\ \|$ denotes the L^2 norm, i.e., $\|F(x)\| = (\int_\Omega |F(x)|^2 dV)^{1/2}$. The estimate given by the previous equation can be proved with energy estimate methods (see, e.g., Refs. 19 and 20). We use a direct solver for the following forward problem,

$$\begin{aligned}
&\frac{1}{\rho c^2}\partial_t p + \nabla\cdot\mathbf{v} = 0, \\
&\rho\partial_t \mathbf{v} + \nabla p = 0, \\
&p_+ = p_+^{(m)}, \quad x\in\Gamma_1, \quad t\in[0,T], \\
&p(x,0) = 0, \quad \mathbf{v}(x,0) = 0,
\end{aligned} \qquad (15)$$

and the following backward dual problem,

$$\begin{aligned}
&\frac{1}{\rho c^2}\partial_t q + \nabla\cdot\mathbf{u} = 0, \\
&\rho\partial_t \mathbf{u} + \nabla q = 0, \\
&q_- = \Phi[p_- - p_-^{(m)}], \quad x\in\Gamma_1, \quad t\in[0,T], \\
&q(x,T) = 0, \quad \mathbf{u}(x,T) = 0,
\end{aligned} \qquad (16)$$

where

$$q_\pm = \tfrac{1}{2}[q \mp \rho_0 c_0 u_n], \quad x\in\Gamma.$$

Note that [cf. Eq. (5)]

$$q(x,t) = 0, \quad \mathbf{u}(x,t) = 0, \quad x\in\Gamma_2, \quad t\in[0,T]. \qquad (17)$$

The system (15) is solved by a finite difference method with a forward time stepping, and the system (16) is solved by a finite difference method with a backward time stepping. In order to avoid any inconsistency between the boundary and initial conditions in the system (16), one should choose the weight function such that

$$\Phi(x,T) = 0. \qquad (18)$$

Using the differential equations in the systems (13), (15), and (16), one obtains

$$\begin{aligned}
\nabla\cdot(\delta p\mathbf{u} + q\,\delta\mathbf{v}) &= [\nabla(\delta p)]\cdot\mathbf{u} + \delta p\nabla\cdot\mathbf{u} \\
&\quad + (\nabla q)\cdot\delta\mathbf{v} + q\nabla\cdot(\delta\mathbf{v}) \\
&= -\partial_t\left[\frac{1}{\rho c^2}(\delta p)q + \rho(\delta\mathbf{v})\cdot\mathbf{u}\right] \\
&\quad + \frac{\delta\rho}{\rho}[-q\nabla\cdot\mathbf{v} + (\nabla p)\cdot\mathbf{u}] - \frac{2\,\delta c}{c} q\nabla\cdot\mathbf{v} \\
&= -\partial_t\left[\frac{1}{\rho c^2}(\delta p)q + \rho(\delta\mathbf{v})\cdot\mathbf{u}\right] \\
&\quad + \frac{\delta\rho}{\rho}[-q\nabla\cdot\mathbf{v} + \nabla\cdot(p\mathbf{u}) - p\nabla\cdot\mathbf{u}] \\
&\quad - \frac{2\,\delta c}{c} q\nabla\cdot\mathbf{v} \\
&= -\partial_t\left[\frac{1}{\rho c^2}(\delta p)q + \rho(\delta\mathbf{v})\cdot\mathbf{u} - \frac{\delta\rho}{\rho^2 c^2}(qp)\right] \\
&\quad + \frac{\delta\rho}{\rho}\nabla\cdot(p\mathbf{u}) - \frac{2\,\delta c}{c} q\nabla\cdot\mathbf{v}.
\end{aligned}$$

Integrating the above equation over the time period $[0,T]$ and the region Ω and using the Gauss divergence theorem, one obtains

$$\begin{aligned}
&\int_0^T \int_\Gamma (\delta p\mathbf{u} + q\,\delta\mathbf{v})\cdot\hat{\mathbf{n}}\, dS\, dt \\
&\quad = \int_0^T \int_\Omega \frac{\delta\rho}{\rho}\nabla\cdot(p\mathbf{u})\, dV\, dt - 2\int_0^T \int_\Omega \frac{\delta c}{c} q\nabla\cdot\mathbf{v}\, dV\, dt.
\end{aligned} \qquad (19)$$

Since [cf. Eq. (14) and noting that $\delta p_+ = 0$ and $q_- = \Phi(p_- - p_-^{(m)})$]

$$\begin{aligned}
&\int_0^T \int_\Gamma (\delta p\mathbf{u} + q\,\delta\mathbf{v})\cdot\hat{\mathbf{n}}\, dS\, dt \\
&\quad = \int_0^T \int_{\Gamma_1} (\delta p u_n + q\,\delta v_n)\, dS\, dt \\
&\quad = -\frac{1}{\rho_0 c_0}\int_0^T \int_{\Gamma_1} [(\delta p_+ + \delta p_-)(q_+ - q_-) \\
&\qquad + (\delta p_+ - \delta p_-)(q_+ + q_-)]\, dS\, dt \\
&\quad = -\frac{2}{\rho_0 c_0}\int_0^T \int_{\Gamma_1} [\,\delta p_+ q_+ - \delta p_- q_-]\, dS\, dt
\end{aligned}$$

$$= \frac{2}{\rho_0 c_0} \int_0^T \int_{\Gamma_1} (\delta p_-) q_- \, dS \, dt$$

$$= \frac{2}{\rho_0 c_0} \int_0^T \int_{\Gamma_1} (\delta p_-) \Phi[p_- - p_-^{(m)}] \, dS \, dt$$

$$= \frac{1}{2\rho_0 c_0} \delta J(\rho, c) + O(\|\delta\rho\|^2 + \|\delta c\|^2),$$

it follows from Eq. (19) that

$$\delta J = \langle G_\rho, \delta\rho \rangle + \langle G_c, \delta_c \rangle + O(\|\delta\rho\|^2 + \|\delta c\|^2), \tag{20}$$

where $\langle , \rangle$ denotes the inner product (with respect to the spatial region Ω) and

$$G_\rho = \frac{2\rho_0 c_0}{\rho} \int_0^T \nabla \cdot (\mathbf{u} p) \, dt, \quad x \in \Omega, \tag{21}$$

$$G_c = -\frac{4\rho_0 c_0}{c} \int_0^T q \nabla \cdot \mathbf{v} \, dt$$

$$= \frac{4\rho_0 c_0}{\rho c^3} \int_0^T q \partial_t p \, dt, \quad x \in \Omega. \tag{22}$$

Equations (21) and (22) give the explicit expressions for the gradients of the objective functional $J(\rho, c)$ with respect to the density $\rho(x)$ and the sound speed $c(x)$, respectively.

Note that the results given in this subsection are valid for arbitrary number n of space dimensions, $n \geqslant 2$.

IV. PARAMETER RECONSTRUCTION

In this section we use an optimization algorithm (the conjugate gradient algorithm) with the analytic gradients derived in the previous section to reconstruct the density and sound speed in the two-dimensional case [i.e., $x = (x_1, x_2)$ in all the formulas given in the previous sections].

A. The direct solver

We use both a leapfrog scheme and a Lax–Wendroff scheme to solve the systems (15) and (16) (cf., e.g., Refs. 21 and 22).

1. A leapfrog scheme

Let $p_{i,j}^n$ be an approximation of p at $t = nk$, $x_1 = ih$, and $x_2 = jh$, and similarly for $\mathbf{v}_{i,j}^n$. At interior points the leapfrog scheme becomes

$$p_{i,j}^{n+1} = p_{i,j}^{n-1} - \rho_{i,j} c_{i,j}^2 2k \nabla_0 \cdot \mathbf{v}_{i,j}^n,$$

$$\mathbf{v}_{i,j}^{n+1} = \mathbf{v}_{i,j}^{n-1} - \frac{2}{\rho_{i,j}} k \nabla_0 p_{i,j}^n,$$

where ∇_0 is the central difference nabla operator [i.e., $\nabla_0 f_{i,j} = (f_{i+1,j} - f_{i-1,j}, f_{i,j+1} - f_{i,j-1})/2h$]. For a finite inhomogeneous object located in a square area $(x_1, x_2) \in [0,1] \times [0,1]$, the fields at the boundary are computed with a one way propagation type of scheme. For example, at the left boundary $x_1 = 0$, the differential equations in Eqs. (1) and (2) are equivalent to the following system of differential equations (for simplicity, here we assume that $\rho_0 = c_0 = 1$),

$$\partial_t p_\pm \pm \partial_{x_1} p_\pm + \tfrac{1}{2} \nabla_T \cdot \mathbf{v}_T = 0,$$

$$\partial_t \mathbf{v}_T + \nabla_T p = 0,$$

where we have used the split fields $p_\pm = \frac{1}{2}[p \mp \rho_0 c_0 v_n] = (p \pm v_1)/2$ at the left boundary $x_1 = 0$, and the subscript T is used to denote the tangential component. The above system of equations can be implemented numerically as follows,

$$(p_+)_{0,j}^{n+1} = (p_+^{(m)})_{0,j}^{n+1}$$

[cf. the boundary condition (12)],

$$(p_-)_{0,j}^{n+1} = (p_-)_{0,j}^n + \frac{k}{h}[(p_-)_{1,j}^n - (p_-)_{0,j}^n] - \frac{k}{2}(\nabla_T)_0 \cdot (\mathbf{v}_T)_{0,j}^n,$$

$$p_{0,j}^{n+1} = (p_+)_{0,j}^{n+1} + (p_-)_{0,j}^{n+1},$$

$$(v_1)_{0,j}^{n+1} = (p_+)_{0,j}^{n+1} - (p_-)_{0,j}^{n+1},$$

$$(\mathbf{v}_T)_{0,j}^{n+1} = (\mathbf{v}_T)_{0,j}^{n-1} - 2k(\nabla_T)_0 p_{0,j}^n.$$

The boundary conditions at the other boundaries are treated similarly.

2. A Lax–Wendroff scheme

The Lax–Wendroff scheme is based on the following Taylor series approximation,

$$p^{n+1} = p^n - k\rho c^2 \nabla \cdot \mathbf{v}^n + \frac{k^2}{2} \rho c^2 \nabla \cdot \left(\frac{1}{\rho} \nabla p^n \right),$$

$$\mathbf{v}^{n+1} = \mathbf{v}^n - \frac{k}{\rho} \nabla p^n + \frac{k^2}{2\rho} \nabla (\rho c^2 \nabla \cdot \mathbf{v}^n),$$

with the second-order approximations for the spatial derivatives. The fields at the boundary are treated in a way that is similar to the one used in the leapfrog scheme, except that the tangential components are implemented with a Lax-type scheme, e.g.,

$$(\mathbf{v}_T)_{0,j}^{n+1} = \tfrac{1}{2}(\mathbf{v}_T)_{0,j-1}^n + \tfrac{1}{2}(\mathbf{v}_T)_{0,j+1}^n - k(\nabla_T)_0 p_{0,j}^n,$$

at the left boundary $x_1 = 0$.

In the gradient calculation the leapfrog scheme is used to solve the systems (15) and (16), as well as in the calculation of the objective functional defined by Eq. (10). The Lax–Wendroff scheme is used to calculate the measured fields $p^{(m)}(x,t)$ and $v_n^{(m)}(x,t)$ at the boundary [cf. Eq. (4)]. Since the measured data are calculated in a way that is different from what is used for the direct solver, we avoid the ''inverse crime'' (see, e.g., Ref. 5) when solving the inverse problem. In other words, we use different numerical methods for forward and inverse problems to avoid simply undoing the forward solution in the inversion.

B. The conjugate gradient method

Once the gradient of the objective functional has been computed, one can use a conventional steepest descent method or conjugate gradient method to minimize the objective functional in an iterative way. The steepest descent

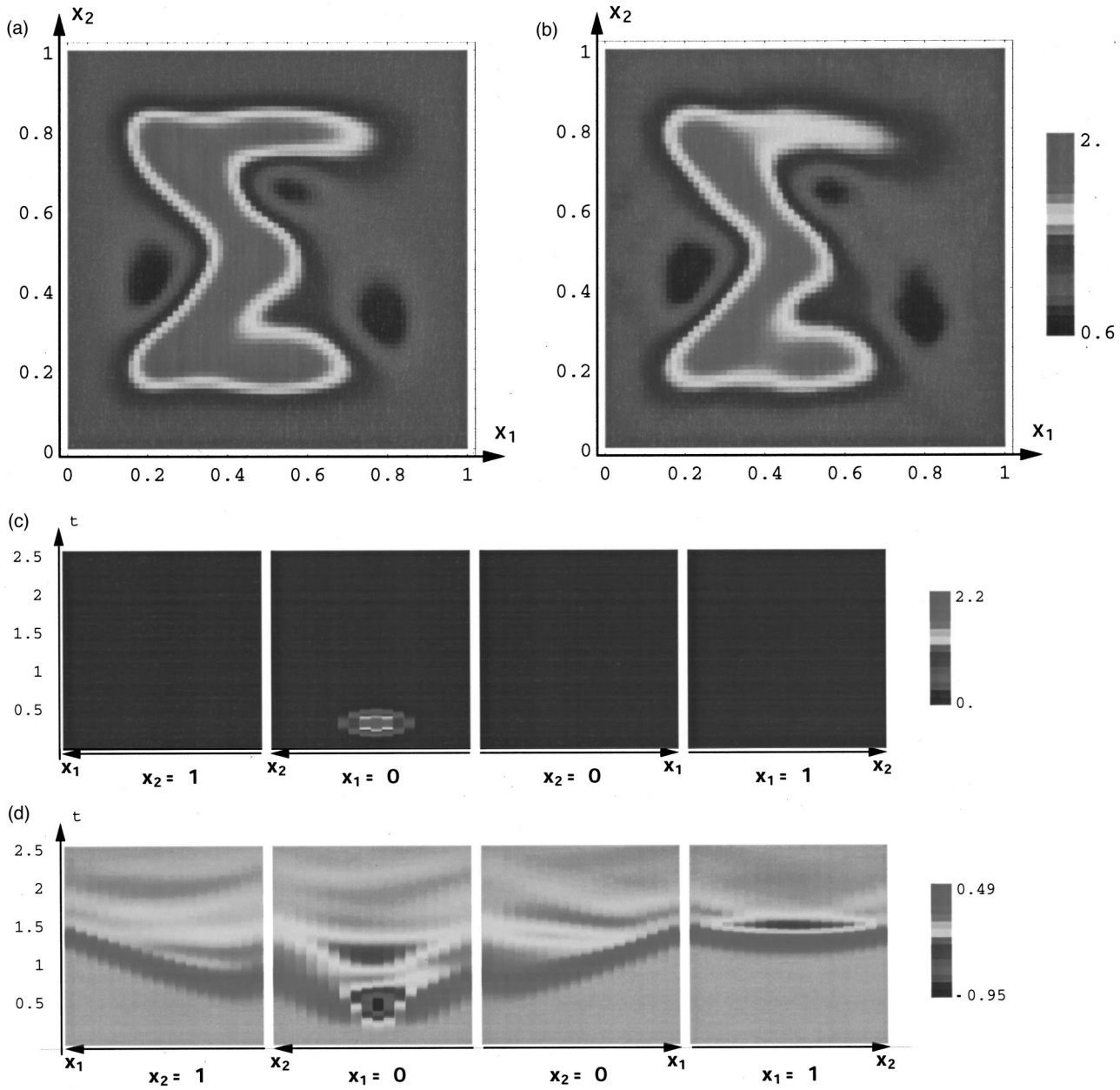

FIG. 2. Reconstruction of the density distribution in a square area using one Gaussian pulse at the left side of the square. (a) The true density distribution; (b) the reconstruction; (c) the input $p_+^{(m)}$ on the four sides of the square; and (d) the output $p_-^{(m)}$ on the four sides of the square.

method usually exhibits slower convergence rates than the conjugate gradient method. In the present article we use a standard conjugate gradient method (Polak–Ribiere algorithm[23]) to minimize the objective functional and reconstruct the density $\rho(x_1,x_2)$ or the sound speed $c(x_1,x_2)$. The iterative algorithm for the reconstruction of $\rho(x_1,x_2)$ is as follows:

Step 0: Select an initial approximation (guess) $\rho=\rho^{(0)}\times(x_1,x_2)$. In all our numerical reconstructions, we take the initial approximation $\rho=\rho_0$ (the constant density value outside the region Ω).

Step 1: Set $i=0$. Solve the direct problem for the system (15) with the leapfrog scheme, and calculate the gradient $G^{(0)}=G(\rho^{(0)})$ using Eq. (21) [**u** is obtained by solving the system (16) with the leapfrog scheme]. Set $H^{(0)}=G^{(0)}$.

Step 2: Compute a scalar stepsize $\lambda_i>0$ such that

$$J(\rho^{(i)}-\lambda_i H^{(i)})=\min\{J(\rho^{(i)}-\lambda H^{(i)})\,|\,\lambda\geqslant 0\}. \tag{23}$$

Step 3: Improve the reconstruction by setting

$$\rho^{(i+1)}=\rho^{(i)}-\lambda_i H^{(i)}. \tag{24}$$

Step 4: Compute the new gradient $G^{(i+1)}=G(\rho^{(i+1)})$ using Eq. (21) [p and **u** are obtained by solving the systems (15) and (16), respectively, with the leapfrog scheme].

Step 5: If $G^{(i+1)}=0$, stop; if not, set

$$H^{(i+1)}=G^{(i+1)}+\gamma_i H^{(i)},$$

$$\text{with}\quad \gamma_i=\frac{\langle G^{(i+1)}-G^{(i)},G^{(i+1)}\rangle}{\langle G^{(i)},G^{(i)}\rangle}, \tag{25}$$

and set $i=i+1$, and go to step 2.

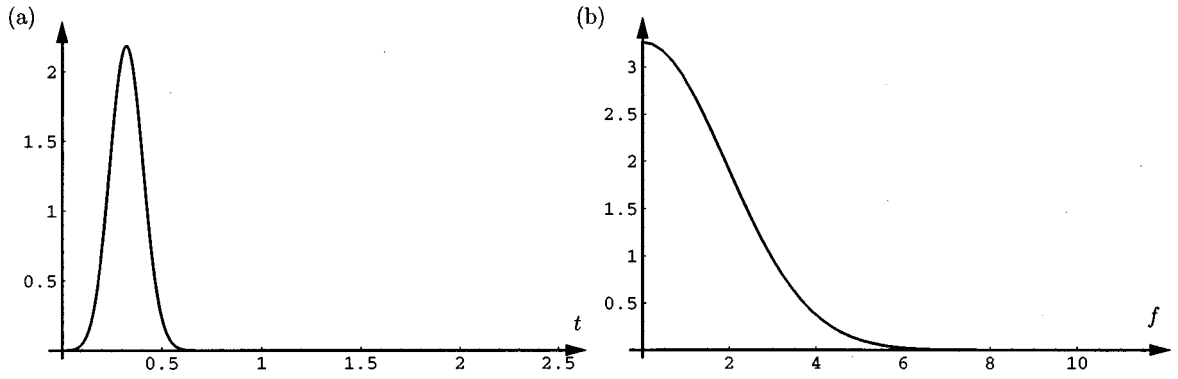

FIG. 3. The time and frequency characteristics of the input field.

The conjugate gradient algorithm may be trapped by a local minimum if the cost function has some local minima other than a global minimum. In order to overcome this local minimum problem, one can use a global optimization method to obtain a rough initial guess before using the conjugate gradient algorithm. Such a combination of a global optimization method and a gradient algorithm has been successfully implemented in a problem of crack identification,[24] where numerical simulation has been given to illustrate the important role of a gradient algorithm in speeding up the minimization procedure. In the present article, we concentrate on the minimization using only the gradient algorithm.

C. Regularization

The parameter reconstruction is ill posed in the sense that the rapid variation of the parameter cannot be determined since the input excitation has a limited frequency band. To get a smooth solution we regularize the problem with a Tikhonov type of regularization.

For example, in the reconstruction of the density $\rho(x_1,x_2)$, we add a term $\int_\Omega \alpha|\nabla\rho|^2\,dV$ to the objective functional, i.e.,

$$J_\alpha(\rho)=J(\rho)+\int_\Omega \alpha(x)|\nabla\rho|^2\,dV.$$

The corresponding increment in the objective functional is

$$\begin{aligned}
&\int_\Omega \alpha\{|\nabla(\rho+\delta\rho)|^2-|\nabla\rho|^2\}\,dV\\
&\quad=\int_\Omega \alpha\{\nabla\delta\rho\cdot\nabla(2\rho+\delta\rho)\}\,dV\\
&\quad=2\int_\Omega\{\nabla\cdot[\delta\rho\alpha\nabla\rho]-\delta\rho\nabla\cdot[\alpha\nabla\rho]\}\,dV\\
&\qquad+\int_\Omega \alpha|\nabla\delta\rho|^2\,dV\\
&\quad=2\int_\Gamma \alpha\delta\rho\partial_n\rho\,dS-2\int_\Omega\{\delta\rho\nabla\cdot[\alpha\nabla\rho]\}\,dV\\
&\qquad+\int_\Omega \alpha|\nabla\delta\rho|^2\,dV.
\end{aligned}$$

Thus one obtains the following gradient with respect to the density (note that $\delta\rho|_\Gamma=0$),

$$G_{\rho,\alpha}=\frac{2}{\rho}\int_0^T\nabla\cdot(\mathbf{u}p)\,dt-2\nabla\cdot[\alpha\nabla\rho]. \tag{26}$$

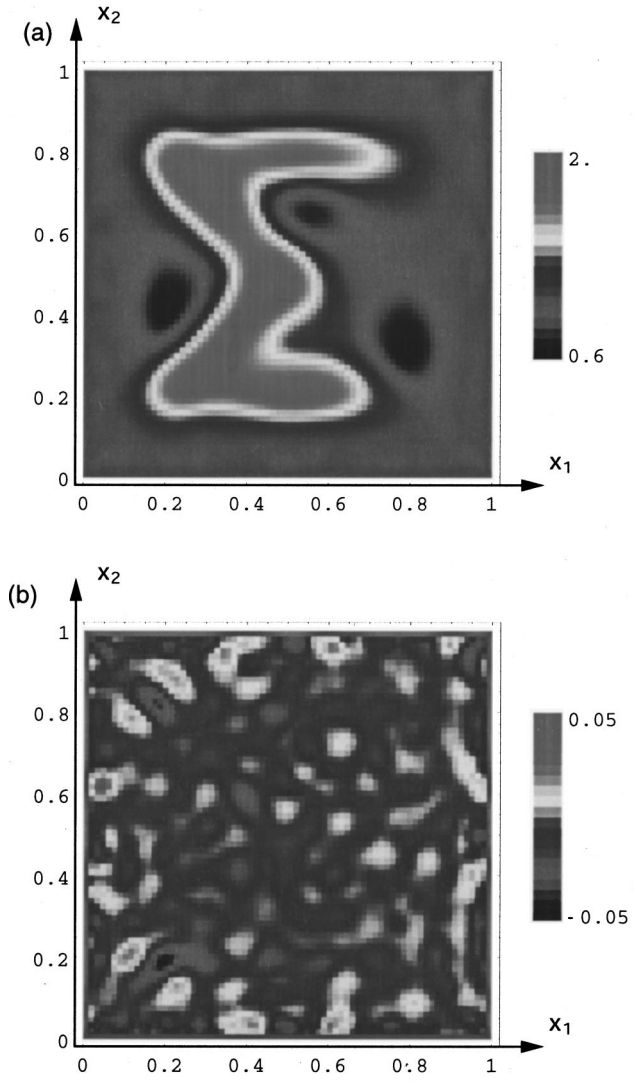

FIG. 4. Reconstruction of the density distribution in a square area using four Gaussian pulses at four different sides of the square [for the same density distribution as shown in Fig. 2(a)]. (a) The reconstruction; (b) reconstruction error of the density.

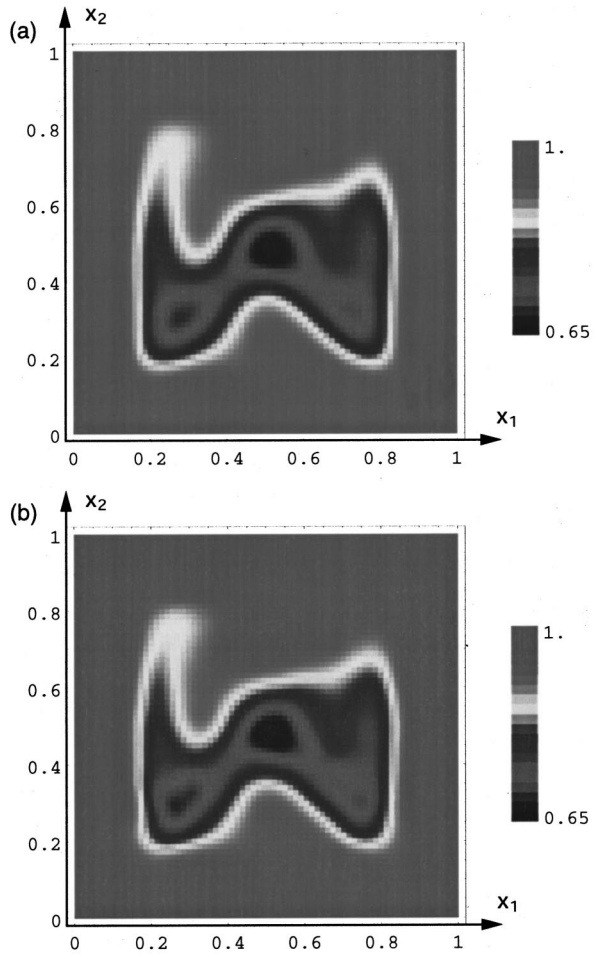

FIG. 5. Reconstruction of the sound speed distribution in a square area using four Gaussian pulses at four different sides of the square. (a) The true sound speed distribution; (b) the reconstruction.

The optimal value of the regularization parameter α can be determined by the generalized cross validation method (see, e.g., 25 and 26) or the largest value which still provides a meaningful fit to the data based on an error statistic such as $J(\rho)$ as commonly used in geophysical inverse theory (see, e.g., Ref. 27).

We can also enforce the known values of ρ at the boundary by adding a term $\beta\int_\Omega \Psi|\rho-\rho_b|^2\,dV$ to the objective functional, i.e.,

$$J_\beta(\rho)=J(\rho)+\beta\int_\Omega \Psi|\rho-\rho_b|^2\,dV,$$

where ρ_b is the known value of ρ at the boundary. The weight function $\Psi(x)$ is large when x is close to the boundary and small in the interior region. In all the numerical reconstructions given in next subsection we use $\Psi(x)=e^{-0.5[\gamma(x)/h]^2}$, where $\gamma(x)$ is the shortest distance to the boundary and h is the spatial discretization. The corresponding increment in the objective functional is

$$\int_\Omega \Psi\{|\rho+\delta\rho-\rho_b|^2-|\rho-\rho_b|^2\}\,dV$$

$$=\int_\Omega \Psi\,\delta\rho(2(\rho-\rho_b)+\delta\rho)\,dV$$

$$=2\int_\Omega \Psi\,\delta\rho(\rho-\rho_b)\,dV+\int_\Omega \Psi\,\delta\rho^2\,dV.$$

Thus one obtains the following gradient with respect to the density (note that $\delta\rho|_\Gamma=0$),

$$G_{\rho,\beta}=\frac{2}{\rho}\int_0^T \nabla\cdot(\mathbf{u}p)\,dt-2\beta\Psi(\rho-\rho_b).$$

Our numerical results show that the reconstruction is not very sensitive to the values of these regularization parameters within a certain region.

D. Reconstruction results

In the first numerical example, we consider an inhomogeneous density distribution in a square area $(x_1,x_2)\in[0,1]\times[0,1]$ as shown in Fig. 2(a). The sound speed is a constant $c=c_0=1$. The inhomogeneous square region is discretized by 72×72 equidistant grid points. One Gaussian pulse of p_+ is used as a source illuminating the square from the left side [as shown in Fig. 2(b)], and the scattered fields are measured on all the four sides of the square [as shown in Fig. 2(c); in the time space plots of Figs. 2(b) and (c) the four plots correspond to the back-, left-, front-, and right-side of the square]. The time and frequency (denoted by f) characteristics of the input field are shown in Figs. 3(a) and (b), respectively. The ''measured'' data are simulated with the Lax–Wendroff scheme. The fields are measured in a time interval [0,2.5] discretized with 360 grid points. Random white noise with a signal-to-noise ratio (SNR) of 130 has been added to the measured fields $p^{(m)}$ and $v_n^{(m)}$ (equivalent to $p_\pm^{(m)}$). The signal-to-noise ratio is estimated by the following formula,

$$\mathrm{SNR}=\frac{\int_0^T\int_\Gamma |p_\pm(x,t)|^2\,dS\,dt}{\int_0^T\int_\Gamma |N(x,t)|^2\,dS\,dt},$$

where $N=N(x,t)$ is the noise added to the fields. In the numerical reconstructions we chose the regularization parameters $\alpha=0.001$, $\beta=10$, and a weight function Φ that goes to zero smoothly over the last 15 time steps. The reconstructed density after 47 iterations is shown in Fig. 2(d) (the starting guess is $\rho=\rho_0=1$ everywhere). The maximum absolute error in the density reconstruction is about 0.29. The reconstruction took about 20 min on a Sun workstation. The reconstruction requires a memory of about 30 MByte in RAM.

The reconstruction can be improved further if four Gaussian pulses at four different sides of the square are used, and the corresponding reconstruction using noisy data with SNR=130 is given in Fig. 3(a) (the starting guess is $\rho=\rho_0=1$ everywhere; 23 iterations are used). In this reconstruction and the reconstructions hereafter, we have smoothed the measured noisy data by the following weighted mean value,

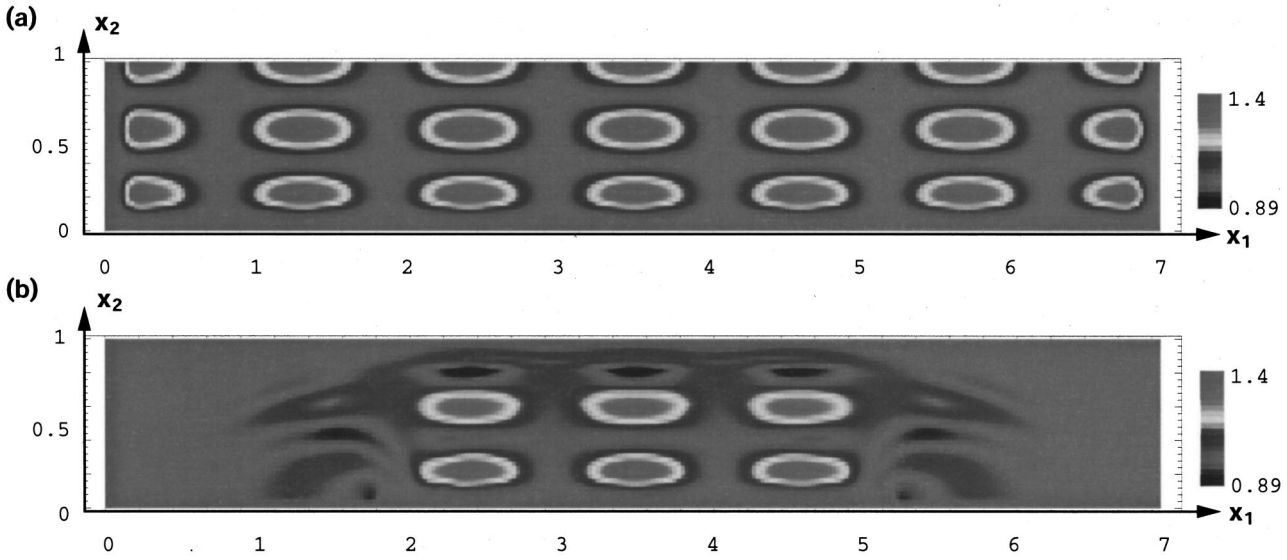

FIG. 6. Reconstruction of the density distribution in an inhomogeneous half-space using one Gaussian pulse and measurement on the part $x_1 \in [0,1]$ of the surface $x_2=0$. (a) The true density distribution; (b) the reconstruction.

$$p_{i,j}^n = \frac{4p_{i,j}^n + p_{i-1,j}^n + p_{i+1,j}^n + p_{i,j-1}^n + p_{i,j+1}^n}{8}.$$

The reconstruction error of the density at each point of the square is shown in Fig. 4(b) [note that the color rules in Figs. 4(a) and (b) are different]. As seen from Fig. 4(b), the maximum absolute error in the density reconstruction is about 0.05.

The reconstruction of the the sound speed can be performed in a completely analogous way, and an example is shown in Figs. 5(a) (the true distribution of the sound speed) and (b) (the corresponding reconstruction). In this reconstruction, noisy data with SNR=130 are used, and the starting guess is $c=c_0=1$ everywhere.

In the last numerical example, we reconstruct the density in an inhomogeneous half-space using the ''measured'' fields on a *finite* part $x_1 \in [0,7]$ of the surface $x_2=0$ for the time period $t \in [0,2.5]$. A plane-wave-like beam field is chosen for the input p_+. The input is supported in $x_1 \in [2,5]$ and the temporal dependence is given in Fig. 3. As one would expect, good reconstruction can be achieved only in a finite region (below the measured surface area) of the inhomogeneous half-space. The true density and the reconstructed density are shown in Figs. 6(a) and (b), respectively.

All numerical examples are given in a dimensionless setting. The quantities are scaled by the background sound speed c_0, the background density ρ_0, and the side length l_0. For given c_0, ρ_0, and l_0 in SI units, the sound speed, density, and temporal parameters are scaled as

$$c_{\mathrm{SI}}(x) = c(x)c_0, \quad \rho_{\mathrm{SI}}(x) = \rho(x)\rho_0, \quad \text{and } t_{\mathrm{SI}} = tl_0/c_0, \tag{27}$$

respectively.

We have carried out many numerical reconstructions in which we never came across a case where the reconstruction failed even with a very bad initial ''guess'' $\rho=\rho_0=1$ or $c=c_0=1$ everywhere (i.e., the whole space is filled with the homogeneous background medium and there is no scatterer at all). It appears that the objective functional is convex in a large area centered at the true profile.

E. Computation efficiency

We compare the computation times for the reconstructions obtained with and without the analytic gradients. When an analytic gradient is not available, one can calculate the gradient numerically through the following set of step functions:

$$\psi_i(x) = \begin{cases} 1 & x \in V_i, \\ 0 & \text{otherwise}, \end{cases}$$

where V_i, $i=1,2,...,N$, are the discretized volume cells. Assume that $\rho(x)=\Sigma_i P_i \psi_i(x)$ [$\rho(x)$ is the density to be reconstructed], and the corresponding gradient $G_\rho(x) = \Sigma_i g_i \psi_i(x)$. Then one can calculate the coefficient G_i numerically through a small perturbation as follows,

$$G_i \approx \frac{J(\langle P_0, P_1, \ldots, P_i+\delta, \ldots, P_N\rangle) - J(\langle P_0, P_1, \ldots, P_i, \ldots, P_N\rangle)}{\delta},$$

where δ is a small quantity. In the present reconstruction algorithm, the computation time is consumed mainly by calling the forward direct solver for the system (15) and the backward direct solver for the system (16) (which takes a time that is roughly equal to that for the forward direct solver). To calculate the gradient, one has to call the forward direct solver N times when the numerical perturbation is used; while using the present analytic expression, one only needs to call the forward and backward direct solvers once. Therefore, the ratio of the computation times for the gradient with and without the analytic expression is about $2/N$. In fact, the ratio of the overall computation time for the reconstruction (if the same number of iterations is required) with and without the analytic gradients is approximately $(2+s)/(N+1+s)$, where s is the average number of steps in the line search within each iteration ($s \approx 2$ if an optimal line search program is used). In a multi-dimensional case, N is large [if one takes N_x discretization points along each orthogonal space direction, then $N=(N_x)^n$, where $n=2,3$ in two- and three-dimensional cases, respectively]. Therefore, the computation time required for the reconstruction can be greatly improved in a multi-dimensional case if an analytic gradient is used.

V. CONCLUSION

In the present article we have treated a multi-dimensional acoustic inverse problem in the time domain with a deterministic gradient search algorithm. The density and/or the sound speed are reconstructed by minimizing an objective functional with an analytic gradient. Wave splitting has been integrated in the optimization algorithm. The wave-splitting provides the best linear combination of the fields for use in this type of inverse problem, as was shown in Ref. 13 with an energy estimate analysis. By introducing some dual functions and using the Gauss divergence theorem, an explicit expression for the gradient of the objective functional has been derived. The density or the sound speed has been reconstructed by a conjugate gradient method (we refer to Ref. 13 for numerical results for a simultaneous reconstruction in an analogous electromagnetic case). The reconstruction algorithm has been tested in the two-dimensional case with noisy data, and shown to be stable and robust. The computation time required for the reconstruction has been greatly improved in the multi-dimensional case when the analytic gradient is used. For the present algorithm, reconstruction using measurement around (i.e., from all sides of) the unknown object seems to be more robust than reconstruction using measurement from only one side of the unknown object. If data is available only from one side of the unknown object, the reconstruction can be improved by using more excitation sources. The present method can be used in many practical applications such as the oceanography, tomography in underwater acoustics, identification of seamounts, etc.

ACKNOWLEDGMENT

The partial support of the Swedish Research Council for Engineering Sciences is also gratefully acknowledged.

[1] F. Santosa, Y. H. Pao, W. Symes, and C. Holland (eds.), *Inverse Problems of Acoustic and Elastic Waves* (SIAM, Philadelphia, 1984).
[2] W. W. Symes, ''Impedance profile inversion via the first transport equation,'' J. Math. Anal. Appl. **94**, 435–453 (1983).
[3] A. E. Yagle and B. Levy, ''A fast algorithm solution of the inverse problem for a layered acoustic medium probed by spherical harmonic waves,'' J. Acoust. Soc. Am. **78**, 729–737 (1985).
[4] S. S. Pan, R. A. Phinney, and R. I. Odem, ''Full-waveform inversion of plane-wave seismograms in stratified acoustic media: Theory and feasibility,'' Geophysics **53**, 21–31 (1988).
[5] D. Colton and R. Kress, *Inverse Acoustic and Electromagnetic Scattering Theory* (Springer-Verlag, Berlin, 1992).
[6] M. Moghaddam and W. C. Chew, ''Simultaneous inversion of compressibility and density in the acoustic inverse problem,'' Inverse Probl. **9**, 715–730 (1993).
[7] J. Cao and S. He, ''Reconstruction of the velocity and density in a stratified acoustic half-space using a short-pulse point source,'' J. Acoust. Soc. Am. **102**, 815–824 (1997).
[8] A. Bamberger and G. Chavent, ''Inversion of normal incidence seismograms,'' Geophysics **47**, 757–770 (1982).
[9] R. E. Kleinman and P. M. van den Berg, ''Non-linearized approach to profile inversion,'' Int. J. Imaging Syst. Technol. **2**, 119–126 (1990).
[10] V. G. Romanov and S. I. Kabanikhin, *Inverse Problems of Geoelectrics* (VNU Science, Utrecht, 1994).
[11] S. He and S. I. Kabanikhin, ''An optimization approach to a three-dimensional acoustic inverse problem in the time domain,'' J. Math. Phys. **36**, 4028–4043 (1995).
[12] S. He, S. Ström, and V. H. Weston, *Time Domain Wave-splittings and Inverse Problems* (Oxford U.P., Oxford, 1998).
[13] M. Gustafsson and S. He, ''A wave-splitting based optimization approach to multi-dimensional time-domain electromagnetic inverse problems,'' Math. Comput. Simul. **50**, 541–551 (1999).
[14] M. I. Taoudakis and M. G. Markaki, ''On the use of matched-field processing and hybrid algorithms for vertical slice tomography,'' J. Acoust. Soc. Am. **102**, 885–895 (1997).
[15] P. Carrion, ''Reflection tomography in underwater acoustics,'' J. Acoust. Soc. Am. **102**, 885–895 (1997).
[16] R. P. Gilbert and Y. Xu, ''The seamount problem,'' in *SIAM* special issue on the occasion of Prof. I. Stakgold's 70th birthday, *Nonlinear Problems in Applied Mathematics*, edited by T. Angell *et al.* (SIAM, Philadelphia, 1996), pp. 140–149.
[17] H. P. Bucker, ''Use of calculated sound fields and matched-field detection to locate sound sources in shallow water,'' J. Acoust. Soc. Am. **59**, 368–373 (1976).
[18] F. G. Friedlander, *Sound Pulses* (Cambridge U.P., Cambridge, 1958).
[19] H.-O. Kreiss and J. Lorentz, *Initial-Boundary Value Problems and the Navier-Stokes Equations* (Academic, San Diego, 1989).
[20] M. Gustafsson, ''Time domain theory of the macroscopic Maxwell equations,'' Technical report LUTEDX/(TEAT-7062)/1-24, Department of Electromagnetic Theory, Lund Institute of Technology, S-211 00 Lund, Sweden, 1997.
[21] J. C. Strikwerda, *Finite Difference Schemes and Partial Differential Equations* (Chapman & Hall, London, 1989).
[22] B. Gustafsson, H.-O. Kreiss, and J. Oliger, *Time Dependent Problems and Difference Methods* (Wiley, New York, 1995).
[23] E. Polack, *Computational Methods in Optimization, a Unified Approach* (Academic, New York, 1971).
[24] M. Popov and S. He, ''Electromagnetic direct and inverse problems for a surface-breaking crack in a conductor at a high frequency,'' J. Appl. Phys. **86**, 3997–4003 (1999).
[25] G. Wahba, ''Practical approximate solutions to linear operator equations when the data are noisy,'' SIAM (Soc. Ind. Appl. Math.) J. Numer. Anal. **14**, 651–667 (1977).
[26] A. Franchois and C. Pichot, ''Microwave imaging—complex permittivity reconstruction with a Levenberg-Marquardt method,'' IEEE Trans. Antennas Propag. **45**, 203–215 (1997).
[27] W. H. Press, S. A. Teukolsky, W. T. Vetterling, and B. P. Flannery, *Numerical Recipes*, 2nd ed. (Cambridge U.P., Cambridge, 1992), Chap. 18.

Spectral integral representations of volume scattering in sediments in layered waveguides

Kevin D. LePage
SACLANT Undersea Research Centre, I-19138 La Spezia, Italy

Henrik Schmidt
Massachusetts Institute of Technology, Cambridge, Massachusetts 02139

(Received 25 June 1999; revised 31 March 2000; accepted 20 June 2000)

In situ measurements of scattering strength are often obtained by analyzing the early-time, high-angle reverberation from bottom and subbottom features. In order to provide insight into the mechanisms which cause bottom reverberation, and to their distinguishing characteristics, it is necessary to have a capability for modeling both the rough surface and the volume scattering mechanisms. For high-angle, early-time backscatter, the most appropriate approach is to use a spectral integral representation, which naturally includes the continuous spectrum important for this angular regime. A rough surface scattering theory developed earlier in this framework has provided important insights into wave scattering and penetration physics at the seafloor. Here a consistent representation for the subbottom scattering is developed and examples are provided which illustrate the observable differences between the two scattering mechanisms. [S0001-4966(00)00810-9]

PACS numbers: 43.30.Bp, 43.30.Gv, 43.30.Hw, 43.30.Vh [SAC-B]

I. INTRODUCTION

Given a model of the seafloor as locally stratified with superimposed roughness at layer interfaces and sound speed and density inhomogeneities distributed between, a combination of mechanisms may be hypothesized to contribute to reverberation: rough surface scattering from the interfaces themselves, and volume scattering from the layers. In order to understand the distinguishing characteristics of these two scattering mechanisms, it is necessary to have some modeling capability, however rudimentary, which as far as possible handles the two mechanisms consistently. Since the underlying physics of the waveguide contributes significantly to the structure of the observed reverberation, it is important for any scattering theory to have the ability to include the stratification of the water column and the bottom. Also, since measurements of the backscattering strength of the seafloor are often conducted using the early time backscatter as a function of angle, the theory must properly treat steep incident and grazing angles, as well as propagation near the critical angle for fast sediments. Both of these requirements are satisfied by scattering theories which are developed around a spectral integral representation of the incident, and by extension, scattered fields. This approach lends itself to the incorporation of arbitrary waveguide effects, and inherently treats high-angle and near critical angle propagation properly.

There has been significant progress in the modeling of volume scattering from sediments in recent years, much of it based around simplified or approximate spectral integral representations of the Green's function. A complete survey of the field would be formidable, however a few references stand out as being particularly relevant to the work presented here. Hines[1,2] has developed a model which treats volume scattering from both slow and fast sediments with three-dimensional correlation functions in closed form, using an approximate Green's function which treats the refracted and the local (forced) backscattering paths found in fast sediments. This work is closest in spirit to our approach since a substantial effort is directed towards modeling the Green's function accurately. The approximate Green's function and some simplifying assumptions allow Hines to obtain closed form expressions for the scattered intensity. We use an exact Green's functions and consequently our results are obtained as realizations. Hines' work is unique because earlier work has treated volume scattering from sediments which are uncorrelated vertically, first in the isovelocity case,[3,4] and more recently for sediments with upward refracting sound speeds.[5] While the bottom model in the latter case may be more realistic than the isovelocity sediment used by Hines, the assumption of vertical incoherence of the scattering volume seems restrictive. More complicated bottoms can also be treated by Tracey *et al.*,[6] who have characterized the effects of volume scattering on long-range propagation in a waveguide. This work also assumes that the sediment inhomogeneities are uncorrelated vertically. While it is one of our goals to treat more complicated bottoms, we wish to treat higher angle scattering than this approach will conveniently allow. Other studies of note have been directed toward evaluating the effects of sediment elasticity[7,8] and toward developing a unified approach to modeling volume and rough surface backscatter.[9,10] Elasticity is ignored in the present work, but one of our goals is to be able to investigate the uniqueness of surface and volume scattering mechanisms.

A rough surface perturbation scattering theory for arbitrary waveguides has been developed systematically in the OASES code[11,12] over the last several years.[13] Arbitrary stratification and elastic properties are handled, properly accounting for the underlying waveguide physics, and the rough surface scattering itself is treated generally, including elastic and slope terms at boundaries and including three-dimensional scattering from anisotropically rough two-

dimensional surfaces.[14] Although the results are valid only for surfaces excursions small relative to the vertical wavelengths, the predictions from the code have proven useful for understanding a variety of underwater acoustic phenomena, including reverberation statistics,[13] sound penetration,[15] and the anisotropic nature of waveguide reverberation.[14] At SACLANTCEN the volume scattering modeling approach developed here will be applied to help analyze bottom backscattering data collected on a vertical array in the Ligurian Sea,[16] where it has already been found to be capable of qualitatively reproducing the time–angle dependency of the experimental backscattering data. Indeed it was the desire to investigate the relative significance of scattering due to seabed roughness and bottom inhomogeneities that initially motivated the development of a consistent small perturbation volume scattering theory within a unified model framework.

II. THEORY

The spectral integral representation of scattering from either a rough seabed or a sediment volume is equivalent to the decomposition of the scattered field into a horizontal wave number spectrum of up-going plane waves originating either at the seabed itself or at the volume scatterers within the bottom. It is well known that volume inhomogeneity scatterers can be represented by a spatial distribution of virtual point sources and dipoles. Within the spectral integral framework the spectral kernels for these sources are easily derived analytically,[17] with the kernels above the source depths representing upward-propagating plane waves. Consequently, a spectral integral representation of the reverberant field in the water column is achieved simply by spatially integrating over the virtual source distribution.

For modeling volume scattering, the wave equation is expanded in the sound speed and density fluctuations, and the total field is decomposed into a mean, or coherent, component p, and a scattered component p_s, which is assumed to be of the order of the perturbations. Collection of terms of equal order in the perturbation then leads to separate equations for the mean and scattered fields, totally analogous to the perturbation treatment of surface roughness.[6,9]

The ocean is here assumed to be a horizontally stratified or range-independent waveguide, where the average geoacoustic properties depend only on depth. Also, the analysis will here be limited to two-dimensional scattering in plane geometry. For sound speed fluctuations (assuming constant density in the scattering layer) the Helmholtz equation for the harmonic field of time dependence $\exp(-\mathbf{i}\omega\mathbf{t})$ is, away from the sources,[1,3]

$$\left\{\nabla^2+k_b(z)^2\left(1-2\frac{\Delta c}{c}(x',z')\right)\right\}(p+p_s)=0. \tag{1}$$

Here $k_b(z)=\omega/c_b(z)$ is the depth-dependent medium wave number. Assuming that the nondimensional sound speed perturbation $\Delta c/c$ is of the same order as the scattered field, collection of the first order terms leads to the inhomogeneous wave equation for the scattered field

$$\{\nabla^2+k_b^2(z)\}p_s(x,z)=2\frac{\Delta c}{c}(x',z')k_b^2p(x',z'), \tag{2}$$

the solution to which is

$$p_s(x,z)=2k_b^2\int_{-\infty}^{\infty}dx'\int dz' \times G(x-x',z;z')\frac{\Delta c}{c}(x',z')p(x',z'), \tag{3}$$

where $G(x-x',z;z')$ is the Green's function for the stratified medium, which for a range-independent waveguide is dependent on the horizontal separation, but the actual depths of source and receiver. Similarly, for density fluctuations, the wave equation is to first order in the nondimensional density fluctuation

$$\left\{(\rho+\Delta\rho)\nabla\cdot\left(\rho^{-1}\left(1-\frac{\Delta\rho}{\rho}\right)\nabla\right)+k_b^2(z)\right\}(p+p_s)=0, \tag{4}$$

which for background density constant in the layer yields the following inhomogeneous wave equation for the scattered field,

$$\{\nabla^2+k_b^2(z)\}p_s(x,z)=\left(\nabla\frac{\Delta\rho}{\rho}\right)\cdot\nabla p(x',z'), \tag{5}$$

with the solution

$$p_s(x,z)=\int_{-\infty}^{\infty}dx'\int dz'\,G(x-x',z;z') \times\left(\nabla\frac{\Delta\rho}{\rho}(x',z')\right)\cdot\nabla p(x',z'). \tag{6}$$

A. Volume scattering in iso-velocity medium

In a bottom half-space with constant background wave number k_b, the integral representation the unperturbed field p, consisting solely of down-going waves below a single interface at depth $z=0$, is

$$p(x',z')=\int_{-\infty}^{\infty}dk\,\tilde{p}(k)T_{12}(k)e^{ik_{bz}z'}e^{ikx'}, \tag{7}$$

where $\tilde{p}(k)$ is the downgoing incident wave spectrum in horizontal wave number k *above the interface*. $T_{12}(k)$ is the wave-number-dependent transmission coefficient into the lower halfspace, and k_{bz} is the vertical wave number, defined as

$$k_{bz}=\sqrt{k_b^2-k^2},\quad k\leqslant k_b \qquad =i\sqrt{k^2-k_b^2},\quad k>k_b, \tag{8}$$

ensuring that the radiation condition is satisfied for $z'\to\infty$. The gradient of the incident field, required in Eq. (6), is easily found from Eq. (7) as

$$\nabla p(x',z')=\int_{-\infty}^{\infty}dk\,(ik\mathbf{e}_x+ik_{zb}\mathbf{e}_z) \times\tilde{p}(k)T_{12}(k)e^{iz'k_{bz}}e^{ikx'}. \tag{9}$$

Similarly, the Green's function from the scatterers to the depth $z=0^-$ just above the interface is[17]

$$G(x-x',0^-;z')=-\frac{i}{4\pi}\int_{-\infty}^{\infty}dq\,q_{bz}^{-1}T_{21}(q)\times e^{iz'q_z}e^{iq(x-x')}, \tag{10}$$

where q is the scattered horizontal wave number, q_{bz} is the corresponding vertical wave number in the bottom, and $T_{21}(q)$ is the spectral transmission coefficient from the lower half-space to the upper half-space.

Using the representations (7), (9), and (10) in Eqs. (3) and (6) and integrating over x' (see Ref. 18 for details) then yields an integral representation of the scattered field. For sound speed inhomogeneity the result for a receiver at depth $z<0$ in the water is

$$p_s(x,z)=-ik_b^2\int_{-\infty}^{\infty}dk\,\tilde{p}(k)T_{12}(k)\times\int_{-\infty}^{\infty}dq\,q_{bz}^{-1}T_{21}(q)e^{iqx}e^{-izq_{wz}}\times\int dz'\frac{\widetilde{\Delta c}}{c}(q-k,z')e^{iz'(q_{bz}+k_{bz})}, \tag{11}$$

where $\widetilde{\Delta c}/c$ represents the horizontal Fourier transform of the volume perturbation, and q_{wz} is the vertical wave number in the water. Assuming the sediment to be lossless ($\mathrm{Im}\{k_b\}\equiv 0$), the contribution from the *propagating* components of the incident and scattered fields ($[k,q]\leqslant k_b$) to the depth integral of Eq. (11) can be simply evaluated by a two-dimensional Fourier transform of the sound speed inhomogeneities, with the result

$$p_s(x,z)=-2\pi ik_b^2\int_{-\infty}^{\infty}dk\,\tilde{p}(k)T_{12}(k)\times\int_{-\infty}^{\infty}dq\,\frac{e^{-izq_{wz}}}{q_{bz}}T_{21}(q)\times\frac{\widetilde{\Delta c_c}}{c}(q-k,-q_{bz}-k_{bz})e^{iqx}. \tag{12}$$

For lossy sediments, and for cases where the contribution from the the *evanescent* components ($[k,q]>k_b$) of the incident and scattered field is significant, i.e., for fast bottoms the scattered field no longer has a direct interpretation in terms of the depth Fourier transform of the sound speed inhomogeneities, and the depth integral in Eq. (11) must be evaluated explicitly.

For density inhomogeneities the spectral integral representation of the scattered field is

$$p_s(x,z)=-i\frac{k_b^2}{2}\int_{-\infty}^{\infty}dk\,\tilde{p}(k)T_{12}(k)\times\int_{-\infty}^{\infty}dq\,\frac{e^{-izq_{wz}}}{q_{bz}}T_{21}(q)e^{iqx}\times\int dz'\left(\frac{k^2-kq}{k_b^2}+\frac{ik_{bz}}{k_b^2}\frac{\partial}{\partial z'}\right)\times\frac{\widetilde{\Delta\rho}}{\rho}(q-k,z')e^{iz'(q_{bz}+k_{bz})}. \tag{13}$$

Ignoring loss, the depth derivatives and the depth integral may also be formulated here as a two-dimensional Fourier transform for the propagating incident and scattered spectrum, yielding

$$p_s(x,z)=-\pi i\int_{-\infty}^{\infty}dk\,\tilde{p}(k)T_{12}(k)\times\int_{-\infty}^{\infty}dq\,\frac{e^{-izq_{wz}}}{q_{bz}}T_{21}(q)e^{iqx}(k_b^2-kq+k_{bz}q_{bz})\times\frac{\widetilde{\Delta\rho}}{\rho}(q-k,-q_{bz}-k_{bz}). \tag{14}$$

Once again, the depth integrals must be explicitly evaluated using Eq. (13) when the vertical wave numbers are complex, i.e., for the evanescent components of the incident and scattered fields, and when the sediment is lossy.

Notice that the wave-number-dependent factor in the kernel of Eq. (14) reaches its maximum for k and q large and of opposite sign, corresponding to horizontal backscatter, or for k_{bz} and q_{bz} large, corresponding to vertical backscatter. This enhanced backscatter is a distinguishing characteristic of scattering from density inhomogeneities.

The theory presented in this section has several restrictions. The three most important are that it is a two-dimensional theory, that small perturbations in sound speed and density have been assumed, and that the single scattering approximation has been taken. The first assumption can be eliminated in an analogous way to which two-dimensional rough surface scattering results have recently been extended to three dimensions using the Fourier spectral approach.[14] The multiple scattering effects between scatterers can be important and have been the subject of recent investigations.[19,20] The present work does not attempt to address the effects of multiple scattering between the individual scatterers, but does include multiple scattering of the scattered field at the waveguide boundaries.

B. Volume scattering in media with sound speed gradient

Strong sediment gradients can substantially influence the characteristics of volume scattering contributions.[5] In order to treat volume scattering from such sediments, it is possible to replace the spectral integral representations for the incident field in Eq. (7) and the scattered field Green's function in Eq. (10) with their equivalent forms for layers with sound

speed gradients which obey the relation $k^2 = az + b$. For such sound speed gradients the depth-separated Helmholtz equation

$$\left\{ \frac{\partial^2}{\partial z^2} + (k_b^2(z) - k^2) \right\} p = 0$$

may be written[17] as an Airy partial differential equation

$$\left\{ \frac{\partial^2}{\partial Z^2} - Z \right\} p = 0,$$

where

$$Z(z,k) = a^{-2/3}(k^2 - (az+b)).$$

In this case two independent vertical eigenfunctions are the Airy functions

$$\mathrm{Ai}(Z(z,k)),$$

which have the characteristic of a standing wave with a turning point at depth $z = -b/a$, and the linear combination[21]

$$\mathrm{Ai}(Z(z,k)) - iBi(Z(z,k)) = 2e^{-2\pi i/6}\mathrm{Ai}(Z(z,k)e^{2\pi i/3}),$$

which have the characteristic of a wave propagating from the turning point depth, and therefore satisfying the radiation condition in the direction of decaying sound speed. Thus for propagation into scattering layers with positive sound speed gradients, Eq. (7) takes the form

$$p(x',z') = \int_{-\infty}^{\infty} dk\, \tilde{p}(k) T_{12}(k) \frac{\mathrm{Ai}(Z(z',k))}{\mathrm{Ai}(Z(0,k))} e^{ikx'}, \quad (15)$$

while for propagation into layers with negative gradients, the result is

$$p(x',z') = \int_{-\infty}^{\infty} dk\, \tilde{p}(k) T_{12}(k) \frac{\mathrm{Ai}(Z(z',k)e^{2\pi i/3})}{\mathrm{Ai}(Z(0,k)e^{2\pi i/3})} e^{ikx'}. \quad (16)$$

Using the integral representation for the Green's function in such a refracting medium, e.g., derived in Ref. 17, the field scattered into the upper half-space by a virtual source in an upward-refracting sediment is

$$G(x-x',0^-;z') = \int_{-\infty}^{\infty} dq \left\{ \frac{T_{21}(q)}{4\pi} e^{iq|x-x'|} \frac{2a^{-1/3}\mathrm{Ai}(Z(z',q))\mathrm{Ai}(Z(0,q)e^{2\pi i/3})}{\mathrm{Ai}'(Z(z',q))\mathrm{Ai}(Z(z',q)e^{2\pi i/3}) - \mathrm{Ai}'(Z(z',q)e^{2\pi i/3})\mathrm{Ai}(Z(z',q))} \right\}, \quad (17)$$

while for a downward refracting sediment the field radiated into the upper half-space is, immediately above the interface at $z = 0$,

$$G(x-x',0^-;z') = \int_{-\infty}^{\infty} dq \left\{ \frac{T_{21}(q)}{4\pi} e^{iq(x-x')} \frac{2a^{-1/3}\mathrm{Ai}(Z(z',q)e^{2\pi i/3})\mathrm{Ai}(Z(0,q))}{\mathrm{Ai}'(Z(z',q))\mathrm{Ai}(Z(z',q)e^{2\pi i/3}) - \mathrm{Ai}'(Z(z',q)e^{2\pi i/3})\mathrm{Ai}(Z(z',q))} \right\}. \quad (18)$$

These equations replace Eq. (10) for refractive media.

C. Volume scattering in general layered media

The volume scattering formulations derived above for a fluid half-space can be easily generalized to horizontally stratified media within the *Direct Global Matrix* (DGM) approach to the solution of the depth-separated wave equation in such environments.[17] Consequently, they are straightforwardly implemented into a spectral integral code. In direct analogy to the handling of physical sources, the contributions from the virtual scattering sources within a layer are introduced by superimposing their free-field radiation with a set of homogeneous solutions, the amplitudes of which are found by satisfying the boundary conditions of continuous stress and particle velocity at all interfaces in the stratification. As is the case for physical sources, only upgoing waves contribute above the virtual sources, while below only downgoing waves contribute.

Adopting the Born approximation,[22] the up- and downgoing waves of the unperturbed field are used to determine the wave number spectrum of upgoing scattered waves at the upper interface and downgoing scattered waves at the lower interface using the integral expressions derived above, but without accounting for the transmission through the interfaces. The up-and downgoing mean field amplitudes $\tilde{a}^{\pm}(k)$ in each layer are provided by first solving for the mean field in the absence of scattering. For a layer of thickness D, the upgoing scattered field at wave number q at the upper interface then is, treating sound speed and density inhomogeneity scattering together,

$$\begin{aligned} \tilde{p}_s(q,0^+) = &-\frac{i}{2q_{bz}} \int_{-\infty}^{\infty} dk \int dz'\, \tilde{a}^+(k) e^{iz'(q_{bz}-k_{bz})} e^{iDk_{bz}} \\ &\times \left(2k_b^2 \widetilde{\frac{\Delta c}{c}}(q-k,z') + \left(k^2 - kq - ik_{bz}\frac{\partial}{\partial z'} \right) \right. \\ &\left. \times \widetilde{\frac{\Delta\rho}{\rho}}(q-k,z') \right) - \frac{i}{2q_{bz}} \int_{-\infty}^{\infty} dk \int dz'\, \tilde{a}^-(k) \\ &\times e^{iz'(k_{bz}+k_{bz})} \left(2k_b^2 \widetilde{\frac{\Delta c}{c}}(q-k,z') \right. \\ &\left. + \left(k^2 - kq + ik_{bz}\frac{\partial}{\partial z'} \right) \widetilde{\frac{\Delta\rho}{\rho}}(q-k,z') \right), \end{aligned} \quad (19)$$

while at the lower interface the downgoing scattered field is

$$\tilde{p}_s(q,D^-) = -\frac{i}{2q_{bz}}\int_{-\infty}^{\infty} dk \int dz'\, \tilde{a}^+(k) e^{i(D-z')(q_{bz}+k_{bz})} \times \left(2k_b^2 \widetilde{\frac{\Delta c}{c}}(q-k,z') + \left(k^2 - kq - ik_{bz}\frac{\partial}{\partial z'} \right) \times \widetilde{\frac{\Delta\rho}{\rho}}(q-k,z') \right) - \frac{i}{2q_{bz}}\int_{-\infty}^{\infty} dk \int dz'\, \tilde{a}^-(k) \times e^{iz'(k_{bz}-q_{bz})} e^{iDq_{bz}} \left(2k_b^2 \widetilde{\frac{\Delta c}{c}}(q-k,z') + \left(k^2 - kq + ik_{bz}\frac{\partial}{\partial z'} \right) \widetilde{\frac{\Delta\rho}{\rho}}(q-k,z') \right). \quad (20)$$

The interface conditions satisfied at fluid interfaces are the continuity of pressure and vertical velocity. The volume scattering contributions to the boundary conditions for pressure at each interface are given directly by Eqs. (19) and (20). The corresponding contributions to the velocity boundary condition at the upper and lower interfaces are

$$\tilde{v}_{\mathbf{n}_s}(q,0^+) = -\frac{i}{2\omega\rho}\int_{-\infty}^{\infty} dk \int dz'\, \tilde{a}^+(k) e^{iz'(q_{bz}-k_{bz})} e^{iDk_{bz}} \times \left(2k_b^2 \widetilde{\frac{\Delta c}{c}}(q-k,z') + \left(k^2 - kq - ik_{bz}\frac{\partial}{\partial z'} \right) \times \widetilde{\frac{\Delta\rho}{\rho}}(q-k,z') \right) - \frac{i}{2\omega\rho}\int_{-\infty}^{\infty} dk \int dz'\, \tilde{a}^-(k) \times e^{-iz'(q_{bz}+k_{bz})} \left(2k_b^2 \widetilde{\frac{\Delta c}{c}}(q-k,z') + \left(k^2 - kq + ik_{bz}\frac{\partial}{\partial z'} \right) \widetilde{\frac{\Delta\rho}{\rho}}(q-k,z') \right), \quad (21)$$

and

$$\tilde{v}_{\mathbf{n}_s}(q,D^-) = \frac{i}{2\omega\rho}\int_{-\infty}^{\infty} dk \int dz'\, \tilde{a}^+(k) e^{i(D-z')(q_{bz}+k_{bz})} \times \left(2k_b^2 \widetilde{\frac{\Delta c}{c}}(q-k,z') + \left(k^2 - kq - ik_{bz}\frac{\partial}{\partial z'} \right) \times \widetilde{\frac{\Delta\rho}{\rho}}(q-k,z') \right) - \frac{i}{2\omega\rho}\int_{-\infty}^{\infty} dk \int dz'\, \tilde{a}^-(k) \times e^{iz'(k_{bz}-q_{bz})} e^{iDq_{bz}} \left(2k_b^2 \widetilde{\frac{\Delta c}{c}}(q-k,z') + \left(k^2 - kq + ik_{bz}\frac{\partial}{\partial z'} \right) \widetilde{\frac{\Delta\rho}{\rho}}(q-k,z') \right), \quad (22)$$

The inhomogeneous boundary conditions for the scattered field coming from a refractive layer are given in Ref. 18.

The implementation of this formulation is straightforward. First, the mean up-and downgoing plane wave amplitudes of the field due to the presence of physical sources are determined. These amplitudes are then used together with a random realization of the perturbation and Eqs. (1)–(18) to provide a virtual source contribution at the upper and lower boundary of the scattering layer, and the standard DGM solution, which includes waveguide effects, followed by the evaluation of the spectral integral over scattered wave numbers, then yields the realization of the scattered field.

III. RESULTS

The theory outlined in the previous section has been implemented into the OASES code.[12] In order to benchmark the results, plane wave scatter cross sections from a layer of scatterers imbedded in a uniform background sound speed of 1500 m/s were computed and compared to theoretical values (see Ref. 18 for the derivation of the theoretical values). The results are shown in Fig. 1 for 360 and 3600 Hz, respectively, at various angles of incidence. Both the numerical and the closed form results were frequency averaged over a 200-Hz bandwidth, in order to smooth the numerical results, which are computed for one realization of scatterers. The results indicate that the numerical implementation closely approximates the known closed form solution, with the forward scattered resonance condition and the angular dependence faithfully reproduced. The remaining disagreement, in general less than 2 dB, may be attributed to details of the numerical implementation which are inconsistent with the plane wave and infinite aperture scattering hypothesis of the theoretical result. These are (1) the use of complex frequency in the numerical calculation, which causes some small decay in the plane wave amplitude as it propagates through the layer, and (2) the use of a finite depth scattering layer to approximate the exact Bragg scattering resonance, on which the closed form theory depends. The finite aperture has the effect of slightly increasing backscattering cross section, as the sidelobes of the forward scattered resonance can pollute the backscattered response. Of course, for actual scattering simulations from finite depth scattering layers, this is a real effect and does not cause errors.

A. Example 1: Volume scattering from a slow layer

In this example we compute a broadband volume scattering realization for a thick, slow sediment layer with the properties shown in Fig. 2. The scattering is caused by a point source which is situated at a height of 28 m above the sediment–water interface. In order to clarify the resulting scattered field calculations, the source is prevented from exciting negative wave numbers. The resulting scattered field, shown in Fig. 3 at various times after the shot, has an asymmetrical nature which eases the identification of the forward and backscattered components of the field. Any scattered energy seen to the left of the source is by definition backscattered, while the field to the right of the source may be either forward or backscattered.

The results show an interesting but predictable evolution in time and space. To the far right of the scattered field at any particular time step is the ''forward scattered'' field which is the strongest component. The only portion of this forward-scattered component which is truly forward scattered, i.e., traveling in the same direction as the incident field, is the

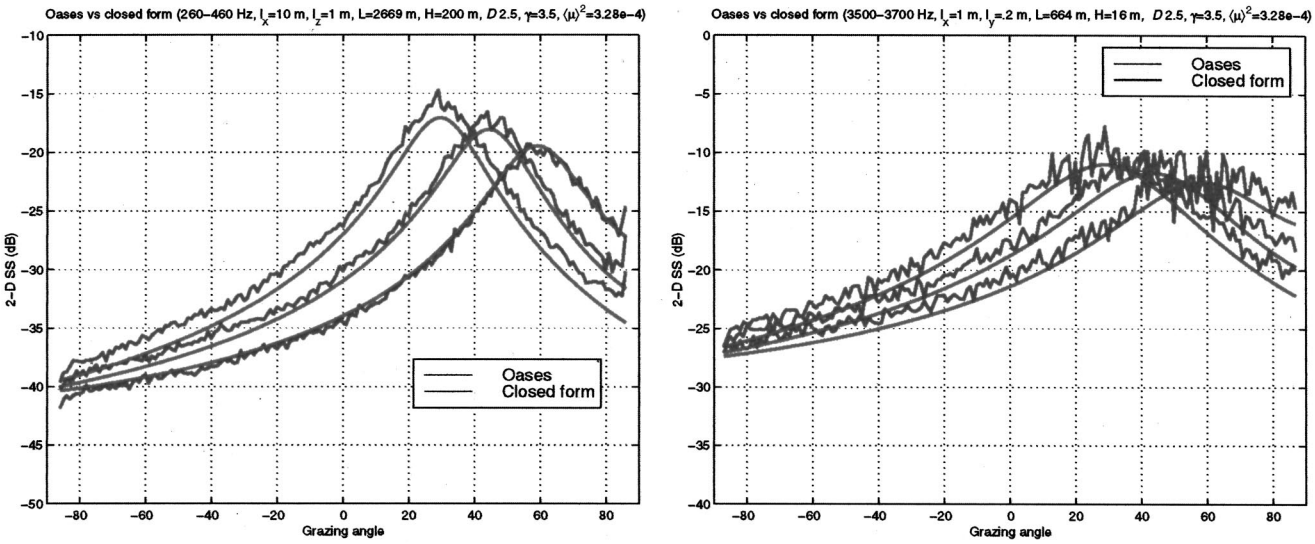

FIG. 1. Benchmark results for the spectral integral representation of volume scattering from sound speed and density inhomogeneities. The red curves are closed form values for the two-dimensional volume scattering strength and the green curves are OASES results. Both curves are averaged over a 200-Hz band. The panel on the left shows results for 30, 45, and 60 degrees incidence at 360 Hz. The correlation length scales are $l_x=10$ m and $l_z=2$ m, with a dip angle $\phi=0$ from horizontal. The right panel illustrates the results at 3600 Hz, with $l_x=1$ m and $l_z=0.2$ m. In both examples the nondimensional variance of the sound speed inhomogeneities is $3.28E-4$, and the density and sound speed inhomogeneities are 100% correlated with a proportionality constant $2\gamma=7.0$.

scattered field right along the sediment–water interface. The scattered waves form a cloud which is most intense along the sediment–water interface and for some distance above it. The vertical extent of the most intense part of the scattered field is defined by the vertical correlation length scale of the scatterers; if the vertical correlation length scale is very short, then more vertical ''smearing'' of the forward scattered energy is expected.

Behind the forward-scattered field is a band of high scattered energy whose thickness is defined by the difference in the travel time between the top and bottom layer for any position, multiplied by the average sound speed. In this case, since the sound speed in the sediment is almost the same as in the water column, the result is that for receivers at zero range the thickness of this band corresponds to twice the thickness of the sediment layer, or 400 m. The thickness decreases as the receiver range is increased, consistent with the fact that the travel time difference between the two paths goes towards zero in this case.

To the left of the source, the field is purely backscattered. For this reason there is a slight asymmetry to the results, as the backscatter slightly retards the forward scatter by a spatial extent roughly corresponding to the $c\tau$, the spatial extent of the incident pulse. This characteristic is observable in the results if one looks closely at the bottom panel of Fig. 3.

If the scattering layer has the same properties as the enclosing upper and lower half-spaces, then the features just described complete the description of the scattered field. However, if there is partial reflection of the scattered field at the upper and lower interface, then there will be a second ring of scattered arrivals of lower amplitude. If the amplitude of the first scattered arrival is proportional to

$$A_1 \propto T_{12} R_{23} T_{21},$$

where T_{12} is the transmission coefficient through the sediment–water interface, R_{23} is the reflection coefficient at the sediment–basement interface, and T_{21} is the transmission coefficient from the sediment back into the water, then the amplitude of the Nth subsequent arrival will be

$$A_N \propto A_1 (R_{21} R_{23})^N,$$

where R_{21} is the internal reflection in the sediment layer at the upper interface. Of course these types of rough arguments are only so useful and are no substitute for the general scattered field calculations which include the angular dependence of the reflection and transmission coefficients and the resonant behavior of both of the incident and the scattered field within the layer.

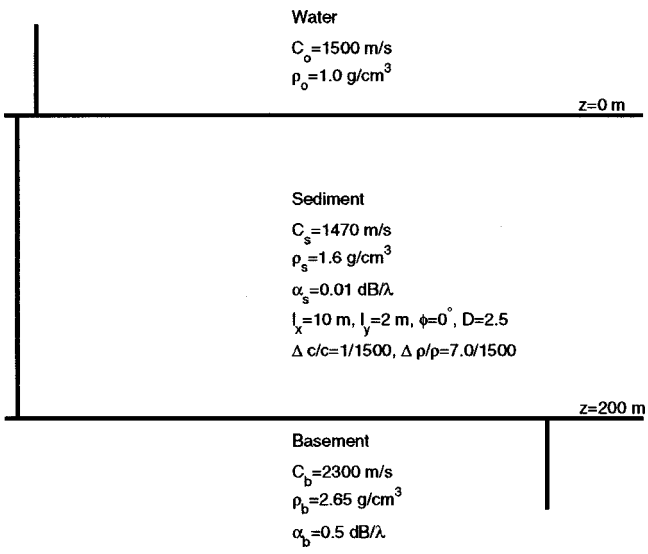

FIG. 2. The environment for example 1. A slow sediment layer 200 m thick is sandwiched between the upper half-space of water and a dense, heavy basement.

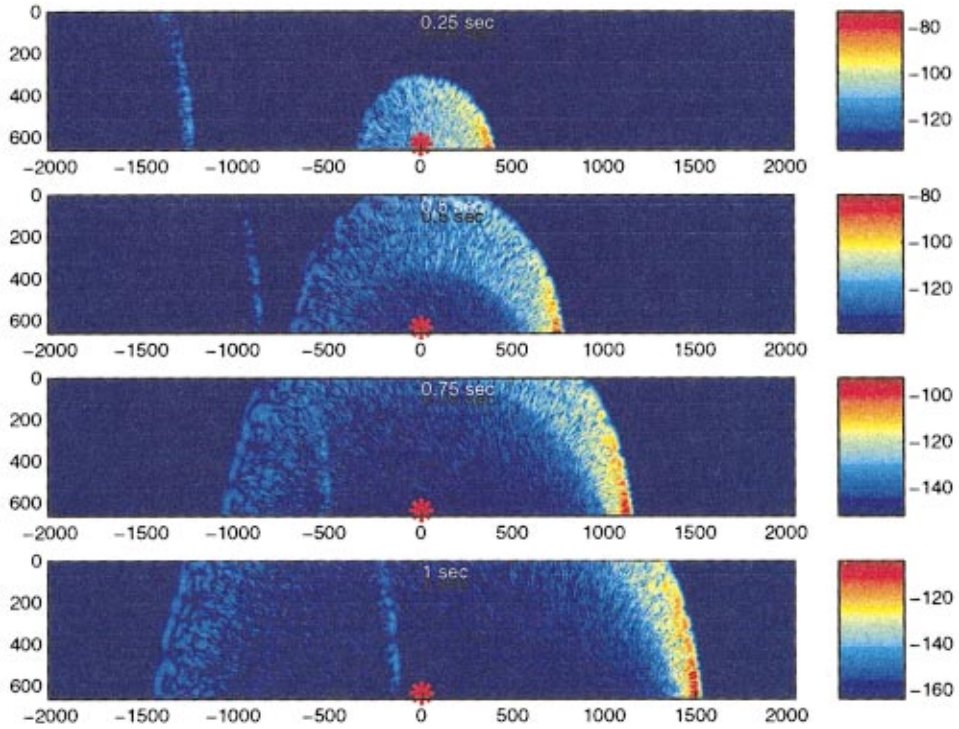

FIG. 3. Spatial snapshots of the evolution of the scattered field for example 1. The center frequency is 500 Hz with 200 Hz of bandwidth. The source is placed 28 m above the water–sediment interface, and is designed to radiate only right-traveling waves, hence the asymmetrical nature of the result. The region to the left of the source by definition has only left-traveling waves, to the right of the source, both left- and right-traveling waves exist. The region of strongest scattering is the forward-scattered regime, to the far right and near the sediment–water interface. The axes of the figure are in meters and the scale is scattered field amplitude in dB re μPa for a unity amplitude point source.

Since a finite reflection coefficient exists in this example at both the upper and lower interface, the scattered field calculations show late time components consistent with the reverberation of the incident and scattered field within the sediment layer. These effects become more evident as the forward scattering regime to the right of the source is approached.

The numerical artifact seen propagating from the left to the right in all panels of Fig. 3 is the time-aliased forward-scattered field. By the time this artifact reaches the source it

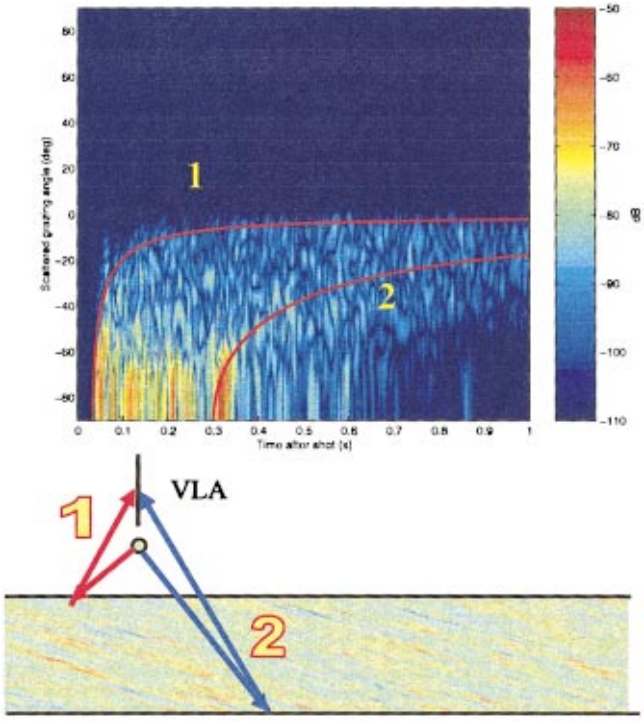

FIG. 4. Time–angle plot of scattered field received on a VLA at $r=0$. Two traces are superimposed, the upper red curve represents the time–angle evolution of returns from scatterers on the sediment–water interface (ray **1** on the ray diagram), while the lower red curve represents return from the sediment–basement interface (ray **2** on the ray diagram). Scattered returns which lie below the lower curve are scattered mutipaths from within the sediment layer.

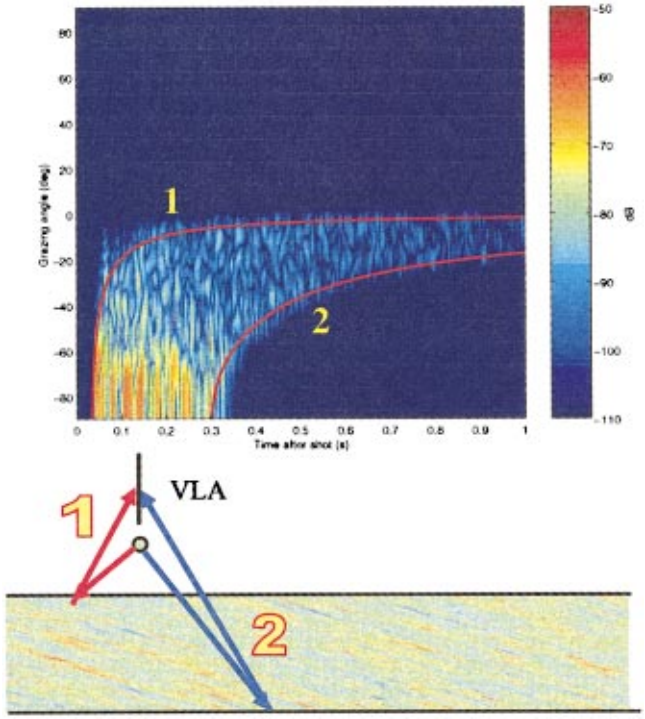

FIG. 5. Time–angle plot of volume scattering in a homogeneous background. Here all the scattered energy lies between the scattering angle trajectories for the top (ray **1** on the ray diagram) and the bottom of the scattering layer (ray **2**). There is no multipath.

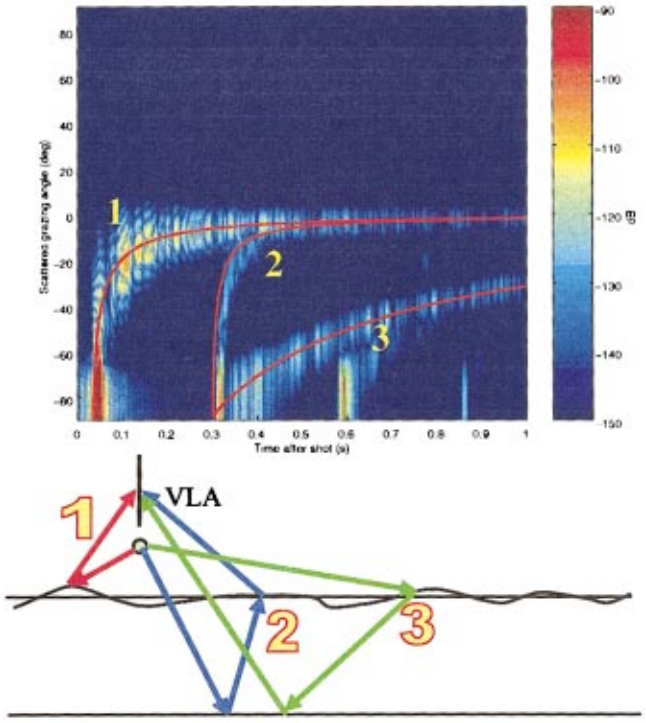

FIG. 6. Time–angle plot for rough surface scattering for the environment in example 1. There are three main branches to the response. The most quickly evolving trajectory (corresponding to ray **1** on the ray diagram) is the direct backscatter from the water–sediment interface. The second trajectory (corresponding to ray **2**) is the scattered field excited by the basement reflected wave, while the lower right trajectory (ray **3**) is the downward scattered field form the direct blast which has reflected off the basement and come back to the receiver.

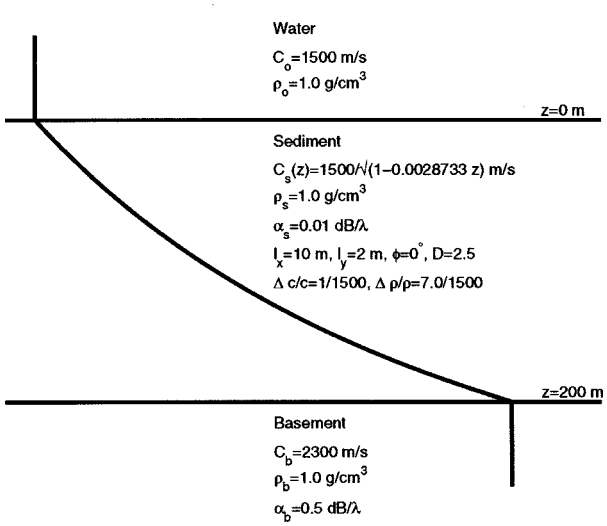

FIG. 7. The environment for example 2. On a homogeneous background of uniform density, a increase in sound speed from 1500 to 2300 m/s occurs over a depth of 200 m. There is 0.01 dB/λ attenuation in the sediment and 0.5 dB/λ in the basement.

suffers a 54-dB attenuation due to the use of a complex frequency offset of $\Delta\omega$ in the calculations. It is important in any Fourier synthesis application to be aware of aliasing features. In wave propagation problems, these aliasing features propagate like late time waves and their effects have to be ameliorated by the use of the complex frequency during the calculation of the Green's functions[12] and by restricting attention to the valid time window of the synthesis

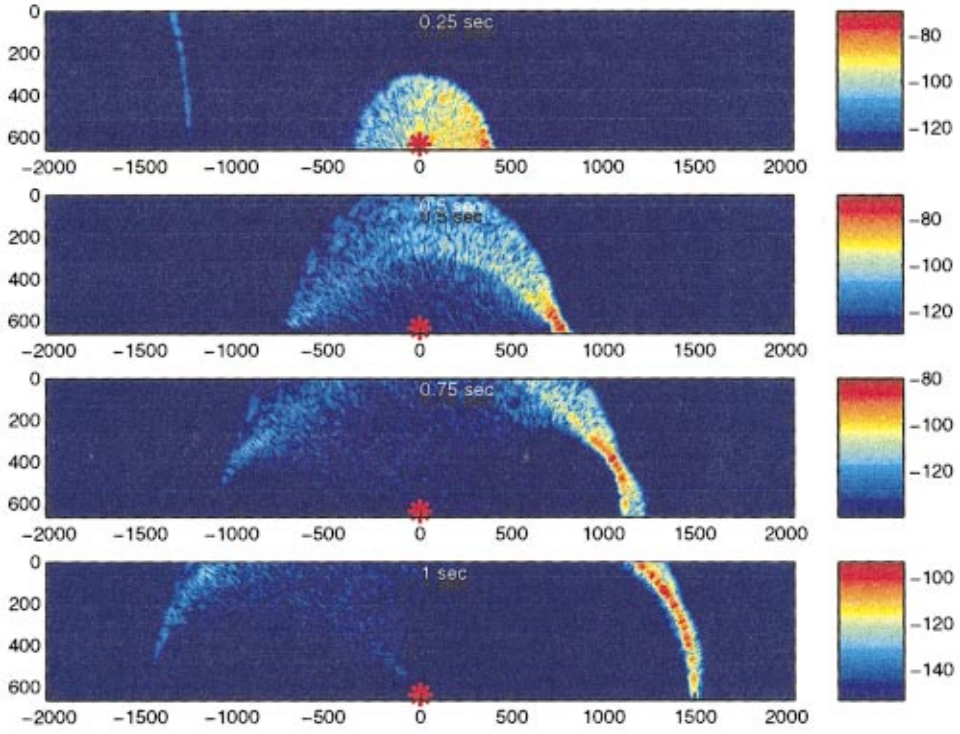

FIG. 8. Spatial snapshots of the evolution of the scattered field in example 2. The deep-diving incident field entering the sediment at grazing angles less than 49 degrees turns and exits the sediment layer at a range of approximately 750 m. The forward-scattered field is therefore comprised of two strong contributions, one associated with grazing incidence along the sediment–water interface and the second associated with downward scattered energy which is turned by the strong gradient in the sediment and exits upward. The backscattered field suffers focusing, so that by a time of 0.95 s, corresponding to the lowest panel, the backscattered field is only evident at the source range. This refocusing of the backscattered energy is a unique phenomena of scattering from layers with strong gradients. The axes of the figure are in meters and the scale is scattered field amplitude in dB re μPa for a unity amplitude point source.

$T_0 \leqslant T \leqslant T_0 + 2\pi/\Delta\omega$. When complex frequency techniques are not used, $T_0 \equiv 0$ and $\Delta\omega \ll 2\pi/\tau$, where τ is the maximum temporal extent of the response of the waveguide, including scattering, for the desired receiver position.

In Fig. 4 the response of a Hanning shaded Bartlett beamformer with 50 m of aperture placed 25 m above the sediment is shown. Overlayed on the figure are the time–angle trajectories of hypothetical scatterers placed on the water–sediment interface [the upper curve (1), evolving to low angles more quickly in time] and the sediment–basement interface [lower curve (2)]. The primary scattered field from the volume scatterers lies between these two trajectories. The thickness of the band in angle is determined by the thickness of the scattering layer. The abruptness of the temporal evolution is determined by the proximity of the source and the receiver array to the sediment–water interface. The later scattered returns fill in the lower right quadrant in the time–angle plane. With homogeneous background properties there would be no multipath and this region would be empty, as is shown in Fig. 5. The simplicity of the interpretation relies to some degree on the assumption that the sediment layer has the same sound speed as the upper half-space.

In Fig. 6 the beamformer response for scattering from a rough sediment–water interface is shown for comparison. The results are very different from the volume scattering results. In the absence of the sediment–basement interface, there would simply be the upper-most beam–time trajectory (1), representing scattering from the interface. With the existence of the sediment–basement interface, there are two additional trajectories which are strongly evident. The trajectory (2) in the closest proximity to the sediment–water interface trajectory is caused by scattering of the basement-reflected incident field when it passes through the sediment–water interface, while the slowest evolving trajectory (3) is the downward scattered energy which has been reflected by the basement and is now seen in the upper half-space. These results together with those shown in Fig. 4 indicate that volume and surface scattering mechanisms should be resolvable in experiments which follow the basic configuration of a monostatic source receiver geometry with a vertical aperture, as has been proposed by Holland.[16]

B. Example 2: Volume scattering from a sediment layer with a strong gradient

In this example we evaluate the scattered field from a layer with a strong gradient of 4 s^{-1}, as shown in Fig. 7. We are interested in understanding how the strong gradient changes the scattering characteristics from those outlined for the isospeed layer in the first example. However, to simplify the interpretation, we begin by eliminating the sound speed and density contrasts at the sediment–water and sediment–basement interfaces.

For scattering from sediments with strong sound speed gradients, the refracted characteristics of the incident field turn out to be extremely important for understanding and interpreting the scattered field results. This is because in strongly upward refracting sediments like the one under consideration the incident field cannot ensonify the entire sediment layer. Instead the bulk of the incident field turns and exits the sediment layer at a range defined by the thickness of the layer and its gradient. In this example this range is only 750 m from the source. The large gradient causes an internal reflection which is responsible for redirecting propagating incident and scattered energy with shallow enough grazing angles (in this case less than roughly 50 degrees) into the upper half-space. At the exit point of the deepest diving internal reflected incident energy, the deep diving forward-scattered field overtakes the grazing incidence forward-scattered field traveling along the sediment–water interface, causing a focusing phenomena in both the incident field and the scattered field, and as can be seen for the lower three panels of Fig. 8. This strong focusing causes much higher amplitudes of forward-scattered energy in the vicinity of the exit point of the incident field.

At later times the phenomena become even more interesting. It is clear that in cases with negligible reflection at the upper and lower interfaces of the sediment layer, there are two spatial regions where scattered energy is excluded from propagating. The first is in the forward-scattered direction directly behind the region of strong focusing, while the second is in the backscattered direction at low grazing angles following the backscattered halo. The cause of these regions of negligible presence of the scattered field is the strong effect of the sediment gradient on the scattered field, which must travel through the sediment before it can be observed in the water column. Looking at the lowermost panel of Fig. 8, it is clear that at approximately 1 s after the shot, the backscattered field is exiting the sediment layer only in the vicinity of the source, at a grazing angle of approximately 50 degrees. In fact a travel time of about 0.9 s is consistent for round-trip deep-refracted backscatter from the scattering volume near the sediment–water interface at the range of 750 m, where the incident field exits the sediment and radiates into the upper half-space.

The angular focusing of the scattered field at later times for sediments with strong sound speed gradients is confirmed by the Bartlett beamformer response illustrated in Fig. 9. For times beyond approximately 0.5 s after the source firing, the scattered field separates into two branches in the time–angle plane. The most significant branch of the late scattering response lies between the time–angle trajectory of scatterers at the top of the sediment layer which are observed through a deep refracted path (**3**), and the angle of total internal reflection of the sediment layer, which in this case is approximately 50 degrees. At approximately 0.9 s, the deep refracted backscatter from the uppermost scatterers within the sediment layer arrive at this angle, and is sharply cut off for later times. The upper branch of the late response, associated with the forced backscatter of the shallowest volume scatterers within the sediment, is a much weaker contributor to the total scattered response at late time, which conforms to the upper boundary of the trajectory (**1**) familiar from the isospeed sediment scattering in the first example. Beyond 0.9 s, this is the only backscattering path observable.

At early time the lower boundary of the backscatter angular response is determined by the time–angle trajectory of scatterers at the bottom of the sediment layer (**2**). These scat-

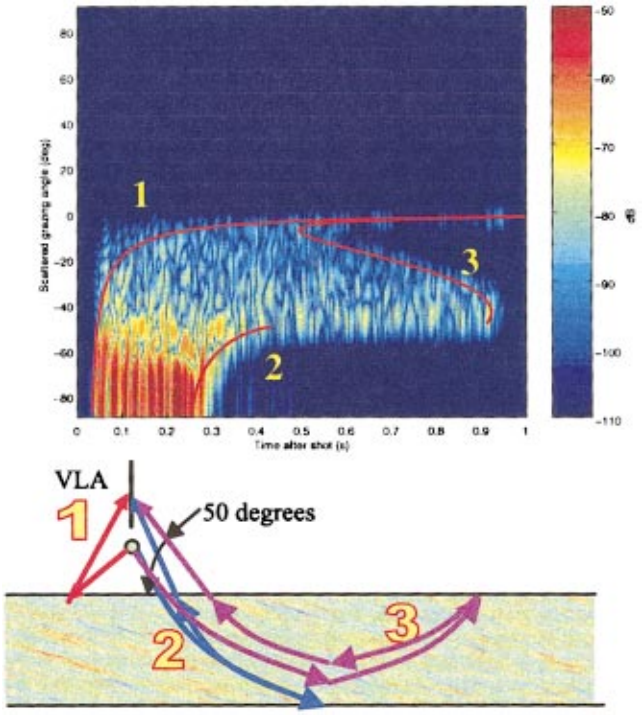

FIG. 9. Time–angle plot for backscatter received at $r=0$ in example 2. For times less than approximately 0.5 s, the scattered energy is confined between the time–angle trajectory of scatterers on the sediment–water interface (ray **1**) and the scatterers on the bottom of the sediment layer (ray **2**). At later times the direct-path backscatter from the uppermost scatterers persists (ray **1**), but the bulk of the response is confined between the time–angle trajectory of scatterers on the top of the sediment layer which are observable as deep refracted backscatter (ray **3**) and the angle of total internal reflection of the sediment, which is approximately 50 degrees. At approximately 0.9 s, the deep refracted backscatter cuts off as all downward-propagating backscattered energy escapes into the lower half-space for scatterers beyond the corresponding range of approximately 750 m. These scattering characteristics are very distinguishable from those of an iso-speed scattering layer.

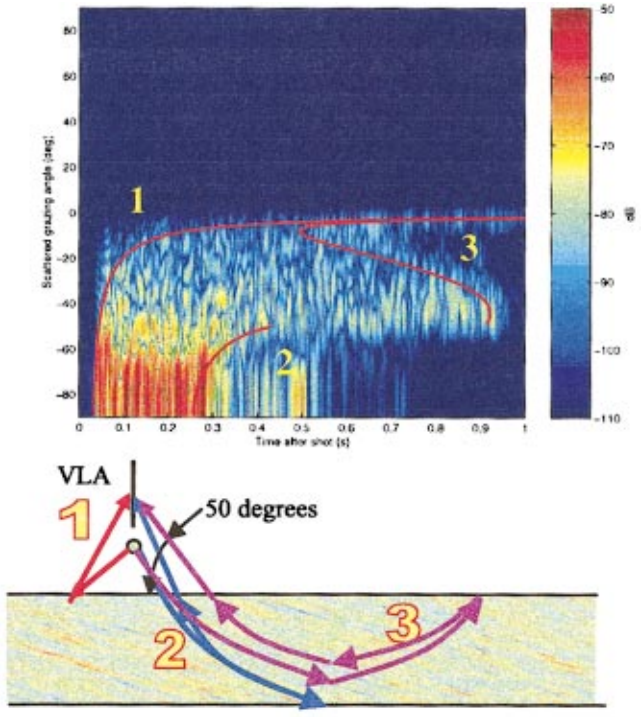

FIG. 10. Time–angle plot for example 1 with the sound speed gradient in the sediment of example 2. Here the effects of late-time resonance of the scattered field are evident in the lower right-hand side of the plot. Otherwise the results are nearly identical to those in Fig. 9.

terers no longer contribute to the backscatter after approximately 0.45 s, which is why this trajectory is shown cut off. At later times progressively shallower scatterers are excluded from contributing to the deep refracted path (**3**) until, finally, the scatterers at the top of the layer are excluded and the response cuts off. Comparison of these results with the iso-speed results in Fig. 4 clearly indicates that in the absence of interface discontinuities, the late time bifurcation and cutoff of the scattering are a dominant characteristic of scattering from a thick sediment with a strong sound speed gradient. The presence of this behavior, confirmed by the overlayed refractive raytrace results, is a unique identifying characteristic of upward refracting sediments. Provided further analysis confirms the observability and robustness of this phenomenon under real ocean conditions, it may provide opportunities for ''through-the-sonar'' environmental assessment concepts.

The combined effects of gradients and realistic interface contrasts are illustrated in Fig. 10, showing the beam–time response from the scattering layer in the case where the density contrasts from example 1 are restored. In this case multipath high-angle arrivals at intermediate time are observed persisting for grazing angles greater than 50 degrees for times between 0.3 and 0.6 s. However, at later times the

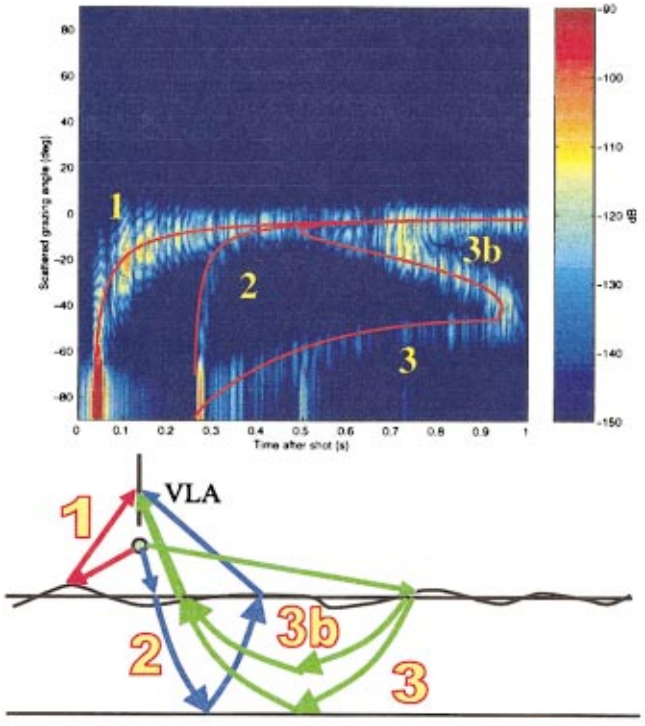

FIG. 11. Time–angle plot of rough surface scattering from the environment of example 1 with the layer sound speed gradient from example 2. Three branches of the backscattered response correspond to those for the iso-speed layer in Fig. 6, but the arrival times of the reflected branches (rays **2** and **3**) are significantly modified by the refractive properties of the waveguide. In addition a new upper branch to the refracted arrival (ray **3b**) is found. This branch corresponds to backscattered paths which have a turning point within the sediment and therefore do not reflect off the sediment–basement interface.

bifurcation and cutoff associated with the strong gradient are still the dominant feature.

The analogous result for rough surface scattering in the presence of the gradient is shown in Fig. 11. The overlayed time trajectories are similar to those in Fig. 6, but indicate the differences that refraction can make. While the general characteristics of the rough surface scattering result in Fig. 6 persist, an additional branch of arrival (**3**), denoted (**3b**), is noted. This branch corresponds to deep refracted backscattering. This path suffers an internal reflection, corresponding to a ray turning point, within the sediment layer. As with volume scattering, the presence of the deep refracted branch is an identifying characteristic of rough surface scattering from interfaces of strongly refractive sediments.

IV. CONCLUSIONS

Volume scattering realizations have been obtained for general layered media in two dimensions, including volume scattering from a layer with a sound speed gradient. Results show that the background characteristics of the waveguide can be as important as the scattering characteristics of the volume scatterers themselves in determining the temporal and angular characteristics of the scattered field. Multipath propagation of the scattered field can be an important effect, whether it is the reverberation of the scattered field within the scattering layer, or the more general refractive properties of the waveguide between the scattering volume and the source and receiver, which are often important in real waveguides.

The layered media formulation presented here has several advantages over a two half-spaces approach. The ability to include free surface effects when evaluating experimental configurations or results is a valuable asset. Also, cases where volume scatterers are dispersed through a general layered media can be evaluated more easily with the present approach. Finally, the treatment of layer gradients conforming to Airy function solution more appropriate under the multilayered approach. This is because half-spaces with these types of gradients have the unphysical property that all energy, no matter how high the propagation angle, is returned from the depth $z=-a/b$, where the sound speed becomes infinite. With the multilayered approach, these types of gradient layers can be truncated and a radiation condition applied before the caustic depth is reached.

The results shown here indicate that OASES has become a more flexible tool for evaluating scattering and reverberation scenarios with the volume scattering extension described in this article. Results show that volume scattering is quite distinguishable for surface scattering for the cases investigated. It is likely that the two mechanisms become increasingly difficult to separate from one another as the pulse width becomes large with respect to the layer thickness. These effects can now be explored in a unified model framework, with the flexibility that affords.

The modeling described here is the simplest generally used to describe volume reverberation. However, essential characteristics, including a two-dimensional roughness correlation structure to the scatterers, as well as sound speed and density scattering, and scattering in refractive layers, have all been treated so as to make the model as useful as possible to those wishing to design experiments or evaluate scenarios or data sets.

ACKNOWLEDGMENT

The MIT part of this work was funded by the Office of Naval Research, Ocean Acoustics Program under Contract No. N00014-97-1-0202.

[1] P. C. Hines, ''Theoretical model of acoustic backscatter from a smooth seabed,'' J. Acoust. Soc. Am. **88**, 324–334 (1990).
[2] P. C. Hines, ''Theoretical model of in-plane scatter from a smooth sediment seabed,'' J. Acoust. Soc. Am. **99**, 836–844 (1996).
[3] A. N. Ivakin and Y. P. Lysanov, ''Theory of underwater sound scattering by random inhomogeneities of the bottom,'' Sov. Phys. Acoust. **27**, 61–64 (1981).
[4] D. Tang, ''Acoustic Wave Scattering from a Random Ocean Bottom,'' doctoral dissertation, MIT-WHOI Joint Program, WHOI-91-25, June 1991.
[5] P. D. Mourad and D. R. Jackson, ''A model/data comparison for low frequency bottom backscatter,'' J. Acoust. Soc. Am. **94**, 344–358 (1996).
[6] B. H. Tracey and H. Schmidt, ''A self-consistent theory for seabed volume scatter,'' J. Acoust. Soc. Am. **106**, 2524–2534 (1999).
[7] D. R. Jackson and A. N. Ivakin, ''Scattering from elastic sea beds: First-order theory,'' J. Acoust. Soc. Am. **103**, 336–345 (1998).
[8] A. N. Ivakin and D. R. Jackson, ''Effects of shear elasticity on sea bed scattering: Numerical examples,'' J. Acoust. Soc. Am. **103**, 346–354 (1998).
[9] A. N. Ivakin, ''A unified approach to volume and roughness scattering,'' J. Acoust. Soc. Am. **103**, 827–837 (1998).
[10] D. Tang, ''A note on scattering by a stack of rough interfaces,'' J. Acoust. Soc. Am. **99**, 1414–1418 (1996).
[11] H. Schmidt, ''SAFARI: Seismo-acoustic fast field algorithm for range independent environments. User's Guide,'' Rep. SR-113 (SACLANT Undersea Research Centre, La Spezia, Italy, 1988).
[12] H. Schmidt, ''OASES Version 2.2: User Guide and Reference Manual,'' Massachusetts Institute of Technology, 1999.
[13] H. Schmidt and W. Kuperman, ''Spectral representations of rough interface reverberation,'' J. Acoust. Soc. Am. **97**, 2199–2209 (1995).
[14] H. Schmidt and J. Lee, ''Physics of 3-D scattering from rippled seabeds and buried targets in shallow water,'' J. Acoust. Soc. Am. **105**, 1605–2617 (1999).
[15] A. Maguer, W. L. J. Fox, H. Schmidt, E. Pouliquen, and E. Bovio, ''Mechanisms for subcritical penetration into a sandy bottom: Experimental and modeling results,'' J. Acoust. Soc. Am. **107**, 1215–1225 (2000).
[16] C. W. Holland, R. Hollett, and L. Troiano, ''Bottom scattering measurements in shallow water,'' Rep. SM-364 (SACLANT Undersea Research Centre, La Spezia, Italy, 1999).
[17] F. B. Jensen, W. A. Kuperman, M. B. Porter, and H. Schmidt, *Computational Ocean Acoustics* (Springer, New York, 2000).
[18] K. D. LePage and H. Schmidt, ''Spectral integral representations of scattering from volume inhomogeneities,'' Rep. SM-363 (SACLANT Undersea Research Centre, La Spezia, Italy, 1999).
[19] C. D. Jones and D. R. Jackson, ''Integral equation method for bistatic volume scattering from the seafloor,'' J. Acoust. Soc. Am. **103** (Pt. 2), 3061 (1998).
[20] D. H. Berman, ''Reverberation in waveguides with rough surfaces,'' J. Acoust. Soc. Am. **105**, 672–686 (1999).
[21] Z. Schulten, D. G. M. Anderson, and R. G. Gordon, ''An algorithm for the evaluation of the complex Airy functions,'' J. Comput. Phys. **31**, 60–75 (1979).
[22] A. D. Pierce, *Acoustics—An Introduction to its Physical Principles and Applications* (McGraw-Hill, New York, 1981).

Acoustic measurements of boundary layer flow and sediment flux

Peter D. Thorne[a)]
Proudman Oceanographic Laboratory, Bidston Observatory, Birkenhead, Merseyside CH43 7RA, United Kingdom

Jon Taylor
School of Environmental Sciences, University of East Anglia, Norwich, Norfolk NR4 7TJ, United Kingdom

(Received 17 August 1999; revised 5 June 2000; accepted 14 June 2000)

Results are reported on an assessment of the application of coherent Doppler and cross-correlation techniques to measure nearbed boundary layer flow. The approaches use acoustic backscattering from sediments entrained into the water column from the bed, to obtain high-resolution profiles of the nearbed hydrodynamics. Measurements are presented from a wave tunnel experiment in which sediment was entrained by unidirectional, oscillatory, and combined flows. The data collected have been used to evaluate the capability of the two flow techniques to measure boundary layer mean, turbulent, and intrawave velocity profiles. Further, the backscattered signal has been used to measure suspended sediment concentration profiles, which have been combined with the velocity profiles to obtain high-resolution measurements of boundary layer sediment flux.
 [S0001-4966(00)03609-2]

PACS numbers: 43.30.Ft, 43.30.Gv, 43.30.Pc, 43.30.Xm [DLB]

I. INTRODUCTION

Over the past decade the application of single and multifrequency acoustic backscatter systems, ABS, to the measurement of suspended sediment concentration and particle size, has become an increasingly accepted methodology by marine sedimentologists.[1–6] These systems typically operate at frequencies between 0.5 and 5 MHz, are normally mounted about 1 m above the bed, and provide centimetric resolution measurements of suspension profiles in the nearbed boundary layer region. Acoustics has significant advantages over traditional measurement methods because it is nonintrusive, uniquely provides profiles of the suspension, typically to within a centimeter of the bed, with sufficient temporal resolution to allow an examination of intrawave and turbulent suspension processes, and also provides a measurement of the bed location and its variation over time.

It has, however, been recognized for some time that to fully realize the potential of the acoustic backscatter measurements, complementary observations of the hydrodynamics of the boundary layer with similar temporal and spatial resolution would be of significant benefit. To this end the potential of using coherent Doppler and cross-correlation methods have been examined in recent years, and the results from these approaches are beginning to emerge.[7–11] These techniques use the same backscattered signal as the ABS systems, and therefore colocated velocity and suspension profiles, and hence direct measurements of boundary layer sediment flux should in principal be obtainable. The correlation approach employs pairs of horizontally separated transducers directed vertically downward. The assumption is made that there are structures in the suspension field, which have sufficient temporal coherence, that a transducer pair record comparable backscattered signals as the sediments advect beneath them. These signals are cross-correlated, and the advection lag obtained, from which the velocity profile can be calculated. The approach is inherently incoherent with only the backscattered amplitude being used to obtain vertical profiles of the horizontal current. The coherent Doppler technique, on the other hand, is based on pulse-to-pulse coherence between successive transmissions, and utilizes the rate of change of phase of the backscattered signal to measure the radial component of the velocity profile along the transducer beam axis. In this case the assumption is made that there is sufficient continuity in the relative particle locations within the insonified volume, that the phase change of the backscattered signal between consecutive transmissions is associated with a bodily movement of the scattering particles toward or away from the insonifying transducer. Since the coherent approach utilizes within signal phase changes, it potentially offers substantially higher temporal resolution than the cross-correlation approach.

To date, reported assessments of both the coherent Doppler and the cross-correlation approaches have primarily been made under conditions of unidirectional flow, with the focus generally being on an evaluation of accuracy and mean flow measurements, although some detailed coherent Doppler temporal mapping of the flow field has been presented.[12] In the present study the analysis of the two techniques has been extended to cover conditions of unidirectional, oscillatory, and combined flow, and the capability of the two methods to measure mean, turbulent, and intrawave flow has been assessed under laboratory conditions. To assess the acoustic flow measurements, a laser Doppler system was used as the absolute velocity reference. Further, acoustic measurements of suspended sediment concentration profiles were obtained from the backscattered signal, and these profiles have been combined with the flow data to obtain boundary layer sedi-

[a)]Electronic mail: pdt@pol.ac.uk

ment flux profiles. The present study focuses on the capability of acoustics to measure contemporaneous colocated boundary layer hydrodynamics and sediment dynamics. Sedimentological analysis of the observed processes is not central to the present report, and is deferred to future works.

II. MEASUREMENT PRINCIPLES

A. Coherent Doppler velocity profiler, CDVP

To obtain velocities with both high temporal and spatial resolution, a coherent Doppler approach was used. This method utilizes the rate of change of phase from consecutive transmissions to obtain the Doppler frequency. In the present study a commonly used pulse-pair technique[7,8] was employed. This approach leads to a Doppler frequency, f_d, which can be expressed as

$$f_d = \frac{1}{2\pi\tau}\tan^{-1}\left\{\frac{\langle I(t)R(t+\tau) - R(t)I(t+\tau)\rangle}{\langle R(t)R(t+\tau) + I(t)I(t+\tau)\rangle}\right\}, \tag{1}$$

where $R(t)$ and $I(t)$ are the in-phase and quadrature components of the backscattered signal, τ is the time between transmissions, and $\langle\ \rangle$ represents an average over a number of pulse pairs. For the condition $v_d \ll c$,

$$v_d = \frac{c f_d}{2 f_0}, \tag{2}$$

where v_d is the Doppler velocity, c is the velocity of sound in water, and f_0 is the transmit frequency. To obtain unambiguous range information $\tau \leqslant 2r_m/c$, where r_m is the maximum operating range, and since the maximum unaliased value for f_d is $f_d \leqslant 1/2\tau$, this leads to the standard range velocity ambiguity equation

$$r_m \cdot v_{dm} \leqslant \frac{c^2}{8 f_0}, \tag{3}$$

where v_{dm} is the maximum unaliased velocity. The present system was limited to a minimum value for τ of 2.13 ms, and the transmission frequency was 526 kHz. The maximum unaliased value for f_d was therefore 235 kHz, which with Eq. (2) and using $c = 1480\ \mathrm{ms}^{-1}$, gives $v_{dm} = 0.33\ \mathrm{ms}^{-1}$. Using this value for v_{dm} in Eq. (3) gives $r_m = 1.57$ m; the actual maximum operating range employed was 1.28 m. In the data analysis, however, phase tracking was used to unwrap the phase and de-alias the velocities. Therefore the upper velocity limit was greater than 0.33 ms^{-1}, and radial velocities of up to 0.8 ms^{-1} were phase tracked and measured.

B. Cross-correlation velocity profiler, CCVP

Unlike the coherent Doppler technique, which utilizes the phase coherence between successive transmissions, the cross-correlation approach simply uses the amplitude of the backscatter signal from pairs of transducers. The basic requirement is that there is sufficient temporal coherence in the suspension field that two horizontally separated transducers will observe comparable concentration fluctuations. The method is seen as complementary to the coherent Doppler approach.

The ensemble-average square backscattered pressure, P^2, from a suspension of incoherent scatters, for a transceiver can be written as[13–16]

$$P^2 = \left\{\frac{K_s K_t}{r\psi}\right\}^2 M e^{-4\{r\alpha_\omega + \int_0^r \zeta M dr\}}. \tag{4}$$

K_t is a system-dependent constant, K_s is a function of the scattering properties of the suspended sediment, M is the suspended sediment concentration, r is the range from the transducer, ψ accounts for the departure from spherical spreading within the transducer nearfield, α_ω is the water attenuation, and ζ is the sediment attenuation constant. It is the fluctuations in M, measured through P^2, that are used in the correlation approach. Using the backscattered signals from a transducer pair, the cross-correlation function, $R_{12}(\nu)$, at range r, is given by

$$R_{12}(\nu) = \int_{-\infty}^{\infty} P_1^2(t,r) P_2^2(t+\nu,r)\, dt, \tag{5}$$

where $P_1^2(t,r)$ and $P_2^2(t+\nu,r)$ are the zero mean backscattered ensemble-average square pressures from the transducer pair, and ν is the cross-correlation lag. For the present work the normalized cross-correlation function, $\rho_{12}(\nu)$, was used; this is given by

$$\rho_{12}(\nu) = \frac{R_{12}(\nu)}{\sqrt{R_{11}(0)R_{22}(0)}}. \tag{6}$$

The time lag at which the normalized cross-correlation function reaches its maximum value is expressed as

$$\rho_{12}(\nu^*) = \max(\rho_{12}(\nu)). \tag{7}$$

The cross-correlation velocity, v_c, is given by

$$v_c = \frac{d_{12}}{\nu^*}, \tag{8}$$

where d_{12} is the transducer pair separation. An estimate for the error in the cross-correlation measurements, is given by[9,17]

$$\sigma(v_c) = \left|\frac{-d_{12}}{\nu^{*2}}\right|\left\{\frac{0.038(2\varepsilon_{12})^3}{T}\left(\frac{1}{\rho_{12}^2(\nu^*)} - 1\right)\right\}^{1/2}, \tag{9}$$

where T is the record length, and ε_{12} is the width of the cross-correlation function $\rho_{12}(\nu)$ at $2/\pi$ of the maximum value $\rho_{12}(\nu^*)$.

Using Eq. (8), the maximum and minimum velocities and resolution can be estimated. Differentiating Eq. (8) and taking the magnitude gives

$$\frac{dv_c}{d\nu} = \frac{v_c^2}{d_{12}}. \tag{10}$$

The correlation time discrimination is $\pm\delta\nu/2$, where $\delta\nu$ is the time interval between consecutive transmission. The fractional velocity discriminator can therefore be written as

$$\frac{\delta v_c}{v_c} = \frac{v_c \delta\nu}{2 d_{12}}. \tag{11}$$

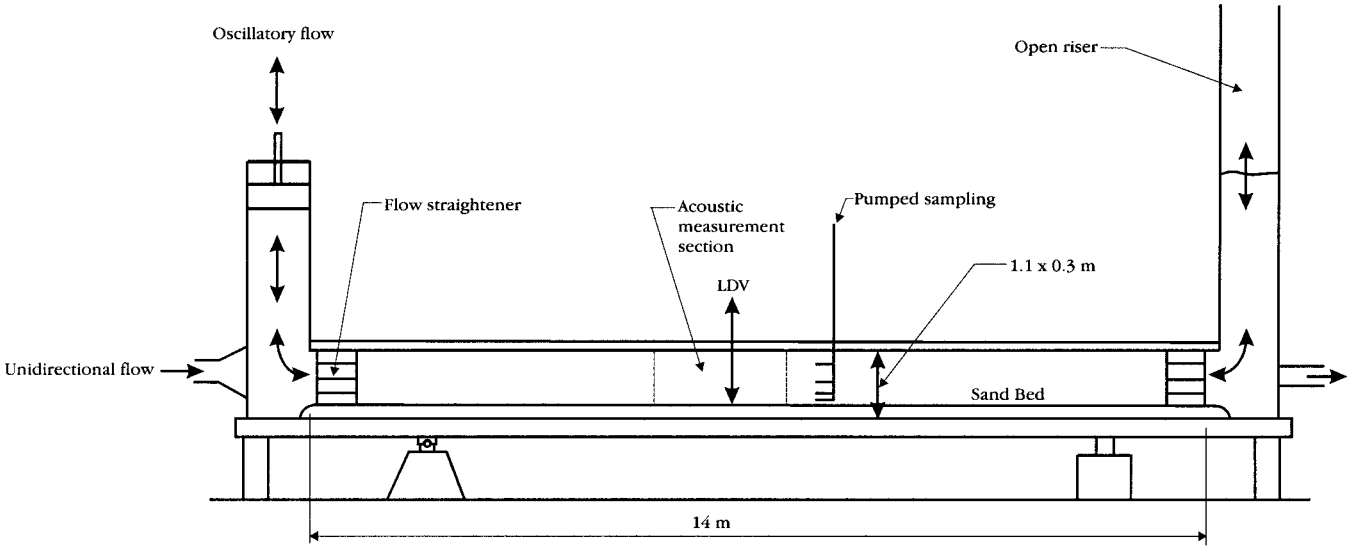

FIG. 1. Schematic of the wave tunnel showing the piston for the oscillatory flow, the input of the unidirectional flow, and the locations of the acoustics, the LDV, and the pumped sample measurements.

In the present study various $\delta\nu$ and d_{12} were used; however, using typical values of $\delta\nu = 2.10^{-3}$ s and $d = 0.1$ m, gives $\delta v / v_c = 0.01 v_c$. Therefore if a resolution of 1% is required, the maximum velocity would need to be 1 m s^{-1} or less. The minimum velocity is given by the maximum value of $\nu^*_{\max}$ which must be less than the record length; therefore,

$$v_{c(\min)} \leqslant \frac{d_{12}}{\nu^*_{\max}}. \tag{12}$$

Present records were typically 60 s, and again using $d = 0.1$ m gives a minimum measurable velocity of 0.0017 m s^{-1}. However, this system minimum velocity is of little consequence because significantly higher velocities are required to suspend the sediments used in the present work.

C. Concentration profiles

Recent developments on the interaction of sound with suspensions of marine sediments have provided a theoretical framework for interpreting the backscattered signal.[13–16] To obtain suspended sediment concentration and particle size from the backscattered pressure, the usual methodology for inverting Eq. (4) has been to use an implicit iterative solution.[16] However, for the present work use is made of suspended sediment pumped samples collected during the experiment, and this allowed an explicit inversion method to be employed. This method has been previously described,[18] and is briefly summarized here for completeness. Taking the natural logarithm of Eq. (4) and differentiating gives a nonlinear differential equation of the Bernoulli type

$$M' - M\gamma = 4\zeta M^2, \tag{13}$$

$$\gamma = 2\left\{\frac{P'}{P} + \frac{1}{r} + \frac{\psi'}{\psi} - \frac{k_s'}{k_s}\right\} + 4\alpha_\omega, \tag{14}$$

where the prime denotes differentiation with respect to range. Equation (13) reduces to a first-order linear equation by the substitution $z = M^{1-n}$, where n is the power to which M is raised on the right-hand side of Eq. (13), i.e., $n = 2$ and $z = 1/M$. Applying this substitution gives

$$z' + \gamma z = -4\zeta. \tag{15}$$

This can now be solved using the standard integrating factor method[19] and gives

$$z e^{\int \gamma dr} = -\int 4\zeta e^{\int \gamma dr} dr. \tag{16}$$

The integral for γ is readily evaluated and results in

$$M = \frac{\chi^2}{(\chi_0^2/M_0) - \int_{r_0}^{r} 4\zeta\chi^2 dr}, \quad \chi = \{P\psi r/k_s\} e^{2r\alpha_\omega}, \tag{17}$$

where at range r_0, $\chi_0 = \chi(r_0)$ and $M_0 = M(r_0)$. In the present work M_0, and the dependence of k_s and ζ on particle size with height above the bed, were obtained from pumped sample measurements.

Equation (17) provides mean concentration profiles; however, to examine concentration fluctuations at the turbulent and intrawave time scales K_t needs to be evaluated. Since the mean concentration profile can be obtained from Eq. (17), Eq. (4) can be used to provide K_t using

$$K_t = \chi_0 M_0^{-1/2} \exp 2\left\{ r_0\alpha_w + \int_0^{r_0} \zeta M dr \right\}. \tag{18}$$

Using the value of k_t derived from the mean concentration profiles, Eq. (4) can be rearranged to make M the dependent variable on the left-hand side of the equation, and an implicit iterative solution used with the mean particle size profile from the pumped sample measurements to obtain the required high temporal resolution concentration profiles.

III. EXPERIMENTAL ARRANGEMENT

The measurements were collected in September 1997, using the large-scale oscillating wave tunnel, at Delft Hydraulics, De Voorst Laboratories in The Netherlands. Figure 1 shows a diagram of the facility. The tunnel's measurement

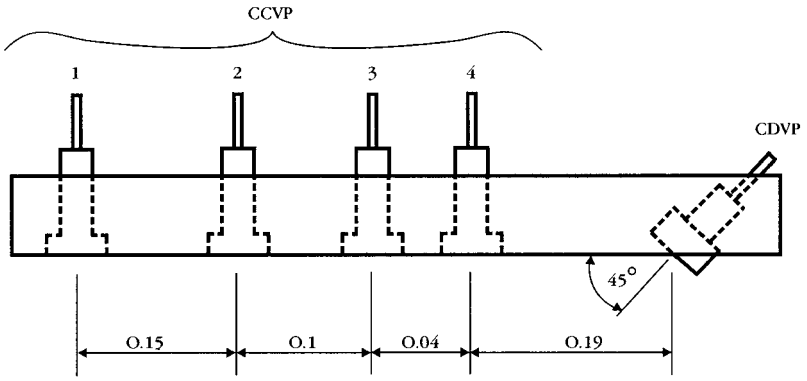

FIG. 2. Diagram of the top plate showing the positions of the cross-correlation, CCVP transducers, and the coherent Doppler, CDVP, transducer.

section was 14 m long, 0.3 m wide, and 1.1 m deep. The tunnel is configured as a vertical U-tube with a piston in one riser and with the other riser open to the atmosphere. The upward and downward motion of the piston generated an oscillatory horizontal flow in the measurement section. In addition to the oscillatory flow, unidirectional currents could be obtained using a recirculating pump system. This allowed unidirectional, oscillatory, and combined flows to be generated. The tunnel was capable of providing oscillatory flow with periods between 2–16 s, with a maximum orbital velocity of 1.8 m s^{-1}, and unidirectional currents of up to 0.7 m s^{-1}. For the flow experiments reported here, a 0.3-m-thick bed of fine sand with a median grain diameter of $d_{50} = 130\,\mu$m was placed along the base of the tunnel. The sediment was suspended by the currents, and the backscattered signal used to measure velocity and concentration profiles.

The top of the 14-m wave tunnel measurement section consisted of a series of steel plates. To conduct the acoustic measurements a series of transducers were set into one of the tunnel top plates approximately halfway along the tunnel. This is shown in Fig. 2. The cross-correlation velocity profile measurements were collected on four 2-MHz transducers, 1–4, with separations of $d_{12}=0.15$, $d_{23}=0.1$, and $d_{34} = 0.04$ m. The transducers were directed vertically downward, located at 0.8 m above the bed, and aligned centrally along the flume axis. A 526-kHz transducer was used to obtain the coherent Doppler velocity profile measurements; this was aligned at 45° to the vertical. For both measuring systems the backscattered signals were digitized at 75.232 kHz, thereby providing a range sampling interval of 0.01 m. The maximum operating range was 1.28 m. The pulse repetition frequency was 471 Hz and the pulse length was normally 15 μs. For the CDVP measurements, the in-phase, quadrature, and amplitude of the backscattered signal were recorded, while for the CCVP only the latter measurement was collected. To reduce the statistical variability of the measured velocities f_d was obtained using 32 pulse-pair samples,[8] and the CCVP data employed a 0.1-s running average on the individual backscattered samples to reduce configuration noise.[2,14]

To assess the acoustic flow measurements, concurrent laser Doppler velocity, LDV, measurements were collected. This provided 50-Hz measurements of the vertical and horizontal flow components. The acoustic and laser velocity measurements were synchronized using an output gate from the acoustic system which was logged with the laser measurements. To make comparisons with the acoustic velocity profiles, the laser Doppler system was traversed vertically to obtain data at a number of heights above the bed. Pumped sampling of the suspended sediments was also taken concurrently with some of the acoustic measurements and these have been used in the evaluation of Eqs. (17) and (18).

IV. MEASUREMENTS AND RESULTS

As mentioned in the previous section, measurements were collected under conditions of unidirectional, oscillatory, and combined flow, for a number of currents and oscillatory velocity amplitudes and periods. A representative selection of the data is presented here which covers the range of flows used to assess the acoustic measurements.

A. Unidirectional flow

1. Mean measurements

Measurements were collected for nominal flow rates of 0.3, 0.5, and 0.7 m s^{-1}. Below 0.3 m s^{-1}, the suspension levels were too low to extract velocity profiles. For each flow rate acoustic data were collected for a period of 60 s, and four runs were carried out at each flow rate.

The results from the CDVP measurements are shown in Fig. 3. Figure 3(a) shows vertical profiles of the mean horizontal flow. The data points are the average velocity from the four 60-s runs, and the error bars are the standard deviation obtained from the four mean velocity profiles collected at each flow rate. The first 10 cm below the top plate were not used to extract velocities due to breakthrough from the transmitter to the receiver electronics. The velocity profiles clearly show the expected trend, with reductions in flow near the steel plates on the upper surface of the tunnel and toward the sand bed. The mean normalized standard error, $\langle \sigma(v_d)/v_d \rangle$, where $\langle\ \rangle$ represents an average over the profile, was calculated for each flow rate and gave values, respectively, of 0.029, 0.016, and 0.012 at 0.3, 0.5, and 0.7 m s^{-1}. These low normalized standard deviations demonstrate the internal consistency of the data over the four runs at each flow rate. It can be seen that near the boundaries the error bars increase, particularly close to the sediment bed; however, this could in part be due to actual flow variability associated with turbulence near the bed. Similar analysis on LDV data, collected at 0.4 m above the bed at 0.5 and 0.7 m s^{-1}, gave $\sigma(v_l)/v_l$ values of 0.0035 and 0.0041. These appear to be considerably lower than the CDVP values; how-

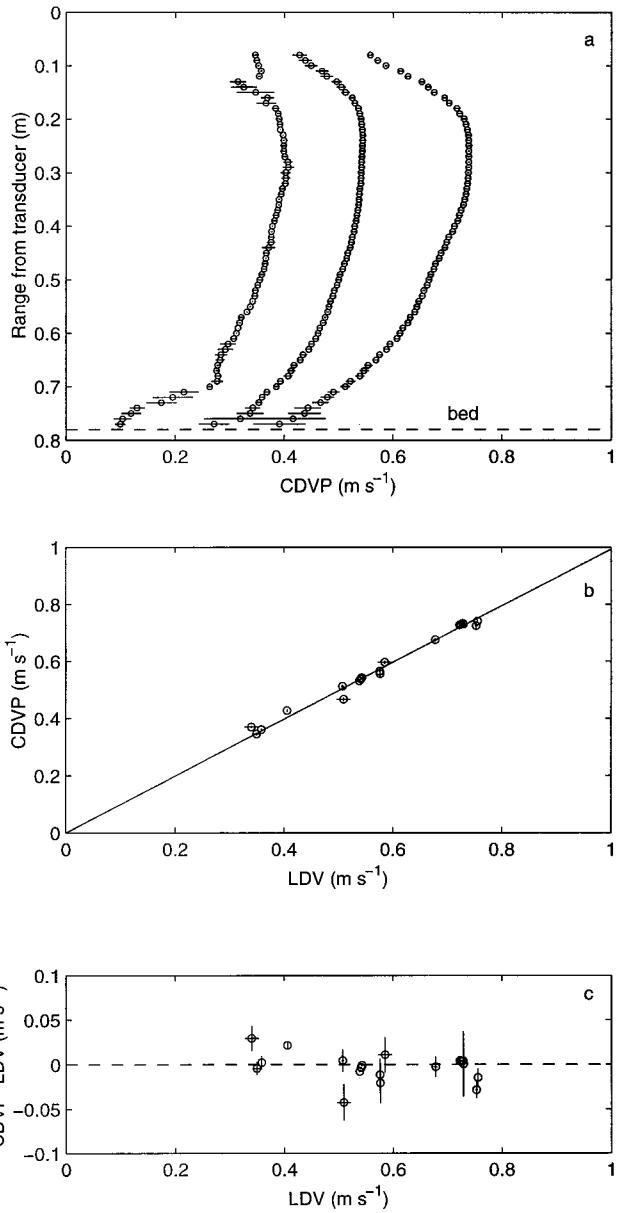

FIG. 3. (a) Coherent Doppler velocity profiles for unidirection flows of nominally 0.3, 0.5, and 0.7 m s^{-1}. (b) Regression plot of the coherent Doppler and laser Doppler measurements. (c) Plot of the difference between the coherent Doppler and laser Doppler measurements against the measured laser velocity.

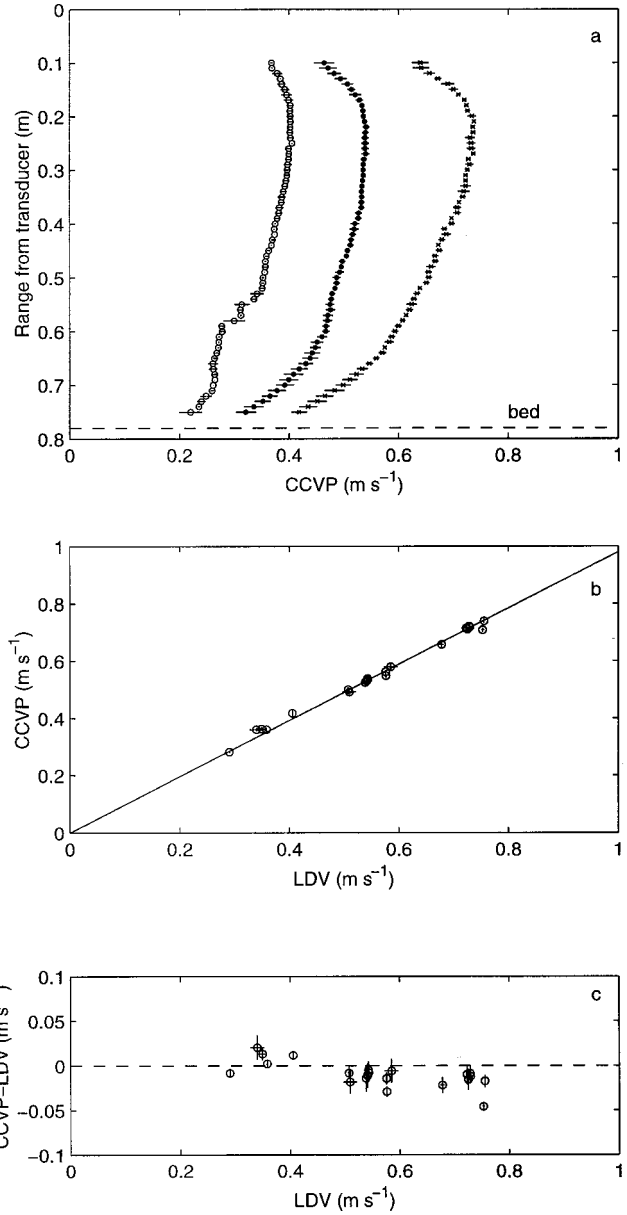

FIG. 4. (a) Cross-correlation velocity profiles for unidirectional flows of nominally 0.3, 0.5, and 0.7 m s^{-1}. (b) Regression plot of the cross-correlation and laser Doppler measurements. (c) Plot of the difference between the cross-correlation and laser Doppler measurements against the measured laser velocity.

ever, if the CDVP measurements coincident with the LDV are chosen, $\sigma(v_{d40})/v_{d40}$, this give values of 0.0085, 0.0089, and 0.0036 at 0.3, 0.5, and 0.7 m s^{-1}, respectively. The CDVP values of $\sigma(v_{d40})/v_{d40}$ are therefore comparable to the LDV values, and suggest for the velocities covered here that the instrumental normalized standard deviation was of the order of 0.005. In Fig. 3(b) a regression plot of v_d against v_l is presented. This shows data with error bars derived from repeated runs under the same conditions. Using normal axis regression gave a regression equation of $v_d=(0.993 \pm 0.03)v_l$, where the error is at the 95% confidence limits, and with a regression coefficient of 0.994. The regression equation gradient is well within the confidence limits for unity, and using the standard student's t distribution test[20] the possibility of obtaining the regression coefficient by chance was less than 0.1%. To assess in detail velocity differences, Fig. 3(c) shows a plot of v_d-v_l with v_l. The plot shows the data scattered about the line $v_d-v_l=0$, with 70% of the measurements lying within the region $|v_d-v_l| \leqslant 0.01\,\mathrm{m\,s^{-1}}$, and with a mean difference between v_d and v_l of $-0.003 \pm 0.016\,\mathrm{m\,s^{-1}}$.

The CCVP data were collected under similar conditions to the CDVP, and the same analysis has been used. For the CCVP the different runs were associated with a different transducer pair separation, $d_{34}=0.04$, $d_{23}=0.1$, $d_{12}=0.15$, and $d_{14}=0.29$ m. The results from the d_{34} transducer pair had noticeably more variability than the other transducer's pairs. The source of this error has been discussed elsewhere,[9] therefore the results presented here are associated with the d_{12}, d_{23}, and d_{14} measurements. The outcome of the analy-

sis is shown in Fig. 4. In Fig. 4(a) the average velocity profiles are presented, with error bars derived from the mean velocity profiles obtained for the three transducer pair separations. As with the CDVP, the trend in velocity is as anticipated, and again the standard deviation in the velocity estimates is seen to increase near the flow boundaries. The values for $\langle \sigma(v_c)/v_c \rangle$ were 0.015, 0.017, and 0.019, respectively, for flow rates of 0.3, 0.5, and 0.7 $\mathrm{m\,s^{-1}}$. These relatively small standard errors show the consistency of the velocity measurements for the three transducer pair separations. This was confirmed by detailed analysis of ϵ_{12} and $\rho_{12}(\nu^*)$, which showed only marginal changes as the transducer pair separation varied between 0.04 and 0.29 m, and hence from Eq. (9) a nominally constant or reducing $\sigma(v_c)$ was to be expected. The values for $\langle \sigma(v_c)/v_c \rangle$ are, as with the CDVP, greater than $\langle \sigma(v_l)/v_l \rangle$; however, if as before, like is compared with like, the values for $\sigma(v_{c40})/v_{c40}$ are 0.011, 0.011, and 0.0077 for flow rates of 0.3, 0.5, and 0.7 $\mathrm{m\,s^{-1}}$. This is larger than the LDV values, and suggests for the CCVP an indicative value for $\sigma(v_c)/v_c$ of the order of 0.01. Figure 4(b) shows a regression of v_c against v_l. Again a normal axis regression was carried out which gave $v_c = (0.980 \pm 0.026) v_l$ with a regression coefficient of 0.997. As with the CDVP results the regression coefficient is highly significant, and the gradient of the line is not significantly different from unity. The final Fig. 4(c) shows a plot of $v_c - v_l$; the data are scattered about the line $v_c - v_l = 0$, although with some tendency to lie beneath the line for larger v_l. Examination shows that 70% of the data lie in the region $|v_c - v_l| \leq 0.02\ \mathrm{m\,s^{-1}}$ with a mean difference between v_c and v_l of $-0.0097 \pm 0.014\ \mathrm{m\,s^{-1}}$.

2. Turbulence measurements

The previous section assessed the capability of the coherent Doppler and cross-correlation techniques to measure vertical profiles of mean horizontal current flow. The present section examines the capability of the two methods to measure boundary layer turbulence, the aim being to establish if accurate turbulence measurements can be obtained with such systems at the typical sampling rates used in marine boundary layer studies.

We consider the CCVP first since it can readily be shown that it is not possible to measure turbulence with an incoherent cross-correlation system. This is simply demonstrated by the results in Fig. 5. This shows results for $\sigma(v_c)/v_c$ obtained from a number of runs at different velocities as the cross-correlated record length was reduced to increase the temporal resolution of the velocity measurement. The measured values for $\sigma(v_c)/v_c$ are given by the open circles and the predicted values from Eq. (9) are shown by the crosses. It can be seen that the predicted and observed normalized standard deviations are in reasonable agreement, although the predicted error overestimates the measured error for the longer record lengths. However, the salient feature for this analysis is the rapid increase in the value for $\sigma(v_c)/v_c$ as the record length decreased. A similar analysis for the LDV gave values of $\sigma(v_l)/v_l \approx 0.02$; therefore, the significant increase in $\sigma(v_c)/v_c$ with record length was not due to turbulent velocity fluctuations, but arose from the

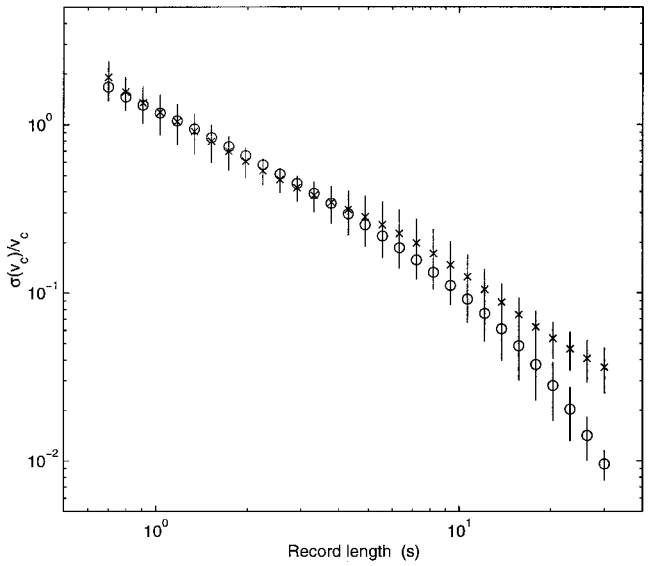

FIG. 5. Measurement (○) and prediction (×) of the normalized standard error $\sigma(v_c)/v_c$ as the cross-correlation record length reduced.

measurement method. The results clearly demonstrate that the turbulence in the flow cannot be measured using an incoherent cross-correlation approach.

For the coherent Doppler the results were different, and the values for $\sigma(v_d)/v_d$ as the record length was reduced were comparable to those from the LDV. Therefore an assessment of the turbulent flow measurements was carried out. The common sampling frequency used in the marine environment to measure turbulence is of the order of 5 Hz, and therefore the velocity time series from the CDVP and LDV were Fourier transformed, a window applied with a cutoff frequency of 2.5 Hz, the resulting spectra inverse Fourier transformed, and the data resampled. This allowed direct high temporal resolution comparisons between the CDVP and LDV measurements to be conducted.

The turbulent component of velocity is defined as $v' = v - \langle v \rangle$, where v was the measured velocity and $\langle v \rangle$ was the mean velocity over the run, the duration of which was typically 60 s. Since the CDVP measured radial velocity, and the transducer was angled at 45°, the turbulent flow comparisons used the vertical and horizontal flow components measured by the LDV and these were combined to give the flow along the radial direction of the CDVP. Examples of typical turbulent flow measurements are presented in Fig. 6. The solid line and the solid line with solid circles are, respectively, the LDV and the CDVP measurements. The CDVP measurements have been offset by $-0.05\ \mathrm{m\,s^{-1}}$ for clarity. Visual inspection of the data clearly shows significant similarities between the CDVP and LDV turbulent velocity time series. To quantify the degree of similarity a number of analyses have been carried out. First, the data from a number of runs were plotted as a scatter plot and a normal axis regression applied to the data. The result is shown in Fig. 7(a). The regression equation for the turbulence data gave $v'_d = \{0.87 \pm 0.02\} v'_l$, and with a regression coefficient of 0.79. Root-mean-square (rms) turbulent velocities, v'_{rms}, were calculated for the time series data in Fig. 7(a) and for other runs, and these gave $v'_{d_{\mathrm{rms}}}/v'_{l_{\mathrm{rms}}} = 0.91 \pm 0.06$. Both the regression

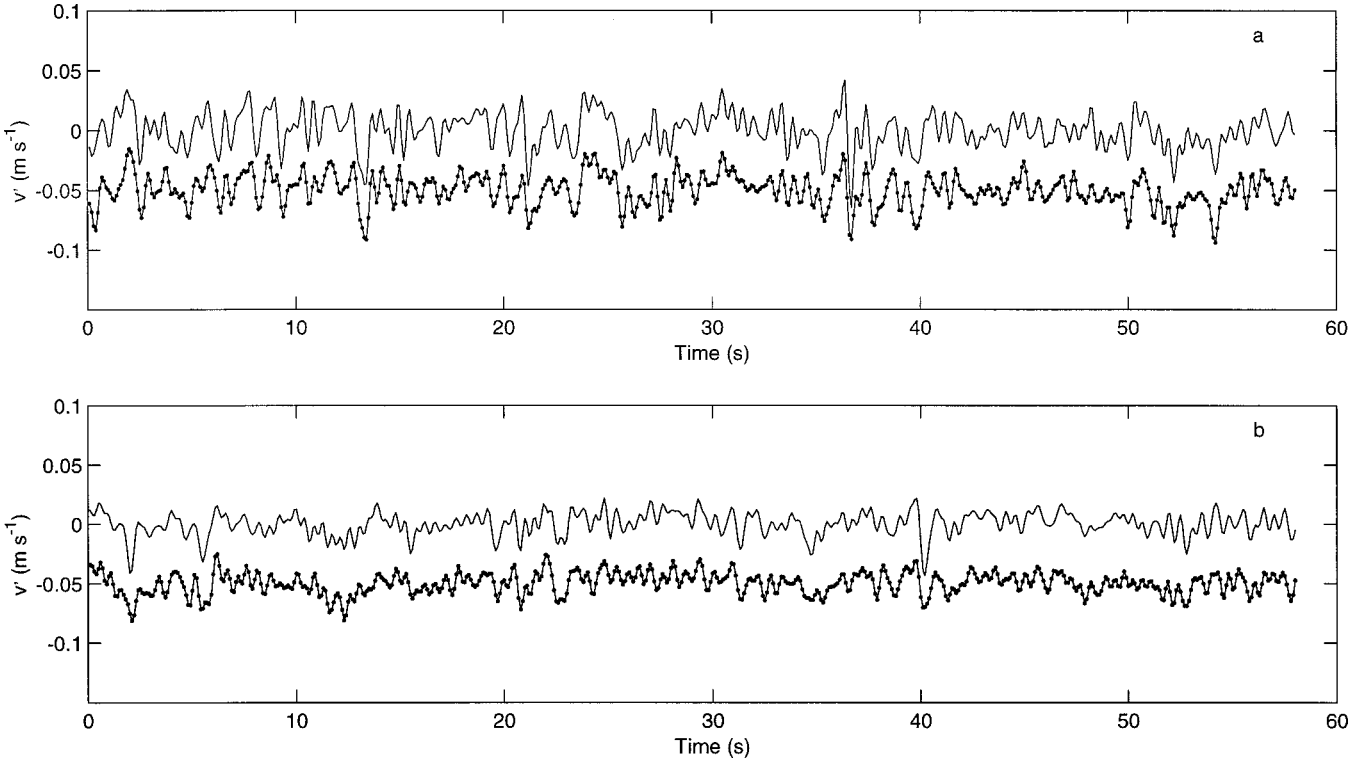

FIG. 6. High temporal resolution turbulent velocity measurements, — LDV, –•–•– CDVP. (a) and (b) are for two different experimental runs with nominal mean velocities of 0.7 and 0.5 m s^{-1}, respectively. The CDVP data have been offset by -0.05 m s^{-1}.

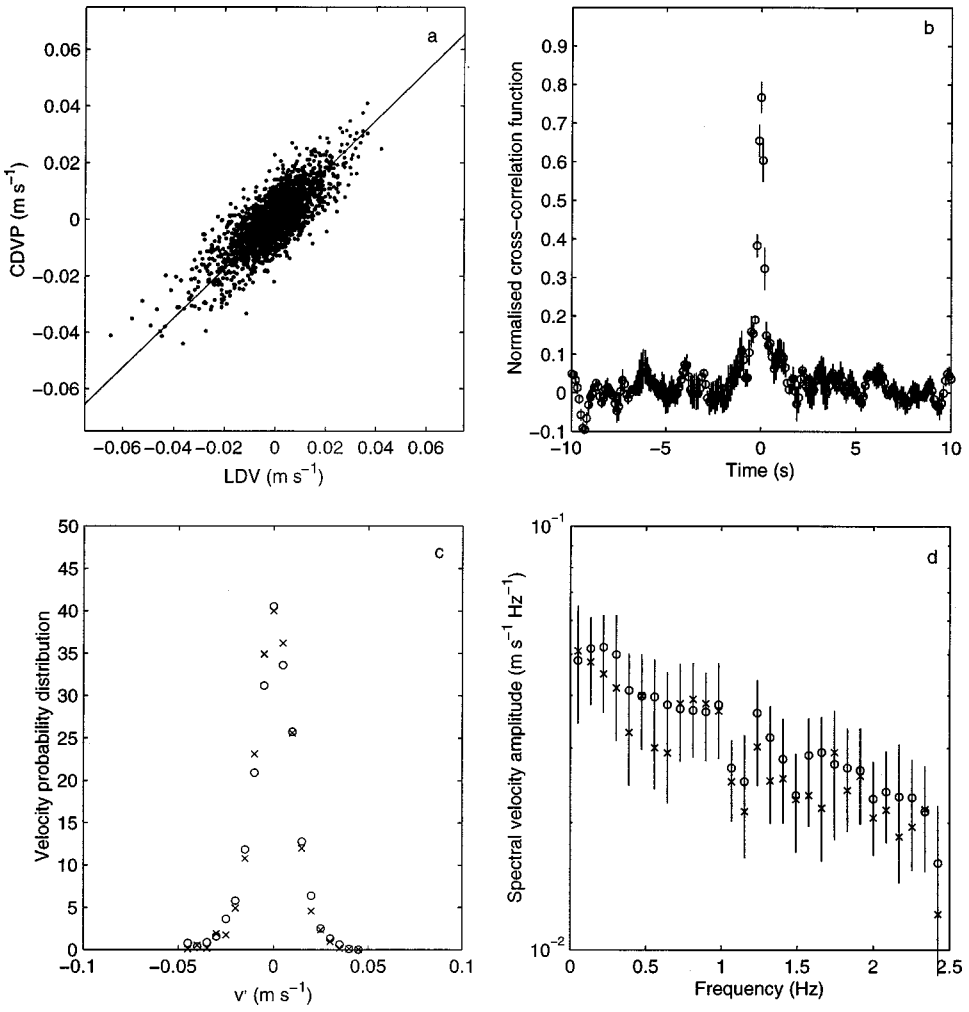

FIG. 7. (a) Regression plot of the coherent Doppler data and the laser Doppler data for turbulent velocity measurements from a number of experimental runs. (b) The mean cross-correlation function of the turbulent velocity from a number of runs for the coherent Doppler and laser Doppler data. (c) The mean probability density distribution for the turbulent velocity from the coherent Doppler profiler (×) and the laser Doppler (○) from a number of experimental runs. (d) Measurement of the turbulent spectra averaged over a number of experimental runs from the coherent Doppler profiler (×) and the laser Doppler (○).

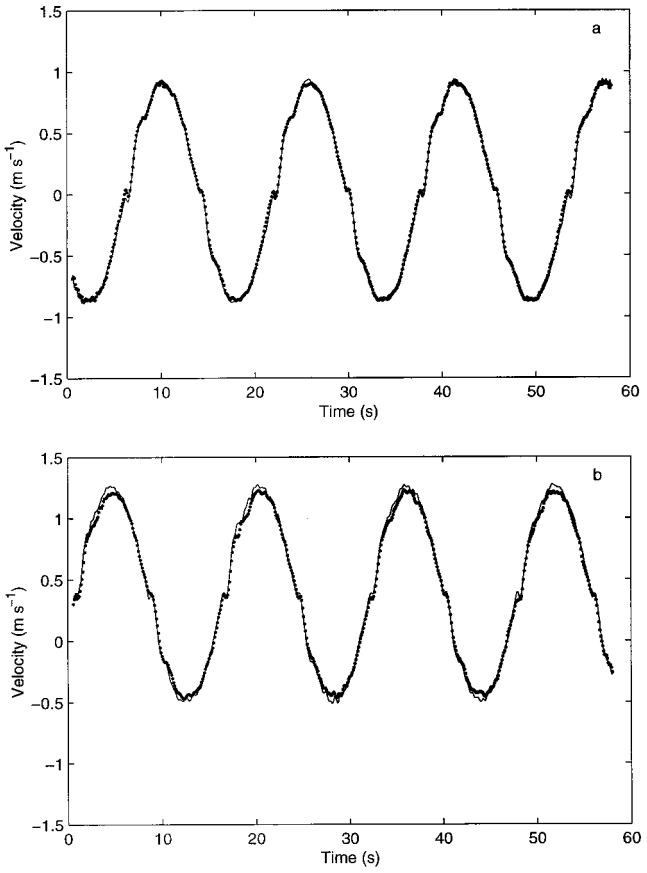

FIG. 8. Measurements of velocity from the LDV (—) and the CDVP (···) for: (a) oscillatory flow alone, and (b) combined unidirectional and oscillatory flow.

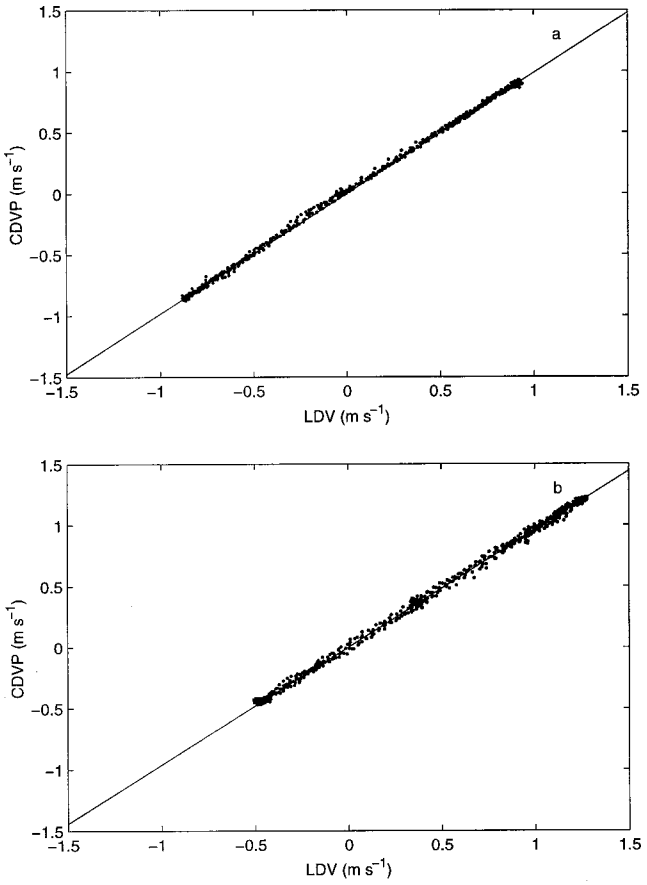

FIG. 9. Regression plots of the CDVP against the LDV for: (a) oscillatory flow alone, and (b) combined unidirectional and oscillatory flow.

and rms analysis indicate that v_d' is of the order of 10% lower than v_l'; however, it should be noted that root mean-square turbulence currents were of the order of 0.01–0.02 m s^{-1}. It is therefore a relatively small difference in small turbulent fluctuations. Cross-correlation analysis on the time series was also carried out on a number of data sets and the mean cross-correlation function with error bars is shown in Fig. 7(b). The normalized cross-correlation function has a clear and readily identifiable peak, with a maximum value of 0.78. Using the usual student's t test on the normalized cross-correlation peak value gave $t=19$. t distribution tables show there was less than an 0.1% probability that the observed correlation coefficient could have arisen by chance; the observed value for the normalized peak cross-correlation function is therefore extremely significant. Figure 7(c) shows a probability turbulent velocity density distribution, $P(v')$, calculated from a number of runs for the LDV (○) and the CDVP (×). The forms for the $P(v')$ are seen to be very similar. To establish the degree of similarity a chi-squared test was applied to the observations. This analysis showed that at the 99% significance level there was no difference between $P(v_d')$ and $P(v_l')$. Finally, turbulent velocity spectra were computed for several runs at comparable velocities, and the mean result is shown in Fig. 7(d). The spectra are seen to be very similar in form and amplitude, with the error bars from the CDVP and LDV overlapping. As well as the comparisons with the LDV, adjacent independent CDVP range bins were compared. If the assumption is made that adjacent range bins were measuring approximately the same turbulence, then the absolute difference in velocity should be close to zero. A number of files were analyzed and $\langle |v_{di}' - v_{d(i+1)}'| \rangle$ was in the range 0.004–0.006 m s^{-1}, where $\langle\ \rangle$ represent an average over 10 range bins at middepth in the tunnel. These small differences in adjacent independent range bins further support the turbulence measuring capability of the CDVP.

B. Oscillatory and combined flow

As previously mentioned, data were collected under conditions of oscillatory, and combined oscillatory and unidirectional flow. Wave periods varied between 4 and 16 s, wave velocity amplitude covered the range 0.8–1.2 m s^{-1}, and unidirectioned flow was between 0 and 0.35 m s^{-1}. Measurement duration was normally 60 s.

Typical examples of the results obtained using the CDVP are shown in Figs. 8–10. Figure 8(a) shows the time series of the flow for the case of oscillatory flow alone, and Fig. 8(b), for oscillatory flow combined with a unidirectional current of nominally 0.35 m s^{-1}. The solid line is the LDV measurements and the solid circles the CDVP data. These figures show that the CDVP is measuring velocities very comparable to those recorded by the LDV. Measurements of the wave period, T_w, amplitude, A_w, and unidirectional current, v_0, for the LDV data in Figs. 8(a) and (b), respectively, gave 15.96 s, 0.89 m s^{-1}, 0.008 m s^{-1}, 15.96 s, 0.86 m s^{-1},

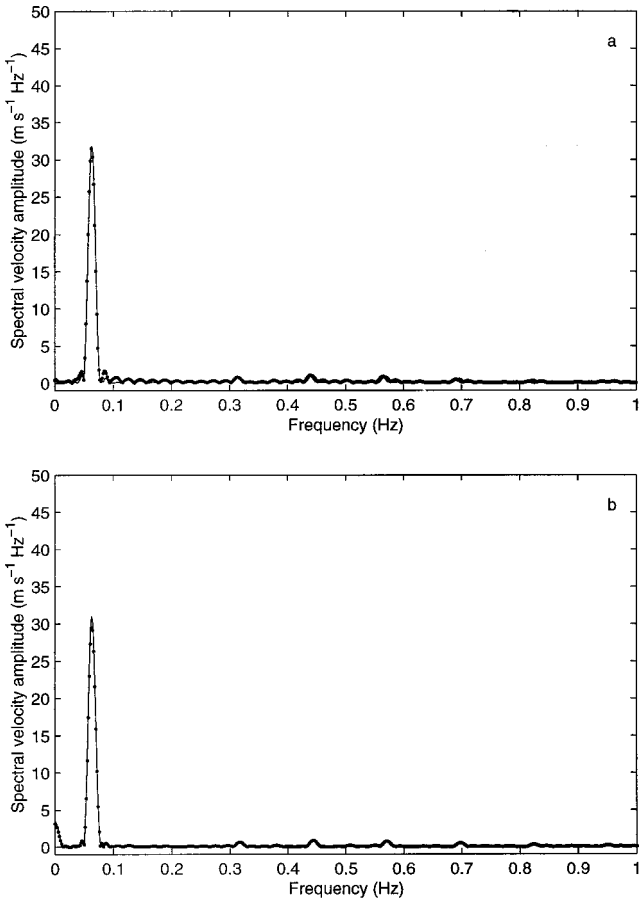

FIG. 10. Spectra of the velocity from the LDV (—) and CDVP (···) for: (a) oscillatory flow alone, and (b) combined unidirectional and oscillatory flow.

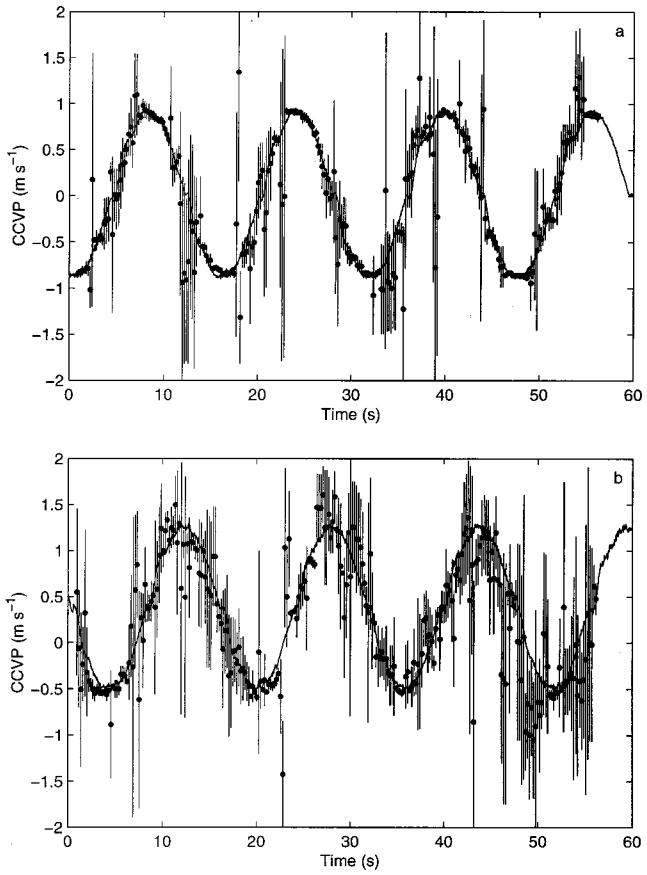

FIG. 11. Measurement of velocity from the LDV (—) and the CCVP (···), for: (a) oscillatory flow alone, and (b) combined unidirectional and oscillatory flow.

and 0.39 m s^{-1}. The CDVP measured values for T_w, A_w, and v_0 were 15.94 s, 0.89 m s^{-1}, 0.009 m s^{-1}, 15.94 s, 0.83 m s^{-1}, and 0.38 m s^{-1}. The measurements from the two instruments are seen to be in very close agreement. To further assess the comparability of the LDV and CDVP, regression plots of the data are shown in Figs. 9(a) and (b). The regression equations and correlation coefficients gave $v_d=\{1.00 \pm 0.02\}v_l$ and $r=0.999$ for Fig. 9(a) and $v_d=\{0.97 \pm 0.02\}v_l$ and $r=0.999$ for Fig. 9(b). The correlation coefficients are highly significant, and the gradients are close to unity. For the combined oscillatory and unidirectional flow measurements shown in Fig. 9(b), the suspended sediment concentration levels were high, of the order of 10 kg m^{-3} near the bed, and these high levels did have a demonstrable effect on the LDV performance, which may account for the reduced gradient in Fig. 9(b). Figures 10(a) and (b) show the spectra obtained, the solid line shows the LDV data, and the solid circles the CDVP measurements. The form and amplitude of the spectra are seen to be very comparable for the two measurement methods, with the spectral peaks being at 0.063 and 0.063 Hz for the LDV and 0.063 and 0.063 Hz for the CDVP, for Figs. 10(a) and (b), respectively. To illustrate that the results from Figs. 8–10 are typical, Table I shows the outcome from other measurements. Using the results from Table I, the mean gradient is given by $\overline{\beta}=0.995 \pm 0.018$ and the ratio of the unidirectional currents, $\overline{v_{0d}/v_{0l}} = 0.988 \pm 0.024$. The results, therefore, show no significant difference between the LDV and CDVP measurements of the flow. An analysis of adjacent range bins was again carried out and comparable results to the unidirectional flow were obtained, with $|v_{di}-v_{d(i+1)})|$ lying in the range 0.004–0.006 m s^{-1}.

Although it was not possible with the CCVP to extract turbulent velocities, the approach was examined to assess its potential to measure intrawave flow. Examples of the results obtained are shown in Fig. 11. The velocities were calculated by cross-correlating record lengths of 2 s and shifting this window through the record with a step interval of 0.2 s. Results are only shown for $d_{23}=0.1$ m; this separation gave the most consistent results under the varying conditions. Figure 11(a) shows the case for oscillatory flow alone, and Fig. 10(b) with the addition of unidirectional flow. The solid line denotes the LDV measurements, and the solid circles the velocities from the CCVP. The data clearly show that intrawave velocities can be measured using the CCVP approach; however, there is considerable scatter around zero velocity, which was not unexpected, and under conditions of combined flow there is increased variability. As can be seen in Fig. 11, precisely tracking the detailed intrawave velocity can be somewhat problematic; however, extracting the mean parameters of A_w, T_w, and v_0 is much more readily obtained. Figure 12 shows profiles of these parameters for the case of a 4-s period wave, with a velocity amplitude of 1.0 m s^{-1}, and a unidirectional current of 0.26 m s^{-1}. As can be

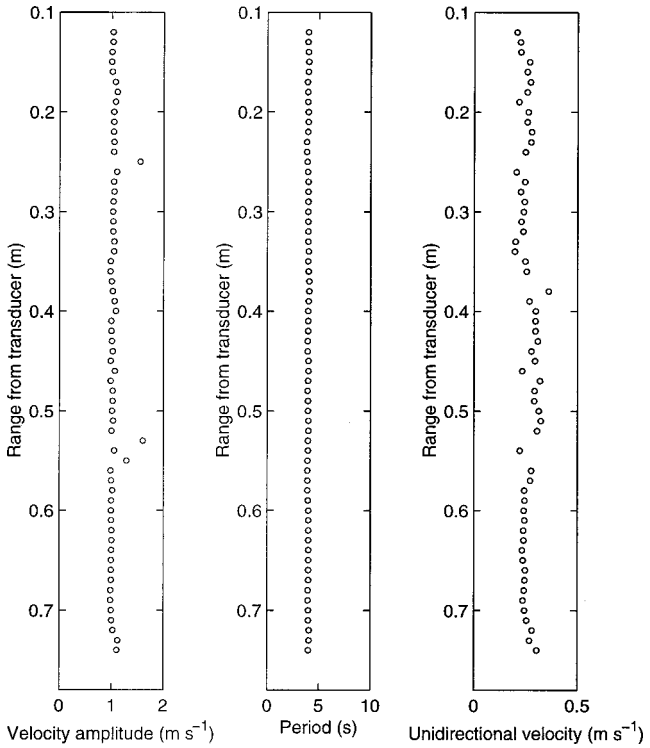

FIG. 12. CCVP profiles of: (a) oscillatory velocity amplitude, (b) period, and (c) unidirectional flow.

seen in the figure, apart from a few data points the CCVP measurements are consistent over the profile. Table I shows that to first order the CCVP approach can be used to obtain mean parameters under conditions of oscillatory and combined flow.

C. Suspended sediment concentration and flux

Using the explicit formulation for the suspended sediment concentration given in Eq. (17), in conjunction with the pumped sample data, suspended sediment concentration profiles were calculated. Figure 13(a) shows the variation of suspended sediment concentration with height above the bed obtained from the acoustic measurements (○) and from the pumped sampled data (△) for unidirectional currents alone of nominally 0.7 m s^{-1}. Figure 13(b) shows the results for combined flow with $v_0 = 0.3\,\mathrm{m\,s^{-1}}$, $A_w = 1.0\,\mathrm{m\,s^{-1}}$, and $T_w = 12\,\mathrm{s}$. The error bars for the acoustic data were obtained from repeated measurements under the same conditions, and those for the pumped samples estimated from reports on the system used.[21,22] As can be seen, the acoustic profiles are very comparable with the pumped sample data both in form and absolute value.

To quantify the agreement between the results shown in Figs. 13(a) and (b), and the data collected from other runs, Fig. 13(c), shows a regression plot of the concentration measurements. The regression equation for the data gave $M_a = (0.94 \pm 0.02)\ M_p$ and regression coefficient of $r = 0.998$. M_a and M_p are the concentration measurements from the acoustic data and pumped sample measurements, respectively. The regression gradient is close to unity, and using the students t distribution test the possibility of obtaining the regression coefficient by chance was less than 1%. The ratio

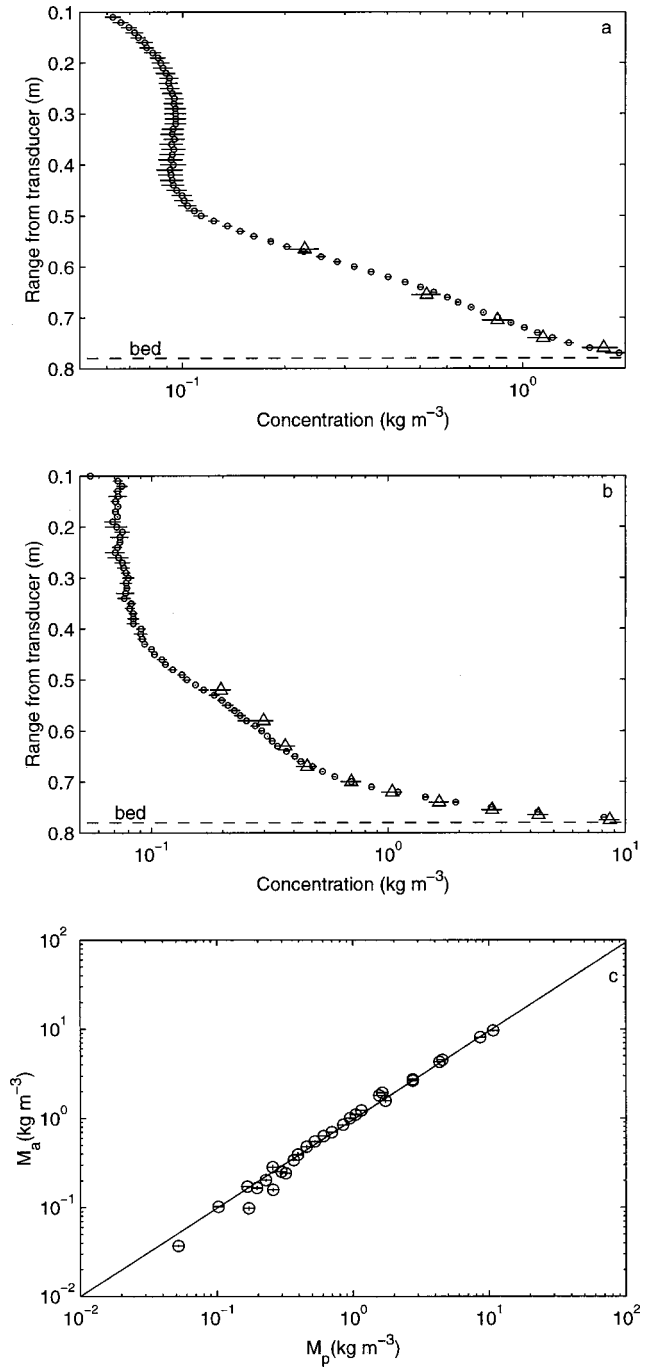

FIG. 13. Measurements of suspended sediment concentration using acoustic backscattering (○) and pumped samples (△). (a) Unidirectional flow with a nominal current of 0.7 m s^{-1}. (b) Combined unidirectional and oscillatory flow. $A_w = 1.1\,\mathrm{m\,s^{-1}}$, $T_w = 12\,\mathrm{s}$, and $v_0 = 0.25\,\mathrm{m\,s^{-1}}$. (c) Regression plot of the acoustic concentration M_a and the pumped sample concentration M_p.

of the acoustic concentration measurement to the pumped sample data gave $M_a/M_p = 0.95 \pm 0.14$. The data in Fig. 13, and the results from the analysis, therefore, clearly show that the backscattered signal could be used to accurately measure the suspended sediment concentration.

Combining the concentration profiles with the profiles of horizontal velocity, mean flux profiles, $\overline{v_d} \cdot \overline{M_a}$, were obtained. The results presented in Fig. 14 show the velocity (×), the concentration (○), and the flux (●) obtained from the acoustics, and the flux obtained using the LDV and pumped sample data (□). Figure 14(a) shows the results for

TABLE I. Results from a number of experimental runs. T_w is the wave period, A_w is the wave velocity amplitude, v_0 is the unidirectional current, and β is the gradient of the line obtained from the regression equation with the LDV.

	CDVP					CCVP			LDV		
Experiment	T_w(s)	A_w(m s)$^{-1}$	v_0(m s)$^{-1}$	Regression gradient (β)	Regression coefficient	T_w(s)	A_w(m s)$^{-1}$	v_0(m s^{-1})	T_w(s)	A_w(m s^{-1})	v_0(m s^{-1})
1	15.94	0.889	⋯	0.995	0.999	15.8	0.86	⋯	15.96	0.892	⋯
2	15.98	0.883	⋯	0.985	1.000				15.95	0.901	⋯
3	15.94	0.882	⋯	0.979	0.999				15.95	0.901	⋯
4	15.95	0.840	0.369	0.961	0.999	15.8	0.86	0.34	15.95	0.877	0.378
5	15.95	0.828	0.383	0.967	0.999				15.96	0.864	0.387
6	4.002	1.065	0.260	0.965	0.995				4.004	1.103	0.277
7	4.004	1.048	0.260	0.960	0.996	3.95	0.98	0.24	4.034	1.092	0.270
8	12.10	1.109	0.251	1.002	0.997	12.1	1.00	0.20	12.11	1.110	0.263
9	12.11	1.078	0.279	1.136	0.976				12.08	1.015	0.253

unidirectional flow alone with a nominal velocity of 0.7 m s^{-1}. The measurements show increasing concentration and reducing flow as the bed is approached, with a flux profile that continues to increase to within approximately 0.04 m of the bed. Below 0.04 m there is a reduction in the rate of increase of the flux; however, even at 0.01 m above the bed, the sediment flux is close to maximum. Figure 14(b) shows the outcome from measurements collected under combined flow with $A_w = 1.1$ m s^{-1}, $T_w = 12$ s, and $v_0 = 0.25$ m s^{-1}. The results shown were calculated over an integer number of

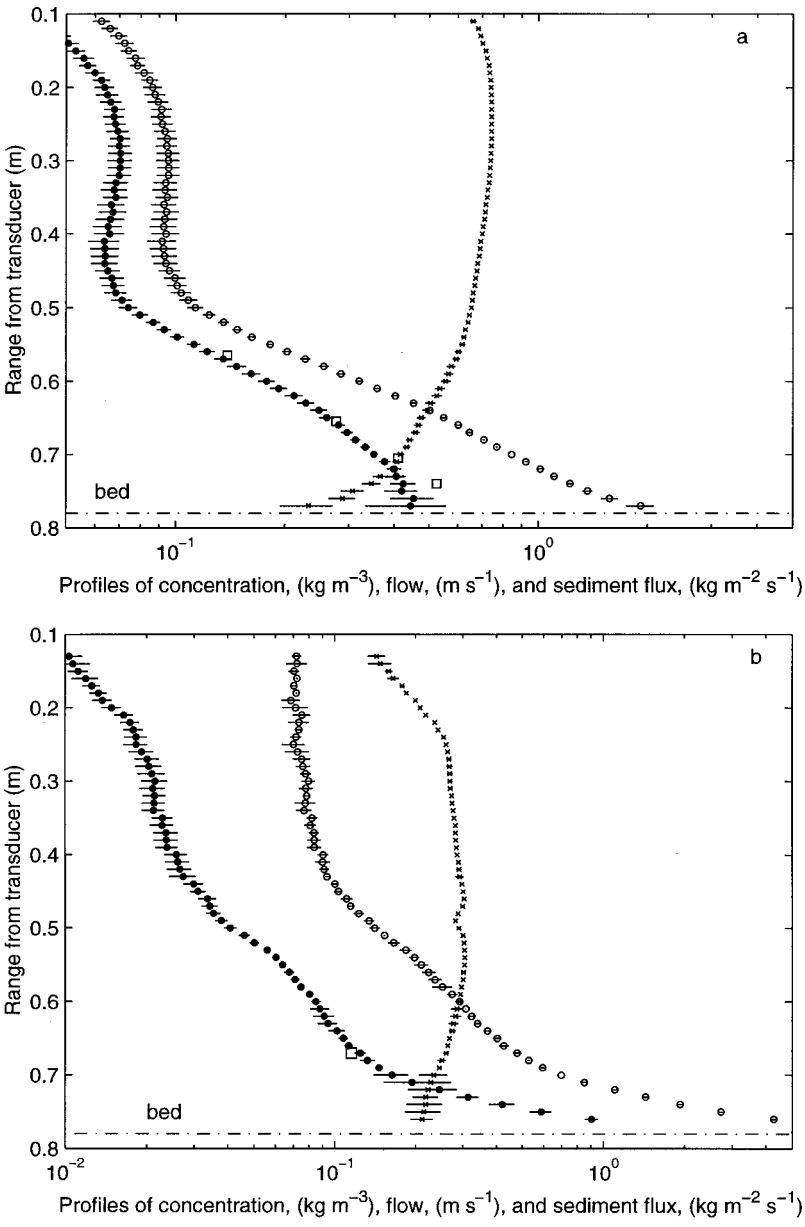

FIG. 14. Profiles of acoustic measurements of flow (×), suspended sediment concentration (○), and flux (●), and measurements of the flux (□) using the LDV and pumped sample data. (a) Unidirectional conditions with a nominal flow velocity of 0.7 m s^{-1}. (b) Combined flow condition with $A_w = 1.1$ m s^{-1}, $T_w = 12$ s, and $v_0 = 0.26$ m s^{-1}.

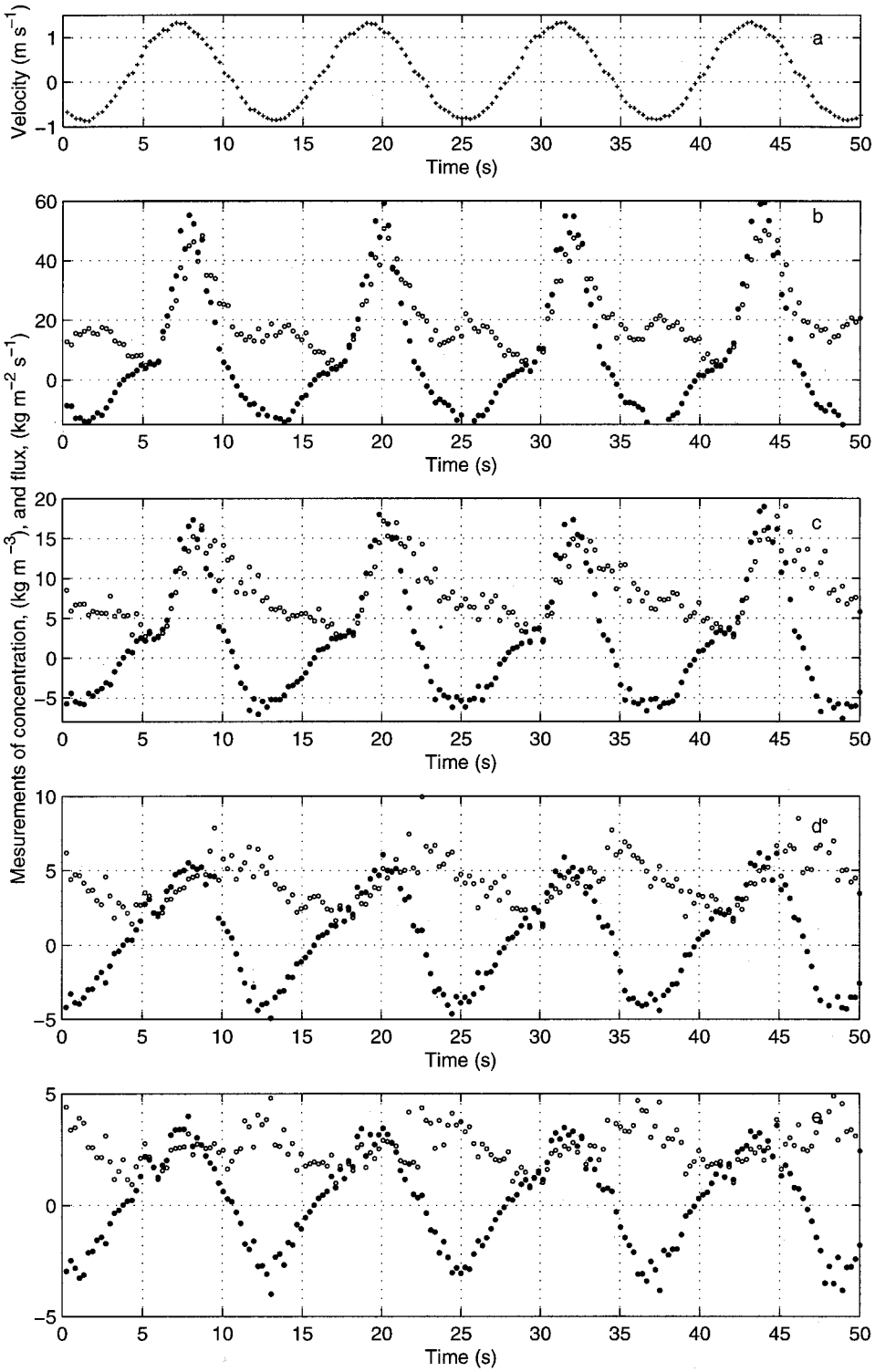

FIG. 15. (a) Measurement of the flow velocity at 0.01 m above the bed. (b)–(e) Measurements of suspended sediment concentration, (○) kg m^{-3}, and suspended sediment flux, (●) kg m^{-2} s^{-1}, at 0.01, 0.02, 0.03, and 0.04 m above the bed, respectively.

wave cycles. In this case the sediment flux is seen to rapidly increase as the bed is approached, with no indication of a reduction even within 0.02 m of the bed. The bed was nominally plane for the results shown in Fig. 14(b), and there was therefore the possibility of sheet flow[23] occurring, and sediment flux increasing to within a few grain diameters of the immobile bed. These measurements show the capability of acoustics to measure boundary layer sediment flux unobtrusively to within typically a centimeter of the bed, and that sediment flux very close to the bed is high and needs to be directly measured if sediment transport is to be correctly modeled, rather than inferred from the usual point measurements normally collected several centimeters above the bed.

Figure 14 provides a mean estimate for the sediment flux; however, acoustics has the potential to provide both high temporal and spatial resolution, and this is illustrated in Fig. 15. Figure 15(a) shows coherent Doppler measurements of the velocity at 0.01 m above a plane bed for combined oscillatory and unidirectional flow. Figures 15(b)–(e) show high-resolution time series of the concentration (○) and sedi-

ment flux (●) at 0.01, 0.02, 0.03, and 0.04 m above the bed. The 0.01-cm measurements clearly show sediment concentration peaks which are located at the same position in the wave cycle, occurring approximately 1 s after maximum flow. The lag between the flow and the suspended sediments increases with height above the bed, although the linkage between the flow and the suspended sediments weakens as the suspension becomes more homogeneous. The increase in lag is associated with the time for the mobile sediments to diffuse up from the bed. However, the maximum flux essentially remains at the same location owing to the dominant current effect on an increasingly homogeneous suspension with height above the bed. It is expected that presentations such as shown in Fig. 15, which illustrate clearly the value of combined acoustic flow and suspended sediment measurements, will be used to assess and develop process-based sediment transport models.

V. CONCLUSIONS

The development of techniques to nonintrusively measure with both high temporal and spatial resolution boundary layer flow is of interest to many scientists who study marine hydrodynamics, and particularly to those involved in developing fundamental descriptions of sediment transport processes at turbulence and intrawave scales. The present study has aimed at measuring the flow at these scales using the two emerging acoustic approaches of coherent Doppler and cross-correlation. The techniques have been assessed at the typical temporal sampling frequency used in boundary layer marine studies. The measurements were collected in the large wave tunnel facility of Delft Hydraulic, De Voorst, which enabled observations to be made under conditions of unidirectional, oscillatory, and combined flow. This has allowed an examination of the coherent Doppler velocity profiler and the cross-correlation velocity profiler performance over a wide range of boundary layer flow conditions, and provided the opportunity to measure and assess mean, turbulence, and intrawave velocity profiles.

The measurements of mean velocity under conditions of unidirectional flow showed results from the CDVP and CCVP which were internally consistent with indicative normalized standard errors from repeated runs of the order of 0.005–0.01. Regression analysis of the mean flow data with the LDV gave CDVP and CCVP gradients which had no significant difference from unity, and highly significant regression coefficients. Examination of the turbulent flow showed that for the incoherent cross-correlation approach, as the cross-correlation record length reduced to increase temporal resolution, the normalized standard error in the measurements increased to values significantly greater than the turbulence of the flow. The coherent Doppler measurements were not subject to this limitation, and turbulence velocities were obtained. The CDVP turbulence measurements were compared with the LDV velocities and close agreement observed. Regression analysis indicated some underestimate of the CDVP turbulent velocity measurements relative to the LDV; however, other statistical tests showed no significant differences between the two methods of measurement. Further, the internal consistency of independent adjacent range bin measurements of the turbulent flow showed a high degree of consistency with an average absolute velocity difference of 0.005 m s^{-1}.

Analysis of CCVP measurements under oscillatory and combined flows showed that intrawave velocities could be obtained, though with a relatively high degree of scatter for the instantaneous velocities. However, the mean parameters of velocity amplitude, period, and unidirectional current could be estimated with a reasonable degree of accuracy. The CDVP intrawave velocity measurements showed excellent agreement with the LDV. The intrawave velocities were accurately measured, and regression analysis showed no significant difference between the CDVP and LDV intrawave velocity measurements. Also, as shown in Table I, A_w, T_n, and v_0 were very comparable. Comparison of velocities from adjacent range bins again gave an average absolute velocity difference of 0.005 m s^{-1}.

Utilization of an explicit inversion scheme to obtain suspended sediment concentration from the backscattered signal gave suspension profiles which were very comparable with the pumped sampled data. Regression analysis of the acoustic and pumped sample concentrations gave a gradient close to unity with a highly significant correlation coefficient. Combining the acoustic suspended sediment and flow measurements, nearbed boundary layer sediment flux profiles were obtained. The mean flux sediment profiles for unidirectional flow showed increasing values as the height above the bed reduced, with near maximum values observed at 0.01 m, while for the plane bed with combined flow, no maximum was observed, and the flux continued to increase. Comparison of the mean acoustic flux measurements with those obtained from the LDV and pumped sample data showed very comparable results. Nearbed intrawave concentration time series showed variations in the suspended sediment concentration that were clearly linked with the phase of the wave, and lagging maximum positive and negative going flow. However, this linkage reduced significantly within a few centimeters of the bed as the sediment diffused away from the bed and the suspension time series became more homogeneous. Intrawave sediment flux measurements showed that within a couple of centimeters of the bed the concentration significantly effected the form of the flux time series, while farther above the bed the flux time series was close in form to the flow velocity.

Finally, the reported series of measurements have attempted to assess the capability of acoustic coherent Doppler and cross-correlation techniques to measure nearbed boundary layer flow under various combinations of unidirection, oscillatory, and combined flows. These flow measurements have been combined with acoustic measurements of the suspended sediments to provide measurements of the nearbed sediment flux. It is anticipated that this combination of contemporaneous collocated nonintrusive high temporal and spatial resolution profiles of the flow and the suspended sediments should make a valuable contribution to the development of our understanding of suspended sediment entrainment and transport processes.

ACKNOWLEDGMENTS

The authors would like to thank Dr. V. Humphery for his many contributions to this work, Dr. C. Vincent for his management of the program of which this work was part, Marc Perennes for the hardware development, and Peter Hardcastle who contributed to the development of the coherent Doppler system. P.D.T. would also like to thank Ulrich Lemmin for his invitation to visit the Laboratoire de Racherches Hydraulics, Ecole Polytechnique Federale, Lausanne, Switzerland, and their discussions on coherent Doppler systems. This work was cofunded by EU Contract No. TRIDISMA MAS3-CT95-0017, and NERC, UK.

[1] D. M. Hanes, C. E. Vincent, D. A. Huntley, and T. L. Clarke, ''Acoustic measurements of suspended sand in the C^2S^2 experiment at Stanhope Lane,'' Prince Edward Island Mar. Geol. **81**, 175–183 (1988).

[2] C. Libicki, K. W. Bedford, and J. F. Lynch, ''The interpretation and evaluation of a 3-MHz acoustic backscatter device for measuring benthic boundary layer sediment dynamics,'' J. Acoust. Soc. Am. **85**, 1501–1511 (1989).

[3] J. F. Lynch, J. D. Irish, C. R. Sherwood, and Y. C. Agrawal, ''Determining suspended sediment particle size information from acoustical and optical backscatter measurements,'' Cont. Shelf Res. **14(10/11)**, 1139–1165 (1994).

[4] T. H. Lee and D. M. Hanes, ''Comparisons of field observations of the vertical distribution of suspended sand and its prediction by models,'' J. Geophys. Res. **101**(C2), 3561–3572 (1996).

[5] L. J. Hamilton, ''Calibration and interpretation of acoustic backscatter measurements of suspended sediment concentration profiles in Sydney Harbour,'' Acoust. Australia **26**(3), 3–87 (1998).

[6] J. J. Williams, C. R. Rose, P. D. Thorne, B. A. O'Connor, J. D. Humphery, P. J. Hardcastle, S. P. Moores, J. A. Cook, and D. J. Wilson, ''Field observations and predictions of bed shear stresses and vertical suspended sediment concentration profiles in wave-current conditions,'' Cont. Shelf Res. **19**, 507–536 (1999).

[7] L. Zedel, A. E. Hay, R. Cabrera, and A. Lohrmann, ''Performance of a single-beam pulse to pulse coherent Doppler profiler,'' IEEE J. Ocean Eng. **21**, 290–297 (1996).

[8] U. Lemmin and T. Rolland, ''Acoustic velocity profiler for laboratory and field studies,'' J. Hydr. Eng. **123**(12), 1089–1098 (1997).

[9] R. F. van Unen, P. D. Thorne, H. Cox, and S. D. Kamminga, ''Laboratory measurements of current flow using cross correlations on acoustic backscattering from suspended sediments,'' J. Acoust. Soc. Am. **104**(3), 1345–1355 (1998).

[10] A. E. Adams, O. R. Hilton, E. M. Valentine, and A. D. Tweedy, ''An acoustic imaging system for the concurrent measurement of suspended sediment concentration and particle velocity,'' J. Acoust. Soc. Am. **104**(4), 2160–2166 (1998).

[11] L. Zedel and A. E. Hay, ''A coherent Doppler profiler for high resolution particle velocimetry in the ocean: Laboratory measurements of turbulence and particle flux,'' J. Atmos. Ocean. Technol. **16**, No. 8, 1102–1117 (1999).

[12] D. Hurther and U. Lemmin, ''A constant-beam-width transducer for 3D acoustic Doppler profile measurements in open-channel flows,'' Meas. Sci. Technol. **9**, 1706–1714 (1998).

[13] A. E. Hay and J. Sheng, ''Vertical profiles of suspended sand concentration and size from multifrequency acoustic backscatter,'' J. Geophys. Res. **97**, No. C10, 15661–15677 (1992).

[14] P. D. Thorne, P. J. Hardcastle, and R. L. Soulsby, ''Analysis of acoustic measurements of suspended sediments,'' J. Geophys. Res. **98**, No. C1, 899–910 (1993).

[15] A. M. Crawford and A. E. Hay, ''Determining suspended sand size and concentration from multifrequency acoustic backscatter,'' J. Acoust. Soc. Am. **94**(6), 3312–3324 (1993).

[16] P. D. Thorne and P. J. Hardcastle, ''Acoustic measurements of suspended sediments in turbulent currents and comparison with *in-situ* sampling,'' J. Acoust. Soc. Am. **101**, 2603–2614 (1997).

[17] M. S. Beck and A. Plaskowski, *Cross-Correlation Flow Meters—Their Design and Application* (Hilger, Bristol, 1987).

[18] T. H. Lee and D. M. Hanes, ''Direct inversion method to measure the concentration profile of suspended particles using backscattered sound,'' J. Geophys. Res. **100**, 2649–2657 (1995).

[19] K. Weltner, J. Grosjean, P. Schuster, and W. J. Weber, *Mathematics for Engineers and Scientists* (Stanley Thomes, UK, 1986), Chap. 10, p. 512.

[20] J. B. Kennedy and A. M. Neville, *Basic Statistical Methods for Engineers and Scientists* (Dun-Donnelley, New York, 1964), p. 490.

[21] J. J. Bosman, E. T. J. M. Van Der Velden, and C. H. Hulsbergen, ''Sediment concentration measurement by transverse suction,'' Coastal Eng. **10**, 353–370 (1987).

[22] C. M. Janssen, W. N. Hassan, R. J. van der Wal, and J. S. Ribberink, ''Net sand transport rates and transport mechanisms of fine sand in combined wave-current sheet flow conditions,'' Delft Hydraulics Report H2462, Part IV, Data Report (1996).

[23] J. S. Ribberink, ''Sediment transport in oscillatory boundary layers in cases of rippled beds and sheet flow,'' J. Geophys. Res. **99**, No. C6, 12707–12727 (1994).

Source ranging with minimal environmental information using a virtual receiver and waveguide invariant theory

Aaron M. Thode[a)]
Ocean Engineering Department, Massachusetts Institute of Technology, Cambridge, Massachusetts 02139

(Received 24 January 2000; revised 19 June 2000; accepted 20 June 2000)

A method is presented for estimating the range of an unknown broadband acoustic source in a waveguide, using a vertical array and a signal sample from another broadband source at a known location relative to the array. The method requires no modeling of the acoustic field, and little to no environmental information for flat bathymetries. Waveguide invariant theory [e.g., D'Spain and Kuperman, J. Acoust. Soc. Am **106**, 2454–2468 (1999)] is applied to the ''virtual receiver'' [Siderius *et al.*, J. Acoust. Soc. Am. **102**, 3439–3449 (1997)] to create a ''virtual aperture'' (VA). In effect, the method effectively converts a source at known range r_g into a continuum of receivers lying between ranges $(1\pm\alpha/\beta)*r_g$, where β is a scalar parameter called the acoustic invariant, and $\alpha\sim 0.1$. This effective displacement is achieved by correlating the known source field, measured at frequency component ω, with the unknown source field, measured at frequency component $\omega+\omega_s$. When the VA output is plotted as a function of ω and ω_s, the slope of the resulting correlation contours yields the unknown source range. The concept is illustrated via both simulation and analysis of data collected from a pseudo-random noise source with 75–150-Hz bandwidth during SWellEx-3, a shallow water experiment conducted off the San Diego coast. The virtual aperture can be reformulated for range-dependent environments, if adiabatic propagation assumptions are valid, and if the bathymetry surrounding the array is known. © *2000 Acoustical Society of America.* [S0001-4966(00)01010-9]

PACS numbers: 43.30.Pc, 43.30.Sf [DLB]

I. INTRODUCTION AND REVIEW

Several years ago guide source concepts in astronomy[1] were reformulated for use in an acoustic waveguide,[2–4] yielding a concept variously dubbed a ''holographic array'' or a ''virtual receiver'' (VR). Under this approach a vertical array receives two time-separated broadband signals, one from a source (S_g) at a known location (z_g,r_g), and one from an ''objective'' source (S_o) at an unknown location (z_o,r_o), as illustrated in Fig. 1(a). Guide sources could be deliberately deployed at a known location, or they could be transient sources of opportunity, whose position relative to the array has been determined via visual sighting or radar. The figure shows three examples of possible broadband guide sources: a bottom-mounted transponder, a ship, and a whale. (Certain species of baleen whale produce intense broadband low-frequency sounds that may propagate tens of kilometers in shallow water. These species include the blue,[5] bowhead,[6] humpback,[7] and sperm whales.[8] A guide source might even consist of the direct path from an explosion, and the objective source would be the time-delayed return[4] from a distant scatterer.

If the array spans sufficient waveguide depth, the VR algorithm can estimate the objective source field at the guide source location, effectively converting the guide source into a ''virtual receiver'' [Fig. 1(b)]. Siderius *et al.*[4] showed via simulation that the concept should still work under mild cases of mode coupling, and used broadband matched-field processing methods to estimate the unknown range of a simulated source. This approach required extensive knowledge about the ocean environment to generate the time-series replica used by the matched-field processor.

The VR algorithm is mathematically similar to both phase-conjugation[9–12] and Bartlett matched-field processing algorithms.[13] Recent work on both topics[13–15] has profited from the application of waveguide invariant theory,[14,16,17] which demonstrates how the propagation characteristics of a waveguide can be summarized in a single robust scalar parameter, β, called the waveguide invariant. To first order β is independent of frequency and mode number, and is relatively insensitive to environmental parameters like ocean depth and bottom composition. It is reasonable to expect the VR method would also benefit from application of waveguide invariant concepts, provided that both the guide and objective source are continuously broadband and have moderately high signal-to-noise (SNR) ratios. ''Continuously broadband'' is defined here as a signal that has a continuous bandwidth of at least 10% around its center frequency.

In Sec. II waveguide invariant theory is applied to the VR algorithm, allowing recovery of not only the objective source field intensity received at (z_g,r_g), but also along a continuum of ranges between $(1\pm\alpha/\beta)*r_g$, where α lies between ± 0.1. In effect, a ''virtual aperture'' can be created around the guide source [Fig. 1(c)]. This aperture reconstruction is fundamentally possible because the propagating acoustic field intensity measured at range r and frequency $\omega+\Delta\omega$ is similar to the intensity that would have been measured at range $r_g(1-\Delta\omega/\beta\omega)$ and frequency ω. Therefore, the field from the guide source at one frequency component

[a)]Also at Marine Physical Laboratory, Scripps Institution of Oceanography, San Diego, CA 92093-0205.

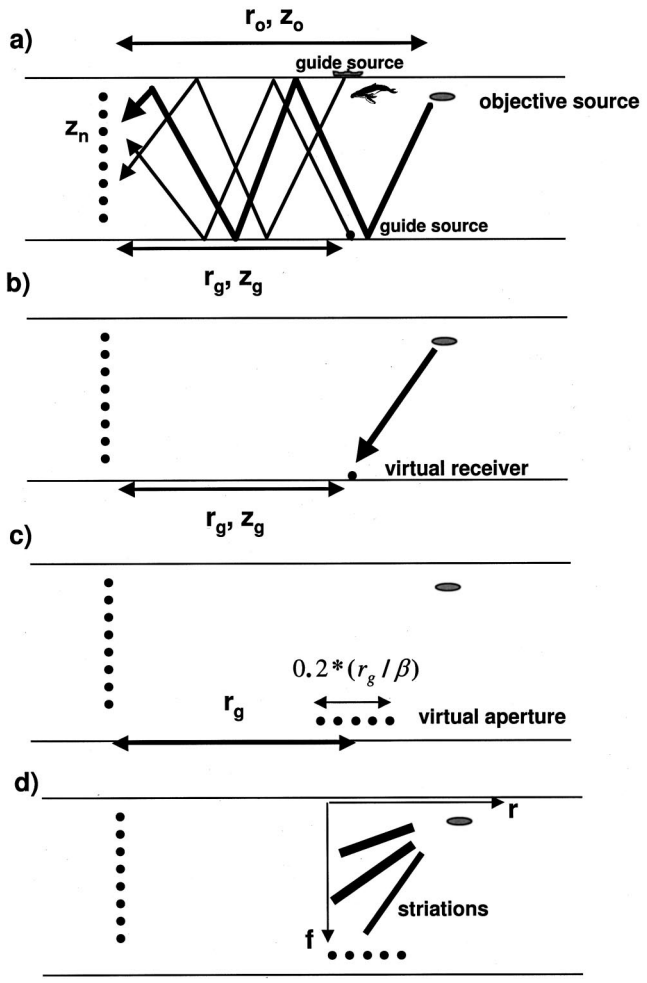

FIG. 1. Heuristic explanation of virtual aperture concept. (a) A signal from a guide source at known range r_g is detected on a vertical array, and at a different time a signal from an objective source at unknown range r_o is also detected. Potential guide sources can include a bottom-mounted transponder, a ship, or a whale at a known range. (b) The virtual receiver formula estimates the objective source field received at (r_g, z_g) from the source at (r_o, z_o), illustrated here for the bottom-mounted guide source. (c) Waveguide invariant concepts allow estimation of the objective source intensity along a continuum of ranges between $r_g^*(1 \pm 0.1/\beta)$, effectively creating a ''virtual aperture.'' (d) When the reconstructed intensity field is plotted in the virtual range-frequency plane, the slopes of the intensity contours yield the objective source range to the vertical array.

may be used to model the acoustic field at a different range, for a different frequency component. If the virtual aperture output is plotted as a function of frequency and virtual range, as suggested in Fig. 1(d), the correlation contour slopes can be related to the objective source range relative to the vertical array.

An intriguing property of the virtual aperture is that although the invariant β is used twice in the derivation—once in constructing the aperture, and once in converting striation slopes into an objective source range estimate—the final range estimation formula has only a weak dependence on β when the waveguide is range independent. Indeed, a reasonable range estimate may be obtained without knowledge of β, and thus without knowledge the waveguide environment. In effect, a modeling problem has been converted into an image-processing problem of slope estimation from an image. The primary assumption behind the derivation is that the waveguide propagation characteristics do not change substantially between the times at which the guide and unknown source signals are sampled.

Section III simulates the virtual aperture concept in shallow-water (bottom-interacting) propagation environments, and explores a computational method for extracting range estimates, using a Radon transform. Section IV demonstrates that the concept works on data collected during the Arc 2 event of the SWellEx-93 experiment, conducted off the San Diego coast.[18] Finally, in Appendix A the concept is revised to incorporate mildly range-dependent environments. Under these circumstances additional information is required to obtain a range estimate, including both source azimuths, and the bathymetry surrounding the array. However, the algorithm does not require detailed information about the local sound-speed profile and bottom composition.

II. THEORY AND METHOD

A. Derivation of the virtual endfire array for constant depth waveguide

The derivation begins with the scenario envisioned in Fig. 1(a), using notation similar to that of Siderius *et al.*[4] For the moment it is assumed that the objective source S_o, the guide source S_g, and the receiving vertical array all lie in the same vertical plane in a waveguide of constant depth, and that the vertical array is not tilted. The field received from the guide source by array element n at a depth z_n and radial frequency ω can be written as the weighted sum of the waveguide normal modes:[19]

$$P_g(z_n, z_g, r_g, \omega) = \frac{ie^{-i\pi/4}}{\rho(z_g)\sqrt{8\pi r_g}} \sum_l e^{-\alpha_l r_g} \Psi_l(z_g) \times \Psi_l(z_n) \frac{e^{ik_l r_g}}{\sqrt{k_l}}. \quad (1)$$

Here k_l and α_l are the horizontal wave numbers and attenuation coefficients of mode Ψ_l at radial frequency ω, respectively. The attenuation coefficients and mode functions are now assumed to remain unchanged with small changes in frequency. Consider a separate signal received from an unknown source at range r_o and depth z_o:

$$p_o(z_n, z_o, r_o, \omega) = \frac{ie^{-i\pi/4}}{\rho(z_o)\sqrt{8\pi r_o}} \sum_l e^{-\alpha_l r_o} \Psi_l(z_o) \times \Psi_l(z_n) \frac{e^{ik_l r_o}}{\sqrt{k_l}}. \quad (2)$$

In the frequency domain the normalized virtual receiver output $V(z_g, r_g, \omega)$ is defined in a fashion identical in form to the Bartlett matched-field processor:[20]

$$V(z_g, r_g, \omega) = \frac{\Sigma_n p_g^*(z_n, z_g, r_g, \omega) p_o(z_n, z_o, r_o, \omega)}{\sqrt{\Sigma_n |p_g(z_n, z_g, r_g, \omega)|^2} \sqrt{\Sigma_n |p_o(z_n, z_o, r_o, \omega)|^2}}. \quad (3)$$

The normalization scheme shown here divides each vertical field vector by its norm, removing possible source spectrum effects. If the receiver array has sufficient aperture, the orthogonality of the modes can be exploited to obtain the following expression:

$$V(z_g, r_g, \omega) = N \sum_l e^{-\alpha_l'(r_g + r_o)} \Psi_l(z_o) \Psi_l(z_g) \frac{e^{ik_l(r_o - r_g)}}{|k_l|}. \tag{4}$$

Here N is a normalization constant that is independent of mode number or frequency. This expression is similar to that of a receiver placed at the guide source location, except for the magnitude of the sediment attenuation term and the extra factor of $\sqrt{k_l}$ present in the denominator. Multiplying Eq. (4) by its complex conjugate yields the acoustic intensity of the objective source at the virtual receiver:

$$\begin{aligned} I_V(z_g, r_g, \omega) &= N^2 \sum_m \sum_l e^{-(\alpha_l + \alpha_m)(r_g + r_o)} \\ &\quad \times A_l A_m \cos[(r_o - r_g)\chi_{lm}(\omega)], \\ A_i &\equiv \frac{\Psi_i(z_o)\Psi_i(z_g)}{|k_i|}, \quad \chi_{lm}(\omega) \equiv k_l(\omega) - k_m(\omega). \end{aligned} \tag{5}$$

Equation (5) makes the frequency dependence of the horizontal wave numbers k_l and wave number differences χ_{lm} explicit.

What would happen if, instead of Eq. (3), one computed a new quantity of the form

$$V(z_g, r_g, \omega, \omega_s) = \frac{\Sigma_n p_g^*(z_n, z_g, r_g, \omega + \omega_s) p_o(z_n, z_o, r_o, \omega)}{\sqrt{\Sigma_n |p_g(z_n, z_g, r_g, \omega + \omega_s)|^2} \sqrt{\Sigma_n |p_o(z_n, z_o, r_o, \omega)|^2}}, \tag{6}$$

where the guide and objective sources are now ''mismatched'' in frequency, with ω_s representing the relative frequency shift between the two signal samples? Assuming that the mode functions do not change significantly with a slight frequency shift, the orthonormality condition can still be used, and the following expression for the intensity I_V is obtained:

$$\begin{aligned} I_V(z_g, r_g, \omega, \omega_s) &= N^2 \sum_m \sum_l e^{-(\alpha_l + \alpha_m)(r_g + r_o)} \\ &\quad \times A_l A_m \cos[r_o \chi_{lm}(\omega) - r_g \chi_{lm}(\omega + \omega_s)]. \end{aligned} \tag{7}$$

The horizontal wave number differences (i.e., modal phase slowness differences) at different frequencies may be related to one other by using the definition of the waveguide invariant β as originally defined by Chuprov,[16] and discussed in detail in more recent literature.[13–15,21] The invariant β is derived by conducting a first-order Taylor expansion of the modal phase slowness (inverse phase velocity) in terms of the group slowness (inverse group velocity):

$$\beta = -\frac{d(1/c_p)}{d(1/c_g)} = -\frac{\chi_{lm}(\omega)/\omega}{\partial \chi_{lm}(\omega)/\partial \omega}. \tag{8}$$

Here c_p is the modal phase velocity, c_g is the modal group velocity, the differentiation is with respect to mode number, and β is considered to be a constant or ''invariant.'' Equation (8) asserts that given the difference in phase slowness between any two modes, the difference in the group slowness may be obtained without knowledge of either the frequency or the mode orders involved. Fundamentally, Eq. (8) assumes that a relationship exists between the modal group and phase velocities in a waveguide that is independent of frequency and mode number.

For example, an ''ideal'' waveguide with perfectly reflecting boundaries obeys the following relationship between group and phase velocity:

$$c_p c_g = c^2. \tag{9}$$

From this expression the value of β in Eq. (8) may be derived as $\beta = (k_r/k)^2 \sim 1$. For a variety of propagation environments characterized by surface and bottom reflections, the invariant β has indeed been demonstrated to be near unity, regardless of the ocean depth or bottom composition.[16,21] Thus, as long as the boundary interactions remain primarily reflective, one would expect the value of β to remain nearly constant, a point that will be explored further in Sec. V.

If β can be treated as a constant, then the first-order differential equation implied by Eq. (8) can be solved for χ_{lm}:[17]

$$\chi_{lm}(\omega) = C_{lm} \omega^{-1/\beta}, \tag{10}$$

where C_{lm} is independent of frequency. Combining Eqs. (10) and (7) and regrouping terms yields the final output for the virtual aperture algorithm:

$$\begin{aligned} I_V(\omega, \omega_s) &= N^2 \sum_m \sum_l e^{-(\alpha_l + \alpha_m)(r_g + r_o)} \\ &\quad \times A_l A_m \cos\left[\left(r_o - \left\{1 + \frac{\omega_s}{\omega}\right\}^{-1/\beta} r_g\right) \chi_{lm}(\omega)\right]. \end{aligned} \tag{11a}$$

The explicit dependence of I_V on the guide source location has been dropped. Comparison of Eq. (11a) with Eq. (5) shows that Eq. (6) is equivalent to a virtual receiver located at a shifted range $r_g + \Delta r_g$:

$$\begin{aligned} r_g + \Delta r_g &\equiv \left(1 + \frac{\omega_s}{\omega}\right)^{-1/\beta} r_g, \\ \Delta r_g &\sim \frac{-\omega_s r_g}{\beta \omega}. \end{aligned} \tag{11b}$$

In effect, the acoustic field at range r_g and frequency $\omega + \omega_g$ has been used to estimate the acoustic intensity at range $r_g(1 - \omega_s/\beta\omega)$ and frequency ω. By repeating the process with different values of ω_s, a continuum of virtual receivers between $r_g(1 \pm \alpha/\beta)$ can be constructed [Fig. 1(b)], where $\alpha = \omega_s/\omega$ has a maximum value of around 0.1. Whenever the relative frequency shift $\alpha = \omega_s/\omega$ exceeds this value, the first-order Taylor approximations implicit in Eqs. (8) and (11b) cease to be valid. In addition, as α becomes large, the mode functions Ψ_l start changing shape, and

modes may emerge or vanish from the system, invalidating the derivation assumptions.

One can imagine mapping this virtual ''aperture'' output as a function of ω and Δr_g, creating a range-frequency plot of the objective source intensity across the virtual aperture. This intensity plot would show contours of constant correlation, over which the frequency of the intensity maxima would shift by $\Delta\omega_I$, over a change Δr_g in range. If the objective source intensity field had been physically measured over this range aperture, the slope of the resulting contours could have been related to the objective source range, as derived by Brekhovskih[21] and Chuprov[16]:

$$\left(\frac{\Delta\omega_I}{\Delta r_g}\right)_{\text{contour}} = \beta\frac{\omega}{(r_o - r_g)}. \tag{12}$$

The actual virtual aperture output is a function of ω and ω_s, not Δr_g, so Eq. (12) must be modified. To determine how contours of constant correlation in the virtual aperture output are related to the objective source range, the total differential of the virtual aperture output must be computed and set to zero:

$$dI_\nu = \frac{\partial I_\nu}{d\omega}\Delta\omega_I + \frac{\partial I_\nu}{\partial\omega_s}\Delta\omega_s = 0. \tag{13}$$

This yields an expression for the slope of the lines of constant correlation:

$$\left(\frac{\Delta\omega_I}{\Delta\omega_s}\right)_{\text{contour}} = -\frac{\partial I_\nu/\partial\omega_s}{\partial I_\nu/\partial\omega}. \tag{14}$$

The partial derivatives are most conveniently derived from Eqs. (7) and (10):

$$\partial I_V/\partial\omega_s = -N^2\sum_m\sum_l A_l A_m \chi_{lm}(\omega+\omega_s) \times\left\{\frac{r_g}{\beta(\omega+\omega_s)}\right\}\sin[E_{lm}], \tag{15a}$$

$$\partial I_V/\partial\omega = -N^2\sum_m\sum_l A_l A_m \chi_{lm}(\omega+\omega_s) \times\left\{-\frac{r_o}{\beta\omega}\left(1+\frac{\omega_s}{\omega}\right)^{1/\beta} + \frac{r_g}{\beta(\omega+\omega_s)}\right\}\sin[E_{lm}], \tag{15b}$$

$$E_{lm} = r_o\chi_{lm}(\omega) - r_g\chi_{lm}(\omega+\omega_s). \tag{15c}$$

Factoring out the quantities independent of mode number and applying the results to Eq. (14) yields an expression for the range of the unknown objective source:

$$r_o = r_g\frac{(1+[\Delta\omega_s/\Delta\omega_I]_{\text{contour}})}{(1+\omega_s/\omega)^{1+1/\beta}}. \tag{16}$$

Thus if the virtual receiver output is plotted as a function of ω and ω_s, as is shown in the simulations in Figs. 2(a)–2(c), the measured slopes of the intensity extrema will yield the unknown source range via Eq. (16), given knowledge of both the guide source range and β. Comparison of Eq. (16) with Eq. (12), however, shows that the virtual aperture slopes have a much weaker dependence on β than a physical aperture, due to both the form of the exponent, and the fact that $\omega_s/\omega = \alpha$ is typically small ($\sim$0.1). The only effect of the β-dependent denominator in Eq. (16) is to add a slight curvature to the striations crossing the aperture. Thus the following approximation can be made:

$$r_o \approx r_g(1+[\Delta\omega_s/\Delta\omega_I]_{\text{contour}}). \tag{17}$$

This simplified result is notable in that all the input parameters are either known or measured quantities—all assumptions about the ocean waveguide have been removed. By neglecting the denominator in Eq. (16), any curvature across the aperture is ignored, and the aperture striations are assumed linear. As demonstrated in the next sections, this approximation is surprisingly robust. Equation (17) remains unchanged for waveguides with upward-refracting profiles, as is the case for deep-water and Arctic propagation. However, this article will focus on shallow-water environments characterized by reflective interactions on both the surface and ocean bottom, a situation under which $\beta\simeq 1$, and for which data were available. As shown in Appendix A, if the waveguide has range-dependent features, then the bathymetry around the vertical array and guide source must be known to achieve an accurate range estimate.

III. SIMULATIONS OF SHALLOW-WATER ENVIRONMENTS

Simulations of virtual aperture output are shown in Figs. 2 and 3, for the range-independent shallow-water environment illustrated in Fig. 4. This environment is characteristic of the region over which the data of Sec. IV were collected, and the frequencies and ranges over which the simulations are conducted have been chosen to facilitate comparison with the data examples that follow in Sec. IV. A normal mode code was used to compute the pressure fields, which were then inserted into Eq. (6). No additive background noise has been incorporated into the simulations, under the implicit assumption that the received signals have high signal-to-noise ratios.

Figures 2(a)–2(c) show virtual aperture outputs for three different vertical array geometries, when applied to a guide source at 2.25-km range and 50-m depth, and an objective source at the same depth, but 5.25-km range. All ranges displayed in the figures refer to the objective source range from the vertical array. In (a), a 64-element array spans the full depth of the waveguide, in (b) the more realistic waveguide geometry illustrated in Fig. 4 is used (1.875-m element spacing), and in (c), only eight evenly spaced elements of the latter array are used. Clearly, the more flagrant the violation of the orthonormality assumption, the more corrupted the striations become. However, even for the eight-element case in (c) the striation contours are clearly visible.

As noted in the previous section, these striations will curve slightly, a consequence of the denominator in Eq. (16). When this curvature is neglected, the striation slopes may be summarized by a rotation angle φ, measured counterclockwise from the image's vertical axis. Redefined in terms of this quantity, Eq. (17) becomes

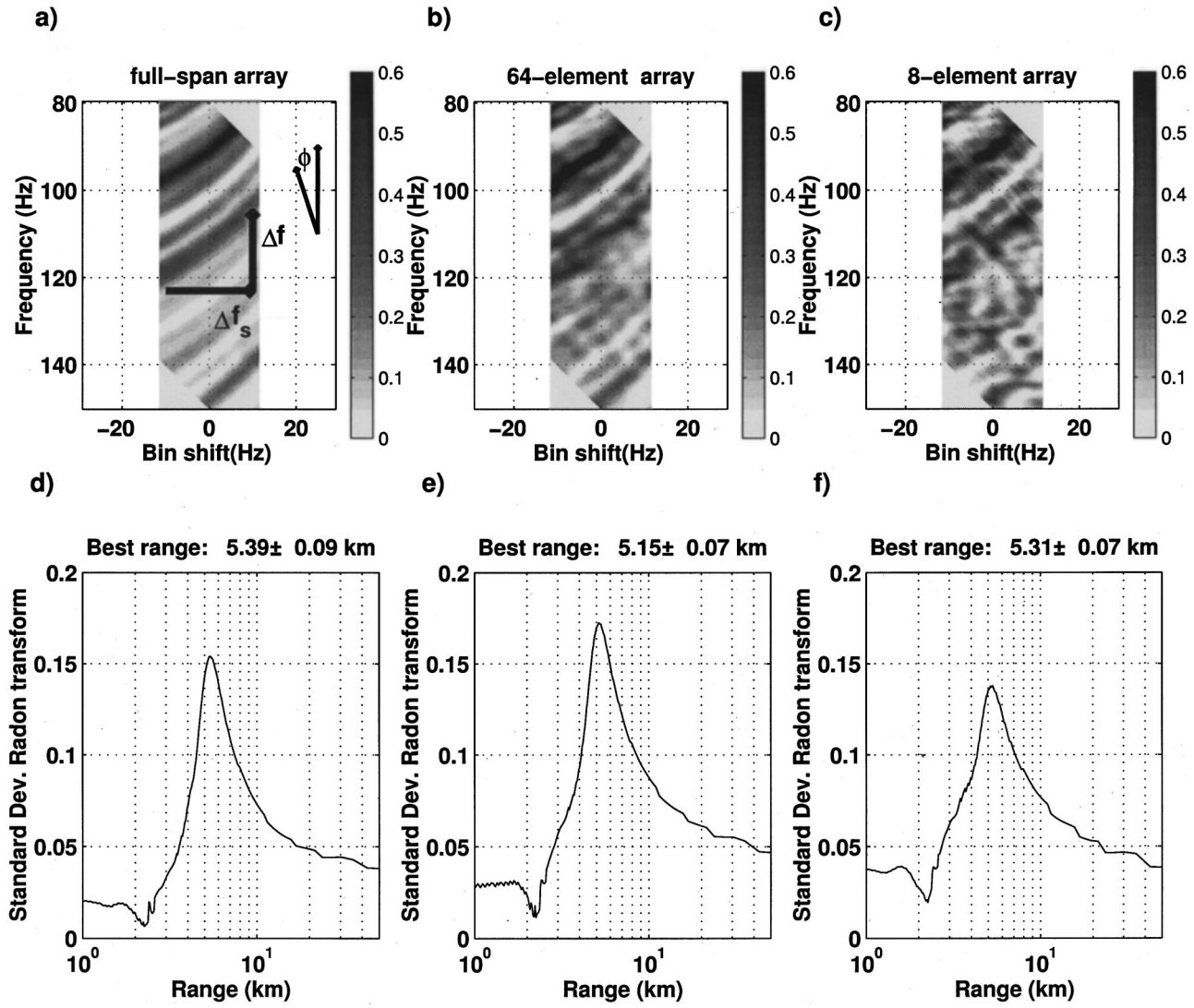

FIG. 2. Simulations of a virtual aperture centered around a 2.25-km guide source, detecting an objective source at 5.25-km range, with both sources at 50-m depth. The horizontal axis represents ω_s, and the vertical axis represents ω in Eqs. (16) and (17). (a) Virtual aperture generated using a 64-element array with complete coverage of the water column, between 5 and 195 m. (b) Virtual aperture generated using the 64-element array depicted in Fig. 4. (c) Virtual aperture generated using only eight elements from (b). (d)–(f) Radon range estimator outputs derived from the contour slopes in (a)–(c), using Eq. (18). The vertical axis represents the standard deviation of all the line integrals computed along an angle φ with respect to the vertical. Line integrals that run parallel to the intensity striations should yield the largest standard deviations. Discretization uncertainties have been estimated using Eq. (19).

$$r_o = r_g[1+\cot(\varphi-\pi/2)]. \tag{18}$$

The Radon transform[13,22,23] is a natural procedure for estimating φ. As outlined in Appendix B, the standard deviation of the modified Radon transform of a virtual aperture image provides an automated method for extracting slopes from an image. The Radon range estimator computes a set of parallel line integrals across the image along an angle φ with respect to the image vertical. The standard deviation of these integrals provides a rough measure of the contrast between the integrals. The greater this contrast, the more likely the integrals have been aligned along image ridges and troughs. Each rotation angle is converted into a hypothetical test range using Eq. (18).

Figures 2(d)–2(f) show the Radon range estimator output for each of the images in (a)–(c). The horizontal axis displays the hypothetical test range, and the vertical axis shows the standard deviation of the Radon transform output for the appropriate φ value. The test range that maximizes the Radon estimator is listed at the top of each figure. The estimates are clearly not perfect, because the estimation errors are as large as 200 m. These errors arise in part from the simplifications of Eq. (16), the width of the correlation bands in 2(d)–2(f), and the fact that ω and $\Delta\omega_s$ are discrete. This last effect arises because Eq. (1) is typically obtained via a fast fourier transform (FFT) of measured data, and thus ω and $\Delta\omega_s$ are discretized with a bin width inversely proportional to FFT sample length. Thus, the range estimate has an inherent uncertainty given by

$$\delta r_o = r_g \delta\omega \sqrt{\left(\frac{1}{\Delta\omega_s}\right)^2+\left(\frac{1}{\Delta\omega}\right)^2}, \tag{19}$$

where $\delta\omega$ is the FFT bin width in Hertz, and $\Delta\omega_g$ and $\Delta\omega$ represent the respective ''width'' and ''height'' of a typical striation. Equation (19) was used to estimate the errors ap-

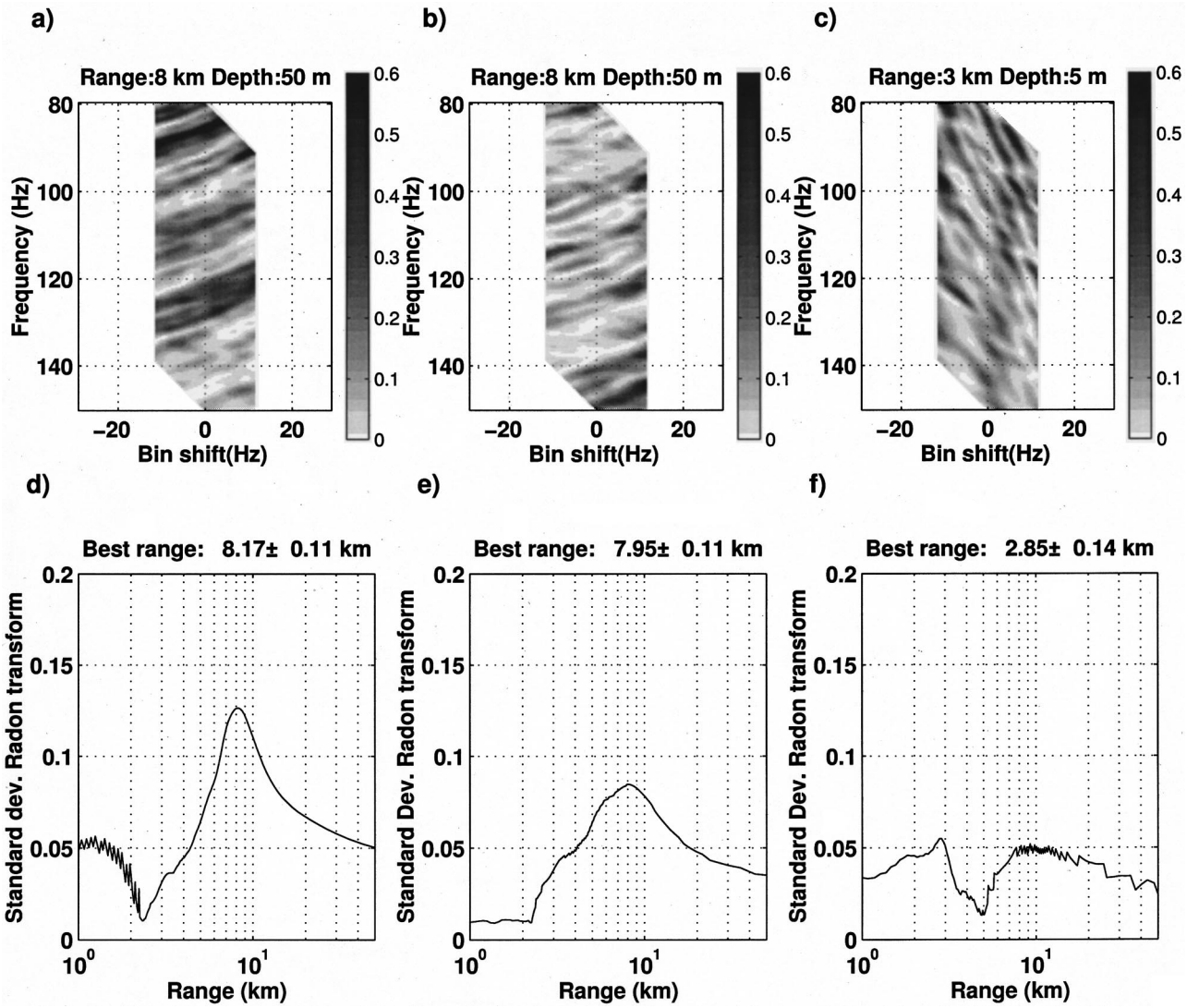

FIG. 3. Simulations of other possible virtual aperture arrangements, modeled using the realistic 64-element vertical array geometry in Fig. 4. (a) Guide source at 50-m depth, 2.25-km range; objective source at 50-m depth, 8-km range. (b) Same as (a), except guide source depth is 198 m, simulating a bottom-mounted source. (c) Guide source at 198-m depth, 5-km range; unknown source at 3-km range and 5-km depth, simulating a ship source. (d)–(f) Radon range estimator outputs obtained from (a)–(c), respectively.

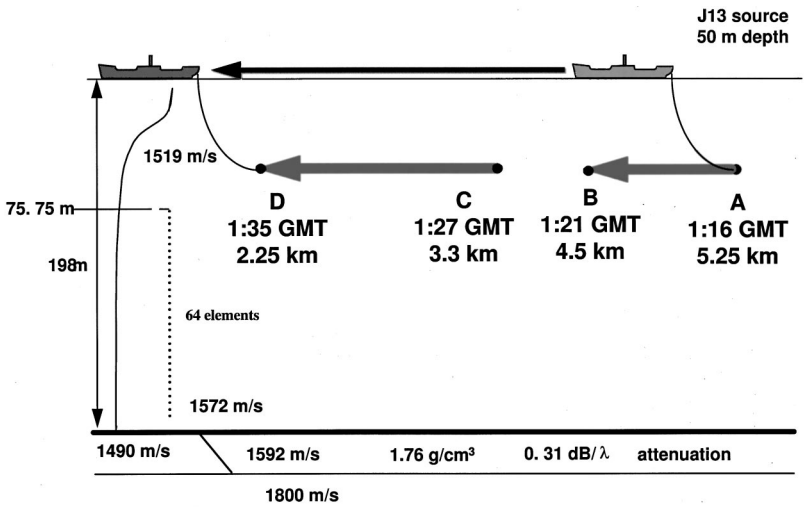

FIG. 4. Schematic of the shallow-water waveguide environment under which the data analyzed in this article were collected. The environment represents summer conditions off Point Loma, San Diego, CA. The data presented in Sec. IV were collected from a J13 source towed at 50-m depth, along a radial toward the vertical array. The ranges over which the source broadcast broadband (75–150 Hz) pseudo-random noise are indicated by the gray shaded arrows. The data used in this article were sampled at ranges A, C, and D. Between 1:21 and 1:27 GMT the source was broadcasting a ten-tone ''comb'' signal.

pended to the best range estimate in subplots (d)–(f), and these quantization errors seem to account for most of the observed discrepancy between the estimated and true objective source range.

Figure 3 demonstrates virtual aperture striations for various combinations of guide and objective source locations, using the realistic 64-element array geometry of Figs. 2(b) and 4. Figure 3(a) shows the striations from a guide source at the same location as Fig. 2, but with the objective source now located at 8-km range from the vertical array. Figure 3(b) keeps the objective source at 8 km, but models the guide source on the ocean bottom. The result suggests that the guide source depth does not need to be the same as the unknown source depth to achieve a satisfactory result. Finally, Fig. 3(c) illustrates the aperture pattern that would be produced by a 3-km range objective source at 5-m depth, across a bottom-mounted guide source at 5-km range. This last example was intended to simulate how the broadband signal from a surface ship might appear using a bottom-mounted transponder. This shallow objective source excites many high-order modes, which are responsible for the finely scaled striations visible in the output. The Radon estimator outputs for all three scenarios are plotted in Figs. 3(d)–3(f). In all cases the range errors lie within the discretization uncertainties computed from Eq. (19), although the estimator nearly fails to extract the correct range from Fig. 3(c).

The preceding results suggest that a virtual aperture can estimate source range to within 10% of the true value, even when using the approximate expression in Eq. (17).

IV. RESULTS FROM SHALLOW-WATER ENVIRONMENT

A. Data description

The virtual aperture algorithm is now demonstrated using data from the SWellEx-3 experiments, conducted off the coast of Point Loma, CA, in 1993.[14,18,24] Ideally, the concept should have been illustrated using two independent sources that overlap in bandwidth. However, as this data set was not available, an artificial example has been constructed wherein data samples from a towed J13 source have been used as both a guide and objective source from different times during its transit.

The situation analyzed here is illustrated in Fig. 4, which depicts part of the ''ArcMFP-2 event'' on Julian day 204. During the event the source was towed at 50-m depth along a radial towards a 64-element array suspended from the research platform FLIP,[25] in approximately 200-m depth water. The water depth between FLIP and the tug remained constant to within a few meters over this time period, and the tug had a differential global positioning system (DGPS) that recorded data every 10 s, so its position was always known to within 10 m. This particular data sequence is the focus of Ref. 14, and further details and references concerning this data set can be found therein.

Between GMT 1:16 and GMT 1:36 the source range decreased from 5.25 to 2.25 km (points ''A'' to ''D'' in Fig. 4). Between 1:16 GMT and 1:21 GMT (points ''A'' and ''B'') the source broadcast pseudo-random noise with a frequency-integrated source level of 150 dB *re* 1 μPa at 1 m, and a flat spectrum between 75 and 150 Hz. Given the background additive noise levels present at the time, the received signal-to-noise ratio at the array was about 10 dB for a single element.

Between points B and C the source broadcast a ten-tone ''comb'' signal. This data segment is unusable by the virtual aperture, because the received signals must contain energy distributed continuously across the frequency band of interest. Between 1:27 and 1:35 GMT (points ''C'' and ''D'') the source again broadcast pseudo-random noise until final cutoff at point D. All data were sampled at 1500 Hz, and all data analyses utilized a FFT length of 4096.

In this section the measured signal at point D will be treated as a ''guide'' source at 2.25 km, and the range of the ''objective'' source at points A and C will be estimated using the virtual aperture technique. This example has been contrived simply to demonstrate the principle, and is not intended to be an example of a practical use.

B. Implementation issues

Before applying the methods in Sec. II to real data, two additional complications must be addressed: vertical array tilt and noise contamination.

No vertical array is perfectly vertical. Currents can incline an array from less than 1 degree to over 15 degrees.[26] When performing matched-field processing with a vertical array, the tilt effects can simply be incorporated into the replica. By contrast, the VA algorithm requires that the tilt effects be stripped from both the guide and objective data sets before applying Eq. (6). This correction is achieved by applying a phase shift of $\exp(i*\omega*(z_n-z_0)*\tan(\theta))/c$ to each array element, where θ is the tilt of the array with respect to the vertical, z_0 is the depth of the point where the offset is defined to be zero, and z_n is the depth of phone n. If the tilt were not removed before implementing the VA, a phase offset of $\exp(i*\omega_s*(z_n-z_0)*\tan(\theta)/c)$ would exist along the array. For large values of θ this phase shift becomes significant, the orthonormality condition used to derive Eq. (7) will be violated, and the technique will fail. The vertical tilt of the array was small throughout the ArcMFP2 event, measuring only 0.5 to 1.4 degrees, but the tilt effects were stripped as a precaution.

The existence of extraneous uncorrelated noise in either the guide and/or the objective source data samples will produce ''streaks'' in the virtual aperture along $\varphi = 45$ degrees. The reason behind this observation is that when extraneous noise exists in a data segment at frequency ω_0, then the corrupted output will appear in $I_v(z_g, r_g, \omega_0, 0)$. Inspection of Eq. (6) shows that this same corrupted frequency bin will also be used when computing $I_v(z_g, r_g, \omega_0 - \omega_s, \omega_s)$ for any ω_S, and thus the noise will appear as a 45-degree streak when the virtual aperture output is plotted as a function of ω and ω_s. These streaks become particularly damaging whenever the objective source lies closer to the vertical array than the guide source, because then the noise streak slopes are similar to the desired striation slopes, a situation that can destroy a range estimate.

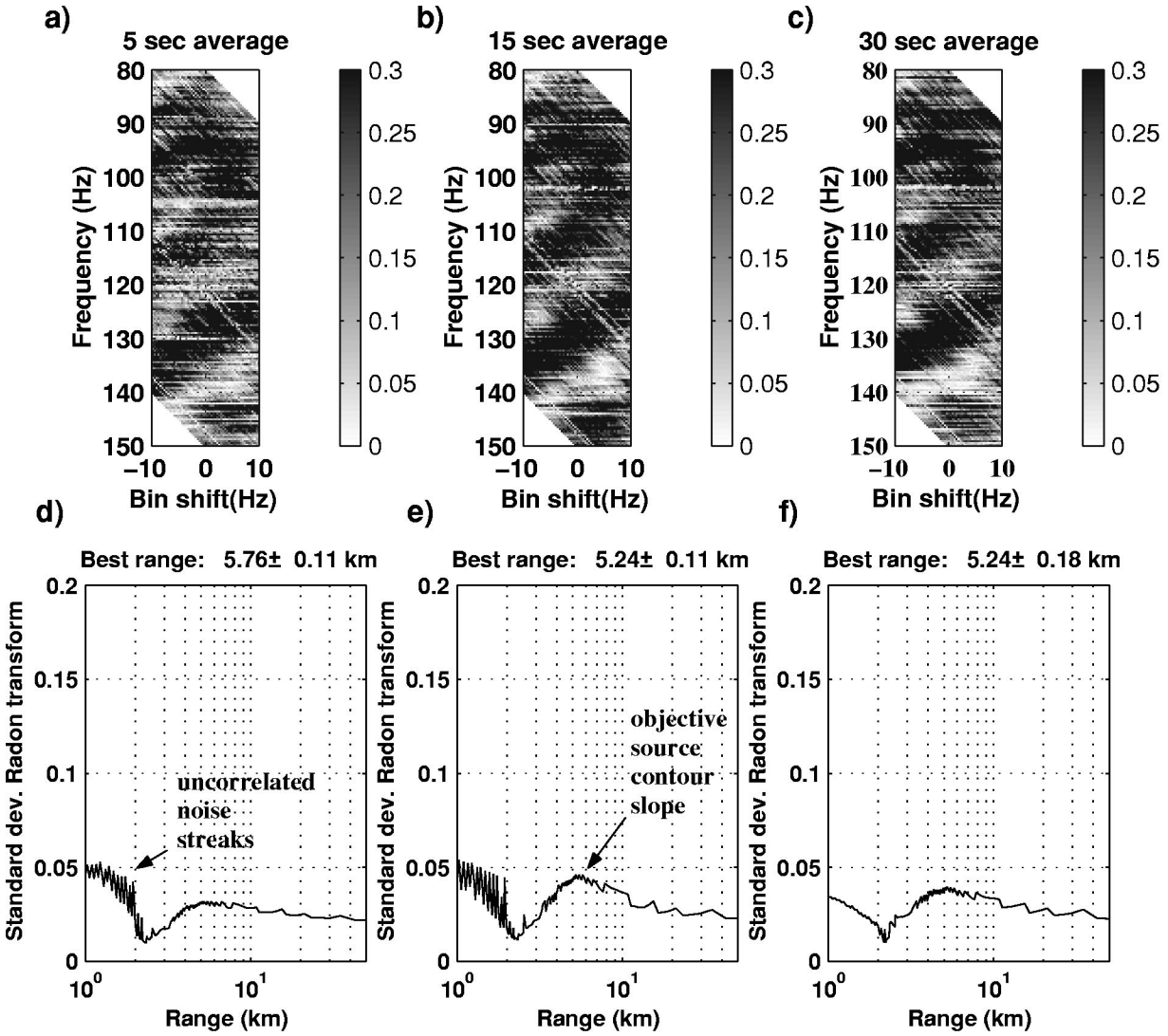

FIG. 5. Virtual apertures constructed around 2.25-km range, using a 15-s sample of pseudo-random noise measured at point D in Fig. 4 as the guide source. The objective source data were averaged at point A (5.25-km range) for (a) 5, (b) 15, and (c) 30 s. Note the existence of 45-degree streaks due to background noise contamination, and the different grayscale map range compared with Figs. 2 and 3. (d)–(f) Radon range estimator outputs of objective source range for (a)–(c). The search for the best range has been limited to ranges greater than the guide source range of 2.25 km, because the Radon output becomes swapped by the noise contamination whenever the integration angle φ is positive.

C. Position A used as objective source

Figure 5 illustrates the virtual aperture constructed by combining the guide source data at point D with data recorded at point A, once array tilt effects have been removed. The data samples were averaged as a cross-spectral density matrix (CSDM), and then the dominant eigenvector was extracted to represent $p(\omega,r)$ in Eq. (6). All data samples used a 4096 pt. FFT with a 75% overlap between successive samples. The guide source data consists of a 15-s average of the signal at point D, and subplots in Figs. 5(a)–5(c) show the effects of using different time averages on the objective source data recorded at point A. Note that the grayscale maps for the data analysis in Figs. 5 and 7 differ from the simulations in Figs. 2 and 3, because the virtual receiver outputs from the data are typically lower than the simulation outputs. A comparison between Figs. 5(a)–5(c) and the analogous simulation in Fig. 2(b) suggests that the striation bands produced by the data are wider than those predicted by the simulations. The most plausible explanation for this observation is that only the lower-order modes are interfering in Fig. 5, and the higher-order modes have suffered greater attenuation than what has been assumed in Fig. 4. Another possibility is that the array has not sampled the higher-order modes adequately, due to uncertainties in accounting for the array shape. Whatever the reasons for the different striation widths, the contour slopes for both the data and simulations are similar.

The Radon range estimator outputs are shown in subplots in Figs. 5(d)–5(f) for the different objective source data averaging times. For short averaging times, the 45-degree noise streaks discussed in Sec. IV B swamp the estimator output, so for these cases the best range estimate has been restricted to ranges greater than the guide source range. However, if the objective source data is averaged for 30 s, Fig. 5(f) shows that the noise contamination seems to be mitigated, and the Radon range estimator reaches a global

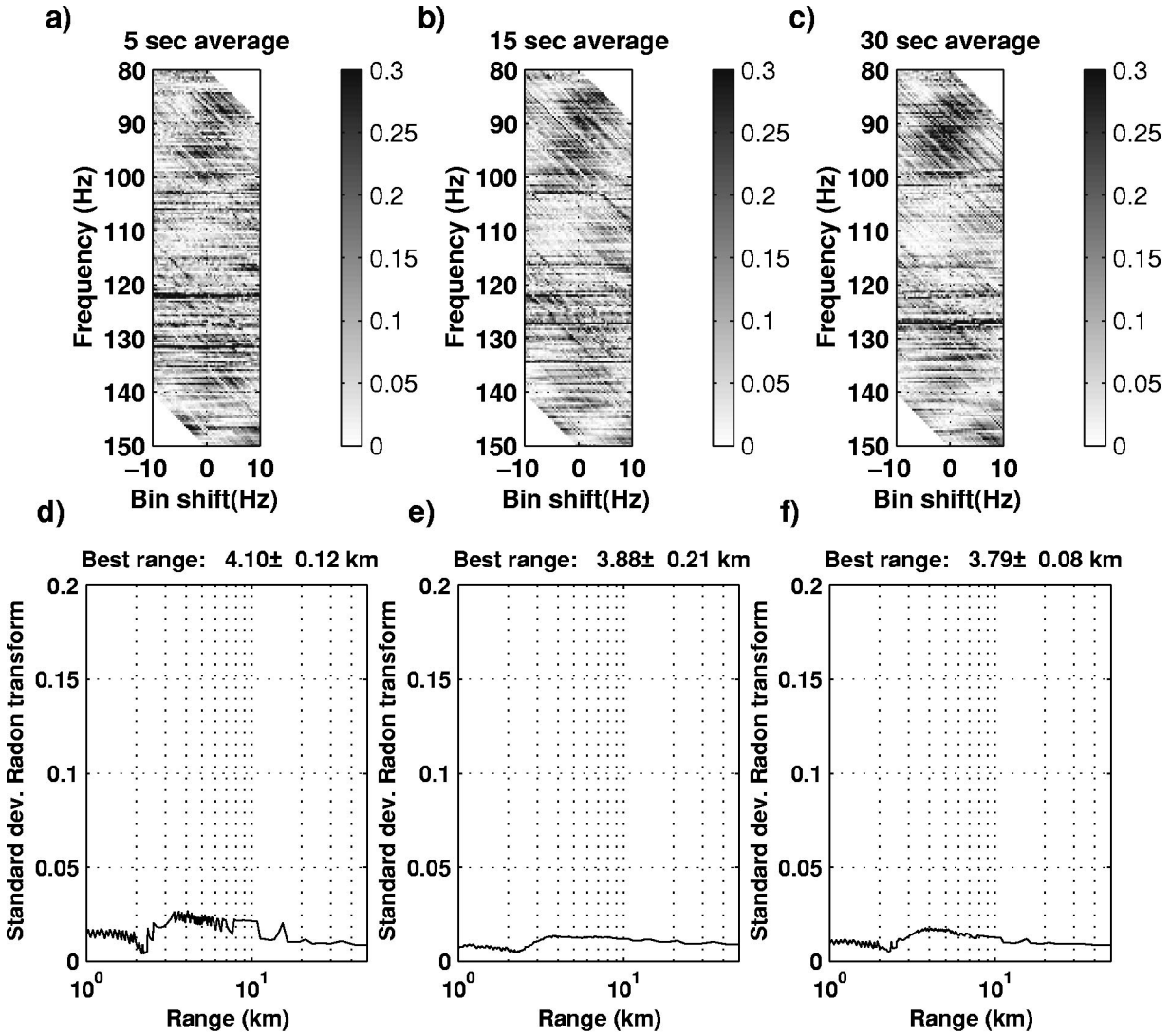

FIG. 6. Same as Fig. 5, except the objective source consists of data collected point C in Fig. 4, when the source tow is 3.3 km from the vertical array.

maximum at the true objective source range. Because of the broad width of the estimation peak, the potential range variance is probably larger than the discretization errors computed from Eq. (19), using a bin size of 0.37 Hz. It is not clear whether the ''half-power bandwidth'' would be an appropriate measure of the estimator variance.

D. Point C used as objective source

Figure 6 illustrates the virtual aperture output constructed by combining the guide source data measured at point D with data measured at point C, where the towed source was 3.3 km away from FLIP. Figures 6(a)–6(c) plot the virtual aperture output for different objective source data averaging times, and subplots in Figs. 6(d)–6(f) show the corresponding Radon range estimator outputs. The objective source signal intensity measured at point C should be greater than that measured at point A, because the source is closer. However, the background noise level, presumably from the tug, has also increased. As a result the uncorrelated noise streaks are more noticeable in Fig. 6, in comparison with Fig. 5. While faint striations are visible in Figs. 6(a)–6(c), the Radon range estimator has trouble extracting the correct range from the broad peaks in Figs. 6(d)–6(f), and the range estimates are biased by around 500 m.

V. DISCUSSION

The data analysis of the previous section demonstrates that the virtual aperture can succeed under favorable experimental conditions, for moderate SNR broadband signals in a range-independent environment. Furthermore, most range estimates computed from Eq. (17) are within 10% of the true source range, even when the environmentally dependent curvature in the intensity contours is neglected. Therefore, it appears possible to obtain reasonable range estimates without assuming any knowledge of the propagation environment (i.e., β).

Clearly several issues must be addressed before this concept can be considered practical. First, the effects of a range-dependent bathymetry must be considered. When adiabatic propagation assumptions are valid, the extension of Eq. (16) is straightforward and is derived in Appendix A. The final result reveals that the bathymetry surrounding the array must

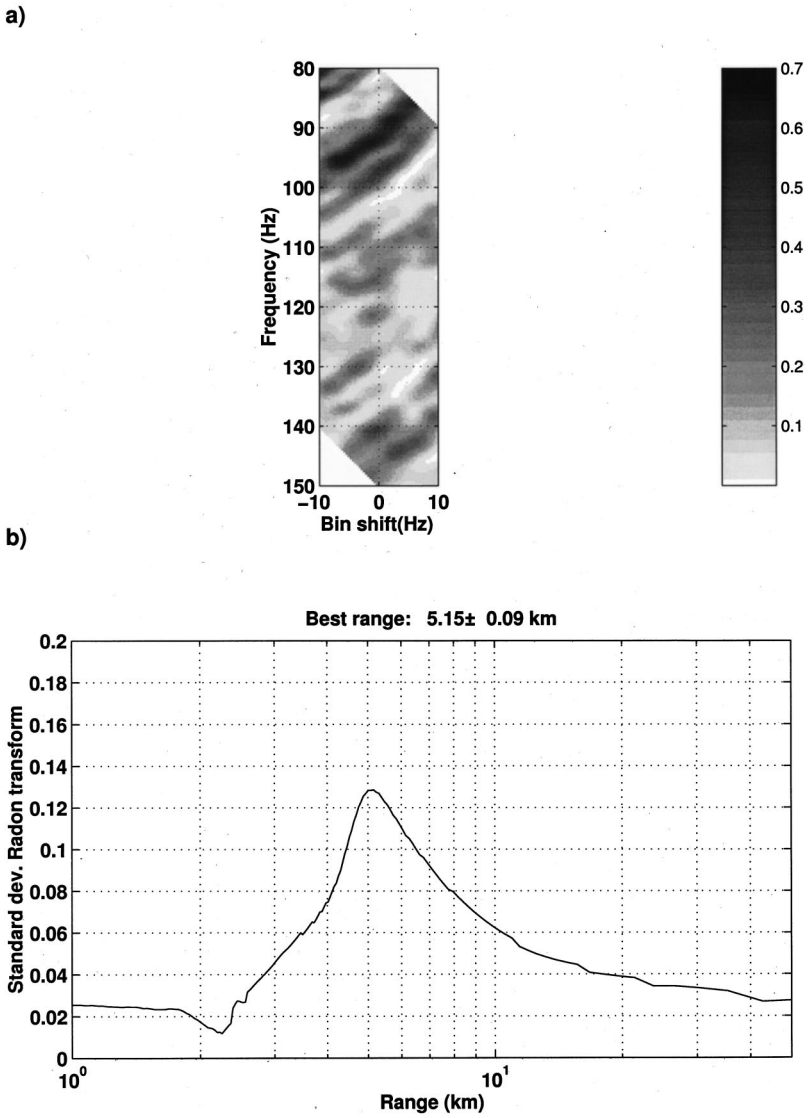

FIG. 7. Example of the potential robustness of the virtual aperture. The objective and guide source fields have been computed using the sound-speed profile in Fig. 4, and an isovelocity sound-speed profile, respectively. (a) Virtual aperture output using the environmentally mismatched guide and objective source fields. (b) Radon range estimator output of (a), for comparison with Fig. 2(e).

be known in order to obtain an accurate source estimate. Second, it would be desirable to derive some image-processing scheme that could implement Eq. (16) directly, by incorporating a rough knowledge of β. Third, better data and image-processing techniques are needed to remove or mitigate the effects of uncorrelated noise. Averaging the data, extracting the dominant eigenvector, and spatially filtering the virtual aperture image has shown some promise. However, as Fig. 6 demonstrates, more sophisticated approaches are needed if the concepts illustrated here are to succeed on signals contaminated with high levels of background noise. A fourth practical problem is whether the vertical array tilt can be measured with enough spatial and temporal resolution to allow effective ''tilt-stripping,'' as discussed in Sec. IV B.

A final, fundamental issue concerns the temporal scale over which the ocean propagation channel evolves. The utility of a virtual aperture would increase tremendously if the guide source signal could be applied to signals recorded days, even weeks later, despite changes in the sound speed profile over that interval. There are some theoretical reasons to believe that this longevity may be possible, as Fig. 7 demonstrates. Here a simulation of a virtual aperture is performed that uses the same objective source model as Fig. 2(b), but then uses an isovelocity profile to compute the guide source signal. The mean value of the original downward-refracting profile has been used for the isovelocity sound speed. Due to the environmental mismatch, the number and magnitude of the striations in Fig. 7(a) have been reduced relative to Fig. 2(b). However, the striation slopes have remained unaltered, as a comparison of Fig. 7(b) with Fig. 2(e) makes clear.

The reason behind this apparent robustness is that the virtual aperture striation slopes are not dependent on individual modal phase or group slownesses, which can vary substantially with changes in the sound speed profile. Instead, the slopes are primarily a function of the *ratio of differences* between these quantities, which is the fundamental definition of β in Eq. (8). Thus, as long of the value of β does not change substantially in a waveguide with time, guide source signals should have a long useful lifetime. When introducing the concept of β, in Sec. II the discussion was restricted to the particular class of waveguide dominated by surface and bottom reflections. This situation describes most shallow-water propagation environments. As long as a waveguide remains primarily characterized by reflections off

the medium boundaries, and not refractions within the water column, β would not be expected to deviate substantially from its initial value, because the fundamental relationship between the modal group and phase velocities [e.g., Eq. (9)] has not been altered. Stated less abstractly, a virtual aperture is predicted to be robust in shallow-water environments, provided that the thermocline does not steepen to the point where the majority of the rays associated with the propagating modes become refracted before contacting the ocean surface.[16]

There is some experimental evidence supporting this prediction of guide source longevity. Recent demonstrations of phase conjugation in the ocean[15] have shown that a narrow-band time-reversed signal received from a probe below the thermocline will still refocus at its original origin, even when retransmitted a week after being recorded. This result hints that guide source signals may be viable for at least days, particularly if they lie beneath the thermocline. Additional experimental information on this topic will probably be gathered in the near future, and a virtual aperture might even provide a convenient framework for characterizing the long-term temporal and spatial evolution of an oceanic waveguide.

VI. CONCLUSION

Waveguide invariant theory has been used to extend the virtual receiver concept into a virtual aperture. With this construct, the range of an unknown acoustic source can be estimated, if a signal sample is available from a second acoustic source at a known location. For range-independent bathymetries the range estimator can be simplified into a form that requires no knowledge about the ocean environment. However, for mildly range-dependent environments, the bearings of both sources, along with the bathymetry surrounding the vertical array, must be available as well. A simple image-processing method using the Radon transform has been developed to automatically extract the unknown source range from a virtual aperture image. A practical implementation of this approach requires that the vertical array tilt be accurately known. These ideas have been successfully demonstrated on data recorded from a pseudo-random noise source in a typical shallow-water environment, but the results also illustrate the need for more sophisticated image processing algorithms. Further development and demonstration of the concept on additional data sets will be necessary to fully explore the advantages and limitations of this approach for ranging unknown sources in complex propagation environments.

ACKNOWLEDGMENTS

The author thanks Bill Kuperman, Gerald D'Spain, and Hee Chun Song for discussions and advice about the ideas presented here. He would also like to thank Gerald for assistance in obtaining the data and background information presented here. This research was supported in part by the Office of Naval Research Grant Nos. N00014-97-0593 and N00014-96-1-0603, and in part by a postdoctoral position funded by the SECNAV/CNO Chair and ONR/MIT Scholar of Oceanographic Science award N00014-99-1-0087. The author also thanks the two anonymous reviewers who helped strengthen the paper.

APPENDIX A: VIRTUAL APERTURE FORMULATION FOR RANGE-DEPENDENT ENVIRONMENTS

In this section, a generalization of Eq. (16) is derived for a more realistic scenario wherein the bathymetry around the vertical array varies as a function of range r and azimuth θ. Let the guide source be located at range r_g and azimuth θ_g, and the unknown objective source be located at range r_o and azimuth θ_o. It is assumed that both bearings have been obtained by independent means, and that adiabatic propagation conditions hold. Equation (7) may then be adjusted as follows:

$$I_V(z_g,r_g,\omega,\omega_s)=N^2\sum_m\sum_l A_lA_m \times\cos\left[\int_0^{r_o}\chi_{lm}(\theta_o,r,\omega)dr-\int_0^{r_g}\chi_{lm}(\theta_g,r,\omega+\omega_s)\,dr\right]. \quad \text{(A1)}$$

Here the modal attenuation coefficients have been dropped, and the horizontal wave number differences χ_{lm} are shown as an explicit function of azimuth, range, and frequency. The integrals can be rewritten using the range-dependent definition of β originally derived by Chuprov,[16] and also defined in Eq. (14) of Ref. 14:

$$\frac{1}{\beta(r,\theta)}=-\left[\frac{1}{r}\int_0^r\frac{\partial\chi_{lm}(\theta,r,\omega)}{\partial\omega}dr\right]\left(\frac{\chi_{lm}^{\mathrm{rcvr}}(\omega)}{\omega}\right)^{-1}, \quad \text{(A2)}$$

where the quantity labeled ''rcvr'' is evaluated at zero range (i.e., at the vertical receiver array). Clearly β is a function of the range-averaged modal group velocity differences, and thus in general will be a function of both range and azimuth. However, its value will still be approximately independent of frequency and wave number.

Rearranging the order of integration and differentiation in Eq. (A2) and applying Eq. (10) yields

$$\int_0^r\chi_{lm}(\theta,r,\omega)\,dr=r\,\frac{\beta^{\mathrm{rcvr}}}{\beta(r,\theta)}\,\chi_{lm}^{\mathrm{rcvr}}(\omega), \quad \text{(A3)}$$

where β^{rcvr} is the value of the invariant at the vertical receiving array. Combining Eqs. (A1)–(A3) yields the following expression:

$$I_V(z_g,r_g,\omega,\omega_s)=N^2\sum_m\sum_l A_lA_m\cos\left[\frac{\beta^{\mathrm{rcvr}}r_o\chi_{lm}^{\mathrm{rcvr}}(\omega)}{\beta(r_o,\theta_o)}-\frac{\beta^{\mathrm{rcvr}}r_g\chi_{lm}^{\mathrm{rcvr}}(\omega+\omega_s)}{\beta(r_g,\theta_g)}\right]. \quad \text{(A4)}$$

Another use of Eq. (10), followed by a repetition of the procedure described in Eqs. (14) and (15), yields the range-dependent version of Eq. (16):

$$r_o = r_g \frac{\beta(r_o,\theta_o)(1+[\Delta\omega_s/\Delta\omega_I]_{\text{contour}})}{\beta(r_g,\theta_g)(1+\omega_s/\omega)^{1+1/\beta^{\text{rcvr}}}}. \quad \text{(A5)}$$

Equation (A5) must be iterated, because each estimate of r_o must be used to readjust $\beta(r_o,\theta_o)$, which in turn yields an improved estimate of r_o. This procedure should converge after a few iterations.

For the particular case of low-order modes in a shallow-water propagation environment, where both the surface and bottom boundary conditions are reflective (not refractive), Eq. (A2) has been shown to be primarily a function of bathymetry:[14]

$$\frac{1}{\beta(r,\theta)} \approx D_{\text{rcvr}}^2 \left[\frac{1}{r}\int_0^r \frac{1}{D(x,\theta)^2}\,dx\right], \quad \text{(A6)}$$

where D_{rcvr} is the water depth at the vertical array, and $D(r,\theta)$ is the water depth at range r and azimuth θ from the array. As a result evaluation of Eq. (A5) requires knowledge of the bathymetry surrounding the array. However, by invoking the same argument used to convert Eq. (16) into Eq. (17), it can be argued that the term dependent on β^{rcvr} in Eq. (A5) can be neglected. Thus, neither the sound speed profile nor bottom composition are needed to recover a range estimate. Thus it is possible that Eq. (A5) would still be a robust, and hence useful, estimator.

APPENDIX B: THE RADON RANGE ESTIMATOR

In this Appendix some details of the Radon range estimator algorithm are presented. More detailed descriptions of this technique have been previously presented elsewhere.[13]

The virtual aperture output consists of nearly straight intensity contours, all rotated at an angle ϕ with respect to the vertical. A natural computational method for estimating this angle is the Radon transform, which performs line integrals across an image along different rotation angles and different offsets from the image center. Specifically

$$\begin{aligned}\Re(p,\varphi,I_v(\omega_0,\omega_s)) &\equiv \Re(p,\varphi)|_{\omega_0,\omega_s} \\ &= \int_{-\infty}^{\infty} I_v \\ &\quad \times (p\cos\varphi + t\sin\varphi,\, p\sin\varphi + t\cos\varphi)\,dt|_{\omega_0,\omega_s}. \quad \text{(B1)}\end{aligned}$$

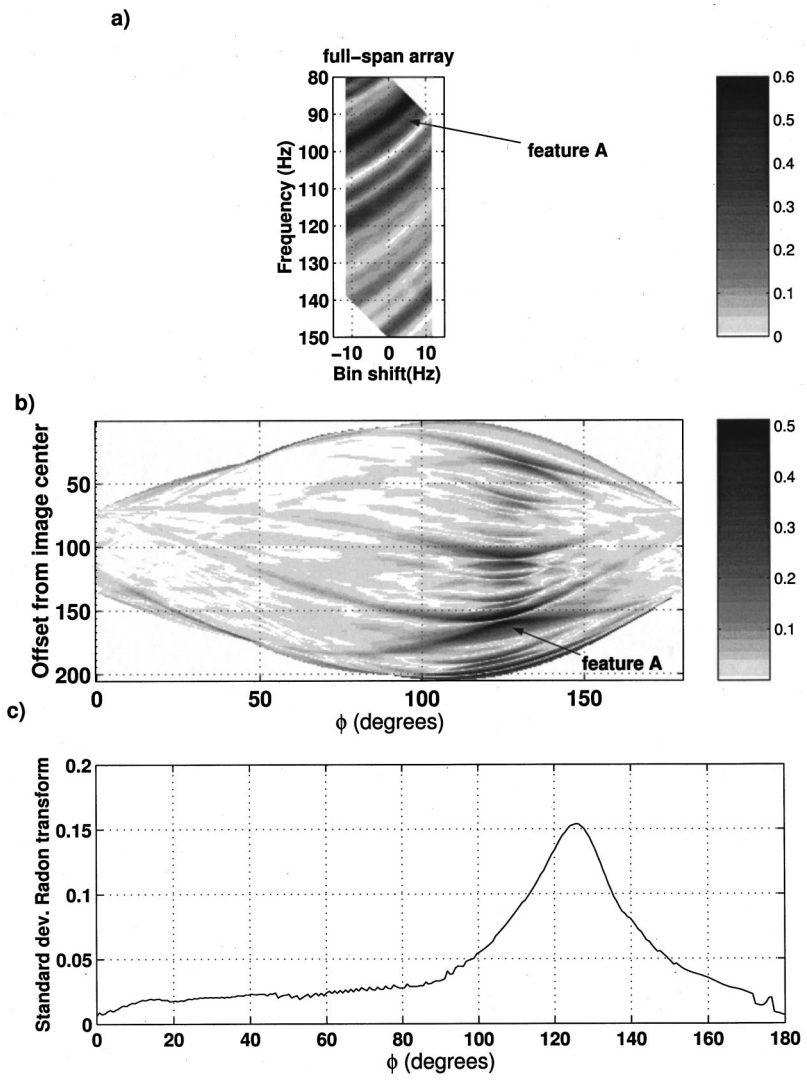

FIG. B1. Example of the Radon range estimation algorithm. (a) Reproduction of Fig. 2(a). (b) Output of Radon transform of Eq. (B2). (c) Standard deviation of subplot along the vertical (p) axis, as a function of rotation angle φ. The φ axis is transformed into a range axis via Eq. (18).

Here p represents a unitless distance from a reference point in an image, which is typically the center pixel. A line lying at an angle φ with respect to the vertical (ω) axis and passing a minimum distance of p units away from the image center will be mapped into a point at the coordinates (p,φ). In practice, a more effective way to estimate the rotation angle is to perform a Radon transform of the modified aperture image I_{vg}:

$$I_{vg}(\omega,\omega_s) \equiv \text{sign}\left(\frac{\partial I_v}{\partial \omega_s}\right) I_v . \tag{B2}$$

As discussed in Ref. 13, multiplying an image by the sign of its horizontal gradient tends to cancel line integrals that are not exactly parallel to the intensity striations.

The Radon processor is illustrated using the virtual aperture image from Fig. 2(a), which is reproduced in Fig. B1(a). After application of Eqs. (B2) and (B1), the resulting output is plotted in Fig. 2(b), as a function of rotation angle φ and offset distance p. The arrows show how one prominent linear striation in subplot (a) is mapped into subplot (b). Instead of summing along the vertical (p) axis, computing the standard deviation appears to be more effective in identifying the striations, and this latter procedure is used to construct Fig. B1(c). The standard deviation operation provides a rough measure of the contrast between the minimum and maximum outputs along the p axis for a given φ value. The final step consists of using Eq. (18) to covert the horizontal axis into units of objective source range.

[1] R. Benedict, Jr., J. B. Breckinridge, and D. L. Fried, ''Atmospheric-compensation technology (feature),'' J. Opt. Soc. Am. A **11**, 257–451 (1994).

[2] A. A. Al-Kurd and R. P. Porter, ''Performance analysis of the holographic array processing algorithm,'' J. Acoust. Soc. Am. **97**, 1747–1763 (1995).

[3] P. D. Mourad, D. Rouseff, R. P. Porter, and A. Al-Kurd, ''Source localization using a reference wave to correct for oceanic variability,'' J. Acoust. Soc. Am. **92**, 1031–1039 (1992).

[4] M. Siderius, D. R. Jackson, D. Rouseff, and R. Porter, ''Multipath compensation in shallow water environments using a virtual receiver,'' J. Acoust. Soc. Am. **102**, 3439–3449 (1997).

[5] J. A. Rivers, ''Blue whale, *Balaenoptera musculus*, vocalizations from the waters off central California,'' Marine Mammal Sci. **13**, 186–195 (1997).

[6] C. W. Clark and J. H. Johnson, ''The sounds of the bowhead whale, *Balaena mysticetus*, during the spring migrations of 1979 and 1980,'' Can. J. Zool. **62**, 1436–1441 (1984).

[7] K. Payne and R. Payne, ''Large scale changes over 19 years in songs of humpback whales in Bermuda,'' Z. Tierpsychol. **68**, 89–114 (1985).

[8] J. C. Goold and S. E. Jones, ''Time and frequency domain characteristics of sperm whale clicks,'' J. Acoust. Soc. Am. **98**, 1279–1291 (1995).

[9] W. A. Kuperman, W. S. Hodgkiss, H. C. Song, and T. Akal, ''Phase conjugation in the ocean: Experimental demonstration of an acoustic time-reversal mirror,'' J. Acoust. Soc. Am. **103**, 25–40 (1998).

[10] A. Parvulescu, ''Matched-signal (mess) processing by the ocean,'' J. Acoust. Soc. Am. **98**, 943–960 (1995).

[11] D. R. Jackson and D. R. Dowling, ''Phase conjugation in underwater acoustics,'' J. Acoust. Soc. Am. **89**, 171–181 (1991).

[12] A. Parvulescu and C. S. Clay, ''Reproducibility of signal transmissions in the ocean,'' Radio Electron. Eng. **29**, 223–228 (1965).

[13] A. M. Thode, W. A. Kuperman, G. L. D'Spain, and W. S. Hodgkiss, ''Matched-Field Processing using Bartlett sidelobe interference structures,'' J. Acoust. Soc. Am. **107**, 278–286 (2000).

[14] G. L. D'Spain and W. A. Kuperman, ''Application of waveguide invariants to analysis of spectrograms from shallow water environments that vary in range and azimuth,'' J. Acoust. Soc. Am. **106**, 2454–2468 (1999).

[15] W. S. Hodgkiss, H. C. Song, and W. A. Kuperman, ''A long-range and variable focus phase-conjugation experiment in shallow water,'' J. Acoust. Soc. Am. **105**, 1597–1604 (1999).

[16] S. D. Chuprov, ''Interference Structure of a Sound Field in a Layered Ocean,'' in *Akustika Okeana. Sovremennoe Sostoyanie (Ocean Acoustics, Current State)*, edited by L. M. Brekhovskikh and I. B. Andreevoi (Nauka, Moscow, 1982), pp. 71–91.

[17] G. A. Grachev, ''Theory of acoustic field invariants in layered waveguide,'' Acoust. Phys. **39**, 33–35 (1994).

[18] J. Rice and J. Determan, ''SWellEx-3 Data Report,'' NCCOSC RDT&E Division, Code 541, Tech Rept. 1995.

[19] F. B. Jensen, W. A. Kuperman, M. B. Porter, and H. Schmidt, *Computational Ocean Acoustics* (American Institute of Physics, New York, 1994).

[20] A. B. Baggeroer, W. A. Kuperman, and P. N. Mikhalevsky, ''An overview of matched field methods in ocean acoustics,'' IEEE J. Ocean Eng. **18**, 401–424 (1993).

[21] L. M. Brekhovskikh and Y. Lysanov, *Fundamentals of Ocean Acoustics*, 2nd ed. (Springer-Verlag, Berlin, 1991).

[22] S. R. Deans, *The Radon Transform and Some of its Applications* (Wiley, New York, 1983).

[23] J. R. Fricke and A. B. Baggeroer, ''Modal-slowness analysis of plate vibrations,'' J. Acoust. Soc. Am. **92**, 3228–3238 (1992).

[24] N. O. Booth, P. A. Baxley, J. A. Rice, P. W. Schey, W. S. Hodgkiss, G. L. D'Spain, and J. J. Murray, ''Source localization with broad-band matched-field processing in shallow water,'' IEEE J. Ocean Eng. **21**, 402–412 (1996).

[25] E. D. Bronson and L. R. Glosten, ''FLIP; Floating Instrument Platform,'' Marine Physical Laboratory, SIO, MPL Tech. Memo MPL-U-27/85 (1985).

[26] A. M. Thode, G. L. D'Spain, and W. A. Kuperman, ''Matched-field processing and geoacoustic inversion of blue whale vocalizations,'' J. Acoust. Soc. Am. **107**, 1286–1300 (2000).

Backscatter of high-frequency (200 kHz) acoustic wavefields from ocean turbulence

Marshall H. Orr
Code 7120, Naval Research Laboratory, 4555 Overlook Avenue, S.W., Washington, D.C. 20375-5350

Loren R. Haury
145 Copper Cliff Lane, Sedona, Arizona 86336

Peter H. Wiebe
Department of Biology, Woods Hole Oceanographic Institution, Woods Hole, Massachusetts 02543

Melbourne G. Briscoe
Code 322, Office of Naval Research, 800 North Quincy Street, Arlington, Virginia 22217-5660

(Received 5 March 1999; revised 6 December 1999; accepted 16 May 2000)

Near space and time coincident 200-kHz acoustic backscatter and CTD measurements were taken during an interdisciplinary study of the internal wave packets that propagate through Massachusetts Bay. The data strongly support the contention that acoustic wavefields can be backscattered from turbulent mixing events (microstructure) associated with the internal wave packets. © *2000 Acoustical Society of America.* [S0001-4966(00)04308-3]

PACS numbers: 43.30.Vh, 43.30.Ft, 43.30.Pc [DLB]

INTRODUCTION

Goodman[1] has expanded the theoretical treatment of the scatter of acoustic signals from oceanic microstructure. In the same paper he presented a review of measurements that suggest acoustic signals can be scattered from sound-speed fluctuations associated with oceanic microstructure. His review revealed that the space-time coincident detection of acoustic signals scattered by oceanic microstructure and measurement of temperature and salinity fluctuations in the immediate vicinity of the scattering volume had not been reported.

Recently, Seim *et al.*[2] have presented data that suggest acoustic signals can be scattered from turbulent microstructure. The experiment was performed in a stratified tidal channel (Admiralty Inlet near Puget Sound, Washington). Trevorrow[3] has detected acoustic signals that were thought to be backscattered by turbulent microstructure associated with internal waves off the coast of Oregon, and Sandstrom *et al.*[4] have compared the time series of backscattered acoustic signals to conductivity, temperature versus depth (CTD) measurements made at the same depth as the acoustic scattering volume. The Sandstrom experiment was performed near the shelf break of Nova Scotia, Canada, and suggests that the acoustic signals were scattered from regions associated with active turbulence. In addition to the above, Farmer has used acoustic backscatter systems for many years to generate flow visualization of hydraulic processes generated by flow over sills.[5,6] He has associated some backscattered acoustic signals with oceanic mixing.

None of the above oceanic or near oceanic data sets were supported by space-time coincident acoustic and temperature and salinity measurements. Sandstrom *et al.*'s[4] CTD and acoustic measurements were separated in time by about 27 sec and in space by ~100 m, the Seim *et al.*[2] acoustic and fine structure measurements were separated in time by 10 to 50 sec with initial spatial separations of 6–26 m, and the Trevorrow[3] acoustic and temperature measurements were spatially separated by ~470 m.

In non oceanic settings, Thorpe and Brubaker,[7] and Pelech *et al.*,[8] have reported evidence for acoustic scatter from turbulent wakes generated by bodies towed through the large temperature gradients at the base of the mixed layer in a fresh water lake and pond, respectively. They infer the acoustic scattering was caused by temperature fluctuations in the turbulent wake.

Near space-time coincident acoustic and CTD measurements that further support the conjecture that 200-kHz acoustic signals can be scattered from temperature and conductivity variability associated with ocean turbulence are presented below. The acoustic scattering volume and CTD were separated by about ~3 m and were nearly in the same vertical plane. The scattering volume was sampled by the CTD ≤6 sec after the acoustic signal was scattered from it.

EXPERIMENT

An interdisciplinary study (oceanic biology, Haury and Wiebe; physical oceanography, Briscoe; and ocean acoustics, Orr) of internal wave packet generation, propagation, decay, and impact on the distribution of biota was conducted from 27 August to 2 September 1977. The site of the experiment was in Massachusetts Bay between Boston and the northwest tip of Cape Cod, Massachusetts. Some results of the study[9,10] have been previously reported.

A 2° beamwidth, 200-kHz acoustic system[11,12] designed to detect acoustic backscatter from sound velocity fluctuations caused by oceanic turbulence was used during the experiment to image ocean microstructure, shear instabilities, and the spatial and temporal evolution of the internal wave packets. The acoustic system could detect target strengths of about −100 dB at a range of 100 m. At a range of 10 m it

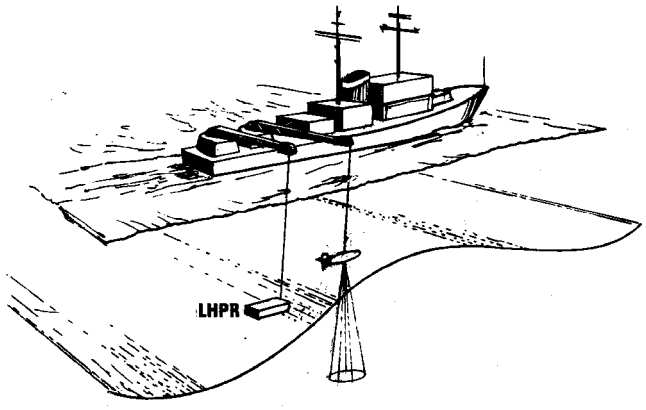

FIG. 1. Deployment geometry of the acoustic tow body and the Longhurst-Hardy Plankton Recorder equipped with a CTD-fluorometer package.

could detect scatters with target strengths of about -150 dB and resolve an individual scatterer in a water volume of about 6.8×10^{-2} m^3, i.e., a cylinder 108 cm in diameter and 7.5 cm in thickness. The tow body housing the acoustic transducer was lowered to a depth of 1 m below the ocean surface and was horizontally displaced about 6 m from the RV Oceanus (Fig. 1). The acoustics data were displayed with an EPC graphics recorder. The acoustic system used either a $20\log R$ time varying gain (TVG) or no TVG. TVG was used only in one of the acoustic records presented below (Fig. 2). The ping rate for all data presented was 4 pings per sec.

A Longhurst-Hardy Plankton Recorder (LHPR) equipped with an *in situ* fluorometer and CTD instrument package was towed in the immediate vicinity of the acoustic tow body (Fig. 1) to provide near space-time coincident *in situ* measurements of the temperature and salinity field in the vicinity of the water volume from which acoustic signals were scattered. On several occasions the CTD instrument package was deployed at a depth of about 16 m, 1–2 m to the side and, depending on tow speed, 1 to 3 m to the rear of the acoustic tow body. Tow speed was ~0.75 m/sec. Temperature and conductivity data were recorded at a 16 sample per second rate. The temperature probe had a response time of ~25 msec. The temperature data presented in Fig. 3 was averaged over 1 sec. The conductivity probe had a flushing length of 2.5 cm. The salinity data presented was not averaged. A representative temperature and salinity profile for the experiment site has been scaled from Haury *et al.*[10] and is shown in Fig. 4. Temperature and salinity profiles in the experiment area were quite variable and depended upon both location and the presence or absence of internal wave packets.

RESULTS

Twelve separate internal wave packets were acoustically detected during the seven-day experiment. The wave packets were tracked from their generation point near the western edge of Stellwagen Bank westward across Massachusetts Bay into shoaling water where they, on occasion, degenerated into internal bores. Each packet was formed when a lee wave[9] generated by an easterly tidal flow across a sill (Stellwagen Bank) propagated, as the tidal flow slackened, to the west across the sill into Massachusetts Bay. The packets' propagation speed over ground ranged from ~0.5–0.8 m/s.

A portion of an internal wave packet that was imaged with the 200-kHz acoustic system (pulse width 100 μsec, 7.5-cm vertical resolution) illustrates the nature of the signal backscatter from the water column (Fig. 2). The first 10 min of the record was taken as the ship moved from west to east, opposite to the direction of propagation of the wave packet. The water depth was about 83 m.

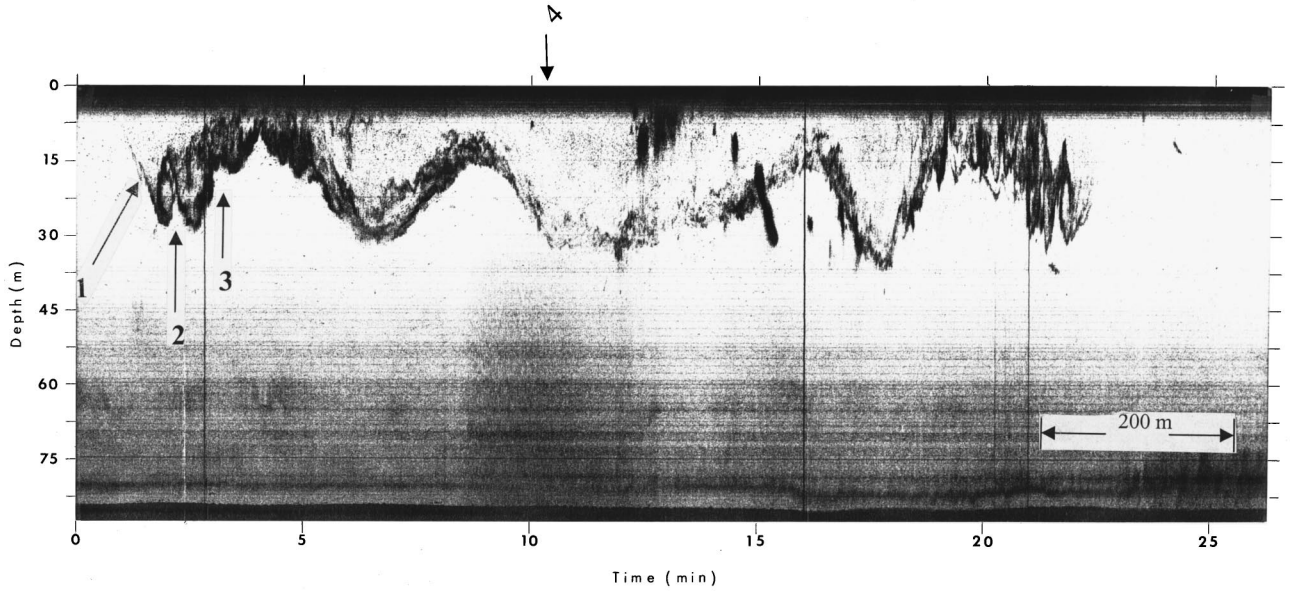

FIG. 2. Two hundred kilohertz acoustic backscattering image of an internal wave packet, associated shear instabilities (arrow 1, 2), and zones of microstructure or turbulent mixing (arrow 3). During the 0–10 min-interval the ship was moving in a direction opposite the propagation direction of the wave packet; the ship reversed course (arrow 4) and attained a stable reciprocal heading at about the 14-min mark. Note the sudden appearance of a thin scattering layer outlining shear instabilities to the left of arrow 1. The dark scattering patch near the surface in the 12–13-min time interval is from the ship's wake.

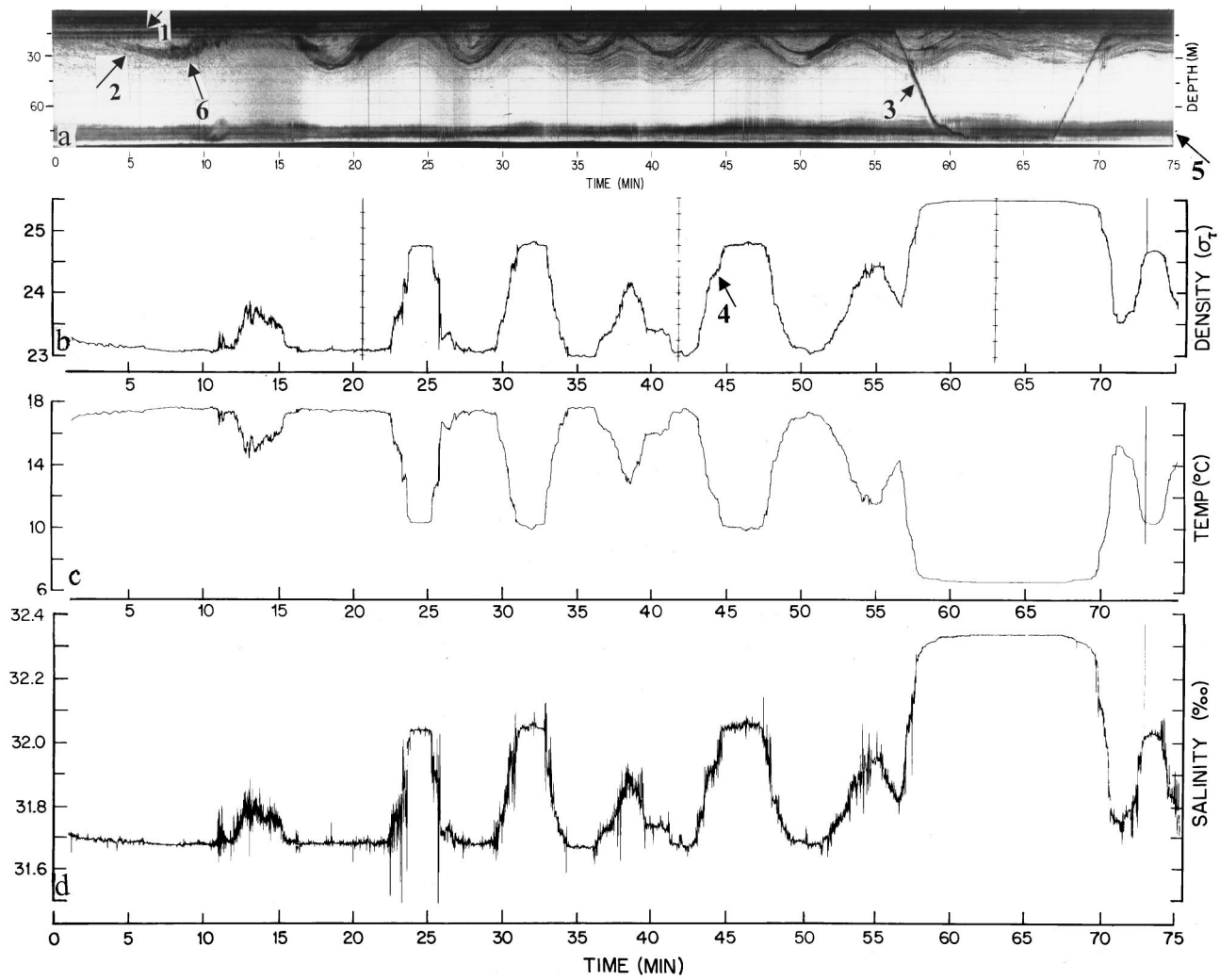

FIG. 3. Salinity, temperature, and potential density records plotted at the same time scale as a 200-kHz acoustic backscattering record. The CTD was held at constant depth (~16 m, arrow 1) as the passing internal wavefield displaced the base of the mixed layer and associated zones of intense acoustic backscatter (turbulent mixing) past the CTD. The salinity record shows large variability during the vertical displacement of the acoustically detected turbulent mixing layers past the CTD package. Note the acoustic detection of multiple scattering or turbulent mixing layers and the corresponding large variability detected by the conductivity sensor. The multiple scattering layers were separated by water with a smaller slope in the density field, indicating that mixing had occurred in the region (see the double shoulder on the temperature, salinity, and density records, arrow 4). The CTD was lowered and held at a constant depth in the vicinity of the bottom in the 57–70-min time interval. No fluctuations are evident in the salinity record during that time. The scattering layer at this depth is due to a dense euphausiid layer (Thysanoessa rauschii) (Ref. 10).

The leading edge of the packet was crossed near the 1 min mark. The downward displacement of the thermocline by the internal wavefield was initially acoustically imaged as a thin scattering layer. That scattering layer (left and above arrow 1) first appeared near the 12 m depth. The thin scattering layer ($\ll$1 m thick) outlined shear instabilities of increasing vertical displacement (arrow 1, 2). An enlargement of the first lobe of the wave packet (Fig. 5) shows shear instabilities with amplitudes ranging from about 1 m (to the left of arrow 1) to nearly 15 m (arrow 2). The thickness of the acoustic scattering zone (Fig. 5) increased from a few cm near the 1 min mark to a maximum of ~7 m (near arrow 3).

At 10 min (arrow 4, Fig. 2), the ship reversed course and attained a westerly heading at ~14 min. As the ship moved to the west, multiple large amplitude shear instabilities were again outlined by an acoustic scattering layer ranging from a few centimeters to a few meters in thickness. The scattering layer persisted until the leading edge of the wave packet was

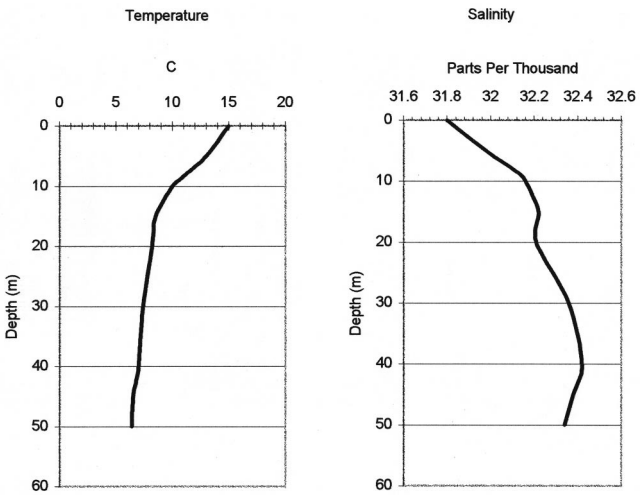

FIG. 4. A representative temperature and salinity profile taken in the experiment area (Ref. 10).

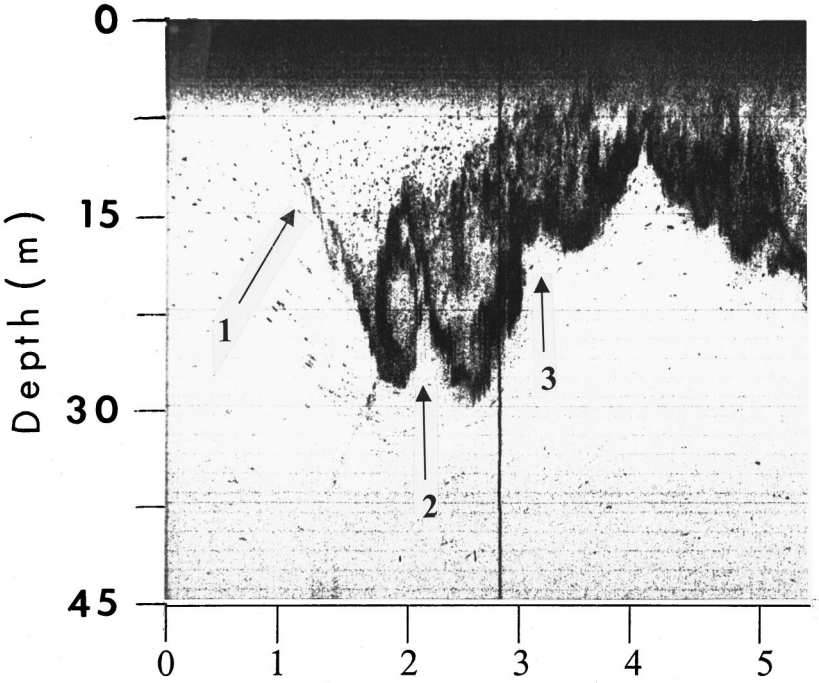

FIG. 5. Enlarged section of the first 5 min of Fig. 4. Small shear instabilities (0.5 to 3 m in amplitude) are to the left of arrow 1. Large-scale instabilities (15 m in amplitude) at arrow 2 and thick zones of scatter (arrow 3) from microstructure associated with shear instabilities are clearly seen.

crossed at the 23 min mark. Note the scattering layer disappeared at the leading edge of the internal wave packet. The horizontal distance (referenced to the ground) scale shown above the 25 min mark is accurate for all time except when the ship turned, i.e., the 10- to 14-min time interval. The acoustic record has not been corrected for the spatial Doppler shift caused by moving with or against the mean speed of the internal wave packet (~0.5 m/sec).

The acoustic scattering zone, which varied from a very thin (few cm) to a thick (meters) scattering region near the rear of the first lobe of the internal wave packet, permits the imaging of the vertical displacement of the mixed layer by the internal wave packet. The thin scattering region outlined active mixing events (shear instabilities). The initial thickness of the thin scattering region is that expected from mixing associated with oceanic microstructure, e.g., Fig. 4.20 in Turner.[13]

A key observation is that the thin scattering layer that outlines the shear instabilities at the leading edge of the internal wave packet was not present in the acoustic record prior to the encounter of the internal wave packet (to the left of arrow 1) nor was it present upon leaving the internal wave packet at ~23 min into the record. The sudden appearance and disappearance of the scattering layer in waters that had no evidence of biologic scatterers indicates that a physical process is causing the scattering. The sudden appearance of acoustic scattering layers within an internal wave packet has also been noted by Sandstrom *et al.*[4] (see their Fig. 2).

Internal wave propagation theory, e.g., Turner[13] Chap. 2; Sandstrom *et al.*;[4] shows that in the presence of an internal wave the base of the mixed layer (a region of high density gradient) is a region of high shear. Shear is known to initiate dynamic instabilities if the Richardson number becomes $\leqslant 1/4$. The existence of instabilities in Fig. 2 suggests that a Richardson number $\leqslant 1/4$ existed at the time the data were taken. Instabilities similar to those appearing in the acoustic records presented here are routinely detected in laboratory fluid dynamics experiments using tracers and in clear air via radar scattering, e.g., see Turner,[13] Figs. 4.10–4.15 or Ottersten.[14]

Based on the above acoustic flow visualization record and many others of similar nature it is our contention that the shear instabilities and internal wave displacement of the mixed layer boundary were partially imaged by acoustic wave fields scattered from temperature and salinity fluctuations associated with bands of shear induced mixing (oceanic microstructure) in the vicinity of the base of the mixed layer boundary. Several observations support this contention. They are:

(1) Acoustic backscatter from organisms that acted as passive tracers of the water column displacement did not change in character during the passage of the internal wave packets. They were merely displaced in depth by the internal waves and were discrete in nature. In addition, scattering layers outlining the shear instabilities in internal waves suddenly appeared in areas known to be high shear zones.
(2) Analysis of plankton recorder samples[10] showed that zooplankton abundance variations were not correlated to the acoustic signal scattered from regions of shear instabilities, therefore, supporting the contention that the acoustic signal imaging the shear instabilities was scattered by another process, namely, temperature and salinity fluctuations associated with active mixing at microstructure scales.
(3) Previously reported density profiles[9] calculated from yo-yo CTD measurements taken in space-time coincidence with acoustic detection or imaging of shear instabilities showed that density inversions were associated with the acoustic scattering layers near the base of the

mixed layer, substantiating the presence of active small scale mixing (<0.5-m thickness) at microstructure scales.

(4) Oscilloscope traces of the envelop of the acoustic signal scattered from the scattering layers associated with shear instabilities were distinctly different than the signal scattered from organisms distributed through the water column. This point will be expanded upon.

The contention that the scattering of acoustic energy can be caused by temperature and salinity fluctuations associated with oceanic microstructure is supported by near space-time coincident acoustic and CTD data (Fig. 3) taken as an internal wave packet propagated past the sensors. The placement of the acoustic transducer tow body and the CTD package was noted in Fig. 1. Both the CTD and acoustic tow body were nearly in the same vertical plane and were within ~3 m of each other in space and separated from each other by <6 sec in time.

The acoustic data [Fig. 3(a), 200 kHz, pulse width 250 μsec, vertical resolution 18.75 cm] shows a dark scattering layer that suddenly appears in the leading trough of the internal wave field at about the 5-min mark [Fig. 3(a), arrow 2]. The scattering layer is repeatedly displaced by the internal wavefield past the CTD package which was held at a constant depth of ~16 m (Fig. 3, arrow 1) during the 0–52-min time interval. The scattering layer evolves from a single scattering layer to multiple layers in the ~27–52 min interval. The intensity of the dark scattering area decreases toward the rear of the internal wave packet where biological scatters outline the vertical displacement of the water column.

Note that the density, temperature, and salinity fluctuations are very small in the 0–5 min time interval [Figs. 3(b), 3(c), and 3(d)] when the strong scattering layer is below the CTD package. Also note that the initial downward displacement of the water column is visualized by the vertical displacement of discrete biological scatterers prior to the sudden development of the dark scattering area. As the high intensity acoustic scattering layer is displaced upward past the CTD package, the salinity [Fig. 3(d)] and temperature [Fig. 3(c)] records and the density [Fig. 3(b)] show a burst of high-frequency variability during the 11–15, 22–24, 29–31, 33–34 min and several later time intervals. When the intense acoustic scattering zone moves above the CTD package there is a noticeable decrease in the temperature and the salinity variability. Due to the range of the scales for the temperature and salinity plots the salinity variability stands out most clearly. Near the 55-min mark the CTD package was lowered into the near-bottom biological scattering layer (75–80-m-depth range, the 57–67-min time period). The bottom is the dark line at ~86 m. The CTD appears as a diagonal line as it was lowered [Fig. 3(a) arrow 3]. The lack of T/S fluctuation as the CTD was lowered away from the mixed layer boundary (high shear zone) helps corroborate the interpretation that dark acoustic scattering layers near the mixed layer boundary are caused by temperature and salinity fluctuations associated with oceanic mixing.

As noted above, the original single scattering layer breaks up into multiple intense scattering layers (see the ~35–45-min interval). In this time interval the T, S variability increases and decreases with the passage of each of the scattering layers past the CTD package. As a result, the temperature and salinity variability appears more continuous in the records. The magnitude of the variability is, however, declining, as is the darkness or intensity of the associated acoustic scattering zones as compared to the variability seen in the first internal wave lobe. The appearance of multiple acoustic scattering layers in internal wavefields has also been noted by Sandstrom *et al.*[4] and was postulated to be caused by the erosion of the density gradient by mixing with the consequent generation of two or more areas of large density gradient at which shear instabilities and mixing would occur. The erosion of the density gradient is seen as a change of slope in the density field [Fig. 3(a), arrow 4]. Note at this time two large-amplitude scattering layers are present in Fig. 3(a).

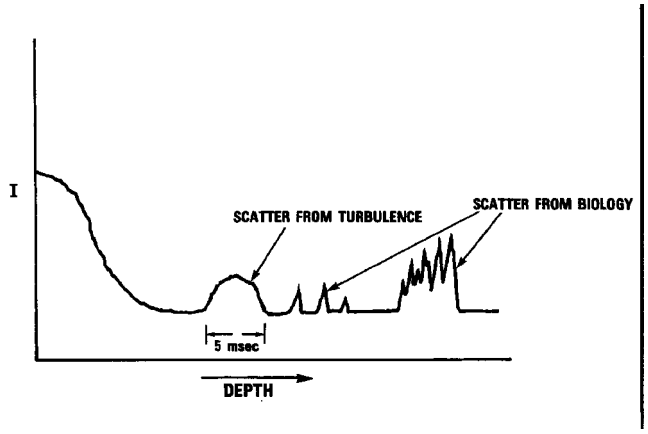

FIG. 6. Replication of an oscilloscope display of signal intensity versus depth. The signal scattered from zones of turbulence had an envelope that was distinctly different than that from biological scatters.

In summary, each displacement of the intense acoustic scattering layer past the CTD was accompanied by increases in the salinity and temperature fluctuations and density fluctuations. There was a distinct decrease in significant temperature/salinity fluctuations as the intense microstructure causing the acoustic scattering layer was displaced above or below the CTD package. The intense acoustic scattering layer that suddenly appears in the first lobe of the internal wave packet is the result of scattering from the temperature and salinity variability caused by mixing and evidenced by the presence of shear instabilities [Fig. 3(a), arrow 6]. These instabilities have a different shape than those in Figs. 2 and 5 because the ship was moving through the internal wave packet at a slower speed.

In addition to the temperature and salinity fluctuations that are associated with the intense acoustic scattering layer, oscilloscope records of the acoustic signals scattered from the zones' turbulence, i.e., high temperature and salinity variability (fine structure and microstructure) were distinctly different than those signals scattered from biological scatterers. A replication of a full wave rectified acoustic signal is displayed (Fig. 6). The scattering from the biology resulted in an envelope that was a superposition of individual discrete

scatterers, while the scatter from the microstructure had a relatively smooth variation in amplitude because of the lack of discrete scatterers within the scattering volume. On a ping-to-ping basis, the signal scattered from the turbulence would vary in amplitude while the amplitude of the discrete scatter from the biology would change more slowly, depending on the rate at which the discrete scatters moved out of the transducer beam pattern. Broadband laboratory measurements have seen similar differences between signals scattered independently from zooplankton and turbulence.[15] Although not pointed out by Sandstrom *et al.*,[4] their acoustic backscattering profiles (see their Fig. 7, 25–30 sec time interval) showed a somewhat similar acoustic signal character in the region of high shear. Their record showed discrete scatter from the biology at other depths versus an expanding smooth envelop of the acoustic signal scattered from the high shear zone. It should be noted that their acoustic data are a two-ping average (one ping per second data rate) versus the 4-ping per sec data presented in Fig. 3.

The acoustic system used to acquire the data was of new design and had not been calibrated prior to this experiment. Consequently, absolute scattering strengths were not extracted from the data. The volume scattering strengths, using the expressions developed by Goodman,[1] could be estimated if the wave number spectrum of the index of refraction spectrum were known. Due to limitations on the temporal and spatial resolution of the conductivity and temperature sensors, the wave number spectrum cannot be calculated. Consequently, the volume backscattering scattering strengths have been estimated using the Born approximation development of Pelech *et al.*,[8] Eq. (8), and the measured temperature and salinity fluctuations. The Pelech *et al.* Eq. (8) has been modified to include the effects of salinity fluctuations. This expression is written as

$$\sigma \approx 0.12(\delta c/c)^2 k^4 L_1 L_2 L_3 [1+(1.33kL_1)^2]^{-11/6}, \qquad (1)$$

where σ=backscattering scattering strength (m^{-1}), k=wave number of incident sound, c=mean sound speed, δc=the sound-speed variance around c, L_1=integral scale length of the sound-speed fluctuations in the direction of the incident radiation, L_2, L_3=integral scale length of the sound-speed fluctuations in the two axes orthogonal to the incident radiation. It should be noted that Pelech *et al.* development used an index of refraction correlation function for fully developed turbulence in the inertial connective region. The authors did generalize the correlation function to include anisotropy for large-scale turbulence.

Volume scattering strengths [in dB ($10\log\sigma$)] calculated using Eq. (1) ranged from ~ -85 to -53 dB *re* 1 m^{-1} for temperature and salinity fluctuations ranging from $\sim 6\times10^{-3}$ °C to $\sim 2\times10^{-1}$ °C and 0.02 to 0.1‰, respectively. The estimated scattering strengths are within the range anticipated from the acoustic measurements and exceeded the noise threshold of the acoustic system by more than 40 dB. The scattering strength range is similar in magnitude to that estimated by previous investigators.[2,4,7,8] An isotropic integral scale length of 0.2 m was used. The temperature and salinity fluctuations were estimated from the CTD record and the sound speed was calculated using Wilson's equation as presented in Tolstoy and Clay.[16] The scale length is an upper bound determined from the thickness of the acoustic scattering layer as the appropriate supporting microstructure measurements necessary to determine the lower bound were not made. The magnitude of the scattering strengths will increase if the scale lengths decrease and are anisotropic since the scattering strength varies as $L^{-2/3}$. For this experiment L is expected to be smaller than 0.2 m.

Goodman[1] has calculated the microstructure scattering strength using the one-dimensional wave number spectrum of index of refraction fluctuations. His volume scattering strength Eq. (46a) is written as

$$\sigma = 0.008\,66\;\; N^2 \varepsilon^{5/8} f^{1/2} [\sin\psi_1]^{-7/2}, \qquad (2)$$

where N=buoyancy frequency (c/hr), ε=turbulent kinetic energy dissipation rate (w/kg), f=acoustic frequency, ψ_1=angle of acoustic axis of source with respect to the horizontal plane=$\pi/2$ for a backscattering geometry. He used a buoyancy frequency of 12 c/hr and a measured turbulent kinetic energy dissipation rate of 3.6×10^{-5} watt/kg to estimate a scattering strength for 200 kHz of -56 dB *re* 1 m^{-1}. This number is similar in magnitude to the estimates made above using the Massachusetts Bay CTD data. The Massachusetts Bay numbers are expected to be a lower order estimate since the effects of anisotropy in the turbulence have not been accounted for.

CONCLUSIONS

Near time and space coincident acoustic backscattering and CTD measurements indicate that the acoustic signals that imaged oceanic mixing events within internal wave packets are scattered by temperature and salinity fluctuations resident within those mixing events. The acoustic scattering often appeared abruptly (in the absence of biology related scatters) in areas of the internal wave packets known to be high shear zones. Estimated volume backscattering strengths for microstructure scattering range from ~ -85 to ~ -53 dB *re* 1 m^{-1}. These acoustic backscattering and CTD measurements, which are very close to time and space coincident, collaborate the interpretation,[2–4,9,10] that acoustic scattering in high shear zones can be caused by temperature and salinity variability related to oceanic mixing.

ACKNOWLEDGMENTS

This work was supported by grants from NSF, NORDA, and NOAA. This paper has been assigned a Woods Hole Oceanographic Institution Contribution Number 9853. The late Fredrick R. Hess designed the acoustic backscattering system used during these measurements.

[1] L. Goodman, ''Acoustic scattering from ocean microstructure,'' J. Geophys. Res., [Oceans] **95**, 11557–11573 (1990).
[2] H. E. Seim, M. C. Gregg, and R. T. Miyamoto, ''Acoustic scatter from turbulent microstructure,'' J. Atmos. Ocean. Technol. **12**, 367–380 (1995).
[3] M. V. Trevorrow, ''Observation of internal solitary waves near the Oregon coast with an inverted echo sounder,'' J. Geophys. Res., [Oceans] **103**, C4, 7671–7680 (1998).
[4] H. Sandstrom, J. A. Elliot, and N. A. Cochrane, ''Observing groups of

solitary internal waves and turbulence with BATFISH and echo-sounder,'' J. Phys. Oceanogr. **19**, 987–997 (1989).
[5] D. M. Farmer and H. J. Freeman, ''The physical oceanography of fjords,'' Prog. Oceanogr. **12**, 147–219 (1983).
[6] L. Armi and D. M. Farmer or D. M. Farmer and L. Armi, ''The flow of Mediterranean through the Strait of Gibraltar'' or ''The flow of Atlantic water through the Strait of Gibraltar,'' Prog. Oceanogr. **21**, 1–105 (1988).
[7] S. A. Thorpe and J. M. Brubaker, ''Observations of sound reflection by temperature microstructure,'' Limnol. Oceanogr. **28**, 601–613 (1983).
[8] I. Pelech, G. G. Zipfel, and R. L. Holford, ''A wake-scattering experiment in thermally stratified water,'' J. Acoust. Soc. Am. **73**, 528–538 (1983).
[9] L. R. Haury, M. B. Briscoe, and M. H. Orr, ''Tidally generated internal wave packets in Massachusetts Bay,'' Nature (London) **278**, 312–317 (1979).
[10] L. R. Haury, P. H. Wiebe, M. H. Orr, and M. B. Briscoe, ''Tidally generated high frequency internal wave packets and their effects on plankton in Massachusetts Bay,'' J. Mar. Res. **41**, 65–112 (1983).
[11] F. R. Hess and M. H. Orr, ''A wide range sonar system for oceanic investigations,'' Proc. Oceans, September 1979, IEEE CH 1478-7/79/0000-0027.
[12] F. R. Hess and M. H. Orr, ''A towed multi-frequency high frequency sonar system for scattering and ocean dynamics studies,'' WHOI Technical Memo 79-76, 1979.
[13] J. S. Turner, *Buoyancy Effects in Fluids* (Cambridge University Press, Cambridge, 1973).
[14] H. Ottersten, ''Atmospheric structure and radar backscattering in clear air,'' Radio Sci. **4**, 1179–1193 (1969).
[15] T. K. Stanton, P. H. Weibe, D. Chu, and L. Goodman, ''Acoustic characterization and discrimination of marine zooplankton and turbulence,'' ICES J. Mar. Sci. **51**, 469–479 (1994).
[16] I. Tolstoy and C. S. Clay, *Ocean Acoustics* (American Institute of Physics, New York, 1987).

An analysis of Freedman's "image pulse" model in air

Janos Tsakiris and Phillip McKerrow
Intelligent Systems Group, School of Information Technology and Computer Science, University of Wollongong, Wollongong, NSW, 2522, Australia

(Received 1 September 1999; accepted for publication 3 May 2000)

The ''image pulse'' model developed by Freedman calculates the echoes generated from convex objects in an underwater environment after insonification with a narrow-band transient signal. The model uses the source radiation and the solid angle subtended at the transducer by the scattering body to determine the echo structure. Work has been completed in adapting this model for use in an air environment using noncoincident transmitters and receivers. Experiments were conducted to measure the amplitudes of the echoes off a range of convex objects, at distances up to 1.4 m, after insonification with a Polaroid transducer. These measured amplitudes were compared to those predicted by the model, with the results for cones highlighting the limitations of the model. Spheres, however, performed significantly better, with an average error of under 5%, indicating that the model should be reasonably accurate at calculating the echoes off convex objects with a smoothly varying surface. © *2000 Acoustical Society of America.* [S0001-4966(00)02608-4]

PACS numbers: 43.35.Ae, 43.20.Bi, 43.20.Fn, 43.20.Px [HEB]

INTRODUCTION

In the field of mobile robotics, the validity of using ultrasonics for object recognition has been questioned in recent years because of its failure to progress beyond simple tasks such as identifying the ranges to walls. To address some of the problems associated with ultrasonic sensing in air, we are investigating acoustic backscatter models. While numerical models abound, they are inadequate because of their inability to be inverted. Freedman's[1] model uses the scatterer's geometry to predict the echoes it produces after insonification. It is investigated here because it is an analytical model and hence can be inverted to calculate object geometry from the echo. Before it can be inverted and used for object recognition, though, the forward model must be extended to work in air.

Freedman's model has been discussed by several researchers.[2–4] The primary prediction of his model is that echoes are generated on a scattering body at those points where there are step discontinuities in the derivatives, with respect to range, of the solid angle subtended at the transducer by the scatterer. The amplitudes of the echoes are a linear combination of the magnitudes of these discontinuities. Freedman conducted a number of experiments in an underwater environment to test this model.[5] These proved inconclusive, since the calculated amplitudes deviated significantly from the experimental results obtained. Freedman claimed this quantitative variation was due to the inadequate equipment used to gather the experimental data and to internal penetration of the signal into the scattering bodies, which compromised the hard target approximation of his model. However, his experiments did provide qualitative validation of the model because the echoes were generated at the points on the objects predicted by the model.

This paper will discuss the experimental results obtained after extending the model from water to air.[6–8] Tests were conducted using three spheres, three truncated cones and three regular cones. These were made of wood, turned on a lathe and painted with acrylic paint. Each object had unique dimensions and was placed at different ranges in the far field (0.800 m to 1.400 m) and insonified with a 50 kHz wave. The amplitude of the echo from one of the spheres at a certain range was used to calibrate the model, enabling the prediction of the amplitudes of the echoes off the other spheres at different ranges. The same method was subsequently used to calibrate the model for the truncated and plain cones.

I. FREEDMAN'S ''IMAGE PULSE'' MODEL

The model makes several assumptions. First, the transmitter is assumed to be a point source radiator. Second, scattering of the incident radiation off the object is assumed to follow Kirchoff's approximation. This approximation states that the scattering surface is composed of an infinite number of elemental areas, each of which reflects incoming radiation into half space. The model also assumes that the scattering body is convex, rigid and in the far field with respect to the transmitter. The expression derived for the receiver voltage resulting from an echo from an object at range r_g is

$$E_g = i\frac{VP(f)H(f)}{r_m^2\lambda}\exp(i\omega t)\int_0^{r_s}\frac{dW_w(r)}{dr}\times\exp(-2ikr)dr, \quad (1)$$

where E_g = voltage at the receiver due to an echo originating at range r_g, V = voltage applied to the transmitter during transmission, r_m = mean range to the object, P and H are frequency dependent sensitivity factors for the transmitter and receiver, respectively, and λ, ω and k, are the wavelength, angular frequency and wave number of the acoustic pulse, respectively.

The solid angle subtended at the receiver by the reflecting surface at range r is given by $W(r)$, where $W(r) = A(r)/r^2$, $A(r)$ being the area that the reflecting surface projects toward the receiver. A weighting is applied to $A(r)$ to account for the variation in the transmitter and receiver directivities with $A_w(r)$ and $W_w(r)$ being the directivity weighted equivalents of $A(r)$ and $W(r)$, respectively.

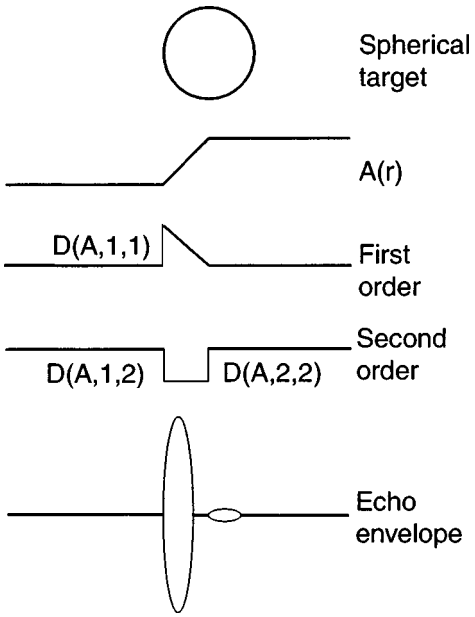

FIG. 1. Echoes from a sphere predicted by Freedman's model.

The term $D(A_w,g,n)$ is introduced to represent the amplitude of the discontinuity, if any, in the nth order derivative, with respect to range, of the directivity weighted projected area $A_w(r)$ and is defined as follows:

$$D(A_w,g,n)=\frac{d^nA_w}{dr^n}(r_{g-})-\frac{d^nA_w}{dr^n}(r_{g+}), \tag{2}$$

where r_{g-} and r_{g+} represent the ranges infinitesimally prior to and beyond the discontinuity. Freedman goes on to replace the continuous integration in Eq. (1) with a discrete summation:

$$E_g=i\frac{VP(f)H(f)}{r_m^2\lambda}\exp(i\theta)\sum_{n=0}\frac{D(A_w,g,n)}{(2ik)^n}, \tag{3}$$

where $\theta=\omega t-2kr_g$.

To provide a physical interpretation of Eq. (3), we break it down into several modules. The term $VP(f)H(f)$ is, at a fixed frequency, a constant of proportionality and represents the dependence of the voltage at the receiver on (a) the voltage applied to the transmitter, (b) the transmissivity of the transmitter and (c) the sensitivity of the receiver. The λ in the denominator is a product of Kirchoff's approximation and results in diminished reflection from the scatterer's surface at lower frequencies.

r_m^2 in the denominator comes from the inverse distance law for geometrical spreading loss from a point source, but is applied *twice*, since we have transmission *and* reflection, for a range r_m, which is defined as the mean range to all points that contribute to the echo. For example, in the case of the sphere in Fig. 1, the regions that contribute to the echo are the leftmost point and all points around the sphere's equator. Therefore, the mean range to these two regions is the range to the leftmost point plus half the radius.

Turning attention back to Eq. (3), the exponential term is the complex form of the solution to the wave equation. The terms within the summation represent, in the case of zeroth order components, the magnitude of the direct backscatter to the receiver and, in the case of higher order components, the magnitude of the diffracted signals transmitted toward the receiver.

The implications of the discontinuities in Eq. (3) are best illustrated by example. At an arbitrary range r_g on a *smoothly varying* section of the scatterer's surface, the nth order derivative at ranges infinitesimally prior to and beyond r_g will be the same. Hence, Eq. (2) will be zero, thus there is no discontinuity and so no echo is generated. At those ranges r_g where there is a discontinuity in one of the nth order derivatives, Eq. (2) will have a nonzero value and hence an echo will be generated. Thus discontinuities in the cross sectional area or any of its higher order derivatives with respect to range are responsible for the formation of echoes. Freedman has termed these echoes ''image pulses'' since their structure is identical to the transmitted pulse in all but amplitude.

Taking the example of the sphere of radius a in Fig. 1, with its closest point located at r_1 and its equator at r_2, Freedman[5] showed that the nth order derivatives of projected area with respect to range, between r_1 and r_2, are as follows:

$$A_w(r_g)=\pi(a^2-(r_2-r_g)^2), \tag{4a}$$

$$\frac{dA_w}{dr}(r_g)=2\pi(r_2-r_g), \tag{4b}$$

$$\frac{d^2A_w}{dr^2}(r_g)=-2\pi, \tag{4c}$$

$$\frac{d^3A_w}{dr^3}(r_g)=0. \tag{4d}$$

The magnitudes of the discontinuities at r_1 and r_2 are then calculated using Eq. (2) and are as follows:

$$D(A_w,r_1,0)=0, \tag{5a}$$

$$D(A_w,r_1,1)=-2\pi a, \tag{5b}$$

$$D(A_w,r_1,2)=2\pi, \tag{5c}$$

$$D(A_w,r_2,0)=0, \tag{5d}$$

$$D(A_w,r_2,1)=0, \tag{5e}$$

$$D(A_w,r_2,2)=-2\pi. \tag{5f}$$

The cross sectional area of the sphere, as ''seen'' by a transducer located to the far left of the sphere, is not discontinuous at any point. However, at r_1 the first and second order derivatives are discontinuous and so each produces an echo. These are in phase and superimposed to form the echo from r_1. Similarly, at r_2, i.e., the equator of the sphere, the second order derivative is discontinuous and an echo *should* originate from there too. It will be shown later that no echo will be generated at the equator, despite the predictions of Freedman's model.

II. EXTENSIONS TO THE MODEL

Freedman's model, as it stands, is idealized in that it only works for objects in nonattenuating media, such as water, using a coincident point source transmitter and receiver.

To enable the model to work in air with real transducers and receivers, which may be noncoincident, we need to modify it. Several factors come into play that need to be compensated for. These are: (a) attenuation due to air, (b) breakdown of the assumption $r_m^{-2} \approx r_g^{-2}$, (c) polar directivity field of the transducer, (d) directivity of the receiver and (e) noncoincident transmitter and receiver. Although (c) and (d) do not represent additions to the model, as Freedman already accounts for transmitter and receiver directivities, we will provide an alternative method for calculating them. Finally, the real component of the model needs to be extracted, since this corresponds to the physically observable signal.

A. Signal attenuation due to air

Several mechanisms are responsible for the loss in energy of a wave traveling through air. Apart from the obvious geometrical spreading loss, which Freedman's model accounts for, atmospheric absorption causes the wave to decay exponentially with range. In the 50 kHz region, this absorption is due primarily to the vibrational relaxation of oxygen molecules.[9]

Atmospheric absorption is incorporated into the model by the addition of the term $\exp(-2r_g\alpha)$ into Eq. (3):

$$E_g = i\frac{VP(f)H(f)}{r_m^2\lambda}\exp(-2r_g\alpha + i\theta)\sum_{n=0}\frac{D(A_w,g,n)}{(2ik)^n}. \tag{6}$$

The new term is the attenuation factor and α is the absorption coefficient. The path length $2r_g$ is used because the radiation travels to the scattering object and then back to the receiver.

The absorption coefficient α can be determined either theoretically or experimentally. Theoretical values can be determined using the series of equations specified by the American national standard method for calculating attenuation in air.[9] At the frequencies we use (50 to 55 kHz), these give us an absorption coefficient accurate to within 10%. Given that the amplitude of a spherical wave traveling through an attenuating medium is given by $E=[E_0 \times \exp(-\alpha r)]/r$, where E_0 is a constant of proportionality, the amplitudes of the wave at two distinct ranges r_1 and r_2 would be given by $E_1=[E_0\exp(-\alpha r_1)]/r_1$ and $E_2=[E_0 \times \exp(-\alpha r_2)]/r_2$, respectively. These equations can be rearranged and equated to produce the following:

$$\alpha = \frac{\ln(E_1 r_1/E_2 r_2)}{r_2 - r_1}. \tag{7}$$

Experimental values can therefore be determined by positioning the receiver at two distinct ranges, r_1 and r_2, from the transmitter and inserting the amplitudes of the received waves E_1 and E_2 into Eq. (7),

Now, voltage E can only be measured to within a 0.8% accuracy in 95% of cases, for reasons to be outlined later. In the worst case scenario where E_1 is 0.8% too large and E_2 is 0.8% too small, the absorption coefficient will be in error by 10%. Consequently, both the experimental and theoretical methods can only claim accuracy to within 10% and so the method chosen is arbitrary. Since the absorption coefficient can be calculated relatively quickly with the aid of a mathematical package, provided environmental conditions are known, we chose the theoretical route.

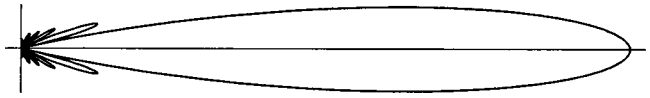

FIG. 2. Directivity pattern of a 1.9-cm radius transducer at 50 kHz.

B. Breakdown of the $r_m^{-2} \approx r_g^{-2}$ assumption

To simplify the derivation of the model, Freedman assumed that the object was sufficiently far from the transducer that the ranges to different points on the scatterer could reasonably be approximated with the mean range, r_m, for the purposes of calculating the geometrical spreading loss. At ranges under 2 m though, this approximation clearly does not hold when we are dealing with objects of up to 0.1 m in size.

An analysis of Freedman's derivation reveals that the approximation is only necessary if one treats the separate echoes coming from different points on the scatterer as all part of the same wave train. If we treat each echo as a separate entity, we can justifiably use the exact range r_g instead of r_m. Hence we can replace r_m with r_g in Eq. (6) to give us

$$E_g = i\frac{VP(f)H(f)}{r_g^2\lambda}\exp(-2r_g\alpha + i\theta)\sum_{n=0}\frac{D(A_w,g,n)}{(2ik)^n}. \tag{8}$$

As an example of how this increases the accuracy of the model, for a typical 0.1 m radius sphere at a distance of 0.8 m, with an absorption coefficient of 0.2, this amounts to a 15% increase in the amplitude of the calculated echo.

C. Polar directivity of the transducer

Because the transducer is not a point source but is instead analogous to an oscillating plane piston, there will be an angular variation in the strength of the field. This occurs because the field at any point is a summation of waves coming from different points across the face of the transducer. Consequently, not all waves arrive in phase and we get interference, producing the characteristic series of maxima and minima.

We used a Polaroid transducer with a radius of 1.9 cm in our experiments and its directivity field, calculated using the plane piston model,[10] is drawn to scale in Fig. 2. The central lobe insonifies a region of 15° around the axis of the transducer, giving it a total coverage of 30°. From Fig. 2 it is clear that the field strength falls off rapidly once we deviate from the axis. Consequently, when modeling the echo generated from a point on an extended object, we need to take into account the diminished field strength of the incoming radiation at that point.

Freedman's model compensates for the directivity of the transducer, as well as the receiver, by requiring that the reflecting area $A(r)$ on extended scatterers be weighted for directivity, to give us $A_w(r)$. This addresses the problem in an indirect manner by retaining an assumption of uniform directivity in transmission and reception, by virtue of the

model's point source approximation, and replacing the true area with the notion of a pseudo area. Our approach is to retain the true area and instead replace the assumption of uniform directivity with a model governing the directivity of the field. Although mathematically both approaches are ultimately equivalent, the strength of the latter is that it is physically and intuitively valid also. This is because it does not require the introduction of the abstract notion of a pseudo area and does not retain an incorrect model of the directivity of the transducer.

The directivity field of a plane piston is given by the following:[10]

$$\beta(\phi)=\frac{2J_1(k\alpha\sin\phi)}{k\alpha\sin\phi},\quad \phi\neq 0,$$

$$=1,\quad \phi=0, \tag{9}$$

where $k=2\pi f/c=$wave number of the transmitted wave, and $J_1=$Bessel function of the first order.

Factor $P(f)$ in Freedman's model represents the transducer's capacity for transmission with its value denoting the pressure produced at 1 m along the axis, per volt applied to the transducer, for a given frequency. To incorporate the directivity of the transducer into Freedman's model, we need to scale this factor with Eq. (9). The resulting model follows:

$$E_g=i\frac{VP(f)\beta_P(\phi)H(f)}{r_g^2\lambda}\exp(-2r_g\alpha+i\theta)$$

$$\times\sum_{n=0}\frac{D(A,g,n)}{(2ik)^n}. \tag{10}$$

For echoes originating from points along the axis, the directivity takes on the unit value. Echoes from points off the axis are now compensated for by taking into account the angle they make with it.

D. Directivity of the receiver

In our research we examine two distinct cases for each scatterer, i.e., the results when the receiver is coincident with the transmitter and the results when it is separated by a small distance. For the coincident receiver setups, the Polaroid transducer switches into reception mode after transmission. For the noncoincident ones, we use a 7 mm diameter Bruel & Kjaer condenser microphone (type 4135), separated from the transducer by 44 mm.

Freedman's model assumes that the receiver is not an extended object and as such has a uniform directivity in reception. By virtue of its small size, this assumption holds true for the microphone with its directivity relatively uniform over the range of angles ($-4°$ to $+10°$) that it receives echoes from (Ref. 11). Consequently, the directivity of the receiver is not an issue for noncoincident setups.

For the coincident cases, though, the directivity of the transducer must be accounted for. The angular sensitivity of the transducer in reception mode is exactly the same as it is in transmission mode and is governed by Eq. (9). This is because the directivity is a function of the transducer's geometry, which remains the same in both cases and so the directivity does not change.

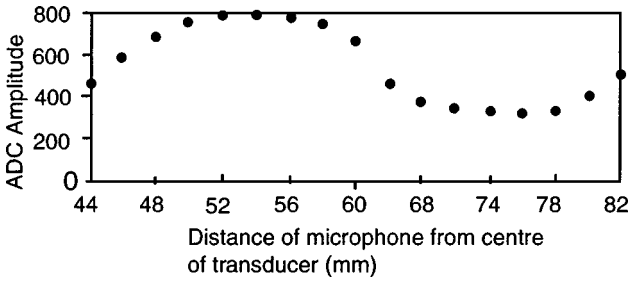

FIG. 3. Maximum amplitude of the echo versus separation of the microphone from the center of the transducer.

Factor $H(f)$ in Freedman's model represents the receiver's sensitivity in the direction of the axis for a given frequency. To incorporate the receiver's directivity into the model, we need to scale this factor with Eq. (9). The resulting model is given in Eq. (11):

$$E_g=i\frac{VP(f)\beta_P(\phi)H(f)\beta_H(\phi)}{r_g^2\lambda}$$

$$\times\exp(-2r_g\alpha+i\theta)\sum_{n=0}\frac{D(A,g,n)}{(2ik)^n}. \tag{11}$$

As stated earlier, when using the microphone, the directivity takes on unit value to indicate uniformity.

E. Noncoincident transmitter and receiver

Although our setup does not strictly satisfy this assumption in half of our experiments, Freedman's model assumes that the transmitter and receiver are coincident. The advantage of this is that, when dealing with echoes originating from a ring of radially equidistant points around the axis, such as the base of a cone, the echoes from each point will all arrive at the receiver in phase. This eliminates the problem of wave interference.

To examine the effect of unchecked interference, we measured the maximum amplitude of echoes from the base of a cone as the microphone was shifted progressively further away from the transducer. The results are shown in Fig. 3. As can be seen in Fig. 3, the results show a sinusoidal variation in amplitude which is characteristic of an interference pattern.

As mentioned before, in half of our cases the transducer doubles as both a transmitter and receiver, satisfying the above assumption and so noncoincidence is not an issue in these cases. For the remainder, though, the problem is dealt with by aligning the axis of the scatterer with a point midway between the center of the transducer and the microphone. This ensures that the path lengths from the transducer to the scatterer and then to the microphone remain equal at all times, ensuring the echoes arrive in phase.

F. Extraction of the real component

Although waves are regularly represented by complex equations, the measurement process can only detect the real component. Consequently, before we can utilize Eq. (11), we need to extract its real part. This is given in Eq. (12):

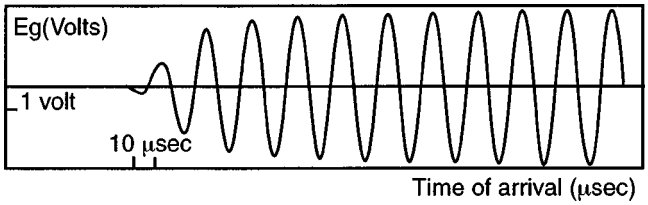

FIG. 4. Echo off the large truncated cone at a range of 0.800 m for noncoincident transmitter and receiver.

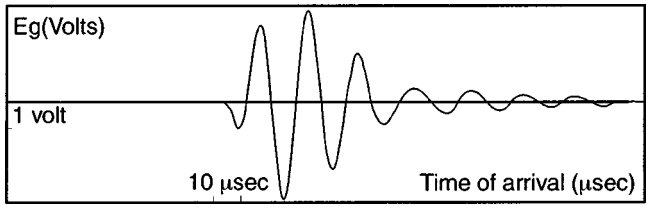

FIG. 5. Echo off the large truncated cone at a range of 0.800 m for a coincident transmitter and receiver.

$$E_g = A(f)\,\frac{GV\beta_P(\phi)\beta_H(\phi)}{r_g^2}\exp(-2r_g\alpha)\left(D(0)\sin\theta - \frac{D(1)}{2k}\cos\theta - \frac{D(2)}{4k^2}\sin\theta\right). \tag{12}$$

Factor G, signifying gain, has been added to account for any amplification that may be applied to the received signal. In Eq. (12) factors $P(f)$, $H(f)$ and λ, which we use $\lambda \approx c/f$ to calculate, have been combined into a single function $A(f)$. This is because the individual factors need not be measured independently, for a given frequency, then combined in order to calibrate the model. Instead, by measuring the echo off an object of known dimensions at a given range, we can insert the echo amplitude, scatterer's discontinuity values, range, frequency and calculated values of speed of sound and attenuation, from the environmental conditions, into Eq. (12) to determine $A(f)$. Since $A(f)$ is independent of the scattering body, the calibrated model is thus suitable for use with a range of objects at a range of distances, provided we use the same frequency that was used to calibrate the model and the speed of sound remains the same.

III. ECHO MEASUREMENT

Our experimental setup consists of several components. First, we have a chirp generator card connected to a Macintosh Quadra. The output of this card is controlled via software that enables variation of the significant parameters, such as the output voltage, number of wave cycles, frequency, etc., to allow production of a signal of arbitrary shape. For noncoincident measurements, we produce a 10 to 20 cycle wave with an amplitude of 4 V at a frequency of 50 kHz. The analog signal produced by the card, by virtue of a digital to analog converter at its output, is fed to an amplifier with a gain of 30, and then a 150 V bias is added. The amplified signal is then applied to the Polaroid transducer and transmission ensues. The first few cycles of the transmitted wave steadily increase in amplitude, since the transducer cannot respond instantaneously to the applied voltage, and by the fifth or sixth cycle the wave has reached its maximum value. This can be seen in Fig. 4, i.e., where the captured echo off the large truncated cone is at a range of 0.800 m for a noncoincident transmitter and receiver. The last several cycles of the wave (not shown in Fig. 4 but visible in Fig. 6) are the result of ''ring down''after the applied voltage has been terminated and these decay exponentially.

For coincident measurements the process differs in that the initial output of the chirp card is a step function which drops from 5 V to 0 within 0.2 ms. At the transducer, this causes the applied ac voltage to drop from 300 V to 0 almost instantaneously, causing the transducer to exponentially ring down at its natural frequency of approximately 55 kHz. Typically, the transmission in this case contains one or two well defined cycles at the start of the wave and a number of trailing cycles that are progressively buried in noise. This is shown in Fig. 5, where the echo off the large truncated cone is at a range of 0.800 m for a coincident transmitter and receiver.

The echo off the scattering body is received via an ultrasonic microphone, with a corresponding preamplifier, in the noncoincident case and the transducer in the coincident case, which goes into reception mode immediately after the step function is applied. In both cases, the signal is then optionally amplified before being sampled at 1 MHz with 12 bit resolution by a chirp capture card, also connected to the Quadra. Custom software is then used to display the signal on screen and export it to a file for later analysis with a mathematical package.

Figure 6 shows a typical received signal that includes two echoes from the one object; in this case the echoes off the medium sized truncated cone are at 0.600 m for a noncoincident transmitter and receiver. The larger echo is from the truncated face of the cone and the second, smaller echo is from its base. The transmitted pulse was shorter than usual to ensure no overlap between the two echoes.

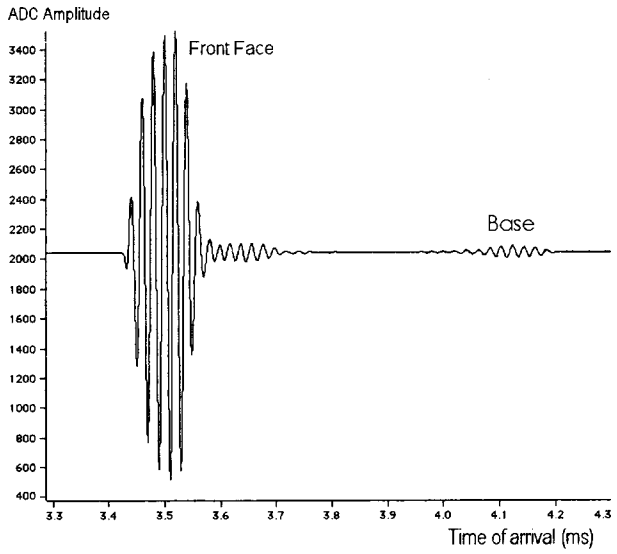

FIG. 6. Echoes off the medium-sized truncated cone at a range of 0.600 m for a noncoincident transmitter and receiver.

IV. NOISE MINIMIZATION

Localization and minimization of noise sources is essential in this work because of the weak echoes with which we often have to deal. Also, the amplitude of the $(n+1)$th order image pulse, represented by the $(n+1)$th order term within Eq. (12), is typically at least two orders of magnitude smaller than the nth. Consequently, we need a signal with a high signal to noise ratio in order to see the higher order contributions.

The noise we examine here comes from three main sources: the environment, the transducer and the chirp capture card.

A. Environment

Short term fluctuations in air pressure from drafts, doors opening/closing, power supply fans, people walking, etc. can cause amplitude variations of up to 10% between any two echo measurements. We minimized these variations by averaging the amplitudes of the echoes over multiple readings to improve the signal to noise ratio. The standard deviation, obtained over numerous trials, of the mean amplitude of a set of echoes was found to be only 0.4% when 50 echoes were sampled. Thus for echo amplitudes obtained by this method, in 95% of cases the value will fall within 0.8% (two standard deviations) of the true value, assuming a normal (Gaussian) distribution. Consequently, in all of our subsequent measurements we averaged over a minimum of 50 echoes before analyzing the results. In each case, the measurements were completed within 30 s because the capture software was able to average the echoes in real time.

Over the course of several hours, the environmental conditions in a room, such as temperature, pressure and humidity, will change. This will affect the time of flight, via the speed of sound, and amplitude, via attenuation factor, of an echo. The model is designed to compensate for these changes provided we know what the environmental conditions are at the time of measurement. Thus, continual monitoring of these conditions is required.

B. Transducer

As mentioned earlier, the final cycles of a transmitted wave are the result of ''ring down'' after the voltage applied to the transducer has terminated and these cycles decay exponentially. This decay is very long though and often the ringing has not completely died away by the time the echo arrives. When the transducer is being used as a receiver, the ring down signal will be superimposed on the incoming echo, corrupting the received signal as a result. When the microphone is used for reception, it will pick up the ring down signal via one of the outer side lobes (see Fig. 2), again resulting in corruption. To solve this problem, the ring down signal, which is fairly repeatable, is recorded separately in the absence of any scattering body and later on, as part of the echo analysis, is subtracted from the measured echo. This also has the advantage of canceling any extraneous echoes, from objects in the environment unaccounted for, which may be present in the signal.

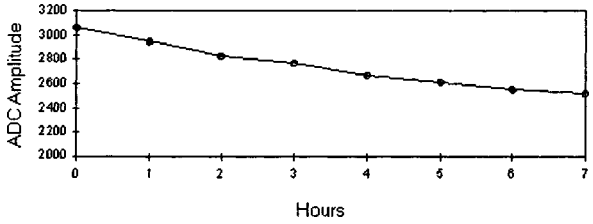

FIG. 7. Variation in amplitude with time of the echo off a target.

A different problem, which reveals itself only after several hours, is the slow but significant reduction over time in the amplitude of the received echo off a scatterer. This was measured off a reference target and the results, given in Fig. 7, show a 4% reduction within 1 h and 18% over 7 h, after which the amplitude no longer decreases significantly. We concluded, after isolating the source of the drift to the transducer itself, that the changes are a result of the transducer losing its ability over time to produce a given pressure for a given voltage. We believe this reduction in transmissivity may be due to the mylar film used in the transducer stretching under a constant 150 V bias and losing its rigidity as a consequence.

To compensate for this drift we switched off the bias to the transducer between measurements. This relieves the tension on the mylar film between chirps and allows it to restore its rigidity.

C. Chirp capture card

The capture card is a host for several potential noise sources. Because the card is in close proximity to the chirp generator card, as well as numerous electronic components within the host computer, the potential for electromagnetic interference is great. To minimize this, we used coaxial cable for the wiring between the input socket and the analogue to digital converter (ADC). The ADC itself was shielded by copper plates to prevent interference from external and onboard noise sources.

The capture card begins sampling the incoming signal as soon as the generator card begins transmitting. Because we are superimposing the echoes in real time for the purpose of averaging them to increase the signal to noise ratio, the incoming waves must be in phase with one another, otherwise they will experience interference. As a consequence, the circuit was designed to ensure that the start of the transmit and receive cycles are synchronized to within half a microsecond, to prevent phase mismatch.

Finally, the sampling rate of the ADC places a constraint on the accuracy of the captured signal. At a sampling frequency of 1 MHz, a typical 50 kHz wave will be sampled 20 times per cycle, or every 18°. Since our objective is to measure the amplitude of the peaks, for reasons to be outlined shortly, the best case scenario, in terms of accuracy, occurs when the wave is sampled exactly at its peaks. The worst case is when the sampling occurs at a separation of 9° on either side of the peak, leading to an inaccuracy in the measured peak of 1.2%. To resolve this issue, we use interpolation[12] to reconstruct the shape of the wave between

the sample points. This is done with the aid of a mathematical package during the analysis stage, the details of which will be explained next.

V. ECHO ANALYSIS

The capture software allows us to export the returned signal to a file for later analysis by a mathematical package. We used Mathematica, but any comparable package should be sufficient. Once the file is imported into Mathematica, the first step is to cut out the unnecessary parts of the trace. Since a typical trace consists of an appreciable period of no signal followed by the echo and then no signal again, it is advantageous to remove the regions that are not part of the main echo since it will reduce processing time markedly later on. Once this is done, the trace of the signal received in absence of any scattering body is imported and subtracted from the echo, as outlined in Sec. IV B.

Interpolation of the processed echo follows and we have chosen to interpolate ten points per sample, giving us a virtual sampling frequency of 10 MHz. The interpolation is more accurate when the wave is monotonic and of constant magnitude. Consequently, the highest accuracy in the interpolated echo occurs in its central region, where the wave's magnitude has stabilized and ring down has yet to begin. This stable central region has the added advantage of conforming more closely to Freedman's assumption of a nonvarying echo envelope. Since the objective of our work is to compare the measured amplitude with the predicted amplitude of the echo at a point in time, we need to find an appropriate region within the echo from which to select our measurement point. For the reasons detailed above, the central region of the echo is the most appealing for this. The appropriate tools within the mathematical package are then used to determine the maximum value of the newly interpolated echo. This will always be a positive peak located within the central region. Now that we have the measured value of E_g, we can turn our attention to using the model to calculate a theoretical value of E_g.

By this stage, we know, or can easily calculate, almost all of the factors that are needed for calculating the theoretical value of E_g. The only unknown remaining is the phase to be used within the trigonometric functions. To determine the phase we utilize the fact that for the three trigonometric terms in Eq. (12), one will always dominate the others. To determine which term dominates, prior knowledge of the wave number and the nth order discontinuities of the scatterer are required, in order to calculate the coefficients for the trigonometric terms. Consequently, if the cosine term dominates, then the positive peaks of the echo correspond to phases of $2\pi n$ where $n=1,2,3$, etc. If one of the sine terms dominate, then the positive peaks correspond to phases of $2\pi n+\pi/2$ where $n=1,2,3$, etc. Even though we do not know the value of n corresponding to the peak that we measured, it does not matter because the trigonometric function takes on the unit value for all integer values of n. Thus the value that one uses is arbitrary, provided it is an integer.

The treatment given above assumes that the nondominant terms play a negligible role in affecting the phase of the wave. But is this assumption valid? By plotting the echo, as predicted by the model, for several typical cases of spheres, cones and truncated cones, we find that when the nondominant terms are included, the phases of the positive peaks deviate from those predicted above by less than 2°. This corresponds to a deviation in the amplitude of less than 0.06%, confirming the validity of our assumptions.

Once the phase has been chosen, the predicted amplitude of the peak in question can be calculated and compared with its measured counterpart. The next section will detail the results of such comparisons for a variety of objects at different ranges.

VI. RESULTS

For the experimental work, we use spheres, regular cones and truncated cones of varying dimensions at ranges of 0.800 m, 1.000 m and 1.400 m, accurate to within 1 mm. The range is defined as the distance from the face of the transducer to the point(s) on the scatterer from which the echo originates. For example, when discussing the echo off the base of a 0.100 m high cone, a range of 1.000 m refers to the distance from the transducer to the base, as opposed to the distance to the vertex, which would be only 0.900 m.

The spheres we used have diameters of 0.100 m, 0.150 m and 0.200 m. The regular cones have a height (distance from base to vertex) of 0.100 m and base diameters of 0.100 m, 0.150 m and 0.197 m. The truncated cones have a height (distance from base to truncated face) of 0.100 m, base diameter of 0.197 m and truncated face diameters of 0.052 m, 0.097 m and 0.149 m.

Unless stated otherwise, for each class of scatterer (i.e., sphere, regular cone or truncated cone), the model was calibrated with a member of that class positioned at the greatest distance. In our experiments the smallest member was always used, but the choice is arbitrary provided that the object is at least several wavelengths wide in order to satisfy Kirchoff's approximation.[5] For example, when dealing with spheres, the model was calibrated with the 0.100 m diameter sphere at 1.400 m. The reason for calibrating with an object at the greatest distance is that the far field approximation, which is central to the model, is most accurate when dealing with scatterers that are as far as possible from the source of the wave. Consequently, the calibration constant $A(f)$ is most accurate when obtained from an object at the greatest range.

Even though $A(f)$ is independent of the geometry of the scattering body and so once calibrated could be used for other object classes, this presumes that all measurements are to be taken within a short time span because $A(f)$ is dependent upon the speed of sound, which varies with temperature. In our experiments, the set of measurements for each object class were taken on different days, with different temperatures, necessitating recalibration of the model for each new set.

All objects were mounted on a precision positioner with three degrees of freedom that has a range limit of 1.5 m.

A. Spheres

As stated earlier, it was suspected that despite the predictions of Freedman's model, the equator of a sphere may

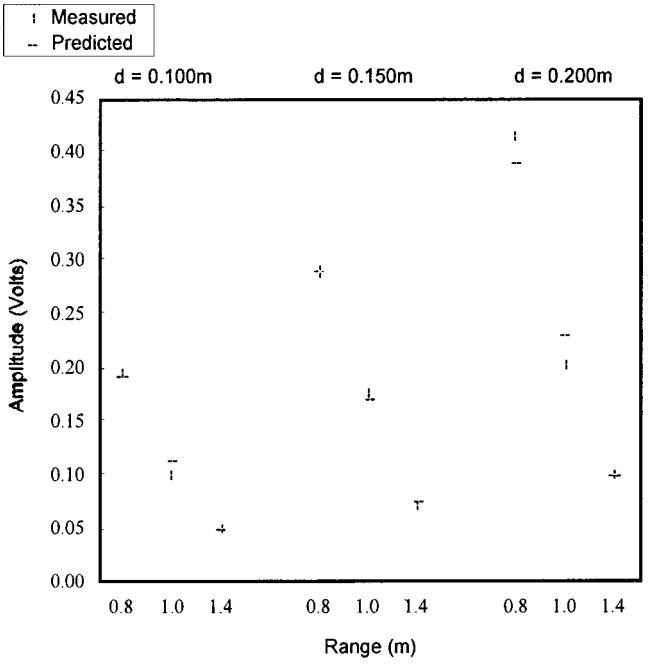

FIG. 8. Measured and predicted amplitudes of echoes off spheres of diameter d when the transmitter and receiver are not coincident.

not generate an image pulse when insonified. The reason for this is that Freedman assumes that the contributions from the geometrical shadow region, generally known as ''creeping waves,'' are negligible at the high frequencies we have used. Rudgers,[4] though, claimed that for the case of a sphere, these contributions are equal in magnitude and are the inverse of those generated by Freedman's mechanism, the net result being a cancellation of the equator echo. To test Rudgers' assertion, we captured the echo off a sphere and analyzed the region where the image pulse from the equator should be.

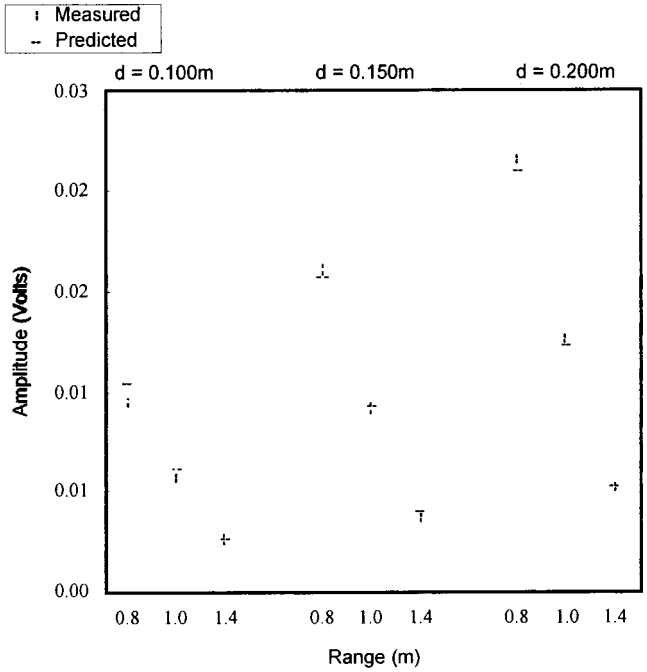

FIG. 9. Measured and predicted amplitudes of echoes off spheres of diameter d when the transmitter and receiver are coincident.

TABLE I. Data for Fig. 8.

Diameter (m)	Range (m)	Meas. amplitude	Pred. amplitude	Pred./Meas.
0.100	0.800	0.1949	0.1910	0.98
	1.000	0.0996	0.1129	1.13
	1.400	0.0490	0.0490	1.00
0.150	0.800	0.2885	0.2882	1.00
	1.000	0.1749	0.1704	0.97
	1.400	0.0710	0.0739	1.04
0.200	0.800	0.4137	0.3886	0.94
	1.000	0.2020	0.2287	1.13
	1.400	0.0998	0.0988	0.99

Given that the equator's echo would be extremely weak, i.e., only $(2ka)^{-1}$ that of the stronger echo from the closest point on the sphere, it was necessary to use an amplification of 10^3 in order to see it, if it existed. Despite the noise floor being significantly lower than the predicted amplitude of the equator's echo, no echo was observed, confirming Rudger's analysis. Consequently, the results presented here are only for the echoes off the closest points on the spheres.

The discontinuity equations for the closest point on a sphere of radius a were given previously:

$$D(0)=0, \tag{5a}$$

$$D(1)=-2\pi a, \tag{5b}$$

$$D(2)=2\pi. \tag{5c}$$

The results of comparing the measured and predicted amplitudes of the echoes are given in Fig. 8 for the case of a noncoincident transmitter and receiver and in Fig. 9 for the coincident case. The data for these figures are shown in Tables I and II to enable better discrimination of the results by readers than is possible in the graphs. For the noncoincident case, the predictions deviated from the measured amplitudes by an average of 4.7%, the worst case being 13%. The coincident case provided better results, though, with the predictions deviating from the measured amplitudes by an average of only 3.3%, the greatest error being 10%.

B. Regular cones

Freedman's model predicts that two echoes should be generated from an insonified regular cone—one from its vertex and the other from its base. The base echo is readily

TABLE II. Data for Fig. 9.

Diameter (m)	Range (m)	Meas. amplitude	Pred. amplitude	Pred./Meas.
0.100	0.800	0.009 49	0.010 42	1.10
	1.000	0.005 70	0.006 07	1.06
	1.400	0.002 60	0.002 60	1.00
0.150	0.800	0.016 08	0.015 69	0.98
	1.000	0.009 14	0.009 23	1.01
	1.400	0.003 71	0.003 94	1.06
0.200	0.800	0.021 51	0.020 99	0.98
	1.000	0.012 66	0.012 30	0.97
	1.400	0.005 24	0.005 24	1.00

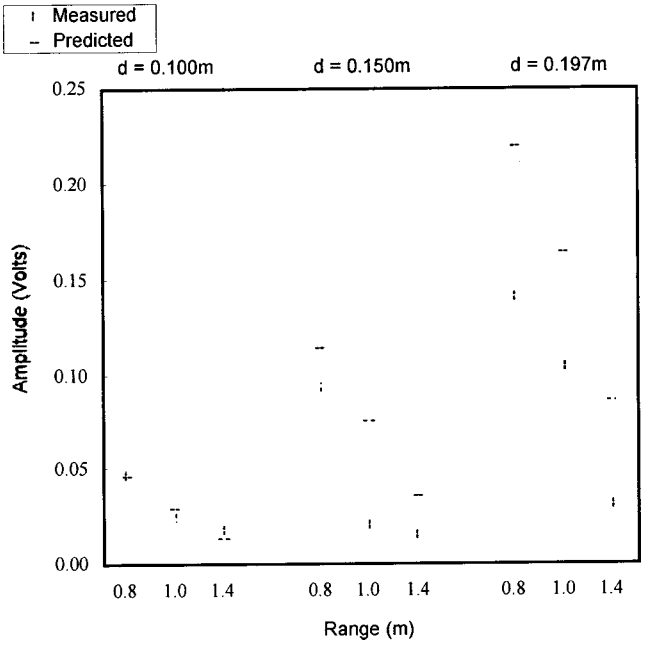

FIG. 10. Measured and predicted amplitudes off the bases of regular cones of base diameter d when the transmitter and receiver are not coincident.

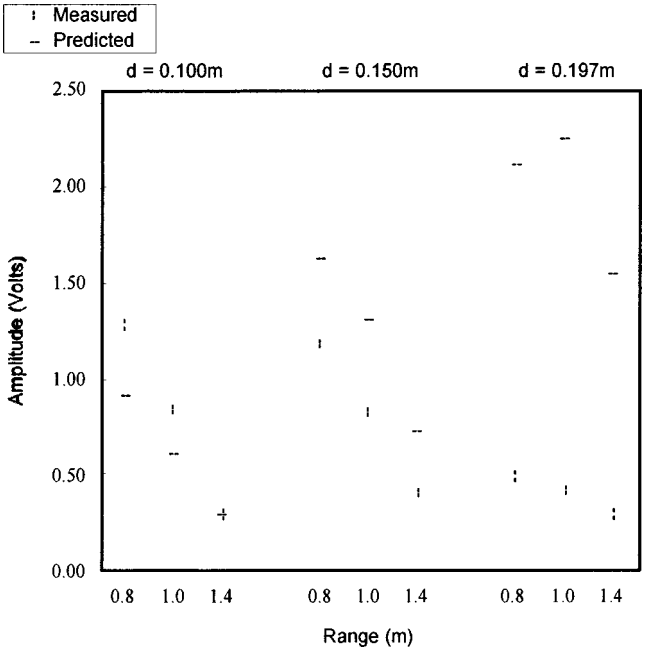

FIG. 11. Measured and predicted amplitudes of echoes off the bases of regular cones of base diameter d when the transmitter and receiver are coincident.

observable but the image pulse off the vertex cannot be seen. This is because it is a point and so has a negligible reflecting area, consequently causing the echo to be buried in noise, despite attempts to observe it with amplifications as high as 10^3. Thus we can only present the results involving the echo off the base.

The discontinuity equations for the base of a regular cone are given below:[5]

$$D(0)=0, \tag{13a}$$

$$D(1)=2\pi h \tan^2 \gamma, \tag{13b}$$

$$D(2)=2\pi \tan^2 \gamma, \tag{13c}$$

where h is the cone's height and γ is the angle between its central axis and any line connecting the vertex to the rim.

Comparison between the measured and predicted amplitudes of the echoes is given in Fig. 10 for the case of a noncoincident transmitter and receiver and in Fig. 11 for the coincident case. For the results presented in Fig. 10, the model was not calibrated at 1.400 m as usual but at 0.800 m because the echo was too weak, allowing noise to dominate, thus rendering it unsuitable for use as a calibrating signal. Also, high amplification was required to extract the echo from the noise in all cases, hence the larger than usual voltages of the captured signals.

For the noncoincident case, the predictions are, on average, almost twice the size of their measured counterparts, the most extreme case being more than 3.6 times the measured value. The coincident case proved no better, with the average prediction being more than three times the measured value, the most extreme case taking it to five times. Results from the smallest cone were an exception to this, having predicted values smaller than those measured.

In Sec. VII we will discuss the reasons these predictions deviate so markedly from the measured values.

C. Truncated cones

As with a regular cone, Freedman's model predicts that two echoes will be generated when a truncated cone is insonified. One will originate from the base and will be identical to that generated by a regular cone with the same shaped base. The other will come from the truncated face and will be significantly strong, given the large reflecting area of the face. As the mechanism of echo formation at the base of a truncated cone is identical to that at the base of a regular cone, we need not examine it again. Instead we will focus on the echo produced by the truncated face.

The discontinuity equations for the face of a truncated cone follows:[5]

$$D(0)=-\pi(h-b)^2 \tan^2 \gamma, \tag{14a}$$

$$D(1)=-2\pi(h-b)\tan^2 \gamma, \tag{14b}$$

$$D(2)=-2\pi \tan^2 \gamma, \tag{14c}$$

where b is the truncated cone's height and γ is the angle between its central axis and any line connecting the virtual vertex to the rim of the base. The virtual vertex is defined here as the vertex that would be present if the truncated cap could be reattached. The term h represents the distance from the base of the truncated cone to the virtual vertex.

The measured and predicted amplitudes of the echoes are given in Fig. 12 for the case of a noncoincident transmitter and receiver and in Fig. 13 for the coincident case. For the noncoincident case, the predicted amplitudes are, on average, 50% in error, the largest errors being predictions twice the size of the measured values. The coincident case has predicted amplitudes that are 60% too large, on average, the worst case being nearly three times larger than the measured value.

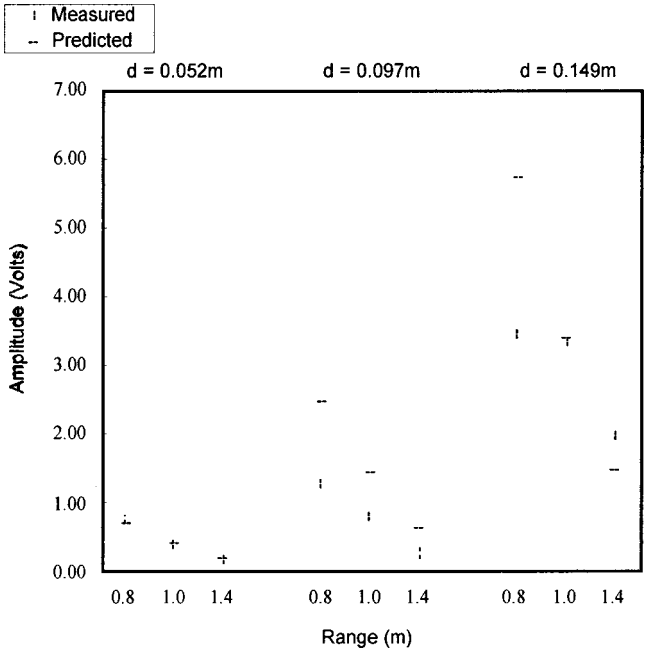

FIG. 12. Measured and predicted amplitudes off the faces of truncated cones of truncated face diameter *d* when the transmitter and receiver are not coincident.

In the next section we will explore the reasons why these results, like those for the regular cones, show such a large discrepancy between theory and measurement.

VII. DISCUSSION

The results for the echoes off the closest points on spheres clearly show that Freedman's model works well for this class of object. Although the largest error was 13%, the average error was less than 5% for noncoincident setups and as low as 3.3% for coincident ones. Sources of error for the results were irregularities in the radii of the spheres, which were measured and found to be 1%. Given that the amplitude of the received echo is approximately proportional to the first order discontinuity, which is itself proportional to the sphere's radius, it follows that such radial irregularities can account for errors of up to 1% in the echo's amplitude.

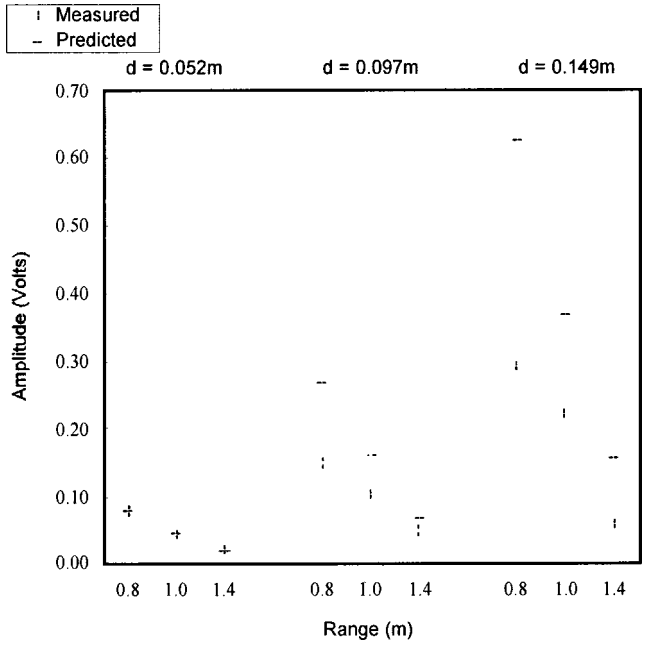

FIG. 13. Measured and predicted amplitudes of echoes off the faces of truncated cones of truncated face diameter *d* when the transmitter and receiver are coincident.

The results from the regular cones highlighted the limitations of Freedman's model. Earlier, we discussed Rudgers'[4] work which showed that Freedman had made an incorrect assumption about the negligibility of creeping waves generated at geometrical shadow boundaries. Because Freedman's model does not account for these waves, we can only speculate as to what effect they may have on echoes originating from geometrical shadow boundaries, such as the bases of cones. We believe the large deviations between the predictions of the model and the measured values for the echoes off the bases of cones can be attributed to these creeping waves from the shadow region.

On a smaller scale, though, there are a couple of features of a cone's shape that could introduce errors. The first is the slope of the cone across its surface. If discontinuities in this parameter occur, or in any of its derivatives with respect to range, which in this case could have occurred had the wood not been turned properly, they can lead to additional echoes being generated, in accordance with Freedman's model. Also, since the slope of the cone at the base affects the echo generated, if there is a deviation in the cone's slope near the base, then the generated echo will differ from that predicted. We measured the slopes of the cones and found smoothly varying and near negligible deviations in the slopes from their means, thereby ruling out discontinuities as a source of error. Likewise, we found the slopes at the bases did not deviate from their overall means.

A second feature of cones that could have affected the results is the radii of curvature, or ''sharpness'' of the base rims. Since the echo at the base is generated by the process of diffraction, a curved base rim will produce an echo of lower magnitude than an ideal ''sharp'' rim. Because the wavelength we used is between 6 mm and 7 mm and the observed radii of curvature at the rims is never greater than about 0.5 mm, the radii of curvature will play no part in the results obtained.

The significant deviations from theory of the measured echoes off the faces of the truncated cones have a different origin than that given for the bases of regular cones. The model assumes that the separation between the scattering body and the receiver is great enough to ensure that the normal vectors at all points on the truncated cone's face are pointing directly toward the receiver. Under such conditions the amplitude of the received echo would vary linearly with the area of the truncated face, as the predicted echo amplitudes in Figs. 12 and 13 indicate. Because of the relative proximity of the transducer to the truncated cone (1.400 m at most), the signal insonifying the truncated face is only *approximated* by a spherical wave front. A more accurate description is that the area of this wave front along the axis of the transducer is actually planar and equal in area to the face

of the transducer, with the remainder of the wave front spherical.

As expected, the spherical regions of the wave front incident on the scattering body are reflected at angles that do not transmit them back to their source and hence are not picked up by the receiver. The central planar region of the wave front experiences direct backscatter to the receiver. The upshot of this is that the only region on the truncated face contributing to the signal captured at the receiver is that area which is irradiated with the central planar section of the wave front. Consequently, if the truncated face is larger than the planar section of the wave front, the amplitude of the echo received will be less than that predicted by the model. This is confirmed by the results in Figs. 12 and 13 which show that the amplitudes of the measured echoes do not increase with the truncated area at the same rate as the predicted amplitudes. The consequence of this is that the model can only be applied to truncated faces of very small area, generally of the order of the area of the transducer's face or smaller.

As with regular cones, irregularities in the slopes of the truncated cones could have been a source of error but as with regular cones we found the slope variations to be negligible. The radii of curvature at the rims of the truncated faces, observed to be less than 0.5 mm, are not as crucial to the results as they had been for the base rims. This is because the dominant echoes result from direct backscatter, the diffracted echoes making only a minor contribution.

As well as those problems discussed above that are specific to a class of object, there are general issues that could affect the results from all scatterers. One is the model's use of the far field approximation, which is valid only if condition $kr \gg 1$ is satisfied.[5] In these cases, though, with ranges over 0.8 m and wave numbers typically near 10^3, it is clear that this condition is satisfied. Even for the results of previous experiments, not given here, which showed slightly worse agreement between experiment and theory at ranges from 0.400 m to 0.800 m, the condition is still satisfied and consequently a breakdown in the far field approximation cannot be blamed for the larger discrepancies.

Small variations in the parameters of the model during the course of a set of measurements may also effect the results. In Eq. (12), the only terms that can vary during the course of a measurement session are the speed of sound and the absorption coefficient. The speed of sound, which is one of the terms that make up $A(f)$, by virtue of $\lambda = c/f$, has a dependence on temperature given by the following:[6]

$$c = c_0 \sqrt{T_K/273}, \tag{15}$$

where $c_0 =$ the speed of sound at $273\,\mathrm{K} = 331.6\,\mathrm{ms}^{-1}$, and $T_K =$ air temperature in Kelvin.

The speed of sound also has a dependence on humidity and pressure, but the variations in these that can occur over a measurement period of, at most, 2 h, will cause a negligible change in the speed of sound. The greatest change in temperature during any measurement period was 2 °C, the minimum and maximum temperatures being 292 K and 298 K, respectively, throughout the entire series of measurements. Using Eq. (15), this +2 °C change represented a change in the speed of sound of +0.3%. Consequently, the change in the inverse of c, to which the amplitude of the echo is proportional, would have been −0.3%. This is too small to produce any significant error in the calculated echo.

The other component of the model that can be a source of experimental error is the absorption coefficient α. Since the coefficient is rated to be accurate to within 10%, at a typical range of 1 m with a typical value of $\alpha = 0.2$, the error in the attenuation factor will be 4%. The reality is that an error in the absorption coefficient of 10% does not mean it can vary from one moment to the next by up to that amount. Consequently, even if the absorption coefficient used is inaccurate by the given amount, provided the measurements are done soon after the model is calibrated, the error in the coefficient will be absorbed by the calibration process. On the other hand, if the model is calibrated one day and used on another, i.e., when the environmental conditions have changed markedly, then there is justifiable concern that the calibration is no longer valid. For the work presented here, though, all the calibration data were part of the same set as the data used to test the model.

Although the model has only been verified for spheres to within an average error of 3.3%, with the worst case being 10%, for coincident cases, this is a significant improvement over the results obtained by Freedman in his original work. He was able to verify only some qualitative aspects of the model, the quantitative results being too noisy (20%–30%) to allow conclusions to be drawn. Subsequent references[2–4] to his work have discussed only the theoretical aspects of the model and have not touched on the failings in his experimental data. Neither has any follow up work been done since 1962 to verify the model, in either air or water, to the best of our knowledge.

VIII. CONCLUSIONS

Freedman's model, when translated to air, is limited in that it cannot be used for modeling the echoes from the geometrical shadow boundaries of objects, such as the base of a cone. It is fairly accurate though in calculating the echoes off the closest points on spheres and may potentially be used for modeling the echoes off the faces of truncated cones, provided these faces have a small area. It should also be reasonably accurate for predicting the echoes off objects with smoothly varying convex surfaces.

The model is of special interest to workers in the field of mobile robotics because of its potential to be used as the basis for an inverse model of ultrasonic imaging. This could lead to the development of a real-time object recognition system that would complement current systems by specializing in the recognition of nonconcave scatterers or their modeling with equivalent symmetrical objects. Major applications of such a system include map building by mobile robots and object recognition on conveyor belts.

[1] A. Freedman, ''A mechanism of acoustic echo formation,'' Acustica **12**, 10–21 (1962).
[2] K. Sasaki *et al.*, ''Classification of objects' surface by acoustic transfer function,'' in Proceedings of the 1992 IEEE/RSJ Int. Conf. on Intelligent Robots and Systems (1992), pp. 821–828.
[3] R. J. Wyber, ''The recognition of targets from their echo signals,'' Doc-

toral Thesis, Department of Electrical Engineering, University of Sydney, 1973.
[4] A. J. Rudgers, ''Separation and analysis of the acoustic field scattered by a rigid sphere,'' J. Acoust. Soc. Am. **52**, 234–246 (1972).
[5] A. Freedman, ''The formation of acoustic echoes in fluids,'' Doctoral Thesis, University of London, 1961, pp. 5–8, 34–58, 95–108.
[6] P. J. McKerrow, D. Crook, and J. Tsakiris, ''Modelling ultrasonic sensing for mobile robots,'' in Proceedings of the Sixth International Symposium on Robotics and Manufacturing (1997), pp. 497–502.
[7] J. Tsakiris and P. J. McKerrow, ''A model of ultrasonic echolocation,'' in Proceedings of the 1996 National Conference of the Australian Acoustical Society (1996).
[8] D. Crook and P. J. McKerrow, ''Models of ultrasonic sensing,'' in Proceedings of the 1995 National Conference of the Australian Robot Association (1995), pp. 158–165.
[9] *American National Standard: Method for the Calculation of the Absorption of Sound by the Atmosphere* (American Institute of Physics, New York, 1978).
[10] E. Skudrzyk, *The Foundations of Acoustics* (Springer-Verlag, New York, 1972), pp. 603, 631.
[11] *Condenser Microphones and Microphone Preamplifiers for Acoustic Measurements* (Bruel and Kjaer, New York, 1982), p. 62.
[12] A. V. Oppenheim and R. W. Schaffer, *Discrete-Time Signal Processing* (Prentice-Hall, New York, 1989), p. 87.

Extension of the mode method for viscoelastic media and focused ultrasonic beams

J. Vandeputte, O. Leroy, R. Briers, and G. Shkerdin[a)]
Interdisciplinary Research Center, K. U. Leuven Campus Kortrijk, B-8500 Kortrijk, Belgium

(Received 17 November 1999; accepted for publication 30 March 2000)

In the present study viscoelasticity is introduced in the mode model and the orthogonality condition is adapted for viscous media. The expansion of convergent acoustic Gaussian beams in terms of radiation modes for viscoelastic media is studied as well. The effects on the reflected and transmitted profiles of acoustic beams incident from an ideal liquid onto a viscoelastic plate are shown and physically explained. It is shown that focusing the incident beam can suppress divergence effects and gives the possibility to measure shear wave attenuation coefficients. © *2000 Acoustical Society of America.* [S0001-4966(00)01907-X]

PACS numbers: 43.35.Mr [HEB]

INTRODUCTION

In the past, the mode method[1,2] was developed to investigate the interaction of bulk and surface waves with inclusions, cracks, abrupt transitions, and other kinds of discontinuities. Only elastic media were considered, and focused Gaussian beams were never taken into account in the mode method. Wave propagation in viscoelastic media has been frequently addressed by several models in the literature: the spectral representation (Fourier integral),[3–5] inhomogeneous wave model,[6]... . At the moment, more absorbing new materials, such as polymers, composites, etc. are considered in NDT. In this paper we introduce viscoelasticity in the mode method formulas by means of the stress–strain relation for viscoelastic media, and by adapting the orthogonality condition for viscous structures. Also, focused Gaussian beams are handled. We consider in this paper only one structure without any discontinuity and illustrate the influence of viscoelasticity and focusing on the bounded beam reflection and transmission. Lamb profiles are strongly dependent on absorption and focusing and are discussed in this paper. In particular, the study of focused beams will be very interesting in case of inclusions, cracks, or all kinds of discontinuities.

In Sec. I the introduction of viscoelasticity in the mode method formulas is described. The decomposition of an arbitrary acoustic field in a viscoelastic multilayered structure into the complete and orthogonal set of acoustic modes (radiation modes and eigenmodes) is described. In Sec. II the introduction of acoustic Gaussian focused beams is handled. In Sec. III numerical calculations are given in order to illustrate the effects of viscoelasticity and incident focused acoustic beams. Describing viscoelasticity and focusing in more complex structures will be done more extensively in future papers.

I. MODE EXPANSION IN VISCOELASTIC MEDIA

The general description of the mode method for isotropic elastic media was given by Briers *et al.*[2] It is based on the construction of a complete and orthogonal set of radiation modes and eigenmodes for the structure to be considered. A radiation mode is the resulting field of the fields created by plane waves emitted by acoustic sources at $+\infty$ and $-\infty$ (assumption).

Assuming harmonic time dependence with angular frequency ω, the stress–strain relation for isotropic viscoelastic media is given by[6]

$$T_{ij}=\delta_{ij}(\lambda'-i\omega\lambda'')\sum_{k=1}^{3} e_{kk}+2(\mu'-i\omega\mu'')e_{ij}, \tag{1}$$

with T_{ij} and e_{ij}, respectively, the stress tensor and strain tensor component; λ', μ' the Lamé constants; λ'', μ'' the viscosity constants, and δ_{ij} the Kronecker symbol. To determine the values of λ'' and μ'', small absorption is assumed by requiring that

$$\omega\lambda''\ll\lambda' \quad \text{and} \quad \omega\mu''\ll\mu'. \tag{2}$$

Only the calculation of μ'' will be shown; the calculation of λ'' can be done in an analogous way. Considered the shear velocity

$$v_t=\sqrt{\frac{\mu'-i\omega\mu''}{\rho}}=v_t'+iv_t'', \tag{3}$$

with ρ the density. Using Taylor series approximations, the real and imaginary parts of v_t can be expressed as

$$v_t'\approx\sqrt{\frac{\mu'}{\rho}}, \tag{3a}$$

$$v_t''\approx-\frac{v_t'\omega\mu''}{2\mu'}. \tag{3b}$$

The shear wave number then becomes

$$k_t=\frac{\omega}{v_t'+iv_t''}\approx\frac{\omega}{v_t'}-\frac{i\omega v_t''}{v_t'^2}. \tag{3c}$$

Denoting with a_1 and a_t the loss parameters defined[3] as attenuation per wavelength for the longitudinal and shear waves, the longitudinal and shear absorption coefficients are

[a)]Permanent address: Institute of Radioengineering and Electronics, Russian Academy of Sciences, Moscow, Russia.

defined as $\alpha_1=\omega^2 a_1$ and $\alpha_t=\omega^2 a_t$.[6,7] In fact, these are two times the imaginary parts of the corresponding complex longitudinal and shear wave numbers. Inserting (3a) and (3b) in (3c) and using $\alpha_t=2k_t''$ leads to

$$\mu''=\frac{\alpha_t v_t'\mu'}{\omega^2}. \tag{4}$$

In an analogous way, it can be shown that

$$\lambda''=\frac{v_l'\lambda'\alpha_l+2\mu'(v_l'\alpha_l-v_t'\alpha_t)}{\omega^2}, \tag{5}$$

with $v_1=v_1'+iv_1''$ the longitudinal velocity.

Since all the parameters on the right-hand sides of (4) and (5) are known, μ'' and λ'' can be calculated. From these results, the complex velocities can be calculated and consequently, the complex wave numbers k_l and k_t too. Using these complex values of wave numbers, viscoelasticity is introduced in the mode method formulas for isotropic elastic media.

For a multilayered viscoelastic structure, homogeneous in the *X*- and *Z* direction, immersed in an elastic liquid, the mode expansion for the displacement vector and stress tensor component is given by[1,2]

$$\mathbf{U}(y,z)=\sum_{m_1,m_2}\int_0^{+\infty} C^{(m)}(k_{ly})\mathbf{U}^{(m)}(y,z;k_{ly})dk_{ly} + \sum_m C^{(s_m)}\mathbf{U}^{(s_m)}(y,z), \tag{6}$$

$$T_{ij}(y,z)=\sum_{m_1,m_2}\int_0^{+\infty} C^{(m)}(k_{ly})T_{ij}^{(m)}(y,z;k_{ly})dk_{ly} + \sum_m C^{(s_m)}T_{ij}^{(s_m)}(y,z), \tag{7}$$

where k_{ly} denotes the y component of the wave vector $\mathbf{k}_l$ in the liquid; the index m_1 refers to the radiation modes generated by plane waves emerging from $+\infty$, and m_2 to the radiation modes generated by plane waves emerging from $-\infty$. The summation is taken over the two types of radiation modes and over the Stoneley modes; integration is taken over the continuous spectrum of radiation modes. $C^{(m)}$ and $C^{(k_m)}$ are, respectively, the expansion coefficients for the radiation modes and the Stoneley modes. All the acoustic waves are assumed to be propagating in the (*Y*,*Z*) plane and to be uniform along the direction perpendicular to the plane of incidence (two-dimensional profiles) (Fig. 1). In order to calculate the expansion coefficients, orthogonality relations are needed. These relations have been handled extensively in previous papers[1,2] for nonabsorbing structures. When absorption is taken into account, they transform into

$$\int_{-\infty}^{+\infty}[T_{yz}^{(m_1)}(y)U_y^{(m_2)}(y)-T_{zz}^{(m_2)}(y)U_z^{(m_1)}(y)]dy = Q_r^{(m_1,m_2)}\delta(k_{ly}^{(m_1)}-k_{ly}^{(m_2)}). \tag{8}$$

Note that the complex conjugate does not occur anymore as was the case in the nonabsorptive situation. A radiation mode can be labeled by k_{ly}, the y component of its wave vector in the liquid. As shown in a previous paper,[1] two radiation modes are orthogonal when the corresponding k_{ly} components are different. Consequently, two radiation modes of types m_1 and m_2 with the same value of k_{ly} and $m_1\neq m_2$ are generally not orthogonal. As a consequence, we have to construct two new orthogonal combinations to remedy this deficiency. Further, we will consider the simplest case of a viscoelastic plate immersed in a liquid. Performing a similar orthogonalization procedure as in Ref. 1 leads to two new orthogonal types of radiation modes

$$\mathbf{U}^{(r')}=\mathbf{U}^{(m_1)}+\mathbf{U}^{(m_2)}, \tag{9a}$$

$$\mathbf{U}^{(r'')}=\mathbf{U}^{(m_1)}-\mathbf{U}^{(m_2)}. \tag{9b}$$

Putting these two new types of radiation modes in (8), the right-hand side becomes

$$Q_r^{(r',t'')}=\tilde{Q}_r^{(r',r'')}\delta_{r',r''} \quad (\delta_{r',r''}=\text{the Kronecker symbol}). \tag{10}$$

For this symmetrical structure, the new types of radiation modes are the symmetrical and the antisymmetrical radiation modes.[1,2] Expressions for the displacement fields and normalization constants $\tilde{Q}_r^{(s)}$ (for the symmetrical modes) and $\tilde{Q}_r^{(a)}$ (for the antisymmetrical modes) are given in the Appendix.

The expansion coefficients can be calculated as follows. Rewriting (6) and (7) for the incident profile, where the z component of the displacement vector and the yz component of the stress tensor in $z=z_0$ is considered, leads to

$$U_z^{\text{inc}}(y,z_0)=\sum_{s,a}\int_0^{+\infty} C^{(m)}(k_{ly})U_z^{(m)}(y,z_0;k_{ly})dk_{ly} + \sum_{s,a} C^{(s_m)}U_z^{(s_m)}(y,z_0), \tag{11}$$

$$T_{yz}^{\text{inc}}(y,z_0)=\sum_{s,a}\int_0^{+\infty} C^{(m)}(k_{ly})T_{yz}^{(m)}(y,z_0;k_{ly})dk_{ly} + \sum_{s,a} C^{(s_m)}T_{yz}^{(s_m)}(y,z_0). \tag{12}$$

Note that summation is taken now over the symmetrical ($m=s$) and antisymmetrical ($m=a$) radiation modes and over

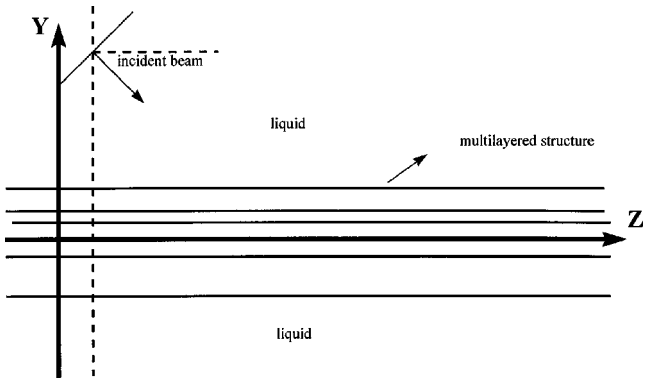

FIG. 1. Liquid/multilayered/liquid-structure.

the symmetrical ($s_m=s$) and the antisymmetrical ($s_m=a$) Stoneley modes. Taking an arbitrary fixed radiation mode and considering $T_{zz}^{(m')}$ and $U_y^{(m')}$, where the superscript $'$ refers to the fixed character, we multiply (11) with $T_{zz}^{(m')}$ and (12) by $U_y^{(m')}$, and integrate over y, from $-\infty$ to $+\infty$. Then, subtracting these two equations leads to the next equality

$$\int_{-\infty}^{+\infty}(U_z^{\mathrm{inc}}T_{zz}^{(m')}-T_{yz}^{\mathrm{inc}}U_y^{(m')})dy$$

$$=\sum_{s,a}\int_0^{+\infty}C^{(m)}(k_{ly})$$

$$\times\left\{\int_{-\infty}^{+\infty}(T_{zz}^{(m')}U_z^{(m)}-T_{yz}^{(m)}U_y^{(m')})dy\right\}dk_{ly}. \tag{13}$$

The summation over the Stoneley modes has already been omitted, because these are orthogonal to the fixed radiation mode. Using the orthogonality condition (8) in the right-hand side of (13) and assuming that $T_z^{\mathrm{mc}}\approx 0$ (the incident wave is concentrated in the liquid), it follows from (13) that

$$C^{(m)}(k_{ly})=-\frac{\int_{-\infty}^{+\infty}U_z^{\mathrm{inc}}(y,z_0)T_{zz}^{(m)}(y,z_0;k_{ly})dy}{\tilde{Q}_r^{(m)'}(k_{ly})}. \tag{14}$$

This expression can be used when $y_0>(\sqrt{2}L)/\cos(\theta)$. If the incident wave is represented by a volume wave (the acoustic transducer is located far from the plate), Stoneley modes are not excited because of the orthogonality and can be neglected.

Then, using (6), we are able to calculate the acoustic field in an arbitrary region of the structure. Note that the mode theory is based on the knowledge of the z component of the displacement of the incident field along the Y axis (or along an axis parallel to the Y axis). When the angle of incidence (with respect to the normal) is very large, the mode model is especially useful, while the Fourier integral fails to describe narrow-bounded beams accurately.

II. FOCUSED GAUSSIAN BEAMS

Consider an incident Gaussian bounded beam passing through a thin acoustic lens in $z'=0$ [see Fig. 2(a)]. Before interaction with the acoustic lens, the acoustic displacement is given by:

$$\mathbf{U}^{\mathrm{inc}}(y',0)=\mathbf{U}_0e^{-y'^2/2L^2}. \tag{15}$$

After passage through the acoustic lens, the profile becomes

$$\mathbf{U}^{\mathrm{inc}}(y',0)=\mathbf{U}_0e^{-y'^2/2L^2}e^{-iy'^2/2L_1^2}e^{-i\omega t}$$

$$=\mathbf{U}_0e^{-(y'^2/2L^2)(1+ai)}, \tag{16}$$

where L denotes the halfwidth and L_1 the phase modification, $a=L^2/L_1^2$. In this way, focused Gaussian beams are described by modifying the halfwidth L to $L/\sqrt{1+ia}$. Using the expression for the diffraction length

$$L_D=k_lL^2, \tag{17}$$

we obtain

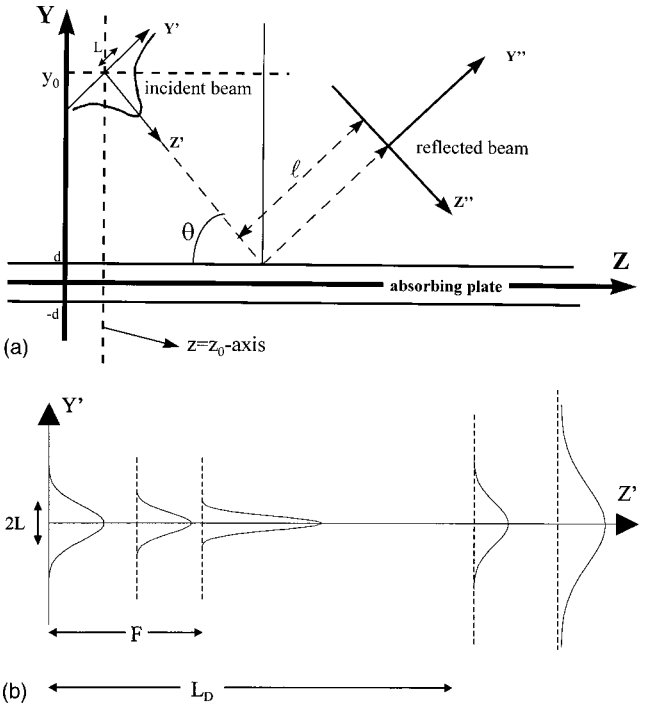

FIG. 2. (a) Incident Gaussian beam on a viscoelastic plate in a liquid. (b) Propagating focused Gaussian beam; parameters L, F, and L_D.

$$a=\frac{L_D}{F}, \tag{18}$$

with

$$F=k_lL_1^2. \tag{19}$$

It can be shown that the effect of focusing appears only if the condition $a\gg 1$ is fulfilled and in this case the focal length is close to F.

Expression (16) enables us to calculate the acoustic profile at an arbitrary point by means of the Fourier integral.[3] Letting $z=z_0$, we have the profile along the $z=z_0$ axis, which is needed to calculate the expansion coefficient given by (14). As a consequence, double integrals are involved to calculate the expansion coefficient. Therefore, the calculations will be strongly simplified when we use the projection of the field given by (16) on the plane $z=z_0$ instead of explicit calculations using the Fourier integral. As a result, we obtain the incident profile adapted for the mode theory:

$$U_z^{\mathrm{inc}}(y,z_0)=U_0\cos(\theta)e^{[(y-y_0)^2\cos^2(\theta)/2L^2](1+ia)}$$

$$\times e^{-ik_l(y-y_0)\sin(\theta)}. \tag{20}$$

Under the assumption that

$$Ltg(\theta)<\min\left(\frac{F}{\sqrt{1+\left(\frac{F}{L_D}\right)^2}},\frac{2F^2}{L_D\left(1+\frac{F^2}{L_D^2}\right)}\right), \tag{21}$$

it can be shown that this simplified formula (20) is acceptable.

In Fig. 2(b), a scheme of the focusing behavior is given.

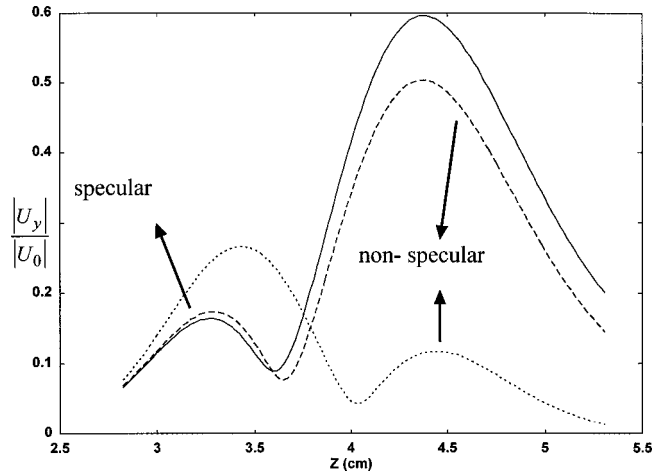

FIG. 3. Influence of absorption on the reflected profile at $y=2$ cm (plane parallel to the plate), angle of incidence: Rayleigh angle. Solid line: no absorption; dashed line: absorption; dotted line: high absorption.

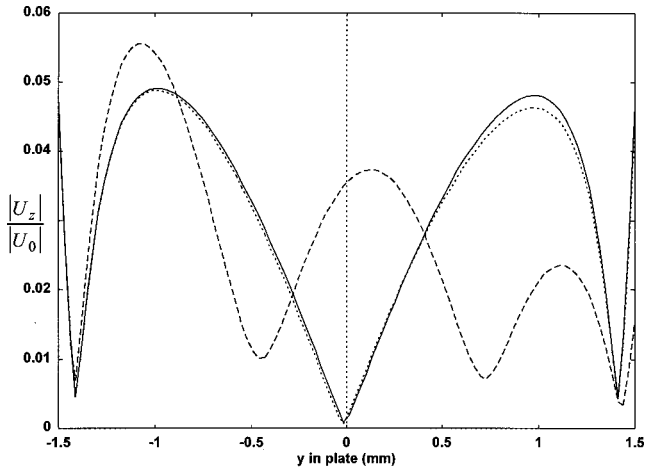

FIG. 4. Influence of focusing on the profile at a cross section in the plate of the A_0 mode, for different values of F, after 5 cm propagation in the plate. Solid line: no focusing; dashed line: focal point on plate; dotted line: focal point 2 m under the plate.

III. NUMERICAL RESULTS

We move to some numerical results in order to illustrate the effects of absorption and focusing on the reflected and transmitted beam using the mode method formulas. We are considering a brass plate immersed in water. In our calculations we always used next values and parameters: frequency$=3$ MHz, $d=1.5$ mm (with $d=$the half-thickness of the plate), velocity in water$=1480$ m/s, $v_1=4410$ m/s (longitudinal velocity in the plate), $v_t=2150$ m/s (transversal velocity in the plate), $v_R=2700$ m/s (Rayleigh wave velocity), $\rho=8600\ \mathrm{kg/m^3}$, $a_1=30\cdot 10^{-15}\ \mathrm{s^2/m}$, $a_t=130\cdot 10^{-15}\ \mathrm{s^2/m}$, $z_0=0$. The angle of incidence wil be mentioned in each example itself. When the angle of incidence is the ''Rayleigh angle,'' we mean the angle corresponding to the A_0-and S_0 mode. These coincide for large values of the product of d and frequency, and this will be the case in our examples. In all examples handled these values remain fixed (unless otherwise mentioned). The values of the other parameters are chosen specifically to make the pictures very illustrative.

A. Influence of viscoelasticity on the reflected bounded profile

We study the reflected profile[8] of an incident nonfocused ($a=0$) Gaussian beam with half-beamwidth $L=2.8$ mm, $y_0=1.5$ cm, and incident at the Rayleigh angle $\theta_R=42.31°$. Figure 3 shows $|U_y|/|U_0|$ as a function of the position z at the plane $y=2$ cm (parallel to the plate). Three curves are represented. First, when we neglect absorption; then, we consider absorption with the absorption values of a_1 and a_t as mentioned above, and finally when arbitrary absorption is chosen: a_1 and a_t are ten times larger than the given values; this in order to understand better the influence effects of high absorption. Analyzing the graphs, we conclude that the specular-reflected component increases and the nonspecular-reflected component decreases with increasing absorption values. Due to the absorption, the excited leaky Rayleigh wave decreases more rapidly in amplitude during the propagation than in the nonabsorptive case; as a consequence, the reradiated field has decreased. The unshifted beam has increased because the phase-match condition between the incident beam and the leaky Rayleigh wave is deteriorated due to the introduction of the viscoelasticity. We also remark that the minimum region, which corresponds to a phase jump of 180° between the shifted and unshifted lobes, moves to the right for increasing absorption values. Specular reflection increases, nonspecular reflection decreases, and as a result the canceling region moves to the right.

B. Influence of focusing on the Lamb profile propagating in the plate

Here, we consider Lamb-angle incidence: 47.11°, the A_0-Lamb mode; $y_0=10$ cm, $L=1.4$ cm. Absorption has been neglected. Figure 4 plots $|U_z|/|U_0|$ as a function of y in the plate, after 5 cm propagation in the plate. Clearly, when the beam is effectively focused, the Lamb profile is disturbed. Due to the focusing, additional Lamb modes with angle of incidence in the neighborhood of 47.11°, are excited. As a result, the observed profile is an interference of Lamb modes and other excited propagating waves. When the focal point is moved very far away from the plate, the profile converges to the nonfocused case. In Fig. 5, the profile after a longer distance of propagation (10 cm) is shown. Of course, the amplitudes have decreased because of the reradiation into the liquid.

C. Influence of focusing on the reflected propagating bounded beam profile

Next, we study the reflected bounded-beam profile[9–12] of a Gaussian beam incident at the Rayleigh angle, 59.01°, on a steel plate with parameters: $v_1=5790$ m/s, $v_1=3100$ m/s, frequency$=4$ MHz, $\rho=7900\ \mathrm{kg/m^3}$, $d=2.5$ mm, $y_0=2$ cm, and $L=2$ mm. Figure 6(a) plots the reflected profile at planes perpendicular to the propagation direction [Fig. 2(a)] for different propagation distances l, without focusing. We see some divergence in propagation and a slightly changing minimum region. Introducing focusing, we show in Fig. 6(b) that it is possible to recreate per-

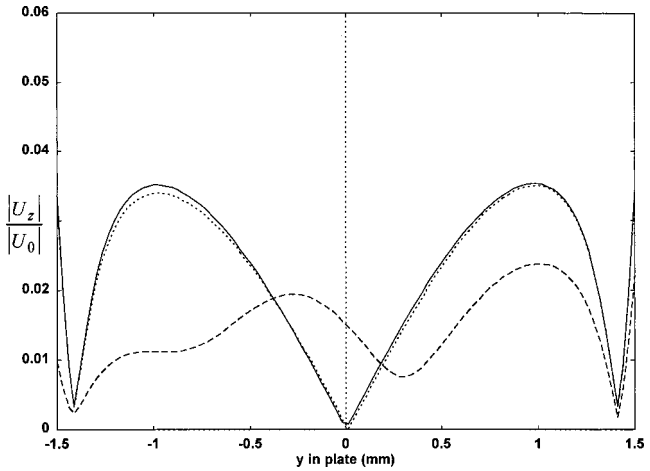

FIG. 5. Influence of focusing on the profile at a cross section in the plate of the A_0 mode, for different values of F, after 10 cm propagation in the plate. Solid line: no focusing; dashed line: focal point on plate; dotted line: focal point 2 m under the plate.

fectly the null region. We also remark a small deformation of the profile, when focusing is taken into account. Due to the focusing, a range of angles of incidence, $59.01° \pm 5°$ (focal point on the plate), $59.01° \pm 2.5°$ (focal point 2 cm under the plate), has to be considered. As a consequence, additional waves and propagating transversal waves (transversal critical angle$=61.48°$) are excited. This declares the distortion in Fig. 6(b).

In a second example, we consider a Gaussian beam with a larger beamwidth, $L=4.2$ mm, incident on a brass plate at the Rayleigh angle, 42.31°; $y_0=4$ cm. Again, absorption is neglected. Figure 7(a) shows the reflected profile at the plane perpendicular to the propagation direction, at 5 cm propagation after reflection ($l=5$ cm). Apparently, ''optimal'' focal lengths [dotted line in Fig. 7(a)] exist which maximize the separation between the two reflected components and recreates the null region. In this example we add a study concerning the phase jump of both lobes affected by focusing. Figure 7(b) represents the different phase curves of $|U|/|U_0|$, plotted as a function of the position z''. We remark a good agreement in the sense that the phase jump exhibits more clearly when the minimum in the null region is closer to zero.

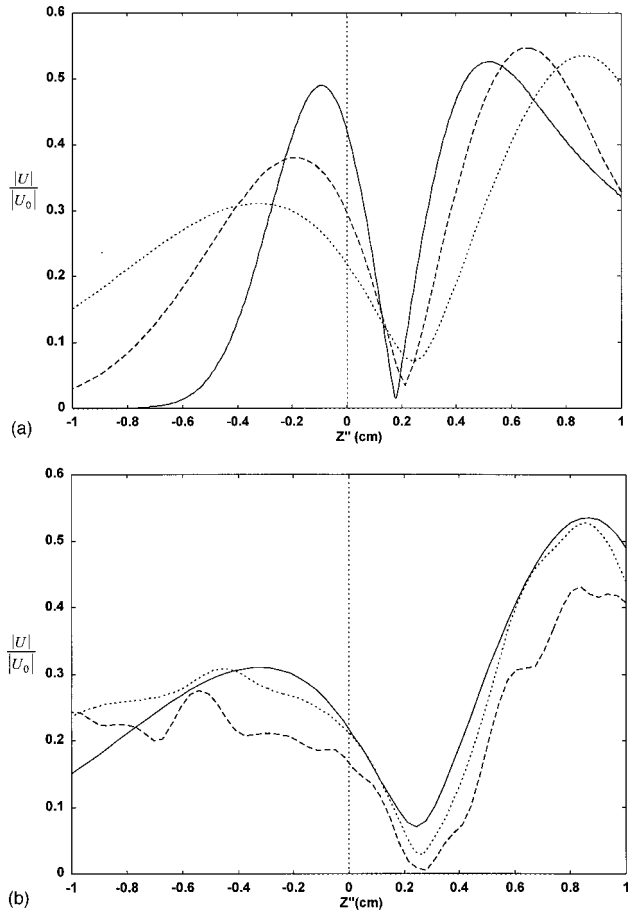

FIG. 6. (a) Effects of propagation divergence on the reflected profile at the plane perpendicular to the propagation direction, for different propagation distances l; angle of incidence=Rayleigh angle. Solid line: $l=1.5$ cm; dashed line: $l=10$ cm; dotted line: $l=20$ cm. (b) Effects of focusing on the reflected profile at the plane perpendicular to the propagation direction, $l=20$ cm, for different focal lengths; angle of incidence=Rayleigh angle. Solid line: no focusing; dashed line: focal point on plate; dotted line: focal point 2 cm under the plate.

D. Influence of focusing and absorption on the reflected and transmitted bounded beam profile

We consider a Gaussian beam with halfwidth $L=8$ mm, incident at an arbitrary angle of 64° on a brass plate; $y_0=20$ cm. Effects of absorption and focusing are studied together here. When focusing is considered, the focal point will always be situated on the top of the plate. The reflected profile is studied at $y=3$ cm in Fig. 8. The transmitted profile is studied at $y=-3$ cm in Fig. 9. In both figures, $|U_y|/|U_0|$ is plotted as a function of the position z. The interpretation of Fig. 8 and Fig. 9 leads to the following conclusions:

(i) When we do not focus and consider the influence of absorption as well on the reflected as on the transmitted profile, we conclude that there is a very small influence on the amplitude distribution.

(ii) When we focus on the top of the plate, we remark a great influence of the absorption on the amplitude by a progressive decrease of the amplitude of the created peaks.

(iii) Focusing generates several peaks as well in the reflected as in the transmitted beam. Those peaks are created because the incident profile becomes very small (4.6 mm) at the top of the plate and leads to multiple reflection and transmission at the interfaces. The multiple interferences are revealed by the different maxima.

Note that the excited propagating waves in the brass plate are the shear waves because the longitudinal critical angle ($=71°\ 60'$) has been exceeded. The incident beam is very narrow when reaching the plate and the range of angles of incidence to be considered is very small ($64° \pm 2°$); as a result, the observed profiles are created by a narrow propagating shear wave in the plate. The distance between two

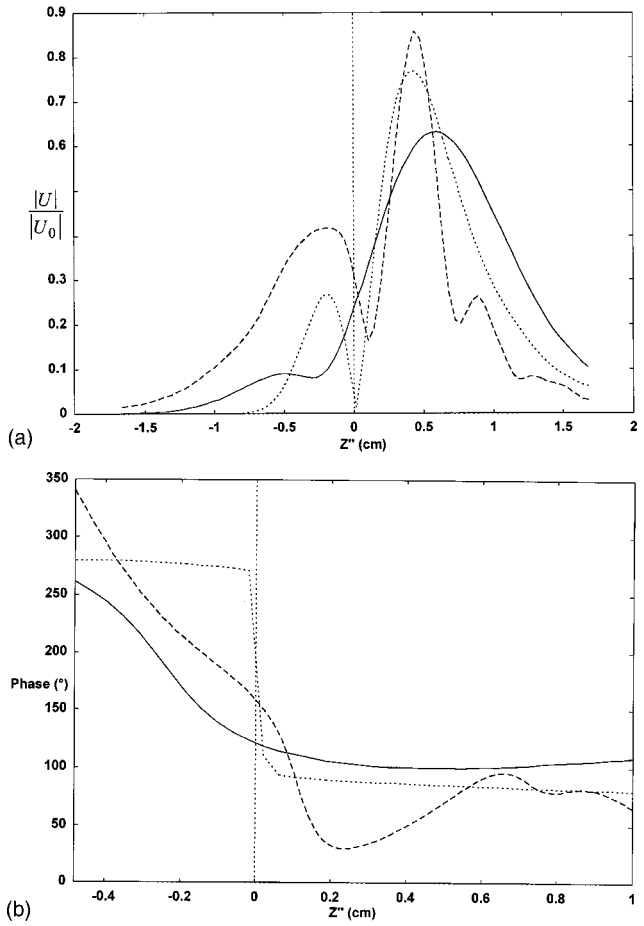

FIG. 7. (a) Influence of focusing on the reflected profile in the plane perpendicular to the propagation direction, $l=5$ cm; angle of incidence=Rayleigh angle. Solid line: no focusing; dashed line: focal point on plate; dotted line: focal point 10 cm under the plate. (b) Influence of focusing on the phase of the reflected profile in the plane perpendicular to the propagation direction, $l=5$ cm; angle of incidence=Rayleigh angle. Solid line: no focusing; dashed line: focal point on plate; dotted line: focal point 10 cm under the plate.

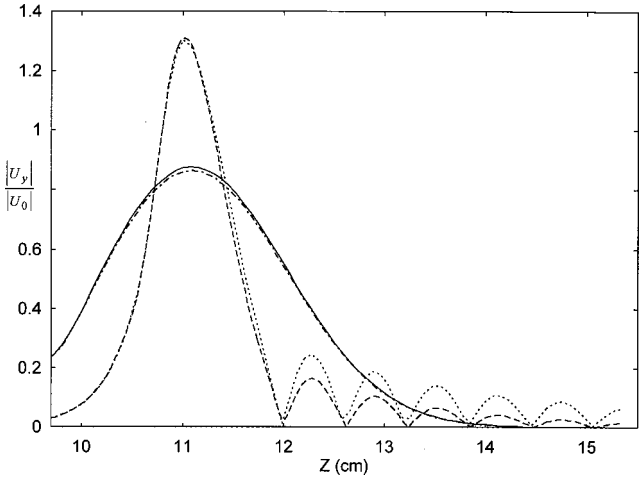

FIG. 8. Influence of absorption and focusing on the reflected profile at $y=3$ cm (plane parallel to the plate); angle of incidence=64°. Solid line: no absorption, no focusing; dashed line: absorption, focusing; dotted line: no absorption, focusing; dash-dot line: absorption, no focusing.

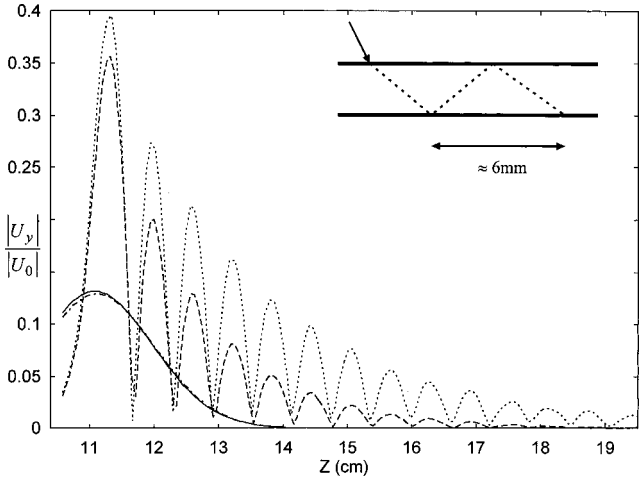

FIG. 9. Influence of absorption and focusing on the transmitted profile at $y=-3$ cm (plane parallel to the plate); angle of incidence=64°. Solid line: no absorption, no focusing; dashed line: absorption, focusing; dotted line: no absorption, focusing; dash-dot line: absorption, no focusing.

adjacent peaks in the transmitted profile can be calculated and is equal to ± 0.6 cm (see the right-hand corner of Fig. 9). As we see that absorption leads to a strong reduction of the amplitudes of the reflected as well of the transmitted peaks, we conclude that the absorption coefficient of the shear waves in the plate can accurately be measured, both in reflection and transmission. In Fig. 10, we consider explicitly different absorption coefficients and plot the transmitted focused beams. The ratio between two adjacent peaks has to be a constant, so the amplitudes of the different peaks decrease exponentially or, in a logarithmic scale, decrease linearly (see the right-hand corner of Fig. 10). As a result, the absorption coefficient of the shear waves can be measured by the inclination of this line.

IV. CONCLUSION

The acoustic mode method has been extended for absorbing structures and focused acoustic beams. It was illus-

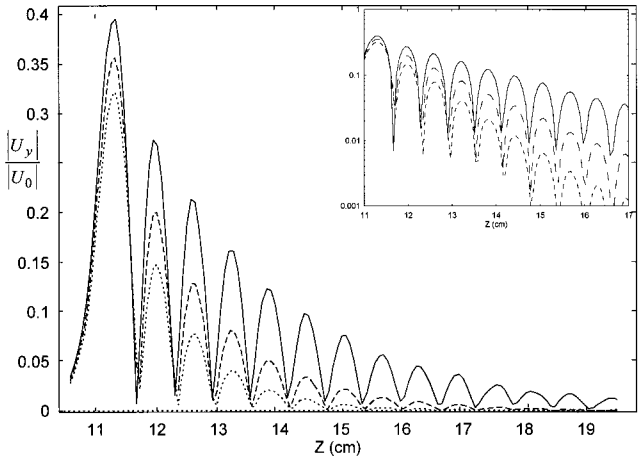

FIG. 10. Influence of the shear wave absorption on the amplitude of the transmitted profile at $y=-3$ cm (plane parallel to the plate); angle of incidence=64°; focal point on plate. Solid line: no absorption; dashed line: absorption coefficient=$a_t=130\cdot 10^{-15}$ s^2/m; dotted line: absorption coefficient=$a_t\times 2$.

trated that absorption weakens the shifted component and amplifies the unshifted component of the reflected profile of a Gaussian beam incident at critical angles. It was shown that the propagating reflected profile leads to disappearance of the null region between the specular- and nonspecular-reflected component, while focusing can restore the null region again. We showed that focusing disturbs the Lamb profile in the plate. The reflected and transmitted profile exhibits several peaks, which can be explained by multiple reflection and transmission effects of the narrow focused beam inside the plate. This phenomenon can be used in order to determine very accurately the shear wave absorption coefficient in the plate.

ACKNOWLEDGMENTS

The authors would like to thank the Research Council of the K. U. Leuven for the fellowship awarded to Professor G. N. Shkerdin, which enabled us to write this paper.

APPENDIX

The displacement fields for the symmetrical ($m=s$) and the antisymmetrical ($m=a$) radiation modes, omitting $e^{ik_z z}$, is described by

$y>d$ (in the liquid above the plate):

$$U_y^{(m)}=-\frac{k_{ly}}{k_l^2 2}\left[\alpha_m e^{ik_{ly}(y-d)-i\phi_m}+e^{i\phi_m-ik_{ly}(y-d)}\right], \quad \text{(A1)}$$

$$U_z^{(m)}=-\frac{k_z}{k_l^2 2}\left[\alpha_m e^{ik_{ly}(y-d)-i\phi_m}-e^{i\phi_m-ik_{ly}(y-d)}\right]. \quad \text{(A2)}$$

y

$y<-d$ (in the liquid beneath the plate):

$$U_y^{(m)}=\pm\frac{k_{ly}}{k_l^2 2}\left[\alpha_m e^{-ik_{ly}(y+d)-i\phi_m}+e^{i\phi_m+ik_{ly}(y+d)}\right] \quad \text{(A3)}$$

$$U_z^{(m)}=\pm\frac{k_z}{k_l^2 2}\left[-\alpha_m e^{-ik_{ly}(y+d)-i\phi_m}+e^{i\phi_m+ik_{ly}(y+d)}\right], \quad \text{(A4)}$$

where in $\pm$ the plus is used in case of $m=s$ and the minus is used in case of $m=a$.

$-d<v<d$ (in the plate):

$$U_y^{(s)}=\frac{k_{ly}}{k_l^2|\Delta_s|}\left[\frac{2k_z^2-k_{1t}^2}{k_{1t}^2}\frac{\sin(k_{1ly}y)}{\sin(k_{1ly}d)}-\frac{2k_z^2}{k_{1t}^2}\frac{\sin(k_{1ty}y)}{\sin(k_{1ty}d)}\right], \quad \text{(A5)}$$

$$U_z^{(s)}=-i\frac{k_z k_{ly}}{k_l^2 k_{1ly}|\Delta_s|}\left[\frac{2k_z^2-k_{1t}^2}{k_{1t}^2}\frac{\cos(k_{1ly}y)}{\sin(k_{1ly}d)}+\frac{2k_{1ty}k_{1ly}}{k_{1t}^2}\frac{\cos(k_{1ty}y)}{\sin(k_{1ty}d)}\right]. \quad \text{(A6)}$$

$$U_y^{(a)}=\frac{k_{ly}}{k_l^2|\Delta_a|}\left[-\frac{2k_z^2-k_{1t}^2}{k_{1t}^2}\frac{\cos(k_{1ly}y)}{\cos(k_{1ly}d)}+\frac{2k_z^2}{k_{1t}^2}\frac{\cos(k_{1ty}y)}{\cos(k_{1ty}d)}\right], \quad \text{(A7)}$$

$$U_z^{(a)}=-i\frac{k_z k_{ly}}{k_l^2 k_{1ly}|\Delta_a|}\left[\frac{2k_z^2-k_{1t}^2}{k_{1t}^2}\frac{\sin(k_{1ly}y)}{\cos(k_{1ly}d)}+\frac{2k_{1ty}k_{1ly}}{k_{1t}^2}\frac{\sin(k_{1ty}y)}{\cos(k_{1ty}d)}\right], \quad \text{(A8)}$$

with

$$v\Delta_s=1+i\frac{\rho_1}{\rho}\frac{k_{ly}}{k_{1ly}}F_s, \quad \text{(A9)}$$

$$F_s=\frac{\cos(k_{1ly}d)}{\sin(k_{1ly}d)}\frac{(k_{1t}^2-2k_z^2)^2}{k_{1t}^4}+\frac{\cos(k_{1ty}d)}{\sin(k_{1ty}d)}\frac{4k_z^2k_{1ty}k_{1ly}}{k_{1t}^4}, \quad \text{(A10)}$$

$$\Delta_a=-1+i\frac{\rho_1}{\rho}\frac{k_{ly}}{k_{1ly}}F_a, \quad \text{(A11)}$$

$$F_a=\frac{\sin(k_{1ly}d)}{\cos(k_{1ly}d)}\frac{(k_{1t}^2-2k_z^2)^2}{k_{1t}^4}+\frac{\sin(k_{1ty}d)}{\cos(k_{1ty}d)}\frac{4k_z^2k_{1ty}k_{1ly}}{k_{1t}^4}, \quad \text{(A12)}$$

$$\alpha_m=\frac{1+\left(\frac{\rho_1}{\rho}\frac{k_{ly}}{k_{1ly}}F_m\right)^2}{|\Delta_m|^2}, \quad \text{(A13)}$$

$$e^{i\phi_m}=\frac{\Delta_m}{|\Delta_m|}. \quad \text{(A14)}$$

The normalization constants of (8) are given by

$$\tilde{Q}_r^{(m)}=\frac{i\pi\lambda k_z\alpha_m e^{2iq_z z}}{k_l^2},$$

where ρ_1 denotes the density in the solid, k_{1l} the longitudinal wave number in the solid, k_{1t} the transversal wave number in the solid, and k_{1ly}, k_{1ty} the y components of the longitudinal and transversal wave vectors in the solid.

[1] R. Briers, O. Leroy, and G. N. Shkerdin, ''Conversion of a Stoneley wave at the extremity of a fluid loaded plate,'' J. Acoust. Soc. Am. **101**, 1347–1357 (1997).

[2] R. Briers, O. Leroy, G. N. Shkerdin, and Yu. V. Gulyaev, ''Mode theory as a framework for the investigation of the generation of a Stoneley wave at a liquid/solid interface,'' J. Acoust. Soc. Am. **95**, 1953–1966 (1994).

[3] T. D. K. Ngoc and W. G. Mayer, ''A general description of ultrasonic nonspecular reflection and transmission effects for layered media,'' IEEE Trans. Sonics Ultrason. **SU-27**(5) (1980).

[4] L. M. Brekhovskikh, *Waves in Layered Media* (Academic, New York, 1960).

[5] H. L. Bertoni and T. Tamir, ''Unified theory of Rayleigh-Angle Phenomena for Acoustic Beams''

[6] K. Van Den Abeele and O. Leroy, ''Complex harmonic wave scattering as the framework for investigation of bounded beam reflection and transmission at plane interfaces and its importance in the study of vibrational modes,'' J. Acoust. Soc. Am. **93**, 308–323 (1993).

[7] J. P. Charlier and F. Crowet, ''Wave equations in linear viscoelastic materials,'' J. Acoust. Soc. Am. **79**, 895–900 (1986).
[8] C. Potel and J.-F. de Belleval, ''Surface waves in an anisotropic periodically multilayered medium: Influence of the absorption,'' J. Appl. Phys. **77**, 6152–6161 (1995).
[9] P. B. Nagy, K. Cho, and L. Adler, ''Focal shift of convergent ultrasonic beams reflected from a liquid–solid interface,'' J. Acoust. Soc. Am. **81**, 835–839 (1987).
[10] H. L. Bertoni, C. W. Hsue, and T. Tamir, ''Non-specular reflection of convergent beams from liquid–solid interface,'' Traitement de Signal, Vol. 2, No. 1, 1985.
[11] A. E. Siegman, *An Introduction to Lasers and Masers* (McGraw-Hill, New York, 1971).
[12] T. E. Matikas, M. Rousseau, and P. Gatignol, ''Experimental study of focused ultrasonic beams reflected at a fluid–solid interface in the neighborhood of the Rayleigh angle,'' IEEE Trans. Ultrason. Ferroelectr. Freq. Control **39**, 737–744 (1992).

Bounded beam interaction with thin inclusions. Characterization by phase differences at Rayleigh angle incidence

R. Briers,[a] O. Leroy, and G. Shkerdin[b]
Interdisciplinary Research Center, K. U. Leuven Campus Kortrijk, B-8500 Kortrijk, Belgium

(Received 6 May 1999; accepted for publication 20 June 2000)

A theoretical study of the reflection of a bounded Gaussian ultrasonic beam, incident onto a rectangular inclusion located near a fluid/solid half-space interface, is presented. The thickness of the inclusion is assumed to be much smaller than the ultrasonic wavelength in the solid. It is shown that, at critical Rayleigh angle incidence, the phase in the point of maximum amplitude of the shifted reflected lobe is very sensitive to dimension variations of the inclusion, and thus useful for inclusion characterization. The modelization of the problem is based on mode theory. © *2000 Acoustical Society of America.* [S0001-4966(00)01510-1]

PACS numbers: 43.35.Cg [HEB]

I. INTRODUCTION

From the work of Brekhovskikh[1] it is seen that for a thin layer—of thickness much smaller than the ultrasonic wavelength—placed upon a solid half-space the dependence of the modulus of the reflection coefficient on the thickness is very small and unmeasurable. Therefore Devolder *et al.*[2] studied the dependence of the *phase* of the reflection coefficient on the thickness of a layer and showed that near the critical Rayleigh angle of the substrate a sensitive phase shift between the incident and reflected ultrasound appears. A new nondestructive technique (the acousto-optic technique[3]) was elaborated to measure these phase differences, confirming the results obtained from the theoretical model based on the classical Fourier theory and the inhomogeneous wave theory.[4,5] This technique measures in the optical near-field[6] the amplitude and phase modulation of the ultrasound reflected by a layered material. The motivation for the present work is to provide a theoretical model for the preliminary acousto-optical measurements[4] of phase variations caused by the presence of a subsurface inclusion (which is modeled by a *finite* thin layer included in a substrate). Unnecessary to notice that when a bounded ultrasonic beam is incident onto a rectangular inclusion, complicated mode conversion and scattering phenomena arise. Due to the complexity of the problem a description with Fourier or inhomogeneous wave theory is not self-evident anymore. Therefore a mode theory will be used that is very suited to these kinds of problems. The mode theory has already been applied to analyze the interaction of *surface waves* with rectangular inclusions,[7] a topic that also was studied experimentally.[8] Only the most relevant equations of the mode theory, necessary for this work, will be presented. For a more detailed description of the fundamentals and applications of the mode theory we refer the reader to other publications.[9–11] The importance of phase information especially for inclusion characterization was recently shown by Maslov *et al.*[12] They developed a new ultrasonic technique that can distinguish small sperical voids from small spherical elastic and rigid inclusions. Convential acoustic techniques that use only amplitude information and ignore the phase information cannot make this distinction.

II. ANALYTICAL EXPRESSION FOR THE AMPLITUDE AND PHASE DISTRIBUTION OF A GAUSSIAN BEAM REFLECTED FROM A RECTANGULAR INCLUSION

Figure 1 shows an incident ultrasonic beam bounded in the (y,z) plane and uniform in the x direction. The beam of angular frequency $\omega=2\pi f$ is seen to be incident at an angle θ_i onto an inclusion of length L and thickness d that is situated near the surface of a fluid loaded solid half-space, which is assumed to be isotropic. Its intensity profile is contained by an effective width $2w$ (w represents the half beamwidth in this work). The inclusion has density ρ_1, dilatational velocity v_{d1}, and shear velocity v_{s1}; the medium constants of the substrate and those of the fluid are ρ_2, v_{d2}, v_{s2}, respectively, ρ and v.

The configuration in Fig. 1 is divided in three structures: two fluid/solid structures (named structures 1a and 1b) with the same medium constants, and a fluid/thin layer/substrate structure (named structure 2). Due to mode conversion and scattering at the plane $z=0$, the incident bounded beam generates in structure 1a ($z<0$) a reflected bulk and Stoneley surface wave as well as a transmitted bulk and Stoneley wave in structure 2 ($0<z<L$). When the latter two encounter the vertical plane $z=L$, they excite a reflected bulk and Stoneley wave in structure 2, and a transmitted bulk and Stoneley wave in structure 1b ($z>L$). In the approximation of a thin inclusion, i.e., when d is much smaller than the ultrasonic wavelength in the substrate, the reflections at the vertical boundaries of the inclusion are very small and negligible. In the context of mode theory the displacement fields in the structures 1a, 2, and 1b are described by, respectively,[9]

$$\mathbf{u}_{1a}(y,z)=\int C_{1a}^{i}(k_{y,i})\mathbf{u}_1^a(k_{y,i};y,z)dk_{y,i}, \tag{1}$$

[a]Electronic mail: Rudy.Briers@kulak.ac.be
[b]Permanent address: Institute of Radioengineering and Electronics, Russian Academy of Sciences, Moscow, Russia.

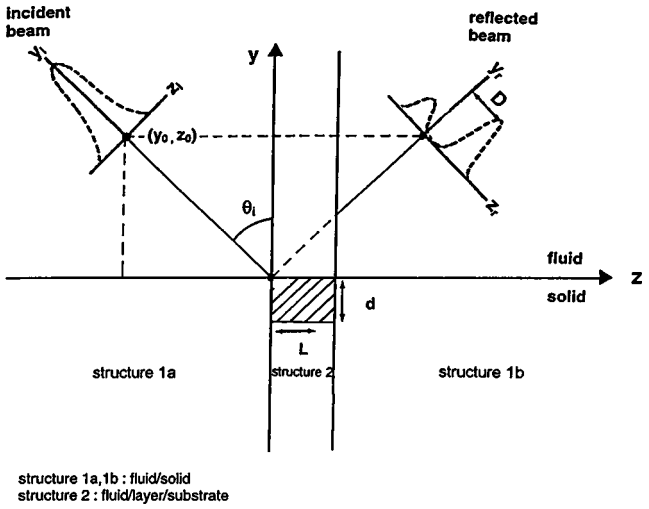

FIG. 1. The reflection of a Gaussian beam onto an inclusion near a fluid/solid interface. Geometrical configuration and definition of the parameters.

$$\mathbf{u}_2(y,z)=\int C_2^t(k_{y,2})\mathbf{u}_2^a(k_{y,2};y,z)dk_{y,2}, \tag{2}$$

$$\mathbf{u}_{1b}(y,z)=\int C_{1b}^t(k_{y,1})\mathbf{u}_1^a(k_{y,1};y,z)dk_{y,1}, \tag{3}$$

from which mode expansions can be written down for the components of the stress tensors in these structures; for instance, the stress tensor components in structure 2 are given by

$$T_{k1,2}(y,z)=\int C_2^t(k_{y,2})T_{k1,2}^a(k_{y,2};y,z)dk_{y,2} \quad (k,1=x,y,z). \tag{4}$$

The integration variables are defined as

$$k_{y,i}=(k^2-k_{z,i}^2)^{1/2} \quad \text{and} \quad k_{y,\alpha}=(k^2-k_{z,\alpha}^2)^{1/2} \quad (\alpha=1,2), \tag{5}$$

with k the longitudinal wave number in the liquid; $k_{z,i}$ and $k_{z,\alpha}$ are the z components of the wave vectors of the acoustic modes that appear in the mode expansions.

The integrals are only calculated within the interval $[0,(k^2-k_{s2}^2)^{1/2}]$, with k_{s2} the shear wave number of the substrate. In other words, only radiation modes of the so-called *type a* are used in the mode expansions. These modes are generated by plane waves incident from the fluid at an angle greater than the shear critical angle.[9] Note from Eq. (3) that since structure 1b is the same as structure 1a, its displacement field is expanded in the same set of radiation modes (denoted by $\mathbf{u}_1^a$) used for the description of the displacement field in structure 1a. The restriction to *type a* radiation modes is justified since further on we will consider Rayleigh angle incidence (the Rayleigh angle is greater than the shear critical angle) and, second, because only beamwidths for which the spectrum of the incident beam consists of namely these modes will be considered. The expressions for the displacement field of *type a* radiation modes for a fluid/solid structure ($\mathbf{u}_1^a$) and those for a fluid/thin layer/substrate structure ($\mathbf{u}_2^a$, in a linear approximation on d) were derived in Refs. 9 and 11. We remark that radiation modes already satisfy the boundary conditions that have to be fulfilled along the interfaces of the structures to which they belong. The expansion of a bounded beam in terms of *type a* radiation modes for a fluid/solid structure [determination of the coefficient $C_a^i(k_{y,i})$] was shown in Ref. 10. The unknown expansion coefficients C_2^t and C_{1b}^t of the transmitted bulk waves in the structures 2 and 1b are determined as follows. From the boundary conditions (continuity of displacement and stresses) along the plane $z=0$ it follows[9] that

$$\int_{-\infty}^{+\infty}[T_{zz,1}u_{z,2}^{a*}-T_{yz,2}^{a*}u_{y,1}]dy=\int_{-\infty}^{+\infty}[T_{zz,2}u_{z,2}^{a*}-T_{yz,2}^{a*}u_{y,2}]dy, \tag{6}$$

in which $u_{z,2}^a$ and $T_{yz,2}^a$ are the components of a fixed radiation mode belonging to the fluid/thin layer/substrate structure. An asterisk stands for the complex conjugate. Taking into account the orthogonality relations[9] that exist among radiation modes results in the solution

$$C_2^t(k_{y,2})=[I_2^a(k_{y,2})+K_2^a(k_{y,2})]^{-1}\int C_a^i(k_{y,i}) \times[I_{12}^{aa}(k_{y,i};k_{y,2})+K_{12}^{aa}(k_{y,i};k_{y,2})]dk_{y,i}, \tag{7}$$

with I_{ij}^{aa} and K_{ij}^{aa} the overlap integrals,[9]

$$I_{ij}^{aa}(k_{y,i};k_{y,j})=\int_{-\infty}^{+\infty}[T_{yz,i}^a(k_{y,i})u_{y,j}^{a*}(k_{y,j}) - T_{zz,j}^{a*}(k_{y,j})u_{z,i}^a(k_{y,i})]_{z=0}\,dy, \tag{8}$$

$$K_{ij}^{aa}(k_{y,i};k_{y,j})=\int_{-\infty}^{+\infty}[T_{zz,i}^a(k_{y,i})u_{z,j}^{a*}(k_{y,j}) - T_{yz,j}^{a*}(k_{y,j})u_{y,i}^a(k_{y,i})]_{z=0}\,dy. \tag{9}$$

These integrals count for the coupling between all radiation modes in one specific plane (in this case the plane $z=0$). For example, $I_{12}^{aa}(k_{y,i};k_{y,2})$ count for the coupling between the radiation modes of the *type a* in structure 1a that were used for the expansion of the incident beam, and the radiation modes of the *type a* that were used to describe the scattered bulk wave in structure 2.

In expression (7), the quantities I_2^a and K_2^a are defined by

$$K_{22}^{aa}(k_{y,2};k'_{y,2})=K_2^a\delta(k_{y,2}-k'_{y,2})$$

and (10)

$$I_{22}^{aa}(k_{y,2};k'_{y,2})=I_2^a\delta(k_{y,2}-k'_{y,2}),$$

with δ the Dirac delta function.

Repeating this procedure, but now using the boundary conditions along the plane $z=L$, the following solution is found for the unknown expansion coefficient C_{1b}^t of the transmitted bulk wave in structure 1b:

$$C_{1b}^{t}(k_{y,1})=[I_1^a(k_{y,1})+K_1^a(k_{y,1})]^{-1}\int C_2^t(k_{y,2})[I_{21}^{aa}(k_{y,2};k_{y,1})+K_{21}^{aa}(k_{y,2};k_{y,1})]\exp[i(k_{z,2}-k_{z,1})L]dk_{y,2}. \tag{11}$$

Substitution of expression (7) into expression (11) and evaluating all overlap integrals K_{ij}^{aa} and I_{ij}^{aa} gives, after longwinded but straightforward analytical calculations,

$$\begin{aligned}C_{1b}^{t}(k_{y,1})=&C_a^i(k_{y,i}=k_{y,1})\cos^2[\varphi_1(k_{y,1})-\varphi_2(k_{y,1})]+\frac{1}{\pi}\frac{\rho_2}{\rho}\frac{1}{k_{z,1}}\cos[\varphi_1(k_{y,1})-\varphi_2(k_{y,1})]\int C_a^i(k_{y,i})[k_{z,i}I_0(k_{y,i};k_{y,1})\\&+k_{z,1}K_0(k_{y,i};k_{y,1})]dk_{y,i}+\frac{1}{\pi}\frac{\rho_2}{\rho}\frac{1}{k_{z,1}}\int C_a^i(k_{y,i})\cos[\varphi_1(k_{y,i})-\varphi_2(k_{y,i})][k_{z,1}I_0(k_{y,1};k_{y,i})+k_{z,i}K_0(k_{y,1};k_{y,i})]\\&\times\exp[i(k_{z,i}-k_{z,1})L]dk_{y,i}+\frac{1}{\pi^2}\left(\frac{\rho_2}{\rho}\right)^2\frac{1}{k_{z,1}}\int\int C_a^i(k_{y,i})\frac{1}{k_{z,2}}[k_{z,1}I_0(k_{y,i};k_{y,2})+k_{z,2}K_0(k_{y,i};k_{y,2})]\\&\times[k_{z,1}I_0(k_{y,1};k_{y,2})+k_{z,2}K_0(k_{y,1};k_{y,2})]\exp[i(k_{z,2}-k_{z,1})L]dk_{y,i}\,dk_{y,2}.\end{aligned} \tag{12}$$

In the Appendix is explained in more detail how the cumbersome expressions for the functions I_0, K_0, φ_1, and φ_2 must be evaluated. Substituting this expansion coefficient in Eq. (3) we can calculate the amplitude and phase distribution of the reflected bounded beam in the structure 1b.

III. NUMERICAL CALCULATIONS

For the numerical calculations a stainless steel half-space is considered with parameters $v_{2d}=5720$ m/s, $v_{2s}=3100$ m/s, $\rho_2=7800$ kg/m^2. This stainless steel half-space is separated from water, having a longitudinal velocity $v=1480$ m/s and a density $\rho=1000$ kg/m^3. The Rayleigh angle for this water/steel structure is $\theta_{\mathrm{Rayl}}=30.448°$. As an example, a copper and a tungsten inclusion layer will be taken with parameters $v_{1d}=4700$ m/s, $v_{1s}=2260$ m/s, $\rho_1=8900$ kg/m^2, respectively, $v_{1d}=5220$ m/s, $v_{1s}=2890$ m/s, $\rho_1=19300$ kg/m^2. In all examples the thickness of the inclusion is much smaller than the ultrasonic wavelength in the substrate.

Let us first explain with an example what is meant by the term ''*phase difference*'' in this work. Suppose that a 4 MHz Gaussian beam ($w=12$ mm) is incident from the plane $y_i=0$ (see Fig. 1) onto the stainless steel half-space *at the critical Rayleigh angle*. The center of the incident beam is assumed to be located at the position ($y_0=85$ mm, $z_0=-50$ mm). It is well known[13] that, depending on the beamwidth, the amplitude profile of the reflected beam consists of a specular and of a shifted reflected lobe separated by a ''null intensity'' strip, as shown in Fig. 2(a) by the solid line. The dashed line in Fig. 2(a) shows in the plane $y_r=0$ the reflected amplitude profile for a thin copper layer of 5 μm placed upon the stainless steel solid (calculated on the basis of expressions in Ref. 11), while the circles line represents the reflected amplitude profile for a copper inclusion of length $L=15$ mm and thickness $d=5$ μm in steel [calculated on the basis of Eqs. (3) and (12)]. One sees that the variation of the maximum amplitude of the shifted lobe due to the presence of a coating or the existence of an inclusion is very small and, in practice, unmeasurable. We focus our attention on the shifted (big) lobe since this is the most convenient one to perform measurements in an experimental setup (in some cases the specular small lobe does not even appear).

However, Fig. 2(b) shows that the phase in the point of maximum amplitude of the shifted lobe is much more sensitive than the amplitude. In this specific example the phase difference (indicated by the double arrow) for a steel half-space with and without an inclusion is 21°. With the acousto-optic technique,[4] phase differences of 1° still can be detected. Note that the phase difference due to the existence of an inclusion (a finite layer) is smaller than the phase difference due to the existence of an infinite layer on the half-space. This is not surprising at all since the latter one is a limiting case of the finite layer. In this paper, only Rayleigh angle incidence will be considered. The presented method for inclusion characterization is exclusive based on phase differences considerations of the shifted reflected lobe (see Fig. 1), and the latter one only appears at critical Rayleigh angle incidence.

In Fig. 3 the above defined phase difference due to the existence of an inclusion is presented for an incident Gaussian beam of half-beamwidth $w=7.5$ mm ($y_0=85$ mm, $z_0=-50$ mm) as a function of the length L of the inclusion (d was fixed at 5 μm). The incident beam is in a fixed position while increasing the length L of the inclusion. So, the amplitude of the reflected shifted lobe is always maximum at a fixed position, in which the phase difference is calculated. Notice that starting from some value L_0 (about 11 mm) the phase difference remains constant. This can be explained as follows. At the Rayleigh angle the incident beam undergoes

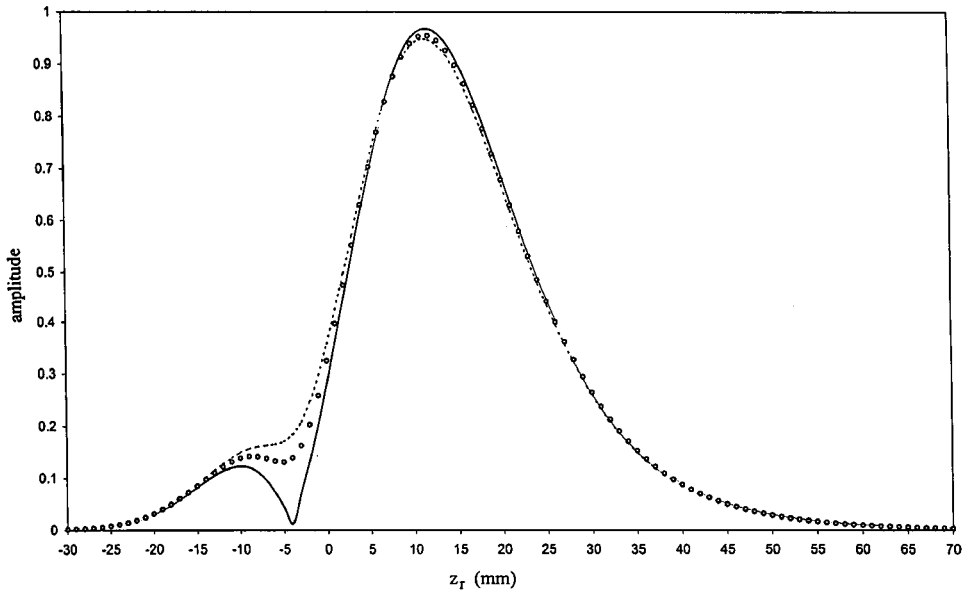

(a)

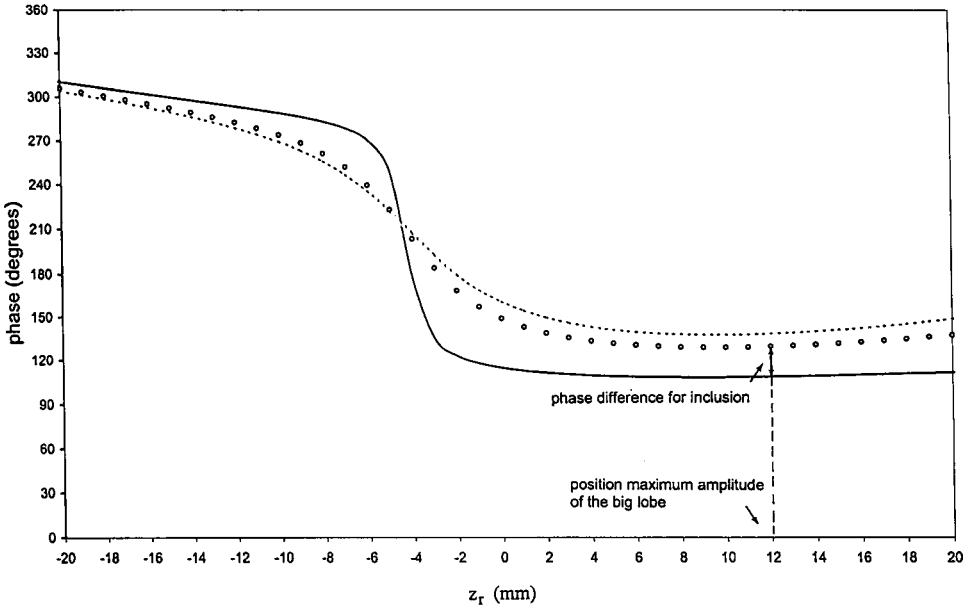

(b)

FIG. 2. Amplitude distribution (a) and phase distribution (b) of the reflected 4 MHz Gaussian beam ($w=12$ mm) onto a stainless steel half-space (solid line), onto a thin layer (5 μm) placed upon a stainless steel substrate (dashed line), onto an inclusion of thickness $d=5$ μm and length $L=15$ mm in stainless steel (circles line). The Gaussian beam is incident at the critical Rayleigh angle. The arrow defines the phase difference.

along the water/steel interface a lateral shift D,[14] as defined in Fig. 1. This makes that the ultrasonic beam, while shifting, can detect the inclusion near the interface. We found that for the water/steel structure this shift D is equal to 11.2 mm. Once the length of the inclusion becomes larger than the shift D, it is as if the incident beam feels an infinite copper coating of thickness d on a steel substrate. In the latter case it can be calculated that the phase difference must be 23.8° (for tungsten this value is 18°). However, according to Fig. 3, for $L>11$ mm, the constant phase difference is equal to 21°. Why this small discrepancy? In the chosen frame (Fig. 1) the inclusion becomes in fact only a *semi-infinite* coating if the value of L is increased (the length does not increases in the negative z direction). In order to check the correctness of our model in the limiting case of an infinite coating, an inclusion of length $L'=2L$ was considered and the bounded beam is now incident under the Rayleigh angle at the middle (L,0) of the inclusion while increasing L'. As can be seen from Fig. 4, the constant phase difference for $L=11$ mm or $L'=22$ mm is now 23°. The difference of 0.8° that still exists is a consequence of the approximations we made in the theoretical model: the *type a* radiation modes for a fluid/thin layer/solid structure were derived in the approximation of a *linear on d* dependence. In any case this error will further decrease when considering thinner inclusions. For instance, if we reduce the thickness of the inclusion to 1 μm, the error is only 0.15°. In Fig. 5 the phase difference is presented as a function of the thickness d of the inclusion (L was fixed at 5 mm). For relative thicker inclusions our theoretical model predicts a phase difference of about 15°. The same order of magnitude was found experimentally by Devolder,[4] who investigated with the acousto-optic technique the phase change of a reflected bounded beam due to the presence of an inclusion ($L=5$ mm) in a steel sample. In the same work

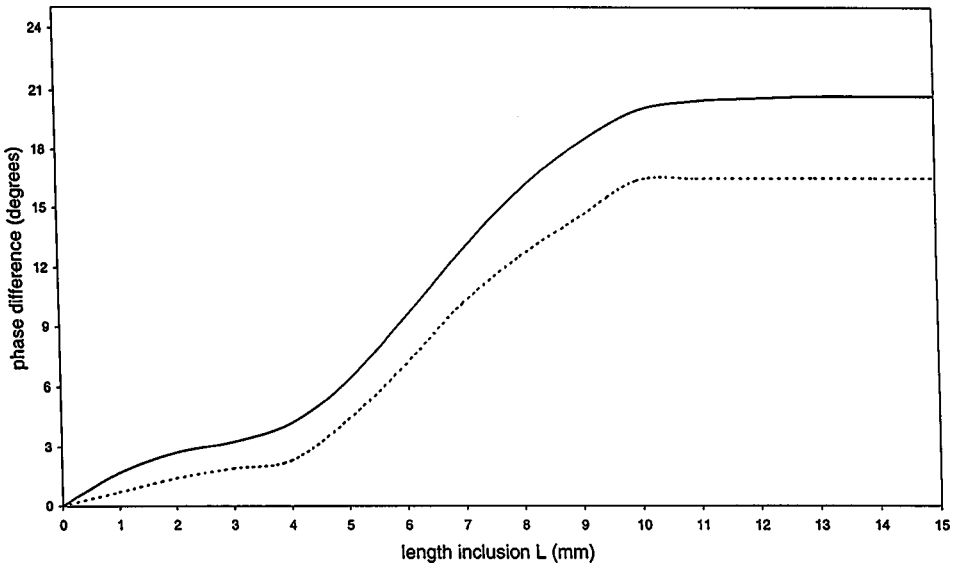

FIG. 3. Phase difference as a function of the length L of the inclusion ($d=5$ μm) for a Gaussian beam ($w=7.5$ mm) incident at the Rayleigh angle. The center of the incident beam located at ($y_0=85$ mm, $z_0=-50$ mm). Solid line: copper inclusion in steel; dashed line: tungsten inclusion in steel.

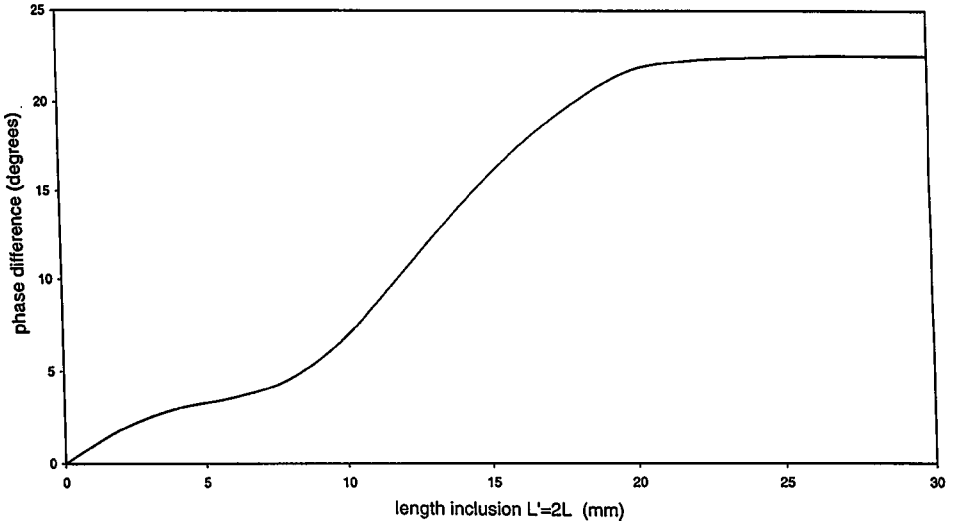

FIG. 4. Phase difference as a function of the length $\mathbf{L}'=2\mathbf{L}$ of the inclusion ($d=5$ μm) for a Gaussian beam ($w=7.5$ mm) incident *at the middle* of the inclusion under the Rayleigh angle. Copper inclusion in steel.

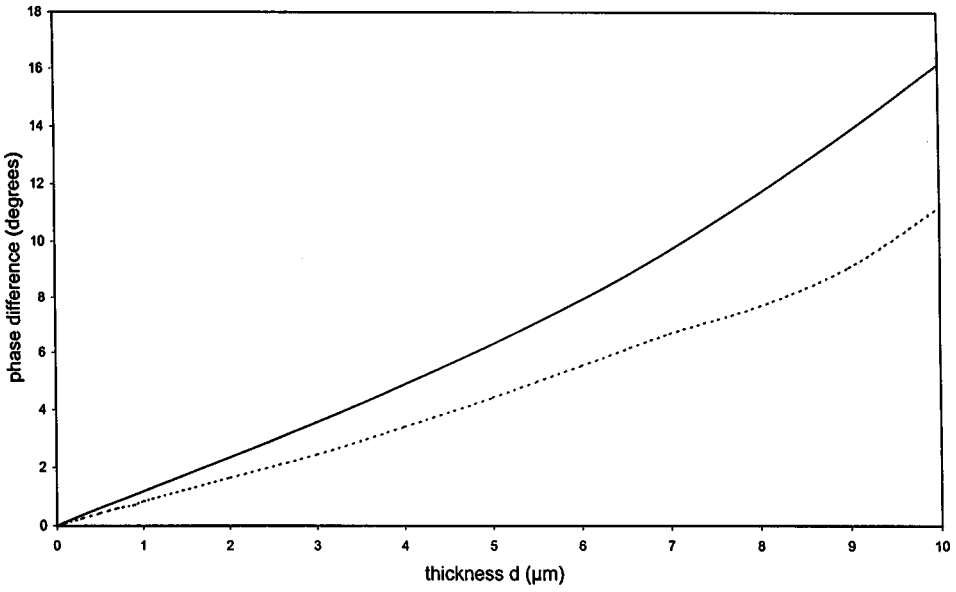

FIG. 5. Phase difference as a function of the thickness d of the inclusion ($L=5$ mm) for a Gaussian beam ($w=7.5$ mm) incident at the Rayleigh angle. Solid line: copper inclusion in steel; dashed line: tungsten inclusion in steel.

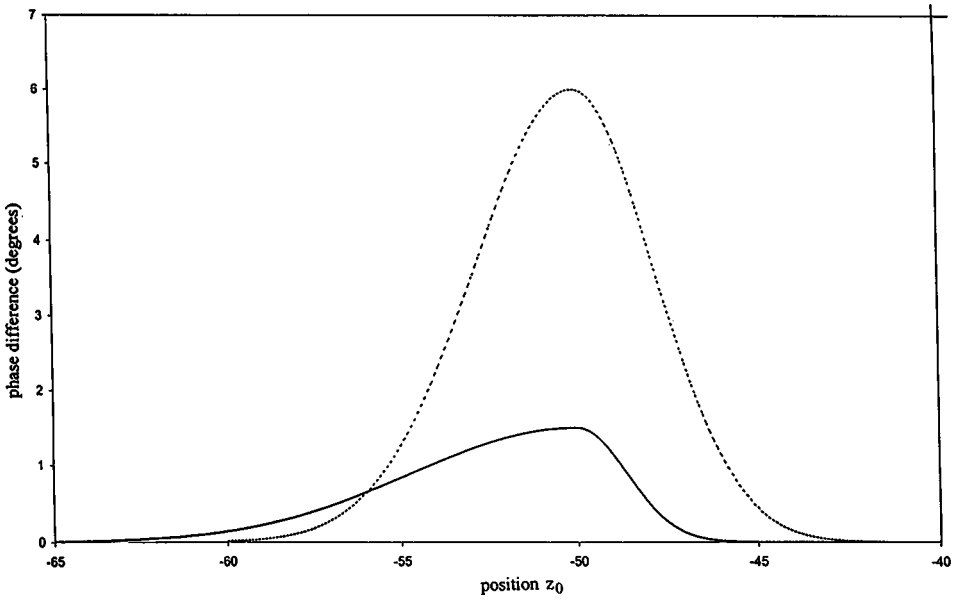

FIG. 6. A 4 MHz Gaussian beam of half-beamwidth $w=7.5$ mm is moving (under Rayleigh angle incidence) along a water/steel interface containing a copper inclusion of length $L=5$ mm. The phase difference as a function of the position z_0 (see Fig. 1) of the center of the incident beam is presented ($y_0=85$ mm). Solid line: inclusion of thickness $d=1$ μm; dashed line: inclusion of thickness $d=5$ μm.

Devolder measured a phase difference of 2° for a coating of 0.4 μm thickness on a steel substrate. Calculations on the basis of our model predicts a phase difference of 1.86°. Since the smallest measurable phase difference with the acousto-optic technique is 1°, it follows from Fig. 5 that in the case of a steel substrate inclusions with a thickness of 0.5 μm still are detectable. It is interesting to notice that for *small* dimensions d and L of the inclusion, the phase difference dependence is linear (see Figs. 4 and 5) and thus *invariant* for the product dL (the surface area of the inclusion).

For the result presented in Fig. 6 the incident Gaussian beam was moved parallel ($y_0=85$ mm) with the fluid/solid interface, which is usually the case in an experimental setup. Each graph describes the phase difference variation in the point of maximum amplitude of the reflected big lobe as a function of the z_0 coordinate of the center of the incident beam. When the center of the Gaussian beam is pointed at the starting point of the inclusion [here when $(z_0)_{\text{begin}}=-50$ mm], the phase difference curve shows a maximum. This result can be used to locate the starting position of an inclusion. The phase difference curve is and should be *asymmetrical* with a small slope at the left side of its maximum and a rather steep descent at the right side of the maximum. This can be understood as follows. Since for the incident Gaussian beam considered, the lateral shift D is 11.2 mm, the shifted reflected beam can already interact with the inclusion layer when the z_0 coordinate is approximately equal to -60 mm [$=(z_0)_{\text{begin}}-D$]. In other words, overlapping between the shifted beam and a part of the inclusion layer begins to take place. This interaction gradually increases when the incident beam is moved farther to the right (more and more overlapping length with the inclusion) until the maximum phase difference has been reached (when $z_0=-50$ mm). From then on the effective overlap region between the lateral shifted beam and the inclusion decreases

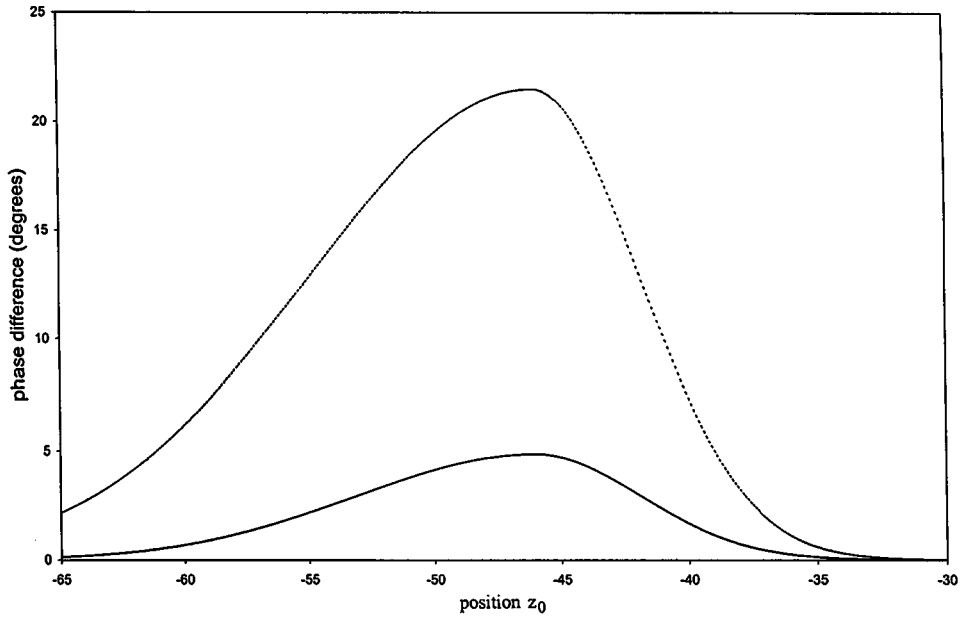

FIG. 7. The same as in Fig. 6 but for $L=15$ mm ($L>D=11.2$ mm).

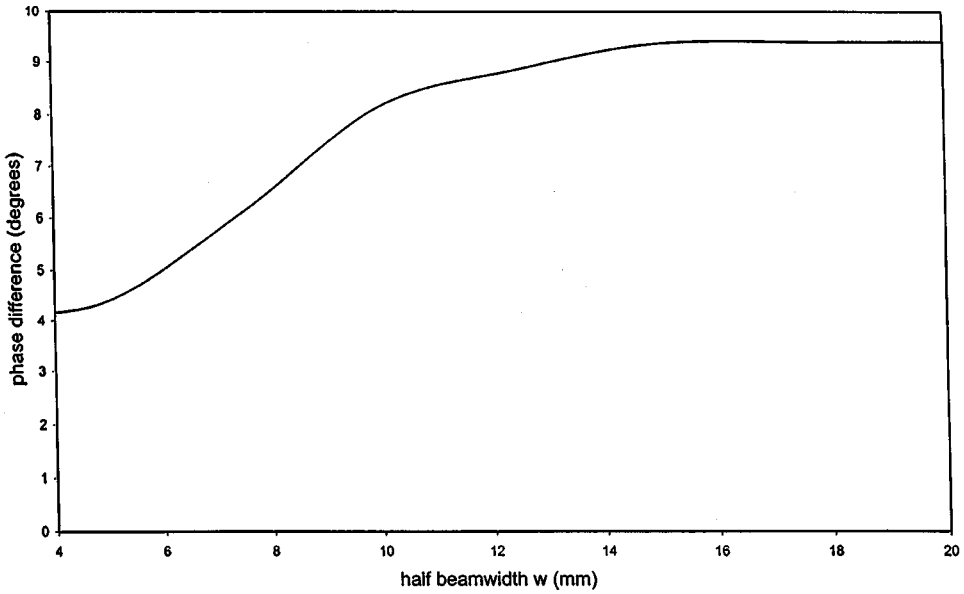

FIG. 8. Phase difference as a function of the half-beamwidth w of the incident beam (Rayleigh angle incidence). Copper inclusion ($d=5\ \mu$m, $L=5$ mm) in steel.

rapidly (over a distance of only 5 mm, being the length L of the inclusion) resulting in a fast diminishing phase difference. We also showed the curve for an inclusion of 5 μm thickness. The asymmetrical character of the phase difference curve still exists but is less pronounced. This can be attributed again to the fact that for increasing thickness of the inclusion the expressions derived for fluid/thin layer/substrate *type a* radiation modes are approximate, although they still provide a good qualitative and quantitative description of the physical phenomenon. As shown in Fig. 7, when the length L of the inclusion is greater than the length of the lateral shift D, the position of maximum phase difference is shifted to the right.

Finally, in Fig. 8 the dependence of the phase difference on the half-width w of the incident beam was investigated. To obtain this graph one first has to calculate for each value of w, the corresponding point where the amplitude of the reflected shifted lobe is maximum, since this position depends on the beamwidth. Once the position is found, the relative phase difference for a structure with and without an inclusion again can be calculated. Bertoni and Tamir[14] showed that the shift D increases for a wider beam. At some beamwidth the reflected beam consists of only a shifted lobe (the specular lobe disappears and the energy is transferred into the shifted one). The authors illustrate that even under these circumstances the shift D can still increase for enlarging beamwidth before the shift D takes a constant value. Here we have a similar effect for the phase difference. The wider the incident beam, the greater the shift D and thus the incident beam interacts with a greater part of the inclusion, resulting in an increasing phase difference. However, when, for example, $w=7.5$ mm, we already mentioned that D is equal to 11.2 mm, which is greater than the inclusion length $L=5$ mm. The phase difference still increases for some while before reaching a constant value (saturation). The graph in Fig. 8 starts from $w=4$ mm. In the beginning of this paper, we already mentioned that only bounded beams would be considered that can be properly described by an expansion in only *type a* radiation modes; 4 mm is the minimum beamwidth that can be considered. For smaller beamwidths it is necessary to take into account other type of radiation modes in the mode expansion for the incident beam.[9]

IV. CONCLUSION

In this work the reflection of a *bounded Gaussian beam* onto a finite inclusion layer of thickness d (smaller than the ultrasonic wavelength in the substrate) and length L, located near a fluid/solid interface was investigated. On the basis of a mode theory an expression was derived to calculate the amplitude as well as the phase distribution of the reflected beam in an arbitrary plane. It was shown that at Rayleigh angle incidence the phase in the point of maximum amplitude of the big (shifted) lobe is very sensitive to dimension variations (L and/or d) of the inclusion, and thus can be used to characterize the inclusion. These phase variations can be measured accurate (up to 1°) by the recently developed acousto-optic technique. As a limiting case the phase difference for a very long inclusion was considered. The value of this phase difference tends to the one for a (infinite) coating on a substrate and confirms the validity of the new developed theoretical model. The results presented in this paper will be used for a rigorous study of detecting inclusions that are situated *at an arbitrary position within* a fluid loaded plate, a work that is now in progress.

ACKNOWLEDGMENTS

This work was supported by the Fund for Scientific Research–Flanders (F.W.O.–Belgium). The authors also would like to thank the Research Council of the K. U. Leuven for the fellowship awarded to Professor Dr. G. Shkerdin.

APPENDIX

The value of the function $I_0(k_{y,1};k_{y,2})$ in Eq. (12) must be evaluated as follows:

$$I_0(k_{y,1};k_{y,2})=\frac{1}{2}\frac{\rho}{\rho_2}\left(\sin[\varphi_1(k_{y,1})-\varphi_2(k_{y,2})]\mathbf{P}\left(\frac{1}{k_{y,1}-k_{y,2}}\right)+\sin[\varphi_1(k_{y,1})+\varphi_2(k_{y,2})]\frac{1}{k_{y,1}+k_{y,2}}\right)$$

$$+\frac{2\,dk_{y,1}k_{y,2}k_{dy,2}\sin[\varphi_1(k_{y,1})]\sin[\varphi_2(k_{y,2})]}{k_{z,1}k_{s2}^2}I_1(k_{y,1};k_{y,2})$$

$$+\frac{2k_{y,1}k_{y,2}\sin[\varphi_1(k_{y,1})]\sin[\varphi_2(k_{y,2})]}{k_{s2}^2[1+\psi(k_{y,2})]}I_2(k_{y,1};k_{y,2}). \tag{A1}$$

The symbol **P** stands for ''principal value.'' The value of the functions $\psi(k_{y,2})$, $I_1(k_{y,1};k_{y,2})$, and $I_2(k_{y,1};k_{y,2})$ are determined by

$$\psi(k_{y,2})=\frac{d}{k_{dy,2}k_{s2}^2}\left[\frac{\rho_1 v_{s1}^2}{\rho_2 v_{s2}^2}(k_{z,2}^2-k_{dy,2}k_{sy,2})\left(2k_{z,2}^2-k_{s1}^2-\frac{2k_{z,2}^2}{k_{s1}^2}(2k_{d1}^2-2k_{s1}^2)\right)\right.$$

$$\left.+2k_{z,2}^2\left(1-\frac{2k_{d1}^2}{k_{s1}^2}\right)(k_{s2}^2-2k_{z,2}^2+2k_{dy,2}k_{sy,2})-\frac{\rho_2}{\rho_1}\frac{k_{d1}^2}{k_{s2}^2}(k_{s2}^2-2k_{z,2}^2)^2+4\frac{\rho_2}{\rho_1}\frac{k_{d1}^2k_{z,2}^2k_{dy,2}k_{sy,2}}{k_{s2}^2}\right], \tag{A2}$$

$$I_1(k_{y,1};k_{y,2})=\left[\frac{k_{z,1}}{k_{dy,1}}\left(1-\frac{2k_{z,1}^2}{k_{s2}^2}\right)+\frac{2k_{z,1}k_{dy,1}}{k_{s2}^2}\right]\left[\left(1-\frac{2k_{z,2}^2}{k_{s2}^2}\right)\frac{k_{s2}^2+2k_{dy,2}^2}{2k_{dy,2}k_{sy,2}}+\frac{2k_{z,2}^2}{k_{s2}^2}\right], \tag{A3}$$

$$I_2(k_{y,1};k_{y,2})=\left(1-\frac{2k_{z,1}^2}{k_{s2}^2}\right)\left[\left(1-\frac{2k_{z,2}^2}{k_{s2}^2}\right)(1+\alpha(k_{z,2})dk_{sy,2})\left(\frac{\exp(-dk_{dy,1})}{k_{dy,1}+k_{dy,2}}-\frac{\exp(-dk_{sy,1})}{k_{sy,1}+k_{dy,2}}\right)\right.$$

$$\left.+\frac{2k_{z,2}^2}{k_{s2}^2}(1+\beta(k_{z,2})dk_{sy,2})\left(\frac{\exp(-dk_{dy,1})}{k_{dy,1}+k_{sy,2}}-\frac{\exp(-dk_{sy,1})}{k_{sy,1}+k_{sy,2}}\right)\right]$$

$$+\left(1-\frac{2k_{z,2}^2}{k_{s2}^2}\right)\frac{k_{s2}^2+2k_{dy,2}^2}{2k_{dy,1}k_{dy,2}}(1+\alpha(k_{z,2})dk_{sy,2})\left[\left(1-\frac{2k_{z,1}^2}{k_{s2}^2}\right)\frac{\exp(-dk_{dy,1})}{k_{dy,1}+k_{dy,2}}+\frac{2k_{dy,1}k_{sy,1}}{k_{s2}^2}\frac{\exp(-dk_{sy,1})}{k_{sy,1}+k_{dy,2}}\right]$$

$$+\frac{2k_{z,2}^2}{k_{s2}^2}\frac{k_{sy,2}}{k_{dy,1}}(1+\beta(k_{z,2})dk_{sy,2})\left[\left(1-\frac{2k_{z,1}^2}{k_{s2}^2}\right)\frac{\exp(-dk_{dy,1})}{k_{dy,1}+k_{sy,2}}+\frac{2k_{dy,1}k_{sy,1}}{k_{s2}^2}\frac{\exp(-dk_{sy,1})}{k_{sy,1}+k_{sy,2}}\right]. \tag{A4}$$

In the latter equation, α and β are abbreviations for

$$\alpha(k_{z,2})=\frac{1}{2k_{z,2}^2-k_{s2}^2}\alpha_0(k_{z,2}), \tag{A5}$$

$$\beta(k_{z,2})=\frac{1}{2k_{dy,2}k_{sy,2}}\left(\alpha_0(k_{z,2})-\frac{v_{s1}^2}{v_{s2}^2}(2k_{d1}^2-k_{s1}^2)\right), \tag{A6}$$

with

$$\alpha_0(k_{z,2})=(2k_{z,2}^2-k_{s1}^2)\left(\frac{\rho_1}{\rho_2}\frac{v_{s1}^2}{v_{s2}^2}+\frac{2k_{z,2}^2\left(1-\frac{v_{s1}^2\rho_1}{v_{s2}^2\rho_2}\right)}{k_{s1}^2}\right)$$

$$-4\frac{k_{z,2}^2}{k_{s1}^2}(k_{z,2}^2-k_{d1}^2)\left(1-\frac{v_{s1}^2\rho_1}{v_{s2}^2\rho_2}\right). \tag{A7}$$

The functions φ_1 and φ_2 represent, respectively, the phase of *type a* radiation modes for a fluid/solid structure, and the phase of *type a* radiation modes for a fluid/thin layer/substrate structure. These phases were derived in Refs. 9 and 11.

As usual, the wave vector components $k_{z,i}$ and $k_{\sigma y,i}$ ($\sigma=d,s$; $i=1,2$) are calculated as

$$k_{z,i}=(k^2-k_{y,i}^2)^{1/2} \quad \text{and} \quad k_{\sigma y,i}=(k_{\sigma i}^2-k_{z,i}^2)^{1/2}, \tag{A8}$$

with $k_{\sigma i}$ the dilatational ($\sigma=d$) or shear ($\sigma=s$) wave number in the inclusion ($i=1$) or in the substrate ($i=2$).

The expression for the function K_0 is formally the same as the one for I_0 wherein the components $k_{z,1}$ and $k_{sy,2}$ must be replaced by, respectively, $k_{z,2}$ and $k_{sy,1}$. The functions I_1 and I_2 must be replaced, respectively, by functions K_1 and K_2. For what concerns the function K_1, take Eq. (A3) and replace subindex 1 by subindex 2 and vice versa. The function K_2 now is given by

$$
\begin{aligned}
K_2(k_{y,1};k_{y,2}) = & \left(1-\frac{2k_{z,2}^2}{k_{s2}^2}\right)\left[\left(1-\frac{2k_{z,1}^2}{k_{s2}^2}\right)\exp(-dk_{dy,1})\left(\frac{1+\alpha\, dk_{sy,2}}{k_{dy,1}+k_{dy,2}}-\frac{1+\beta\, dk_{sy,2}}{k_{dy,1}+k_{sy,2}}\right)\right. \\
& \left.+\frac{2k_{z,1}^2}{k_{s2}^2}\exp(-dk_{sy,1})\left(\frac{1+\alpha\, dk_{sy,2}}{k_{sy,1}+k_{dy,2}}-\frac{1+\beta\, dk_{sy,2}}{k_{sy,1}+k_{sy,2}}\right)\right] \\
& +\left(1-\frac{2k_{z,1}^2}{k_{s2}^2}\right)\frac{k_{s2}^2+2k_{dy,1}^2}{2k_{dy,1}k_{dy,2}}\exp(-dk_{dy,1})\left[\left(1-\frac{2k_{z,2}^2}{k_{s2}^2}\right)\frac{1+\alpha\, dk_{sy,2}}{k_{dy,1}+k_{dy,2}}+\frac{2k_{dy,2}k_{sy,2}}{k_{s2}^2}\,\frac{1+\beta\, dk_{sy,2}}{k_{dy,1}+k_{sy,2}}\right] \\
& +\frac{2k_{z,1}^2}{k_{s2}^2}\,\frac{k_{sy,1}}{k_{dy,2}}\exp(-dk_{sy,1})\left[\left(1-\frac{2k_{z,2}^2}{k_{s2}^2}\right)\frac{1+\alpha\, dk_{sy,2}}{k_{sy,1}+k_{dy,2}}+\frac{2k_{dy,2}k_{sy,2}}{k_{s2}^2}\,\frac{1+\beta\, dk_{sy,2}}{k_{sy,1}+k_{sy,2}}\right]. \qquad \text{(A9)}
\end{aligned}
$$

[1] L. M. Brekhovskikh, *Waves in Layered Media* (Academic, New York, 1960).

[2] S. Devolder, O. Leroy, M. Wevers, and P. De Meester, ''Relation between the phase of the reflected ultrasound and the thickness of a thin layer placed on a solid halfspace,'' Acta Acust. (China) **82**, 372–375 (1996).

[3] S. Devolder, O. Leroy, M. Wevers, and P. De Meester, ''Acousto-optic technique: A new nondestructive technique to evaluate thin layered structures,'' Appl. Phys. Lett. **66**, 1466–1468 (1995).

[4] S. Devolder, ''A new nondestructive acousto-optic technique for the quality control of layered materials,'' Ph.D. in Dutch, K. U. Leuven Campus Kortrijk, Promotor O. Leroy, 1996.

[5] J. M. Claeys and O. Leroy, ''Reflection and transmission of bounded sound beams on half-spaces and through plates,'' J. Acoust. Soc. Am. **72**, 585–590 (1982).

[6] E. Blomme and O. Leroy, ''Plane wave analysis of the near field of light diffracted by ultrasound,'' J. Acoust. Soc. Am. **91**, 1474–1483 (1992).

[7] R. Briers, O. Leroy, and G. Shkerdin, ''Influence of an inclusion on the phase of a Stoneley wave,'' J. Acoust. Soc. Am. **101**, 1358–1365 (1997).

[8] J. R. Chamuel, ''Ultrasonic studies of transient seismo-acoustic waves in bonded solids and liquid/solid interfaces,'' Sonoquest Report No. JRC-34-91, 1991, National Technical Information Document No. AD-A243441.

[9] R. Briers, O. Leroy, G. Shkerdin, and Yu. Gulyaev, ''Mode theory as a framework for the investigation of the generation of a Stoneley wave at liquid/solid interfaces,'' J. Acoust. Soc. Am. **95**, 1953–1966 (1994).

[10] R. Briers, O. Leroy, and G. Shkerdin, ''A fundamental study of the excitation of a Stoneley wave at a liquid–solid interface: Rayleigh angle and Gaussian beam incidence,'' J. Acoust. Soc. Am. **95**, 1967–1976 (1994).

[11] R. Briers, O. Leroy, and G. Shkerdin, ''Stoneley wave excitation by a bounded beam at the downstep of a thin layer on a substrate,'' J. Acoust. Soc. Am. **102**, 2108–2112 (1997).

[12] K. I. Maslov, T. Kundu, and O. I. Lobkis, ''Acoustic microscopy for sperical inclusion characterization,'' J. Acoust. Soc. Am. **100**, 80–85 (1996).

[13] T. D. K. Ngoc and W. G. Mayer, ''A general description of ultrasonic nonspecular reflection and transmission effects for layered media,'' IEEE Trans. Sonics Ultrason. **SU-27**, 229–236 (1980).

[14] H. L. Bertoni and T. Tamir, ''Unified theory of Rayleigh angle phenomena for acoustic beams at liquid–solid interfaces,'' J. Appl. Phys. **2**, 157–172 (1973).

Fan beam and double crosshole Lamb wave tomography for mapping flaws in aging aircraft structures

Eugene V. Malyarenko and Mark K. Hinders[a)]
Department of Applied Science, College of William & Mary, Williamsburg, Virginia 23187-8795

(Received 10 November 1999; accepted for publication 20 June 2000)

As the worldwide aviation fleet continues to age, methods for accurately predicting the presence of structural flaws—such as hidden corrosion and disbonds—that compromise airworthiness become increasingly necessary. Ultrasonic guided waves, Lamb waves, allow large sections of aircraft structures to be rapidly inspected. However, extracting quantitative information from Lamb wave data has always involved highly trained personnel with a detailed knowledge of mechanical waveguide physics. The work summarized here focuses on a variety of different tomographic reconstruction techniques to graphically represent the Lamb wave data in quantitative maps that can be easily interpreted by technicians. Because the velocity of Lamb waves depends on thickness, for example, the traveltimes of the fundamental Lamb modes can be converted into a thickness map of the inspection region. This article describes two potentially practical implementations of Lamb wave tomographic imaging techniques that can be optimized for in-the-field testing of large-area aircraft structures. Laboratory measurements discussed here demonstrate that Lamb wave tomography using either a ring of transducers with fan beam reconstructions, or a square array of transducers with algebraic reconstruction tomography, is appropriate for detecting flaws in multilayer aircraft materials. The speed and fidelity of the reconstruction algorithms as well as practical considerations for person-portable array-based systems are discussed in this article. [S0001-4966(00)02110-X]

PACS numbers: 43.35.Pt [HEB]

I. INTRODUCTION

Ultrasonic nondestructive evaluation of platelike structures is of interest in many areas, including the inspection of aging military and civilian aircraft, where there is an ongoing need to develop efficient and cost effective techniques for detection and characterization of flaws in laminated structures with extended surface areas. Lamb waves are guided ultrasonic waves capable of propagating relatively long distances in such structures, providing an efficient means of detecting disbonds, corrosion and fatigue cracks. If Lamb wave measurements are made for a number of relative transducer positions (projections), then an image of the flawed region can be reconstructed tomographically to give a quantitative map of a quantity of interest, e.g., thickness loss due to corrosion. Previous Lamb wave tomography work by Hutchins *et al.*,[1–5] Achenbach,[6] and Degertekin[7] used a parallel projection technique with the velocity and attenuation of Lamb waves as input for the tomographic reconstruction. McKeon *et al.* have investigated a ''crosshole'' tomographic scheme which has many practical advantages for aging aircraft,[8–13] although the reconstructions are inferior. Hildebrand *et al.* have performed a preliminary study[14] of a double crosshole technique using arrays of transducers that appears to be the appropriate mix of practicality and reconstruction quality. Our work explores this technique further and compares it to fan beam tomography, using a variety of flaw types, transducer frequencies and number of sources/receivers.

Our measurements are typically performed at a frequency thickness of $fd \approx 2$ MHz-mm where only the lowest order symmetric and antisymmetric (S_0 and A_0) modes propagate appreciably in aluminum. We use contact transducers excited by tone burst and then allow the Lamb wave modes to develop as the ultrasonic energy propagates. This is in contrast to other researchers who use angle-block transducers to select particular Lamb wave modes. We find that, for measurements outside the laboratory, the careful coupling required to select particular waveguide modes via Snell's law is not practical. Instead we drive the transducers at a high enough frequency that the S_0 mode has sufficient dispersion to give sensitivity to thickness variations, but low enough that all higher-order modes are cut off or negligible. The S_0 mode at $fd \approx 2$ MHz-mm is appreciably faster than the A_0 mode so that in our pitch-catch measurements the S_0 signal will be distinct from the A_0 signal. For corrosion detection we find it convenient to monitor changes in arrival time of the S_0 signals, but depending on the flaws of interest we can monitor any combination of changes in arrival time or amplitude of the S_0 and A_0 modes. Although amplitude measurements are often most sensitive to the presence of flaws, the received signals are more strongly affected by the variations in coupling inherent in field measurements with contact transducers. Since tomographic reconstructions require many individual measurements to develop the projection data, we have concentrated our efforts on those measurement schemes which have the most promise for being fully automated.

Lamb wave techniques have the inherent advantage for large structures that they are not point-by-point measure-

a)Electronic mail: hinders@as.wm.edu

ments. Instead, the Lamb waves propagate between pairs of transducers in a pitch-catch setup that interrogates the entire region between the transducers. Because useful diagnostic signals can be propagated tens of inches in aircraft structures, by moving the transducer pair perpendicular to the direction of propagation it is possible to rapidly inspect large areas. This ''structural screening'' has been a demonstrated benefit of Lamb waves for over a decade, and puts Lamb wave ultrasonography in the same league with rapid full-field techniques such as thermography and photoelasticity. What we are reporting in this article extends considerably the usefulness of Lamb waves, by adding detailed quantitative measurement capability without sacrificing the rapid large-area capabilities inherent in the method. Scanning pairs of transducers is unavoidably slow and mechanically cumbersome. Although successful in the laboratory on small samples, we do not feel that mechanical scanners are appropriate in the field, no matter how cleverly robotic they are conceived. We have laid the groundwork that allows arrays of transducers to take large area snapshots using Lamb waves. Fully automated and person-portable, the instrumentation is intended to be configured as plug-in boards in a lunchbox computer while the transducer arrays are lightweight and handheld.

This article is organized as follows. In the next section we discuss standard fan beam tomography as we have implemented it in the laboratory using Lamb waves. The algorithms used and measurements performed are discussed, as are the difficulties that would have to be overcome in a practical array implementation of this technique. The following section then discusses double crosshole Lamb wave tomography algorithms and experiments, and shows reconstructions from a number of flawed aluminum specimens. We conclude by discussing some areas of further work that will be necessary for practical implementation of this promising technique.

II. FAN BEAM TOMOGRAPHY

A. General discussion of the method

In a parallel projection tomography measurement, a source-receiver pair has to linearly scan over the length of a projection, then rotate and scan the next projection until a specified number of them is recorded. The method requires either rotation of the sample or rotation of the transmitter-receiver assembly (which is slow and cumbersome). Both are impractical in field conditions with large objects being scanned and with real-time requirements for the data acquisition process. Using transducer arrays does not solve these problems because in the parallel projection case we cannot completely exclude mechanical motion in the system. A fast and practical alternative to the parallel projection scheme is the so-called ''fan beam'' scheme, now widely used in medical imaging. In this case, the projections are generated by a single transmitter emanating a fanlike beam which is recorded by an array of receivers. One can arrange the receivers in different ways, but usually they are located either along an arc centered on the transmitter at equiangular intervals, or equally spaced along a straight line. The data acquisition is much faster than in the parallel case, but there are still mechanically moving parts in the system because the transmitter-detector assembly is rotated to measure projections at corresponding angles.

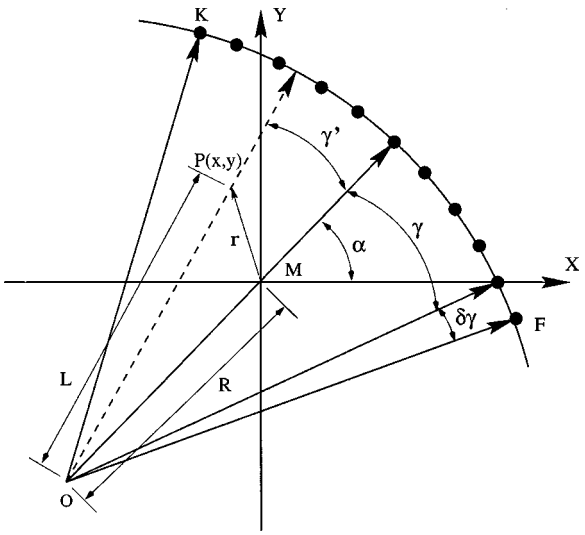

FIG. 1. Fan beam coordinate systems and variables used in reconstruction.

Figure 1 shows the main components of a typical fan beam scanning geometry. The current transmitter is located at O and α is the current projection angle. M is the rotation center and Cartesian origin of the system. Receivers are spread along the arc $\widehat{FK}$ symmetrically about the middle ray OM. The receiver spacing being considered is equiangular with the angle increment $\delta\gamma$. Current receiver angle γ is measured with respect to the central ray ($\gamma=0$) and ranges from $-\gamma_m$ to γ_m. The next projection can be taken if the whole system is rotated about M by incrementing the projection angle α. In the most straightforward implementation α covers the complete range $(0,2\pi)$.

Image reconstruction from fan beam projections is very similar to that from parallel projections except for small changes in algebra. Here we outline the three basic steps of the algorithm and explain some details of its computer implementation. The filtered back-projection formula is as follows:

$$f(x,y)=\int_0^{2\pi}\frac{1}{L^2}Q_\alpha(\gamma')\,d\alpha, \tag{1}$$

where L is the distance $|OP|$ from the point P with coordinates (x,y) to the transmitter O for the current projection. The quantity $Q_\alpha(\gamma')$ is the filtered projection data along the line $\gamma=\gamma'$ for the current projection and $f(x,y)$ is the ''image'' being reconstructed.

Below is the practical realization of this formula.[15]

(1) Assume that each projection $R_\alpha(\gamma)$ has N data points (N is odd) sampled with sampling interval $\delta\gamma$, where α is the projection angle in Fig. 1. Angle γ varies in the range $(-\gamma_m,\gamma_m)$ and takes N values $n\cdot\delta\gamma, n\in(-(N-1)/2,(N-1)/2)$. First modify the projection data and build intermediate values

$R'_\alpha(n\cdot\delta\gamma)=R_\alpha(n\cdot\delta\gamma)\cdot R\cdot\cos(n\cdot\delta\gamma)$.

Here $n=0$ corresponds to the ray passing through the center of projection.

(2) Convolve each modified projection $R'_\alpha(n\cdot\delta\gamma)$ with the impulse response filter $g(\gamma)$, samples of which are given by

$$g(n\cdot\delta\gamma)=\begin{cases}\dfrac{1}{8(\delta\gamma)^2}, & n=0,\\ 0, & n \text{ even},\\ -0.5\cdot\dfrac{1}{(\pi\cdot\sin(n\cdot\delta\gamma))^2}, & n \text{ odd},\end{cases}$$

to get the corresponding filtered projection $Q_\alpha(n\cdot\delta\gamma)$:

$$Q_\alpha(n\cdot\delta\gamma)=R'_\alpha(n\cdot\delta\gamma)*g(n\cdot\delta\gamma). \tag{2}$$

Kak and Slaney[15] also recommend convolving the result with an additional smoothing filter, e.g., Hamming window, to enhance the reconstruction quality.

(3) Perform a weighted back-projection of each filtered projection (2) along the fan:

$$f(x,y)\approx\Delta\alpha\sum_{i=1}^{M}\frac{1}{L^2(x,y,\alpha_i)}Q_{\alpha_i}(n\cdot\delta\gamma'). \tag{3}$$

Here γ' is the angle of the fan beam ray that passes through the point (x,y) and $\Delta\alpha=2\pi/M$ where M is the number of projections. The value of γ' in general does not correspond to one of $n\cdot\delta\gamma$ for which the filtered projection $Q_\alpha(n\cdot\delta\gamma)$ is known. We therefore perform a cubic spline interpolation to calculate (3). L in the last formula is the distance from the transmitter to the current point (x,y).

Note that the transmitter rotating around M covers the circle with radius $|OM|=R$, and so if the fan beam opening angle is $2\cdot\gamma_m$, then the usable reconstruction area, where all the fan beams intersect, is the circle of a smaller radius $R_{in}=R\cdot\sin(\gamma_m)$. This means that the wider the opening angle of a fan beam, the better the effective area coverage is. To increase γ_m we need either more receivers or wider angular spacing $\delta\gamma$. In the first case we are physically restricted by the number of receivers available in the array or by the time necessary for stepping a single receiver along the arc. In the second case we lose information by decreasing the ray density, which can also be improved by increasing the number of projections. The problem therefore reduces to optimization of the number of receivers, projections and receiver angular spacing. Since the scanning geometry is symmetrical about the origin M it seems reasonable to make the reconstruction region be the square with side $a=R\cdot\sqrt{2}$. This square is embedded into the big circle and cannot be made larger since we cannot provide information for pixels outside the circle.

If the transducers are equally spaced along the big circle at the angle interval $\delta\theta$, see Fig. 2, the fan beam originates and ends on the same circle. This geometry could easily be implemented via a ''ring array'' for mapping large areas with Lamb waves. Fortunately, we still can use the previously described reconstruction algorithm for equiangular

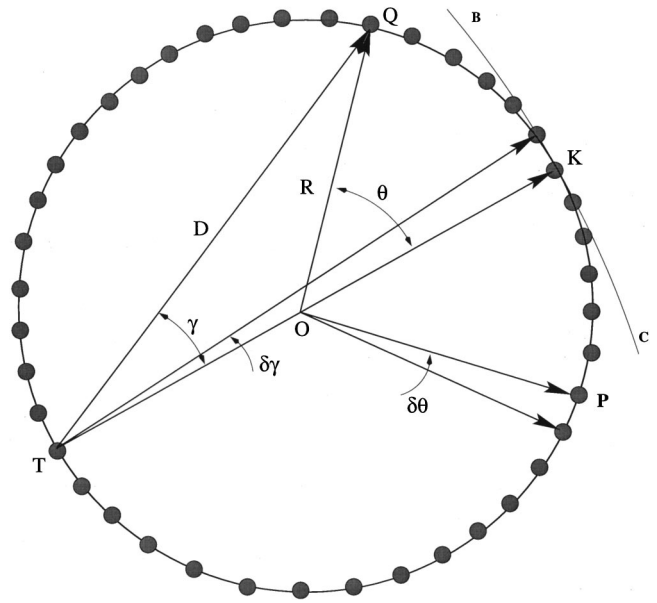

FIG. 2. Fan beam variables with circular array of evenly spaced transducers.

spacing. This is because the angle increment $\delta\gamma$ used in the reconstruction procedure still remains constant ($\delta\gamma=0.5\delta\theta$, and $\delta\theta$ is constant).

However, there is an important difference between this and the original equiangular fan beam geometry: now rays within a fan beam have different lengths. This is not a problem in medical x-ray CT scanners where the target is located essentially near the center and rays travel most of their paths in air. Therefore it does not matter whether the receivers are placed along the arc $\widehat{BC}$ (original version) or along the arc $\widehat{PQ}$ (current version). In our experiments the Lamb waves spend all their time in the material, and when the sources and receivers are placed on the same circle, we have to take into account the variation in ray lengths, because dispersion of the Lamb waves is key to sensitivity to subtle flaws such as minor corrosion thinning.

Since the parameter of interest is arrival time and it changes not only due to defects but also due to geometrical differences in ray lengths, we need some quantity independent of the latter, such as the average wave velocity for a given ray. This can be easily calculated as $\overline{V}=D/t$, where D is the length of the current ray and t is the measured arrival time for that ray. It is clear that $\overline{V}$ does not depend on the ray length explicitly, but still incorporates all the information about defects that the arrival time did.

In the experimental setup the receiving transducer Q moves along the circular arc of radius R centered at O (Fig. 2). OQ is, in fact, a rigid arm geared to the stepper motor. Scanning angle $\theta=\angle QOK$ is the angle between the central ray TK of the fan beam and the current direction of the arm OQ. The actual ray angle $\gamma=\angle QTO$ used by the reconstruction algorithm is $\gamma=\theta/2$. It is desirable to open the fan beam at the right angle having the holder arm OQ sweep the whole 180 degrees. In this case the circle formed as an intersection of all fan beams is exactly embedded into the image square with side $a=R\cdot\sqrt{2}$. This image has the biggest possible size

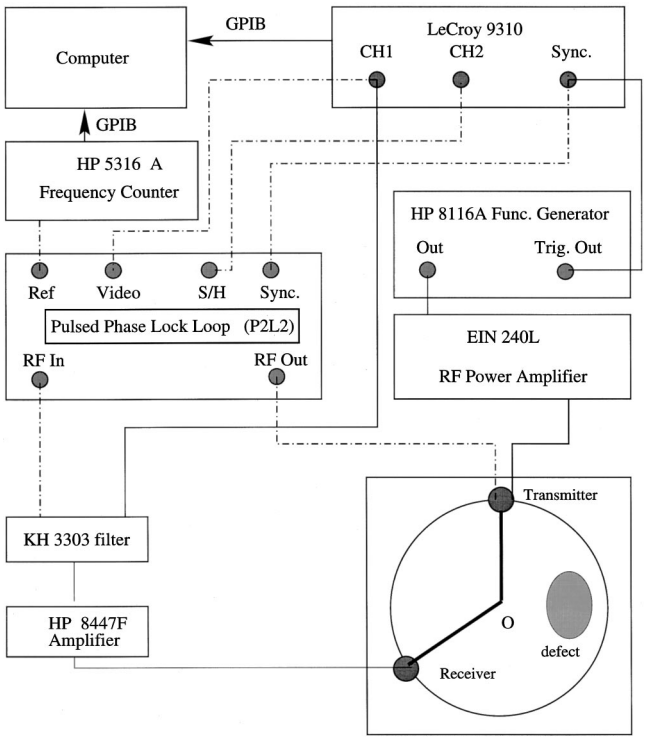

FIG. 3. Fan beam equipment setup for P2L2 spike position measurement (dashed lines) and for waveform capture mode (solid lines).

because it is, in turn, embedded into the transducer array circle.

Since we use a straight ray assumption (nondiffracting case) for the tomographic reconstruction, we can define the ray length as the distance $D=|TQ|$ between the transmitting and receiving transducers. Both transducers have a footprint of radius ≈ 7 mm. The distance between their centers will serve as a first guess of the ray length,

$$L=2\cdot R\cdot\cos(\gamma)=2\cdot R\cdot\cos\left(\frac{\theta}{2}\right). \tag{4}$$

We use (4) in the software that corrects experimental data for changing ray lengths.

B. Data collection and reconstruction

Projection data for fan beam tomographic reconstruction has been collected in three different ways. The first two use a pulsed phase lock loop (P2L2), a device that proved to be extremely helpful in parallel projection tomography, and the third method of data retrieval is borrowed from cross borehole tomography.[11] Below is a brief description of all three methods.

A block diagram of the first method is shown in Fig. 3 (dashed lines). The P2L2 sends a tone burst (typically three to ten cycles of a sine wave) to the transmitting transducer T (1.0 to 2.25-MHz Panametrics longitudinal contact transducer) which generates Lamb waves in the sample plate. The receiving transducer Q of the same type as T is positioned on the moving holder arm (Fig. 2). The amplified and filtered signal from Q comes to the input of the P2L2, which is synchronized with the LeCroy oscilloscope. The P2L2 also generates a spike indicating the chosen sampling point on the signal in CH1 of the oscilloscope. The spike is displayed in CH2. The actual data is retrieved from the ''Ref'' socket of the P2L2 and is proportional to the time shift of the reference point if the Loop is locked. The data from the frequency counter is transferred to the computer via GPIB IEEE 288. The mechanical motion of the holder arm and rotary table, as well as data acquisition, is controlled by a computer. The receiving transducer makes a specified number of steps sweeping a fan beam and the data is retrieved after each step, thus forming a single tomographic projection. The rotary table then turns the sample and the next projection is acquired. Both the step size and the speed of the rotary table need to be fairly small for the P2L2 to not lose the reference point, which is an inherent limitation of the method. Moreover, the total range of ray lengths within a fan beam must be rather small, or the P2L2 also loses the reference point. This happens because the length increment for the adjacent rays varies within the fan beam, getting bigger at the edges. The wider the fan beam, the more different are the lengths of adjacent rays and our P2L2 eventually cannot follow the corresponding abrupt phase shifts.

A block diagram for the second method is similar except that now we retrieve the time delay of the reference point in the signal. To do this we lock the P2L2 and read the signal from CH2 of the oscilloscope via GPIB into the computer. This signal is merely the spike generated by the P2L2 and follows the reference point of the signal. The position of the spike's sharp maximum will thus indicate the delay time of the reference point and can be easily found in software. This method allows us to accurately determine the delay of the signal point with the same phase.

The third method of data acquisition (Fig. 3, solid lines) does not rely on any additional hardware to solve the arrival time problem. Instead it saves the entire digitized waveform from the LeCroy oscilloscope at each scanning point and then extracts the parameters of interest in software. We use an HP8116A Function Generator to generate a tone burst similar to that in the first and second methods. We also use an ENI 240L (or 3100L) RF Power Amplifier to drive the transmitting transducer. As a result, the method produces a long file of stacked 5000-point waveforms that is analyzed by custom software.

The most important parameter to be extracted from the digitized waveforms is the arrival time of the fastest mode. This time depends upon the presence of defects and, obviously, upon the distance between transmitter and receiver. We therefore need to detect rather small variations in the arrival time carrying the information about defects, with error smaller than the effect itself. We also have to remove the regular trend associated with changing of the ray lengths during the scan. This is done by applying (4) to all the rays and then calculating the average velocities. To eliminate some of the uncertainty in ray length determination it is important to use contact transducers with small footprint area. To accomplish this we have chosen 7-mm-diam 2.25-MHz delay-line Panametrics transducers and fabricated cone-shaped acrylic resin delay lines for them. The lower ends of delay lines, contacting with the sample, have a diameter of 2 mm. The delay time of compressional elastic waves penetrat-

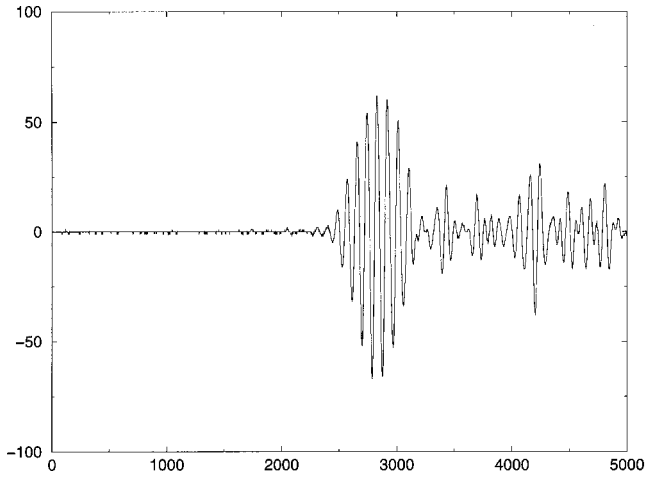

FIG. 4. Typical Lamb waveform in Al plate. S_0 is first arrival.

ing both delay lines is measured to be 12.1 μs. The drawback of this footprint reduction is the loss of received energy and therefore the need to amplify the signal. Since standard HP 8447F amplifiers are rather broadbanded ones, they amplify noise at all frequencies including the operating band. We reduce this noise by signal averaging in software. A typical recorded waveform is shown in Fig. 4.

We have collected fan beam velocity data for 18-projection scans taking 241 steps per projection at every 0.25 degrees. The radius R (Fig. 2) was equal to 108 mm. The opening angle of the fan beam was thus equal to 60 degrees, which was the largest physically possible opening angle for the apparatus, and the best covered area could not be greater than the circle of radius $r = R \cdot \sin(30 \text{ degrees}) = 56$ mm. We applied the fan beam reconstruction algorithm to this data, and the image reconstructed from it for a plate with a single 1-in.-diam flat bottom hole is shown in Fig. 5. The image shows very good quantitative agreement with the defect size. However, the fraction of the area inside the scanning ring that is free of tomographic artifacts—the ''fill factor''—is quite small. Since any practical implementation of this technique with a ring-array of transducers would cover a large area via a composite of many such scanned areas, in actual practice it would be merely the included square area that is useful. We have concluded that this low fill factor issue is such a serious limitation that fan beam tomography using Lamb waves is not practical for the purposes that have motivated our research. At the outset we had hoped that using the P2L2 with the fan beam method would provide a simple and accurate way to extract Lamb wave arrival times in hardware, but this has not been the case. A further question was whether or not there was something inherently advantageous in the fan beam tomography algorithm that would make the method attractive. Its primary advantage was the speed of reconstruction via the convolution–back-projection algorithm, but this was outweighed by sensitivity to experimental noise. On the other hand, the ART/SIRT algorithms together with the fan beam data acquisition scheme could make this technique more robust, especially for problems with axisymmetric geometry.

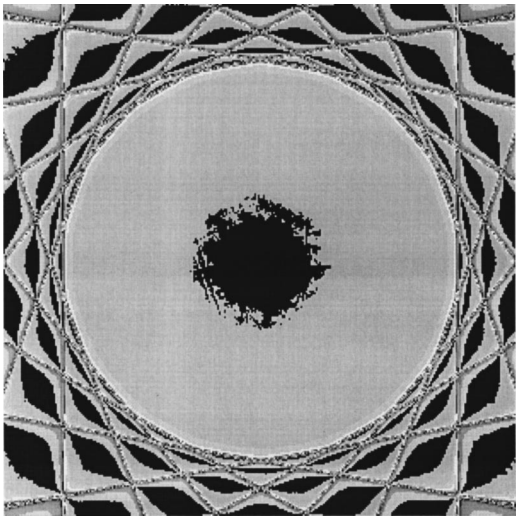

FIG. 5. Fan beam tomographic reconstruction of aluminum plate with single 1-in. 50% flat bottom hole shown as dark region in center. Note the relatively small useful area of reconstruction.

III. DOUBLE CROSSHOLE TOMOGRAPHY DEVELOPMENT

A. General discussion of the method

Seismologists have developed a distinct tomographic literature and set of techniques which can also be adapted for use with Lamb wave applications. Perhaps the best known is algebraic reconstruction tomography (ART)[16] which serves the same purpose as the previously described parallel projection and fan beam algorithms. Namely, it allows solution of the inverse problem of recovering an object from its projections. What makes it useful for Lamb wave tomography is its iterative nature and great flexibility allowing practically any scanning geometry and incomplete data sets. The parallel projection and fan beam algorithms both belong to the convolution–back-projection family, which requires strictly determined scanning configuration and is very sensitive to incompleteness or noise in the experimental data.

For the sake of clarity we will briefly describe the ART algorithm for our particular scanning setup as shown in Fig. 6, in which circles are the transducer positions that all can be occupied by transducers in the case of a square-perimeter array. In the current laboratory implementation only two positions are occupied at a time since we use only one transmitter-receiver pair. Both transducers are attached to linear slider screws and can be moved back and forth using two stepper motors controlled by the computer. The transmitting transducer steps along the lower edge from left to right incrementing i from 0 to $N-1$. The receiving transducer steps along the upper edge sweeping all N available j-positions for the fixed i. For each relative position the whole wave train is recorded and stacked into a data file. After the N^2 measurements the first set of cross-hole projections is completed. We then make the transmitter step down from the upper left corner and the receiver go up and down along the right side. Again, the N^2 measurements complete the second set of projections.

We assume all the rays to be straight lines connecting transmitters and receivers. Each ray$[i,j]$ crosses a certain

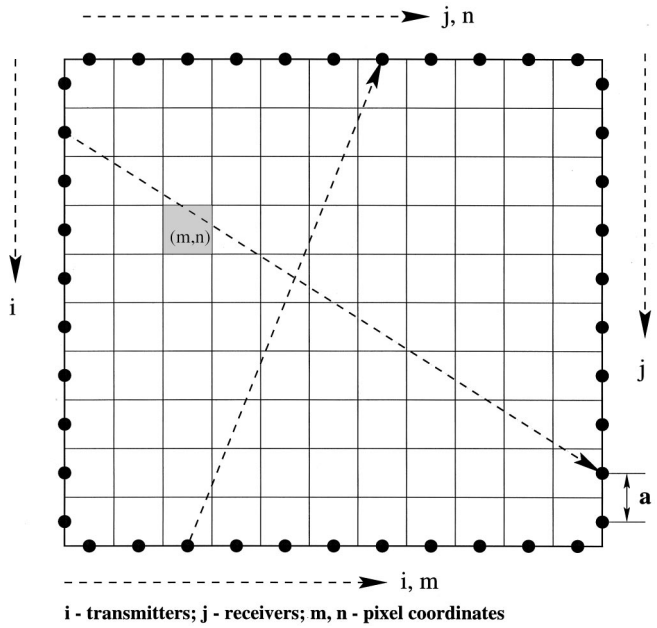

FIG. 6. Geometry for double crosshole tomography.

number of cells on its way. We assume the velocity to be constant for each cell and denote it as $v[m,n]$, where $m.n$ are the cell's coordinates starting from the bottom left corner. The time the wave spends crossing the cell is $t[i,j,m,n] = \delta[i,j,m.n]/v[m,n]$, where $\delta[i,j,m.n]$ is the length of a segment that cell$[m,n]$ cuts from the ray$[i,j]$. To get the experimentally measured arrival time for a given ray$[i,j]$ we need to sum all partial times $t[i,j,m,n]$ over the cells involved:

$$T[i,j]=\sum_{m,n\in \mathrm{ray}[i,j]} t[i,j,m,n]=\sum_{m,n\in \mathrm{ray}[i,j]} \frac{\delta[i,j,m.n]}{v[m,n]}. \quad (5)$$

Equation (5) is a system of linear equations with unknown slownesses $1/v[m,n]$. We can calculate the segment lengths $\delta[i,j,m.n]$ theoretically and measure $T[i,j]$ experimentally. Solving the matrix equation will yield the velocity pattern of a given Lamb wave mode throughout the whole square region. Since the operating frequency is known we can easily transform the velocity map into a thickness map.

For the chosen scanning geometry the total number of equations in a single crosshole projection equals N^2, where N is the number of transmitter positions. In our experiments, for example, we often use $N=100$ as a compromise between reconstruction quality and scanning time. To avoid the direct inversion of such a large matrix the less computationally intensive iterative algebraic reconstruction technique is commonly used. When applied to our case it leads to the following sequence of operations.

(1) Determine the segment lengths $\delta[i,j,m.n]$, then estimate cell velocities (an initial guess) and calculate estimated values for the arrival time of each ray:

$$T^0[i,j]=\sum_{m,n\in \mathrm{ray}[i,j]} \frac{\delta[i,j,m,n]}{v^0[m,n]}. \quad (6)$$

(2) For each ray calculate the update for velocities in the cells containing that ray:

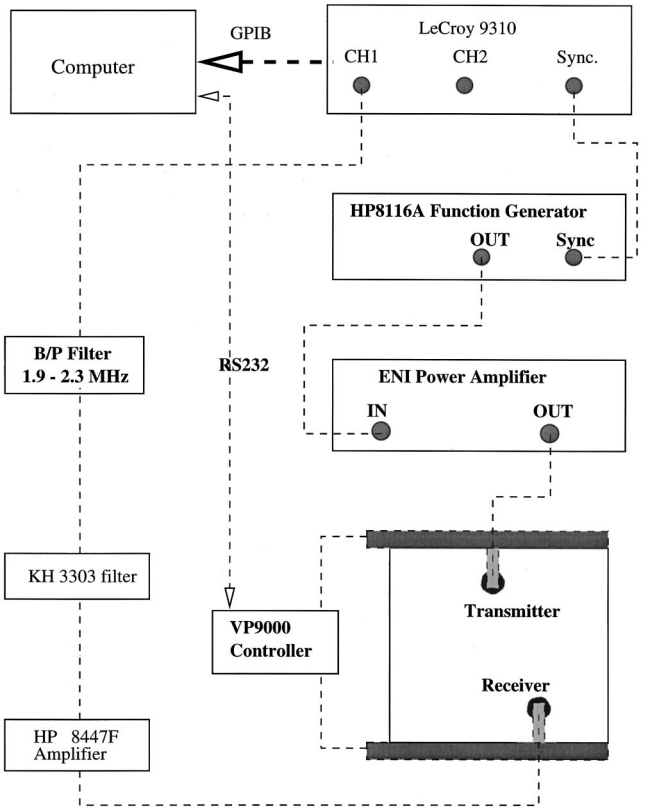

FIG. 7. Data acquisition block diagram for crosshole tomography.

$$\Delta \frac{1}{v_{m,n\in \mathrm{ray}[i,j]}[m,n]}=\frac{T[i,j]-T^0[i,j]}{L[i,j]}, \quad (7)$$

where $L[i,j]$ is the length of the ray$[i,j]$ and $T[i,j]$ is the arrival time for the ray$[i,j]$, measured in the experiment.

(3) Add the update to the current $1/v[m,n]$ values for that ray, thus completing the first iteration:

$$\frac{1}{v^1[m,n]}=\Delta \frac{1}{v[m,n]}+\frac{1}{v^0[m,n]}, \quad m,n\in \mathrm{ray}[i,j]. \quad (8)$$

(4) The values $v^1[m,n]$ can be used as an input for the second iteration and, finally, we continue iterations repeating the above steps (6)–(8) until the required accuracy is reached.

The above algorithm updates cell velocities ray-by-ray, leading to the so-called ''salt and pepper'' noise[15] in the resulting image. To eliminate it, at each iteration one can first calculate the updates for all the rays and only then update all the cell velocities simultaneously. This modified method is called SIRT (simultaneous iterative reconstruction technique) and is the version used in the reconstructions shown here.

B. Data collection and reconstruction

A block diagram of the data acquisition equipment for double crosshole tomography is presented in Fig. 7. The HP8116A Signal/Function Generator is used to form a tone burst, containing four to ten cycles. After amplification, the tone burst drives the transmitting transducer, which excites Lamb waves in the sample. The received signal is amplified,

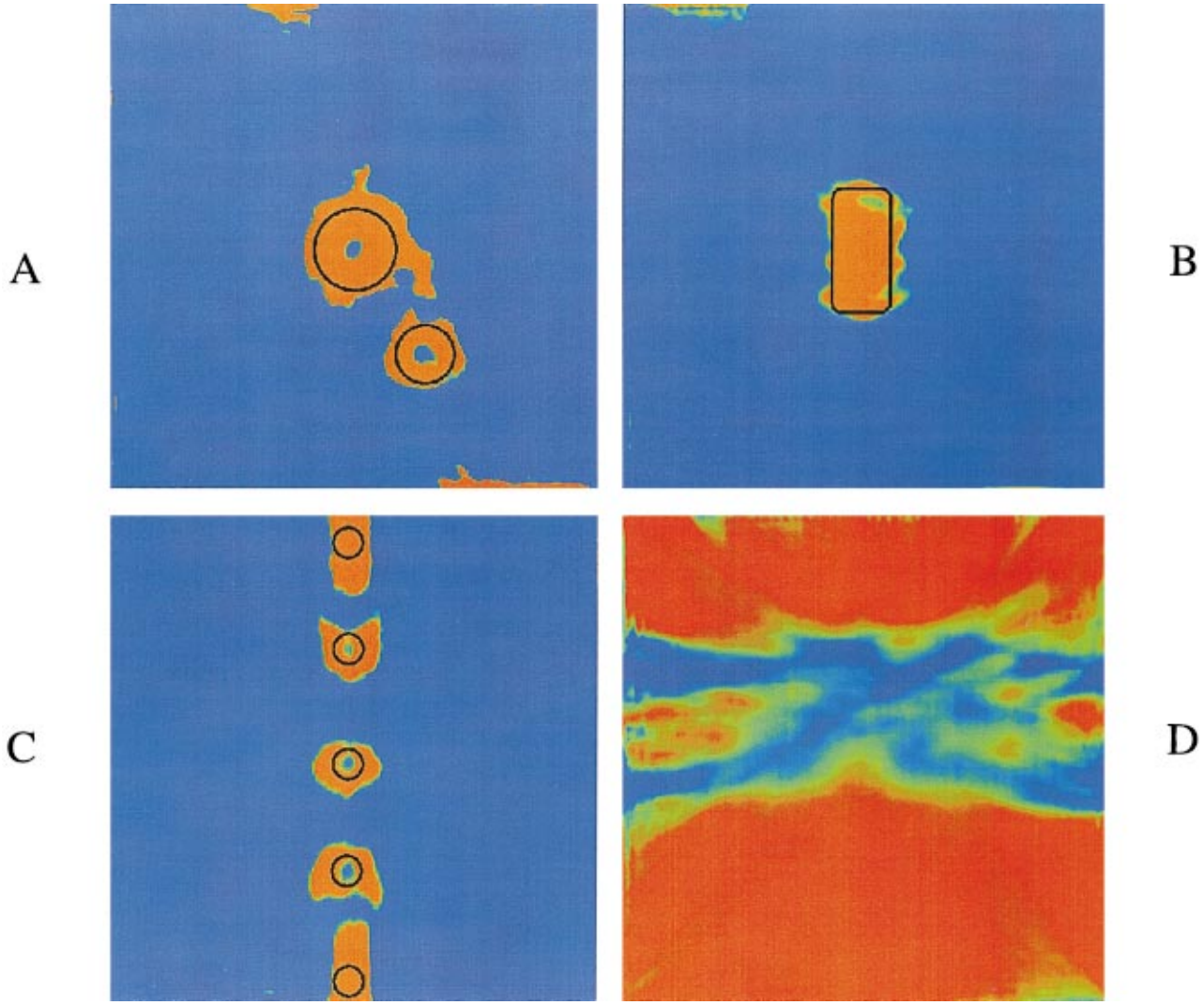

FIG. 8. SIRT reconstructions of (a) two flat bottom holes in plate; (b) rectangular thinned region in plate; (c) line of five through holes in plate; and (d) partially disbonded doubler sample. Red maps to single thickness regions and disbonded areas.

filtered and recorded by a computer. The same computer also controls motion of both transmitting and receiving transducers, which step along the two linear sliders placed parallel to each other. It is relatively easy to take one set of cross-hole projections this way, but it is much harder to take additional sets because the sample must stay in place while we move and align the sliders. Each of the sliders can be mounted along any of the four sides without moving the sample which is secured in place at its edges. After measuring the first cross-hole projection we put sliders along the other sides and take another set of projections. Some adjustment of the transducer starting position is always necessary to make sure that both sets of projections cover exactly the same area.

Each crosshole experiment results in a stack of N^2 5000-point wave trains which needs to be processed in order to extract one or several values of interest from every wave train. Currently we extract only one value—the arrival time of the fastest Lamb wave mode. At our operating frequency that is usually S_0—the first symmetric mode. Although fairly robust, the extraction algorithm is not perfect. It produces various estimation errors ranging from fractions of the quarter-wavelength to complete failure to localize the signal. Fortunately, the percentage of severe errors is small enough ($\approx 1\%$) that they do not distort the entire data set. In addition, we correct the above failures by assigning out-of-range data points the values of their closest neighbors. As a result, the code runs well on experimental data and produces satisfactory images even at this early stage of the software and hardware development.

Figure 8(a) shows a double crosshole SIRT reconstruction of a 2.3-mm-thick Al plate with two 10% thinnings indicated by the black circles. The thinnings have diameters of 29 and 25 mm, the distance between centers is 53 mm, and the scanning frequency is 1.2 MHz. The scanning geometry for this and the following figures is 100×100 with a step size of 2 mm. In all cases we used a thin layer of water for coupling purposes, and the transducers were equipped with cone-shaped delay lines made of acrylic resin. The footprint diameter of the delay line was 2 mm. Figure 8(b) is a similar scan and reconstruction, but for a 1.3-mm-thick Al plate with 30% rectangular thinning indicated by the black rectangle with rounded corners. The thinning size is 52×26 mm and the scanning frequency is 2.2 MHz. Figure 8(c) shows a reconstruction for a 2.3-mm-thick Al plate with five circular

through holes indicated by the black circles. The holes have diameters of 14 mm, the distances between centers are 45 mm, and the scanning frequency is 1.2 MHz. Figure 8(d) shows a 1.3-mm-thick Al plate with a 72-mm-wide doubler of the same material bonded to it. We were not able to receive a good signal at our usual frequency of 2.2 MHz for a 1.274-mm-thick plate, with the optimal signal quality achievable only at 1.5 MHz. Here the S_0-mode is less dispersive in the plate than at 2.2 MHz, and is also less dispersive in the doubled region than at 1.1 MHz. Blue maps to the double-thickness region and red to the single plate. The sample has been disassembled and carefully compared against the image. Qualitative agreement between the spots of missing adhesive and red single plate areas on the image has been observed.

Although all the images Figs. 8(a)–(c) were contrast-stretched to eliminate insignificant ''salt-and-pepper'' noise, they still bear residual artifacts of either reconstruction or diffraction origin. We have reconstructed several images from simulated data for different acquisition geometries including single, double and triple crosshole projections. The distribution of reconstruction artifacts on the resulting images is closely correlated with chosen acquisition geometry. This is because the ray density varies from cell to cell, together with the set of ray angles (wave vector coverage) in characteristic ways for particular geometric setups. The wave vector coverage per cell for two crosshole projections is much more uniform than that for just one, but is still imperfect, resulting in the type of diagonal and edge artifacts, apparent in Figs. 8(a), (b), and (d). Reconstruction artifacts can be substantially reduced, and both ray density and ray directivity patterns are kept the same for all cells. In the case of a square array this can be accomplished via the ''one send all receive'' technique, first reported in Ref. 14. Diffraction artifacts show up as defect enlargements, shape distortions and null values in the centers. We believe they are caused by the limitations of the straight ray approach and can be reduced by means of diffraction tomography, discussed later.

IV. DISCUSSION

Fan beam Lamb wave tomography is able to accurately reconstruct flaws with fidelity comparable to parallel projection methods, but we do not consider it a practical fieldable technique even though it could be implemented via a ring-array of transducers. The ''fill factor'' of useful reconstructed area is very small, and the convolution–backprojection family of algorithms is unforgiving to the errors and uncertainties inherent in any real-world measurement. Moreover, the P2L2 was not particularly useful in extracting the arrival times of Lamb wave modes, so we found it necessary to resort to digitizing the waveforms and processing them in software.

Double crosshole Lamb wave tomography is likewise able to accurately reconstruct flaws with fidelity comparable to (or better than) parallel projection methods. It allows for a good quality of reconstruction even from noisy, corrupted and incomplete data, such as Lamb wave arrival times estimated with custom software. Moreover, it works for a variety of scanning geometries so that specialized, nonsquare arrays can be used for hard-to-scan locations in service. The SIRT algorithm preserves all the advantages of the conventional ART, being in addition the lower-noise and lower-artifact technique.

The 100×100 square perimeter array of transducers that our laboratory measurements have mimicked provides an acceptable quality of the reconstruction from the two mutually perpendicular sets of crosshole projections for the area of 20×20 cm. For larger areas, or for better resolution, more transducers may be desired. Costs of multiplexer electronics and transducer elements will likely be the limiting factor on array size in a fieldable instrument, since even for very large arrays the measurement time, processing/memory capability, and computer storage requirements are not limits. Both the expert system software that extracts the arrival times and the reconstruction algorithms run in near real-time on modest PCs.

The tomography theories that we have used here assumed that the Lamb waves travel along straight rays. For corrosion this is a relatively good assumption, since the main effect of a region of thinning in the path of the S_0 Lamb waves is to speed them up and give earlier arrivals. As the corrosion gets more severe, scattering will take place in addition to the speeding up of the S_0 modes. This scattering can involve mode coupling so that some of the energy is converted to *other* Lamb wave modes. Moreover, the Lamb wave beam is finite, which means that a ray-tracing type of description is inadequate. For flaws which are of the same size or smaller than the diameter of the beam, some of the Lamb wave energy will interact with the flaw and some will skirt past it. The complicated interplay of these effects introduces artifacts into the tomographic reconstruction, such as the null regions in the middle of the holes in Figs. 8(a) and (c). For example, small through holes are interpreted by the algorithm as slowing down of the Lamb waves because that portion of the beam which is not blocked by the hole must travel the longer path around the obstruction. To take ray bending effects into account and thus to improve the resolution of reconstruction methods, Lamb wave diffraction tomography is needed.[17] There is no reliable universal algorithm yet,[18–21] but one scheme that has been found to be successful is to use the straight-ray reconstruction as a first pass to find the large scale variations, and then account for the varying ray paths with diffraction tomography as a second pass. The reconstruction is then refined to delineate more subtle features and enhance the resolution significantly. A good but relatively slow candidate for the second pass of the Lamb wave tomography could be the curved ray (or refraction) tomography, which uses Fermat's principle for the ray path computation. Well developed in the fields of geophysics and acoustics, this method accounts for ray bending due to the variations in the index of refraction and is reported to yield better resolution than the straight ray method. A more comprehensive approach may be diffraction tomography based on wave field inversion techniques requiring detailed analysis of propagation and scattering of guided waves and their interaction with defects. For Lamb waves an appropriate scattering theory seems to be the Mindlin higher-order plate theory.

ACKNOWLEDGMENTS

The authors would like to thank Chris Domack and Jonathan Stevens for their help in design and construction of the fanbeam scanner. Support for this work was provided by ONR under Contract No. N00014-99-M-0185 and by Virginia's Center for Innovative Technology.

[1] W. Wright, D. Hutchins, D. Jansen, and D. Schindel, ''Air-coupled Lamb wave tomography'' IEEE Trans. Ultrason. Ferroelectr. Freq. Control **44**(1), 53–59 (1997).

[2] D. P. Jansen, D. A. Hutchins, and J. T. Mottram, ''Lamb Wave Tomography of Advanced Composite Laminates Containing Damage,'' Ultrasonics **32**(2), 83–89 (1994).

[3] D. A. Hutchins, D. P. Jansen, and C. Edwards, ''Lamb Wave Tomography Using Non-Contact Transduction,'' Ultrasonics **31**(2), 97–103 (1993).

[4] D. P. Jansen and D. A. Hutchins, ''Immersion tomography using Rayleigh and Lamb waves,'' Ultrasonics **30**(4), 245–254 (1992).

[5] D. P. Jansen and D. A. Hutchins, ''Lamb wave tomography,'' in 1990 Ultrasonics Symposium, p. 1017.

[6] Y. Nagata, J. Huang, J. D. Achenbach, and S. Krishnaswamy, ''Lamb Wave Tomography Using Laser-Based Ultrasonics,'' in *Review of Progress in QNDE*, Vol. 14, edited by D. O. Thompson and D. E. Chimenti (Plenum, New York, 1995), p. 561.

[7] F. L. Degertekin, J. Pei, B. T. Khuri-Yakub, and K. C. Saraswat, ''*In situ* acoustic temperature tomography of semiconductor wafers,'' Appl. Phys. Lett. **64**(11), 1338–1340 (1994).

[8] J. C. P. McKeon, ''Tomography Applied to Lamb Wave Contact Scanning,'' doctoral dissertation, College of William and Mary, 1998.

[9] M. K. Hinders and J. C. P. McKeon, ''Lamb Wave Tomography for Corrosion Mapping,'' in *Proceedings of the 2nd Joint NASA/FAA/DoD Conference on Aging Aircraft*, edited by C. E. Harris, NASA CP-1999-208982732 (1998).

[10] M. K. Hinders, E. V. Malyarenko, and J. C. P. McKeon, ''Contact scanning Lamb wave tomography,'' J. Acoust. Soc. Am. **104**, 1790(A) (1998).

[11] J. C. P. McKeon and M. K. Hinders, ''Parallel projection and crosshole contact scanning Lamb wave tomography,'' J. Acoust. Soc. Am. **106**, 2568–2577 (1999).

[12] J. C. P. McKeon and M. K. Hinders, ''Lamb Wave Contact Scanning Tomography,'' in *Review of Progress in QNDE*, Vol. 18, edited by D. O. Thompson and D. E. Chimenti (Plenum, New York, 1999), p. 951.

[13] M. K. Hinders, E. V. Malyarenko, and J. C. P. McKeon, ''Ultrasonic Lamb Wave Tomographic Scanning,'' edited by A. Mal, Proc. SPIE **3586**, 279–291 (1999).

[14] B. P. Hildebrand, T. J. Davis, G. J. Posakony, and J. C. Spanner, ''Lamb Wave Tomography for Imaging Erosion/Corrosion in Piping'' in *Review of Progress in QNDE*, edited by D. O. Thompson and D. E. Chimenti (Plenum, New York, 1999), Vol. 18, p. 967.

[15] A. C. Kak and M. Slaney, *Principles of Computerized Tomographic Imaging* (IEEE, New York, 1988).

[16] K. A. Dines and R. J. Lytle, ''Computerized geophysical tomography,'' Proc. IEEE **67**(7), 1065–1073 (1979).

[17] J. C. P. McKeon and M. K. Hinders, ''Lamb Wave Scattering from a Through Hole,'' J. Sound Vib. **224**(5), 843–862 (1999).

[18] G. T. Herman and A. Kuba, eds., *Discrete Tomography* (Birkhauser, Boston, 1999).

[19] F. Natterer, *The Mathematics of Computerized Tomography* (Wiley, New York, 1986).

[20] K. T. Ladas and A. J. Devaney, ''Application of an ART Algorithm in an Experimental Study of Ultrasonic Diffraction Tomography,'' Ultrason. Imaging **15**, 48–58 (1993).

[21] T. A. Dickens and G. A. Winbow, ''Spatial resolution of diffraction tomography,'' J. Acoust. Soc. Am. **101**, 77–86 (1997).

Dynamics of gas bubbles in viscoelastic fluids. II. Nonlinear viscoelasticity

John S. Allen
Department of Biomedical Engineering, University of California, Davis, One Shields Avenue, Davis, California 95616-5294

Ronald A. Roy
Department of Aerospace and Mechanical Engineering, Boston University, 110 Cummington Street, Boston, Massachusetts 02215

(Received 3 December 1999; accepted for publication 20 June 2000)

The nonlinear oscillations of a spherical, acoustically forced gas bubble in nonlinear viscoelastic media are examined. The constitutive equation [Upper-Convective Maxwell (UCM)] used for the fluid is suitable for study of large-amplitude excursions of the bubble, in contrast to the previous work of the authors which focused on the smaller amplitude oscillations within a linear viscoelastic fluid [J. S. Allen and R. A. Roy, J. Acoust. Soc. Am. **107**, 3167–3178 (2000)]. Assumptions concerning the trace of the stress tensor are addressed in light of the incorporation of viscoelastic constitutive equations into bubble dynamics equations. The numerical method used to solve the governing system of equations (one integrodifferential equation and two partial differential equations) is outlined. An energy balance relation is used to monitor the accuracy of the calculations and the formulation is compared with the previously developed linear viscoelastic model. Results are found to agree in the limit of small deformations; however, significant divergence for larger radial oscillations is noted. Furthermore, the inherent limitations of the linear viscoelastic approach are explored in light of the more complete nonlinear formulation. The relevance and importance of this approach to biomedical ultrasound applications are highlighted. Preliminary results indicate that tissue viscoelasticity may be an important consideration for the risk assessment of potential cavitation bioeffects. [S0001-4966(00)01210-8]

PACS numbers: 43.35.Wa [HEB]

LIST OF SYMBOLS

τ	stress tensor
$\dot{\gamma}$	rate of deformation tensor
λ_1	relaxation time
η_o	zero shear-rate viscosity
ρ	fluid density
σ	fluid static surface tension
κ	polytropic exponent
p_{go}	initial internal gas pressure
p_o	ambient pressure
p_A	acoustic pressure amplitude
ω	acoustic frequency
$R(t)$	instantaneous bubble radius
R_o	equilibrium bubble radius
T_a	acoustic period
$\overline{t}=\omega t$	nondimensional time
$\overline{r}=r/R_o$	nondimensional radial coordinate
$\overline{R}=R/R_o$	nondimensional bubble radius
$\overline{\tau}=\tau R_o/\eta_o\sqrt{\rho/p_o}$	nondimensional radial stress
$a=p_A/p_o$	ratio of pressure amplitudes
$\mathrm{De}=\lambda_1\omega$	Deborah number
$\mathrm{Re}=\rho_o\omega R_o^2/\eta_o$	Reynolds number
$\mathrm{We}=2\sigma/p_oR_o$	Weber number
$y=r^3-R^3(t)$	Lagrangian transformation

I. INTRODUCTION

Since the development of the Rayleigh-Plesset equation, the growth and collapse of spherical gas bubbles has been the subject of numerous studies (see Ref. 1 for a comprehensive summary). Some of this research has concentrated on the oscillatory behavior of a single bubble in an acoustic field,[1] where for sufficiently high pressure amplitudes of forcing the bubble oscillates nonlinearly about its equilibrium radius. Most of these studies of forced oscillations considered bubble behavior in Newtonian fluids.

The inclusion of polymeric additives to many fluids of interest has motivated the study of bubble dynamics in non-Newtonian media. As a first-order attempt to account for non-Newtonian shear thinning behavior, some researchers utilized empirical formulas modeling viscosity as a function of shear stress.[2] Throughout the years, a few studies have attempted to investigate the role of viscoelasticity on bubble dynamics. In 1970, Fogler and Goddard published pioneering work in this area,[3] with their work forming the foundation for many subsequent studies on viscoelastic bubble dynamics. Using the linear Maxwell model for the constitutive relation for the fluid, they obtained an integro-differential equation governing the radial bubble dynamics. (The linear Maxwell model is a constitutive equation that can be ex-

pressed as a linear differential equation.) For simplicity, the bubble was modeled as an empty void. The equation was examined in certain asymptotic limits and solved numerically for a few cases. Some general conclusions were presented on how elasticity effects the bubble collapse. However, their results and subsequent conclusions were somewhat limited by numerical difficulties encountered in solving the integro-differential equation. Spurious numerical artifacts made it difficult to carefully discern the nature of the collapse and rebound for more than a few cycles.

Subsequently, the Fogler and Goddard's integro-differential formulation was coupled with a three-constant Oldroyd constitutive equation, which allows for strain relaxation of the fluid and is more suitable to greater deformations.[4,5] Ting[4] was only able to partially resolve a single collapse without rebound due to numerical problems. Tanaswa and Yang[5] carried out their integration for a few oscillations but also encountered numerical difficulties. Forced oscillations of a bubble in a three-constant Oldroyd fluid were studied by Shima *et al.*,[6] who computed the bubble's frequency response as a function of the different viscoelastic time constants. They obtained some interesting results but their pioneering study leaves many questions open. For instance, their paper does not include radius-versus-time (R-T) plots, making it difficult to appreciate the differences between viscoelastic and Newtonian bubble dynamics. Furthermore, potential implications for biomedical applications were not addressed.

The above researchers attempted to solve a single bubble dynamics equation formulated along the lines of the Fogler and Goddard derivation. In other studies, the more formidable task of simultaneously solving the continuity and momentum equations for the fluid along with a respective constitutive equation has been tackled. Zana and Leal numerically solved the conservation equations of mass and momentum along with a gas diffusion equation for a single bubble collapse.[7] A complicated constitutive equation incorporating several material parameters was employed and the results were compared with the corresponding Newtonian case. Approximate analytical solutions were obtained for specific cases. They did not investigate subsequent rebounds or oscillations, and found that viscoelastic effects coupled with gas diffusion had profoundly impacted the collapse. More recently, Kim solved the continuity and momentum equations in a Lagrangian frame for the study of the free oscillations of a bubble in an Upper-Convective Maxwell (UCM) fluid.[8] This is a generalized Maxwell model with derivatives of the stress expressed in a formulation that preserves ''objectivity'' such that properties are independent of the reference frame.[8] Kim implemented a complicated finite element method for solving these equations in spherical coordinates and compared some of his results with those obtained by Fogler and Goddard. In doing so, he reached some conclusions about the differences between linear Maxwell and the UCM models. He also attempted to interpret the physical behavior from his results in terms of certain nondimensional quantities, notably the Reynolds and Deborah numbers.

Several questions regarding viscoelastic bubble dynamics persist to this day. Fogler and Goddard's formulation is based on a traceless stress tensor consistent with a linear viscoelastic constitutive equation. Subsequent researchers implemented this traceless assumption for objective constitutive relationships in bubble dynamics equations without an extensive explanation.[4,5] Some general formulations of non-Newtonian bubble dynamics relied on this traceless assumption[9] while other researchers adopted a form consistent with a finite trace.[7] More recent work, such as that of Kim, suggests that a traceless formulation is not necessarily appropriate; however, little discussion is presented with respect to reasons why. Furthermore, some non-Newtonian fluid dynamics literature indicates that certain constitutive equations such as the Upper-Convective Maxwell (UCM) model can be derived from a molecular theory which specifies a finite trace.[10]

What is the proper form of the bubble dynamics equation for a given constitutive equation? For bubble dynamics, a rigorous comparison between models based on objective vs linear viscoelastic relations of a respective constitutive equation has not be performed. In recent work by the authors, governing equations for the linear viscoelastic bubble dynamics were re-derived such that they could be readily solved in a robust numerical fashion.[11] The advantage of this formulation is that it eliminates the numerical difficulties encountered by Fogler and Goddard's form of the equations. Likewise, it offers a direct means for benchmarking calculations of corresponding objective constitutive equations for dynamic responses within the linear viscoelastic limit.

Many applications involving viscoelastic bubble dynamics entail relatively large deformations, thus the use of equations valid in these regimes seems warranted. For instance, medical ultrasound applications involve the forced oscillations of bubbles in biological media. Pressing issues include understanding the dynamics of ultrasound contrast agents in biological fluids and the assessment of cavitation bioeffects from diagnostic and therapeutic ultrasound. For certain biomedical applications, such as ultrasound-enhanced drug delivery, it may be desirable to mediate cavitation-induced transport through viscoelastic tissue layers of the skin. The determination of safety criteria for prevention of potential cavitation bioeffects has been a subject of ongoing experimental and theoretical studies.[12–14] An important consideration that has only recently received much attention is the role of tissue rheology on the bubble dynamics.[11] The currently accepted exposure criteria and understanding of bubble dynamics in the body originates from a study of bubble dynamics in Newtonian fluids. The nearly ubiquitous viscoelastic nature of biological fluids and tissue may have a profound influence on the cavitation collapse and rebound behavior. Since cavitation damage in general has been linked to large bubble expansions, the use of an appropriate constitutive equation is desirable. Earlier work by the authors attempted to address some of these issues within a linear viscoelastic framework.[11]

In this study, we investigate the oscillatory behavior of a spherical bubble in an Upper-Convective Maxwell fluid. We address issues related to the trace of the stress tensor and respective form of the equations. The numerical approach

used for solving the equations is explained in some detail. We compare our results for the UCM model in the limit of small deformation to solutions of our linear viscoelastic formulation.[11] Examples related to potential biomedical applications are highlighted.

II. BUBBLE DYNAMICS EQUATIONS

Fogler and Goddard's work on a bubble in an incompressible, linear viscoelastic fluid builds on the fact that the stress tensor is traceless for linear constitutive relationships.[3] In general, the spherical symmetry of the problem allows one to write

$$\tau_{\theta\theta} = \tau_{\phi\phi}, \tag{1}$$

and for a traceless tensor, trace $(\tau) = 0$, the diagonal components of the stress tensor can be related by

$$\tau_{\theta\theta} + \tau_{\phi\phi} = -\tau_{rr}. \tag{2}$$

Researchers have employed a variety of constitutive relationships in conjunction with radial bubble dynamics equations. Fogler and Goddard's work is often cited as a reference by later researchers who use Eq. (2), but not necessarily for linear viscoelastic equations.[4,5] An important point is that there is disagreement in the literature about use of Eq. (2). Some rigorous arguments based on continuum mechanics considerations have been made for using a traceless stress tensor for the bubble problem for non-Newtonian fluids in general.[9] However, Kim's recent work on bubble collapse and free oscillations in a UCM fluid follows a nontraceless formulation, though limited justification for adopting this formulation is given.[8] Since the form of stress tensor remains an open question, we follow a more general formulation that does not require the assumption given by Eq. (2).

In accordance with the above discussion, we write the Rayleigh–Plesset equation with acoustic forcing in a general form that includes the theta component of the stress tensor, τ,

$$R\ddot{R} + \frac{3}{2}\dot{R}^2 = \frac{1}{\rho}\left[\rho_{go}\left(\frac{R_o}{R}\right)^{3\kappa} - (p_o + p_A \sin(\omega t)) - \frac{2\sigma}{R} - 2\int_R^\infty \left(\frac{\tau_{rr} - \tau_{\theta\theta}}{r}\right) dr\right]. \tag{3}$$

This equation describes the motion of a spherically symmetric bubble of radius $R(t)$ in incompressible liquid of density ρ, subject to a static surface tension σ, an initial internal gas pressure p_{go}, and an ambient pressure p_o. The acoustic pressure amplitude and forcing frequency are given by p_A and ω, respectively. For simplicity, we assume the internal gas follows a polytropic relationship with exponent κ. Some limitations of this assumption are presented below.

We assume the UCM model describes the fluid and its rheology. It is desirable to seek a general understanding of the bubble dynamics for a basic viscoelastic fluid before investigating more complicated constitutive relations. The UCM model may be written as

$$\tau + \lambda_1 \tau_{(1)} = -\eta_o \dot{\gamma}. \tag{4}$$

The subscript ''(1)'' refers to the first contravariant (upper) convective time derivative which can be defined as acting on a second-order tensor as

$$\tau_{(1)} = \frac{D}{Dt}\tau - ((\nabla u)^{\perp} \cdot \tau + \tau \cdot (\nabla u)), \tag{5}$$

where the symbol $\perp$ indicates the transpose and D/Dt is the material derivative. Defining the notation, λ_1 refers to the relaxation time, $\dot{\gamma}$ to the rate of deformation tensor, u to the velocity field, and η_o to the zero-shear-rate viscosity. The UCM model offers one of the simplest descriptions of elasticity available, yet still poses a challenge for accurate numerical evaluation when coupled with a bubble dynamics equation.

The numerical problem consists of solving Eq. (3) coupled with the radial and theta equations from Eq. (4). The introduction of the upper convective time derivative, Eq. (5), introduces terms in the formulation that prevent the use of a previously developed technique for reducing the problem to a series of ordinary differential equations by first solving for the stress in terms of the spatial variable.[11] For the spherical bubble problem, the radial and theta components of the UCM model can be expressed as

$$\tau_{rr} + \lambda_1\left(\frac{\partial \tau_{rr}}{\partial t} + \frac{R^2\dot{R}}{r^2}\frac{\partial \tau_{rr}}{\partial r} + \frac{4R^2\dot{R}}{r^3}\tau_{rr}\right) = 4\eta_o \frac{R^2\dot{R}}{r^3}, \tag{6}$$

$$\tau_{\theta\theta} + \lambda_1\left(\frac{\partial \tau_{\theta\theta}}{\partial t} + \frac{R^2\dot{R}}{r^2}\frac{\partial \tau_{\theta\theta}}{\partial r} - \frac{2R^2\dot{R}}{r^3}\tau_{\theta\theta}\right) = -2\eta_o \frac{R^2\dot{R}}{r^3}. \tag{7}$$

Following the nondimensionalization employed in our previous study of linear viscoelastic bubble dynamics,[11] we introduce the following definitions of nondimensional time, radial spatial variable, radius, and stress (the choice for the stress nondimensionalization originates from the considerations of a Newtonian fluid, where $\tau \sim \eta_o \partial u/\partial r$),

$$\bar{t} = \omega t; \quad \bar{r} = r/R_o; \quad \bar{R} = R/R_o; \quad \bar{\tau} = \tau \frac{R_o}{\eta_o}\sqrt{\rho/p_o}. \tag{8}$$

We obtain the nondimensional parameter known as the Deborah number through our choice nondimensionalizing time by the acoustic forcing frequency. The Deborah number describes the ratio of the characteristic time scale of the fluid to that of the flow,

$$\mathrm{De} = \lambda_1 \omega. \tag{9}$$

This choice of time scales is partially motivated by the consideration that in cases where the bubble is driven off resonance the acoustic forcing mediates the elastic response of the fluid. The Reynolds number for this nondimensionalization is given by

$$\mathrm{Re} = \frac{\rho \omega R_o^2}{\eta_o}. \tag{10}$$

Equation (3) is rewritten in nondimensional form (dropping the bars),

$$R\ddot{R}+\frac{3}{2}\dot{R}^2=\frac{p_o}{\rho\omega^2R_o^2}\left[\left(1+\frac{2\sigma}{p_oR_o}\right)\left(\frac{1}{R}\right)^{3\kappa}-\left(\frac{2\sigma}{p_oR_o}\right)\left(\frac{1}{R}\right)-(1+a\sin(t))\right]-\frac{2}{\mathrm{Re}}\frac{1}{\omega R_o}\sqrt{\frac{p_o}{\rho}}\int_R^\infty\left(\frac{T_{11}-T_{\theta\theta}}{r}\right)dr, \quad (11)$$

where a is the ratio of the acoustic forcing pressure amplitude to the ambient pressure. A further nondimensional quantity, the Weber number, is defined as the ratio of surface tension to inertial forces,

$$\mathrm{We}=\frac{2\sigma}{p_oR_o}. \quad (12)$$

This study considers how the viscoelastic fluid properties affect the bubble for a fixed surface tension value approximating that of water (72.5 dyn/cm). Actual values in tissue may be different, but since these values have not been well established it suffices for this initial study to choose a fixed value. Finally, the stress tensor components, Eqs. (6) and (7), are rewritten as (again dropping the bars),

$$\tau_{rr}+\mathrm{De}\left(\frac{\partial\tau_{rr}}{\partial t}+\frac{R^2\dot{R}}{r^2}\frac{\partial\tau_{rr}}{\partial r}+\frac{4R^2\dot{R}}{r^3}\tau_{rr}\right)=4\left(\omega R_o\sqrt{\frac{\rho}{p_o}}\right)\frac{R^2\dot{R}}{r^3}, \quad (13)$$

$$\tau_{\theta\theta}+\mathrm{De}\left(\frac{\partial\tau_{\theta\theta}}{\partial t}+\frac{R^2\dot{R}}{r^2}\frac{\partial\tau_{\theta\theta}}{\partial r}-\frac{2R^2\dot{R}}{r^3}\tau_{\theta\theta}\right)=-2\left(\omega R_o\sqrt{\frac{\rho}{p_o}}\right)\frac{R^2\dot{R}}{r^3}. \quad (14)$$

There are several bubble damping considerations that are not included in these governing equations. Radiation damping is not considered because the constitutive equations used are based on the incompressible assumption.[10] How compressibility changes the character of the model predictions, particularly for those expressions that are derived from molecular-based theories, is currently not well understood. Furthermore, this study is conducted for the most part at a level of amplitude oscillation where radiation damping is likely to play only a minor role in the overall character of the bubble dynamics. The thermal damping of the bubble oscillations is neglected in this study. The polytropic exponent relationship for the gas was employed for computational simplicity and this assumption has limitations. Thermal damping becomes significant when a bubble is driven such that interior gas reaches a high temperature.[1] Thermal effects are in general less important than viscosity for micron size bubbles driven at MHz frequencies.[1] However, the reader should carefully view the results in light of the polytropic assumption. Finally, these approximations seem somewhat justified given the scope and nature of this initial study. Likewise, the same assumptions were followed for our study of linear viscoelastic bubble dynamics,[11] the results of which are used as a benchmark in this work.

III. NUMERICAL APPROACH

The problem posed by Eqs. (11), (13), and (14) is difficult to solve numerically in its present form. Part of this difficulty stems from tracking the movement of the bubble boundary in the liquid, which is coupled to Eqs. (13) and (14). To overcome similar problems, previous researchers have introduced Lagrangian coordinates to immobilize the boundary.[7] Following this approach, we introduce the transformation

$$y=r^3-R^3(t). \quad (15)$$

The problem can thus be expressed as a system of first-order ordinary differential equations and an integro-differential equation for all the points in the liquid such that $y_i=0,N$, where the first point represents the bubble wall and the last point the boundary condition where the stresses are zero,

$$\frac{dR}{dt}=U, \quad (16)$$

$$\frac{dU}{dt}=\left[-\frac{3}{2}U^2+\frac{p_o}{\rho\omega^2R_o^2}\left\{(1+\mathrm{We})\left(\frac{1}{R}\right)^{3\kappa}-\mathrm{We}\left(\frac{1}{R}\right)-(1+a\sin(t))\right\}\right]\frac{1}{R}-\frac{1}{R}\frac{2}{3\,\mathrm{Re}}\left(\frac{1}{\omega R_o}\sqrt{\frac{p_o}{\rho}}\right)\times\int_0^\infty\left(\frac{\tau_{rr}(y_i,t)-\tau_{\theta\theta}(y_i,t)}{y_i+R^3}\right)dy, \quad (17)$$

$$\frac{d\tau_{rr}(y_i,t)}{dt}=\left(\left(\frac{-4R^2\dot{R}}{y_i+R^3}\right)-\frac{1}{\mathrm{De}}\right)\tau_{rr}+\frac{4}{De}\left(\omega R_o\sqrt{\frac{\rho}{p_o}}\right)\left(\frac{R^2\dot{R}}{y_i+R^3}\right), \quad (18)$$

$$\frac{d\tau_{\theta\theta}(y_i,t)}{dt}=\left(\left(\frac{2R^2\dot{R}}{y_i+R^3}\right)-\frac{1}{\mathrm{De}}\right)\tau_{\theta\theta}-\frac{2}{\mathrm{De}}\left(\omega R_o\sqrt{\frac{\rho}{p_o}}\right)\left(\frac{R^2\dot{R}}{y_i+R^3}\right). \quad (19)$$

The initial conditions are taken as

$$R(0)=1[R_o], \quad (20)$$

$$\tau_{\theta\theta}(0)=\tau_{rr}(0)=0, \quad (21)$$

$$U(0)=0. \quad (22)$$

This study is conducted for $\mathrm{De}\sim O(1)$ to avoid numerical difficulties because of the division by this quantity in Eqs. (18) and (19). This permits us to explore the parameter range of interest where the elastic characteristics of fluid become comparable to the viscous. For small Deborah numbers that are less than one, the behavior will only slightly deviate from the Newtonian case.

Although the problem has been reduced to ordinary differential equations coupled to an integro-differential equation, several computation problems must still be addressed. The first consideration is how the equations should be discretized in time to allow for proper computation of the integral term in Eq. (7) and to allow for sufficiently small time steps to capture a rapid bubble collapse and rebound. Another is how the spatial resolution in the y coordinate should be discretized to allow sufficient resolution of the stress components at the bubble wall and still preserve the $\tau_{\theta\theta}(\infty,t)=\tau_{rr}(\infty,t)=0$ boundary condition. Moreover, global checks are needed in order to monitor whether the simulations are working properly. One such check will be to see if the results converge to those computed from the linear viscoelastic equation formulation with the linear Maxwell model.[11] A comparison of these two cases is also of scientific interest and this aspect will be examined in detail in a later section.

One approach used to monitor the solution behavior is to track the global conservation of energy in the system. The sum of the kinetic and potential energy should balance the work done by the acoustic forcing and resulting dissipation of the system. For a conservative version of the Rayleigh-Plesset equation, assuming a polytropic exponent behavior for the gas, this energy balance has been demonstrated using Lagrangian methods.[15] A similar energy balance is obtained by multiplying the generalized Rayleigh-Plesset Eq. (3) by $4\pi\rho\dot{R}R^2$ and grouping the quantities into terms representing the kinetic, and potential energies,

$$\frac{d}{dt}[2\pi\rho\dot{R}^2R^3]+\frac{4\pi}{3}\frac{d}{dt}\left[R^3\left(p_o+\frac{p_{go}}{\kappa-1}\left(\frac{R_o}{R}\right)^{3\kappa}+\frac{3\sigma}{R}\right)\right]$$
$$=-4\pi p_o a\sin(\omega t)\dot{R}R^2-8\pi\dot{R}R^2\int_{R(t)}^{\infty}\left(\frac{\tau_{rr}-\tau_{\theta\theta}}{r}\right)dr. \tag{23}$$

The first term in Eq. (23) represents the time rate of change of the kinetic energy, the second the time rate of change of the potential energy, and the two terms of the right-hand side are the forcing and dissipation, respectively. This can be expressed in a manner that is more amenable to numerical simulations by integrating with respect to time,

$$2\pi\rho\dot{R}^2R^3+\frac{4\pi}{3}R^3\left(p_o+\frac{p_{go}}{\kappa-1}\left(\frac{R_o}{R}\right)^{3\kappa}+\frac{3\sigma}{R}\right)$$
$$=-4\pi p_o a\int_0^t\sin(\omega t)\dot{R}R^2dt$$
$$-8\pi\int_0^t\left[\dot{R}R^2\int_{R(t)}^{\infty}\left(\frac{\tau_{rr}-\tau_{\theta\theta}}{r}\right)dr\right]dt+E_o, \tag{24}$$

where the constant E_o is determined from the initial conditions. By computing this quantity, normalized by the initial energy (E_o), a description of the energy of the system is obtained. The difference between the sum of the kinetic and potential energies and the work done by dissipation and forcing gives a measure of the error involved in the calculation. As outlined below, a set of regularization variable transformations was performed on equations to alleviate time stepping difficulties. In practice, the relative difference between quantities from a regularized version of (24) proved to be a reasonable indicator of numerical problems.

The choice of time integration for the system described by Eqs. (16)–(19) is complicated by the addition of the integral in Eq. (17). This integral must be computed in the y coordinate for each time step. A multistep method, which uses information from previous mesh points, was found to be best suited for this problem. A third-order explicit predictor-corrector Adams-Bashforth-Moulton method was chosen. Simpson's Rule was used to compute the integral in Eq. (17) at each time step. A ''variable step-size method'' was used to change step size, which involves using a variable coefficient multistep formula to change step sizes.[16] This method is both faster than interpolation methods and does not have the same stability restrictions on the rate of step-size changes.[16] Despite the use of adaptive step techniques, the integration in time of Eqs. (16)–(19) resulted in numerical difficulties at the cusplike points of bubble collapse and checks of the energy balances indicated problems with the numerical accuracy at these points.

To overcome these difficulties, some analytical temporal-transformation methods were employed. These involve a set of variable transformations which make the solution of the differential equation behave more smoothly at the cusp points. Many of these methods were originally developed in astrophysics to treat numerical difficulties caused by close approach or near-collision orbits.[17] The methods have proven to be of particular value in the integration of bubble dynamics equations driven by explosive tensile wave.[18] We follow the approach taken by Lastman *et al.*[18] and ask the reader to examine that reference for more complete information. The benefit of employing these transformations for solving Eqs. (16)–(19) is evidenced by the fact that the error in the energy balance associated with integration through the cusp regions is greatly reduced in a comparison with the unregularized versions of equations.

Another numerical problem involves determining the proper grid distribution of the spatial coordinate y. It is important that the system obeys the boundary conditions at infinity and that the stress tensor is properly resolved. It was found, depending on the magnitude of the bubble collapse that is dictated by its maximum expansion, and the elastic-viscous coupling occurring in the fluid, that the radial component of the stress tensor becomes steep in a region near the bubble wall, requiring a fine grid. The sharpness of this region is not known *a priori* and is ultimately determined by the maximum bubble radius and its subsequent collapse. The spatial grid length must be an adequate distance from the bubble wall so that the stress component is small at the last mesh point, otherwise elastic reflections can occur and the bubble growth cycle is distorted. Several different methods were used to determine the optimal distribution of mesh points. None has proven completely satisfactory, and future work on this problem might be best approached using an adaptive mesh method. Limitations in the ability to properly resolve the mesh near the bubble wall and in finding a proper distribution through the liquid imposes some restrictions in the allowable amplitude of acoustic forcing considered in

this study. Nevertheless, the current method is capable of obtaining results in many physically relevant regimes.

A rudimentary, straightforward method was adopted to address some of these concerns. Some of these procedures proved time consuming because it was necessary to rerun the calculations. The spatial y region was subdivided into five regions of various grid resolutions, which were based on an estimate derived from knowledge of the governing physics. This allows for a nonuniform distribution of mesh points over the entire region bearing some resemblance to the actual physics of the problem. The distributions were set with more mesh points near the bubble wall in an effort to resolve the steep collapse scenario during a run. At various points, usually corresponding to a threshold error level in the energy balances during a sharp bubble collapse, the mesh distribution was monitored. Numerical techniques used to solve differential boundary layer equations were implemented to find a better mesh distribution.[19] In particular, a mesh was sought which would equally distribute the variation of the solution at the time, t_c, of the steepest collapse for a given case,

$$|\tau_{rr}(y_{i+1},t_c)-\tau_{rr}(y_i,t_c)|=\Lambda. \tag{25}$$

After an initial calculation, the mesh points in a boundary layer type region were redistributed in subsequent calculations in an attempt to satisfy (25). A suitable constant Λ was determined through numerical experiments for each case. The radial component was found to undergo greater spatial fluctuations than the theta component so τ_{rr} was chosen for Eq. (25). The boundary condition at infinity was also monitored to determine if the stress components remain below a predetermined small quantity, δ,

$$\tau_{rr}(y_N,t)\leqslant\delta \quad \text{and} \quad \tau_{\theta\theta}(y_N,t)\leqslant\delta. \tag{26}$$

If either of these criteria fails, the mesh length was increased by either increasing the spacing in the last region while maintaining the same resolution in each of the other regions, or increasing the size of the entire mesh.

IV. RESULTS AND DISCUSSION

Several example cases have been chosen to illustrate some of the physical features of the UCM model and also to highlight some of the computation difficulties in solving this system of equations. Furthermore, we investigate how the UCM and Linear Maxwell models compare and explore the limitations and ultimate breakdown of the linear viscoelastic formulation. In particular, the implications for medical ultrasound applications will be highlighted. Though numerical limitations do not permit a detailed study in a parameter space broadly relevant to medical diagnostic ultrasound, our results reveal some novel behavior that can be directly related to cavitation bioeffects considerations.

First, we explore the effects of elasticity with the linear and UCM models on the 2/1 harmonic forcing (2 local maximum per acoustic cycle) of a 1.7-μm bubble at 1.0 MHz. This secondary harmonic response has been observed previously for water.[20] One of our goals is to investigate the bubble behavior in tissue. Hence, we study the cases of Re $=0.6$ and 0.45, which correspond to the zero-order, shear viscosities of 30 and 40 cP, respectively. These values are our best estimates for possible values for interstitial fluid in connective tissue.[21,22]

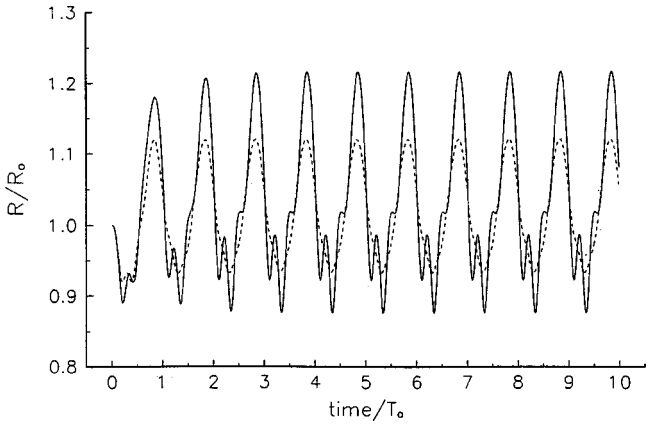

FIG. 1. Shown is a comparison of the Re=0.45 (dashed line) and Re=0.6 (solid line) cases of a 1.7-μm equilibrium radius bubble forced at 0.1 MPa, 1.0 MHz for De=1.0. Notice the appearance of the second harmonic in the Re=0.6 case. Time is shown in terms of acoustic periods denoted by T_a.

The results over several cycles are shown in Fig. 1 (the dashed line corresponds to Re=0.45 and solid line the Re $=0.6$ case). The time is shown in terms of acoustic periods (T_a) for Fig. 1 and all the following figures. The increased viscosity damps out the oscillations as seen in the lower Re number case. In this case, the second harmonic is not present, although its appearance is manifest for a decrease of 10.0 cP in the zero-order shear viscosity value. It should be noted that the Newtonian case was also examined at these Reynolds numbers for comparison and the second harmonic was not as prominent. This result suggests that elasticity may contribute to pronounced second harmonic generation—an observation of relevance to bubble harmonic imaging, a medical ultrasound imaging modality that relies on the generation of second harmonics. These results indicate that in tissue, the presence of the second harmonic may be governed by the combined viscous and elastic properties of the tissue. Depending on the forcing amplitude, certain combinations of these numbers may determine the overall strength of the second harmonic signal used for imaging. However, the actual extent to which contrast agents will enter interstitial space remains an open question subject to ongoing experimental research.

For the Re=0.45 case, the radial (solid line) and theta stresses (dashed line) at the bubble wall are shown in more detail in Fig. 2. The theta component is greatest during the bubble growth cycle and radial component dominates during the collapse phase. The growth of the harmonic peaks corresponds directly with the symmetric rise and fall of the radial and theta stress components. This result makes sense physically, since the growth of a spherical bubble is a biaxial elongation and the following collapse is an uniaxial elongation.[7]

Figure 3, obtained at 5.3 cycles in terms of nondimensional time, shows how the radial stress components develop in the liquid as a function of the nondimensional y variable (recall that $y=0$ corresponds to the bubble wall). The solid line corresponds to the Re=0.6 case and the Re=0.45 case is

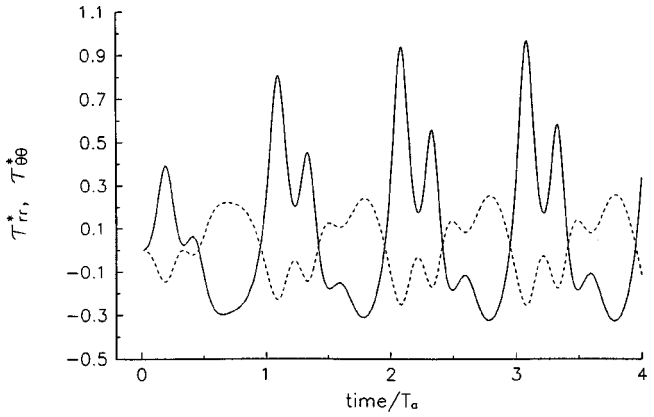

FIG. 2. The nondimensional radial and theta components of the stress tensor at the bubble wall (for the Re=0.6 case as in Fig. 1) grow and shrink as the bubble oscillates. The theta component (dashed line) dominates the growth phase while the radial part is greatest during the collapse.

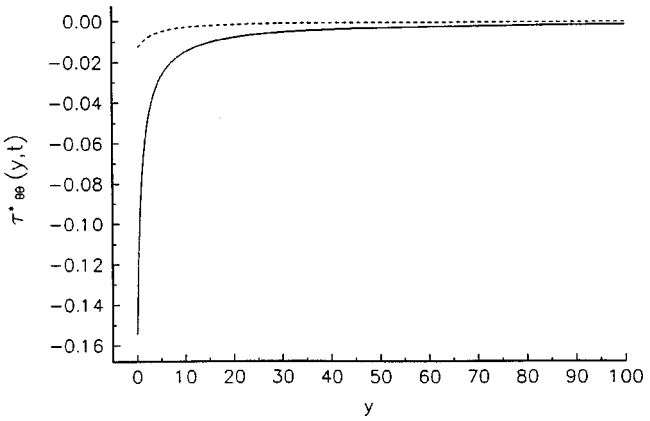

FIG. 4. The theta stress component in the liquid is shown as a function of y at the time corresponding to 5.3 cycles. Notice the magnitude of stress for the Re=0.6 (solid line) and Re=0.45 (dashed line) cases is much less than that shown in Fig. 3.

given by the dashed line. Notice how the stresses fall off steeply from the bubble wall and reach an asymptotic value farther out in the liquid. In particular, the change in radial component is quite steep for y less than about 10, which can lead to computational difficulties near the bubble wall. This illustrates one of the computational challenges of this problem outlined previously. The theta component reaches its maximum during growth so it does not pose as great a computation problem during the collapse, as seen in Fig. 4. The solid and dashed lines correspond to the Re=0.6 and Re =0.45 cases, respectively, as in Fig. 3. For these calculations, approximately 4000–5000 grid points were required to proper resolve the Lagrangian coordinate y. A large group of tightly spaced points is needed near the bubble wall to resolve the boundary layer region. However, it proved to be cumbersome and too computationally intensive to pick a fine mesh throughout this coordinate. Also y needs to be of a length such that the stress tensors are sufficiently small at the last grid point. Hence a nonuniform distribution of points was sought with a fine resolution near the bubble wall and with increasing coarseness away from the wall.

For increasing pressure amplitudes, the bubble collapses more violently, causing steeper gradients in the radial stress components, exacerbating the computational problems associated with the grid distribution. By tracking the energy balance differences, we were able to crudely determine when our grid choice was in significant error, and monitor the behavior of the global error associated with the calculation. Spikes present in plots of our balances indicated it is difficult to accurately resolve the minimum collapse point with this type of calculation. Care was thus taken to look for possible numerical artifacts from a spurious grid.

One illustrative exercise that has not been made before (for bubble oscillations) is the direct comparison of results obtained using the linear Maxwell and UCM constitutive models. Kim reaches some conclusions based on his calculations and an examination of Fogler and Goddard's results, but he does not do a direct comparison with the two models. For the linear viscoelastic bubble dynamics, we solve the system of nonlinear ordinary differential equations developed previously for the linear Maxwell model (see Ref. 11). Figure 5 shows a comparison of the two models for the previously given Re=0.45 case; the agreement is excellent. This offers some confidence in the calculations, because for sufficiently small deformation UCM (dashed line) should re-

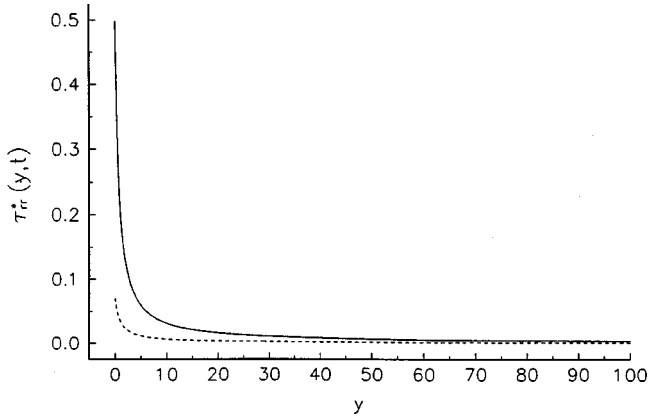

FIG. 3. The radial stress component in the liquid is plotted as a function of y at the time corresponding to 5.3 cycles. The Re=0.6 (solid line) collapse is much more violent than the Re=0.45 (dashed line) case. Resolving this collapse with sufficient spatial resolution presents a computational challenge.

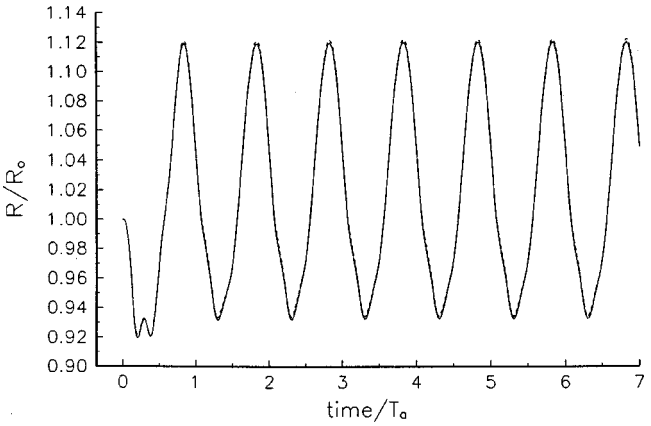

FIG. 5. Excellent agreement is found with the linear Maxwell formulation (solid line) and the UCM model (dashed line) for the 1.7-μm radius bubble for the Re=0.45 case from Fig. 1. This direct comparison between the two models has not been reported previously.

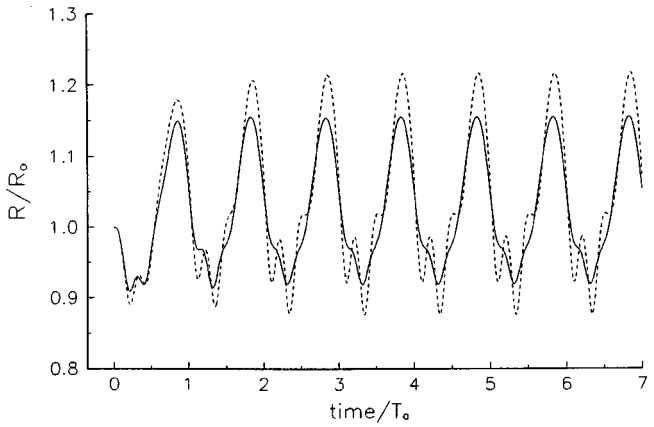

FIG. 6. A comparison between the linear Maxwell (solid line) and UCM (dashed line) for the Re=0.6 case from Fig. 1 suggests that the UCM predicts a second harmonic response that is not visible in the linear constitutive formulation.

duce to the linear Maxwell (solid line). The additional terms in the UCM model do not appear to contribute significantly for cases involving small deformations. For the Re=0.60 case, we see in Fig. 6 (UCM—dashed line, linear Maxwell—solid line) that some differences exist between the two treatments. In the UCM-based model, the damping seems less and greater radial expansion occurs. The second harmonic component is prominent in the UCM formulation, but is not observed in the linear case. The overall bubble excursion amplitude for the UCM case is higher.

A plot of the corresponding radial stress components is shown in Fig. 7 (UCM—dashed line, linear Maxwell—solid line). From the radial stress tensor, we see that the collapse predicted by the UCM model is faster in the final stages as it overtakes the linear model. Also, the stress induced in the liquid is much more narrowly peaked. For the theta component comparison, shown in Fig. 8 (UCM—dashed line, linear Maxwell—solid line), we see that the bump and dip associated with the growth cycle is much more pronounced in the UCM model. The additional terms in the objective derivative introduce additional quadratic nonlinearities into the problem, which may be the mathematical origin of these second harmonics.

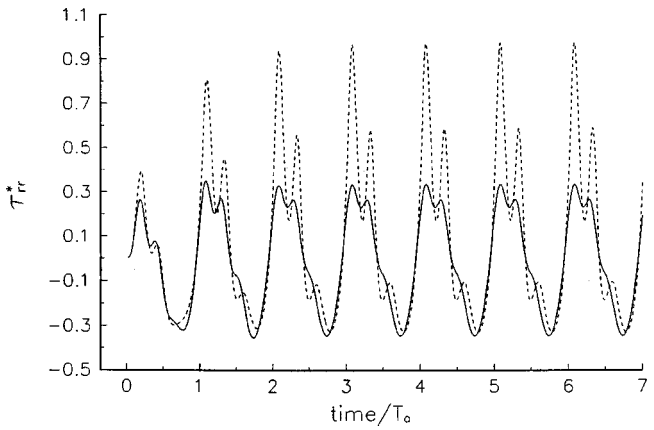

FIG. 7. The radial stress tensor at the bubble wall (Re=0.6) for the UCM (dashed line) and linear Maxwell (solid line) models. Note the latent harmonic formation in the linear Maxwell formulation.

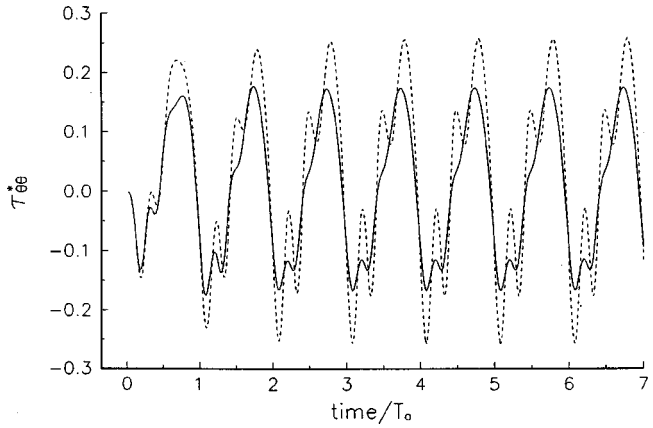

FIG. 8. The differences in harmonic structure and formation are also seen for the theta stress component at the bubble for the case from Fig. 7.

Kim[8] finds some qualitative differences between his results for free oscillations and those of Fogler and Goddard.[3] He attributes the differences seen in the collapse rate to the characteristic behavior of the UCM versus the linear Maxwell models. However, we find excellent agreement between the two models in the limit of small-amplitude oscillations. It is important to note that Kim compares his results at a finite Reynolds number (Re=2.0) to Fogler and Goddard's results in the inviscid limit (infinite Reynolds number). The differences noted are most likely due to this discrepancy.

We consider now the case of near-resonance forcing for much larger Re and at different forcing amplitudes. We chose a 1.0-μm radius bubble forced at 3.0 MHz for various pressure amplitudes and at Re=2.5, which corresponds to a viscosity of 7.5 cP. This case roughly approximates a bubble in blood. Shown in Fig. 9 is the case for 0.05 MPa of forcing. We note again excellent agreement between the linear Maxwell (solid line) and UCM models (dashed line), which is expected for such low amplitude radial response. Dramatic differences are seen if the pressure amplitude is increased to 0.2 MPa, as shown in Fig. 10. For the first cycle, there is good agreement between the two models, after which the linear model (solid line) predicts explosive growth while the UCM model (dashed line) exhibits a stable oscillation. These

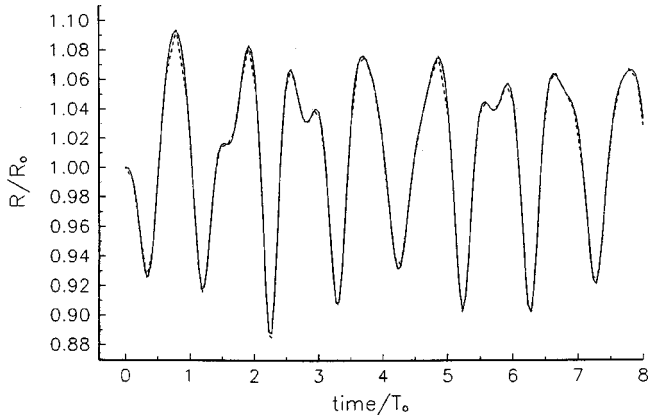

FIG. 9. A comparison shows the linear and nonlinear model predictions for small-amplitude forcing. The physical parameters are: $p_A=0.05$ MPa, $f=3.0$ MHz, $R_o=1.0$ μm, De=3.0 and Re=2.5. Good agreement is found between the UCM (dashed line) and linear Maxwell (solid line) models.

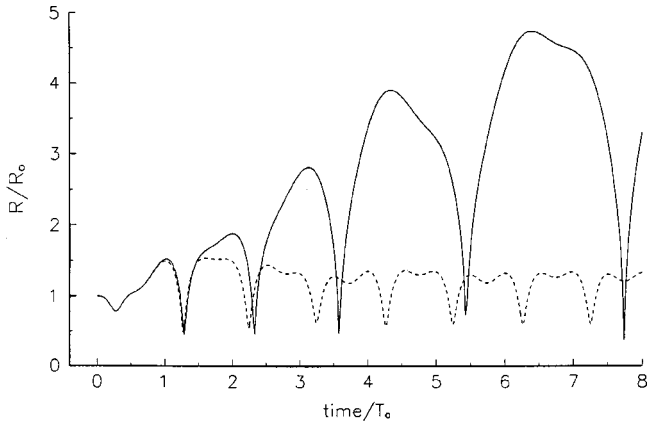

FIG. 10. Radius versus time for the same conditions as in Fig. 9, except the pressure amplitude has been increased to 0.2 MPa. The UCM model (dashed line) undergoes stable oscillations while the linear Maxwell (solid line) predicts an explosive growth.

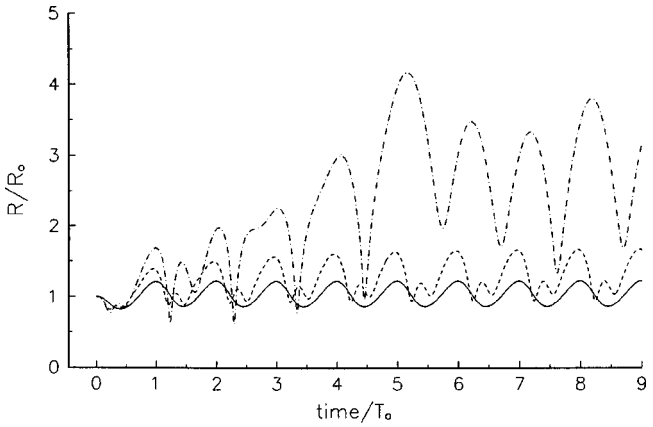

FIG. 12. A 1.0-μm radius bubble forced at 3.0 MHz, 0.4 MPa is shown for the Newtonian case (solid line), De=1.0 (dashed line) and De=2.0 (dot-dash line) using the UCM model. For increasing Deborah number, the oscillation amplitude increases, as does the overall bubble minimum radius.

differences are elucidated in the plots of the radial and theta stresses, and the normal stress difference, the latter of which is given in Fig. 11. The normal stress difference is purported to be directly related to the driving force of the collapse.[4,8] Figure 11 shows that the linear Maxwell model (solid line) collapse is both later and slower relative to the UCM model (dashed line), and that the normal stress difference reaches a greater negative value during the expansion cycle. This case reveals a more powerful collapse than in previous cases, such as those shown in Fig. 2, as indicated by the spiked nature of the peaks in Fig. 11. Physically, this can be attributed to the higher Reynolds number and the near-resonance forcing.

The linear Maxwell model, which is based on empirical considerations, has difficulties handling these effects. The model can be derived heuristically using a linear combination of a spring and dashpot representing the respective elastic and viscous contributions.[22] Radial bubble growth corresponds with some extension of the elastic spring. Bubble growth beyond some point suggests that the spring is stretched so far out so it no longer has a normal restoring force. We notice that the greater negative normal stress difference leads to an explosive bubble growth, which has not been demonstrated previously. Finally, this example clearly illustrates that there are limits in forcing parameters in combination with Reynolds number at a given Deborah number for the linear viscoelastic formulations. It is easy to get unphysical results if one is not careful and does not realize the model's limitations—an observation that is important to keep in mind when selecting a model for biomedical applications. Linear viscoelastic constitutive equations have received the most attention in the literature and texts on biomaterials and biomechanics.[22] However, quite often the inherent assumptions and limitations of these equations are not fully emphasized. Potentially damaging inertial cavitation effects are often linked to a bubble expansion to roughly more than two times its equilibrium radius. Obviously in this case one would not want to rely on a linear viscoelastic model.

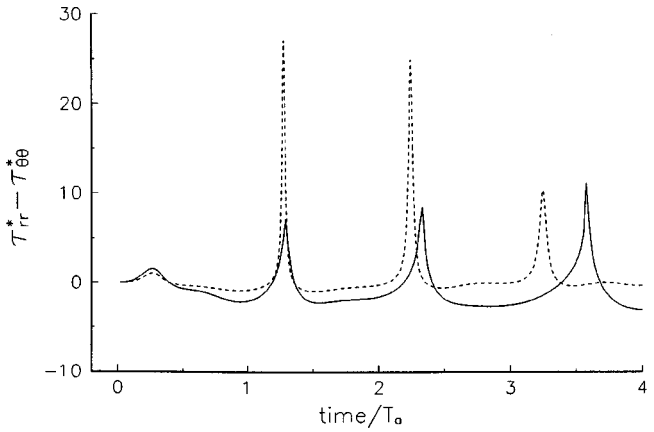

FIG. 11. The normal stress difference, computed for the same conditions as in Fig. 10, gives a measure of the magnitude of the collapse. A less violent collapse and more growth is seen in the linear Maxwell (solid line) compared with UCM (dashed line) model.

Shown in Fig. 12 is a plot of a 1.0-μm radius bubble at Re=0.63 (30 cP) and for De=1.0, De=2.0, De=0.0 (Newtonian fluid) in an UCM fluid. These cases correspond with the solid, dashed and dot-dashed lines respectively. The acoustic forcing amplitude and frequency are 0.4 MPa and 3.0 MHz, respectively. This is a sufficiently high pressure amplitude to get a sense of viscoelastic bubble behavior at medically relevant conditions. The Newtonian case is damped by viscosity and undergoes small oscillations about its equilibrium radius. The De=1.0 case shows increased amplitude of oscillations, along with the presence of an additional harmonic. The bubble, however, still undergoes stable oscillations about its equilibrium radius. For the De =2.0 case we see the rapid growth to a transient cavity such that the bubble is more than 2.3 times its equilibrium size. *This rapid growth for increasing elasticity at the same pressure amplitude indicates that viscoelasticity may be important to the definition of cavitation thresholds and the assessment of bioeffects in non-Newtonian media.*

Several key features depicted in Fig. 12 could be tested in future experiments. These include emissions from the additional harmonics and the presence of an ''elastic threshold'' criteria for violent bubble growth. In the latter case, inertial cavitation effects would be monitored as a function of the viscoelastic properties of the material. The same features were seen in studies at higher Reynolds numbers; how-

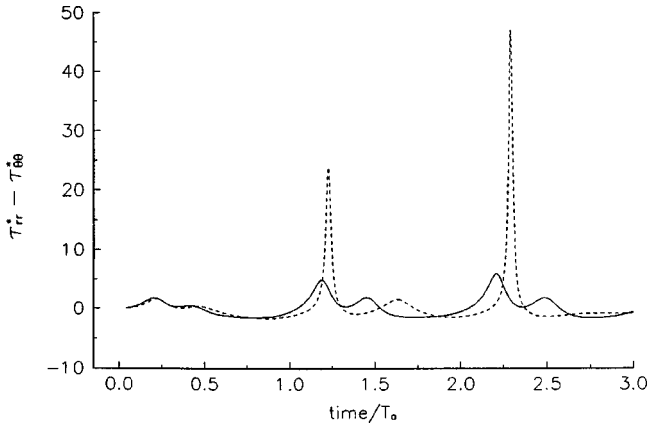

FIG. 13. The normal stress difference is plotted for the De=1.0 (solid line) and De=2.0 (dashed line) cases from Fig. 12. Increasing Deborah number retards the collapse.

ever, for increasing Deborah numbers the bubbles grew beyond our present computational capabilities. Another feature of note is the transition from a periodic motion at De=1.0 to the transient oscillations at the larger De=2.0. Also the overall minimum bubble radius steadily increases for the first five cycles. This may be due to the fact that, for sufficiently high dissipation and forcing, the elasticity builds up to a point that it retards the collapse much more quickly for increasing Deborah number. This point is further illustrated in Fig. 13, which is a plot of the normal stress differences for the De =1.0 (solid line) and De=2.0 (dashed line) cases. The magnitude of the collapse is much greater for the higher Deborah number; however, the collapse is delayed in time. Also the presence of a small secondary harmonic is retarded in time for the higher Deborah number case. During the second major collapse, the De=2.0 case becomes even more delayed relative to the De=1.0 case. This may be attributed to the increasing contribution from the elasticity of the fluid.

Further study is required in order to understand completely the effects of elasticity in relationship to medical ultrasound applications. Moreover, a retardation effect is seen after a few cycles. The extent to which this diminishes potentially damaging effects is not readily apparent. It should be noted that many medical imaging modalities employ short-pulse ultrasound, which may not permit sufficient time for the elastic effects to respond. On the other hand, pulse Doppler modalities use longer pulses and could couple with elasticity dependent effects leading to significant material-dependent behavior. Also, an important consideration for regions of interstitial fluid is that they cannot withstand large expansion forces.[21] The mucopolysaccharide fibers begin to fragment as the cross links break and the free fluid spaces grow within the gel.[21] Therefore, it is possible that after a large bubble expansion the sources for the elastic forces would be disrupted before they have time to continue to affect the bubble dynamics. We surmise that this scenario is perhaps more likely in loosely connected tissue rather than ones with organized collagen and elastin fibers.

V. CONCLUSIONS

This study addresses several issues related to bubble dynamics in viscoelastic fluids. Previous work by the authors concentrated on linear viscoelastic bubble dynamics formulations and applications.[11] Here the study is extended to include constitutive equations that hold for larger deformations. In particular, we find solutions for bubble oscillations in an UCM fluid and compare results with those obtained for a linear Maxwell fluid. Excellent agreement is found in the limit of small deformations while the solutions diverge for increasing radial excursions. It is revealed that elasticity can enhance the generation of secondary harmonics and can serve to increase the maximum bubble radius attained. The behavior of the stress tensor components reveals the elongation nature of the fluid behavior during collapse and growth. The normal stress difference highlights the magnitude of bubble collapse.

Another aspect of this study, besides investigating the underlying physics, is to examine the implications of these results to biomedical ultrasound applications. Numerical examples reveal that the generation of a bubble's second harmonic response in a viscoelastic fluid is highly sensitive to both the acoustic forcing and material parameters. Tissue modeled as a viscous Newtonian fluid neglects what appears to be an important contribution of elasticity to harmonic generation. Numerical spatial resolution complications limit a direct comparison of model predictions at acoustic pressure amplitudes associated with the Mechanical Index of order unity.[13] However, at ''low-end'' diagnostic ultrasound amplitudes we notice drastic differences between the predicted bubble response as a function of Deborah number. Indeed, these results suggest that the pressure threshold for inertial cavitation is a function of both the acoustic pulse duration and elasticity of the medium. This indicates tissue rheology and, in particular, elastic properties should be considered in future investigations of ultrasound cavitation bioeffects.

Scant discussion has been given in biomedical literature on the limitations in the use of linear viscoelastic constitutive equations.[21,22] The topic *is* addressed, however, in standard rheology texts.[10] In this study, we do a direct comparison of bubble dynamics based on the linear Maxwell model to that of its counterpart, the UCM. The comparisons reveal the limitations of the linear constitutive model in capturing large radial bubble excursions.

The differences in computational effort involved in solving the two models should be noted. The linear viscoelastic formulation can be solved quite easily for most cases. The corresponding cases with the UCM can require several hours to a day (or more) on a workstation due to the large system of equations. These cases would often have to be rerun to ensure their validity. Finding the proper spatial resolution for a given case was particularly difficult. Future work might be directed to improving the computational efficiency of solving the UCM-based bubble model. Another limitation of this work is the neglect of thermal damping of the gas and this aspect should be addressed in future studies.

Finally, it is essential that these theoretical predictions be compared with experimental data. Currently, little or no experimental evidence is available that affords direct comparison with these results. As an initial step, the current theories might be compared with experimentally measured bubble-radius-versus-time curves (such as those employed in

single-bubble sonoluminescence studies[23]) for fluids of different Deborah numbers. Also, if the parameter range of the computational model is expanded to include higher acoustic pressures, inertial cavitation threshold measurements might be compared against model predictions. Only once these potentially important viscoelastic effects are better understood can one hope to understand and more completely model cavitation bubble dynamics in complex tissue environments.

ACKNOWLEDGMENTS

The authors wish to acknowledge the generous support of ONR, NIH and DARPA. We thank Lawrence Crum for all manner of support and Steven Kargl for assistance with the use of computational resources. Suggestions and guidance on the numerical calculations by James Riley were greatly appreciated and proved invaluable to the completion of this work. Also, we wish to thank Lewis Wedgewood for enlightening discussions on viscoelastic bubble dynamics and, in particular, for elucidating key points about the nature of the trace of the stress tensor.

[1] T. J. Leighton, *The Acoustic Bubble* (Academic, San Diego, 1994).
[2] A. Shima and T. Tsujino, ''On the dynamics of bubbles in polymer aqueous solutions,'' Appl. Sci. Res. **38**(2), 255–263 (1982).
[3] H. S. Fogler and J. D. Goddard, ''Collapse of spherical cavities in viscoelastic fluids,'' Phys. Fluids **13**(5), 1135–1141 (1970).
[4] R. Y. Ting, ''Viscoelastic effect of polymers on single bubble dynamics,'' AIChE J. **21**(4), 810–813 (1975).
[5] I. Tanasawa and W. J. Yang, ''Dynamic behavior of a gas bubble in viscoelastic liquids,'' J. Appl. Phys. **41**(1), 4526–4531 (1970).
[6] A. Shima, T. Tsujino, and H. Nanjo, ''Nonlinear oscillations of gas bubbles in viscoelastic fluids,'' Ultrasonics **24**, 142–147 (1986).
[7] E. Zana and L. G. Leal, ''Dissolution of a stationary gas bubble in a quiescent, viscoelastic liquid,'' Ind. Eng. Chem. Fundam. **14**(30), 175–182 (1975).
[8] C. Kim, ''Collapse of spherical bubbles in Maxwell fluids,'' J. Non-Newtonian Fluid Mech. **55**, 37–58 (1994).
[9] A. Prosperetti, ''A generalization of the Rayleigh-Plesset equation of bubble dynamics,'' Phys. Fluids **25**(3), 409–410 (1982).
[10] R. B. Bird, R. C. Armstrong, and O. Hassager, *Dynamics of Polymeric Liquids*, 2nd ed. (Wiley, New York, 1987), Vol. 2.
[11] J. S. Allen and R. A. Roy, ''Dynamics of gas bubbles in viscoelastic fluids I. Linear viscoelasticity,'' J. Acoust. Soc. Am. **107**, 3167–3178 (2000).
[12] R. E. Apfel, ''Possibility of microcavitation from diagnositc ultrasound,'' IEEE Trans. Ultrason. Ferroelectr. Freq. Control **33**, 139–142 (1986).
[13] R. E. Apfel and C. K. Holland, ''Gauging the likelihood of cavitation from short pulse, low-duty cycle diagnostic ultrasound,'' Ultrasound Med. Biol. **17**, 179–18 (1991).
[14] R. A. Roy and J. B. Fowkles, ''Cavitation in water generated by pulse Doppler ultrasound,'' J. Acoust. Soc. Am. **96** (Pt. 2), 3306 (1994).
[15] M. Ceschina, A. Francescutto, and R. Naberjgoj, ''Threshold energy for transient cavitation-free bubbles,'' Acustica **40**, 105–107 (1978).
[16] C. W. Gear and K. W. Tu, ''The effect of variable mesh size on the stability of multistep methods,'' SIAM (Soc. Ind. Appl. Math.) J. Numer. Anal. **11**(5), 1025–1043 (1974).
[17] E. L. Stiefel and G. Scheifele, *Linear and Regular Celestial Mechanics* (Springer-Verlag, New York, 1971).
[18] G. J. Lastman, R. A. Wentzell, and A. C. Hindmarsh, ''Numerical solution of a bubble cavitation problem,'' J. Comput. Phys. **28**, 56–64 (1978).
[19] C. E. Pearson, ''On a differential equation of boundary layer type,'' J. Math. Phys. **47**, 134–154 (1968).
[20] H. G. Flynn and C. C. Church, ''Transient pulsations of small gas bubbles in water,'' J. Acoust. Soc. Am. **84**, 985–998 (1988).
[21] A. C. Guyton, A. E. Taylor, and H. Granger, *Circulatory Physiology II: Dynamics and Control of Body Fluids* (W. B. Saunders, Philadelphia, 1975).
[22] J. F. Vincent, *Structural Biomaterials* (Princeton University Press, Princeton, 1990).
[23] D. F. Gaitan, L. A. Crum, C. C. Church, and R. A. Roy, ''Sonoluminscence and bubble dynamics for a single stable cavitation bubble,'' J. Acoust. Soc. Am. **91**, 3166–3183 (1992).

Analysis and comparison of four anhysteretic polarization models for lead magnesium niobate[a)]

Jean C. Piquette[b)]
Naval Undersea Warfare Center, 1176 Howell Street, Newport, Rhode Island 02841

Ralph C. Smith
Center for Research in Scientific Computation, North Carolina State University, Raleigh, North Carolina 27695-8205

(Received 29 February 2000; revised 6 May 2000; accepted for publication 25 July 2000)

Four anhysteretic polarization models that have been used in the literature to evaluate data acquired from lead magnesium niobate (PMN) are analyzed and compared. Derivations of two of the models from assumed spatial distributions of dipole energy states, using first physical principles, are presented. A third model is derived from a suitable integral averaging calculation. These derivations are used as the basis for developing an integral equation for determining an energy-state distribution that produces a fourth model, which was not originally formulated in terms of an assumed distribution. A new polarization function is also presented. Excellent approximations to each of the four polarization functions of interest can be deduced from this new polarization function by adjusting the numerical value of just a single parameter. An application of two of the models to data is presented. It is shown that it can be necessary to consider a sample to be an admixture of two distinct species of poles, in the sense that two polarization functions must be added together in order to accommodate the data. © *2000 Acoustical Society of America.* [S0001-4966(00)06110-5]

PACS numbers: 43.38.Ar [SLE]

I. INTRODUCTION

Four anhysteretic polarization models have been used in the literature to analyze data acquired from lead magnesium niobate (PMN). These include (1) a model introduced by Langevin[1] (the ''Langevin'' model); (2) a model introduced by Zhang and Rogers[2] (the ''Ising Spin'' model); a model introduced by Piquette and Forsythe[3] (the ''Square Root'' model); and a model introduced by Smith and Hom[4] (the ''Preferred Orientation'' model). As part of an ongoing research program that seeks to understand the basic physics of this particular group of active acoustical (transducer) materials, we review, analyze, and compare the existing models, and provide a framework in which all four are shown to be equivalent in the sense that they are special cases of a physical discrete polarization model.

The fact that four apparently quite different mathematical functions can be used to accommodate PMN data may seem quite troubling, since the mathematical structure of the models is so different. However, it will be seen here that when viewed from a fundamental physical perspective, each of these very different polarization functions merely represents a slightly different distribution of energy states available to the system.

Introducing a dimensionless electric field parameter x, and considering numerical parameters that cause all the models to have a unity slope near $x=0$ and to saturate to unity polarization as $x\to\infty$, the models can be expressed by the following equations:

$$P_{\text{Langevin}}(x)=\coth(3x)-\frac{1}{3x}, \tag{1}$$

$$P_{\text{Ising Spin}}(x)=\tanh(x), \tag{2}$$

$$P_{\text{Square Root}}(x)=\frac{x}{\sqrt{1+x^2}}, \tag{3}$$

and

$$P_{\text{Preferred Orientation}}(x)=-1+\frac{\pi^2}{27x^2}+\frac{4\ln(1+e^{3x})}{3x}+\frac{4\,\text{Li}_2(-e^{3x})}{9x^2}, \tag{4}$$

where Li_2 denotes the polylogarithm function[5] of order 2. The dimensionless field parameter x is defined as

$$x\equiv\frac{p_0E}{k_BT}, \tag{5}$$

where p_0 denotes an elementary dipole strength of a single dipole, E is the electric field, T is the (absolute) temperature, and k_B is Boltzmann's constant.

A plot comparing all four functions of interest, in dimensionless terms, is given in Fig. 1. In view of the significant differences in the theoretical formulations of the models, as well as the evident differences between the equations that express the models as shown in Eqs. (1)–(4), the plots are unexpectedly similar. Moreover, the similarity seen between the Square Root and Preferred Orientation models is remarkable.

In Sec. II we present a brief review of solution methods from statistical mechanics. Here we also derive the Langevin and Ising Spin models from assumed dipole energy-state distributions, and we review how the discrete sums arising in

[a)]A preliminay version of this article was presented at the 1999 PMN meeting held at Alfred University, Alfred, NY, 4 October 1999.
[b)]Electronic mail: piquettejc@npt.nuwc.navy.mil

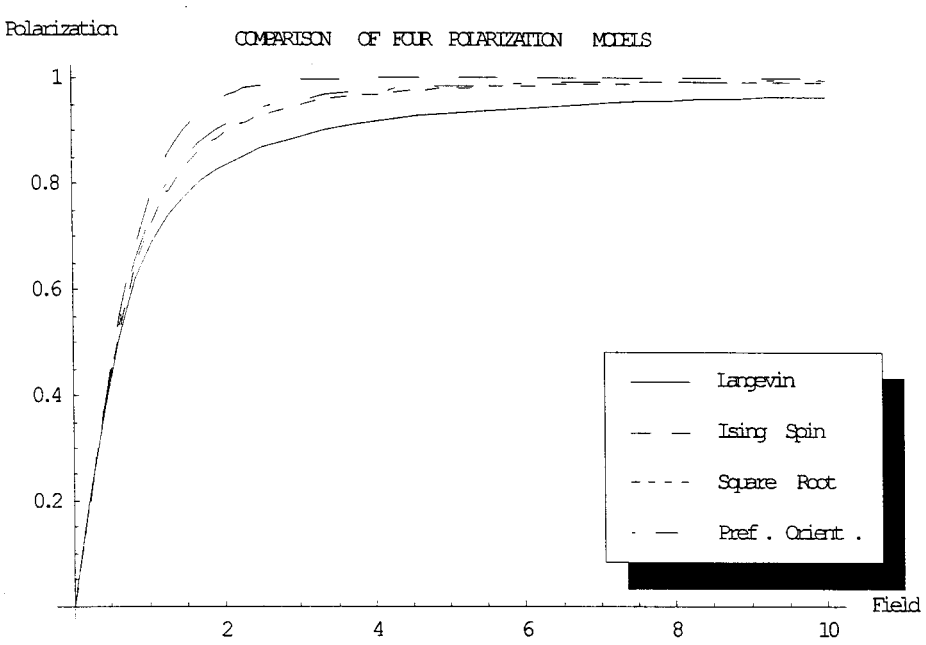

FIG. 1. A comparison of the four polarization functions expressed in dimensionless terms. All functions have been normalized to have unity slope near the origin and to saturate to unity polarization.

the statistical derivations can be replaced by integrals. We also introduce a ''weighting'' function w for describing the energy-state distribution. A physical interpretation of w is provided. An integral equation that can be used to deduce a dipole energy-state distribution from a given polarization function is developed in Sec. III. The equations arising in the derivations presented in Sec. II are used as ''templates'' to produce this integral equation. In Sec. IV we present a demonstration of a symmetry property of w. A method for solving the integral equation is presented in Sec. V, and solutions are obtained in Sec. VI. In Sec. VII, the continuous dipole energy-state distributions considered in the preceding sections are interpreted in terms of a new model, the ''Discrete'' polarization model. This one model subsumes all four of the polarization models considered here. Two of the polarization models (Ising Spin and Square Root) are fitted to data in Sec. VIII. Here it is pointed out that two species of poles appear to be present in the sample analyzed, owing to the fact that a sum of two polarization functions is required to effect the fit. A summary, discussion, and the conclusions are presented in Sec. IX. Finally, a derivation of the interval of convergence of the Taylor series for the Square Root model, which is needed to establish the validity of the solution, is provided in an Appendix.

II. DERIVATIONS FROM STATISTICAL MECHANICS

The correct statistical distribution for analyzing the behavior of polarization domains is the Maxwell–Boltzmann distribution, because the domains are *distinguishable*. We therefore formulate each of the polarization functions using this distribution.

The average number of particles in energy state j for a system of particles obeying the Maxwel–Boltzmann statistics is given by[6]

$$\overline{n}_j = N \frac{e^{-\beta u_j}}{\Sigma_i e^{-\beta u_i}}, \tag{6}$$

where N is the total number of particles in the system, u_j is the energy of state j, and $\beta \equiv 1/k_B T$, where k_B is Boltzmann's constant and T is the (absolute) temperature. The exponential in the numerator is usually called the Boltzmann factor. The sum in the denominator is called the partition function,[7] and is usually denoted by Z. The sum is taken over all energy states available to the system. Often the density of energy states available to a system is such that the partition-function sum can be replaced by an integral. This approach will be used here.

For a dipole of strength p_0, oriented at angle ϑ with respect to an external electric field E, the energy is given by[8] $u = -p_0 E \cos\vartheta$. In deriving the distributions of interest to us, we assume all dipoles have the same strength p_0 and that such dipoles differ only in their orientation angle ϑ. Hence, the partition function is given by

$$Z = \sum_j e^{p_0 E \cos\vartheta_j / k_B T}. \tag{7}$$

Rewriting the equation for the average number of particles in the jth state, given by Eq. (6), in terms of the partition function Z gives

$$\overline{n}_j = \frac{N}{Z} \mathrm{Exp}\left(\frac{p_0 E \cos\vartheta_j}{k_B T} \right). \tag{8}$$

The total sample polarization P is computed by summing the contributions from all states; thus

$$P = \sum_j \overline{n}_j p_0 \cos\vartheta_j, \tag{9}$$

where $\overline{n}_j$ is given by Eq. (8). Here, as previously mentioned, it has been assumed that every dipole is characterized by the same elementary pole strength p_0. Thus $p_0 \cos\vartheta_j$ in Eq. (9) denotes, for a dipole oriented at angle ϑ_j, the component of the elementary polarization pointing in the direction of the external electric field. (In all the polarization models considered here, it is assumed that there is no *net* polarization com-

ponent transverse to the applied field. This is equivalent to assuming azimuthal symmetry, meaning that the distribution of dipoles in all cases is independent of the spherical coordinate angle φ.)

A. Replacing sums by integrals

When the density of states available to the system is sufficiently high, the summation of the partition function in Eq. (7) may be replaced by an integral of the form

$$Z(E)=\int_0^{\pi} w(\vartheta)\mathrm{Exp}\left(\frac{p_0 E\cos\vartheta}{k_B T}\right)\sin\vartheta\, d\vartheta. \tag{10}$$

Here, $w(\vartheta)$ denotes the density of states and the $\sin(\vartheta)d\vartheta$ factor derives from the area of the unit sphere, $d\Omega = 2\pi\sin\vartheta\, d\vartheta$, which is associated with the volume of a unit cell in phase space for spherical coordinates under the presumption of azimuthal symmetry. The density function $w(\vartheta)$ is defined to include the factor 2π.

Under circumstances in which the partition-function summation of Eq. (7) can be replaced by the integration of Eq. (10), Eq. (8) is also replaced with a corresponding expression that represents a continuous, rather than a discrete, distribution. The continuous-system version is

$$dN=\frac{N}{Z(E)}w(\vartheta)e^{p_0 E\cos\vartheta/k_B T}\sin\vartheta\, d\vartheta, \tag{11}$$

where the differential dN represents the number of ''particles'' (dipoles in the cases of interest) between ϑ and $\vartheta+d\vartheta$. Here, as in Eq. (10), $w(\vartheta)$ is considered to be a ''weighting'' function related to the density of dipole energy states. It also should be noted that Eqs. (10) and (11) are consistent, in the sense that integrating both sides of Eq. (11) yields Eq. (10).

The continuous-system analog of Eq. (9) is

$$P=\frac{p_0 N}{Z(E)}\int_0^{\pi} w(\vartheta)e^{p_0 E\cos\vartheta/k_B T}\cos\vartheta\sin\vartheta\, d\vartheta. \tag{12}$$

As in Eq. (9), $p_0\cos\vartheta$ denotes the component of an elementary dipole pointing in the direction of the applied electric field E. Equation (12) is formulated from Eq. (11) by multiplying by $p_0\cos\vartheta$ and integrating on ϑ from 0 to π.

When the density of states available to a system is low, the usual procedure adopted is to formulate the statistics using the discrete equations given by Eqs. (7)–(9), and to reserve integral formulations such as given in Eqs. (10)–(12) for systems having a continuous density of available states. Although initially we will follow this prescription, eventually we will adopt the procedure of using Eqs. (10)–(12) even for discrete systems that have only a small number of available states. We do so because we are interested in both discrete and continuous systems, and it is important that all systems are formulated in a similar fashion. As we will see, this can be done by including suitable Dirac delta functions in the definition of the weighting function w appearing in the continuous-system equations.

B. Langevin polarization

The Langevin model incorporates the assumption that the dipoles are free to align with any position in space, with the density of energy states being uniformly distributed in phase space. The *probability* of selecting a particular state is controlled by the Boltzmann factor, $\mathrm{Exp}(p_0 E\cos\vartheta/k_B T)$. The assumption that the density of energy states is uniformly distributed in phase space means that the weighting function w becomes

$$w_{\mathrm{Langevin}}(\vartheta)=1. \tag{13}$$

Thus, the partition function of Eq. (10) becomes

$$Z_{\mathrm{Langevin}}=\int_0^{\pi}\mathrm{Exp}(p_0 E\cos\vartheta/k_B T)\sin\vartheta\, d\vartheta. \tag{14}$$

Carrying out the integral in Eq. (14) gives

$$Z_{\mathrm{Langevin}}=\frac{2k_B T}{p_0 E}\sinh\left(\frac{p_0 E}{k_B T}\right). \tag{15}$$

Equation (12) for the total polarization becomes

$$P_{\mathrm{Langevin}}=p_0(N/Z_{\mathrm{Langevin}})\times\int_0^{\pi}\mathrm{Exp}(p_0 E\cos\vartheta/k_B T)\cos\vartheta\sin\vartheta\, d\vartheta. \tag{16}$$

Carrying out the integral and substituting Z_{Langevin} as given by Eq. (15) produces the Langevin polarization function,

$$P_{\mathrm{Langevin}}=p_0 N\left[\coth\left(\frac{p_0 E}{k_B T}\right)-\frac{k_B T}{p_0 E}\right]. \tag{17}$$

C. Ising spin and preferred orientation models

The Ising Spin model incorporates the simple assumption that the available energy states are all oriented at an angle of $\vartheta=0$ or $\vartheta=\pi$ with respect to the external field. (The probability of a dipole *occupying* either orientation, however, is mediated by the Boltzmann factor.) The Preferred Orientation model involves orientations over more general angles with respect to the field. This model can be derived as an average over the polarizations obtained when the available energy states are associated with a ''preferred'' angular orientation. (The average is carried out over *all possible energy-state orientations with respect to the external field*. The ''with or against the external field'' orientation assumed by the Ising Spin model is only one such orientation out of a continuum infinity of possible orientations.) Both the Ising Spin and Preferred Orientation models can be formulated in a similar manner if a two-state system is considered in which the orientation angle associated with the available energy states is initially treated as arbitrary.

Consider therefore a two-state system in which the dipoles can orient only at the two angles $\vartheta=\vartheta_0$ and $\vartheta=\vartheta_0+\pi$ with respect to the external field, where ϑ_0 is an arbitrary fixed angle. Evaluating the discrete partition function of Eq. (7) as a sum over the two states available to the system gives

$$Z = 2\cosh\left(\frac{p_0 E\cos\vartheta_0}{k_B T}\right). \tag{18}$$

Using Eq. (8) to evaluate the average number of particles in state j yields

$$\overline{n}_j = \frac{N\,\mathrm{Exp}\left(\frac{p_0 E\cos\vartheta_j}{k_B T}\right)}{2\cosh\left(\frac{p_0 E\cos\vartheta_0}{k_B T}\right)}, \tag{19}$$

where the partition function given by Eq. (18) has been substituted. Using Eq. (19) to help evaluate total polarization given by Eq. (9), with the sum again taken over the two states available to the system, gives

$$P(\vartheta_0) = p_0 N\cos\vartheta_0\tanh\left(\frac{p_0 E\cos\vartheta_0}{k_B T}\right). \tag{20}$$

This is the polarization function for dipoles that can orient only at the two angles ϑ_0 and $\vartheta_0+\pi$ with respect to the external field, which we have been seeking. By letting $\vartheta_0 = 0$ in Eq. (20) we obtain the Ising Spin polarization function,

$$P_{\text{Ising Spin}} = p_0 N\tanh\left(\frac{p_0 E}{k_B T}\right). \tag{21}$$

Next, to deduce the Preferred Orientation model, we calculate a weighted average of the polarization function given by Eq. (20), evaluated over all angles ϑ_0 between 0 and π, with weight specified by the differential area of the unit sphere. That is, we formulate the Preferred Orientation model as

$$P_{\text{Preferred Orientation}} = \frac{\int_0^\pi P(\vartheta_0)\sin\vartheta_0\,d\vartheta_0}{\int_0^\pi \sin\vartheta_0\,d\vartheta_0}, \tag{22}$$

with $P(\vartheta_0)$ given by Eq. (20). Carrying out the integrations of Eq. (22) gives

$$P_{\text{Preferred Orientation}} = -\frac{Np_0}{2} + \frac{\pi^2 k_B^2 N T^2}{24E^2 p_0} + \frac{k_B N T\ln\left[1+\mathrm{Exp}\left(\frac{2Ep_0}{k_B T}\right)\right]}{E} + \frac{k_B^2 N T^2\,\mathrm{Li}_2\left[-\mathrm{Exp}\left(\frac{2Ep_0}{k_B T}\right)\right]}{2E^2 p_0}. \tag{23}$$

Here, $E>0$ has been assumed so that this (somewhat) simplified result will obtain. [This derivation differs somewhat from the original one given in Ref. 4, but the result given by Eq. (23) is mathematically identical to the result given there, at least for positive E. In Eq. (23), Li_2 again denotes the polylogarithm of order 2.]

We now follow our program of expressing even the discrete cases in terms of the continuous-system description, and reformulate the Ising Spin model in terms of Eqs. (10)–(12). This can be done by introducing a weighting function w given by

$$w_{\text{Ising Spin}}(\vartheta) = \frac{\delta(\vartheta)+\delta(\vartheta-\pi)}{\sin\vartheta}, \tag{24}$$

as can be verified by direct substitution. (Here, δ denotes the Dirac delta function.) That is, substituting Eq. (24) into Eq. (10) recovers the partition function [Eq. (18), with ϑ_0 set to zero]. Similarly, substituting Eq. (24) into Eq. (12) recovers the Ising Spin polarization function of Eq. (21). Finally, substituting Eq. (24) into Eq. (11) for the total number of particles produces a tautology when integrated, thus establishing the validity of the expression given by Eq. (24) for the Ising Spin weighting function.

D. Physical interpretation of the weighting function *w*

At this point we develop a physical picture for the weighting function w. From its appearance in the calculation of the partition function of Eq. (10), it is clear that w represents *the number of dipole energy states per unit area available to the system*. This interpretation follows from the fact that the partition function derives from a sum (or integral) over all energy states. The ''area'' referred to here is not the surface area of the sample, of course, but rather the differential area of the unit sphere, $2\pi\sin\vartheta\,d\vartheta$. This area is associated with an elementary volume in phase space, as expressed in the spherical coordinate system. (Recall that ϑ is the angle between an elementary dipole and the applied field. Consequently, the interpretation of w as the ''number of dipole energy states per unit area'' includes *all* states throughout the sample that happen to point in the direction ϑ, regardless of the physical location of the dipoles that happen to occupy these states.) As the applied electric field strength approaches zero, w can be seen to represent the actual spatial distribution of dipoles assuming the angular direction ϑ with respect to the ever-weakening field. On the other hand, as the external field strength E increases, the Boltzmann factor appearing in Eq. (10) modifies the probability of a dipole occupying any particular angular position. Owing to its mathematical structure, it is clear that the Boltzmann factor makes the energy state at $\vartheta=0$ increasingly probable as the strength of the applied field increases. As the external field strength increases without bound (that is, as saturation is approached), only the $\vartheta=0$ position will have a nonzero probability of occupation.

The weighting function is independent of all variables but ϑ. This can be understood on a purely mathematical basis, in that the function w arises in replacing the partition function summation over energy states (which differ from each other only through the orientation angle ϑ) by an integral over ϑ. Physical variables such as E and T do not affect the presence, or character, of the energy states available to the system, only their level of occupation. Thus, as the electric field changes the number of dipoles occupying any given state varies, but not the state itself. So, for example, the uniform weighting function w that characterizes the Langevin model [Eq. (13)] remains uniform as the external field increases or decreases in strength. However, the number of these states that are actually occupied by physical dipoles is determined by the Boltzmann factor, which indeed does depend on the physical variables E and T.

Without the presence of the Boltzmann factor the functional forms assumed by w for the cases studied thus far, given in Eqs. (13) and (24), would be rather confusing. For example, consider the fact that w in the Langevin case is independent of ϑ. If w were the only factor present, the dipoles would be completely randomly distributed in space, and no net polarization could arise. Since the Boltzmann factor approaches unity as E approaches zero, a random distribution of dipoles is precisely what the Langevin model predicts as the cause of a vanishing net sample polarization at the zero applied field. (Of course, *all* the models predict zero net polarization at zero field strength, as Fig. 1 shows. However, the cause of the zero net is different for each polarization model.)

On the other hand, referring to Eq. (24), the physical picture for the Ising Spin case is rather different. The presence of the two delta functions shows that only the energy states corresponding to $\vartheta=0$ and $\vartheta=\pi$ can *ever* have a nonnegligible probability of occupation, regardless of the electric field strength. Thus, *all* the dipoles in this model always align either with or against the external electric field. So as E approaches zero in this case, the zero net polarization (see Fig. 1) is achieved from an *equal* number of dipoles occupying states that are aligned with and against the external field, rather than the random spatial dipole distribution of the Langevin case. As E increases in strength the Boltzmann factor causes the energy state at the $\vartheta=0$ position to become increasingly probable, as in the Langevin model, and becomes the only occupied state at saturation.

III. FORMULATION OF THE INTEGRAL EQUATION

We now seek a weighting function for the distribution of energy states that will produce the Square Root polarization function. (Also of ancillary interest is the weighting function for the Preferred Orientation case.) We do so by formulating the problem in terms of an integral equation.

We start by noting that Eqs. (10) and (12) can be combined to give

$$P(x)=P_{\text{sat}}\frac{\int_0^{\pi} w(\vartheta)\text{Exp}(x\cos\vartheta)\sin\vartheta\cos\vartheta\,d\vartheta}{\int_0^{\pi} w(\vartheta)\text{Exp}(x\cos\vartheta)\sin\vartheta\,d\vartheta}, \quad (25)$$

where we have introduced the notation

$$P_{\text{sat}}=p_0 N, \quad (26)$$

for the saturation polarization, and have used the dimensionless field parameter x defined in Eq. (5).

Rearranging Eq. (25), we obtain

$$\int_0^{\pi}[P_{\text{sat}}\cos\vartheta-P(x)]\text{Exp}[x\cos\vartheta]w(\vartheta)\sin\vartheta\,d\vartheta=0. \quad (27)$$

Equation (27) is a Fredholm equation of the first kind[9] for the unknown weighting function $w(\vartheta)$.

IV. SYMMETRY OF THE SOLUTION

Prior to attempting to solve Eq. (27) for the unknown weight $w(\vartheta)$ for the cases of interest, it is useful to show that the solution can be taken to be symmetric about $\vartheta=\pi/2$. To do so, it is only necessary to assume that $P(x)$ is an odd function, that is, $P(-x)=-P(x)$. This is a well-known polarization characteristic in the absence of hysteresis, and is exhibited by each of the functions given in Eqs. (1)–(4).

First, change the integration variable in Eq. (27) such that $\vartheta\rightarrow\pi-\vartheta$. Doing this and rearranging slightly gives

$$\int_0^{\pi}[P_{\text{sat}}\cos\vartheta+P(x)]\times\text{Exp}[-x\cos\vartheta]w(\pi-\vartheta)\sin\vartheta\,d\vartheta=0. \quad (28)$$

Now, letting $x\rightarrow-x$ in Eq. (28) and imposing the assumed odd symmetry of $P(x)$ gives

$$\int_0^{\pi}[P_{\text{sat}}\cos\vartheta-P(x)]\times\text{Exp}[x\cos\vartheta]w(\pi-\vartheta)\sin\vartheta\,d\vartheta=0. \quad (29)$$

A comparison of Eq. (29) with Eq. (27) shows that $w(\vartheta)=w(\pi-\vartheta)$, which demonstrates symmetry about $\vartheta=\pi/2$. Strictly, this final comparison necessarily requires the equality of $w(\vartheta)$ and $w(\pi-\vartheta)$ only if the solution to the integral equation is unique, which it is not [as is evident from the fact that replacing $w(\vartheta)$ with itself multiplied by an arbitrary constant in Eq. (27) will not affect the equality]. However, the present demonstration suggests that a solution with this symmetry is *sufficient* for solving the integral equation of interest, and is clearly consistent with the odd symmetry of the known polarization function $P(x)$.

V. SOLVING THE INTEGRAL EQUATION

Since the Fourier cosine series is complete with respect to functions in the interval $\pi\geqslant\vartheta\geqslant0$, it is convenient to represent the unknown function w in terms of such a series.[10] Moreover, the symmetry of the solution about $\pi/2$ permits further simplification, in that only the even terms need be retained under such symmetry. Thus, we will introduce the representation

$$w(\vartheta)=a_0+\sum_{n=1}^{m} a_n\cos(2n\vartheta), \quad (30)$$

for the unknown weight $w(\vartheta)$. The constant m denotes the number of terms in the Fourier cosine series. Here, a_0-a_m are unknown expansion coefficients.

Equation (30) and the polarization function $P(x)$ for which it is desired to determine w are both substituted into Eq. (27) as a first step in the solution process. The expansion coefficients are determined by expanding the integrand of Eq. (27) in a Taylor series about a selected expansion point $x=x_0$. The resulting series can be integrated term by term. Coefficients of the individual terms of the resulting Taylor series can then separately be set equal to zero to produce simultaneous algebraic equations, which are then solved for the unknown expansion coefficients of Eq. (30).

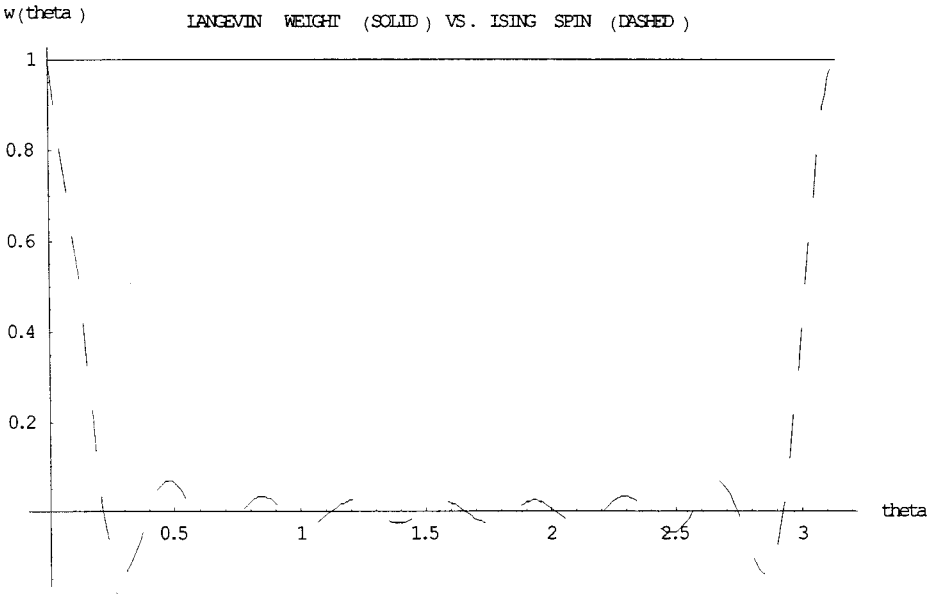

FIG. 2. A comparison of weights recovered by solving the integral equation given by Eq. (27) for the Langevin (solid line) and Ising Spin (dashed line) cases. The plots should be compared with the analytical expressions given by Eq. (13) and Eq. (24). Weights have been normalized to unity.

VI. SOLUTIONS

A. Recovering the known cases

As a verification of the solution methodology, we first recover the weighting functions in the known cases, viz., the Ising Spin and Langevin cases. (Although the Preferred Orientation model has been derived analytically, strictly speaking we have not yet obtained a dipole distribution that directly produces that polarization function. Rather, we have deduced the Preferred Orientation model by performing an averaging calculation over polarization functions for which the distribution is known.)

To recover the weights for the two known cases, we substitute the dimensionless forms of these polarization functions, Eqs. (1) and (2), into the integral equation and solve for $w(\vartheta)$, using the approach described in Sec. V. The results of this procedure are presented in Fig. 2. (Here, and in what follows, the weights have been normalized to unity.) In producing the results shown in Fig. 2, the value $m=8$ was used in Eq. (30). The result for the weighting function obtained for the Langevin model (solid line) is clearly suggestive of the unity analytical result of Eq. (13). In the case of the Ising Spin model (dashed line) although the delta functions (and the singularity caused by the sine function in the denominator) cannot be recovered exactly, the shape of the recovered function seen in Fig. 2 is clearly suggestive of the analytical weight given by Eq. (24).

B. Weighting functions for the Square Root and Preferred Orientation cases

Since part of the solution procedure requires carrying out a Taylor series expansion of the integrand of Eq. (27), it is important to establish the interval of convergence of the Taylor series of the polarization function for the Square Root model. This matter is addressed in the Appendix. (Strictly, the interval of convergence should be determined for the Preferred Orientation model as well. Since this case is only of ancillary interest here though, and owing to its complexity, we will simply assume that the interval of convergence is at least as great as for the Square Root case, derived in the Appendix. The similarity of the Square Root and Preferred Orientation models seen in Fig. 1 suggests this is reasonable.)

Applying the solution methods outlined in Sec. V to the Square Root polarization function given by Eq. (3), and using $m=8$ again in Eq. (30), produces the weighting function shown in Fig. 3, solid line. For this calculation the required Taylor series expansion of the integrand was carried out about the dimensionless field value of $x_0=2$. The interval of convergence of this series, as determined from Eq. (A9) of the Appendix, is $-0.23<x<4.23$.

Next, we turn to the case of the Preferred Orientation model. The result of solving for the weight in this case is shown in Fig. 3, dashed line. The similarity to the Square Root weight is evident. Negative values occurring in each of the distributions of Fig. 3 are probably artifacts of the solution methodology used. Elimination of the negative values is accomplished in Sec. VII.

C. Recovery of the polarization functions

By substituting the various weighting functions, as depicted in Figs. 2 and 3, into Eq. (25) the original polarization functions are recovered. In Figs. 4(a)–(d) are shown the results obtained for all four of the polarization functions under consideration. The recovered functions are denoted by dots, and are sampled at several points. For comparison, the known exact functions (solid line curves) are also presented. As can be seen, the recoveries are quite good in all cases.

VII. THE "DISCRETE" POLARIZATION MODEL

The continuous weighting functions plotted in Fig. 3 are suggestive of the energy-state distributions required to produce the Square Root and Preferred Orientation models. The distributions suggest a strong concentration of states in the $\vartheta=0$ and $\vartheta=\pi$ directions, with additional nonzero contributions at other angular positions. However, it is difficult to ascertain the physical significance of the distributions at po-

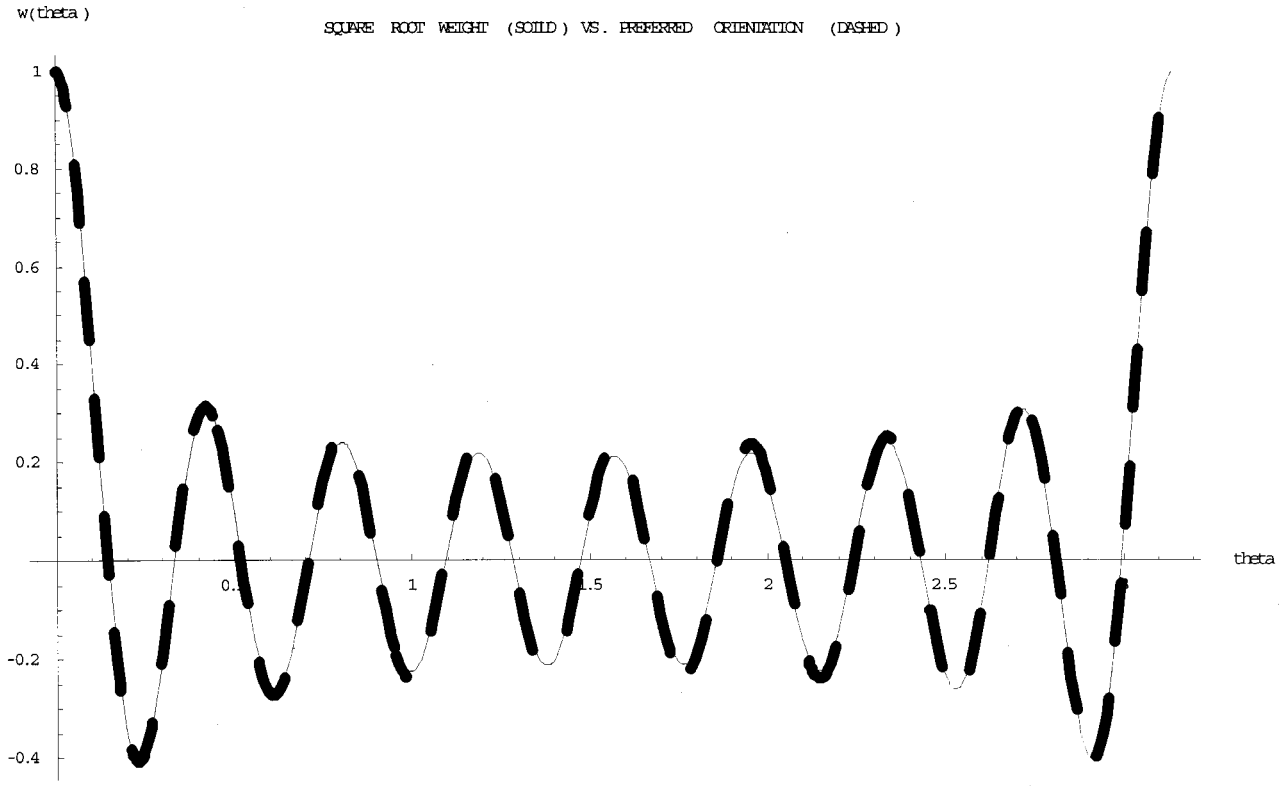

FIG. 3. A comparison of weights recovered by solving the integral equation given by Eq. (27) for the Square Root (light solid line) and Preferred Orientation (heavy dashed line) cases.

sitions between the extremes, owing to what are apparently artifacts of the methodology used to produce the results shown. One obvious artifact is reflected by the nonphysical negative values seen for the weighting functions for various angle ranges. Nonetheless, the results of Fig. 3 can be used to guide further analysis. In particular, we now seek a *discrete* energy-state distribution having characteristics similar to those seen for the continuous cases shown in Fig. 3, but with only non-negative weighting contributions.

We begin the analysis by seeking a discrete analog of Eq. (25). To achieve this end, suppose first that the energy states available to the system correspond to discrete angular positions. Assume that these positions are separated by M uniform angular increments between $\vartheta=0$ and $\vartheta=\pi/2$, and that there is a corresponding set of increments between $\vartheta=\pi/2$ and $\vartheta=\pi$. Thus, between $\vartheta=0$ and $\vartheta=\pi/2$ there are dipole energy states occurring at the $M+1$ uniformly spaced angular positions given by $\vartheta=\vartheta_j=j\pi/2M$, for $j=0,1,...,M$. There are also corresponding dipole energy states between $\vartheta=\pi/2$ and $\vartheta=\pi$, at the $M+1$ symmetrically located angular positions $\vartheta=\pi-\vartheta_j$. With these definitions, it is seen that the discrete partition function of Eq. (7) may be written in the form

$$Z=\sum_{j=0}^{M}\left\{\mathrm{Exp}\left[x\cos\left(\frac{j\pi}{2M}\right)\right]+\mathrm{Exp}\left[x\cos\left(\pi-\frac{j\pi}{2M}\right)\right]\right\}, \tag{31}$$

with x the dimensionless field parameter defined in Eq. (5). Equation (31) can be re-expressed as

$$Z=2\cosh(x)+2\sum_{j=1}^{M}\cosh\left[\cos\left(\frac{j\pi}{2M}\right)\right], \tag{32}$$

where the $j=0$ term has been broken off from the sum for convenience. Evaluating Eq. (9) in a similar way for this model gives

$$P=P_{\mathrm{sat}}\frac{\sinh(x)+\Sigma_{j=1}^{M}\cos\left(\frac{j\pi}{2M}\right)\sinh\left[x\cos\left(\frac{j\pi}{2M}\right)\right]}{\cosh(x)+\Sigma_{j=1}^{M}\cosh\left[x\cos\left(\frac{j\pi}{2M}\right)\right]}, \tag{33}$$

with P_{sat} the saturation polarization defined in Eq. (26).

Equation (33) expresses the polarization when there is a distribution of energy states at equally spaced angles [although the state-counting scheme as described yields two (degenerate) states at $\vartheta=\pi/2$)]. Consider next a related situation in which there is also a large cluster of energy states near $\vartheta=0$, and an identical cluster near $\vartheta=\pi$, in addition to the uniformly spaced states. Such clusters would lead to a large number of terms of the approximate form $\sinh(x)$ in the numerator, and an (equally) large number of terms of the approximate form $\cosh(x)$ in the denominator, of Eq. (33). In other words, such a system would have a polarization function similar to Eq. (33), except that there would be many almost-equal terms of the form of the two broken-off terms. To good accuracy, these similar terms could be lumped into a single $\sinh(x)$ term (in the numerator) and a single $\cosh(x)$ term (in the denominator), with each such term having a (common) multiplier greater than unity. (This assumes all the

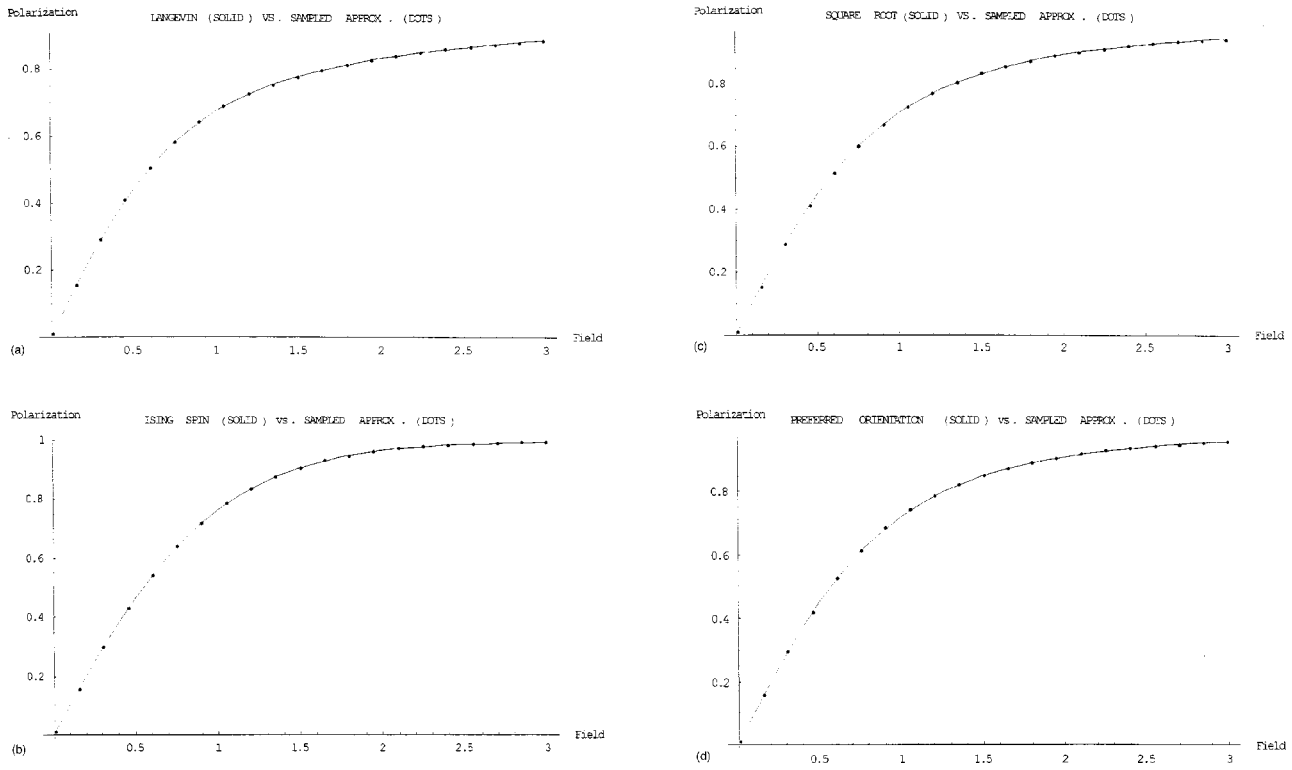

FIG. 4. A comparison of the recovered polarization functions [obtained by substituting the computed weights into Eq. (25)] sampled at discrete values of x (dots) compared with known exact polarization functions in each case (solid lines). The integrals of Eq. (25) were evaluated numerically. The value $m=8$ was used in Eq. (30) in the determination of the weights in all cases: (a) Langevin; (b) Ising Spin; (c) Square Root; and (d) Preferred Orientation.

other angular positions remain equally likely, but are much less likely than either $\vartheta=0$ or $\vartheta=\pi$.) Dividing through both the numerator and denominator of Eq. (33) by this common multiplier would then give an equation of the form

$$P=P_{\text{sat}}\frac{\sinh(x)+w\sum_{j=1}^{M}\cos\left(\frac{j\pi}{2M}\right)\sinh\left[x\cos\left(\frac{j\pi}{2M}\right)\right]}{\cosh(x)+w\sum_{j=1}^{M}\cosh\left[x\cos\left(\frac{j\pi}{2M}\right)\right]}. \tag{34}$$

In Eq. (34), w now represents a single numerical value, which is positive and *less* than (or equal to) unity. [Note the similarity of the discrete equation (34) to the continuous equation (25). Even greater similarity could be achieved if the broken-off sinh and cosh terms were reincorporated into the sums. This could readily be done by introducing a weight w_j, where $w_j=1$ for $j=0$ and $w_j=w$ for $j>0$.] In order to permit normalization of the kind used in producing Fig. 1, we now modify the dimensionless field parameter x to include a constant coefficient k, giving

$$P=P_{\text{sat}}\frac{\sinh(kx)+w\sum_{j=1}^{M}\cos\left(\frac{j\pi}{2M}\right)\sinh\left[kx\cos\left(\frac{j\pi}{2M}\right)\right]}{\cosh(kx)+w\sum_{j=1}^{M}\cosh\left[kx\cos\left(\frac{j\pi}{2M}\right)\right]}, \tag{35}$$

where the value of k is to be adjusted to give unity slope at the origin. If k is taken to have the value

$$k=\frac{2+2Mw}{2+(M-1)w}, \tag{36}$$

and if P_{sat} is taken to be unity, the polarization model of Eq. (35) is then normalized as in Fig. 1.

It will be appreciated that the ''Discrete'' polarization model of Eq. (35) has characteristics of all the models of interest. For example, notice that substituting $w=0$ in Eq. (35) [and Eq. (36)] immediately recovers the Ising Spin model of Eq. (21). Also, if w is taken equal to unity and M is taken to be large, the Discrete model of Eq. (35) will approach the Langevin model. As a test of this, w was set equal to 1 and M was set equal to 1000, and the resulting polarization function numerically compared with the Langevin function. The results of this calculation are shown in Fig. 5(a). As can be seen, the polarization associated with the continuous dipole distribution (solid line) and that associated with the discrete dipole distribution (dashed line) are quite similar. [However, the discrete Langevin model approaches the continuous Langevin model rather slowly as M is increased. For example, the difference between the normalized polarizations for the discrete and continuous models, averaged over 100 equally spaced points, is 3.58×10^{-3} for $M=100$. The average difference reduces to 3.54×10^{-3} for $M=1000$, and to 3.50×10^{-3} for $M=10\,000$.]

The Square Root model can be recovered from the Discrete polarization model of Eq. (35) to an excellent approximation by evaluating this equation for a large value of M and using a suitable numerical value for w. The required value for w can be determined from a least-squares calculation.

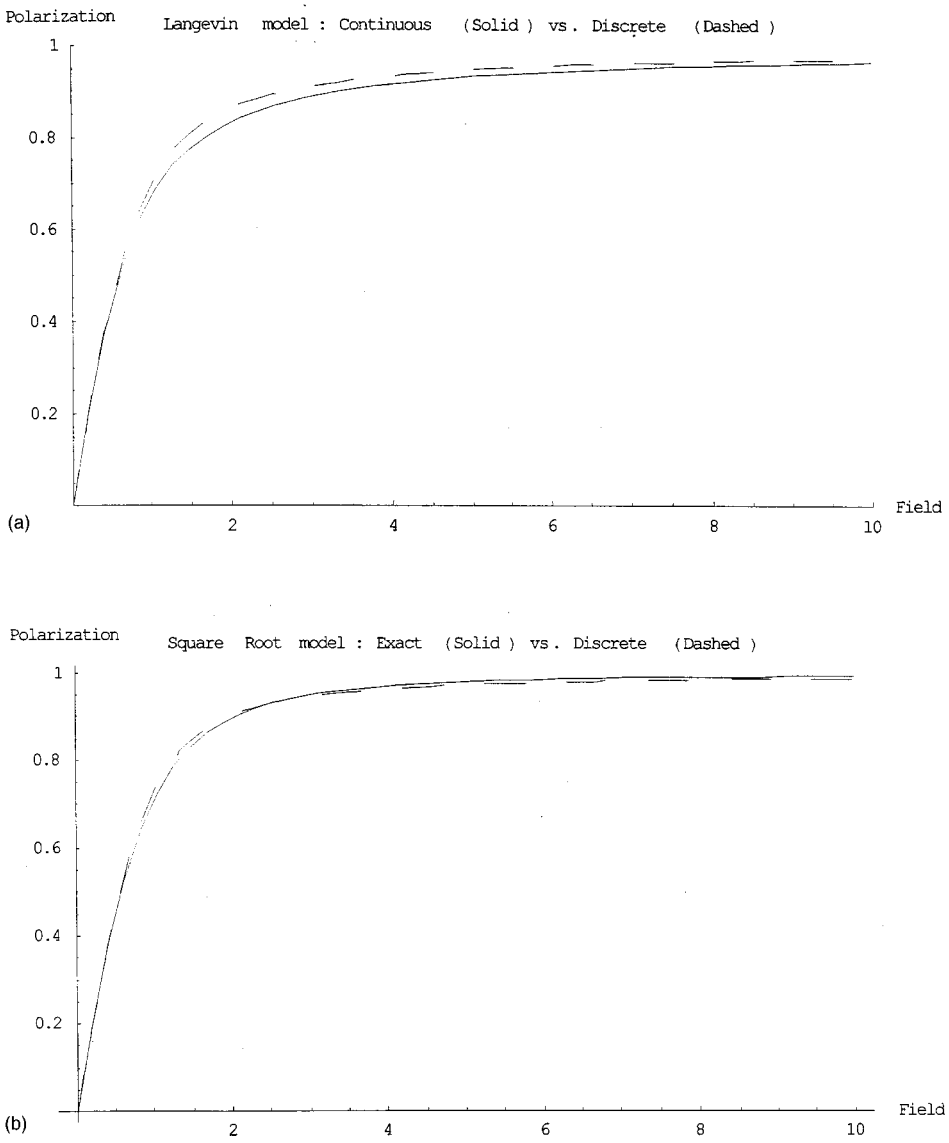

FIG. 5. Results obtained from analyzing the Discrete polarization model of Eq. (35). (a) Continuous dipole-distribution version of the Langevin polarization model (solid line) compared with the discrete version resulting from evaluating Eq. (35) with $w=1$ and $M=1000$ (dashed line). (b) Exact Square Root model (solid line) compared with the discrete version resulting from evaluating Eq. (35) with $M=100$ and least-squares fitting the resulting equation to 100 equally spaced samples of the exact equation (dashed line). The weight determined in the fit was $w=0.021\,457\,5$.

This was carried out by fitting Eq. (35) to the Square Root function sampled at 100 equally spaced points between $x=0$ and $x=10$, taking $M=100$ and using for k the value given by Eq. (36). The value of w produced by the fit is $w=0.021\,457\,5$. The results are summarized in Fig. 5(b). Here, the solid line is the exact Square Root model function, and the dashed line is Eq. (35) evaluated using $M=100$ and the fitted value of w. As can be seen, the agreement is quite good. This calculation is strongly suggestive of the fact that the Square Root model is consistent with a dipole distribution of the type considered here. This is a distribution having a high concentration of dipoles in the $\vartheta=0$ and $\vartheta=\pi$ directions, together with a uniform distribution of dipoles in the other angular directions with the constant weight as determined in the least-squares fit. (Thus, this is the sought-after distribution that produces the Square Root model with all non-negative weighting contributions.) Although the concentration of dipoles around any one angular position away from either $\vartheta=0$ or $\vartheta=\pi$ is significantly less than at either of these two dominant angles, the concentration is nonetheless sufficient to change the overall polarization value significantly. In fact, if only the $\vartheta=0$ and $\vartheta=\pi$ directions were contributing, the Ising Spin model would result [as is suggested from the fact that setting $w=0$ in Eq. (35) recovers the Ising Spin model]. If *all* directions were contributing equally, the Langevin model would result, as Fig. 5(a) suggests. Consequently, by taking M to be large and by continuously varying w from 0 to 1, the Discrete polarization function is seen to change in a continuous manner from the Ising Spin case to the Langevin case, with the specific numerical value of $w=0.021\,457\,5$ (for $M=100$) yielding the Square Root model.

Although the Discrete polarization model was not explicitly fitted to the Preferred Orientation model, the similarity of the Preferred Orientation model to the Square Root model, as seen in Fig. 1, suggests this would be no less successful than the results of Fig. 5(b).

VIII. APPLICATION TO DATA

In applications to experimental data, the four polarization functions tend to produce fits of similar quality. We consider only one explicit example, viz., the analysis of data acquired by Hackenberger.[11] In the interest of conciseness

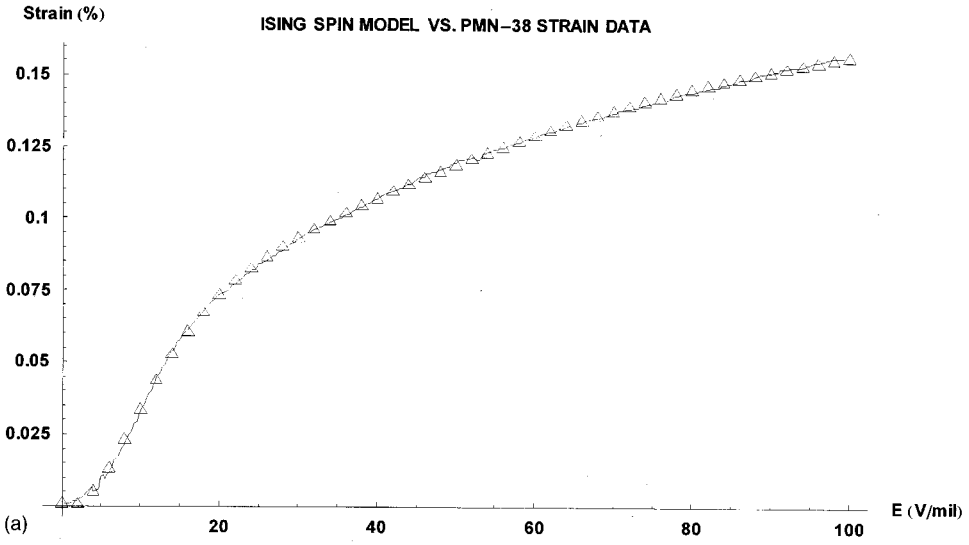

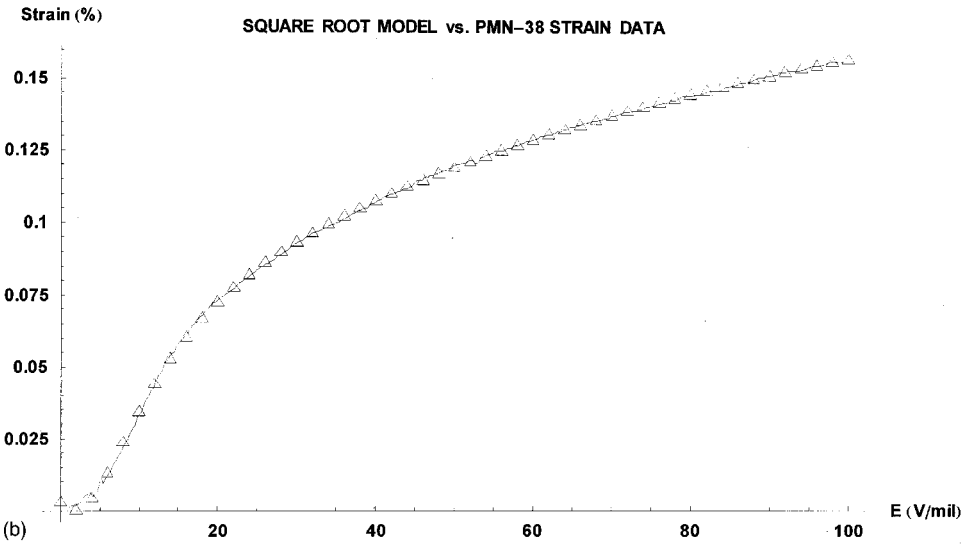

FIG. 6. Comparisons of models (open triangles) least-squares fitted to PMN-38 data (solid lines). To effect the fits, it was necessary to assume the samples contained two species of poles, in the sense that two of the respective polarization functions were added together. In each case, a constant term was also included in the fits to account for remanence. The units of the horizontal axis are those used in the original (Ref. 11) plots. (a) Ising Spin. (b) Square Root.

we consider applications of only two of the polarization models, viz., the Ising Spin and Square Root.

In Figs. 6(a) and (b) are shown fits of the data to these two polarization models. Open triangles are the fitted functions while solid lines represent the original data. In order to effect each of the fits, it was necessary to assume the sample contains two species of poles. That is, two independent functions had to be added together and simultaneously adjusted in order to fit the data. For each of the summed terms, two free parameters were adjusted. In addition, a single constant term was added to account for the effects of remanence. Thus, a total of five parameters were adjusted to produce the theoretical curves shown in each figure. Finally, since the data presented are strain and not polarization, the assumption of quadratic dependence of the strain upon polarization was also imposed.[3] (While five adjusted parameters used here might seem somewhat large, the reader should bear in mind that both the Ising Spin and Square Root models have been repeatedly shown to well accommodate PMN measurements. The present application merely suggests what each of these well-tested models might predict to occur should two types of PMN materials be mixed.)

As can be seen, the quality of the fits is quite good and is similar for the two models. This behavior is typical of that seen whenever these models are applied to data.

IX. SUMMARY, DISCUSSION, AND CONCLUSIONS

We have reviewed four polarization models that have been used in the literature to fit PMN polarization data. These are the Langevin, Ising Spin, Square Root, and Preferred Orientation models. The Langevin model assumes an initially random distribution of dipoles. The Ising Spin model assumes that all the dipoles always remain aligned either with or against the external field. The Square Root and Preferred Orientation models each subsume aspects of both the Langevin and Ising Spin models.

A new model, the Discrete polarization model, was introduced. This model can reproduce, to an excellent approximation, each of the four polarization models of interest by simply varying a single parameter between 0 and 1. The

most significant aspect of this new model is that it shows that the Square Root and Preferred Orientation models can be physically interpreted as arising partially from each of the mechanisms that give rise to the Ising Spin and Langevin models. That is, the two dominant energy states at $\vartheta=0$ and $\vartheta=\pi$, combined with a background of uniformly spaced energy states, is responsible for producing the Square Root and Preferred Orientation polarization models.

The Square Root and Preferred Orientation models produce remarkably similar normalized curves, as can be seen in Fig. 1, and these models may be indistinguishable in applications to data. However, it is sometimes necessary to consider a sample to be an admixture of two species of poles, in the sense that a sum of polarization functions may be required to fit the observations.

All four models do quite well in accommodating experimental data. The Discrete polarization model perhaps gives an understanding of why this is so, since differences between the models can be understood as corresponding to variations in the levels of uniform ''background'' dipoles.

ACKNOWLEDGMENTS

The Office of Naval Research (Jan Lindberg) supported the work of the first author. We gratefully acknowledge Dr. Guomao Yang of Royal Military College, Canada, for calling to our attention the data of Hackenberger, and for providing a digitized version of that data for our analysis. We also acknowledge helpful technical conversations with Dr. Craig L. Hom of Lockheed-Martin, Palo Alto, California.

APPENDIX. INTERVAL OF CONVERGENCE OF THE TAYLOR-SERIES EXPANSION OF THE SQUARE ROOT MODEL

The solution method employed here for determining the weighting function involves using a Taylor series expansion, in terms of the dimensionless field parameter x, of the integrand of Eq. (27). The integrand consists of a portion that contains the Boltzmann factor, which is an exponential with an infinite interval of convergence for all its Taylor series in x, and another portion that contains the polarization function $P(x)$. (It is sufficient to establish the convergence of the individual portions of the integrand, because then the convergence of the entire integrand follows. See Ref. 12.) For those polarization models for which there exist known weighting functions, it is not essential to establish the convergence of the Taylor series owing to the availability of the known functions, which can be used to check the validity of the recovered weights. (In fact, we recover the known cases primarily as a ''sanity check'' of the solution methodology.) However, in the case of the Square Root polarization model, no known weighting function is available. Hence, it is important to establish the interval of convergence of the underlying Taylor series representation in that case, since that establishes the field values over which the solution method is valid.

We first note that the Square Root polarization model, Eq. (3), is the derivative of the somewhat simpler function

$$g(x)=\sqrt{1+x^2}. \tag{A1}$$

Since the Taylor series for $g'(x)$ has the same interval of convergence[13] as that of $g(x)$, it suffices to determine the interval of convergence of $g(x)$.

It is helpful to deduce a formula for the nth derivative of $g(x)$. Re-expressing a formula from a standard table[14] in a more compact form, we get

$$\frac{d^n}{dx^n}(1+x^2)^p=\frac{\Gamma(p+1)n!(2x)^n}{(1+x^2)^{n-p}} \times\sum_{m=0}^{[n/2]}\frac{1}{m!(n-2m)!\Gamma(p-n+m+1)} \times\left(\frac{1+x^2}{4x^2}\right)^m, \tag{A2}$$

where $p=\frac{1}{2}$ for the case of interest, and the [ ] notation denotes truncation to the smallest integer value. The finite sum can be re-expressed using Gegenbauer polynomials[15] $C_n^{\lambda}(x)$, giving

$$\frac{d^n}{dx^n}(1+x^2)^p=(-1)^n n!\frac{x^n}{(1+x^2)^{n-p}} \times(1+1/x^2)^{n/2}C_n^{-p}\left(\frac{1}{\sqrt{1+1/x^2}}\right). \tag{A3}$$

The Taylor-series coefficients of $g(x)$ are given by $g^{(n)}(x_0)/n!$, where x_0 denotes the expansion point and the derivatives are evaluated with the aid of Eq. (A3). Thus, the Taylor series representation is

$$(1+x^2)^p=\sum_{n=0}^{\infty}(-1)^n(1+1/x_0^2)^{n/2}x_0^n(1+x_0^2)^{p-n} \times C_n^{-p}\left(\frac{1}{\sqrt{1+1/x_0^2}}\right)(x-x_0)^n. \tag{A4}$$

To determine the interval of convergence, we focus our attention on the nth term u_n of this series,

$$u_n=(-1)^n(1+1/x_0^2)^{n/2}x_0^n(1+x_0^2)^{p-n}C_n^{-p}\left(\frac{1}{\sqrt{1+1/x_0^2}}\right) \times(x-x_0)^n. \tag{A5}$$

The leading term of an asymptotic form[16] for the Gegenbauer polynomials is

$$C_n^{\lambda}(\cos\vartheta)=2\frac{(\lambda)_n}{n!}\left[\frac{\cos[(n+\lambda)\vartheta-\lambda\pi/2]}{(2\sin\vartheta)^{\lambda}}+O(n^{-3/2})\right], \quad n\to\infty, \tag{A6}$$

thus,

$$C_n^{-p}(\cos\vartheta)=2\frac{\Gamma(n-p)\cos[(n-p)\vartheta+p\pi/2][2\sin\vartheta]^p}{\Gamma(-p)n!}, \quad n\to\infty, \tag{A7}$$

where $\vartheta = \cos^{-1}(1/\sqrt{1+1/x_0^2})$ and the principal value of the arccosine is intended. [The $(\lambda)_n$ notation used in Eq. (A6) is defined in Ref. 17.] The presence of the cosine factor in the asymptotic expression for $C_n^{-p}(\cos\vartheta)$ as given in Eq. (A7) causes this expression not to have a well-defined value as $n \to \infty$. However, we note that if the cosine factor is replaced by unity the resulting expression is *larger* than the original expression. So, we may safely replace the cosine factor by unity, in view of the comparison test.[18] Thus, forming the ratio test[19] for u_n as given in Eq. (A5), but using for the Gegenbauer polynomial the asymptotic form of Eq. (A7) with the cosine factor replaced by unity, gives

$$\lim_{n\to\infty}\left|\frac{u_{n+1}}{u_n}\right| = \lim_{n\to\infty}\left|\frac{(n-p)(x-x_0)}{(n+1)\sqrt{1+x_0^2}}\right| = \left|\frac{x-x_0}{\sqrt{1+x_0^2}}\right| < 1. \tag{A8}$$

Solving the final inequality gives the interval of convergence,

$$x_0 - \sqrt{1+x_0^2} < x < x_0 + \sqrt{1+x_0^2}, \tag{A9}$$

with x_0 presumed positive.

[1] M. P. Langevin, J. Phys. (France) **4**, 678 (1905).
[2] X. D. Zhang and C. A. Rogers, ''A macroscopic phenomenological formulation for coupled electromechanical effects in piezoelectricity,'' J. Intell. Mater. Syst. Struct. **4**, 307–316 (1993).
[3] J. C. Piquette and S. E. Forsythe, ''A nonlinear material model of lead magnesium niobate (PMN),'' J. Acoust. Soc. Am. **101**, 289–296 (1997).
[4] R. C. Smith and C. L. Hom, ''Domain wall theory for ferroelectric hysteresis,'' J. Intell. Mater. Syst. Struct. **10**, 195-213 (1999).
[5] S. Wolfram, *The Mathematica Book* (Cambridge University Press, Cambridge, UK, 1996), p. 1168.
[6] F. Reif, *Fundamentals of Statistical and Thermal Physics* (McGraw-Hill, New York, 1965), p. 345, Eq. (9.4.7).
[7] See Ref. 6, p. 343, Eq. (9.4.1).
[8] D Haliday and R. Resnick, *Physics* (Wiley, New York, 1967), p. 679, Eq. (27-12).
[9] G. Arfken, *Mathematical Methods for Physicists* (Academic, New York, 1970), p. 725.
[10] E. Butkov, *Mathematical Physics* (Addison-Wesley, Reading, MA, 1968), p. 161.
[11] W. Hackenberger, ''PMN-PT materials for sonar applications,'' 1998 PMN Measurements Workshop held 19 October 1998 at Alfred University, Alfred, NY.
[12] K. Knopp, *Infinite Sequences and Series* translated by F. Bagemihl (Dover, New York, 1956), p. 111, Eq. (2). See also footnote 1 on p. 111. We conclude that the interval of convergence of the Taylor series of a function formed from a product is *at least as great* as the smallest interval of convergence of the Taylor series of the individual functions forming the product.
[13] See Ref. 12, pp. 107–108.
[14] I. S. Gradshteyn and I. M. Ryzhik, *Tables of Integrals, Series, and Products* (Academic, New York, 1965), p. 20, Eq. (0.432.3).
[15] See Ref. 14, pp. 1029–1031.
[16] H. Bateman, *Higher Transcendental Functions* (McGraw-Hill, New York, 1953), Vol. 2, p. 198, Eq. (7).
[17] See Ref. 14, p. xliii.
[18] See Ref. 12, p. 56.
[19] See Ref. 12, pp. 57–58.

An efficient model of an equipment loaded panel for active control design studies

G. S. Aglietti
School of Engineering Sciences, Aeronautics and Astronautics, University of Southampton, Southampton SO17 1BJ, England

R. S. Langley
Department of Engineering, University of Cambridge, Cambridge CB2 1PZ, England

E. Rogers
Department of Electronics and Computer Science, University of Southampton, Southampton SO17 1BJ, England

S. B. Gabriel
School of Engineering Sciences, Aeronautics and Astronautics, University of Southampton, Southampton SO17 1BJ, England

(Received 13 August 1999; revised 5 June 2000; accepted 6 June 2000)

An effective investigation of alternative control strategies for the reduction of vibration levels in satellite structures requires realistic, yet efficient, structural models to simulate the dynamics of the system. These models should include the effects of the sources, receivers, supporting structure, sensors, and actuators. In this paper, a modeling technique which meets these requirements is developed and some active control strategies are briefly investigated. The particular subject of investigation is an equipment-loaded panel and the equations of motion are derived using the Lagrange–Rayleigh–Ritz (LRR) approach. The various pieces of equipment on the panel are mounted on active or passive suspensions, and resonators are used to represent the internal dynamics of the mounted equipment. Control of the panel, which transmits vibrations from sources to receivers, is by means of piezoelectric patches and the excitation consists of dynamic loads acting on the equipment enclosures and/or directly on the panel. The control objective is to minimize the displacement at an arbitrary output location. The LRR model developed is verified against one produced by using the finite-element method. Finally, some initial controller design studies are undertaken to investigate and compare the effectiveness of different control strategies (e.g., minimization at the source, along the vibration path, or at the receiver). [S0001-4966(00)01909-3]

PACS numbers: 43.40.Dx, 43.40.Vn [CBB]

INTRODUCTION

Over the past 20 years there has been a dramatic increase of research in the field of active control of variations, with particular interest in aerospace applications. One of the principal focuses of this research have been large space structures (LSS),[1] which are characterized by very low rigidity and damping. The objective of this research is to reduce the large oscillations of the structure produced by various dynamic disturbances or maneuvers. In particular, the large model uncertainties which characterize LSS have been the subject of much work and pose challenging problems for the control community. A range of controller algorithms, designed using, for example, linear optimal control and implemented using different types of actuators and sensors, has emerged from this work. Also, some of these algorithms have been the subject of ground-based hardware tests as a prelude to actual implementation in space.

The onward development of real LSS has been significantly hindered by the delays in the plans to build the space station and this has, in turn, led to increased research effort on more realistic and immediate issues.[2] These include the active control of microvibrations on satellite structures, which is now quite an active area and is prompted by ''real world'' problems. For example, mirror pointing systems,[3] such as those used in space telescopes which require extremely accurate targeting, are very sensitive to vibrations and even small mechanical disturbances can produce jitter that results in blurred images. It is estimated that the new generation of precision pointing mirror systems will be extremely sensitive to even the smallest vibrations, and that to (usefully) exploit their capability a decrease in satellite jitter of at least three orders of magnitude will be required. In other equipment, such as laser communications systems, these vibrations induce oscillations of the beam which can cause problems at the receiving station.

Consider now the case onboard a spacecraft.[4] In this situation there is often no alternative to mounting sensitive equipment on structures where vibrations are induced by the functioning of other necessary pieces of equipment. This situation often occurs on satellites where microgravity experiments or accurately targeted optical instruments are frequently mounted on panels which are subject to vibrations induced by reaction wheels, crycoolers, and other subsystems.

The minimization of vibrations at sensitive locations on a spacecraft can be undertaken either by minimizing the

strength of the vibration source(s), or by modifying the design of a relevant component, or by reducing the transmission between source(s) and receiver(s).[5] Assuming that everything possible has been done to reduce the level of disturbance, there are three areas where the vibration transmission can be reduced. These are (i) at the source(s) by mounting the vibration equipment on a suspension system designed to minimize the level of vibrations injected into the supporting structure; (ii) at the receiver(s) by mounting sensitive equipment on a suitable suspension system, and (iii) along the supporting structure(s) which is the media for vibration propagation between source(s) and receiver(s) location(s).

To assess which one of the above strategies is the most effective in a given situation, it is clearly essential to have a mathematical model of the system which includes all the essential elements of the vibration path(s). Suppose also that the essential task is to minimize the vibration transmission via the panel. Then, the model used must include (as appropriate/relevant) the source(s) and receiver(s) dynamics, the dynamics of the sensor(s) and actuator(s) of their suspension systems, and the dynamics of the supporting panel and its sensor(s) and actuator(s). Given that further analysis based on a single model which includes all of these elements is not really possible (due to the size/complexity of the resulting model), research to date has focused on a single strategy for vibration transmission reduction. For example, minimization at the receiver(s) has been considered in Refs. 6 and 7, minimization at the source(s) in Refs. 8 and 9, minimization along the transmitting structure in Ref. 10.

In previous work, the authors have used an efficient Lagrange–Rayleigh–Ritz (LRR)[11] method to develop a model[12] for active control of microvibrations in a mass-loaded panel actively controlled through the use of piezoelectric patches as both sensors and actuators. In comparison to the finite-element method (FEM)[13] of structural modeling, this method requires the use of relatively few degrees of freedom to retain the essential dynamics of the real system. This fact, together with the immediate delivery of the model in the state form on which many modern controller design techniques are based, makes this LRR-based model a powerful tool in the design of active control schemes for microvibration suppression on mass-loaded panels.

In this paper the LRR modeling technique is extended to include a more detailed representation of the source(s) and receiver(s) dynamics which incorporates the possible use of active mounting systems. The use/relevance of the resulting models is demonstrated by the design and basic evaluation of controllers designed using the linear quadratic Gaussian (LQG)[14] approach for control at the source, receiver, and along the transmission path. Some conclusions on the relative performance of these controllers is also given, together with recommendations for further work.

I. PLANT DESCRIPTION

The three characteristic elements of a vibration transmission problem are, respectively,

(i) source(s);
(ii) transmitting structure;
(iii) receiver(s).

If active control is to be implemented, sensors and actuators also have to be included in the plant model. Sources and receivers are pieces of equipment with different mechanical interfaces to secure them to the structure underneath, the most common mounting geometry being four mounting feet positioned at the corners of the equipment enclosure. For this reason a typical piece of equipment will be modeled as a rectangular box fixed to the underlying structure through mounting feet positioned at its corners, as illustrated in Fig. 2. The mounting feet, piezoelectric stacks, are the actuators for control at a source or at a receiver, whilst piezoelectric patches bonded onto the panel are the sensors/actuators for control along the structure.

The transmitting structure consists of a simply supported panel on which the pieces of equipment are mounted. Lumped masses can be positioned on the panel to represent small pieces of equipment. Piezoelectric patches bonded on the faces of the panel act as sensors and actuators for the control system and are used to apply control along the transmitting structure.

The mathematical model of the complete plant is the assembly of the model of the actively controlled supporting panel with the model of the equipment on their suspension systems. Both models are built using Lagrange's equations of motion, with the model coordinates of the bare panel and the equipment enclosure displacements as mechanical generalized coordinates, and the voltages at the piezoelectric elements as the electrical generalized coordinates.

A. Transmitting structure (actively controlled panel)

The mathematical model of the actively controlled panel (ACP) is derived using the procedure described in Ref. 12. The displacement field (out-of-plane displacements of the panel) is obtained using a Rayleigh Ritz approach as a superposition of shape functions $S_{m,n}$ multiplied by the time-dependent modal coordinates $\phi_{m,n}$

$$w(x,y,t)=\sum_{n=1}^{Nm}\sum_{m=1}^{Nn} S_{n,m}(x,y)\,\phi_{n,m}(t)=\mathbf{s}^t\boldsymbol{\phi}, \tag{1}$$

where $\mathbf{s}$ is the vector of the shape functions, $\boldsymbol{\phi}$ is the vector of the modal coordinates, and x and y are the in-plane coordinates on the panel.

Once suitable expressions for the kinetic and potential energy associated with the elements of the ACP, i.e., panel and piezoelectric patches have been written (see Ref. 12 for full details), using the Lagrange's equation of motion, the equations governing the dynamic of the system are obtained as

$$(\mathbf{M}_{\mathrm{pl}}+\mathbf{M}_{\mathrm{pz}})\,\ddot{\boldsymbol{\phi}}+(\mathbf{K}_{\mathrm{pl}}+\mathbf{K}_{\mathrm{pz}}^{\mathrm{elast}})\,\boldsymbol{\phi}+(\mathbf{K}_{\mathrm{pz}}^{\mathrm{elastoelect}})^t\mathbf{v}=\mathbf{Q}, \tag{2a}$$

$$\mathbf{K}_{\mathrm{pz}}^{\mathrm{elastoelect}}\boldsymbol{\phi}+\mathbf{K}_{\mathrm{pz}}^{\mathrm{elect}}\mathbf{v}=0. \tag{2b}$$

$\mathbf{M}_{\mathrm{pl}}$ and $\mathbf{M}_{\mathrm{pz}}$ are the mass matrices associated with the panel and piezoelectric patches, respectively, $\mathbf{K}_{\mathrm{pl}}$ and $\mathbf{K}_{\mathrm{pz}}^{\mathrm{elast}}$ are the stiffness matrices, $\mathbf{K}_{\mathrm{pz}}^{\mathrm{elastoelect}}$ is the matrix accounting for the piezoelectric effect, $\mathbf{K}_{\mathrm{pz}}^{\mathrm{elect}}$ is the matrix of the capacitances of

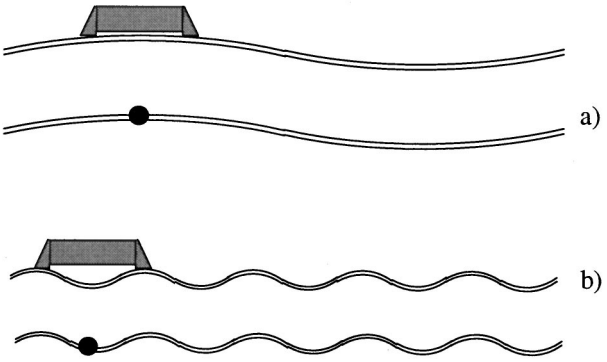

FIG. 1. Lumped mass approximation (a) deformation wavelength longer than equipment mounting feet distance, (b) deformation wavelength shorter than equipment mounting feet distance.

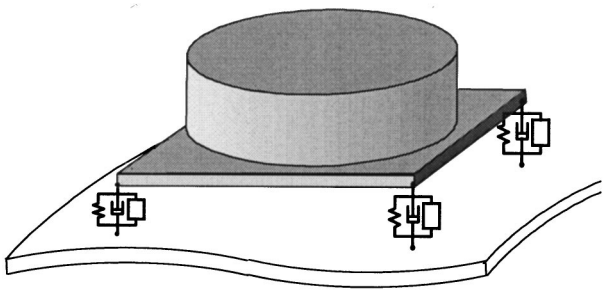

FIG. 2. Equipment with active suspensions mounted on a flexible panel.

the piezoelectric patches, and **v** contains the generalized coordinates representing the voltage at each piezoelectic patch.

Equation (2a) describes the dynamics of the system when the piezoelectric patches are used as actuators (externally driven) and can be rewritten as[12]

$$\mathbf{M}_{\mathrm{acp}}\ddot{\boldsymbol{\phi}}+\mathbf{C}_{\mathrm{acp}}\dot{\boldsymbol{\phi}}+\mathbf{K}_{\mathrm{acp}}\boldsymbol{\phi}=\mathbf{V}_{\mathrm{a}}\mathbf{v}_{\mathrm{a}}+\mathbf{S}_{\mathrm{t}}\mathbf{f}, \tag{3}$$

where damping has been introduced via the matrix $\mathbf{C}_{\mathbf{acp}}$. Equation (2b) can be rewritten as

$$\mathbf{v}_s=-(\mathbf{K}_s^{\mathrm{elect}})^{-1}\mathbf{K}_s^{\mathrm{elastoelect}}\boldsymbol{\phi}, \tag{4}$$

and used to retrieve the voltages at the patches acting as sensors.

B. Source(s) and receiver(s)

The simplest method to model equipment mounted on a panel is by using lumped masses, Fig. 1(a), but if the equipment internal dynamics have to be represented, or the wavelength of deformations of the panel is equal to or smaller than the distance between the mounting points, Fig. 1(b), the lumped mass approximation is no longer valid. Hence, a more detailed representation of the mounting geometry needs to be considered.

Source(s) and receiver(s) are usually mounted on suspensions, whose basic function is to secure the piece of equipment to the underlying structure and at the same time minimize the transmission of dynamic disturbances, i.e., vibrations. These two requirements are in principle contradictory, since the first one requires strong coupling between the equipment and the underlying structure, while in order to meet the second requirement it is necessary to isolate the equipment, thus uncoupling it from the supporting structure. This contradiction can be solved by using latching mechanisms, which are locked when the equipment needs to be strongly constrained to the structure, e.g., the launch phase of a satellite, and open during phases in which the equipment needs to be isolated, e.g., equipment for microgravity experiments. The complications of using a two-mode suspension system can be avoided by having suspensions which are stiff at low frequency, thus allowing the transmission of low-frequency loads, such as those produced by maneuvers or static loads, and soft at high frequency, in order to avoid the transmission of dynamic disturbances (which usually occur at higher frequencies). The suspension therefore acts as a low-pass filter and provided that the bandwidth of the mechanical disturbances is at a frequency high enough to be well separated from the deliberately transmitted loads, the problem could then be solved by passive suspensions.

Conversely, there are many uncertainties in the system and this fact, together with the high performance level required, means that active control, possibly implemented in a closed-loop configuration, must be employed. This is the only real option available to achieve the required performance levels in the presence of unknown disturbances. The first task in this strategy is to construct a mathematical model of the particular structure under consideration, as discussed next.

In terms of sources, these are basically pieces of equipment where the motion of the internal parts to perform their function produces unwanted forces/reactions which are transmitted to the supporting structure. Each particular piece of equipment has a different mechanical interface to secure it to the structure underneath, the most common mounting geometry being four mounting feet positioned at the corners of the equipment enclosure. For this reason a typical piece of equipment is modeled here as if it were connected to the underlying structure through mounting feet, positioned at its corners (see Fig. 2).

Since the mechanical enclosure of the equipment is quite stiff, compared to the panel, it can be modeled as a rigid body connected to the panel through flexible elements, which represent the mounting feet. The description of the dynamics of a free rigid body in a three-dimensional space requires six degrees of freedom (DOF), which are usually taken as three translations and three rotations relative to a fixed reference system. In this case the in-plane translations (along x and y axes) of the enclosure can be neglected, assuming strong mechanical coupling with the panel along these directions and the high in-plane stiffness of the panel itself. Rotations about the axis (z) perpendicular to the panel are transmitted to the panel as x and y translations of the mounting feet, and therefore can be neglected for the same reasons as those given above.

Each enclosure is therefore assumed to have only three degrees of freedom, i.e., off-plane displacement ζ and pitch and roll angles α and β, as illustrated by Figs. 3(a), 3(b), and 3(c).

Most of the equipment, even though included in quite

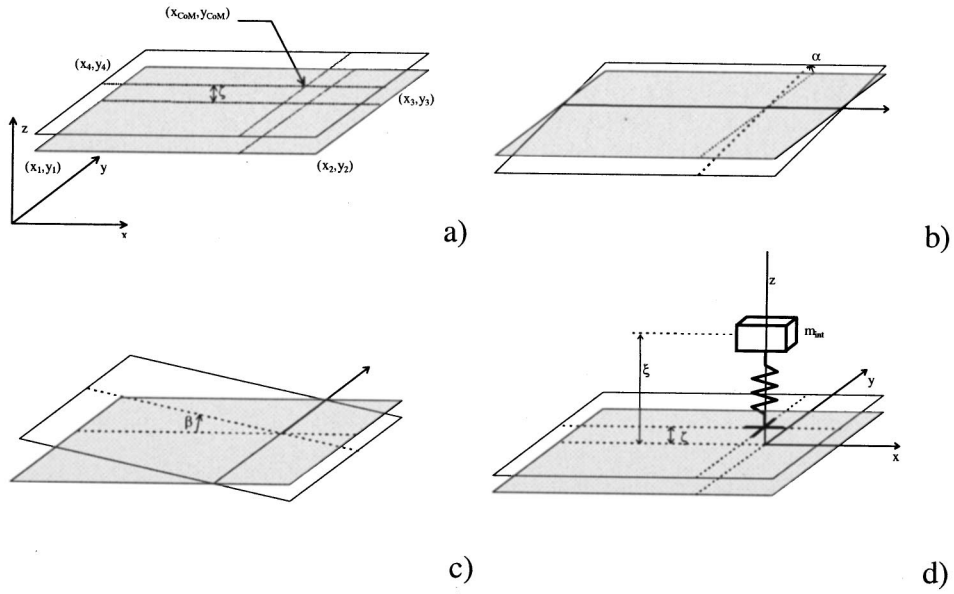

FIG. 3. Degrees of freedom of the equipment enclosures x_i, y_i: coordinates of the mounting feet; $x_{\mathrm{COM}}, y_{\mathrm{COM}}$: coordinates of the box center of mass.

stiff enclosures (such as electronic boxes), will have internal flexible parts whose resonance could be within the frequency bandwidth of the active control system. Consequently it is necessary to account for the resulting internal dynamics, where the approach adopted here relies on the assumption that there is only one resonance within the frequency range of interest. In this case the internal dynamics can be represented by adding an extra degree of freedom (ξ) to the set of three detailed above to describe the equipment motion. This new DOF describes the z displacement of an internal mass linked through a spring to the center of mass (COM) of the equipment enclosure, as shown in Fig. 3(d). This internal resonator can be tuned to the internal resonance frequency of the equipment by varying its mass and spring stiffness.

Given these assumptions, it is possible to write suitable expressions for the energy associated with the equipment as a function of its degrees of freedom (which are taken as generalized coordinates). The expressions for the energies obtained will then be derived and Lagrange's equations of motion applied, to obtain the mathematical model of the dynamics of the plant.

1. Kinetic energy

Suppose that $\boldsymbol{\phi}_{\mathrm{eqp}}$ denotes the column vector of the equipment degrees of freedom (Fig. 3)

$$\boldsymbol{\phi}_{\mathrm{eqp}}=\{\alpha \quad \beta \quad \zeta \quad \xi\}^t, \tag{5}$$

and $\mathbf{M_{eqp}}$ the inertia matrix

$$\mathbf{M_{eqp}}=\mathrm{diag}\{I_{yy} \quad I_{xx} \quad m_{\mathrm{enc}} \quad m_{\mathrm{int}}\}, \tag{6}$$

where I_{yy} and I_{xx} are the moments of inertia of the equipment, m_{int} is the internal mass, i.e., the mass of the resonating element, and m_{enc} is the mass of the equipment enclosure. Then, it is possible to write the kinetic energy as

$$T_{\mathrm{eqp}}=\tfrac{1}{2}\dot{\boldsymbol{\phi}}^t_{\mathbf{eqp}}\mathbf{M_{eqp}}\dot{\boldsymbol{\phi}}_{\mathbf{eqp}}. \tag{7}$$

2. Potential energy

Assuming that the equipment enclosure can be regarded as a rigid body on comparatively soft suspensions, the potential energy is essentially the energy stored in the suspension system, plus the energy stored in the ''spring'' of the internal resonator. Modeling the suspension system (Fig. 2) as a parallel connection of a spring, a damper and an active element, i.e., a piezoelectric prism whose stiffness is included in the spring stiffness, the elastic energy stored can be expressed as

$$U^{\mathrm{ela}}_{\mathrm{eqp}}=\frac{1}{2}\left(k_s\sum_{i=1}^{4}\Delta z_i^2+k_{\mathrm{res}}\Delta z_{\mathrm{res}}^2\right), \tag{8}$$

where k_s is the total stiffness of the suspension, k_{res} the stiffness of the internal resonator, Δz_i $(i=1,...,4)$ is the linear deformation of the ith suspension foot and Δz_{res} is the linear deformation of the internal resonator stiffness. The linear deformation of the ith suspension can be obtained as the difference between the out-of-plane displacement of the panel surface $z_{\mathrm{str}}(x_i, y_i, t)$ evaluated at the mounting foot location (x_i, y_i) and the vertical displacement $z_i(t)$ of the ith corner of the box. Both of these displacements can be written in terms of shape functions $\mathbf{s}$, multiplied by time-dependent coordinates $\boldsymbol{\phi}$ as

$$(z_{\mathrm{str}})_i=(\mathbf{s}_{\mathrm{str}})^t_i\boldsymbol{\phi}_{\mathrm{str}}, \tag{9}$$

where the subscript str denotes the modal coordinates of the panels, and

$$z_i=(\mathbf{s_{eqp}})^t_i\boldsymbol{\phi}_{\mathrm{eqp}}. \tag{10}$$

The shape functions used for the supporting structure will be described in the following section, while those used for the equipment are simply (see Fig. 3)

$$(\mathbf{s}_{\mathrm{eqp}})^t_i=\{(y_i-y_{\mathrm{COM}}) \quad (x_i-x_{\mathrm{COM}}) \quad 1 \quad 0\}^t. \tag{11}$$

Hence, the linear deformation can be written as

$$\Delta z_i=\{(\mathbf{s}_{\mathrm{str}})^t_i \quad -(\mathbf{s_{eqp}})^t_i\}\begin{Bmatrix}\boldsymbol{\phi}_{\mathrm{str}}\\ \boldsymbol{\phi}_{\mathrm{eqp}}\end{Bmatrix}, \tag{12}$$

and the deformation of the spring of the internal resonator can be written as

$$\Delta z_{\text{res}} = (\mathbf{s_{res}})^t \boldsymbol{\phi}_{\text{eqp}}, \tag{13}$$

with

$$\mathbf{s}^i_{\text{res}} = \{0 \quad 0 \quad 1 \quad -1\}^t. \tag{14}$$

Consequently, the total elastic energy associated with any piece of equipment is

$$U^{\text{ela}}_{\text{eqp}} = \tfrac{1}{2} \boldsymbol{\phi}^t \mathbf{K}^{\text{ela}}_{\text{eqp}} \boldsymbol{\phi}, \tag{15}$$

where

$$\boldsymbol{\phi} = \begin{Bmatrix} \boldsymbol{\phi}_{\text{str}} \\ \boldsymbol{\phi}_{\text{eqp}} \end{Bmatrix} \tag{16}$$

and

$$\mathbf{K}^{\text{ela}}_{\text{eqp}} = k_s \sum_{i=1}^{4} \begin{bmatrix} (\mathbf{s}_{\text{str}})_i (\mathbf{s}_{\text{str}})^t_i & -(\mathbf{s}_{\text{str}})_i (\mathbf{s}_{\text{eqp}})^t_i \\ -(\mathbf{s}_{\text{eqp}})_i (\mathbf{s}_{\text{str}})^t_i & (\mathbf{s}_{\text{eqp}})_i (\mathbf{s}_{\text{eqp}})^t_i \end{bmatrix} + k_{\text{res}} \begin{bmatrix} 0 & 0 \\ 0 & \mathbf{s}_{\text{res}} \mathbf{s}^t_{\text{res}} \end{bmatrix}. \tag{17}$$

The elastic energy is not the only potential energy which can be stored in the suspensions. In particular, the stress produced by the piezoelectric effect, multiplied by the strain of the material and integrated over the volume of the piezoelectric element, produces another form of energy, termed elastoelectric energy here.

The stress produced in a piezoelectric prism along the direction (z in the reference system used here) of the applied electric field is given by the expression

$$(\sigma_{\text{elect}})_i = E_{\text{pz}} d_{zz} \frac{v_i}{h_{pz}}, \tag{18}$$

where d_{zz} is the piezoelectric constant of the material, h_{pz} is the height of the prism, E_{pz} is the Young's modulus and v_i is the applied voltage. Assuming that the strain in the material is constant and equal to

$$(\varepsilon_z)_i = \frac{\Delta z_i}{h_{\text{pz}}}, \tag{19}$$

then the elastoelectic energy stored in each piezoelectric support is

$$(U^{\text{elastoelec}}_{\text{eqp}})_i = \frac{1}{2} \int_{\text{pz}} \int \int (\sigma_{\text{elect}})_i (\varepsilon_z)_i \, dx \, dy \, dz = \frac{1}{2} v_i E_{\text{pz}} d_{zz} \frac{A_{\text{pz}}}{h_{\text{pz}}} \Delta z_i. \tag{20}$$

Letting $\mathbf{v_{eqp}}$ be the column vector of the voltages v_i ($i = 1,...,4$) existing at the electrodes of each mounting foot, the total elastoelectric energy stored in the equipment suspension system can be written as

$$U^{\text{elastoelect}}_{\text{eqp}} = \mathbf{v}^t_{\text{eqp}} \mathbf{K}^{\text{elastoelect}}_{\text{eqp}} \boldsymbol{\phi}, \tag{21}$$

where

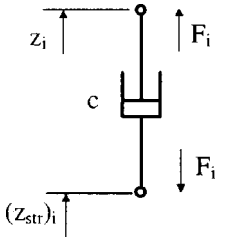

FIG. 4. Dashpot.

$$K^{\text{elastoelect}}_{\text{eqp}} = E_{\text{pz}} d_{zz} \frac{A_{\text{pz}}}{2 h_{\text{pz}}} \begin{bmatrix} \{(\mathbf{s}_{\text{str}})^t_1 & & -(\mathbf{s}_{\text{eqp}})^t_1\} \\ & \vdots & \\ & \vdots & \\ \{(\mathbf{s}_{\text{str}})^t_4 & & -(\mathbf{s}_{\text{eqp}})^t_4\} \end{bmatrix}, \tag{22}$$

under the assumption that all supports have the same characteristics.

The last form of energy stored in the piezoelectric material is the electric energy, which can be calculated directly as

$$(U^{\text{elect}}_{\text{eqp}})_i = \tfrac{1}{2} C \nu_i^2, \tag{23}$$

where C is the capacitance of the elements given by

$$C = \varepsilon_{\text{pz}} \frac{A_{\text{pz}}}{h_{\text{pz}}}. \tag{24}$$

Hence, the total electric energy stored can be written in matrix form as

$$U^{\text{elect}}_{\text{eqp}} = \tfrac{1}{2} \mathbf{v}^t_{\text{eqp}} \mathbf{K}^{\text{elect}}_{\text{eqp}} \mathbf{v}_{\text{eqp}}, \tag{25}$$

where $\mathbf{K}^{\text{elect}}_{\text{eqp}}$ is the four-by-four diagonal matrix whose diagonal elements are all equal to the capacitance.

3. Dissipative forces

The dissipative forces produced by dashpots in the mounting feet can be calculated as an extra term in the generalized forces which will represent the externally applied disturbance forces. This term, denoted by Q_{dp} here, accounts for the nonconservative forces

$$F_i = c \Delta \dot{z}_i, \tag{26}$$

generated by each of the i ($i = 1,...,4$) dashpots of the mountings. Equation (26) in this case can be rewritten in matrix form as

$$F_i = c \{(\mathbf{s}_{\text{str}})^t_i - (\mathbf{s}_{\text{eqp}})^t_i\} \begin{Bmatrix} \dot{\boldsymbol{\phi}}_{\text{str}} \\ \dot{\boldsymbol{\phi}}_{\text{eqp}} \end{Bmatrix}, \tag{27}$$

and adopting the sign convention of Fig. 4, it is possible to write the vector of the generalized forces acting on the panel and on the equipment, respectively, as

$$\mathbf{Q}_{\text{str}_l} = F_i (-\mathbf{s}_{\text{str}})_i, \tag{28a}$$

$$\mathbf{Q}_{\text{eqp}_l} = F_i (\mathbf{s}_{\text{eqp}})_i. \tag{28b}$$

By assumption, the equipment has four mounting feet and Eqs. (27) and (28a), (28b) can be used to write the generalized force vector as

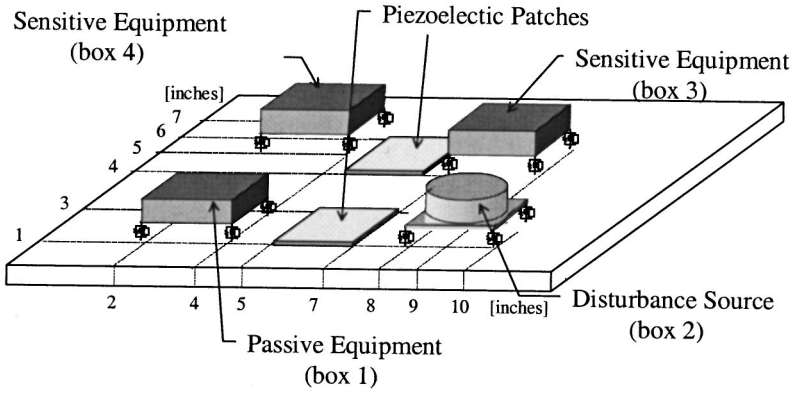

FIG. 5. Model assembly.

$$\mathbf{Q}_{dp} = \mathbf{C}_{dip}\dot{\boldsymbol{\phi}}, \tag{29}$$

where

$$\mathbf{C}_{dp} = c\sum_{i:1}^{4}\begin{bmatrix} (\mathbf{s}_{str})_i(\mathbf{s}_{str})_i^t & (-\mathbf{s}_{str})_i(\mathbf{s}_{eqp})_i^t \\ (-\mathbf{s}_{eqp})_i(\mathbf{s}_{str})_i^t & (\mathbf{s}_{eqp})_i(\mathbf{s}_{eqp})_i^t \end{bmatrix}. \tag{30}$$

In addition to the damping of the mounts, proportional damping is added to the internal resonator.

C. Assembly of equations of motion for *Ne* pieces of equipment

The methodology developed in the previous sections can be applied repeatedly to obtain expressions for the energies associated with more pieces of equipment mounted on the panel. The matrices produced can then be assembled in a finite-element fashion.

Assuming *Ne* pieces of equipment mounted on the panel, the mechanical generalized coordinates of the whole system can be expressed as the column vector **r**

$$\mathbf{r} = \begin{Bmatrix} \boldsymbol{\phi}_{str} \\ \hline (\boldsymbol{\phi}_{eqp})_1 \\ \vdots \\ (\boldsymbol{\phi}_{eqp})_{Ne} \end{Bmatrix}. \tag{31}$$

In the case of the kinetic energy, the choice of DOFs made to describe the equipment motion has produced expressions which are decoupled from the DOFs used to describe the motion of the panel. The mass matrices of all the components (actively controlled panel and pieces of equipment) can therefore be augmented with rows and columns of zeros to obtain square matrices with dimensions equal to that the vector **r**, to allow the assembly of the model of the whole system. The mass matrix $\mathbf{M}_{eqp}$ of this model is obtained as

$$\mathbf{M}_{eqp} = \sum_{j=1}^{Ne}\left[\begin{array}{c|ccc} 0 & & 0 & \\ \hline & \ddots & & 0 \\ 0 & & (\mathbf{M}_{eqp})_j & \\ & 0 & & \ddots \end{array}\right]. \tag{32}$$

In the case of the potential energies, the assembly procedure is slightly more complex due to the coupling between the DOFs of the boxes and the panel. By partitioning the stiffness matrix of an equipment box (say the *j*th in accordance with the panel and equipment DOFs $\boldsymbol{\phi}_{str}$ and $\boldsymbol{\phi}_{eqp}$, i.e.,

$$\left(\mathbf{K}_{eqp}^{ela}\right)_j = \left[\begin{array}{c|c} \left(\mathbf{K}_{pp}\right)_j & \left(\mathbf{K}_{pe}\right)_j \\ \hline \left(\mathbf{K}_{ep}\right)_j & \left(\mathbf{K}_{ee}\right)_j \end{array}\right], \tag{33}$$

it is possible to obtain the matrix for the whole system as

$$\mathbf{K}_{eqp}^{ela} = \sum_{j=1}^{Ne}\left[\begin{array}{c|ccc} \left(\mathbf{K}_{pp}\right)_j & \cdots & \left(\mathbf{K}_{pe}\right)_j & \cdots \\ \hline \vdots & \ddots & & \mathbf{0} \\ \left(\mathbf{K}_{ep}\right)_j & & \left(\mathbf{K}_{ee}\right)_j & \\ \vdots & \mathbf{0} & & \ddots \end{array}\right]. \tag{34}$$

An identical procedure for the generalized forces produced by the dashpots yields

$$\mathbf{C}_{dp} = \sum_{j=1}^{Ne}\left[\begin{array}{c|ccc} \left(\mathbf{C}_{pp}\right)_j & \cdots & \left(\mathbf{C}_{pe}\right)_j & \cdots \\ \hline \vdots & \ddots & & \mathbf{0} \\ \left(\mathbf{C}_{ep}\right)_j & & \left(\mathbf{C}_{ee}\right)_j & \\ \vdots & 0 & & \ddots \end{array}\right]. \tag{35}$$

where $(\mathbf{C_{pp}})_j(\mathbf{C_{pe}})_j(\mathbf{C_{ep}})_j(\mathbf{C_{ee}})_j$ are the partitions of $\mathbf{C_{dp}}$ relating to the panel (subscript p) or to the equipment (subscript e).

The same procedure can be applied to the matrix in the elastoelectric energy expression, which can be partitioned as

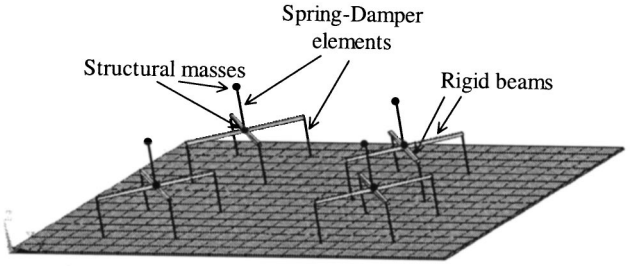

FIG. 6. FEM model.

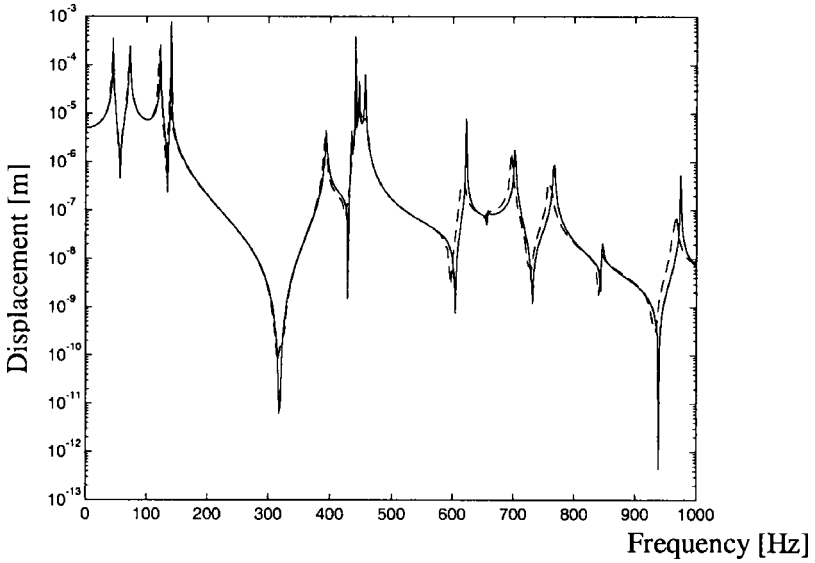

FIG. 7. Displacement of receiver 1 produced by 1N point force applied at the source. Continuous line: LRR model; dashed line: FE model.

$$\mathbf{K}_{eqp}^{elasrtoelect} = \left[\mathbf{K}_{\mathbf{vp}} \;\vdots\; \mathbf{K}_{\mathbf{ve}}\right] . \tag{36}$$

This time, the vector of the voltages has also to be expanded to assemble together all voltages at the suspensions of each box

$$\mathbf{v}_e = \begin{Bmatrix} (\mathbf{v}_{\mathrm{eqp}})_1 \\ \vdots \\ (\mathbf{v}_{\mathrm{eqp}})_j \end{Bmatrix} . \tag{37}$$

Subsequently, $\mathbf{K}_{\mathrm{eqp}}^{\mathrm{elastoelect}}$ is expanded to be compatible with the vectors $\mathbf{v_e}$ and $\mathbf{r}$. Finally, the total elastoelectric stiffness of the suspensions of all j pieces of equipment can be written as

$$\mathbf{K}_{eqp}^{elastoelect} = \sum_{j=1}^{Np} \begin{bmatrix} \vdots & \ddots & \mathbf{0} \\ \left(\mathbf{K}_{\mathbf{vp}}\right)_{\mathbf{j}} & \left(\mathbf{K}_{\mathbf{ve}}\right)_{\mathbf{j}} & \\ \vdots & \mathbf{0} & \ddots \end{bmatrix} . \tag{38}$$

The last matrices to be expanded are those relating to the electric energy in the system, which are augmented with rows and columns of zeros in order to be dimensionally compatible with the vector $\mathbf{v}$. The matrix related with the total electric energy will be

$$\mathbf{K}_{\mathrm{eqp}}^{\mathrm{elect}} = \sum_{j=1}^{Ne} \begin{bmatrix} \ddots & & 0 \\ & (\mathbf{K}_{\mathrm{eqp}}^{\mathrm{elect}})_j & \\ 0 & & \ddots \end{bmatrix} . \tag{39}$$

The equations of motion for the whole system therefore take the form

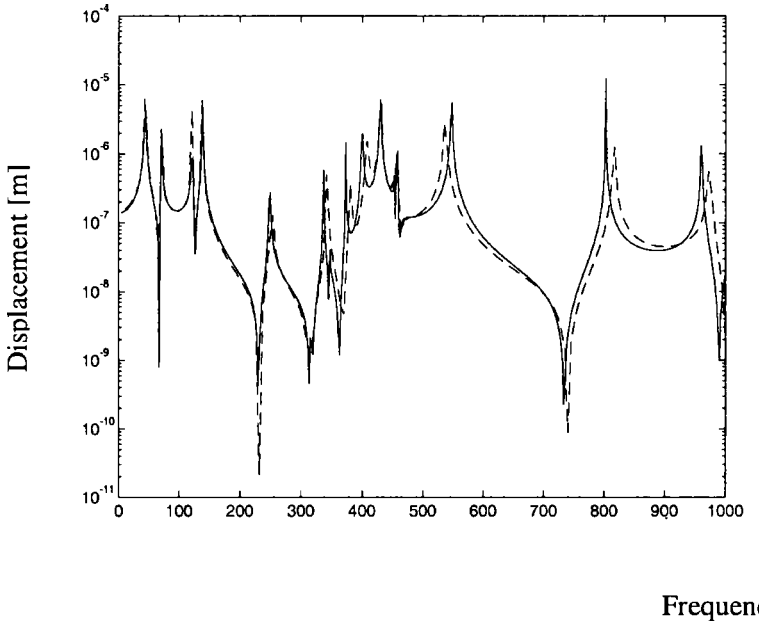

FIG. 8. Displacement of receiver 1 produced by 1 V applied at one active mount of the source. Continuous line: LRR model; dashed line: FE model.

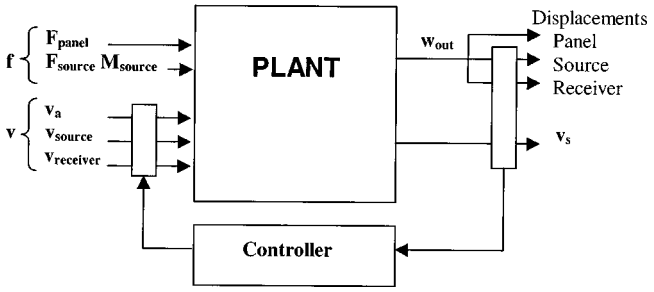

FIG. 9. Plant input/output block diagram.

$$(\mathbf{M}_{acq}+\mathbf{M}_{eqp})\ddot{\mathbf{r}}+\mathbf{C}_{acp}\dot{\mathbf{r}}+(\mathbf{K}_{acp}+\mathbf{K}_{eqp}^{elast})\mathbf{r} = \mathbf{C}_{dp\dot{r}}+(-\mathbf{K}_{eqp}^{elastoelect})^{t}\mathbf{v}_e+\mathbf{V}_a\mathbf{v}_a+\mathbf{Sf}, \tag{40}$$

which can be rewritten as

$$\mathbf{M}_{acs}\ddot{\mathbf{r}}+\mathbf{C}_{acs}\dot{\mathbf{r}}+\mathbf{K}_{acs}\mathbf{r}=\mathbf{V}_e\mathbf{v}_e+\mathbf{V}_a\mathbf{v}_a+\mathbf{Sf}, \tag{41}$$

This expression governs the motion of the actively controlled structure excited by the external forces **f**, voltage inputs at the active suspensions, $\mathbf{v}_e$, and at the piezoelectric patches acting as actuators $\mathbf{v}_a$.

Once this equation is solved for *r*, the displacements at any point on the panel can be obtained from

$$w=\left\{\mathbf{s}^{t} \;\vdots\; 0\right\}\mathbf{r}\ , \tag{42}$$

while the displacement of the equipment enclosures will simply be given by the corresponding elements of the vector **r**.

An augmented version of Eq. (4) can be used to retrieve the voltages at the piezoelectric patches acting as sensors

$$\mathbf{v}_s=\left[-\left(\mathbf{K}_s^{elect}\right)^{-1}\mathbf{K}_s^{elastoelect} \;\vdots\; 0\right]\mathbf{r}\ . \tag{43}$$

For the case in which the vibrations of the actively controlled equipment have to be monitored, suitable transformation matrices can be assembled into a matrix $\mathbf{B}_e$ to yield the signals produced as a function of the enclosure DOFs

$$\mathbf{v}_{se}=[0 \;\vdots\; \mathbf{B}_e]\mathbf{r}\ . \tag{44}$$

II. MODEL VERIFICATION

The mathematical model derived in the previous sections is verified by comparing the results with those obtained by modeling the same system with the standard FEM (ANSYS code[15]). The simulation of the dynamics of the example structure shown in Fig. 5, performed by using the LRR method, was carried out using MATLAB.[16] The panel is a simply supported aluminum plate 304.8 by 203.2 mm, and 1.52 mm thick. Box 1 is a passive equipment box, such as an electronic box, box 2 is a source of vibration, and boxes 3 and 4 are the receivers. Boxes 2, 3, and 4 are mounted on active suspensions, while box 1 is mounted on springs. All boxes have an internal resonator, to simulate internal dynamics. The mass of each box is taken to be 0.5 kg, equally divided between the mass of the enclosure and the mass of the resonator, and the rotational inertia of the boxes is 10^{-4} kg/m^2. The four suspension springs have stiffness $k=10^6$ N/m, and the internal resonators, which are positioned at the center of each box to avoid coupling between linear (axial) and rotational (rocking) modes of the boxes, also have $k=10^6$ N/m. Figure 6 shows a schematic view of the structure as modelled using the FEM. Note that the FE model has approximately 3500 DOFs compared to 80 DOFs for the LRR models.

A comparison of the results obtained by using the two different models is shown in Figs. 7 and 8. A very good agreement between the models is present, with only a slight frequency shift at high frequencies, which can be avoided by extending the modal base used for modeling the panel displacements, and refining the mesh used in the FE model. More details about the LRR modeling technique and its validation can be found in Ref. 17.

III. CONTROL SYSTEM FORMULATION

The aim of the control system, shown in block diagram form in Fig. 9, is to minimize the displacement at selected location(s) in the presence of the dynamic disturbances **f**. Once the mathematical model of the plant dynamics is available, the next step is to write it in a form suitable for active

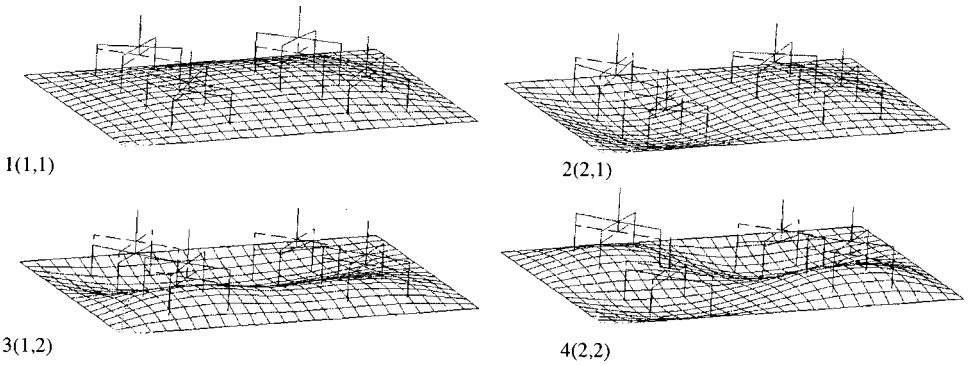

FIG. 10. First four modal shapes of the structure (FEM).

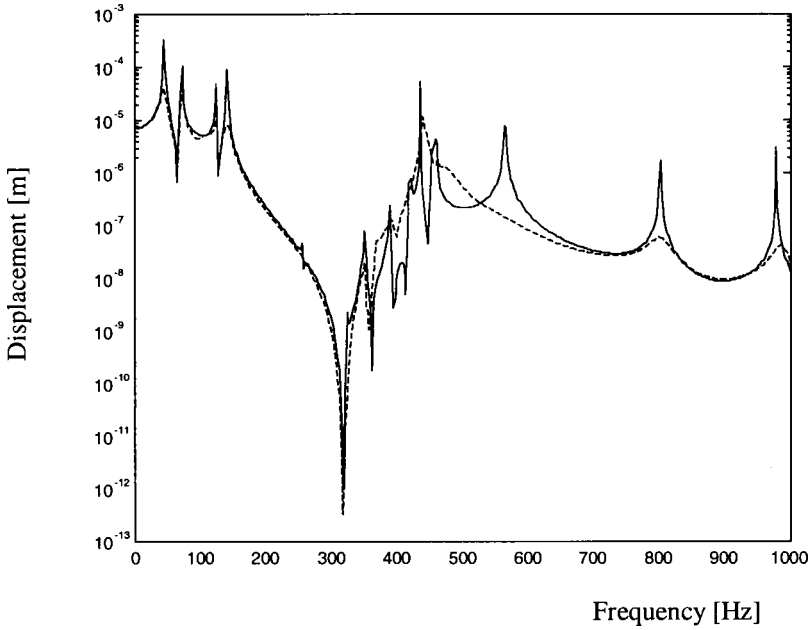

FIG. 11. Vertical displacements of receiver 1 without (continuous line) and with (dashed line) control at source using signals from the source, designed using the 4-by-4 modal base—applied to plant with 6-by-6 modal base.

control studies. In particular, it is a straightforward task to write the LRR model [Eq. (41)] in state-space form

$$\begin{aligned}\dot{\mathbf{x}}&=\mathbf{A}\mathbf{x}+\mathbf{B}_1\mathbf{v}+\mathbf{B}_2\mathbf{f},\\ \mathbf{v}_s&=\mathbf{C}_v\mathbf{x},\\ \mathbf{w}_{\text{out}}&=\mathbf{C}_w\mathbf{x},\end{aligned} \tag{45}$$

where

$$\mathbf{x}=\begin{pmatrix}\mathbf{r}\\ \dot{\mathbf{r}}\end{pmatrix} \tag{46}$$

is the state variable vector, containing the modal coordinates of the panel and the displacements of the equipment enclosures in the column vector **r**, and their derivatives

$$\mathbf{A}=\begin{bmatrix}\mathbf{0} & \mathbf{I}\\ -\mathbf{M}_{\text{acs}}^{-1}\mathbf{K}_{\text{acs}} & -\mathbf{M}_{\text{acs}}^{-1}\mathbf{C}_{\text{acs}}\end{bmatrix}, \tag{47}$$

is the state matrix

$$\mathbf{B}_1=\begin{bmatrix}\mathbf{0} & \mathbf{0}\\ \mathbf{M}_{\text{acs}}^{-1}\mathbf{V}_{\text{e}} & \mathbf{M}_{\text{acs}}^{-1}\mathbf{V}_{\text{a}}\end{bmatrix} \tag{48a}$$

and

$$\mathbf{B}_2=\begin{bmatrix}\mathbf{0}\\ \mathbf{M}_{\text{acs}}^{-1}\mathbf{S}\end{bmatrix} \tag{48b}$$

are the control input and disturbances input matrices,

$$\mathbf{v}=\begin{pmatrix}\mathbf{v}_{\text{e}}\\ \mathbf{v}_{\text{a}}\end{pmatrix}, \tag{49a}$$

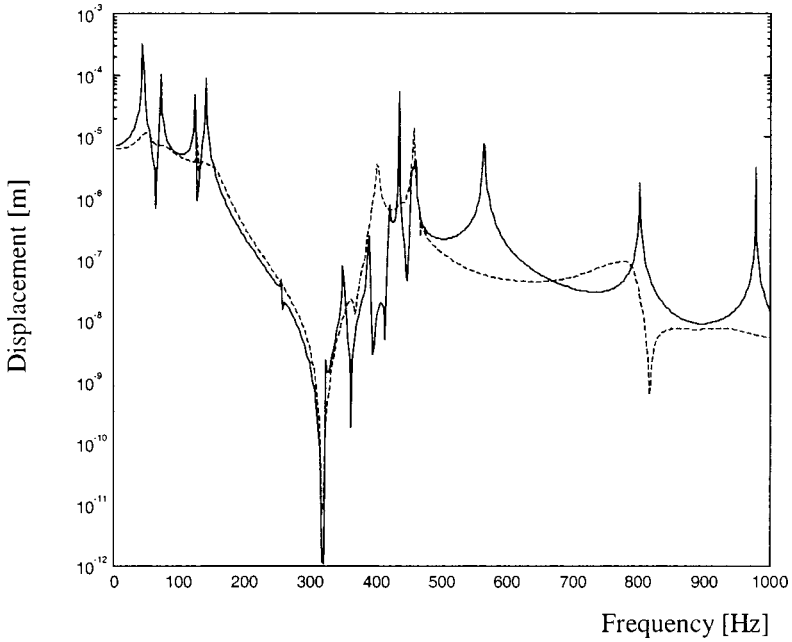

FIG. 12. Displacement of receiver 1 without (continuous line) and with (dashed line) control—sensors and actuators at receiver—6-by-6 mode shapes plant.

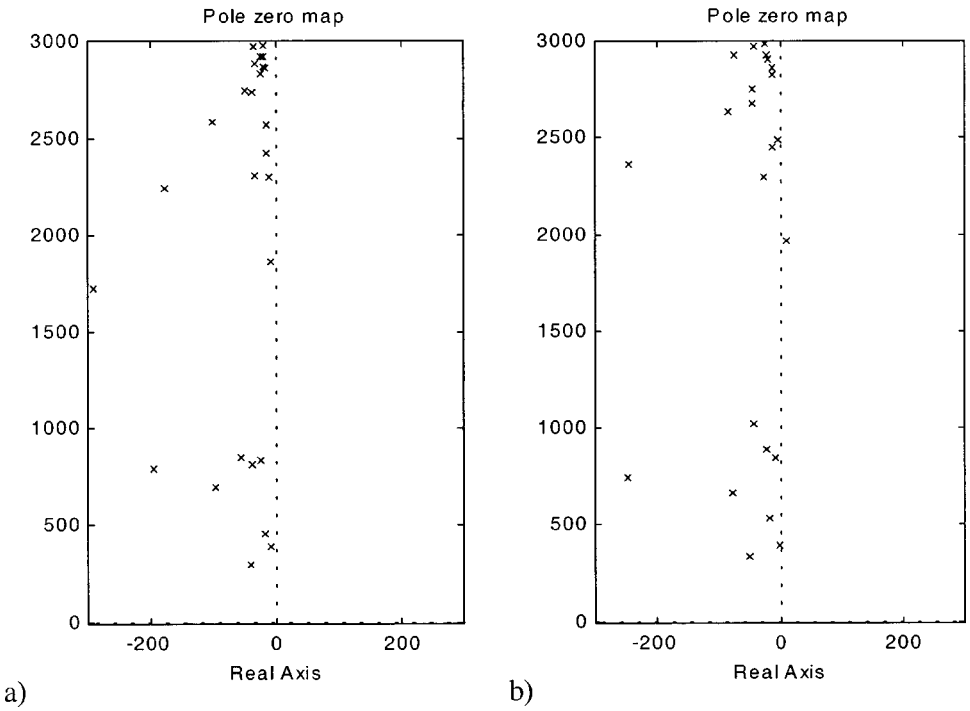

FIG. 13. Poles for the controlled plant (a) nominal plant, (b) plant with thicker panel.

and

$$\mathbf{f}, \tag{49b}$$

are the control input and disturbances input. Also,

$$\mathbf{C_v} = [(-\mathbf{K}_{\mathrm{pzs}}^{\mathrm{elect}})^{-1} \quad \mathbf{K}_{\mathrm{pzs}}^{\mathrm{elastelect}} \quad \mathbf{0}], \tag{50a}$$

and

$$\mathbf{C_w} = \begin{bmatrix} \mathbf{s}^{\mathbf{t}} & \mathbf{0} \\ \mathbf{s}_{\mathbf{rc}}^{\mathbf{t}} & \mathbf{0} \\ \mathbf{s}_{\mathbf{sr}}^{\mathbf{t}} & \mathbf{0} \end{bmatrix} \tag{50b}$$

are the observed output and controlled output matrices, respectively, where the *sr* and *rc* subscripts identify output vectors for source and receiver, respectively.

Once the model of the plant is available in state-space form, it is possible to design appropriate controllers, e.g., LQG, using the routines available in MATLAB.

Furthermore, the mathematical model offers the possibility of connecting different inputs and outputs to investigate various strategies for vibration transmission reduction, e.g., minimization at the source, minimization at the receiver, or minimization along the transmitting structure. In the case of the structure investigated here, the control along the transmission path, attempted using the piezoelectric patches directly bonded on to the panel, as sensors and actuators, did not give acceptable results. This is mainly due to the relatively low level of force which can be produced by the patch used as actuator. In particular, the controller was only able to reduce slightly the amplitude of the peaks of the frequency response corresponding to the first and third mode, and it was not effective in reducing the response at the other resonances. The reason for this particular behavior is due to the position of the actuator patches which lie along a nodal line of most of the modes, and in particular of modes 2 and 4 (see Fig. 10). The situation does not improve if the controller has other signals available, e.g., the displacements of the receivers, which confirms that the problem of this configuration lies in the position of the actuators. Better results can be obtained when the control is applied at the mechanical interface of the source or receiver, as described in the following sections.

A. Control at source

In this case the control system drives (independently) the four suspensions of the equipment enclosure which generates the vibrations (source). The objective is to minimize the displacements and rotations of the two receivers. The signals available to the controller are numerous, and the option considered here is to use the displacements and rotations of the source as sensor signals.

The controller design is based on a plant model which uses the first 4-by-4 modal shapes of the bare panel, and afterwards, the performance of the controlled structure is simulated by using a more accurate plant model (built using a 6-by-6 modal base). Figure 11 shows the vertical displacements of a receiver (which correspond to box 3 in Fig. 5) with and without control.

B. Control at receiver

The vibrations at the sensitive equipment can be reduced by acting on the equipment's suspensions. In this case the signals available to the control system are taken as the displacements and rotations of the receivers, and the controller drives the active suspensions of the receivers in order to minimize their displacements and rotations. The results are reported in Fig. 12. Note that, compared with the active control at source (Fig. 11), this strategy allows a stronger reduction of the vibration level at the receivers location. Also, this

type of controller is relatively easy to implement because the sensors and actuators are located very close to each other.

Note that, even if the control strategies (A and B) presented in this paper are local, the panel plays an important role in the overall dynamics of the plant. The importance of a correct model of the panel in the global model of the plant is highlighted by the fact that the plant may become unstable for small changes in the panel characteristics. As an example, the controller designed in the case A, which produces a stable controlled plant (Fig. 13), becomes unstable for a change of 5% in the panel in the panel thickness.

IV. CONCLUSIONS

This paper has used a Lagrange Rayleigh Ritz (LRR) approach to develop state-space models of the dynamics of an equipment-loaded panel on which to undertake the design of active control strategies based on feedback control schemes. The equipment enclosures have been modeled as rigid rectangular boxes mounted on a flexible panel. The enclosures have internal resonators to simulate internal dynamics and there is provision for rigid or flexible mounting elements to allow for active/passive suspensions.

Piezoelectric patches are used as sensors and actuators on the panel, and piezoelectric stacks are used for the box suspensions.

A comparison of the results obtained, with results obtained by modeling the same system with the FE method, has established the validity and efficiency of the LRR approach to simulate the dynamics of this type of system. The reduced size of this LRR model, in comparison with the FE model, makes it particularly suitable for investigations into the active control of vibrations, since it is able to capture the essential dynamics of the plant in a model of manageable size. Thus, the LRR approach provides a convenient way of assessing various control algorithms and strategies. Furthermore, the efficiency of the model implies that Monte Carlo studies of the effects of uncertainties on the controller performance could realistically be undertaken: an ensemble of perturbed plants could be considered, and a controller designed for the nominal plant could be applied to the perturbed plants to investigate robustness.

In this paper, as an example application of the use of an LRR model, various control strategies, i.e., active control at the source, at the receiver, or along the transmission path have been briefly investigated. Active control along the transmission path, using piezoelectric patches bonded onto the panel, gave the worst results, mainly due to the position of the patches. In realistic applications most of the space on the panel will be taken by the equipment, and therefore the possibility of optimizing the position of the patches is very limited. The best option is control at the receiver location, which is also relatively easy and safe to implement since the sensors and actuators will be at roughly the same location.

[1] E. Schmitz, K. E. Richards, and C. T. Voth, ''An Integrated Active & Passive Control Design Methodology for the NASA LaRC CSI Evolutionary Model,'' in Proceedings of the SPIE, Smart Structures and Materials, Vol. 2193, 1994 (unpublished).

[2] H. R. Stark and C. Stavrinidis, ''ESA microgravity and microdynamics activities—An overview,'' Acta Astronaut. **34**, 205–221 (1994).

[3] J. Su, C. Huang, F. Austin, and G. Knowles, ''Vibration control of an active mirror pointing system,'' in Proceedings of the SPIE, Smart Structures and Materials, Smart Structures and Intelligent Systems, Vol. 1917, pp 37–48 (1993) (unpublished).

[4] S. J. Dine, D. E. L. Tunbridge, and P. P. Collins, The Vibration Environment on A Satellite in Orbit, IEE Colloquium On High Accuracy Platform Control in Space (1993) (unpublished).

[5] B. Garnier, D. Bondoux, and C. Clerc, ''Microvibration Control: Practical Tools for the Designer,'' in Proceedings of the 1st International Symposium On Space Microdynamics and Accuracy Control, 30 Nov. 1992, Nice, France (1992) (unpublished).

[6] C. M. Grodsinsky and K. A. Logsdon, ''Microgravity Vibration Isolation Technology: Development To Demonstration,'' in Proceedings of the 1st International Symposium On Space Microdynamics and Accuracy Control, 30 Nov. 1992, Nice, France (1992) (unpublished).

[7] S. A. Collins and A. H. Von Flotow, ''Active vibration control for spacecraft,'' 42nd Congress of the International Astronautical Federation, IAF Paper 91-289 (1991).

[8] A. H. von Flotow, ''An Expository Overview Of Active Control Of Machinery Mounts,'' in Proceedings of the 27th IEEE International Conference on Decision and Control, Austin, TX, pp. 2029–2033 (1988) (unpublished).

[9] P. Gardonio, S. J. Elliot, and R. J. Pinnington, ''Active isolation of structural vibrations on a multiple degree-of-freedom system,'' J. Sound Vib. **207**, 61–93 (1997).

[10] S. J. Elliot and L. Billet, ''Adaptive control of flexural waves propagating in a beam,'' J. Sound Vib. **163**, 295–310 (1993).

[11] L. Meirovitch, *Elements of Vibration Analysis* (McGraw-Hill, London, 1986).

[12] G. S. Aglietti, S. B. Gabriel, R. S. Langley, and E. Rogers, ''A modeling technique for active control design studies with application to spacecraft microvibrations,'' J. Acoust. Soc. Am. **102**, 2158–2166 (1997).

[13] O. C. Zienkiewicz, *The Finite Element Method* (McGraw-Hill, London, 1977).

[14] B. D. O. Anderson and J. B. Moore, *Optimal Control Linear Quadratic Methods* (Prentice-Hall, Englewood Cliffs, NJ, 1989).

[15] ANSYS Release 5.3, ANSYS Inc.

[16] MATLAB, Mathworks Inc. (1997).

[17] G. S. Aglietti, ''Active Control of Microvibrations for Equipment Loaded Spacecraft Panels,'' Ph.D. Thesis, University of Southampton, Southampton, UK (1999).

Estimation of structural wave numbers from spatially sparse response measurements[a)]

J. Gregory McDaniel
Department of Aerospace and Mechanical Engineering, Boston University, 110 Cummington Street, Boston, Massachusetts 02215

W. Steve Shepard, Jr.
Department of Mechanical Engineering, The University of Alabama, Box 870276, Tuscaloosa, Alabama 35487-0276

(Received 26 January 2000; revised 10 July 2000; accepted 24 July 2000)

A method is presented for estimating the complex wave numbers and amplitudes of waves that propagate in damped structures, such as beams, plates, and shells. The analytical basis of the method is a wave field that approximates response measurements in an aperture where no excitations are applied. At each frequency, the method iteratively adjusts wave numbers to best approximate response measurements, using wave numbers at neighboring frequencies as initial estimates in the search. In comparison to existing methods, the method generally requires far fewer measurement locations and does not require evenly spaced locations. The number of locations required by the method scales with the number of waves that propagate in the structure, whereas the number of locations required by existing methods scales with the minimum wavelength. In addition, the method allows convenient inclusion of the analytic relationships between wave numbers that exist for flexural vibrations of beams and plates. Advantages of the method are illustrated by an example in which a beam is excited by a transverse force at one end. Using analytic data and experimental measurements, the method produces a wave field that matches response measurements to within 1 percent. One interesting feature of the new method is that, when applied to analytic data, it supplies more robust wave number estimates using responses at unevenly spaced locations. [S0001-4966(00)05910-5]

PACS numbers: 43.40.At, 43.40.Cw, 43.35.Mr [CBB]

I. INTRODUCTION

This paper presents a method for constructing wave fields from spatially sparse response data. The wave descriptions include dispersion relations of the waves that propagate in the structure as well as the associated wave amplitudes. The method applies to structures such as beams, plates, and shells that support waves along one coordinate. This includes structures that are nonhomogeneous in the cross-sectional coordinates, such as composite layered structures, as long as their dynamics are represented by equivalent homogeneous structures. The constrained-layer damping of a beam as analyzed by Kerwin[1] and Ross *et al.*[2] is an example of such a structure.

The dispersion relations are useful in that they contain information about the structure's viscoelastic properties that is otherwise difficult to experimentally measure. One of the most important of these is the material loss factor of the structure, which is easily derived from the dispersion relations. Extraction of such parameters from relatively simple experiments allows one to construct more accurate finite-element models of structural assemblages. For example, experiments on a single beam can be used to characterize viscoelastic properties for use in a finite-element model of a truss composed of beams with varying lengths.

Other methods of estimating the loss factor derive from modal descriptions of the structural response. These include the half-power point method and the many variations of modal analysis and testing.[3] These methods are more general than the proposed method in that they make very few assumptions about the structure. However, they only yield estimates of the loss factor near the resonance frequencies of the structure, whereas the proposed method is capable of estimating the loss factor at any frequency. This difference is important when the loss factor varies significantly over the frequency range of interest and the resonance frequencies are not close enough to track the variations. Loss factors that vary substantially over small frequency bands have been realized through a variety of damping technologies, an example being a box beam filled with small viscoelastic spheres.[4]

Estimation of the loss factor by the measurement of spatial wave attenuation has been used by others and is described in the text by Cremer and Heckl.[5] However, to date the concept appears to have been limited to experiments that either generate one wave propagating in one direction or to experiments in which the boundary conditions are known precisely. The former generally requires long structures with high damping, so that a wave generated at one end is mostly attenuated before it reaches the other end. Bland and Lee[6] developed a method that allowed for more than one wave but assumed a precise knowledge of the boundary conditions.

[a)]A portion of this work was presented at the 130th Meeting of the Acoustical Society: J. Gregory McDaniel, Kevin D. LePage, and Nathan C. Martin, ''Computation of Complex Wave Numbers and Amplitudes on Vibrating Structures from Response Data,'' J. Acoust. Soc. Am. **98**, Pt. 2 (1995).

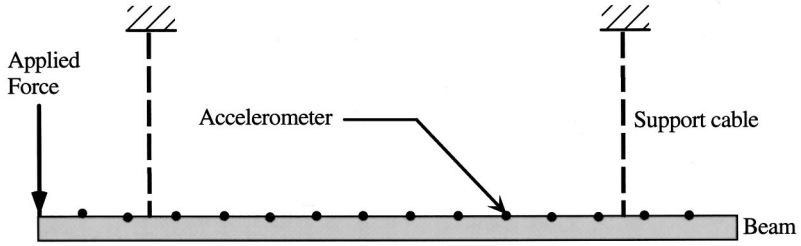

FIG. 1. A schematic of the beam experiment.

Their method required an experiment in which a damped beam was excited by a time-harmonic force at one end while the other end was either free or held fixed. By measuring the ratio of the velocities at each end of the beam and knowing the boundary conditions, their method yielded estimates of the loss factor at each frequency of excitation.

In recent years, a variety of methods has been developed and used to construct wave fields from finely sampled response measurements. The foundation for much of this work was laid over two centuries ago by Prony,[7,8] who developed a method for estimating the parameters of damped sinusoids from evenly spaced measurements. His elegant analysis transformed the problem into one of finding the complex roots of a polynomial equation. As originally presented, Prony's method was very sensitive to noise. To overcome this difficulty, improvements were made that resulted in the total-least-squares Prony's method (TLS)[9,10] and the singular-value decomposition Prony's method (SVD).[11,12] Another method that has received much attention in the literature is the matrix pencil method,[13–15] which has been shown to have a lower variance of parameter estimates than Prony-based methods.

Prony-based methods have been successfully applied to analytic and experimental responses of cylindrical shells. Plona *et al.*[16] estimated dispersion relations of fluid-loaded cylindrical shells by applying Prony's method to response measurements at 20–40 locations along the axis of the shell. The estimated dispersion relations agreed with theoretical estimates obtained by Sinha *et al.*[17] Grosh and Williams[18] developed a modified Prony's method that addressed backward and forward propagating waves and applied it to analytic response data. Vollmann *et al.*[19] used a complex spectrum technique to estimate the dispersion relations of cylindrical shells filled with various viscoelastic media. Their dispersions agreed with theoretical predictions.[20]

For the problem of structural wave estimation, Prony-based methods and their derivatives have the advantages of being computationally efficient and requiring very little *a priori* knowledge of the vibrating structure. However, they generally suffer from three disadvantages that are overcome by the present work. First, they require response measurements at a relatively large number of locations on the structure in order to model highly attenuated waves in the presence of measurement noise, as discussed by Grosh and Williams.[18] In their work, responses at 64 axial locations on a cylindrical shell were used in a modified Prony's method. Although propagating waves were accurately identified, evanescent waves were unrecoverable in the presence of a 50–60 SNR. Second, these methods require substantial reformulation to include relationships between wave numbers. For example, evanescent and flexural waves on beams are related by a factor of $\sqrt{-1}$. Finally, these methods require evenly spaced data. Even though most experiments collect data at evenly spaced locations, the failure of a single sensor destroys the applicability of the method. More importantly, it is not clear that evenly spaced measurement locations are optimal for constructing wave fields.

The present work provides analytical and experimental demonstrations of a method that requires far fewer response measurements to construct wave solutions. In particular, the new method overcomes the Nyquist sampling criteria in cases where the complex wave numbers may be roughly estimated. In addition, the method allows exploitation of relationships between wave numbers in order to reduce the number of wave numbers that are extracted from data. A simplified form of the method was used in a previous paper by one of the authors.[21] The present paper provides a more general and complete account of the method, including its application beyond the Nyquist criterion and its application to unevenly spaced measurement locations.

The method requires that the steady-state response is measured at locations within an aperture in which no excitation is applied to the structure. An example experimental arrangement, which is used in examples presented in Secs. IV and V, is shown in Fig. 1. In such experiments, the structure supports a finite set of waves that propagate back and forth across the aperture and that decays due to the damping of the structure. At each frequency, a wave is characterized by a complex wave amplitude and a complex wave number. The proposed method fits a linear combination of these waves to measured responses by adjusting the complex wave numbers and amplitudes to best approximate the data.

This fitting of waves to data is performed iteratively. In brief, initial wave number estimates are made and wave amplitudes are calculated by performing a least-squares fit to data. A wave field is constructed by simply adding the contributions of the individual waves. This wave field is evaluated at the measurement locations and the error between the wave field and the data is calculated. This error is used to refine the estimates of the trial wave numbers. This process, which may be facilitated by a variety of nonlinear optimization techniques, continues until the error between the data and the wave field is sufficiently small. As is the case for Prony-based methods, time-domain equivalents of the iterative method used here have been previously developed.[22–25] In addition, some investigations have shown that the iterative

approach avoids ill-conditioning problems inherent in Prony-based approaches.[26]

In the following section, an analytical basis for the wave field is presented for a broad class of structures. In Sec. III, an iterative method for estimating wave numbers and wave amplitudes is described. In Sec. IV, the method is applied to an example problem consisting of a beam excited into flexural vibrations by a transverse force at one end. These analytic data are polluted with noise and sampled at nine locations along the beam in order to simulate the experimental data used in Sec. V.

II. ANALYTICAL BASIS FOR THE WAVE FIELD

The method is based on the solution of a homogeneous linear partial differential equation that describes the motion of the neutral surface or axis of a structure. For simplicity, this development considers a displacement w that only varies with respect to a spatial coordinate, x. Using a harmonic time dependence of $w=\Re\{We^{-i\omega t}\}$, the governing differential equation for the steady-state displacement amplitude, W, with no distributed loading is of the form

$$-\omega^2 W+\mathcal{L}\{W\}=0, \tag{1}$$

where $\mathcal{L}$ is a linear operator that involves derivatives with respect to x and structural parameters. Boundary conditions are assumed to be of the form

$$\mathcal{L}_b\{w\}|_{x=x_b}=\Re\{Be^{-i\omega t}\}, \tag{2}$$

where x_b represents the boundaries of the aperture and B is complex valued. The number of such boundary conditions depends on the order of differentiation contained in the linear operator $\mathcal{L}$. Note that other response fields, such as velocity or acceleration, may also be used as these quantities are proportional to the displacement field at each frequency.

The steady-state solution of Eq. (1) subject to a set of boundary conditions of the form given in Eq. (2) is a summation of damped waves

$$W(x)=\sum_{n=1}^{N}\{F_n\exp[ik_n x]+B_n\exp[ik_n(L-x)]\}. \tag{3}$$

Each value of n represents a distinct wave type that naturally propagates on the structure with a complex-valued wave number, k_n. For uniqueness, the real and imaginary parts of each wave number are assumed positive. The complex-valued amplitudes of the forward and backward propagating waves are denoted by F_n and B_n, respectively, and are determined by the boundary conditions.

The wave numbers can usually be estimated if the cross-sectional dimensions and parameters are known. For convenience of referral, dispersion relations for flexural, longitudinal, and torsional waves in homogeneous beams of constant cross section will be given here. For flexural waves in beams, the wave number is

$$k_f=\left(\sqrt{\frac{\rho A\omega^2}{E(\omega)[1-i\eta(\omega)]I}}\right)^{1/4}, \tag{4}$$

where ρ is the mass density, A is the cross-sectional area, I is the area moment of inertia, E is the real part of the Young's modulus, and η is the material loss factor. Beams in flexure also support a highly attenuated evanescent wave, whose wave number is related to the flexural wave number by $k_e=ik_f$. Algebraic manipulation of this equation yields the following relationship between loss factor and wave number:

$$\eta=\frac{\Im\{k_f^4\}}{\Re\{k_f^4\}}. \tag{5}$$

For longitudinal waves in beams, the wave number is

$$k_l=\sqrt{\frac{\rho\omega^2}{E(\omega)[1-i\eta(\omega)]}}. \tag{6}$$

and the loss factor is related to wave number by

$$\eta=\frac{\Im\{k_l^2\}}{\Re\{k_l^2\}}. \tag{7}$$

Relations for torsional waves may be found from Eqs. (6) and (7) by replacing E with the shear modulus, $G=E/[2(1+\nu)]$.

By convention, each wave is required to decay in its propagation direction. Therefore, $\Im\{k_n\}>0$ is a forward-propagating wave and $\Im\{k_n\}<0$ is a backward-propagating wave. The choice of the $\exp[ik_n(L-x)]$ dependence in Eq. (3) for the backward-propagating waves, as opposed to the simpler form of $\exp[-ik_n x]$, is motivated by numerical issues. All backward propagating waves are generated at $x=L$. If a backward propagating wave is described by the form in the above equation, its amplitude B_n corresponds to the value of the wave field at its point of origin. The wave could also be described by the simpler form $b_n\exp[-ik_n x]$, where $b_n=B_n\exp[ik_n L]$. However, as $\Im\{k_n\}L$ increases, b_n decreases and might underflow to a zero value during a finite precision calculation.

III. ITERATIVE ESTIMATION OF WAVE NUMBERS FROM DATA

The present method adjusts the wave numbers and wave amplitudes in Eq. (3) so that the resulting wave field approximates measured data. For the present discussion, the measured response consists of the complex amplitudes of displacement at locations denoted by x_m, where $m=1,2,...,M$. These amplitudes are denoted by $\tilde{W}_m$ and are assumed to be measured at each frequency of interest.

For the moment, let us consider a single response frequency. The method begins with rough initial estimates of the wave numbers at this frequency. These may be obtained either from a simplified processing of the measured response, from a knowledge of the material properties and dimensions of the structure, or from an application of the method at a neighboring frequency. For example, the real parts of the wave numbers may be estimated by locating peaks in a wave number transform of the spatial data. If the structural cross section is approximately homogeneous, then the analytical dispersion relations given in Eqs. (4) and (6) can be used to obtain estimates.

Given initial wave number estimates, the wave amplitudes are found by requiring the wave field in Eq. (3) to

approximate the data at the measurement locations

$$W_m \approx \tilde{W}_m \quad \text{for} \quad m=1,2,\ldots,M. \tag{8}$$

Each W_m is the sum of all of the individual wave fields evaluated at the mth measurement position and is found from Eq. (3)

$$W_m = \sum_{n=1}^{N} \{F_n \exp[ik_n x_m] + B_n \exp[ik_n(L-x_m)]\}. \tag{9}$$

For modeling either longitudinal or torsional responses, $N=1$ in the above equation, as only one wave propagates. For beams in flexure, $N=2$ is required, as flexural and evanescent waves must be included. The fields produced by the evanescent waves, which are sometimes referred to as ''near fields,'' insure that the model is accurate even at lower frequencies.

Writing the approximations in Eq. (8) in matrix form gives

$$[[\Phi][\beta]]]\begin{Bmatrix}\{F\}\\ \{B\}\end{Bmatrix} \approx \{\tilde{W}\}, \tag{10}$$

where the forward and backward propagation matrices, $[\Phi]$ and $[\beta]$, are given by

$$\Phi_{mn} = e^{ik_n x_m} \quad \text{and} \quad \beta_{mn} = e^{ik_n(L-x_m)}. \tag{11}$$

If $M \leqslant 2N$, then the number of unknowns exceeds the number of equations and the wave field can identically reproduce the data for any choice of wave numbers. It must therefore be required that $M > 2N$, which makes Eq. (10) overconstrained. The wave amplitudes are found by satisfying this equation in a least-squares sense. As a consequence, the number of necessary measurement locations required by the method scales with the number of waves that propagate in the structure.

Once the wave numbers and amplitudes are initially estimated, the wave field is evaluated and an error norm is used to quantify errors between the wave field and response measurements. The examples presented here use the normalized mean square error defined by

$$\varepsilon = \sqrt{\left(\sum_{m=1}^{M} |W_m - \tilde{W}_m|^2\right) \Big/ \left(\sum_{m=1}^{M} |\tilde{W}_m|^2\right)}. \tag{12}$$

Based on this error norm, the wave number estimates are refined and the process repeats. This repetition continues until the error norm is below a set tolerance.

This procedure may be automated by using nonlinear optimization routines[27] to simultaneously adjust the real and imaginary parts of each k_n to minimize ε. The stability and efficiency of the method may be improved by recognizing that, in most cases, the wave dispersion is desired at many frequencies over a frequency band. Therefore, one begins by estimating the loss factor at one end of the frequency band and stepping in frequency, at each step using the wave number estimates from the previous frequency as initial estimates in the search at the new frequency.

In cases where the wave field is dependent on a single wave number, such as the flexural, longitudinal, and torsional wave fields described in the previous section, one has the luxury of computing an error surface in which the two planar axes are the real and imaginary parts of the wave number. An estimate of the wave number may then be obtained by locating the global minimum of the surface. In practice, this is an advisable approach for obtaining a good initial wave number estimate at the first considered frequency. This estimate may be then be iteratively refined, as described above, and the search procedure at other frequencies may use the final estimate at a neighboring frequency as an initial estimate. This process will be illustrated in the following two sections.

In practice, the wave numbers are not known and one may develop confidence in the estimates in two ways. First, the error norm in Eq. (12) may be evaluated using the final wave number estimates. Large errors indicate that the wave field poorly matches the measured response and the wave number estimates are therefore far from the actual. In the authors' experience, a value of ε that is less than 0.05 generally implies an accurate wave number estimate. Second, the continuity of the wave number over the frequency band is an important measure of confidence. This requires a sufficiently fine sampling in frequency, so that any apparent discontinuities are not caused by undersampling in frequency.

IV. APPLICATION TO AN ANALYTICAL MODEL OF A VIBRATING BEAM

In this section, the method is applied to an analytical model of a beam in flexural vibration. The purpose of this example is to illustrate the performance of the method in a circumstance where the estimated wave numbers may be compared to known values. The example will include the effects of noise and sparse spatial sampling, which are expected in the experimental data analyzed in Sec. V. The beam considered in the example has one end free while the other end is excited by a transverse force. These boundary conditions are close to those used in experiment.

For generality of the numerical results, a normalized frequency Ω is defined using the first resonance frequency of the free-free beam[28]

$$\Omega = \omega\left(\frac{2L}{3\pi}\right)^2 \sqrt{\frac{\rho A}{EI}}. \tag{13}$$

In this example, the frequency-dependent loss factor of the beam will be taken as

$$\eta = \frac{2\Omega}{1+\Omega^2}, \tag{14}$$

and the Young's modulus will be assumed constant over the considered frequency range. The flexural wave number is evaluated using Eq. (4), which simplifies to

$$k = \frac{3\pi}{2L}\frac{1}{4}\sqrt{\frac{\Omega^2}{1-i\eta}}. \tag{15}$$

The real and imaginary parts of the normalized wave number, kL, are plotted and labeled ''Actual'' in Figs. 4 and 5.

The beam response is obtained by applying boundary conditions to the wave field in Eq. (3), where the wave num-

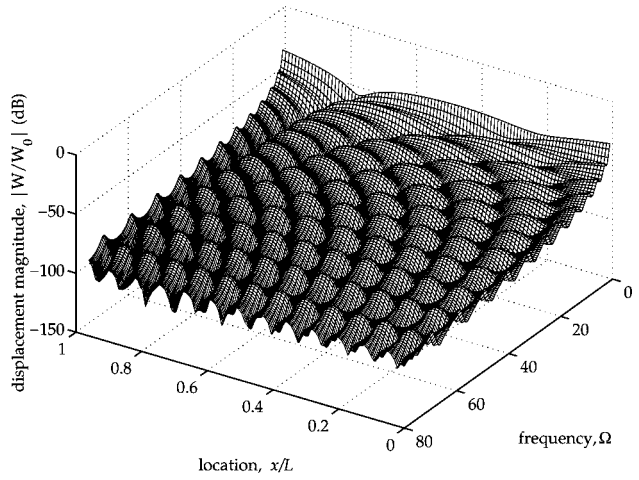

FIG. 2. A plot of the normalized displacement magnitude of the beam due to a transverse load at $x=0$.

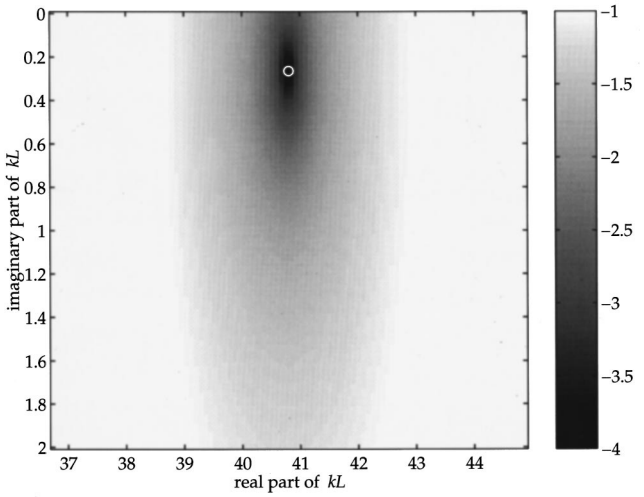

FIG. 3. Plot of the logarithm of the normalized mean-square error, $\log_{10}(\varepsilon)$, for $\Omega=75$. The actual value of kL is indicated by the circle.

bers are $k_1=k_f$ and $k_2=ik_f$. For this example, the boundary conditions require zero bending moment at both ends of the beam

$$E(1-i\eta)I\frac{\partial^2 W}{\partial x^2}\bigg|_{x=0}=0 \quad \text{and} \quad E(1-i\eta)I\frac{\partial^2 W}{\partial x^2}\bigg|_{x=L}=0, \tag{16}$$

a zero shear force at $x=L$

$$E(1-i\eta)I\frac{\partial^3 W}{\partial x^3}\bigg|_{x=L}=0, \tag{17}$$

and a shear force equal to the applied force at $x=0$,

$$E(1-i\eta)I\frac{\partial^3 W}{\partial x^3}\bigg|_{x=L}=-F. \tag{18}$$

Application of these four conditions to the wave solution yields a linear set of equations that is solved for the four wave amplitudes. Substitution of the amplitudes into the wave solution allows evaluation of the displacement at any location on the beam. A normalized displacement is defined by W/W_0, where $W_0=FL^3/EI$.

A surface plot of the displacement amplitude versus frequency and position is given in Fig. 2. In this figure, one observes summations of forward- and backward-going waves that produce spatial oscillations governed by the flexural wavelength. In addition, a decay envelope due to damping is observed as one moves away from either end of the beam, where the waves originate. At any location on the beam, one observes relative maxima that correspond to damped resonances of the beam. Using a modal method, the loss factor could only be estimated near the resonance frequencies.

In order to simulate experimental conditions, the response is sampled at a small number of locations and corrupted with Gaussian noise. The measurement locations are equally spaced along the beam and the aperture is chosen to include the entire length of the beam. Nine measurement locations are chosen, so that the Nyquist sampling criterion is violated at $\Omega>30$. The real and imaginary parts of the noise are assumed to be Gaussian distributions with zero mean and unity standard deviation multiplied by 1 percent of the mean displacement magnitude at each frequency. According to the definition used by Grosh and Williams,[18] the SNR is approximately 40 dB at each frequency. The final set of response data consists of the noise-corrupted displacement amplitudes at nine specified beam locations for 200 evenly spaced excitation frequencies over the range $1<\Omega<75$.

Figure 3 contains a plot of the logarithm of the normalized mean square error versus the real and imaginary parts of the flexural wave number at the highest frequency in the band, $\Omega=75$. This plot indicates a clear minimum near the actual value, indicated by the white circle. This wave number was used as an initial estimate in a search for the final estimate at that frequency. For the results presented here, the search was automated by using a simplex algorithm. The wave number at the next lower frequency was extracted using the wave number estimated at the previous frequency as an initial estimate. This procedure continued down in frequency until the end of the band was reached.

The real and imaginary parts of the normalized wave number estimated by this procedure are shown in Figs. 4 and 5. The different scales on the two plots leave the erroneous impression that the imaginary part of the wave number is more sensitive to the noise, when in fact only the relative errors in the imaginary part are greater. To observe this, the errors in the real and imaginary parts of the wave number are plotted on the same scale in Fig. 6, where they are seen to be the same magnitude. Note that the horizontal axis is the ratio between Δ, which is the spacing between the response locations, and λ, the wavelength of the flexural wave. The Nyquist criterion is exceeded when Δ/λ exceeds 0.5. The wave number is accurately predicted above the Nyquist criterion; however, relatively large errors are seen near the criterion.

These large errors near the Nyquist criterion result from sampling the response field at equally spaced locations. Since the method does not require equally spaced locations, this situation may be improved by sampling the response at unequally spaced locations. To illustrate this, the response was resampled at the ends of the beam and at seven ran-

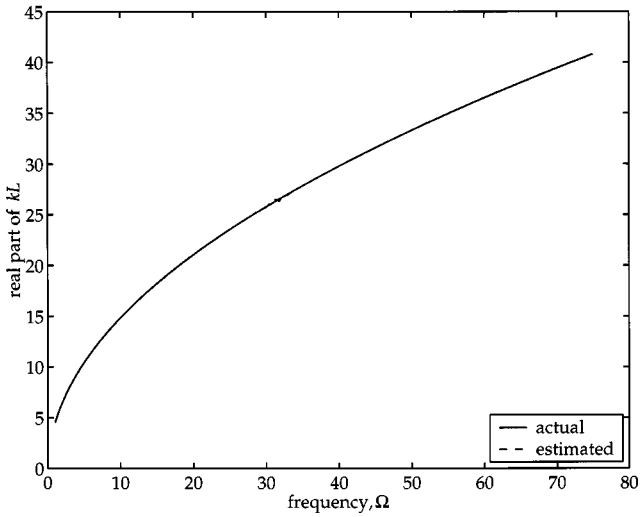

FIG. 4. A plot of the real part of normalized wave number versus normalized frequency.

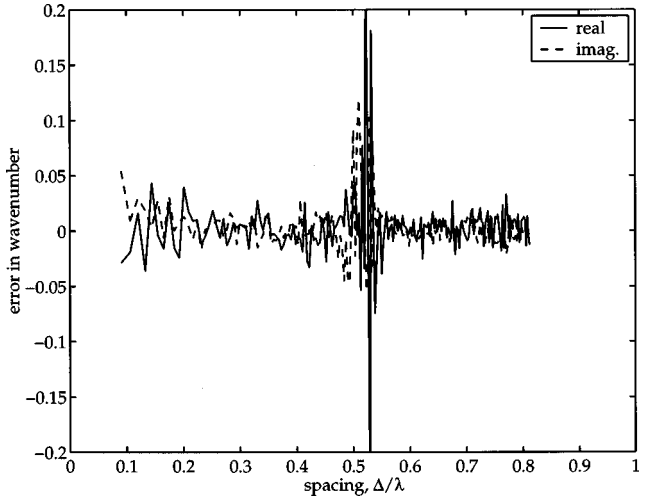

FIG. 6. Plot of the errors in the real and imaginary parts of the normalized wave number, kL, using equal spacing of response locations.

domly chosen locations in between, so that the total number of locations was kept the same. The method was applied to this response data and the resulting errors are plotted in Fig. 7 using the same horizontal axis as in Fig. 6. Large errors near the Nyquist criterion have been eliminated by the unequal spacing.

V. APPLICATION TO EXPERIMENTAL DATA FROM A VIBRATING BEAM

In this section, the method is applied to experimental measurements taken on a damped beam. A schematic of the experiment is shown in Fig. 1. The acceleration of the beam was measured by nine evenly spaced accelerometers that spanned the length the beam and an electromagnetic shaker produced a transverse force at one end. The shaker was driven by a random time signal and the measured beam acceleration was Fourier transformed to obtain the complex amplitude of acceleration at the nine locations. The acceleration magnitudes at the middle and ends of the beam are plotted versus frequency, which is again normalized by the first resonance frequency of the beam, in Fig. 8. The second resonance occurs near $\Omega=3$ and the third resonance near $\Omega=6.5$. Spatial decay of the measured response, due to the intrinsic material damping of the beam, is evidenced in this figure by large reductions in vibration from the forced end at $x/L=0$ and the far end at $x/L=1$. This substantial and frequency-dependent damping is expected from the design of the beam.

As in the previous section, the wave number estimation began at the highest frequency in the band, $\Omega=8$. In order to determine a starting guess for the complex wave number at this frequency, a plot of the logarithm of the normalized mean-square error versus the real and imaginary parts of wave number is shown in Fig. 9. One local minimum is observed near a wave number of $kL\approx 10+i0.6$. The real part of this wave number is close to an estimate based on the dimensions and material of the beam. Another local minimum appears at $kL\approx 33+i0.6$; however, the real part is more than three times the value estimated from the cross-

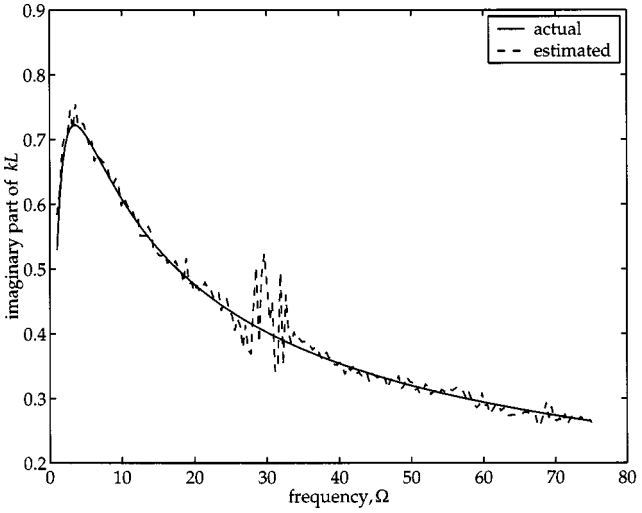

FIG. 5. A plot of the imaginary part of normalized wave number versus normalized frequency.

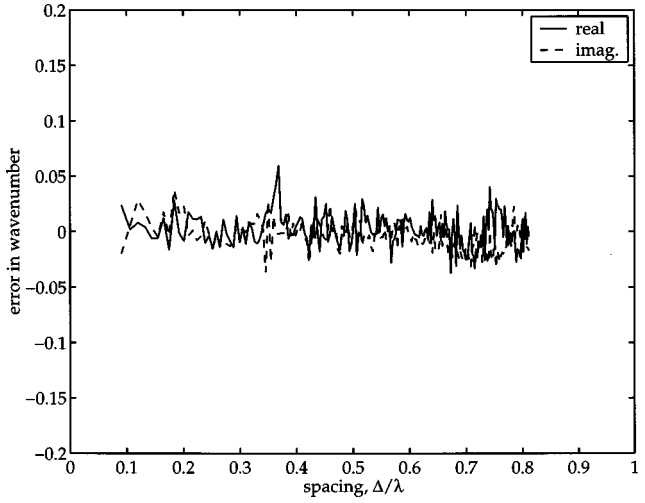

FIG. 7. Plot of the errors in the real and imaginary parts of the normalized wave number, kL, using unequal spacing of the response locations.

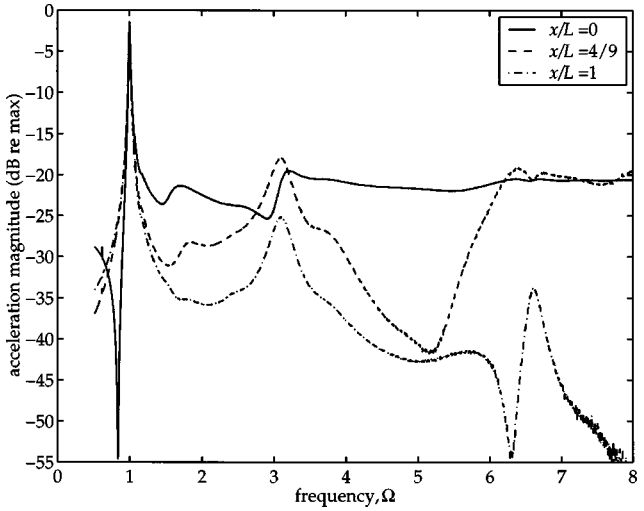

FIG. 8. Plot of the acceleration measured at three locations on a free–free beam that is excited at one end by a mechanical shaker.

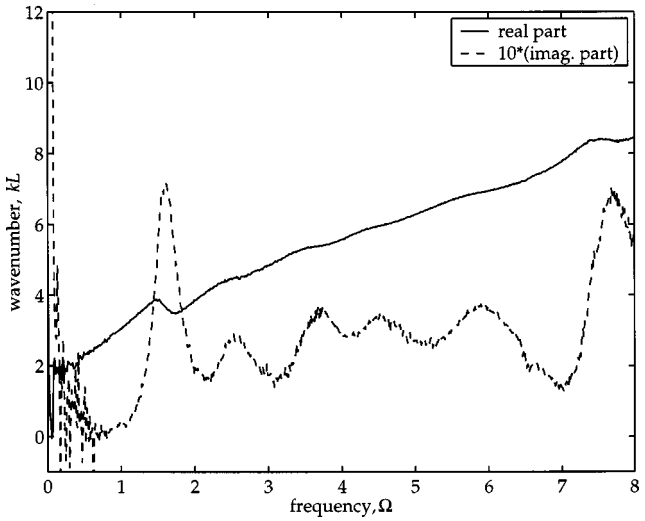

FIG. 10. Plot of the complex wave number estimated from the experimental data using the method.

sectional dimensions and material of the beam. Therefore, $k \approx 10 + i0.6$ is used as an initial estimate.

This estimate is used by a simplex algorithm that varies the real and imaginary parts of the wave number to minimize the normalized mean-square error. After the algorithm refines this guess, the wave number at the next lower frequency is estimated using the final wave number estimate at $\Omega = 8$ as an initial estimate. The process continues in this way down to zero frequency. The normalized wave number is plotted in Fig. 10. Dramatic variations in the wave number at frequencies below $\Omega = 0.75$ indicate that the method is not capable of accurately extracting the wave number, as such variations are physically unrealizable. Over the rest of the frequency band, the continuity of the wave number is one indication that the method succeeded.

Another indication is given in Fig. 11, where the normalized mean-square error is plotted versus frequency. This plot was produced by using the wave numbers in Fig. 10. Low errors indicate the accuracy of the method, which involves five adjustable parameters, to best approximate the nine measured values of acceleration. While the errors are less than 1 percent, the rapid variations in wave number at frequencies below $\Omega = 0.75$ lead to the conclusion that a large range of wave numbers would produce low errors. An analytical explanation for the low-frequency failure of the method has been developed and is included in the Appendix. The method appears to produce acceptable results above $\Omega = 0.75$ as the errors are small and the estimated wave numbers are continuous functions of frequency.

As an additional verification, the loss factor of the beam was evaluated by fitting a modal description to the first three modes of the beam. To do this, the impulse response of the beam in the time domain was calculated by taking the inverse Fourier transform of the frequency response. Using the matrix pencil method,[13–15] six damped sinusoids were fit to the acceleration at the center of the beam. The center of the beam was used because the first three modes produced accelerations of roughly the same magnitude at that location. Note that the second mode of a symmetric free–free beam would have a node at the midpoint of the beam; however, small nonsymmetries in the beam produced a finite response

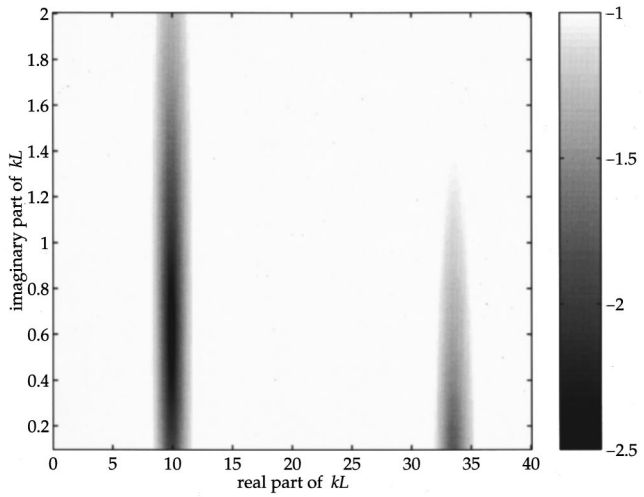

FIG. 9. Plot of the logarithm of the error at $\Omega = 8$.

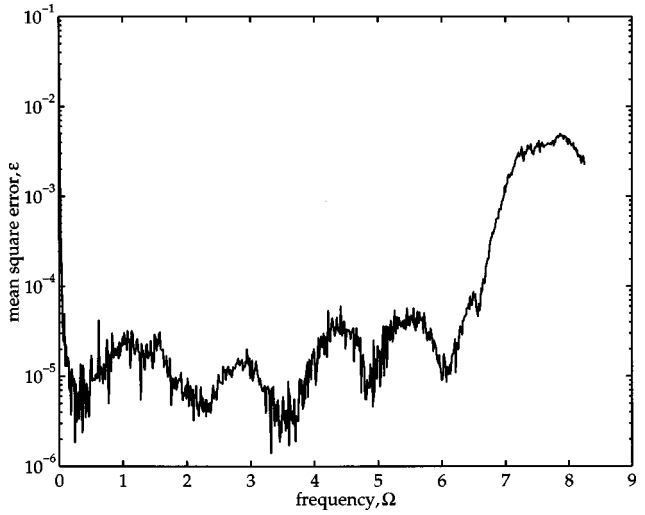

FIG. 11. Plot of the error in fitting the acceleration of the beam by using the complex wave numbers shown in Fig. 10.

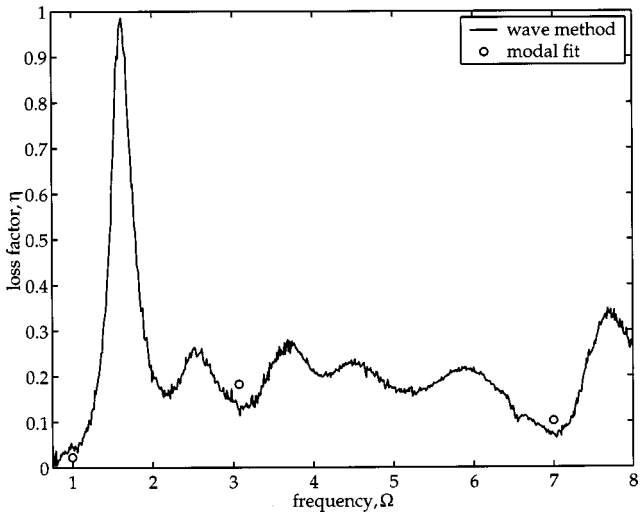

FIG. 12. Plot of the loss factor estimated from the experimental data using the method and a modal fit.

there. Accelerometers at the ends of the beam were not used because the large accelerations of the first mode prevented accurate estimation of the modal properties of the second and third modes. The results are shown in Fig. 12, where the modal loss factor estimates agree with those predicted by using the estimated wave number. Note, however, that the new method estimates the loss factor at all measured frequencies whereas the modal estimates may only be obtained at the modal frequencies.

VI. CONCLUSIONS

The present method provides an accurate means of estimating the dispersion relations of waves in damped structures from a small number of measured response amplitudes at frequencies above the first structural resonance. The method expresses the steady-state response amplitudes as a sum of damped waves that propagate forward and backward across an aperture in which no external force is applied. For time-harmonic flexural vibrations of a beam, one complex wave number and four wave amplitudes completely describe the response anywhere on the structure. For pure longitudinal or shear vibrations at a single frequency, one complex wave number and two wave amplitudes describe the response anywhere. The method does not require any knowledge of the boundary conditions, material properties, or cross-sectional dimensions of the structure.

The method offers the distinct advantage of working even when the Nyquist criterion for the distance between response locations is not satisfied. This advantage is gained by having an estimate of the structural wave numbers, which is usually available given cross-sectional dimensions and material parameters. While the method appears to produce large errors at sampling spacings equal to half of the structural wavelength, this weakness can be overcome by sampling the response at unevenly spaced locations. Additional analysis may reveal sets of sampling locations for which the wave numbers may be optimally estimated.

ACKNOWLEDGMENTS

The authors would like to thank Newport News Shipbuilding for collaborations in the experimental portion of the work. The first author gratefully acknowledges the support of the Office of Naval Research for a portion of this work and, in particular, the encouragement of Dr. Geoffrey Main and Dr. Vernon Simmons. The first author wishes to thank Dr. Nathan Martin who motivated the development of the method at BBN, Dr. Kevin LePage and Dr. Terrence Bazow, who provided useful insights into the application of optimization routines, and Dr. Pierre DuPont who offered advice on the writing of the manuscript.

APPENDIX: LOW-FREQUENCY FAILURE OF THE METHOD

In this section, a low-frequency analysis is presented that accounts for the failure of the method at low frequency, where the structural wavelengths are a fraction of the aperture over which the response is measured. Note that this aperture length, L, may be considerably different than the actual length of the structure. For clarity, consider a wave field that is composed of a single wave type. According to Eq. (3), this field is

$$W(x)=F_1\ \exp[ik_1x]+B_1\ \exp[ik_1(L-x)]. \tag{A1}$$

Now examine the situation where the wavelength is much larger than L, which corresponds to small values of k_1L. Performing a Taylor series expansion about $k_1L=0$ gives

$$W(x)\approx F_1(1+ik_1x)+B_1[1+ik_1(L-x)]. \tag{A2}$$

This equation may be rewritten as

$$W(x)\approx C_1+C_2(x/L), \tag{A3}$$

where

$$C_1=F_1+B_1(1+ik_1L)\ \text{ and }\ C_2=ik_1L(F_1-B_1). \tag{A4}$$

In this limit, the wave field is reduced to a linear function of position. Assuming that C_1 and C_2 are accurately found by fitting Eq. (A3) to data, this information is not sufficient to estimate the wave number. To see this, rewrite Eq. (A4) in matrix form as

$$\begin{bmatrix} 1 & 1+ik_1L \\ ik_1L & -ik_1L \end{bmatrix}\begin{Bmatrix} F_1 \\ B_1 \end{Bmatrix}=\begin{Bmatrix} C_1 \\ C_2 \end{Bmatrix}. \tag{A5}$$

This equation indicates an ambiguity in the wave number search, as the wave amplitudes F_1 and B_1 may be found to produce the linear fit coefficients C_1 and C_2 for any choice of wave number. This causes the method to fail, as the normalized mean-square error becomes independent of wave number in this limit.

[1] E. M. Kerwin, Jr., ''Damping of flexural waves by a constrained layer,'' J. Acoust. Soc. Am. **31**, 952–962 (1959).
[2] D. Ross, E. E. Ungar, and E. M. Kerwin, Jr., *Structural Damping* (ASME, New York, 1959), pp. 49–88.
[3] D. J. Ewins, *Modal Testing: Theory and Practice* (Wiley, New York, 1995).
[4] J. R. House, ''Damping hollow tubular structures with lightweight viscoelastic spheres,'' Polymeric Materials: Science and Engineering, Proceed-

ings of the ACS Division, 1989, Vol. 60, pp. 734–738.
[5] L. Cremer and M. Heckl, *Structure-Borne Sound*, 2nd ed. (Springer, New York, 1987). Translated and revised by E. E. Ungar.
[6] D. R. Bland and E. H. Lee, ''Calculation of the complex modulus of linear viscoelastic materials from vibrating reed measurements,'' J. Appl. Phys. **26**(12), 1497 (1955).
[7] R. de Prony, ''Essai experimental et analytique,'' J. Ec. Polytech. (Paris) **1**, 24–76 (1795).
[8] F. B. Hildebrand, *Introduction to Numerical Analysis* (McGraw-Hill, New York, 1956), pp. 378–383.
[9] G. H. Golub and C. F. Van Loan, ''An analysis of the total least squares problem,'' SIAM **17**, 883–893 (1980).
[10] W. M. Steedly, C. H. J. Ying, and R. L. Moses, ''Statistical analysis of TLS-based Prony techniques,'' Automatica **30**, 115–129 (1994).
[11] D. W. Tufts and R. Kumaresan, ''Estimation of frequencies of multiple sinusoids: Making linear prediction perform like maximum likelihood,'' Proc. IEEE **70**, 975–989 (1982).
[12] R. Kumaresan and D. W. Tufts, ''Estimating the parameters of exponentially damped sinusoids with pole-zero modeling in noise,'' IEEE Trans. Acoust., Speech, Signal Process. **ASSP-30**, 833–840 (1982).
[13] Y. Hua, ''On techniques for estimating parameters of exponentially damped/undamped sinusoids in noise,'' Ph.D. thesis, Syracuse University, Syracuse, NY, August 1988.
[14] Y. Hua and T. K. Sarkar, ''Matrix pencil method for estimating parameters of exponentially damped/undamped sinusoids in noise,'' IEEE Trans. **38**(5), 814–824 (1990).
[15] T. K. Sarkar and O. Pereira, ''Using the matrix pencil method to estimate the parameters of a sum of complex exponentials,'' IEEE Antennas Propag. Mag. **37**(1), 48–55 (1995).
[16] T. J. Plona, B. K. Sinha, S. Kostek, and S.-K. Chang, ''Axisymmetric wave propagation in fluid-loaded cylindrical shells. II. Theory versus experiment,'' J. Acoust. Soc. Am. **92**, 1144–1155 (1992).
[17] B. K. Sinha, T. J. Plona, S. Kostek, and S.-K. Chang, ''Axisymmetric wave propagation in fluid-loaded cylindrical shells. I. Theory,'' J. Acoust. Soc. Am. **92**, 1132–1143 (1992).
[18] K. Grosh and E. G. Williams, ''Complex wave-number decomposition of structural vibrations,'' J. Acoust. Soc. Am. **93**, 836–848 (1993).
[19] J. Vollmann, R. Breu, and J. Dual, ''High-resolution analysis of the complex wave spectrum in a cylindrical shell containing a viscoelastic medium. Part I. Theory and numerical results,'' J. Acoust. Soc. Am. **102**, 896–908 (1997).
[20] J. Vollmann, R. Breu, and J. Dual, ''High-resolution analysis of the complex wave spectrum in a cylindrical shell containing a viscoelastic medium. Part II. Experimental results versus theory,'' J. Acoust. Soc. Am. **102**, 909–920 (1997).
[21] J. G. McDaniel, P. Dupont, and L. Salvino, ''A wave approach to estimating frequency-dependent damping under transient loading,'' J. Sound Vib. **231**, 433–449 (2000).
[22] M. Lal and E. Moore, ''An iterative technique for fitting exponentials,'' Int. J. Numer. Methods Eng. **10**(5), 979–990 (1976).
[23] S. J. Wright and J. N. Holt, ''Algorithms for nonlinear least squares with linear inequality constraints,'' SIAM J. Sci. Comput. **6**(4), 1033–1048 (1985).
[24] R. Kumaresan, L. L. Scharf, and A. K. Shaw, ''An algorithm for pole-zero modeling and spectral analysis,'' IEEE Trans. Acoust., Speech, Signal Process. **ASSP-34**(3), 637–640 (1986).
[25] L. Kirkup and J. Sutherland, ''Curve stripping and nonlinear fitting of polyexponential functions to data using a microcomputer,'' Comput. Phys. **2**, 64–68 (1988).
[26] G. E. Bromage, ''A quantification of the hazards of fitting sums of exponentials to noisy data,'' Comput. Phys. Commun. **30**(3), 229–233 (1983).
[27] W. H. Press, B. P. Flannery, S. A. Teukolsky, and W. T. Vetterling, *Numerical Recipes, The Art of Scientific Computing ([FORTRAN] Version)* (Cambridge University Press, New York, 1989).
[28] R. E. D. Bishop and D. C. Johnson, *Vibration Analysis Tables* (Cambridge University Press, Cambridge, 1956).

Acoustic noise during functional magnetic resonance imaging[a)]

Michael E. Ravicz
Eaton-Peabody Laboratory, Massachusetts Eye and Ear Infirmary, 243 Charles Street, Boston, Massachusetts 02114 and Research Laboratory of Electronics, Massachusetts Institute of Technology, 77 Massachusetts Avenue, Cambridge, Massachusetts 02139

Jennifer R. Melcher
Eaton-Peabody Laboratory, Boston, Massachusetts 02114 and Department of Otology and Laryngology, Harvard Medical School, Boston, Massachusetts 02115

Nelson Y.-S. Kiang
Eaton-Peabody Laboratory, Boston, Massachusetts 02114, Department of Otology and Laryngology, Harvard Medical School, Boston, Massachusetts 02115, Harvard-MIT Joint Division of Health Sciences and Technology and Department of Brain and Cognitive Sciences, MIT, 77 Massachusetts Avenue, Cambridge, Massachusetts 02139, and Neurology Service, Massachusetts General Hospital, Boston, Massachusetts 02114

(Received 27 May 1999; accepted for publication 16 July 2000)

Functional magnetic resonance imaging (fMRI) enables sites of brain activation to be localized in human subjects. For studies of the auditory system, acoustic noise generated during fMRI can interfere with assessments of this activation by introducing uncontrolled extraneous sounds. As a first step toward reducing the noise during fMRI, this paper describes the temporal and spectral characteristics of the noise present under typical fMRI study conditions for two imagers with different static magnetic field strengths. Peak noise levels were 123 and 138 dB *re* 20 μPa in a 1.5-tesla (T) and a 3-T imager, respectively. The noise spectrum (calculated over a 10-ms window coinciding with the highest-amplitude noise) showed a prominent maximum at 1 kHz for the 1.5-T imager (115 dB SPL) and at 1.4 kHz for the 3-T imager (131 dB SPL). The frequency content and timing of the most intense noise components indicated that the noise was primarily attributable to the readout gradients in the imaging pulse sequence. The noise persisted above background levels for 300–500 ms after gradient activity ceased, indicating that resonating structures in the imager or noise reverberating in the imager room were also factors. The gradient noise waveform was highly repeatable. In addition, the coolant pump for the imager's permanent magnet and the room air-handling system were sources of ongoing noise lower in both level and frequency than gradient coil noise. Knowledge of the sources and characteristics of the noise enabled the examination of general approaches to noise control that could be applied to reduce the unwanted noise during fMRI sessions. [S0001-4966(00)04610-5]

PACS numbers: 43.50.Cb, 43.50.Gf, 43.50.Ki [MRS]

I. INTRODUCTION

Magnetic resonance imaging (MRI) permits mapping of bodily structure and function and is now used routinely for both clinical and basic research studies. However, an undesirable aspect of present-day MRI is the high-level sounds produced by the imager and associated equipment. These unwanted sounds, or ''acoustic noise,'' pose particular difficulties for functional MRI (fMRI) studies that measure brain activation in response to sound stimuli. For example, the background noise can mask the stimuli (Shah *et al.*, 1999; Eden *et al.*, 1999), and the noise itself can produce brain activity that is not related to the intended stimuli (Bandettini *et al.*, 1998; Ulmer *et al.*, 1998; Talavage *et al.*, 1999; Edmister *et al.*, 1999). If the noise can be heard, then the auditory system presumably is in a different state than during quiet conditions more typical of physiological or psychophysical experiments on hearing. Earmuffs or earplugs are commonly used to reduce noise levels heard by subjects (e.g., Savoy *et al.* 1999), but they are insufficient to achieve acceptably quiet conditions (Ravicz and Melcher, 1998a, b). Although some modifications to the timing of imaging acquisition have been shown to reduce the *influence* of the noise on brain activity, these modified paradigms compromise either the temporal resolution of measurements or the efficiency with which data are acquired (Edmister *et al.*, 1999; Hall *et al.*, 1999; see Melcher *et al.*, 1999 for a discussion).

Acoustic noise in most imaging environments arises from various sources. Continuous noise can originate from ancillary equipment located in the room that houses the imager. This equipment often includes a pump for liquid helium used to supercool the imager's permanent magnet, a fan for supplying ventilation to the patient, and the air-handling equipment for the imager room. The highest-level noise,

[a)]Portions of this material were presented at the 1997 American Speech-Language-Hearing Association meeting, Boston, MA, 23 November 1997, the Twentieth and Twenty-first Midwinter Meetings of the Association for Research in Otolaryngology, St. Petersburg Beach, FL, 5 February 1997 and 18 February 1998, and the Fourth International Conference on Functional Mapping of the Human Brain, Montreal, PQ Canada, 11 June 1998.

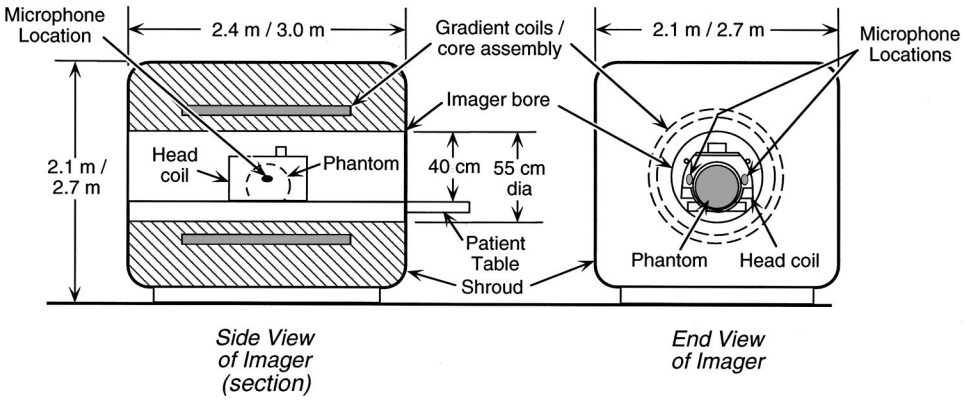

FIG. 1. Side view (left—in section) and end view (right) of a typical imager showing the gradient coils, bore, and location of microphones for noise measurements. The gradient coils and the cylindrical core on which they are wound surround the imager bore (the cylindrical opening through the center of the imager in which subjects lie during imaging). For noise measurements, a liquid-filled spherical plastic ''phantom'' (shown dashed in the side view) installed in a head coil was positioned where a subject's head would be during brain imaging. The measurement microphones appear larger than their actual size (Shure: 4×6×10 mm, Knowles: 3×4×6 mm). Outer dimensions are given for the 1.5-T imager first, then the 3-T imager; bore diameter applies to both imagers.

however, is intermittent and is produced whenever an image is acquired. To generate images, MRI uses both the static field of a permanent magnet and temporally varying magnetic field gradients to manipulate the nuclear spins of hydrogen nuclei (protons) in the body (e.g., Bushong, 1996; Cohen, 1998). Three sets of coils wound on a cylindrical fiberglass core are used to set up magnetic field gradients orthogonal and parallel to the long axis of the imager bore (e.g., Hedeen and Edelstein, 1997; see Fig. 1). When current is passed through these coils to set up the gradients, the resulting magnetic forces on the coils cause them to flex and thereby generate audible acoustic noise (e.g., Hurwitz *et al.*, 1989; Schmitt *et al.*, 1998). Flexure of the gradient coils can also produce acoustic noise secondarily. For example, vibration of the coils and the core on which they are wound can be conducted through the core supports to the rest of the imager's structure, which responds by vibrating noisily. Where the connections between the core and its supports are not rigid, parts can rattle against each other, further adding to the noise (Hurwitz *et al.*, 1989; Kelley, 1994). Although the exact noise may differ somewhat between imaging facilities, the generating mechanisms and characteristics may well be similar among commercial imagers. In this paper, acoustic noise produced directly or indirectly by the action of the gradient coils will be referred to as ''gradient noise.''

Previous reports of acoustic noise in the imaging environment have included measurements during functional MRI (Cho *et al.*, 1997; Shellock *et al.*, 1998; Prieto *et al.*, 1998; Miyati *et al.*, 1999) as well as during conventional anatomical imaging (e.g., Hurwitz *et al.*, 1989; Shellock *et al.*, 1994; McJury *et al.*, 1994; McJury, 1995; Counter *et al.*, 1997). All of the fMRI studies used protocols based on echo-planar imaging (EPI), a high-speed imaging method that involves rapid (e.g., 1 kHz) gradient switching (e.g., Cohen, 1998). Because most of these reports were, at least in part, motivated by concerns that exposures to high-level imaging noise might damage hearing (e.g., Brummett *et al.*, 1988), previous studies of the noise during EPI-based fMRI sought data that are relevant for estimating damage risk criteria, such as peak levels and/or time- and frequency-weighted time-average noise levels[1] (e.g., OSHA, 1996; ANSI S1.4-1985). A few studies have included some spectral information (Cho *et al.*, 1997; Miyati *et al.*, 1999) or qualitative descriptions of the noise (Wessinger *et al.*, 1997; Ulmer *et al.*, 1998). Still, as yet no study has provided a quantitative temporal and spectral description of the noise or examined the relationship between gradient noise and gradient activity—information essential for understanding the mechanisms of noise generation and examining possibilities for noise reduction.

The present study characterizes the entire ensemble of acoustic noise during EPI-based fMRI in our facility for the purpose of examining noise reduction options. Because our interest is not focused on assessing the risks to hearing, we did not use the measurement protocols typically used for estimating noise hazard. Instead, we concentrated on describing features of the noise that have direct implications for noise control. Thus, we related temporal and spectral characteristics of the noise to specific noise sources in the imaging environment and to particular gradients in the imaging pulse sequence, and we demonstrated the repeatability of the noise and the effects of variations in imaging parameters on the noise. We discuss several possibilities for treating imaging noise: (1) reduce the noise at its source; (2) reduce noise transmission from its source to the subject; (3) reduce noise levels at the subject's ears; and (4) apply active noise reduction techniques.

II. METHODS

A. Measurement location and imager parameters

Acoustic noise was measured in two General Electric Signa imagers equipped with resonant echo-planar imaging (EPI) gradient systems by Advanced NMR Systems (Wilmington, MA). The imagers had static magnetic field strengths of 1.5 and 3 tesla (T) and maximum magnetic gradients of 25 and 34 mT/m, respectively, and were located at the Massachusetts General Hospital's NMR Imaging Center in Charlestown, MA.[2] The imagers were situated in large rooms (approximate dimensions 5.0×8.0×2.7 m) with acoustic tile ceilings and hard walls and floors.

Acoustic measurements were made with two small microphones positioned in a standard transmit–receive head coil (General Electric) at the approximate locations of a subject's ears during imaging[3] (Fig. 1). A plastic, liquid-filled ''phantom'' (target used in calibrating the imager) was installed in the head coil and positioned where a subject's head would be during brain imaging. The microphones were attached by their cables to the phantom with tape. This attachment was such that the microphones were suspended by their cables and did not touch the phantom, thus avoiding direct vibrational coupling between phantom and microphone. The microphones were spatially separated from the phantom by approximately 5 mm.

Most measurements were made using a set of ''standard'' imaging parameters and while acquiring images of a single oblique slice.[4] For the 1.5-T imager, the pulse sequence for these standard measurements was asymmetric spin echo[5] [(ASE); interimage interval (TR)=2 s; slice thickness=7 mm; matrix size 128×64]. For the 3-T imager, the standard pulse sequence was spin echo[6] [(SE); TR=2 s; slice thickness=5 mm; matrix size 128×64]. The effect of individually varying certain imaging parameters was also examined. Specifically, for some measurements (a) the slice thickness was reduced to 3 mm or increased to 7 mm; (b) the imaging plane was rotated by 90° (examined for 1.5 T only);[7] (c) the pulse sequence was changed to gradient echo[8] [(GE); TR=2 s; 1.5 T only]; (d) the matrix size was increased to 256×128; and (e) the number of imaged slices was increased to 5 or 15 (1.5 T only).

B. Equipment and procedure

Condenser microphones were chosen for acoustic measurements because the high magnetic fields in the imaging environment have little or no effect on their sensitivity to acoustic signals (e.g., Hurwitz *et al.*, 1989). Two microphones with complementary characteristics were used: a Shure SM93 pro audio condenser microphone was used for gradient noise measurements because it could measure high sound pressures without appreciable distortion. For measurements in the 3-T imager, where noise levels were highest, cellophane tape was placed over the input port of the Shure microphone.[9] The tape reduced noise levels at the microphone diaphragm by approximately 35 dB, thereby reducing the effective microphone sensitivity. A Knowles EK3103 hearing-aid electret microphone with the short tube at the input port removed was used to measure pump- and air-handling noise because it had a better low-frequency response than the Shure microphone.

Low-level, low-impedance microphone outputs[10] were conducted through 10 m of shielded twisted-triplet cable to custom bias voltage power supplies located in the control room. The cables were taped at intervals to the patient table and to the floor to prevent movement and to eliminate loops. The Shure microphone used a 15-V bias from an external power supply; the Knowles microphone used a 9-V bias provided by a conventional battery. The microphone cable shields were tied to the power supply ground (Shure) or case (Knowles). Microphone signals were conducted through coaxial cables from the power supplies to differential amplifiers (20–40-dB gain) also located in the control room. Ten- to 20-s segments of the amplified microphone output were digitized at 48 kHz with a National Instruments A2100 A/D board and streamed to the hard disk of a Macintosh Quadra 950 computer [running LABVIEW 2 (1991)]. The microphone frequency response had a sharp, high-frequency rolloff above 10–12 kHz which effectively provided automatic antialiasing filtering. A trigger signal from the imager controller was digitized concurrently. Further computations were performed in MATLAB (1998).

The functional characteristics of the microphones were tested over the course of the measurement series in three ways: (1) The sensitivity of each microphone was checked in the control room immediately before and after each measurement session using a 250-Hz electronic pistonphone (Larson-Davis CA250). Differences in microphone sensitivity (pre- vs post-measurements) were less than 2 dB. For the 3-T imager, the cellophane tape over the port of the Shure microphone remained in place for the entire measurement session, including assessments of sensitivity [and of frequency response—see (3) below]. (2) The output of the Shure microphone in response to a 1.4-kHz tone was measured with the microphone at two locations, in the bore of the 3-T imager and in the imager room approximately 1.5 m from the opening of the bore (where the static magnetic field strength was lower). The tone was produced by an MRI-compatible audio transducer (positioned at a fixed location) and was conducted by tubes to a headset. The microphone (positioned under the headset) produced the same output at the two locations, indicating an insensitivity to static magnetic field strength. (3) Microphone sensitivities and frequency responses were measured before or after each session by examining the microphone's response to a calibration stimulus (broadband chirp, 24 Hz–14 kHz) when the microphone was sealed to the end of a custom-made acoustic source. The level of the calibration stimulus at the microphone diaphragm was approximately 105 dB SPL for both the Knowles microphone and the Shure without tape, and 70 dB SPL for the Shure with tape. All spectra are corrected for the microphone frequency response (note that the response of the rest of the measurement system was flat).

The arrangement used to measure microphone frequency response was also used to check that the measured noise levels at the harmonics of the primary frequency of the highest-level gradient noise were not due to harmonic distortion in the Shure microphone. We established that the harmonic distortion of the Shure microphone output to a pure tone at the level and primary frequency of the highest-level gradient noise was below the harmonics in the noise measurements. For a 1-kHz tone at 122 dB SPL, the second and third harmonics were below the fundamental by 33 and 50 dB, respectively.[11] In the imager, noise levels at the microphone diaphragm were less than 120 dB SPL for all measurements, and measured spectral levels at the second and third harmonics of the primary noise frequency were down only about 20 and 35 dB, respectively, from the primary. Since the noise levels measured in the imager were lower at the primary frequency and higher at the harmonics than for

the tonal test stimulus, harmonic distortion did not contribute appreciably to the measured noise spectrum.

C. Artifact identification and treatment

The time-varying electric and magnetic fields present during imaging could potentially cause electrical artifacts in the measured signals, so procedures were established to identify and eliminate the effects of any such artifacts. Artifacts were identified using an approach that involved encasing the microphones in a heavy clay that reduced sound pressure at the microphone diaphragm by at least 40 dB.[12] With the microphones positioned in the imager bore (Fig. 1), acoustic noise measurements were made alternately with and without clay encasing the microphone. Electrical artifacts were defined as any part of the microphone output signal that was not attenuated when clay was applied (see also Hedeen and Edelstein, 1997).[13]

Artifacts were either eliminated or shown to have no significant effect on measurements: (1) Preliminary measurements showed that the radio-frequency (rf) pulses in the imaging sequence (which excite proton spins during image acquisitions) produced an electrical artifact that was substantially higher in amplitude than the electrical representation of the acoustic noise. This fact meant that the gains of the amplifiers had to be reduced to avoid saturating their outputs, which resulted in a reduction in the usable dynamic range of the recording equipment. Disconnecting the rf transmitter eliminated the artifact without changing the electrical representation of the acoustic signal (see also Hurwitz *et al.*, 1989; NEMA MS 4, 1989), so the transmitter was disconnected for all noise measurements presented in this paper. (2) In the 1.5-T imager with the rf transmitter disconnected, clay reduced the entire measured signal by at least 40 dB, indicating that there were no significant artifacts and that the outputs of the microphones (without clay) were uncontaminated representations of the acoustic noise. (3) In the 3-T imager with the rf transmitter disconnected, clay reduced most of the measured signal by at least 40 dB, but a ''square wave'' electrical artifact was still present during part of the waveform. No further steps were taken to eliminate this artifact, for two reasons: (a) it occurred well before the most intense acoustic noise started [see Fig. 2(B)], so it did not contaminate measurements of peak noise levels or maximum spectral levels (see Sec. III A 1);[14] and (b) the artifact was lower in amplitude than the electrical representation of the acoustic noise, so it did not limit the usable dynamic range of the recording equipment.

III. RESULTS

Acoustic noise in the imaging environment came from four main sources: the gradient coils, the pump for the liquid helium used to cool the imager's permanent magnet, the room air-handling system, and a fan that provides a cooling breeze to the patient in the imager bore. The gradient coils produced the loudest noise, tonal ''beeps'' coinciding with each image acquisition. The pump produced an ongoing

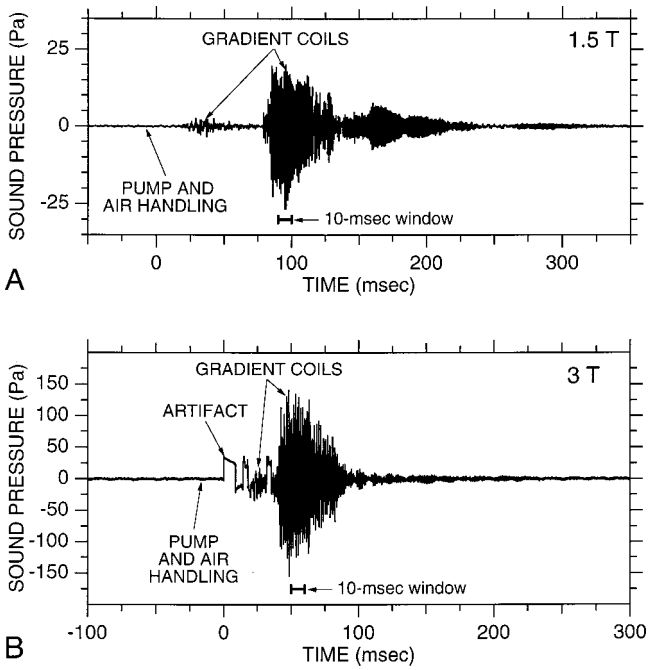

FIG. 2. Acoustic noise measured over a time period including one image acquisition in the 1.5-T (A) and 3-T (B) imagers. Our standard imaging parameters were used (1.5 T: asymmetric spin echo, TE=70 ms, offset =−25 ms, field of view (FOV)=40×20 cm, TR=2 s, matrix size 128×64, slice thickness 7 mm; 3 T: spin echo, TE=35 ms, FOV=40×20 cm, TR=2 s, matrix size 128×64, slice thickness 5 mm). The imaged slice was in a plane that would be approximately parallel to the Sylvian fissure in a supine subject. A trigger pulse from the imager controller occurred at time=0. The rf transmitter was disconnected. The noise waveform for the remainder of the 2-s TR [i.e., time $t>350$ ms in (A), $t>300$ ms in (B)] resembles that for $t<0$ at this scale. Short horizontal bars below each waveform indicate waveform segments used in Fig. 3.

''growling'' or ''throbbing'' noise. The air-handling equipment and patient fan produced ongoing ''whooshing'' sounds.

Typical noise waveforms[15] measured in the 1.5-T and 3-T imagers during one image acquisition are shown in Fig. 2. The gradient noise accounted for the highest amplitudes of the waveform, while the pump- and air-handling sounds were much lower in level, appearing virtually as flat lines at the scales of Fig. 2. Fan noise levels were lower than pump- and air-handling noise levels and will not be considered further because they could be eliminated merely by turning the fan off. Noise from the other three sources presented more of a problem and is examined in detail.

A. Noise from the gradient coils

1. Gradient noise levels

Peak noise levels[16] (L_{pk}, ANSI S1.13-1995) were higher in the 3-T than in the 1.5-T imager. At 1.5 T, the highest L_{pk} was 123 dB *re* 20 μPa (peak sound pressure 27 Pa) among all of the noise waveforms (17) recorded with our standard imaging parameters during one 6-h session (session I). At 3 T, the highest L_{pk} was 138 dB *re* 20 μPa (peak sound pressure 157 Pa) among all of the noise waveforms (24) recorded with our standard imaging parameters during one 4-h session (session II). For each imager, the range of L_{pk} was less than 1 dB. The fact that peak noise levels were higher in the 3-T

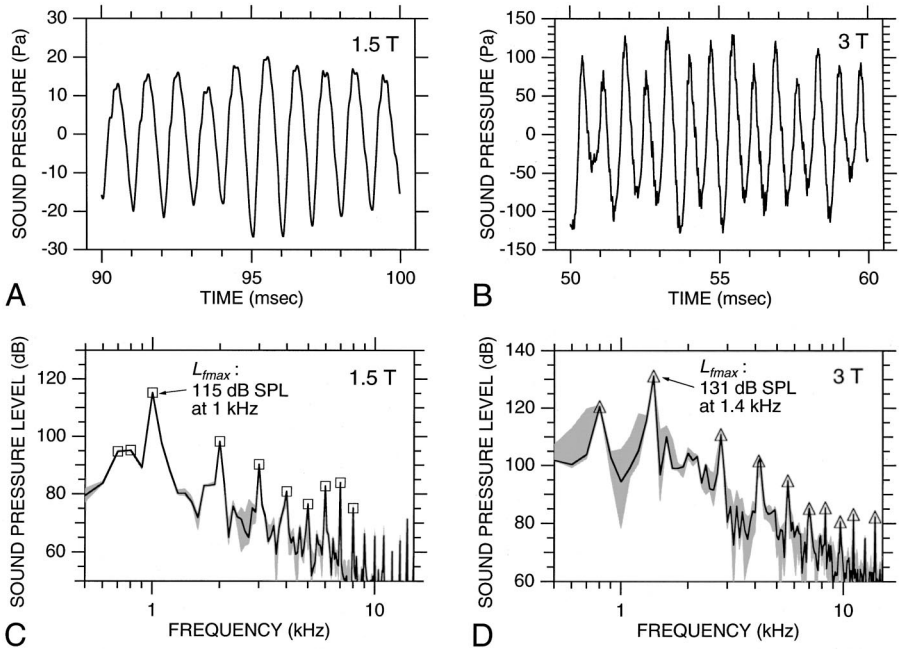

FIG. 3. Temporal and spectral characteristics of gradient coil noise. (A) and (B) 10-ms segments of the gradient noise in Figs. 2(A) and (B), respectively. In each case [(A) and (B)], the plotted segment corresponds to the 10-ms time window containing $L_{f\,\max}$. These windows are indicated by the short thick bars below the waveforms in Fig. 2. (C) and (D) Spectra computed from the waveforms in (A) and (B), respectively (solid curves). Shading indicates the range of spectra seen for the other waveforms recorded during the same session [using our standard imaging parameters as in (A) and (B), and for the 10-ms time window corresponding to $L_{f\,\max}$]. Squares (C) and triangles (D) indicate the spectral peaks that were tracked versus time as described in Sec. III A 3. The maximum spectral level $L_{f\,\max}$ is indicated. Spectral resolution: 100 Hz.

than in the 1.5-T imager makes sense because two of the factors that determine the magnitude of the Lorenz forces on the gradient coils, the amplitude of the gradient currents and the strength of the static magnetic field, were higher in the 3-T than in the 1.5-T imager.

Because L_{pk} conveys no information as to frequency content, we developed a second descriptor of the highest amplitude gradient noise that does. This descriptor was calculated as follows for each noise waveform. First, the waveform was divided into overlapping 10-ms time windows displaced from each other by 5 ms.[17] Then, the sound-pressure level spectrum was calculated for each 10-ms waveform segment.[18] The highest level observed among all of these spectra was defined as the ''maximum spectral level'' $L_{f\,\max}$ for that waveform.[19] This level and its corresponding frequency constitute our second descriptor of the noise. For the 1.5-T imager, the highest $L_{f\,\max}$ was 115 dB SPL at 1 kHz [Fig. 3(C)] among waveforms recorded during session I using our standard parameters. For the 3-T imager, the highest $L_{f\,\max}$ was 131 dB SPL at 1.4 kHz [Fig. 3(D)] among waveforms recorded during session II using our standard parameters. Within both sessions I and II, the range of $L_{f\,\max}$ was less than 1 dB.

Because reported noise levels are often frequency-weighted to account for the frequency dependence of human equal-loudness curves (e.g., Earshen, 1986), we considered the effects of standard A and C weightings on $L_{f\,\max}$. For the 1.5-T imager, $L_{f\,\max}$ is unchanged by either an A- or C weighting because both weightings are 0 dB at 1 kHz, the frequency of $L_{f\,\max}$ at 1.5 T. Although these weightings are nonzero at 1.4 kHz, the frequency of $L_{f\,\max}$ for the 3-T imager, their effect is still small; $L_{f\,\max}$ for the 3-T imager increases by approximately 0.7 dB when an A weighting is applied and changes by less than 0.1 dB with a C weighting.

We also computed time-average noise levels[20] (see ANSI S1.1-1994) over short (10-ms) and long (2-s) intervals. $L_{f\,\max}$ and the time-average noise level over the 10-ms window containing $L_{f\,\max}$ differed by less than 1 dB for all measurements in both imagers (based on an analysis of the waveforms recorded for our standard parameters in sessions I and II).[21] This agreement reinforces what can be seen from the spectra in Figs. 3(C) and (D): almost all of the noise energy is at the frequency of the spectral peak.

For our standard imaging parameters, 2 s is the time from the onset of one waveform to the onset of the next; so, the time-average noise level over a 2-s window L_{2s} represents the steady-state noise level. The highest L_{2s} was 97 and 114 dB SPL for the 1.5-T and 3-T imagers, respectively (based on an analysis of the waveforms recorded with our standard parameters during sessions I and II); the range among all measurements was less than 1 dB. These unweighted values for L_{2s} were reduced by less than 0.5 dB when either an A- or C weighting was applied.

2. Relationship between gradient noise and imaging pulse sequence

The acoustic noise waveforms included several distinct features which were correlated with the occurrence of the various gradients in the imaging pulse sequence. This is illustrated in Fig. 4(A) for the 1.5-T imager and our ''standard'' imaging parameters. There was always an initial low-level burst of noise [beginning at about 20 ms in Fig. 4(A)] that began just after the onset of the ''chemical saturation'' gradient in the imaging pulse sequence (used to suppress the contribution from fatty tissue to the image). This burst continued throughout the ''slice-select'' gradients (the gradients that determine the thickness and position of the imaged slice, centered at 24 and 34 ms).[22] The onset of the next burst in the noise waveform coincided with the readout and phase-encode gradients (the gradients used to extract two-dimensional information within the selected slice plane).[23] While the readout and phase-encode gradients were on (between 78 and 110 ms), this noise reached a maximum in

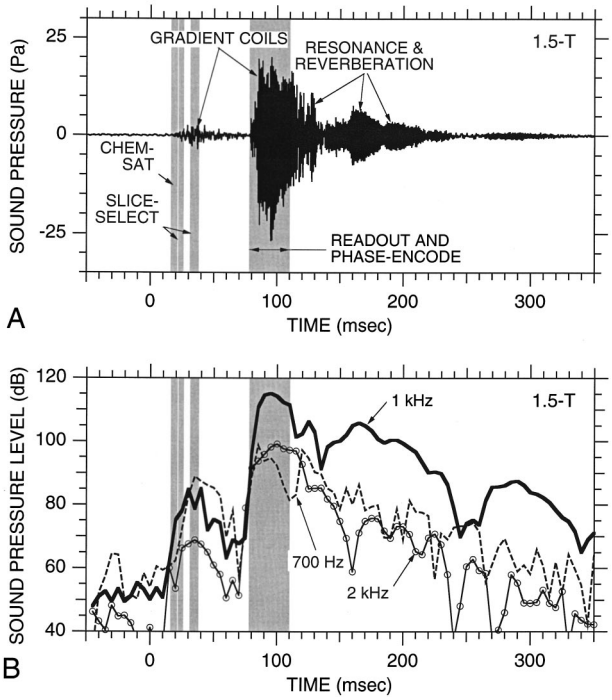

FIG. 4. Relationship between gradient coil noise and imaging pulse sequence (1.5 T). (A) Acoustic noise waveform from Fig. 2(A). Gray shading indicates when various gradients were on: (1) a brief ''chemical saturation'' gradient; (2) two slice-select gradients; and (3) readout and phase encode gradients. (B) Time course of the 1-kHz (thick solid curve), 2-kHz (thin solid curve and circles), and 700-Hz components (dashed curve) of the waveform in (A). Levels were computed from spectra of waveform segments obtained from a 10-ms rectangular window moved along the waveform in (A) at 5-ms intervals. Each data point in (B) corresponds to the center of the appropriate 10-ms window. Gray shading indicates gradient activity as in (A).

amplitude, then decayed nonmonotonically over a period of approximately 300–500 ms after the gradients were turned off. Although not shown or discussed in detail, the timing of components in the acoustic waveform in the 3-T imager was also correlated with the occurrence of the various gradients in the imaging sequence.

The waveform and frequency spectrum of the noise during and after the readout and phase-encode gradients indicated that the noise in this time period was primarily caused by the readout gradients. During the readout and phase-encode gradients, the noise waveform was quasisinusoidal in shape [Figs. 3(A), (B)] with a dominant frequency of 1 kHz in the 1.5-T imager and 1.4 kHz in the 3-T imager [Figs. 3(C), (D)]. These temporal and spectral characteristics mirrored those of the readout gradient (which varied sinusoidally at 1 kHz in the 1.5-T imager and at 1.4 kHz in the 3-T), rather than the phase-encode gradient (which consisted of monophasic pulses occurring twice per period of the readout gradient). The spectrum of the noise [Figs. 3(C), (D)] included a local maximum at the fundamental frequency of the phase-encode gradient (i.e., at 2 kHz in the 1.5-T imager and at 2.8 kHz in the 3-T), so the phase-encode gradient may account for a substantial fraction of this spectral peak. Alternatively, this spectral maximum and the maxima at higher multiples of the readout gradient frequency may represent nonlinearities in the mechanical response to the readout gradient [for instance, the ''flattened'' positive excursions of the waveform in Fig. 3(A) suggest that inward motion of the gradient coils may have been constrained]. After the readout and phase-encode gradients were turned off, the noise waveform remained quasisinusoidal in shape as it decayed nonmonotonically in amplitude. The dominant frequency over the course of this decay was equal to the readout gradient frequency.

3. Gradient noise spectral levels versus time

Further insights into the nature of noise generation and transmission were gained by tracking the spectral content of the acoustic noise over time, as described here for the 1.5-T imager. In our analyses (of 17 waveforms measured using our standard parameters), we examined all of the labeled frequencies in the noise spectrum in Fig. 3(C) (indicated by squares). The following trends were seen consistently across waveforms: Levels at the fundamental frequencies of the readout and phase-encode gradients [1 and 2 kHz; Fig. 3(C)] and harmonics increased when the gradients were turned on, were sustained at a high level while the gradients were on, and decreased after the gradients were turned off [Fig. 4(B)]. In contrast, the time course of the 700-Hz component consistently deviated from this behavior in subtle but notable ways. No 700-Hz component was present in the gradient currents except at the switch-on and switch-off transients at 78 and 110 ms, respectively. Immediately after switch-on at 78 ms, the level of the 700-Hz component reached a maximum. However, unlike the 1- and 2-kHz components, the level of the 700-Hz component subsequently decayed. In addition, after the gradients were switched off at 110 ms, the 700-Hz component again increased and decayed, approximately exponentially. One possible interpretation of these responses to transients is that the 700-Hz component represents a natural mechanical response of the imager structure that was excited by the broadband transients in the gradient currents.

The 1-kHz component decayed slowly after the gradient currents were switched off, possibly because (1) the gradient coils continued to resonate after the driving current was switched off; (2) other structures in the imager or imager room continued to resonate; (3) the noise reverberated in the imager room; or (4) a combination of these factors. The 300–500-ms decay to pump noise levels (60–75 dB down—see Sec. B and Fig. 7) is comparable to the roughly 500-ms reverberation time (time necessary for the noise level to decay by 60 dB) estimated from the dimensions of the imager room (by Sabine's equation,[24] e.g., Kinsler *et al.*, 1982).[25]

4. Repeatability of gradient noise

For a given set of imaging parameters, the pulse sequence is identical from image acquisition to acquisition, suggesting that the acoustic noise produced by the gradient coils should be highly repeatable. This idea is in agreement with the fact that the spectrum of the highest amplitude gradient noise showed little variability [Figs. 3(C) and (D)]. However, to further examine the degree of noise repeatability, we performed an additional analysis sensitive to wave-

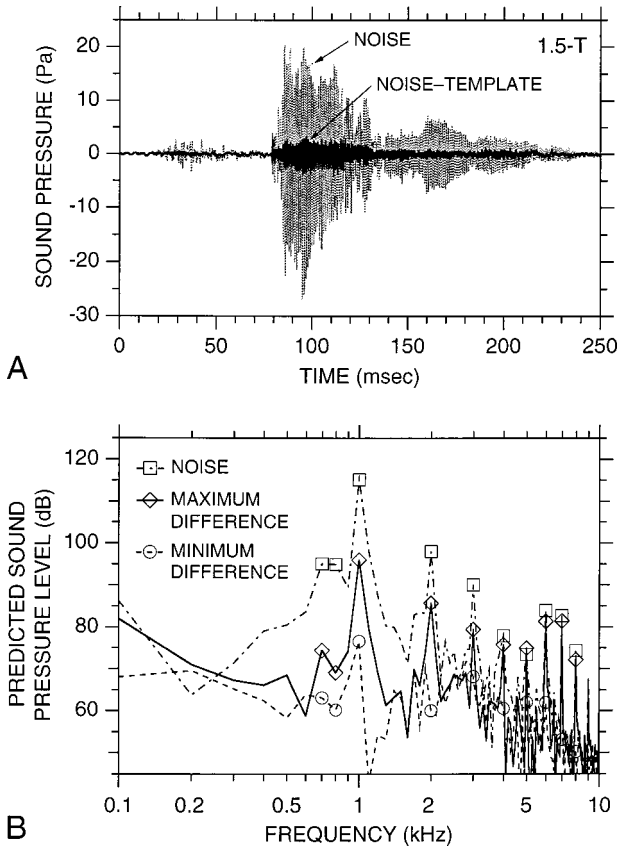

FIG. 5. Investigation of the repeatability of gradient coil noise (1.5 T). (A) A noise waveform before (light curve) and after (dark curve) an earlier noise waveform (i.e., a ''template waveform'') was subtracted from it. The difference waveform shown (i.e., ''noise–template'') had the greatest amplitude of all the difference waveforms calculated in our analyses. (B) Spectra computed over a 10-ms window from the noise waveform in (A) (dot-dashed curve, squares), the maximum difference waveform in (A) (solid curve, diamonds), and the minimum difference waveform in our analyses (dashed curve, circles). In each case, the 10-ms window coincided with the waveform peak.

form timing. For this analysis, the digitized noise waveform from the first acquisition in a 1.5-T measurement session (i.e., the ''template waveform'') was subtracted from each of the 16 subsequent noise waveforms recorded during the same session using our standard imaging parameters.[26] The amplitudes of the resulting difference waveforms indicated the degree of similarity between each noise waveform and the template waveform, where zero amplitude would indicate that the waveforms were identical in shape and timing. Subtraction of the template waveform reduced the amplitude of the gradient noise waveform at all points in time [Fig. 5(A)]. $L_{f\,\max}$ at 1 kHz for the difference waveforms was 19–38 dB lower than that for the template noise waveform [Fig. 5(B)].[27] L_{2s} was 13–15 dB lower. These reductions indicate that both the gradient noise amplitude and timing were highly repeatable.

5. Dependence of gradient noise on imaging parameters

Because the readout gradients are the source of the most intense acoustic noise, we expected that $L_{f\,\max}$ and L_{2s} would be insensitive to changes in the slice-select gradients or to changes in the timing of the readout gradients (i.e., changes that do not alter the amplitude or duration of the readout gradients). This proved to be the case when we examined the effects of varying imaging parameters away from our standard values. For example, when slice orientation was changed (by 90 deg) or slice thickness was changed [from 7 to 3 mm (1.5 T) or from 5 to 3 or 7 mm (3 T)], $L_{f\,\max}$ and L_{2s} were within 1 dB of the values obtained using our standard parameters. These alterations in slice parameters did change the acoustic waveform at the time of the slice-select gradients, which is to be expected since the slice-select gradients control the orientation and thickness of the imaged slice but do not affect the readout gradients. Changes in imaging pulse sequence (from ASE to GE, 1.5 T) are associated with changes in the relative timing of the various gradients and therefore resulted in corresponding changes in the timing of the various components of the acoustic noise waveform. However, for each imager, the readout gradient waveform was the same regardless of pulse sequence. Consequently, $L_{f\,\max}$ and L_{2s} were insensitive to pulse sequence (i.e., they varied by less than 1 dB).

Doubling the duration of the readout and phase-encode gradient trains,[28] from 32 to 64 ms in the 1.5-T imager, did result in an approximately twofold increase in the duration of the highest-amplitude portion of the noise waveform [compare Fig. 6(B) to Fig. 6(A)] and hence an approximate doubling of the energy per 2-s TR. Because the amplitude and frequency of the gradients were unchanged, the level and frequency of $L_{f\,\max}$ did not change [Fig. 6(C)]. However, the doubling in duration did result in a 2-dB increase in L_{2s}, which is close to the expected value of 3 dB for a doubling in energy.

Increasing the number of slices imaged in a given 2-s time interval did not change $L_{f\,\max}$ but did increase L_{2s}, because the total gradient noise energy in the time interval increased. Specifically, L_{2s} increased by 7 dB when the number of slices was increased from 1 to 5 and increased by approximately 12 dB when the number of slices was increased from 1 to 15.[29] These increases are consistent with five- and 15-fold increases in energy, respectively. In other words, noise energy increased in proportion to the number of slices. This relationship is consistent with our observation that the noise waveforms from successive acquisitions were largely nonoverlapping and thus did not interact with one another to a significant degree, even for the case of 15 slices.[30]

B. Noise from the pump and air-handling system

The noises produced by the liquid helium pump and the room air-handling system were much lower in both level and frequency than the noise produced by the gradient coils. Figure 7 shows the spectra of noise from the pump and air-handling system for the 1.5-T imager. The pump noise fluctuated cyclically with a period of 1.7 s, showed spectral peaks at 125, 240, and 490 Hz, and decreased in level at higher frequencies. Levels at 240 Hz, the highest spectral peak, fluctuated between 57 and 76 dB SPL (unweighted, when evaluated over a moving 100-ms window, analogous to our analysis technique described in Sec. A 1). The steady-

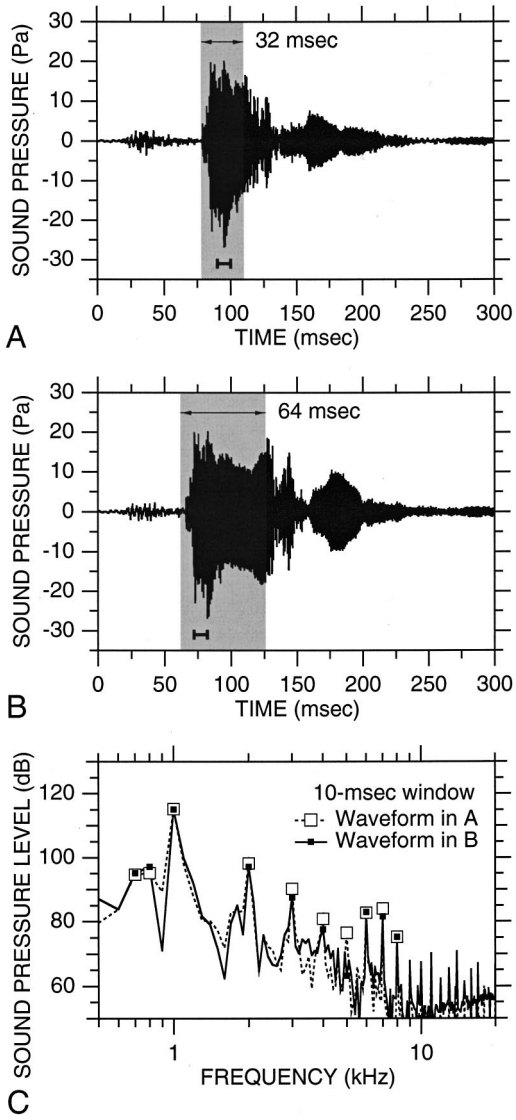

FIG. 6. Effect of doubling the duration of the readout and phase-encode gradient trains on the waveform and spectrum of acoustic noise (1.5 T). (A) Noise waveform from Fig. 4(A) obtained using our standard 1.5-T imaging parameters (matrix size 128×64). Gray shading indicates readout and phase-encode gradient activity. (B) Noise waveform obtained using the same parameters as in (A) except that the gradient duration was doubled (matrix size 256×128). (C) Spectrum of waveform in (A) (dashed line, open squares) and waveform in (B) (solid line, filled squares) computed over a 10-ms window coinciding with the peak noise [short bars under waveforms in (A) and (B)].

state level of pump and air-handling noise evaluated over the 1.7-s period was 80 dB SPL (unweighted), 71 dB SPL (A-weighted), 79 dB SPL (C-weighted), considerably lower than L_{2s} for the 1.5-T gradient noise with our standard parameters (97 dB SPL). When the pump was turned off, only the air-handling noise remained. The steady-state noise level was then 77 dB SPL (unweighted), 65 dB (A-weighted), 76 dB (C-weighted). The spectrum (computed over 1 s) showed a peak at 80 Hz and decreased with increasing frequency. The pump and air-handling noise spectra and levels in the 3-T imager were similar to the 1.5-T.

IV. DISCUSSION

(1) Our analyses showed that the most intense noise produced by the gradient coils was much higher in level and frequency than the noises produced by the coolant pump and air-handling equipment in the imager room. For the gradient noise, peak levels L_{pk} of 123 and 138 dB *re* 20 μPa were observed in a 1.5-T and a 3-T imager, respectively, during EPI-based fMRI. Maximum spectral levels $L_{f\,\mathrm{max}}$ were 115 and 131 dB SPL at 1 and 1.4 kHz in the 1.5-T and 3-T imagers; steady-state levels L_{2s} with our standard imaging parameters were 97 and 114 dB SPL (single slice in 2-s period). (These levels, unlike those in previous reports by other authors, were measured without a time weighting.) Noise levels were unchanged by applying either an A- or C-frequency weighting.

(2) The frequency content and timing of the most intense gradient noise indicated that it was primarily attributable to the readout gradients rather than to other gradients in the imaging pulse sequence. This interpretation was supported by the fact that the highest-level noise (a) did not change when imaging parameters were varied in a way that did not affect the readout gradients (e.g., changes in slice thickness or orientation), and (b) changed predictably when the readout gradients were affected (e.g., increasing image matrix size or number of imaged slices).

(3) Noises produced by the coolant pump and air-handling equipment in the imager room were much lower in frequency and level than the gradient noise: 80 dB SPL (unweighted), 71 dB SPL (A-weighted). The fan could be turned off, so there was no point in studying it further.

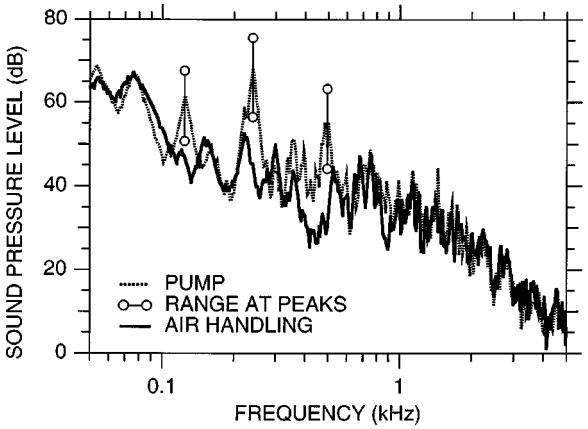

FIG. 7. Time-average spectra (unweighted) of noises produced by the combination of the 1.5-T imager coolant pump and the air handling system in the 1.5-T imager room (dotted curve) and the air-handling system alone (solid curve). For the peaks in the pump spectrum at 125, 240, and 490 Hz, the circles connected by vertical bars show the range of levels observed as a 100-ms time window was moved through the 1.7-s pump cycle.

A. Comparison to previous measurements of fMRI noise

The noise measurements presented in this paper extend previous descriptions of acoustic noise during EPI-based fMRI by providing a more comprehensive description of the spectrum and timing of the noise (previous reports generally included only peak and time-average levels). By computing spectra and levels from digitized waveforms, we have also avoided a limitation of sound-level meters (used in most previous studies) that can cause time-average levels of short-duration sounds to be underestimated.[31] We estimate that L_{2s}

in the 1.5-T imager, in which the duration of the highest-level noise is comparable to the gradient currents (32 ms for our standard parameters), would be underestimated by a sound-level meter by at least 5 dB on the fast setting and at least 13 dB on the slow setting (ANSI S1.4-1985). This potential for underestimation should be kept in mind when comparing our time-average levels with previous reports. Peak levels should be unaffected by differences in measurement method.

Of the four studies reporting noise levels, two included peak levels. Prieto *et al.* (1998) examined noise levels in a 3-T imager (Bruker Biospec) with a custom insert head gradient system[32] for a range of imaging parameters and reported peak levels of 126–139 dB (unweighted), a range that brackets the peak levels measured for the 3-T imager in the present study (137–138 dB). Miyati *et al.* (1999) reported peak levels of 104–115 dB SPL in nine 1.5-T imagers during single-shot EPI, levels considerably lower than the peak levels in our 1.5-T imager (122–123 dB).

Four previous studies reported time-average noise levels during imaging, measured with a sound-level meter. Prieto *et al.* (1998) and Miyati *et al.* (1999) measured time-average A-weighted noise levels (L_{eq}) with a ''fast'' time weighting. The $L_{A,\mathrm{eq}}$ measured by Prieto *et al.* (1998) in their 3-T imager for a 2-s TR (most analogous to our L_{2s}) was 104 dB SPL. This is approximately 10 dB lower than the A-weighted L_{2s} measured in our 3-T imager (113–114 dB SPL), but roughly 5 dB of the difference may be due to the different measurement methods. Another point of comparison with Prieto *et al.* (1998) is the effect of increasing the rate at which images were acquired on peak and average noise levels. When Prieto *et al.* increased the number of images per 2-s interval (by reducing TR from 2 s to as little as 74 ms), peak levels remained constant but average levels increased, similar to our results; however, unlike our results, the increases they observed did not indicate a proportional relationship between noise energy and the number of images acquired. The range of $L_{A,\mathrm{eq}}$ measured by Miyati *et al.* (1999) in their nine imagers (seven slices in a 2.5-s TR) was 92–100 dB SPL, which is lower than our L_{2s} under similar conditions (104 dB for five slices in a 2-s TR).

The two other previous studies reporting noise levels also used a sound-level meter (Cho *et al.*, 1997; Shellock *et al.*, 1998) but did not specify the time weighting used. Levels (C-weighted) reported by Cho *et al.* (1997) for a General Electric 1.5-T imager (103 dB SPL; TR=3.2 s) are comparable to L_{2s} for our 1.5-T imager. The highest levels (A-weighted) reported by Shellock *et al.* (1998) for two 1.5-T imagers (General Electric Vision: 115 dB SPL, TR=5 s; Siemens Magnetom: 114 dB; TR=300 ms)[33] are considerably higher than L_{2s} in our 1.5-T imager and are very similar to our $L_{f\,\max}$.

Two reports noted the frequency content of the noise during EPI-based fMRI. Cho *et al.* (1997) presented a noise spectrum from a General Electric 1.5-T imager with a dominant peak at about 1.3 kHz. Miyati *et al.* (1999) presented octave-band noise spectra (A-weighted) from a General Electric Horizon 1.5-T imager that peaked in the 2-kHz band. In addition, Wessinger *et al.* (1997) observed that the gradient noise in a Bruker Biospec 3-T imager had a dominant frequency of 2.5 kHz. These studies did not comment on the relationship between these dominant noise frequencies and the gradient activity in their imaging pulse sequence.

B. Noise reduction approaches: Gradient noise

After characterizing the gradient noise during fMRI, we examined ways to reduce the noise. Well-established approaches for reducing unwanted sound offer possibilities in at least four areas: (1) Reduce the noise produced by the gradient coils or by structures that are vibrationally coupled to the gradient coils; (2) Reduce the noise transmitted to the imager bore; (3) Reduce noise at the subject's ears (using passive hearing protection devices, i.e., earmuffs and/or earplugs); (4) Reduce the noise actively through the introduction of ''antinoise'' (e.g., Ravicz *et al.*, 1997). In this section we discuss these various noise reduction possibilities in detail.

1. Gradient noise: Reduction at the source

Several approaches have been tried for reducing the gradient noise produced by the imager. Mansfield, Bowtell, and their colleagues (Mansfield *et al.*, 1995; Bowtell and Mansfield, 1995; Bowtell and Peters, 1999) redesigned the coils such that the forces generated by the gradient currents opposed each other (a ''force balance''). This reduced gradient noise by 7–15 dB. Cho *et al.* (1998) replaced the time-varying readout gradients by a constant magnetic field rotated mechanically (the ''silent MRI'' technique), which reportedly reduced noise levels by 20 dB but imposed constraints on imaging parameters. The effect of these techniques on image quality was not addressed.

Approaches not yet tried can be grouped into two categories. One category involves altering the electrical currents used to set up the gradients, especially the readout gradients since these account for the most intense noise. Perhaps the most direct approach would be to reduce the forces that act on the readout gradient coils by reducing the amplitude of the electrical currents, but doing so would have an adverse effect on image resolution or quality (e.g., Cohen, 1998). If the frequency of the gradient current is sufficiently close to a natural mechanical frequency of the coils[34] that their flexure is amplified, the flexure could be reduced by changing the gradient current frequency. However, varying gradient frequency leads to reductions in image quality or resolution due to imaging and equipment constraints (Wald, 1999). If there is indeed a mechanical resonance at 700 Hz (Sec. III A 3), then increasing the readout gradient frequency above its current value of 1 kHz might decrease gradient coil flexure and therefore gradient noise.

The second category involves modifying the mechanical properties of the gradient coils, the core on which the coils are wound, or the attachment of the coil/core assembly to the rest of the imager structure. Stiffening the coil/core assembly would reduce flexure unless it also moves natural frequencies of the assembly closer to gradient current frequencies. The natural frequencies of the assembly could be moved further from gradient frequencies by changing the assembly's stiffness or mass. Mansfield *et al.* (1998) have proposed relocating the gradient coils on the core and changing the stiff-

ness of the assembly to manipulate its vibration. The assembly's attachment to the rest of the imager structure could be modified to reduce its motion, though care would have to be taken not to increase the vibration of other parts of the imager because this could degrade image quality (Kelley, 1999) or result in radiated noise into the bore or the room. Active vibration control might reduce coil/core assembly flexure or aid in isolating the rest of the imager structure from vibrations of the assembly. Of the approaches mentioned here, modifications to the mechanical properties of the coil/core assembly or their attachment to the rest of the imager hold the most promise for reducing noise at its source without adversely affecting image quality. Such a solution requires active cooperation of the imager manufacturer.

2. Gradient noise: Reducing transmission

Comparing the frequency content of the most intense gradient noise to the properties of typical sound-attenuating materials indicates that gradient noise transmission from source to subject can be reduced significantly by passive means. In the frequency range of the most intense gradient noise (1–1.4 kHz), sound-attenuating materials such as acoustic barrier–foam composite can provide on the order of 30 dB of attenuation (transmission loss),[35] suggesting that the gradient noise reaching a subject could be reduced substantially if attenuating materials were suitably interposed between noise source and subject. A recent experiment confirmed the feasibility of this approach. In this demonstration, a ''helmet'' made of barrier–foam composite and enclosing the head reduced simulated gradient noise heard by a subject by 15–25 dB (Ravicz and Melcher, 1998a, b).

Preliminary tests suggest that gradient noise transmission can also be reduced by applying passive attenuation materials directly to the imager or imager room (Ravicz *et al.*, 1999). In these tests, noise was measured with a microphone in the bore of the 3-T imager examined in the present study. Lining the bore with barrier–foam composite reduced peak gradient noise levels by approximately 12 dB. This result implies that an important path of noise transmission is directly from source to subject through the walls of the imager bore. That this was not the only important transmission route was shown by an additional test that involved blocking the ends of the bore in addition to lining the bore with acoustic foam (see Fig. 1). Blocking the ends substantially reduced the ''resonance and reverberation'' part of the noise waveform [after the gradients were turned off, e.g., Fig. 4(A)] recorded within the imager bore, indicating that noise also reaches a subject via a route through the imager room and the ends of the bore. This means that noise transmission to the subject could be reduced further by applying sound-attenuating material to the outer imager shroud to suppress transmission into the imager room, by applying sound-absorbing materials to the walls of the imager room to reduce reverberations, or by applying both treatments. Additional tests indicated that other transmission routes involving vibration of structures inside the bore such as the patient table were less important. Thus, through a combination of passive treatments applied to the most important routes of noise transmission, it is possible to reduce substantially the gradient noise at the location of a subject during fMRI.

3. Gradient noise: Passive hearing protection devices

The simplest and most economical approach for reducing the noise heard by a subject during fMRI is to reduce noise at the ears using passively attenuating earmuffs, earplugs, or both, but there is a limit on the reductions that this approach can provide. Earmuffs and earplugs (when used properly) provide 31–38 and 25–29 dB of attenuation respectively at dominant gradient noise frequencies (1 and 1.4 kHz; Berger, 1983; Berger *et al.*, 1998; Ravicz and Melcher, 1998a,b). However, when the two devices are used together, the reduction in noise heard by a subject (38–43 dB at 1–1.4 kHz) is far less than the sum of the attenuations provided by each device alone. This is because noise conduction through the head and body, though not significant under normal circumstances, becomes a dominant mode of hearing at gradient noise frequencies when earmuffs and earplugs are used together (e.g., Zwislocki, 1957; Berger, 1983; Ravicz and Melcher, 1998a,b). Thus, hearing protection devices alone cannot eliminate the gradient noise heard by a subject during fMRI. Fortunately, this approach can be combined with the other approaches discussed so far.

4. Gradient noise: Active reduction

Several active noise reduction (ANR) systems[36] have been developed that reduce gradient noise levels at a subject's ears (Goldman *et al.*, 1989; Pla *et al.*, 1995; Palmer, 1998). Although these systems demonstrated that a reduction in gradient noise at the ear can be achieved with ANR, this reduction does not necessarily translate into an equal reduction in the noise *heard* by a subject. This is because ANR applied only at the ear (as with the headset systems of Goldman *et al.* and Palmer) reduces the noise conducted through the *ear canal* without reducing conduction through the *head and body*. For example, in a subject wearing earmuffs and earplugs, ANR at the ear should have virtually no effect on the gradient noise heard because the earmuffs and earplugs reduce noise conduction along the ear canal to the point that conduction through the head and body dominates the noise heard[37] (Ravicz *et al.*, 1998a,b). The free-field system of Pla *et al.*, which reduces noise in a region around the head, may provide additional noise reduction when used with hearing protection devices, but this has not been tested, and noise conduction through the body would still limit the total noise reduction achievable with this system.

The limitation imposed by head and body conduction in applying ANR at the ears could, in theory, be avoided if the gradient noise signal could be canceled at every point on a closed surface encompassing the subject's head and body. However, implementing a system that approximates this theoretical situation is beyond the scope of today's technology. The difficulty arises partly because the wavelength of the most intense gradient noise is small compared to the dimensions of the subject, so noise amplitude and phase variations over a surface enclosing the subject would have to be taken

into account. Regular bore geometry (Fig. 1), knowledge of gradient coil vibration patterns (e.g., Hedeen and Edelstein, 1997), and the repeatability and predictability of imager noise (Sec. III A 4) may eventually make this problem tractable. Given the technical challenges, the other approaches discussed in this section are more practical options for reducing the effects of gradient noise at this time.

C. Noise reduction approaches: Pump- and air-handling noise

Since the pump and air-handling equipment are not essential for imaging, a simple, short-term approach to reducing the noise from these sources is to turn this equipment off temporarily during imaging during particularly noise-sensitive parts of an fMRI experiment. This approach has the drawback that it can be used for only short periods of time. In addition, turning the pump off increases the coolant boiloff rate. It is therefore worth considering alternative approaches.

The four noise reduction possibilities discussed in the previous section are also applicable to the noise produced by the coolant pump and air-handling system. If we assume that minimizing the noise output was not a primary consideration in pump or air-handling system design, substantial reductions in noise at the source may be achievable through simple alterations to this equipment. The use of passive materials to attenuate noise transmission from source to subject or passive hearing protection devices should also be effective approaches. However, they will be less effective in this case than for the case of gradient noise because the pump and air-handling noises are lower in frequency than the gradient noise and passively attenuating materials are less effective at low than high frequencies (Beranek, 1954; Vér and Holmes, 1988). One consequence of this poorer low-frequency performance is that reducing noise at the ear with earmuffs and earplugs does not attenuate low-frequency noise conduction through the ear canal to the point where conduction through the head and body dominates the noise heard (Berger, 1983; Ravicz and Melcher, 1998a,b). This means that ANR applied at the ear can provide a reduction in the (low-frequency) pump and air-handling noise heard by a subject over and above that provided by earmuffs and earplugs, unlike the situation for the higher-frequency gradient noise.[38] This, coupled with the fact that ANR is well-suited to reducing low-frequency noise, makes ANR a promising complement to other approaches for reducing the pump and air-handling noise.

D. Importance of noise reduction for all fMRI of brain activity

It is clear that the acoustic background noises present during imaging can adversely affect fMRI studies that use auditory stimuli. However, it may also be that noise affects all fMRI studies of brain activity in as yet unassessed ways. Though the discomfort and anxiety experienced by many patients during conventional MRI is apparently unrelated to the noise (Dantendorfer *et al.*, 1997), the higher noise levels during fMRI could cause discomfort, which may lead to an increase in motion artifacts from unintended head movements that could reduce the detectability of brain activity (Elliott *et al.*, 1999). Noise has been shown to interfere with the performance of some cognitive tasks by reducing a subject's attentiveness to the task (e.g., Paschler, 1998). Since changes in attentiveness have been demonstrated to affect brain activity (Woodruff *et al.*, 1996), the noise potentially can affect the results of *any* fMRI study of subject performance or response to *any* stimulus, not just auditory stimuli. Two studies have reported different effects of *increasing* time-average noise levels during nonauditory tasks (Elliott *et al.*, 1999; Cho *et al.*, 1998), but no study to date has examined the effect of *reducing* the noise. This issue will mostly likely remain unresolved until quieter imaging facilities are available.

V. CONCLUSIONS

(1) The nature of the high noise levels present during fMRI makes total elimination of imager noise perceived by subjects impractical at this time. However, significant noise reduction is possible using existing methods.

(2) Because noise levels are high and the gradient noise and the pump- and air-handling noise occupy different parts of the frequency spectrum, substantial noise reduction will undoubtedly require a combination of approaches.

(3) Substantial reductions in gradient noise levels have been demonstrated using passive noise reduction approaches such as hearing protection devices (earmuffs and earplugs) or the use of noise attenuation material to reduce noise transmission from the gradient coils to the subject. This result is to be expected, since these approaches are more effective for high-frequency components than low.

(4) Although MRI-compatible active noise reduction (ANR) systems have been developed, they are less effective at reducing high-frequency gradient noise than passive techniques and therefore seem less practical for most applications. The effectiveness of present ANR systems in conjunction with hearing protection devices that reduce sound conduction through the *ear canal* (e.g., an ANR headset) is limited by noise conducted through the *head and body* that bypasses these treatments. To solve this problem, ANR must be applied over the subject's head and body, an approach that cannot be implemented with present technology.

(5) Pump noise levels can also be reduced by passive noise reduction approaches and could probably be eliminated by appropriate pump design and placement. Because the effectiveness of ANR increases at low frequencies, ANR may be a more effective option for reducing pump- and air-handling noise than passive techniques.

(6) Even a combination of approaches is unlikely to reduce unwanted sounds to levels below the threshold of hearing. Therefore, optimal imaging conditions can be achieved only by redesigning the imaging equipment to reduce the noise at its sources.

ACKNOWLEDGMENTS

The authors wish to thank Douglas Kelley at ANMR, General Electric Medical Systems, and MGH for many help-

ful discussions on the sources of imager noise; Larry L. Wald, Terence A. Campbell, Whitney B. Edmister, Thomas M. Talavage, Bruce Rosen, and Randy Benson at the MGH Imaging Center for technical information and support; John J. Guinan, William T. Peake, John J. Rosowski, Mark N. Oster, and Larry L. Wald for comments on earlier versions of the manuscript; Knowles Electronics for supplying microphones; Barbara E. Norris for assistance in document preparation; and the staff of the Eaton-Peabody Laboratory for general help. Supported by NIH/NIDCD No. P01 DC00119.

[1]Time-average noise levels (root-mean-square sound pressure over a given time interval, expressed in dB *re* 20 μPa—ANSI S1.1-1994) used for assessing noise hazard include a time weighting (e.g., fast, slow) that de-emphasizes sudden changes in level and a frequency weighting (e.g., A,C) that relates sound levels to human loudness curves (e.g., Earshen, 1986). A-weighted sound levels have been shown to be a good predictor of observed threshold shifts and hearing losses (e.g., von Gierke and Nixon, 1992).

[2]Note that these imagers did not include the noise-attenuating material under the imager shroud which is sometimes supplied with GE Signa imagers. When installed, this material reportedly reduces noise by 5 dB (Counter *et al.*, 1997).

[3]Our measurement technique differs slightly from the National Electrical Manufacturers Association (NEMA) MS 4 maximum clinical acoustic noise (MCAN) procedure in that (1) our microphones were positioned approximately at the location of a subject's ears rather than at the imager isocenter; (2) we digitized waveforms instead of using a sound meter, which allowed us to compute accurate noise spectra; (3) we measured noise in a typical imaging paradigm rather than with maximal gradient activity; and (4) our imager bore contained a phantom. In fact, the primary frequencies of imager noise are sufficiently high that the sound pressure probably varies over the volume of the bore [for instance, Hedeen and Edelstein (1997) and Shellock *et al.* (1998) measured differences in sound pressure of several dB between the center and the ends of the bore, all on the bore axis, and we have observed differences in sound pressure between the axis of the (empty) bore and a point approximately 10 cm off-axis]. To our knowledge, no systematic study of the sound field over the entire bore has been performed. Noise levels measured approximately at the location of the ears with a phantom in place (which serves as a dummy head for this purpose), rather than at the center of the symmetric bore, may provide a more realistic estimate of the actual noise levels experienced by subjects in the imager.

[4]The slice would have been approximately parallel to the Sylvian fissure in a supine subject.

[5]TE=70 ms, offset=−25 ms, field of view (FOV)=40×20 cm, frequency-encode direction: right–left.

[6]TE=35 ms, FOV=40×20 cm, frequency-encode direction: right–left.

[7]The slice would have been approximately perpendicular to the Sylvian fissure in a supine subject.

[8]TE=50 ms, flip angle=90 deg, FOV=40×20 cm, frequency-encode direction: right–left.

[9]Care was taken not to let the tape touch the microphone diaphragm.

[10]Both the Shure and the Knowles microphone had integral preamps that provided a low-impedance output.

[11]Harmonic distortion at 1.4 kHz (the primary frequency of the gradient noise at 3 T) would presumably be comparable to that at 1 kHz because harmonic distortion for condenser microphones is typically fairly constant across frequency (e.g., Zuckerwar, 1995).

[12]Microphone outputs in response to a 250-Hz pistonphone source were reduced by at least 40 dB when the microphones were encased in clay. (Note that the clay did not touch the microphone diaphragm and that the microphones were immersed in the sound field within the pistonphone cavity for these measurements.) We know that the clay did not damage the microphones because microphone outputs were the same after removing the clay as before applying the clay.

[13]Encasing the microphone in this way may be a more rigorous test of artifact than using a dummy microphone, in that the measurement microphone is still in place and functional. Several other investigators have also established that condenser microphones are largely immune to electrical artifact in the imager (e.g., Hurwitz *et al.*, 1989; Shellock *et al.*, 1994; Counter *et al.*, 1997).

[14]For computations of time-average levels, the waveform was high-pass filtered at 240 Hz to minimize the artifact.

[15]The sound-pressure waveforms $p[t]$ (sound pressure as a function of time t) shown were computed from the microphone voltage output waveform $w[t]$ by dividing $w[t]$ by the microphone sensitivity r_m (in V/Pa) measured in a pistonphone at 250 Hz.

[16]For the sound-pressure waveform $p[t]$, the peak level $L_{\mathrm{pk}} = 10 \log_{10}(p_{\mathrm{pk}}/20\ \mu\mathrm{Pa})^2$, where p_{pk} is the maximum of $|p[t]|$ (ANSI S1.13-1995).

[17]For this waveform with time-varying amplitude, a 10-ms window provided a good combination of time and frequency resolution. The 10-ms waveform segment included an integral number of cycles at the frequency of the peak in the noise spectrum, which allowed us to use a rectangular window to minimize spectral smearing (e.g., Oppenheim and Schafer, 1989).

[18]For the ith 10-ms (N-point) windowed waveform segment $w_i[t]$, the sound-pressure spectrum $S_{pi}[f]$ (in Pa) was computed from the Fourier transform $S_i[f]$ of $w_i[t]$ and the frequency response of the microphone and amplifier $S_m[f]$ (V/Pa) by $S_{pi} = (|S_i| \cdot 2/N)/|S_m|$. Shown in Figs. 3(C) and (D) is the spectrum containing $L_{f\ \max}$ for positive frequencies, divided by $\sqrt{2}$ to obtain root-mean-square pressures and expressed in dB SPL ($S_{\mathrm{SPL}i} = 20 \log_{10}[(S_{pi}/\sqrt{2})/20\ \mu\mathrm{Pa}]$).

[19]Note that $L_{f\ \max}$ is defined slightly differently from the ''maximum sound level'' or ''spectral level'' described in ANSI S1.1 (1994). We call $L_{f\ \max}$ the ''maximum spectral level'' because this term has the same sense as the ANSI terms: the highest of spectral levels computed over short time intervals.

[20]Time-average noise levels were derived from the acoustic energy in the noise signal ($L_T = 10 \log_{10}[1/T \int_0^T p^2 dt/(20\ \mu\mathrm{Pa})^2]$—see ANSI S1.1-1994). For our calculations T was either 10 ms or 2 s. We chose to compute time-average levels from the energy in the sound pressure spectrum $S_{pT}[f]$ rather than the time waveform $p[t]$ because correcting for the nonflat frequency response of our microphones was easier in the frequency domain; the two methods are equivalent by Parseval's theorem (Oppenheim and Schafer, 1989). For example, the time-average level over a 2-s time window L_{2s} (N points) was computed from the sound-pressure spectrum over the 2-s interval S_{p2s} by $L_{2s} = 10 \log_{10}[1/N \Sigma(|S_{p2s}|^2/N)/(20\ \mu\mathrm{Pa})^2]$.

[21]With one exception: For the last measurement in session II in the 3 T, $L_{f\ \max}$ underestimated the time-average noise level over the 10-ms window containing $L_{f\ \max}$ by less than 2 dB.

[22]Normally, the chemical-saturation gradient would be preceded by an rf pulse, and each of the slice-select gradients would be centered on an rf pulse. For these measurements, the rf transmitter was disconnected.

[23]The readout and phase-encode gradients were each immediately preceded by a 1-ms pulse, and the phase-encode gradient was followed by a 5-ms pulse (not shown in Fig. 4).

[24]Time for 60-dB decay $T_{60} \approx 0.161\ V/a$, where V is the volume of the room, the mean absorption $a = \Sigma\ S_i \alpha_i$, and S_i and α_i are the area and absorption coefficient, respectively, of each plaster wall, the acoustical tile ceiling, and the concrete floor. Absorption coefficients from Kinsler *et al.*, 1982.

[25]An experiment in the 3-T imager suggested that most of the noise in the bore 20 ms or more after the switch-off of the gradient currents was due to room reverberation (Ravicz *et al.*, 1999).

[26]For these calculations, the trigger pulses (from the imager controller, to which the noise and template waveforms were synchronized) were aligned, and the waveforms were subtracted on a sample-by-sample basis.

[27]This may be a conservative estimate of the reduction achievable because of uncertainty in our measurements of the timing of the imager trigger: Measurements of trigger timing had an uncertainty of 21 μs due to the 48-kHz sample rate of our A/D converter.

[28]This was accomplished by changing the image matrix size from 128×64 to 256×128.

[29]Note that when multiple (5 or 15) slices were specified, there was a corresponding number of equally spaced image acquisitions (one per slice) during each TR.

[30]The noise waveforms for successive image acquisitions were largely nonoverlapping because the time between acquisitions [repetition time (TR)/number of slices=2 s/15=133 ms] was comparable to the duration (~140

ms) of the highest-amplitude noise in the 1.5-T imager [occurring between roughly 80 and 220 ms in Fig. 4(A)].

[31]Though sound-level meters provide a quick and simple way of estimating average noise levels, the most commonly used meter time weighting settings (fast and slow) are inherently not well-suited for accurate time-average measurements of short-duration sound (e.g., ANSI S1.13-1995). The fact that the time constants associated with these settings (fast: 125 ms; slow: 1 s) are comparable to or longer than the duration of our high-level imager noise means that time-average noise levels, if measured with these settings, could have been significantly underestimated (ANSI S1.4-1985; Earshen, 1986).

[32]The insert gradient coil was designed and fabricated at the Medical College of Wisconsin Biophysics Research Institute and is approximately 33 cm in diameter, considerably smaller than the scanner bore (Prieto, 1999).

[33]Note that the field of view was also varied among these measurements. Prieto *et al.* (1998) have shown that FOV influences noise levels.

[34]For example, the apparent resonance at 700 Hz observed in our 1.5-T imager—see Sec. III C.

[35]For example, E·A·R E-0-10-25 (see E·A·R, 1999).

[36]Active noise reduction (ANR) involves introducing an acoustic signal (''antinoise'') into a noise field that combines destructively with the noise. Of the two main ANR strategies (feedforward and feedback), most commercial ANR headsets use a feedback strategy (e.g., Olson and May, 1953) in which noise is sensed at a particular location and antinoise is computed and delivered to the sensing location in ''real time.'' There is, however, an inherent delay due to processing time that causes the noise and antinoise to become out of phase as frequency increases; hence, with increasing frequency, the antinoise produces a diminishing reduction and eventually an amplification of the noise (e.g., Elliott and Nelson, 1993). Since the effectiveness of such ANR systems decreases as frequency increases, systems using this strategy are inherently less suitable for reducing the most intense gradient noise (e.g., 1 kHz and above). [For instance, the effectiveness of most commercial ANR headsets decreases above a few hundred hertz, and most are ineffective above 1 kHz (e.g., Casali and Berger, 1996).] Alternatively, if the timing of the noise is predictable (such as for the gradient noise), the time delay problem can be overcome by synchronizing the antinoise to the imager controller—a feedforward approach (e.g., Lueg, 1936; Elliott and Nelson, 1993; Fuller and von Flotow, 1995). The antinoise itself can be synthesized from measured transfer functions between the gradient current and the resulting sound (e.g., Hedeen and Edelstein, 1997) or can be an inverted copy of a previously measured noise waveform. All ANR systems developed for MRI to date have employed a feedforward strategy.

[37]In support of this idea, Palmer and his colleagues have observed that, for subjects wearing their ANR headset, reductions in the noise *heard* were smaller than the reduction in noise *level* at the entrance of the ear canal at frequencies above 1 kHz (Palmer, 1998).

[38]In the frequency range of pump and air-handling noise (<500 Hz), commercially available ANR headsets (using feedback control) typically provide 10–20 dB additional noise reduction at the ear (e.g., Casali and Berger, 1996). Though not currently magnet-compatible, these headsets could be adapted for use during MRI. ANR with feedforward control may also be appropriate because the pump noise is periodic.

ANSI (**1985**). S1.4, ''Specification for Sound Level Meters (amended)'' (American National Standards Institute, New York).

ANSI (**1994**). S1.1, ''Acoustical Terminology'' (American National Standards Institute, New York).

ANSI (**1995**). S1.13, ''Measurement of Sound Pressure Levels in Air'' (American National Standards Institute, New York).

Bandettini, P. A., Jesmanowicz, A., Van Kylen, J., Birn, R. M., and Hyde, J. S. (**1998**). ''Functional MRI of brain activation induced by scanner acoustic noise,'' Magn. Reson. Med. **39**, 410–416.

Beranek, L. L. (**1954**). *Acoustics* (McGraw-Hill, New York), 481 pp.

Berger, E. H. (**1983**). ''Laboratory attenuation of earmuffs and earplugs both singly and in combination,'' Am. Ind. Hyg. Assoc. J. **44**, 321–329.

Berger, E. H., Franks, J. R., Behar, A., Casali, J. G., Dixon-Ernst, C., Kieper, R. W., Merry, C. J., Mozo, B. T., Nixon, C. W., Ohlin, D., Royster, J. D., and Royster, L. H. (**1998**). ''Development of a new standard laboratory protocol for estimating the field attenuation of hearing protection devices. III. The validity of using subject-fit data,'' J. Acoust. Soc. Am. **103**, 665–672.

Bowtell, R. W., and Mansfield, P. (**1995**). ''Quiet transverse gradient coils: Lorentz force balanced designs using geometrical similitude,'' Magn. Reson. Med. **34**, 494–497.

Bowtell, R. W., and Peters, A. (**1999**). ''Analytic approach to the design of transverse gradient coils with co-axial return paths,'' Magn. Reson. Med. **41**, 600–608.

Brummett, R. E., Talbot, J. M., and Charuhas, P. (**1988**). ''Potential hearing loss resulting from MR imaging,'' Radiology **169**, 539–540.

Bushong, S. C. (**1996**). ''Magnetic Resonance Imaging: Physical and Biological Principles,'' 2nd ed. (Mosby, St. Louis), 497 pp.

Casali, J. G., and Berger, E. H. (**1996**). ''Technology advancements in hearing protection circa 1995: Active noise reduction, frequency/amplitude sensitivity, and uniform attenuation,'' Am. Ind. Hyg. Assoc. J. **57**, 175–185.

Cho, Z. H., Chung, S. T., Chung, J. Y., Park, S. H., Kim, J. S., Moon, C. H., and Hong, I. K. (**1998**). ''A new silent magnetic resonance imaging using a rotating dc gradient,'' Magn. Reson. Med. **39**, 317–321.

Cho, Z. H., Park, S. H., Kim, J. H., Chung, S. C., Chung, S. T., Chung, J. Y., Moon, C. W., Yi, J. H., Sin, C. H., and Wong, E. K. (**1997**). ''Analysis of acoustic noise in MRI,'' Magn. Reson. Imaging **15**, 815–822.

Cohen, M. (**1998**). ''Theory of echo-planar imaging,'' in *Echo-Planar Imaging: Theory, Technique and Application*, edited by F. Schmitt, M. K. Stehling, and R. Turner (Springer, Berlin), pp. 11–30.

Counter, S. A., Olofsson, Å, Grahn, H. F., and Borg, E. (**1997**). ''MRI acoustic noise: Sound pressure and frequency analysis,'' JMRI **7**, 606–611.

Dantendorfer, K., Amering, M., Bankier, A., Helbich, T., Prayer, D., Youssefzadeh, S., Alexandrowicz, R., Imhof, H., and Katschnig, H. (**1997**). ''A study of the effects of patient anxiety, perceptions and equipment on motion artifacts in magnetic resonance imaging,'' Magn. Reson. Imaging **15**, 301–306.

E·A·R. (**1999**). Materials Summary Sheet MSS3 Barrier Composites. E·A·R Specialty Composites, Indianapolis IN. Available at ⟨http://www.earsc.com/new/pdfs/mss/BarrCompositesMSS3.pdf⟩. Viewed 30 August 2000.

Earshen, J. J. (**1986**). ''Sound measurement: Instrumentation and noise descriptors,'' in *Noise and Hearing Conservation Manual*, edited by E. H. Berger, W. D. Ward, J. C. Morrill, and L. H. Royster (American Industrial Hygiene Association, Akron, OH), pp. 37–95.

Eden, G. F., Joseph, J. E., Brown, H. E., Brown, C. P., and Zeffiro, T. A. (**1999**). ''Utilizing hemodynamic delay and dispersion to detect fMRI signal change without auditory interference: The behavior interleaved gradients technique,'' Magn. Reson. Med. **41**, 13–20.

Edmister, W. B., Talavage, T. M., Ledden, P. J., and Weisskoff, R. M. (**1999**). ''Improved auditory cortex imaging using clustered volume acquisitions,'' Hum. Brain Mapp **7**, 89–97.

Elliott, M. R., Bowtell, R. W., and Morris, P. G. (**1999**). ''The effect of scanner sound in visual, motor, and auditory functional MRI,'' Magn. Reson. Med. **41**, 1230–1235.

Elliott, S. J., and Nelson, P. A. (**1993**). ''Active noise control,'' IEEE Signal Process. Mag. **10**(4), 12–35.

Fuller, C. R., and von Flotow, A. H. (**1995**). ''Active control of sound and vibration,'' IEEE Control Syst. Mag. **15**(6), 9–19.

Goldman, A. M., Gossman, W. E., and Friedlander, P. C. (**1989**). ''Reduction of sound levels with antinoise in MR imaging,'' Radiology **171**, 549–550.

Hall, D. A., Haggard, M. P., Akeroyd, M. A., Palmer, A. R., Summerfield, A. Q., Elliott, M. R., Gurney, E., and Bowtell, R. W. (**1999**). '''Sparse' temporal sampling in auditory fMRI,'' Hum. Brain Mapp. **7**, 213–223.

Hedeen, R. A., and Edelstein, W. A. (**1997**). ''Characterization and prediction of gradient acoustic noise in MR imagers,'' Magn. Reson. Med. **37**, 7–10.

Hurwitz, R., Lane, S. R., Bell, R. A., and Brant-Zawadzki, M. N. (**1989**). ''Acoustic analysis of gradient-coil noise in MR imaging,'' Radiology **173**, 545–548.

Kelley, Douglas A. C. (**1994**). Personal communication to M.E.R. and J.R.M.

Kelley, Douglas A. C. (**1999**). Personal communication to M.E.R.

Kinsler, L. E., Frey, A. R., Coppens, A. B., and Saunders, J. V. (**1982**). *Fundamentals of Acoustics*, 3rd ed. (Wiley, New York), 480 pp.

LABVIEW, Version 2 (**1991**). (National Instruments, Austin, TX).

Lueg, P. (**1936**). ''Process of silencing sound oscillations,'' U.S. Patent 2,043,416, 19 June 1936.

Mansfield, P., Chapman, B. L. W., Bowtell, R., Glover, P., Coxon, R., and Harvey, P. R. (**1995**). ''Active acoustic screening: Reduction of noise in

gradient coils by Lorentz force balancing,'' Magn. Reson. Med. **33**, 276–281.
Mansfield, P., Glover, P. M., and Beaumont, J. (**1998**). ''Sound generation in gradient coil structures for MRI,'' Magn. Reson. Med. **39**, 539–550.
MATLAB, Version 5.2 for Macintosh (**1998**). The Mathworks, Natick, MA.
McJury, M. J. (**1995**). ''Acoustic noise levels generated during high field MR imaging,'' Clin. Radiol. **50**, 331–334.
McJury, M. J., Blug, A., Joerger, C., Condon, B., and Wyper, D. (**1994**). ''Acoustic noise levels during magnetic resonance imaging scanning at 1.5 T,'' Br. J. Radiol. **67**, 413–415.
Melcher, J. R., Talavage, T. M., and Harms, M. P. (**1999**). ''Functional MRI of the Auditory System,'' in *Medical Radiology, Diagnostic Imaging and Radiation Oncology: Functional MRI*, edited by C. Moonen and P. Bandettini (Springer, Berlin), pp. 393–406.
Miyati, T., Banno, T., Fujita, H., Mase, M., Narita, H., Imazawa, M., and Ohba, S. (**1999**). ''Acoustic noise analysis in echo planar imaging: Multicenter trial and comparison with other pulse sequences,'' IEEE Trans. Med. Imaging **18**, 733–736.
NEMA (**1989**). MS 4-1989: *Acoustic Noise Measurement Procedure for Diagnostic Magnetic Resonance Imaging Devices* (National Electrical Manufacturers Association, Washington, DC).
OSHA (**1996**). *OSHA Regulations (Standards-29 CFR), Occupational noise exposure-1910.95*. Occupational Safety and Health Administration: Washington, DC, 7 March 1996. Available: ⟨http://www.osha-slc.gov/OshStd_data/1910_0095.html⟩. Viewed 4 May 2000.
Olson, H. F., and May, E. G. (**1953**). ''Electronic sound absorber,'' J. Acoust. Soc. Am. **25**, 1130–1136.
Oppenheim, A. V., and Schafer, R. W. (**1989**). *Discrete-Time Signal Processing* (Prentice-Hall, Englewood Cliffs, NJ), 879 pp.
Palmer, A. R., Bullock, D. C., and Chambers, J. D. (**1998**). ''A high-output, high-quality sound system for use in auditory fMRI,'' NeuroImage 7(4), S359.
Palmer, A. R. (**1998**). Personal communication to M.E.R.
Paschler, H. E. (**1998**). *The Psychology of Attention* (MIT Press, Cambridge, MA), 494 pp.
Pla, F. G., Sommerfeldt, S. D., and Hedeen, R. A. (**1995**). ''Active control of noise in magnetic resonance imaging,'' in *Proceedings of Active 95* (Noise Control Foundation, Poughkeepsie, NY), pp. 573–582.
Prieto, T. E., Bennett, K., and Weyers, D. (**1998**). ''Acoustic noise levels in a head gradient coil during echo planar imaging,'' in Proceedings of the International Society for Magnetic Resonance in Medicine, Sixth Scientific Meeting and Exhibition, p. 750.
Prieto, T. E. (**1999**). Personal communication to M.E.R.
Ravicz, M. E., and Melcher, J. R. (**1998a**). ''Reducing imager-generated noise at the ear during functional magnetic resonance imaging: Passive attenuation,'' *Abstracts of the Twenty-first Midwinter Meeting of the Association for Research in Otolaryngology* (ARO, Mt. Royal, NJ), p. 208.
Ravicz, M. E., and Melcher, J. R. (**1998b**). ''Imager noise and noise reduction during fMRI,'' NeuroImage **7**(4), S556.
Ravicz, M. E., Melcher, J. R., Talavage, T. M., Benson, R. R., Rosen, B. R., and Kiang, N. Y. S. (**1997**). ''Characterization and reduction of imager-generated noise during functional magnetic resonance imaging (fMRI),'' *Abstracts of the Twentieth Midwinter Meeting of the Association for Research in Otolaryngology* (ARO, Des Moines, IA), p. 205.
Ravicz, M. E., Melcher, J. R., and Wald, L. L. (**1999**). ''Reducing acoustic noise transmission from gradient coils to subject during fMRI: An approach and preliminary results,'' Neuroimage **9**, S1.
Savoy, R. L., Ravicz, M. E., and Gollub, R. (**1999**). ''The Psychophysiological Laboratory in the Magnet: Stimulus Delivery, Response Recording, and Safety,'' in *Medical Radiology, Diagnostic Imaging and Radiation Oncology: Functional MRI*, edited by C. Moonen and P. Bandettini (Springer, Berlin), pp. 347–365.
Schmitt, F., Irnich, W., and Fischer, H. (**1998**). ''Physiological side effects of fast gradient switching,'' in *Echo-Planar Imaging: Theory, Technique and Application*, edited by F. Schmitt, M. K. Stehling, and R. Turner (Springer, Berlin), pp. 201–252.
Shah, N. J., Jäncke, L., Grosse-Ruyken, M.-L., and Müller-Gärtner, H. W. (**1999**). ''Influence of acoustic masking noise in fMRI of the auditory cortex during phonetic discrimination,'' JMRI **9**, 19–25.
Shellock, F. G., Morisoli, S. M., and Ziarati, M. (**1994**). ''Measurement of acoustic noise during MR imaging: Evaluation of six 'worst-case' pulse sequences,'' Radiology **191**, 91–93.
Shellock, F. G., Ziarati, M., Atkinson, D., and Chen, D.-Y. (**1998**). ''Determination of acoustic noise during MRI using echo planar and three dimensional, fast spin echo techniques,'' JRMI **8**, 1154–1157.
Talavage, T. M., Edmister, W. B., Ledden, P. J., and Weisskoff, R. M. (**1999**). ''Quantitative assessment of auditory cortex responses induced by imager acoustic noise,'' Hum. Brain Mapp. **7**, 79–88.
Ulmer, J. L., Biswal, B. B., Yetken, F. Z., Mark, L. P., Mathews, V. P., Prost, R. W., Estkowski, L. D., McAuliffe, T. L., Haughton, V. M., and Daniels, D. L. (**1998**). ''Cortical activation response to acoustic echo planar scanner noise,'' J. Comput. Assist. Tomogr. **22**, 111–119.
Vér, I. L, and Holmes, C. I. (**1988**). ''Interaction of sound waves with solid structures,'' in *Noise and Vibration Control*, edited by L. L. Beranek (Institute of Noise Control Engineering, Washington, DC), pp. 270–361.
Von Gierke, and Nixon, C. W. (**1992**). ''Damage risk criteria for hearing and human body vibration,'' in *Noise and Vibration Control Engineering: Principles and Applications*, edited by L. L. Beranek and I. L. Vér (Wiley, New York), pp. 585–616.
Wald, L. L. (**1999**). Personal communication to M.E.R. and J.R.M.
Wessinger, C. M., Buonocore, M. H., Kussmaul, C. L., and Mangun, G. R. (**1997**). ''Tonotopy in human auditory cortex examined with functional magnetic resonance imaging,'' Hum. Brain Mapp. **5**, 18–25.
Woodruff, P. W. R., Benson, R. R., Bandettini, P. A., Kwong, K. K., Howard, R. J., Talavage, T., Belliveau, J., and Rosen, B. R. (**1996**). ''Modulation of auditory and visual cortex by selective attention is modality-dependent,'' NeuroReport **7**, 1909–1913.
Zuckerwar, A. J. (**1995**). ''Principles of operation of condenser microphones,'' in *AIP Handbook of Condenser Microphones*, edited by G. S. K. Wong and T. F. W. Embleton (AIP, Woodbury, NY), pp. 37–69.
Zwislocki, J. (**1957**), ''In search of the bone-conduction threshold in a free sound field,'' J. Acoust. Soc. Am. **29**, 795–804.

Sound absorption of cellular metals with semiopen cells

Tian J. Lu[a)]
Engineering Department, Cambridge University, Cambridge CB2 1PZ, United Kingdom

Feng Chen and Deping He
Department of Materials Science & Engineering, Southeast University, Nanjing 210096, People's Republic of China

(Received 24 August 1999; accepted for publication 8 May 2000)

A combined experimental and theoretical study is presented for the feasibility of using aluminum foams with semiopen cells for sound-absorption applications. The foams are processed via negative-pressure infiltration, using a preform consisting of water-soluble spherical particles. An analytical model is developed to quantify the dependence of pore connectivity on processing parameters, including infiltration pressure, particle size, wetting angle, and surface tension of molten alloy. Normal sound-absorption coefficient and static flow resistance are measured for samples having different porosity, pore size, and pore opening. A theory is developed for idealized semiopen metallic foams, with a regular hexagonal hollow prism having one circular aperture on each of its eight surfaces as the unit cell. The theory is built upon the acoustic impedance of the circular apertures (orifices) and cylindrical cavities due to viscous effects, and the principle of electroacoustic analogy. The predicted sound-absorption coefficients are compared with those measured. To help select processing parameters for producing semiopen metallic foams with desirable sound-absorbing properties, emphasis is placed on revealing the correlation between sound absorption and morphological parameters such as pore size, pore opening, and porosity. © *2000 Acoustical Society of America.* [S0001-4966(00)03608-0]

PACS numbers: 43.50.Gf, 43.55.Ev, 43.20.Mv [MRS]

INTRODUCTION

Cellular metal foams having either closed or open cells are currently being developed for structural, thermal, and acoustical applications.[1–8] Cellular metals with closed cells are, in general, poor sound absorbers, owing to the difficulty of sound having access to the interior cellular structure. The sound-absorption performance of close-celled metallic foams can nevertheless be much enhanced by partially fracturing the cell walls via rolling[6,8]—the resulting small but sharp-edged cracks on the cell faces become passageways for the in-and-out movement of air particles, resulting in sound-absorption improvement. Here, the dissipation of sound energy is realized mainly through viscous and thermal losses; other energy-dissipating mechanisms also exist in a cellular metal, including Helmholtz resonators, vortex shedding from sharp ligaments, and structural vibration, but their effects on sound absorption are likely to be small compared to viscous and thermal forces.[6] One type of such aluminum foam, trade name Alporas, has been developed by Shinko Wire, Japan, for use as sound-absorbing material; it has been installed as soundproofing inside factories/shopping malls, along the side of a road/tunnel, underneath an expressway, amongst many other applications (e.g., underwater sound absorption). In addition to its attractive sound-absorbing property,[6] aluminum foams are stable and do not generate toxic gases in the presence of a flame,[4] have high durability and resistance to weathering, and can shield against electromagnetic waves.[1] Consequently, they may be implemented in harsh conditions such as the discharge chamber of a high-repetition-rate excimer laser used in optical lithography where sound may reach a level as high as 190 dB. Since the laser charge chamber is filled with 99% neon and 1% fluorine gas, the latter being chemically extremely aggressive, Al alloy foam sound absorbers would be suitable.

Open-celled aluminum foams are widely used as compact heat exchangers for high-power electronics due to their low relative density, superior surface area density, and high thermal conductivity of the cell edges.[3] To minimize flow resistance due to restrictions on pumping power, a high open porosity with cell sizes larger than 1 mm is usually required. Experimentally, it is found that these foams are poor sound absorbers. This is expected, as our previous study[7] has established that the cells of an open-celled foam must have sizes on the order of 10^{-1} mm for the foam to be a good sound absorber. However, the capability of a cellular foam to absorb sound does not always increase with decreasing cell size—the foam becomes a poor sound absorber again if its cell size falls below 0.1 mm because most of the sound is thence reflected back to the source.[7]

Sound absorption in porous materials has been a subject of significance in many practical applications, and has been studied extensively in the past. Delany and Bazley[9] developed empirical power-law relationships between fundamental acoustic properties, i.e., characteristic impedance and propagation constant, and the ratio of static flow resistivity to frequency. Despite their popularity and successful application in a large number of sound absorbers, the Delany–Bazley equations can nevertheless lead to physically unrealistic predictions, especially at low frequencies. Also, because

a)Electronic mail: TJL21@eng.cam.ac.uk

these equations are phenomenological, they cannot be used to study the effect of microstructural parameters on sound absorption. Similarly, although the Morse–Ingard model[10] is based on physically sound principles, it is not directly applicable to a porous material with a particular microstructure. Based on the general frequency dependence of the viscous forces derived by Johnson *et al.*,[11] Allard and Champoux[12] developed a new empirical relationship for highly porous rigid-framed fibrous materials. Here, two parameters are needed, one related to the pore geometry and the other being the ratio of two length scales associated separately with viscous and thermal dissipation processes. A notable feature of Allard and Champoux's approach is that correct predictions both at low and high frequencies are obtained. On the other hand, Zwikker and Kosten[13] and Biot[14] provided different but equivalent solutions for uniform, circular tubes that lay the foundation of another type of popular theory. To extend these solutions for circular tubes to more complicated pore geometries, Attenborough,[15] Allard *et al.*,[16] and Stinson and Champoux[17] introduced pore shape factors to account for the discrepancy between the cross-sectional geometry of an actual pore and that of a circular tube. Another theoretical approach for sound propagation through porous media is Wilson's[18] relaxation-matched method built on previous work of Johnson *et al.*[11] In contrast to models based on matching low- and high-frequency asymptotic behaviors, Wilson's relaxation-type model is physically more realistic for all frequencies. It is based on the concept of modal wave modes and the dominance of a particular mode in the description of complex density and compressibility. Three parameters are needed in the relaxation model, i.e., static flow resistance and two relaxation times characterizing the process of wave fields to establish either viscous or thermal equilibrium in the material.

In the present investigation, aluminum foams with semiopen cells are developed for implementation as a sound absorber. The foam is made by infiltrating molten aluminum alloy under a controlled high pressure into the pores of a preform consisting of water-soluble particles [cf. Fig. 1(a)]. The cells of the foam are interconnected by small circular openings with sizes adjustable by varying the infiltration pressure, particle size, surface tension of molten alloy, and wetting angle between molten alloy and particle. A typical microstructure of the foam is shown in Fig. 1(b). An analytical model is developed to quantify the dependence of pore connectivity upon infiltration pressure, particle size, surface tension, and wetting angle. Acoustic performance of the foam is then characterized by sound-absorption measurement with the impedance tube method and by the static flow resistance measurement, with special emphasis placed on exploring the roles of structural parameters such as pore size, pore connectivity, and porosity in sound absorption. Note that the size of the pores does not have to be small for the porous metal to be a good sound absorber, as long as the size of the pore openings is on the order of 10^{-1} mm. However, due to this feature (i.e., abrupt change in cross-sectional area as sound enters or leaves the pore opening), the resulting material may not be adequately characterized by previous theoretical models. Consequently, a theory, built upon the acoustic impedance of circular apertures and cylindrical cavities, is developed to establish the structure–property relationship for metallic foams having idealized, semiopen cellular structures, and to identify optimized structures that would maximize sound absorption. The predicted absorption properties are compared with those measured. It is found that the end effects of small pore openings—modeled as circular apertures in the present approach—must be considered to determine the sound-absorption coefficient of the infiltration-processed porous metal. These effects are not modeled by most previous theories, e.g., those of Zwikker–Kosten, Attenborough, Allard–Champoux–Stinson, and Wilson, which mainly deal with homogeneous porous materials where the pores do not change abruptly in cross-sectional area. Another important feature of the present model is that no fitted parameter is introduced, and that it can be directly applied to nonhomogeneous materials with, for example, a gradient of pore size and pore opening distribution. However, it is emphasized here that the new model is not a replacement of existing models, but rather introduced to deal with the three-dimensional small apertures in our material. In other words, if a porous material does not contain such apertures, then the use of our model is not recommended.

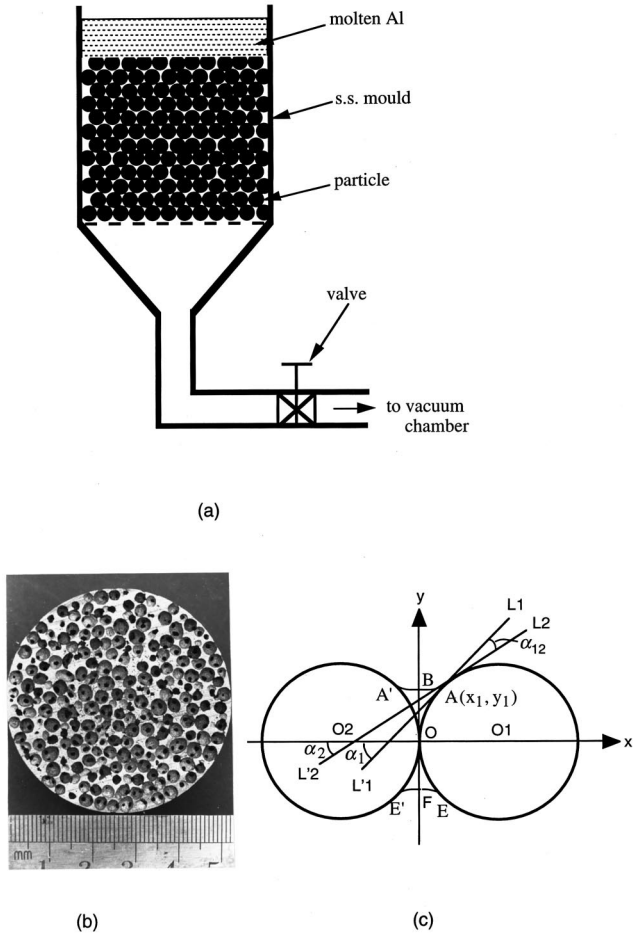

FIG. 1. (a) Schematic of negative-pressure infiltration processing of semiopen aluminum foams; (b) typical microstructure of semiopen aluminum foam; (c) geometry and notations of an infiltration element.

I. MATERIALS

A. Processing of materials

Spherical particles are made by a specially designed machine which mixes very fine Al_2O_3 powders with a binder solution—composed of inorganic salt (e.g., Na_2CO_3) and water—to form round particles and ''roll'' these particles until they become (approximately) spherical. The selection of Al_2O_3 powder is based on its high temperature resistance, excellent removability after foaming, good formability, high stiffness and strength, low thermal conductivity, and, most importantly, nonwettability with molten aluminum alloy. After baking (in order to make the inorganic salt crystallize), the particles are separated, via screening, into groups with varying sizes: 0.3–0.45, 0.45–0.6, 0.6–1.0, 1.0–1.25, 1.25–1.6 mm, with those obviously less spherical discarded. The particles from a selected group are randomly packed, assisted by mechanical vibration, into a cylindrical stainless-steel mold of diameter 200 mm. The mold is then preheated in a specially designed oven, maintained at 700 °C for about 30 min to ensure uniform heating of the particles. Molten aluminum of temperature ~720 °C is subsequently infiltrated into the preform under controlled pressure [Fig. 1(a)]. After the mold cools down to room temperature, the particle/Al composite is removed; the particles are then separated from the Al skeleton and washed away by a water jet. In addition to pure Al, the casting alloy comprises about 6.5%–7.5% Si and 0.25%–0.45% Mg. The aluminum alloy has a density of 2.68 Mg/m^3 and melting temperature of 615 °C.

B. Pore connectivity

With reference to Fig. 1(c), let $I=d/D$ denote the connectivity between two neighboring spherical particles, where D is the particle diameter and $d=\overline{BF}$. Here, O lies midway between the centers O_1 and O_2 of two identical, neighboring particles, with $\overline{OO}_1=\overline{OO}_2=D/2$, and B is the bottom of surface ABA' of the molten alloy between the spherical particles. During infiltration, air is trapped inside the volume formed by revolving the surface $ABA'E'FE$ with respect to the x axis. When the particles are removed, d becomes the diameter of the hole connecting two neighboring pores of diameter D. The shape of surface ABA' depends on surface tension γ of the molten alloy, wetting angle θ between molten alloy and particle, and pressure drop ΔP across surface ABA'. When ΔP drops below a critical value ΔP_c, the surface ABA' collapses to a point O (i.e., $d=0$), with[19]

$$\Delta P_c = 6\gamma\cos\theta\frac{V_p}{(1-V_p)D}. \tag{1}$$

Here, $V_p=M\pi D^3/6$ is the relative density of the preform, with M representing the number of particles per unit volume of the preform. To ensure successful infiltration without the molten alloy entering the gap spontaneously, it is required that the wetting angle satisfies the condition $\pi/2<\theta\leqslant\pi$.

In general, the pore connectivity I depends upon infiltration pressure ΔP, particle size D, wetting angle θ, and surface tension γ. However, an elementary dimensional analysis reveals that I is only dependent upon two dimensionless parameters, $\Delta pD/\gamma$ and θ, i.e., $I=\zeta(\Delta pD/\gamma,\theta)$. By assuming that the surface ABA' is parabolic, the dimensionless function ζ can be determined analytically, as follows. With reference to Fig. 1(c), let L_1L_1' be the tangent line of circle O_1 at $A(x_1,y_1)$, which intersects with the x axis at angle α_1; let L_2L_2' be the tangent line of surface ABA' at A, which intersects with the x axis at angle α_2. With the angle sustained by L_1L_1' and L_2L_2' denoted by α_{12}, the wetting angle θ between the molten alloy and particle is simply

$$\theta=\pi-\alpha_{12}=\pi-(\alpha_1-\alpha_2), \tag{2}$$

where $\pi/2<\theta\leqslant\pi$ is assumed. From equilibrium (with the gravity effect neglected), the pressure drop Δp across the surface ABA' is related to the surface tension γ by

$$\Delta p=\gamma(1/r_1-2/d), \tag{3}$$

where r_1 is the radius of curvature of surface ABA' at B, and $d=\overline{BF}$ is the pore opening size. As a first approximation, let the molten alloy surface ABA' be parabolic, with

$$y=x^2/k+d/2, \tag{4}$$

where k is a length scale to be determined. Combining Eq. (4) with Eq. (3) results in

$$\Delta p=2\gamma(1/k-1/d). \tag{5}$$

On the other hand, the coordinates (x_1,y_1) of A must satisfy

$$y_1=x_1^2/k+d/2, \tag{6}$$

and

$$(x_1-D/2)^2+y_1^2=D^2/4. \tag{7}$$

Finally, with the surface ABA' taken to be of parabolic shape as defined by Eq. (4), Eq. (2) can be rewritten as

$$tg\ \theta=\frac{x_1(1+2y_1/k)-D/2}{y_1+2(x_1/k)(D/2-x_1)}. \tag{8}$$

Equations (5)–(8) provide a set of four equations for four unknowns x_1, y_1, d, and k, for given values of Δp, D, γ, and θ. With the introduction of the following dimensionless parameters:

$$\frac{\Delta pD}{\gamma},\ I\equiv\frac{d}{D},\ \overline{x_1}\equiv\frac{x_1}{D},\ \overline{y_1}\equiv\frac{y_1}{D},\ \overline{k}\equiv\frac{k}{D}, \tag{9}$$

Eqs. (5)–(8) can be rewritten as

$$\Delta pD/\gamma=2(1/\overline{k}-1/I), \tag{10}$$

$$\overline{y_1}=\overline{x_1}^2/\overline{k}+I/2, \tag{11}$$

$$(\overline{x_1}-1/2)^2+\overline{y_1}^2=1/4, \tag{12}$$

$$tg\ \theta=\frac{\overline{x_1}(1+2\overline{y_1}/\overline{k})-1/2}{\overline{y_1}+2(\overline{x_1}/\overline{k})(1/2-\overline{x_1})}. \tag{13}$$

Equations (10)–(13) have no closed-form solutions, and must be solved numerically. However, it is evident from this set of dimensionless equations that the pore connectivity I is a function of only two nondimensional parameters, namely, $\Delta pD/\gamma$ and θ. The predicted connectivity I is shown in Fig. 2(a) as a function of $\Delta pD/\gamma$ for selected values of θ, and in

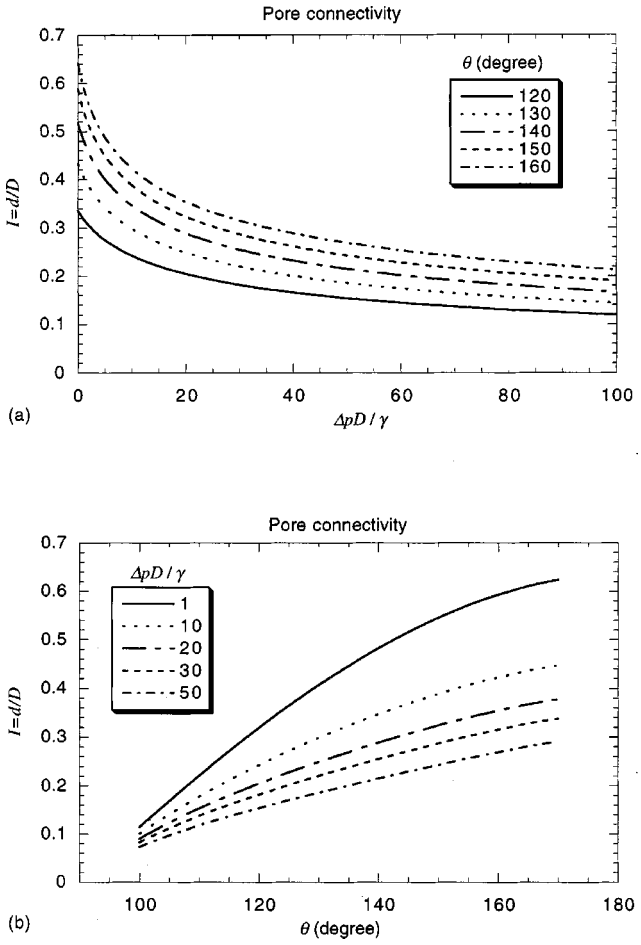

FIG. 2. Predicted pore connectivity $I=d/D$ as a function of (a) $\Delta pD/\gamma$ for selected values of wetting angle θ; (b) θ for selected values of $\Delta pD/\gamma$.

Fig. 2(b) as a function of θ for selected values of $\Delta pD/\gamma$. From Fig. 2, it is seen that the pore connectivity decreases with increasing values of $\Delta pD/\gamma$, and increases with increasing values of wetting angle θ. For a given wetting angle θ, the pore connectivity decreases sharply with increasing $\Delta pD/\gamma$ when $\Delta pD/\gamma$ is small (<10), but then descends slowly as $\Delta pD/\gamma$ is further increased. On the other hand, for a fixed value of $\Delta pD/\gamma$, the pore connectivity increases nearly linearly with increasing θ. These results clearly indicate that, to achieve a predetermined pore connectivity at a known wetting angle θ, it is critical to adjust the value of $\Delta pD/\gamma$ according to the master curves given in Fig. 2. This can be realized by changing separately the infiltration pressure Δp, particle size D, surface tension γ, or a combination of all three parameters. The model predictions have been compared with experimental measurements for varying particle size D (1–6 mm) and infiltration pressure Δp (2–40 MPa), with $\gamma=0.914$ N/m for aluminum and $\theta=152°$ (measured from a microscope); excellent agreement between predictions and measurements is obtained.[20]

C. Porosity

The porosity Ω of the foam is, in general, larger than V_p (the relative density of the perform), because the molten alloy is not fully infiltrated into the space between neighboring particles [Fig. 1(c)]. The air entrapped in the volume $ABA'E'FE$ adds to the porosity of the foam, resulting in

$$\Omega = V_p(1+3NV_a/\pi D^3), \tag{14}$$

where N is the coordination number (i.e., the number of nearest neighbors) of an individual particle, and V_a is the volume of $ABA'E'FE$. Once x_1, d, and k are found by solving Eqs. (10)–(13), the volume V_a of the air trapped inside the space formed by revolving the surface $ABA'E'FE$ around the x axis can be calculated as

$$\frac{V_a}{2\pi} = \int_0^{x_1}\left\{\left(\frac{x^2}{k}+\frac{d}{2}\right)^2 - \left[\frac{D^2}{4}-\left(x-\frac{D}{2}\right)^2\right]\right\}dx$$

$$= \frac{x_1^5}{5k^2} + \frac{(d/k+1)}{3}x_1^3 - \frac{Dx_1^2}{2} + \frac{x_1 d^2}{4}. \tag{15}$$

On the other hand, an extensive experimental study has established the following relationship between V_p and N:[21]

$$V_p = 34 + 9.2(N-4) - 0.35(N-4)(N-6) - 0.2(N-4) \times (N-6)(N-8) + 0.07(N-4)(N-6) \times (N-8)(N-10). \tag{16}$$

Experimentally, the packing density of the particles is first measured, which is then used together with Eq. (16) to determine N. Note that when the particles are closely packed with $N=12$ (face-centerd cubic), we have $V_p=74.0\%$ according to Eq. (16). If $N=8$ (body-centerd cubic), then $V_p=68.0\%$. If the particles are loosely packed with $N=6$, then $V_p=52.4\%$. For the present porous aluminum, we found that the coordination number $N=7-7.5$, which depends weakly on the pore size D. The predicted porosities from Eqs. (14)–(16) for a range of semiopen aluminum foams compare closely with measured values.[21]

II. EXPERIMENTAL MEASUREMENTS

A. Sample preparation

Cylindrical specimens of diameter 100 mm and thickness 100 mm are spark cut by an electrodischarge machine from foams having six different grades of pore size, and are denoted separately as samples ''a,'' ''b,'' ''c,'' ''d,'' ''e,'' and ''f.'' For each grade of pore size two nominally identical samples are prepared. Figures 3(a) and 3(b) show separately the scanning electron microscopy (SEM) images of the surface and cross-sectional area of a typical sample. The average pore size, pore opening, porosity, and bulk density of each specimen are listed in Table I.

B. Sound-absorption coefficient

The standard impedance tube method is used to measure the sound-absorption coefficient of each sample as a function of frequency and air cavity depth behind the sample. Details of the impedance tube method can be found in Lu *et al.*[6] It suffices to say that special care has been taken to minimize the effect of boundary conditions on sound-absorption measurements: here, a tight fit between the sample and impedance tube is not as difficult to achieve as in the case of much softer materials such as glass wool and polymeric foams.

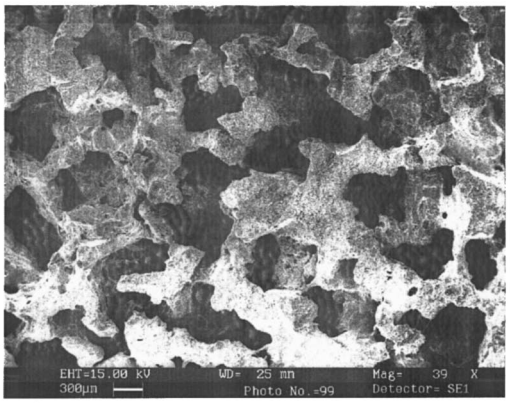

(a)

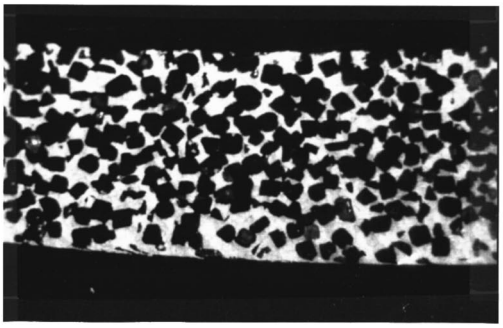

(b)

FIG. 3. SEM images of (a) surface; (b) cross-sectional area of a semiopen aluminum foam sample.

Also, it has been checked that the maximum sound level recorded in the tube is about 100 dB, and hence the assumption of linearity of sound is valid in the present investigation.

C. Static airflow resistance

Amongst the various parameters that may affect the acoustic performance of a porous material (e.g., porosity, tortuosity, pore shape factor, etc.), it has been well established that the static flow resistance σ is the most important and, often, it is a good approximation to use it alone.[22] Several analytical and semianalytical models have been developed to characterize cellular and fibrous materials on the basis of f/σ (where f is the frequency), including the empirical model of Delany and Bazley,[9] the semiempirical model of Allard and Champoux,[12] and the relaxation model of Wilson.[18]

The static airflow resistance σ of each sample is measured by a specially designed experimental setup as illustrated in Fig. 4. The samples are spark cut from the same specimens used for sound-absorption measurements. The test rig in the main consists of an air supply system, flowmeter and controller, and manometer. The air is supplied from a pressurized tank that is connected to the flowmeter via a network of in-series valves and quarter-inch tubings. A pressure regulator maintains a 2-bar overpressure upstream of the installation. A mass flow controller is used to ensure a stable gas supply to the sample. The specimen is mounted on a brass tube attached to the platform. An O-ring seals off the brass tube inside a quartz tube which is also sealed by a O-ring. A digital manometer having a resolution of ± 0.01 mbar is used to measure the pressure drop of airflow across the specimen after the flow has reached a steady stage. A number of readings are made at different flow rates to check whether the flow is in the laminar regime. Finally, from the measured data in the laminar regime, the airflow resistivity σ (defined here as the specific airflow resistance per unit thickness) is obtained as

$$\sigma = \frac{\Delta p}{UL/A}, \tag{17}$$

where Δp is the pressure drop across the sample, L and A are the sample thickness and surface area, respectively, and U is the volume flow rate of air. Note that the above method of static flow resistance measurement is similar to that developed by Stinson and Daigle.[23]

III. EXPERIMENTAL RESULTS

A. Sound-absorption coefficient

Figure 5 plots the measured normal sound-absorption coefficients for samples ''a,'' ''b,'' ''c,'' ''d,'' and ''f,'' each 20-mm thick, as functions of frequency in the range of 0–1800 Hz. (The majority of sound-absorption applications for semiopen Al foams is in the relatively low frequency range, with $f < 4000$ Hz.) Here, all samples are placed against a rigid wall, with no air cavity in between. Note that Fig. 5 also includes theoretical predictions which will be discussed in detail later in Sec. IV. Sound absorption is seen to be generally poor at frequencies below 1000 Hz, but increases sharply as the frequency is further increased. Overall, the best sound absorption is achieved in sample ''a,'' having the smallest pore size and pore opening (Table I). In Fig. 6, the measured sound-absorption coefficient of sample ''ad'' is compared with that of a 40-mm-thick glass wool layer. Here and below, a sample labeled as, for example, ''cb,'' is created by combining samples ''c'' and ''b,'' each 20-mm

TABLE I. Properties of Al foam samples.

Sample	Bulk density (g/cm^3)	Porosity (%)	Pore size (mm)	Pore opening (mm)	Static flow resistance (MKS rayls m^{-1})
a	0.911	66.26	0.433	0.138	147.0
b	1.010	62.58	0.836	0.250	49.2
c	0.919	65.98	0.861	0.344	31.3
d	0.932	65.47	1.06	0.400	27.9
e	0.853	68.41	0.800	0.329	28.0
f	1.084	59.84	0.999	0.300	47.7

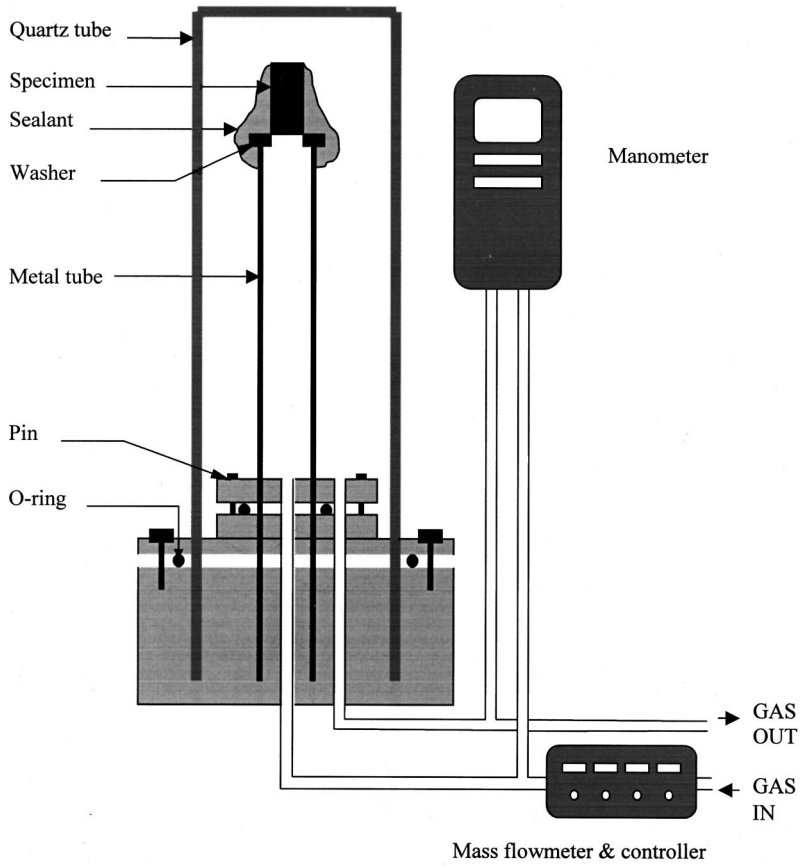

FIG. 4. Experimental setup for static airflow resistance measurement.

thick, with sample ''b'' facing the approaching sound wave and sample ''c'' facing the rigid wall. Note that, except for a small phase shift of peak absorption, the 40-mm-thick Al foam performs nearly as well as the 40-mm-thick glass wool, a known good sound absorber. For completeness, the measured sound-absorption coefficient versus frequency curves for 20-mm-thick sample ''a'' and ''d'' are also included in Fig. 6.

The effect of placing an air cavity between the sample and rigid wall is shown in Fig. 7(a) for the 20-mm sample ''a.'' As expected, the peak point of sound absorption is increasingly shifted towards lower frequencies as the depth of air cavity is increased. Figure 7(b) shows the effect of placing an air cavity between two 10-mm-thick panels of sample ''a'' on the sound absorption versus frequency curve; the combined specimen is placed directly against the rigid wall. The effect is similar to that shown in Fig. 7(a), although slightly better overall sound-absorption performance is observed in Fig. 7(b). The sound-absorption coefficients of sample ''bc'' and sample ''cb'' were also measured, with no air cavity placed behind the sample or between samples. It is found that switching sample ''b'' with sample ''c'' so as to alter the cellular morphology of the sample surface facing the impinging sound wave has only a minimal effect on sound absorption: the two curves are nearly identical (for brevity, the experimental results are not shown here). Similarly, it is found that it is not important which type of sample is used to pair with sample ''a''—the best sound absorber amongst all 20-mm-thick samples; for instance, the sound-absorption performance of sample ''ba'' is nearly identical to that of sample ''ca'' or ''ea.'' The predicted effect of air cavity is also included in Fig. 7. A summary of the sound-absorption coefficients at three frequencies, 500, 1000, and 1500 Hz, is given in Table II for samples backed against a rigid wall.

The variation of normal sound-absorption coefficient with porosity, pore size, and pore opening size is shown in Figs. 8(a), 8(b), and 8(c), respectively. Here, the data corresponding to samples ''a,'' ''b,'' ''c,'' ''d,'' ''f,'' each 20-mm thick and backed by rigid wall, are plotted (i.e., these data are taken directly from Fig. 5). There appears to be no apparent correlation between sound absorption and porosity from Fig. 8(a), which may be attributed to the small range of porosity investigated in the experiments. Figure 8(b) also reveals that the correlation between sound absorption and pore size amongst the samples is rather poor, suggesting more data are needed to establish a more definite trend. However, it is quite obvious from Fig. 8(c) that the sound-absorbing capability of a semiopen Al foam increases with decreasing pore opening size, consistent with the analytical results reported by Wang and Lu.[7] More discussions on the effects of morphological parameters on sound absorption will be given later in Sec. IV C.

B. Static flow resistance

Extensive measurements of pressure drop (Δp) as a function of volume flow rate (U) established that laminar flow is maintained for all six samples considered, allowing σ to be directly calculated from the slope of each Δp versus U

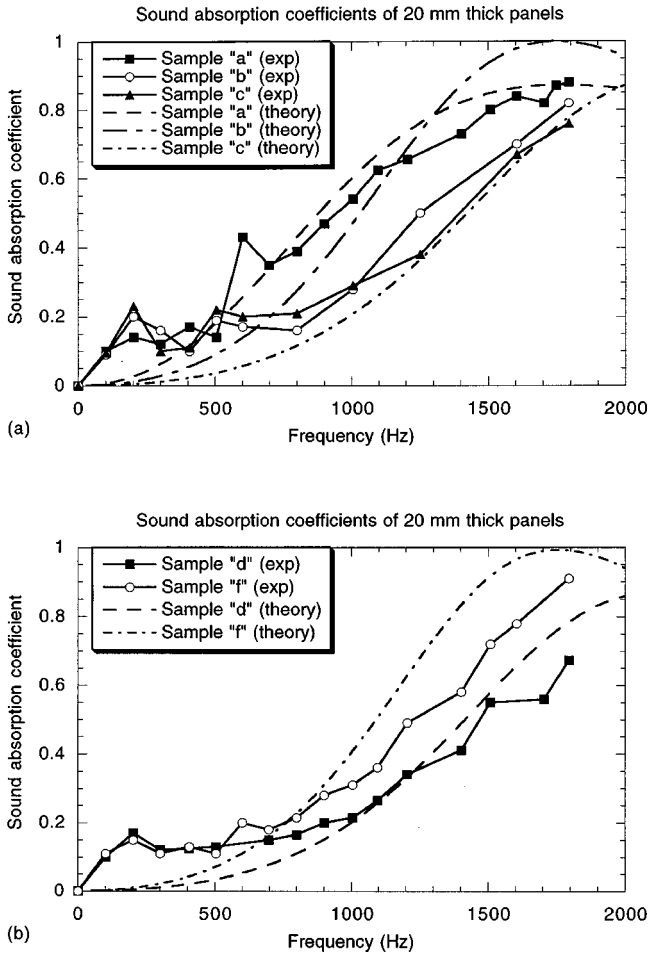

FIG. 5. Measured and predicted normal sound-absorption coefficient versus frequency curves for 20-mm-thick samples backed by rigid wall: (a) samples ''a,'' ''b,'' ''c,'' and (b) samples ''d,'' ''f.'' The error of measurement is on the order of 5%–10%.

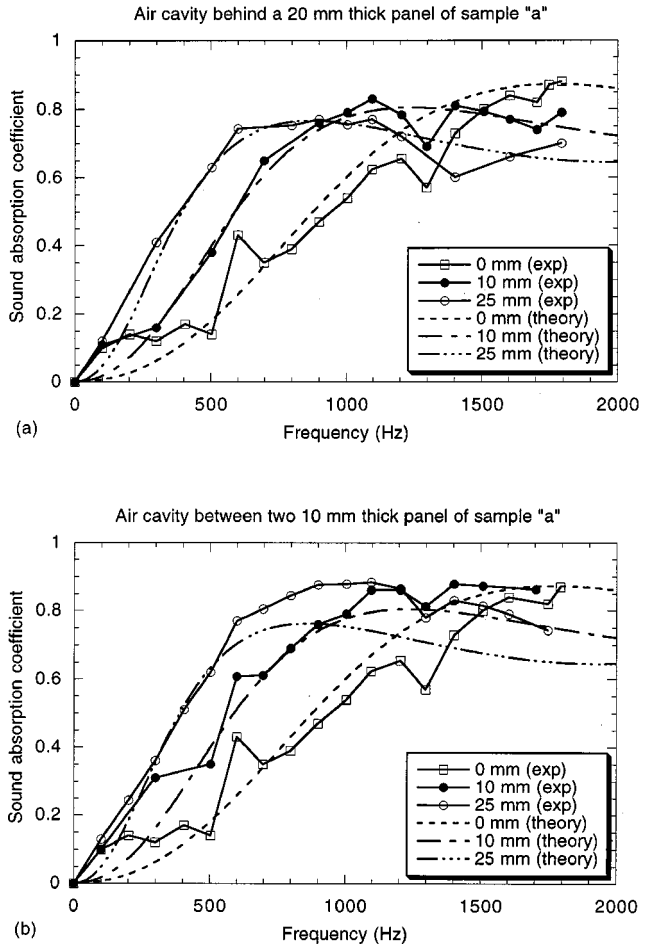

FIG. 7. Measured and predicted normal sound-absorption coefficient versus frequency curves: (a) effect of air cavity behind 20-mm-thick sample ''a;'' (b) effect of air cavity between two 10-mm-thick samples ''a.'' The error of measurement is on the order of 5%–10%.

curve; the results are summarized in Table I. The dependence of σ on pore size and pore opening is plotted in Fig. 9, where it is seen that σ decreases with increasing pore opening size, but the correlation between σ and pore size is poor. The knockdown in σ is particularly acute when the pore opening size is doubled from about 0.15 to 0.3 mm. However, for the samples considered in the present study, no correlation between σ and porosity was found. The dependence of normal sound-absorption coefficient on σ is shown in Fig. 8(d); as expected, sound absorption is enhanced as the static flow resistance is increased, especially at higher frequencies ($>$500 Hz).

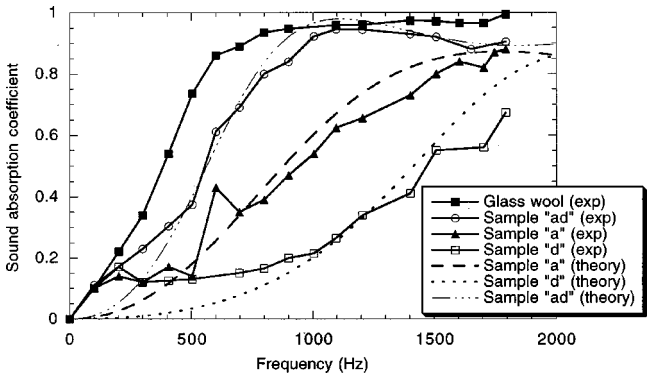

FIG. 6. Comparison of normal sound-absorption coefficient versus frequency curves of porous aluminum with that of 40-mm-thick glass wool. All samples are backed by a rigid wall. The 40-mm-thick sample ''ad'' is made by combining samples ''a'' with ''d,'' each 20-mm thick. The error of measurement is on the order of 5%–10%.

TABLE II. Sound absorption coefficients of Al foams with semi-open cells.

Sample[a]	Absorption coefficient		
	500 Hz	1000 Hz	1600 Hz
a	0.14	0.54	0.84
b	0.19	0.28	0.70
c	0.22	0.29	0.67
d	0.13	0.22	0.52
f	0.11	0.31	0.78
ae	0.40	0.91	0.88
ea	0.48	0.74	0.69
bd	0.34	0.98	0.78
db	0.31	0.94	0.89
ba	0.51	0.75	0.70
da	0.47	0.75	0.69

[a]Samples ''a'' to ''f'' are 20-mm thick, the rest 40 mm thick. All samples are backed by rigid wall.

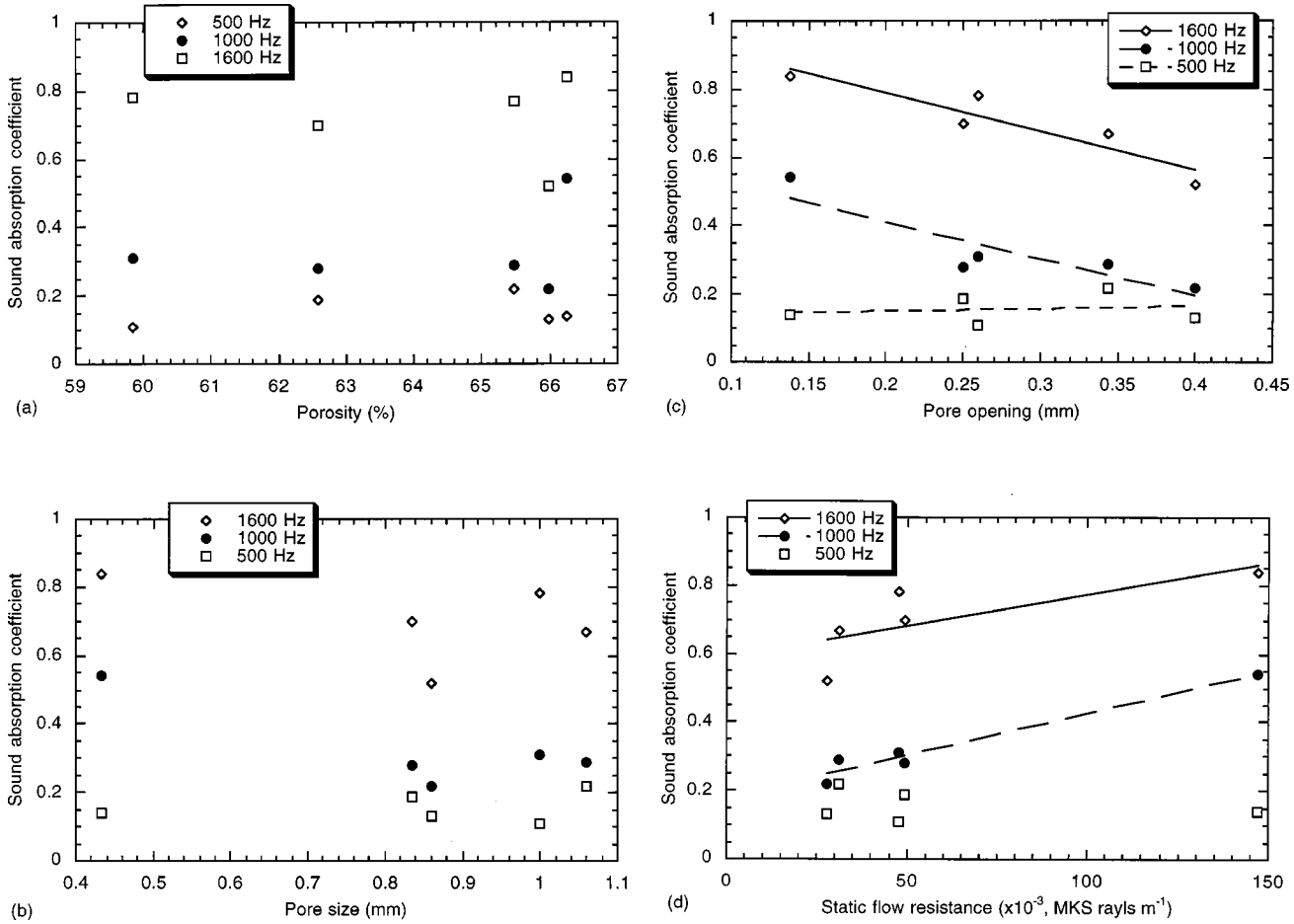

FIG. 8. Measured normal sound-absorption coefficient as a function of (a) porosity; (b) pore size; (c) pore opening size; (d) static airflow resistance at selected frequency levels. Samples ''a,'' ''b,'' ''c,'' ''d,'' ''f,'' each 20-mm thick and backed by rigid wall are used, which correspond to those of Fig. 5. The error of measurement is on the order of 5%–10%.

IV. THEORY

This section attempts to develop a simple analytical model to describe sound absorption in model semiopen foams having idealized cellular structures. The validity of the theory will be checked by comparing the predicted normal sound-absorption coefficients with experimental measurements on real porous metals. A parameter study is subsequently performed to explore the underlying sound-absorption mechanisms, and to quantify the effects of varying pore size, pore opening, and porosity on the absorption performance.

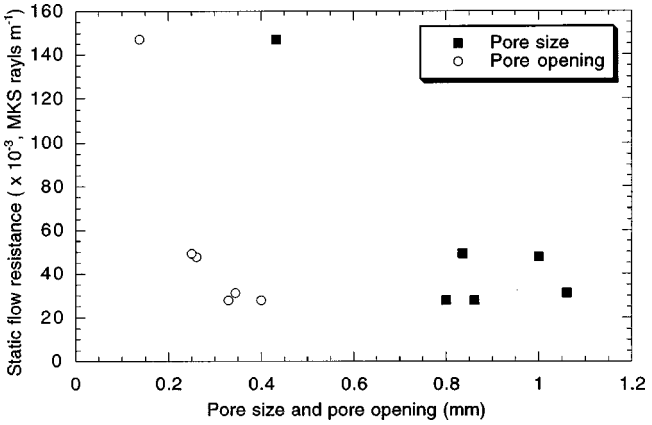

FIG. 9. Measured static airflow resistance as a function of pore size and pore opening size.

A. The model

Consider an idealized cellular structure as shown in Fig. 10; the model foam is transversely isotropic, with circular pore openings arranged in a regular hexagonal lattice in the $x-y$ plane [Fig. 10(b)]. The unit cell of the foam is shown in Fig. 10(c), with one circular aperture of diameter d placed on each of the eight surfaces (i.e., the coordination number N of the cell is taken to be 8, which is close to the experimentally measured value of 7.0–7.5). Other arrangements of apertures such as regular square array or random distribution may also be considered, but the resulting absorption performance is not expected to be significantly different from that associated with the hexagonal arrangement.[7,24] Here, the model material is introduced to represent a real porous metal characterized by pore size D, pore opening d, and porosity Ω. For the model foam, let D be the separation distance between two neighboring apertures, t be the cell-wall thickness (uniform cell-wall thickness is assumed and each cell wall is assumed to have identical thickness t), $\overline{D}$ be the distance between the middle planes of end walls of the unit cell in the longitudinal direction (z direction), and L be the thickness of the foam.

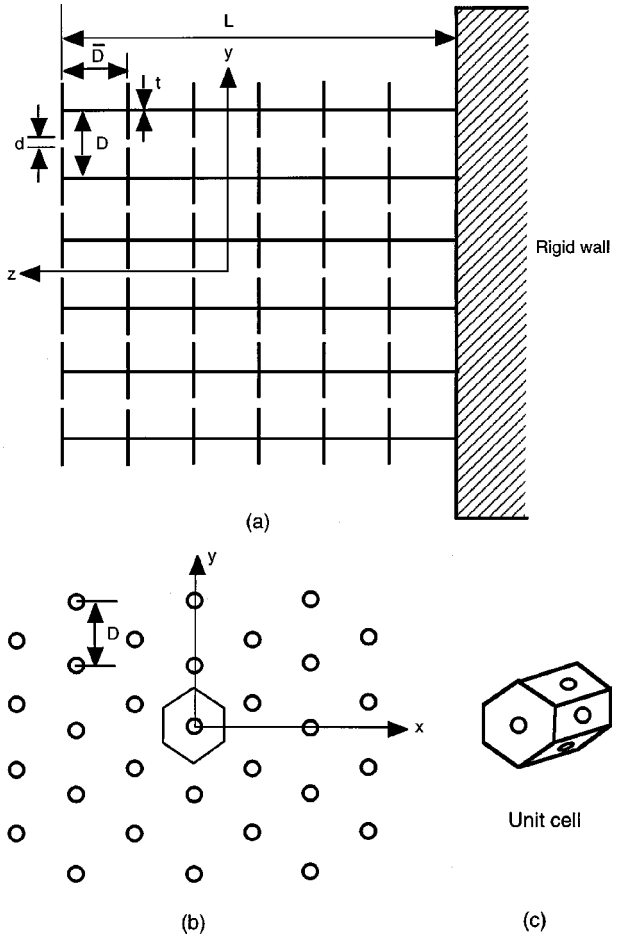

FIG. 10. Model metallic foam with idealized cellular structure backed by rigid wall: (a) cross-sectional area; (b) regular hexagonal array arrangement of circular apertures; (c) unit cell.

For simplicity, it is assumed that the diameter of the circular apertures on the surfaces of the unit cell equals that of the pore opening of a real porous metal, and that the porosity of the model material is identical to that of the real material, namely, Ω. Consequently, the model material and the real material have identical pore connectivity $I=d/D$. On the other hand, $\overline{D}$ is chosen such that the volume of the unit cell, $3\sqrt{3}D^2\overline{D}/8$, is equal to the volume of a spherical pore of diameter D, resulting in $\overline{D}=0.806D$. Furthermore, the cell walls are assumed to be thin, such that $t \ll D$. The transverse dimensions of the foam may be taken as infinite, or as periodic, or as impermeable with finite extent, and hence do not enter the following. Under these assumptions and with reference to the unit cell of Fig. 10(c), the porosity Ω of the model material can be calculated as

$$\Omega = 1 - \frac{[3D\overline{D} + 2(3\sqrt{3}D^2/8) - 8(\pi d^2/4)](t/2)}{3\sqrt{3}D^2\overline{D}/8}, \quad (18a)$$

which can be simplified to obtain

$$t \approx \frac{(1-\Omega)D}{3.55-6I^2}. \quad (18b)$$

The aim is to follow the motion of the air, initially at rest, when the system is subjected to a global pressure gradient in the form $\nabla p e^{i\omega \hat{t}}$ (where $i=\sqrt{-1}$, ω is angular frequency, and $\hat{t}$ is time), and to determine the fraction of sound energy that is absorbed by the model semiopen foam as a function of frequency, foam thickness, porosity, pore connectivity, and pore size. It is assumed that the stimulus is sufficiently small to render a linear analysis adequate. Thus, the metal skeleton is essentially motionless, given its large density and stiffness compared to those of air. In addition, the wavelength of the sound traveling in air is assumed to be much larger than D (which, in the acoustic range of interest—$f<4000$ Hz—it always is), and that the sound wave is normally impinging upon the foam surface (i.e., the incoming wave is traveling along the negative direction of the z axis).

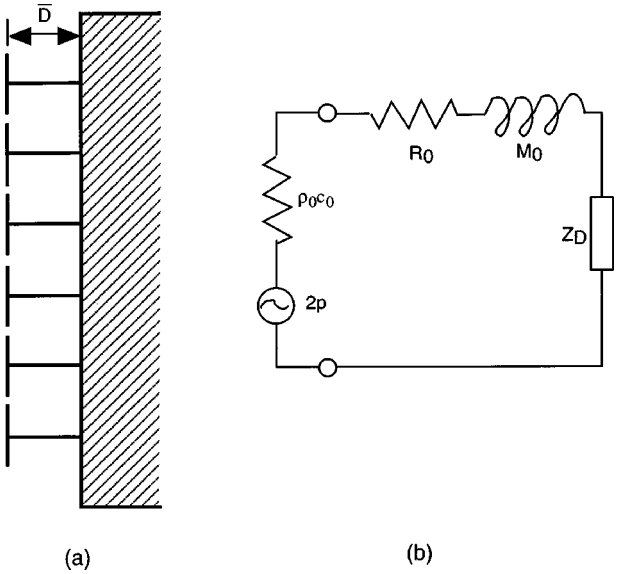

FIG. 11. (a) Model metallic foam with one cell in thickness direction backed by rigid wall; (b) electroacoustic analogy.

Consider first a model foam of thickness $L=\overline{D}$, i.e., with only one cell in the z direction [Fig. 11(a)]. The acoustical system may be modeled, following the principle of electroacoustic analogy,[13,25] by an equivalent electrical circuit depicted in Fig. 11(b). For simplicity, the hexagonal prismatic pore is modeled by a circular cylindrical pore of equal cross-sectional area, i.e., the diameter $\overline{D}_c$ of the cylindrical pore is related to D by $\overline{D}_c=0.909D$. Three levels of acoustic impedance are considered: internal resistance of air $\rho_0 c_0$ (ρ_0 and c_0 are the density of air and sound speed in air, respectively), the impedance of apertures $Z_0=R_0+iM_0$, and the impedance of air inside the cell $Z_D=-i\rho_0 c_0 \cot(\omega\overline{D}_c/c_0)$ (for simplicity, additional impedance due to viscous resistance along cell walls and thermoplastic dissipation is neglected). The latter can be simplified to $Z_D \cong -i\rho_0 c_0^2/\omega\overline{D}_c$ because, in general, $\omega\overline{D}_c/c_0 \ll 1$. Our previous study on sound absorption in regular hexagonal honeycombs found that, to an excellent approximation, a hexagonal tube can be replaced by a circular tube as long as they have the same cross-sectional area.[7] Also observe that, due to periodicity, only those apertures normal to the z axis are permeable to sound waves; subsequent calculations are greatly simplified

by this observation. To solve for the aperture impedance Z_0, we note that the thermal and viscous forces governing sound propagation in a (short) circular tube, of length t, can be treated separately.[13,26] The decoupled equation for time-harmonic propagation along the tube is

$$\frac{i\rho_0}{\eta}\omega v - \frac{\partial}{\partial r}\left(r\frac{\partial v}{\partial r}\right) = \frac{1}{\eta}\frac{\delta p}{t}, \tag{19}$$

where v is the particle velocity along the tube axis of z, r is the radial vector, δp is the drop of sound pressure over length t, and η is the dynamic viscosity of air. Equation (19) can be solved exactly, with the boundary condition that the velocity v vanishes on the tube walls due to viscous effects, yielding[27,28]

$$v(r) = -\frac{\delta p}{\eta t \chi^2}\left[1 - \frac{J_0(\chi r)}{J_0(\chi d/2)}\right], \tag{20a}$$

where $\chi = \sqrt{-i\omega\rho_0/\eta}$, and J_0 and J_1 are cylindrical Bessel functions of zeroth- and first order, respectively. By calculating the average particle velocity $\langle v\rangle$ over the cross-sectional area of the tube, the specific impedance of the hole Z_0 is then obtained as

$$Z_0 = \frac{\delta p}{\langle v\rangle} = i\omega\rho_0 t\left[1 - \frac{2}{\sqrt{-i}\beta}\frac{J_1(\sqrt{-i}\beta)}{J_0(\sqrt{-i}\beta)}\right]^{-1}, \tag{20b}$$

where $\beta = \sqrt{\omega\rho_0/\eta}d/2$. Note that the dimensionless parameter β is related to the quotient of two stresses caused separately by sound pressure and viscosity, and is commonly known as the acoustic Reynolds number.

In the low-frequency (or small aperture radius) limit such that $\beta < 1$, the acoustic impedance Z_0 simplifies to[27]

$$Z_0 \cong 32\eta t/d^2 + (4/3)i\omega\rho_0 t, \quad \beta < 1. \tag{21a}$$

Similarly, in the other limit where $\beta > 10$ (high frequency, or large aperture radius)[27]

$$Z_0 \cong (8\eta t\beta/\sqrt{2}d^2)(1+i) + i\omega\rho_0 t, \quad \beta > 10. \tag{21b}$$

To cover the intermediate range $1 < \beta < 10$, Maa[27] found that, to an excellent approximation, Eq. (20b) can be replaced by the following relaxation-matching solution:

$$Z_0 \cong (32\eta t/d^2)\sqrt{1+\beta^2/32} + i\omega\rho_0 t(1 + 1/\sqrt{9+\beta^2/2}), \quad 1 < \beta < 10. \tag{21c}$$

Equation (21c) reduces to (21a) when $\beta \to 0$, and to (21b) when $\beta \to \infty$. We note that Eq. (21c) is similar to the relaxation approach of Wilson.[18] For short tubes, it is not necessary to modify the expression (21c) to include thermal effects, although the contribution to the acoustic impedance from the end effects must be appropriately accounted for.[27,29] For sound propagation in air-saturated circular apertures in a metallic material under standard conditions of temperature and pressure, (21c) becomes[25,27]

$$\frac{R_0}{\rho_0 c_0} = \frac{32\eta t}{d^2}\{\sqrt{1+\beta^2/32} + \sqrt{\beta d/4t}\}, \tag{22a}$$

$$\frac{M_0}{\rho_0 c_0} = \omega\rho_0 t\{1 + 1/\sqrt{9+\beta^2/2} + 0.85d/t\}. \tag{22b}$$

Note that, the second term in Eq. (22a) is the end correction for resistance, and the last term in Eq. (22b) is the end correction for mass reactance. Finally, once Z_0 is determined, the acoustic impedance of the acoustic system [Fig. 11(a)] is simply given by

$$Z = z_0 + Z_D = R + iM, \tag{23a}$$

where $z_0 = Z_0(\overline{D_c^2}/d^2)$ is the relative specific acoustic impedance of the apertures. Finally, from Eq. (23a), the normal sound-absorption coefficient is calculated as

$$\alpha = \frac{4R/\rho_0 c_0}{(1 + R/\rho_0 c_0)^2 + (M/\rho_0 c_0)^2}. \tag{23b}$$

If the number of cells $(= L/\overline{D})$ in the z direction is larger than 1, the sound-absorption coefficient of the model foam backed by rigid wall or air cavity is still calculated according to Eq. (23b), except that its acoustic impedance Z must now account for the impedance of additional cells and air cavity. This can be achieved straightforwardly by using the electroacoustic analogy. For instance, in the case of two cells across the foam thickness with rigid wall backing, we have

$$Z = z_0 + \frac{1}{\dfrac{1}{Z_D} + \dfrac{1}{z_0 + Z_D}}. \tag{24}$$

Note that our calculations have established that, if the end effects are ignored in Eq. (22), the agreement between predictions and measurements is rather poor. This is the main reason why existing models such as those of Champoux and Stinson, Allard, Attenborough, and Wilson (to name just a few) are not used, because these models mostly deal with porous materials where the pores do not abruptly change in cross section. The Delaney–Bazley model is not chosen either, because the poor correlation between measured values of static flow resistance and pore size, pore opening, and porosity would not allow us to use the model to study the influence of these pore parameters on sound absorption (which is the main purpose of this paper). Furthermore, while the current model can be easily applied to study porous materials having nonuniformly distributed pore sizes and pore openings (e.g., gradient porous materials), conventional models of Champoux and Stinson, Attenborough, Allard, Wilson, and others cannot be directly applied to these nonuniform materials because, for nonhomogeneous materials, it is not possible to define characteristic impedance and propagation constant. The application of the present model to characterize porous metals processed with a gradient of pore size and pore opening distribution will be the subject of a future study. However, it must be stated that the new model is not a replacement of existing models, but rather introduced to deal with the unique microstructural features of the infiltration-processed material. In other words, if a porous material does not contain such features, then our model should not be used—use of conventional models is recommended.

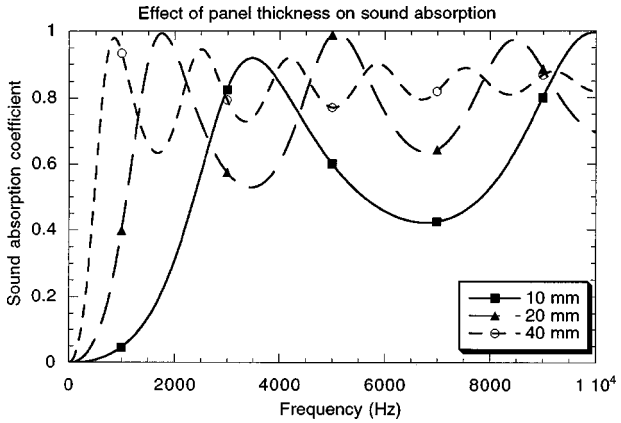

FIG. 12. Predicted effect of sample thickness on normal sound-absorption coefficient versus frequency curve for sample ''f.''

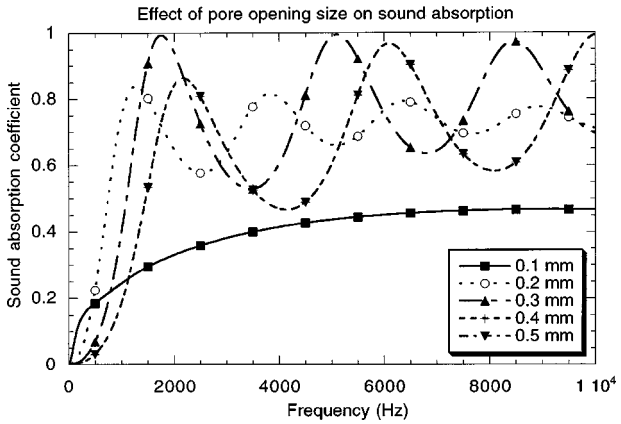

FIG. 13. Predicted effect of pore opening size on normal sound-absorption coefficient versus frequency curve for sample ''f.''

B. Comparison with experimental measurements

The predicted normal sound-absorption coefficient versus frequency curves for samples ''a,'' ''b,'' ''c,'' ''d,'' and ''f,'' each 20-mm thick and backed by a rigid wall, with the geometrical parameters chosen identical to those listed in Table I, are presented in Fig. 5. The validity of the model is further checked against the measured data for a panel combining samples ''a'' and ''d'' and the result is shown in Fig. 6. Figure 7(a) presents the predicted effect of placing an air cavity behind a 20-mm-thick panel of sample ''a'' on sound absorption compared to that measured. In Fig. 7(b), the predicted effect of placing an air cavity between two 10-mm-thick panels of sample ''a'' on sound absorption is compared to that measured. In general, fairly close agreement between theoretical predictions and experimental measurements are observed from Figs. 5–7. Given the idealized nature of the model, this close agreement between theory and experiment is quite remarkable. It is important to point out here that, in all these calculations, no parameter has been adjusted for best fit in plotting Figs. 5–7.

C. Parameter study

Because the range of geometrical parameters explored in the experiments is rather limited, it would be illuminating to use the theoretical model to study the effect of more parameter variations on acoustical performance of model metallic foams. The good agreement between theory and experiment as shown in Figs. 5–7 suggests that the results from the following parameter study may be used to guide acoustic design with semiopen metallic foams for sound-absorption applications. For reference, a 20-mm-thick sample ''f'' backed by rigid wall is selected as the reference, with $D=1.0\,\mathrm{mm}$, $d=0.3\,\mathrm{mm}$, and $\Omega=60\%$. In addition, it is assumed that all samples are backed by a rigid wall in the parameter study. Figure 12 plots the normal sound-absorption coefficient as a function of frequency for sample ''f'' with its thickness varying from $L=10$, 20 to 40 mm. As expected, the increasing of sample thickness reduces the resonance frequencies as well as the spacing between neighboring resonances, and improves the overall sound-absorption performance. In Fig. 13, the effect of varying pore opening size d while maintaining the remaining parameters unchanged is demonstrated for a 20-mm-thick sample ''f.'' In general, the resonance frequency is reduced by decreasing pore opening size, i.e., the absorption is enhanced in the low-frequency range. However, it is not always beneficial to reduce d, as it is seen from Fig. 13 that $d\approx 0.3\,\mathrm{mm}$ provides the best acoustic performance for panel ''f'': increasing or reducing d from $\sim$0.3 mm would lead to weakened absorption performance. The effect of varying pore size D on sound absorption whilst maintaining other parameters unaltered is shown in Fig. 14 for a 20-mm-thick sample ''f'' backed by a rigid wall. Again, an optimal cell size $D\approx 1$ mm exists, which tends to maximise sound absorption in the low-frequency range ($f<4000\,\mathrm{Hz}$). Similar conclusions are reached by Wang and Lu[7] in a theoretical study of optimized cellular structures for maximum sound absorption. Also, from Figs. 13 and 14, we may conclude that the foam should be processed with an optimal pore connectivity $I\approx 0.3$. Finally, the predicted effect of porosity on sound absorption is shown in Fig. 15 for the 20-mm-thick panel ''f'' backed by a rigid wall, with Ω varying from 50%, 60% to 70%. Increasing porosity slightly increases the resonance frequencies, but otherwise has insignificant influence on sound absorption, at least for the range of porosity considered.

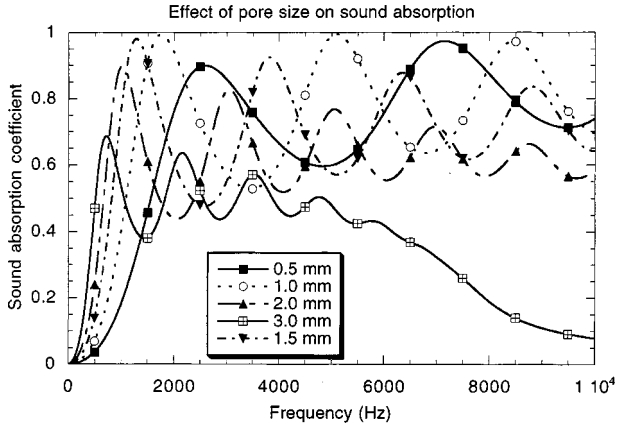

FIG. 14. Predicted effect of pore size on normal sound-absorption coefficient versus frequency curve for sample ''f.''

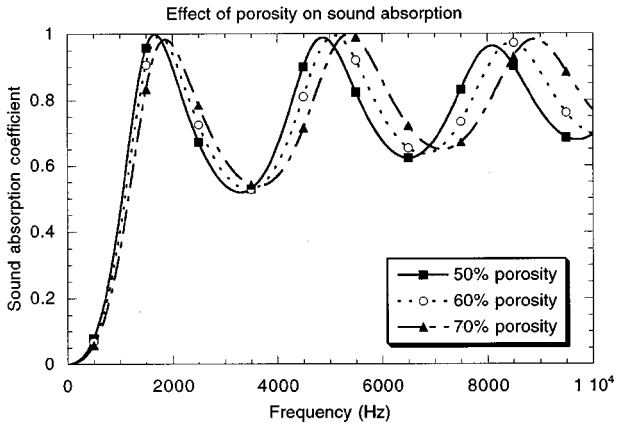

FIG. 15. Predicted effect of porosity on normal sound-absorption coefficient versus frequency curve for sample ''f.''

These results can be used to guide the selection of processing parameters to produce semiopen metallic foams with desirable sound-absorbing properties.

V. CONCLUDING REMARKS

Aluminum foams with semiopen cells for sound-absorption applications are developed. The foams are processed via negative-pressure infiltration, using a preform consisting of water-soluble spherical particles. The most important structural parameter for the foam is the connectivity between neighboring pores, which depends on two dimensionless parameters. An analytical model is developed to quantify the dependence of pore connectivity on processing parameters, including infiltration pressure, particle size, wetting angle, and surface tension of molten alloy. It is found that, to obtain a given pore connectivity by adjusting processing parameters, increasing infiltration pressure is equivalent to increasing particle size or decreasing surface tension.

Normal sound-absorption coefficient and static flow resistance are measured for six samples having different grades of porosity, pore size, and pore opening. It is found that a sound-absorption coefficient larger than 0.8 in the frequency range of 800–2000 Hz can be achieved in selected samples. No apparent correlation between sound absorption and porosity or cell size is observed, which may be attributed to the limited parameter range explored. However, there exists a good correlation between sound absorption and pore opening size, with sound absorption increasing as pore opening decreases. Similarly, a relatively high static flow resistance is beneficial for sound absorption. For the samples considered, the static flow resistance decreases as the pore opening size is increased, although more test data are needed to establish a more definite trend.

An acoustical model is developed for semiopen metallic foams having idealized cellular structures; a regular hexagonal prismatic cell is chosen as the unit cell, with one circular aperture placed on each of its eight surfaces. The theory is built upon the acoustic impedance of the apertures (orifices) and cavities due to viscous effects, and the electroacoustic analogy. Good agreement between theoretical predictions and experimental measurements is obtained. Subsequent parameter studies reveal that there exists an optimal pore size, an optimal pore opening size, and an optimal pore connectivity for best sound absorption; sound absorption is enhanced by increasing the thickness of the foam panel, but is only slightly affected by varying the foam porosity. The new model is introduced not to replace existing models, but rather to deal with the unique pore structures of the infiltration-process porous materials. In other words, if a porous material does not contain such geometrical features, then the use of our model is not recommended—conventional models have been proven highly successful in most situations.

ACKNOWLEDGMENTS

This work was partially supported by the EPSRC, U.K., by the DARPA/ONR MURI program, U.S.A., on Ultralight Metal Structures (No. N00014-1-96-1028), and by the National Natural Science Foundation, P. R. China. The authors would like to thank R. S. K. Yiin, J. M. Ong, Alice Fox, and T. W. Clyne of Cambridge University for assistance in experimental measurements.

[1] M. F. Ashby, J. W. Hutchinson, A. G. Evans, and N. A. Fleck, *Cellular Metals—A Design Guide* (Cambridge University, Cambridge, England, 1999).
[2] Y. Sugimura, J. Meyer, M. Y. He, H. Bart-Smith, J. L. Grenestedt, and A. G. Evans, ''On the mechanical performance of closed cell Al alloy foams,'' Acta Mater. **45**, 5345–5359 (1997).
[3] T. J. Lu, H. A. Stone, and M. F. Ashby, ''Heat transfer in open-cell metal foams,'' Acta Mater. **46**, 3619–3635 (1998).
[4] T. J. Lu and C. Chen, ''Thermal transport and fire retardance properties of cellular aluminium alloys,'' Acta Mater. **47**, 1469–1485 (1999).
[5] T. J. Lu, ''Heat transfer efficiency in metal honeycombs,'' Int. J. Heat Mass Transf. **42**, 2031–2040 (1999).
[6] T. J. Lu, A. Hess, and M. F. Ashby, ''Sound absorption in metallic foams,'' J. Appl. Phys. **85**, 7528–7539 (1999).
[7] X. W. Wang and T. J. Lu, ''Optimized acoustic properties of cellular solids,'' J. Acoust. Soc. Am. **106**, 756–765 (1999).
[8] F. Han, Z. Zhu, and C. Liu, ''Examination of acoustic absorption characteristics of foamed aluminium,'' Acust. Acta Acust. **84**, 573–576 (1998).
[9] M. E. Delany and E. N. Bazley, ''Acoustical properties of fibrous absorbent materials,'' Appl. Acoust. **3**, 105–116 (1969).
[10] P. M. Morse and K. U. Ingard, Theoretical Acoustics (McGraw-Hill New York, 1968).
[11] D. L. Johnson, J. Koplik, and R. Dashen, ''Theory of dynamic permeability and tortuosity in fluid-saturated porous media,'' J. Fluid Mech. **176**, 379–402 (1987).
[12] J. F. Allard and Y. Champoux, ''New empirical equations for sound propagation in rigid frame fibrous materials,'' J. Acoust. Soc. Am. **91**, 3346–3353 (1992).
[13] C. Zwikker and C. W. Kosten, Sound Absorbing Materials (Elsevier, New York, 1949).
[14] M. A. Biot, ''Theory of propagation of elastic waves in a fluid-saturated porous solid. I. Low frequency range,'' J. Acoust. Soc. Am. **28**, 168–178 (1956).
[15] K. Attenborough, ''Acoustical characteristics of rigid fibrous absorbents and granular materials,'' J. Acoust. Soc. Am. **73**, 785–799 (1983).
[16] J. F. Allard, C. Depollier, J. Nicolas, W. Lauriks, and A. Cops, ''Proprietes acoustiques des materiaux poreux satures d'air et theorie de Biot,'' J. Acoust. **3**, 29–38 (1990).
[17] M. R. Stinson and Y. Champoux, ''Propagation of sound and the assignment of shape factors in model porous materials having simple pore geometries,'' J. Acoust. Soc. Am. **91**, 685–695 (1992).
[18] D. K. Wilson, ''Relaxation-matching modeling of propagation through porous media, including fractal pore structure,'' J. Acoust. Soc. Am. **94**, 1136–1145 (1993).
[19] J. Bear, *Dynamics of Fluids in Porous Media* (Dover, New York, 1988).
[20] F. Chen, A. Zhang, and D.-P. He, ''Control of the degree of pore-opening for porous metals,'' Chin. J. Mater. Res. (to be published).
[21] L. Ma and D.-P. He, ''Fabrication and pore structure control of new type aluminium foams,'' Chin. J. Mater. Res. **8**, 11–17 (1994).

[22] D. A. Bies and C. H. Hansen, ''Flow resistance information for acoustical design,'' Appl. Acoust. **13**, 357–391 (1980).
[23] M. R. Stinson and G. A. Daigle, ''Electronic system for the measurement of flow resistance,'' J. Acoust. Soc. Am. **83**, 2422–2428 (1983).
[24] V. Tarnow, ''Airflow resistivity of models of fibrous acoustic materials,'' J. Acoust. Soc. Am. **100**, 3706–3713 (1996).
[25] J. Kang and H. V. Fuchs, ''Predicting the absorption of open weave textiles and micro-perforated membranes backed by an air space,'' J. Sound Vib. **220**, 905–920 (1999).
[26] M. Stinson, ''The propagation of plane sound waves in narrow and wide circular tubes, and generation to uniform tubes of arbitrary cross-sectional shape,'' J. Acoust. Soc. Am. **89**, 550–558 (1991).
[27] D. Y. Maa, ''Microperforated-panel wideband absorbers,'' Noise Control Eng. J. **29**, 77–84 (1987).
[28] I. B. Crandall, *Theory of Vibrating Systems and Sound* (Van Nostrand, New York, 1926).
[29] M. R. Stinson and E. A. G. Shaw, ''Acoustic impedance of small, circular orifices in thin plates,'' J. Acoust. Soc. Am. **77**, 2039–2042 (1985).

Surface diffusion coefficients for room acoustics: Free-field measures

Tristan J. Hargreaves, Trevor J. Cox,[a] and Y. W. Lam
School of Acoustics and Electronic Engineering, University of Salford, Salford M5 4WT, United Kingdom

Peter D'Antonio
RPG Diffusor Systems, Inc., 651-c Commerce Drive, Upper Marlboro, Maryland 20772

(Received 14 October 1999; revised 10 July 2000; accepted 15 July 2000)

A surface diffusion coefficient is needed in room acoustics to enable the quality of diffusing surfaces to be evaluated. It may also facilitate more accurate geometric room acoustic models. This paper concentrates on diffusion coefficients derived from free-field polar responses. An extensive set of two- and three-dimensional measurements and predictions was used to test the worth of different diffusion coefficient definitions. The merits and problems associated with these types of coefficients are discussed, and past parameters reviewed. Two new coefficients are described. The new measure based on the autocorrelation function is forwarded as the best free-field coefficient. The strengths and weaknesses of the coefficient are defined. © *2000 Acoustical Society of America.* [S0001-4966(00)04810-4]

PACS numbers: 43.55.Br, 43.20.El [JDQ]

I. INTRODUCTION

Surface diffusion can play a key role in determining the sound field within an enclosed space. For example, the correct use of diffusion in performance spaces may enhance the acoustic for both the audience and musicians.[1] Given the important role that diffuse reflections can play in determining the sound field, it is necessary to have a measure to gauge the degree of diffusion created by a surface. Only by having a numerical measure of surface diffusion is it possible to readily compare the performance of different treatments, and to develop design specifications for diffusers. Indeed, by creating a *language* to describe the degree of diffusion, it is hoped to improve the understanding of diffuse reflection phenomena among practitioners.

The development of a diffusion coefficient is also of interest to developers of geometric room acoustic models. A round robin test of geometric room acoustic computer models[2] showed that the common feature of the most successful predictions was the inclusion of some form of diffusion modeling. The implementation of diffusion in geometric models currently requires some single-figure random incidence measure—a diffusion coefficient. Unfortunately, at the moment the diffusion coefficient has to be chosen empirically[3] since there are no clear relationships between the physical properties of a surface and the diffusion coefficients adopted by computer models. Indeed, Lam[4] showed that existing diffusion modeling algorithms generally require different diffusion coefficient values to model the same room surface.

The current interest in diffusion coefficients is acknowledged by the fact that two international standard working groups are currently looking at this issue. The diffusion coefficient outlined in this paper is the method likely to be enshrined in one of the international standards.

[a]Electronic mail: t.j.cox@salford.ac.uk

The literature contains a number of methods that have been proposed to characterize the diffuse scattering from surfaces. Unfortunately, there is not one diffusion coefficient in the literature or proposed in this paper that does not have flaws. While at first it may appear possible to produce a watertight definition of a diffusion coefficient, detailed examination reveals that it is impossible. The choice of diffusion coefficient is application dependent. While this may appear unsatisfactory, it should be remembered that room acoustics has been using an absorption coefficient for a hundred years, which has well-defined limitations in application. For example, there are two primary techniques for measuring absorption: the impedance tube and reverberation chamber methods. Each method has advantages and disadvantages and is used for different reasons.

In an analogous manner, the methods for characterizing diffusion can be classified either as free- or diffuse field. The diffuse-field methods have the advantage of quickly obtaining a random incidence coefficient, but are difficult to predict. The free-field methods are often more laborious to carry out, but can be readily predicted. Probably the best known diffuse-field method is the technique suggested by Mommertz and Vorländer.[5,6] This method looks at the invariant and variant portions of the sound-pressure decay in a reverberation chamber as the test surface is rotated. Another diffuse field method[7] investigates the effect that surface diffusers have on the diffuseness of the space.

This paper, however, concentrates on free-field methods. Most publications have dealt with diffusion coefficients based on polar distributions. Essentially, these coefficients gauge the spatial evenness of energy scattering around the surface, in a way similar to how the omnidirectionality of a sound source might be tested. A different type of free-field method investigates how much energy is scattered into and away from the specular reflection angle. This latter method appears to grow out of the type of definition certain geometric computer models have used in diffusion modeling. In this

case complete diffusion is defined as the case where no energy is reflected into the specular reflection direction. The free-field method of Mommertz and Vorländer[5] can be used to measure this type of coefficient. In a similar way to the diffuse-field technique, the measurement method gauges the invariance of the scattered pressure to surface movements measured at the specular reflection position. The diffusion coefficient derived is then the ratio of nonspecular to total reflected energy.

In this paper, however, the concern will be with the ability of diffusers to uniformly scatter in all directions, rather than with just the ability of a surface to move energy away from the specular angles. This restriction is placed because of experiences of diffuser design that some of the authors have. From the standpoint of the diffuser designer, it is important that a diffusion coefficient differentiates between redirection and dispersion. Diffusers are usually applied to treat first-order reflections, for example to prevent echoes from the rear wall of concert halls. If all the diffuser achieves is redirection, there is a risk that the echo problem will simply move to another place in the hall. On the other hand, if the diffuser achieves dispersion, this has the potential to reduce the echo problem without creating new difficulties for other listeners. For this reason, despite all its merits, the Mommertz and Vorländer free-field method will not be discussed further here.

Consequently, this paper returns to its main concern, free-field methods based on polar distributions. The general method is as follows. First, the scattering from a surface is measured or predicted in terms of a polar distribution. Then, the diffusion coefficient is a frequency-dependent, single figure of merit derived from the polar distribution. This is evaluated in one-third octaves, which has the advantage of smoothing out some of the local variations in the polar responses, so the diffusion coefficient is based more on the overall envelope. There have been various statistical operations suggested to calculate a diffusion coefficient from the polar distributions: standard deviation[8–10] directivity,[11,12] specular zone, and spherical harmonics.[13] In any such data reduction, there is a risk of losing essential detail. Diffusion coefficients, however, have been applied to enable the quality of specialist diffusing surfaces to be evaluated and designed, for example by using the diffusion coefficient as a cost function in a numerical optimization scheme.[8,9] Consequently, this supports the common belief that a single figure of merit can be useful. The main aim of this paper is to review the previously published diffusion coefficients based on polar distributions, and to forward a new coefficient based on the autocorrelation coefficient which seems to offer significant advantages over previous published techniques.

II. EVALUATION CRITERIA

The diffusion coefficients must be evaluated against a set of criteria. For the basis of this project, it was decided that an ideal diffusion coefficient would:

(i) have a solid physical basis;
(ii) be clear in definition and concept, and related to the current role of diffusion in room acoustics;
(iii) consistently evaluate and rank the performance of diffusers;
(iv) apply to all the different surfaces and geometries found in rooms;
(v) be measurable by a simple process;
(vi) be bounded;
(vii) be easy to predict.

FIG. 1. Photograph of the automated goniometer for measuring hemispherical scattering being assembled in an anechoic chamber at the University of Salford. The lower part of the structure is covered with absorbent when operating.

The various diffusion definitions found in literature, and new ones developed during the project were tested against the above criteria to test their suitability. This could be done by combining philosophical thought experiments with measurements and predictions of the coefficients for a wide variety of surfaces. It was also important to relate the assessment to current industry practice in diffuser design, and the application of diffusion in geometric room acoustic models.

III. MEASUREMENT AND PREDICTION

There are various techniques for obtaining the scattered pressure distributions to enable the coefficients to be calculated. Boundary element methods (BEMs) have been shown to be accurate in predicting the scattering from a variety of diffusing surfaces both in two and three dimensions[14–16] and so have been used for this project. Measurements on reflecting surfaces were based on maximum length sequence signals using time gating to separate the reflected from the incident sound. Such a system has been used in the past to enable measurements to be made in a single plane on a semicircle.[17] A capability to measure the surface scattering over the hemisphere using a goniometer was especially developed for this project. This is shown in Fig. 1. Measure-

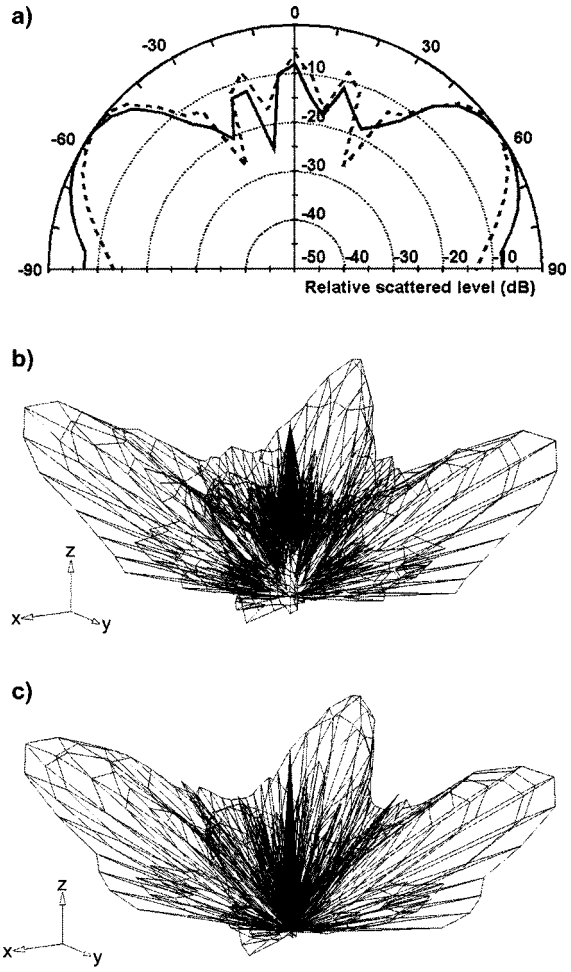

FIG. 2. Comparison of measured and predicted polar responses. (a) ——— Two-dimensional measurement, – – – single-plane BEM prediction for square-based pyramid, 1 kHz, normal incidence source. (b) Three-dimensional measurement for square-based pyramid, 2 kHz, normal incidence. (c) BEM prediction, square-based pyramid, 2 kHz, normal incidence.

ments were mostly carried out at 1:5 scale. To avoid confusion, frequencies and distances given here are always equivalent full-scale values.

Unless otherwise stated, for hemispherical measurement the source was 15 m and the receivers 7.5 m from the surface, and for the single-plane measurement the source was 10 m and the receivers 5 m from the surface. One of the criteria given above for the diffusion coefficient is that it should be easy to measure. This is certainly true for the single-plane measurements, which are routinely undertaken on a boundary in a large room, which forms a pseudo-hemianechoic space, or an anechoic chamber. Measurements in the goniometer, however, require considerably more complex engineering to achieve the necessary microphone and source positioning in an anechoic chamber. They are also more time consuming due to the great increase in the number of measurements required. A spatial resolution of 5 deg was used between receivers, resulting in 1369 measurement positions for a single angle of incidence. Figure 2 compares the measured and predicted scattering from a surface measured both on a single plane and a hemisphere. The agreement between theory and measurement is good. Incidentally, the measurement resolution of 5 deg was chosen because tests showed that this was a sufficient resolution to gain the diffusion coefficient accurately without overburdening measurements with excessive sampling points.

Table I and Fig. 3 show some of the surfaces used in the test. The surfaces were chosen so that there was as little as possible redundancy in the surface set. In addition, each surface was chosen to test a particular attribute such as redirection, focusing, periodicity, randomness, partial absorption, good and poor diffusion. The concept was to cover a wide range of generic surface types to make the outcomes from the work as generalizable as possible. Incidentally, experience has shown that where possible the sample tested

TABLE I. Details of a selection of the samples measured.

Sample	Dimensions (unless stated otherwise)	Reason for use
Plane	Various. 0.57 m wide for single plane measurements	Reference.
Concave prism	1.5 m wide.	Practical worst-case diffuser.
Cone	1.5 m diameter, 0.35 m deep.	Redirects specular reflection.
Square-based pyramid	1.5 m square, 0.35 m deep.	Comparison with cone in 3D.
Periodic and random binary	≈3 m square. Cross section of parallel battens 90 mm square.	To examine periodic and aperiodic structures.
Semicylinder	0.55 m diameter.	Very effective diffuser.
Triangular prism	0.54 m wide, 0.27 m deep. Cross section is right-angled isosceles triangle.	Redirects in single plane.
QRD®	$N=7$, Maximum well depth 0.2 m. Well width 60 mm.	Commercial single-plane diffuser.
Skyline®	≈0.55 m square×0.225 m deep.	Commercial hemispherical diffuser.
BAD™ Panel	0.6 m square.	Diffusion from variation in surface absorption. Commercial product.
Periodic hemispheres	Hemispheres are 0.375 m diameter. Arrangements of 1, 7, and 19 used.	To compare single and periodic arrangements

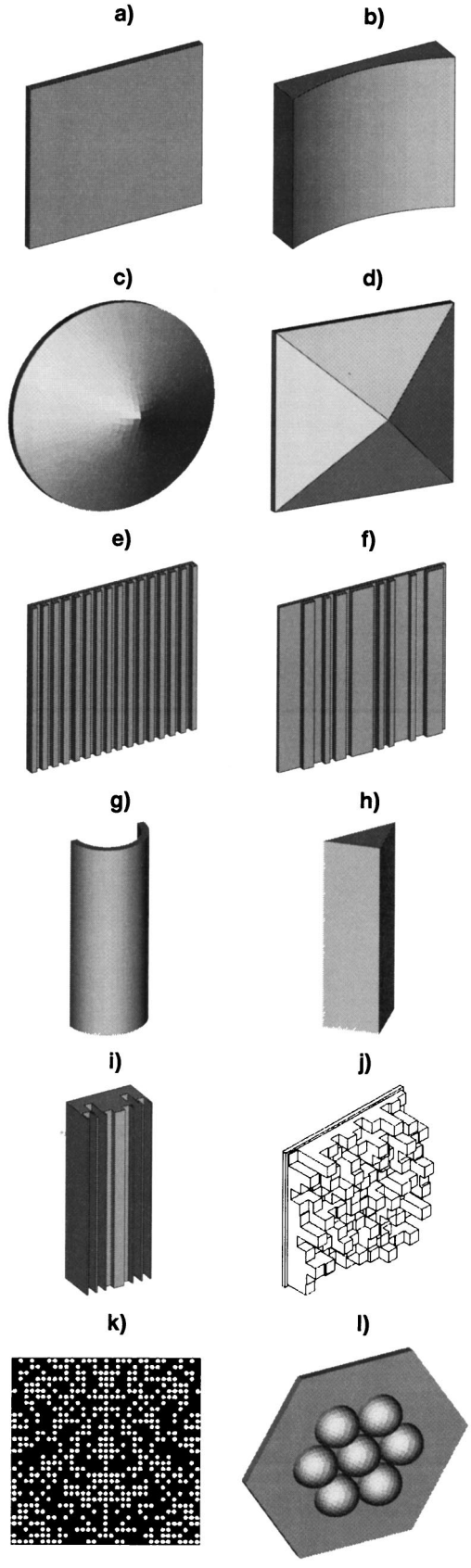

FIG. 3. Selection of samples measured. (a) Plane. (b) Concave prism. (c) Cone. (d) Square-based pyramid. (e) Periodic binary. (f) Random binary. (g) Semicylinder. (h) Triangular prism. (i) QRD®. (j) Skyline®. (k) BAD™ Panel. (l) Periodic hemispheres.

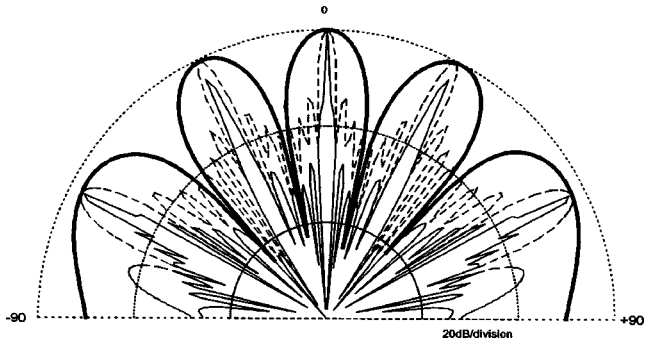

FIG. 4. Effect of number of periods of a diffuser on scattering lobe width. Single-plane Fraunhoffer prediction, 1130 Hz, normal incidence. Quadratic residue diffuser, $N=53$, well width 12.7 mm, design frequency 1130 Hz. ——— 2, – – – 8, ——— 32 periods.

should be the entire structure to be applied in a real application. This is because the method measures the diffraction effects of the edges and surface roughness together. While it may be possible to separate edge and surface diffraction effects for large surfaces with small roughness, for the majority of surfaces, such a separation is impossible. Where the whole sample cannot be tested, because of geometric constraints on source and receiver distance, the following techniques are suggested for reducing the sample size. For a periodic sample at least three complete repeat sequences should be included so the effects of lobing from repetition is measured. The width of the diffraction lobes, however, depends on the number of repeat units in the sample.[18] This is illustrated in Fig. 4, where the scattering from a Schroeder diffuser is shown for 2, 8, and 32 periods. Lobe narrowing is seen as the number of periods increases. So, if possible, the number of periods tested should be similar to the number used in real applications. The requirement for at least three periods is based on results from studies where an increasing number of periods of a sample were introduced and the effect on the diffusion coefficient monitored. For random surfaces, representative samples of the surface roughness should be tested, large enough so that surface rather than edge effects are more prominent in the scattering.

IV. NEAR AND FAR FIELDS

Ideally, any diffusion coefficient should apply to all geometries that usually occur in room designs. One variable geometric factor is the distances from the source and receivers to the surface. All free-field measurements suffer from the problem that the relative levels within the polar response are dependent on these distances unless the source and receivers are in the far field. (The far field being where the scattered pressure falls by 6 dB per distance doubling for 3D geometries.) Unfortunately, in most room applications, it is usual for sources and receivers to be in the near rather than the far field. Figure 5 shows the scattering from a plane surface for a variety of receiver distances. As the receiver approaches the surface a *top hat* effect occurs; a plane surface appears to be a very good diffuser when measurements are close to the surface. (In fact, close enough to the surface, the reflection is provided by an approximate image source that radiates the same energy to all receivers except for any

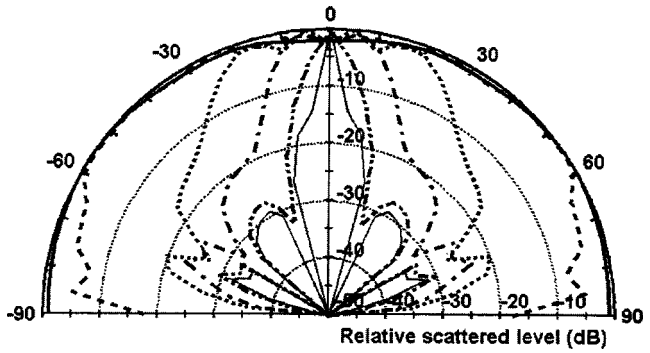

FIG. 5. Effect of receiver arc radius on the polar response of a 1 m square plane panel. Single-plane BEM prediction, 5 kHz, normal incidence, source distance=100 m. ——— 0.1 m, – – – 0.5 m, --- 1 m, —·—·—·— 2 m, —··—··—·· 5 m, ——— 100 m.

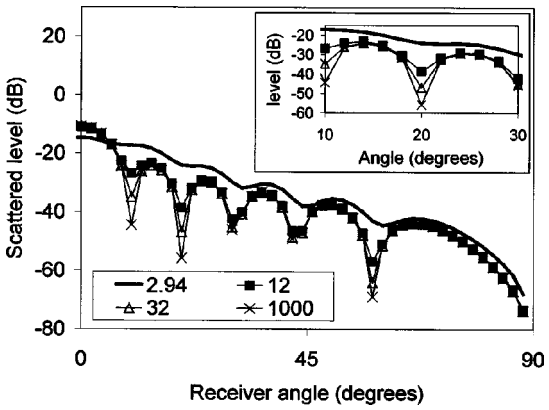

FIG. 6. Variation of scattered polar response with receiver distance, as shown in the legend, to illustrate extent of near field. Receiver angle on a linear scale for clarity; insert graph is an enlargement of a section of the main graph. 1 m plane surface at 1 kHz using BEM predictions. A distance correction of $1/\sqrt{r}$ has been used to correct for cylindrical wave spreading.

minor effects due to spherical spreading.) This seemingly contradicts conventional wisdom in room design, which would have us believe that a plane surface is a poor diffuser.

To understand this contradiction, it is necessary to understand why plane surfaces can cause problems in real applications. Problems can occur with plane surfaces with directional sources, such as trumpets. The reflected energy will be concentrated over a narrow solid angle, leading to a risk of detrimental effects such as echoes, coloration, or image shift. The results shown in Fig. 5 were produced using an omnidirectional source. Consequently, one solution would be to carry out the polar response measurements using a directional source that would better simulate the real sources that cause problems. But, the well-defined scientific nature and universality of the point-test source makes an omnidirectional source a better choice.

Another solution is to move to a different characterizing regime,[9] as has been adopted for baffled surfaces, but this also has problems. Consequently, the preferred solution is for diffusion measurements based on polar distributions to be taken in the far field. There are standard formulations for approximately calculating the required distance for measurements to be in the far field.[19] There are two criteria to satisfy: the receiver radius should be large compared to wavelength and the differences between path lengths from points on the surface to the receiver are small compared to wavelength. With the geometries and frequencies used for acoustic diffuser scattering, it is the latter criterion that is most exacting. Unfortunately, the common far-field formulations are not applicable to the case of oblique sources and receivers. In Fig. 6 the polar response from a 2-m wide plane surface is shown for four receiver radii. A distance correction of $1/\sqrt{r}$ has been used to correct for cylindrical wave spreading to aid comparison of the relative distributions. The first distance of 2.94 m represents the far-field criteria given in Ref. 18, and the distance of 12 m comes from a more complete consideration of Fresnel diffraction and the critical frequency for plane panels.[20] Neither of these distances, however, is sufficient to get the true far-field response; this is achieved when the receiver radius is many hundreds of meters. Problems arise for angles where significant destructive interference occurs, because the amount of destructive interference is very sensitive to the relative magnitudes of the waves coming from the secondary sources on the scattering surface (assuming the scattering is modeled following Huygen's principle). Consequently, the receiver distance required to achieve the true far field for oblique receivers is often so large that measurements cannot be accommodated in normal test facilities.

A pragmatic approach may be taken, however, to enable polar response measurements to be obtained using conventional methods and in normal test facilities. The calculation of the diffusion coefficient involves reducing the many scattered pressure values to a single figure of merit; consequently, detail such as the slight misrepresentation of the notches in the polar response will tend to average out. So, the true far field does not have to be obtained. It is sufficient to ensure that the majority of receivers is outside the specular zone so that the diffuser effects can be seen. Then, a reasonable approximation to the far-field diffusion coefficient value can be obtained. (The specular zone is defined in Fig. 7; it is the region over which a geometric reflection point exists on the surface. Although the specular zone is strictly a high-frequency construction, practice has shown it to be a useful concept for the geometries and frequencies typically used in diffuser design.) In the spatial domain, the effect of a diffuser should be to move energy from the specular zone to other positions. So, unless receivers are placed both outside and

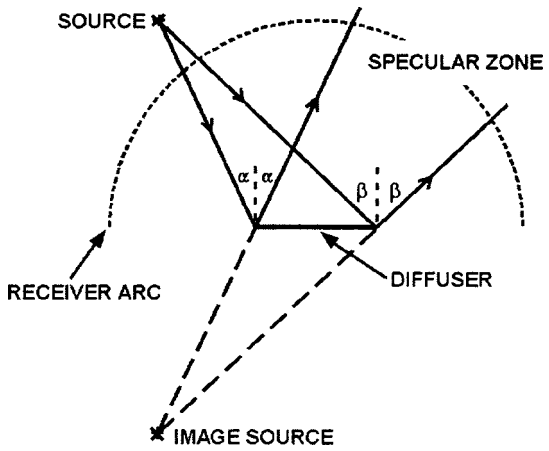

FIG. 7. Definition of specular zone.

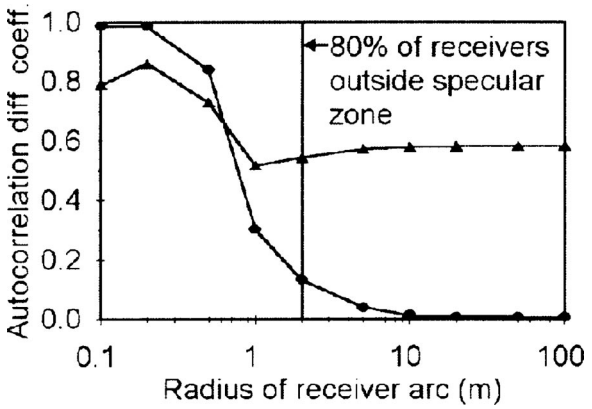

FIG. 8. Effect of receiver arc radius on a diffusion coefficient. Single-plane BEM predictions, normal incidence, source distance=100 m. –●– 1 m wide plane panel, 5 kHz. –▲– 1 m wide random binary panel, 400 Hz.

within the specular zone, measuring energy levels alone will not detect the effects of diffusion. In tests carried out for this project, typically 80% of receivers were outside the specular zone. In Fig. 8 the diffusion coefficient for two surfaces as a function of receiver distance is shown. The point where 80% of the receivers are outside the specular zone is shown. The plane panel case shown is one of the worst-case scenarios, and the error introduced into the diffusion coefficient is only 0.1. Furthermore, this is a single frequency prediction. Once averaging effects across one-third octave bands are introduced, this error approximately halves. This illustrates that a reasonable approximation to the true far-field value can be obtained. Alternatively, systems such as near-field acoustic holography could be performed[21] to enable near-field measurements to be projected into the far field, but they have their own different disadvantages such as the problems of mounting the surface in an application realistic manner. Another solution is to use validated prediction models; then, projecting to the far field is always possible.

For some surfaces, however, it is not sufficient just to measure in the far field. For concave surfaces, and others that might have significant aberrations closer to the surface, it is necessary to monitor in the near field as well as the far field to ensure that effects such as focusing are found. This is illustrated in Fig. 9, where the scattering from a concave surface is shown as a function of distance. It can be seen that receivers very close to the surface detect a good diffuser, but

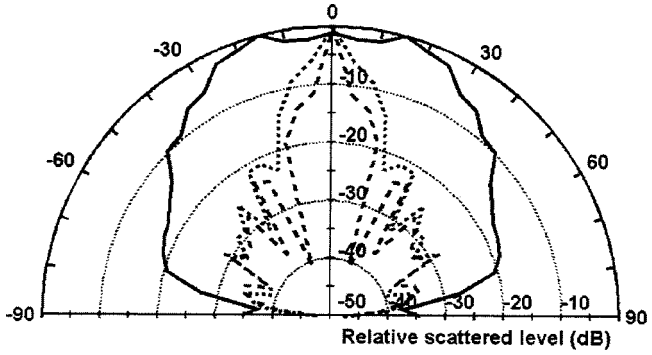

FIG. 9. Effect of receiver arc radius on the polar response of a concave prism. Single-plane BEM predictions, 2 kHz, normal incidence. ——— Near field, ––– focal distance, --- far field.

a little further out the scattering becomes highly focused. This is as expected because the concave surface effectively focused the far-field scattered pressure distribution into the near field. In the far field, the diffusion is improved, the concave surface appearing to behave somewhat like a plane surface. In summary, a pragmatic approach requires receivers to be both inside and outside the specular zone; measurements at application realistic distances are also needed to check for focusing as a concave surface can focus far-field aberrations into the near field. If measurements are made at different radial distances from the surface, it is necessary to apply a correction to allow for the normal drop in level due to spherical or cylindrical spreading. Otherwise, the diffusion coefficient is overly biased by drops in levels that naturally occur due to effects that are not related to a surface's ability to diffuse. Incidentally, for the purpose of this paper, measures will be defined in terms of *energy*. Strictly speaking, as some of the measurements were not in the far field, the true outward propagating energy was not always measured. Consequently, in reality, measures are actually based on the squared pressure.

V. SINGLE PLANE AND HEMISPHERICAL DIFFUSERS

Diffusers can be designed to cause scattering in one or more planes. The examples of one-plane surfaces shown in Fig. 3 are the battens, cylinder, triangle, and one-dimensional quadratic residue diffuser (QRD). The terminology one-dimensional arose from Schroeder-style diffusers, although it is less confusing to use the term single-plane diffusers. Often results for diffusion coefficients for single-plane surfaces are obtained from semicircular measurements in the plane of maximum diffusion. Strictly speaking, when evaluating the diffusion from such surfaces, it is best to calculate the diffusion coefficient in two directions—in the case of the cylinder across the width where diffusion is greatest and along the length where diffusion is smallest. More complex surfaces may create scattering in a more hemispherical manner. For example, an appropriate-sized sphere is effective at distributing energy in all directions. A two-dimensional Schroeder diffuser has two planes of maximum diffusion. In these cases, the polar distribution has to be measured over the surface of a hemisphere.

VI. REVIEW OF PREVIOUS COEFFICIENTS

In this section, the previous parameters appearing in literature will be reviewed. The advantages and disadvantages of the coefficients will be presented, drawing on the large body of measured and predicted results generated for this work.

The simplest parameter to define is a measure that forms a ratio between the energy reflected outside the specular zone to the total reflected energy. This is similar in philosophy to the coefficient defined by Lam.[22] If the squared pressure in a particular direction is given by $E(\Omega)$, then the coefficient, d_z, is given by

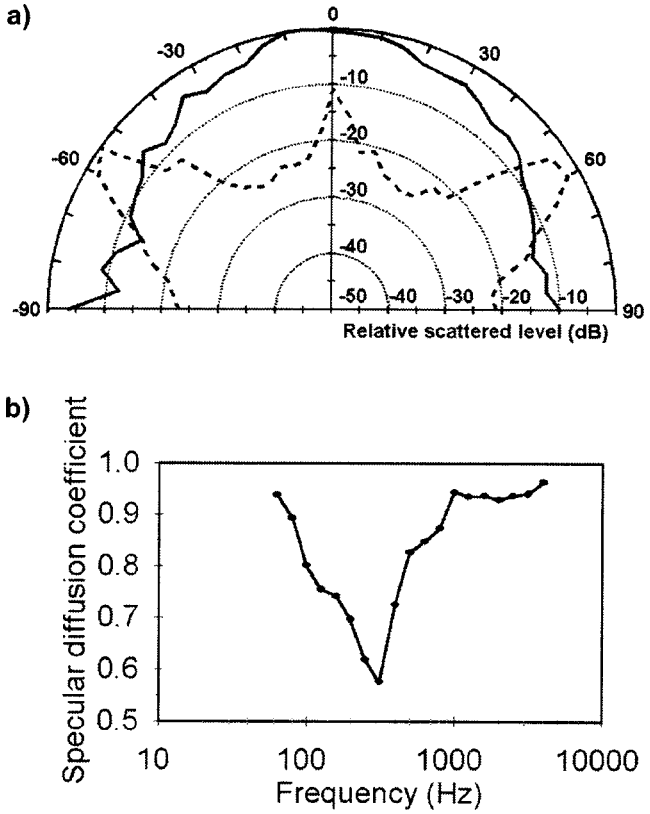

FIG. 10. Illustration of the simple specular zone diffusion coefficient failing due to incident sound being redirected as opposed to scattered. Two dimensional measurements of cone, normal incidence. (a) Polar responses: ——— 250 Hz, diffusion=0.619. – – – 4 kHz, diffusion=0.963. (b) Variation of the specular zone diffusion coefficient with frequency.

$$d_z = 1 - \frac{\int_{s_z} E(\Omega)\, d\Omega}{\int_s E(\Omega)\, d\Omega} = 1 - \frac{\sum_{i=1,(\theta_i,\phi_i)\in s_z}^{n_z} E_i \Delta A_i}{\sum_{i=1}^{n} E_i \Delta A_i}, \qquad (1)$$

where s_z denotes the area of the specular zone; s the area of a hemisphere or semicircle centered on the surface depending on whether this is a one-plane or hemispherical measure, and Ω is the solid angle. The second discrete form uses n for the total number of measurements and n_z the number of measurements in the specular zone. ΔA_i is the area sampled by the ith measurement point. For a single-plane measurement with an evenly spaced set of receivers on an arc these factors can be ignored; for a hemispherical measurement, these give a weighting equivalent to changing the sampling to be linear with respect to area before calculation of the diffusion coefficient.

This definition has several qualities to recommend it. The definition is simple in concept, easy to explain, and links to some of the styles of diffusion modeling used in computer prediction models. Not only is it bounded, it also has values between the extremes which are easy to conceptualize. Furthermore, it links to the perceived role of diffusers in rooms, which is to move reflected energy from specular reflection directions.

There are, however, two main difficulties with the measure. The first is that according to Eq. (1) a complete diffuser would have no energy in the specular reflection direction and so creates a notch in the polar response. This is not a good definition of complete diffusion for two reasons. First, there are no known useful surfaces that can produce a significant notch in specular reflected energy over a significant bandwidth and for random incidence. While a primitive root diffuser and modified forms[23–25] can generate notches at specific frequencies, the notches are not broadband. Using optimization[25] can produce a more broadband notch, but this can only be achieved for single specified angles of incidence. An alternative diffuser design, such as a simple triangle or pyramid, can produce such a notch, but this is achieved by redirection and not by dispersion. In addition, the notch is not achieved for all angles of incidence, and so these are not random incident surfaces. The second reason is that the term *diffusion* is defined as meaning to scatter in all directions, not to produce a specific diffusion distribution such as a notch. Consequently, it is a semantic misdefinition to term Eq. (1) a diffusion coefficient. Fortunately, a simple redefinition enables the above parameter to have complete diffusion as even scattering in all directions

$$d_z' = \left(1 - \frac{\sum_{i=1,\theta_i\in s_z}^{n_z} E_i \Delta A_i}{\sum_{i=1}^{n} E_i \Delta A_i}\right) \frac{n}{n-n_z}. \qquad (2)$$

This does not cure the second difficulty with specular zone measures, which is the inability of the formulation to differentiate between redirection and dispersion. The scattering from a simple cone is shown as a function of frequency in Fig. 10 in terms of polar distributions and diffusion coefficients. The polar distributions show the scattering becoming distinctly less diffuse as frequency increases from 250 Hz to 4 kHz. At 250 Hz the cone is a reasonable diffuser; the surface roughness is small compared to wavelength and the cone behaves as a small flat surface, producing good diffusion because the surface size is much smaller than the wavelength. But, at 4 kHz the surface detail of the cone sides is significant compared to wavelength and specular-like reflections off the two cone sides occur, producing two distinct lobes shown on the semicircular polar response. This is not seen in the calculated diffusion coefficient values, however, where the diffusion coefficient wrongly implies increasing diffuseness with frequency above 250 Hz.

Diffuser designers, as discussed previously, have to worry about the difference between redirection and dispersion because specialist surfaces are used more often than not to treat first-order reflections. (Admittedly, specialist diffusers usually have some influence on the diffuseness of the reverberation in the space, but this is of secondary importance. Indeed, if the only consideration of diffuser design was to treat the diffuseness of the late-arriving sound field, surfaces which cause redirection would probably be just as effective as those that cause dispersion.) Consequently, specular zone measures in all their various guises are rejected.

The most popular form of diffusion definition, if this is measured on the number of publications using it, is the standard deviation.[8–10] These have taken slightly different forms.

Splitting these into generic types, two diffusion parameters, $D_{\sigma,E}$ and $D_{\sigma,L}$ can be defined

$$D_{\sigma,E}=\sqrt{\frac{1}{n}\sum_{i=1}^{n}(E_i-\overline{E})^2};\quad \overline{E}=\sum_{i=1}^{n}E_i \tag{3}$$

$$D_{\sigma,L}=\sqrt{\frac{1}{n}\sum_{i=1}^{n}(L_i-\overline{L})^2};$$

$$\overline{L}=\sum_{i=1}^{n}L_i;\quad L_i=10\log_{10}(E_i). \tag{4}$$

These equations have assumed a single-plane measurement with evenly spaced receivers for clarity so the complication of terms to deal with uneven area sampling—seen in Eqs. (1) and (2)—can be removed. If all the energies in a polar distribution are the same, then the standard deviation is zero. Any deviation from the case of complete diffusion causes the standard deviation to increase. The parameters are simple in concept and relatively easy to explain as they use a common statistical operation. Values can be interpreted for average to good diffusers, as the standard deviation is a measure of spread, particularly if Eq. (4) is used. For example, two standard deviations would define within what limits 95% of scattered pressure levels lie if a normal distribution is assumed (incidentally, this is actually an incorrect supposition as most polar distributions are not normal distributions). For poor diffusers, as discussed below, the standard deviation formulation falls down and so does the usefulness of defining the range of levels for 95% of receivers.

The essential difference between Eqs. (3) and (4) is whether the standard deviation is taken of the measured levels or energy. The philosophy of taking the standard deviation of the levels is that the polar distribution of levels forms a more linear perceptual scale to listeners than the polar distribution of energies. Indeed, when evaluating the quality of diffusion, designers will view level polar distributions rather than those based on energy. So, the linear perceptual scale also applies to the visual evaluation of polar distributions used by practitioners. Unfortunately, the simple level formulation fails for poor diffusers. The highest standard deviation achievable occurs when all the scattered energy is reflected into half the receivers, the remaining receivers measuring the background level. (This occurs because level values are interval and not ratio.) This contradicts accepted philosophy of diffusers and reflectors where the worst case would be expected to be when all the scattered energy is reflected to one receiver. Consequently, although the standard deviation ranks moderate to good diffusers correctly, it does not rank poor diffusers in the right order. In fact, poor diffusers can be rated as very good. The problem is that the standard deviation measures the deviation from the mean. In Fig. 9, the scattering from a concave prism was shown at the focal distance. In this case the mean level is close to the low-level scattering, and so the standard deviation sees this as a reasonable diffuser as the vast majority of the scattering is close to the mean level. In reality, however, it is a very poor diffuser suffering from a strong specular reflection. A simple solution to this is to calculate the mean level via energy[9]

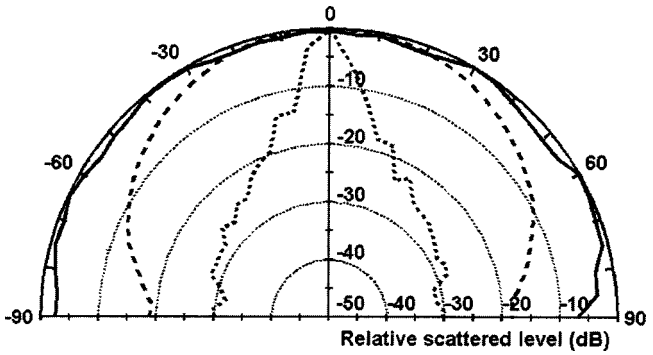

FIG. 11. Illustration of the ranking of polar responses by standard deviation. 2D measurements, normal incidence. ——— Convex semicylinder, 2 kHz, $d_{\sigma,E}=0.950$. −−− Two concave semicylinders, 250 Hz, $d_{\sigma,E}=0.748$. --- Plane panel, 4 kHz, $d_{\sigma,E}=0.685$.

$$\overline{L}=10\log\sum_{i=1}^{n}10^{L_i/10}. \tag{5}$$

This then shifts the mean level upwards, so penalizing poor diffusers. It does not completely remove the problem. For example, when measuring a single-plane measurement over a semicircle with a 5° resolution, the worst case occurs with all the reflected energy being scattered to 9 out of the 37 receivers. It has, however, ameliorated the problem to the point where it is more of a philosophical worry than a difficulty in real situations.

These types of standard deviation criteria have been used to design diffusers.[8,9] Except for the difficulty discussed above, they have been shown to rank diffuser performance correctly. This is illustrated in Fig. 11. A further refinement of standard deviation coefficients was suggested by Angus;[26] this was the concept of diffusion gain. He used this to evaluate the performance of large arrays of Schroeder diffusers. The diffusion gain is the ratio between the standard deviation values for the diffuser and an equivalent-sized flat surface. While this neatly illustrates the performance of diffusers over a flat surface, it is unbounded and so fails to meet a crucial criterion for a diffusion coefficient. In fact, the main problem with the standard deviation formulations is that they are not bounded in one direction. A normalization can be most readily achieved by considering the worse case. For Eq. (3), the worst case is where all the energy is scattered in one direction. Then, the diffusion coefficient, $d_{\sigma,E}$, is

$$d_{\sigma,E}\approx 1-\frac{1}{nE}\sqrt{\sum_{i=1}^{n}(E_i-\overline{E})^2};\quad n\gg 1. \tag{6}$$

The subtraction from 1 is done so that the coefficient value is unity for a good diffuser and zero for a bad diffuser to be consistent with other measures given here. The diffusion coefficient now only depends on the relative distribution of energies within the polar response. It is independent of total scattered energy and hence any absorption that might occur. This seems a desirable characteristic, as there already exists a coefficient to measure absorption. For Eq. (4), the worst case is when all the scattered energy is evenly scattered into half the measurement points, and the other measurement points measure background noise. Using the mean of Eq. (5) results

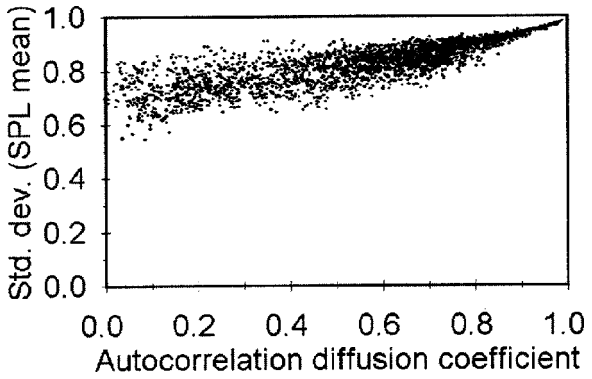

FIG. 12. Relationship between autocorrelation diffusion coefficient and standard deviation diffusion coefficient values for all 2D measurements and predictions. Each point represents a different measured frequency for a different surface.

in a different worst case that is n dependent. Furthermore, once normalization has been performed, a problem arises because for many surfaces the diffusion coefficients are bunched at one end of the scale. This problem is even worse for the energy-based formulation than the level equation. In Fig. 12 the diffusion coefficients for a wide variety of surfaces is shown; it can be seen that really only about half the standard deviation scale is being used. For this reason, the standard deviation is no longer the favored parameter for characterizing scattering.

Another characterization method that has been suggested[11,12] is based on a directivity-style measure. Subtle differences have appeared in the literature, but in the simplest, single-plane form, the coefficient, d_d, is

$$d_d = 1 - \frac{1}{n}\sqrt{\sum_{i=1}^{n}\left(\frac{E_i}{E} - 1\right)^2}. \tag{7}$$

Essentially, the directivity measures utilize the fact that complete diffusion occurs when the energy scattered in direction i is a constant equal to the reciprocal of the number of measurements. While at first this appears to be a unique measure, it in fact is almost identical to the energy-based standard deviation normalized to between 0 and 1 as shown in Eq. (6) and so will not be discussed further.

Spherical harmonics have been suggested by Angus[13] as another method for characterizing hemispherical scattering. The polar distributions are transformed into a set of amplitudes for the spherical harmonic basis functions. The fundamental spherical harmonic is a sphere and so represents even scattering in all directions. Higher harmonics are more complex in shape, for example dipoles, and so represent deviations from uniform scattering. A single-figure parameter can then be derived from the ratio of the fundamental to the higher-harmonics amplitudes. This coefficient has not been thoroughly tested and further work is needed to prove its worth. Conceptually, however, it has one major drawback. The calculation of the harmonics is complex, and difficult to explain to nonacademics. It is feared that this would make such a coefficient unacceptable to many practitioners.

In summary, all the published coefficients have flaws in one or more respects. Consequently, new coefficients have been developed to overcome some of the difficulties.

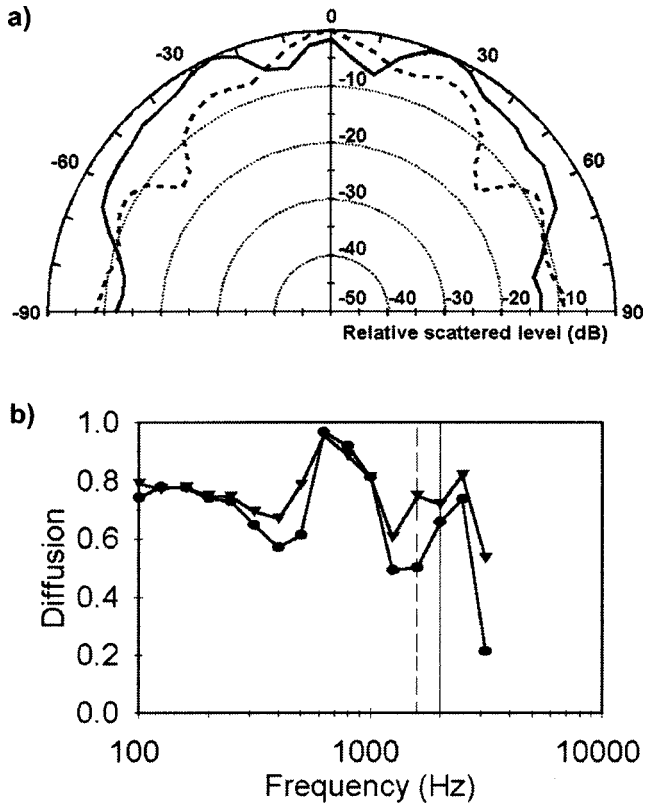

FIG. 13. Illustration of a case where d_{90} fails to quantify diffusion correctly. 2D measurements of $N=7$ QRD, normal incidence. (a) Polar responses: ——— 2 kHz, – – – 1.6 kHz. (b) Variation of diffusion coefficient with frequency. –●– Autocorrelation diffusion coefficient, d_a; –▼– d_{90}.

VII. NEW COEFFICIENTS

A parameter can be defined in terms of the cumulative probability distribution. The advantage of doing this is that it creates a parameter where the physical meaning of all values can be easily interpreted. This 90% energy coefficient, d_{90}, is defined as follows:

$$d_{90} = \frac{n_{90}}{0.9n}, \tag{8}$$

where n_{90} is the number of directions that 90% of the energy is scattered into and can be found from the cumulative probability distribution. The choice of 90% is purely empirical. Higher percentile values lead to a coefficient with a lack of discrimination and lower values lead to a coefficient which no longer ranks diffusers correctly. The coefficient can be easily interpreted. A value of 0.6 means that all the energy is scattered into ≈60% of the directions (strictly speaking, 54%). The coefficient works well for nearly all the required criteria; for example, it is bounded. The only problem is that for a small but significant minority of cases it fails to rank diffusers correctly. This is illustrated in Fig. 13. The solid line at 2 kHz displays better diffusion than the dashed 1.6-kHz line, yet the ranking shown by the 90% diffusion coefficient has it the wrong way around. Consequently, the following coefficient based on the autocorrelation function is preferred.

The autocorrelation function is most familiar in acoustics as a technique for assessing the similarity between two

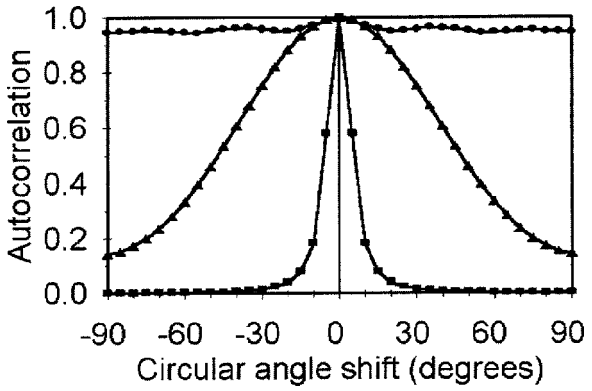

FIG. 14. Normalized circular autocorrelation functions of the polar responses in Fig. 9. –●– Convex semicylinder, 2 kHz. –▲– 2 *H* concave semicylinders, 250 Hz. –■– Plane panel, 4 kHz.

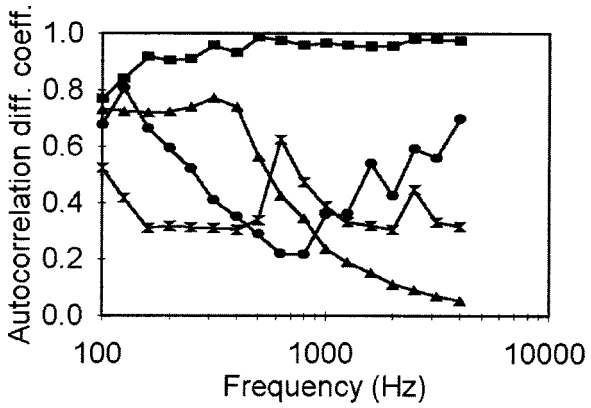

FIG. 15. Variation of d_a with frequency for a selection of samples. 2D measurements, normal incidence. –●– 2×Skyline units differently orientated. –▲– Plane panel. –■– Convex semicylinder. –⧗– Random binary panel.

or more sections of the same signal measured at different times. The function can also be used spatially to measure the similarity between different sections of polar responses. The technique is to first calculate the circular autocorrelation coefficient. Figures 11 and 14 show some typical polar responses and their circular autocorrelation functions. A perfect diffuser will have an autocorrelation value of 1 at all times; a complete specular reflector will only have a nonzero value at one sample point. The circular autocorrelation is then averaged across all displacements to give a single diffusion measure. At first this might appear to be a moderately involved calculation, but in fact the procedure reduces to a simple to calculate formulation. The autocorrelation diffusion coefficient, d_a, is given by

$$d_a = \frac{(\Sigma_{i=1}^{n} E_i)^2}{n\Sigma_{i=1}^{n} E_i^2}. \tag{9}$$

This is automatically bounded between $1/n$ and 1. A simple scaling can be carried out to make the bounding between 0 and 1. The autocorrelation coefficient generally ranks diffusers in the same order as the energy-based standard deviation as there is a single-valued function relating the coefficients

$$\frac{1}{d_a} = (1 - d_{o,E})^2 (n-1) + 1. \tag{10}$$

Essentially, the difference between standard deviation and autocorrelation is how the values are distributed along the diffusion axis. At this point, it would be good to know which scale, autocorrelation or standard deviation, forms the most linear scale in terms of the effect that diffusers have on the room acoustic and the response of listeners. But, this information is unavailable. Consequently, it is assumed that the autocorrelation is a better measure of diffusion than the standard deviation because practical values are distributed over the whole range of possible values rather than being bunched together. This is illustrated in Fig. 12. As the standard deviation has been thoroughly tested in diffuser design, this lends evidence that the autocorrelation ranks diffusers correctly. For example, in Fig. 11 the autocorrelation coefficients are 0.956, 0.529, and 0.055 for the semicylinder, two convex semicylinders, and plane surface, respectively. Further evidence of correct ranking can be seen in Fig. 15, where some typical autocorrelation diffusion spectra are given. Again, the diffusion coefficient is independent of the absolute values and so the coefficient is correctly characterizing diffusion, not absorption. The only real drawback of the autocorrelation coefficient is that only the extremes of the scale are well defined. It is hard to put an exact physical meaning on intermediate coefficient values. Attempts were made to relate values to the spread of the polar distribution, but the relationship is too vague to be of much use and the necessary assumption of polar distribution normality is usually incorrect.

VIII. CONCLUSIONS

Techniques for characterizing the degree of diffusion produced by a surface have been discussed. This paper has concentrated on free-field methods. Previous suggested diffusion coefficients have been investigated and their strengths and weaknesses highlighted. There is no ideal diffusion coefficient that can meet all the desired criteria. For this reason, the new coefficient will not be perfect, but this is also true of the absorption coefficient that acousticians have been using for nearly a century. The best diffusion coefficient is the one that has fewest flaws and must be of use to practitioners. A new surface diffusion coefficient based on the autocorrelation function has been developed and demonstrated to be superior to previous measures.

ACKNOWLEDGMENTS

This work was funded by the Engineering and Physical Research Council (UK) (No. GR/L13124), with support from RPG Diffusor Systems, Inc.

[1] P. D'Antonio and T. J. Cox, ''Diffusor application in rooms,'' Appl. Acoust. **60**, 113–142 (2000).
[2] M. Vorländer, ''International Round Robin on Room Acoustical Computer Simulations,'' in Proceedings of the 15th ICA, Norway. II, pp. 689-692 (1995).
[3] Y. W. Lam, ''The dependence of diffusion parameters in a room acoustics prediction model on auditorium sizes and shapes,'' J. Acoust. Soc. Am. **100**, 2193–2203 (1996).
[4] Y. W. Lam, ''A comparison of three diffuse reflection modeling methods

used in room acoustics computer models,'' J. Acoust. Soc. Am. **100**, 2181–2192 (1996).
[5] E. Mommertz and M. Vorländer, ''Measurement of Scattering Coefficients of Surfaces in the Reverberation Chamber and in the Free Field,'' in Proceedings of the 15th ICA II (1995), pp. 577–580.
[6] E. Mommertz and M. Vorländer. The authors have submitted a paper on the method to a special edition of Applied Acoustics to be published in 1999.
[7] A. C. Pantelides, ''The Effect of Absorbing and Diffusing Surfaces in a Rectangular Shaped Recording Studio,'' MSc thesis, University of Salford (1995).
[8] T. J. Cox, ''Optimization of profiled diffusers,'' J. Acoust. Soc. Am. **97**, 2928–2941 (1995).
[9] T. J. Cox, ''Designing curved diffusers for performance spaces,'' J. Audio Eng. Soc. **44**, 354–364 (1996).
[10] P. D'Antonio, ''The Disc Project: Directional Scattering Coefficient Determination and Auralization of Virtual Environments,'' in Proceedings Noise-Con 93 (May 1993), pp. 259–264.
[11] J. Angus, A. C. Marvin, J. Clegg, and J. F. Dawson, ''A Practical Metric for Evaluating Sound Diffusers,'' Presented at the 98th Audio Engineering Society Convention, Preprint 3955 (D5) (February, 1995).
[12] D. Takahashi, ''Development of optimum acoustic diffusers,'' J. Acoust. Soc. Am. **16**, 51–58 (1995).
[13] J. A. S. Angus, ''Diffuser assessment using surface spherical harmonics,'' J. Acoust. Soc. Am. **104**, 1857–1858 (1998).
[14] T. J. Cox, ''Predicting the scattering from reflectors and diffusers using 2D boundary element methods,'' J. Acoust. Soc. Am. **96**, 874–878 (1994).
[15] T. J. Cox and Y. W. Lam, ''Evaluation of methods for predicting the scattering from simple rigid panels,'' Appl. Acoust. **40**, 123–140 (1993).
[16] T. J. Cox and Y. W. Lam, ''Prediction and evaluation of the scattering from quadratic residue diffusers,'' J. Acoust. Soc. Am. **95**, 297–305 (1994).
[17] P. D'Antonio, J. H. Konnert, and P. Kovitz, ''The Disc Project: Experimental Measurement of the Directional Scattering Properties of Architectural Acoustic Surfaces,'' 1p, AAd2, 141–144 (June 1994).
[18] P. D'Antonio and J. H. Konnert, ''The reflection phase grating diffusor: Design theory and application,'' J. Audio Eng. Soc. **32**, No.4, 228–238 (1984).
[19] L. E. Kinsler, A. R. Frey, A. B. Coppens, and J. V. Sanders, *Fundamentals of Acoustics*, 3rd ed. (Wiley, New York, 1982), pp. 187–188.
[20] J. H. Rindel, ''Attenuation of Sound Reflections due to Diffraction,'' Nordic Acoustical Meeting. NAM86 (1986).
[21] M. Kleiner, H. Gustafsson, and J. Backman, ''Measurement of directional scattering coefficients using near-field acoustic holography and spatial transformation of sound fields,'' J. Audio Eng. Soc. **45**(5), 331–346 (1997).
[22] Y. W. Lam, ''A boundary integral formulation for the prediction of acoustic scattering from periodic structures,'' J. Acoust. Soc. Am. **105**(2), 762–769 (1999).
[23] M. R. Schroeder, ''Toward better acoustics for concert halls,'' Phys. Today **33**(10), 24–30 (1980).
[24] E. Feldman, ''A reflection grating that nullifies the specular reflection: A cone of silence,'' J. Acoust. Soc. Am. **98**, 623–634 (1995).
[25] T. J. Cox, ''Acoustic phase gratings for reduced specular reflection,'' Appl. Acoust. **60**(2), 167–186 (2000).
[26] J. A. S. Angus, ''Using Modulated Phase Reflection Gratings to Achieve Specific Diffusion Characteristics,'' presented at the 99th Audio Engineering Society Convention, Preprint 4117 (October 1995).

Predicting reverberation times in a simulated classroom

Sylvio R. Bistafa[a] and John S. Bradley[b]
Institute for Research in Construction—Acoustics, National Research Council Canada, 1500 Montreal Road, Ottawa, Ontario K1A 0R6, Canada

(Received 3 March 2000; revised 9 July 2000; accepted 17 July 2000)

By varying the sound-absorption treatments in a simulated classroom, experimental results were compared with analytical and computer predictions of reverberation time. Analytical predictions were made with different absorption exponents, which are the result of different weighting procedures involving room surface areas and the sound-absorption coefficients. Sound scattering was found to influence measured reverberation times. With the amount of sound scattering provided, more accurate analytical predictions were obtained with absorption exponents that give reverberation times longer than those obtained with the Sabine absorption exponent, which consistently underpredicted reverberation times. However, none of the absorption exponents could be singled out as more adequate because of similar average accuracy. Computer predictions of reverberation time were accomplished with two commercially available ray-based programs, RAYNOISE 3.0 and ODEON 2.6, with specular and calibrated diffuse reflection procedures. Neither type of procedure, in either program, was more accurate than the best analytical predictions. With RAYNOISE, neither the specular nor the calibrated diffuse reflection procedure could be singled out as more adequate. For ODEON, the calibrated diffuse reflection procedure gave consistently more accurate predictions than its specular reflection procedure, with the best accuracy of the computer predictions. [S0001-4966(00)04710-X]

PACS numbers: 43.55.Br, 43.55.Dt, 43.55.Fw, 43.55.Ka [JDQ]

I. INTRODUCTION

It is often required to predict reverberation times in rooms for speech communication such as school classrooms. This paper compares the ability of several analytical expressions and two room acoustics computer programs to predict reverberation times in a simulated classroom with varied absorptive treatments.

The Sabine and Eyring reverberation formulas are most commonly used to predict reverberation time. These formulas are slightly different, because they are derived from somewhat different considerations,[1,2] but both are based on the assumption of a diffuse sound field. For high total sound absorption, the Sabine formula gives longer reverberation times than the Eyring formula, but the differences become smaller as the total amount of sound absorption decreases.

Many other formulas have been proposed for predicting reverberation times.[3–7] The development of some of these formulas was motivated by the lack of accuracy in reverberation time prediction when using the traditional Sabine/Eyring reverberation formula, in certain rooms with nonuniform surface absorption. This is a very important issue for many rooms, including classrooms, where the sound absorption is typically applied only to the ceiling area.

As far as having sound absorption located mostly on a single surface is concerned, classrooms are very similar to auditoriums because of the high audience absorption on the floor area in this type of room. A fundamental difference, however, is that recommended reverberation times for classrooms are well below 1 s,[8] whereas in larger rooms, such as opera houses and concert halls, values well above 1 s are usually recommended.[9]

Over the last three decades many room acoustical computer programs have been developed and used for predicting room acoustics quantities. These programs can be classified as wave-based programs and ray-based programs. Ray-based programs are the most common type of room acoustic programs available today.

The main objective of the present work was to systematically study the accuracy of seven reverberation formulas and two contemporary ray-based programs, RAYNOISE 3.0[10] and ODEON 2.6,[11] to predict reverberation times in a simulated classroom for varied absorption treatments. Another objective was to compare the effect of different absorption treatments to achieve recommended reverberation times in classrooms.

II. REVERBERATION TIME FORMULAS

All reverberation time formulas that have been used in the present work reduce to the form given, in SI units, by

$$T = 0.161 \frac{V}{Sa + 4mV}, \tag{1}$$

where V and S are the volume and the total surface area of the room, respectively, m is the sound attenuation constant of the air, and a is the so-called absorption exponent.

Different absorption exponents have been proposed. As we shall see, these are in fact the result of different weighting procedures involving the areas S_i of each of the room surfaces and the corresponding absorption coefficients α_i.

[a]Visiting Scientist, Department of Mechanical Engineering, Polytechnic School, University of São Paulo, São Paulo, Brazil.
[b]Electronic mail: John.Bradley@nrc.ca

Sabine[1] considered the absorption exponent as the average absorption coefficient $\overline{\alpha}$, given by

$$\overline{\alpha}=\frac{1}{S}\sum_i \alpha_i S_i, \tag{2}$$

where $S=\Sigma_i S_i$. Hence, according to Sabine, the absorption exponent is

$$a_{\text{Sab.}}=\overline{\alpha}. \tag{3}$$

Equation (1), with $a=a_{\text{Sab.}}$, is known as the Sabine reverberation formula.

Eyring[2] was concerned with the fact that when $a_{\text{Sab.}}=1$, that is, for the case where the average absorption coefficient $\overline{\alpha}$ is unity, the reverberation time does not become zero. Eyring proposed a reverberation formula in which the absorption exponent is calculated according to

$$a_{\text{Eyr.}}=-\ln(1-\overline{\alpha}). \tag{4}$$

The Eyring reverberation formula—Eq. (1) with $a=a_{\text{Eyr.}}$—gives reverberation time equal to zero for $\overline{\alpha}=1$. It reduces to the Sabine formula for $\overline{\alpha}\ll 1$.

Millington[3] was concerned with the fact that when the absorption coefficients of highly absorbing materials are measured, the Eyring formula gives absorption coefficients greater than unity. Millington then developed a reverberation formula, which when used for the calculation of the absorption coefficient of samples in reverberation chambers, always results in sample absorption coefficients less than unity. The Millington formula is given by Eq. (1) with the absorption exponent given by

$$a_{\text{Mil.}}=-\frac{1}{S}\sum_i S_i \ln(1-\alpha_i). \tag{5}$$

The Millington formula has the drawback that when one of the surfaces of the room, even if very small, has an absorption coefficient $\alpha_i=1$, $a_{\text{Mil.}}$ would be infinitely large and hence the reverberation time would be zero. This happens because, as mentioned above, absorption coefficients obtained using the Millington formula are always less than unity. Therefore, the traditional absorption coefficients obtained in the reverberation chamber using the Sabine formula cannot be used in the $a_{\text{Mil.}}$ formula as given by Eq. (5). To enable the Millington formula to be used correctly, Dance and Shield[12] have created a conversion graph, so that Millington absorption coefficients can simply be estimated from the standard absorption coefficients.

The fundamental difference between the Eyring and Millington approaches is that the former considers the energy to be uniformly spread out after each reflection, whereas the latter considers the acoustical energy in a series of confined sound cones, reflected in sequence by each of the room surfaces S_i. A recommendation by Cremer and Müller[4] consists of dividing the total room surface area S into several large ''principal surfaces,'' which can be regarded as encountered by the sound cones in sequence (Millington's approach), and to subdivide these principal surfaces into smaller surfaces, which can be regarded as being uniformly acoustically irradiated (Eyring's approach).

The smaller subdivisions in each of the principal surfaces are first averaged according to Eq. (2), to determine the mean absorption coefficient for each of the principal surfaces. These are then inserted into Eq. (5) giving Cremer's absorption exponent as

$$a_{\text{Cre.}}=\frac{1}{S}\sum_i S_i\left[-\ln\left(1-\frac{1}{S_i}\sum_j \alpha_{ij}S_{ij}\right)\right]. \tag{6}$$

S_{ij} is the surface area of each subdivision j, of the principal surface i, which has the absorption coefficient α_{ij}. In the case where the principal surfaces have a uniform absorption coefficient, $\alpha_{ij}=\alpha_i$, and $a_{\text{Cre.}}=a_{\text{Mil.}}$. For that reason we have used Eq. (6) with the Millington absorption coefficients. This combined formula embraces both the Eyring and Millington formulas where they are adequate, but avoids their physically impossible results.

Because nonuniform distribution of absorption in rooms often occurs in practice, the condition of a diffuse sound field is frequently not fulfilled. Kuttruff[13] obtained sound decay curves at different points in a rectangular room, with nonuniform surface absorption but with surfaces that reflect energy in an ideally diffuse way (Lambertian scattering), by numerically solving an integral equation. He found that the initial decay is characterized by fluctuations. After the time that it takes for the sound to travel a few mean free-path lengths, these initial fluctuations fade out, leaving an exponential decay with the same decay constant throughout the whole room. He then numerically calculated absorption exponents, in cubic and rectangular rooms, with different distributions of surface absorption.

In another related study, Kuttruff[5,9] proposed a correction to the Eyring absorption exponent, to take into account the influence of nonuniform surface absorption in the room. An additional correction factor was added to $a_{\text{Eyr.}}$, that takes into account the influence of unequal path lengths. This correction is based on the variance of the path length distribution γ^2, which is given by $\gamma^2=(\overline{l^2}-\overline{l}^2)/\overline{l}^2$. $\overline{l}$ is the mean free path given by $\overline{l}=4V/S$, and $\overline{l^2}$ is the mean squared value of the free paths between two subsequent wall reflections. When both corrections are combined, Kuttruff's absorption exponent is given by

$$a_{\text{Kut.}}=a_{\text{Eyr.}}\left(1-\frac{\gamma^2}{2}a_{\text{Eyr.}}\right)+\frac{\Sigma_i(1-\alpha_i)(\overline{\alpha}-\alpha_i)S_i^2}{S^2(1-\overline{\alpha})^2}. \tag{7}$$

The first term in Eq. (7) reflects the influence of unequal path lengths, and the second, the nonuniform surface absorption. For rectangular room shapes, such as classrooms, γ^2 is close to 0.4.[9]

Fitzroy[6] experimentally verified, in rooms where the absorption is nonuniformly distributed, that the Sabine and Eyring reverberation formulas give reverberation time predictions that usually ''vary widely'' from measurements. According to his experience these formulas underpredicted reverberation times, especially in rooms that were heavily damped in the vertical direction. This is the case for rooms with an acoustical ceiling, as typically found in classrooms, or with high audience absorption as found in auditoriums. He then proposed a reverberation formula in which the absorp-

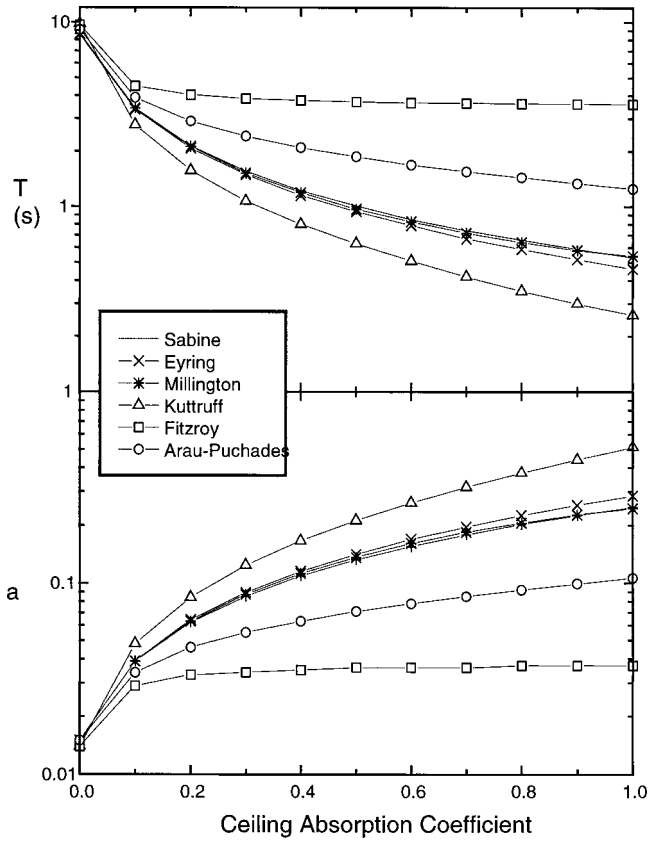

FIG. 1. Reverberation times (upper plot) and values of the absorption exponents (lower plot) versus the ceiling absorption coefficient. These results are for the room used to simulate the classroom, in which sound absorption is applied to the ceiling area.

tion exponent is calculated by an area-weighted arithmetic mean of an Eyring-type absorption exponent in the three orthogonal directions. Fitzroy's absorption exponent is given by

$$a_{\text{Fit.}} = -S\left[\frac{S_x}{\ln(1-\overline{\alpha}_x)} + \frac{S_y}{\ln(1-\overline{\alpha}_y)} + \frac{S_z}{\ln(1-\overline{\alpha}_z)}\right]^{-1}. \quad (8)$$

In Eq. (8), S_x is the ceiling plus the floor surface area, S_y is the surface area of both side walls, and S_z is the surface area of both end walls. Here α_x, α_y, and α_z are the mean absorption coefficients of the surface areas S_x, S_y, and S_z, respectively, which are calculated according to Eq. (2).

Based on Fitzroy's idea, Arau-Puchades[7] has proposed a reverberation formula in which the absorption exponent is given by weighting an Eyring-type absorption exponent in each one of the main directions according to

$$a_{\text{ArP.}} = [-\ln(1-\overline{\alpha}_x)]^{S_x/S} \cdot [-\ln(1-\overline{\alpha}_y)]^{S_y/S} \cdot [-\ln(1-\overline{\alpha}_z)]^{S_z/S}. \quad (9)$$

Arau-Puchades experimentally confirmed the adequacy of his absorption exponent in auditoriums, theaters, and television broadcasting studios.

Figure 1 shows values of the various absorption exponents and the corresponding reverberation times as functions of the ceiling absorption coefficient. The sound-absorbing configuration chosen for this comparison is typical of classrooms, in which sound absorption is applied to the ceiling area. For this type of sound-absorbing configuration, $a_{\text{Cre.}}$ is equal to $a_{\text{Mil.}}$. It can be seen that the absorption exponents of Sabine, Eyring, and Millington give reverberation times that are practically the same. This is because, even for the extreme case of a ceiling absorption coefficient equal to 1, the average sound-absorption coefficient $\overline{\alpha}$ is only equal to approximately 0.25, for this particular sound-absorbing configuration. This gives $a_{\text{Cre}} = a_{\text{Mil}} \approx a_{\text{Sab}} = 0.25$, and $a_{\text{Eyr}} = 0.29$. The absorption exponent of Arau-Puchades gives longer reverberation times, and that of Fitzroy even longer. The Kuttruff absorption exponent gives the shortest reverberation times compared to the other proposals. For the largest values of the ceiling absorption coefficient, Fig. 1 shows differences in reverberation time up to one order of magnitude. One of the objectives of the present study is to compare predictions of reverberation time by the various absorption exponents with measurements in a simulated classroom, for different sound-absorbing configurations.

III. EXPERIMENTAL PROCEDURES

A. The room and the sound-absorbing configurations

In the present study, the classroom was simulated in a rectangular and reverberant laboratory enclosure. The room is 9.20 m long by 4.67 m wide and 3.56 m high. Sound absorption in the simulated classroom was varied by laying different amounts of sound-absorbing ceiling tiles on the floor and walls of the room. The maximum amount of ceiling tiles used was 42.24 m^2. Figure 2 shows schematics depicting the application of the ceiling tiles in different amounts and configurations.

For ease of handling, the ceiling tiles were laid on the floor to simulate ceiling absorption. The untreated room, configuration (0) in Fig. 2, was tested first. Thereafter, the amount of sound-absorbing material was progressively increased, in different configurations, which corresponded to areas of 26.2%, 52.4%, 78.7%, and 98.3% of the total ceiling area of 42.96 m^2, and are referred to as configurations (25), (50), (75), and (100), respectively.

The amount of sound-absorbing material of configuration (50) (52.4% of the ceiling area) was also tested in different configurations to evaluate their effectiveness. In Fig. 2, configuration (HR) represents covering the ceiling on the receiver side; configuration (HS) represents covering the ceiling on the source side; configuration (EW) represents covering the end wall and part of the ceiling; configuration (PW) represents covering the upper part of the walls; and configuration (PF) represents covering a ring on the ceiling. All had exactly the same area of added sound-absorbing material corresponding to 52.4% of the complete ceiling area.

The sound-absorbing material used consisted of 25-mm-thick Luna Perforated Ceiling Tiles; they were semirigid glass-fiber panels (0.60×1.21 m) for ceiling applications. In tests conducted in a reverberation chamber according to ASTM C423, the following sound-absorption coefficients were obtained in the six-octave frequency bands from 125 Hz to 4 kHz: 0.08, 0.44, 0.94, 1.15, 1.01, and 0.75. The room surfaces are painted, nonporous masonry.

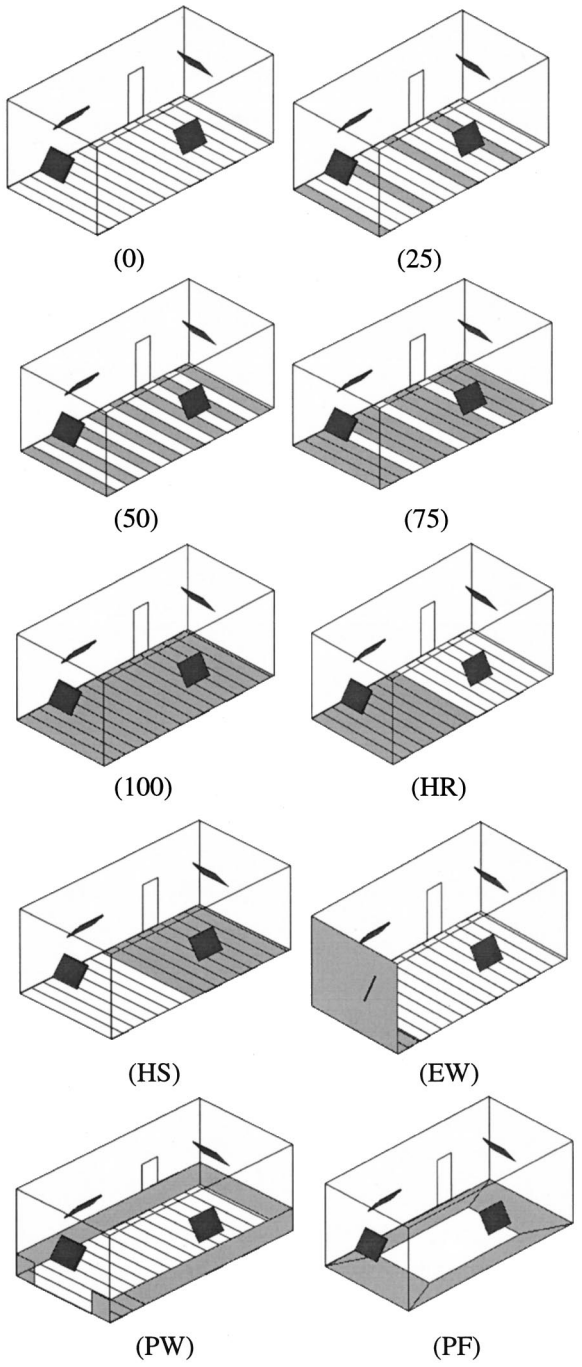

FIG. 2. Schematics depicting the application of the sound-absorbing ceiling tiles in different amounts and configurations. Configuration (0) depicts the room with no absorption. Configurations (25), (50), (75), and (100) depict the room with ceiling tiles applied, respectively, on 26.2%, 52.4%, 78.7%, and 98.3% of the floor area. Configurations (HR), (HS), (EW), (PW), and (PF) depict sound-absorbing configurations that have areas equal to 52.4% of the floor area. Also shown are the diffuser panels and the room door.

B. The measurements and the measuring system

For practical reasons, reverberation time measurements are in general conducted in unoccupied classrooms, because reverberation times in occupied classrooms would vary with the number of people in the classroom.

As will be discussed later, it was found necessary to add sound scattering to the room used to simulate the classroom. This was accomplished by fitting the room with diffuser panels, made of gypsum board (1.2×0.9 m). Figure 2 shows the room fitted with four diffuser panels, which were placed at an approximately 45° angle with each wall.

The temperature and relative humidity at the time of the tests were also measured to obtain the applicable air attenuation constant. The reverberation times measured in the bare room, configuration (0), were used to estimate the sound-absorption coefficients of the bare room surfaces using the Eyring formula.

In the results included here, the microphone was omnidirectional, and was located at a height of 1.1 m in six positions distributed where students would sit. The measured reverberation times reported here are given as position-averaged values. Two sound sources were used, one approximately omnidirectional and the other with an average directivity index at midfrequencies of 5 dB straight ahead, to better approximate the directivity of a human talker. The sources were positioned on the centerline of the room, 1.5 m from the front wall and the floor. Reverberation time measurements with the omni source were used in comparisons with the analytical predictions, and those with the directional source with the computer predictions. For these two sources, the average difference between measured reverberation times in all configurations was 4.1%.

Reverberation time measurements were accomplished with the RAMSOFT measuring system. This system uses a maximum-length-sequence (MLS) signal and a fast Hadamard transform procedure to obtain measured impulse responses at particular locations in rooms. A program filters the measured impulse responses into standard octave frequency bands and calculates decay times by means of Schroeder's backward integral. The validity of the measurement program was verified in various situations, including in an international round robin of room acoustics measurement systems.[14]

IV. RESULTS AND DISCUSSION

A. Effect of sound scattering on reverberation time measurements

Hodgson[15] investigated the effects of increasing sound scattering on the decay times and the stationary sound-pressure levels in a rectangular room. In his work, both quantities were predicted by ray-tracing simulations and by using the Eyring formula for diffuse sound fields. In the ray-tracing simulations, sound scattering was accomplished by two different types of scattering mechanisms: a Lambert model for surface scattering, and volume scatterers. He then found, that independent of the scattering mechanism used, as scattering increases, sound decays predicted by ray tracing tended to better approximate the results obtained using the Eyring reverberation formula.

Although surface and volume scattering have similar effects on the room sound field, they are quantified differently. Surface scattering is measured by the *scattering coefficient* δ, which is defined as the ratio of non-specularly reflected sound energy to totally reflected energy. Volume scattering is measured by the *scattering frequency* v [m^{-1}], obtained by

multiplying the density of scatterers by the average scattering cross section.[16]

There have been some attempts to measure surface scattering,[17] and studies on the scattering of sound by fittings in industrial rooms.[16,18] However, these are still the objects of ongoing research. Surface and volume scattering are present during measurements in real classrooms. Unlike the absorption coefficient, the scattering coefficients of room surfaces are not available. Although in unoccupied classrooms volume scattering by the occupants is not an issue, the presence of desks and other furniture could be considered to be volume scatterers. These considerations point to the need of quantifying the amount of scattering in real classrooms. For obvious reasons, this was not possible. It was decided to experimentally verify the influence of volume scattering on measured reverberation times, and to report reverberation times based on a reference value for the scattering frequency.

A recommendation by Kuttruff[9] for achieving a diffuse sound field in reverberation chambers is to have the scattering frequency in the range $0.5/H < \upsilon < 2.0/H$, where H is the distance of the test specimen from the wall opposite to it. In the room used to simulate the classroom, this would give a range for the scattering frequencies of $0.141\ \mathrm{m}^{-1} < \upsilon < 0.562\ \mathrm{m}^{-1}$. The corresponding range for the number of diffuser panels (1.2×0.9 m) N would be $40 < N < 160$.

However, the results of the computer simulations performed by Hodgson[15] revealed that a scattering frequency of $0.050\ \mathrm{m}^{-1}$ was sufficient for the sound decay to agree with that predicted by the Eyring formula. Benedetto *et al.*[19] investigated the effect of stationary diffuser panels in the measurement of sound-absorption coefficients in a reverberation chamber. They found experimentally that a scattering frequency of $0.024\ \mathrm{m}^{-1}$ was sufficient to obtain absorption coefficients practically equal to those obtained with a scattering frequency of $0.032\ \mathrm{m}^{-1}$. This means that increasing the scattering frequency above $0.024\ \mathrm{m}^{-1}$ had no effect on the degree of diffusion in the reverberation chamber. Based on these results, the number of diffuser panels (1.2×0.9 m) necessary to achieve diffuse field conditions in the simulated classroom would be $N = 14$ according to the former study, and $N = 7$ according to the latter.

To get an idea of the influence of the number of panels on reverberation time, a limited number of reverberation time measurements were made in the room for some of the sound-absorbing configurations, and with the number of diffuser panels varying from zero to 12 panels. These would give scattering frequencies ranging from 0 to $0.042\ \mathrm{m}^{-1}$. It was then found that as the number of diffuser panels increase, the measured reverberation times decrease, and tend to better approximate predictions obtained using the Eyring formula.

The better agreement between measured and predicted reverberation times as the number of diffuser panels increase was expected, since increasing scattering also increases the randomization of the incidence of sound on the room surfaces, resulting in a sound field that is more diffuse. However, even with 12 diffuser panels, significant differences were still apparent between measured and predicted reverberation times. A natural course would be to keep increasing the number of diffuser panels beyond 12, to attempt to achieve a diffuse sound field, here indicated by the agreement between measured and predicted reverberation times. This, however, was not pursued because the objective was to reproduce acoustical conditions found in typical classrooms, which usually are not ideal diffuse sound fields. The creation of a diffuse sound field was not sought since it would represent an unrealistic approximation to unoccupied classrooms.

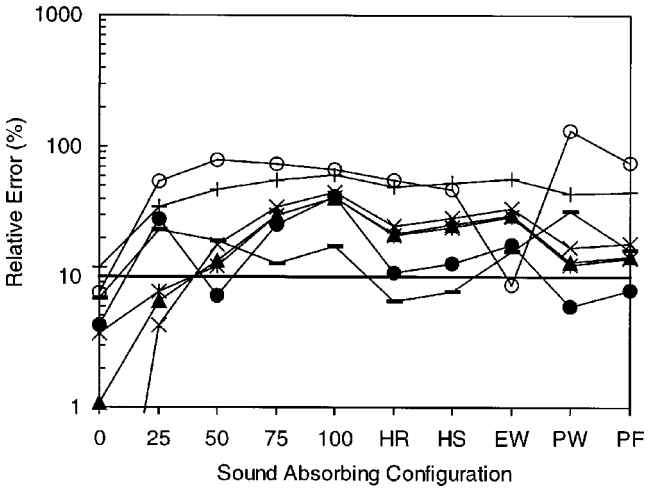

FIG. 3. Average relative error in reverberation time prediction across the six octave bands from 125 Hz to 4 kHz, for each sound-absorbing configuration. Analytical predictions using absorption exponents of: (▲) $a_{\mathrm{Sab.}}$, (×) $a_{\mathrm{Eyr.}}$, (*) $a_{\mathrm{Mil.}}$, (●) $a_{\mathrm{Cre.}}$, (+) $a_{\mathrm{Kut.}}$, (○) $a_{\mathrm{Fit.}}$, and (−) $a_{\mathrm{ArP.}}$. Also shown in this figure is a horizontal line across the plot area that corresponds to an accuracy of 10%.

According to both studies mentioned above,[15,19] a value for the scattering frequency of $0.012\ \mathrm{m}^{-1}$ was about the minimum necessary for the most pronounced changes to occur in the values of the parameters used to indicate the degree of sound diffusion. These parameters were reverberation time in the first study,[15] and the sound-absorption coefficient in the second.[19] Therefore, both studies seem to indicate that a scattering frequency of around $0.012\ \mathrm{m}^{-1}$ is a ''borderline'' value for the most significant changes in the sound field to occur. This was taken as a convenient reference value for the measurements in the simulated classroom. Therefore, all reverberation time measurements reported here were obtained with the room fitted with four diffuser panels (1.2×0.9 m), giving a scattering frequency of $0.014\ \mathrm{m}^{-1}$.

B. Accuracy of reverberation time formulas

For each sound-absorbing configuration in the simulated classroom, Fig. 3 shows the average relative error in reverberation time prediction, across the six octave bands from 125 Hz to 4 kHz, using the different absorption exponents. Also shown in this figure is a horizontal line across the plot area that corresponds to an accuracy of 10%, which was adopted by Hodgson[20] as an engineering-type accuracy for reverberation time predictions in practical applications. Although a just-noticeable difference in reverberation time is about 5%,[21] the 10% accuracy is more indicative of a minimum practically important difference.

It can be seen in Fig. 3 that for the bare room [configuration (0)], all absorption exponents are capable of predicting

reverberation time with an accuracy of 10%. This was expected since in the absence of ceiling tiles, all predictions for the bare room tend to approximate Eyring's prediction. As mentioned earlier, the absorption coefficients of the room surfaces were obtained from measurements in the bare room using the Eyring formula.

For configuration (25), the Sabine, Eyring, and Millington absorption exponents were all capable of predicting reverberation times with an accuracy of 10%; and for configurations (50), (PW), and (PF), only the Cremer absorption exponent predicted with this accuracy. For configuration (EW), only the Fitzroy absorption exponent was successful in predicting with an accuracy of 10%, and for configurations (HR) and (HS), only the Arau-Puchades absorption exponent predicted reverberation times with this accuracy. Predictions for configurations (75) and (100) could not be made with an accuracy of 10% by any absorption exponent. For these two configurations, predictions with the smallest average relative error were obtained with the Arau-Puchades absorption exponent, with values of 12.6% and 17.4%, respectively.

Figure 4 shows experimentally obtained reverberation times in octave bands, together with the prediction that gives the smallest average relative error for the specific sound-absorbing configuration (best prediction). Also shown in Fig. 4 are the predictions using the Sabine formula. As mentioned earlier, configuration (0) was used to estimate the absorption coefficients of the bare room surfaces using the Eyring formula. Therefore, for configuration (0), Fig. 4 shows that the average relative error using the Eyring formula is 0.0%.

It can be seen in Fig. 4 that the Sabine formula tends to underpredict reverberation times in the simulated classroom, with different amounts and configurations of sound absorption. Therefore, predictions obtained with lower values of the absorption exponent tend to be more accurate because they give longer reverberation times. For the sound-absorbing configurations tested, more accurate predictions than those obtained using the Sabine formula were obtained with the absorption exponent of Arau-Puchades in four configurations [(75), (100), (HR), (HS)]; of Cremer, in three configurations [(50), (PW), (PF)], and even with Fitzroy's absorption exponent in configuration (EW). Based on these results, the Arau-Puchades and Cremer absorption exponents better follow the measured changes in reverberation time with configuration.

To get an idea of the degree of uniformity of the predictions in different frequency bands, the average relative error at midfrequencies (500 Hz, 1 kHz, and 2 kHz) was also calculated for each sound-absorbing configuration, together with the relative errors in the 1-kHz frequency band. These relative errors, and the average relative errors across the six octave bands from 125 Hz to 4 kHz, were used to determine the ''overall quality'' of the predictions by averaging the relative errors for all configurations tested.

Table I shows the *overall average relative errors* in reverberation time predictions for each absorption exponent. This table shows that as more bands are included in the averages, the relative errors are reduced. In fact, the relative errors in the 1-kHz band are larger than the average relative errors at midfrequencies, which are larger than the average

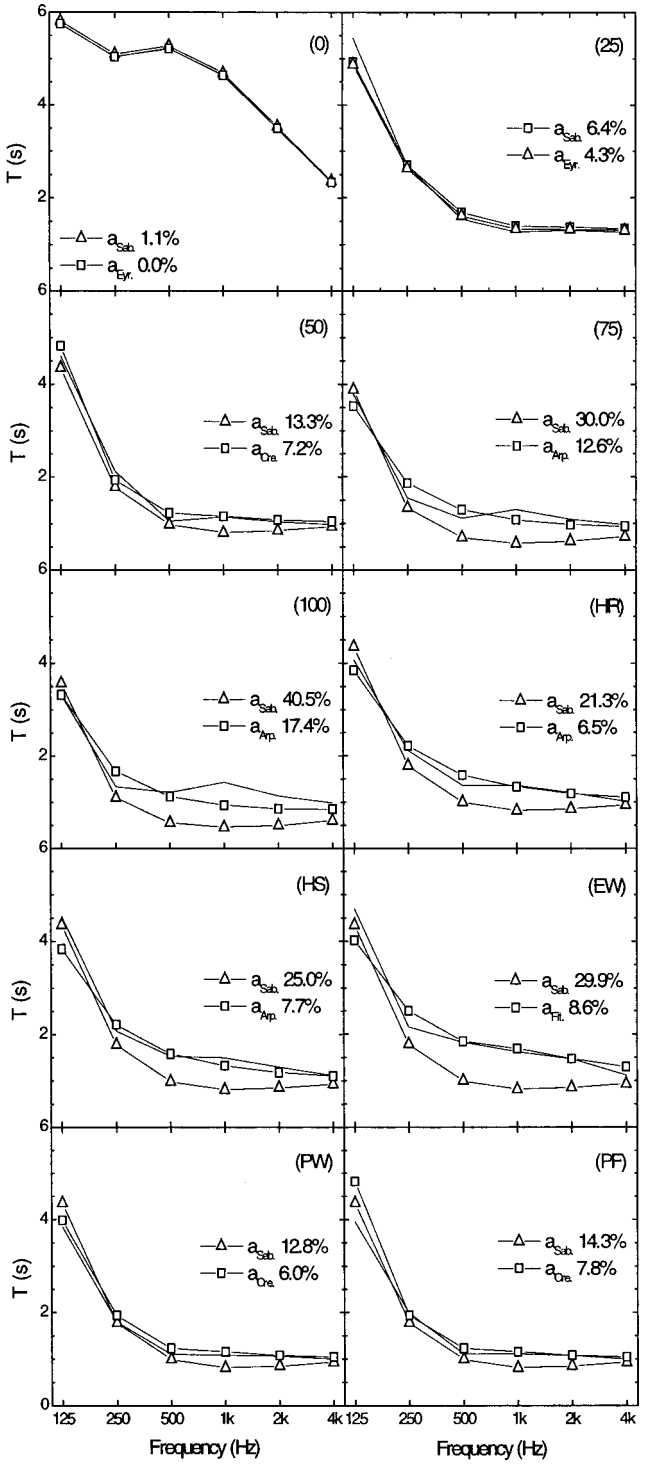

FIG. 4. (———) Experimental and analytical predictions of reverberation time. (△) predicted by the Sabine formula; (□) analytical prediction that gives the smallest average relative error (best prediction). Indicated in each configuration is the average relative error of the prediction across the six octave bands from 125 Hz to 4 kHz.

relative errors across the six octave bands from 125 Hz to 4 kHz. This result reveals that the quality of the predictions is nonuniform throughout the frequency range, and the average relative errors in reverberation time prediction tend to become smaller as more frequency bands are included in the averages.

In Table I, by comparing the overall average relative

TABLE I. Overall average relative errors of the analytical predictions of reverberation time for ten sound-absorbing configurations in the simulated classroom.

	Overall average relative error (%)		
	Frequency bands included in the averages		
Absorption exponent	1 kHz	500 Hz–2 kHz	125 Hz–4 kHz
Sabine	38.8	31.6	21.5
Eyring	42.6	35.7	24.7
Millington	36.1	30.4	21.1
Cremer	26.7	23.9	17.4
Kuttruff	68.0	63.5	49.3
Fitzroy	92.0	95.8	65.7
Arau-Puchades	22.9	22.7	16.7

errors across the six octave bands from 125 Hz to 4 kHz, it can be seen that the Arau-Puchades and Cremer absorption exponents predict reverberation times with the smallest average relative errors of 16.7% and 17.4%, respectively. The largest average relative errors were obtained by predicting reverberation times with the Kuttruff and Fitzroy absorption exponents, with values of 49.3% and 65.7%, respectively.

Dance and Shield,[12] using the Sabine, Eyring, and Millington reverberation formulas, predicted reverberation times in a recording studio with average relative errors of 12.8%, 20.1%, and 10.9%, respectively. In a concert hall the average relative errors were 35.6%, 27.9%, and 36.6%, respectively. Table I shows that the average relative errors in reverberation time predictions using these formulas in the simulated classroom, fall more or less in the middle of both sets of average relative errors, with values of 21.5%, 24.7%, and 21.1%. However, a fundamental difference between both studies is that these reverberation formulas had consistently overpredicted reverberation times in the concert hall, while the results of the present study reveal that these same formulas have consistently underpredicted reverberation times in the simulated classroom.

Figure 4 shows that absorption exponents that give reverberation times longer than those predicted by using the Sabine absorption exponent would lead to more accurate predictions of conditions in the simulated classroom. However, Table I shows that the average relative errors produced by these absorption exponents are comparable to those produced using the Sabine and Eyring absorption exponents. The most accurate absorption exponents resulted in average relative errors in the range between 17% and 25%. Therefore, with the rather limited amount of experimental data available, it seems prudent not to single out any of these absorption exponents as more adequate because of similar average relative errors.

This reveals a considerable uncertainty in choosing a particular absorption exponent for predicting reverberation times for a given room condition. In other words, a given absorption exponent may predict the reverberation time accurately in one situation but fail in another. This is the main drawback of reporting average values. These results do not justify the need to use the more complex analytical expressions to predict reverberation times because they do not in general lead to greater accuracy. Because of its simplicity and average accuracy comparable to the best predictions, the Sabine/Eyring formula is concluded to be a reasonable choice among the analytical expressions compared here.

C. Accuracy of computer models

Both RAYNOISE and ODEON can be used with pure specular or with diffuse reflection procedures. Modeling surface reflections as partially diffuse, at least for the later reflections, is more realistic relative to actual conditions in rooms. It additionally provides greater flexibility for modeling, but at the same time introduces another variable that one must consider. However, data describing the diffusing properties of common room surfaces are simply nonexistent. Usually, in ray-based programs in which reflections are modeled as diffuse, the diffusion coefficient assigned to a given surface is treated as the probability that a given ray hitting the surface will be diffusely reflected. If the reflection happens to be diffusing instead of specular, the ideal Lambertian model determines the new ray direction and the intensity reaching the receivers.

Experience in dealing with diffuse reflections in ray-based computer programs is very limited. One approach is to start with a purely specular model, and to compare sound decays thus obtained with those derived from the classical Sabine/Eyring formula. It was found that in the case of lack of agreement, reverberation times predicted by a diffuse model could be made to approximately agree with those obtained from the classical reverberation formulas by arbitrary adjustments to the diffusion coefficients of various surfaces. This is in general easy to accomplish by a rather crude trial-and-error procedure, in which the surfaces that are assigned as diffuse reflectors and the respective diffusion coefficients are varied. However, no consistent general procedure could be established by analyzing the results thus obtained. Modeling reduces to an exercise of matching the computer results with those obtained from classical reverberation formulas. If one were to rely on these formulas to make the computer modeling successful, there would be no need for computer modeling, at least for predicting reverberation times.

The real advantage of computer models is to deal with nondiffuse fields where the classical Sabine formula may not be appropriate. Since these are to various degrees very common, an approach is required to model these rooms. The approach adopted by the present work was that of ''calibrating'' the diffuse model. The calibration procedure consisted of first modeling a room of ''similar characteristics'' for which the reverberation time was known, from measurements, for instance. If the specular model did not predict the measured reverberation time, then one hoped that a diffuse model could be found to approximate the expected results. The diffusion coefficients of the surfaces, considered as diffuse reflectors, were varied until predicted and measured reverberation times agreed within a certain accuracy. This approach seems realistic for classrooms because many classrooms have quite similar characteristics. However, it may not be applicable at the design stage of most types of new rooms, where a combination of scale models and computer models may be required to study the acoustical properties of the new room.

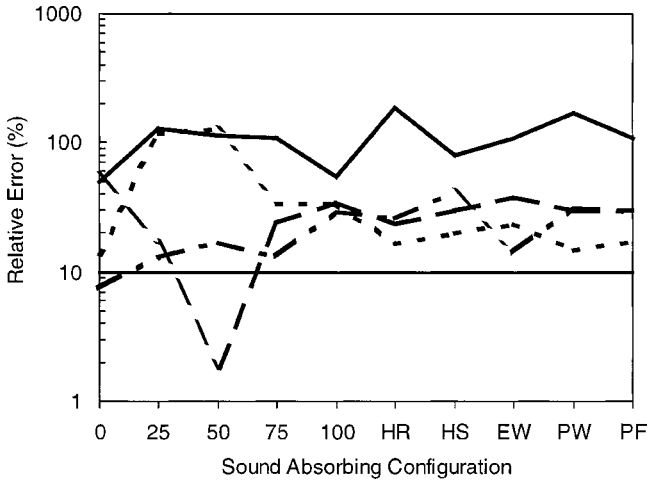

FIG. 5. Average relative errors in reverberation time predictions across the six octave bands from 125 Hz to 4 kHz, for each sound-absorbing configuration. Computer predictions using: (---) RAYNOISE specular model; (––) RAYNOISE diffuse model; (———) ODEON specular model; and (–·–·–) ODEON diffuse model. Also shown in this figure is a horizontal line across the plot area that corresponds to an accuracy of 10%.

In the present study, the classroom used for model calibration was the simulated classroom fitted with the sound-absorbing configuration (50). In both programs, sound decays varied not only with the diffusion coefficient but also according to the surfaces that are assigned as diffuse reflectors. A first attempt in the model calibration was to consider all the room surfaces as diffuse reflectors. In ODEON, however, a slightly smaller average relative error in reverberation time prediction was obtained by modeling only the ceiling and the front wall as such in all configurations. These same surfaces were then modeled as diffuse reflectors also in RAYNOISE.

Unlike ODEON, and in accord with physical reality, RAYNOISE treats the diffusion coefficient as a frequency-dependent quantity. This gives greater flexibility for model calibration with RAYNOISE. This characteristic allowed the average relative error in reverberation time prediction across the six octave frequency bands from 125 Hz to 4 kHz to be reduced to 1.8% in the room chosen for calibration. In ODEON, because the diffusion coefficient is set as a frequency-independent quantity, the average relative error could only be reduced to 17.1% in the same room.

Figure 5 shows the average relative error in reverberation time prediction for RAYNOISE and ODEON, across the six octave bands from 125 Hz to 4 kHz, using both specular and calibrated diffuse models in all configurations. This figure reveals that with both programs, neither the specular model nor the calibrated diffuse model could predict reverberation times in the simulated classroom with an accuracy of 10%, in any of the sound-absorbing configurations. The only exceptions are the ODEON diffuse model prediction for configuration (0), and the RAYNOISE diffuse model prediction for configuration (50). The latter is an expected and obvious result since this configuration was used to calibrate the diffuse model.

Figures 6 and 7 compare experimentally obtained reverberation times with those predicted by RAYNOISE and ODEON,

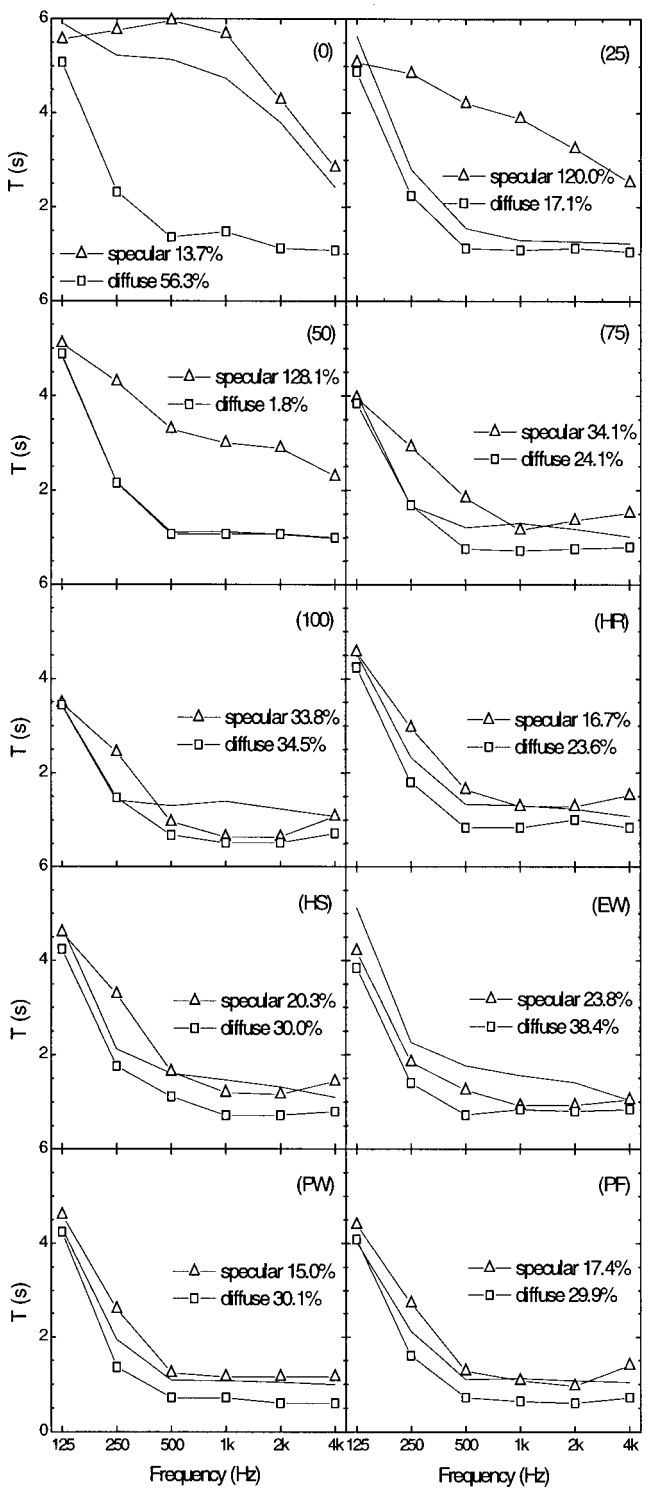

FIG. 6. (———) Experimental and RAYNOISE predictions of reverberation time. (△) RAYNOISE specular model; (□) RAYNOISE diffuse model. Indicated in each configuration is the average relative error of the prediction across the six octave bands from 125 Hz to 4 kHz.

respectively, using both specular and calibrated diffuse models. Figure 6 shows that, for some sound-absorbing configurations, the RAYNOISE specular model is a more accurate predictor of reverberation time than the diffuse model, while for others, the calibrated diffuse model predictions are more accurate. Figure 7, which shows ODEON predictions, reveals that the calibrated diffuse model is more accurate than the

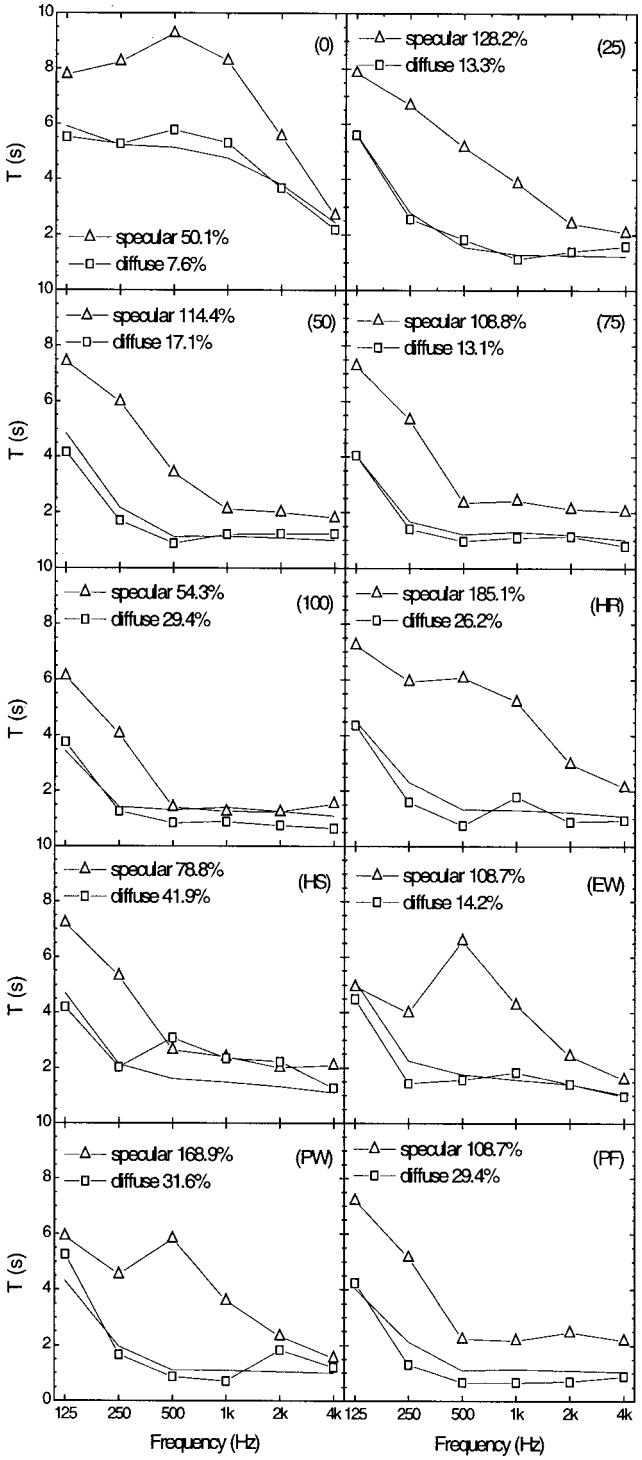

FIG. 7. (———) Experimental and ODEON predictions of reverberation time. (△) ODEON specular model; (□) ODEON diffuse model. Indicated in each configuration is the average relative error of the prediction across the six octave bands from 125 Hz to 4 kHz.

specular model in all configurations. Figure 7 also shows that the ODEON specular model consistently overpredicts reverberation times in the simulated classroom in all configurations.

Table II shows the overall average relative errors in reverberation time predictions for each computer program and reflection procedure. These average values do not include the room chosen for calibration—configuration (50). Similar to Table I, which gives the average relative errors of the different absorption exponents, Table II also shows that as more bands are included in the averages, the relative errors of the computer models are also reduced.

TABLE II. Overall average relative errors of the computer predictions of reverberation time for ten sound-absorbing configurations in the simulated classroom.

Computer program		Overall average relative error (%)		
		Frequency bands included in the averages		
		1 kHz	500 Hz–2 kHz	125 Hz–4 kHz
RAYNOISE 3.0	Specular	40.1	37.8	32.8
	Diffuse	44.7	42.7	31.6
ODEON 2.6	Specular	136.7	133.5	110.2
	Diffuse	29.5	30.8	23.0

The data in Table II do not provide a basis to rank the relative adequacy of the specular or the diffuse calculation procedures with RAYNOISE. This is because the RAYNOISE specular and calibrated diffuse models predict reverberation times with practically equal average relative errors, with values of 32.8% and 31.6%, respectively. The ODEON calibrated diffuse model gave the smallest average relative error of the computer predictions, with a value of 23.0%. On the other hand, the ODEON specular model gave the largest average relative error of the computer predictions, with a value of 110.2%.

Dance and Shield[12] also found that the average relative errors in reverberation time prediction of three computer programs in a concert hall were 14.0%, 14.3%, and 18.2%, using the standard absorption coefficients in the simulations. When the Millington absorption coefficients were used in the computer simulations, these errors were reduced, respectively, to 11.0%, 7.2%, and 11.7%. These errors are smaller than the smallest average relative error of the computer simulations obtained by the present study with the ODEON calibrated diffuse model (23.0% average relative error).

In an international round robin of 14 ray-based computer programs,[21] most programs predicted reverberation times in the 1-kHz octave band with relative errors between 5% and 10%, when absorption and diffusion coefficients were given. However, a considerably larger scatter of the results was obtained when the user had free choice of absorption coefficients.

D. Effect of sound-absorption treatments

Table III shows the average reverberation time at mid-frequencies for the ten sound-absorbing configurations in the simulated classroom. It can be seen that when sound absorption is added to the bare room [configuration (0)], a significant reduction in the average reverberation time is achieved, from 4.4 to 1.4 s, by covering 25% of the floor area with ceiling tiles [configuration (25)]. As more absorption is added, the corresponding reductions in the average reverberation times are not as significant. For instance, increasing absorption by a factor of 4 [from (25) to (100)] does not lower the average reverberation time by the same factor. In

TABLE III. Average reverberation times at midfrequencies (500 Hz–2 kHz) measured in the simulated classroom with different sound-absorbing configurations.

Sound-absorbing configuration	Average reverberation time at midfrequencies (500 Hz–1 kHz) (s)
(0)	4.4
(25)	1.4
(50)	1.1
(75)	1.2
(100)	1.3
(HR)	1.3
(HS)	1.4
(EW)	1.6
(PW)	1.1
(PF)	1.1

the simulated classroom, the corresponding reduction in the average reverberation time was from 1.4 to 1.3 s.

Also according to Table III, the shortest average reverberation time was not achieved when the room was most absorbing [configuration (100)]. The shortest average reverberation time, with a value of 1.1 s, was achieved when 50% of the floor area was covered [configuration (50)]. An average reverberation time value of 1.1 s was also achieved when the same amount of absorption that corresponds to configuration (50) was applied in other configurations [configurations (PW) and (PF)]. It is surprising that when this same amount of absorption was used in configurations (HR), (HS), and (EW), the average reverberation times were amongst the longest measured in the simulated classroom, with values of 1.3, 1.4, and 1.6 s, respectively. These results reveal that concentration of sound absorption on some room surfaces, as occurs in configurations (HR), (HS), and (EW), tends to produce longer reverberation times than those obtained when the same amount of absorption is more uniformly distributed, as in configurations (50), (PW), and (PF).

As a summary, the reverberation times that were measured in the simulated classroom for different sound-absorbing treatments show that increasing the amount of absorption does not necessarily produce reductions in reverberation time as predicted by the Sabine formula. This formula also predicts the same reverberation time for the same total absorption. Nevertheless, in some cases, different reverberation times were measured when the same amount of absorption was used in different configurations.

In a previous study,[8] a reverberation time of around 0.5 s was recommended for 100% speech intelligibility in very quiet classrooms. None of the absorptive treatments that was tested in the simulated classroom could produce the recommended reverberation time. As discussed above, the shortest average reverberation time at midfrequencies measured in the simulated classroom was 1.1 s, and it was not for the most absorbing configuration [configuration (100)]. This average reverberation time was measured by covering an area equal to 50% of the ceiling area in three different configurations [configurations (50), (PW), and (PF)].

V. SUMMARY AND CONCLUSIONS

The present study has evaluated the ability of several analytical expressions and two room acoustics computer programs to predict reverberation times measured in a simulated classroom. Although many reverberation time prediction schemes assume diffuse sound fields, these rarely occur and it is therefore important to evaluate predictions of reverberation times for more realistic conditions.

Increased sound scattering in the simulated classroom led to reduced reverberation times and better agreement with the predictions of the Sabine/Eyring formula. Increased scattering surfaces led to more diffuse conditions that better approximated the case of ideal diffusion on which these analytical expressions are based. However, even when the scattering frequency was increased up to 0.042 m^{-1}, complete agreement between measured and predicted values could not be achieved. It is therefore important that the conditions in the simulated classroom approximated those in a real unoccupied classroom. In these tests, conditions corresponded to a scattering frequency of 0.014 m^{-1} and this was assumed to represent conditions in a typical unoccupied classroom.

In the current evaluations of reverberation time predictions, it was assumed that a prediction accuracy of 10% would be satisfactory for most practical situations. However, none of the analytical expressions or the computer models could consistently predict reverberation times within this accuracy. Because these results were obtained for measurements in a simulated unoccupied classroom, they should not be generalized to other conditions.

The range of the average relative errors of the most accurate absorption exponents was found to lie approximately between 17% and 25%. The average relative error of the Sabine formula was 21.5%. In the simulated classroom, the Sabine formula consistently underpredicted reverberation times for all of the tested sound-absorbing configurations. The inaccuracy of the Sabine formula in the present case seems to be due to the sound field being less than ideally diffuse. Sound scattering was found to be a factor, but other factors including the amount and distribution of sound-absorbing material also appear to play a major role in the degree of diffusion of the sound field. There seems to be an interaction of these factors that results in unreliable predictions of reverberation times using the Sabine formula and other formulas based on the diffuse-field assumption.

Better reverberation time predictions were those that indicated longer reverberation times than the Sabine formula. However, none of the absorption exponents was within the required 10% accuracy and none could be singled out as more accurate for the ten different absorption configurations tested. They had similar average relative errors.

The RAYNOISE specular and calibrated diffuse models predicted reverberation times with similar average relative errors of 32.8% and 31.6%, respectively. Neither was more accurate than the other. Reverberation time predictions with the ODEON specular model were particularly inaccurate and the 110.2% average relative error of this method was the highest of all the predictive methods. However, the ODEON calibrated diffuse model consistently gave more accurate

predictions than the ODEON specular model and had the smallest average relative error of all of the computer model predictions. The average relative error of the ODEON calibrated diffuse model was 23.0%, which is comparable with the accuracy of the best analytical expressions.

Covering the total floor area of the simulated classroom with highly absorbing ceiling tiles was not sufficient to achieve the recommended reverberation time for classrooms of 0.5 s.[8] For this condition, the measured midfrequency reverberation time was 1.3 s. Three different configurations that covered the equivalent of half of the ceiling area reduced the midfrequency reverberation time to 1.1 s. Various special configurations of the absorbing material that have been recommended in previous studies were not found to be significant improvements.

ACKNOWLEDGMENTS

The first author is spending sabbatical leave, granted by the University of São Paulo, São Paulo, Brazil, with the Acoustic Group at the National Research Council—NRC Canada. The first author would like to acknowledge the personal financial support for the development of the classroom acoustic project currently underway, granted by Fundação de Amparo à Pesquisa do Estado de São Paulo—FAPESP. The generous donation of the sound-absorbing material by Ottawa Fibre is gratefully acknowledged, as is the assistance of Keith Lay in making the reverberation measurements.

[1] W. C. Sabine, *Collected Papers on Acoustics* (Peninsula, Los Altos, CA, 1992), pp. 43–52.
[2] C. F. Eyring, ''Methods of calculating the average coefficient of sound absorption,'' J. Acoust. Soc. Am. **4**, 178–192 (1933).
[3] G. Millington, ''A modified formula for reverberation,'' J. Acoust. Soc. Am. **4**, 69–82 (1932).
[4] L. Cremer and H. A. Müller, *Principles and Applications of Room Acoustics* (Applied Science, London, 1982), Vol. 1, p. 235.
[5] H. Kuttruff, ''Sound decay in enclosures with non-diffuse sound field,'' in *Proceedings of the Wallace Clement Sabine Centennial Symposium, Cambridge, MA, 5–7 June 1994* (Acoustical Society of America, Woodbury, NY), pp. 85–88.
[6] D. Fitzroy, ''Reverberation formula which seems to be more accurate with nonuniform distribution of absorption,'' J. Acoust. Soc. Am. **31**, 893–897 (1959).
[7] H. Arau-Puchades, ''An improved reverberation formula,'' Acustica **65**, 163–180 (1988).
[8] S. R. Bistafa and J. S. Bradley, ''Reverberation time and maximum background-noise level for classrooms from a comparative study of speech intelligibility metrics,'' J. Acoust. Soc. Am. **107**, 861–875 (2000).
[9] H. Kuttruff, *Room Acoustics* (Elsevier Applied Science, London, 1991), pp. 204–207, 123–128, 118–120, 255.
[10] RAYNOISE is registered trademark of LMS Numerical Technologies NV, Leuven, Belgium.
[11] ODEON is the main part of a room acoustic modeling system developed at the Department of Acoustic Technology, Technical University of Denmark, Lyngby, Denmark.
[12] S. M. Dance and B. M. Shield, ''Modeling of sound fields in enclosed spaces with absorbent room surfaces,'' Appl. Acoust. **58**, 1–18 (1999).
[13] H. Kuttruff, ''A simple iteration scheme for the computing of decay constants in enclosures with diffusely reflecting boundaries,'' J. Acoust. Soc. Am. **98**, 288–293 (1995).
[14] J. S. Bradley, ''An international comparison of room acoustics measurement systems,'' Report IR-714 (National Research Council Canada, Ottawa, Canada, 1996).
[15] M. Hodgson, ''On measures to increase sound-field diffuseness and the applicability of diffuse-field theory,'' J. Acoust. Soc. Am. **95**, 3651–3653 (1994).
[16] A. M. Ondet and J. L. Barbry, ''Modeling of sound propagation in fitted workshops using ray tracing,'' J. Acoust. Soc. Am. **85**, 787–796 (1989).
[17] E. Mommertz and M. Vorländer, ''Measurement of scattering coefficients of surfaces in the reverberation chamber and in the free field,'' in Proceedings of the 15th International Congress on Acoustics, Trondheim, Norway, 26–30 June 1995, pp. 577–580.
[18] H. A. Akil, ''The scattering of sound by fittings in industrial buildings,'' Ph.D. thesis, University of Liverpool, UK, 1995.
[19] G. Benedetto, E. Brosio, and R. Spagnolo, ''The effect of stationary diffusers in the measurement of sound absorption coefficients in a reverberation room: An experimental study,'' Appl. Acoust. **14**, 49–63 (1981).
[20] M. Hodgson, ''When is diffuse-field theory applicable?,'' Appl. Acoust. **49**, 197–207 (1996).
[21] M. Vorländer, ''International round robin on room acoustics computer simulations,'' in Proceedings of the 15th International Congress on Acoustics, Trondheim, Norway, 26–30 June 1995, pp. 689–692.

Comparison of an integral equation on energy and the ray-tracing technique in room acoustics

A. Le Bot[a] and A. Bocquillet
Laboratoire de Tribologie et Dynamique des Systèmes—UMR 5513 CNRS, École Centrale de Lyon, 36, Avenue Guy de Collongue 69131 BP163 Ecully, France

(Received 31 May 1999; revised 12 December 1999; revised 5 May 2000; accepted 5 June 2000)

This paper deals with a comparison of two room acoustic models. The first one is an integral formulation stemming from power balance and the second is the ray-tracing technique with a perfectly diffuse reflection law. The common assumptions to both models are the uncorrelated wave hypothesis and the perfectly diffuse reflection law. The latter allows the use of these methods for nondiffuse fields beyond the validity domain of Sabine's formula. Comparisons of numerical simulations performed with the softwares RAYON and CeReS point out that these results are close to each other and finally, a formal proof is proposed showing that both methods are actually equivalent. © *2000 Acoustical Society of America.* [S0001-4966(00)02309-2]

PACS numbers: 43.55.Ka, 43.55.Br, 43.50.Jh [JDQ]

INTRODUCTION

The high-frequency range in acoustics and structural vibrations is often considered with the help of two simplifying assumptions. The first consists of neglecting the effects of interference. As an immediate consequence, energies of traveling waves can be added. This fact explains why energy quantities are more often used as the primary variables of high-frequency models instead of kinetic variables. Justifications for this assumption are numerous and have been largely discussed in the literature.[1] Let us recall that these descriptions are well suited, especially when the modal density is high. The second hypothesis usually introduced is the diffuse-field assumption. Energy inside the system is uniformly and isotropically distributed. This crude simplification is surprisingly as much adapted to most current cases as their geometry is complex. In fact, the theoretical study of conditions that lead to a diffuse field is done by the mathematical theory of billiards.[2,3] This theory introduces the concept of mixing billiards for which two initially adjacent rays are arbitrarily distant in phase space after a sufficient time.[4] But it is well-known that the simplest billiards, such as rectangular or parallepipedic ones, are not mixing! The more the geometry of the system is complex, the more the mixing property is assured. Applied to room acoustics, the diffuse-field concept results in a very simple relationship for time-reverberation: Sabine's formula, the success and popularity of which have not decreased for a century. More recently and in structural vibration, the so-called Statistical Energy Analysis (SEA)[1] has given rise to increasing interest. The diffuse-field assumption is constantly used and allows the evaluation of exchanged powers in terms of the vibrational energy of adjacent sub-systems. Sabine's formula and SEA make use of energy balance, and take the form of simple relationships for well-chosen variables; time-reverberation for the former and energies of sub-systems for the latter. The diffuse-field assumption leads to a major simplification; the exact geometry of systems is of no importance. Only a few global parameters such as the areas and volumes of the systems matter.

Nevertheless, many authors have emphasized that the diffuse-field assumption is somewhat inadequate.[5] A perfect diffuse field cannot exist in the presence of absorbing walls because the isotropy imposes that energy flow should vanish everywhere, even in the vicinity of the walls. It is certainly the simplest approximation, whose efficiency results in useful relationships. However, it is sometimes necessary to account for anisotropy and inhomogeneous fields with an appropriate model. That case arises in the presence of highly absorbing walls, or rooms with one dimension much larger than the others, such as long corridors.[6]

For these unusual enclosures, the image-source method[7] and the ray-tracing technique[8] may be applied with efficiency. The diffuse-field assumption is no longer necessary, and the sound pressure level may be calculated for each observation point. On the other hand, the amount of calculation required is greater and, for instance, details of the geometry are taken into account. Many variations of the ray-tracing technique may be found in the literature: cones or rays, with or without phase, specular or diffuse reflection.[9–11] In this work, we are concerned with the approach which adopts the perfectly diffuse reflection law, namely Lambert's law. This law is valid for rough surfaces that cannot be described in a deterministic way, or for plane surfaces when a great number of rays impinge on them from all directions. Interference effects are neglected; that is to say, no phase is attached to rays or source magnitudes.

On this subject, one might also point out the method proposed by Kuttruff.[12] Under similar physical assumptions, a power balance at the boundary leads to an integral equation that determines the incident power. Carroll and Chien[13] solved this equation for spherical enclosures and showed how Sabine's formula should be modified. In a similar way, Miles[14] was interested in applying this method to rectangular enclosures and demonstrated that, after cutting-off the sound sources, and after a short instability period, ''the field will

[a]Electronic mail: lebot@mecasola.ec-lyon.fr

ultimately decay exponentially and at the same rate everywhere in the enclosure but it will not be diffuse during decay.'' This confirms the time-reverberation concept, as well as correcting Sabine's model. On the other hand, this method has been applied to structural vibrations in the steady state in Ref. 15. The coupling conditions between structural components involve reflection and transmission efficiencies whose mean values are also used in the calculation of coupling loss factors in SEA. All these studies emphasize the interest of this method concerning both the theoretical view and the numerical purpose.

The goal of this study is to compare results from geometrical acoustics with those of the integral method. To this end, two softwares have been used. One is the ray-tracing software RAYON designed by EDF; the second is the software CeReS especially built for the solving of the integral equation in vibroacoustic problems. Numerical simulations for some rooms are presented and predicted sound pressure level maps are compared.

I. INTEGRAL EQUATION ON ENERGY

The aim of this method is to determine the energy density W and the energy flow $\mathbf{I}$ resulting from sources in a domain Ω with boundary $\partial\Omega$. To this purpose, the fields due to direct radiation have to be calculated first. They are, respectively, denoted by $G(S,M)$ for the energy density at the observation point M induced by a unit excitation located at S, and $\mathbf{H}(S,M)$ for the energy flow in similar conditions. We introduce specific notations G and $\mathbf{H}$ for direct fields which will be frequently used in what follows, in order to avoid a confusion with complete fields W and $\mathbf{I}$ which generally result from a superposition of many direct fields. Only steady-state equations are considered, since numerical simulations for transient-state problems have not been carried out. At first one has to write the energy-balance relationship to be verified,

$$\mathrm{div}_M \cdot \mathbf{H}(S,M) + mcG(S,M) = \delta_S(M), \tag{1}$$

where the first term is the net outgoing power per volume, the second term is the power density being dissipated (m is the usual atmospheric absorption factor and c the velocity of sound) and the right hand side is the injected power. As the fields G and $\mathbf{H}$ propagate in an open space, they are related by a simple proportionality relationship,

$$\mathbf{H}(S,M) = cG(S,M)\mathbf{u}_{SM}, \tag{2}$$

where $\mathbf{u}_{SM}$ is the unit vector from S toward M. The solutions of Eqs. (1), (2) are[15]

$$G(S,M) = \frac{1}{4\pi c}\frac{e^{-mSM}}{SM^2}, \tag{3}$$

$$\mathbf{H}(S,M) = \frac{1}{4\pi}\frac{e^{-mSM}}{SM^2}\mathbf{u}_{SM}, \tag{4}$$

where SM denotes the distance between S and M. Thus the energy of the direct field decreases for two reasons. First, the exponential term is due to the atmospheric absorption and, second, the geometric expansion imposes the attenuation factor $1/SM^2$; that is, a decrease of 6 dB per doubling of distance.

The second step in developing the method is to find the complete fields W and $\mathbf{I}$ in a domain Ω with boundary $\partial\Omega$. Indeed they can be separated into direct fields previously determined, and reverberant fields caused by multiple reflections of energy impinging on the boundary. *All of these waves are assumed to be uncorrelated.* Many reasons enable to use such an assumption. For instance, the boundary may be irregular so that the exact position of the reflection is unknown. The phase of the reflected wave may then be considered as a random variable, and the results of the model are interpreted as the expected values of the actual variables. It should be remarked that such imperfection of boundary is most important, as the frequency increases, especially when the wavelength is comparable to the size of the irregularities. Another point of view is to consider that the exact positions of the excitation and observation points are imperfectly known. Furthermore, at high frequencies, a small displacement of one of these points leads to a drastically different response. Then a reasonable model should predict only the expected value of the response or, in other words, a local space-average of the response. A straightforward consequence of this hypothesis is that the energies of all waves may be summed without difficulties. This is a common fact in room acoustics, and explains why the use of energy quantities is so popular in high-frequency modeling. Referring to a classical integral representation, such as the Helmholtz–Kirchhoff formula, fields may be viewed as a superposition of spherical waves created by both actual sources located inside the domain Ω and a source layer located on the boundary $\partial\Omega$. A direct transposition on energy fields leads to the following representation formulas,

$$W(M) = \int_\Omega \rho(S)G(S,M)dS + \int_{\partial\Omega} \sigma(P,\theta_P)G(P,M)dP, \tag{5}$$

$$\mathbf{I}(M) = \int_\Omega \rho(S)\mathbf{H}(S,M)dS + \int_{\partial\Omega} \sigma(P,\theta_P)\mathbf{H}(P,M)dP, \tag{6}$$

where ρ is the magnitude of the actual sources, obviously known, and σ denotes the magnitude of the secondary sources, yet to be determined. The directivity function of the secondary sources depends on the angle θ_P between the outward normal at P and the emanating direction. We assume that *this directivity does not depend on the point P*. In other words, and following Joyce,[16] this is a memoryless law, since the reflected directions are independent of the incident direction. A strong consequence of the second law of thermodynamics is that the only memoryless directivity function permitted is Lambert's law,

$$\sigma(P,\theta_P) = \sigma(P)\cos\theta_P. \tag{7}$$

This is the law of perfectly diffuse reflection.

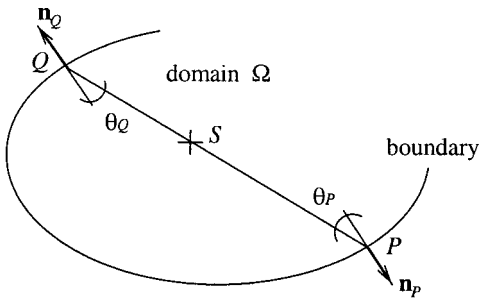

FIG. 1. Energy balance on the boundary $\partial\Omega$. The reflected power at P is the incident power stemming from actual sources S and other secondary sources Q, times the reflection coefficient $1-\alpha$.

The third step is to develop an equation for secondary sources σ. This is achieved by applying the power balance at a point P on the boundary (see Fig. 1). The boundary dissipates a part of the incident energy; therefore, an absorption coefficient α, defined as the ratio of reflected power to incident power, is then associated with it. The power balance is then

$$\mathcal{P}_{\text{refl}}=(1-\alpha)\mathcal{P}_{\text{inc}}, \tag{8}$$

where the left hand side is the reflected power at point P, and $\mathcal{P}_{\text{inc}}$ is the incident power of both the actual and secondary sources. The latter is the sum of all normal components of intensity vectors evaluated at P. Thus

$$\mathcal{P}_{\text{inc}}=\left[\int_{\Omega}\rho(S)\mathbf{H}(S,P)dS + \int_{\partial\Omega}\sigma(Q)\cos\theta_Q\mathbf{H}(Q,P)dQ\right]\cdot\mathbf{n}_P, \tag{9}$$

where $\mathbf{n}_P$ is the outward normal vector at point P. The reflected power can now be related to the source magnitude $\sigma(P)$. Consider a small hemisphere HS_ϵ of radius ϵ surrounding point P. The power flow crossing this hemisphere is

$$\mathcal{P}^{\epsilon}_{\text{refl}}=\sigma(P)\int_{HS_\epsilon}\frac{e^{-m\epsilon}}{4\pi\epsilon^2}\cos\theta_P\,dQ=\frac{\sigma(P)}{4}e^{-m\epsilon}. \tag{10}$$

The emitted power at point P is deduced by taking the limit for small ϵ:

$$\mathcal{P}_{\text{refl}}=\lim_{\epsilon\to 0}\mathcal{P}^{\epsilon}_{\text{refl}}=\frac{\sigma(P)}{4}. \tag{11}$$

The power balance Eq. (8) can now be rewritten,

$$\frac{\sigma(P)}{4}=(1-\alpha)\left[\int_{\Omega}\rho(S)\mathbf{H}(S,P)dS + \int_{\partial\Omega}\sigma(Q)\cos\theta_Q\mathbf{H}(Q,P)dQ\right]\cdot\mathbf{n}_P. \tag{12}$$

This is a Fredholm integral equation of the second kind on the layer σ.

The software CeReS has been especially written to solve this equation in various circumstances. In this text, Ω is an acoustical enclosure bounded by a surrounding surface $\partial\Omega$.

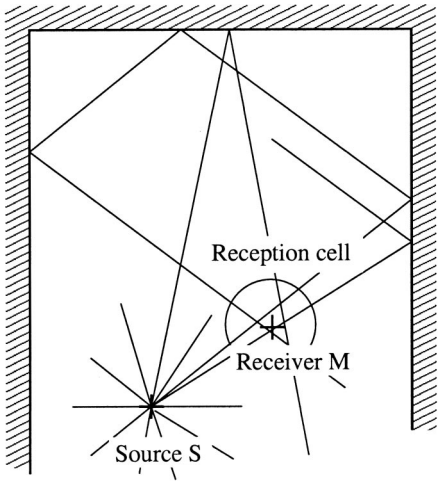

FIG. 2. Principle of the ray-tracing technique. Numerous rays are emitted from the source S, propagate in the room, are subjected to reflections on walls and, finally, arrive in the vicinity of the receiver point M. Energy at a point is evaluated by summing energies of all rays which cross the reception cell.

The CeReS software is able to treat other systems, such as assembled plates, for which the equations are slightly different from Eq. (12) (see Ref. 15). It seems that no attempt has previously been made to develop a software suitable for acoustical enclosures of arbitrary shape and size. The numerical simulations presented in Refs. 14, 12 are limited to parallepipedic enclosures.

In the CeReS software, the boundary is assumed to be constructed with polyhedra of arbitrary shape and size, and the domain may be convex or not. The boundary is discretized into a sufficient number of triangles, and a collocation method with constant elements is implemented. Numerical integrals are evaluated with a standard Gaussian quadrature. Note that these integrals are regular, unlike the singular integrals involved in the classical boundary-element method, allowing a fast and accurate computation. The stability and the robustness of the algorithm depend on the existence and uniqueness of solutions for Eq. (12). This question is investigated in the following section. The theoretical formalism introduced to this end will turn out to be very useful for comparison with the ray-tracing method.

II. EXISTENCE AND UNIQUENESS OF SOLUTION

In this section, we are interested in proving existence and uniqueness of solution for Eq. (12) in the special case of a convex domain Ω. To this end, the boundary $\partial\Omega$ is assumed to be compact. Equation (12) has no meaning if the outward normal does not exist. So, as a premise, we shall assume that such a normal vector exists almost everywhere. Now, let us write the integral operator involved in Eq. (12):

$$T:\sigma\mapsto\int_{\partial\Omega}\sigma(Q)K(Q,P)dQ, \tag{13}$$

where $K(Q,P)$ is the kernel expressed as follows:

$$K(Q,P)=[1-\alpha]\frac{e^{-mPQ}}{\pi PQ^2}\cos\theta_Q\cos\theta_P\geqslant 0 \tag{14}$$

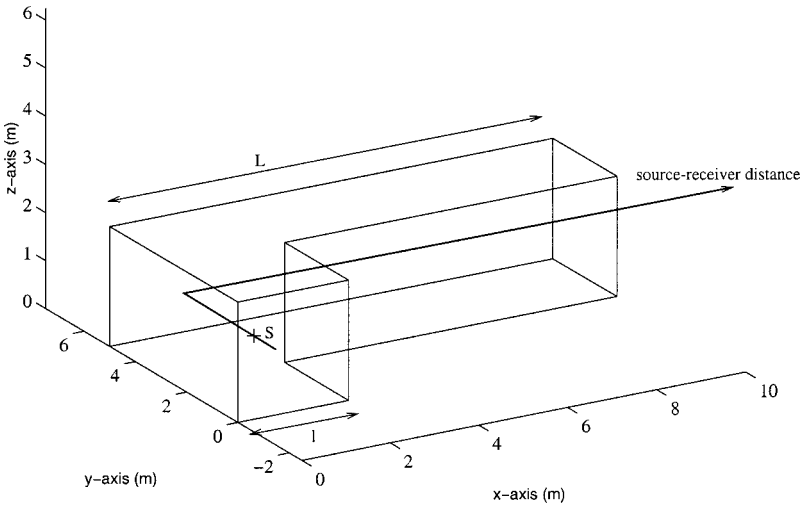

FIG. 3. View of the L-shaped room: the length ratio $\lambda = L/l$ may vary. The source–receiver distance is taken along the thick line.

which is nonnegative by virtue of the convex assumption. Equation (12) can now be rewritten:

$$(Id - T)\sigma = g, \tag{15}$$

where

$$g(P) = [1-\alpha]\int_{\partial\Omega} \rho(S)\,\frac{e^{-mSP}}{\pi SP^2}\cos\theta_P\, dS. \tag{16}$$

In practice, we are concerned with functions $\rho(S)$ which are finite sums of Dirac functions representing point sources inside the domain (not on the boundary). For these functions ρ, g is bounded over $\partial\Omega$. In the general case, we shall assume that function g is essentially bounded: $g \in L^{\infty}(\partial\Omega)$. A direct calculation gives

$$\int_{\partial\Omega} \frac{\cos\theta_P \cos\theta_Q}{\pi PQ^2}\, dQ = 1 \quad \text{for almost all} \quad P \in \partial\Omega. \tag{17}$$

So the partial function $Q \mapsto K(P,Q) \in L^1(\partial\Omega)$ is integrable over $\partial\Omega$; its resulting integral $P \mapsto \int_{\partial\Omega} K(P,Q)dQ \leqslant 1 \in L^{\infty}(\partial\Omega)$; the operator T maps the set $L^{\infty}(\partial\Omega)$ of all essentially bounded functions into itself. And the following inequality:

$$\|T\sigma\|_{\infty} \leqslant \left\| \int_{\partial\Omega} K\, dQ \right\|_{\infty} \|\sigma\|_{\infty} \tag{18}$$

shows that T is a continuous operator whose norm is

$$\|T\| = \left\| \int_{\partial\Omega} K\, dQ \right\|_{\infty} \leqslant \sup_{\partial\Omega}(1-\alpha). \tag{19}$$

For equality, check with $\sigma = 1$. Whenever $\inf_{\partial\Omega}\alpha > 0$, i.e., all the boundary is absorbing, the norm of the operator is less than one ($\|T\| < 1$) and, following a well-known result valid for all Banach algebra, and, in particular, the Banach algebra $L(L^{\infty}(\partial\Omega))$ of all continuous linear maps from $L^{\infty}(\partial\Omega)$ into itself, the operator $Id - T$ is invertible, so that Eq. (12) has a unique solution which can be written $\sigma = (Id-T)^{-1}g \in L^{\infty}(\partial\Omega)$.

III. A REVIEW OF THE RAY-TRACING TECHNIQUE

The ray-tracing technique is of considerable interest for room-acoustic studies. Numerous softwares are available which attest to the industrial efficiency of such an approach. There are several approaches for the ray-tracing technique but, for the sake of brievety, we just describe the one adopted in the software RAYON2.1 of EDF (France)[11,17] that we used for the numerical simulations presented in this paper.

The basis of the method is as follows (see Fig. 2): A great number N of rays start from each sound source with power magnitude ρ in any direction. For instance, when sources are isotropic, the number of rays in a specific direction depends only on the solid angle, all rays having the same initial energy $\epsilon(0) = \rho/cN$. Rays propagate in straight lines and lose energy because of the sound absorption. After a distance x, the energy of the rays is $\epsilon(x) = \rho e^{-mx}/cN$. Rays reflect from surfaces they encounter. At each reflection, they lose a part α of the incident energy so that, after n reflections and a total distance x, the residual energy is: $\epsilon(x) = \rho e^{-mx}\Pi_{i=1}^{n}(1-\alpha_i)/cN$. In RAYON, *reflections may be specular or diffuse*. In the first case, reflected angle is equal to incident angle whereas, in the second case, reflected direction is a probabilistic variable following the cosine law of Lambert. For the sake of consistency with the integral method of Sec. I, all numerical tests done with RAYON2.1 in the next section adopt Lambert's law of diffuse reflection.

One can finally calculate the energy at any observation point M inside the domain. Interference effects are not taken into account in the ray-tracing technique since multiple reflections of rays tend to uncorrelate the acoustic field. Thus energy at any spatial position is merely obtained by summing the energies of all rays reaching this location. Indeed, the probability for a ray to encounter the point is null. This difficulty is avoided in RAYON by introducing the notion of reception cells. These are spheres surrounding observation points. Energy density at any observation point is the energy contained in the reception cell—that is, the sum of energies of rays crossing the cell—divided by the sphere volume.

Rays are stopped when their energies become negligible or after a specified number of reflections. In both cases, re-

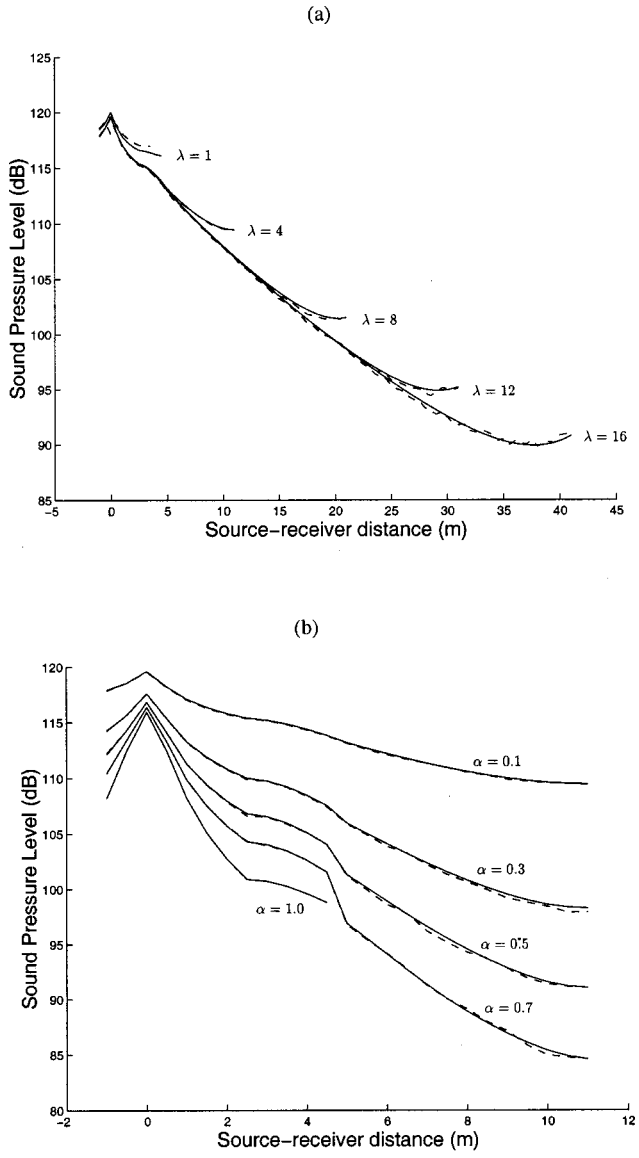

FIG. 4. Sound pressure level in a L-shaped room: comparison of sound pressure level (Lp-dB) from the ray-tracing technique (- -) and from the collocation method (——) as a function of the source–receiver distance along the thick line crossing the room (see Fig. 3). (a) SPL for different values of λ with a uniform absorption factor $\alpha = 0.1$. (b) SPL for different values of α for $\lambda = 4$.

sidual energy is considered to be diffuse and is equally distributed over the whole domain.

IV. NUMERICAL SIMULATIONS

We have systematically compared both codes for numerous examples. Two different rooms with diffuse reflection are presented in this section. The first example is intended to examine the effect of varying shape, from a parallepiped to a long corridor, and varying absorbing factors, from perfectly reflecting walls to totally absorbing walls. The second example is intended to demonstrate the applicability of the collocation method to more realistic rooms with complex shape and obstacles and floors contained inside. Our purpose is limited to the comparison of the two methods, and thus no experimental results are presented.

The first example is an L-shaped room with absorbing walls. Width and height are equal to $l = 2.5\,\mathrm{m}$, whereas the length L may vary. The nondimensional parameter $\lambda = L/l$ characterizes the shape of the enclosure. Its value starts from 1 for a parallepipedic room and increases to 16 for a long corridor. The source is located in the corner of the room at position $x = 1.25\,\mathrm{m}$, $y = 1.25\,\mathrm{m}$, $z = 1.7\,\mathrm{m}$ (see Fig. 3). The response is evaluated along a horizontal line centered inside the room. All of these features are shown in Fig. 3. The atmospheric absorption is $m = 0.0007\,\mathrm{m}^{-1}$ which is a typical value at 1000 Hz. The calculation with the RAYON software was performed with 64 000 rays, which may be reflected up to 100 times. Their residual energy is 0.01% of the initial energy. The calculation with CeReS software was performed with a mesh of triangles with areas of $0.4\,\mathrm{m}^2$. Results of the comparison are shown in Fig. 4. The top graph compares the sound pressure level, *Lp*, for different values of the ratio λ, with a uniform absorption factor $\alpha = 0.1$. The second graph compares the sound pressure level, *Lp*, for different absorption factors, with $\lambda = 4$. In the case of totally absorbing walls, $\alpha = 1$, the acoustical energy cannot reach any point in the right part of the room since it vanishes at the first reflection. All these comparisons show a good agreement between the ray-tracing technique and the integral method.

The second example is a hypothetical factory with sound-absorbing walls, floors and obstacles. The geometry is shown in Fig. 5. This is a nonconvex room with volume V

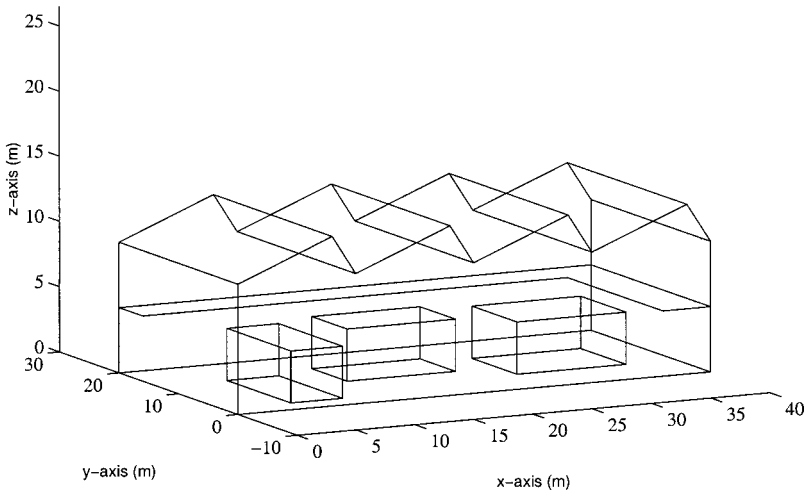

FIG. 5. View of the factory: ground, first floor and obstacles are located inside.

TABLE I. Absorption factors for the factory. Obstacles are numbered 1 to 3 from left to right in Fig. 5.

Surface	Absorption factor α	Area (m^2)
ground floor	0.05	627.4
first floor (both sides)	0.1	448
ceiling	0.05	972
front and back walls $x=0$ m, $x=40$ m	0.02	400
lateral walls $y=0$ m, $y=20$ m	0.02	460
surfaces of obstacle 1	0.2	169.1
surfaces of obstacle 2	0.3	176.8
surfaces of obstacle 3	0.25	204.3

$=8509\,m^3$ and total surface area $S=2305\,m^2$. The absorption factors are summarized in Table I. Floors, ceiling and walls are highly reflective; the absorption is essentially due to obstacles inside the factory. The area-averaged absorption coefficient is $\overline{\alpha}=0.12$. Thus the room constant is $R=\overline{\alpha}S/(1-\overline{\alpha})=319\,m^2$. The atmospheric absorption is $m=0.0007\,m^{-1}$. The critical radius is $r_c=(R/16\pi)^{1/2}=2.5\,m$; that gives an indication of how far from the source the direct field is predominant. Three sources are located in the factory. Their positions are: $x=5$ m, $y=5$ m, $z=1$ m for source 1; $x=20\,m$, $y=5$ m, $z=1$ m for source 2; and $x=35\,m$, $y=15\,m$, $z=1$ m for source 3. The power levels of these sources are 120 dB (1 W). The calculation with RAYON is performed with 64 000 rays which may be reflected up to 100 times. Their residual energy is 1% of the initial energy. The calculation with CeReS is performed with a mesh of 586 triangles for boundary elements. Results are shown in Figs. 6, 7 and 8 with, respectively, one, two and three sources active. In each case, the top map is the sound pressure level (Lp-dB) computed with RAYON on a plane 2 m above the ground floor, and the bottom map is computed with CeReS on the same plane. The additional graphs on the right com-

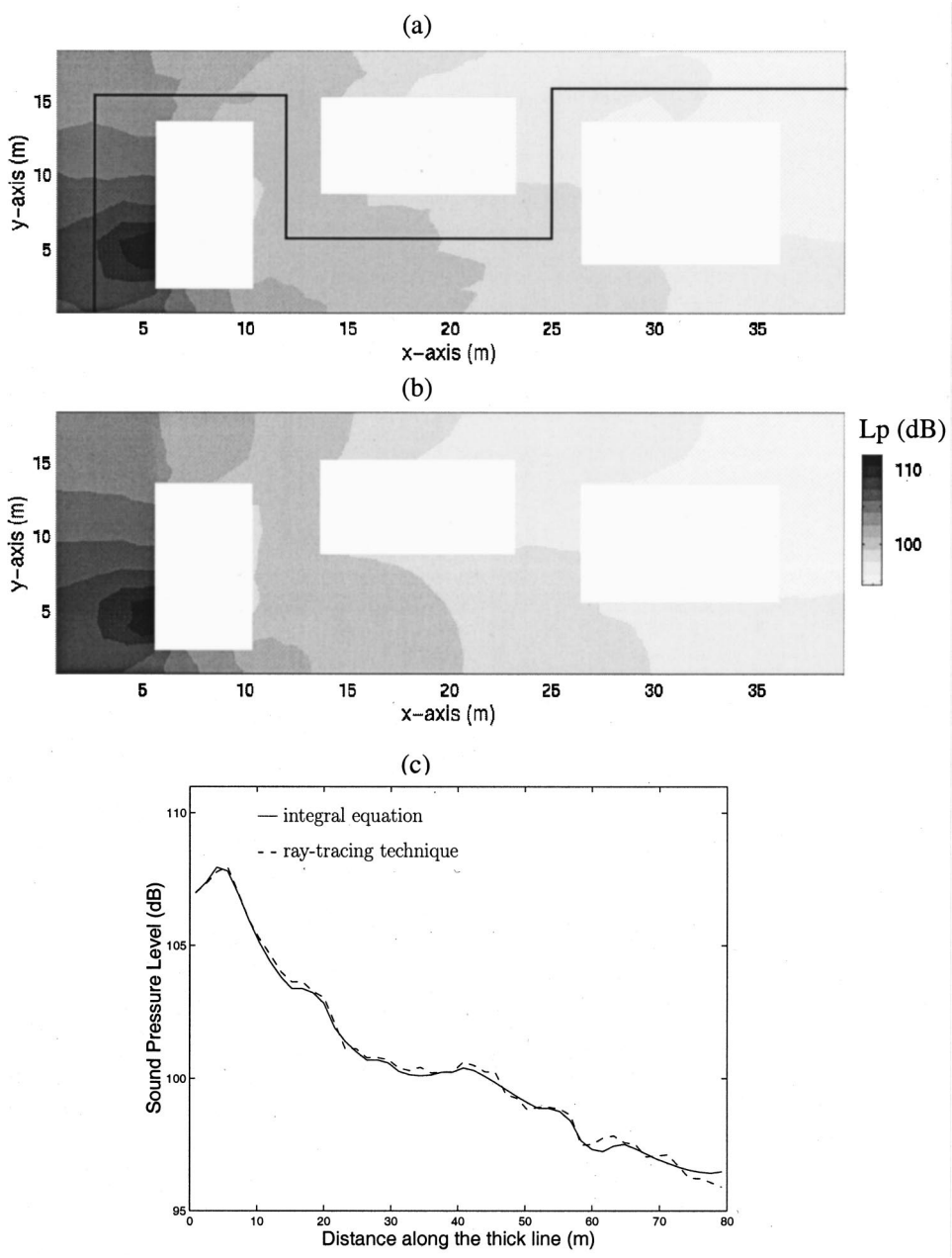

FIG. 6. Noise in a factory: comparison of sound pressure level (Lp) by (a) the ray-tracing technique, and by (b) the integral formulation on a horizontal receiver plane 2 m above the floor. (c) Direct comparison of SPL along the thick line. One source is active.

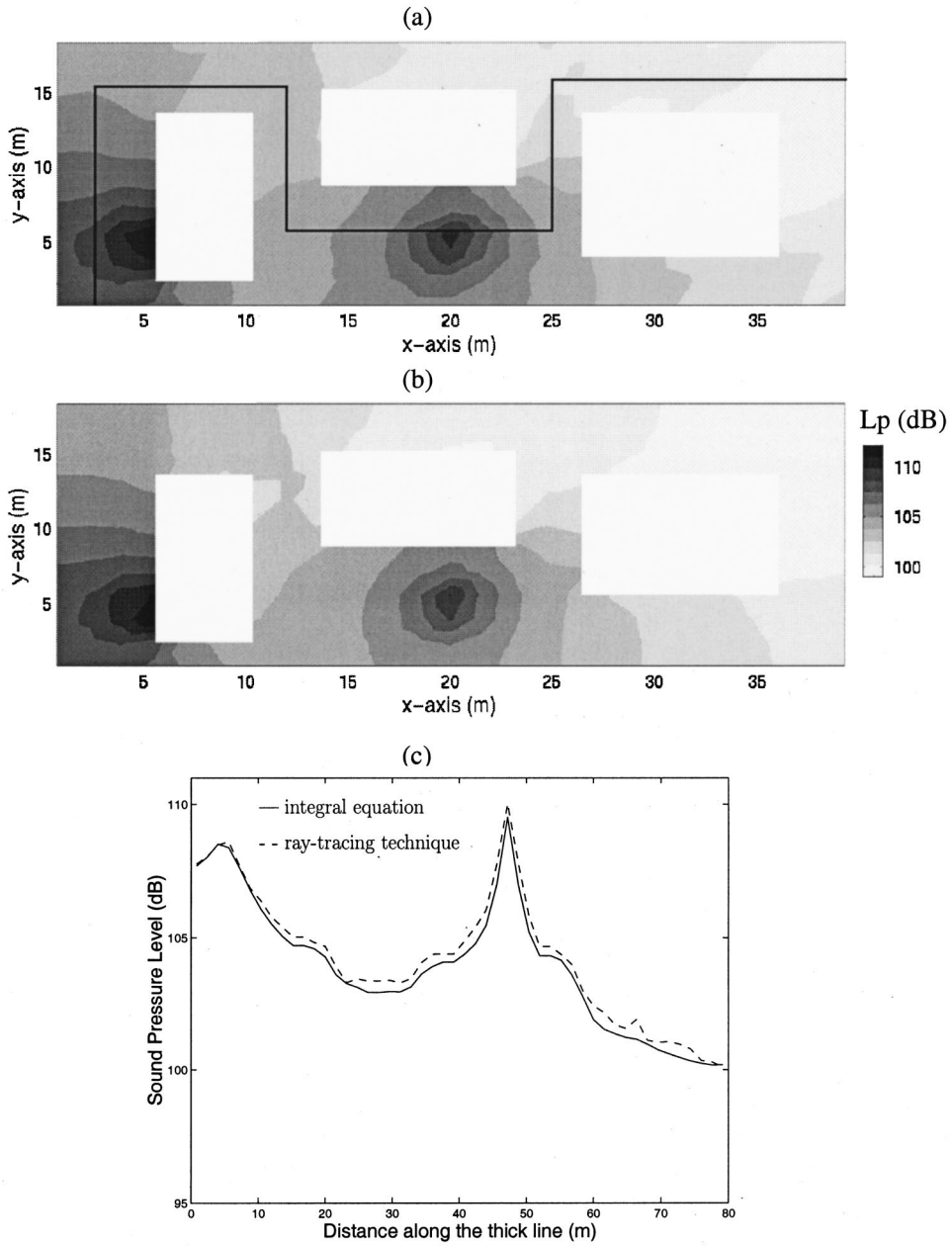

FIG. 7. Noise in a factory: same conditions as Fig. 6 with two sources active.

pare directly the SPL along the axis of the thick line visible on the maps.

Results of these examples highlight an excellent agreement between the two algorithms. Although the numerical schemes are quite different—Monte Carlo for RAYON and collocation method for CeReS—the physical assumptions are similar: interference effects neglected and diffuse reflection on walls. These numerical simulations suggest that the two methods are equivalent. The next section proposes a formal proof for this equivalence.

V. EQUIVALENCE OF THE METHODS

To prove that the ray-tracing technique is close to the integral method, consider the operator T defined in Sec. II. We saw that its norm is less than one (in the mathematical meaning of norm of bounded linear mappings of Banach spaces; see for instance Ref. 18, Chapter 4) and we deduced the existence and the uniqueness of the solution for Eq. (12). However, the fact that $\|T\|<1$ leads to an additional result. The operator $(Id-T)^{-1}$ can be developed into a Neumann series:

$$(Id-T)^{-1}=Id+T+T^2+\cdots+T^n+\cdots \in L(L^\infty(\partial\Omega)). \tag{20}$$

Thus

$$\sigma=g+Tg+T^2g+\cdots+T^ng+\cdots\in L^\infty(\partial\Omega). \tag{21}$$

At each point P, σ is the reflected power. It is the sum of the reflected part of the incident power of the direct field g and those of the powers after one reflection, two reflections, and so on. Finally, the energy inside the domain at M is

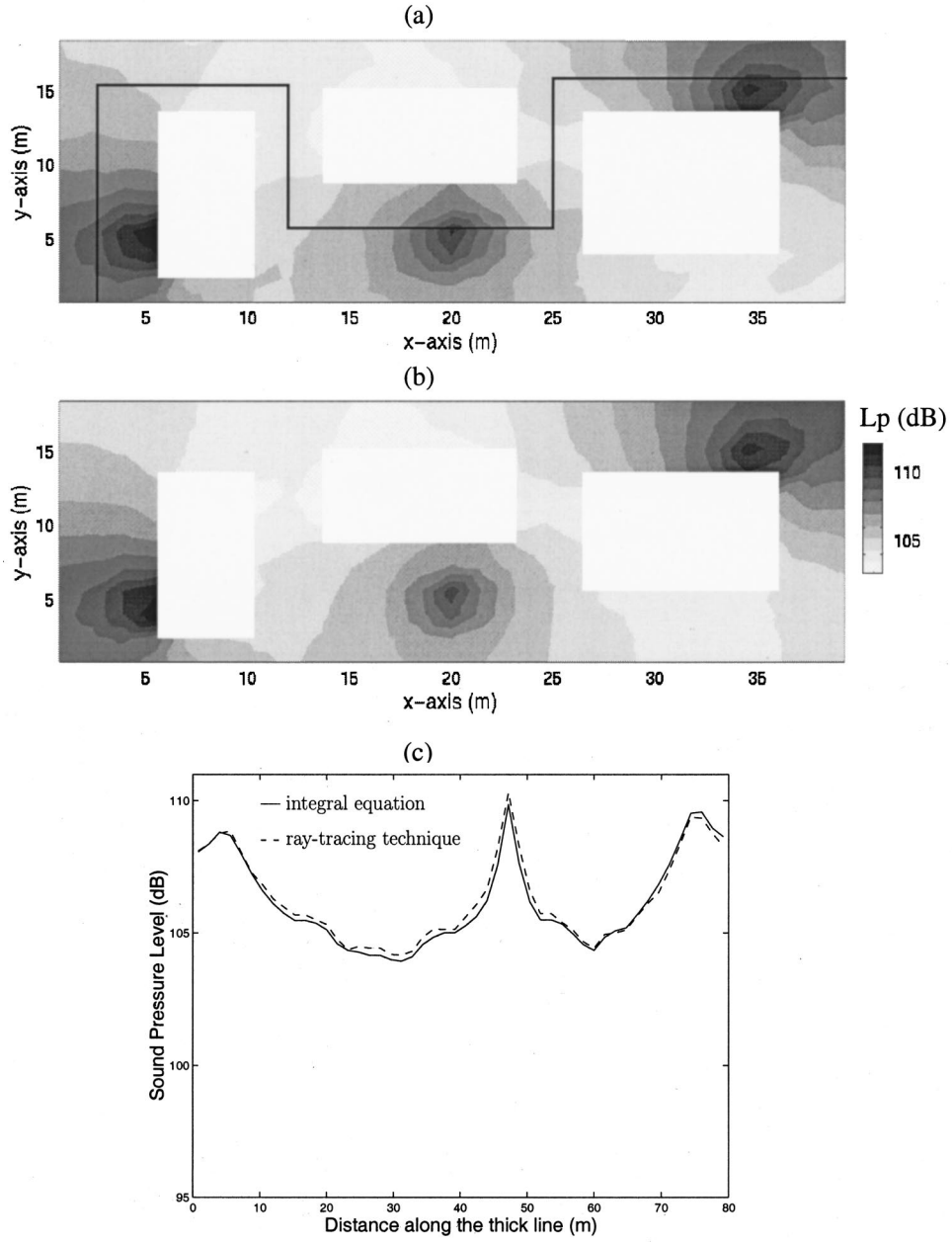

FIG. 8. Noise in a factory: same conditions as Fig. 6 with three sources active.

$$W(M)=\int_{\Omega}\rho(S)G(S,M)dS+\int_{\Omega}g\cos\theta_P G(P,M)dP+\int_{\Omega}Tg\cos\theta_P G(P,M)dP+\cdots+\int_{\Omega}T^n g\cos\theta_P G(P,M)dP+\cdots, \quad (22)$$

and we find that the energy at M is the sum of the energy of the direct field and the energies carried by rays which have been reflected once, twice, and so on. It is clear from this development how the ray algorithm is hidden in the integral equation (12). The ray-tracing technique is seen to be a numerical evaluation by the Monte Carlo method of the above integrals Eq. (22).

VI. CONCLUSION

In this study, we have compared results of two methods for calculating acoustic pressure fields in rooms. The first is the well-known ray-tracing technique; the second is based on an integral equation obtained by balancing powers at any points of the boundary.

The methods were implemented into softwares called RAYON and CeReS that can solve all cases of acoustic enclosures limited by arbitrary polyhedra. The numerical examples that we treated show that the two methods give identical results. Actually, both methods are based on the same physical assumptions, which are energy superposition and diffuse reflection.

The formal proof of the equivalence of the two methods stems from the Neumann development of the integral operator. This has been possible because the norm of the operator

is less than one. The ray-tracing technique is seen be a numerical method for the computation of the integrals Eq. (22) by the Monte Carlo procedure, whereas the CeReS software uses a collocation method for the evaluation of the same integrals.

It is not clear whether the numerical method has advantages over the other method. Computing times for the RAYON and CeReS softwares are similar. The ray-tracing technique is simpler to implement. In any case, this method is well established, and highly optimized algorithms are available.

The advantages of the integral method are rather theoretical. The formulation is continuous, in contrast to the discrete description of the ray-tracing method. In addition, with the integral equation, we have the use of an equation that has a closed-form solution in contrast to the ray-tracing technique that only leads to numerical solutions. For instance, in Ref. 13, Caroll and Chien give a closed-form solution for the energy field inside a spherical enclosure. It would be very difficult to obtain such a result with the ray-tracing technique.

ACKNOWLEDGMENTS

The authors gratefully acknowledge L. Ricol and E. Luzzato (EDF) for their advice, numerical computations with RAYON, and financial support.

[1] R. H. Lyon, *Statistical Energy Analysis of Dynamical Systems: Theory and Application* (MIT Press, Cambridge, MA, 1975).
[2] M. Berger, ''La mathématique du billard,'' Pour la Science **163**, 76–85 (1991).
[3] V. I. Arnold and A. Avez, *Problèmes Ergodiques de la Mécanique Classique* (Gauthier-Villars, 1967).
[4] J. D. Polack, ''Playing billiards in the concert hall: The mathematical foundations of geometrical acoustics,'' Appl. Acoust. **38**, 235–244 (1993).
[5] H. Kuttruff, *Room Acoustics*, 3rd ed. (Elsevier, New York, 1991), p. 102.
[6] J. Kang, ''Reverberation in rectangular long enclosures with geometrically reflecting boundaries,'' Acust. Acta Acust. **82**, 509–516 (1996).
[7] J. Borish, ''Extension of the image model to arbitrary polyhedra,'' J. Acoust. Soc. Am. **75**, 1827–1836 (1984).
[8] A. Krostad, S. Strom, and S. Sorsdal, ''Calculating of the acoustical room response by the use of a ray-tracing technique,'' J. Sound Vib. **8**, 118–125 (1968).
[9] J. L. Barbry, ''Techniques des images et des rayons (locaux vides),'' *Publication de l'Institut National de Recherche et de Sécurité*, 51 (1984).
[10] D. Maercke and J. Martin, ''The prediction of echograms and impulse responses within the epidaure software,'' Appl. Acoust. **38**, 93–114 (1993).
[11] L. Ricol and F. Junker, ''A ray tracing software: RAYON2.0,'' in *Euro-Noise 95, Lyon France*, pp. 49–54, 1995.
[12] H. Kuttruff, ''A simple iteration scheme for the computation of decay constants in enclosures with diffusely reflecting boundaries,'' J. Acoust. Soc. Am. **98**, 288–293 (1995).
[13] M. M. Carroll and C. F. Chien, ''Decay of reverberent sound in a spherical enclosure,'' J. Acoust. Soc. Am. **62**, 1442–1446 (1977).
[14] R. N. Miles, ''Sound field in a rectangular enclosure with diffusely reflecting boundaries,'' J. Sound Vib. **92**, 203–226 (1984).
[15] A. Le Bot, ''A vibroacoustic model for high frequency analysis,'' J. Sound Vib. **211**, 537–654 (1998).
[16] W. B. Joyce, ''Sabine's reverberation time and ergodic auditoriums,'' J. Acoust. Soc. Am. **58**, 643–655 (1975).
[17] E. Luzzato and D. Taillifet, ''Les modèles de l'acoustique prévisionnelle intérieure,'' *EDF-Bulletin de la Direction des Études et Recherches*, 1 Série C 5–37 (1988).
[18] W. Rudin, *Functional Analysis* (McGraw-Hill, New York, 1991).

Application of a finite-element model to low-frequency sound insulation in dwellings

Sophie P. S. Maluski[a] and Barry M. Gibbs
Acoustics Research Unit, School of Architecture and Building Engineering, The University of Liverpool, Liverpool L69 3BX, United Kingdom

(Received 20 October 1999; accepted for publication 18 July 2000)

The sound transmission between adjacent rooms has been modeled using a finite-element method. Predicted sound-level difference gave good agreement with experimental data using a full-scale and a quarter-scale model. Results show that the sound insulation characteristics of a party wall at low frequencies strongly depend on the modal characteristics of the sound field of both rooms and of the partition. The effect of three edge conditions of the separating wall on the sound-level difference at low frequencies was examined: simply supported, clamped, and a combination of clamped and simply supported. It is demonstrated that a clamped partition provides greater sound-level difference at low frequencies than a simply supported. It also is confirmed that the sound-pressure level difference is lower in equal room than in unequal room configurations. © *2000 Acoustical Society of America.* [S0001-4966(00)05510-7]

PACS numbers: 43.55.Rg, 43.55.Ti [JDQ]

I. INTRODUCTION

Noise from adjoining dwellings increasingly is recognized to occur below 100 Hz due to powerful modern hi-fi and home cinema systems with enhanced bass response.[1,2] Laboratory measurements at these frequencies are known to be highly variable, because of the nondiffuse sound fields in the source room and in the receiving room.[3–5] The room resonances also are pronounced because the effects of room absorption are less at low frequencies than at mid- and high frequencies. Rooms in dwellings are much smaller than the standard volumes in laboratories and the modal character of the sound fields is even more influential. Even if laboratory measurement conditions could be adjusted to reduce modal effects,[6,7] the sound reduction index obtained could not simply translate to the sound-level difference in the field.

Analytical and numerical methods have been employed in previous studies of the sound insulation of separating (party) walls in simulated test and field conditions.[8,9] Using analytical methods[10–15] and finite-element methods (FEM),[16–19] the effect of room dimension on the sound insulation of a party wall has been considered. The reliability of the methods is strongly dependent on the way the model is defined, but good agreements between prediction and measurement have been obtained.[11,12,14] Using these methods, it has been demonstrated that the sound-level difference between rooms is not only a characteristic of the party wall, but also of the room configuration. However, in previous studies, the party walls were modeled as simply supported[17,18] or as mass controlled.

The work reported here is of an investigation using FEM of the effect of wall-edge condition on the sound insulation of party walls between rooms of volume less than $50m^3$, at low frequencies. The *in situ* sound insulation properties of the party wall are expressed as the sound-pressure level difference between rooms, thereby eliminating the need of initially estimating the reverberation time, which is problematic at low frequencies.[20–22] The selected FEM model was validated by comparing the predicted with the measured frequency response of a full-scale and a 1:4 scale room. In addition, comparisons were made for the sound-pressure level difference between 1:4 scale model rooms. An investigation then followed of the effect of edge conditions on the sound-pressure level difference across masonry walls and of the effect of room configuration.

II. EFFECT OF EDGE CONDITION

Although the FEM model could include party wall-edge conditions, ranging from the simply supported to the clamped, it was not immediately obvious how real masonry walls should be treated. Therefore, as a prelude to the main study, the structural eigenfrequencies of two full-scale walls were measured and compared with the expected eigenfrequencies for a range of classical edge conditions.

Two brick and mortar walls were used with dimensions $2.88\times2.49\times0.115$ m and $1.84\times2.49\times0.115$ m. The brick dimensions were $0.223\times0.180\times0.070$ m and the mortar joints were typically 13 mm. Both walls were bonded into side walls of the same brickwork, and joined with concrete floor and roof slabs. An electrodynamic shaker was attached at a position which did not correspond to expected vibrational nodes, within a frequency range 0–200 Hz. An accelerometer was used to record the acceleration amplitudes at points on a 0.300×0.355-m grid for the first wall and on a 0.305×0.250-m grid for the second. The measured signal was displayed on an oscilloscope and compared with a reference signal. The nodal lines were determined when the measured signal was a minimum and/or when the measured signal changed phase with respect to the reference signal. By this method, it was possible to identify modes (1,1), (2,1), (3,1), and (1,3) for the first wall and modes (1,1), (1,2), (2,1), (2,2), and (1,3) for the second.

[a]Electronic mail: S.Maluski@liv.ac.uk

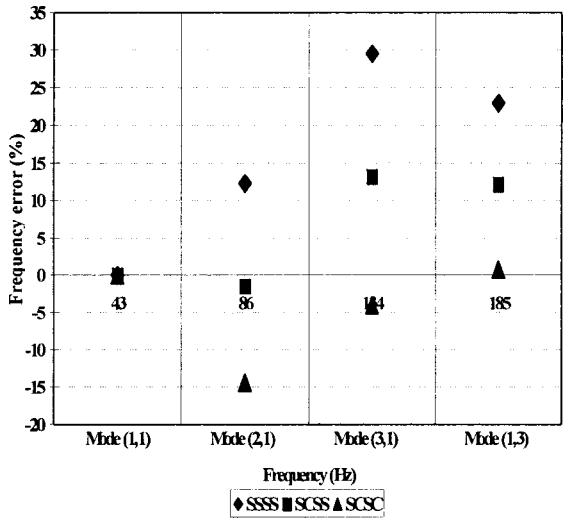

FIG. 1. Frequency error for a 2.88×2.49×0.115-m brick wall.

In order to distinguish the likely corresponding edge conditions, the eigenfrequencies and their order were compared with theoretical prediction according to Leissa.[23] It was assumed that the two walls are isotropic, although it was recognized that they had different bending stiffness in the vertical and horizontal directions due to the differences in the number of mortar joints per unit length. The properties of the wall being unknown, the factor containing the stiffness and the surface density was calculated from the eigenfrequencies of the mode (1,1). The edge conditions were identified by calculating the frequency error ε, obtained between the theoretical and measured eigenfrequencies for simply supported (SSSS), simply supported with one clamped edge (SCSS), simply supported with two clamped edges (SCSC), as

$$\varepsilon = \frac{\text{predicted value} - \text{measured value}}{\text{predicted value}} \times 100. \tag{1}$$

Figures 1 and 2 display the frequency error for the first and second walls, respectively. Large discrepancies result if all edges are assumed simply supported. The smallest discrepancies are obtained when the wall is assumed to have

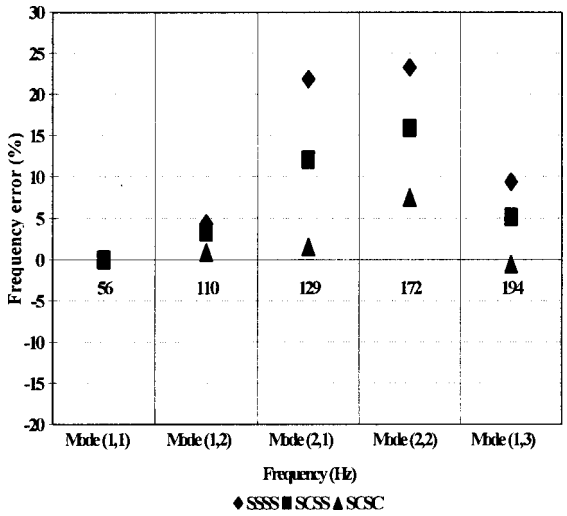

FIG. 2. Frequency error for a 1.84×2.49×0.115-m brick wall.

two simply supported edges with two clamped edges. The edge conditions of a typical party wall therefore lie between simply supported and clamped, a phenomenon already observed by Balike.[24] The walls investigated formed corner junctions and it was recognized that party walls would form T- or cross junctions with the side walls and thus have a stiffer edge constraint. The approach, therefore, was to investigate the range of possible edge conditions likely, including simply supported, clamped, and mixed. The real conditions could be assumed to lie somewhere in this range.

III. TWO-ROOM MODEL

A. Acoustic field

The sound pressure throughout the volume of an enclosure with the dimensions L_x, L_y, and L_z is governed by the wave equation[25]

$$\frac{\partial^2 p}{\partial x^2} + \frac{\partial^2 p}{\partial y^2} + \frac{\partial^2 p}{\partial z^2} = \frac{1}{c_0^2}\frac{\partial^2 p}{\partial t^2}, \tag{2}$$

where p is the pressure, t is the time, and c is the speed of sound in air.

Equation (2) can be rewritten as a Helmholtz equation

$$\nabla^2 p + k^2 p = 0, \tag{3}$$

where $k = 2\pi f/c$.

In order to obtain the normal modes of the enclosure, the six surfaces were assumed hard, i.e., the air particle velocity is equal to zero and the variation of the pressure normal to the surface of the walls also is equal to zero

$$\frac{\partial p}{\partial n} = 0, \tag{4}$$

where ∂n is the normal to the surface of the wall.

Using separable functions, the boundary condition is satisfied by the form

$$p = p_o \cos\left[\frac{\pi n_x x}{L_x}\right]\cos\left[\frac{\pi n_y x}{L_y}\right]\cos\left[\frac{\pi n_z x}{L_z}\right], \tag{5}$$

for $0 \leqslant x \leqslant L_x$, $0 \leqslant y \leqslant L_y$, $0 \leqslant z \leqslant L_z$ where n_x, n_y, n_z are integers and p_o is the maximum pressure amplitude.

The corresponding wave number components are

$$k_x = \frac{\pi n_x}{L_x}, \quad k_y = \frac{\pi n_y}{L_y}, \quad k_z = \frac{\pi n_z}{L_z}, \tag{6}$$

with

$$k^2 = k_x^2 + k_y^2 + k_z^2. \tag{7}$$

The eigenfrequencies can then be calculated from Eq. (7), where

$$f_{n_x n_y n_z} = (c/2)[(n_x/L_x)^2 + (n_y/L_y)^2 + (n_z/L_z)^2]^{1/2}. \tag{8}$$

The acoustic field can be discretized into finite elements,[26] by considering the pressure function p in each element as

$$\{p\} = [N]_e \{p\}_e, \tag{9}$$

where $\{p\}_e$ are the nodal values of the pressure function associated with the element and $[N]_e$ is a listing of so-called shape functions of the coordinates only.

Using a Rayleigh–Ritz method, which considers the total acoustic sound energy as the sum of the acoustic potential energy and the acoustic kinetic energy,[27] Eq. (9), Eq. (3) can then be discretized to give a matrix equation of the form

$$([K]-\omega^2[M])\{p\}=-i\rho_0\omega\{Q\}, \tag{10}$$

where K is the stiffness matrix and M is the mass matrix, where $\{p\}$ and $\{Q\}$ are the amplitudes of nodal pressures and flows, respectively. The two matrices are only calculated once and are independent of the frequency.

The eigenfrequencies f of the enclosure are obtained when there is no acoustic force $\{Q\}=0$

$$[K]-\omega^2[M]=0. \tag{11}$$

The frequency response of the enclosure is calculated according to Eq. (10). This is called the acoustic finite element (AFE) method.[28]

B. Structural field

The wall separating the two rooms was modeled as a finite isotropic panel. According to Cremer,[29] the wall can be considered as a thin plate when $\lambda_b \geqslant 6h$, where λ_b is the governing bending wavelength and h is the wall thickness. Thus, a wall of 200-mm brick can be assumed to be a thin plate below 619 Hz. Such a condition is confirmed by Ljunggren,[30] who was able to assume a lower limit for thin plate theory as $\lambda_b \geqslant 2h$.

The vibration displacement w of the wall[23,31] is expressed as

$$B\left(\frac{\partial^2 w}{\partial y^2}+\frac{\partial^2 w}{\partial z^2}\right)^2=-\rho_s\frac{\partial^2 w}{\partial t^2}, \tag{12}$$

where ρ_s is the mass per unit area, B is the bending stiffness where $B=Eh^3/12(1-\nu^2)$, E is the Young's modulus, and ν is Poisson's ratio.

A solution of this equation is

$$w(y,z,t)=\tilde{w}\exp[j(\omega t-k_y y-k_z z)], \tag{13}$$

where $\tilde{w}$ is the maximum amplitude displacement and

$$k_y^2+k_z^2=k_b^2=(\omega^2\rho_s/B)^{1/2}, \tag{14}$$

where k_b is the free-bending wave number at angular frequency ω.

The rectangular wall initially was assumed simply supported, i.e., no translational displacement at the edges. The normal vibration velocity distribution takes the form

$$v(y,z)=v_{n_y n_z}\sin[\pi n_y y/L_y]\sin[\pi n_z z/L_z], \tag{15}$$

where L_y and L_z are the panel dimensions, n_y, n_z are integers, and $0\leqslant y\leqslant L_y$, $0\leqslant z\leqslant L_z$, and $k_y=\pi n_y/L_y$, $k_z=\pi n_z/L_z$.

Substituting k_y and k_z into Eq. (14), the natural frequencies of a simply supported wall are given by[23]

$$f_{n_y n_z}=\frac{\pi}{2}\left(\frac{B}{\rho_s}\right)^{1/2}\left[\left(\frac{n_y}{L_y}\right)^2+\left(\frac{n_z}{L_z}\right)^2\right]. \tag{16}$$

Using a variational method,[27] the thin panel is also discretized into finite elements and gives an equation of a form

$$([K_s]-\omega^2[M_s])\{w\}=-j\rho_0\omega\{F\}, \tag{17}$$

where $[K_s]$ and $[M_s]$ are the stiffness and the mass matrices, respectively, $\{w\}$ is the displacement vector, and $\{F\}$ is the force applied to the surface of the wall.

As for the acoustic modes, the structural eigenfrequencies are obtained when no force is applied on the surface of the wall, i.e., $j\rho_0\omega\{F\}=0$

$$([K_s]-\omega^2[M_s])\{w\}=0. \tag{18}$$

Again, K_s and M_s are both calculated only once. The numerical method used to define the structural modes and the displacements is called the structural finite-element (SFE) method.[28]

C. Sound transmission between rooms

Sound transmission between two rooms is modeled by taking into account the sound fields of the source room and of the receiving room, the structural behavior of the party wall and the coupling. A link is formed between the structural and acoustical systems to model the sound transmission. Equations (10) and (18) are grouped into a global coupled system of equations

$$\begin{bmatrix} K_s-\omega^2 M_s & \mathbf{C}^t \\ \mathbf{C} & K-\omega^2 M \end{bmatrix}\begin{Bmatrix} w \\ p \end{Bmatrix}=\begin{bmatrix} Q \\ F \end{bmatrix}, \tag{19}$$

where $\mathbf{C}$ is the geometrical coupling matrix.

The acoustic model and the structural model are subdivided into connected finite elements. The number of elements is dependent upon the upper frequency of interest with the initial assumption that six elements would be required to properly represent the pressure/displacement over the governing wavelength.[32] If the number of elements is too few, then numerical errors result,[33] if too large, computer processing time becomes too long. In the investigation described here, the simulation run was longer than processing time, since the network system was shared with other users. Consequently, an optimum between accuracy of simulation and required CPU power was required. It was found that for dimensions representative of rooms in attached dwellings, $4\times4\times2.5$ m and $3.5\times4\times2.5$ m, the difference between FEM predicted eigenfrequencies and values obtained from Eq. (8) was less than 10% for an 8-mesh model, i.e., 8^3 elements.[34] For a brick party wall, the error was less than 10% for an 11-mesh model, i.e., 11^3 elements. However, for the software package employed, both mesh sizes had to be the same when linking the acoustic model with the structural model.[28] By selecting the 10 AFE mesh model, the simulation ran within an error of 7%. When the panel was modeled with a 10-mesh model, the simulation ran within an error of 8%. The coupled system was therefore modeled using a 10-mesh model for room and party wall.

IV. VALIDATION

The results of the FEM model were first compared with measurements of a 1:4 scale model of a single room of di-

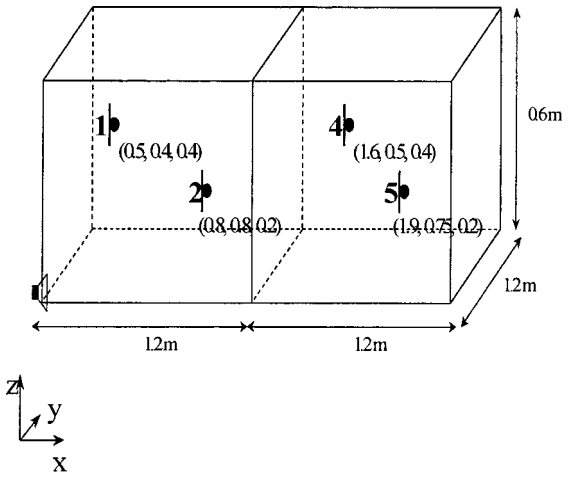

FIG. 3. Dimensions of the model transmission rooms, with microphone positions indicated.

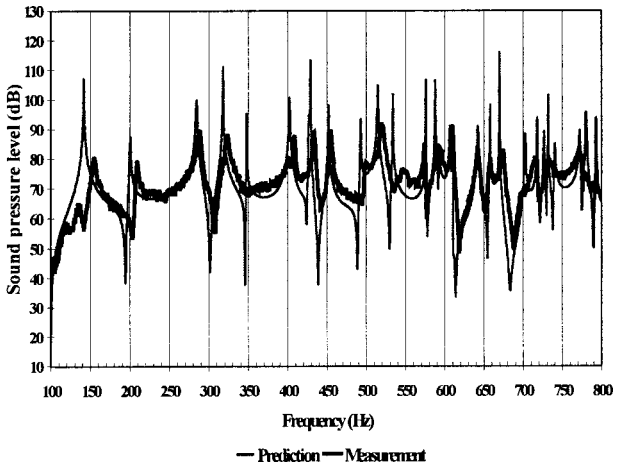

FIG. 4. Frequency response at microphone position 1.

mensions 1.2×1.2×0.6 m. The measurement bandwidth was 100–800 Hz, corresponding to 25–200 Hz, full scale. The enclosure mesh model was designed using P3/PATRAN,[35] then transferred into SYSNOISE 5.3 where the values of mass density and sound velocity were assigned to the sound field of the enclosure. Absorption was not included at this stage. Ninety room modes, 30 of which had eigenfrequencies above the frequency range of interest, were then processed. A point source with a specified power level was assigned to one corner, opposite to the party wall, in order to excite the maximum number of room modes. The level of the experimental sound power being unknown, only a specified power level was assigned to the point source. This was not likely to be a problem since the effect of source power cancels on calculating the level difference between the two rooms. The frequency response was obtained with a resolution of 1 Hz. A field-point mesh was processed to produce the sound-pressure levels at position 1 (0.4,0.5,0.6 m) and position 2 (0.8,0.8,0.2 m), as shown in Fig. 3, to allow a comparison with measurement.

The 1:4 scale room was made of 24-mm blockwood, with one wall of 10-mm perspex. The model was placed in a small acoustic chamber with low background noise level, and was positioned on resilient foam to reduce vibration from the floor. To provide a sound source which approximated a point source, a loudspeaker was placed outside of the model room and radiated through a 10-mm hole in one corner. Two 1/2-in. microphones were placed at the same positions as selected in the simulation. A maximum length sequence (MLS) signal was used as a source of excitation.[36] The spectra of the sound levels at two microphone positions were obtained with a resolution of 0.5 Hz. Predicted and measured sound-pressure levels are shown in Fig. 4 and Fig. 5 for two microphone positions. In both cases, the level of the predicted frequency response was altered to adapt to the level of the measured frequency response. As expected, the sound field shows peaks and dips, corresponding to the modes of the enclosure and the agreement in the predicted and measured response signature is promising. This was despite the fact that the computer model did not include absorption. The finite peaks in the prediction were the results of storage and processing limitations of the computer. This gave a false absorption to the model which, when translated into an equivalent reverberation time, gave values varying between 2.2 and 2.75 s. These values are similar to measurements for hard-walled chambers. At high frequencies, the agreement between prediction and measurement is not as good because of the limited number of elements used to describe the frequency response and because of the expected increased effect of absorption. The simulation also indicates the effect of the perspex panel resonances on the sound field at 350, 430, and 630 Hz while the measured frequency response did not show such effects.

The predicted and measured sound levels also were calculated with a 1/12-octave band resolution and results are presented as a level difference between predicted and measured sound-pressure levels in Fig. 6. Large differences often are the results of quite small shifts between the observed and expected resonant frequency peaks. The discrepancy between prediction and measurement decreases with increase in measured bandwidth as indicated in Fig. 7, which shows level difference calculated with a 1/3-octave band resolution. A peak at 141 Hz, which corresponds to the first room mode, is evident in all curves. The discrepancy is less for microphone position 1 than for position 2. This can be explained by the fact that the former was closer to the loudspeaker than

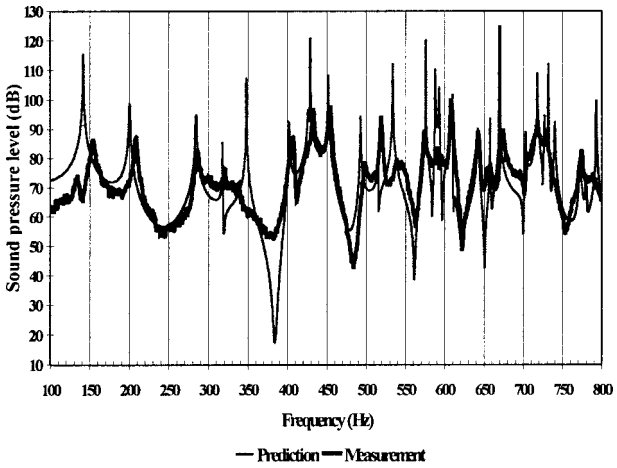

FIG. 5. Frequency response at microphone position 2.

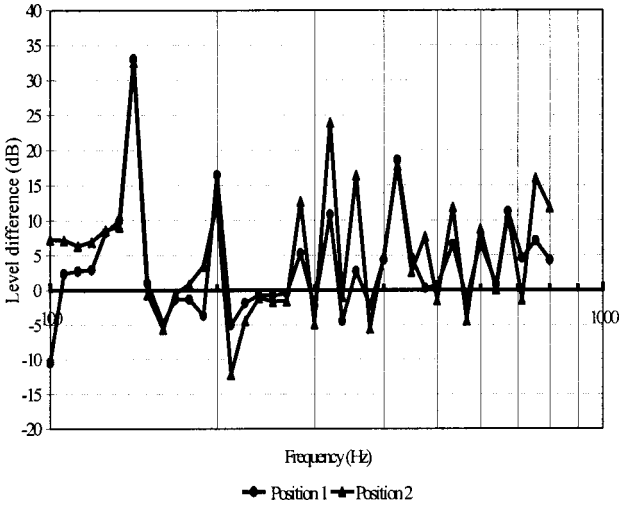

FIG. 6. Level difference between predicted and measured sound-pressure levels, in 1/12-octave bands.

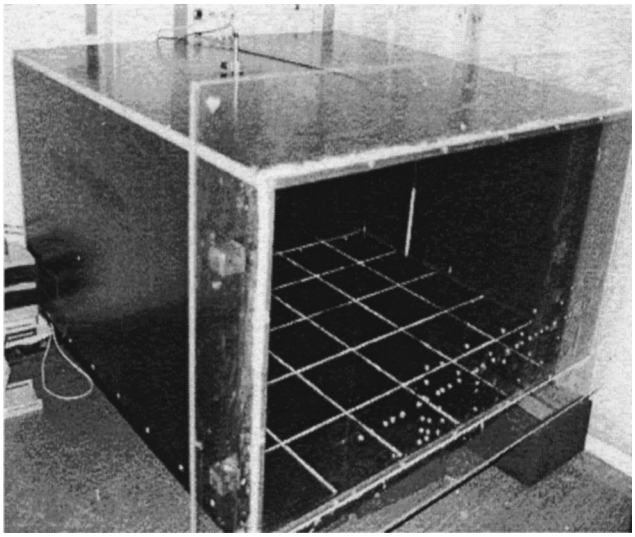

FIG. 8. Perspex panel fixed to source room model.

the latter, and was therefore less affected by the room.

The simulation overestimates the overall sound level by approximately 5–10 dB. This could be for two reasons. The first is that the sound power of the point source and its position may have been incorrectly assigned. Second, as stated earlier, damping was not included in this FEM model. The simulation therefore overestimates the sound field when processed inside any room of hard walls. The effects of the two causes would be expected to partially cancel when calculating sound-level difference between rooms.

A transmission room model was created by linking the acoustic FE model with the structural FE model. It was then compared to the same 1:4 scale model to which a second identical enclosure was added to form the transmission room. Four microphone positions were selected, the two positions (1 and 2) defined previously and two more (4 and 5) in the receiving room as seen in Fig. 3. Measurements were conducted for two perspex walls, of thickness 10 and 5 mm as shown in Fig. 8. The plate was attached to the source room using wood screws at 100-mm centers along the perimeter. The two sides of the perspex panel were sealed with flexible mastic to prevent acoustic leaks.

It is by no means straightforward to physically model required edge conditions. A clamped condition[24,37,38] is particularly difficult to model since plastic deformation occurs when too firmly clamped and small displacements result when not clamped sufficiently. Simply supported edges can be created by cutting a notch parallel to the edges, with the plate beyond the notch clamped[37] as shown in Fig. 9. The simply supported condition is approximated with a rotational stiffness

$$\Lambda = \left(\frac{h_b}{h}\right)^3 \left(\frac{B}{\Delta l}\right), \tag{20}$$

where B is the bending stiffness of the plate, notch width $\Delta l = 3$ mm and notch depth $h_b = 2$ mm for the 5-mm, plate and $h_b = 2.5$ mm for the 10-mm plate. This gives a rotational stiffness of 1.5 10^3 N which is 6.4% of the plate stiffness and 2.9 10^3 N for the 10-mm plate, which is 12.5% of the plate

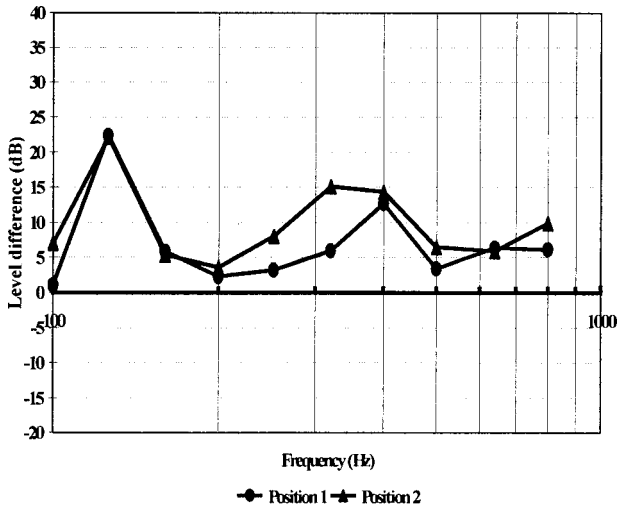

FIG. 7. Level difference between predicted and measured sound-pressure levels, in 1/3-octave bands.

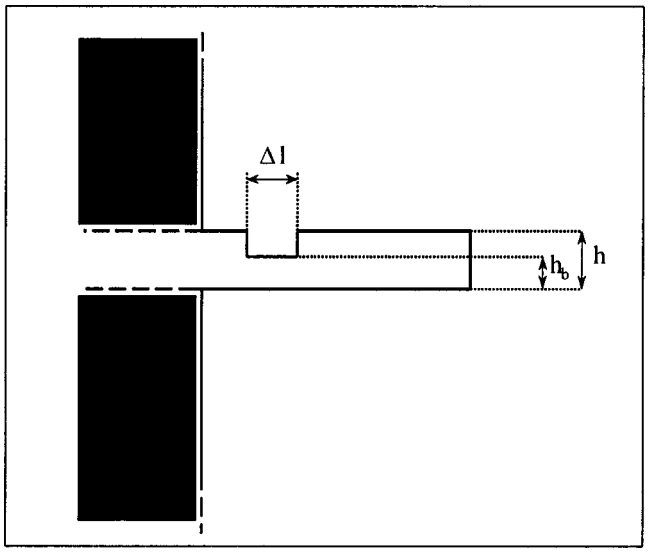

FIG. 9. Dimensions of the notch.

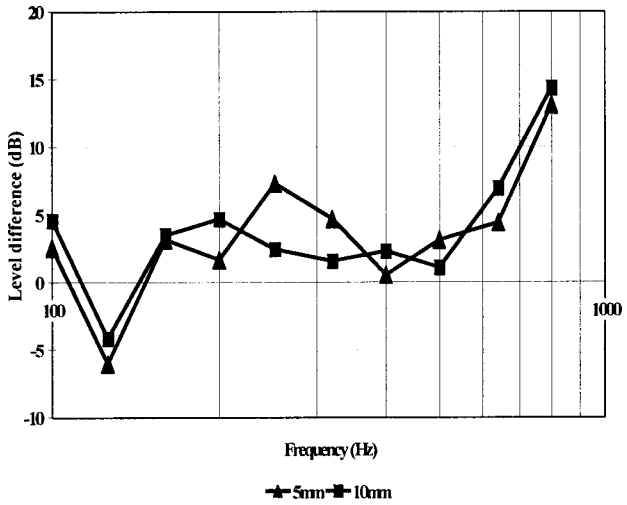

FIG. 10. Level difference between predicted and measured sound-pressure levels, in 1/3-octave band.

stiffness. Flanking transmission in this case was assumed to have little effect.

The sound-level difference was calculated between positions 1 and 4 for the 5-mm and 10-mm simply supported panels. They were then compared with the predicted sound-pressure level difference in 1/3-octave bands as shown in Fig. 10. The FEM prediction underestimates the sound-pressure level difference by 5 dB over much of the frequency range with increasing discrepancy at high frequencies. This can be explained in part by the fact that the simply supported edge condition was physically modeled with a nonzero rotational stiffness.

So far, the damping had not been assigned to the acoustic model, for reasons of simplicity and increased computational speed. Therefore, full-scale measurements of the frequency response of a 5.75×4.89×4.28-m chamber were compared with the predicted response of the same enclosure with no damping and with surface absorption included. The results are presented in Fig. 11. The three curves display the same signature with good agreement between the measured and the two predicted frequency responses. With no damping, the large peaks and dips in the predicted frequency response do not correspond to measured resonances above 100 Hz. When a surface admittance was assigned to the six surfaces, corresponding to a surface absorption coefficient of 0.02, the agreement was better over the whole frequency range. However, importantly, the effect of surface absorption was small up to 100 Hz and could be neglected. This allowed the FEM models to remain simple and the resultant computational times to be short enough for the following survey.

V. EFFECT OF WALL BENDING STIFFNESS AND EDGE CONDITION

The validated FEM model now provided a tool for a parametric survey of the effect of wall and room characteristics on sound-level difference. The effect of wall-edge condition was investigated by numerically modeling a fixed room configuration of 40 m^3 and 35 m^3. The party wall was assumed to be of brick with dimensions 4×2.5 m. Three thicknesses were considered: 0.05, 0.1, and 0.2 m. The sound-pressure level difference was calculated from 31.5 to 160 Hz. One point source was assumed positioned in one corner of the 40-m^3 room, opposite to the party wall.[11] The frequency response in each room was calculated to a frequency resolution of 1 Hz. A field mesh box in each room was defined with 152 points in each. The points were at least 0.5 m from the walls and 0.3 m from the ceilings and floors. The 152 points were then averaged and the narrow-band values recalculated to give the 1/3-octave band level difference.

The narrow-band sound-pressure level difference of a 0.05-m and 0.2-m thick wall for simply supported and clamped conditions are shown in Figs. 12 and 13, respectively. The presence of alternative maxima and minima due

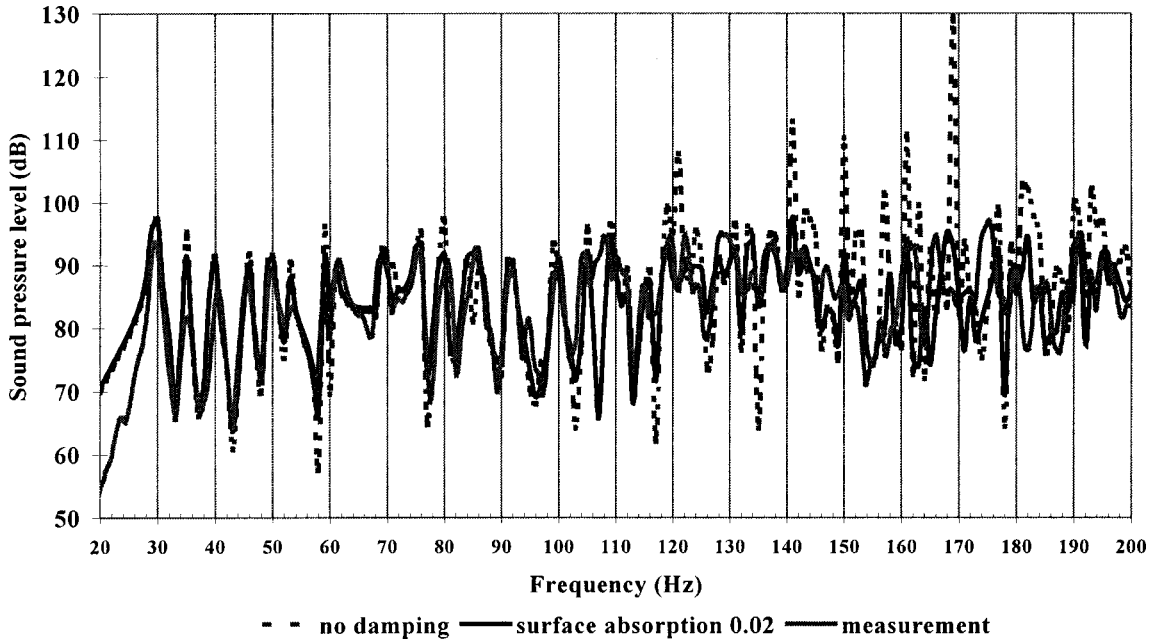

FIG. 11. Effect of the introduction of surface absorption in the numerical model.

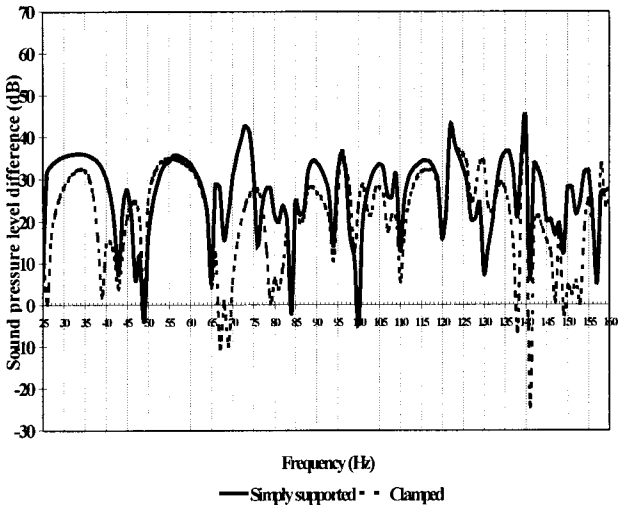

FIG. 12. Sound-pressure level difference across a 0.05-m brick wall.

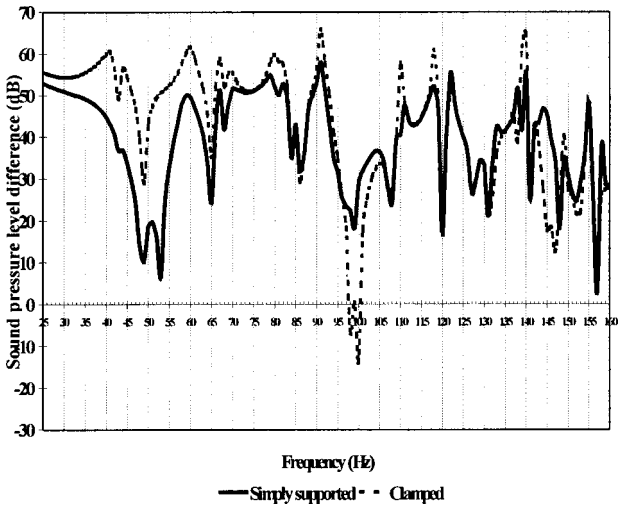

FIG. 13. Sound-pressure level difference across a 0.2-m wall.

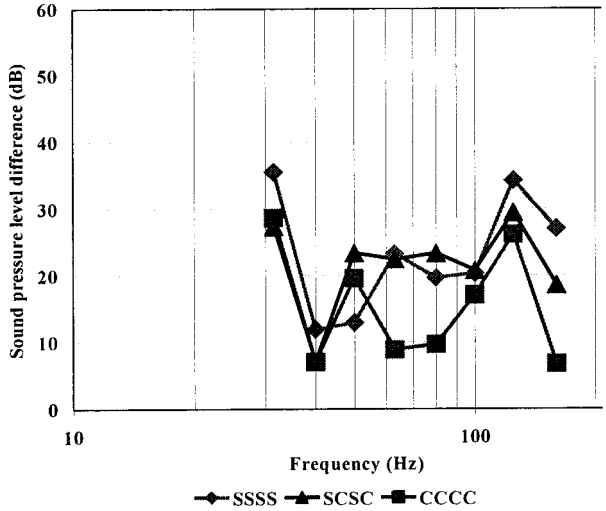

FIG. 14. Sound-pressure level difference of the 0.05-m wall in 1/3-octave bands.

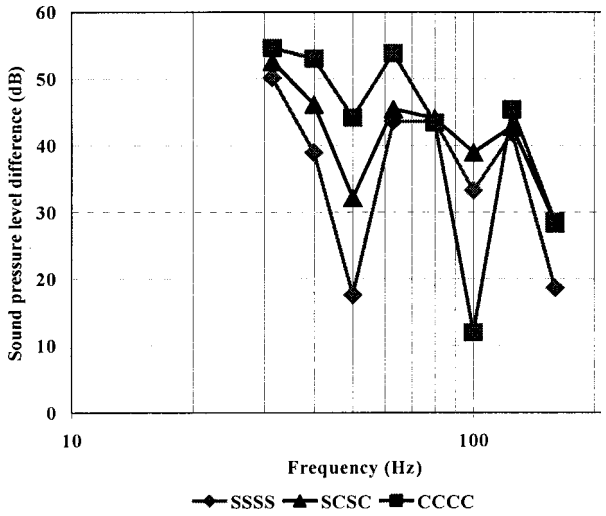

FIG. 15. Sound-pressure level difference of the 0.2-m wall.

to room and wall resonances is observed.[14] When presented as 1/3-octave values (Figs. 14–16), the sound-pressure level difference still displays maxima and minima. The sound-level difference of the simply supported 0.05-m wall (Fig. 14) increases with increasing frequency, with a gradient of about 6-dB/octave and the sound insulation can be assumed to be mass controlled. The sound-level difference of a simply supported 0.2-m thick wall (Fig. 15) decreases with increasing frequency at about 6-dB/octave. The sound insulation can be assumed to be stiffness controlled and this supports the findings of Parkin,[39] Bergassoli,[40] Gargliardini,[11] Gibbs,[41] and Osipov.[14] The clamped edge condition adds to the stiffness of the thick wall and gives the largest level difference overall. The beneficial effects of clamping, also, are observed for the 0.1-m wall (see Fig. 16), but not for the 0.05-m wall.

The positions of the first excited structural mode of the two edge conditions explain the different trends. In the cases of the simply supported 0.05-m and 0.1-m walls, both have their first structural modes excited below the first acoustic mode and the sound transmission can be assumed mass-law controlled. In the cases of the clamped 0.1-m wall and of the

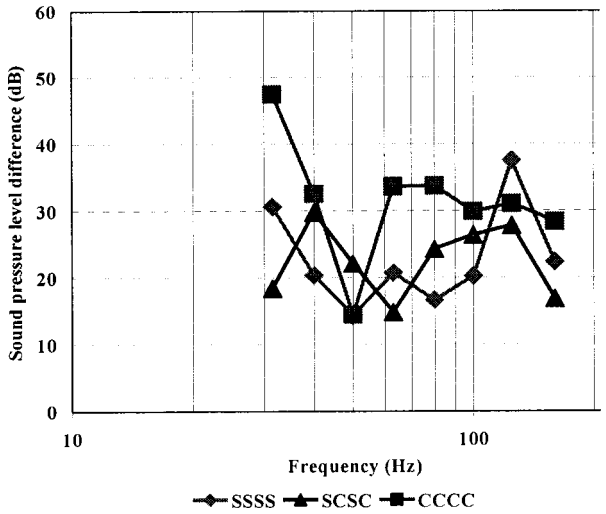

FIG. 16. Sound-pressure level difference of the 0.1-m wall.

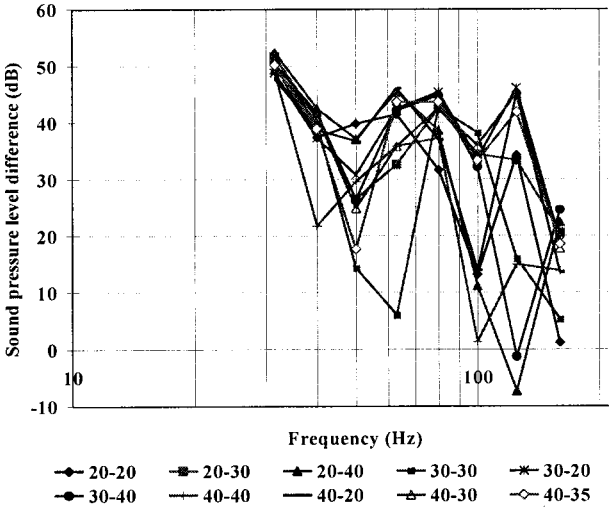

FIG. 17. Effect of room configuration on a simply supported 0.2-m brick wall.

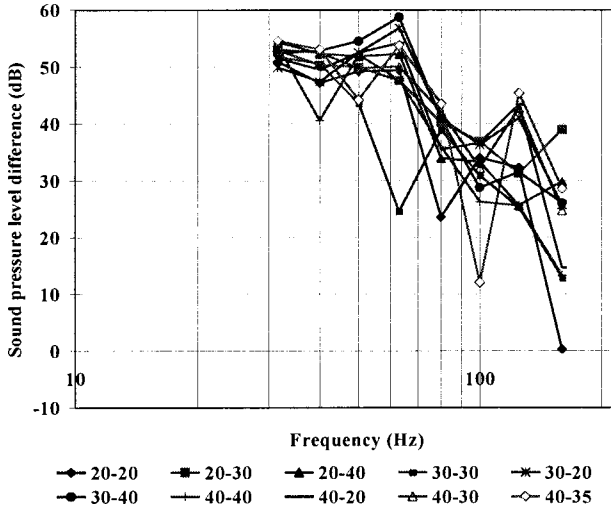

FIG. 18. Effect of room configuration on a clamped wall.

0.2-m wall, the first structural mode is excited above the first acoustic modes and the sound transmission is stiffness controlled. The sound-level difference of the 0.1-m wall displays a transition between stiffness and mass control.[42] The effects of the mixed edge conditions present less strong dips than the simply supported cases and change with the wall thickness. The sound-pressure level difference of the 0.05-m and 0.1-m wall tends to be greater than that of the simply supported. The sound-pressure level difference of the 0.2-m wall lies between that of simply supported and clamped.

Consequently, it has been demonstrated that edge conditions control sound insulation at low frequencies and their effect alters with wall thickness. The classic monotonic decrease and increase with frequency for the stiffness-controlled and mass-controlled regions, respectively, are not observed. However, despite the fact that the sound fields in the source room and in the receiving room are not statistical, the curves display trends which can be interpreted by reference to the classical mechanisms.

VI. EFFECT OF ROOM CONFIGURATION

Room configurations, representative of dwellings in the U.K.,[43] were considered to examine their effect on the sound-level difference of a 0.2-m brick wall with different edge conditions. This thickness was selected as representative of single-leaf party walls typical of attached dwellings. A small sample of ten room configurations, varying from 20 m^3 to 40 m^3, was selected. The volume of the two rooms was modified by changing the room length only, keeping room width and height at 4 and 2.5 m, respectively. Figures 17–19 show the spread of data for a simply supported, clamped, and mixed edge conditions wall when placed in equal and unequal room configurations. In all cases, the sound-pressure level difference decreases with increasing frequency but with gradients ranging from −6 to −15 dB octave. The spread of data varies with edge condition and is greatest for the simply supported condition. Changes in acoustic–acoustic couplings and acoustic–structural couplings and structural resonances are the reasons for those differences. This confirms the work of Pietrzyk.[18] Coupling and panel resonances cause fluctuations over the frequency range 40–160 Hz. Strong coupling takes place when the acoustic modes have the same distribution, as in equal rooms. If data for equal rooms are removed, the spread of data is reduced for all edge conditions. Also, the spread is small when no structural modes are present, recalling the work of Kropp[12] and Pietrzyk[13] on limp walls.[44]

Figures 20 and 21 display the average sound-pressure level difference for each edge condition for even rooms and uneven rooms, respectively. Again, the simply supported wall is found to insulate less than the clamped wall. Values for the mixed edge condition lie between those for the simply supported and clamped. Between equal rooms, the sound insulation decreases faster with increasing frequency than that in unequal rooms.

The sound-level difference data for the three edge conditions were averaged for equal and unequal rooms and are presented in Fig. 22. As expected, a decrease in sound-level difference with increasing frequency has been observed for both cases and the mean sound-level difference in equal rooms is lower than that in unequal room configurations. Such behavior is expected as strong acoustic–acoustic cou-

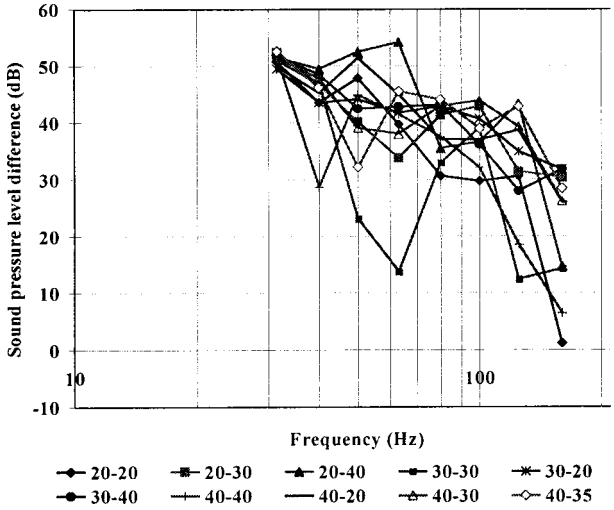

FIG. 19. Effect of room configuration wall with mixed edge conditions.

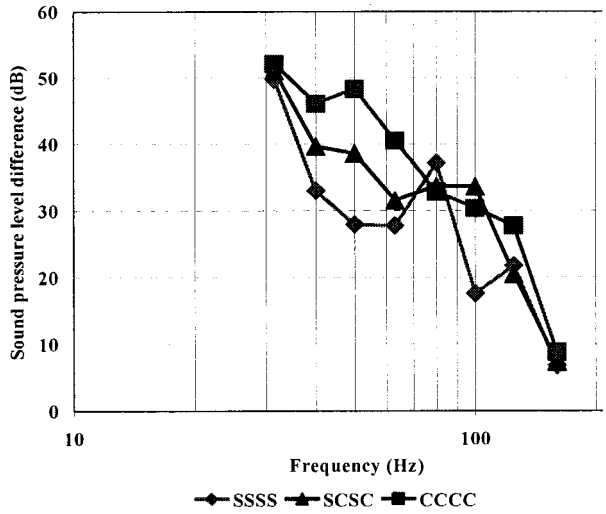

FIG. 20. Sound-level difference between equal rooms.

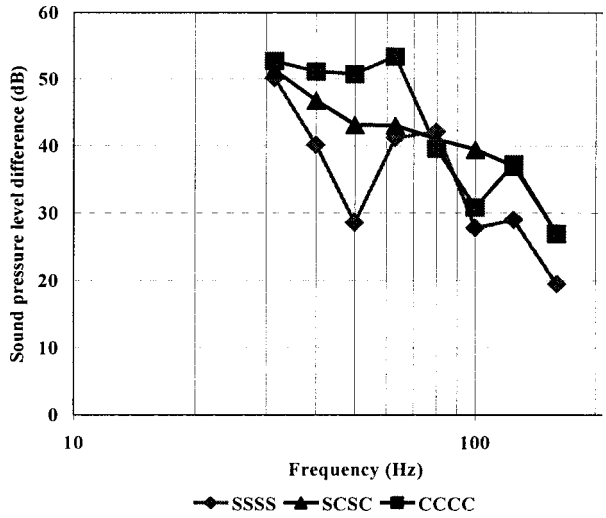

FIG. 21. Sound-level difference between unequal rooms.

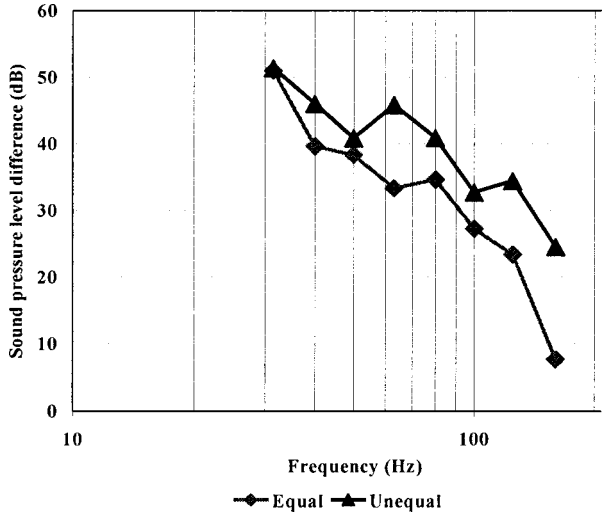

FIG. 22. Effect of room configuration on the sound-level difference.

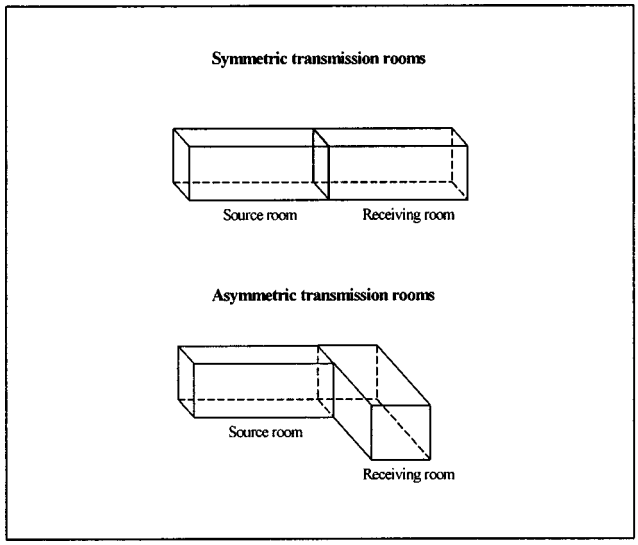

FIG. 23. Symmetric and asymmetric transmission rooms.

pling takes place between identical modes.[8,12,44] The effects of the equal room configurations are therefore true not only for the mid and high frequencies,[45,46] but also for low frequencies in small rooms.

Attached dwellings can have asymmetric rooms as seen in Fig. 23. To investigate the effects of this room configuration on the sound insulation of the 0.2-m wall, the area of the party wall could not be maintained at 10 m^2, otherwise the room volumes would have to be in excess of 50 m^3. Therefore, rooms with volumes of 20 m^3 and 30 m^3 with party walls of areas 2×2.5 m^2 and 3×2.5 m^2 were investigated. The difference in room-level difference between asymmetric and symmetric room configurations is shown in Fig. 24 for the 20-m^3 configuration and in Fig. 25 for the 30-m^3 configuration. In general, the sound insulation of the party wall in the asymmetric configuration is 3 dB greater than in the symmetric configuration, but with increased differences depending on the degree of mode coupling. The asymmetric room configurations thus tend to improve the sound insulation of party walls by weakening the coupling between the acoustic

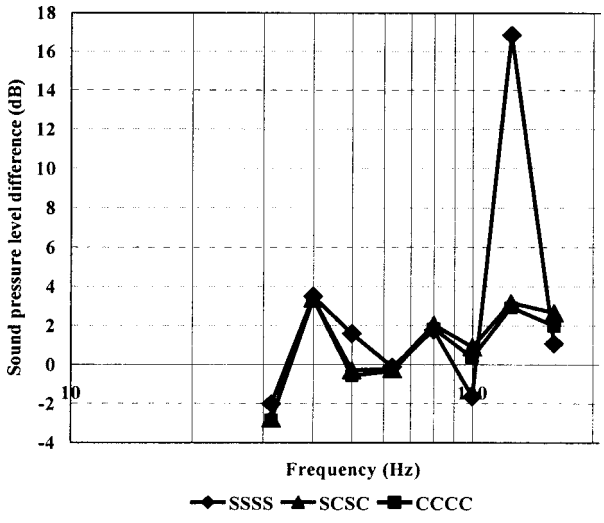

FIG. 24. Difference between asymmetric and symmetric sound-level differences for a 0.2-m wall between 20-m^3 rooms.

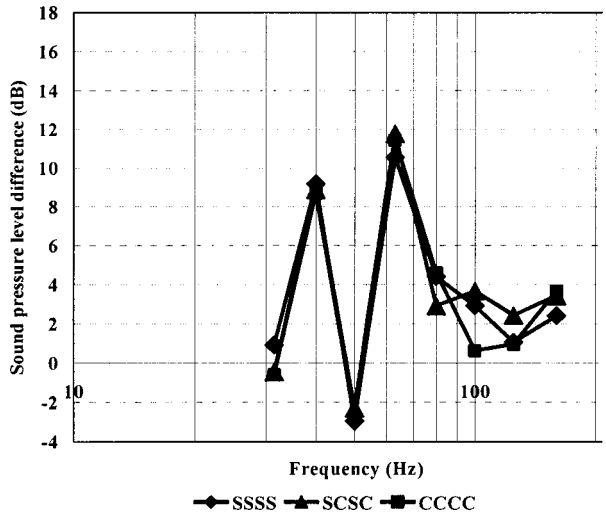

FIG. 25. Difference between asymmetric and symmetric sound-level differences for a 0.2-m wall between 30-m^3 rooms.

modes. Figures 24 and 25 also show that the edge conditions have negligible effect since the wall area is small and therefore few structural modes are excited in the frequency range of interest.

VII. CONCLUDING REMARKS

The sound transmission between dwellings at low frequencies has been investigated using an FEM model. The FEM utilization was justified by good agreements between measured and predicted sound-pressure level and level difference in 1:4 scale and full-scale rooms.

The effect of party wall-edge condition on the sound-pressure level difference between rooms was investigated for walls of different thickness and different room configurations. It was found that the sound-level difference between rooms is strongly influenced by the modal characteristics of the rooms, as well as of the party wall, producing a large spread in data below 100 Hz.

The wall edge conditions affect the sound-pressure level difference since they alter the structural modal frequency distribution, a phenomenon already observed by other workers.[46–49] The level difference produced by clamped thin walls is lower than the simply supported case, since the rigidity of the wall is increased and structural eigenfrequencies are shifted upwards towards room eigenfrequencies.[46–48,50] The level difference of clamped thick walls is higher than the simply supported case,[46,47,49,50] since the edge condition adds to the controlling mechanism which is stiffness.

The different room configurations existing in dwellings tend not to alter the effect of edge conditions on the sound-pressure level difference of party walls. The sound-pressure level difference is lower when the volumes of the two rooms are equal, because of increased acoustic coupling. This is unfortunate since the majority of attached dwellings has a floor plan which mirrors that of their neighbor. Therefore, the rooms on each side of the party wall will be of the same dimensions. If the room volumes could be made to differ by about 40%, then the reduced acoustic coupling obtained would increase the sound insulation by 3 dB and more.

[1] J. R. Brooks and K. Attenborough, ''The implication of measured and estimated domestic source levels for insulation requirements,'' Proceedings of I.O.A. **11**, 19–27 (1989).
[2] C. Grimwood, ''Complaints about poor sound insulation between dwellings,'' I.O.A. Acous. Bull. **20**, 11–16 (1995).
[3] J. Roland, ''Adaptation of existing test facilities to low frequency measurements,'' Proceedings of Inter-Noise 95 **2**, 1113–1116 (1995).
[4] H. Goydke, ''Investigations on the precision of laboratory measurements of sound insulation of building elements according to the revised Standard ISO 140,'' Proceedings of Inter-Noise 98, 480 (1998).
[5] ISO 140, Part 3: Acoustics—Measurements of sound insulation in buildings and of building elements. Part 3. Laboratory measurements of airborne sound insulation of building elements (1995).
[6] H. V. Fuchs, X. Zha, M. Spah, and M. Pommerer, ''Qualifications of small freefield and reverberation rooms for low frequencies,'' Proceedings of Euro-Noise 98 **2**, 657–662 (1998).
[7] D. B. Pedersen, ''Laboratory measurement of the low frequency sound insulation,'' D.A.G.A. 97, Kiel, 105–106 (1997).
[8] A. J. Pretlove, ''Free vibration of a rectangular panel backed by a closed rectangular cavity,'' J. Sound Vib. **2**(3), 197–209 (1965).
[9] R. Josse and C. Lamure, ''Transmission du son par une paroie simple,'' Acustica **14**, 267–280 (1964).
[10] L. Gargliardini, ''Simulation numerique de la mesure en laboratoire de l'indice d'affaiblissement acoustique: Effects des sources et de la geometrie de la paroie,'' Colloq Phys., Colloq. C2, Supplement au no. 2, Tome 51, Fevrier 1990, 1081–1084 (1990).
[11] L. Gargliardini, J. Roland, and J. L. Guyader, ''The used of functional basis to calculate acoustic transmission between two rooms,'' J. Sound Vib. **145**(3), 457–478 (1991).
[12] W. Kropp, A. Pietrzyk, and T. Khilman, ''On the meaning of the sound reduction index at low frequencies,'' Acta Acust. (China) **2**, 379–392 (1994).
[13] A. Pietrzyk, ''Optimization of sound insulation at low frequencies by selecting partition location,'' Nordic Acoustical Meeting, Helsinki, 12–14 June 1996, pp. 71–76 (1996).
[14] A. Osipov, P. Mees, and G. Vermeir, ''Low frequency airborne sound transmission through single partitions in Buildings,'' Appl. Acoust. **52**(3–4), 273–288 (1997).
[15] V. Cutanda and A. Pietrzyk, ''Low frequency sound transmission measurements and numerical simulations: A comparative study,'' Proceedings of Inter-Noise 97 **3**, 1449–1452 (1997).
[16] Y. J. Kang and J. S. Bolton, ''A finite element model for sound transmission through foam lined double panel structures,'' J. Acoust. Soc. Am. **99**, 2755–2765 (1996).
[17] A. Pietrzyk and T. Khilman, ''The sensitivity of sound insulation to partition location—Case of heavyweight partitions,'' Proceedings of Inter-Noise 97 **2**, 727–730 (1997).
[18] A. Pietrzyk, ''Sound insulation at low frequencies,'' PhD thesis, Report F 97-01, Chalmers University of Technology, Sweden, 1997.
[19] A. Osipov, P. Mees and G. Vermeir, ''Numerical simulation of airborne sound transmission at low frequencies: The influence of the room and the partition parameters,'' Proceedings of Inter-Noise 97 **2**, 759–762 (1997).
[20] B. Yegnaranayana, ''Wave analysis of sound decay in rectangular rooms,'' J. Acoust. Soc. Am. **56**, 534–541 (1974).
[21] R. E. Halliwell, ''Inter laboratory variability of sound absorption measurements,'' J. Acoust. Soc. Am. **73**, 880–886 (1983).
[22] J. L. Davy, ''The variance of decay rate at low frequencies,'' Appl. Acoust. **23**, 63–79 (1988).
[23] A. Leissa, *Vibration of Plates* (Acoustical Society of America, Woodbury, 1993).
[24] M. Balike, R. B. Bhat, and S. Rakheja, ''Noise transmission through a cavity backed flexible plate with elastic edge constraints,'' Third International congress on air- and structure-borne sound and vibration, Montreal, Canada, pp. 335–343 (1994).
[25] P. M. Morse, *Vibration and Sound* (McGraw-Hill, New York, 1948).
[26] M. Petyt, J. Lea, and G. H. Koopman, ''A finite element method for determining the acoustic modes of irregular shaped cavities,'' J. Sound Vib. **45**(4), 495–502 (1976).
[27] O. C. Zienkiewicz, *The Finite Element Method in Engineering Science*, 4th ed. (McGraw-Hill, New York, 1991).
[28] SYSNOISE, 1993, User Manual, Version 5.3.
[29] L. Cremer, M. Heckl, and E. E. Ungar, *Structure Borne Sound* (Springer-Verlag, Berlin, 1988), p. 104.

[30] S. Ljunggren, ''Airborne sound insulation of thick walls,'' J. Acoust. Soc. Am. **89**, 2338–2345 (1991).
[31] F. Fahy, *Sound and Structural Vibration: Radiation, Transmission and Response* (Academic, New York, 1985).
[32] R. J. Astley, ''Finite elements in acoustics,'' Proceedings of Inter-Noise 98, 538 (1998).
[33] N. Atalla and R. J. Bernhard, ''Review of numerical solutions for low frequency structural-acoustic problems,'' Appl. Acoust. **43**, 271–294 (1994).
[34] S. Maluski and H. Bougdah, ''Predicted and measured low frequency response of small rooms,'' J. Build. Acoust. **4**(2), 73–85 (1997).
[35] P3/PATRAN, *User Manual* (PDA Engineering, 1993).
[36] MLSSA, Version 9.01.
[37] B. M. Gibbs and Y. Shen, ''The predicted and measured bending vibration of an *L*-combination of rectangular thin plates,'' J. Sound Vib. **112**(3), 469–485 (1987).
[38] C. C. Sung and J. T. Jan, ''The response of sound power radiated by a clamped rectangular plate,'' J. Sound Vib. **207**(3), 301–317 (1997).
[39] P. H. Parkin, H. J. Purkis, and W. E. Scholes, *Field and Measurements of Sound Insulation Between Dwellings* (Her Majesty's Stationery Office, London, 1960).
[40] A. Bergassoli and M. Brodut, ''Transparence des murs et des cloisons,'' Acustica **23**, 315–322 (1970).
[41] B. M. Gibbs and J. Lewis, ''Sound insulation of brick diaphragm walls I. Scale model measurements and statistical energy analysis,'' Build. Envir. **26**(2), 165–172 (1991).
[42] S. Maluski and B. M. Gibbs, ''The influence of partitions boundary conditions on sound level difference between rooms at low frequencies,'' Proceedings of Euro-Noise 98, V.2, 681–686 (1998).
[43] S. Maluski, ''Low frequency sound insulation in dwellings,'' Ph.D. thesis, Sheffield Hallam University, U.K., 1999.
[44] S. Maluski and B. M. Gibbs, ''Variation of sound level difference in dwellings due to room modal characteristics,'' Proceeding of Acoustics Performances of Medium-Rise Timber Buildings, 3–4 December 1998, Dublin (1998).
[45] M. C. Bhattacharya and R. W. Guy, ''The influence of the measuring facility on the measured sound insulating property of a panel,'' Acustica **26**, 344–348 (1972).
[46] A. C. Nilsson, ''Reduction index and boundary conditions for a wall between two rectangular rooms, Parts I and II,'' Acustica **26**, 1–23 (1972).
[47] T. Kihlman, *Report on the Influence of Boundary Conditions on the Reduction Index* (Report No. ISO/TC43/SC2/WG2, Chalmers Tekniska Hogskila, Goteborg, Sweden, 1970).
[48] G. Maidanik, ''Response of ribbed panels to reverberant acoustic fields,'' J. Acoust. Soc. Am. **34**, 809–826 (1962).
[49] T. Kihlman and A. C. Nilsson, ''The effects of some laboratory designs and mounting conditions on reduction index measurements,'' J. Sound Vib. **24**, 349–364 (1972).
[50] A. Berry and J. Nicolas, ''Structural acoustics and vibration behaviour of complex panels,'' Appl. Acoust. **43**, 185–215 (1994).

Detection of Gaussian signals in Poisson-modulated interference

Roy L. Streit[a)]
Naval Undersea Warfare Center, Newport, Rhode Island 02841

(Received 21 August 1998; revised 26 June 2000; accepted 7 July 2000)

Passive broadband detection of target signals by an array of hydrophones in the presence of multiple discrete interferers is analyzed under Gaussian statistics and low signal-to-noise ratio conditions. A nonhomogeneous Poisson-modulated interference process is used to model the ensemble of possible arrival directions of the discrete interferers. Closed-form expressions are derived for the recognition differential of the passive-sonar equation in the presence of Poisson-modulated interference. The interference-compensated recognition differential differs from the classical recognition differential by an additive positive term that depend on the interference-to-noise ratio, the directionality of the Poisson-modulated interference, and the array beam pattern. [S0001-4966(00)03910-2]

PACS numbers: 43.60.Cg, 43.30.Wi [JCB]

I. INTRODUCTION

Passive broadband (incoherent) detection of a known Gaussian target signal in independent Gaussian noise by an array of hydrophones is a classical and well-understood problem. The processing chain of the optimal detector is depicted in Fig. 1. After time delaying and summing the outputs $\{u_m(t)\}$ of individual array hydrophones, the sum $v(t)$ passes through a predetection filter, the output $x(t)$ is squared to obtain $y(t)$, and then $y(t)$ is sent through a postdetection low-pass filter. The output $z(t)$ is compared to a threshold to determine the presence or absence of signal. The optimal predetection, or Eckart, filter maximizes the deflection coefficient, denoted by d, that parametrizes the receiver operating characteristic (ROC) curves of probability of detection, P_{D}, versus probability of false alarm, P_{FA}, when the variance of $z(t)$ remains approximately constant in the presence and absence of signal.

Interfering signals contribute coherently to the output of the array beamformer, and they inevitably degrade detection performance when present. The classic paper by Schultheiss[1] derives the deflection coefficient d for a Gaussian signal and a single interferer for the conventional processor in the case of an equispaced line array. Because there is only one interferer, he is able to discuss performance in terms of the behavior of d as a function of the angular separation between the signal and interferer. For more than one interferer, however, this approach is intractable because it requires examining all possible separations between signal and interferers.

When many interferers are present, it is reasonable to consider adopting a statistical model for both the number and arrival directions of the interferers. In this paper the expected values of the numerator and denominator of the expression for the deflection coefficient d are obtained in closed form under the assumption that the interference is Poisson modulated (PM). These explicit, but average, expressions facilitate insight into the problem while avoiding the otherwise intractable enumeration over all possible deterministic interference locations. PM interference models are used to study both conventional and optimal (Eckart) processors for a general hydrophone array. The PM interference model is especially well suited to study processors operating on linear beamformer outputs, but extensions to adaptive processors such as minimum variance distortionless response (MVDR) requires further work and are not considered here.

In some applications, the PM interference model can be obtained from a specified surface shipping density function $\mathrm{SD}(x,y)$. Thus, $\mathrm{SD}(x,y)$ is the probability that a surface ship is located at the point (x,y) at a randomly chosen time. Acoustic propagation transforms the given shipping density into a directional source distribution at the sensor, as depicted in Fig. 2 for the special case of straight-line propagation and a flat bottom with only two dominant paths, direct and bottom bounce. The directional source distribution at the sensor is denoted by $\Lambda(\xi)$, and it is in general determined by the propagation paths for nonconstant sound-speed profiles. In other applications, a volumetric source density might be employed to model biologics such as whales. Whatever the application, however, the investigation in this paper begins by assuming that the function $\Lambda(\xi)$ is given. Thus, the source distribution function $\Lambda(\xi)$ implicitly incorporates the effects of acoustic propagation.

PM interference is used to model both ''temporally nonresolvable'' and ''temporally resolvable'' interference. Temporally nonresolvable interference is essentially a shot noise model; that is, interferers are short duration and have a rapid occurrence rate compared to the averaging time T of the postdetection filter. The variance of the detector output is essentially stationary in this case and is directly related to the beamformer output variance. It is shown in Sec. III that there is essentially no difference between this kind of interference and classical nonisotropic noise. In contrast, temporally resolvable interference is long duration and has a slow occurrence rate compared to the averaging time T of the postdetection filter. In this case, the variance of the detector output varies over time, and the expected value of the variance of the detector output is computed with respect to the PM interference process. The expected variance involves the fourth power of the array beam pattern and is derived in Sec. IV.

Interference correction terms to the classical recognition differential of the passive-sonar equation are given in closed

[a)]Electronic mail: streitrl@npt.nuwc.navy.mil

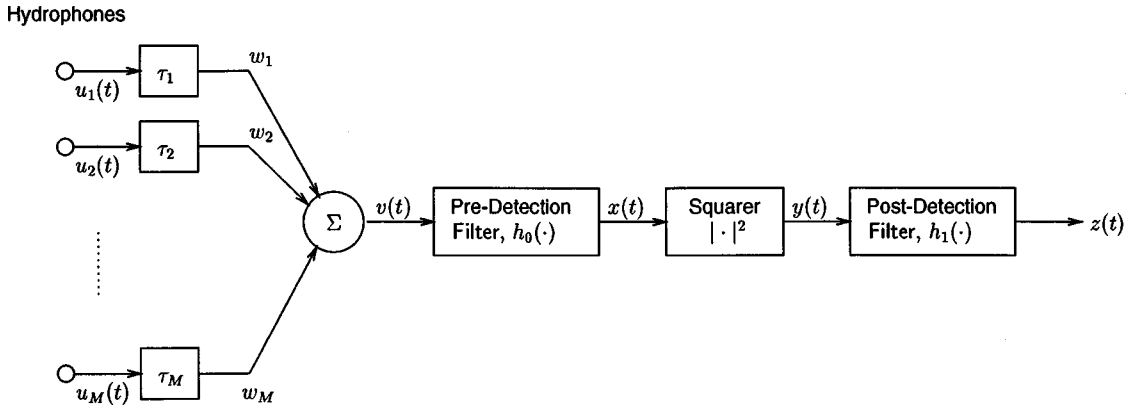

FIG. 1. Processing chain for detecting Gaussian signals in additive independent Gaussian noise.

form in Sec. V. These correction terms are derived directly from the deflection coefficient d of the conventional processor for fixed interference and for PM interference. [The quantity d is known by several other names, including the deflection signal-to-noise ratio (SNR), the detection coefficient, and simply the deflection.] Section VI summarizes the results obtained and presents some concluding remarks. Appendix A provides relevant background information on the Poisson process and its expectation operator. Appendix B discusses the deflection coefficient, the optimal predetection filter for Gaussian processes, and the Gaussian signals that are least detectable by the optimal processor.

Throughout the paper, target signal and (hydrophone) noise are assumed to be Gaussian random processes with stationary spectra. Noise is assumed statistically independent from hydrophone to hydrophone in the receiving array. Each interferer in a realization of a set of PM interferences, whether resolvable or nonresolvable, is assumed to be a stationary Gaussian random process. Interferences in the same and in different realizations of the PM interference process are assumed statistically independent. Finally, all interferers are assumed to have identical power spectra. Nonidentical interference spectra can be incorporated into the current approach via so-called ''marked'' Poisson processes (if the spectral mark process is independent of the arrival direction process), but this topic is not pursued here.

Nonhomogeneous Poisson point processes have been used previously in the sonar context. Heitmeyer, Davis, and Yen[2] study the special case of azimuthal directional arrays and use Poisson processes to model shipping anisotropy. Their formulation of the problem differs significantly from the one used in this paper, and they describe their results in

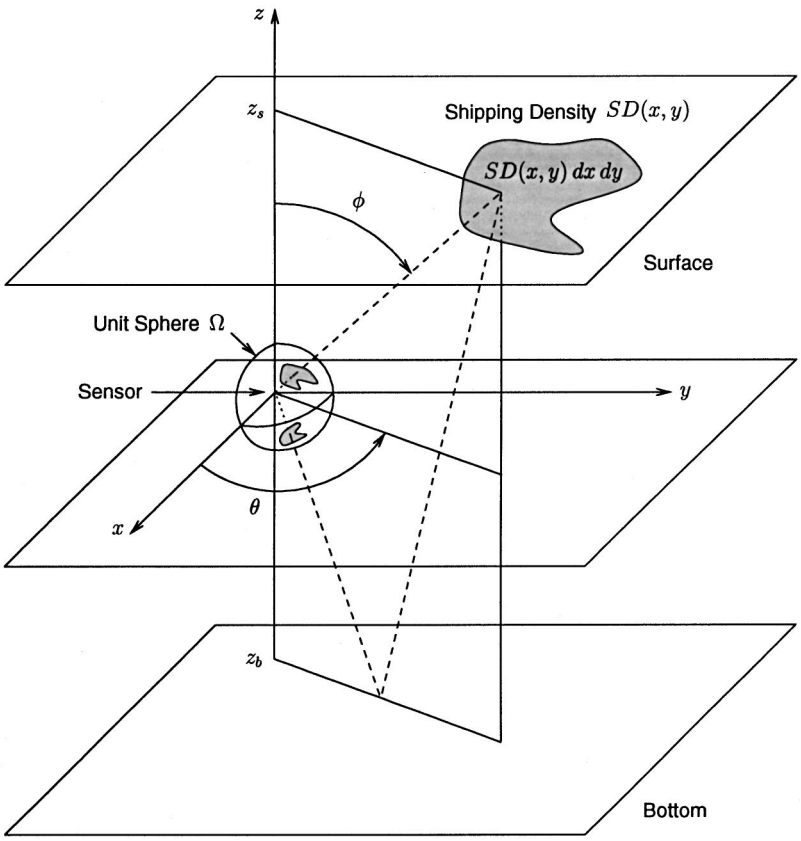

FIG. 2. Acoustic propagation transformation of shipping density SD(x,y) to interference intensity $\Lambda(\xi)$ on the sphere $\Omega=\{\xi\in R^3:\|\xi\|=1\}$. The case of constant sound speed, direct and bottom bounce paths, and flat bottom is depicted.

terms of a (suitably defined) ''detection opportunity function'' and ''ship resolution gain.'' In any event, they do not obtain correction terms to the classical expression for recognition differential of the passive-sonar equation. Liu and Nolte[3] obtain closed-form expressions for the probabilities of detection and false alarm for a single interferer from a fixed, known direction. They cite several papers related to spatial discrimination of array signal processors against interference. Claus, Kadota, and Romain[4] present a method for estimating spatially localized noise embedded in spatially and temporally white ambient noise, and apply it to the narrowband signal detection problem. Their method may be useful for estimating the intensity function of a PM interference field. Van Trees[5] uses nonhomogeneous Poisson processes to model spatially distributed interference (reverberation) in the problem of detecting the (active sonar) return from a slowly fluctuating point target. He states that the spatial Poisson process model is an adequate model of the reverberant environment in many situations.

II. FIXED INTERFERENCES

Deflection coefficients are derived in this section for a fixed number of interferences with specified arrival directions and one signal arrival direction. Let ξ_l denote a unit vector in the look, or steer, direction of an M hydrophone passive array, and let $p_m=(x_m,y_m,z_m)$ denote the locations of the array's hydrophones. The (voltage) beamformer output is the weighted and time-delayed coherent sum of the hydrophone outputs

$$v(t)=\sum_{m=1}^{M} w_m u_m(t-\mu(p_m,\xi_l)), \tag{2.1}$$

where $\{u_m(t)\}$ are the hydrophone outputs, $\{\mu(p_m,\xi_l)\}$ are the time delays corresponding to the wavefront curvature of the signal as it propagates across the array, and $\{w_m\}$ are the array weights. Plane wave propagation is assumed in this paper, so the time-delay function referenced to the origin (which is taken to be the acoustic center of the array) for arbitrary propagation directions ξ and locations p is given by $\mu(p,\xi)=(p\cdot\xi)/c$, where c denotes wave speed across the array. The output of hydrophone m due to a fixed far-field target signal with plane wave arrival direction ξ_s and array hydrophone noise $n_m(t)$ is given by

$$u_m(t)=s(t+\mu(p_m,\xi_s))+n_m(t), \tag{2.2}$$

where $s(t)$ is the output due to signal alone of a hypothetical reference hydrophone located at the origin. Let $V(\omega)$, $S(\omega)$, and $N_m(\omega)$ denote the power spectra of the beamformer output $v(t)$, signal $s(t)$, and hydrophone noises $\{n_m(t)\}$, respectively. The beamformer output spectrum is

$$V(\omega)=S(\omega)|B(\omega;\xi_s,\xi_l)|^2+\sum_{m=1}^{M} N_m(\omega)w_m^2, \tag{2.3}$$

where the beam pattern (or transfer function) of the array is defined for arbitrary plane wave arrival angles ξ by

$$|B(\omega;\xi,\xi_l)|^2=\left|\sum_{m=1}^{M} w_m \exp[-i\omega(\mu(p_m,\xi)-\mu(p_m,\xi_l))]\right|^2. \tag{2.4}$$

The array weights are normalized so that

$$B(\omega;\xi_l,\xi_l)=\sum_{m=1}^{M} w_m=M. \tag{2.5}$$

The hydrophone noises are now assumed to have identical spectra, so that $N_m(\omega)\equiv N(\omega)$, $m=1,\ldots,M$. Define the (dimensionless) ratio

$$G=\frac{[\Sigma_{m=1}^{M} w_m]^2}{\Sigma_{m=1}^{M} w_m^2}=\frac{M^2}{w'w}, \tag{2.6}$$

where $w=(w_1,\ldots,w_M)'$ denotes the array weight vector (and primes denote matrix/vector transpose). G is the array gain for a plane wave and uncorrelated hydrophone noise. Substituting (2.5) and (2.6) into (2.3) gives the more intuitive form

$$V(\omega)=S(\omega)|B(\omega;\xi_s,\xi_l)|^2+G^{-1}N(\omega)|B(\omega;\xi_l,\xi_l)|^2. \tag{2.7}$$

The expression (2.7) is valid for any array weight normalization. In the absence of signal, the beamformer output spectrum is the noise spectrum multiplied by the scalar $G^{-1}|B(\omega;\xi_l,\xi_l)|^2=w'w$.

Fixed interference arises when (point) sources other than the target lie in the far field and contribute coherently to the beamformer output. Let K denote the number of interfering sources, and let $\{\xi_k\}$ denote unit vectors in their arrival directions. For $k=1,\ldots,K$, let $\iota_k(t)$ denote the output of a hypothetical reference hydrophone located at the origin when only interferer k is present. Output $\iota_k(t)$ is modeled as a stationary Gaussian process. Interfering sources are assumed independent of each other; that is, outputs $\iota_k(t)$ and $\iota_j(t)$ are statistically independent for $k\neq j$. Signal, interference, and noise are independent, so the beamformer output power spectrum in the presence of K interference sources is, by linear superposition,

$$V(\omega)=S(\omega)|B(\omega;\xi_s,\xi_l)|^2+G^{-1}N(\omega)|B(\omega;\xi_l,\xi_l)|^2+\sum_{k=1}^{K} I_k(\omega)|B(\omega;\xi_k,\xi_l)|^2, \tag{2.8}$$

where $I_k(\omega)$ is the spectrum of the interfering source arriving from direction ξ_k.

Interferences are stationary Gaussian random processes by assumption; thus, detector performance is governed by the deflection coefficient d, where d is the difference in the mean output level of $z(t)$ under the two hypotheses

$\{\mathbf{H}_0$: interference and noise present$\}$,

$\{\mathbf{H}_1$: signal, interference, and noise present$\}$,

divided by the $\mathbf{H}_0$ standard deviation. (Some authors use the detection index, defined as d^2.) The mean of $z(t)$ under $\mathbf{H}_1$ is obtained from (2.8), and its mean under $\mathbf{H}_0$ is obtained

from (2.8) by setting $S(\omega)=0$; hence, the difference in the means of $z(t)$ is

$$\Delta=\int_{-\infty}^{\infty} S(\omega)|B(\omega;\xi_s,\xi_l)|^2 d\omega. \tag{2.9}$$

Assuming low signal to aggregate interference plus noise ratio, the variance of $z(t)$ is approximately the same under both hypotheses. The time constant T of the postdetection low-pass filter is assumed large compared to the correlation times of the interference and noise, so that the approximation (B2) can be used. The low-pass filter used here has weight $1/T$ for $|t|\leqslant T/2$, and weight zero otherwise.

The deflection coefficient for the (nonadaptive) conventional detector is obtained using a predetection filter whose transfer function is constant. In this case, from Eq. (B7) in Appendix B,

$$d^K_{\mathrm{conv}}(\xi_l)=\frac{\frac{1}{2}\sqrt{T/\pi}\int_{-\infty}^{\infty}S(\omega)|B(\omega;\xi_s,\xi_l)|^2 d\omega}{\{\int_{-\infty}^{\infty}[G^{-1}N(\omega)|B(\omega;\xi_l,\xi_l)|^2+\Sigma_{k=1}^{K}I_k(\omega)|B(\omega;\xi_k,\xi_l)|^2]^2 d\omega\}^{1/2}}. \tag{2.10}$$

If the noise spectrum is strictly positive (i.e., nonzero) for all ω, and if there is no multipath and the array is steered on target, so that $\xi_s=\xi_l$, then $d^K_{\mathrm{conv}}(\xi_l)$ takes the more intuitive form

$$d^K_{\mathrm{conv}}(\xi_l)=\sqrt{\pi T}GS\left\{\int_{-\infty}^{\infty}N^2(\omega)\left[1+\sum_{k=1}^{K}\frac{I_k(\omega)}{N(\omega)}\frac{|B(\omega;\xi_k,\xi_l)|^2}{w'w}\right]^2 d\omega\right\}^{-1/2}, \tag{2.11}$$

where $S=1/2\pi\int_{-\infty}^{\infty}S(\omega)d\omega$ denotes signal power.

The Eckart filter maximizes the deflection coefficient by choice of the optimal predetection filter. Using (2.8) and substituting into expression (B8) in Appendix B gives the Eckart filter as

$$|H^K_{\mathrm{Eckart}}(\omega,\xi_l)|^2=\frac{S(\omega)|B(\omega;\xi_s,\xi_l)|^2}{[G^{-1}N(\omega)|B(\omega;\xi_l,\xi_l)|^2+\Sigma_{k=1}^{K}I_k(\omega)|B(\omega;\xi_k,\xi_l)|^2]^2}. \tag{2.12}$$

Using the array weight normalization (2.5), the deflection coefficient (B9) is

$$d^K_{\mathrm{Eckart}}(\xi_l)=\frac{1}{2}\left\{\frac{T}{\pi}\int_{\Psi}\frac{S^2(\omega)|B(\omega;\xi_s,\xi_l)|^4}{[G^{-1}M^2N(\omega)+\Sigma_{k=1}^{K}I_k(\omega)|B(\omega;\xi_k,\xi_l)|^2]^2}d\omega\right\}^{1/2}, \tag{2.13}$$

where Ψ is the (radian) frequency band of interest in the application for which the processor is being designed. If the noise spectrum is strictly positive on Ψ, and the array is steered on target, $\xi_s=\xi_l$, the expressions (2.12) and (2.13) take the more insightful forms

$$|H^K_{\mathrm{Eckart}}(\omega,\xi_l)|^2=\frac{S(\omega)}{N^2(\omega)}\times\left[1+\sum_{k=1}^{K}\frac{I_k(\omega)}{N(\omega)}\frac{|B(\omega;\xi_k,\xi_l)|^2}{w'w}\right]^{-2}, \tag{2.14}$$

and

$$d^K_{\mathrm{Eckart}}(\xi_l)=\frac{G}{2}\left\{\frac{T}{\pi}\int_{\Psi}\left[\frac{S(\omega)}{N(\omega)}\right]^2\times\left[1+\sum_{k=1}^{K}\frac{I_k(\omega)}{N(\omega)}\frac{|B(\omega;\xi_k,\xi_l)|^2}{w'w}\right]^{-2}d\omega\right\}^{1/2}. \tag{2.15}$$

When interference is absent, these results reduce to the corresponding expressions in Appendix B when the array gain $G=1$, that is, when the array comprises a single hydrophone.

III. TEMPORALLY NONRESOLVABLE INTERFERENCES

Temporally nonresolvable interference in the beamformer output arises in complex environments in which both the number and location of the interferences change rapidly. If the time duration of an interferer is sufficiently short and the occurrence rate is sufficiently high when compared to the averaging time T of the postdetection filter, then the detector output $z(t)$ is essentially stationary. The post- and predetection filters are linear and time invariant, so the beamformer output $v(t)$ is also essentially stationary. Consequently, the conventional and Eckart filters for nonresolvable interference can be approximated by this stationary limiting case. It will be shown that nonresolvable PM interference is closely related to classical (planewave) nonisotropic noise.

Assuming nonresolvable interference, the power spectrum of the beamformer output $v(t)$ is evaluated as a double expectation. The first expectation yields the beamformer output power spectrum (2.8), conditioned on a fixed number and location of interferences. The second expectation is the ensemble average of (2.8) with respect to the number K and the directions $\{\xi_1,\xi_2,\ldots,\xi_K\}$ of the nonresolvable interferences.

The PM interference model is defined on the set of all possible arrival directions, namely the unit sphere, denoted by Ω. Let $\Lambda(\xi)\geqslant 0$ denote the occurrence intensity of the

Poisson process in the direction ξ. The subset of Ω over which the intensity attains its maximum value is the set of directions from which interference is most likely to arrive. Similarly, the subset of Ω for which $\Lambda(\xi)=0$ gives the set of directions from which interference is impossible (with probability one). The magnitude of $\Lambda(\xi)$ determines the number of interferers from direction ξ to expect over time, that is, over the statistical ensemble defining the Poisson process. Further discussion of Poisson processes is given in Appendix A.

The expected value of $V(\omega)$ with respect to the PM interference process with intensity $\Lambda(\xi)$ is the PM power spectrum of the beamformer output, denoted by $\overline{V}_P(\omega)$. Denote the interference-weighted expected beam-response pattern by the surface integral

$$\overline{B}_\Lambda(\omega,\xi_l)=\int_\Omega |B(\omega;\xi,\xi_l)|^2\Lambda(\xi)d\xi, \tag{3.1}$$

where the surface area element on Ω is $d\xi=\sin\phi\, d\phi\, d\theta$. It is now assumed that the interferers have identical power spectra, $I_k(\omega)=I(\omega)$ for all k. Using Eq. (2.8) and the identity (A6) of Appendix A, the PM power spectrum is easily shown to be given by

$$\begin{aligned}\overline{V}_P(\omega)&=E_\Lambda[V(\omega)]\\&=S(\omega)|B(\omega;\xi_s,\xi_l)|^2+G^{-1}N(\omega)|B(\omega;\xi_l,\xi_l)|^2\\&\quad+I(\omega)\overline{B}_\Lambda(\omega,\xi_l).\end{aligned} \tag{3.2}$$

Application-specific expressions for $\overline{V}_P(\omega)$ are obtained by evaluating $\overline{B}_\Lambda(\omega,\xi_l)$ for particular interference intensity functions $\Lambda(\xi)$.

The expectation $\overline{V}_P(\omega)$ for the Poisson interference model differs from nonisotropic (plane wave) ambient noise models only in the interpretation that is made of the intensity function $\Lambda(\xi)$. Ambient noise in the vicinity of the array is classically modeled as the linear superposition of independent plane waves from every possible arrival direction ξ. In contrast to the PM interference model, the plane waves comprising nonisotropic noise are always present. Noise intensity varies with direction ξ. Let $\Lambda(\xi)d\xi$ be the plane wave intensity in direction ξ and differential element $d\xi$. The power spectrum $I(\omega,\xi)\equiv I(\omega)$ of the nonisotropic noise field is spatially homogeneous. Thus, the component of the beamformer output power spectrum due to nonisotropic ambient noise is the integral

$$I(\omega)\int_\Omega |B(\omega;\xi,\xi_l)|^2\Lambda(\xi)d\xi, \tag{3.3}$$

which is identical to the third term on the right-hand side of (3.2). At the beamformer output, therefore, PM interference is equivalent to a nonisotropic ambient noise field with intensity $\Lambda(\xi)$. In other words, sufficiently rapid intermittent fluctuations of PM distributed interference is indistinguishable from nonisotropic ambient noise.

If a temporally nonresolvable PM signal model is employed to model signal multipath effects, then it is also necessary to take the expectation of (2.8) with respect to the PM signal process. Let $\Gamma(\xi)$ denote the Poisson intensity of signal arrival direction. Signal and interference PM processes are independent; hence, paralleling the above discussion for interference gives the PM spectrum with respect to signal and interference processes as

$$\begin{aligned}\bar{\bar{V}}_P(\omega)&=E_\Gamma[\overline{V}_P(\omega)]\\&=S(\omega)\overline{B}_\Gamma(\omega,\xi_l)+G^{-1}N(\omega)|B(\omega;\xi_l,\xi_l)|^2\\&\quad+I(\omega)\overline{B}_\Lambda(\omega,\xi_l),\end{aligned} \tag{3.4}$$

where $\overline{B}_\Gamma(\omega,\xi_l)$ is given by (3.1) with Γ replacing Λ. If the signal arrives from a single direction, say ξ_{s_0}, then $\Gamma(\xi)\equiv\gamma_0\delta(\xi-\xi_{s_0})$, where $\delta(\cdot)$ denotes the Dirac delta function; the result (3.4) reverts to (3.2) exactly if the intensity $\gamma_0=1$.

From Eq. (3.4), the difference in means of $z(t)$ for PM signal and interference processes under hypotheses $\mathbf{H}_0$ and $\mathbf{H}_1$ is

$$\Delta=\int_{-\infty}^{\infty} S(\omega)\overline{B}_\Gamma(\omega,\xi_l)d\omega. \tag{3.5}$$

The deflection coefficients are obtained from (3.5) and the variance of the PM spectrum (3.4) under a low SNR assumption. From Eq. (B4) in Appendix B and the normalization $B(\omega;\xi_l,\xi_l)=M$, it follows that

$$\begin{aligned}\mathrm{Var}[\bar{\bar{V}}_P(\omega)]&=\frac{1}{\pi T}\int_{-\infty}^{\infty}|H_0(\omega)|^4[G^{-1}M^2N(\omega)\\&\quad+I(\omega)\overline{B}_\Lambda(\omega,\xi_l)]^2d\omega,\end{aligned} \tag{3.6}$$

assuming the correlation times of noise and interferences are small compared to T, the averaging time of the postdetection filter. For short-duration interferers, this assumption is valid. The predetection filter is omitted from the conventional detector, so that $x(t)\equiv v(t)$ in Fig. 1, that is, $|H_0(\omega)|\equiv 1$. From (B7) of Appendix B

$$d_{\mathrm{conv}}^{\mathrm{nonres}}(\xi_l)=\frac{\frac{1}{2}\sqrt{T/\pi}\int_{-\infty}^{\infty}S(\omega)\overline{B}_\Gamma(\omega,\xi_l)d\omega}{\{\int_{-\infty}^{\infty}[G^{-1}M^2N(\omega)+I(\omega)\overline{B}_\Lambda(\omega,\xi_l)]^2d\omega\}^{1/2}}. \tag{3.7}$$

If there is no signal multipath and $\Gamma(\xi)\equiv\gamma_0\delta(\xi-\xi_{s_0})$ with $\gamma_0=1$, if the array is steered on target, so that $\xi_{s_0}=\xi_l$, and if the noise spectrum is strictly positive, then (3.7) can be written in the more insightful form

$$\begin{aligned}d_{\mathrm{conv}}^{\mathrm{nonres}}(\xi_l)=\sqrt{\pi T}GS\Bigg\{&\int_{-\infty}^{\infty}N^2(\omega)\\&\times\left[1+\frac{I(\omega)}{N(\omega)}\frac{\overline{B}_\Lambda(\omega,\xi_l)}{w'w}\right]^2d\omega\Bigg\}^{-1/2}.\end{aligned} \tag{3.8}$$

This result is what would be obtained from Eq. (2.11) by setting $I_k(\omega)\equiv I(\omega)$ for all k and replacing the finite sum by its expectation with respect to the PM interference model.

If the noise spectrum is strictly positive, the optimal Eckart filter is

$$|H^{\text{nonres}}_{\text{Eckart}}(\omega,\xi_l)|^2=\frac{S(\omega)\overline{B}_\Gamma(\omega,\xi_l)}{N^2(\omega)}\times\left[1+\frac{I(\omega)}{N(\omega)}\frac{\overline{B}_\Lambda(\omega,\xi_l)}{w'w}\right]^{-2},\qquad(3.9)$$

and the deflection coefficient is

$$d^{\text{nonres}}_{\text{Eckart}}(\xi_l)=\frac{G}{2}\left\{\frac{T}{\pi}\int_\Psi\left[\frac{S(\omega)\overline{B}_\Gamma(\omega,\xi_l)}{N(\omega)}\right]^2\times\left[1+\frac{I(\omega)}{N(\omega)}\frac{\overline{B}_\Lambda(\omega,\xi_l)}{w'w}\right]^{-2}d\omega\right\}^{1/2}.\qquad(3.10)$$

The results (3.9) and (3.10) are the same as would be obtained from (2.14) and (2.15), respectively, by replacing finite sums with their analogous Poisson expectations.

IV. TEMPORALLY RESOLVABLE INTERFERENCES

Temporally resolvable interference occurs when interferences in the far field of the array are of long duration compared to the averaging time T of the postdetection filter. The start and end times of such interferers can be estimated to within an error depending on T. These interferers are, essentially, models of distant ship traffic. In practice, the arrival directions of these interferers can be estimated and their effect on detection analyzed using the fixed interference model of Sec. II. This approach is useful for specific interference distributions, but it does not give insight into detection capabilities when the specific traffic pattern is unknown. In this section, ensemble averages (expectations) of mean levels and standard deviations are evaluated explicitly under the assumption that the number and location of the interferers follow the PM interference statistical model. The resulting expression for the deflection coefficient d depends on the PM interference intensity function, but it is independent of specific interference patterns.

Because only the signal contribution remains after differencing the conditional mean of the output $z(t)$ under hypotheses $\mathbf{H}_1$ and $\mathbf{H}_0$, the deflection coefficient is easily computed from the variance of $z(t)$ under $\mathbf{H}_0$. Conditioned on a fixed number and location of interferences, the variance of $z(t)$, denoted

$$\text{Var}[z]\equiv E[(z-\overline{z})^2|\text{fixed interference}],\qquad(4.1)$$

is stationary; that is, $\text{Var}[z]$ is constant because the ensemble used to define $\text{Var}[z]$ comprises only realizations of $z(t)$ having a fixed interference pattern. However, PM interference is nonstationary, and $\text{Var}[z]$ fluctuates over time. As a result, it is necessary to compute the expectation of $\text{Var}[z]$ with respect to the PM interference model. The expectation $E_\Lambda[\text{Var}[z]]$ is thus a double expectation of the same statistical character as used above for nonresolvable interference.

An explicit expression for the variance (4.1) is obtained by assuming that the correlation time of an interferer is small compared to the averaging time T of the postdetection filter. Thus, in comparison to T, resolvable interferers have long durations and short correlation times. Correlation time is approximately inversely proportional to bandwidth, so the assumption is satisfied in applications in which the interference bandwidth is large compared to $2\pi/T$.

From the small SNR assumption, it follows from (2.8) with $I_k(\omega)=I(\omega)$ for all k and from (B4) of Appendix B that

$$\text{Var}[z]=\frac{1}{\pi T}\int_{-\infty}^{\infty}|H_0(\omega)|^4\left[G^{-1}M^2N(\omega)+I(\omega)\sum_{k=1}^{K}|B(\omega;\xi_k,\xi_l)|^2\right]^2d\omega,$$

where the normalization $B(\omega;\xi_l,\xi_l)=M$ has been used. Linearity of the expectation operator gives the expectation of $\text{Var}[z]$ with respect to the PM interference model as

$$E_\Lambda[\text{Var}[z]]=\frac{1}{\pi T}\int_{-\infty}^{\infty}|H_0(\omega)|^4E_\Lambda\left[\left[\frac{M^2}{G}N(\omega)+I(\omega)\sum_{k=1}^{K}|B(\omega;\xi_k,\xi_l)|^2\right]^2\right]d\omega.\qquad(4.2)$$

Interchanging the integral and the expectation operator is justified here because the integral is absolutely convergent. From (A9) of Appendix A, the required expectation in the integrand of (4.2) is

$$\left[G^{-1}M^2N(\omega)+I(\omega)\int_\Omega|B(\omega;\xi,\xi_l)|^2\Lambda(\xi)d\xi\right]^2+I^2(\omega)\int_\Omega|B(\omega;\xi,\xi_l)|^4\Lambda(\xi)d\xi.$$

The first term was encountered earlier with nonresolvable interference; the second term is contributed by the nonstationary character of resolvable PM interference. The predetection filter is omitted from the conventional detector, so that $|H_0(\omega)|=1$; hence, from (B7) of Appendix B, the deflection coefficient for the conventional processor in resolvable PM interference is

$$d^{\text{res}}_{\text{conv}}(\xi_l)=\frac{\frac{1}{2}\sqrt{\frac{T}{\pi}}\int_{-\infty}^{\infty}S(\omega)\overline{B}_\Gamma(\omega,\xi_l)d\omega}{\tilde{\sigma}_{\text{res}}},\qquad(4.3)$$

where

$$(\tilde{\sigma}_{\text{res}})^2=\int_{-\infty}^{\infty}\left[G^{-1}M^2N(\omega)+I(\omega)\int_\Omega|B(\omega;\xi,\xi_l)|^2\Lambda(\xi)d\xi\right]^2d\omega+\int_{-\infty}^{\infty}\int_\Omega I^2(\omega)|B(\omega;\xi,\xi_l)|^4\Lambda(\xi)d\xi\,d\omega.\qquad(4.4)$$

If there is no signal multipath and $\Gamma(\xi)=\delta(\xi-\xi_{s_0})$, if the array is steered on target so that $\xi_l=\xi_{s_0}$, and if the noise spectrum is positive, then

$$d_{\mathrm{conv}}^{\mathrm{res}}(\xi_l)=\sqrt{\pi T}GS\left\{\int_{-\infty}^{\infty}N^2(\omega)\left[1+\frac{I(\omega)}{N(\omega)}\frac{\overline{B}_{\Lambda}(\omega,\xi_l)}{w'w}\right]^2 d\omega + \int_{-\infty}^{\infty}I^2(\omega)\left[\frac{\int_{\Omega}|B(\omega;\xi,\xi_l)|^4\Lambda(\xi)d\xi}{(w'w)^2}\right]d\omega\right\}^{-1/2}. \tag{4.5}$$

The deflection coefficient reduces to the interference-free case if $I(\omega)=0$.

The Eckart filter is given by

$$|H_{\mathrm{Eckart}}^{\mathrm{res}}(\omega,\xi_l)|^2=\frac{S(\omega)\overline{B}_{\Gamma}(w,\xi_l)}{N^2(\omega)}\left\{\left[1+\frac{I(\omega)}{N(\omega)}\frac{\overline{B}_{\Lambda}(\omega,\xi_l)}{w'w}\right]^2 + \left[\frac{I(\omega)}{N(\omega)}\right]^2\frac{\int_{\Omega}|B(\omega;\xi,\xi_l)|^4\Lambda(\xi)d\xi}{w'w}\right\}^{-1}, \tag{4.6}$$

and the corresponding deflection coefficient is

$$d_{\mathrm{Eckart}}^{\mathrm{res}}(\xi_l)=\frac{G}{2}\left\{\frac{T}{\pi}\int_{\Psi}\left[\frac{S(\omega)\overline{B}_{\Gamma}(w,\xi_l)}{N(\omega)}\right]^2 \times\left\{\left[1+\frac{I(\omega)}{N(\omega)}\frac{\overline{B}_{\Lambda}(\omega,\xi_l)}{w'w}\right]^2 + \left[\frac{I(\omega)}{N(\omega)}\right]^2\frac{\int_{\Omega}|B(\omega;\xi,\xi_l)|^4\Lambda(\xi)d\xi}{w'w}\right\}^{-1}d\omega\right\}^{1/2}. \tag{4.7}$$

These results reduce to the interference-free case if $I(\omega)=0$.

V. RECOGNITION DIFFERENTIALS

Classical expressions for the recognition differential (N_{RD}) are obtained by imposing simple spectral models on both signal and noise and then taking the logarithm of the deflection coefficient for the conventional processor in the interference-free case (Cox[6]). In this section, these spectral models are supplemented with an equally simple interference spectral model. Interference correction (IC) factors for the classical N_{RD} expression are derived via the appropriate deflection coefficient expression for fixed interferences and for both temporally resolvable and nonresolvable interferences. (Alternatively, the classical N_{RD} expression can be retained if the IC term is treated as a noise term and added to the sonar equation.)

Creese[7] uses the results presented in this section to evaluate N_{RD} expressions numerically for a uniformly shaded line array. He considers several ocean environments with different shipping densities and sea states. Multiple types of interference spectra are modeled by superposition of several PM interference models, one for each spectral type. For further details, the interested reader is referred to Creese.[7]

The classical N_{RD} analysis is straightforward. If there is no interference, $I(\omega)\equiv 0$; if the noise spectrum is flat and equals N_0 (per Hertz) over a frequency band of (radian) bandwidth W, and if there are no signal multipath effects, then from (2.11)

$$d_{\mathrm{conv}}^{K}(\xi_l)|_{K=0}=G\sqrt{\frac{TW_0}{2\pi}}\frac{S}{N}, \tag{5.1}$$

where

$$N=\frac{1}{2\pi}\int_{-\infty}^{\infty}N(\omega)d\omega=\frac{WN_0}{2\pi} \tag{5.2}$$

is the noise power and $W_0=W/2$ denotes the (radian) bandwidth of the one-sided noise spectrum. In this case, the deflection coefficient for the conventional processor is directly proportional to the array gain G, the square root of the time-bandwidth product TW_0, and the signal-to-noise ratio. Let d_{thresh} denote the detection threshold determining the (P_D,P_{FA}) operating point on the detector's ROC curve. Converting to decibels (dB) by taking 10 log of (5.1) and solving for signal gives

$$N_{\mathrm{RD}}=SL-NL+AG, \tag{5.3}$$

where

$$SL=10\log S,\quad NL=10\log N,\quad AG=10\log G,$$

and

$$N_{\mathrm{RD}}=DT-5\log\left(\frac{TW_0}{2\pi}\right), \tag{5.4}$$

where $DT=10\log d_{\mathrm{thresh}}$. Equation (5.3) is the classical passive-sonar equation if SL, the received signal level, is set equal to the target source level minus the one-way transmission loss. In practice, background noise level is estimated from beams that are free of signal and interference; however, such procedures are unnecessary in a theoretical analysis if noise and interference models are given.

The classical recognition differential (5.4) does not depend on the look direction ξ_l when the assumptions under which it is derived are met; that is, when there is no interference. When interference is present, the recognition differential is written

$$N_{\mathrm{RD}}=DT-5\log\left(\frac{TW_0}{2\pi}\right)+\mathrm{IC},$$

where the term IC depends on the specific nature of the interference.

For fixed interferences, the deflection coefficient (2.11) holds. Assuming that the noise and interference spectra are flat over the same bandwidth W, and that interferences have identical spectra equal to I_0 (per Hertz), the IC term is

$$\mathrm{IC}^K=5\log\left[\frac{1}{W}\int_W\left[1+\frac{I}{N}\sum_{k=1}^{K}\frac{|B(\omega;\xi_k,\xi_l)|^2}{w'w}\right]^2 d\omega\right], \tag{5.5}$$

where $I=1/2\pi\int_{-\infty}^{\infty}I(\omega)d\omega=WI_0/2\pi$ is the interference power. For the case $K=0$, the correction term $\mathrm{IC}^K\equiv 0$.

The correction term (5.5) simplifies if the integral over the bandwidth W is approximated by the product of W and

the integrand evaluated at the center frequency ω_c of the one-sided band W_0. With this approximation, (5.5) becomes

$$\mathrm{IC}^K \cong 10\log\left[1+\frac{I}{N}\sum_{k=1}^{K}\frac{|B(\omega_c;\xi_k,\xi_l)|^2}{w'w}\right]. \tag{5.6}$$

The IC term (in dB) for K-independent interferences is not the linear sum of K individual IC terms, as is clear from both (5.5) and the approximation (5.6).

The derivation of the correction term for nonresolvable PM interference proceeds in essentially the same manner, but with the sum in (5.5) replaced by an integral. Using the deflection (3.8), the IC term takes the form

$$\mathrm{IC}^{\mathrm{nonres}} = 5\log\left[\frac{1}{W}\int_W\left[1+\frac{I}{N}\int_\Omega\frac{|B(\omega;\xi,\xi_l)|^2}{w'w}\Lambda(\xi)d\xi\right]^2 \times d\omega\right]. \tag{5.7}$$

If the interference power $I=0$, the correction term (5.7) is zero. The correction term (5.7) simplifies if the product of W and the integrand evaluated at the center frequency ω_c approximates the integral over ω. Substituting this approximation in (5.7) gives

$$\mathrm{IC}^{\mathrm{nonres}} \cong 10\log\left[1+\frac{I}{N}\int_\Omega\frac{|B(\omega_c;\xi,\xi_l)|^2}{w'w}\Lambda(\xi)d\xi\right]. \tag{5.8}$$

Limiting values of (5.8) as $I/N\to 0$ and as $I/N\to\infty$ are of interest. Using the approximation $\log_e(1+x)\cong x$, $x\to 0$, gives the low interference-to-noise limit, in dB, as

$$\mathrm{IC}^{\mathrm{nonres}} \cong 4\left\{\int_\Omega\frac{|B(\omega_c;\xi,\xi_l)|^2}{w'w}\Lambda(\xi)d\xi\right\}\frac{I}{N}, \quad \frac{I}{N}\to 0, \tag{5.9}$$

where $4\cong 10\log e$. Thus, (5.9) approaches zero as $I/N\to 0$. The high interference-to-noise limit is

$$\mathrm{IC}^{\mathrm{nonres}} \cong 10\log\left[\frac{I}{N}\int_\Omega\frac{|B(\omega_c;\xi,\xi_l)|^2}{w'w}\Lambda(\xi)d\xi\right], \quad \frac{I}{N}\to\infty,$$
$$= IL - NL + 10\log\left[\frac{\int_\Omega|B(\omega_c;\xi,\xi_l)|^2\Lambda(\xi)d\xi}{w'w}\right], \tag{5.10}$$

where $IL = 10\log I$ is the interference power in dB. The high interference-to-noise limit is obtained merely by noting that the constant 1 in (5.8) is small compared to I/N.

The correction term for resolvable PM interference proceeds from the deflection coefficient given by (4.5). The IC term is

$$\mathrm{IC}^{\mathrm{res}} = 5\log\left[\frac{1}{W}\int_W\left\{\left[1+\frac{I}{N}\int_\Omega\frac{|B(\omega;\xi,\xi_l)|^2}{w'w}\Lambda(\xi)d\xi\right]^2 + \left(\frac{I}{N}\right)^2\int_\Omega\frac{|B(\omega;\xi,\xi_l)|^4}{(w'w)^2}\Lambda(\xi)d\xi\right\}d\omega\right]. \tag{5.11}$$

Using the product of W and the integrand evaluated at the center frequency ω_c to approximate the integral over ω gives

$$\mathrm{IC}^{\mathrm{res}} \cong 5\log\left[\left[1+\frac{I}{N}\int_\Omega\frac{|B(\omega_c;\xi,\xi_l)|^2}{w'w}\Lambda(\xi)d\xi\right]^2 + \left(\frac{I}{N}\right)^2\int_\Omega\frac{|B(\omega_c,\xi,\xi_l)|^4}{(w'w)^2}\Lambda(\xi)d\xi\right]. \tag{5.12}$$

The low interference-to-noise limit is the same as (5.9), as is seen from (5.12) by noting that the ratio $(I/N)^2$ is small compared to I/N. The high interference-to-noise limit is

$$\mathrm{IC}^{\mathrm{res}} \cong 5\log\left[\left(\frac{I}{N}\right)^2\left\{\left[\int_\Omega\frac{|B(\omega_c;\xi,\xi_l)|^2}{w'w}\Lambda(\xi)d\xi\right]^2 + \int_\Omega\frac{|B(\omega_c;\xi,\xi_l)|^4}{(w'w)^2}\Lambda(\xi)d\xi\right\}\right]$$
$$= IL - NL + 10\log\left[\frac{I}{N}\int_\Omega\frac{|B(\omega_c;\xi,\xi_l)|^2}{w'w}\Lambda(\xi)d\xi\right], + 5\log\left[1+\frac{\int_\Omega|B(\omega_c;\xi,\xi_l)|^4\Lambda(\xi)d\xi}{\{\int_\Omega|B(\omega_c;\xi,\xi_l)|^2\Lambda(\xi)d\xi\}^2}\right]. \tag{5.13}$$

Thus, as $I/N\to\infty$, the IC term for resolvable interference differs from that for nonresolvable interference by the last term in (5.13), which depends on the directional process $\Lambda(\xi)$ but not on the ratio I/N.

VI. SUMMARY AND CONCLUDING REMARKS

A quantitative analysis of the degradation of performance for the conventional and optimal detector for arrays of arbitrary geometry has been presented for fixed interference and for nonresolvable and resolvable PM interference. Rapid, short duration, temporally nonresolvable interference leads to expressions that are essentially the same as those obtained from classical nonisotropic noise models. Long duration, temporally resolvable interference is slowly varying when compared to the averaging time of the postdetection filter, and it leads to novel expressions for the deflection coefficient. Interference correction terms for the conventional detector are derived from the deflection coefficients for all three kinds of interference.

Poisson interference models for specific scenarios with slowly changing, but relatively stable, interference fields can be obtained by extending the work presented here to doubly stochastic Poisson models; that is, to models in which the Poisson interference intensity is a function of time. Resolvable and nonresolvable interferences are limiting cases of this more general temporal–directional PM interference model. The approach requires parametrizing the Poisson intensity functions of signal and interference appropriately and estimating the constituent parameters adaptively over time. The beam level deflection coefficients $\{d(\xi_l)\}$ are thus a collection of coupled (especially at lower frequencies in which interference arrival directions are not spatially resolvable) sufficient statistics of a family of generalized likelihood ratio tests in which the signal, noise, and interference spectra are jointly statistically estimated by maximum likelihood or maximum *a posteriori* multibeam procedures. Generalized likelihood ratio tests are often, but not always, very effective in practice, and their performance is usually difficult to as-

certain theoretically. An adaptive approach should improve the performance of the conventional and optimal processors in changing interference environments; however, adaptive multibeam filters and similar interesting topics lie outside the scope of the present paper.

Finally, practical experience suggests that the split-beam (or split-array) cross-correlation processor may sometimes offer better performance than the optimum processor in difficult interference environments. The application of PM interference models to analyze the detection performance of the cross-correlation processor may facilitate comparisons between it and the optimal (full-array) processor discussed in this paper.

ACKNOWLEDGMENTS

This work was supported by the Office of Naval Research. The author thanks J. R. Short, R. R. Kneipfer, T. E. Luginbuhl, and M. J. Walsh for many stimulating discussions.

APPENDIX A: NONHOMOGENEOUS POISSON PROCESSES

Poisson point processes are discrete–continuous stochastic processes. The discrete component determines the number of events, or points, that occur in a given realization and the continuous component determines where the points lie in a specified space, or domain, denoted by X. The intensity $\Lambda(x)$ of the process is a non-negative function defined for every point $x \in X$, and it completely determines both the discrete and continuous components of the distribution. If $\Lambda(x)$ is constant over X, then the process is said to be homogeneous; otherwise, it is nonhomogeneous. Simulation of one realization of a Poisson process on a given region $S \subset X$ is a two-step procedure. Step 1 samples the discrete component to determine the number of events that occur. The discrete distribution governing this sample is the Poisson distribution with parameter $\lambda_S = \int_S \Lambda(x)dx$, where dx denotes the appropriate differential of ''volume'' in the space X. Because the intensity is non-negative, λ_S is non-negative also. The discrete Poisson distribution is

$$P[k] = \frac{(\lambda_S)^k}{k!} \exp[-\lambda_S], \quad k = 0,1,2,\ldots . \tag{A1}$$

Suppose, then, that the realization of the discrete Poisson distribution with parameter λ_S is K; that is, K is the number of points that must now be sampled from the set S. Step 2 of the simulation samples these K points as independent realizations of a random variable whose probability density function is

$$p_S(x) = \frac{\Lambda(x)}{\int_S \Lambda(\xi)d\xi}, \quad x \in S. \tag{A2}$$

This completes the simulation of one realization of the Poisson process. The two-step procedure depends on the choice of the subset S via the parameter λ_S and the density $p_S(x)$. If λ_S is zero for some set S, then with probability one the outcome of *step* 1 is $K=0$, so that no points need be sampled in *step* 2; thus, the possible division by zero in (A2) is avoided. The sample points in *step* 2 are independent of the number K of sample points drawn, so that for all $K \geqslant 1$

$$p_S(x_1,\ldots,x_K|K) = p_S(x_1,\ldots,x_K) = \prod_{k=1}^{K} p_S(x_k). \tag{A3}$$

This important result is used below in the definition of the expectation operator.

The domain X over which a Poisson process can be defined is as general as the concept of integration; that is, it can be defined on any domain X for which $\int_S \Lambda(\xi)d\xi$ is defined for any (measurable) region $S \subset X$. The process is temporal if X is a time interval, say T, spatial if $X = R^p$ for integers $p \geqslant 1$, spatial–temporal if $X = R^k \times T$, directional if $X = \Omega \equiv \{x \in R^3 : \|x\| = 1\}$, and directional–temporal if $X = \Omega \times T$. It is an azimuthal process if X is the unit circle Ω in R^2. The details change with the space X, but Eqs. (A1) and (A2) always hold.

The expectation operator on the region $S \subset X$ is defined for real or complex valued functions F as

$$\begin{aligned} E_\Lambda[F] &= \sum_{K=1}^{\infty} P[K] \int \cdots \int_{S^K} F(x_1,\ldots,x_K) \\ &\quad \times p_S(x_1,\ldots,x_K|K)dx_1,\ldots,dx_K \\ &= \sum_{K=1}^{\infty} P[K] \int \cdots \int_{S^K} F(x_1,\ldots,x_K) \\ &\quad \times \prod_{k=1}^{K} p(x_k)dx_1, \ldots, dx_K, \end{aligned} \tag{A4}$$

where the integral is over the K-fold Cartesian product $S \times \cdots \times S \equiv S^K \subset X^K$, the probability $P[K]$ is given by (A1), and where the conditional independence of sample points (A3) is substituted in the second expression. It is evident from (A4) that the function F must be defined for any number of arguments, so F cannot be a traditional function having a fixed number of arguments; in other words, F must be defined for every possible outcome of the Poisson process. The kind of function most relevant to this paper is, for $K > 0$,

$$F = F(x_1,\ldots,x_K) = \sum_{k=1}^{K} f(x_k), \tag{A5}$$

where $f(x)$ is a traditional function having a single argument. For $K=0$, F is defined to be 0. The expected value of F is

$$E_\Lambda[F] \equiv E_\Lambda\left[\sum_{k=1}^{K} f(x_k)\right] = \int_S f(x)\Lambda(x)dx. \tag{A6}$$

Intuitively, this expectation weights terms in the sum (A5) by the intensity with which those terms can occur. If $f(x) = 1$, then (A6) is λ_S, and if $f(x) = \exp(i\omega \cdot x)$, $\omega \in X \equiv R^p$ for some $p \geqslant 1$, then (A6) is the characteristic function of $\Lambda(x)$ restricted to the region S.

The expected value of the product of two functions of the form (A5) is

$$E_\Lambda\left[\sum_{k=1}^{K} f(x_k)\sum_{k=1}^{K} g(x_k)\right]=\int_S f(x)g(x)\Lambda(x)dx + \int_S f(x)\Lambda(x)dx\int_S g(x)\Lambda(x)dx. \tag{A7}$$

Setting $f\equiv g^*$ gives the important result

$$E_\Lambda\left[\left|\sum_{k=1}^{K} f(x_k)\right|^2\right]=\int_S |f(x)|^2\Lambda(x)dx + \left|\int_S f(x)\Lambda(x)dx\right|^2. \tag{A8}$$

The proofs of (A6) and (A7) given by Hero[8] hold for intensities $\Lambda(x)$ such that $\int_S\Lambda(x)dx<\infty$, and for real-valued functions f and g such that

$$\int_S |f(x)|^2\Lambda(x)dx<\infty \quad \text{and} \quad \int_S |g(x)|^2\Lambda(x)dx<\infty.$$

The proof for complex valued functions follows easily by separating them into real and imaginary parts. Finally, if f_0 is an arbitrary constant, then

$$E_\Lambda\left[\left|f_0+\sum_{k=1}^{K} f(x_k)\right|^2\right]=\left|f_0+\int_S f(x)\Lambda(x)dx\right|^2 + \int_S |f(x)|^2\Lambda(x)dx, \tag{A9}$$

as is seen by expanding the squared magnitude in (A9) and substituting the results (A6) and (A8).

For further discussion of Poisson processes, the alternative tradition in signal processing, see Snyder and Miller[9] and Kingman.[10]

APPENDIX B: DETECTION OF GAUSSIAN SIGNALS IN ADDITIVE NOISE

The deflection coefficient for a stationary Gaussian signal in additive independent stationary Gaussian noise is reviewed in this Appendix, as is the optimal predetection, or Eckart, filter. The spectrum of the Gaussian signal that is least detectable by the Eckart processor is also discussed. Robust versions of the Eckart filter that are insensitive to variations in signal and noise spectra are discussed by Al-Husseini and Kassam.[11]

The processing stream is limited to the portion of Fig. 1 from input $v(t)$ to output $z(t)$, inclusive. Predetection and postdetection filters are assumed linear and time invariant. The input $v(t)$ is assumed real valued, zero mean, Gaussian, and stationary, so $x(t)$ is also real valued, zero mean, Gaussian, and stationary. Due to the nonlinear square-law device, $y(t)$ and $z(t)$ are real valued and stationary, but neither zero mean nor Gaussian. (If the input process is complex valued instead of real valued, as assumed in this Appendix, the Eckart filter and corresponding deflection coefficient differ from the expressions given below by a constant.) A complete but standard derivation of the deflection coefficient can be found in Streit.[12]

Assuming small SNR, the output variance under the hypotheses

$\{\mathbf{H}_0$: noise only is present$\}$,

$\{\mathbf{H}_1$: signal plus noise is present$\}$,

are approximately equal. The difference of the means of the output $z(t)$ under these hypotheses is divided by the standard deviation under the null hypothesis to obtain the so-called deflection coefficient, denoted by d. The ROC curves of the detector are completely parametrized by d under Gaussian signal and noise statistical assumptions.

Let $h_1(\tau)$ denote the impulse response function of the postdetection filter normalized so that

$$\int_{-\infty}^{\infty} h_1(\tau)d\tau=1. \tag{B1}$$

The simplest low-pass postdetection filter satisfying the normalization (B1) is $h_1(t)=1/T$ for $|t|\leqslant T/2$ and $h_1(t)=0$ for $|t|\geqslant T/2$. The variance of the output $z(t)$ is given by (see, for example, Thomas[13] for a careful discussion)

$$\mathrm{Var}[z]=\frac{2}{T}\int_{-T}^{T} R_x^2(\tau)\left(1-\frac{|\tau|}{T}\right)d\tau\cong\frac{1}{\pi T}\int_{-\infty}^{\infty} S_x^2(\omega)d\omega, \tag{B2}$$

where $S_x(\omega)$ is the power spectrum of $x(t)$. The approximation (B2) is reasonable if T is large compared to the correlation time. Denoting the impulse response and transfer functions of the predetection filter by $h_0(\tau)$ and $H_0(\omega)$, respectively, gives

$$S_x(\omega)=|H_0(\omega)|^2S_v(\omega). \tag{B3}$$

Substituting (B3) into (B2) gives

$$\mathrm{Var}[z]=\frac{1}{\pi T}\int_{-\infty}^{\infty}|H_0(\omega)|^4S_v^2(\omega)d\omega. \tag{B4}$$

The difference in the means of $z(t)$ under hypotheses $\mathbf{H}_0$ and $\mathbf{H}_1$ is computed from the power spectra of the input $v(t)$ under hypotheses $\mathbf{H}_0$ and $\mathbf{H}_1$, denoted by $S_v^N(\omega)$ and $S_v^{S+N}(\omega)$, respectively. Signal and noise are statistically independent, so their power spectra add; that is, $S_v^{S+N}(\omega)=S_v^S(\omega)+S_v^N(\omega)$, where $S_v^S(\omega)$ denotes the spectrum of the signal. The predetection filter is linear and time invariant, so the difference in the mean of the output $z(t)$ under hypotheses $\mathbf{H}_0$ and $\mathbf{H}_1$ is

$$\Delta\equiv E[z|H_1]-E[z|H_0]=\frac{1}{2\pi}\int_{-\infty}^{\infty}|H_0(\omega)|^2S_v^S(\omega)d\omega. \tag{B5}$$

The deflection coefficient for Gaussian random variables with identical variances is defined by $d=\Delta/\sigma$, where σ denotes the approximately equal standard deviations of $z(t)$ under $\mathbf{H}_0$ and $\mathbf{H}_1$. Substituting (B5) and (B4) gives

$$d=\frac{\frac{1}{2}\sqrt{\frac{T}{\pi}}\int_{-\infty}^{\infty}|H_0(\omega)|^2 S_v^S(\omega)\,d\omega}{[\int_{-\infty}^{\infty}|H_0(\omega)|^4[S_v^N(\omega)]^2 d\omega]^{1/2}}. \tag{B6}$$

If the signal spectrum is unknown, the predetection filter is sometimes omitted, so that

$$d=\frac{\frac{1}{2}\sqrt{\frac{T}{\pi}}\int_{-\infty}^{\infty}S_v^S(\omega)\,d\omega}{[\int_{-\infty}^{\infty}[S_v^N(\omega)]^2 d\omega]^{1/2}}, \tag{B7}$$

which is the expression used in the main body of the paper for the conventional processor.

The deflection (B6) can be maximized by a particular choice of $H_0(\omega)$ in any specified frequency band, say Ψ, for which the noise spectrum is bounded away from zero; that is, $S_v^N(\omega)\geqslant\varepsilon>0$ for $\omega\in\Psi$. The maximizing filter is called the Eckart filter, after its discoverer,[14] and it is denoted here by $H_{\text{Eckart}}(\omega)$. Straightforward application of the Cauchy–Schwarz inequality (see, e.g., Burdic[15]) gives

$$|H_{\text{Eckart}}(\omega)|^2=\frac{S_v^S(\omega)}{[S_v^N(\omega)]^2}. \tag{B8}$$

Substituting (B8) into (B6) gives

$$d_{\text{Eckart}}=\frac{1}{2}\left[\frac{T}{\pi}\int_{\Psi}\left[\frac{S_v^S(\omega)}{S_v^N(\omega)}\right]^2 d\omega\right]^{1/2}. \tag{B9}$$

Given the noise spectrum $S_v^N(\omega)$ and a specified signal power, say S_{power}, the least detectable signal $S_{\text{opt}}(\omega)$ is the signal for which the deflection coefficient d_{Eckart} is a minimum. Let $\alpha\geqslant 0$ denote the SNR. Then, $S_{\text{opt}}(\omega)$ is the solution of the following constrained optimization problem:

$$\min_{S(\omega)}\int_{\Psi}\left[\frac{S(\omega)}{S_v^N(\omega)}\right]^2 d\omega, \tag{B10}$$

subject to the SNR constraint

$$\frac{S_{\text{power}}}{\int_{\Psi}S_v^N(\omega)\,d\omega}=\frac{\int_{\Psi}S(\omega)\,d\omega}{\int_{\Psi}S_v^N(\omega)\,d\omega}=\alpha. \tag{B11}$$

Applying the calculus of variations to the Lagrangian function, it is straightforward to show (see Streit[12] for a detailed discussion) that the minimizing signal is

$$S_{\min}(\omega)=S_{\text{power}}\frac{[S_v^N(\omega)]^2}{\int_{\Psi}[S_v^N(\omega)]^2 d\omega}. \tag{B12}$$

In other words, the spectrum of the least detectable signal is directly proportional to the normalized square of the noise spectrum, and the proportionality constant is the specified signal power.

If noise power is finite and its spectrum is continuous and bounded on the band Ψ, then the deflection coefficient d_{Eckart} can be made arbitrarily large for any specified signal power $S_{\text{power}}>0$. For example, if the signal spectrum is

$$S_\epsilon(\omega)=\begin{cases}\epsilon^{-1}S_{\text{power}}, & a\leqslant\omega\leqslant a+\epsilon,\\ 0, & \text{otherwise,}\end{cases}$$

where a and $\epsilon>0$ are such that the interval $[a,a+\epsilon]$ is a subset of Ψ, then it is straightforward to show that $\int_{\Psi}S_\epsilon(\omega)\,d\omega=S_{\text{power}}$ and

$$\int_{\Psi}\left[\frac{S_\epsilon(\omega)}{S_v^N(\omega)}\right]^2 d\omega=\frac{1}{\epsilon}\frac{S_{\text{power}}^2}{[S_v^N(\omega_\epsilon)]^2}\geqslant\frac{1}{\epsilon}\left[\frac{S_{\text{power}}}{\max_{\omega\in\Psi}S_v^N(\omega)}\right]^2. \tag{B13}$$

The noise spectrum is bounded above on Ψ, so the maximum in (B13) is finite. Thus, d_{Eckart} is made arbitrarily large by choosing ϵ sufficiently small. In other words, the most detectable signals are those whose spectra contain at least one component of finite power and very narrow bandwidth.

[1] P. M. Schultheiss, ''Passive Sonar Detection in the Presence of Interference,'' J. Acoust. Soc. Am. **43**, 418–425 (1968).
[2] R. M. Heitmeyer, L. J. Davis, and N. Yen, ''Implications of Noise Source Resolution on Detection Performance for Horizontal Directional Systems Operating in Ship-Induced Noise Fields,'' Naval Research Laboratory Report 8863, 7 February 1985.
[3] S. C. Liu and L. W. Nolte, ''Performance Evaluation of Array Processors for Detecting Gaussian Acoustic Signals,'' IEEE Trans. Acoust., Speech, Signal Process. **ASSP-28**, 328–333 (1980).
[4] A. J. Claus, T. T. Kadota, and D. M. Romain, ''Efficient Approximation of a Family of Noises for Application in Adaptive Spatial Processing for Signal Detection,'' IEEE Trans. Inf. Theory **IT-26**, 588–595 (1980).
[5] H. Van Trees, *Detection, Estimation, and Modulation Theory*, Reprint ed. (Krieger, Malabar, FL, 1992), Part 3, pp. 459–482.
[6] H. Cox, private communication, 1971.
[7] M. A. Creese, ''Numerically Modeling the Impact of Multiple Interferences on the Recognition Differential (NRD),'' NUWC-NPT Reprint Report 11 229, Naval Undersea Warfare Center Division, Newport, Rhode Island (to be published).
[8] A. O. Hero, ''Lower Bounds on Estimator Performance for Energy-Invariant Parameters of Multidimensional Poisson Processes,'' IEEE Trans. Inf. Theory **IT-35**, 843–858 (1989).
[9] D. L. Snyder and M. I. Miller, *Random Point Processes in Time and Space* (Springer, New York, 1991).
[10] J. F. C. Kingman, *Poisson Processes* (Clarendon, Oxford, 1993).
[11] E. K. Al-Husseini and S. A. Kassam, ''Robust Eckart Filters for Time Delay Estimation,'' IEEE Trans. Acoust., Speech, Signal Process. **ASSP-32**, 1052–1063 (1984).
[12] R. L. Streit, ''Broadband Detection of Gaussian Signals,'' NUWC-NPT Technical Memorandum 990037, Naval Undersea Warfare Center, Newport, Rhode Island, 5 April 1999.
[13] J. B. Thomas, *An Introduction to Statistical Communication Theory* (Wiley, New York, 1969), Equation (6.4-19).
[14] C. Eckart, ''Optimal Rectifier Systems for the Detection of Steady Signals,'' Scripps Institution of Oceanography, La Jolla, CA, SIO Reference 52-11, 4 March 1952.
[15] W. S. Burdic, *Underwater Acoustic System Analysis* (Prentice-Hall, Englewood Cliffs, NJ, 1984).

Turboprop and rotary-wing aircraft flight parameter estimation using both narrow-band and broadband passive acoustic signal-processing methods

Brian G. Ferguson[a] and Kam W. Lo
Defence Science and Technology Organisation, PO Box 44 Pyrmont, NSW 2009, Australia

(Received 23 December 1999; revised 28 February 2000; accepted 30 March 2000)

Flight parameter estimation methods for an airborne acoustic source can be divided into two categories, depending on whether the narrow-band lines or the broadband component of the received signal spectrum is processed to estimate the flight parameters. This paper provides a common framework for the formulation and test of two flight parameter estimation methods: one narrow band, the other broadband. The performances of the two methods are evaluated by applying them to the same acoustic data set, which is recorded by a planar array of passive acoustic sensors during multiple transits of a turboprop fixed-wing aircraft and two types of rotary-wing aircraft. The narrow-band method, which is based on a kinematic model that assumes the source travels in a straight line at constant speed and altitude, requires time-frequency analysis of the acoustic signal received by a single sensor during each aircraft transit. The broadband method is based on the same kinematic model, but requires observing the temporal variation of the differential time of arrival of the acoustic signal at each pair of sensors that comprises the planar array. Generalized cross correlation of each pair of sensor outputs using a cross-spectral phase transform prefilter provides instantaneous estimates of the differential times of arrival of the signal as the acoustic wavefront traverses the array. [S0001-4966(00)03807-8]

PACS numbers: 43.60.Gk, 43.28.Tc [JCB]

INTRODUCTION

Unattended ground sensors are often deployed in remote areas for surveillance and early warning purposes. Sources of focal interest to land-based surveillance systems are ground vehicles (whether tracked or wheeled) and aircraft (jets, propeller-driven aircraft, and helicopters). Owing to the high levels of acoustic energy radiated by the propulsion systems of aircraft and by the engines of vehicles, it is possible to detect these sources using passive acoustic sensors mounted close to the ground.[1] The presence of an acoustic source can be detected automatically (and most simply) by comparing the received acoustic signal level with a preselected or adaptively controlled threshold. Data from acoustic sensors can also be processed for source classification, localization, and tracking.[2] When an aircraft travels at constant velocity and constant altitude, its trajectory is completely specified by a set of flight parameters. The retardation effect,[3] which arises when the speed of the source is comparable with the speed of sound propagation in the medium, enables the estimation of some or all of the aircraft flight parameters using passive acoustic methods.[4–7]

In the first part of the paper, the narrow-band parameter estimation method[5] is reviewed to facilitate its comparison with the broadband flight parameter estimation method,[7] as both methods are based on a nonlinear least-squares (LS) approach. For the narrow-band method, the spectral line corresponding to the blade-passage frequency of the turboprop aircraft's propeller (that is, the propeller blade rate) is selected for processing because it has the highest signal-to-noise ratio (SNR). Similarly, for the rotary-wing aircraft, the spectral line corresponding to the main-rotor blade rate is selected for analysis. However, the performance of the narrow-band method is comparable when another harmonic spectral line of the main-rotor blade rate, or even one of the harmonic spectral lines of the tail-rotor blade rate, is selected for analysis. The performance of the narrow-band method is evaluated by processing real data from only the center sensor of a cross array for a large number of aircraft transits. The narrow-band method estimates the aircraft speed, time, and slant range at which the aircraft is at the closest point of approach (CPA) to the sensor, along with the propeller blade rate or main-/tail-rotor blade rate.

In the second part of the paper, the broadband method[7] is reviewed and the data from each sensor of the cross array are used to evaluate its performance. SNR considerations for the broadband method suggest using the bandwidth 10–300 Hz when computing the generalized cross-correlation function with the cross-spectral phase transform prefilter (that is, the magnitude of the cross-spectral density function is set to unity in the selected bandwidth and to zero elsewhere). Phase transform prefiltering is necessary to suppress the ambiguous peaks in the cross-correlation function caused by the strong narrow-band tones, which correspond to the fundamental and higher harmonics of the blade-passage frequency. The broadband method estimates the aircraft speed and altitude, along with the time, ground range, and azimuth angle at which the aircraft is at the CPA to the center sensor of the cross array.

Both the narrow-band and broadband methods process the sensor data from the same array for the same sources. A significant advance is that these passive acoustic signal-

[a]Electronic mail: brian.ferguson@dsto.defence.gov.au

processing methods provide unattended land-based surveillance systems with the capability to extract reliable tactical information concerning the type of aircraft and its flight parameters by exploiting both the narrow-band and broadband features of the aircraft's acoustic spectrum. Evaluating the performance of these acoustic methods using real data requires conducting a controlled scientific experiment involving three different turboprop and rotary-wing aircraft with pilots flying a total number of 39 transits, each along a prescribed flight path at a designated speed and altitude.

I. NARROW-BAND METHOD

A. Background

For ground vehicles, propeller-driven aircraft and helicopters, the acoustic signal emitted by the source consists of one or more sets of harmonic tones superimposed on a broadband random component. The frequency of a narrow-band tone from a transiting source, when received by a stationary sensor, changes with time due to the acoustical Doppler effect. Processing the acoustic data from a single sensor enables the source frequency and source speed to be estimated along with the time and slant range at which the source is at the CPA to the sensor.[4,5] The method involves measuring the temporal variation of the instantaneous frequency (IF) of a received narrow-band tone and then minimizing the sum of the squared deviations of the IF estimates from their predicted values over a period of time. Moreover, by processing the fundamental tone of the harmonic series, the method can provide an estimate of the propeller blade rate of a turboprop aircraft, which is an important classification parameter. The main- or tail-rotor blade rate of a helicopter and the engine firing rate of a ground vehicle can be estimated in the same way. This narrow-band method has been successfully applied to real data to estimate the speed, altitude, and propeller blade rate of a turboprop aircraft flying directly over and along the axis of a linear array of 15 microphones.[4,5] In order to reduce the variability in the IF observations due to atmospheric fluctuations and noise, the sequences of IF estimates from all the microphones were appropriately shifted in time and then combined to provide a spatially averaged IF sequence for the parameter estimation. However, in practice, an aircraft seldom flies directly over and along the array axis, and a long linear array is often not available. An important contribution of this paper is to assess the performance of the narrow-band method *without* any spatial averaging, that is, by processing only the data from a *single* sensor.

B. Time-frequency model

Consider an acoustic source moving along a straight line at a constant (subsonic) speed v so that at time τ_c it is at the CPA to a stationary acoustic sensor at a separation distance (or slant range) of R_c—see Fig. 1(a). Suppose the source emits an acoustic tone of constant frequency f_o and the speed of sound in air is c. The frequency of the signal, as received by the sensor, changes with time due to the acoustical Doppler effect. The IF of the signal received by the sensor at time t is given by[5]

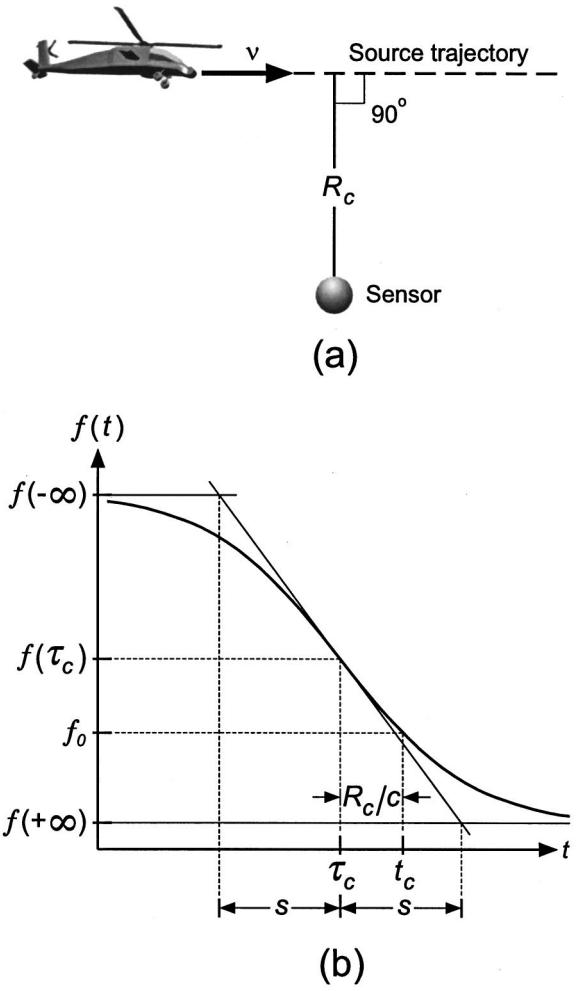

FIG. 1. (a) Geometry of a stationary sensor and a moving source traveling in a straight line at constant speed. (b) A typical time-frequency curve.

$$f(t)=\alpha+\beta p(t;\tau_c,s), \tag{1a}$$

where

$$\alpha=f_o c^2/(c^2-v^2), \tag{1b}$$

$$\beta=-f_o cv/(c^2-v^2), \tag{1c}$$

$$s=\frac{R_c(c^2-v^2)^{1/2}}{vc}, \tag{1d}$$

and

$$p(t;\tau_c,s)=\frac{t-\tau_c}{[s^2+(t-\tau_c)^2]^{1/2}}. \tag{1e}$$

Figure 1(b) shows a typical time-frequency curve obtained by plotting the IF $f(t)$ versus time t. When the source is at a long distance from the CPA, the IF of the received signal decreases slowly with time as the source moves towards or away from the CPA. The asymptotic expressions for $f(t)$, which can be derived from Eqs. (1a)–(1e) by taking the limit $t\rightarrow\pm\infty$, are given by

$$f(\pm\infty)=f_o(1\pm v/c)^{-1}. \tag{2}$$

When the source is near the CPA, the IF of the received signal decreases rapidly with time. The maximum magnitude

for the rate of change of $f(t)$, which occurs when $t=\tau_c$, is given by

$$g_{\max}=\left|\frac{df(t)}{dt}\right|_{t=\tau_c}=\frac{f_o c^2 v^2}{R_c(c^2-v^2)^{3/2}}. \tag{3}$$

The corresponding IF of the received signal at $t=\tau_c$ is

$$f(\tau_c)=\alpha=\tfrac{1}{2}[f(-\infty)+f(+\infty)], \tag{4}$$

which is larger than the source frequency f_o. Owing to the propagation delay, the IF of the received signal is equal to f_o at a later time $t_c=\tau_c+R_c/c$, where R_c/c is the time delay for the sound to propagate at a constant speed c from the source to the sensor when the source is at the CPA. Note that $f(t)-\alpha$ is antisymmetric about $t=\tau_c$.

C. Parameter estimation

The parameters $\{f_o,v,\tau_c,R_c\}$, or equivalently $\{\alpha,\beta,\tau_c,s\}$, are estimated using a nonlinear LS approach, that is, by minimizing the sum of the squared deviations of the noisy IF estimates from their predicted values.[5] Specifically, the (nonlinear LS) estimates of $\{\alpha,\beta,\tau_c,s\}$ are given by

$$\{\tilde{\alpha},\tilde{\beta},\tilde{\tau}_c,\tilde{s}\}=\arg\min_{(\alpha',\beta',\tau_c',s')}\sum_{k=1}^{K}[\alpha'+\beta' p(t_k;\tau_c',s')-\tilde{f}(t_k)]^2, \tag{5}$$

where $\tilde{f}(t_k)$ is the IF estimate at time $t=t_k$ and K is the number of IF estimates. The four-dimensional minimization in Eq. (5) can be reduced to a two-dimensional maximization, and consequently the estimates of $\{\alpha,\beta,\tau_c,s\}$ are given by[5]

$$\{\tilde{\tau}_c,\tilde{s}\}=\arg\max_{\{\tau_c',s'\}}\frac{|\Sigma_{k=1}^{K}[\tilde{f}(t_k)-\bar{\tilde{f}}]p(t_k)|^2}{\Sigma_{k=1}^{K}[p(t_k)-\bar{p}]^2}, \tag{6a}$$

$$\tilde{\beta}=\frac{\Sigma_{k=1}^{K}[\tilde{f}(t_k)-\bar{\tilde{f}}]\tilde{p}(t_k)}{\Sigma_{k=1}^{K}[\tilde{p}(t_k)-\bar{\tilde{p}}]^2}, \tag{6b}$$

$$\tilde{\alpha}=\bar{\tilde{f}}-\tilde{\beta}\bar{\tilde{p}}, \tag{6c}$$

where $\bar{\tilde{f}}=(1/K)\Sigma_{k=1}^{K}\tilde{f}(t_k)$, $p(t_k)=p(t_k;\tau_c',s')$, $\bar{p}=(1/K)\Sigma_{k=1}^{K}p(t_k)$, $\tilde{p}(t_k)=p(t_k;\tilde{\tau}_c,\tilde{s})$, and $\bar{\tilde{p}}=(1/K)\Sigma_{k=1}^{K}\tilde{p}(t_k)$. Solving Eqs. (1b) and (1c) using the estimated values for α and β gives the estimates of the source speed v and source frequency f_o as

$$\tilde{v}=-(\tilde{\beta}/\tilde{\alpha})c, \tag{7}$$

$$\tilde{f}_o=\tilde{\alpha}(1-\tilde{v}^2/c^2). \tag{8}$$

From Eq. (1d), the estimate of the CPA range R_c is given by

$$\tilde{R}_c=\tilde{s}\tilde{v}c/(c^2-\tilde{v}^2)^{1/2}. \tag{9}$$

The maximization in Eq. (6a) is performed using the quasi-Newton method, where the initial estimates of τ_c and s are given by the method described in Ref. 5, or alternatively, by the following procedure:

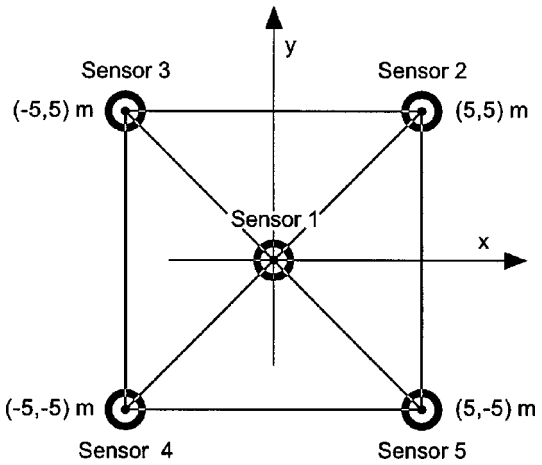

FIG. 2. The cross array used in the field experiment.

Step 1: Calculate the initial estimate of τ_c [refer to Eq. (4)]:

$$\tilde{\tau}_c^o=t_{k0}, \tag{10a}$$

where

$$k0=\arg\min_k|\tilde{f}(t_k)-\tfrac{1}{2}[\tilde{f}(t_1)+\tilde{f}(t_K)]|. \tag{10b}$$

In Eq. (10b), $\tilde{f}(t_1)$ and $\tilde{f}(t_K)$ are the estimates of $f(-\infty)$ and $f(+\infty)$, respectively.

Step 2: Estimate $g_{\max}$

$$\tilde{g}_{\max}^o=\left|\frac{\tilde{f}(t_{k0+1})-\tilde{f}(t_{k0-1})}{t_{k0+1}-t_{k0-1}}\right|. \tag{11}$$

Step 3: Estimate the source speed and the source frequency [refer to Eq. (2)]

$$\tilde{v}^o=c\frac{\tilde{f}(t_1)-\tilde{f}(t_K)}{\tilde{f}(t_1)+\tilde{f}(t_K)}, \tag{12}$$

$$\tilde{f}_o^o=\frac{2\tilde{f}(t_1)\tilde{f}(t_K)}{\tilde{f}(t_1)+\tilde{f}(t_K)}. \tag{13}$$

Step 4: Estimate the source CPA range [refer to Eq. (3)]

$$\tilde{R}_c^o=\frac{\tilde{f}_o^o(c\tilde{v}^o)^2}{[c^2-(\tilde{v}^o)^2]^{3/2}\tilde{g}_{\max}^o}. \tag{14}$$

Step 5: Calculate the initial estimate of s by substituting the estimated values $\tilde{v}^o$ and $\tilde{R}_c^o$ (for v and R_c, respectively) into Eq. (1d).

D. Experimental results

A field experiment is conducted in which five microphones are located on flat ground just above ground level. Figure 2 shows the sensors arranged in a cross configuration, where there is a sensor at each corner of a 10-×10-m square and a fifth sensor at the center. Data are collected for a total of 39 transits made by three different aircraft: one turboprop aircraft and two helicopters referred to as types A and B. During each transit, the aircraft travels at constant velocity and constant altitude so that it flies directly over the center

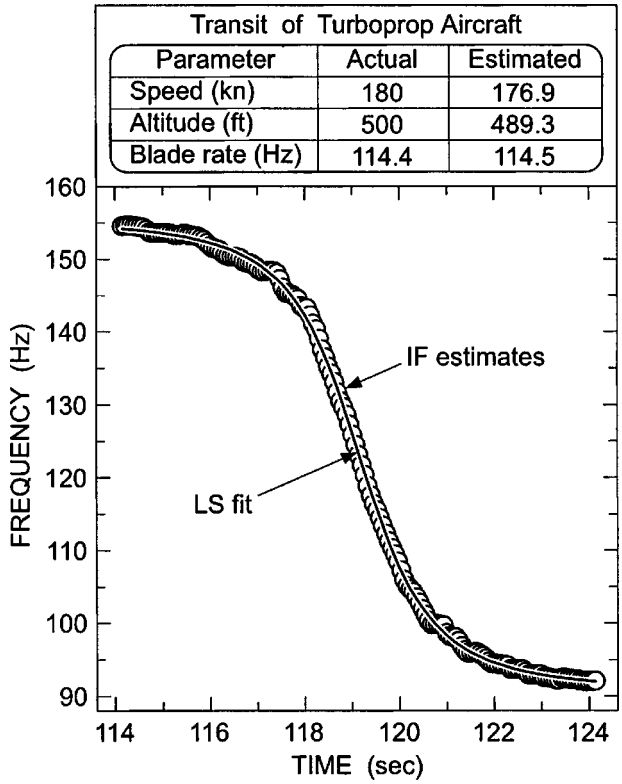

FIG. 3. Time sequence of IF estimates (circles) and the LS fit (solid line) for a transit of the turboprop aircraft.

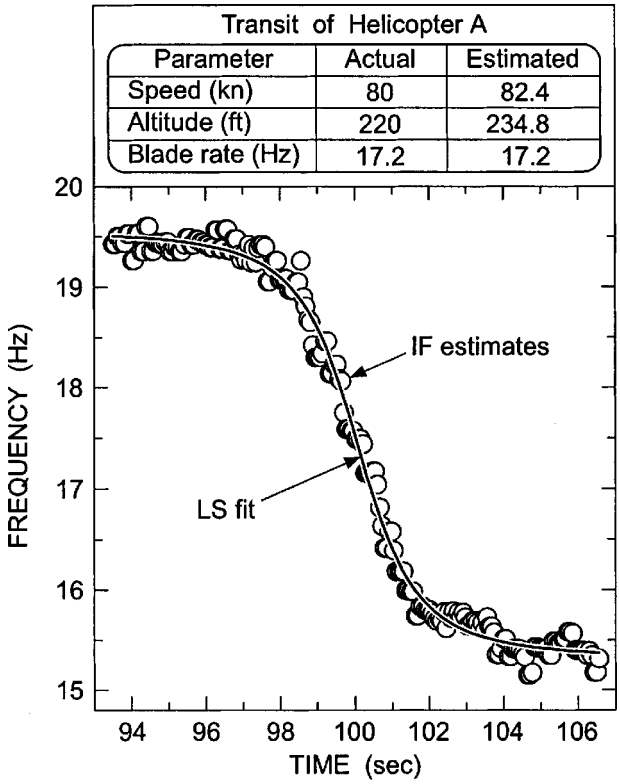

FIG. 4. Similar to Fig. 3 but for a transit of helicopter A.

sensor. In this case, the aircraft's CPA range with respect to the center sensor is the same as its altitude. For the turboprop aircraft, there are 19 transits in total at various combinations of speeds: 130, 180, and 220 kn, and altitudes: 500, 1000, and 2000 ft. For the two helicopters A and B, there are 20 transits in total at various combinations of speeds: 50, 60, 70, 80, 90, 110, 112, and 135 kn, and altitudes: 220, 232, 247, 250, 253, 260, and 500 ft. The output of each sensor is sampled at 1 kHz. The narrow-band method is applied to the data from the *center* sensor in order to estimate the aircraft parameters $\{f_o, v, \tau_c, R_c\}$. The short-time Fourier transform is used for the time-frequency signal analysis.[5] The resulting spectrogram (which shows the distribution of acoustic energy as a joint function of frequency and time) provides a time sequence of IF estimates for each received narrow-band tone. The spectrogram is computed using a 1024-point fast Fourier transform (FFT) for each data block consisting of 256 data samples (tapered with a Hanning window and padded with 768 zeros) with 75% overlap between two consecutive data blocks. The IF estimates of a spectral peak can be refined either by using three-point quadratic interpolation (inverse parabolic interpolation) or by extending the zero padding and using a longer FFT.

For the turboprop aircraft, the strongest line in the spectrogram is the fundamental tone and it is selected for further processing because its source (or rest) frequency corresponds to the propeller blade rate of the aircraft. With the narrow-band method, the estimates of the aircraft's speed, CPA time, CPA range (altitude), and blade rate correspond to the set of parameter values that provides a LS fit of the time-frequency model to the IF estimates. For example, Fig. 3 shows, as circles, the time sequence of IF estimates for the fundamental tone during a particular transit of the turboprop aircraft. The solid curve represents the LS fit of the model to the IF estimates. The actual and estimated values of the aircraft's speed, altitude, and propeller blade rate are shown in the inset of Fig. 3. The corresponding results for a typical transit of helicopter A are shown in Fig. 4. In this case, the source frequency of the selected narrow-band tone corresponds to the main-rotor blade rate of the helicopter.

The results of processing the acoustic data using the narrow-band method for all 19 transits of the turboprop aircraft are shown in Figs. 5 and 6, where the estimated values (denoted by white-filled circles) are compared with the actual values (denoted by diamonds) for the aircraft's speed and altitude, respectively. For the narrow-band method, the root-mean-square (rms) errors in the speed and altitude estimates (relative to the actual values) are 7.5 kn and 85 ft., respectively. These results are consistent with those reported previously[5] for the transits of a different type of turboprop aircraft where the rms errors in the speed and altitude were 5 kn and 90 ft., respectively. (Estimated values obtained using the broadband method are also shown in the figures as black-filled circles for comparison—see Sec. II E.) The corresponding results for all 20 transits of the two helicopters A and B are shown in Figs. 7 and 8. The rms errors in the speed and altitude are 8.9 kn and 54 ft., respectively.

Also, the estimated values for each aircraft's blade rate are compared with the actual value. The rms errors in the blade-rate estimates for the turboprop aircraft and the two helicopters (A and B) are 0.4, 0.2, and 0.1 Hz, respectively. The result for the turboprop aircraft is the same as the rms

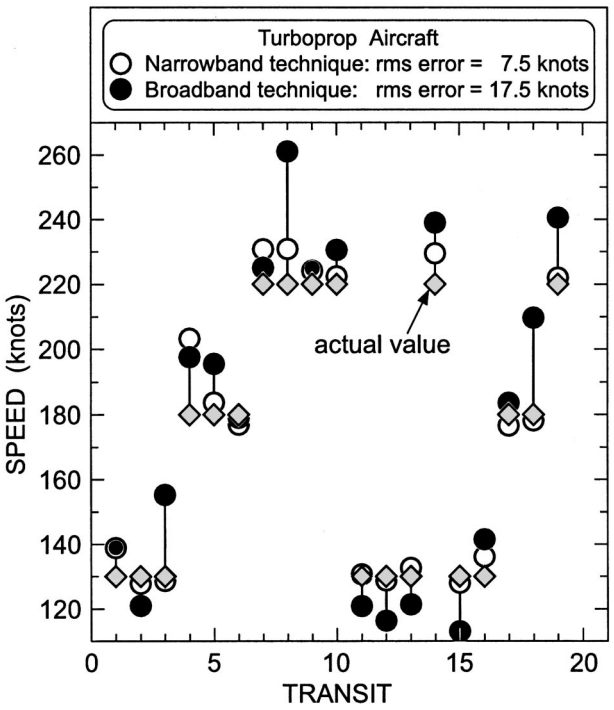

FIG. 5. Estimated and actual speeds for all 19 transits of the turboprop aircraft.

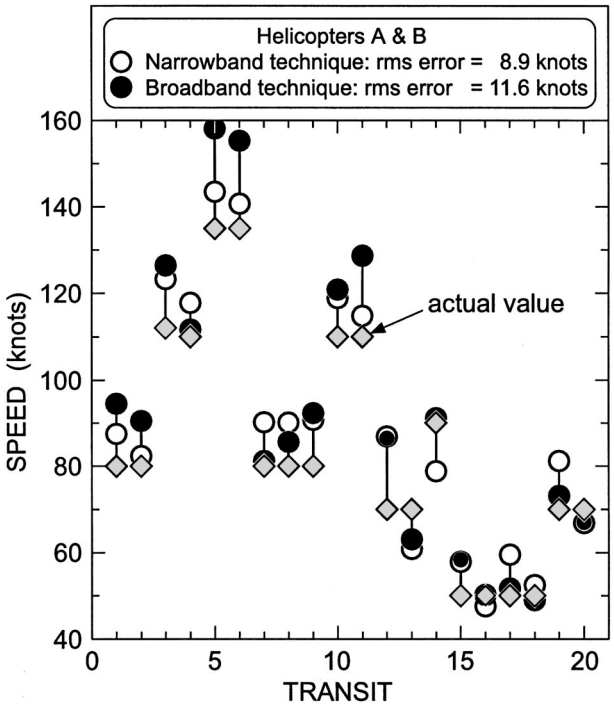

FIG. 7. Estimated and actual speeds for all 20 transits of the two helicopters.

error in the blade-rate estimate reported previously for a different turboprop aircraft.[5]

The results for all 39 aircraft transits are used to compute the cumulative probability distributions of the relative errors in the estimates of the speed and altitude (CPA range) of an aircraft. Here, the cumulative probability distribution of a relative error at ε, denoted by $P(\varepsilon)$ where $0 \leqslant P(\varepsilon) \leqslant 1$, is the probability that the magnitude of the relative error is less than or equal to the value ε. Figure 9 shows, as white-filled circles, the cumulative probability distributions of the relative errors in the narrow-band estimates of (a) the speed, and (b) the altitude of an aircraft. The probabilities that the magnitudes of the relative errors for the estimated speed and altitude of an aircraft are within 20% of the actual values are greater than 0.98 and 0.88, respectively.

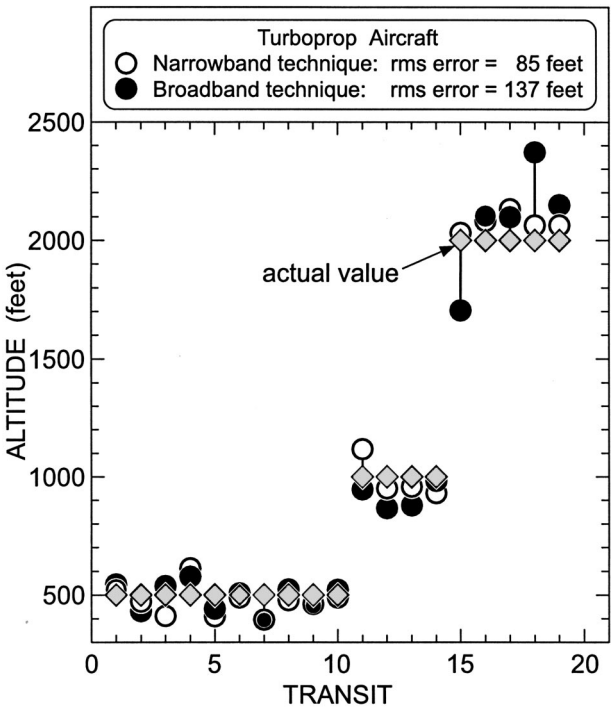

FIG. 6. Estimated and actual altitudes for all 19 transits of the turboprop aircraft.

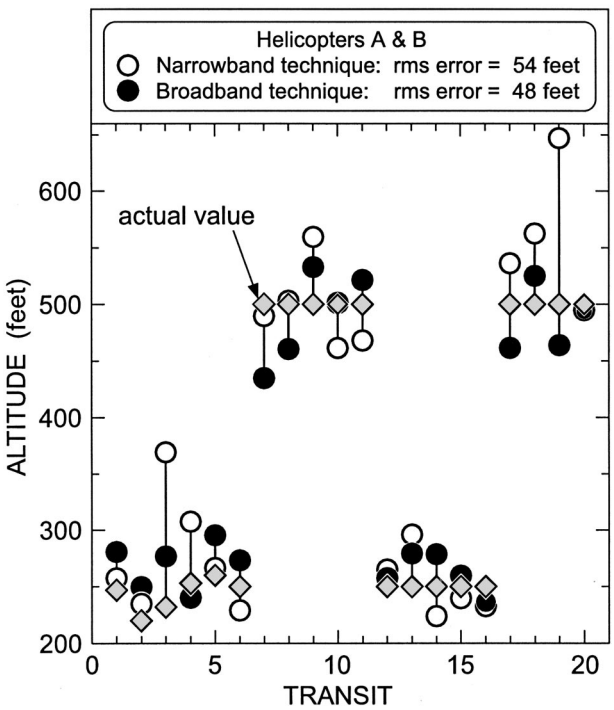

FIG. 8. Estimated and actual altitudes for all 20 transits of the two helicopters.

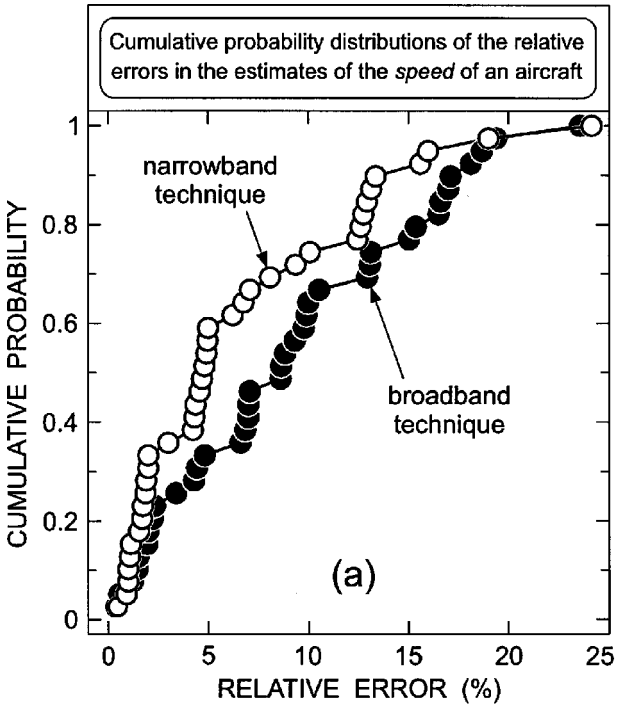

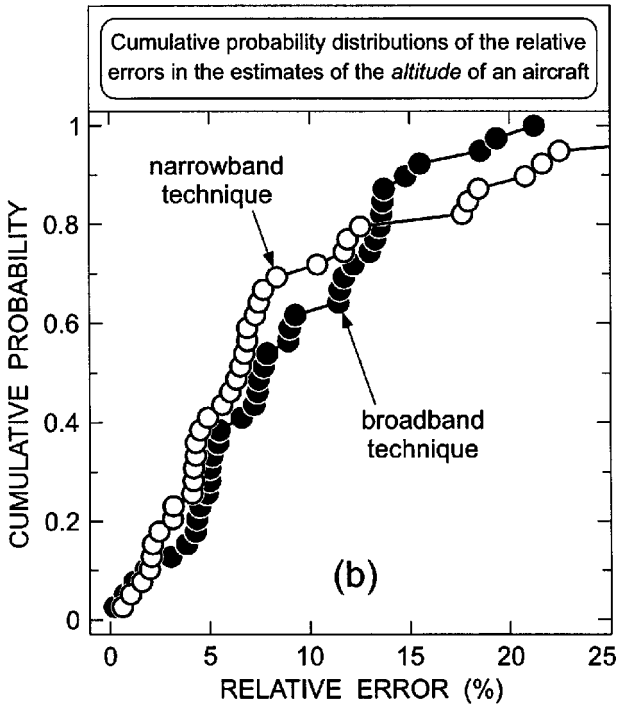

FIG. 9. Cumulative probability distributions of the relative errors in the estimates of (a) the speed, and (b) the altitude of an aircraft.

II. BROADBAND METHOD

A. Background

A broadband passive acoustic method for source motion parameter estimation has been described recently,[7] where the broadband random acoustic energy emitted by the source is sensed by an array of microphones. The temporal variation of the differential time of arrival (or time-delay) estimates of the acoustic signal at each pair of sensors is estimated and then the sum of the squared deviations of the noisy time-delay estimates from their predicted values is minimized over a period of time and over all sensor pairs. The effectiveness of the method has been verified using real data for different types of ground vehicles that made multiple transits past a planar array.[7]

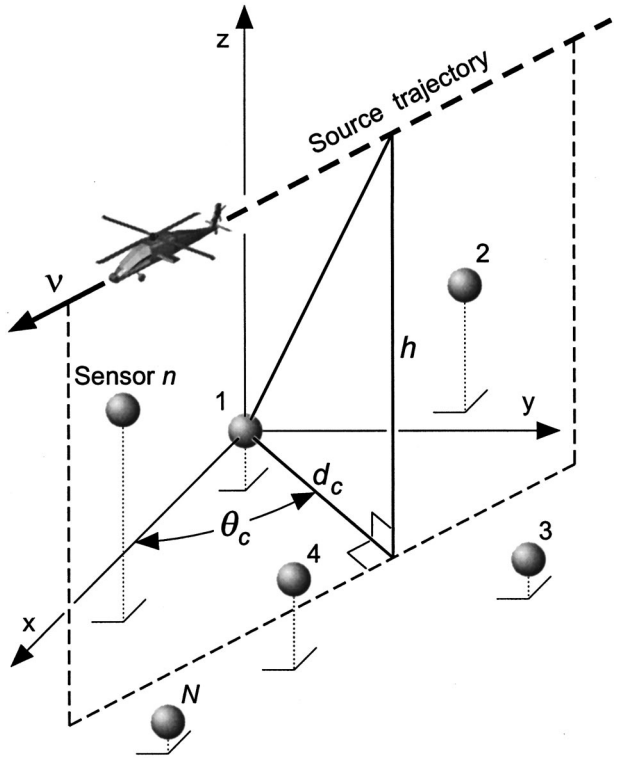

FIG. 10. Geometry of N stationary sensors and a moving source traveling at constant velocity and constant altitude.

B. Flight parameters for an airborne source

Figure 10 shows the geometry of N stationary sensors and a moving source traveling at constant velocity and constant altitude. The source position at time τ can be described by

$$x(\tau)=d_c\cos\theta_c+(\tau-\tau_c)v\sin\theta_c,$$
$$y(\tau)=d_c\sin\theta_c-(\tau-\tau_c)v\cos\theta_c, \tag{15}$$
$$z(\tau)=h,$$

where v $(-c<v<c)$ is the source speed, τ_c is the time at which the source is at CPA (to sensor 1), d_c is the source ground range at CPA, h is the source altitude, and θ_c is the source azimuth angle at CPA. The source trajectory is completely specified by the five flight parameters $\{v,\tau_c,h,d_c,\theta_c\}$. In other words, estimating the source trajectory is equivalent to estimating the source flight parameters. Note that the source speed in Eqs. (15) is allowed to be negative. The sign convention is that v is positive (negative) when sensor 1 is on the source's right- (left-) hand side as the source moves along its trajectory.

C. Time-delay model

Sensor 1 is located at the origin and sensor m at (x_m,y_m,z_m), $2\leqslant m\leqslant N$. At time τ, the source is at a distance

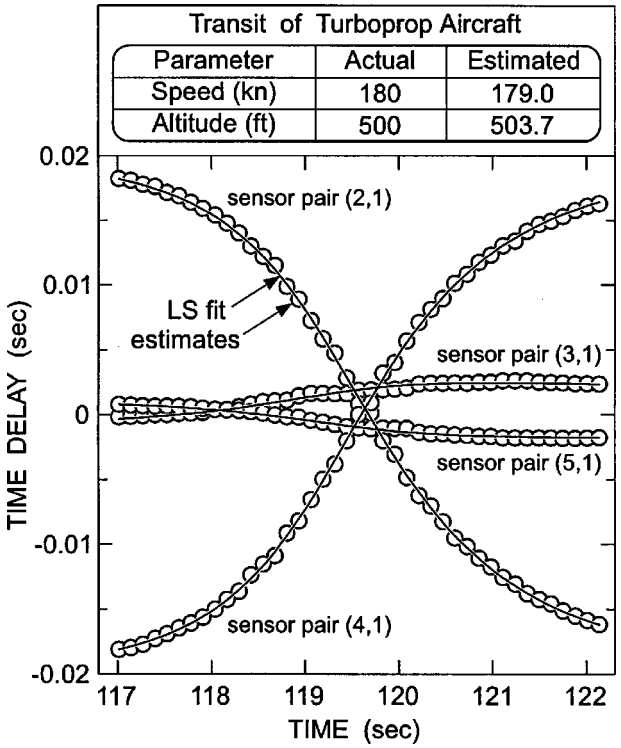

FIG. 11. Estimated time delays for the four sensor pairs of the cross array as a function of time for the same aircraft transit considered in Fig. 3.

$R_n(\tau)$ from sensor n, $1 \leq n \leq N$. Due to the propagation delay, the signal emitted at time τ arrives at sensor n at a later time $t^{(n)}$ given by

$$t^{(n)} = \tau + R_n(\tau)/c, \quad 1 \leq n \leq N. \tag{16}$$

The time delay between sensor 1 and sensor m, β_{m1}, at time $t = t^{(1)}$ is defined as $\beta_{m1}(t) = t^{(m)} - t^{(1)}$. It follows from Eq. (16) that

$$\beta_{m1}(t) = \frac{R_m(\tau) - R_1(\tau)}{c}, \quad 2 \leq m \leq N. \tag{17}$$

The absolute value of β_{m1} is bounded by the time required for sound to propagate from sensor 1 to sensor m or vice versa, that is, $|\beta_{m1}| \leq d_{m1}/c$ where $d_{m1} = (x_m^2 + y_m^2 + z_m^2)^{1/2}$ is the separation distance between the two sensors. Note that in Eq. (17) τ is the time of emission of the acoustic signal (or *source* time), while t is the time of reception of the signal (or *sensor* time). By measuring the time delays for the $N-1$ sensor pairs at time t, it is possible to estimate the source position at an earlier time τ.[7] Since the speed of an aircraft is comparable with the speed of sound propagation in air, the source position at time t is significantly different from that at time τ, and this is commonly referred to as the retardation effect.

For the assumed motion of the source, it can be shown that

$$R_1(\tau) = \{v^2(\tau - \tau_c)^2 + R_c^2\}^{1/2}, \tag{18}$$

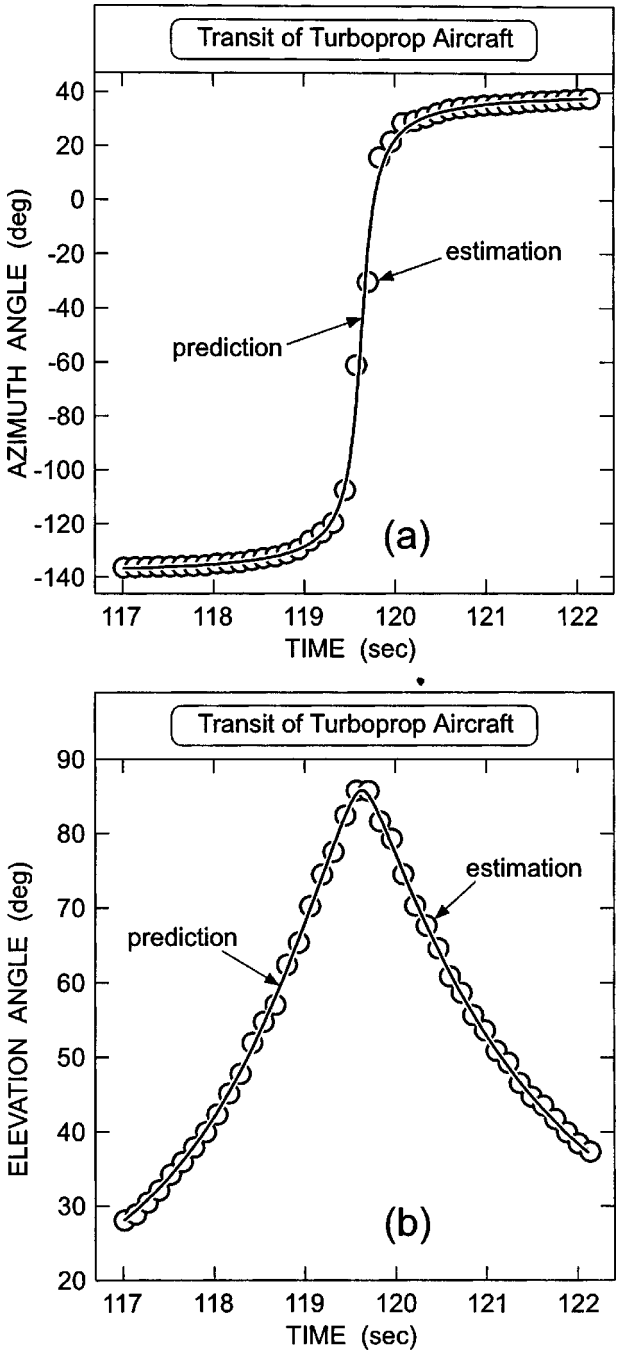

FIG. 12. (a) Azimuth angle, and (b) elevation angle of the turboprop aircraft as a function of time for the same aircraft transit considered in Fig. 3.

$$R_m(\tau) = \{R_1^2(\tau) + d_{m1}^2 - 2d_c(x_m \cos\theta_c + y_m \sin\theta_c) - 2v(\tau - \tau_c)(x_m \sin\theta_c - y_m \cos\theta_c) - 2z_m h\}^{1/2}, \quad 2 \leq m \leq N, \tag{19}$$

where $R_c^2 = d_c^2 + h^2$ is the source (slant) range at CPA. By substituting Eq. (18) into Eq. (16) (with $n=1$), then solving the resulting quadratic equation for τ and recalling $t = t^{(1)}$, it can be shown that

$$\tau = \tau_c + \frac{c^2(t - \tau_c) - \sqrt{R_c^2(c^2 - v^2) + v^2c^2(t - \tau_c)^2}}{c^2 - v^2}. \tag{20}$$

Using Eqs. (17)–(20), the time delay between sensor 1 and sensor m at a specified time t can be computed for a given set of flight parameters. A time-delay curve for sensor 1 and sensor m is obtained by plotting the time delay between the two sensors, $\beta_{m1}(t)$, as a function of time t.

D. Flight parameter estimation

Define the source flight parameter vector $\lambda = [v, \tau_c, h, d_c, \theta_c]^T$, where the superscript T denotes matrix transpose. The nonlinear LS estimate of λ, denoted by $\tilde{\lambda} = [\tilde{v}, \tilde{\tau}_c, \tilde{h}, \tilde{d}_c, \tilde{\theta}_c]^T$, is obtained by minimizing the cost function $P_d(\lambda)$ defined by

$$P_d(\lambda) = \sum_{m=2}^{N} \sum_{k=1}^{K} [\beta_{m1}(t_k) - \tilde{\beta}_{m1}(t_k)]^2, \tag{21}$$

where $\tilde{\beta}_{m1}(t_k)$ is the time-delay estimate for sensor 1 and sensor m at time $t = t_k$, and K is the number of time-delay estimates for each pair of sensors. The minimization of $P_d(\lambda)$ is performed using the quasi-Newton method. The initial estimate of λ for the minimization is calculated using the method described in Ref. 7.

E. Experimental results

The broadband method is applied to the real data from the cross array—see Fig. 2. The data from each of the five sensors are processed in blocks, each containing 256 data samples. There is a 50% overlap between two consecutive data blocks so that the observation rate of the time delay for each sensor pair is $(0.128)^{-1}$ Hz. Each data block of sensor 1 is cross correlated with the corresponding data block of each of the other four sensors. The cross correlation is implemented in the frequency domain using the FFT, with a spectral window from 10 to 300 Hz. Only the phase of the cross spectrum is used by the inverse FFT in computing the cross-correlation function. This phase transform prefiltering technique[7,8] suppresses the undesirable effects of the strong narrow-band tones in the received signals (which would otherwise cause ambiguous peaks in the cross-correlation function). A three-point quadratic interpolation routine[9] is used to refine the peak of the cross-correlation function and the time-lag position of the refined peak gives the time-delay estimate. The sequence of time-delay estimates for each sensor pair is then used in the flight parameter estimation.

For the purpose of illustration, consider the same transit of the turboprop aircraft used previously to demonstrate the narrow-band method (see Fig. 3). Figure 11 shows, as circles, the time sequence of time-delay estimates for each of the four sensor pairs of the cross array. The solid curves in Fig. 11 represent the LS fit of the model to the time-delay estimates. The actual and estimated values of the aircraft's speed and altitude are shown in the inset of Fig. 11. The time-delay estimates for all four sensor pairs at a particular time t are used to calculate the instantaneous range, azimuth angle, and elevation angle of the aircraft at an (unknown) earlier time τ (see Ref. 7 for the details of the localization method). Figure 12 shows only the estimated azimuth and elevation angles of the aircraft as a function of the sensor time t; the instantaneous range estimates are not presented because they are inaccurate due to the aircraft being in the far field. The solid curves in Fig. 12 represent the angular trajectory predicted by the estimated flight parameters of the aircraft.

Figures 5 and 6 show the speed and altitude estimates (denoted by black-filled circles) obtained by processing the acoustic data using the broadband method for all 19 transits of the turboprop aircraft. For the broadband method, the rms errors in the speed and altitude estimates (relative to the actual values) are 17.5 kn and 137 ft., respectively. Also shown, for comparison purposes, are the estimates from the narrow-band method (denoted by white-filled circles) and the actual values (denoted by diamonds). Similarly, the results for all 20 transits of the two helicopters are shown in Figs. 7 and 8. The rms errors in the speed and altitude estimates (relative to the actual values) are 11.6 kn and 48 ft., respectively.

The cumulative probability distributions of the relative errors in the speed and altitude estimates are computed using the broadband results for all 39 aircraft transits. These broadband distributions (denoted by black-filled circles) are compared with the narrow-band distributions (denoted by white-filled circles) in Figs. 9(a) and 9(b), respectively. With the broadband method, the probabilities that the magnitudes of the relative errors in the estimated speed and altitude of an aircraft are within 20% of the actual values are greater than 0.98.

III. CONCLUSIONS

Both the narrow-band and broadband flight parameter estimation methods provide reliable estimates of the speed and altitude of a transiting aircraft, whether turboprop fixed wing or rotary wing. In addition, the narrow-band method provides a reliable estimate of the blade-passage frequency, which is useful for aircraft classification purposes. Based on the empirical cumulative probability distribution of the relative errors in the source-speed estimates, the narrow-band method performs better than the broadband method for the present experiment. This is also the case for the source altitude estimates, providing the relative error does not exceed 13.5%. It is recommended that both methods be considered for land-based acoustic surveillance applications.

ACKNOWLEDGMENTS

The authors gratefully acknowledge the contributions of their colleague Mr. Lionel Criswick to this paper and the field trial support provided by the Commanding Officer (Lieutenant Colonel Rik Modderman) and the soldiers of 1 RISTA Regiment, Australian Army.

[1] B. G. Ferguson, ''Time-delay estimation techniques applied to the acoustic detection of jet aircraft transits,'' J. Acoust. Soc. Am. **106**, 255–264 (1999).
[2] B. G. Ferguson and K. W. Lo, ''Passive wideband cross-correlation with differential Doppler compensation using the continuous wavelet transform,'' J. Acoust. Soc. Am. **106**, 3434–3444 (1999).
[3] F. M. Dommermuth, ''A simple procedure for tracking fast maneuvering aircraft using spatially distributed acoustic sensors,'' J. Acoust. Soc. Am. **82**, 1418–1424 (1987).

[4] B. G. Ferguson, ''A ground-based narrow-band passive acoustic technique for estimating the altitude and speed of a propeller-driven aircraft,'' J. Acoust. Soc. Am. **92**, 1403–1407 (1992).
[5] B. G. Ferguson and B. G. Quinn, ''Application of the short-time Fourier transform and the Wigner–Ville distribution to the acoustic localization of aircraft,'' J. Acoust. Soc. Am. **96**, 821–827 (1994).
[6] F. Dommermuth and J. Schiller, ''Estimating the trajectory of an accelerationless aircraft by means of a stationary acoustic sensor,'' J. Acoust. Soc. Am. **76**, 1114–1122 (1984).
[7] K. W. Lo and B. G. Ferguson, ''Broadband passive acoustic technique for target motion parameter estimation,'' IEEE Trans. Aerosp. Electron. Syst. **36**, 163–175 (2000).
[8] B. G. Ferguson, ''Improved time-delay estimates of underwater acoustic signals using beamforming and prefiltering techniques,'' IEEE J. Ocean Eng. **14**, 238–244 (1989).
[9] G. Jacovitti and G. Scarano, ''Discrete time techniques for time delay estimation,'' IEEE Trans. Signal Process. **41**, 525–533 (1993).

On the relationships between the fixed-f_1, fixed-f_2, and fixed-ratio phase derivatives of the $2f_1-f_2$ distortion product otoacoustic emission

Arnold Tubis
Department of Physics, Purdue University, West Lafayette, Indiana 47907

Carrick L. Talmadge
National Center for Physical Acoustics, University of Mississippi, University, Mississippi 38677

Christopher Tong
Department of Physics, Purdue University, West Lafayette, Indiana 47907

Sumit Dhar
Department of Audiology and Speech Sciences, Purdue University, West Lafayette, Indiana 47907

(Received 17 November 1999; revised 14 July 2000; accepted 21 July 2000)

For primary frequency ratios, f_2/f_1, in the range 1.1–1.3, the fixed-f_1 (''f_2-sweep'') phase derivative of the $2f_1-f_2$ distortion product otoacoustic emission (DPOAE) is larger than the fixed-f_2 (''f_1-sweep'') one. It has been proposed by some researchers that part or all of the difference between these delays may be attributed to the so-called cochlear filter ''build-up'' or response time in the DPOAE generation region around the f_2 tonotopic site. The analysis of an approximate theoretical expression for the DPOAE signal [Talmadge *et al.*, J. Acoust. Soc. Am. **104**, 1517–1543 (1998)] shows that the contributions to the phase derivatives associated with the cochlear filter response is small. It is also shown that the difference between the phase derivatives can be qualitatively accounted for by assuming the approximate scale invariance of cochlear mechanics. The effects of DPOAE fine structure on the phase derivative are also explored, and it is found that the interpretation of the phase derivative in terms of the phase variation of a single DPOAE component can be quite problematic. © *2000 Acoustical Society of America.*
[S0001-4966(00)05710-6]

PACS numbers: 43.64.Bt, 43.64.Ha, 43.64.Jb [BLM]

I. INTRODUCTION

Distortion product otoacoustic emissions (DPOAEs) (Kemp, 1979) are pressure signals resulting from the cochlear nonlinear interaction of two external primary tones of frequency f_1 and f_2 ($f_2>f_1$) that may be measured in the ear canal. Studies of the correlation of DPOAE levels with hearing loss, and the effects of suppressor tones, noise exposure, and ototoxic drugs on DPOAEs, have suggested that these emissions may constitute clinically important indicators of the health status of the nonlinear active cochlear function (see, e.g., the reviews in Robinette and Glattke, 1997).

The distortion product (DP) energy is initially generated in the strong overlap region (or ''generation region'') of the primary tone cochlear activity patterns (around the f_2 tonotopic place). The generated DP waves travel in both the apical and basal directions. In the case of apical DPOAEs such as the one with the frequency $2f_1-f_2$, in which the DPOAE tonotopic site is apical to the f_1 and f_2 sites, the initially apical moving generated DP wave may be reflected by cochlear inhomogeneities around the DP tonotopic place (Shera and Zweig, 1993; Zweig and Shera, 1995). The resulting interference of this reflected wave (the ''reflection site component'') and the initially basally generated wave (the ''generator site component'') is observed as DPOAE fine structure in the ear canal, in which the DPOAE level varies with DPOAE frequency in a pseudoperiodic fashion (e.g., He and Schmiedt, 1993, 1996, 1997; Kummer *et al.*, 1995; Brown *et al.*, 1996; Gaskill and Brown, 1996). A comprehensive theoretical description of DPOAE fine structure as well as the fine structure of other types of otoacoustic emissions and the psychoacoustic microstructure of the hearing threshold has been recently developed (Talmadge *et al.*, 1996, 1997, 1998, 1999a). It should be noted that Kim (1980) was actually first to suggest cochlear wave reflection around the DP tonotopic site as the agent for DPOAE fine structure. A similar suggestion was made by Kemp and Brown (1983).

The phase and phase derivatives of DPOAEs as functions of the primary frequency have been of great interest to many researchers. As discussed in Talmadge *et al.* (1999a), the phase derivatives complement in many respects the usual DPOAE level measurements, and comparisons of the two sets of quantities provide additional information on the underlying mechanics responsible for DPOAE generation. Because of this potential for new theoretical insights, it is useful to have a quasirealistic analytic description of the DPOAE signal. The model of Talmadge *et al.* (1998) provides such a description in terms of the nonlinear component of the cochlear partition dynamics and the cochlear response to single-tone stimuli. Moreover, it can be used to give a connection between the temporal DPOAE response to pulsed tones (from which physical time delays may be inferred) and

the steady-state response (Talmadge *et al.*, 1999b; Tubis *et al.*, 2000).

This paper will be focused mainly on the differences between $\tau_{\text{fixed-}f_1}$ and $\tau_{\text{fixed-}f_2}$, the negatives of the respective fixed-f_1 and -f_2 phase derivatives (which are usually referred to as group delays) of the $f_{dp}=2f_1-f_2$ DPOAE (e.g., O'Mahoney and Kemp, 1995; Bowman *et al.*, 1997, 1998; Schneider *et al.*, 1999a,b). Specifically, if the complex DPOAE signal is written as

$$S_{dp}=A_{dp}e^{i\varphi_{dp}}, \tag{1}$$

where A_{dp} and φ_{dp} are the real amplitude and phase of the $2f_1-f_2$ DPOAE, respectively, with the convention that the time dependence is $\exp(2\pi i f_{dp})$, then

$$\tau_{\text{fixed-}f_1}=-\frac{1}{2\pi}\left.\frac{\partial\varphi_{dp}}{\partial f_{dp}}\right|_{f_1}, \tag{2}$$

$$\tau_{\text{fixed-}f_2}=-\frac{1}{2\pi}\left.\frac{\partial\varphi_{dp}}{\partial f_{dp}}\right|_{f_2}. \tag{3}$$

Both of these phase derivatives are generally functions of f_1 and f_2. Bowman *et al.* (1997, 1998) have proposed that if $\tau_{\text{fixed-}f_1}$ and $\tau_{\text{fixed-}f_2}$ are interpreted as physical time delays, then all or a significant part of the difference between them is associated with the ''filter build-up'' time or response time of the cochlear elements around the f_2 tonotopic site. This proposal is evaluated in the present paper using the theoretical framework of the Talmadge *et al.* (1998) model. *The filter referred to by Bowman et al. (1997, 1998) will be assumed to be associated with the resonance response of the cochlear partition in the neighborhood of the f_2 tonotopic place (the initial DP generation region).*

It will be shown that the effect of this cochlear filter on the DPOAE phase and phase derivatives is very small, and that the approximate scale invariance of cochlear mechanics (e.g., Shera and Zweig, 1993; Zweig and Shera, 1995) can give rise to a substantial difference between $\tau_{\text{fixed-}f_1}$ and $\tau_{\text{fixed-}f_2}$ in the range of primary frequency ratios f_2/f_1 between 1.1 and 1.3, without the need for a significant contribution from the cochlear filter (Talmadge *et al.*, 1999b; Schneider *et al.*, 1999b; Tubis *et al.*, 2000; Prijs *et al.*, 2000). In particular, it is shown in the papers just cited that

$$\frac{\tau_{\text{fixed-}f_1}}{\tau_{\text{fixed-}f_2}}\approx\frac{2f_1}{f_2}, \tag{4}$$

which is in qualitative agreement with typical data (e.g., Bowman *et al.*, 1997; Schneider *et al.*, 1999a).

In order to simplify the discussion, only $f_{dp}=2f_1-f_2$ DPOAEs for which fine structure effects are negligible will be considered at first; i.e., reflection of apically moving DP waves from around the f_{dp} tonotopic site will not be taken into account initially. [Time-domain and frequency-domain techniques for separating the two DPOAE components have been recently presented (Talmadge *et al.*, 1998, 1999a,b).] Also, $\tau_{\text{fixed-}f_1}$ and $\tau_{\text{fixed-}f_2}$, as defined above in terms of the steady-state DPOAE phase, are considered without discussing to what extent they correspond to physical time delays. In other papers (Talmadge *et al.*, 1999b; Tubis *et al.*, 2000), it is shown that considerable care must be exercised in attempts to associate them with physical time delays. It is also found that DPOAE fine structure can have a dramatic effect on $\tau_{\text{fixed-}f_1}$ and $\tau_{\text{fixed-}f_2}$, and that the interpretation of these delays in terms of the phase behavior of a DPOAE component originating from a single cochlear source can give very misleading results.

The essential elements of the Talmadge *et al.* (1998) model for the DPOAE are reviewed in Sec. II. The extent to which the cochlear filter behavior around the f_2 tonotopic site contributes to the DPOAE phase behavior is discussed in Sec. III using an analytic argument and several simplifying approximations. With the assumption that these approximations do not grossly distort the results, it is found that this contribution is fairly small and cannot be the main source of the difference between $\tau_{\text{fixed-}f_1}$ and $\tau_{\text{fixed-}f_2}$. This conclusion is supported by extensive numerical calculations in Sec. VII, in which the above-mentioned approximations are *not* made. In Sec. IV, the derivation of results such as Eq. (4) is reviewed using (1) simplified forms for the DPOAE phase and phase derivatives and the assumption that the generator region component is dominant, and (2) the assumption of scale invariance (e.g., Shera and Zweig, 1993; Zweig and Shera, 1995; Talmadge *et al.*, 1998). Group delays are obtained in Section V for the case in which only the reflection site component is important. Unlike the situation in Sec. IV, it is found that the phase derivatives are approximately independent of the measurement paradigm, and correspond to the approximate round-trip travel time of a signal at the DP frequency from the cochlear base to its tonotopic (reflection) site and back to the base. The case in which neither of the DPOAE components may be neglected is considered in Sec. VI. Here, it is found that significant deviations of the group delays from those for a dominant generator region (or reflection region) component can be present. The various assumptions used in obtaining the results in Secs. III, IV, V, and VI are justified in Sec. VII via numerical calculations. The fixed-f_1 and fixed-f_2 group delays for higher-order apical DPOAEs are considered in Sec. VIII, and a summary of results and conclusions is presented in Sec. IX. An outline of the perturbative method used to obtain the pressure wave equation for the $2\omega_1-\omega_2$ DP is given in the Appendix.

II. MODEL FOR DPOAE PHASE

The analysis of this paper is based on an approximate expression for the DPOAE signal derived in Talmadge *et al.* (1998), to which the reader is referred for a detailed definition of symbols, and discussions of assumptions and approximations involved.

For a steady-state ''calibrated'' (complex) driving pressure $P_{dr}(t)$, given by

$$P_{dr}(t)=P_{dr}e^{i\omega t}, \tag{5}$$

the steady-state complex DPOAE amplitude of frequency $\omega_{dp}=2\omega_1-\omega_2$ is given by (Talmadge *et al.*, 1998)

$$P_{dp}^{ss}(\omega_1,\omega_2,\omega_{dp}) = \frac{P_l(\omega_1,\omega_2,\omega_{dp}) + R_a(\omega_{dp})P_r(\omega_1,\omega_2,\omega_{dp})}{1 - R_a(\omega_{dp})R_b(\omega_{dp})}, \quad (6)$$

where

$$P_l(\omega_1,\omega_2,\omega_{dp}) = -T_{pd}(\omega_{dp})\frac{k_{ow}(\omega_{dp})}{k_r(\omega_{dp})+k_{ow}(\omega_{dp})} \times \frac{\rho_p(\omega_1,\omega_2)}{\Delta_{sm}(0,\omega_{dp})}F_r(\infty,\omega_1,\omega_2), \quad (7)$$

$$P_r(\omega_1,\omega_2,\omega_{dp}) = -T_{pd}(\omega_{dp})\frac{k_{ow}(\omega_{dp})}{k_r(\omega_{dp})+k_{ow}(\omega_{dp})} \times \frac{\rho_p(\omega_1,\omega_2)}{\Delta_{sm}(0,\omega_{dp})}F_l(\infty,\omega_1,\omega_2). \quad (8)$$

[As usual, the complex temporal dependence is $\exp(i\omega_{dp}t)$.]

Here, $P_l(\omega_1,\omega_2,\omega_{dp})$ is the amplitude of the contribution to the DPOAE ear-canal pressure directly from the DP generation region, $R_a(\omega_{dp})P_r(\omega_1,\omega_2,\omega_{dp})$ is the amplitude from the reflection-site contribution, and $R_a(\omega_{dp})$ and $R_b(\omega_{dp})$ are, respectively, the cochlear apical and basal reflectances. As noted in Talmadge *et al.* (1999a), the quantity $P_r(\omega_1,\omega_2,\omega_{dp})$ gives the ear-canal contribution from the reflection-site component in the limit that $R_a(\omega_{dp})\to 1$ and $R_b(\omega_{dp})\to 0$. As noted in the Introduction, the reflection from the DP site will be neglected for the initial modeling considerations, so that Eq. (6) becomes

$$P_{dp}^{ss}(\omega_1,\omega_2,\omega_{dp}) \approx P_l(\omega_1,\omega_2,\omega_{dp}). \quad (9)$$

Some of the relevant expressions for the terms in Eqs. (7) and (8) are

$$F_{r,l}(x,\omega_1,\omega_2) = \int_0^x dx'\ \gamma_0(x')\chi_r^2(x',\omega_1) \times \chi_r^*(x',\omega_2)\chi_{r,l}(x',\omega_{dp}), \quad (10)$$

$$\chi_r(x,\omega) = \frac{\Delta_{sm}(0,\omega)}{\Delta_{sm}(x,\omega)}\psi_r(x,\omega), \quad (11)$$

$$\psi_r(x,\omega) \cong \sqrt{\frac{k(0,\omega)}{k(x,\omega)}}\exp\left\{-i\int_0^x k(x',\omega)dx'\right\}, \quad (12)$$

$$\psi_l(x,\omega) \cong \sqrt{\frac{k(0,\omega)}{k(x,\omega)}}\exp\left\{+i\int_0^x k(x',\omega)dx'\right\}, \quad (13)$$

$$k(x,\omega) = \frac{k_0\omega}{\sqrt{\Delta_{sm}(x,\omega)}}, \quad (14)$$

$$\Delta_{sm}(x,\omega) = \omega_0^2(x) - \omega^2 + i\omega\gamma_0(x) + \rho f\omega_0^2(x)e^{-i\psi_f\omega/\omega_0(x)} + \rho_s\omega_0^2(x)e^{-i\psi_s\omega/\omega_0(x)}, \quad (15)$$

$$\rho_p(\omega_1,\omega_2) = \frac{i\sigma_{bm}k_0^2(2\omega_1-\omega_2)^3 b_r^2(0,\omega_1)b_r^*(0,\omega_2)}{b_{nl}^2}, \quad (16)$$

$$b_r(0,\omega) = \frac{-G_{me}(\omega)k_{ow}(\omega)P_{dr}(\omega)}{\sigma_{bm}\Delta_{sm}(0,\omega)(k_r(0,\omega)+k_{ow}(\omega))}, \quad (17)$$

$$\omega_0(x) \cong \omega_{0c}e^{-k_\omega x}, \quad (18)$$

where b_{nl} is the nonlinear saturation level. The reader is referred to Talmadge *et al.* (1998) for the explanation of the above formulas, as well as further discussion of the notation. It should be noted that Talmadge *et al.* (1998) further assumed that

$$\gamma_0(x) = \varepsilon_\gamma\omega_0(x), \quad (19)$$

where $\varepsilon_\gamma = \gamma_0(x)/\omega_0(x)$ is a constant in their analysis. In terms of their notation,

$$F_{r,l}(x,\omega_1,\omega_2) \cong \varepsilon_\gamma I_{r,l}(x,\omega_1,\omega_2), \quad (20)$$

$$\varepsilon_\gamma\rho_p(\omega_1,\omega_2) = \rho_0(\omega_1,\omega_2), \quad (21)$$

$$I_{r,l}(x,\omega_1,\omega_2) = \int_0^x dx'\ \omega_0(x')\chi_r^2(x',\omega_1) \times \chi_r^*(x',\omega_2)\chi_{r,l}(x',\omega_{dp}). \quad (22)$$

Equation (19) will be assumed in the derivation of the results. This assumption will be relaxed in Sec. VII, where the semianalytic results are compared to those obtained from a numerical model in which $\varepsilon_\gamma \neq$ constant. The WKB approximation (e.g., Zweig *et al.*, 1976) is used for the cochlear traveling wave basis function $\psi_r(x,\omega)$, along with the Zweig (1991) form of the cochlear macromechanical transpartition impedance. In order to illustrate in part how these equations were obtained, and to clarify the discussion of the numerical results in Sec. VII, the perturbative analysis for the $2\omega_1-\omega_2$ DP is outlined in the Appendix.

III. COCHLEAR FILTER CONTRIBUTION TO THE DPOAE PHASE

In this section, an analytic argument, based on a number of simplifying approximations (some of which may appear dubious to the reader), is used to make plausible the smallness of the cochlear filter contribution to the DPOAE phase. In Sec. VII, numerical calculations, in which these approximations are *not* made, are shown to confirm the results found here. Therefore, a reader who is not interested in analytic details need only read through this section lightly in order to see where in the formal structure of the DPOAE pressure signal the cochlear filter contribution to the phase arises.

Within the approximations of Eq. (9), the DPOAE phase is that of $I_r(\infty,\omega_1,\omega_2)$ [see Eqs. (8), (10), (19), and (20)] except for a small contribution from the acousto-mechanics of the ear canal and middle ear. Consequently, the focus will be on this factor in the remainder of this section.

Most of the contribution to the integral $I_r(\infty,\omega_1,\omega_2)$ comes from the region around the amplitude maximum of $\chi_r^*(x,\omega_2)$ at

$$x \approx \hat{x}(\omega_2) = \frac{1}{k_\omega}\log\left(\frac{\omega_{0c}}{\omega_2}\right). \quad (23)$$

In order to estimate the phase of $I_r(\infty,\omega_1,\omega_2)$, it is convenient to expand the x dependence of the phase of the inte-

grand of $I_r(\infty,\omega_1,\omega_2)$ in Eq. (22) about $x=\hat{x}(\omega_2)$ to first order in $x-\hat{x}(\omega_2)$. If the phase contributions from the $\Delta_{sm}(x,\omega)$ factors are not taken into account, this phase dependence is approximately given by

$$\begin{aligned}\arg[\text{integrand of } I_r(\infty,\omega_1,\omega_2)] &\cong \int_0^{\hat{x}(\omega_2)} dx' \,\mathrm{Re}[-2k(x',\omega_1)+k^*(x',\omega_2) \\ &\quad -k(x',\omega_{dp})]+\mathrm{Re}[-2k(\hat{x}(\omega_2),\omega_1) \\ &\quad +k^*(\hat{x}(\omega_2)),\omega_2)-k(\hat{x}(\omega_2),\omega_{dp})][x-\hat{x}(\omega_2)], \quad (24)\end{aligned}$$

where $\mathrm{Re}\,z$ denotes the real part of z, and $\arg z$ denotes the phase of z.

It will be shown in Sec. IV that, at least for the case of a scale-invariant wave number function $k(x,\omega)$, the first term on the right-hand side of Eq. (24) does not depend significantly on the behavior of $k(x,\omega_2)$ in the resonance region, $x\approx\hat{x}(\omega_2)$ [see, e.g., Eq. (46)]. Thus, the importance of the sharpness of the filter function for the ω_2 primary in determining the DPOAE phase may be assessed by estimating the difference between the phase of $I_r(\infty,\omega_1,\omega_2)$ and this first term. This difference was previously estimated by Talmadge *et al.* (1998) and shown to be small (see their Secs. V B and C). However, they neglected the additional phase of the integrand of $I_r(\infty,\omega_1,\omega_2)$ which comes from the factor $\Delta^*_{sm}(x,\omega_2)$. For present purposes, therefore, it is sufficient to calculate the phase difference with this additional phase dependence included in the integrand in order to demonstrate the relative importance of the sharpness of the filter function (and thus the relative importance of the filter build-up time). A plausibility argument will now be given to demonstrate that the phase difference remains small even if the additional phase is included in the integrand, and thus that the character of the resonance region for the ω_2 primary is not significant in determining the DPOAE phase.

In order to simplify the evaluation of this extra phase contribution, the time-delayed stiffness terms in $[\Delta^*_{sm}(x,\omega_2)]^{-3/4}$ in Eq. (15) are dropped. These terms are however still included in the numerical treatment of this problem in Sec. VII in order to assess their relative importance. In addition, γ_0 is assumed to be constant, the magnitude of $\chi^*_r(x,\omega_2)$ around $x\approx\hat{x}(\omega_2)$ is approximated by (e.g., Zweig and Shera, 1995; Talmadge *et al.*, 1998)

$$|\chi^*_r(x,\omega_2)|\cong|\hat{\chi}_r(\omega_2)|e^{-[x-\hat{x}(\omega_2)]^2/2\sigma_x^2}, \quad (25)$$

$|\chi_r(x,\omega_1)|$ is replaced by its value at $x=\hat{x}(\omega_2)$, $\omega_0(x)$ is evaluated at $\hat{x}(\omega_2)$, and $[\Delta^*_{sm}(x,\omega_2)]^{3/4}$ is expanded about $x\approx\hat{x}(\omega_2)$

$$\begin{aligned}[\Delta^*_{sm}(x,\omega_2)]^{3/4} &\approx (-i\omega_2\gamma_0)^{3/4}+\frac{3}{4}\frac{1}{(-i\omega_2\gamma_0)^{1/4}} \\ &\quad \times(-2k_\omega\omega_2^2)[x-\hat{x}(\omega_2)] \\ &= -\frac{3}{2}k_\omega\omega_2^2\frac{1}{(-i\omega_2\gamma_0)^{1/4}} \\ &\quad \times\left[x-\hat{x}(\omega_2)+\frac{2i\gamma_0}{3k_\omega\omega_2}\right]. \quad (26)\end{aligned}$$

Since the phase of

$$\frac{-3}{2}k_\omega\omega_2^2\frac{1}{(-i\omega_2\gamma_0)^{1/4}} \quad (27)$$

is constant (i.e., independent of ω_1 and ω_2), the ω_1- and ω_2-dependent part of this phase contribution can be approximately represented as

$$\begin{aligned}\arg\int_0^\infty dx' \exp\{i\,\mathrm{Re}[-2k(\hat{x}(\omega_2),\omega_1)+k^*(\hat{x}(\omega_2),\omega_2) \\ -k(\hat{x}(\omega_2),\omega_{dp})][x'-\hat{x}(\omega_2)]\} \\ \times\frac{|x'-\hat{x}(\omega_2)+iL|}{x'-\hat{x}(\omega_2)+iL}\exp\left\{-\frac{[x-\hat{x}(\omega_2)]^2}{2\sigma_x^2}\right\}, \quad (28)\end{aligned}$$

where $L\approx 2\gamma_0/3k_\omega\omega_2\sim 0.1$ cm. Using the variable substitutions

$$x''=x'-\hat{x}(\omega_2), \quad (29)$$

$$\begin{aligned}K=\mathrm{Re}[&-2k(\hat{x}(\omega_2),\omega_1)+k^*(\hat{x}(\omega_2),\omega_2) \\ &-k(\hat{x}(\omega_2),\omega_{dp})], \quad (30)\end{aligned}$$

the phase contribution given by Eq. (28) may be written approximately as

$$\begin{aligned}\arg\int_{-\infty}^\infty dx''\, e^{-(x'')^2/2\sigma_x^2}e^{iKx''}\frac{x''-iL}{\sqrt{(x'')^2+L^2}} \\ =\arg i\int_{-\infty}^\infty dx''\, e^{-(x'')^2/2\sigma_x^2}\frac{x''\sin Kx''-L\cos Kx''}{\sqrt{(x'')^2+L^2}} \\ =\pm\frac{\pi}{2}. \quad (31)\end{aligned}$$

Since Eq. (31) yields a constant phase, the frequency derivatives of this extra phase contribution are vanishingly small within the approximation scheme used here and are probably very small in general. The ω_1- and ω_2-dependent part of the phase is approximately given by

$$\begin{aligned}\varphi_{\mathrm{gen}}(\omega_1,\omega_2,\omega_{dp}) &\equiv \arg[P^{ss}_{dp}(\omega_1,\omega_2,\omega_{dp})] \\ &\cong \arg[I_r(\infty,\omega_1,\omega_2)] \\ &\cong \int_0^{\hat{x}(\omega_2)} dx' \,\mathrm{Re}[k^*(x',\omega_2) \\ &\quad -2k(x',\omega_1)-k(x',\omega_{dp})], \quad (32)\end{aligned}$$

where the subscript gen indicates that this is the contribution to the DPOAE phase only from the DP generation region. Note that this equation simply states that the DPOAE phase is given by $2\pi\times$[the number of ω_2 wavelengths—twice the number of ω_1 wavelengths—the number of ω_{dp} wavelengths of the associated traveling waves between the cochlear base and the ω_2 tonotopic place].

The calculations of this section are admittedly based on many approximations, including the use of a symmetric [Eq. (25)] rather than a (more realistic) highly asymmetric cochlear activity pattern. However, it will be shown in Sec. VII that numerical calculations, *in which none of the approxima-*

tions used in this section is made, support the general conclusion that taking into account the phase of $\Delta^*_{sm}(x,\omega_2)$, and hence the most important effects of the cochlear filter on the DPOAE phase, gives only very small contributions to the DPOAE phase derivatives.

IV. APPROXIMATE PHASE DERIVATIVES FROM SCALE-INVARIANCE

In this section, it will be demonstrated that the substantial difference between the fixed-f_1 and fixed-f_2 phase derivatives can be understood as a consequence of the approximate scale invariance of the cochlear mechanics (e.g., Shera and Zweig, 1993; Zweig and Shera, 1995; Talmadge *et al.*, 1998) applied to the evaluation of $\varphi_{\rm gen}(\omega_1,\omega_2,\omega_{dp})$ given by Eq. (32).

Scale invariance of the form

$$k(x,\omega)\cong k\left(\frac{\omega}{\omega_0(x)}\right), \tag{33}$$

will be assumed for the wave number function, where $\omega_0(x)$ is given by Eq. (18). Note that the assumption Eq. (19) gives a scale-invariant wave number. From Eqs. (18) and (33), it follows that

$$\frac{\partial k(x,\omega)}{\partial\omega}\cong\frac{\partial k(\omega/\omega_0(x))}{\partial\omega}\cong\frac{1}{\omega_0(x)}k'(\omega/\omega_0(x)), \tag{34}$$

$$\frac{\partial k(x,\omega)}{\partial x}\cong\frac{\partial k(\omega/\omega_0(x))}{\partial x}\cong\frac{k_\omega\omega}{\omega_0(x)}k'(\omega/\omega_0(x)). \tag{35}$$

[The primes indicate differentiation of k with respect to its argument, $\omega/\omega_0(x)$.] Comparison of Eqs. (34) and (35) gives the approximate relationship

$$\frac{\partial k(x,\omega)}{\partial\omega}\cong\frac{1}{k_\omega\omega}\frac{\partial k(x,\omega)}{\partial x}. \tag{36}$$

The phase derivative,

$$\tau_{\rm gen}(\omega_1,\omega_2,\omega_{dp})\equiv-\frac{\partial\varphi_{\rm gen}(\omega_1,\omega_2,\omega_{dp})}{\partial\omega_{dp}}, \tag{37}$$

is usually evaluated under one of three conditions: (i) ω_1 = constant [fixed-f_1 or f_2-sweep paradigm]; (ii) ω_2 = constant [fixed-f_2 or f_1-sweep paradigm]; (iii) ω_2/ω_1 = constant [fixed-f_2/f_1 or fixed-ratio paradigm]. Since $\omega_{dp}=2\omega_1-\omega_2$, the derivatives of ω_1 and ω_2 with respect to ω_{dp} can be expressed in terms of the constants

$$\alpha_1=\frac{\partial\omega_1}{\partial\omega_{dp}},\quad \alpha_2=\frac{\partial\omega_2}{\partial\omega_{dp}}, \tag{38}$$

where

$$\alpha_1=0,\quad \alpha_2=-1:\quad (\omega_1=\text{constant}), \tag{39}$$

$$\alpha_1=\tfrac{1}{2},\quad \alpha_2=0:\quad (\omega_2=\text{constant}), \tag{40}$$

$$\alpha_1=\frac{1}{2-r},\quad \alpha_2=\frac{r}{2-r}:\quad (\omega_2/\omega_1=r=\text{constant}). \tag{41}$$

Also,

$$\frac{\partial\hat{x}(\omega_2)}{\partial\omega_{dp}}=\frac{\partial\hat{x}(\omega_2)}{\partial\omega_2}\frac{\partial\omega_2}{\partial\omega_{dp}}=-\frac{\alpha_2}{k_\omega\omega_2}. \tag{42}$$

Equations (32), (33), (37), and (42) give

$$\begin{aligned}\tau_{\rm gen}(\omega_1,\omega_2,\omega_{dp})=&-\int_0^{\hat{x}(\omega_2)}dx'\,{\rm Re}\left[\frac{\partial k^*(x',\omega_2)}{\partial\omega_{dp}}\right.\\&\left.-2\frac{\partial k(x',\omega_1)}{\partial\omega_{dp}}-\frac{\partial k(x',\omega_{dp})}{\partial\omega_{dp}}\right]\\&+\frac{\alpha_2}{k_\omega\omega_2}{\rm Re}[k^*(\hat{x}(\omega_2),\omega_2)\\&-2k(\hat{x}(\omega_2),\omega_1)-k(\hat{x}(\omega_2),\omega_{dp})].\end{aligned} \tag{43}$$

Applying Eqs. (38) through (43) yields

$$\begin{aligned}\tau_{\rm gen}(\omega_1,\omega_2,\omega_{dp})=&\frac{\alpha_2}{k_\omega\omega_2}{\rm Re}[k^*(\hat{x}(\omega_2),\omega_2)\\&-2k(\hat{x}(\omega_2),\omega_1)-k(\hat{x}(\omega_2),\omega_{dp})]\\&-\int_0^{\hat{x}(\omega_2)}dx'\,{\rm Re}\left[\alpha_2\frac{\partial k^*(x',\omega_2)}{\partial\omega_2}\right.\\&\left.-2\alpha_1\frac{\partial k(x',\omega_1)}{\partial\omega_1}-\frac{\partial k(x',\omega_{dp})}{\partial\omega_{dp}}\right],\end{aligned} \tag{44}$$

which can be further reduced using Eq. (36) to give

$$\begin{aligned}\tau_{\rm gen}(\omega_1,\omega_2,\omega_{dp})=&\frac{\alpha_2}{k_\omega\omega_2}{\rm Re}[k^*(\hat{x}(\omega_2),\omega_2)\\&-2k(\hat{x}(\omega_2),\omega_1)-k(\hat{x}(\omega_2),\omega_{dp})]\\&-\int_0^{\hat{x}(\omega_2)}dx'\,{\rm Re}\left[\frac{\alpha_2}{k_\omega\omega_2}\frac{\partial k^*(x',\omega_2)}{\partial x'}\right.\\&-\frac{2\alpha_1}{k_\omega\omega_1}\frac{\partial k(x',\omega_1)}{\partial x'}\\&\left.-\frac{1}{k_\omega\omega_{dp}}\frac{\partial k(x',\omega_{dp})}{\partial x'}\right].\end{aligned} \tag{45}$$

After the x' integration is carried out, this expression reduces to the final form

$$\begin{aligned}\tau_{\rm gen}(\omega_1,\omega_2,\omega_{dp})=&\frac{2\,{\rm Re}[k^*(\hat{x}(\omega_2),\omega_1)]}{k_\omega\omega_1}\left[\alpha_1-\alpha_2\frac{\omega_1}{\omega_2}\right]\\&+\frac{{\rm Re}[k(\hat{x}(\omega_2),\omega_{dp})]}{k_\omega\omega_{dp}}\left[1-\alpha_2\frac{\omega_{dp}}{\omega_2}\right]\\&+\left\{\frac{\alpha_2}{k_\omega\omega_2}{\rm Re}[k^*(0,\omega_2)]\right.\\&-\frac{2\alpha_1}{k_\omega\omega_1}{\rm Re}[k(0,\omega_1)]\\&\left.-\frac{1}{k_\omega\omega_{dp}}{\rm Re}[k(0,\omega_{dp})]\right\}.\end{aligned} \tag{46}$$

The wave number function $k(x,\omega)$ has the approximate scale-invariant form (Talmadge *et al.*, 1998)

$$k(x,\omega)\cong\frac{k_0\omega}{\sqrt{\omega_0^2(x)-\omega^2}}[=\text{real}],\quad \omega\ll\omega_0(x), \tag{47}$$

where k_0 is a constant (see Talmadge *et al.*, 1998). Evaluating Eq. (47) at $x=0$ for $\omega\ll\omega_{0c}$ gives

$$k(0,\omega)\cong\frac{k_0\omega}{\omega_{0c}}. \tag{48}$$

Since $\omega_{dp}=2\omega_1-\omega_2$, the $\alpha_{1,2}$ are then related by

$$2\alpha_1-\alpha_2=1, \tag{49}$$

which is true for any DPOAE measurement paradigm for which ω_{dp} is varied. Applying Eqs. (47), (48), and (49) to Eq. (46) gives

$$\tau_{\text{gen}}(\omega_1,\omega_2,\omega_{dp})=\left[\alpha_1-(2\alpha_1-1)\frac{\omega_1}{\omega_2}\right]\left(\frac{2k_0}{k_\omega}\right)\times\left(\frac{1}{\sqrt{\omega_2^2-\omega_1^2}}+\frac{1}{\sqrt{\omega_2^2-\omega_{dp}^2}}\right)-\frac{2k_0}{k_\omega\omega_{0c}}. \tag{50}$$

Using the values of k_0, k_ω, and ω_{0c} for humans as quoted in Talmadge *et al.* (1998), $2k_0/k_\omega\omega_{0c}\cong 0.25$ ms, which, for ω_{dp}, ω_1, $\omega_2\ll\omega_{0c}$, is very small compared to other phase derivative contributions associated with scale-invariance violations of the cochlear parameters, as well as those associated with the middle and outer ear. Consequently, the $2k_0/k_\omega\omega_{0c}$ term in Eq. (50) will be neglected for the purpose of this discussion. A brief description of the consequences of including this term is given at the end of this section.

From Eqs. (41) and (50), the fixed-ratio phase derivative is

$$\tau_{\text{fixed-}r}(\omega_{dp})\equiv\tau_{dp}(\omega_1,\omega_2,\omega_{dp})|_{\omega_2/\omega_1=r}\cong 0. \tag{51}$$

The fact that $\tau_{\text{fixed-}r}\cong 0$ for a cochlea which is approximately scale invariant was first pointed out by Kemp and Brown (1983). From Eqs. (39) and (50), the fixed-f_1 (f_2-sweep) phase derivative is

$$\tau_{\text{fixed-}f_1}=\tau_{\text{gen}}(\omega_1,\omega_2,\omega_{dp})|_{\omega_1}=\frac{2\omega_1}{\omega_2}\frac{k_0}{k_\omega}\left(\frac{1}{\sqrt{\omega_2^2-\omega_1^2}}+\frac{1}{\sqrt{\omega_2^2-\omega_{dp}^2}}\right). \tag{52}$$

Finally, using Eqs. (40) and (50), the fixed-f_2 (f_1-sweep) phase derivative is

$$\tau_{\text{fixed-}f_2}=\tau_{\text{gen}}(\omega_1,\omega_2,\omega_{dp})|_{\omega_2}=\frac{k_0}{k_\omega}\left(\frac{1}{\sqrt{\omega_2^2-\omega_1^2}}+\frac{1}{\sqrt{\omega_2^2-\omega_{dp}^2}}\right). \tag{53}$$

Thus, the ratio

$$\frac{\tau_{\text{fixed-}f_1}}{\tau_{\text{fixed-}f_2}}=\frac{2\omega_1}{\omega_2} \tag{54}$$

is significantly larger than 1 for ω_2/ω_1 in the range 1.1–1.3, as was observed experimentally by Bowman *et al.* (1997, 1998) and by Schneider *et al.* (1999a,b). Equation (54) may also be derived from the assumption of scale invariance of the phase (Schneider *et al.*, 1999b; Prijs *et al.*, 2000, and Sec. VIII of this paper). From the additional assumptions needed besides that of wave number scale invariance given by Eq. (33), it is evident that the assumption of phase scale invariance is far more restrictive than wave number scale invariance.

Equation (54) suggests the definition of a new quantity $\mathcal{S}(\omega_{dp})$ that indicates the degree of conformity of the DPOAE phase with the assumption of DPOAE phase scale invariance

$$\mathcal{S}(\omega_{dp})\equiv\left[\left(\frac{2\omega_1}{\omega_2}\right)^{-1}\frac{\tau_{\text{fixed-}f_1}(\omega_1,\omega_2,\omega_{dp})}{\tau_{\text{fixed-}f_2}(\omega_1,\omega_2,\omega_{dp})}\right]. \tag{55}$$

The factor $\mathcal{S}(\omega_{dp})$ is equal to 1 only if phase scale invariance within the cochlea holds, and is close to 1 only if approximate wave number scale invariance within the cochlea is assumed and, in addition, if the effects from the base and apex and from the middle and outer ears on the phase can be neglected. If middle-ear effects are included in the model, significant deviations of $\mathcal{S}$ from 1 should be expected around the resonance frequency of the middle ear. The effect of the neglected factor of $2k_0/k_\omega\omega_{0c}$ (which parametrizes the effects of the cochlear base) becomes relatively more important as the DP frequency is increased, so that a significant deviation of $\mathcal{S}$ from 1 is also expected at DP frequencies approaching ω_{0c}.

It is interesting to compute the deviation of $\mathcal{S}$ from 1 if the assumption that the effects of the base are negligible is relaxed. This assumption amounts to the neglect of the term $2k_0/k_\omega\omega_{0c}$ in Eq. (50). With the assumption that this term is small but non-negligible, the factor $\mathcal{S}$ becomes

$$\mathcal{S}(\omega_{dp},r)\cong 1+(\omega_{dp}/\omega_{0c})f_{\mathcal{S}}(r), \tag{56}$$

$$f_{\mathcal{S}}(r)=\left(\frac{1}{\sqrt{r^2-1}}+\frac{1}{2\sqrt{r-1}}\right)^{-1}. \tag{57}$$

V. APPROXIMATE PHASE DERIVATIVES OF APICAL DPOAE COMPONENT

In Secs. III and IV, the DPOAE phase derivatives were obtained under the assumption that the effects of reflection of the initially generated apical wave from around the DP tonotopic site could be neglected. In this section, the DPOAE phase derivatives will be derived assuming instead that $R_aP_r\gg P_l$, but that $|R_a||R_b|\ll 1$: that is, the DPOAE reflection-site component will be assumed dominant, but the effects of multiple internal reflection will be neglected. In this case, the DPOAE signal is

$$P_{dp}^{ss}(\omega_1,\omega_2,\omega_{dp})\cong R_a(\omega_{dp})P_r(\omega_1,\omega_2,\omega_{dp}). \tag{58}$$

Following the procedures outlined in the previous section, but now assuming that the dominant phase contribution to P_r comes from $\arg I_l$, gives

$$\begin{aligned}\varphi_{\text{refl}}(\omega_1,\omega_2,\omega_{dp}) &\cong \arg[R_a(\omega_{dp})P_r(\omega_1,\omega_2,\omega_{dp})] \\ &\cong \arg[I_l(\infty,\omega_1,\omega_2,\omega_{dp})]+\arg[R_a(\omega_{dp})] \\ &\cong \int_0^{\hat{x}(\omega_2)} dx'\ \text{Re}[k^*(x',\omega_2)-2k(x',\omega_1) \\ &\quad +k(x',\omega_{dp})]+\varphi_a(\omega_{dp}), \end{aligned} \tag{59}$$

where $\varphi_a(\omega_{dp})\equiv\arg R_a(\omega_{dp})$, and where the subscript ''refl'' indicates that this phase represents the contribution only from the DPOAE reflection site component. From Zweig and Shera (1995) and Talmadge *et al.* (1998)

$$\varphi_a(\omega)\cong -\frac{2\hat{k}}{k_\omega}\log\left(\frac{\omega}{\omega_{0c}}\right), \tag{60}$$

where $\hat{k}=\hat{k}(\omega)\equiv\text{Re}[k(\hat{x}(\omega),\omega)]$ (assumed constant with respect to ω under scale invariance) is the real part of the wave number at the basilar membrane activity pattern maximum for an initially apical moving wave of frequency ω. The phase derivative

$$\tau_{\text{refl}}(\omega_1,\omega_2,\omega_{dp})=-\frac{\partial\varphi_{refl}(\omega_1,\omega_2,\omega_{dp})}{\partial\omega_{dp}} \tag{61}$$

is given by

$$\begin{aligned}\tau_{\text{refl}}(\omega_1,\omega_2,\omega_{dp}) &= \frac{2\,\text{Re}[k(\hat{x}(\omega_2),\omega_1)]}{k_\omega\omega_1}\left[\alpha_1-\alpha_2\frac{\omega_1}{\omega_2}\right] \\ &\quad -\frac{\text{Re}[k(\hat{x}(\omega_2),\omega_{dp})]}{k_\omega\omega_{dp}}\left[1-\alpha_2\frac{\omega_{dp}}{\omega_2}\right] \\ &\quad +\left\{\frac{\alpha_2}{k_\omega\omega_2}\text{Re}[k(0,\omega_2)]\right. \\ &\quad -\frac{2\alpha_1}{k_\omega\omega_1}\text{Re}[k(0,\omega_1)] \\ &\quad \left.+\frac{1}{k_\omega\omega_{dp}}\text{Re}[k(0,\omega_{dp})]\right\}+\frac{2\hat{k}}{k_\omega\omega_{dp}}. \end{aligned} \tag{62}$$

Applying Eqs. (47), (48), and (49) to Eq. (62) gives

$$\begin{aligned}\tau_{\text{refl}}(\omega_1,\omega_2,\omega_{dp}) &= \frac{2\hat{k}}{k_\omega\omega_{dp}}-\left[\alpha_1-(2\alpha_1-1)\frac{\omega_1}{\omega_2}\right]\left(\frac{2k_0}{k_\omega}\right) \\ &\quad \times\left(\frac{1}{\sqrt{\omega_2^2-\omega_{dp}^2}}-\frac{1}{\sqrt{\omega_2^2-\omega_1^2}}\right). \end{aligned} \tag{63}$$

The interpretation of Eq. (63) may be facilitated by noting that the physical round-trip travel time of a wave packet of center frequency ω from the base to its tonotopic position and back to the base is just (Lighthill, 1978)

$$\begin{aligned}\tau_{rt}(\omega) &= 2\int_0^{\hat{x}(\omega)} dx'\frac{\partial k(x',\omega)}{\partial\omega} \\ &\cong \frac{2}{k_\omega\omega}\int_0^{\hat{x}(\omega)} dx'\frac{\partial k(x',\omega)}{\partial x'} \\ &= \frac{2}{k_\omega\omega}[\hat{k}(\omega)-k(0,\omega)]\approx\frac{2\hat{k}}{k_\omega\omega}, \end{aligned} \tag{64}$$

where Eq. (36) has been used in obtaining this result. Comparing Eqs. (63) and (64), it is easy to see that the phase derivative for the DPOAE reflection-site component is just the (physical) round-trip travel time minus a small correction term. This correction term just accounts for the phase effects of the variation in the separation between the generation region and the DP reflection site. For fixed-f_1 and fixed-f_2 sweeps in the range of r between 1.1 and 1.3, these corrections are less than 1/6 of $\tau_{\text{fixed-}f_1}$ and $\tau_{\text{fixed-}f_2}$, respectively, for the cases in which the generator region component is dominant [Eqs. (52) and (53)]. This is due to the minus sign between the two terms in the last factor in Eq. (63).

VI. DPOAE PHASE-DERIVATIVE FINE STRUCTURE

In this section, the phase derivative for the case in which neither P_l nor R_aP_r is negligible but $|R_a||R_b|\ll 1$ will be considered. In this case, we have

$$\begin{aligned}P_{dp}^{ss}(\omega_1,\omega_2,\omega_{dp}) &\cong P_l(\omega_1,\omega_2,\omega_{dp}) \\ &\quad +R_a(\omega_{dp})P_r(\omega_1,\omega_2,\omega_{dp}). \end{aligned} \tag{65}$$

To simplify the notation, the following definitions are introduced:

$$P_l(\omega_1,\omega_2,\omega_{dp})=A_{\text{gen}}(\omega_1,\omega_2,\omega_{dp})e^{i\varphi_{\text{gen}}(\omega_1,\omega_2,\omega_{dp})}, \tag{66}$$

$$\begin{aligned}R_a(\omega_{\text{refl}})P_r(\omega_1,\omega_2,\omega_{dp}) &= A_{\text{refl}}(\omega_1,\omega_2,\omega_{dp}) \\ &\quad \times e^{i\varphi_{\text{refl}}(\omega_1,\omega_2,\omega_{dp})}. \end{aligned} \tag{67}$$

From the formalism of Talmadge *et al.* (1998), the amplitudes A_{gen} and A_{refl} are expected to vary slowly compared to φ_{refl}. Consequently, A_{gen} and A_{refl} will be treated as constants with respect to their arguments in the following analysis.

Using Eqs. (66) and (67), the phase of $P_{ss}^{dp}(\omega_1,\omega_2,\omega_{dp})$ is then given by

$$\begin{aligned}\varphi_{dp}(\omega_1,\omega_2,\omega_{dp}) &= \varphi_{\text{gen}}(\omega_1,\omega_2,\omega_{dp}) \\ &\quad +\tan^{-1}\left[\frac{\mathcal{R}\sin(\Delta\varphi(\omega_1,\omega_2,\omega_{dp}))}{1+\mathcal{R}\cos(\Delta\varphi(\omega_1,\omega_2,\omega_{dp}))}\right], \end{aligned} \tag{68}$$

where $\mathcal{R}\equiv A_{\text{refl}}/A_{\text{gen}}$ and

$$\begin{aligned}\Delta\varphi(\omega_1,\omega_2,\omega_{dp}) &\equiv \varphi_{\text{refl}}(\omega_1,\omega_2,\omega_{dp})-\varphi_{\text{gen}}(\omega_1,\omega_2,\omega_{dp}) \\ &= \varphi_{dp0}(\omega_{dp},\omega_2)+\varphi_a(\omega_{dp}), \end{aligned} \tag{69}$$

$$\varphi_{dp0}(\omega_{dp},\omega_2)=2\int_0^{\hat{x}(\omega_2)} dx'\ \text{Re}[k(x',\omega_{dp})], \tag{70}$$

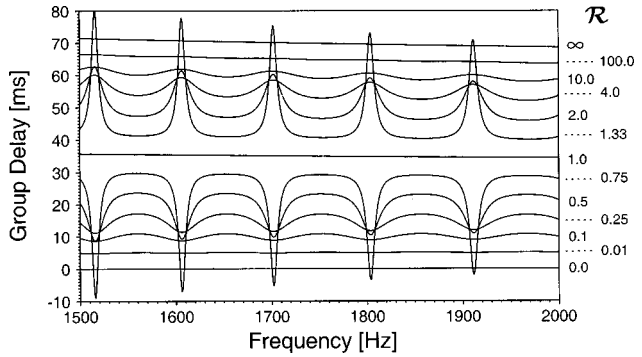

FIG. 1. Plot of the fixed-ratio paradigm phase derivative τ_{dp} using Eq. (74), for various admixtures $\mathcal{R}$ of the generation region and reflection-site DPOAE components. In order to be distinguishable, each successive curve is shifted vertically on the scale by 5 ms.

where Eq. (70) follows from Eqs. (32) and (59). The phase derivative for this case is then

$$\tau_{dp}(\omega_1,\omega_2,\omega_{dp})=\left[\frac{1+\mathcal{R}\cos\Delta\varphi(\omega_1,\omega_2,\omega_{dp})}{1+\mathcal{R}^2+2\mathcal{R}\cos\Delta\varphi(\omega_1,\omega_2,\omega_2)}\right]\times\tau_{\text{gen}}(\omega_1,\omega_2,\omega_{dp})+\left[\frac{\mathcal{R}^2+\mathcal{R}\cos\Delta\varphi(\omega_1,\omega_2,\omega_{dp})}{1+\mathcal{R}^2+2\mathcal{R}\cos\Delta\varphi(\omega_1,\omega_2,\omega_{dp})}\right]\times\tau_{\text{refl}}(\omega_1,\omega_2,\omega_{dp}). \tag{71}$$

As expected, Eq. (71) reduces to $\tau_{dp}=\tau_{\text{gen}}$ when $\mathcal{R}\to 0$ and to $\tau_{dp}=\tau_{\text{refl}}$ when $\mathcal{R}\to\infty$. However, for intermediate values of $\mathcal{R}$, the phase derivative is in general neither a monotonically varying nor even a bounded function.

In order to study in detail the effects of fine structure on the phase derivative, the case of the fixed ratio will be considered. Under the assumption of scale invariance, $\tau_{\text{gen}}\approx 0$ and $\tau_{\text{refl}}\approx\tau_a\equiv-\varphi_a'(\omega)$. Since

$$\varphi_{dp0}(\omega_{dp},\omega_2)=2\int_0^{\hat{x}(\omega_2)}dx'\frac{k_0\omega_{dp}}{\sqrt{\omega_0(x')^2-\omega_{dp}^2}}\cong\frac{2k_0}{k_\omega}\sin^{-1}\frac{\omega_{dp}}{\omega_2}, \tag{72}$$

where Eq. (18) has been used in obtaining this result, and $\omega_{dp}\ll\omega_{0c}$ has been assumed, it follows that

$$\Delta\varphi(\omega_{dp},\omega_2)\cong\varphi_a(\omega_{dp})+\text{constant}, \tag{73}$$

for fixed ω_2/ω_1 (and hence, fixed ω_{dp}/ω_2). For simplicity, $\Delta\varphi\approx\varphi_a(\omega_{dp})$ will be assumed. In this case, Eq. (71) becomes

$$\tau_{\text{fixed-ratio}}(\omega_{dp})\cong\left[\frac{\mathcal{R}^2+\mathcal{R}\cos[(2\hat{k}/k_\omega)\log(\omega_{dp}/\omega_{0c})]}{1+\mathcal{R}^2+2\mathcal{R}\cos[(2\hat{k}/k_\omega)\log(\omega_{dp}/\omega_{0c})]}\right]\frac{2\hat{k}}{k_\omega\omega_{dp}}. \tag{74}$$

This result is displayed in Fig. 1 for varying amounts of $\mathcal{R}$. Note that only for $\mathcal{R}\ll 1$ is the result expected for the case of a dominant generator-region component (Sec. IV) recovered. In addition, the phase derivative can vary quite wildly for $\mathcal{R}\approx 1$. Both of these observations also hold for the cases of the fixed-f_1 and fixed-f_2 paradigms. It was shown in Talmadge *et al.* (1999a) that the phase-derivative fine structure will correlate with the DPOAE level fine structure if $\mathcal{R}<1$ (that is, the maxima and minima will align), but will negatively correlate if $\mathcal{R}>1$ (the phase derivative maxima will correspond to level minima and vice versa). This pattern of positively and negatively correlating fine structure was also observed experimentally in Talmadge *et al.* (1999a).

The results obtained in this section were derived under the assumption that the denominator contribution to the fine structure in Eq. (6) could be ignored. The inclusion of this contribution makes the results correspondingly more complex, both for level and phase-derivative fine structures, as will be demonstrated in a paper now in preparation.

VII. NUMERICAL TESTS AND VALIDATION OF THE APPROXIMATIONS

A significant number of approximations were made in order to obtain the quasianalytic results reported in Secs. III through VI. In this section, the effects of these assumptions will be explored in the context of a number of different numerical methods. In order to clarify the discussion, a short summary of the approximations used in obtaining the results is first given. The specific numerical methods used in the validation are then described. In the final subsection, numerical results which provide a test of the various assumptions made in the analyses are given. Alternative means of verifying some of the results are also given.

A. Summary of the approximations

The approximations made in this analysis are listed in the order that they first appear in this paper.

(1) The cochlear model of Talmadge *et al.* (1998) is assumed.
(2) The validity of the results of Talmadge *et al.* (1998) given by Eqs. (7) and (8) is assumed. It should be noted that these results are themselves approximate, and depend on the following assumptions:
  (a) higher-order contributions in the perturbative expansion of the wave equation may be ignored;
  (b) the effects of nonlinearity on the activity patterns of the various frequency components may be neglected;
  (c) nonlinear cochlear wave reflection may be ignored.
(3) The cochlear basis functions are accurately described by the WKB approximation.
(4) Wave number scale invariance is assumed. This is equivalent to assuming that $\varepsilon_\gamma=\gamma_0(x)/\omega_0(x)$ is constant. This assumption results in the approximate relationships given separately in Eqs. (20) and (36).
(5) The neglect of the effects of time-delayed stiffness on DPOAE phase.
(6) The neglect of the influence of the middle ear on the DPOAE phase. This amounts to approximating the phase of $P_l(\omega_1,\omega_2,\omega_{dp})$ by the phase of $I_r(\omega_1,\omega_2,\omega_{dp})$.
(7) The neglect of the effects of damping on DPOAE phase in order to obtain a closed-form result for $\tau_{\text{gen}}(\omega_1,\omega_2,\omega_{dp})$ [see Eq. (50)].

(8) The neglect of the effects of the base (finite ω_{0c}). This approximation plus Eqs. (39) and (40) give Eqs. (52) and (53), respectively.

B. Numerical methods

The effects of these approximations will be systematically investigated by comparing the quasianalytic result with numerical ones based on the underlying cochlear model. In particular, the differences among the models will be explored by separately comparing the values of $\tau_{\text{fixed-}f_1}$ and $\tau_{\text{fixed-}f_2}$, as well as $\mathcal{S}(\omega_{dp})$ given by Eq. (55). In addition, for the study of the possible effects of the ''filter build-up time,'' alternative numerical tests are reported. These will be described separately in Sec. C.

Four different numerical computations for $\tau_{\text{fixed-}f_1}$, $\tau_{\text{fixed-}f_2}$, and $\mathcal{S}$ versus frequency were carried out. In all calculations, the primary frequency ratio was $f_2/f_1=1.22$, and derivatives were evaluated numerically using the centered-difference method. For the computation of $\mathcal{S}$, the results of these separate numerical calculations were compared to the predictions of DPOAE phase scale invariance ($\mathcal{S}\equiv 1$) and wave number scale invariance [Eq. (56)]. The four computations are described below.

(I) In order to make as few assumptions as possible, time-domain integration for a limited number of discretization points was employed. A cochlear model with 4096 sections, and a time step of 2.5×10^{-6} s was used. The model is that described in Talmadge *et al.* (1998) and includes time-delayed stiffness of the form described by Zweig (1991). However, for this analysis, the basilar membrane stiffness function was smoothly varying, instead of having embedded roughness as was the case in Talmadge *et al.* (1998). This simplification prevented any significant reflection-site DPOAE component from being present in the ear canal. The total integration time was 150 ms, and the final 75 ms of the simulated ear-canal signal were analyzed for the DPOAE signal. The effective stimulation levels for this model were $L_1=35$ dB SPLm and $L_2=35$ dB SPLm. The principal advantages of this approach are that it does not rely on perturbation theory and that it is able to account for distortion of the basilar membrane wave functions as a function of stimulus level. It can also account for secondary distortion product generation via the interaction of other DP products with each other and with the primaries. Its chief disadvantages are (i) that its accuracy decreases with increasing frequency of the primaries, as a result of the fixed step size of the time integration, (ii) the large numerical error for low-frequency components due to the finite-time interval for integration and the nonexact convergence of the numerical results to the steady-state solutions, and (iii) the large amount of required computing time. Nonetheless, it is expected that the utility of this approach should compare well with that of other numerical approaches for the midrange of frequencies (approximately 1000–5000 Hz).

(II) As an intermediate test, the frequency-domain perturbative DP wave equation (see the Appendix) was numerically solved, using 40 960 sections. The model was again that of Talmadge *et al.* (1998) except that it had a smooth basilar membrane stiffness function. The chief advantage of this procedure is its speed, which allows numerical integration with a finer grid spacing to be performed, and the phase derivatives to be obtained for a much larger number of DPOAE frequencies. The main disadvantage is that it cannot take into account nonlinear distortion of the basilar membrane traveling waves, so that results based on this approach must be regarded as the low stimulation level limit of those obtained from the time-domain integration approach. This method is equivalent to using approximations 1 and 2 above.

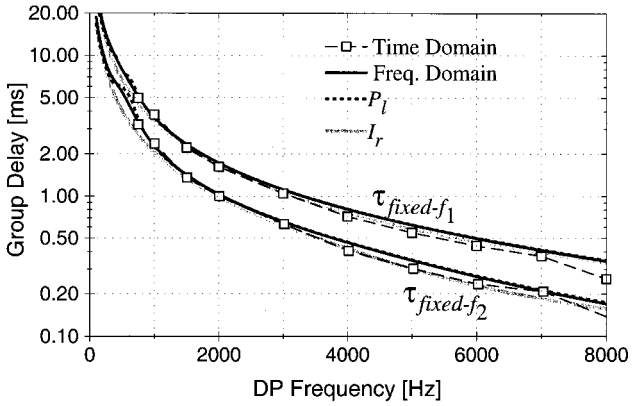

FIG. 2. Plots of $\tau_{\text{fixed-}f_1}$ and $\tau_{\text{fixed-}f_2}$ versus DP frequency for various numerical solutions. The time-domain solution corresponds to primary levels $L_1=L_2=15$ dB SPL. The ''frequency domain'' solution corresponds to the perturbative solution discussed in the text. The solution P_l corresponds to the direct computation of Eq. (7) using the WKB approximation, and I_r corresponds to the direct integration of Eq. (22). As discussed in the text, the use of just I_r to compute the DPOAE phase corresponds to the neglect of middle- and outer-ear effects.

(III) The integral F_r of Eq. (10) was numerically integrated using the basis functions $\psi_{r,l}(x,\omega)$ given by the WKB approximation [Eqs. (12) and (13)]. Because this model is just the Green's function formulation of the frequency-domain perturbative DP wave equation, this procedure can be considered to be nearly identical to that of method II except for the use of the WKB solutions in obtaining the numerical results. This method is equivalent to using approximations 1–3 above.

(IV) The integral F_r was approximated by I_r using Eq. (20). The integral I_r [Eq. (22)] was numerically integrated, using the basis functions $\psi_{r,l}(x,\omega)$ given by the WKB approximation [Eqs. (12) and (13)]. Moreover, I_r does not include effects of the middle ear, so that it cannot be used for frequencies near the middle-ear resonance frequency (500–1000 Hz). It should be noted that for this reason, the quasianalytic results reported upon in this paper are also not valid in this frequency range. This method is equivalent to using approximations 1–6 above.

C. Results

A large number of numerical tests were run during the validation process for this manuscript. As a consequence, a representative but relatively small fraction of the various numerical results will be reported here.

The results of comparisons of the values of $\tau_{\text{fixed-}f_1}$ and $\tau_{\text{fixed-}f_2}$ based on methods I–IV are shown in Fig. 2. These

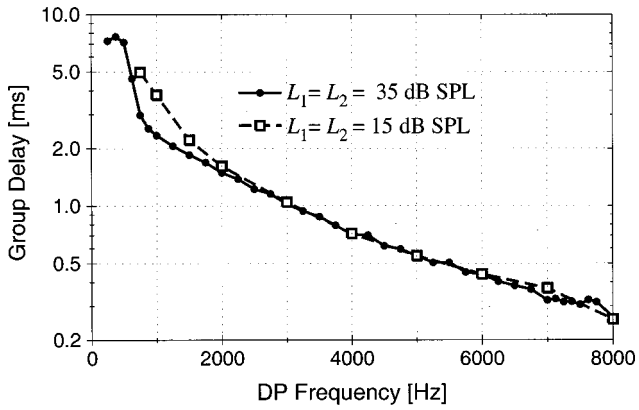

FIG. 3. Effect of level on $\tau_{\text{fixed-}f_1}$. Shown are the computed values based upon the time-domain solutions for primary levels $L_1 = L_2 = 15$ dB SPL and $L_1 = L_2 = 35$ dB SPL. As would be expected from the influence of the middle ear, the dominant effect of level is (initially) seen for DPOAE frequencies in the range 500–1500 Hz.

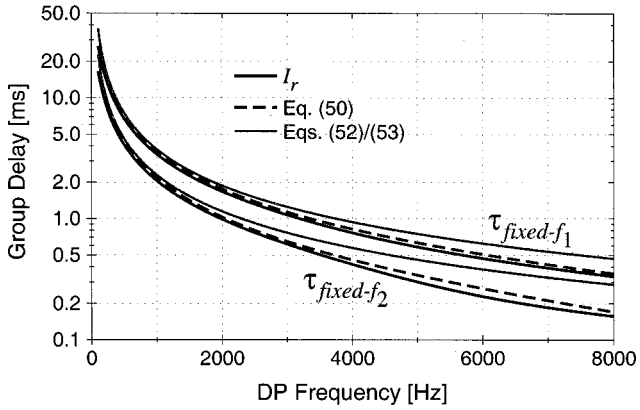

FIG. 4. Comparison of $\tau_{\text{fixed-}f_1}$ and $\tau_{\text{fixed-}f_2}$ computed from I_r to those computed using Eq. (50) and using Eqs. (52) and (52).

results demonstrate the approximate equivalence of the predictions of the mathematical model of Talmadge *et al.* (1998) to those of its approximated forms given by approximations 1–6. It should be noted that the cochlear model used in all four calculations included scale-invariance violating terms for both the place-frequency map and the damping function, as described in Talmadge *et al.* (1998). Consequently the fact that, unlike the other approaches, the direct integration of I_r did not yield significant symmetry violation in the frequency range 500–1000 Hz suggests that the middle and outer ear have a larger effect on the DPOAE phase than the scale-invariant violations of the cochlea at low frequencies.

One of the chief limitations of the approximate forms (frequency-domain perturbative calculation, WKB approximation of P_l, etc.) is the neglect of the frequency shift of the activity pattern maximum of the f_2 primary. The middle ear will transmit acoustic signals more efficiently near its characteristic frequency. Thus, for a fixed ear-canal signal level, there will be a larger basilar membrane amplitude of motion when the signal is near the middle-ear characteristic frequency than when it is well away from that characteristic frequency. If the basilar membrane nonlinear saturating level (b_{nl}) is approximately independent of frequency, as it is in the cochlear models used in this analysis, then it is expected that the effect of the shift of the activity pattern maximum on the phase derivatives will be largest for frequencies near the middle-ear characteristic frequency. This observation is borne out in Fig. 3, where $\tau_{\text{fixed-}f_1}$ is compared for $L_1 = L_2 = 15$ dB SPL to $L_1 = L_2 = 35$ dB SPL. In this figure, the two computed values of $\tau_{\text{fixed-}f_1}$ are seen to diverge only in the range of 500–1500 Hz.

In Fig. 4, the values of $\tau_{\text{fixed-}f_1}$ and $\tau_{\text{fixed-}f_2}$ calculated from I_r are compared to those computed using Eq. (50) and using Eqs. (52) and (53). As discussed above, Eqs. (52) and (53) give the results for a DPOAE wave number scale-invariant model in which the contribution to the phase from the base of the cochlea is neglected, whereas Eq. (50) also corresponds to a wave number scale-invariant model which includes the effect of the cochlear base. In both cases, damping contributions to the DPOAE phase have been neglected. As expected, at high frequencies the results based on Eqs. (52) and (53) deviate substantially from those based on Eq. (50) and I_r. However, the agreement between the phase derivatives computed using I_r and Eq. (50) is quite reasonable, given the level of approximation used to obtain Eq. (50).

Figure 5 displays the computed value of $\mathcal{S}$ from all four numerical approaches. Above approximately 6500 Hz, the time-domain integration error becomes evident for method 1. However, for midrange values (~750–4500 Hz in this simulation), the four approaches give results within approximately 10% with respect to the value of $\mathcal{S}$, and confirm the validity of the approximations used in this analysis for these frequencies. It should be noted that the deviations of $\mathcal{S}$ from 1 are not inconsistent with the model of Talmadge *et al.* (1998), but rather with the more restrictive assumption of DPOAE phase scale invariance. Also, differences among the four approaches are expected because of the varying levels of approximations used in obtaining the results.

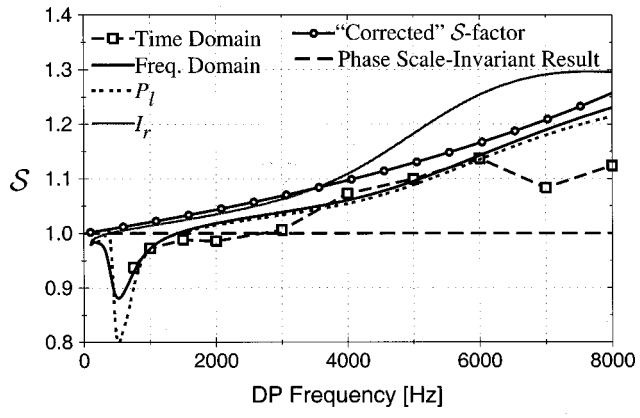

FIG. 5. Plot of $\mathcal{S}$ versus DPOAE frequency, for various numerical solutions. The time-domain, frequency-domain, P_l, and I_r solutions are the same as discussed in the caption for Fig. 2. The factor $\mathcal{S}=1$ corresponds to a phase scale-invariant model, and the ''corrected'' $\mathcal{S}$ factor corresponds to the computed $\mathcal{S}$ factor corrected for the effect of the cochlear base ($\omega_{0c} < \infty$). The large deviations of the computed values of $\mathcal{S}$ from unity for frequencies near 500 Hz are a result of the scale-invariance violations caused by the middle ear.

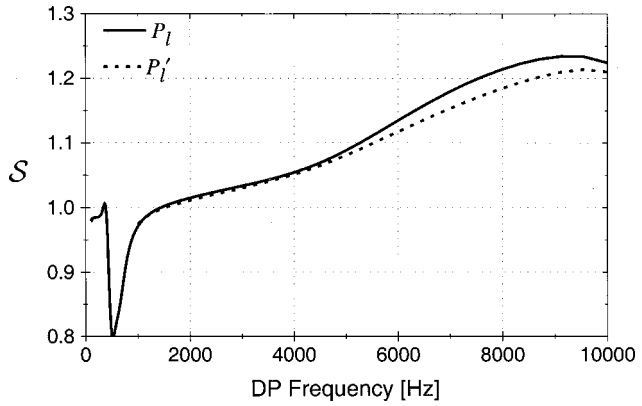

FIG. 6. Comparison of the predicted values of $\mathcal{S}$ versus DPOAE frequency for the perturbative frequency-domain solution P_l and for the modified solution P_l', which is P_l evaluated using $|\Delta(x,\omega)|$ as discussed in the text.

Further insight into the nature of the dependence of the phase derivatives on the basilar membrane damping $\gamma_0(x)$ (and hence on the ''filter build-up'') is obtained by comparing the results of the perturbative frequency-domain calculation, P_l, with P_l', which is the integration of P_l carried out with $\Delta_{sm}^*(x,\omega_2)$ replaced by its magnitude. This was done so as to assess the importance of the resonant phase behavior of $\Delta_{sm}^*(x',\omega_2)$ on the phase derivatives of P_l, which was addressed in an approximate analytic approach in Sec. III. For this evaluation, the integral is labeled as P_l' in Fig. 6. The fact that only a small effect on $\mathcal{S}$ is observed implies that the filter build-up time cannot be the principal explanation for the observed differences between $\tau_{\text{fixed-}f_1}$ and $\tau_{\text{fixed-}f_2}$.

VIII. THE RELATIONSHIP BETWEEN THE FIXED-f_1 AND FIXED-f_2 PHASE DERIVATIVES FOR THE HIGHER-ORDER APICAL DPOAES

[The results obtained in this section have been previously considered in the context of scale invariance by Schneider *et al.* (1999b). See also Prijs *et al.* (2000).] Under the assumption that the generation region component of the DPOAE is dominant, a relationship between $\tau_{\text{fixed-}f_1}$ and $\tau_{\text{fixed-}f_2}$ can be obtained by assuming that the phase of the apical DPOAE from the generator site is scale invariant. In the case of an apical DPOAE of frequency $\omega_{dp}=n\omega_1-(n-1)\omega_2$, scale invariance implies,

$$\varphi_{\text{gen}}(\omega_1,\omega_2,\omega_{dp})=\varphi_{\text{gen}}\left(\frac{\omega_1}{\omega_2},\frac{\omega_{dp}}{\omega_2}\right). \tag{75}$$

Equation (75) is sufficient to establish a general relationship between the two phase derivatives for arbitrary apical order and for an arbitrary form of the nonlinearity, except that the nonlinearity must be of a form that can produce cubic distortion products. With the introduction of the scaling variables

$$\beta_1\equiv\frac{\omega_1}{\omega_2},\quad \beta_{dp}\equiv\frac{\omega_{dp}}{\omega_2}, \tag{76}$$

Eq. (75) becomes

$$\omega_{gen}(\omega_1,\omega_2,\omega_{dp})=\varphi_{\text{gen}}(\beta_1,\beta_{dp}). \tag{77}$$

Evaluating the partial derivatives of φ_{gen} with respect to ω_1 and ω_2 gives

$$\left(\frac{\partial\varphi_{\text{gen}}}{\partial\omega_1}\right)_{\omega_2}=\frac{1}{\omega_2}\frac{\partial\varphi_{\text{gen}}}{\partial\beta_1}+\frac{n}{\omega_2}\frac{\partial\varphi_{\text{gen}}}{\partial\beta_{dp}},$$

$$=\frac{1}{\omega_2}\left[\frac{\partial\varphi_{\text{gen}}}{\partial\beta_1}+n\frac{\partial\varphi_{\text{gen}}}{\partial\beta_{dp}}\right], \tag{78}$$

and

$$\left(\frac{\partial\varphi_{\text{gen}}}{\partial\omega_2}\right)_{\omega_1}=-\frac{\omega_1}{\omega_2^2}\frac{\partial\varphi_{\text{gen}}}{\partial\beta_1}-\left[\frac{n-1}{\omega_2}+\frac{\omega_{dp}}{\omega_2^2}\right]\frac{\partial\varphi_{\text{gen}}}{\partial\beta_{dp}},$$

$$=-\frac{\omega_1}{\omega_2^2}\frac{\partial\varphi_{\text{gen}}}{\partial\beta_1}-\left[\frac{(n-1)\omega_2}{\omega_2^2}+\frac{n\omega_1-(n-1)\omega_2}{\omega_2^2}\right]\frac{\partial\varphi_{\text{gen}}}{\partial\beta_{dp}},$$

$$=-\frac{\omega_1}{\omega_2^2}\left[\frac{\partial\varphi_{\text{gen}}}{\partial\beta_1}+n\frac{\partial\varphi_{\text{gen}}}{\partial\beta_{dp}}\right]. \tag{79}$$

Next, evaluating the phase derivatives with respect to $\omega_{dp}=n\omega_1-(n-1)\omega_2$ gives

$$\tau_{\text{fixed-}f_1}(\omega_{dp})=-\left(\frac{\partial\varphi_{\text{gen}}}{\partial\omega_{dp}}\right)_{\omega_1}$$

$$=\frac{1}{n-1}\left(\frac{\partial\varphi_{\text{gen}}}{\partial\omega_2}\right)_{\omega_1}$$

$$=-\frac{\omega_1}{(n-1)\omega_2^2}\left[\frac{\partial\varphi_{\text{gen}}}{\partial\beta_1}+n\frac{\partial\varphi_{\text{gen}}}{\partial\beta_{dp}}\right], \tag{80}$$

$$\tau_{\text{fixed-}f_2}(\omega_{dp})=-\left(\frac{\partial\varphi_{\text{gen}}}{\partial\omega_{dp}}\right)_{\omega_2}$$

$$=-\frac{1}{n}\left(\frac{\partial\varphi_{\text{gen}}}{\partial\omega_1}\right)_{\omega_2}$$

$$=-\frac{1}{n\omega_2}\left[\frac{\partial\varphi_{\text{gen}}}{\partial\beta_1}+n\frac{\partial\varphi_{\text{gen}}}{\partial\beta_{dp}}\right]. \tag{81}$$

Combining Eqs. (80) and (81) gives

$$\frac{\tau_{\text{fixed-}f_1}(\omega_{dp})}{\tau_{\text{fixed-}f_2}(\omega_{dp})}=\frac{n}{n-1}\frac{\omega_1}{\omega_2}. \tag{82}$$

Finally, it should be noted that if the phase derivatives are evaluated in terms of ω_1 and ω_2 directly, as has been typically done in previous studies (e.g., O'Mahoney and Kemp, 1995; Bowman *et al.*, 1997, 1998), then the ratio of these phase derivatives is just

$$\frac{(\partial\varphi_{\text{gen}}/\partial\omega_2)_{\omega_1}}{(\partial\varphi_{\text{gen}}/\partial\omega_1)_{\omega_2}}\cong\frac{\omega_1}{\omega_2}, \tag{83}$$

independent of the DPOAE order.

IX. SUMMARY AND CONCLUSIONS

The importance of considering the variation of both the DPOAE phase and amplitude with frequency when studying DPOAE fine structure effects has been previously demonstrated by Talmadge *et al.* (1999a). Their results, together with studies such as those of O'Mahoney and Kemp (1995); Bowman *et al.* (1997,1998), Schneider *et al.* (1999a), and Kemp and Knight (2000), underscore the importance of understanding in more detail the proper interpretation of the DPOAE phase and its derivatives. Recent theoretical studies (Talmadge *et al.*, 1999b; Tubis *et al.*, 2000) have already demonstrated that great care must be exercised when attempting to relate DPOAE phase derivatives to the relevant latencies.

In this paper, expressions describing the phase derivatives $\tau_{\text{fixed-ratio}}$, $\tau_{\text{fixed-}f_1}$, and $\tau_{\text{fixed-}f_2}$ have been obtained in Secs. II and III using the theoretical framework of Talmadge *et al.* (1998). In Sec. III, an approximate analytical argument was used to show that the contributions to these phase derivatives from the resonant cochlear partition phase behavior in the generation region (around the f_2 tonotopic site) are small. This contribution is presumably what Bowman *et al.* (1997,1998) associate with the filter build-up time. In Sec. VII, this conclusion was reinforced using four different numerical approaches. It was shown in particular that the cochlear filter contributions to $\mathcal{S}$, and hence to the ratio of $\tau_{\text{fixed-}f_1}$ to $\tau_{\text{fixed-}f_2}$, are small. On this basis, it was concluded that these contributions could not be the main source for the substantial differences between these phase derivatives that have been found experimentally.

In Sec. IV, it was shown that wave number scale invariance applied to the generator region DPOAE component is sufficient to give a general result [Eq. (54)] for the ratio of $\tau_{\text{fixed-}f_1}$ to $\tau_{\text{fixed-}f_2}$, which is in fairly good agreement with experimental data for f_2/f_1 in the range of 1.1 to 1.3. This result has been previously derived by Schneider *et al.* (1999b). Because of the restrictive nature of the assumptions made in obtaining this relationship, however, the effect of small scale-invariance violating contributions cannot be modeled directly using this approach. This situation is in contrast to the results on scale-invariance breaking that can be obtained from the auditory periphery model discussed in Sec. VII.

In the case of a dominant reflection region DPOAE component, it was shown in Sec. V that for any of the measurement paradigms (fixed-f_1, fixed-f_2, fixed-f_2/f_1), the phase derivative is approximately the round-trip travel time for a cochlear wave of the DPOAE frequency between the cochlear base and the DP tonotopic site. When the phase derivative of the DPOAE resulting from the combined effects of the generator and reflection region components was considered in Sec. VI, it was found that significant variations in the DPOAE phase and amplitude can occur as the DPOAE frequency is varied. These variations constitute the DPOAE fine structure, which has been studied in a limited theoretical context and experimentally corroborated by Talmadge *et al.* (1999a).

The numerical results presented in Sec. VII support the approximate validity of scale invariance over a wide range of frequencies (roughly 1000–5000 Hz for humans) for a cochlear model that manifestly contains scale-invariance violations. Some of the variations of the numerical results from the simple analytical expressions obtained in Sec. IV using the assumption of scale invariance were also shown to be explainable by the inclusion of a small scale-invariance violating term related to the cochlear base. The numerical results also suggest that the assumption of scale invariance can be used to describe qualitative properties of cochlear models, even when these models exhibit significant scale-invariance violations, such as a non exponential place-frequency map or the inclusion of a realistic middle ear. An important limitation of the present paper is the restriction of the analysis for the DPOAE phase-derivative fine structure to the case in which the effects of multiple internal cochlear wave reflections can be ignored [that is, it was assumed that $|R_a R_b| \ll 1$ in Eq. (6)]. Consideration of the effects of fine structure on the phase derivative and level of P_{ss}^{dp} will be deferred to a future paper.

ACKNOWLEDGMENTS

This research was supported in part by NIH/NICD Grant No. R29 DC03094. We would like to thank Chris Shera and an anonymous reviewer for their very careful and constructive reviews of this manuscript.

APPENDIX: PERTURBATIVE SOLUTION FOR DPOAES

In this section, the perturbative solution for the $2\omega_1 - \omega_2$ DP will be illustrated. In the one-dimensional cochlear model, the steady-state transpartition pressure wave $P_d(x,\omega)$ of frequency ω is described by the wave equation

$$P_d''(x,\omega) + k^2(x,\omega) P_d(x,\omega) = 0, \tag{A1}$$

where $k(x,\omega)$ is the complex wave number of the traveling wave given by Eq. (14). The $\Delta(x,\omega)$ function that appears in this latter equation is defined by

$$\Delta(x,\omega) = \frac{1}{\sigma_{bm}} \frac{P_d(x,\omega)}{\xi(x,\omega)}. \tag{A2}$$

In order to generalize this expression to the case for an internally generated DP, it is necessary to use the time-domain formulation of the pressure wave equation, namely (e.g., Talmadge *et al.*, 1998)

$$\frac{\partial^2 P_d(x,t)}{\partial x^2} = -k_0^2 \sigma_{bm} \ddot{\xi}(x,t), \tag{A3}$$

$$\ddot{\xi}(x,t) + \gamma_{bm}(x,\xi,\dot{\xi})\dot{\xi}(x,t) + \omega_{bm}^2(x,\xi,\dot{\xi})\xi(x,t) = \frac{1}{\sigma_{bm}} P_d(x,t), \tag{A4}$$

where $\dot{A}(t)$ refers to differentiation with respect to time, and where γ_{bm} and ω_{bm} are, respectively, the basilar membrane damping and stiffness functions. The steady-state solution for the $\omega_{dp} = 2\omega_1 - \omega_2$ DP can then be found by writing

$$\xi(x,t)\approx\xi_1(x,\omega_1)e^{i\omega_1 t}+\xi_2(x,\omega_2)e^{i\omega_2 t}+\xi_{dp}(x,\omega_{dp})e^{i\omega_{dp}t}+\text{complex conjugate}, \quad \text{(A5)}$$

$$P_d(x,t)\approx P_1(x,\omega_1)e^{i\omega_1 t}+P_2(x,\omega_2)e^{i\omega_2 t}+P_{dp}(x,\omega_{dp})e^{i\omega_{dp}t}+\text{complex conjugate}, \quad \text{(A6)}$$

where $\xi_{1,2,dp}$ and $P_{1,2,dp}$ are, respectively, the ω_1, ω_2, and ω_{dp} Fourier components of ξ and P_d.

As in the previous sections, a simple quadratic nonlinear (''Van der Pol-type'') damping is assumed, and possible stiffness feedback terms are neglected. Then, Eq. (A4) becomes

$$\ddot{\xi}(x,t)+\gamma_0(x)\left[1+\frac{\xi^2(x,t)}{b_{nl}^2}\right]\dot{\xi}(x,t)+\omega_0^2(x,\xi,\dot{\xi})\xi(x,t)=\frac{1}{\sigma_{bm}}P_d(x,t), \quad \text{(A7)}$$

where $\gamma_0(x)$ and $\omega_0^2(x)$ are the usual passive linear damping and stiffness, respectively, of the basilar membrane, and b_{nl} is the nonlinear saturation level.

Equations (A3) and (A7) can be solved perturbatively if it is assumed that the nonlinearity is weak; that is, $\xi^2(x,t)/b_{nl}^2\ll 1$. It will be assumed that this nonlinear contribution to Eq. (A7) as well as $\xi_{dp}(x,\omega)$ and $P_{dp}(x,\omega)$ are of first order in perturbation theory. Using the perturbation parameter ε_p to track the order of perturbation, then

$$\xi_1(x,\omega)=\sum_{n=0}^{\infty}\varepsilon_p^n\xi_1^{(n)}(x,\omega),\qquad P_1(x,\omega)=\sum_{n=0}^{\infty}\varepsilon_p^n P_1^{(n)}(x,\omega), \quad \text{(A8)}$$

$$\xi_2(x,\omega)=\sum_{n=0}^{\infty}\varepsilon_p^n\xi_2^{(n)}(x,\omega),\qquad P_2(x,\omega)=\sum_{n=0}^{\infty}\varepsilon_p^n P_2^{(n)}(x,\omega), \quad \text{(A9)}$$

$$\xi_{dp}(x,\omega)=\sum_{n=1}^{\infty}\varepsilon_p^n\xi_{dp}^{(n)}(x,\omega),\qquad P_{dp}(x,\omega)=\sum_{n=1}^{\infty}\varepsilon_p^n P_{dp}^{(n)}(x,\omega), \quad \text{(A10)}$$

where the notation $F^{(n)}(x,\omega)$ is used to denote the nth order of the perturbation theory. Also, by assumption of a weak nonlinearity, Eq. (A10) contains no $n=0$ perturbative contribution. Equation (A7) also becomes

$$\ddot{\xi}(x,t)+\gamma_0(x)\dot{\xi}(x,t)\omega_0^2(x,\xi,\dot{\xi})\xi(x,t)=\frac{1}{\sigma_{bm}}P_d(x,t)-\varepsilon_p\frac{\xi^2(x,t)}{b_{nl}^2}\dot{\xi}(x,t), \quad \text{(A11)}$$

where the extra factor of ε_p has been inserted to denote the assumed first-order perturbative term. Insertion of Eqs. (A8)–(A10) into Eqs. (A3) and (A11) gives the lowest-order pressure wave equations

$$\frac{\partial P_1^{(0)}(x,\omega_1)}{\partial x^2}+k^2(x,\omega_1)P_1^{(0)}(x,\omega_1)=0, \quad \text{(A12)}$$

$$\frac{\partial P_2^{(0)}(x,\omega_2)}{\partial x^2}+k^2(x,\omega_2)P_2^{(0)}(x,\omega_2)=0, \quad \text{(A13)}$$

$$\frac{\partial P_{dp}^{(0)}(x,\omega_{dp})}{\partial x^2}+k^2(x,\omega_{dp})P_{dp}^{(0)}(x,\omega_{dp})=\rho_{dp}(x,\omega_1,\omega_2,\omega_{dp}), \quad \text{(A14)}$$

$$\rho_{dp}(x,\omega_1,\omega_2,\omega_{dp})=\frac{i\sigma_{bm}\gamma_0(x)k_0^2\omega_{dp}^3[\xi_1^{(0)}(x,\omega_1)]^2[\xi_2^{(0)}(x,\omega_2)]^*}{\Delta(x,\omega_{dp})b_{nl}^2}. \quad \text{(A15)}$$

Equations (A12)–(A15) have been solved in Talmadge *et al.* (1998) with $\gamma_0(x)=\varepsilon_\gamma\omega_0(x)$ using the basis function formalism, and it is this solution that is given in Sec. II of this paper.

Bowman, D. M., Brown, D. K., Eggermont, J. J., and Kimberley, B. P. (**1997**). ''The effect of sound intensity on f_1-sweep and f_2-sweep distortion product otoacoustic emissions phase delay estimates in human adults,'' J. Acoust. Soc. Am. **101**, 1550–1559.

Bowman, D. M., Eggermont, J. J., Brown, D. K., and Kimberly, B. P. (**1998**). ''Estimating cochlear filter response properties from distortion product otoacoustic emission (DPOAE) phase delay measurements in normal hearing human adults,'' Hear. Res. **119**, 14–26.

Brown, A. M., Harris, F. P., and Beveridge, H. A. (**1996**). ''Two sources of acoustic distortion products from the human cochlea,'' J. Acoust. Soc. Am. **100**, 3260–3267.

Gaskill, S. A., and Brown, A. M. (**1996**). ''Suppression of human acoustic distortion product: dual origin of $2f_1-f_2$,'' J. Acoust. Soc. Am. **100**, 3268–3274.

He, N.-J., and Schmiedt, R. A. (**1993**). ''Fine structure of the $2f_1-f_2$ acoustic distortion product: Changes with primary level,'' J. Acoust. Soc. Am. **94**, 2659–2669.

He, N.-J., and Schmiedt, R. A. (**1996**). ''Effects of aging on the fine structure of the $2f(1)-f(2)$ acoustic distortion product,'' J. Acoust. Soc. Am. **99**, 1012–1015.

He, N.-J., and Schmiedt, R. A. (**1997**). ''Fine structure of the $2f_1-f_2$ acoustic distortion product: Effects on primary level and frequency ration,'' J. Acoust. Soc. Am. **101**, 3554–3565.

Kemp, D. T. (**1979**). ''Evidence of nonlinearity and frequency selective wave amplification in the cochlea,'' Arch. Oto-Rhino-Laryngol. **224**, 37–45.

Kemp, D. T., and Brown, A. M. (**1983**). ''An integrated view of the cochlear mechanical nonlinearities observable in the ear canal,'' in *Mechanics of Hearing*, edited by E. de Boer and M. A. Viergever (Martinus Nijhoff, The Hague, The Netherlands), pp. 75–82.

Kemp, D. T., and Knight, R. D. (**2000**). ''Indications of different distortion product otoacoustic emissions mechanisms from a detailed f_1, f_2 area study,'' J. Acoust. Soc. Am. **107**, 457–473.

Kim, D. O. (**1980**). ''Cochlear mechanics: Implications of electrophysiological and acoustical observations,'' Hear. Res. **2**, 297–317.

Kummer, P., Janssen, T., and Arnold, W. (**1995**). ''Suppression tuning characteristics of the $2f_1-f_2$ distortion product otoacoustic emission in humans,'' J. Acoust. Soc. Am. **98**, 197–210.

Lighthill, J. (**1978**). *Waves in Fluids* (Cambridge University Press, Cambridge).

O'Mahoney, C. F., and Kemp, D. (**1995**). ''Distortion product otoacoustic emission delay measurement in humans,'' J. Acoust. Soc. Am. **97**, 3721–3735.

Prijs, V. F., Schneider, S., and Schoonhoven, R. (**2000**). ''Group delays of distortion product otoacoustic emissions: Relating delays measured with f_1- and f_2-sweep paradigms,'' J. Acoust. Soc. Am. **107**, 3298–3307.

Robinette, M. S., and Glattke, T. J., editors (**1997**). *Otoacoustic Emissions: Clinical Applications* (Thieme, New York).

Schneider, S., Prijs, V. F., and Schoonhoven, R. (**1999a**). ''Group delays of distortion product otoacoustic emissions in the guinea pig,'' J. Acoust. Soc. Am. **105**, 2722–2730.

Schneider, S., Prijs, V. F., Schoonhoven, R., and van Hengel, P. W. J. (**1999b**). ''f_1- versus f_2-sweep group delays of distortion product otoacoustic emissions in the guinea pig: Experimental results and theoretical predictions,'' in *Proceedings of the 1999 Sendai Symposium on Recent Developments in Auditory Mechanics*, edited by H. Wada, T. Takasaka, K. Ikeda, K. Ohyama, and T. Koike (World Scientific, Singapore), pp. 360–366.

Shera, C. A., and Zweig, G. (**1993**). ''Order from chaos: Resolving the paradox of periodicity in evoked otoacoustic emission,'' in *Biophysics of Hair Cell Sensory Systems*, edited by H. Duifhuis, J. W. Horst, P. van Dijk, and S. M. van Netten (World Scientific, Singapore), pp. 54–63.

Talmadge, C., Long, G. R., Tubis, A., and Dhar, S. (**1999a**). ''Experimental confirmation of the two-source interference model for the fine structure of distortion product otoacoustic emissions,'' J. Acoust. Soc. Am. **105**, 275–292.

Talmadge, C., Tubis, A., Long, G. R., and Piskorski, P. (**1998**). ''Modeling otoacoustic emission and hearing threshold fine structures,'' J. Acoust. Soc. Am. **104**, 1517–1543.

Talmadge, C., Tubis, A., Piskorski, P., and Long, G. R. (**1997**). ''Modeling otoacoustic emission fine structure,'' in *Diversity in Auditory Mechanics*, edited by E. Lewis, G. Long, R. Lyon, P. Narins, and C. Steele (World Scientific, Singapore), pp. 462–471.

Talmadge, C. L., Tubis, A., Long, G. R., and Piskorski, P. (**1996**). ''Evidence for multiple spatial origins of the fine structure of distortion product otoacoustic emissions in humans, and its implications: Experimental and modeling results,'' in Abstracts of the Nineteenth Midwinter Research Meeting of the Association for Research in Otolaryngology, edited by D. J. Lim (unpublished), p. 94, Abstract.

Talmadge, C. L., Tubis, A., Tong, C., Long, G. R., and Dhar, S. (**1999b**). ''Temporal aspects of otoacoustic emissions,'' in *Proceedings of the 1999 Sendai Symposium on Recent Developments in Auditory Mechanics*, edited by H. Wada, T. Takasaka, K. Ikeda, K. Ohyama, and T. Koike (World Scientific, Singapore), pp. 353–359.

Tubis, A., Talmadge, C. L., and Tong, C. (**2000**). ''Modeling the temporal behavior of distortion product otoacoustic emissions,'' J. Acoust. Soc. Am. **107**, 2122–2127.

Zweig, G. (**1991**). ''Finding the impedance of the organ of Corti,'' J. Acoust. Soc. Am. **89**, 1229–1254.

Zweig, G., Lipes, R., and Pierce, J. R. (**1976**). ''The cochlear compromise,'' J. Acoust. Soc. Am. **59**, 975–982.

Zweig, G., and Shera, C. A. (**1995**). ''The origins of periodicity in the spectrum of evoked otoacoustic emissions,'' J. Acoust. Soc. Am. **98**, 2018–2047.

Nonlinear interactions that could explain distortion product interference response areas

P. F. Fahey[a)]
Department of Physics/EE, University of Scranton, Scranton, Pennsylvania 18510

B. B. Stagner
Department of Otolaryngology, University of Miami, Miami, Florida 33101

B. L. Lonsbury-Martin and G. K. Martin
Department of Otolaryngology and Neuroscience Program, University of Miami, Miami, Florida 33101

(Received 16 May 2000; accepted for publication 17 July 2000)

Suppression and/or enhancement of third- and fifth-order distortion products by a third tone that can have a frequency more than an octave above and a level more than 40 dB below the primary tones have recently been measured by Martin *et al.* [Hear. Res. **136**, 105–123 (1999)]. Contours of iso-suppression and iso-enhancement that are plotted as a function of third-tone frequency and level are called interference response areas. After ruling out order aliasing, two possible mechanisms for this effect have been developed, a harmonic mechanism and a catalyst mechanism. The harmonic mechanism produces distortion products by mixing a harmonic of one of the primary tones with the other primary tone. The catalyst mechanism produces distortion products by mixing one or more intermediate distortion products that are produced by the third tone with one or more of the input tones. The harmonic mechanism does not need a third tone and the catalyst mechanism does. Because the basilar membrane frequency response is predicted to affect each of these mechanisms differently, it is concluded that the catalyst mechanism will be dominant in the high-frequency regions of the cochlea and the harmonic mechanism will have significant strength in the low-frequency regions of the cochlea. The mechanisms are dependent on the existence of both even- and odd-order distortion, and significant even- and odd-order distortion have been measured in the experimental animals. Furthermore, the nonlinear part of the cochlear mechanical response must be well into saturation when input tones are 50 or more dB SPL. © *2000 Acoustical Society of America.* [S0001-4966(00)04510-0]

PACS numbers: 43.64.Bt, 43.64.Jb [LHC]

I. INTRODUCTION

The inner ear has a nonlinear mechanical response that has been intensively studied by measuring intermodulation distortion products (DPs). DPs are generated upon the input of two pure tones. If the frequencies of the input tones are labeled f_1 and f_2 (where $f_1<f_2$), DPs with frequencies $f_d=2f_1-f_2$ or $3f_1-2f_2$ or $2f_2-f_1$ or $3f_2-2f_1$ can routinely be measured in the external ear canal as distortion product otoacoustic emissions (DPOAEs). For many f_2/f_1 ratios, the $f_d=2f_1-f_2$ DP has the largest level of all of the DPs; hence, its properties have been the most studied. The generation of DPs has been probed by suppressing them with a third input tone of frequency f_3. As would be expected, the $2f_1-f_2$ DPOAE is suppressed in the regime where the third tone would be expected to suppress the response of the f_2 and/or f_1 tone (e.g., Brown and Kemp, 1984; Martin *et al.*, 1987, 1998b; Kummer *et al.*, 1995). Also, several studies have shown some suppression of this DPOAE when the frequency of the suppressor tone is less than the DP frequency (Gaskill and Brown, 1996; Heitmann *et al.*, 1998; Siegel *et al.*, 2000; Martin *et al.*, 2000). That is, there can be suppression of the DP when one suppresses excitation at the cochlear place that would be excited by a tone at the DP frequency. Making only the very general assumption that the nonlinear part of the cochlear mechanical response is due to a compressive nonlinearity, the first suppression effect would have been expected. The third tone is suppressing the level of one or both of the primary tones at the sites of mixing of the two primary tones. If it assumed that some of the DPOAE energy in the external ear canal has come via reflection/re-emission from the cochlear DP place, the second suppression effect would be expected. The third tone would be suppressing the reflection/re-emission process.

However, Martin, Lonsbury-Martin, and colleagues (Martin *et al.*, 1995, 1999; Whitehead *et al.*, 1995b), and Mills (2000) have recently shown suppression and/or enhancement of the $2f_1-f_2$, $3f_1-2f_2$, and $2f_2-f_1$ DPOAEs by tones much higher in frequency than either of the primary tones and, often, much lower in input level. The following discussion shows how some simple properties of compressive nonlinearities and of known basilar membrane responses predict these effects when the compressive nonlinearity has both even and odd symmetry. The data to be explained are illustrated in Figs. 1 and 2. These figures show the effect that a third tone has on the level of the DPOAEs detected in the ear canal. The contours in these figures are called interference response areas (IRAs). The object of this study to is to

a)Electronic mail: faheypl@uofs.edu

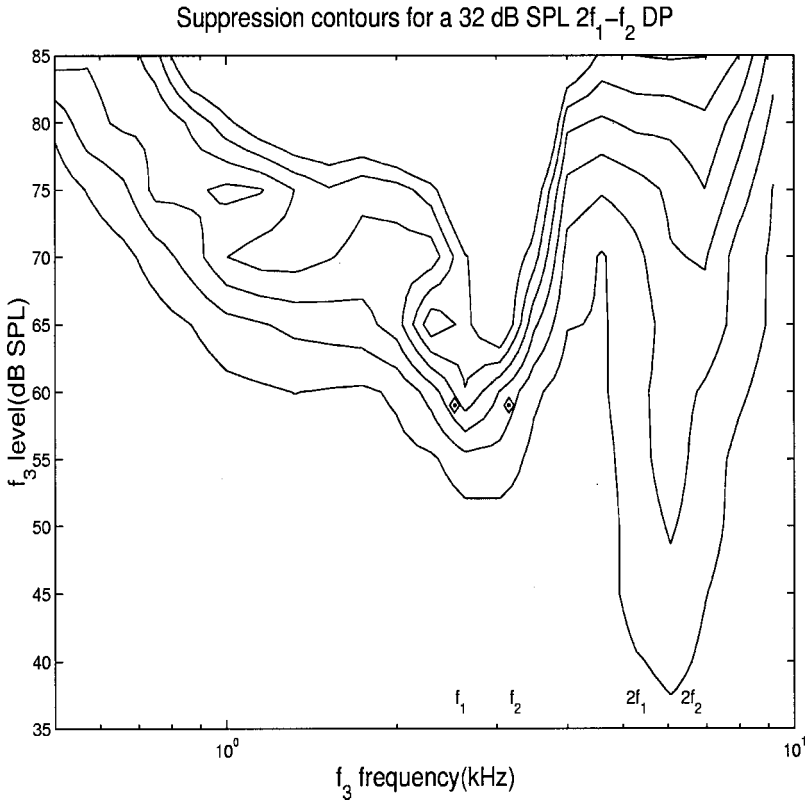

FIG. 1. Suppression contours of 3, 6, 9 dB, etc. that are due to the addition of a third tone at frequency f_3. The levels and frequencies of the primary tones are indicated by the diamonds. Decreases in DPOAE level centered around the primary tones would be expected when f_3 suppresses one or both of the primaries. The region of suppression about an octave or more above f_2 shows the typical ''high-frequency lobe'' that cannot be explained by the suppression of one of the primaries by f_3. In the absence of the third tone, the level of the $2f_1-f_2$ DPOAE is 32 dB SPL. The data in this figure were plotted in a different format in Fig. 1(H) of Martin *et al.* (1999). $f_1=2.530$ and $f_2=3.156$ kHz.

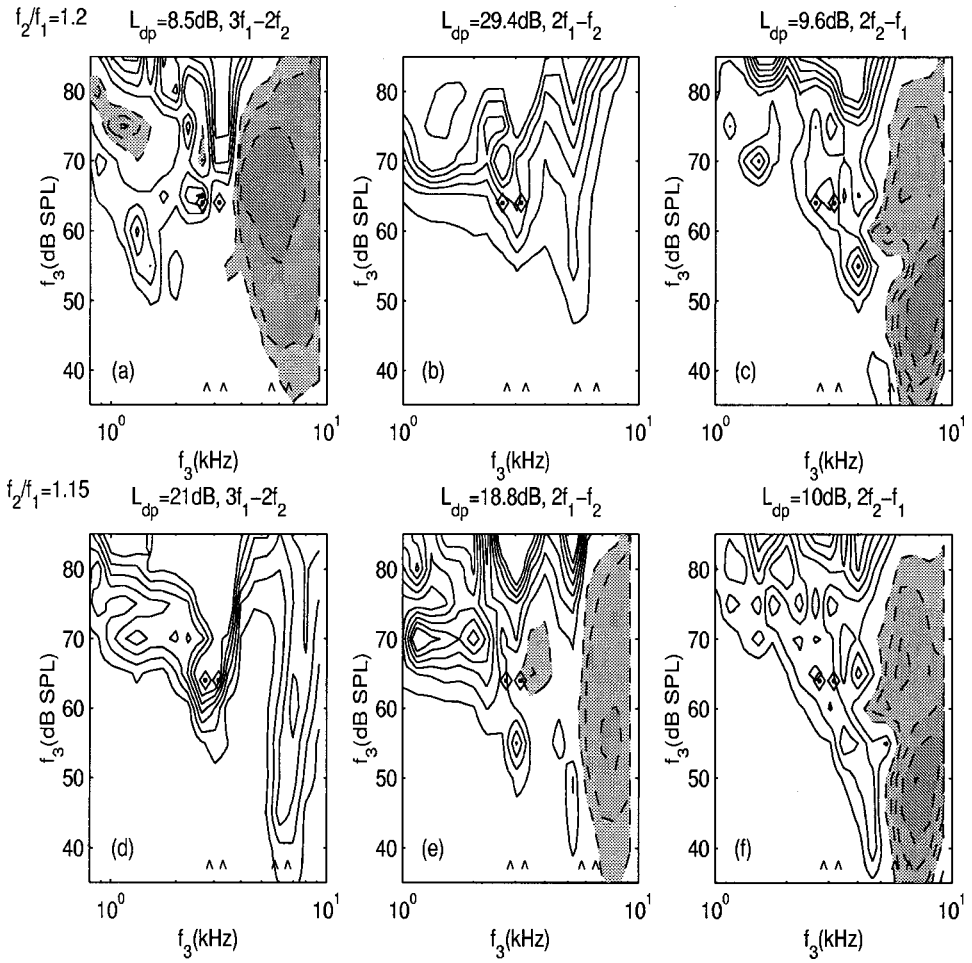

FIG. 2. Adaptation of some panels from Fig. 4 of Martin *et al.* (1999). The suppression contours at 3, 6, 9 dB, etc., are shown with continuous lines, enhancement contours at 3, 6, 9 dB, etc., are shown with dashed lines and the gray field. The lowest-level contour is always the 3-dB contour. The input levels are the same for all of the panels, at $L_1=L_2=65$ dB SPL. The frequency ratio decreases from the top row to the bottom. $f_2=3.165$ kHz in each panel. In the first row of panels, $f_1=2.638$ kHz; in the second row, $f_1=2.745$ kHz; in the third row, $f_1=2.875$ kHz; in the fourth row, $f_1=3.015$ kHz. The diamonds show the input levels and frequencies of f_1 and f_2 and the carets at the bottom of each panel mark the values of f_1, f_2, $2f_1$, $2f_2$. The left-most column is the $3f_1-2f_2$, the middle column is the $2f_1-f_2$, and the right-most column is the $2f_2-f_1$ DPOAE. The level of the DPOAE in the absence of the third tone is given at the top of each panel. The highest value of f_3 in this data was 9 kHz; therefore, what seems to be a high-frequency cutoff at 9 kHz is just the end of the data.

propose mechanisms that underly the high-frequency lobes ($f_3 > 2f_1, 2f_2$) of the IRAs. Much of the low frequency lobe ($f_3 < f_2$) is just an example of the direct suppression of a primary tone.

II. THE PHYSICAL MODEL

A. General approach

After Johnstone *et al.* (1986), Yates (1990), and Withnell and Yates (1998), it is assumed that the amplitude of the basilar membrane response as a function of input amplitude has both a linear and a nonlinear part, such as pictured in Fig. 3(a). Many features of DPs can be explained with the nonlinear part of this input/output (I/O) map, shown in Fig. 3(b). That is, it is not necessary to find the solutions to a time-dependent partial differential equation that emulates the nonlinear system; all that is required is to study a one-to-one mapping of the input of the system to the output. The nonlinear part of I/O maps can be either expansive or compressive. For an expansive nonlinearity, the output increases faster than a linear increase of the input. For a compressive nonlinearity the reverse is true. It is well-known that the cochlear mechanical response I/O function is compressive. Several mappings have been used in the literature to emulate features of signal compression, DP generation, and suppression of the output of one tone by another. Let a general mapping be symbolized as $y = f(x)$, where y is the output and x is the input. The quantity x could represent a scaled value of the stapes displacement and the quantity y could represent the basilar membrane displacement at the site of a nonlinearity. The amplitude of the stapes displacement is proportional to the ear canal pressure amplitude, and nonlinear components in the waveform of the basilar membrane response will have ear canal pressure correlates.

Some examples of nonlinear I/O maps are: $y = \mathrm{sgn}(x) * |x|^{1/3}$ (one of the power-law nonlinearities reviewed in Duifhuis, 1989), $y = \tanh(\alpha x)$, $y = 1/(\alpha + e^{\beta(x_1 - x)}(1 + e^{\gamma(x_2 - x)}))$ (e.g., Frank and Kossl, 1996), where α, β, γ, x_1, and x_2 are constants. The first two of these I/O functions are said to have odd symmetry and the last one has both odd and even symmetry. Odd I/O maps are such that $f(-x) = -f(x)$ and even I/O maps are such that $f(-x) = f(x)$. For any general mapping, $f(x) = f_{\mathrm{odd}}(x) + f_{\mathrm{even}}(x)$, where $2f_{\mathrm{odd}}(x) = f(x) - f(-x)$ and $2f_{\mathrm{even}} = f(x) + f(-x)$. Plots of these representative I/O maps are shown in Figs. 3(b)–(d).

With regard to DPs, compressive nonlinearities have some properties in common. Let A_1 be the amplitude of the tone that has frequency f_1 and A_2 be the amplitude of the f_2 tone. Then, if A_1 is held constant, and A_2 is increased from a value much less than A_1, the amplitude of the $2f_1 - f_2$ DP increases linearly. Eventually it begins to saturate to a maximum. The value of A_1/A_2 at maximum depends upon both the particular I/O map and the value of A_1 relative to the saturation of the I/O map. If A_2 is increased beyond the value

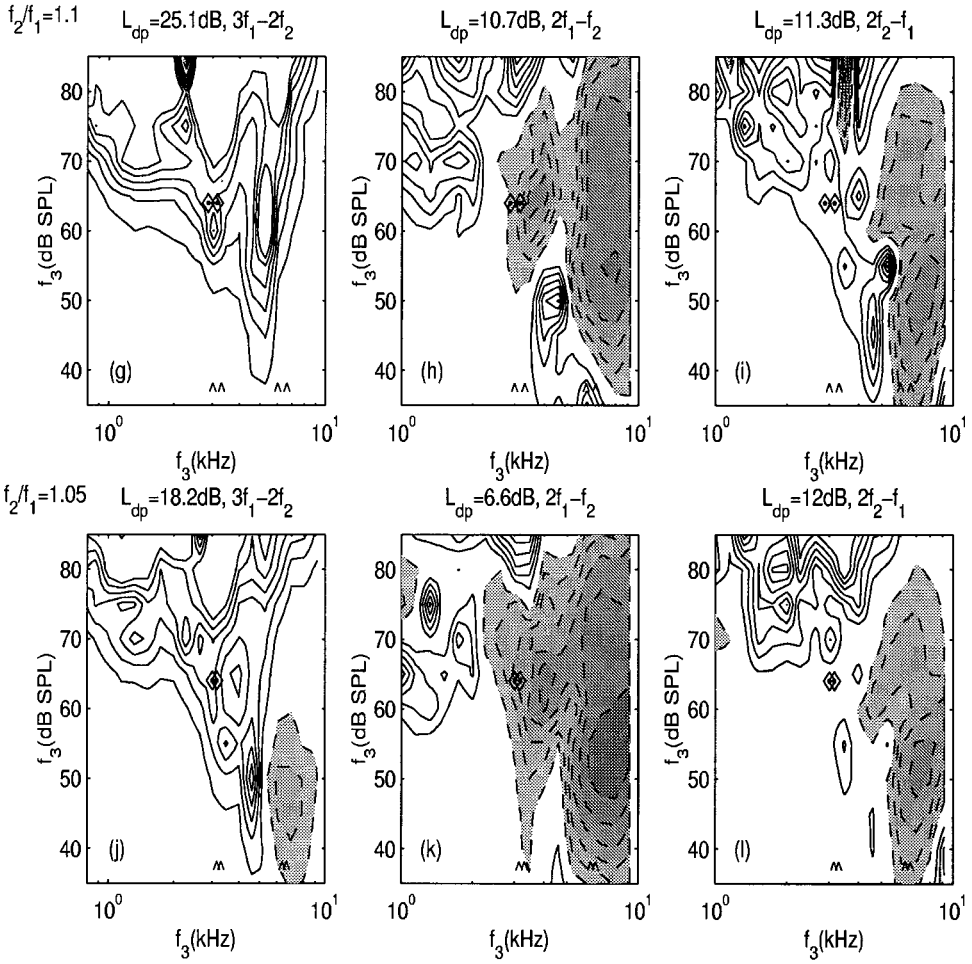

FIG. 2. (*Continued.*)

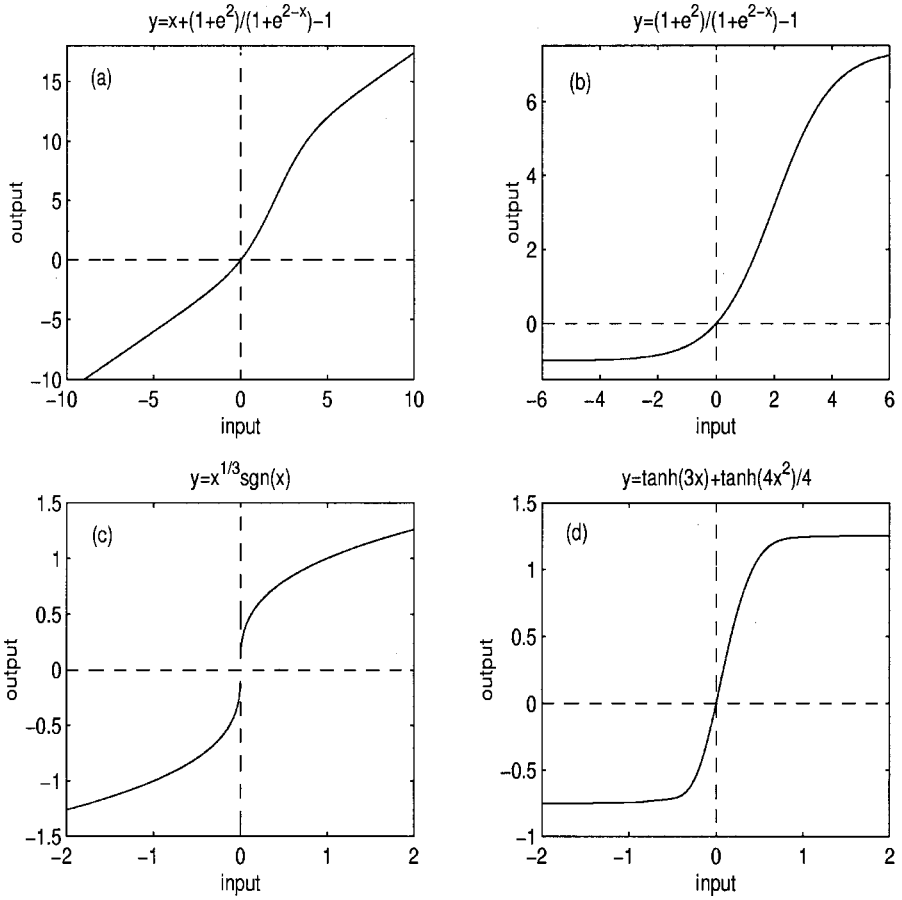

FIG. 3. Four I/O maps. (a) Model basilar membrane response that is linear at the lowest levels, nonlinear at low and intermediate levels, and linear at high levels; (b) is the nonlinear part of (a) and is the map used for all of the simulations of the harmonic and the catalyst mechanisms. It has both even and odd symmetry. (c) is a nonlinear I/O map that has only odd symmetry; (d) is the nonlinear map used to study order aliasing. Like (b), (d) has both even and odd symmetry. The four I/O maps are plotted on linear axes.

where the DP is maximum, the amplitude of the DP decreases, and it decreases faster than linear. If A_2 is held constant and A_1 is increased from a value much less than A_2, the amplitude of the $2f_1-f_2$ DP increases proportional to A_1^2 until the DP reaches a maximum. Then, continued increase of A_1 decreases the amplitude of the DP. For the $2f_2-f_1$ DP, the dependencies of the DP amplitude on A_1 and A_2 are reversed. When A_1 is constant, the DP amplitude increases as A_2^2 when $A_2 \ll A_1$. The general rule is that if A_1 is held constant and A_2 increases from a low value, the amplitude of the Mf_1+Nf_2 DP increases as $A_2^{|N|}$, $A_2 \ll A_1$ (where M,N are integers that can be positive or negative). This scaling has been reviewed in Duifhuis (1989) and Fahey (1989).

Figure 4 illustrates results based up the example I/O mapping in Fig. 3(b). Shown are the growth of three DPs with A_1 and A_2 varied together [Fig. 4(a)]; A_1 held constant [Fig. 4(b)]; A_2 held constant [Fig. 4(c)]; and the second and third harmonic dependence on input level [Fig. 4(d)]. This nonlinear I/O map is of a similar shape to the hair cell receptor voltage vs cilia displacement measured by Hudspeth and Corey (1977) and Russell *et al.* (1986). It is used here for purposes of illustration. Any similar I/O map with large-enough second and third derivatives would produce similar results.

These scaling properties have been been observed in ear canal DPOAE measurements (e.g., Rosowski *et al.*, 1984; Fahey and Allen, 1988; Whitehead *et al.*, 1995a). Indeed, Whitehead *et al.* (1995a) showed that drug administration which substantially reduced DPOAE levels did not change this scaling. The drug changed the particular I/O mapping but did not change the fact that the mapping was compressive. Whitehead *et al.* (1995a) have also confirmed that the ratio of A_2/A_1 where the DPOAE is maximum depends upon the value of primary tones relative to the saturation level of the nonlinearity.

Another general property of compressive nonlinearities is that one tone will significantly (more than 1 dB) suppress the level of a second tone if two conditions are met. First, the suppressor tone must have a level that is at least 1/3 as large (within 10 dB) as the tone being suppressed. Second, the suppressor must be large enough that it is in the saturation region of the nonlinearity. These I/O properties of suppression are shown in Fig. 5. In this figure the amplitude of the f_1 tone is varied while that of the f_2 tone is held constant at three different values. In Fig. 5(a), when $A_2=10$, the tone is in saturation; therefore, its value on output is less than 10 and it suppresses the level of the f_1 tone. It is not until the level of the f_1 tone begins to be comparable in magnitude to the level of the f_2 tone that the f_2 Fourier amplitude is suppressed. When the value of $A_2=1$ or 0.1 [Figs. 5(b) and (c)], the f_2 tone does not significantly suppress the f_1 Fourier amplitude. Moreover, the f_1 tone does not suppress the Fourier amplitude of the f_2 tone until the input amplitude of f_1 reaches the saturation region. Therefore, for suppression to occur the suppressor level must be large enough to be into the saturation region and if the suppressee is into saturation, then the suppressor must be no less than 10 dB below the level of the suppressee. That is, if one tone amplitude is more

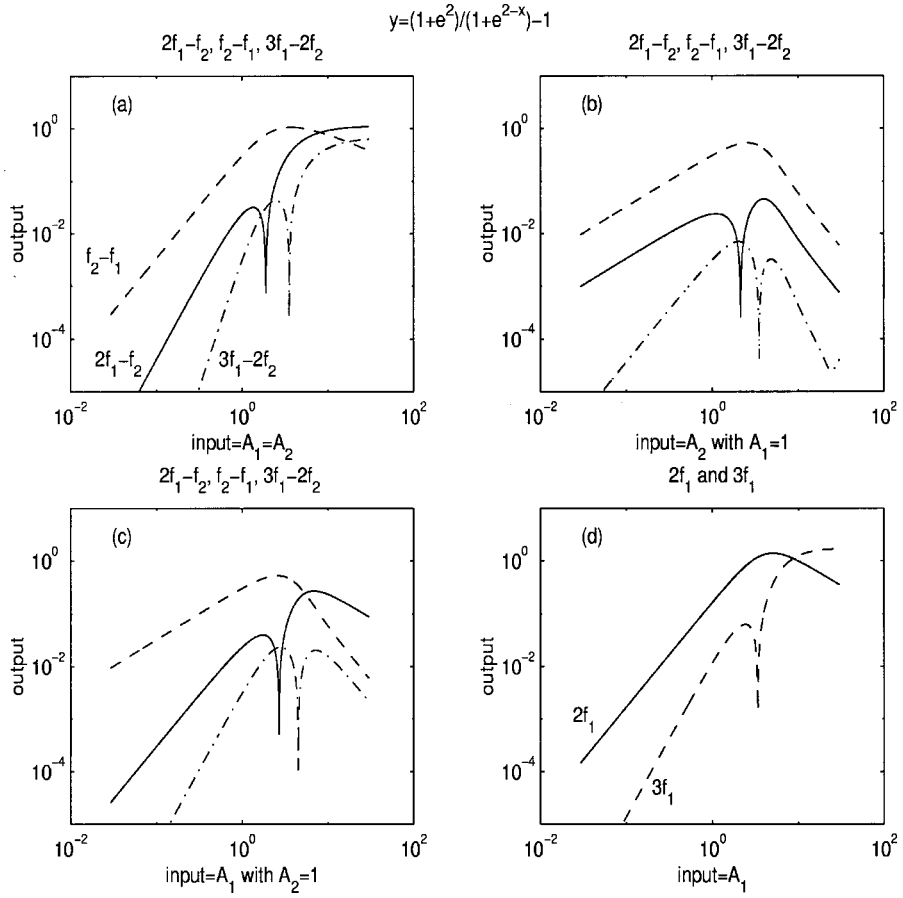

FIG. 4. Simulated $2f_1-f_2$ (solid line), f_2-f_1 (dashed line), and $3f_1-2f_2$ (dashed-dot line) DP levels plotted as a function of input level. In (a) $A_1=A_2$; in (b) $A_1=1.0$ and A_2 amplitude is the abscissa; in (c) $A_2=1.0$ and A_1 amplitude is the abscissa, and in (d) the level of the second and third harmonics of f_1 is plotted as a function of A_1. In each of the panels there are sharp nulls for the odd-order DPs/harmonics that are a function of level. The presence of I/O map nulls is the topic of a paper by Lukashkin and Russell (1999).

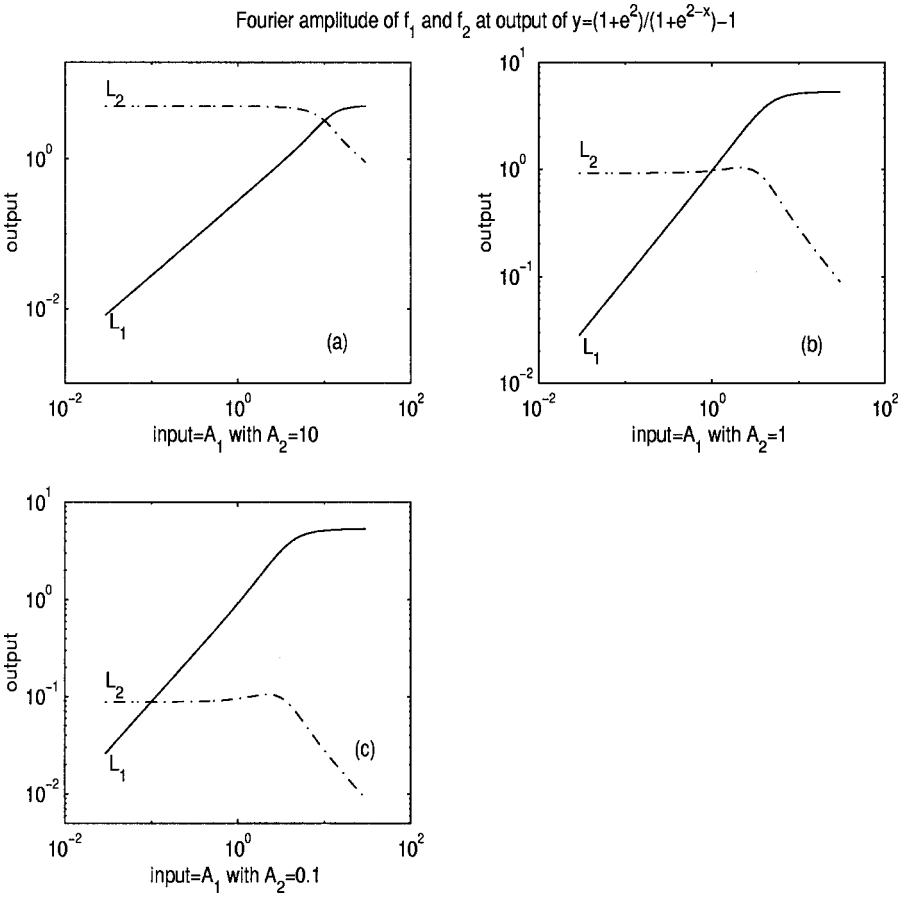

FIG. 5. This figure illustrates the properties of two-tone suppression. The input, A_2, is held constant at three different values, while the other input, A_1, is varied. The Fourier amplitude of f_2, L_2, at the output of the nonlinearity is shown with the dot-dash curves. The Fourier amplitude of f_1 (L_1) at the output of the nonlinearity is shown with the continuous curve. In (a) the value of $A_2=10$, in (b) the value of $A_2=1.0$, and in (c) the value of $A_2=0.1$. In (a) the output, L_1, is suppressed over its whole range [compare L_1 in (a) with L_1 in (b) and (c)].

than about a factor of 3 (or 10 dB) below the second tone amplitude, it will not significantly suppress that second tone. Martin *et al.* (1998a) have shown that this property persists upon drug administration that substantially decreases DPOAEs. This data of Martin *et al.* is consistent with the I/O map changing curvature with drug administration while the saturation levels remain invariant.

A final property of certain I/O mappings and, in particular, of the mapping shown in Fig. 3(b) that was used to generate Fig. 4, is that there are input levels at which sharp nulls in the output level appear. Nulls of this type have been observed in the data and have been the central topic of the work by Lukashkin and Russell (1999). These nulls are not observed in all I/O maps. The nulls correlate with the transition from input amplitudes where only the negative part of the wave is strongly compressed to input amplitudes where both the negative part and the positive part of the wave become strongly compressed.

B. Differences between simple I/O maps and the cochlea

Since the cochlea is a distributed, tuned mechanical system, the simple I/O analysis comes with caveats. First, the levels of the input tones in the ear canal must be translated to the levels of these tones at the sites of the distributed cochlear nonlinearities. Second, DPOAEs measured in the ear canal are the vector sum of all cochlear sources. Hence, the amplitude scaling properties of the compressive I/O maps discussed above will be modulated by the wave mixing of the cochlear DP sources. However, there are experimental conditions where wave interference effects are minimal and the amplitude scaling is close to the ideal as per Fahey and Allen (1988) and Whitehead *et al.* (1995a). Third, some of the DP energy created in the cochlea can be absorbed within the cochlea and never propagate out into the ear canal. The energy that propagates to the ear canal microphone depends upon the impedance from the source to the microphone. Generally, I/O maps correctly predict the scaling of DPOAEs when one of the input levels is held constant. However, when both input levels are varied together the I/O maps that have Taylor series expansions all predict that, at low input amplitudes, the $2f_1-f_2$ DP scales as A^3 where $A_1=A_2=A$ until within a few dB of saturation. Data often show scaling that is between A and A^2 (Withnall and Yates, 1998, Whitehead *et al.*, 1995a) rather than the A^3 scaling predicted from the I/O map.

The maximum levels of the harmonics and the DPs that are shown in Fig. 4 are much greater than those observed in the ear canal. This is expected. All of the harmonics should be attenuated at the site of generation due to basilar membrane filtering. In regions where there is little filtering at the site of generation (i.e., the basilar membrane is broadly tuned) harmonics as large as those predicted from Fig. 4 have been observed by Khanna and Hao (1999). From the site of generation, the harmonics and the DPs must propagate to the ear canal. In general, these signals can propagate apically and/or basally depending upon the impedance seen by the the signal in the apical and/or basal direction. For DPs lower in frequency than the characteristic frequency of the generation site, apical propagation is both allowed and observed. The energy propagated apically that is absorbed (rather than reflected/re-emitted) will never reach the ear canal. The energy that is propagated basally can partially be reflected at the cochlea/middle-ear interface and, likewise, will never get to the ear canal unless re-reflected. For harmonics and DPs higher in frequency than the characteristic frequency of the generation site, apical propagation is ruled out because the basilar membrane will not respond to such relatively high frequency signals. The energy that is propagated basally will be partially absorbed by the basilar membrane at the characteristic place. The energy not absorbed will, in general, be partially reflected at the cochlea/middle-ear interface. Hence, for harmonics and these higher-frequency DPs, only a fraction of the amplitude predicted by the I/O map will be detectable in the ear canal.

The data of Whitehead *et al.* (1995a) affirms that for most DPOAE measurements there is another reason that ear canal levels are much lower than the maxima predicted in Fig. 4. As discussed by Kummer *et al.* (2000), in order for the f_1 excitation at the f_2 place to be comparable to the f_2 excitation at the f_2 place, the amplitude of the f_1 tone at input must be much larger than the amplitude of the f_2 tone at input. When this adjustment is made, the ear canal amplitude of the $2f_1-f_2$ DP is commonly as large as 1/10 (-20 dB) of the ear canal amplitude of f_2 and can even be as large as 1/3 (-10 dB) of the ear canal amplitude of f_2 (Kummer *et al.*, 1998, Fig. 2). Usually $2f_1-f_2$ DPOAE measurements are made with almost equal ear canal amplitudes of f_1 and f_2; therefore, the relative amplitudes are lower. The signal levels for harmonics and DPs shown in Fig. 4 are, therefore, predictably larger than those observed in most ear canal measurements.

C. Ruling out order aliasing

The data of Martin *et al.* (1999) utilize a third tone of amplitude A_3 and frequency f_3 to affect the level of a DPOAE that was present when only two tones were presented, e.g., the $2f_1-f_2$ DPOAE. For ease of analysis, assume that an I/O map can be represented as a Taylor series expanded about $x=0$. Then, the odd powers of x comprise the odd symmetry part of the nonlinearity and the even powers comprise the even symmetry part. The lowest power odd nonlinear term is the x^3 term. If two tones, $A_1\cos(2\pi f_1 t)+A_2\cos(2\pi f_2 t)$ are the input, x, to the cubic nonlinearity, then the output has tones with frequencies $f=f_1$, $3f_1$, f_2, $3f_2$, $2f_1-f_2$, $2f_2-f_1$. The $2f_1-f_2$ and $2f_2-f_1$ DPs are called cubic or third-order DPs. Two tones input into an x^5 nonlinearity would also generate the two third-order DPs along with several fifth-order DPs at frequencies $3f_1-2f_2$, $3f_2-2f_1$, $4f_1-f_2$, $4f_2-f_1$. In the assumed Taylor series for the compressive I/O function, as the order gets greater the coefficient of the power gets smaller; hence, the amplitudes of the higher-order DPs are smaller than the lower order until the nonlinearity is being driven into saturation.

A major potential complication can arise when a third tone is added to the input. Now the number of possible DPs can increase markedly. For example, for fifth order when only two tones form the input there are 18 components in the

output spectrum (the two input tones and 16 other tones that are either harmonics or intermodulation DPs). If three tones form the input, the output has 73 tones in the spectrum. A general intermodulation DP has a frequency, $f_d = Lf_1 + Mf_2 + Nf_3$ where L, M, N are integers (positive, negative, or zero) and the lowest order of the nonlinearity that produces this DP is $|L|+|M|+|N|$. Hence, there are values of L, M, N, f_3 such that $f_d = Lf_1 + Mf_2 + Nf_3 = 2f_1 - f_2$. That is, a higher-order DP in the presence of f_3 can alias as the third-order DP that is being studied. Depending upon the ratio of f_2/f_1, upon whether f_3 is above or below f_1 and/or f_2, and depending upon how high an order of DP is likely to be important (simulations up to order nine were performed), it was found that the density of aliasing DPs can be as high as 10 points/octave.

To control for ''order aliasing,'' two strategies were employed (Martin *et al.*, 1999). First, order aliasing was measured and f_3 frequencies that produced significant order aliasing were intentionally avoided. Second, the data were gathered using a phase-rotation technique in which the f_3 tone was presented four times, each time with a phase shifted by $\pi/2$ (i.e., the phase of f_3 was successively set to 0, $\pi/2$, π, $3\pi/4$). When the data were added, to first order, all DPs containing f_3 (with the exception of terms with integer multiples of $4f_3$) were canceled. Since the system is nonlinear and the response will be time-waveform dependent, it is possible that the phase-rotation technique might not completely cancel intermodulation DPs containing f_3. The phase-rotation technique was tested with a numerical simulation using the mapping $y = \tanh(3x) + 0.25\tanh(4x^2)$ [the I/O map in Fig. 3(d)]. The simulation showed that even when input levels were in saturation, the phase-rotation technique decreased spectral components due to f_3 (including the f_3 primary itself) to more than 120 dB below the spectral level of $A_1 = A_2$ for the majority of DPs. The exceptions were DPs containing a frequency term with $N4f_3$ (where N is an integer). The $N4f_3$ DPs can be as large as 30 dB below the primary tones when the primaries are in saturation and when $A_1 = A_2 = A_3$. As the primaries decrease from the saturation level and/or as A_3 becomes more than a factor of 2 less than $A_1 = A_2$, the $N4f_3$ DPs soon become more than 80 dB below the levels of the primaries.

For the data of specific interest to this study, A_3 is usually 20 dB down from other the primary levels at the ear canal. The combination of phase rotation and explicitly avoiding frequencies that could alias a DPOAE with a $4f_3$ component, should mitigate order aliasing. In the experimental animal, phase rotation reduces the the level of the f_3 primary itself by at least 70 dB. That order aliasing has been well controlled is evident from the absence of sharp level transitions (level spikes) in the IRA contours.

D. Possible mechanisms for IRAs

The IRAs can be divided into two regions. The first region has a high-frequency cutoff around f_2. This region is consistent with the suppression of the f_2 tone and/or the f_1 tone by the f_3 tone. This first region is called the low-frequency lobe. It has been studied often (e.g., Brown and Kemp, 1984; Martin *et al.*, 1987; Kummer *et al.*, 1995). Many studies have shown that there is a source of DPOAEs at or near the f_2 place (the place of maximal response to the f_2 tone). For a DPOAE to be generated, signals of frequency f_1 and f_2 have to be mixing in the nonlinearity. Given that the basilar membrane response is such that there is negligible excitation by the f_2 tone apical to the f_2 place, the only region of the basilar membrane where it is possible for the two tones to mix is at and very near the f_2 place. It is a property of compressive nonlinearities that the maximal value of the DP is generated when the amplitudes of the two tones are within an order of magnitude of one another at the site of the nonlinearity. Most of the DP is generated where the excitation amplitudes due to the two tones are almost equal. This region is at the f_2 place (and slightly apical to it). This property follows from the I/O function and basilar membrane tuning and has been verified in studies by Kummer *et al.* (1998, 2000). At the site of the nonlinearity, if f_3 is less than f_2 and/or f_1 and is comparable in amplitude to the lower-amplitude primary, then it can suppress the level of that primary. Usually (depending upon A_2/A_1) this will decrease the DPOAE level. Assume that $A_2 < A_1/3$; then, a compressive I/O map would predict that the $2f_1 - f_2$ DP would be suppressed as $f_3 \rightarrow f_2$ and $A_3 > A_2/3$. This is a robust feature of the data. Most of the low-frequency lobe data can be understood in terms of a simple I/O map and its predictions about suppression and DP generation. The mechanics of suppression predicted by an I/O map are shown in Fig. 5 and have been discussed above. The data of Martin *et al.* (1998a), shown in Fig. 6 are consistent with these rules. Here, the DP is suppressed because the f_2 tone is suppressed. And, the f_2 tone is suppressed when the suppressor tone is within a few dB of the f_2 level. Changing the I/O map by drug administration does not change this behavior.

The second IRA region is at higher frequency (even more than an octave above f_2) and this region is called the high-frequency lobe. The high-frequency lobe can be suppressive (i.e., f_3 decreases the DPOAE level) or can be enhancing (i.e., f_3 increases the DPOAE level). The high-frequency lobe commonly has regions where the value of A_3 can be a factor of 30 (30 dB) or more below the levels of the other two primaries. Hence, if the f_3 tone is suppressing a tone, that tone must have an amplitude close to A_3 at the f_3 place.

Because the high-frequency lobe can either be suppressing or enhancing, depending upon the particular DP and/or depending upon the f_2/f_1 ratio (Martin *et al.*, 1999), it will be assumed that the high-frequency lobe is effectively a second source of DPOAEs. The first source is at the f_2 place. The two sources mix in the ear canal to produce the measured DPOAE. The level and phase of the DPOAE depends upon the levels and phases of the sources. If the two sources were in phase at the ear canal microphone, then decreasing the level of either one would be suppressive. On the other hand, if the two sources were almost equal in amplitude but out of phase by π radians, decreasing either source would increase (enhance) the ear canal DPOAE level.

If the upper-frequency lobe is due to two-source interference, then both phase changes and level changes of the second source will participate in the effect. In order to

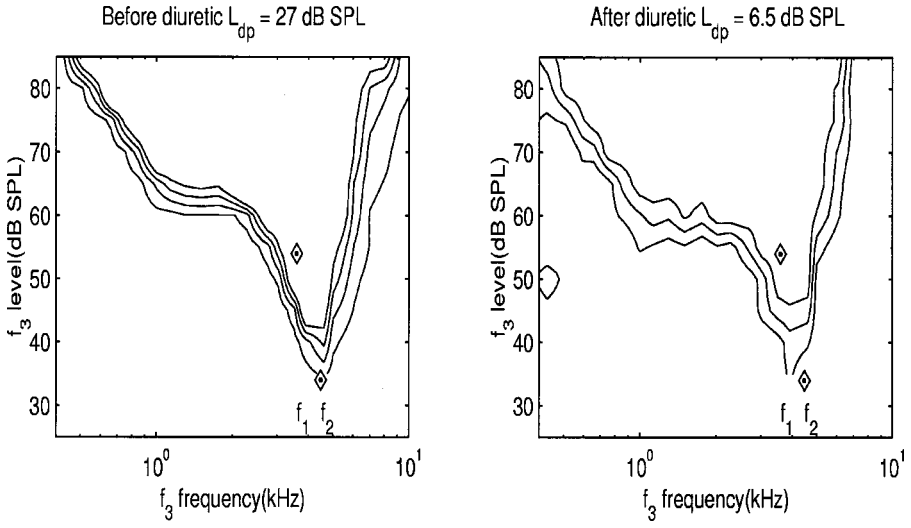

FIG. 6. The suppression contour of the $2f_1-f_2$ DPOAE upon addition of a third tone is shown both before (a), and after (b) diuretic administration to an experimental animal. Note the level of the DPOAE (given at the top of the panel) changes markedly upon drug administration, but that the mechanics of suppression are similar both before and after drug administration indicating that the I/O map changed, but that the system remained nonlinear and compressive. The data plotted in this figure were plotted in a different format than in Fig. 4(C) and (D) from Martin *et al.* (1998a). The diamonds represent the level and frequencies of the two primary tones.

achieve suppressions on the order of 20 dB, this implies that the second source must be generating a DPOAE that is comparable in amplitude to the amplitude of the first source DPOAE. What mechanisms could possibly do this? Two possible mechanisms will be discussed: (a) suppression of putative harmonics, sum tones, and/or difference tones, and (b) the f_3 tone acting as a catalyst. The most fundamental difference between the two mechanisms is that the second DPOAE source for the catalyst mechanism only exists if there is a third tone in the input. For the harmonic mechanism there are two (or more) sources when there are only two tones in the input.

Much of the data shown here (with input levels of f_1 and f_2 at around 60–65 dB SPL) can be simply understood if it is assumed that there is a second source for the $2f_1-f_2$, $2f_2-f_1$, and $3f_1-2f_2$ DPOAEs that has strength that can be as large as about 20–25 dB when $f_3 \geqslant 2f_1$ and its level is about 50 dB SPL.

E. Rules for the second-order tones

Both the harmonic and the catalyst mechanisms will utilize second-order tones. The harmonic mechanism uses the simple difference tone of a second harmonic and a primary tone to make either the $2f_1-f_2$ or the $2f_2-f_1$ DPOAE. For the $3f_1-2f_2$ DPOAE the harmonic mechanism uses the third harmonic of f_1 and the third-order difference tone with f_2 or else it can use the second harmonic of f_2 and a fourth-order difference tone with f_1. Matthews and Molnar (1986) proposed a mechanism similar to that above for the $2f_1-f_2$ DPOAE. They found substantial $2f_1-f_2$ in a distributed cochlear model that had only even-order distortion; hence, they proposed that the $2f_1-f_2$ DP was due to the mixing of $f_1-(f_2-f_1)$.

The catalyst mechanism has several possible routes. It may utilize the simple difference tone, the third-order difference tone, and/or third-order intermodulation DPs with all three tones in the product. The simple difference tone (e.g., f_2-f_1) increases linearly as the level of the lower of the two tones gets larger. By way of example, the I/O map $y=(1+e^2)/(1+e^{2-x})-1$ is used to observe how the two mechanisms are possible or are likely. Examination of Fig. 3(b) shows that saturation for the negative-going part of the signal occurs when the signal amplitude is about -2 or -3. A careful study of Fig. 4 would show that A_{f2-f1} has a value of about 0.3 when $A_1=A_2=1$. Hence, the ratio $A_{f2-f1}/A_1=1/3$ (or -10 dB) when the two primaries are near saturation. As the levels approach saturation, A_{f2-f1}/A_1 can be a little greater than 1/3 (still about -10 dB); so, let this be the maximum value of this ratio. As $A_1=A_2=A$ decreases, the value of A_{f2-f1} decreases as A^2. Therefore, the expected value of A_{f2-f1} at $A_1=A_2=0.1$ would be about 1/100 of 1/3 or 1/300. And, this is approximately the value from the graph. If, instead of decreasing both primaries together, just one of the primaries is decreased, then A_{f2-f1} decreases linearly, as in Fig. 4(b) or (c). If $A_1=1$ and $A_2=0.1$, A_{f2-f1} should be about 1/10 of 1/3, or 1/30. This is approximately the value on the graph. If one of the primaries is near saturation, while the other is less than saturation, the $A_{f2-f1}/A_{\text{lower}}$ is about $A_{\text{lower}}/3$ or -10 dB below the level of the smaller input. Figure 4(d) shows that the second harmonic grows with level as the square of the input. It reaches a maximum when $A \approx 4$, when the input is well into saturation. The maximum value of A_{2f1}/A_1 is about 1/3. At $A_1=1$ the value of $A_{2f1}=0.2$. Below saturation, A_{2f1} decreases as A_1^2. These simple scaling rules are the framework for the discussion of the possibilities of a harmonic mechanism or a catalyst mechanism. These rules will be used to yield rough estimates for possible levels of DPOAE and harmonic tones. In discussing the catalyst mechanism there will be also three-tone mixing and four-tone mixing. For three- and four-tone mixing the DPs will be found from the I/O map output curves in Figs. 7 and 8.

III. HARMONIC MECHANISM

A. What I/O maps allow

In Fig. 1 the input tone levels are at 60 dB SPL; the $2f_1-f_2$ DPOAE is at 32 dB SPL. There is 6 dB of suppression when $f_3 \approx f_2$ at a level of f_3 equal to 55 dB SPL. Hence, it appears that f_3 is suppressing both f_1 and f_2. This is characteristic of the low-frequency lobe. Here, it is well understood that f_3 is a suppressor tone.

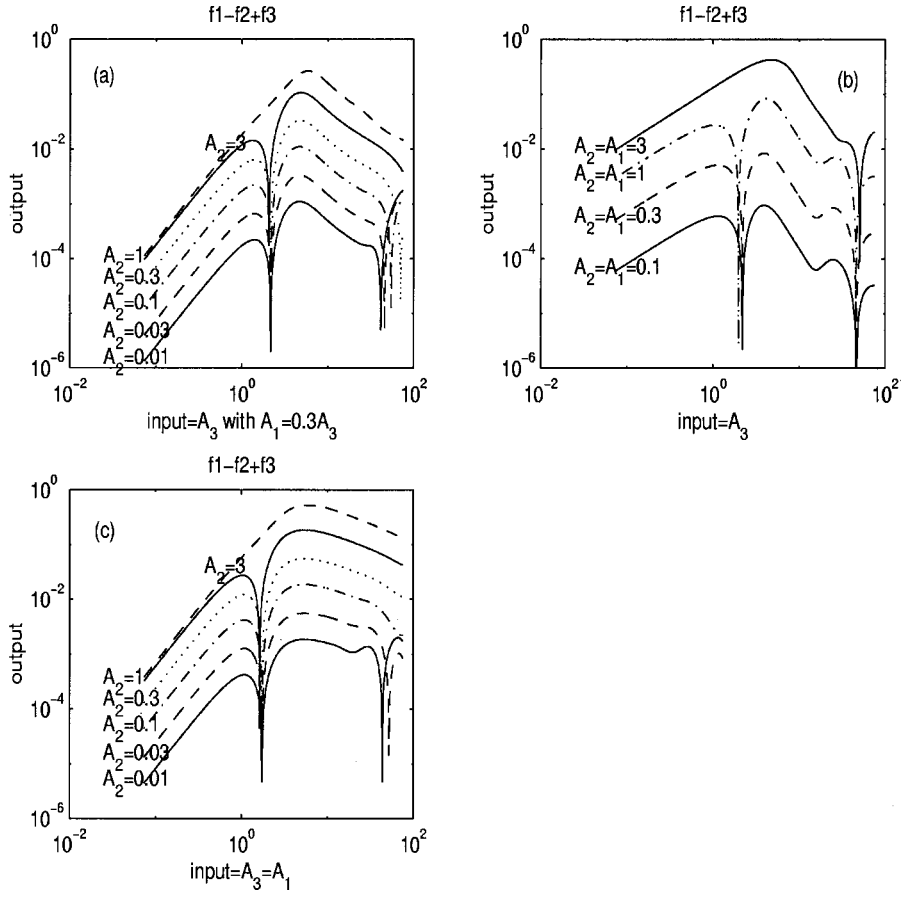

FIG. 7. The output at the frequency $f_1-f_2+f_3$ due to the input of three tones to the I/O map used in Fig. 4 above. In panels (a) and (c) the amplitudes of two of the input tones, A_1 and A_3, are covaried for a constant amplitude of the other tone, A_2. The parameter marking the curves is the amplitude of the constant tone, A_2, and the ratio of the covaried amplitudes is in the horizontal axis label. In panel (b), two of the tones have constant amplitude while the amplitude of the other tone, A_3, is varied. The parameter marking the curves is the amplitude of the two constant tones.

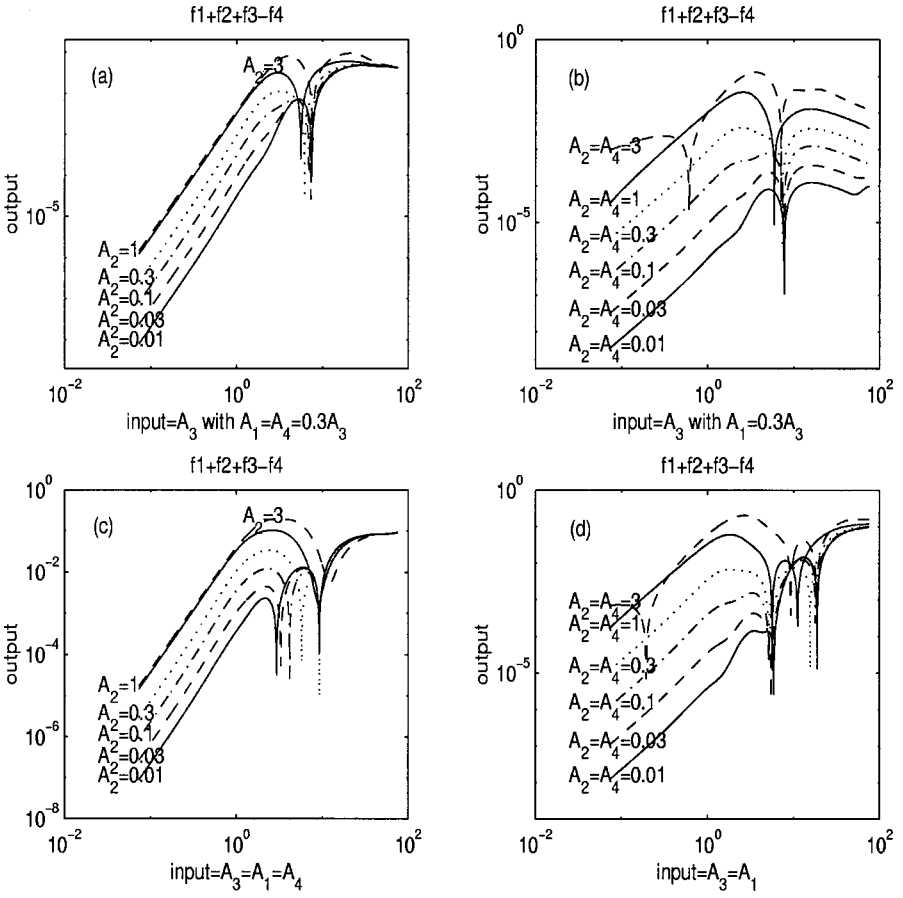

FIG. 8. The output at the frequency $f_1+f_2+f_3-f_4$ that is due to the input of four tones to the I/O map used in Fig. 4. In panels (a) and (c) the amplitudes of three of the input tones, A_1, A_3, and A_4, are covaried for a constant amplitude of the other tone, A_2. The parameter marking the curves is the amplitude of A_2 and the ratio of the covaried amplitudes is in the horizontal axis label. In panels (b) and (c), two of the tones have constant amplitude, A_2 and A_4, while the other two tones, A_1 and A_3, are covaried. The parameter marking the curves is the amplitude of the two constant tones.

Again looking at the 6-dB suppression contour, the high-frequency lobe has a minimum when $2f_1 < f_3 < 2f_2$ and the level of f_3 at that value is 47 dB SPL. If f_3 is suppressing another tone, that other tone must have a level less than 57 dB (as per the rules for suppression). One possibility would be a tone of frequency $2f_1$. The I/O map shown in Fig. 4 can generate a second harmonic that is as large as 10 dB below the primary when the primary is well into the saturation level of the I/O map. Assuming that an even-order nonlinearity can generate a $2f_1$ tone that couples back into the system and produces a substantial excitation at its characteristic place, this tone also should mix with the f_2 tone at the $2f_1$ place. Given that there is an even-order nonlinearity at that place as well, the difference tone of $2f_1$ and f_2 will have the same frequency as the $2f_1 - f_2$ generated by the first source.

Would an I/O map predict that it is possible that the level of this second source $2f_1 - f_2$ difference tone is comparable to the first source cubic DP? Depending on the specifics of rabbit basilar membrane tuning, the f_2 tone could be comparable to the $2f_1$ tone at the $2f_1$ place. If the level of the second harmonic, $2f_1$, at the $2f_1$ place were effectively the equivalent of a 50-dB tone (i.e., within 10 dB of the primary) and if the level of the f_2 excitation were the equivalent of a 30- to 36-dB tone [consistent with basilar membrane response in chinchilla shown in Fig. 1(b) of Ruggero, 1992], then it is possible that the difference tone of $2f_1$ and f_2 would be a 20- to 26-dB source. A 26-dB source would be large enough to enhance or cancel the primary source by 6 dB, depending upon the relative phases of the two sources. Therefore, since the tone at f_3 has a level larger than the putative second harmonic, it would suppress the second harmonic source. Assuming that the two sources are roughly in phase, this suppresses the total level of the DPOAE.

The properties of I/O maps predict that the harmonic mechanism is possible.

B. What the basilar membrane frequency response permits

How large will the $2f_1$ tone be at its characteristic place? At the site of its creation, the f_1 place, it can be as large as 10 dB less than the level of f_1 according to the example I/O map. Levels as large as this have been observed in the mechanical response on the organ of Corti in the apical turn of the guinea pig cochlea (Khanna and Hao, 1999). The apical turn of the guinea pig cochlea is broadly tuned (e.g., Khanna and Hao, 1999). However, in a region of the cochlea that has a sharp high-frequency cutoff, a tone of frequency $2f_1$ that has been created at the f_1 place will be attenuated upon creation because it does not efficiently excite the f_1 place. Both neural and basilar membrane studies show evidence of a sharp high-frequency cutoff in excitation for tones slightly greater than the CF tone in nonapical regions of the cochlea. A tone of frequency $2f_1$ can be well into the high-frequency cutoff region of the f_1 place depending on both the frequency and the level of f_1. When $2f_1$ is greater than the cutoff frequency at the f_1 place, it is an evanescent wave and its amplitude should decrease exponentially with distance toward the stapes until reaching the $2f_1$ place. Neural response data in mammals other than rabbit show that the second harmonic generated along the basilar membrane is more than 30 dB below the primary level at its own characteristic place when $f_1 > 1$ kHz [e.g., Ruggero, 1992, Fig. 1d in both basilar membrane and neural response in chinchilla] or at best 30 dB below the primary level in the basilar membrane response (measured in guinea pig at 16 kHz by Cooper, 1998).

Recently, Cooper (2000) has measured the second harmonic in the 12–19-kHz region of gerbil that is about 40 dB below the primary level for input levels between 30–100 dB SPL. However, some basilar membrane response data show that the high-frequency cutoff diminishes with increasing level (Robles *et al.*, 1997) and with decreasing value of frequency (Cooper and Rhode, 1995). This possibility of the harmonic mechanism can be tested by looking for the second harmonic in either the neural or basilar membrane response of rabbits. However, if the effective level of the second harmonic at its characteristic place is attenuated so that it is the equivalent of 30 dB or less than the primary tone (such as Cooper, 1998), then the difference tone, $2f_1 - f_2$, generated at the $2f_1$ place will be generated by a 30-dB tone (the $2f_1$ tone) and a 36-dB tone (the effective level of f_2). If the 36-dB tone were still in the saturation region of the I/O map, then the mix of the two tones would be a 20-dB source. If the 36-dB tone were not in strong saturation, then the source strength would be several dB less. In any event, suppressing a source that is smaller than 26 dB with the third tone would not give an effect large enough to be consistent with the data in Fig. 1. However, a source of strength of 20 dB or even 10 dB is large enough to be a factor in explaining some other data features. Therefore, the harmonic mechanism appears to be a strong mechanism in regions where, or under circumstances in which, the basilar membrane does not have a sharp high-frequency cutoff. The harmonic mechanism would be not only possible but likely at high levels and/or low frequencies of the primaries.

C. Suppression tuning of the harmonic mechanism

In a compressive nonlinearity, a suppressor tone at the site of the nonlinearity must have a level within 10 dB of the tone that it is suppressing. In the cochlea this implies that tones lower in frequency than the suppressee are more effective suppressors. Higher frequency tones do not drive the nonlinearity at the suppressee tone place unless they are much higher in level than the suppressee tone. This pattern is seen in the low-frequency lobe IRA. Therefore, if f_3 is suppressing $2f_1$, it will be most effective when $f_3 < 2f_1$. The tuning for the high-frequency IRA would be expected to look similar to the tuning for the low-frequency IRA. Because the $2f_1$ is at a lower level than the primaries, it would be expected that the high-frequency IRA could show a sharper tip than the low-frequency lobe and a steep high-frequency slope above $2f_1$. The data in Fig. 1 are suggestive that a tone close to frequency of $2f_1$ is being suppressed. Indeed, this effect is exactly what led to the hypothesis of a suppressed harmonic. Some of the data showing a sharp tip centered on $2f_1$ are consistent with the tuning expected from the suppressed harmonic. However, some of the data exhibit

a low-frequency cutoff at $2f_1$ (rather than showing a high-frequency cutoff at that value) that is not consistent with most basilar membrane suppression experiments and is different from the suppression pattern in the low-frequency lobe of the IRAs. Some of the data show that for $f_3 > 3f_1$ and levels 20 dB or more below the primaries there are significant effects. A tone of such a relatively high frequency and such a relatively low level is not likely to be capable of suppressing a tone at frequency $2f_1$, unless that tone is very small. Of course, if $2f_1$ is very small the second source would be too small to explain the effects seen in the data.

D. Generalizing to other DPs and to other generation sites

The more a nonlinearity is driven into saturation, the more energy in the input tones is output into higher-order DPs and harmonics. Higher-order terms begin to reach the levels of the lower-order terms. Hence, if one ignores the high-frequency cutoff in the basilar membrane response, other possible generation sites develop. For example, at the $3f_1$ place, the third harmonic, $3f_1$, can mix with the f_1+f_2 DP to produce the difference tone $2f_1-f_2$. A little more basally, the $2f_1+f_2$ DP can mix with $2f_2$ to produce $2f_1-f_2$ and even more basal $2f_2+f_1$ can mix with f_2-f_1 to produce $2f_1-f_2$.

For the $2f_2-f_1$ DPOAE, the second site with the greatest potential generator strength would be at the $2f_2$ place. Other sites would be at the $2f_1+f_2$, $2f_2+f_1$, and $3f_2$ places where mixing with, respectively, f_2-f_1, $2f_1$, and f_2+f_1 will produce $2f_2-f_1$.

For the $3f_1-2f_2$ DPOAE, the second site with the greatest strength should be at the $3f_1$ place. Here, the f_2 tone mixing with the $3f_1$ tone would have a third-order DP with frequency $3f_1-2f_2$. Another possible site with smaller generator strength would exist at $2f_2$ place, where a fourth-order DP would produce the right frequency.

E. Summary of harmonic mechanism

For the harmonic mechanism to work, the second and third harmonics of f_1 and f_2 must substantially excite their respective characteristic places. Their effective levels should be no smaller than 30 dB less than the levels of the primary tones and preferably no smaller than 20 dB less. The nonlinearity can easily generate harmonics this large. The major factor limiting the size of the harmonic at its characteristic place is the possible role of the low-pass filtering of the basilar membrane response. If the high-frequency cutoff of the basilar membrane response is sharp, then none of the harmonics is expected to have a large enough amplitude at its own characteristic place to become a large second source of DP. But, if the high-frequency cutoff is gradual, then the harmonic mechanism is a likely second source of DPs.

IV. CATALYST MECHANISMS

At intermediate and high frequencies, the sharp high-frequency cutoff of the basilar membrane response is predicted to attenuate the harmonic mechanism. The catalyst mechanism makes use of the high-frequency cutoff to both explain the mechanism and to explain features in the IRA data. Examination of the right-most column (the $2f_2-f_1$ DPOAE) of Fig. 2 shows the presence of regions that look like hot spots of DP generation at around $f_3=7.0$ kHz for levels between 45 and 55 dB SPL. In the absence of the third tone, the $2f_2-f_1$ DPOAE is about 10 dB and the hot spot region is always enhancing. For the other two DPOAEs, enhancing regions near $f_3 \geqslant 2f_1, 2f_2$ are common when the DPOAE in the absence of the third tone is small enough (less than 20 dB). This is consistent with the presence of a source that arises when $f_3 \geqslant 2f_1, 2f_2$ that has a level of about 20–26 dB and that has a phase that is somewhere between 0 and π radians relative to the DPOAE from the primary source. If the second source were 10 dB or more larger than the first source, then the second source would always be enhancing even if the phase relative to the primary source were π. Because the second source is always suppressing when the $2f_1-f_2$ and the $3f_1-2f_2$ DP in the absence of the third tone are greater than 20 dB, the second source must have a phase greater than $\pi/2$ relative to the first source. Further examination of Fig. 2 shows that there are often significant effects when the f_3 tone is more than three times the value of the f_2 tone and its level is less than the levels of f_1 and f_2. The issue to be resolved is how energy delivered to the cochlea at such high frequencies can somehow be heterodyned down into the relatively low frequencies of the DPs under study. This heterodyning down must be done in such a way that the value of the f_3 frequency is not contained in any final products.

A. The $2f_2-f_1$ DPOAE

The explication of the catalyst mechanism(s) is best understood from the $2f_2-f_1$ IRA data. Notice in Fig. 2 that (in the absence of f_3) as f_2/f_1 becomes smaller, the $2f_2-f_1$ DP becomes larger. This is consistent with what would be expected from the effect of the basilar membrane high-frequency cutoff at the f_2 place. For as $f_1 \rightarrow f_2$, $2f_2-f_1 \rightarrow f_2$ also and the $2f_2-f_1$ DP is less into the cutoff region of the f_2 place. When a third tone is added such that $f_3 \geqslant 2f_2$, the $2f_2-f_1$ DPOAE can become up to 15 dB larger. It is proposed that at the f_3 place, several intermodulation DPs can be generated. Some of these are at the frequencies f_3-f_2, f_3-f_1, f_3-2f_1, f_3-2f_2, $f_3-f_2+f_1$, $f_3-f_1+f_2$ (as $f_2/f_1 \rightarrow 1$), $f_3-2f_2+f_1$, etc. All of these tones have frequencies less than or close to the characteristic frequency of their generation site, f_3, and they all will exist as cochlear excitations. All of these tones have been detected in rabbit ear canal spectra. Once these tones exist in the cochlea, there are many possible ways to combine them.

For example, the tones f_3-f_1 and f_3-2f_2 will both excite the f_3-f_1 place and their difference tone has a value of $2f_2-f_1$. This tone can propagate back to the ear canal microphone and mix with the $2f_2-f_1$ DPOAE generated at the primary site, near the f_2 place. This is the simplest potential catalyst route; so, it will be used to illustrate the catalyst mechanism. This route has a cutoff as $f_3 \rightarrow 2f_2$ from greater than $2f_2$. First, the tone $f_3-2f_2 \rightarrow 0$. Second, when f_3 becomes less than $2f_2$, the DP produced at $2f_2-f_1$ will be in the high-frequency cutoff at the site of generation, the

f_3-f_1 place. Does this particular catalyst route produce a large-enough DPOAE to explain any features in the data? This route is an example of a catalyst route where the second source is the DP of two DPs. It might be expected to be weak but the overall order of the process is fifth order (the difference tone of a simple difference tone and a cubic difference tone). This order is the same as the order of $3f_1-2f_2$ and the data in Fig. 2 show that this particular fifth order product can be as large as 25 dB SPL; therefore, this route seems possible if the DPs are in the saturation regime of the nonlinearity.

For the purposes of discussion, the following assumptions will be used to obtain an estimate of the strength of this route from the I/O map. First, a 50-dB tone is well into saturation. This is consistent with the data. Let a 50-dB tone scale to an input amplitude of 3 in the I/O map simulations (such as Fig. 4). Therefore, a 40-dB tone scales to input amplitude$=1$ and a 30-dB tone scales to an input amplitude$=0.3$ in the I/O map. Second, assume that when the 65-dB tones at f_1 and f_2 are about an octave below f_3, they produce the same displacement amplitude at the f_3 place as a 50-dB f_3 tone [consistent with Fig. 1(b) of Ruggero, 1992]. Third, the f_3-f_1, f_3-f_2, f_3-2f_1, f_3-2f_3, and $f_3-f_2+f_1$ DPs generated at the f_3 place will be the equivalent of 40-dB sources. That is, they will be 10 dB less than either of the 50-dB tones input to the nonlinearity. Fourth, if these DP sources propagate to their characteristic places, they are the equivalent of 40-dB tones. If they are interacting at other places they must be scaled by basilar membrane filtering (for example, Matthews and Molnar, 1986).

An approximate measure of the strength of the route $(f_3-f_1)-(f_3-2f_2)$ can now be found. Assume the data of Fig. 2(c), where $f_1=2.638$ kHz, $f_2=3.165$ kHz, and $f_3=7.0$ kHz, and that their level is 50 dB. Assume that a 50-dB tone is well into the saturation region of the nonlinearity and assume that the 65-dB f_1 and f_2 tones at the f_3 place produce a displacement that is equivalent to the displacement of a 50-dB f_3 tone. Assume that the effective level of the $f_3-f_1=4.362$ tone and effective level of the $f_3-2f_2=0.670$ tone will be about 40 dB. These DPs will mix at the f_3-f_1 place. The f_3-2f_2 tone is about three octaves below the characteristic frequency of the f_3-f_1 place, so its effective level will be much less than 40 dB; assume that it is between 20 and 10 dB. Then, the difference tone of a 40-dB tone with the 10–20-dB tone would be between 0 and 10 dB. Therefore, this catalyst route is too weak to explain the major features of the data.

This first example catalyst route shows the general approach to analyzing a putative catalyst route. It also demonstrates that to find routes of the necessary strength, more energy should go into the mix that makes the final $2f_2-f_1$ DPOAE than the energy in two DPs. This first route was weakened because basilar membrane filtering attentuated one of the components that went into the final mix.

A route that uses two DPs plus a primary tone would be the mixing of tones f_3-f_1, f_3-f_2, and f_2. There is more energy available in this process because two DPs are now mixing with a primary and because the attenuation of the DPs due to basilar membrane filtering is much less. f_3-f_1 and f_3-f_2 are generated at the f_3 place. Making the same assumptions above, they would have effective levels of 40 dB. Now, if $f_3\approx 2f_2$, the three tones will all have comparable frequencies and make the DP $(f_3-f_1)-(f_3-f_2)+f_2=2f_2-f_1$ at the f_3-f_1 place. To get an approximate estimate of the level of the final product, an I/O map was driven with three tones, two 40-dB tones and a 65-dB tone. The results of such a simulation are that the final product has a value less than 0 dB, as per Fig. 7(b). The output was so low because the 65-dB level of the f_2 tone was so large as to be suppressive of the final product. Increasing the value of f_3 beyond $2f_2$ will increase characteristic frequency of the place of interaction, the f_3-f_1 place, and the effective level of f_2 at that place will decrease. Simulations show that if the effective level of f_2 is decreased to 50 dB, then the size of the final product will be close to 20 dB, as per Fig. 7(b) or (c). This is large enough to be a major factor in the data, but is not large enough to be the whole story. Another aspect of this particular catalyst route is that it has a cutoff as $f_3\rightarrow 2f_2$ from above. This is due to the excitation of f_2 becoming so large that it is suppressive and also due to the final product, the $2f_2-f_1$ DP, starting to go into cutoff at the site of generation. Hence, the strength of this catalyst route will be attenuated for both reasons. Just such an effect is seen in the data (Fig. 2).

There is another route that uses two DPs and a primary tone that is worth examination. When $f_2/f_1\rightarrow 1$, the DP $f_3-f_1+f_2$ will not be much into the cutoff region at the site of generation, the f_3 place. Then, the combination $(f_3-f_1+f_2)-(f_3-f_2+f_1)+f_1=2f_2-f_1$. This mix occurs at the $f_3-f_1+f_2$ place. As long as $f_3>f_2$ the DP is not in cutoff. If $f_3\approx 2f_2$, the two DPs are about an octave greater than the f_1 primary. Reasoning as before, the two DPs will have effective levels around 40 dB. The final product will be the mix of two 40-dB tones with a 50-dB tone (the effective level of f_1 at the $f_3-f_1+f_2$ place). The level of $2f_2-f_1$ will be about 20 dB. If $f_3\approx f_2$, the two distortion products and f_1 all have comparable frequencies. Hence, now the final product will be due to the mix of the 40-dB DPs with a 65-dB primary and its value will decrease to below 0 dB due to the suppressive effect of the 65-dB tone. This route has a cutoff as $f_3\rightarrow f_2$ from above.

It is possible to attempt to get even more energy into a catalyst route by using two of the primary tones in the mix that makes the final product. The route $f_3-(f_3-f_2+f_1)+f_2$ will make $2f_2-f_1$ at the f_3 place. Assume that $f_3\approx 2f_2$. As before, let the effective level of f_2 at the f_3 place be 50 dB. Assume that the effective level of the $f_3-f_2+f_1$ tone can be as large as 40 dB. Now, mix a 50-dB tone (f_3), a 50-dB tone (the effective level of f_2 at the f_3 place), and the 40-dB tone. Simulations show that this final DP can have a value of about 24 dB. If the level of f_3 were 40 dB, and the effective level of $f_3-f_2+f_1$ were then 30 dB, the mix would have a strength of about 6 dB. Since this process occurs at the f_3 place, cutoff is not an issue until $f_3\rightarrow 2f_2-f_1$. In Figs. 2(c), (f), and (i), there is a suppression feature that is in the region where $f_3=2f_2-f_1$ that might be due to this mechanism.

As $f_2/f_1 \rightarrow 1$, a complement to this route is the mix of $(f_3+f_2-f_1)-f_3+f_2$. This route will have the same strength as the aforesaid route when the $f_3+f_2-f_1$ DP is not significantly into high-frequency cutoff at the f_3 place.

A third route using one DP and two primary tones is the route $(f_3-f_1)-f_3+2f_2$, with the site of mixing at the f_3 place. While the f_3-f_1 DP could have an effective level of 40 dB at its own place, it will be attenuated at the f_3 place. Assume that $f_3 \approx 2f_2$; then, f_3-f_2 is an octave below f_3 and it will be assumed that it is attentuated by at least 10 dB. The tones in the mix have levels of 50, 40, and 30 dB. The final product has a value around 6 dB. So, this route is too small to explain the major features in the data.

The route $f_3-(f_3-f_2)+f_2-f_1$ uses all three primaries plus one distortion product so it has the potential to use more of the input energy than the routes proposed above. Assume that $f_3 > 2f_2-f_1$ so that the DP is not in cutoff at the site of creation, the f_3 place. The f_3-f_1 signal will be attenuated at the f_3 place because it is a low-frequency tone for that place. Let $f_3=2f_2$, then $f_3-f_2=f_2$, an octave below the characteristic frequency of the generation site. Assuming that f_1 and f_2 are effectively 50-dB tones at the f_3 place, and that the f_3 tone is in saturation, the I/O map creates f_3-f_2 as a 40-dB tone. However, its excitation is filtered by the basilar membrane response because it is an octave below f_3, so let its effective value be 30 dB. The final product will be due to the mixing of three 50-dB tones and a 30-dB tone and it has a level that is about 6 dB, as per Fig. 8(c). This route utilizes four-tone mixing. Simulations show that this process has its best strength when two of the four-tones have an input amplitude to the I/O map that is 20 or larger. This amplitude would scale to a 66-dB tone. When two tones are this large the DP amplitude becomes about 20 dB, independently of the levels of the other two tones [Figs. 8(c) and (d)]. When the f_1 and f_2 primaries are this large, a catalyst mechanism where the f_2 place is the mixing site would have a strong four-tone process due to the large levels of both f_1 and f_2 at that site. This would be effective when f_3 is lower in frequency than the other two primaries. The data in Fig. 2 show several islands of strong suppression that can be understood in terms of a four-tone process. For example, if $f_3=f_2/2$, then the process $f_3+(f_2-f_3)+f_2-f_1$ would have a strength of about 20 dB when the effective level of f_3 at the f_2 place is in the 40- to 50-dB range. In Fig. 2(c) there is an island of suppression at $f_3 \approx 1.5$ kHz that could well be due to this route.

In the region where f_3 is a little greater than $2f_2$, there are four catalyst routes that can significantly contribute to the hot spot. They have levels of 20 and 24 dB and, the closer that $f_2/f_1 \rightarrow 1$, there is another 20-dB route and another 24-dB route. If they are all in phase, they have the potential to make the hot spot a 34-dB source. The sum of these routes would show a cutoff as $f_3 \rightarrow 2f_2$ from above due to the cutoff at $f_3=2f_2$ of one of its components and due to the weakening of the other three components as $f_3 \rightarrow f_2$.

Because f_3 does not appear in the final product, it has to come into the mix of tones twice, once positive and once negative. That implies that the overall order of the catalyst mechanism must be at least 2 greater than the order of the target DP. That is, the lowest overall order process that can produce a catalyst $2f_2-f_1$ or a $2f_1-f_2$ DPOAE is fifth order. And, the lowest overall order producing the $3f_1-2f_2$ DPOAE is seventh order. Hence, for the catalyst mechanism to have much strength the primary tone needs to be into the saturation region of the nonlinearity.

1. Sensitivity to assumptions

All of the catalyst mechanisms discussed above assume that the strength of the effective levels of the f_1 and f_2 primaries at the f_3 place were 50 dB. The basilar membrane response data of Ruggero (1992) Fig. 1(b) show that at the 9-kHz place in chinchilla, the displacement of a 65-dB tone at 4.5 kHz is almost the same as the displacement of a 50-dB 9-kHz tone. To within a few dB, this is also consistent with recent measurements at higher frequencies (13-kHz range) of Cooper (2000) in gerbil, and the measurements at much higher frequencies (30-kHz range) in cat and guinea pig of Cooper and Rhode (1992). Had an effective level of 40 dB been assumed for the excitation of the f_1 and f_2 primaries at the f_3 place, all the DPs generated at the f_3 place would have been smaller, but the three-tone mixing that gives the final product would have produced approximately the same strength catalyst mechanisms. This is because the action of one of the primaries would have been less suppressive.

It has also been assumed that all of the energy in DPs initially created at the f_3 place then went into the final catalyst mix. Some of this energy will end up elsewhere and not be available in the final mix, reducing the strengths of the catalyst mechanisms. For example, if one-half of the energy in the $f_3-f_2+f_1$ DP does not get into the final mix, then the strength of the final product, $f_3-(f_3-f_2+f_1)+f_2$, would have been 18 dB rather than 24 dB.

The discussion above was within the context of a 50-dB tone scaling to an excitation into the I/O map of amplitude $=3$. Had it been assumed that a 50-dB tone scaled to an amplitude$=10$, then the strength of the catalyst mechanism would have been essentially the same. This is because both amplitudes of 3 and 10 bracket the region where the creation of DPs by the example I/O map reaches the maximum effect. However, if a 50-dB tone were scaled to an amplitude$=1$ the catalyst strengths would then be reduced by more than a factor of 3 (smaller by about 13 dB). While this would be large enough to reproduce much of the data, it is not large enough to reproduce all of it.

If it were assumed that the initial DPs generated at the f_3 place were effectively at levels of 30 dB rather than at 40 dB, then the catalyst mechanism would have been weaker by a factor of roughly 10 dB. Hence, the overall strength would have been 24 dB rather than 34 dB.

The last important assumption (not formally stated) was that the example I/O map was a good choice of I/O map for representing the data and for developing the argument. The example map used was of the form $y=(1+e^{\alpha})/(1+e^{\alpha-\beta x})-1$, where $\alpha=2$ and $\beta=1$; α controls the asymmetry of the clipping (saturation) of the waveform and β controls the slope at $x=0$. This map was chosen because of the similarity of its shape to the I/O map of outer hair cell response, because at low levels its generates more f_2-f_1 DP

TABLE I. Some high-frequency lobe catalyst routes.

Reactants	Place of reaction	Final product and overall order
$(f_3-f_1)-(f_3-f_2)+f_2$	(f_3-f_1)	$2f_2-f_1$ (fifth)
$f_3-(f_3-f_2+f_1)+f_2$	f_3	$2f_2-f_1$ (fifth)
$(f_3-f_1+f_2)-f_3+f_2$	$(f_3-f_1+f_2)$	$2f_2-f_1$ (fifth)
$(f_3-f_1+f_2)-(f_3-f_2-f_1)+f_1$	$(f_3-f_1+f_2)$	$2f_2-f_1$ (seventh)
$f_3-(f_3-f_2)+f_2-f_1$	f_3	$2f_2-f_1$ (fifth)
$(f_3-f_2)-(f_3-f_1)+f_1$	(f_3-f_1)	$2f_1-f_2$ (fifth)
$(f_3-f_2+f_1)-f_3+f_1$	f_3	$2f_1-f_2$ (fifth)
$f_3-(f_3-f_1+f_2)+f_1$	$(f_3-f_1+f_2)$	$2f_1-f_2$ (fifth)
$(f_3-f_2+f_1)-(f_3-f_1+f_2)+f_2$	$(f_3-f_1+f_2)$	$2f_1-f_2$ (seventh)
$f_3-(f_3-f_1)+f_1-f_2$	f_3	$2f_1-f_2$ (fifth)
$(f_3-2f_2)-(f_3-2f_1)+f_1$	(f_3-2f_1) if $f_3>3f_1$	$3f_1-2f_2$ (seventh)
$(f_3-f_2+f_1)-(f_3-f_1+f_2)+f_1$	$(f_3-f_1+f_2)$	$3f_1-2f_2$ (seventh)
$(f_3-f_2)-(f_3-f_1)+2f_1-f_2$	(f_3-f_1)	$3f_1-2f_2$ (seventh)
$(f_3-f_2)-(f_3-2f_1)+f_1-f_2$	(f_3-f_2)	$3f_1-2f_2$ (seventh)

than $2f_1-f_2$ DP and at high levels it generates more $2f_1-f_2$ DP than f_2-f_1 DP (similar to the neural population study in cats summarized in Kim, 1980) and because it has a large second harmonic (needed to develop the harmonic mechanism), and because the slope at $x=0$ was unity. Had the simulations been developed with an I/O map that had larger values for β, the odd-order distortion would have been increased and the strongest catalyst route (which had only third-order tones in the mixes) would have been even stronger.

B. The $2f_1-f_2$ and $3f_1-2f_2$ DPOAEs

The same type of arguments applies to the $2f_1-f_2$ and $3f_2-2f_1$ DPOAEs with the exception that the final product cannot possibly be in the high-frequency cutoff regime at the site of creation if any one of the primary tones is involved in the final mixing. The routes that should be effective in the production of the $2f_1-f_2$ DPOAE are the mixes: $(f_3-f_2)-(f_3-f_1)+f_1$; $(f_3-f_2+f_1)-f_3+f_1$; when $f_2/f_1 \rightarrow 1$, $(f_3-f_2+f_1)-(f_3+f_2-f_1)+f_2$ and $f_3-(f_3+f_2-f_1)+f_1$; and, depending upon levels, $f_3-(f_3-f_1)+f_1-f_2$. For the $3f_1-2f_2$ DPOAE, the order of the overall process has to be at least seventh, as the f_3 has to be both added once and subtracted once. Possible routes are: $(f_3-2f_2)-(f_3-2f_1)+f_1$, when $f_3>3f_1,3f_2$; $(2f_1-f_3)-(2f_2-f_3)+f_1$, strongest when $f_3<f_1,f_2$; $(f_3-f_2+f_1)-(f_3+f_2-f_1)+f_1$ [which gets stronger as $f_2/f_1 \rightarrow 1$ and which is a good candidate for the strong suppression source seen at $f_3 \approx 5.5$ kHz in Fig. 2(j) and for the suppression source seen at $f_3 \approx 5.0$ kHz in Fig. 2(g)]; $(f_3-f_2)-(f_3-f_1)+2f_1-f_2$, which can be about 10 dB; and $(f_3-f_2)-(f_3-2f_1)+f_1-f_2$, which also can be about 10 dB.

A summary of important catalyst routes is presented in Table I. A corollary of the catalyst mechanism for making DPs is that there are also catalyst mechanisms for affecting the levels of other tones. For example, a catalyst tone at f_1 can be created by the route $(f_3+f_1-f_2)-f_3+f_2$ and/or by the route $(f_3-f_2)-(f_3-f_1)+f_2$. Even when $f_3>2f_2$, such f_3-dependent tones have been measured at levels up to 25 dB SPL in rabbit ear canals.

C. More catalyst mechanism tuning

The catalyst mechanism assumes that f_1, f_2, and f_3 are all mixing at the f_3 place to create at least one DP that will mix in the final production. Let f_3 be more than an octave greater than f_2. Assuming that the basilar membrane displacement is in saturation at the f_3 place, its frequency response should not exhibit much of a sharply tuned tip near the f_3 place. The excitations of f_1 and f_2 will be in the f_3 tail region, but should have excitation amplitudes within an order of magnitude of the amplitude of f_3. Now, let f_3 increase to a more basal location. The f_1 and f_2 excitations will still be in the tail region at this new place. They will be attenuated compared to the prior f_3 location; their attenuation depends upon the specifics of basilar membrane tuning. This attenuation will attenuate the DPs made at the f_3 place. When f_3 is more than an octave above f_2, the IRA could only be weakly tuned as a function of f_3 if the basilar membrane excitation is weakly tuned in the low-frequency tail of the excitation. If rabbit basilar membrane tuning is similar to guinea pig tuning in the high-frequency regime as shown in Fig. 3(b) of Cooper (1996), then a catalyst mechanism's production could have roughly constant strength as f_3 increases. This is consistent with some regions of the high-frequency IRA. However, if the basilar membrane response in the low-frequency tail decreases at a rate of 9 dB/octave as in squirrel monkey, Rhode (1971), or as the Wentzel–Kramers–Brillouin (WKB) approximation would predict, the catalyst mechanisms that use only two DPs, or that uses two DPs plus one primary, would decrease much more rapidly with increasing f_3.

D. Catalyst mechanism summary

For the catalyst mechanism to work, there are several constraints that must be respected. First, the final DP product should not be into the cutoff region at the site of creation. Second, the intermediate DPs cannot be into the cutoff region at their site(s) of creation. Third, the DP tones should be mixing near their characteristic places. Fourth, the primary tones should not be so great that they exert suppressive effects at the mixing sites of either the intermediate or the final products. That low-order DP production decreases as input

increases beyond a certain level explains why the hot spots exist only within a confined range of f_3 level. When the level of f_3 gets too large the DPs that it generates begin to decrease. Of course, as the level of f_3 gets too low the DP levels decrease. As the frequency, f_3, gets too large the hot spot also attenuates due to the effective levels of the other two primaries decreasing too much at the f_3 place. The catalyst mechanism has the features that are capable of explaining why the hot spot is hottest over both a limited region of the level and value of f_3.

V. PHASE EFFECTS

If the second source had more than twice the amplitude of the first source, the second source would always show enhancement in the catalyst mechanism and would always show suppression in the harmonic mechanism, irrespective of the relative phases of the sources. In the high-frequency IRA a region of enhancement always occurs when the DPOAE, in the absence of the third tone, is small (<15 dB SPL). The catalyst mechanism explains this by positing that there is an f_3-dependent source that has an effective level of 20 dB or more. The harmonic mechanism explains this by positing that the third tone is suppressing the second source that in the absence of the third tone was canceling the first source. In general, to qualitatively explain why the IRAs can be either areas of suppression or of enhancement, the relative phases of the sources must be examined to see if phase changes of at least π radians can result from changes of f_2/f_1. The data show that the transition of the high-frequency IRA from suppressing to enhancing for the $2f_1-f_2$ and $3f_1-2f_2$ DPOAEs is strongly correlated with f_2/f_1. The harmonic mechanism postulates that this is mostly a phase effect, while the catalyst mechanism postulates that this is mostly a level effect. The discussion below seeks to qualitatively determine what phase effects are possible.

At the f_2 generation site, the phase of $2f_1-f_2$ will carry three contributions, the phase of f_2 at the f_2 place (θ_2), twice the phase of f_1 at the f_2 place ($2\theta_1^g$), and the phase that a tone of frequency $2f_1-f_2$ would have at the f_2 place ($\theta^g_{2\,f1-f2}$). The superscript, g, stands for the DP generator site. Let $\theta_2=0$ so that it will serve as the reference phase. The phase of the $2f_1-f_2$ DP will be $2\theta_1^g-\theta^g_{2\,f1-f2}$. Similarly, the phase of the $3f_1-2f_2$ DP will be $3\theta_1^g-\theta^g_{3f1-2\,f2}-\pi$. Because the Taylor series has alternating signs for the successive odd powers in the expansion, there is a factor of π extra in the fifth-order DP relative to the third-order DP. The phase for the $2f_2-f_1$ DP will be $-\theta_1^g-\theta^g_{2\,f2-f1}$. At the f_2 place there is rapid phase change for tones whose frequencies are close to f_2. Therefore, the $\theta^g_{2\,f2-f1}$ can be quite different from $\theta^g_{2\,f1-f2}$ and $\theta^g_{3f1-2\,f1}$. For example, this difference can be up to several π if $3f_1-2f_2$ is more than an octave below f_2. Basilar membrane displacement response measurements in small laboratory mammals show phase differences of between three and four wavelengths (i.e., 6π to 8π) when the eliciting signal is swept across the full range of excitation frequencies.

At the second site of DP generation, the phase situation depends upon the mechanism. For the harmonic mechanism, $2f_1$ and f_2 are mixing at the $2f_1$ site. The DP from this site will have a component that equals the phase with which the f_2 tone excites the $2f_1$ site, and it will have the phase given to $2f_1$ where it was created, and the phase change accumulated during propagation from the f_1 region to the $2f_1$ excitation region. Both the creation phase and propagation phase of $2f_1$ should be fairly independent of f_1. Moreover, in the data presented in this study, $0.5<f_2/2f_1<0.6$, so as f_2/f_1 changes, this phase change should be negligible. Hence, for the harmonic mechanism the phase difference between the two sources as f_2/f_1 changes should be mostly due to the phase changes of the first source.

For the catalyst mechanism, the data in Fig. 2 are consistent with the phase of the second source differing from the first source by more than $\pi/2$, but less than π. A simple example illustrates this point. Suppose that the amplitude of the second source is 1 and that the phase difference between the two sources is $4\pi/6$ radians (120°). If the first source also has amplitude 1, then the vector sum has an amplitude 1. The vector diagram is an equilateral triangle. If the first source has amplitude less than 1, then the vector sum is always greater than the first source amplitude, or enhancement. If the first source has amplitude greater than 1, then the vector sum is always less than the amplitude of the first source, or suppression. Reviewing the $2f_1-f_2$ and $3f_1-2f_2$ data in Fig. 2, a level around 20 dB is the level where there is neither suppression or enhancement, when f_3 is a little greater than $2f_2$, except for very high levels, so this would be the amplitude of the putative second source if it had a phase of $4\pi/6$ radians with respect to the first source.

The overall catalyst mechanism is the vector sum of several possible routes. For the $2f_2-f_1$ DPOAE, when $f_3>2f_2$, the four strongest routes are: $(f_3-f_1)-(f_3-f_2)+f_2$; $f_3-(f_3-f_2+f_1)+f_2$; $(f_3+f_2-f_1)-f_3+f_2$; and $(f_3+f_2-f_1)-(f_3-f_2+f_1)-f_1$. The last two routes are more important as $f_2/f_1\rightarrow 1$. All of these routes have the following similarities. The f_1 or f_2 primary is the lowest-frequency tone in the mix. The other two tones in the mix are relatively close in frequency. For the first three routes the difference in frequency for the two higher frequency tones is f_2-f_1 and for the fourth route the difference is $2(f_2-f_1)$. If $f_3\approx 2f_2$, a dynamical model would be needed to determine the relative phases as the first catalyst route then has all three tones close to the same frequency; hence, the phase of each input to the final product would be important and each is in the region where the ratio of phase change to frequency change is large. However, if $f_3\approx 3f_2$, then it is evident that the last three catalyst routes will all have approximately the same phase. This is because the highest-frequency tone is at or near the f_3 place. The middle-frequency tone is close in frequency to the highest-frequency tone [the relative difference of these two tones is small, being either $(f_2-f_1)/f_3$ in two instances and $2(f_2-f_1)/f_3$ in the other]. The third tone in the mix is a low-frequency tone at the f_3 place. Hence, the products from these last three routes will all have about the same phase. The first catalyst route will have a different phase because the site of generation, the f_3-f_1 place, is near $2f_2$ rather than near $3f_2$. The phase of the $2f_2-f_1$ DP on creation at

the f_3-f_1 place will be only slightly different from the other three catalyst routes, because the relative spacing the two higher-frequency inputs is still fairly small, and because the f_2 tone at the f_3-f_1 place is still a fairly low-frequency tone. The largest diffence in the phase of $2f_2-f_1$ will be due to its larger delay in coming from a lower-frequency place. Assuming that this delay is of the form γ/f_g, where γ is of order one and f_g is the frequency of the generator site, the phase difference due to that larger delay is estimated to be less than $\pi/4$ radians. Hence, as $f_3 \rightarrow 3f_2$, all four catalyst routes are essentially in phase. As $f_3 \rightarrow 2f_2$ the first catalyst route goes out of phase with the other three. However, the first catalyst route also diminishes amplitude as $f_3 \rightarrow 2f_2$, so cancellation of the other three routes by this route ceases to be an issue.

Therefore, as f_3 approaches $3f_2$ or greater, the strongest four routes for the creation of $2f_2-f_1$ are essentially in phase.

A. Phase delays

For the harmonic mechanism, the DPOAE generated at the second site carries twice the phase delay of the f_1 tone at the f_1 place and it also has the delay appropriate for a $2f_1-f_2$ tone generated at the $2f_1$ place. The delay should be almost independent of the value of f_3. For the catalyst mechanisms the DPOAE from the second source should have a phase delay that decreases as $f_3(>2f_2)$ increases.

VI. SUMMARY

Using arguments based upon the properties of compressive I/O maps, two possible mechanisms have been proposed to explain the existence of the high-frequency lobe of the IRAs. The harmonic mechanism is attractive for its simplicity. However, the harmonic mechanism needs the harmonics generated by the primary tones to be large (on the order of the equivalent of a 30- to 40-dB tone) at the characteristic places of the harmonics. This is generally not consistent with observations of neural frequency tuning curves or basilar membrane response curves for intermediate and high frequencies; however, it is consistent for frequencies less than 1 kHz. However, at frequencies in the hundreds of Hz, the harmonic mechanism is not only possible, but likely.

The catalyst mechanisms avoid the problem of the basilar membrane response high-frequency cutoff. Indeed, the catalyst mechanisms invoke the high-frequency cutoff to explain some tuning features of IRAs. While the catalyst mechanism does not have the attractive simplicity of the harmonic mechanism, it is interesting for the variety of ways that distortion tones can be generated. Catalyst routes of the strength proposed here are likely to confound simplistic interpretations of DP suppression experiments. Evidence of a catalyst mechanism in the low-frequency lobe is seen in the islands of suppression that appear in Fig. 2. Furthermore, the catalyst mechanisms could prove useful in understanding the psychophysics of high-level multitone complexes. The experiment of Yates and Withnell (1999) provides an excellent picture of the rich variety of tones in the output spectra when the input is both multitone and high level.

For both mechanisms, it is assumed that at levels of 50 dB the input tones at f_1 and f_2 are driving the basilar membrane well into saturation. This assumption seems valid given that 50-dB tone inputs generate many DPOAE frequencies in the ear canal spectra and given that increasing primary levels beyond 60 dB can lead to the decreases in DPs predicted by the I/O maps. Conclusive tests of these mechanisms can be made with basilar membrane displacement experiments and/or with neural experiments. For both mechanisms, it is assumed that the cochlea has both odd and even distortion. Ear canal spectra show substantial odd and even DPs and second and third harmonics.

ACKNOWLEDGMENTS

Graeme Yates made insightful and valuable comments on an early draft and Christopher Shera did the same on a later draft of this study. This study was supported by NIDCD Grant No. DC00613.

Brown, A.M., and Kemp, D.T. (**1984**). ''Suppressibility of the $2f_1-f_2$ stimulated acoustic emissions in gerbil and man,'' Hear. Res. **13**, 29–37.
Cooper, N.P., and Rhode, W.S. (**1992**). ''Basilar membrane mechanics in the hook region of cat and guinea-pig cochleae: Sharp tuning and nonlinearity in the absence of baseline position shifts,'' Hear. Res. **63**, 163–190.
Cooper, N.P., and Rhode, W.S. (**1995**). ''Nonlinear mechanics at the apex of the guinea-pig cochlea,'' Hear. Res. **82**, 225–243.
Cooper, N.P. (**1996**). ''Two-tone suppression in cochlear mechanics,'' J. Acoust. Soc. Am. **99**, 3087–3098.
Cooper, N.P. (**1998**). ''Harmonic distortion on the basilar membrane in the basal turn of the guinea-pig cochlea,'' J. Physiol. (London) **509**, 277–288.
Cooper, N.P. (**2000**). ''Basilar membrane vibrations in the basal turn of the gerbil cochlea,'' Abstracts of the Midwinter Meeting of the Association for Research in Otolaryngology **23**, 205.
Duifhuis, H. (**1989**). ''Power law nonlinearities: A review of some less familiar properties,'' in *Cochlear Mechanisms: Structure, Function and Models*, edited by J. P. Wilson and D. T. Kemp (Plenum, New York), pp. 395–403.
Fahey, P.F., and Allen, J.B. (**1988**). ''Power law features of acoustic distortion product emissions,'' in *Basic Issues in Hearing*, edited by H. Duifhuis, J. W. Horst, and H. P. Wit (Academic, London), pp. 124–131.
Fahey, P.F. (**1989**). ''Distortion product responses of saturating nonlinearites,'' in *Cochlear Mechanisms: Structure, Function and Models*, edited by J. P. Wilson and D. T. Kemp (Plenum, New York), pp. 405–412.
Frank, G., and Kossl, M. (**1996**). ''The acoustic two-tone distortions $2f_1-f_2$ and f_2-f_1 and their possible relation to changes in the operating point of the cochlear amplifier,'' Hear. Res. **98**, 104–115.
Gaskill, S.A., and Brown, A.M. (**1996**). ''Suppression of human acoustic distortion product: Dual origin of $2f_1-f_2$,'' J. Acoust. Soc. Am. **100**, 3260–3274.
Heitmann, J., Waldmann, B., Schnitzler, H-U., Plinkert, P.K., and Zenner, H-P. (**1998**). ''Suppression of distortion product otoacoustic emissions (DPOAE) near $2f_1-f_2$ removes DP-gram fine structure—Evidence for a second generator,'' J. Acoust. Soc. Am. **103**, 1527–1531.
Hudspeth, A.J., and Corey, D.P. (**1977**). ''Sensitivity, polarity, and conductance change in the response of vertebrate hair cells to controlled mechanical stimulation,'' Proc. Natl. Acad. Sci. U.S.A. **74**, 2407–2411.
Johnstone, B.M., Patuzzi, R., and Yates, G.R. (**1986**). ''Basilar membrane measurements and the travelling wave,'' Hear. Res. **22**, 147–153.
Khanna, S.M., and Hao, L.F. (**1999**). ''Nonlinearity in the apical turn of living guinea pig cochlea,'' Hear. Res. **135**, 89–104.
Kim, D.O. (**1980**). ''Cochlear mechanics: Implications of electrophysiological and acoustical observations,'' Hear. Res. **2**, 297–317.
Kummer, P., Janssen, T., and Arnold, W. (**1995**). ''Suppression tuning characteristics of the $2f_1-f_2$ distortion-product emissions in humans,'' J. Acoust. Soc. Am. **98**, 197–210.

Kummer, P., Janssen, T., and Arnold, W. (**1998**). ''The level and growth behavior of the 2 f1−f2 distortion product otoacoustic emission and its relationship to auditory sensitivity in normal hearing and cochlear hearing loss,'' J. Acoust. Soc. Am. **103**, 3431–3444.

Kummer, P., Janssen, T., Hulin, P., and Arnold, W., (**2000**). ''Optimal $L_1 - L_2$ primary tone level separation remains independent of test frequency in humans,'' Hear Res. **146**, 47–46.

Lukashkin, A.N., and Russell, I.J. (**1999**). ''Analysis of the f_2-f_1 and $2\,f_1-f_2$ distortion components generated by the hair cell mechanoelectrical transducer: Dependence on the amplitudes of the primaries and feedback gain,'' J. Acoust. Soc. Am. **106**, 2661–2668.

Martin, G.K., Probst, P., Scheinin, S.A., Coats, A.C., and Lonsbury-Martin, B.L. (**1987**). ''Acoustic distortion products in rabbits. II. Site of origin revealed by suppression and pure-tone exposures,'' Hear. Res. **28**, 191–208.

Martin, G.K., Whitehead, M.L., Stagner, B.B., and Lonsbury-Martin, B.L. (**1995**). ''Suppression and enhancement of DPOAEs by interference tones above f_2 in rabbits,'' Abstracts of the Midwinter Meeting of the Association for Research in Otolaryngology **18**, 124.

Martin, G.K., Jassir, D., Stagner, B.B., and Lonsbury-Martin, B.L. (**1998a**). ''Effects of loop diuretics on the suppression tuning of distortion-product otoacoustic emissions in rabbits,'' J. Acoust. Soc. Am. **104**, 972–983.

Martin, G.K., Jassir, D., Stagner, B.B., Whitehead, M.L., and Lonsbury-Martin, B.L. (**1998b**). ''Locus of generation for the $2\,f_1-f_2$ vs $2\,f_2-f_1$ distortion-product otoacoustic emissions in normal-hearing humans revealed by suppression tuning, onset latencies, and amplitude correlations,'' J. Acoust. Soc. Am. **103**, 1957–1971.

Martin, G.K., Stagner, B.B., Jassir, D., Telischi, F.F., and Lonsbury-Martin, B.L. (**1999**). ''Suppression and enhancement of distortion-product otoacoustic emissions by interference tones above f_2. I. Basic findings in rabbits,'' Hear. Res. **136**, 105–123.

Martin, G.K., Plummer, J.R., Stagner, B.B., and Lonsbury-Martin, B.L. (**2000**). ''Phase-sensitive residual measures of DPOAE suppression tuning curves: Insights into generation processes,'' in *Recent Developments in Auditory Mechanics*, edited by H. Wada, T. Takasaka, K. Ikida, K. Ohyama, and T. Koike (World Scientific Press, Singapore), pp. 388–394. in press.

Matthews, J.W., and Molnar, C.E. (**1986**). ''Modeling of intracochlear and ear canal distortion product $2\,f_1-f_2$,'' in *Peripheral Auditory Mechanisms*, edited by J. B. Allen, J. L. Hall, A. Hubbard, S. T. Neely, and A. Tubis (Springer, New York), pp. 258–265.

Mills, D.M. (**2000**). ''Frequency responses of two- and three-tone distortion product otoacoustic emissions in Mongolian gerbils,'' J. Acoust. Soc. Am. **107**, 2586–2602.

Rhode, W.S. (**1971**). ''Observation of the vibration of the basilar membrane in squirrel monkeys using the Mossbauer technique,'' J. Acoust. Soc. Am. **49**, 1219–1231.

Robles, L., Ruggero, M.A., and Rich, N.C. (**1997**). ''Two-tone distortion on the basilar membrane of the chinchilla,'' J. Neurophysiol. **77**, 2385–2399.

Rosowski, J. J., Peake, W. T., and White, J. R., (**1984**). ''Cochlear nonlinearities inferred from two-tone distortion products in the ear canal of the alligator lizard,'' Hear Res., **13**, 141–158.

Ruggero, M.A. (**1992**). ''Responses to sound of the basilar membrane of the mammalian cochlea,'' Curr. Opin. Neurobiol. **2**, 449–456.

Russell, I.J., Cody, A.R., and Richardson, G.P. (**1986**). ''The responses of inner and outer hair cells in the basal turn of the guinea-pig cochlea and in the mouse cochlea grown *in vitro*,'' Hear. Res. **22**, 199–216.

Siegel, J., Borneman, A., and Dreisbach, L. (**2000**). ''Suppressor conditions for optimal separation of distortion product otoacoustic emission sources,'' Abstracts of the Midwinter Meeting of the Association for Research in Otolaryngology **23**, 283.

Whitehead, M.L., Stagner, B.B., McCoy, M.J., Lonsbury-Martin, B.L., and Martin, G.K. (**1995a**). ''Dependence of distortion-product otoacoustic emissions on primary levels in normal and impaired ears. II. Asymmetry in $L1$, $L2$ space,'' J. Acoust. Soc. Am. **97**, 2359–2377.

Whitehead, M.L., Stagner, B.B., McCoy, M.J., Lonsbury-Martin, B.L., and Martin, G.K. (**1995b**). ''Enhancement of distortion-product emissions (DPOAEs) in rabbits by high-frequency interference tones: Evidence for a second filter?,'' Abstracts of the Midwinter Meeting of the Association for Research in Otolaryngology **18**, 124.

Withnell, R.H., and Yates, G.K. (**1998**). ''Onset of basilar membrane nonlinearity reflected in cubic distortion tone input–output functions,'' Hear. Res. **123**, 87–96.

Yates, G.K. (**1990**). ''The basilar membrane nonlinear input–output function,'' in *The Mechanics and Biophysics of Hearing*, edited by P. Dallos, C. D. Geisler, J. W. Matthews, M. A. Ruggero, and C. R. Steele (Springer, New York), pp. 106–113.

Yates, G.K., and Withnell, R.H. (**1999**). ''The role of intermodulation distortion in transient-evoked otoacoustic emissions,'' Hear. Res. **136**, 49–64.

Evidence for spatial tuning in informational masking using the probe-signal method[a)]

Tanya L. Arbogast[b)] and Gerald Kidd, Jr.
Department of Communication Disorders and The Hearing Research Center, Boston University, 635 Commonwealth Avenue, Boston, Massachusetts 02215

(Received 18 January 2000; revised 20 June 2000; accepted 22 June 2000)

Auditory spatial attention is one mechanism that may contribute to the ability to identify one sound source in a multi-source environment. The role of auditory spatial attention in a multi-source environment was investigated using the probe-signal method. The experiment took place in a quiet room with seven speakers arranged in a semi-circle in front of the listener. The speakers were placed at 30-degree intervals at a distance of 5 ft from the listener. The signal was comprised of eight contiguous, 60-ms pure-tone bursts arranged in either a rising or falling frequency pattern. Masker components were also comprised of eight contiguous pure-tone bursts but with durations that varied randomly from 20 to 100 ms. The six maskers were played with the signal and were constructed in order to result in informational rather than energetic masking. The frequency of each masker component was chosen randomly on each burst from a narrow frequency band, independent from the signal frequency band. The task was 1I-2AFC fixed-level identification with response time measurement. The listener was instructed to focus attention on a specified speaker (expected location) for a block of trials. Accuracy and response time were compared across two conditions: (1) signal presented at the expected location and (2) signal presented at an unexpected location. Results indicate a significant increase in accuracy and faster response time when the signal was presented at the expected location as compared to an unexpected location. These results suggest that auditory spatial attention plays an important role in multi-source listening, especially when the listening environment is complex and uncertain.
[S0001-4966(00)01710-0]

PACS numbers: 43.66.Ba, 43.66.Dc, 43.66.Pn [SPB]

I. INTRODUCTION

Auditory attention can be focused along a stimulus dimension in order to improve processing at the point of focus. A consequence of focused attention is decreased processing at unattended regions. This pattern of performance resembles the properties of a band-pass filter leading to the concept of an ''attentional filter'' or ''attention band'' (Greenberg and Larkin, 1968; MacMillan and Schwartz, 1975; Scharf *et al.*, 1987; Dai *et al.*, 1991; Wright and Dai, 1994; Mondor and Zatorre, 1995). In the auditory modality, attentional filtering has been well documented in the frequency domain using the probe-signal method. In that method, first described by Greenberg and Larkin (1968), a fixed-frequency target tone is presented for detection in the majority of trials within a block of trials. In the remaining trials, the probe tones are presented at frequencies surrounding the target frequency. The resulting plot of detection performance has a peak at the target frequency and declines as the frequency difference between the probe and the target increases, resulting in a filterlike function (Greenberg and Larkin, 1968; Scharf *et al.*, 1987; Schlauch and Hafter, 1991; Hafter *et al.*, 1993; Wright and Dai, 1994). The outcome is the same or nearly the same regardless of whether the listener is aware of the existence and probability of occurrence of the probe frequencies before the start of data collection (Scharf *et al.*, 1987; Dai *et al.*, 1991). If two frequencies are attended, two filterlike functions result (MacMillan and Schwartz, 1975). The probe-signal method has been adapted to other acoustic dimensions such as signal duration (Wright and Dai, 1994; Dai and Wright, 1995), temporal structure (White and Carlyon, 1997), sinusoidal amplitude modulation (Wright and Dai, 1998), and profile analysis (Hill *et al.*, 1997).

The evidence for filtering in the auditory spatial dimension is not as clear. Most of this research to date has used a paradigm in which a cue to the location of the signal is given prior to each trial. In one variation of the paradigm, the cue is valid (correctly indicates signal location) in the majority of trials and is invalid (incorrectly indicates signal location) in the remaining trials. The listener is informed that the cue indicates the most likely location of the signal. The listener presumably directs attention to the cued location because the cue usually indicates the correct signal location. The expectation is that when the cue is valid, performance is better than when the cue is invalid because attention can be focused at a particular location. In general, the effects of auditory attention on detection have been small or nonexistent. Posner (1978), Buchtel and Butter (1988), and Spence and Driver (1994) all measured the effect of valid and invalid cues in a soundfield for supra-threshold detection tasks. They found no significant difference in response time between valid cue and invalid cue conditions. In a preliminary experiment,

[a)]Portions of this research were presented at the 22nd Midwinter Meeting of the Association for Research in Otolaryngology, St. Petersburg Beach, FL, February 1999.
[b)]Electronic mail: rohtla@bu.edu

Scharf *et al.* (1987) also found no response time difference for detection at expected versus unexpected locations. However, Quinlan and Bailey (1995) and Bedard *et al.* (1993) both found small but significant response time effects for detection tasks under headphones.

The effects of cue validity seem to be more robust for localization and identification tasks. Mondor and Zatorre (1995) investigated spatial cue validity in a soundfield for identification of a 1000-Hz pure tone and a three-tone harmonic complex having a fundamental frequency of 1000 Hz. They found that accuracy was not affected by cue validity, but response times were faster for valid cues than for invalid cues. The plot of response time as a function of spatial location yielded a filterlike function, providing some evidence for spatial tuning. Spence and Driver (1994) also measured the effect of valid versus invalid spatial cues for the tasks of localization and identification in a soundfield. Listeners responded faster for valid cues than for invalid cues on the localization task (front/back judgment) and on the identification task (375 Hz versus 345 Hz). Error rates did not vary with cue validity for localization. A significant cue validity effect was reported for identification accuracy, although the error rates for invalid cues were only 1.5 percentage points higher than for valid cues. Schroger (1993) measured both response time and accuracy in a Go (response)/NoGo (no response) localization task in which Go and NoGo stimuli differed in frequency. The effect of valid versus invalid spatial cues was examined in a soundfield while event-related potentials were simultaneously measured. Localization accuracy for validly cued conditions and invalidly cued conditions was not different. Response time, however, was significantly faster for validly cued conditions than for invalidly cued conditions. Quinlan and Bailey (1995) found significant effects for localization in response time and accuracy measures under headphones. Localization was performed faster and with fewer errors when the cue was valid than when the cue was invalid. Bedard *et al.* (1993) also reported significantly faster response times for valid cues than for invalid cues for a localization task performed under headphones. However, the results of Bedard *et al.* can be explained by response priming because the listener's right finger pressed the right button for stimuli presented to the right ear and the left finger pressed the left button for stimuli presented to the left ear. In response priming, the cue activates a localization response that is appropriate for valid trials, but inappropriate for invalid trials because the localization response parallels stimulus presentation.

The studies discussed above consistently report cue validity effects for identification and localization on the response time measure. The effects on accuracy are mixed. Of the studies that measured identification or localization accuracy, two found no validity effects (Mondor and Zatorre, 1995; Schroger, 1993), another found an extremely small effect of 1.5 percentage points (Spence and Driver, 1994), and another found a significant effect of 7.2 percentage points for data collected under headphones (Quinlan and Bailey, 1995). Error rates in many of these studies (Mondor and Zatorre, 1995; Quinlan and Bailey, 1995; Schroger, 1993) were relatively low and a ceiling effect may have obscured or reduced cue validity effects for accuracy.

In all of the studies above, the sound to be attended to was played in isolation. It is possible that the relatively small and mixed effects for accuracy provided by spatial tuning in those studies were due to the fact that the signal was played in quiet. Spatial tuning would seem to be more important in multi-source environments than in single-source environments. The ''cocktail party problem'' was originally described by Cherry (1953) as the problem of understanding what a single talker is saying in the presence of other competing talkers. One of the factors Cherry identified as contributing to the solution of the cocktail party problem is that the sources come from different spatial locations. Most of the work on the cocktail party problem has focused on binaural analysis (cf. Yost, 1997). However, recent soundfield masking studies have suggested that large listening advantages may occur in multi-source environments that cannot be attributed to binaural analysis as it is usually thought of, but rather appear to be due to perceptual effects related to grouping and segregation. In particular, large listening advantages can occur when the signal is masked by a stimulus that causes large amounts of ''informational masking.'' Informational masking (e.g., Pollack, 1975; Watson *et al.*, 1976; Watson, 1987; Neff and Green, 1987; Lutfi, 1989) is thought to be due to uncertainty and reflects central rather than peripheral limitations. Kidd *et al.* (1998) used a pattern identification task to evaluate the effect of spatial separation of sources on masking. Listeners were trained to identify six frequency patterns. Either Gaussian noise or a multi-tone informational masker masked the patterns. Spatial separation of signal and masker provided very little advantage in the Gaussian noise masker, except at high frequencies due to the head-shadow effect. For the informational masker, however, large improvements in performance were found due to spatial separation for both low and high frequencies. For mid-frequencies, where neither interaural time nor interaural intensity differences provide strong cues to localization, smaller advantages were observed. One possible explanation for these results is the existence of a spatial filter that can be tuned to the signal location. It yields improved signal identification performance when the masker is outside of the pass band, at a different location, than when the masker is presented at the same location as the signal. That study was not intended to examine spatial tuning directly. However, the results suggest that a spatially tuned filter would help the listener select and attend to the target source in a multi-source environment.

Based on the preceding discussion, we believe that it is possible that stronger spatial tuning effects will be found in masked conditions than in quiet, particularly if the masker is informational in nature. Therefore, we designed an experiment in which accuracy and response time for signal identification were measured in an informational masker presented in a soundfield environment, using the probe-signal method. Performance was compared in two conditions: (1) the signal location expected by the listener and (2) the signal location unexpected by the listener.

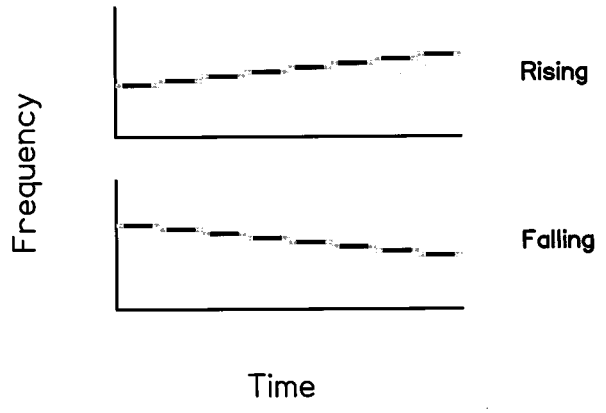

FIG. 1. Schematics of the two signals in spectrogram form. Lighter shading at the onset and offset of each burst indicates the gating.

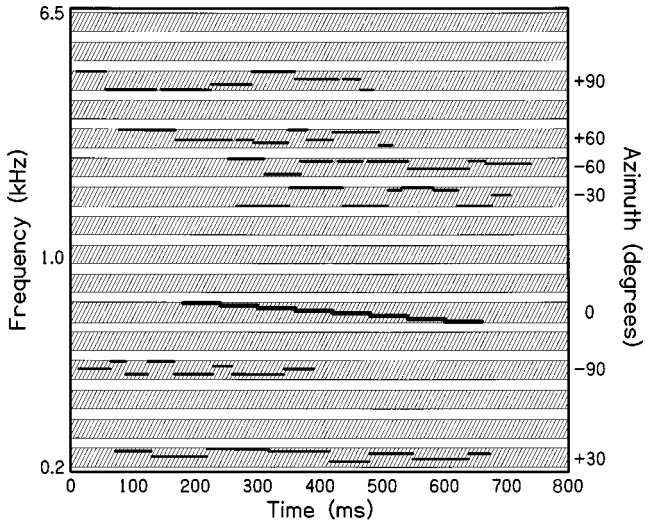

FIG. 2. Schematic of one possible stimulus interval, containing six masker components and the falling signal (in bold, within the frequency band labeled 0° on the right ordinate) in spectrogram form. The hatched areas represent the 16 possible frequency bands. The right ordinate indicates the azimuth at which each component was presented for one possible stimulus interval.

II. METHODS

A. Listeners

The listeners were 12 young adults between the ages of 20 and 31. All had normal hearing, as measured by conventional audiometry, and defined by pure-tone thresholds less than or equal to 20 dB HL at 250–8000 Hz in each ear. The difference in thresholds between ears at any frequency was 10 dB or less. Listeners were paid for their participation. All data from each listener were collected in two 2-h sessions, including rest breaks.

B. Signals

The signal was comprised of eight contiguous tone bursts of 60 ms each (including a 10-ms rise/fall). The frequencies of the eight tone bursts were arranged to make either a rising or falling frequency pattern, as shown in the schematic in Fig. 1. The frequency step between successive tone bursts was constant at 2% of the center frequency, resulting in a total range of 14% of the center frequency. One of four logarithmically spaced, orthogonal frequency bands was used to contain the signal. The center frequencies of the four consecutive bands, spaced by a ratio of 1.25, were 420, 525, 656, and 820 Hz. Each band had a width of 14% of its center frequency. The signal band was picked randomly from these four bands. Once the signal band was chosen, the two adjacent bands, one above and one below, were not permitted to be a masker band. These particular frequency bands were chosen for the signal because (1) they contained frequencies for which localization accuracy is high; and (2) these bands allowed masker components to occur below the signal, as well as above (although the probability of masker components occurring above the signal was greater than below).

C. Maskers

Six masker components were generated. Each component was comprised of eight contiguous tone bursts, varied randomly in duration between 20 and 100 ms (including a 10-ms rise/fall). Duration was randomly varied in order to deter the masker and signal components from being perceptually grouped. Synchronous onset/offset of different frequency components tends to promote perceptual grouping of the components, while asynchronous onset/offset promotes perceptual segregation (cf. Bregman and Pinker, 1978; Dannenbring and Bregman, 1978; Darwin and Ciocca, 1992). Informal listening of the stimuli with synchronous onset/offset resulted in the perception of one or two sound sources, when in fact there were seven sources. When masker burst duration was varied, as above, a diffuse sound source was perceived. Since the goal was to simulate an environment in which sounds originated from multiple sources, we chose to use asynchronous bursts. A schematic of the maskers with the falling signal is shown in Fig. 2. Each masker component, like the signal, was contained within a frequency band. The 16 available frequency bands were spaced logarithmically by a ratio of 1.25 and ranged in center frequency from 215 to 6112 Hz (including the four signal bands). On each presentation, 6 of the 16 frequency bands were chosen randomly to contain a masker component, with the constraint that the signal band and the two adjacent bands could not be chosen in order to keep energetic masking to a minimum. For each component, the frequency of each burst was chosen randomly from one of eight, linearly spaced, discrete frequencies within the band. The eight discrete frequencies were placed at increments of 2% of the center frequency, similar to the signals. The maskers were constructed in this way so that they were as similar to the signals as possible, but it was highly unlikely that one of them formed the same exact spectro-temporal pattern as either of the signals. This type of masker has been shown to be highly ''informational'' in nature because of the similarity in structure between signal and masker components (Kidd and Mason, 1997).

D. Procedures

1. Setting

The experiment took place in a soundfield located in a quiet room. The soundfield was intended to simulate a quiet

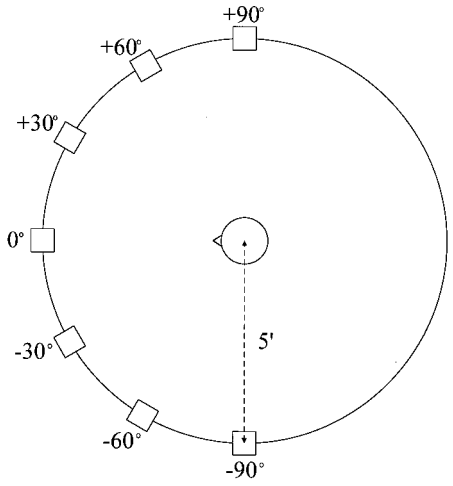

FIG. 3. Schematic of the soundfield. The listener's head is depicted at the center of the circle, facing 0°. The speakers are represented by the squares.

living room environment with a relatively low reverberation time of approximately $\frac{1}{4}$ s. The soundfield consisted of seven speakers, placed 30 degrees apart, in a semicircle located 5 ft in front of the listener (see Fig. 3). Speaker locations were at 0, ±30, ±60, and ±90 degrees azimuth (+ indicating speakers to the right of the listener, − indicating speakers to the left). The speakers were labeled with the numbers 1–7 so that the listener could easily identify and focus attention on a particular speaker. Speakers were numbered sequentially from #1 at 90 degrees to the left to #7 at 90 degrees to the right.

2. Stimulus presentation and generation

The signal was presented to one of the seven speakers and six masker components were presented one each to the remaining speakers. Therefore, on every trial each speaker played either a signal or one masker component (see Fig. 2, *right ordinate*). The maximum possible duration of a masker component was 800 ms (if each burst were 100 ms long) and therefore the stimulus interval was 800 ms long. Stimulus onset was defined as the beginning of this 800-ms interval, whether or not any masker or signal components began at the onset of the interval. The signal, which was 480 ms long, was randomly placed within the stimulus interval; signal onset varied randomly between 0 and 320 ms following stimulus onset. Each masker component's onset was randomly chosen between zero and the last possible value in order for the component to finish playing by the end of the stimulus interval.

The stimulus tones were generated digitally at a 50-kHz sampling rate. Stimuli were sent to a 16-bit, 8-channel D/A converter, a low-pass filter with cutoff at 20 kHz, and programmable attenuators. They were then sent to power amplifiers and played through the speakers. A look-up table of correction values was constructed for each speaker based on its impulse response, in order to flatten and match the effective response of each speaker. The level of each tone burst was modified digitally with use of the look-up table, based on the tone's frequency and assigned speaker. The system was calibrated to result in a tone burst level of 85 dB SPL at a distance of 5 ft. After correction, the desired tone burst level was obtained by further attenuation with the programmable attenuators. Therefore, all stimulus levels are specified in the absence of the room and the listener. Each masker component burst was presented at a fixed level of 53 dB SPL. Signal burst levels were held constant throughout data collection and were adjusted individually for each listener (see Sec. II D 5).

3. Task

The task was one-interval, two-alternative forced-choice identification. Response time was also measured. At the start of each block of trials, the experimenter instructed the listener to focus auditory attention on one speaker for the entire block. Throughout data collection listeners were asked to keep their heads stationary and straight ahead at 0 degrees. A block of trials began when the listener pushed a button on the response box. A trial began with a warning light. The stimulus was played 800 ms following the warning light. One of the signals—rising or falling—was randomly presented on every trial. Listeners identified the signal as rising or falling by pressing one of two response box buttons labeled with the schematic of each signal. Response time was calculated from signal onset to a response button push. Listeners were instructed to use the left forefinger or thumb to indicate the rising signal and the right forefinger or thumb to respond with the falling signal. They were also informed that their first response priority was correct identification of the signal and the second priority was a fast response time. When a response button was depressed, the light directly above it was illuminated to alert the listener that the response was received. If the light did not turn on (the computer did not receive the response due to a partially depressed button, for example), the response time would be artificially delayed. In this situation, the listener was instructed to press a third button, which put an error code in the data file so that the trial would not be analyzed. The allowable response interval began 60 ms following the onset of the signal (after the first signal burst) and ended 2100 ms following the offset of the stimulus interval. Any responses outside of this range were discarded and the listener was notified by a light that indicated the response was too fast or slow; no feedback was provided for response times within the valid range. Correct answer feedback for identification was provided after each response via the lights above the two response buttons.

4. Conditions

The experiment used a multi-probe variation of the probe-signal method (Dai *et al.*, 1991). The stimulus dimension varied was signal location. Data were collected for two conditions: control and experimental. For both conditions, the listener was asked to direct auditory attention to one of the speakers for the entire block of trials (the speaker number was specified by the experimenter at the start of each block). In the control condition, the signal was played at the specified speaker in 100% of trials. The control condition was run separately at each of the seven speakers in random order. Each block contained between 18 and 22 trials (the exact

number of trials was controlled by the experimenter). In the experimental condition, the listener was instructed to direct attention to the 0-degree location for the entire block. Each block contained 64 trials. The signal was played at 0 degrees in 75% of trials (target). In the remaining 25% of trials, the signal was played at one of the six remaining speakers chosen randomly (probe). Trials that contained probes were randomly distributed within the block. The listeners were aware of the two conditions and the fact that in the experimental condition, signals would occasionally be presented at locations other than the attended location. This information was provided in order to counteract the use of a strategy in which unexpected signals are ignored because the listener was led to believe that only expected signals would be presented. The two-alternative forced-choice task was used to deter the use of this strategy also. A response was required on every trial, and therefore the listener could not withhold a response when the signal occurred at an unexpected location.

For both the control condition and the probes of the experimental condition, approximately 40 trials were presented at each speaker. Between 672 and 816 target trials were presented in the experimental condition at 0 degrees. In order to obtain an equal number of control and probe trials at each speaker (other than 0 degrees), approximately three times as many trials were run in the experimental condition than in the control condition, since only 25% of the trials were probes in the experimental condition. Therefore the control condition blocks contained significantly fewer trials than the experimental condition so that they could be roughly alternated with blocks of experimental condition (sometimes two experimental blocks were run in a row). Therefore, any learning effects equally affected both conditions.

5. Training

All training was completed with an expected signal location. Training began with a 20-trial block of signal identification in quiet at 0 degrees (response time not measured). The level of each signal burst was 70 dB SPL. If performance of at least 90% correct was obtained, signal identification in quiet with response time was measured. Each block contained ten trials. Seven blocks were run—one at each speaker in random order. This stage of training gave the listeners more practice with signal identification, but more importantly it gave them practice with the response time measurement. If identification performance was maintained at 80%–90% correct or greater, listeners moved on to the third stage of training.

In the third and last part of training, signal identification and response time were measured in the presence of the maskers. Each block consisted of between 10 and 22 trials, and signal location was randomly varied between blocks. Initially, the signal burst level was fairly high (60 to 75 dB) so the listener could easily hear the signal in the presence of the maskers. The level was lowered gradually in subsequent blocks until performance between 65% and 85% correct was achieved (usually eight to nine blocks). This level was fixed for subsequent data collection in order to avoid ceiling or floor effects. The average percent correct performance at the end of training was 77.0%. Listeners' signal burst levels ranged between 20 and 35 dB SPL, with a median of 29 dB SPL.

A total of 17 listeners began the experiment. Five of those listeners did not complete data collection due to an inability to identify the signals in quiet with greater than 80% accuracy, even toward the end of training. Some scores were at chance, but most ranged between 60% and 80% correct. These listeners may have been able to learn the task, but due to time constraints they were released from the experiment.

III. RESULTS

Response times for trials with incorrect signal identification were not included in the results. The 12 listeners who completed the experiment could easily perform the signal identification task in quiet with very little practice. They progressed through the training stage in approximately 15 to 20 min. When the data from all 12 listeners, all speakers, and both conditions were pooled (training data not included), there were no instances in which a response occurred too early (before the second burst of the signal). Only 0.1% of response times occurred too late (after the time limit of 2100 ms following stimulus offset) and 0.3% of responses were thrown out due to difficulty with a response button. The left hand pushed the rising signal response button, while the right hand pushed the falling signal response button. The data were therefore analyzed to check for differences in response time between the hands. The average response time was 884 ms for the rising signal and 889 ms for the falling signal, which was not significantly different ($p=0.73$) on a paired-sample *t*-test. Accuracy differences were also examined between the two signals to be sure that one signal was not more identifiable than the other was. The overall percent correct was 87% for the rising signal and 84% for the falling signal, which was also not significantly different ($p=0.35$) on a paired-sample *t*-test. Since there were no differences between the signals, data were pooled across the signals for the remaining analysis. In general, percent correct scores increased during the course of the experiment due to practice. The average score at the end of training was 77.0% correct, while the average of all control condition scores was 87.2% correct. This learning effect should have little influence on the data comparisons since the collection of experimental data and control data at each speaker was counterbalanced over time. The Pearson correlation coefficient between all accuracy and response time data was 0.02 and was not significant ($p=0.81$). Therefore, accuracy and response time will be discussed independently.

Mean accuracy data are shown in Fig. 4. Accuracy in percent correct is plotted as a function of signal azimuth. Data points represent the mean across listeners. The triangles are the control condition while the squares are the experimental condition. Error bars are ± 1 standard error. Mean response time data are shown in Fig. 5. Response time is plotted as a function of signal azimuth. The triangles represent the control condition and the squares represent the experimental condition. The error bars are ± 1 standard error.

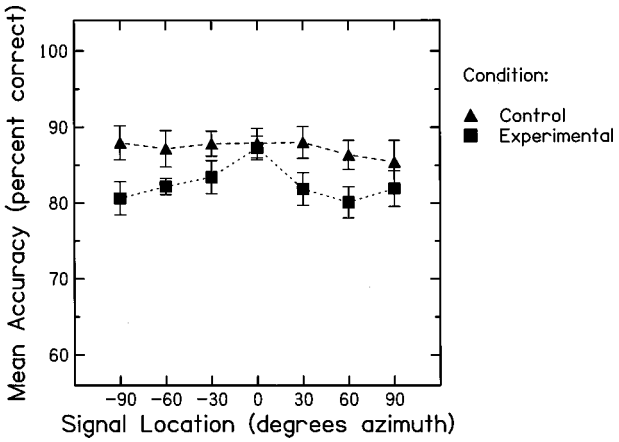

FIG. 4. Mean accuracy in percent correct as a function of signal azimuth in degrees. The control condition is indicated by triangles and the experimental condition is indicated by squares. Error bars are ±1 standard error.

In the control condition, accuracy is fairly constant (±2 percentage points) across the seven speakers. Response time in the control condition is also fairly constant across signal location (±35 ms). The condition categories were transformed from control/experimental to expected/unexpected for the statistical analysis; in the latter arrangement, the value at 0 degrees azimuth in the experimental condition was classified as expected along with all of the control data, and the remaining experimental data were classified as unexpected. A one-factor, repeated measures analysis of variance was performed on the expected signal location data, for accuracy and response time separately. The results revealed no significant main effect of signal location on accuracy ($p = 0.96$) or on response time ($p = 0.61$). These results suggest that neither accuracy nor response time performance was influenced by azimuth alone. Factors such as individual speaker differences and/or room acoustics that may have varied depending on speaker position did not influence the data. It also suggests that performance at the expected 0-degree location in the experimental condition is comparable to performance at other expected locations in the control condition. This indicates that factors other than spatial attention, such as the number of trials per block or the structure of the blocks in the experimental condition (i.e., the presence of probes), did not change performance at the 0 degree expected signal location, relative to other expected locations in the control condition. The results are also consistent with the assumption that the listeners followed the instruction to focus attention at 0 degrees in the experimental blocks. If the listeners diffused their spatial attention so that it covered a larger spatial area due to the existence of probe trials, performance at 0 degrees might be poorer than in the control condition in which the signals were presented at the expected location in 100% of trials.

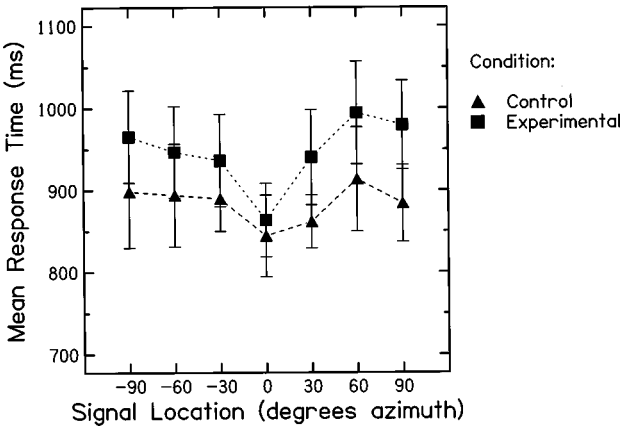

FIG. 5. Mean response time in ms as a function of signal azimuth in degrees. The control condition is indicated by triangles and the experimental condition is indicated by squares. Error bars are ±1 standard error.

The plot of accuracy in the experimental condition reveals a shallow, filterlike function with best performance at 0 degrees azimuth. However, a one-factor, repeated measures analysis of variance on the experimental accuracy data revealed no significant main effect of signal location ($p = 0.06$). The plot of response time performance in the experimental condition appears to take the form of an inverted, shallow filter with the quickest responses at 0 degrees. A one-factor, repeated measures analysis of variance performed on the experimental response time data revealed a significant main effect of signal location ($p < 0.001$). Duncan's multiple range *post hoc* test revealed that response time performance at the 0-degree location was significantly different from all other locations, and +60 degrees was different from both +30 degrees and −30 degrees. All other locations were not significantly different. The response time at 0 degrees was 73 to 131 ms faster than at other locations. The +60-degree location was slower than +30 degrees and −30 degrees by 54 and 58 ms, respectively.

Comparison of accuracy performance between the two conditions reveals a decrease in accuracy for the unexpected signal locations (squares at locations other than 0 degrees) as compared to expected signal locations (all triangles and square at 0 degrees). The average decrease in performance was 5.6 percentage points. For the statistical analysis, the condition factor was transformed from control/experimental to expected/unexpected. A two-factor, repeated measures analysis of variance (general linear models procedure) was performed on the accuracy data to test for the effects of signal location and condition. The main effect of condition was significant ($p < 0.01$). The main effect of signal location was not significant ($p = 0.92$) and the interaction between the signal location and condition was also not significant ($p = 0.94$).

Comparison of response time performance between the conditions reveals an average increase for unexpected locations relative to expected locations of 78.5 ms. For the statistical analysis the conditions were classified, as above, into expected and unexpected signal location. A two-factor, repeated measures analysis of variance (general linear models procedure) was performed on the response time data in order to test for an effect of signal location and condition. The main effect of condition was significant ($p < 0.01$). The main effect of signal location was not significant ($p = 0.16$), nor was the interaction between signal location and condition ($p = 0.85$).

IV. DISCUSSION

Mean accuracy at unattended signal locations was 5.6 percentage points poorer than at attended signal locations. Mean response time performance at unattended signal locations was 78.5 ms slower than at attended locations. When the signal location was expected, performance was significantly more accurate and faster than when the signal location was unexpected. The effect of attention did not appear to decrease gradually as the actual signal location moved further away in azimuth from the expected signal location. Performance at ± 30, ± 60, and ± 90 degrees was essentially equal. However, the ± 30-degree positions may be on the skirts of an attentional filter and the slopes might become apparent if locations at ± 15 degrees, or other small increments in azimuth are investigated.

The average increase in response time and decrease in accuracy for unattended signal locations relative to attended is larger than found in previous research. For identification, response time differences were 22 to 67 ms in the Mondor and Zatorre study, and 18 to 34 ms in the Spence and Driver study, depending on the length of the cue-signal interval. Neither study found an effect of attention on accuracy. This could be the result of a ceiling effect since accuracy was very high, particularly in the Mondor and Zatorre study. In the previous studies, location was cued on a trial-by-trial basis and was randomly varied within a block of trials. In this experiment, listeners focused attention at one location for a block of trials, which may have enabled a stronger lock of attention at that location. This may be characterized by either a narrower attentional filter or less attentional wandering; either case would result in better performance at the focus of attention and poorer performance at unattended locations, resulting in a larger difference between attentional conditions. Absolute response times were also longer in the current study—840 to 1000 ms as compared to a range of 580 to 760 ms reported in the two studies mentioned earlier. Longer signal length and the type of identification required (a temporal-frequency pattern) both served to increase absolute response times in the current study.

It was also anticipated that informational maskers would produce different results than those previously obtained in a quiet background. The task was more challenging than in quiet, due to the uncertainty caused by the informational masking. These maskers were structurally very similar to the signal, so that each spatial location contained a spectro-temporal pattern of identical proportional range. The uncertainty originated from the fact that any one of the seven frequency bands that contained stimuli on any given trial could have contained the signal. The listener needed to discern a particular frequency pattern in order to hone in on the signal band. In quiet, a listener could potentially discern the signal patterns with only the first two bursts (120 ms), but for human listeners to approach such performance was unlikely due to the presence of the informational maskers. The listeners most likely required nearly the entire pattern to make an accurate decision regarding the signal due to the uncertainty; this may have contributed to the longer absolute response times.

The larger attentional effects for both response time and accuracy found in this study were not surprising given that there were multiple sound sources and high uncertainty. When the listener discovered that the signal was not presented at the expected location, there were six other sources to search through in order to find the signal. All but one of the seven sources contained an informational masker component that was structurally similar to the signal. One might expect the attentional effect on performance to be even larger than reported here, given the amount of time it would take to search through each of the remaining six sources for the signal. However, listeners likely used a more time-efficient strategy in which attention was diffused or unfocused when the stimulus at the attended speaker was categorized as a masker. This strategy takes more time than if the signal is played at the expected location, but it does not take as long as searching through each source separately. This strategy could also account for the decrement in accuracy for unexpected locations. Diffused attention results in an effective increase in signal-to-noise ratio, because attention is directed at all the sources—maskers and signal. The size of the accuracy decrement was not larger because diffusing attention to find the signal takes less time than searching each source, and therefore the listener could catch the tail end of the signal and perform the identification based on the last several signal bursts. However, the 5.6 percentage point advantage likely translates into a significant increase in effective signal level, given that psychometric functions in the presence of informational masking are generally much more shallow than those in the presence of energetic maskers (Kidd *et al.*, 1995, 1998; Freyman *et al.*, 1999).

The use of informational, multi-source masking to investigate auditory spatial attention and its effect on signal identification provided evidence for the existence of a spatial auditory filter. The probe-signal method, applied to the spatial dimension, effectively revealed this spatial tuning, as it has revealed attentional tuning in the frequency and temporal domains in previous research. The results of this experiment suggest that the ability to utilize a spatial auditory filter is advantageous in complex, multi-source, and highly uncertain environments. The employment of such a filter results in something equivalent to an increase in the signal-to-noise ratio. Masker components at locations outside of the focus of attention are essentially attenuated. Although experiments performed in quiet conditions also revealed convincing evidence of spatial filtering in audition, that evidence was mainly in the response time domain for identification or localization tasks; there was no strong effect on accuracy. The task studied here was more complex and challenging and therefore revealed the accuracy effects. Thus, our conclusion is that the use of an auditory spatial filter is more advantageous in highly uncertain, multi-source environments than in less complex listening environments.

ACKNOWLEDGMENTS

This work was supported by Grants Nos. DC00100 and DC3281 from NIH/NIDCD, by the ONR-managed MURI #Z883402, by the Dudley Allen Sargent Fund, and by the Boston University Hearing Research Center. The authors are grateful to Christine Mason for comments, suggestions, pro-

gramming assistance, and review of the manuscript, and to Melanie Matthies for assistance with statistical analyses.

Bedard, M. A., Massioui, F. El, Pillon, B., and Nandrino, J. L. (**1993**). ''Time for reorienting of attention: A premotor hypothesis of the underlying mechanism,'' Neuropsychologia **31**, 241–249.

Bregman, A. S., and Pinker, S. (**1978**) ''Auditory streaming and the building of timbre,'' Can. J. Psychol. **32**, 19–31.

Buchtel, H. A., and Butter, C. M. (**1988**). ''Spatial attentional shifts: Implications for the role of polysensory mechanisms,'' Neuropsychologia **26**, 499–509.

Cherry, E. C. (**1953**). ''Some experiments on the recognition of speech with one and two ears,'' J. Acoust. Soc. Am. **25**, 975–979.

Dai, H., and Wright, B. A. (**1995**). ''Detecting signals of unexpected or uncertain durations,'' J. Acoust. Soc. Am. **98**, 798–806.

Dai, H., Scharf, B., and Buus, S. (**1991**). ''Effective attenuation of signals in noise under focused attention,'' J. Acoust. Soc. Am. **89**, 2837–2842.

Dannenbring, G. L., and Bregman, A. S. (**1978**). ''Streaming vs. Fusion of sinusoidal components of complex tones,'' Percept. Psychophys. **24**, 369–376.

Darwin, C. J., and Ciocca, V. (**1992**). ''Grouping in pitch perception: Effects of onset asynchrony and ear of presentation of a mistuned component,'' J. Acoust. Soc. Am. **91**, 3381–3390.

Freyman, R. L., Helfer, K. S., McCall, D. D., and Clifton, R. K. (**1999**). ''The role of perceived spatial separation in the unmasking of speech,'' J. Acoust. Soc. Am. **106**, 3578–3588.

Greenberg, G. Z., and Larkin, W. D. (**1968**). ''Frequency-response characteristic of auditory observers detecting signals of a single frequency in noise: The probe-signal method,'' J. Acoust. Soc. Am. **44**, 1513–1523.

Hafter, E. R., Schlauch, R. S., and Tang, J. (**1993**). ''Attending to auditory filters that were not stimulated directly,'' J. Acoust. Soc. Am. **94**, 743–747.

Hill, N. I., Bailey, P. J., and Hodgson, P. (**1997**). ''A probe-signal study of auditory discrimination of complex tones,'' J. Acoust. Soc. Am. **102**, 2291–2296.

Kidd, Jr., G., and Mason, C. R. (**1997**). ''Pattern-like maskers increase informational masking in a nonspeech identification task,'' program of the 20th Annual Midwinter Research Meeting of the Association for Research in Otolaryngology.

Kidd, Jr., G., Mason, C. R., and Rohtla, T. L. (**1995**). ''Binaural advantage for sound pattern identification,'' J. Acoust. Soc. Am. **98**, 1977–1986.

Kidd, Jr., G., Mason, C. R., Rohtla, T. L., and Deliwala, P. S. (**1998**). ''Release from masking due to spatial separation of sources in the identification of non-speech auditory patterns,'' J. Acoust. Soc. Am. **104**, 422–431.

Lutfi, R. A. (**1989**). ''Informational processing of complex sound. I. Intensity discrimination,'' J. Acoust. Soc. Am. **86**, 934–944.

Macmillan, N. A., and Schwartz, M. (**1975**). ''A probe-signal investigation of uncertain-frequency detection,'' J. Acoust. Soc. Am. **58**, 1051–1058.

Mondor, T. A., and Zatorre, R. J. (**1995**). ''Shifting and focusing auditory spatial attention,'' J. Exp. Psychol. **21**, 387–409.

Neff, D. L., and Green, D. M. (**1987**). ''Masking produced by spectral uncertainty with multicomponent maskers,'' Percept. Psychophys. **41**, 409–415.

Pollack, I. (**1975**). ''Auditory informational masking,'' J. Acoust. Soc. Am. Suppl. 1 **57**, S5.

Posner, M. I. **(1978)**. *Chronometric Explorations of Mind* (Erlbaum, Hillsdale, NJ).

Quinlan, P. T., and Bailey, P. J. (**1995**). ''An examination of attentional control in the auditory modality: further evidence for auditory orienting,'' Percept. Psychophys. **57**, 614–628.

Scharf, B., Quigley, S., Aoki, C., Peachey, N., and Reeves, A. (**1987**). ''Focused auditory attention and frequency selectivity,'' Percept. Psychophys. **42**, 215–223.

Schlauch, R. S., and Hafter, E. R. (**1991**). ''Listening bandwidths and frequency uncertainty in pure-tone signal detection,'' J. Acoust. Soc. Am. **90**, 1332–1339.

Schroger, E. (**1993**). ''Event-related potentials to auditory stimuli following transient shifts of spatial attention in a Go/Nogo task,'' Biol. Psychol. **36**, 183–207.

Spence, C. J., and Driver, J. (**1994**). ''Covert spatial orienting in audition: exogenous and endogenous mechanisms,'' J. Exp. Psychol. **20**, 555–574.

Watson, C. S. (**1987**). ''Uncertainty, informational masking and the capacity of immediate auditory memory,'' in *Auditory Processing of Complex Sounds*, edited by W. A. Yost and C. S. Watson (Erlbaum, Hillsdale, NJ).

Watson, C. S., Kelly, W. J., and Wroton, H. W. (**1976**). ''Factors in the discrimination of tonal patterns: II. Selective attention and learning under various levels of stimulus uncertainty,'' J. Acoust. Soc. Am. **60**, 1175–1181.

White, L. J., and Carlyon, R. P. (**1997**). ''Detection of signals having expected and unexpected temporal structures,'' Hear. Res. **112**, 141–146.

Wright, B. A., and Dai H. (**1994**). ''Detection of unexpected tones in gated and continuous maskers,'' J. Acoust. Soc. Am. **95**, 939–948.

Wright, B. A., and Dai H. (**1998**). ''Detection of sinusoidal amplitude modulation at unexpected rates,'' J. Acoust. Soc. Am. **104**, 2991–2996.

Yost, W. A. (**1997**). ''The cocktail party problem: Forty years later,'' in *Binaural and Spatial Hearing in Real and Virtual Environments*, edited by R. A. Gilkey and T. R. Anderson (Erlbaum, Hillsdale, NJ).

Effects of ipsilateral and contralateral precursors on overshoot

Sid P. Bacon[a] and Li Liu
Psychoacoustics Laboratory, Department of Speech and Hearing Science, Arizona State University, Tempe, Arizona 85287-1908

(Received 14 October 1999; revised 24 April 2000; accepted 8 July 2000)

Overshoot is defined as the decrease in threshold as a brief signal is moved from the beginning to near the temporal center of a longer duration, broadband noise masker. Overshoot can be reduced when another noise (a precursor) is presented just prior to the masker. The purpose of the present investigation was to follow up on a recent psychophysical study which showed that overshoot could be reduced by a precursor presented to the ear contralateral to that receiving the masker and signal. The signal was a 20-ms, 4000-Hz tone that was presented at the beginning or in the temporal center of a 400-ms broadband noise masker. In the first experiment, a 200-ms broadband precursor was presented either to the ipsilateral or to the contralateral ear. The ipsilateral precursor reduced overshoot for all ten subjects, but the contralateral precursor reduced overshoot for only four of the ten subjects. In a supplementary experiment, the contralateral precursor failed to reduce overshoot in a new group of five subjects, both when tested with supra-aural headphones and with insert earphones. In the second experiment, the four subjects who showed an effect of the contralateral precursor in experiment 1 were tested under conditions where the bandwidth of the precursor was manipulated, resulting in either a narrow-band precursor centered at 4000 Hz, a low-band precursor with energy primarily below 4000 Hz, or a high-band precursor with energy primarily above 4000 Hz. There was a tendency for the effectiveness of the ipsilateral and contralateral precursors to be affected similarly (though to different degrees) by changes in the spectral content of the precursor. These results suggest that the effect of the contralateral precursor is not due to a timing cue, and that the processing underlying the effectiveness of ipsilateral and contralateral precursors may be largely the same. [S0001-4966(00)03710-3]

PACS numbers: 43.66.Dc, 43.66.Mk, 43.66.Ba [DWG]

I. INTRODUCTION

The threshold for a brief signal masked by a broadband noise is often higher when that signal occurs at the beginning of the masker than when it occurs later in time. This effect, dubbed ''overshoot'' by Zwicker (1965a), has been the focus of a considerable amount of research (e.g., Zwicker, 1965a, b; Elliott, 1965, 1969; Fastl, 1976; McFadden, 1989; Bacon, 1990; Schmidt and Zwicker, 1991; Bacon and Smith, 1991; Carlyon and White, 1992; Overson *et al.*, 1996). Despite the concerted efforts, a satisfactory understanding of the mechanisms underlying overshoot has remained elusive.

One of the original explanations for overshoot, based on the physiological work of Smith (Smith and Zwislocki, 1975; Smith, 1977, 1979), is adaptation of auditory-nerve fibers. Although adaptation may play a role, it is clear that peripheral adaptation cannot account for the entire effect: Overshoot is typically much larger than the 3–5 dB that is predicted based on neural adaptation (e.g., Zwicker, 1965a, b; McFadden, 1989; Bacon, 1990), and it depends critically upon frequency regions outside the critical band centered at the signal frequency (Zwicker, 1965b; McFadden, 1989; Bacon and Smith, 1991; Schmidt and Zwicker, 1991; Carlyon and White, 1992).

More recently, it has been suggested that overshoot may reflect nonlinear cochlear processing (Champlin and McFadden, 1989; McFadden and Champlin, 1990; Klitzing and Kohlrausch, 1994) typically associated with the ''cochlear amplifier'' (or outer hair cells). This is based at least partly on the fact that temporary hearing loss due to aspirin ingestion (McFadden and Champlin, 1990) or acoustic overstimulation (Champlin and McFadden, 1989), as well as permanent sensorineural hearing loss (Bacon and Takahashi, 1992) significantly reduces overshoot. As noted by Klitzing and Kohlrausch (1994), however, the cochlear amplifier cannot, by itself, account for overshoot, given that the action of the amplifier is essentially instantaneous.

One way in which the cochlear amplifier might contribute to overshoot is via the influence of neurons from the medial olivocochlear system on the outer hair cells. The possibility that the efferent system might be involved with overshoot was first suggested by Schmidt and Zwicker (1991). Consistent with this possibility is the fact that the 100–200 ms that it takes the efferent system to reach its maximum effectiveness (e.g., Warren and Liberman, 1989) is similar to the time it takes masked threshold to reach its minimum (or steady-state) value (e.g., Zwicker, 1965a; Elliott, 1965; Fastl, 1976). Moreover, it has been demonstrated that activation of the efferent system can enhance the response of an auditory-nerve fiber to a tonal signal embedded in noise (Kawase and Liberman, 1993; Kawase *et al.*, 1993). Thus, it is possible that the decrease in threshold with increasing signal delay reflects the relatively slow activation of the efferent system.

Two groups of investigators have attempted to examine

[a]Author to whom correspondence should be addressed. Electronic mail: spb@asu.edu

the role of the efferent system in overshoot by measuring overshoot in patients who have undergone a vestibular neurotomy, during which the olivocochlear bundle was severed. The results from those studies have been mixed. Scharf *et al.* (1994, 1997) found little difference (<2 dB) in overshoot between the operated and unoperated ears in the two patients they tested, whereas Zeng *et al.* (2000) found consistently smaller amounts of overshoot in the operated than in the unoperated ear of the four patients they tested. Zeng *et al.* argued that the effect they observed was not due to hearing loss, which can reduce overshoot (Bacon and Takahashi, 1992), but instead was likely due to the lack of efferent involvement in the operated ear.

Recently, Turner and Doherty (1997) used a different approach to examine the possibility that the efferent system is involved in overshoot. They took advantage of the fact that a minority of the neurons from the medial olivocochlear system responds best to contralateral stimulation (Liberman, 1988), and thus attempted to activate the efferent system with a contralateral stimulus. Their stimulus (a so-called ''precursor'') was a 200-ms broadband noise whose offset preceded the onset of their 400-ms broadband masker by 10 ms. Others have used ipsilateral precursors to study overshoot (e.g., Zwicker, 1965a; McFadden, 1989; Bacon and Smith, 1991; Overson *et al.*, 1996), but unfortunately it is not possible to separate the effects of efferent stimulation from the effects of, say, peripheral adaptation when the precursor is presented to the ear receiving the signal and masker. Turner and Doherty found that their contralateral precursor reduced or eliminated overshoot by reducing the threshold for a signal near masker onset (it had no effect when the signal was in the temporal center of the masker). Inasmuch as the decline in threshold caused by the precursor reflects the same processing responsible for the decline in threshold as a signal is moved in time through a masker, their results are consistent with the possibility that the efferent system is intimately involved in overshoot.

Turner and Doherty (1997) entertained the possibility that the effectiveness of their contralateral precursor was mediated not by efferent involvement, but by the offset of the precursor providing a temporal cue for the onset of the signal (and masker). They tentatively dismissed this latter possibility, though, based on their finding that the precursor was ineffective in subjects with sensorineural hearing loss. This, however, may not be the best test of the ''timing hypothesis,'' given that those subjects did not have any overshoot to begin with, because their thresholds for the signal at masker onset were already relatively low (also see Champlin and McFadden, 1989; McFadden and Champlin, 1990; and Bacon and Takahashi, 1992). Hence, a temporal cue may not have been able to reduce those thresholds for their hearing-impaired subjects. A better way to evaluate this hypothesis would be to use a precursor that provides timing information but is otherwise unlikely to reduce the threshold for a signal at masker onset. Previous work with *ipsilateral* precursors indicates that a narrow-band precursor centered at the signal frequency is ineffective in reducing overshoot (McFadden, 1989; Bacon and Smith, 1991). If ipsilateral and contralateral precursors work in a similar fashion, then it should be possible to use a narrow-band noise precursor to determine whether or not contralateral precursors lower threshold via a timing cue.

The important findings of Turner and Doherty (1997) warrant further investigation, as they may provide new insight into the mechanisms underlying overshoot. It is important not only to replicate their results to determine the generality of their findings, but also to evaluate further the possibility that contralateral precursors reduce threshold at masker onset via a timing cue. These were the goals of the present study. The first experiment was concerned primarily with replicating the results of Turner and Doherty (1997), whereas the second experiment examined how the spectral content of ipsilateral and contralateral precursors influences their effectiveness in reducing overshoot; this enabled us to determine (1) whether the influence of the contralateral precursor was mediated via a timing cue, and (2) whether the effectiveness of ipsilateral and contralateral precursors is similarly affected by their spectral content.

II. EXPERIMENT 1: BROADBAND PRECURSORS

A. Rationale

The primary purpose of this first experiment was to replicate the results of Turner and Doherty (1997). To that end, we used conditions that were nearly identical to theirs. In addition, we included an ipsilateral precursor in order to compare the effectiveness of contralateral to ipsilateral precursors.

B. Apparatus and stimuli

All stimuli were digitally generated and produced at a 20-kHz sampling rate using a digital array processing card (TDT AP2) and digital-to-analog converter, or DAC (TDT DD1). In conditions without a precursor, the signal (quiet thresholds) or signal and masker (masked thresholds) were presented through a single channel of the DAC. When the precursor was presented to the ipsilateral ear, the precursor, masker, and signal were presented through that same single channel. When the precursor was presented to the contralateral ear, the precursor was presented through a second channel. The output of each channel was low-pass filtered at 8 kHz (TDT FT6), attenuated (TDT PA4), and routed via a headphone buffer (TDT HB6) to a TDH-49P headphone mounted in an MX/51 cushion.

The signal was a 4000-Hz tone; its duration was 20 ms. The masker was broadband noise that was generated in the frequency domain and transformed into the time domain via an inverse Fourier transform, using the SigGen software provided by TDT. It had components from 1 to 8000 Hz, and a duration of 400 ms. A new noise sample was used for each masker presentation. In the absence of a precursor, the signal was presented either at the beginning (0-ms delay) or in the temporal center (190-ms delay) of the masker; the difference between those two thresholds defines the magnitude of overshoot. The precursor was generated using the same procedures used to generate the masker; it had components from 1 to 8000 Hz, and a duration of 200 ms. A new noise sample was generated for each precursor presentation. The delay be-

tween the offset of the precursor and onset of the masker was either 0 or 10 ms. A 10-ms delay was used by Turner and Doherty (1997); the 0-ms delay was included here because, at least with ipsilateral precursors, the effectiveness of the precursor increases as its offset approaches the onset of the masker (e.g., Bacon and Smith, 1991). In the presence of a precursor, the signal was only presented at the beginning of the masker, as precursors generally have no effect on the threshold for a signal near the temporal center of a masker (e.g., Bacon and Smith, 1991; Turner and Doherty, 1997). All stimulus durations include 10-ms $\cos^2$ rise/fall times (0 to peak amplitude), and all durations and delays are determined from the 0-voltage points of the stimulus envelope.

The level of the signal was varied adaptively via the array processor. The spectrum level (N_0) of the masker and precursor was 20 or 30 dB SPL. The overall level was thus 59 or 69 dB SPL. These levels were chosen to be similar to the overall level (60 dB SPL) where Turner and Doherty (1997) found the largest effect of a contralateral precursor, and also to be similar to the levels where overshoot is typically maximal (Bacon, 1990; Overson *et al.*, 1996).

C. Procedure

Testing was completed in a single-walled, sound-attenuating chamber located within an acoustically treated room. The masker and signal were presented to the right ear of each subject. An adaptive, two-interval, forced-choice paradigm was used with a three-down, one-up decision rule that tracked 79.4% correct (Levitt, 1971). Subjects responded by pressing one of two buttons on a response panel. Lights were used to indicate when the signal might occur and to provide correct-answer feedback. The time between the two observation intervals always included 500 ms of silence. A run consisted of 12 reversals; the threshold estimate for a given run was the mean of the signal levels at the last 10 reversals. The initial step size of 5 dB was reduced to 2 dB after the second reversal. Runs were discarded on the rare occasions when the standard deviation of the threshold estimate was greater than 3 dB. Following any practice (see below), data were collected on three separate days (2 h per day). On each day all 12 conditions (eight with precursor, four without) were tested in random order, and on some days some conditions were tested more than once. Three threshold estimates, obtained on three separate days, were averaged to produce a threshold for a given condition. If the standard deviation of this average was greater than 3 dB, an additional estimate was obtained and included in the average. This continued until the standard deviation was less than 3 dB, or a total of six estimates was obtained and averaged. All thresholds obtained here had a standard deviation less than 3 dB.

D. Subjects

Ten individuals participated. Of these, six were female (S2–S5, S7, and S9) and four were male (S1, S6, S8, and S10). They ranged in age from 23–43 years, and had thresholds of 15 dB HL or lower (ANSI, 1996) for octave test frequencies from 500 to 8000 Hz. Three of the subjects (S6, the first author; S9, the second author; and S3, a laboratory associate) had prior experience as a subject in overshoot experiments. Subjects S6 and S3 did not undergo any additional practice. Subject S9 and all of the inexperienced subjects had 2 h of practice prior to data collection. The practice consisted primarily of detecting a signal at masker onset both with and without the contralateral precursor, as these were the most difficult conditions. Except for the three subjects associated with the laboratory, the subjects were paid for their participation.

E. Results and discussion

The individual results for the two different masker/precursor levels are shown separately in Figs. 1 ($N_0 = 20$ dB) and 2 ($N_0 = 30$ dB). The results are plotted in terms of the amount of overshoot without a precursor (open bars), with a contralateral precursor (hatched bars), and with an ipsilateral precursor (filled bars). (Recall that, in the presence of a precursor, threshold was only measured for the signal at the beginning of the masker, as precursors generally have no effect on the threshold for a signal near the temporal center of a long masker. Thus, overshoot is referenced to the threshold in the temporal center of the masker without a preceding precursor.) In each figure, the results in the top panel are for the 0-ms precursor–masker delay, and those in the bottom panel are for the 10-ms precursor–masker delay. The subjects are numbered according to the magnitude of their overshoot effect without a precursor at a masker spectrum level of 20 dB (Fig. 1). For the 20-dB masker, the amount of overshoot varied from 19 to 3 dB (average of 8 dB); for the 30-dB masker, it varied from 21 to 5 dB (average of 11 dB). These results are consistent with previous results, both in terms of magnitude and intersubject variability (e.g., Bacon, 1990; Schmidt and Zwicker, 1991; Bacon and Takahashi, 1992; Wright, 1995, 1997). The ipsilateral precursor reduced or eliminated overshoot at both levels for all subjects. Further, consistent with previous results (Bacon and Smith, 1991), the effect of the ipsilateral precursor was somewhat larger at the shorter precursor–masker delay. Averaged across subjects and levels, the ipsilateral precursor reduced overshoot to 1.0 and 2.5 dB at the 0- and 10-ms precursor–masker delay, respectively.

The contralateral precursor was considerably less effective at reducing overshoot. Indeed, when averaged across subjects, masker level, and precursor–masker delay, the precursor had essentially no effect. However, as can be seen in Figs. 1 and 2, there were clear differences among subjects. For the majority of subjects, overshoot either remained about the same or increased in the presence of the contralateral precursor. Although small increases (or decreases) may simply reflect measurement error, overshoot increased as much as 5–9 dB for some subjects. As noted below (Sec. IV A), this rather large increase may reflect a ''distracting'' effect of the contralateral precursor.

Although, when averaged across subjects, the contralateral precursor was ineffective, it did consistently reduce overshoot in some subjects. In two subjects, the contralateral precursor reduced overshoot in all four conditions (both levels and delays); on average, the reduction was 5.5 dB for S3, and 3.2 dB for S4. For two other subjects (S5 and S7), the

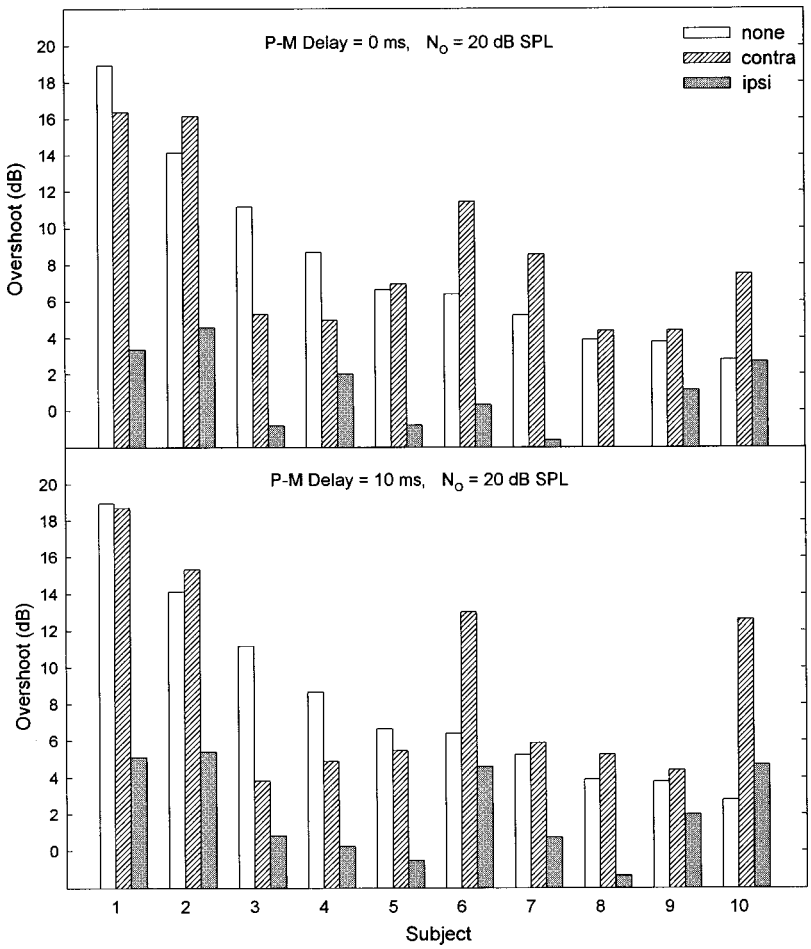

FIG. 1. Results from the ten subjects who participated in experiment 1. Overshoot for a 4000-Hz signal was measured in the absence of a precursor (open bars), in the presence of a contralateral precursor (hatched bars), and in the presence of an ipsilateral precursor (filled bars). The spectrum level of the masker and precursor was 20 dB SPL. The delay between the offset of the precursor and onset of the masker (P–M delay) was 0 ms (top panel) or 10 ms (bottom panel).

contralateral precursor reduced overshoot only at the higher level; averaged across delays, the reduction was 5.0 dB for S5 and 4.5 dB for S7. Thus, the contralateral precursor reduced overshoot in four of our ten subjects. This contrasts somewhat with the results of Turner and Doherty (1997), where the contralateral precursor decreased overshoot in all eight of the ten subjects for whom an overshoot effect (without the precursor) was observed. It is unclear why the contralateral precursor was generally less effective here than in Turner and Doherty, particularly given the fact that our conditions closely matched theirs in terms of durations, delays, frequency content, and levels. One potentially important difference between the two studies is the transducers that were used: Turner and Doherty used insert earphones, whereas we used supra-aural headphones. To determine whether differences in results across studies might be due to the type of transducer, we conducted a supplementary experiment where we recruited five new normal-hearing subjects and tested them with both supra-aural headphones (TDH-49P) and insert earphones (ER-3A). The conditions and procedures were as in experiment 1, except that an ipsilateral precursor was not included and only a 10-ms precursor–masker delay was used, as that was the delay used by Turner and Doherty. The amount of overshoot was similar to that in Figs. 1 and 2. Importantly, the contralateral precursor had little effect, regardless of the transducer. Averaged across subjects and levels, the effect of the precursor was less than 0.2 dB for both transducers. These results indicate that differences between Turner and Doherty (1997) and our experiment 1 in terms of the pervasiveness of the effect of a contralateral precursor cannot be attributed to our use of supra-aural headphones.

III. EXPERIMENT 2: SPECTRAL MANIPULATIONS

A. Rationale and method

Four out of the 15 subjects whose results were described in Sec. II E (including five in the supplemental experiment comparing the two transducers) revealed a consistent effect of the contralateral precursor. It is worth determining whether this effect is due to the presence of a timing cue provided by the precursor (and utilized effectively only by those four subjects), or whether it is due to some other type of processing, perhaps that which is revealed with an ipsilateral precursor. One way to evaluate this is by manipulating the spectral content of the precursor, as it has been shown that the effectiveness of an ipsilateral precursor is dependent upon its spectral content (McFadden, 1989; Bacon and Smith, 1991). If the contralateral precursor reduces overshoot by providing a temporal cue for the onset of the signal (and masker), this cue should be independent of the spectral content of the precursor, as long as the precursor is clearly audible. On the other hand, if the mechanism by which the contralateral precursor reduces overshoot is similar to that by which an ipsilateral precursor reduces overshoot, then the effectiveness of the contralateral precursor should depend upon its spectral content. In the present experiment, the four

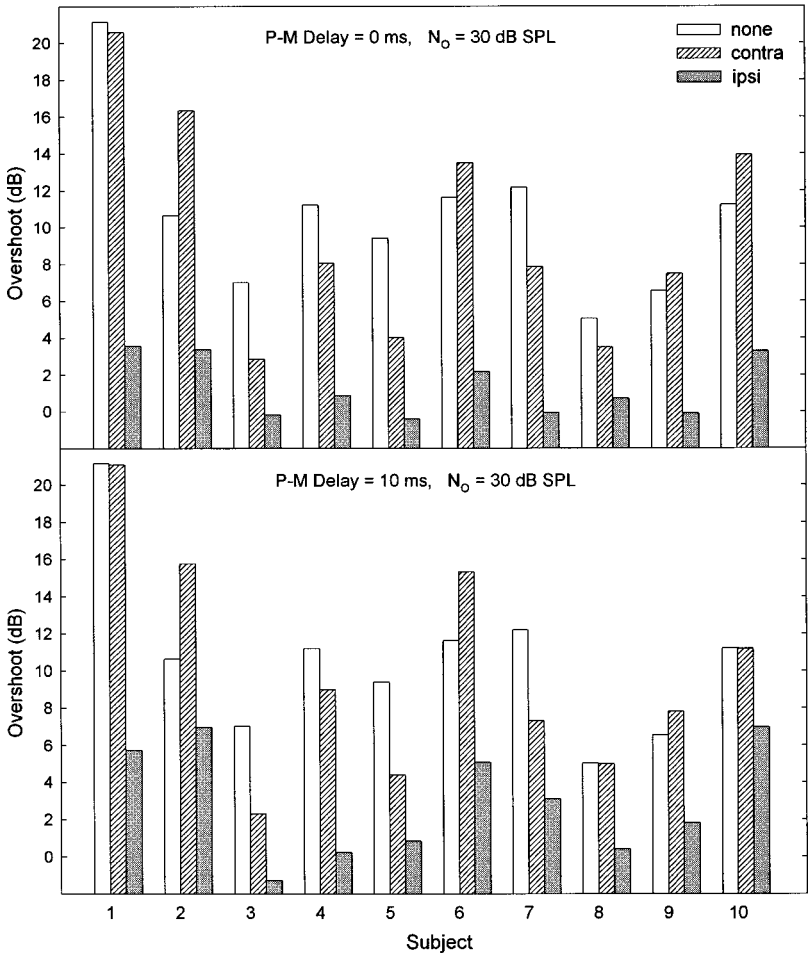

FIG. 2. As Fig. 1, except the spectrum level was 30 dB SPL.

subjects who showed an effect of a contralateral precursor in experiment 1 (S3–S5, S7) were run under the following ipsilateral and contralateral precursor conditions: narrow band (NB), low band (LB), and high band (HB). These results were compared with the no-precursor and broadband (BB) precursor conditions from experiment 1. All data were collected in one 2-h session. The standard deviations of the thresholds obtained here were all less than 3 dB.

The apparatus and stimuli were as in experiment 1. The NB precursor had components between 3800 and 4200 Hz; it was thus centered at the 4000-Hz signal frequency and was approximately the width of a critical band. The LB precursor had components between 1 and 4200 Hz. The HB precursor had components between 3800 and 8000 Hz.

The spectrum level of the masker and precursor was 20 (S3 only) or 30 dB SPL (all four subjects). The precursor–masker delay was 10 ms. The signal occurred at the beginning of the masker (0-ms delay).

B. Results and discussion

Although four subjects were tested, the results from one subject (S7) are not included. This subject alone showed a consistent *increase* in overshoot due to the bandlimited contralateral precursor, and admitted to being tired during the test session due to studying for final exams; S7's data were thus deemed unreliable. The results for the other three subjects are shown in individual panels of Fig. 3. Within each panel, the results for the contralateral precursor are given by the set of histograms on the left, whereas those for the ipsilateral precursor are given by the histograms on the right. The results are displayed in terms of overshoot (where, again, the threshold in the temporal center was obtained without a precursor). From left to right within a set of histograms, the amount of overshoot is shown for the conditions without a precursor and for the following precursor conditions: BB, HB, LB, and NB (the results without a precursor and with a BB precursor are from experiment 1). There is a relatively clear pattern to the data, and that same pattern is observed for both contralateral and ipsilateral precursors. In general, the largest effect on overshoot was produced by the BB precursor, followed in turn by the HB, LB, and NB precursors. The NB precursor had little effect on overshoot.

The results with the ipsilateral precursor confirm previous results (McFadden, 1989; Bacon and Smith, 1991) in showing that (1) narrow-band noise centered at the signal frequency is an ineffective precursor; (2) noise with energy concentrated primarily below the signal frequency is not a particularly effective precursor; (3) noise with energy concentrated primarily above the signal frequency is an effective precursor; and (4) the most effective precursors contain energy broadly distributed on both sides of the signal frequency.

The fact that the pattern of results was more or less the same for both ipsilateral and contralateral precursors is im-

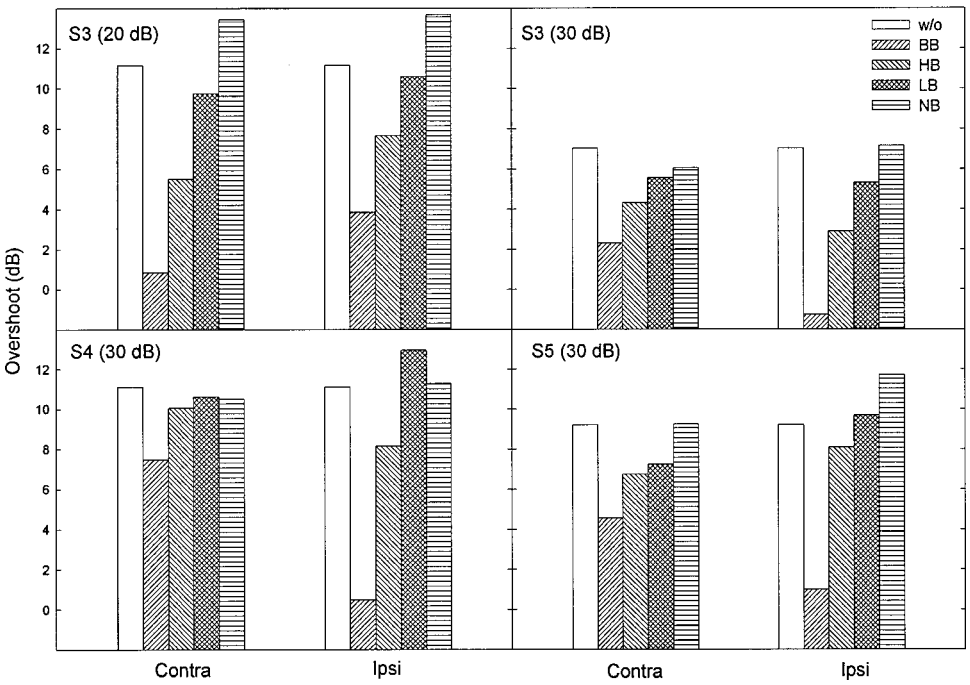

FIG. 3. Results from the three subjects who participated in experiment 3 (these are three of the four for whom the contralateral precursor reduced overshoot in experiment 1). Subject S3 was tested at masker and precursor spectrum levels of 20 and 30 dB, whereas S4 and S5 were tested only at 30 dB. Overshoot for the 4000-Hz signal is shown without a precursor and in the presence of a precursor that was either broadband (BB; 1–8000 Hz), high band (HB; 3800–8000 Hz), low band (LB; 1–4200 Hz), or narrow band (NB; 3800–4200 Hz). The results without a precursor and with the BB precursor are from experiment 1. Within a panel, the histograms on the left are for the contralateral precursor, and those on the right are for the ipsilateral precursor.

portant, as it suggests that the processing underlying the reduction in overshoot may be the same for both types. Further, because the NB (and to a somewhat lesser extent the LB) precursor was ineffective in reducing overshoot, the results strongly suggest that the effect of the precursor is not mediated via a timing cue.

IV. DISCUSSION

A. Comparisons with data in the literature

As discussed in the context of the individual experiments, the results without a precursor and those in the presence of an ipsilateral precursor were similar to those obtained previously. The main intent of the present study was to follow up on Turner and Doherty's (1997) research on the effects of a contralateral precursor on overshoot. That four of the 15 subjects tested in experiment 1 and its supplementary experiment showed a decrease in overshoot in the presence of the contralateral precursor was at least a partial replication of Turner and Doherty (1997). In their experiment, however, overshoot decreased in all eight of their ten subjects who showed a sizable overshoot in the absence of a precursor (two of their subjects were reported not to show a ''reliable overshoot at any masker level''). It is highly unlikely that the differences between the two studies in terms of the pervasiveness of the effect can be accounted for by differences in stimuli, as our stimuli were chosen to be essentially identical to theirs. The differences also cannot be attributed to the fact that they used insert earphones and we typically used supra-aural headphones: In the supplementary experiment, we tested five subjects with both insert and supra-aural phones, and found essentially no difference in performance between the two transducers.

One possibility is that some of the differences between the two studies is related to practice. In other words, it may be that it requires considerable practice for some subjects to benefit from the contralateral precursor. Turner and Doherty (1997) did not mention practice, although Turner (personal communication) has indicated that their subjects received at least 8 h of practice. Our subjects who were inexperienced with overshoot received only 2 h of practice, with the bulk of the practice focusing on detecting a signal at masker onset both with and without a contralateral precursor. It is possible that with additional training, more of our subjects would have shown an effect of the contralateral precursor. To address this possibility, four subjects for whom the contralateral precursor did not reduce overshoot participated in additional testing. For three of those subjects, thresholds were measured in the contralateral condition (10-ms precursor–masker delay) for 2 h a day on 5 separate days (all days were generally within a 2-week period). There was no evidence of a decrease in overshoot with additional practice, either within or across days. For the fourth subject (S6, the first author), who already had considerable prior listening experience with overshoot conditions, thresholds were measured for an additional 3 h distributed over 2 days. For this subject as well, there was no evidence for a decrease in overshoot with practice. The results from this additional testing cast some doubt on the possibility that differences between our results and those of Turner and Doherty (1997) are due to the amount of practice.

Despite the fact that Turner and Doherty (1997) generally found a greater reduction in overshoot than we did in the presence of a contralateral precursor, it is worth noting that for the condition (60-dB masker and precursor) in which individual data are shown (their Fig. 3), the reduction in overshoot was greater than 2 dB in only four of their subjects. Further, in three of those subjects, the reduction was similar in magnitude (about 5 dB) to that observed here in our four subjects who showed a decrease in overshoot in the presence of the contralateral precursor; in their fourth subject—the one with the largest overshoot—the reduction

was almost 11 dB. Thus, given the considerable variability among subjects, the apparent difference between the two studies may merely represent individual differences.

It is important to emphasize that we were able, at least to some extent, to replicate the results of Turner and Doherty (1997). Furthermore, the results from experiment 2, in which we manipulated the spectral configuration of both an ipsilateral and contralateral precursor, provide insight into the way in which the contralateral precursor reduces overshoot. First, the fact that the effectiveness of the contralateral precursor was dependent upon its spectral content indicates that the contralateral precursor does not reduce overshoot via a timing cue. Second, the fact that the spectral manipulations affected the ipsilateral and contralateral precursors in more or less a similar fashion suggests that the way in which a precursor reduces overshoot may be the same whether that precursor is presented ipsilaterally or contralaterally.

B. Underlying mechanisms

Although peripheral adaptation may contribute to overshoot (and to the effects of an ipsilateral precursor), it almost certainly cannot account for the entire effect (see the Introduction). Moreover, the contralateral precursor produces little, if any, peripheral adaptation in the test ear, and thus its effect cannot be mediated by adaptation of the auditory-nerve fibers that process the signal.

More recently, attention has focused on the possibility that the cochlear amplifier may be involved in overshoot. Experimental evidence in favor of this comes from research with individuals with temporary (Champlin and McFadden, 1989; McFadden and Champlin, 1990) or permanent hearing loss (Carlyon and Sloan, 1987; Bacon and Takahashi, 1992; Turner and Doherty, 1997). Both significantly reduce overshoot by lowering the threshold for a signal at or near masker onset; in other words, subjects are more sensitive to signals near masker onset following (presumed) cochlear damage. In a study concerned with the effect of masker level on overshoot, Klitzing and Kohlrausch (1994) argued explicitly that basilar membrane nonlinearities (in particular, the frequency-specific compressive growth of response) may influence overshoot. They noted, for example, that the way in which overshoot changes as a function of masker level (it usually increases and then decreases with increasing masker level) can be understood in terms of a basilar membrane input–output function that can often be divided into three segments—linear, compressive, linear (e.g., Yates, 1990; Ruggero and Rich, 1991; but see Ruggero *et al.*, 1997). They noted further, however, that in order to account for overshoot in terms of a compressive nonlinearity at the basilar membrane, one must assume that the nonlinearity decreases with increasing signal delay (or masker stimulation). Following Schmidt and Zwicker (1991), they suggested that this could be realized through activation of the efferent system, particularly that part of the efferent system that influences the outer hair cells.

The psychophysical experiment of Turner and Doherty (1997) was designed explicitly to examine this possibility. They argued that the decline in overshoot that they observed as a consequence of a contralateral precursor was consistent with the possibility that the efferent system is involved with overshoot. The results from the present study are also consistent with this possibility. The efferent influence is presumably via the medial olivocochlear system, whose neurons synapse directly with the outer hair cells in the cochlea (see Warr, 1992, for a review). As noted in the Introduction, physiological experiments have shown that activation of the efferent system can enhance the auditory nerve's response to a tone in noise (Kawase and Liberman, 1993; Kawase *et al.*, 1993). Further, the efferent system requires about 200 ms to reach its maximum effectiveness (e.g., Warren and Liberman, 1989), and thus its time course is consistent with the time course of overshoot (Zwicker, 1965a; Elliott, 1965; Fastl, 1976). Thus, especially high thresholds near masker onset (reflecting an ''overshoot'' of masking) may reflect the compressive nature of the basilar membrane response in a healthy cochlea (i.e., one with healthy outer hair cells), and the decline in threshold as a function of masker stimulation (i.e., signal delay) may reflect a less compressive response, brought about by the influence of medial olivocochlear neurons on the outer hair cells. This could explain why individuals with cochlear damage do not exhibit much overshoot, and in particular why their thresholds near masker onset are lower than normal. Further, as noted by Klitzing and Kohlrausch (1994), it may explain why overshoot declines and often disappears at high levels (e.g., Bacon, 1990), inasmuch as the compressive nature of the basilar membrane is reduced at high levels.

If the decrease in threshold with increasing signal delay (i.e., overshoot) reflects the relatively slow activation of the efferent system, then it is likely that the reduction in overshoot caused by the ipsilateral precursor reflects the same processing. In the present study, the ipsilateral precursor eliminated or at least significantly reduced overshoot in all (10/10) subjects, whereas the contralateral precursor reduced overshoot by a smaller amount, and then only in some (4/15) subjects. It is possible that some of the differences between the effectiveness of the ipsilateral and contralateral precursors reflect the fact that, with ipsilateral stimulation, peripheral adaptation can also be involved. However, the large and consistent differences between the two precursors almost certainly cannot be explained entirely in this way. Instead, the difference in effectiveness between ipsilateral and contralateral precursors may reflect the fact that the majority of efferent neurons from the medial olivocochlear system responds best to ipsilateral stimulation (Liberman, 1988).

Finally, although the reduction in overshoot caused by a contralateral precursor suggests that the efferent system is involved with overshoot, it is important to recall that the effect of severing the olivocochlear bundle on overshoot has been mixed. As noted in the Introduction, Scharf and his colleagues (1994, 1997) found little difference in overshoot between the operated and unoperated ears in two patients who had undergone a vestibular neurotomy. Zeng and his colleagues (2000), however, found smaller amounts of overshoot in the operated than in the unoperated ear of the four patients they tested. The cause of this discrepancy is unclear.

V. SUMMARY AND CONCLUSIONS

The purpose of the present study was twofold: (1) to replicate a recent study by Turner and Doherty (1997), in which a contralateral precursor was found to reduce overshoot by reducing the threshold for a signal near masker onset; and (2) to evaluate the possibility that the effect of the contralateral precursor is mediated via a timing cue. The results can be summarized as follows:

(1) A broadband precursor consistently reduced overshoot in only four out of 15 subjects when it was presented contralaterally, but it reduced overshoot in all ten subjects for whom it was presented ipsilaterally (experiment 1 and its supplement). In contrast, Turner and Doherty (1997) found that a contralateral precursor reduced overshoot in the eight of their ten subjects for whom overshoot was reliably present. In both studies, however, there was considerable variability among subjects and the effect of the contralateral precursor was generally small. Thus, differences across studies could largely represent individual differences.

(2) For both ipsilateral and contralateral precursors, energy above the signal frequency is more important for reducing overshoot than is energy below the signal frequency. Further, precursor energy contained only within the critical band centered at the signal frequency is ineffective in reducing overshoot (experiment 2). These results suggest that the effect of the contralateral precursor is not mediated via a timing cue, and, moreover, that the processing underlying the effectiveness of ipsilateral and contralateral precursors may be largely the same. The results are consistent with the possibility that the efferent system is involved in overshoot.

ACKNOWLEDGMENTS

This research was supported by NIDCD Grant No. DC01376. We thank Michelle Hicks for her participation as a subject and for her comments on a previous version of this manuscript. We also thank Craig Champlin and an anonymous reviewer for their helpful comments.

ANSI (**1996**). ANSI S3.6-1996, Specifications for audiometers (American National Standards Institute, New York).

Bacon, S. P. (**1990**). ''Effect of masker level on overshoot,'' J. Acoust. Soc. Am. **88**, 698–702.

Bacon, S. P., and Smith, M. A. (**1991**). ''Spectral, intensive, and temporal factors influencing overshoot,'' Q. J. Exp. Psych. **43A**, 373–399.

Bacon, S. P., and Takahashi, G. A. (**1992**). ''Overshoot in normal-hearing and hearing-impaired subjects,'' J. Acoust. Soc. Am. **91**, 2865–2871.

Carlyon, R. P., and Sloan, E. P. (**1987**). ''The 'overshoot' effect and sensory hearing impairment,'' J. Acoust. Soc. Am. **82**, 1078–1081. See also J. Acoust. Soc. Am. **83**, 1193 (E) (**1987**).

Carlyon, R. P., and White, L. J. (**1992**). ''Effect of signal frequency and masker level on the frequency regions responsible for the overshoot effect,'' J. Acoust. Soc. Am. **91**, 1034–1041.

Champlin, C. A., and McFadden, D. (**1989**). ''Reductions in overshoot following intense sound exposures,'' J. Acoust. Soc. Am. **85**, 2005–2011.

Elliott, L. L. (**1965**). ''Changes in the simultaneous masked threshold of brief tones,'' J. Acoust. Soc. Am. **38**, 738–746.

Elliott, L. L. (**1969**). ''Masking of tones before, during, and after brief silent periods in noise,'' J. Acoust. Soc. Am. **45**, 1277–1279.

Fastl, H. (**1976**). ''Temporal masking effects. I. Broad band noise masker,'' Acustica **35**, 287–302.

Kawase, T. K., Delgutte, B., and Liberman, M. C. (**1993**). ''Antimasking effects of the olivocochlear reflex. II. Enhancement of auditory-nerve responses to masked tones,'' J. Neurophysiol. **70**, 2533–2549.

Kawase, T. K., and Liberman, M. C. (**1993**). ''Antimasking effects of the olivocochlear reflex. I. Enhancement of compound action potentials to masked tones,'' J. Neurophysiol. **70**, 2519–2532.

Klitzing, R., and Kohlrausch, A. (**1994**). ''Effect of masker level on overshoot in running- and frozen-noise maskers,'' J. Acoust. Soc. Am. **95**, 2192–2201.

Levitt, H. (**1971**). ''Transformed up–down methods in psychoacoustics,'' J. Acoust. Soc. Am. **49**, 467–477.

Liberman, M. C. (**1988**). ''Response properties of cochlear efferent neurons: Monaural vs binaural stimulation and the effects of noise,'' J. Neurophysiol. **60**, 1779–1798.

McFadden, D. (**1989**). ''Spectral differences in the ability of temporal gaps to reset the mechanisms underlying overshoot,'' J. Acoust. Soc. Am. **85**, 254–261.

McFadden, D., and Champlin, C. A. (**1990**). ''Reductions in overshoot during aspirin use,'' J. Acoust. Soc. Am. **87**, 2634–2642.

Overson, G. J., Bacon, S. P., and Webb, T. M. (**1996**). ''The effect of level and relative frequency region on the recovery of overshoot,'' J. Acoust. Soc. Am. **99**, 1059–1065.

Ruggero, M. A., and Rich, N. C. (**1991**). ''Furosemide alters organ of Corti mechanics: Evidence for feedback of outer hair cells upon the basilar membrane,'' J. Neurosci. **11**, 1057–1067.

Ruggero, M. A., Rich, N. C., Recio, A., Narayan, S. S., and Robles, L. (**1997**). ''Basilar-membrane responses to tones at the base of the chinchilla cochlea,'' J. Acoust. Soc. Am. **101**, 2151–2163.

Scharf, B., Magnan, J., and Chays, A. (**1997**). ''On the role of the olivocochlear bundle in hearing: 16 case studies,'' Hear. Res. **103**, 101–122.

Scharf, B., Magnan, J., Collet, L., Ulmer, E., and Chays, A. (**1994**). ''On the role of the olivocochlear bundle in hearing: A case study,'' Hear. Res. **75**, 11–26.

Schmidt, S., and Zwicker, E. (**1991**). ''The effect of masker spectral asymmetry on overshoot in simultaneous masking,'' J. Acoust. Soc. Am. **89**, 1324–1330.

Smith, R. L. (**1977**). ''Short-term adaptation in single auditory nerve fibers: Some poststimulatory effects,'' J. Neurophysiol. **40**, 1098–1112.

Smith, R. L. (**1979**). ''Adaptation, saturation, and physiological masking in single auditory-nerve fibers,'' J. Acoust. Soc. Am. **65**, 166–178.

Smith, R. L., and Zwislocki, J. J. (**1975**). ''Short-term adaptation and incremental responses in single auditory-nerve fibers,'' Biol. Cybern. **17**, 169–182.

Turner, C. W., and Doherty, K. A. (**1997**). ''Temporal masking and the 'active process' in normal and hearing-impaired listeners,'' in *Modeling Sensorineural Hearing Loss*, edited by W. Jesteadt (Erlbaum, Hillsdale, NJ), pp. 387–396.

Turner, C. W. (**2000**). Personal Communication.

Warr, W. B. (**1992**). ''Organization of olivocochlear efferent systems in mammals,'' in *The Mammalian Auditory Pathway: Neuroanatomy*, edited by D. B. Webster, A. N. Popper, and R. R. Fay (Springer, New York).

Warren III, E. H., and Liberman, M. C. (**1989**). ''Effects of contralateral sound on auditory-nerve responses. I. Contributions of cochlear efferents,'' Hear. Res. **37**, 89–104.

Wright, B. A. (**1995**). ''Detectability of simultaneously masked signals as a function of signal bandwidth for different signal delays,'' J. Acoust. Soc. Am. **98**, 2493–2503.

Wright, B. A. (**1997**). ''Detectability of simultaneously masked signals as a function of masker bandwidth and configuration for different signal delays,'' J. Acoust. Soc. Am. **101**, 420–429.

Yates, G. K. (**1990**). ''Basilar membrane nonlinearity and its influence on auditory nerve rate-intensity functions,'' Hear. Res. **50**, 145–162.

Zeng, F.-G., Martino, K. M., Linthicum, F. H., and Soli, S. D. (**2000**). ''Auditory perception in vestibular neurectomy subjects,'' Hear. Res. **142**, 102–112.

Zwicker, E. (**1965a**). ''Temporal effects in simultaneous masking by white-noise bursts,'' J. Acoust. Soc. Am. **37**, 653–663.

Zwicker, E. (**1965b**). ''Temporal effects in simultaneous masking and loudness,'' J. Acoust. Soc. Am. **38**, 132–141.

Auditory discrimination in a sound-producing electric fish (*Pollimyrus*): Tone frequency and click-rate difference detection

Peter Marvit[a)]
Department of Psychology, University of Pennsylvania, Philadelphia, Pennsylvania 19104

John D. Crawford[b)]
Neuroscience Graduate Group and Department of Psychology, University of Pennsylvania, Philadelphia, Pennsylvania 19104

(Received 7 December 1999; accepted for publication 5 June 2000)

Pollimyrus adspersus is a fish that uses simple sounds for communication and has auditory specializations for sound-pressure detection. The sounds are species-specific, and the sounds of individuals are sufficiently stereotyped that they could mediate individual recognition. Behavioral measurements are presented indicating that *Pollimyrus* probably can make species and individual discriminations on the basis of acoustic cues. Interclick interval (ICI; 10–40 ms) and frequency (100–1400 Hz) discrimination was assessed using modulations of the fish's electric organ discharge rate in the presence of a target stimulus presented in alternation with an ongoing base stimulus. Tone frequency discrimination was best in the 200–600-Hz range, with the best threshold of 1.7% ±0.4% standard error at 500 Hz (or 8.5 Hz ±1.9 SE). The just noticeable differences (jnd's) were relatively constant from 100 to 500 Hz (mean 8.7 Hz), then increased at a rate of 13.3 Hz per 100 Hz. For click trains, jnd's increased linearly with ICI. The mean jnd's for 10- and 15-ms ICI were both 300 μs (SE = 0.8 ms at 10-ms ICI, SE = 0.11 ms at 15-ms ICI). The jnd at 20-ms ICI was only 1.1 ms ±0.25 SE. © *2000 Acoustical Society of America.* [S0001-4966(00)02009-9]

PACS numbers: 43.66.Gf, 43.80.Lb, 43.64.Tk [WA]

INTRODUCTION

Studies of hearing in animals that rely on sounds for basic behaviors such as spatial orientation (Suga, 1990; Konishi, 1993; Knudsen and Brainard, 1995; Yager and Spangler, 1997) and communication (Feng, 1992; Hall, 1994; Wyttenbach *et al.*, 1996; Esser *et al.*, 1997; Alder and Rose, 1998; Bodnar and Bass, 1999; Gerhardt and Schul, 1999) are powerful because the design of experiments, and the interpretation of performance, can be constrained by knowledge of natural function. Performance in auditory discrimination is more easily understood with information about the kinds of signals that are normally encountered and the way they are used to guide behavior. In some instances, the relevant sounds are comparatively simple, and behavioral analyses can be combined with physiological studies of the underlying computational mechanisms. In the present study, we have investigated auditory discrimination in an animal that uses simple sounds for courtship communication, with the goal of learning more about the ability of this species to extract available information from its own natural sounds.

The communication sounds of the weakly electric fish *Pollimyrus adspersus* (Mormyridae) have been studied extensively (Crawford *et al.*, 1997a). These fish have a relatively simple auditory system (Stipetic, 1939; Fletcher and Crawford, submitted) that has yielded to neuroanatomical (Kozloski and Crawford, 1998) and neurophysiological analyses (Crawford, 1997a; Kozloski and Crawford, 2000). The auditory periphery of *Pollimyrus* is specialized for sound-pressure detection, with gas-filled tympanic bladders coupled to each ear (Crawford, 1997b; Fletcher *et al.*, 2000; Fletcher and Crawford, submitted). Because fish lack peripheral specializations for mechanical frequency analysis (i.e., a cochlea), it has been suggested that they do much of their auditory processing in the temporal domain (Wever, 1949; Fay, 1978a, 1994a; Crawford, 1997a; Bodnar and Bass, 1999; Popper and Fay, 1999). Male *Pollimyrus* court females with an acoustic display consisting of a regular alternation between two simple sounds—the grunt and the moan. Grunts are essentially acoustic click trains with an interclick interval (ICI) of 18 ms, and total duration of 250 ms. Moans are tonal with sharp spectral peaks at 240 and 480 Hz, and a duration of 800 ms. The sounds can be modeled with synthesized click trains and pure tones. Recent behavioral studies of acoustic detection in *Pollimyrus* (Marvit and Crawford, 2000a) have shown that these animals are very sensitive to the tones and click trains that correspond to the natural vocalizations. Nevertheless, prior to the present study there has not been an analysis of auditory discrimination in this sound-producing species.

Two key questions, questions that have arisen from previous studies of acoustic behavior, hinge upon new measurements on auditory discrimination. First, is discrimination in *Pollimyrus* sufficient for acoustic species recognition? The sounds of *P. adspersus* and a closely related sympatric species (*P. isidori*) are similar in some respects but are clearly species-specific (Crawford *et al.*, 1997a). Both species make grunts, but the ICIs used by the two species are different.

[a)]Current address: Speech-Language, Pathology and Audiology, Northeastern University, Boston, Massachusetts 02115-5000; electronic mail: marvit@research.neu.edu
[b)]Electronic mail: crawford@psych.upenn.edu

Both species also produce moans, but the dominant frequencies of these tonal sounds are different. Second, is discrimination sufficient for acoustic individual recognition? Both the grunts and the moans of P. adspersus could be used to recognize individual males if discrimination ability were good enough. It is likely that the evolution of acoustic displays by male *Pollimyrus* has been driven by intraspecific sexual selection during mate choice (Crawford *et al.*, 1997a, 1997b). If so, discrimination may be sufficiently fine for recognizing the small acoustic differences that distinguish individuals.

The data presented here show that *Pollimyrus* have access to a considerable amount of the information present in their natural sounds, and are likely to be quite sensitive to species and individual acoustic differences. A preliminary account of these findings has been presented in abstract form (Marvit and Crawford, 2000b).

I. METHODS

Changes in the ongoing temporal pattern of electric organ discharges (EODs) have been used successfully as an assay for stimulus detection in a number of studies of electric fishes (Mandriota *et al.*, 1965, 1968; Kramer *et al.*, 1981; Ciali *et al.*, 1997). In a recent study on hearing (Marvit and Crawford, 2000a), we demonstrated that EOD modulations in conditioned fish are a reliable assay for acoustic detection in the electric fish *Pollimyrus adspersus*. In the present study, we adapted these techniques for measuring discrimination thresholds (i.e., *just noticeable differences*, jnd's) for tones and click trains. The equipment and methods used in the present study are essentially the same as those used for the previous detection study (Marvit and Crawford, 2000a), but are detailed here for clarity.

A. Animals

Our study was based on adult *P. adspersus* that were imported from Nigeria, West Africa. They were housed in laboratory aquaria at 26 °C. Twenty individuals were screened for consistent behavioral responses in the discrimination experiment (85% target detection), and five were used. The subjects, two females and three males, ranged from 57 to 81 mm in standard length (67 mm ± 9 s.d.). None was breeding at the time of the experiment.

B. Experimental tank, stimulus generation, and data acquisition

The equipment setup that we employed for these underwater acoustic experiments has been used successfully by other laboratories in a number of previous studies of hearing in fish (e.g., Fay, 1989; Lu and Fay, 1993), and in our own laboratory for auditory neurophysiology and behavioral experiments (Crawford, 1993, 1997a; Kozloski and Crawford, 1998; Marvit and Crawford, 2000a). Comparisons between the current study and prior behavioral and physiological work are therefore facilitated.

The fish were free to move but confined to the central acoustically calibrated portion of a cylindrical holder centered 25 mm below the water surface in an acoustic tank. The holder was fashioned from a section of polyvinyl chloride (PVC) pipe (l = 80 mm, d = 38 mm) to make a frame with large, elongated windows. The windows were covered with fine fiberglass mesh (1 × 1-mm squares). The holder had three Ag/AgCl electrodes (d = 1 mm) along its top axis for differential recording of EOD activity. During training and testing, EOD times were recorded digitally to the nearest 1.0 μs and analyzed online. An additional pair of Ag/AgCl electrodes was also mounted on the sides of the holder to deliver a weak but aversive current [unconditional stimulus (UCS)].

Each acoustic tank was located inside a sound-attenuating chamber (IAC or Acoustic Systems). The water was kept at 26 °C (±1.5°) and approximately 200 μS/cm conductivity. All stimulus generation was done with hardware from Tucker-Davis Technologies (TDT) and microcomputers. We used a 50-kHz sample rate to output computer-synthesized tone and click stimuli through a 16-bit digital-to-analog converter (TDT DA1) and then to a low-pass filter at 10 kHz (TDT FT5). The analog signals were fed to programmable attenuators (TDT PA4) and then to a power amplifier (Crown D-75). Finally, sounds were presented by an underwater speaker (University UW-30) at the bottom of the acoustic tank. Tones had 30-ms raised-cosine onset/offset ramps. Clicks were synthesized by passing 200-μs monophasic pulses through a bandpass filter set at 300 and 3000 Hz. As recorded in the tank, the clicks were about 5 ms in duration and had flat amplitude spectra from 300 to 3000 Hz.

Calibration was accomplished by placing a pressure hydrophone (B&K 8103) inside the fish holder, at the spot normally occupied by the fish during testing. The hydrophone's output was then amplified with a BMA 202 amplifier, and digitized (TDT AD1). Tones were calibrated (dB rms *re*: 1 μPa) from their amplitude spectra. Clicks were calibrated dB peak *re*: 1 μPa from the digitized waveform.

C. Tone frequency discrimination training

Fish were conditioned to give a change in EOD rate whenever the ongoing *base* stimulus changed in frequency (for tones), or interclick interval (for click trains). This *oddball* design [Fig. 1(A)] has been widely used for discrimination studies in animals (e.g., Fay, 1970).

Fish were presented with an ongoing series of 350-ms tone bursts (30-ms rise/fall) separated by 150 ms of silence (i.e., 2 bursts/s). The mean level of the sounds was set substantially above detection threshold, approximately 110 dB *re*: 1 μPa (Marvit and Crawford, 2000a), but the level of each burst was randomly roved over a uniform 20-dB range. Tone bursts of a single *base* frequency were presented continuously except during trials (Marvit and Crawford, 2000a). The intertrial interval varied randomly over a uniform range from 90 to 150 s and averaged 120 s.

A trial consisted of a 3-s *prestimulus* period recording of EODs during tone bursts at the base frequency. In the subsequent 3 s of *peristimulus* period, the base tone bursts were alternated with *target* tone bursts of a different frequency [Δf = target-base; Fig. 1(A)] and EODs were also recorded. The distributions of inter-EOD times were compared between the prestimulus and peristimulus intervals [Fig. 1(B)], and changes in the ongoing EOD pattern were tested for each

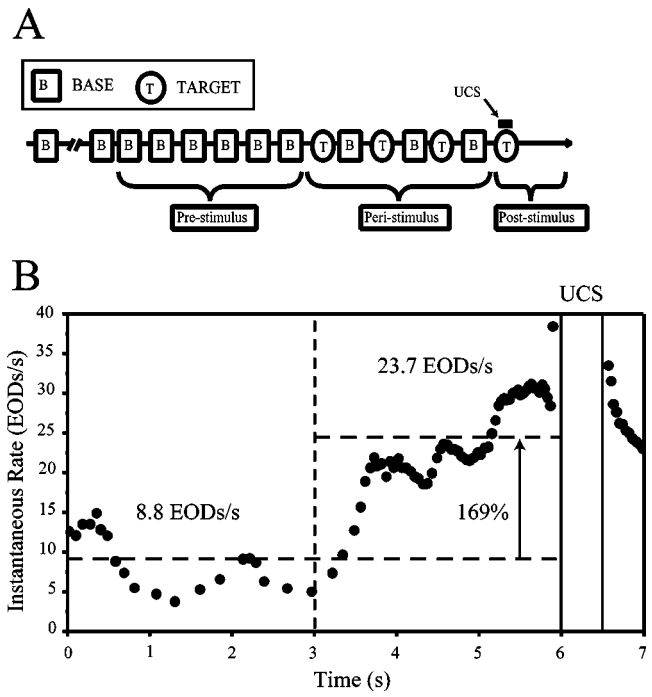

FIG. 1. Discrimination trial schematic (A) and example EOD response (B). The fish was presented with tone bursts at the base frequency (B) during the intertrial period and through the prestimulus period. During the peristimulus period the base (B) alternated with the target (T) tone frequency. At the start of the poststimulus period, the UCS was delivered during a final presentation of the target, and then the base presentations resumed until the next trial. Tone bursts (350 ms) were presented at a rate of 2 per s. Pre- and peristimulus periods were 3 s long. The time between trials was chosen at random (120 ± 30 s). Trained fish increased their EOD rate when the target was detected, often by as much as threefold or more (B). These instantaneous EOD rates were smoothed for plotting.

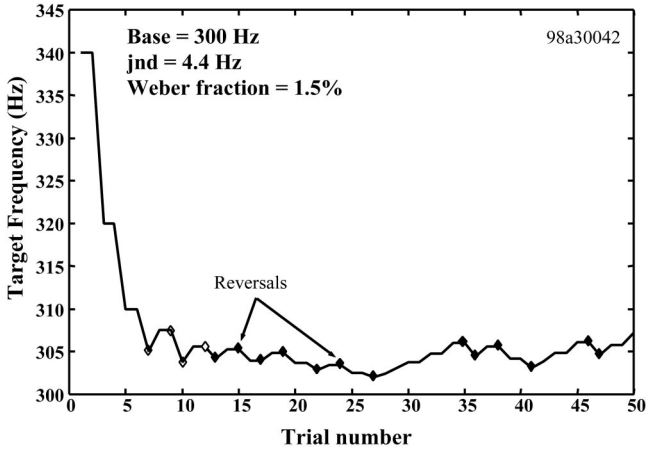

FIG. 2. Example staircase for tone frequency discrimination. The base frequency was 300 Hz, and the initial target was 340 Hz. The filled diamonds show the 13 reversals that correspond to a step size of 25% of *f*. The last 12 of these were used to estimate the threshold. The geometric mean of these 12 reversals was 304.4 Hz, giving a threshold estimate of 4.4 Hz or a Weber fraction of 1.4%. The first four reversals (open diamonds) correspond to steps of 50% of *f* and were not used in the jnd estimate (see the text).

trial using the Kolmagorov–Smirnov nonparametric test of unequal distributions (Hollander and Wolf, 1973). During the following *poststimulus* period, a final target tone burst overlapped with a 500 ms UCS. The UCS was a 500 ms dc pulse of 2–3.5 mA. The fish received the reinforcement (UCS) on every trial. Training sessions consisted of 50 trials, and individuals participated in sessions no more than once per day.

Fish were trained for at least three sessions using a different, randomly selected base frequency between 100 and 1000 Hz each session. None of the training frequencies was used for testing. Target frequencies in training sessions randomly varied from trial to trial from 25% to 60% greater than the base frequency. Most test fish reached 85%-correct performance criterion within 5–10 training sessions.

D. Frequency discrimination testing

Testing sessions were identical to training, except that we used a 1-up, 2-down adaptive staircase procedure (Fig. 2) to estimate jnd's (Levitt, 1971). The initial Δf was set to 10%–25% of the base. Whenever a fish detected a difference between base and target frequencies in a sequence of two adjacent trials, the difference between base and target (Δf) was decreased for the subsequent trial. If the fish missed the target, the difference was increased. These changes in the direction of frequency change were referred to as *reversals* (Fig. 2). The change in stimulus frequency was 50% of the preceding Δf until the first four reversals appeared in the staircase. These reversals were not used for estimating thresholds. The Δf was then reduced to 25% for the subsequent reversals. The jnd for a session was computed as the geometric mean of the last even number of the 25% reversals. If the standard error of an estimate for a frequency exceeded 3% of the base frequency, or there were fewer than six reversals, the fish was retested at that frequency on another day.

Fish were tested at base frequencies of 100, 200, 250, 300, 400, 500, 600, 900, 1200, and 1400 Hz in randomized order. The fish were tested with starting target frequencies 10%–25% greater than the base for 100–900 Hz (''from above''), and 10%–25% less than the base for 1200 and 1400 Hz (''from below''). Three fish were retested at the full set of base frequencies, but using starting target frequencies 10%–25% less than the base (from below) for the 100–900-Hz range.

E. Click-train training and testing

The methods for training and testing differences in click trains were identical to those used for tones, except the stimuli were click trains of 350 ms duration. The mean level of the click trains was 110 dB peak; each click train was independently roved within a 20-dB range. Fish were trained for at least two sessions using a different, randomly selected base ICI between 10 and 100 ms each session. None of the training ICIs was used for testing. All five fish were then tested at ICIs of 10, 15, 20, and 40 ms, in randomized order. At each base ICI, each fish was also tested with target ICI 10%–25% less than the base (from below) and 10%–25% greater than the base (from above), also in randomized order.

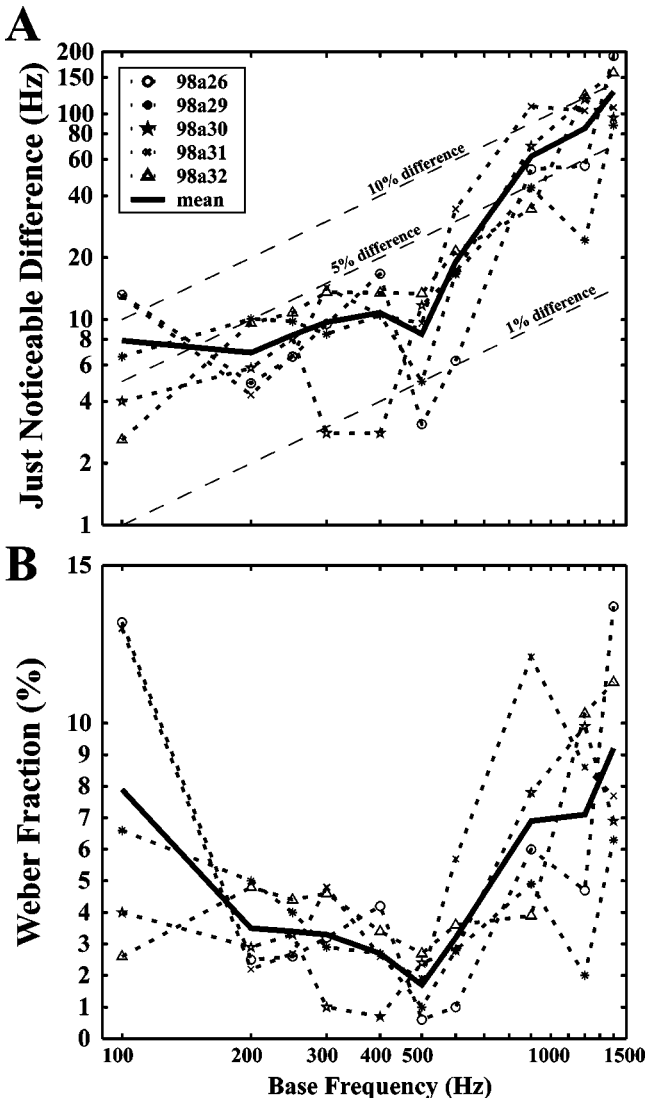

FIG. 3. Tone discrimination as jnd's in Hz on a log–log scale (A) and as Weber fractions (B). A straight diagonal line in A would indicate that the jnd is strictly proportional to the base stimulus (Weber's law). Dashed lines show ideal Weber fractions of 1%, 5%, and 10%. The departures from a simple diagonal shown by the fish indicate changes in relative sensitivity, evident in panel (B). In both (A) and (B), the solid black line shows the mean for the five individuals.

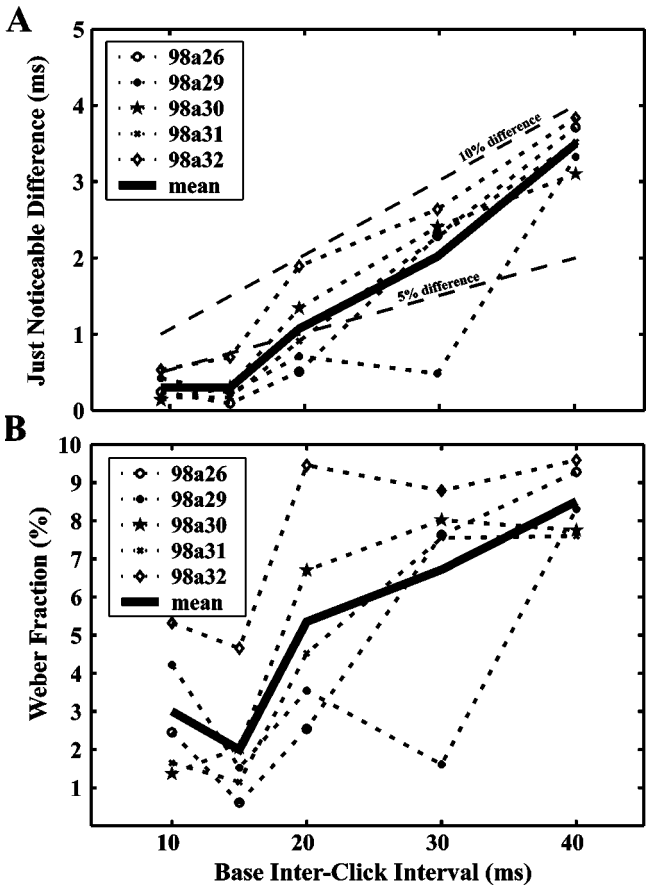

FIG. 4. Click-train discrimination as jnd in ms (A) and as Weber fractions (B). In (A), the diagonal dashed lines represent constant Weber fractions of 5% and 10%. The mean of five individuals is shown by the thick black line.

II. RESULTS

The tested fish provided reliable and consistent threshold estimates, regardless of the direction of change in the frequency or click-train ICI. For both frequency and click-train discrimination, there were no significant differences between trials tested from above and from below (paired *t*-tests on arcsine-transformed Weber ratios, $p > 0.6$). The average difference in the frequency jnd's, expressed as Weber fractions, was $0.41\% \pm 0.66\%$ s.d. The mean difference in the click-train jnd estimates, expressed as Weber fractions, was $-0.01\% \pm 1.6\%$ s.d. The results presented here are therefore the pooled estimates at each stimulus value.

P. adspersus were sensitive to small differences in tones and click trains, especially those frequencies and ICIs corresponding to the natural vocalizations. For tones, the fish were most sensitive to frequency differences in the 200–600-Hz range (Fig. 3). In the 100- to 500-Hz range, the fish had a relatively constant jnd of about 9 Hz. Above 500 Hz, the jnd increased steadily at a rate of 13.3 Hz per 100 Hz [Fig. 3(A)].

The smallest Weber fractions were always near 500 Hz [Fig. 3(B)]. Four of the five individuals had their greatest sensitivity at 500 Hz and one at 400 Hz. The mean Weber fraction at 500 Hz was only $1.7\% \pm 0.4\%$ SE (i.e., 8.5 Hz jnd $\pm$ 1.9 SE). The mean Weber fractions increased substantially at frequencies above and below the middle range, reaching $7.9\% \pm 2.2\%$ SE at 100 Hz (i.e., 7.9 Hz jnd $\pm$ 2.2 SE) and $9.2\% \pm 1.4\%$ SE at 1400 Hz (i.e., 128.4 Hz jnd $\pm$ 20.0 SE). Interindividual variations in jnd were smallest near 500 Hz.

For click trains, the fish showed systematic increases in jnd ranging from about 0.3 ms at the shortest ICIs to about 3 ms for a 40-ms ICI train [Fig. 4(A)]. All the fish showed this general pattern, with significant positive correlations (r) between jnd and base ICI ($0.75 < r < 0.93$). The smallest Weber fractions were obtained at short ICIs, with a fraction of only $2.0\% \pm 0.7\%$ at 15 ms. The mean Weber fraction was over fourfold greater at 40-ms ICI [$8.5\% \pm 0.4\%$ SE; Fig. 4(B)].

III. DISCUSSION

The discrimination thresholds we measured indicate that the natural sounds of *Pollimyrus* could mediate species and

individual recognition. We modeled the two-part acoustic courtship display in terms of click trains and tones, and examined just two of a variety of dimensions that could potentially be exploited by these fish under natural conditions (ICI and frequency).

The aim of the our study was to arrive at an estimate of the average discrimination capability of a single sound-producing species, *P. adspersus*. Our threshold estimates for both frequency and click-train rate discrimination were consistent within individuals. We found no significant difference in estimates when the target frequency or ICI was less than or greater than the base stimulus. However, additional work will be required to obtain a careful assessment of individual differences in this species. Since we were interested in estimating the mean performance for the species in this paper, we have combined data across individuals so as to effectively eliminate individual differences and variability in the estimates for individuals. Future experiments will focus on the variations found within individuals.

Pollimyrus use sounds while breeding in freshwater habitats in central Africa (Crawford *et al.*, 1997a). These waters carry sounds made by a variety of species of animals, including insects, frogs, and other species of fishes including close relatives of *P. adspersus. P. isidori* uses sounds during breeding and is sympatric with *P. adspersus* in the Niger River (Crawford *et al.*, 1997b).

The peak fundamental frequency of the *P. adspersus* moan (240 Hz) is substantially lower than that of *P. isidori* (332 Hz). Based upon discrimination studies of goldfish (*Carassius auratus*; Fay, 1970, 1978a, 1978b), Crawford *et al.* (1997a) predicted that the 92-Hz separation of the moan fundamentals might be separated perceptually by about 9 jnd's. Our new data for frequency discrimination in *P. adspersus* indicate an even larger perceptual separation of 11 jnd's. However, both detection (Marvit and Crawford, 2000a) and discrimination [Fig. 3(B)] are best near the second harmonic of the moan, and this may be where moan discriminations are made. The separation of *P. adspersus* and *P. isidori* near the second harmonic is on the order of 21 jnd's. This is exceptional in the context of species recognition, and leads one to suspect that the fish may also be performing acoustic individual recognition based on the moan.

The mean ICI of *P. adspersus* grunts is 17.9 ms compared to 22.7 ms in *P. isidori* (Crawford *et al.*, 1997a). Again, based upon data from goldfish (Fay and Passow, 1982), Crawford *et al.* predicted that the 5-ms ICI separation for grunts would correspond to about 3 jnd's. The current behavioral measures of click-train discrimination by *P. adspersus* show that the grunts are perceptually separated by about 4.5 jnd's—sufficient for species recognition but not as impressive as the case for moans.

There are several circumstances under which individual recognition might be important. *Pollimyrus* males vocalize to advertise to, and court, potential mates and for territorial defense (Crawford *et al.*, 1986; Crawford, 1997b; Crawford *et al.*, 1997a, 1997b). Males produce isolated grunts while patrolling their territory, and often produce one or a few grunts immediately following a territorial dispute with another male. The most elaborate episodes of sound production

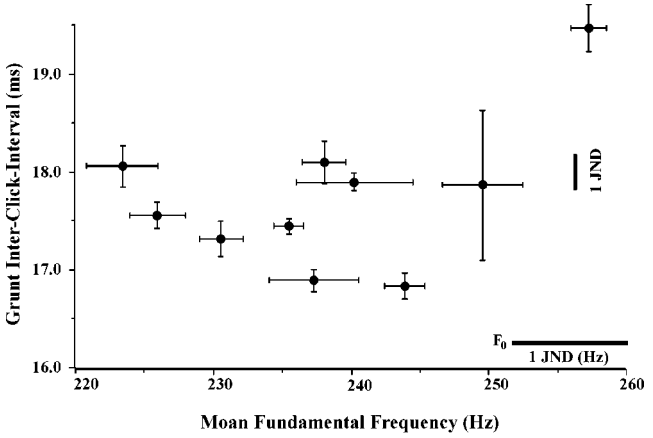

FIG. 5. Individual differences for ten *P. adspersus* plotted as the fundamental frequency of the moan and the interclick intervals (ICI) of the grunts. Each point represents the mean and standard error of eight sounds from one individual (adapted from Crawford *et al.*, 1997a). The just noticeable difference (jnd) in ms is shown as a vertical line (right side) for an ICI of 18 ms, assuming a Weber fraction of 2%. The jnd for tones corresponding to the fundamental is shown at the lower right as a horizontal line.

occur while gravid females visit the male's territory, during the *sonic phase* of courtship. During these 10–20-s interactions, males produce a steady sequence of alternating grunts and moans. It has been proposed that females make decisions about their ultimate mate choice based upon these interactions with males (Crawford *et al.*, 1997a). The moan is a prime candidate for individual recognition because males differ dramatically in the characteristics of the moans they produce during courtship. For example, the fundamental frequency of moans tends to increase with body mass (Crawford *et al.*, 1997a), making this a possible cue for male's fitness (see also Wiegmann *et al.*, 1992, 1997; Myrberg *et al.*, 1993; Lobel and Mann, 1995).

Moans from individuals are stereotyped and have characteristic fundamental frequencies that vary from call to call by only a few Hz. Differences between individuals, on the other hand, can vary as much as 60 Hz. Applying the discrimination thresholds from this study to the moans of a sample of ten individual males (Crawford *et al.*, 1997a), 27/45 (60%) pairs of fish could be uniquely distinguished based on the fundamental of the moan alone (Fig. 5). If the fish were to use the second harmonic, where they are more sensitive and have even better discrimination, the differences between individuals would be even more salient. The importance of the higher-frequency component of the moan may be due in part to the acoustic characteristics of the habitat where these animals broadcast their sounds. In the shallow-water breeding environment, the low-frequency sounds are near the propagation cutoff limit and the higher components may be detectable at greater distances than the fundamental (Crawford *et al.*, 1997b).

The departures from a constant Weber fraction (power function) near 500 Hz also suggest that this region is particularly salient for natural behavior. Although discrimination may have simply been better where the sounds were most easily detected, previous studies on goldfish showed that neither roving intensity (12-dB range) nor mean sensation level

(15–55 dB SL) had a statistically significant effect on frequency discrimination (Fay, 1989).

Discrimination of click-train ICI may also provide information for individual recognition. The grunts of *P. adspersus* have a mean ICI of 17.9 ms—close to the best mean discrimination in the current study. An analysis of ten individuals' grunts shows mean ICI differences ranging from less than 0.5 ms to over 2.5 ms (Crawford *et al.*, 1997a). In the current study, *P. adspersus* had sufficiently small jnd's to be able to discriminate between 33/45 (73%) pairs of individuals based solely upon their grunts.

Pollimyrus could use these single cues for individual identification, or could use both cues in combination for even better resolution of individual differences. Neither pure-tone jnd's (i.e., for moans) nor click-train ICI jnd's (i.e., for grunts) alone are sufficient for uniquely identifying all ten of our sample of individuals (Fig. 5). However, a simple combination of the two cues yields 91% (41/45) separation of these males. It is worth noting that, in a natural setting, it is unlikely that any individual would be within vocalizing range of more than 3–5 other fish at one time, thus making the task easier (Crawford *et al.*, 1997b). Additionally, the natural vocalizations vary over a number of other dimensions that the animals may use (e.g., duration, amplitude modulation, spectral shape).

Tone discrimination in goldfish is generally similar to what we found in *Pollimyrus*, with the best Weber fractions (3.7%) in the 400–500-Hz range (Fay, 1970). However, Weber fractions for goldfish did not vary as much with frequency as they did in *Pollimyrus*. Goldfish Weber fractions declined from 5.3% at 100 Hz to 3.7% at 400 Hz, and then increased to 4.7% at 1000 Hz. *Pollimyrus* had relatively poor sensitivity at the lower and higher frequencies (i.e., 7.9% at 100 Hz and 6.9% at 900 Hz), but better discrimination at 500 Hz (i.e., 1.7%). These differences may reflect the evolution of sound-production mechanisms in *Pollimyrus* (Crawford and Huang, 1999) but not in the goldfish. Human total jnd's in the 500-Hz region are more than an order of magnitude better than any fish tested (Wier *et al.*, 1976, cited in Fay, 1988).

Fay and Passow (1982) and Fay (1994b) have examined comparable aspects of click-train rate discrimination in goldfish, though neither used a task identical to the current study. Fay and Passow (1982) investigated the effects of temporal jitter on the discrimination of different types of periodic stimuli, and derived just noticeable differences as a function of click-train period (ICI). For stimuli approximately matching those in the present experiment, sensitivity also approaches a power function, with a Weber fraction of 3%–15%, depending on the condition. These values are in general agreement with our data on *Pollimyrus*. In generalization experiments with click trains, goldfish required a five- to tenfold greater difference in ICI rate before they responded to a change (Fay, 1994b).

The relative simplicity of the fish ear has lead investigators to hypothesize that fish may rely on temporal analysis of synchronized spike trains for acoustic discrimination (Fay, 1970, 1978a, 1988). If the frequency discrimination were carried out entirely in the time domain, *Pollimyrus* would have to resolve differences on the order of 35 μs for discrimination at 500 Hz. Similarly, if discrimination of small differences in click-train ICI were based entirely on temporal cues, then the fish would need to resolve differences of a few hundred microseconds in the 10- to 20-ms ICI range. Although this kind of fine temporal resolution has been suggested in a variety of other sensory systems (Guo and Kawasaki, 1997; Simmons *et al.*, 1998), additional experiments will be required to determine whether acoustic discrimination in *Pollimyrus* is based purely on an analysis of the timing of synchronized action potentials.

ACKNOWLEDGMENTS

We are indebted to A. P. Cook, L. B. Fletcher, R. Rescorla, V. Richards, J. C. Saunders, and R. Seyfarth for their contributions to the development of the research and the paper. We also thank two anonymous reviewers for helpful comments. This research was supported by grants from the NIH (No. DC01252) and the PA Lions Hearing Research Foundation.

Alder, T., and Rose, G. (**1998**). ''Long-term temporal integration in the anuran auditory system,'' Nat. Neurosci. **1**, 519–523.

Bodnar, D. A., and Bass, A. H. (**1999**). ''Midbrain combinatorial code for temporal and spectral information in concurrent acoustic signals,'' J. Neurophysiol. **81**, 552–563.

Ciali, S., Gordon, J., and Moller, P. (**1997**). ''Spectral sensitivity of the weakly discharging electric fish *Gnathonemus petersi* using its electric organ discharges as the response measure,'' J. Fish Biol. **50**, 1074–1087.

Crawford, J. D. (**1993**). ''Central auditory neurophysiology of a sound-producing mormyrid fish: The mesencephalon of *Pollimyrus isidori*,'' J. Comp. Physiol. A **172**, 1–14.

Crawford, J. D. (**1997a**). ''Feature-detecting auditory neurons in the brain of a sound-producing fish,'' J. Comp. Physiol. A **180**, 439–450.

Crawford, J. D. (**1997b**). ''Hearing and acoustic communication in the mormyrid electric fishes,'' Mar. Freshwater Behav. Physiol. **29**, 65–86.

Crawford, J. D., Cook, A. P., and Heberlein, A. S. (**1997a**). ''Bioacoustic behavior of African fishes (Mormyridae): Potential cues for species and individual recognition in *Pollimyrus*,'' J. Acoust. Soc. Am. **102**, 1200–1212.

Crawford, J. D., Hagedorn, M. M., and Hopkins, C. D. (**1986**). ''Acoustic communication in an electric fish, *Pollimyrus isidori* (Mormyridae),'' J. Comp. Physiol. A **159**, 297–310.

Crawford, J. D., and Huang, X. (**1999**). ''Communication signals and sound production mechanisms of mormyrid electric fish,'' J. Exp. Biol. **202**, 1417–1426.

Crawford, J. D., Jacob, P., and Bénech, V. (**1997b**). ''Sound production and reproductive ecology of strongly acoustic fish in Africa: *Pollimyrus isidori*, Mormyridae,'' Behaviour **134**, 677–725.

Esser, K. H., Condon, C. J., Suga, N., and Kanwal, J. S. (**1997**). ''Syntax processing by auditory cortical neurons in the FM–FM area of the mustached bat *Pteronotus parnellii*,'' Proc. Natl. Acad. Sci. USA **94**, 14019–14024.

Fay, R. R. (**1970**). ''Auditory frequency discrimination in the goldfish (*Carassius auratus*),'' J. Comp. Physiol. Psychol. **73**, 175–180.

Fay, R. R. (**1978a**). ''Phase-locking in goldfish saccular nerve fibers accounts for frequency discrimination capacities,'' Nature (London) **275**, 320–322.

Fay, R. R. (**1978b**). ''Coding of information in single auditory-nerve fibers of the goldfish,'' J. Acoust. Soc. Am. **63**, 136–146.

Fay, R. R. (**1988**). *Hearing in Vertebrates: A Psychophysics Databook* (Hill-Fay Associates, Winnetka, IL).

Fay, R. R. (**1989**). ''Frequency discrimination in the goldfish (*Carassius auratus*): Effects of roving intensity, sensation level, and the direction of frequency change,'' J. Acoust. Soc. Am. **85**, 503–505.

Fay, R. R. (**1994a**). ''The sense of hearing in fishes: Psychophysics and neurophysiology,'' Sens. Syst. **8**, 262–268.

Fay, R. R. (**1994b**). ''Perception of temporal acoustic patterns by the goldfish (*Carassius auratus*),'' Hear. Res. **76**, 158–172.
Fay, R. R., and Passow, B. (**1982**). ''Temporal discrimination in the goldfish,'' J. Acoust. Soc. Am. **72**, 753–760.
Feng, A. S. (**1992**). ''Information processing in the auditory brainstem,'' Curr. Opin. Neurobiol. **2**, 511–515.
Fletcher, L. B., Cook, A. P., and Crawford, J. D. (**2000**). ''Acoustic detection by sound-producing fishes (Mormyridae): The role of tympanic ear-bubbles,'' Paper presented at the Midwinter meeting of the Association for Research in Otolaryngology, St. Petersburg, FL, February (unpublished).
Fletcher, L. B., and Crawford, J. D. ''Acoustic detection by sound-producing fishes (Mormyridae): the role of tympanic ear-bladders,'' submitted to J. Exper. Bio.
Gerhardt, H. C., and Schul, J. (**1999**). ''A quantitative analysis of behavioral selectivity for pulse rise-time in the gray treefrog, *Hyla versicolor*,'' J. Comp. Physiol. A **185**, 33–40.
Guo, Y. X., and Kawasaki, M. (**1997**). ''Representation of accurate temporal information in the electrosensory system of the African electric fish, *Gymnarchus niloticus*,'' J. Neurosci. **17**, 1761–1768.
Hall, J. C. (**1994**). ''Central processing of communication sounds in the anuran auditory system,'' Am. Zool. **34**, 670–684.
Hollander, M., and Wolf, D. A. (**1973**). *Nonparametric Statistical Methods* (Wiley, New York).
Knudsen, E. I., and Brainard, M. S. (**1995**). ''Creating a unified representation of visual and auditory space in the brain,'' Annu. Rev. Neurosci. **18**, 19–43.
Konishi, M. (**1993**). ''Neuroethology of sound localization in the owl,'' J. Comp. Physiol. A **173**, 3–7.
Kozloski, J., and Crawford, J. D. (**1998**). ''Functional neuroanatomy of auditory pathways in the sound producing fish *Pollimyrus*,'' J. Comp. Neurol. **401**, 227–252.
Kozloski, J., and Crawford, J. D. (**2000**). ''Transformations of an auditory temporal code in the medulla of a sound-producing fish,'' J. Neurosci. **20**, 2400–2408.
Kramer, B., Tautz, J., and Markl, H. (**1981**). ''The EOD sound response in weakly electric fish,'' J. Comp. Physiol. A **143**, 435–441.
Levitt, H. (**1971**). ''Transformed up–down methods in psychoacoustics,'' J. Acoust. Soc. Am. **49**, 467–477.
Lobel, P. S., and Mann, D. A. (**1995**). ''Spawning sounds of the damselfish, *Dascyllus albisella* (Pomacentridae), and relationship to male size,'' Bioacoustics **6**, 187–198.
Lu, Z., and Fay, R. R. (**1993**). ''Acoustic response properties of single units in the torus semicircularis of the goldfish, *Carassius auratus*,'' J. Comp. Physiol. A **173**, 33–48.
Mandriota, F. J., Thompson, R. L., and Bennet, M. V. L. (**1965**). ''Classical condition of electric organ discharge rate in mormyrids,'' Science **150**, 1740–1742.
Mandriota, F. J., Thompson, R. L., and Bennet, M. V. L. (**1968**). ''Avoidance conditioning of the rate of electric organ discharge in mormyrid fish,'' Anim. Behav. **16**, 448–455.
Marvit, P., and Crawford, J. D. (**2000a**). ''Auditory thresholds in a sound-producing electric fish (*Pollimyrus*): Behavioral measurements of sensitivity to tones and click trains,'' J. Acoust. Soc. Am. **107**, 2209–2214.
Marvit, P., and Crawford, J. D. (**2000b**). ''Auditory discrimination in a sound producing electric fish: Tone frequency and click-rate difference detection in Pollimyrus,'' Paper presented at the Midwinter meeting of the Association for Research in Otolaryngology, St. Petersburg, FL, February (unpublished).
Myrberg, Jr., A. A., Ha, S. J., and Shamblott, M. J. (**1993**). ''The sounds of bicolor damselfish (*Pomacentrus partitus*): Predictors of body size and a spectral basis for individual recognition and assessment,'' J. Acoust. Soc. Am. **94**, 3067–3070.
Popper, A., and Fay, R. (**1999**). ''The Auditory Periphery in Fishes,'' in *Comparative Hearing: Fish and Amphibians*, edited by A. Popper and R. Fay (Springer, New York).
Simmons, J. A., Ferragamo, M. J., and Moss, C. F. (**1998**). ''Echo-delay resolution in sonar images of the big brown bat, *Eptesicus fuscus*,'' Proc. Natl. Acad. Sci. USA **95**, 12647–12652.
Stipetic, E. (**1939**). ''Über das Gehörorgan der Mormyriden,'' Zeitschrift für vergleichende Physiologie **26**, 740–752.
Suga, N. (**1990**). ''Cortical computational maps for auditory imaging,'' Neural Networks **3**, 3–21.
Wever, E. G. (**1999**). *Theory of Hearing* (Wiley, New York).
Wiegmann, D. D., Baylis, J. R., and Hoff, M. H. (**1992**). ''Sexual selection and fitness variation in a population of smallmouth bass, *Micropterus dolomieui* (Pisces: Centrarchidae),'' Evolution (Lawrence, Kans.) **46**, 1740–1753.
Wiegmann, D. D., Baylis, J. R., and Hoff, M. H. (**1997**). ''Male fitness, body size and timing of reproduction in smallmouth bass, *Micropterus dolomieui*,'' Ecology **78**, 111–128.
Wier, C., Jesteadt, W., and Green, D. (**1976**). ''Frequency discrimination as a function of frequency and sensation level,'' J. Acoust. Soc. Am. **61**, 178–184.
Wyttenbach, R. A., May, M. L., and Hoy, R. R. (**1996**). ''Categorical perception of sound frequency by crickets,'' Science **273**, 1542–1544.
Yager, D. D., and Spangler, H. G. (**1997**). ''Behavioral response to ultrasound by the tiger beetle *Cicindela marutha* Dow combines aerodynamic changes and sound production,'' J. Exp. Biol. **200**, 649–659.

Monaural and binaural detection of sinusoidal phase modulation of a 500-Hz tone

Caroline Witton[a)]
Department of Physiological Sciences, University of Newcastle upon Tyne, The Medical School, Framlington Place, Newcastle upon Tyne NE2 4HH, United Kingdom

Gary G. R. Green and Adrian Rees
Department of Physiological Sciences, University of Newcastle upon Tyne, The Medical School, Framlington Place, Newcastle upon Tyne NE2 4HH, United Kingdom

G. Bruce Henning
SRU, Department of Experimental Psychology, University of Oxford, South Parks Road, Oxford OX1 3UD, United Kingdom

(Received 10 August 1999; revised 17 April 2000; accepted 19 July 2000)

The detectability of phase modulation was measured for three subjects in two-alternative temporal forced-choice experiments. In experiment 1, the detectability of sinusoidal phase modulation in a 1500-ms burst of an 80-dB (SPL), 500-Hz sinusoidal carrier presented to the left ear (monaural condition) was measured. The experiment was repeated with an 80-dB, 500-Hz static (unmodulated) tone at the right ear (dichotic condition). At a modulation rate of 1 Hz, subjects were an order of magnitude more sensitive to phase modulation in the dichotic condition than in the monaural condition. The dichotic advantage decreased monotonically with increasing modulation rate. Subjects ceased to detect movement in the dichotic stimulus above 10 Hz, but a dichotic advantage remained up to a modulation rate of 40 Hz. Thus, although sound movement detection is sluggish, detection of internal phase modulation is not. In experiment 2, thresholds for detecting 2-Hz phase modulation were measured in the dichotic condition as a function of the level of the pure tone in the right ear. The dichotic advantage persisted even when the level of the pure tone was reduced by 50 dB or more. The findings demonstrate a large dichotic advantage which persists to high modulation rates and which depends very little on interaural level differences. [S0001-4966(00)05110-9]

PACS numbers: 43.66.Pn [DWG]

I. INTRODUCTION

The acoustical information for determining the horizontal-plane location of static sound sources arises from differences in the waveforms reaching the two ears; for low-frequency sounds, interaural delays are crucial (Rayleigh, 1907). With moving sources, interaural cues change with time and their relative importance may be altered (Wallach, 1940). For example, when a sound source moves in the horizontal plane relative to a listener, the phase of the sound may change differently at the two ears so that the interaural phase of the sound is modulated. This article is concerned with the ability of human listeners to discriminate between sounds using such temporally changing interaural-phase differences (IPDs).

The earliest observations that temporally varying IPDs can generate a percept of source movement were made by presenting sounds of slightly different frequency to the two ears, resulting in an apparently moving ''binaural beat'' (Rayleigh, 1907). The phenomenon occurs because, over time, the instantaneous phase of the higher-frequency tone advances linearly in comparison with the phase of the lower-frequency tone. The rate of change of interaural phase is dependent on the frequency difference between the tones presented to each ear; the phase advances by one cycle (360 degrees) for each Hz of interaural frequency difference. In other words, a 1-Hz frequency difference results in one binaural beat per second. The percept associated with the binaural beat is highly subject dependent and differs according to conditions: for tones below 1000 Hz and for small frequency differences such as 1 Hz, the phase difference between the ears changes sufficiently slowly that most listeners hear a fused sound image that appears to move as the phase difference progresses between 0 and 360 degrees. For larger frequency differences, listeners hear a sound from a fixed location that varies in loudness (Licklider *et al.*, 1950).

The same type of stimulus has been used in neurophysiological studies to show that the auditory system contains units responsive to interaural phase (e.g., Yin and Kuwada, 1983). Griffiths *et al.* (1994) used the stimulus in a functional imaging study to demonstrate human cortical responses to interaural phase modulation.

Another technique for generating interaural phase modulation (IPM) has been used in a series of psychophysical studies (Green *et al.*, 1976; Henning and Zwicker, 1984; Zwicker and Henning, 1985). Green *et al.* (1976) measured detection thresholds for sinusoidal frequency modulation (FM) presented to one ear in the presence and absence of a

[a)]Present address: University Laboratory of Physiology, Parks Road, Oxford OX1 3PT, UK. Electronic mail: caroline.witton@physiol.ox.ac.uk

pure tone presented to the contralateral ear. In the monaural condition, the task was simply one of FM detection, but when the contralateral pure tone was added, the interaural phase of the sounds was modulated sinusoidally at the same rate as the FM. This stimulus differs from the binaural beat stimulus described above, because the change in interaural phase in binaural beats is linear, not sinusoidal.

Sinusoidal IPM is particularly interesting because it has also been used in the neurophysiological studies of Spitzer and Semple (1991, 1993). Spitzer and Semple modulated the frequency of a tone at one ear of anaesthetized cats and gerbils while presenting a pure tone to the other ear. They demonstrated nonlinear responses to the time-varying IPDs in inferior collicular (IC) neurones. One interesting feature of their work, which illustrates the importance of studying dynamically changing cues, was that the responses to changing IPDs could not be predicted from the responses of the same units to static IPDs. Spitzer and Semple's observations complement findings, derived from experiments using a wide range of acoustical stimuli, that show both movement and directionally sensitive cells at a variety of levels in the auditory system (e.g., Sovijärvi and Hyvärinen, 1974; Wagner and Takahashi, 1990; Toronchuk *et al.*, 1991; Stumpf *et al.*, 1992; Poirier *et al.*, 1997).

Findings in the psychophysical literature do not always support the notion of special responses to moving sounds in the behavior of human observers. It has been reported several times that minimum audible angles measured with moving sounds are larger than those measured with static sounds (Harris and Sargeant, 1971; Grantham, 1986; Chandler and Grantham, 1992). This has led to suggestions that the human binaural system may be less sensitive to sound movement than to the location of static sources. Indeed, it has been suggested that the auditory system has no specialization for moving sound analysis (Grantham, 1986; Chandler and Grantham, 1992).

Grantham and Wightman (1978) suggested that listeners' processing of interaural phase modulation is ''sluggish'' or slow. The suggestion was based on their measurement of thresholds for the discrimination of sinusoidal interaural phase modulation in a broadband stimulus from diotic phase modulation with the same modulation rate and modulation index; performance deteriorated sharply as the modulation rate increased from 2.5 Hz to 10 or 20 Hz. Further, Grantham (1986) showed that detection thresholds for a moving sound (simulated with a fixed two-loudspeaker system by dynamic variation of the amplitudes of the loudspeaker inputs) deteriorated exponentially with decreasing duration for durations less than 300 ms; the detection of sound movement appears to be limited when the processing time is restricted, suggesting that, in detecting movement, the auditory system is slow to respond to dynamic interaural cues.

There are some differences in the results of previous simple comparisons of FM and IPM detection. Green *et al.* (1976) found that at the lowest modulation rates they used (below 3 Hz), subjects were more sensitive to IPM (the dichotic stimulus) than they were to monaural FM alone. Henning and Zwicker (1984) and Zwicker and Henning (1985) also reported detection thresholds for the same stimulus. Their data differed from those of Green *et al.* (1976) because they found that the advantage available to subjects in the dichotic condition persisted to much higher modulation rates (about 40 Hz).

The discrepancy between the findings of these different studies, namely in the modulation rate below which there is a dichotic advantage, might be accounted for by a number of factors. First, these studies used different carrier frequencies for their stimuli (Green *et al.* used 500 Hz; Henning and Zwicker and Zwicker and Henning used 250 Hz). More importantly, each of these studies employed a method of adjustment to obtain a crude estimate of threshold, and that alone could account for the inconsistencies. In the present study, thresholds for detecting this IPM stimulus will be measured using the more reliable standard two-interval, two-alternative forced-choice (2I-2AFC) method. As well as providing more reliable data, this approach will provide baseline data for our subjects upon which to expand the findings of the studies described earlier.

In this study, we examine subjects' responses to interaural phase modulation. The experiments address the issue of binaural processing of IPM by measuring the detection of interaural phase modulation as a function of modulation rate and interaural level.

II. METHODS

A. Subjects

Three subjects, between 23 and 53 years of age, were seated separately in an IAC soundproofed booth and served in standard 2I-2AFC detection experiments. The subjects were all experienced subjects with normal hearing.

B. Stimuli

All the signals were generated using Tucker-Davies Technology equipment (TDT System II). The required waveforms were created digitally and scaled to fill the dynamic range of two independent 16-bit digital-to-analog converters. The sampling rate was 40 kHz, and the signals for each ear were low-pass filtered at 15 kHz, separately attenuated, and used to drive calibrated Sennheisser HD40 earphones working in phase. All the stimuli were gated on and off with 20-ms Gaussian rise/fall times.

The phase-modulated stimulus was given by

$$s(t) = A \sin [2\pi f_c t + \beta \sin (2\pi f_m t)], \quad (1)$$

where A is the amplitude of the signal, f_c (Hz) is the carrier frequency, f_m (Hz) is the rate of sinusoidal modulation, and β is the modulation index. The unmodulated (or static) carrier is given by

$$s(t) = A \sin [2\pi f_c t]. \quad (2)$$

Thus, in one observation interval, the phase (frequency) of the 500-Hz carrier was modulated at a given rate, f_m (Hz), and to a given depth, β [Eq. (1)]. The sinusoidal phase modulation, like the carrier, always began in sine phase. The other observation interval contained the unmodulated 500-Hz carrier [Eq. (2)].

C. Procedure

A 500-Hz sinusoidal carrier was presented monaurally (left ear) in each of the two 1500-ms observation intervals of each trial. In one interval, the phase of the carrier was sinusoidally modulated and the subjects were required to press one of two buttons to indicate whether the modulated signal had occurred in the first or in the second observation interval. Feedback was provided by lights that informed the subjects, after they had responded, which interval had contained the modulated waveform. In some experiments the stimulus in both observation intervals was accompanied by a 500-Hz pure tone (the reference tone) presented to the right ear. The modulated stimulus was presented to the left ear at 80 dB SPL. The level of the reference tone in the right ear, when present, could be adjusted. In all the experiments, subjects were not asked to detect movement or frequency change, but just to report which interval contained the modulated signal.

Trials were run in blocks of 150: 25 at each of six different depths of modulation, centered at the subject's threshold and spaced to span the entire psychometric function. The order of presentation of modulation depths was randomly chosen from trial to trial. Blocks were run at least four times to produce 100 points at each depth of modulation. Each data point on each psychometric function was thus based on a minimum of 100 observations for a single subject.

Data were collected for detection of monaural and binaural phase modulation (with the level of the stimulus equal in both ears in the binaural condition) at modulation rates of 1, 2, 5, 10, 20, 40, 60, and 120 Hz (experiment 1). For experiment 2, detection thresholds for 2-Hz interaural phase modulation (dichotic condition) were measured with the level of the pure tone in the right ear set at successive levels, in seven or eight approximately even steps, below the level of the modulated tone in the right ear.

D. Threshold computation

The psychometric function relating the percentage of correct responses to the depth of modulation was plotted, three-parameter Weibull functions fitted to the data, and threshold defined as the modulation depth giving 75% correct responses on the fitted function.[1]

In addition to the two standard parameters of the Weibull function, the third parameter was the ''lapse rate'' (λ), constrained to be less than 0.06. Nonzero lapse rates are most easily observed in cases where data for a subject asymptote below 100% in Fig. 1. The fitting technique employed in this study also provides nonparametric bootstrap estimation of the standard error of the mean threshold (Wichmann and Hill, 2000a, b) and standard error bars, when appropriate, are plotted for our data.

All thresholds reported in this study are a function of modulation depth, i.e., the degree of interaural phase modulation required for the subject to detect its presence. Modulation depth can be described in several ways. We use the modulation index, β, defined in Eq. (1). It equals the maximum change in phase, in units of radians, although it is conventionally reported without units. Modulation index in radians can be converted to depth of phase modulation, or phase-modulation angle ($\Delta\theta$), in units of degrees [Eq. (3)]:

$$\Delta\theta = \frac{\beta}{2\pi} \times 360. \tag{3}$$

Further, the phase-modulation angle has an equivalent delay, Δt s. This quantity can be calculated from $\Delta\theta$ in degrees [Eq. (4)]:

$$\Delta t = \frac{\Delta\theta}{360 f_c}. \tag{4}$$

Phase-modulation index (in radians) can also be converted to frequency deviation, Δf, in Hz, which is a function of the modulation rate, f_m:

$$\Delta f = \beta \times f_m. \tag{5}$$

All the data here are reported in terms of β, although the equivalent delay, Δt, is also reported where appropriate, to enable comparison with other literature. A good review of phase and frequency modulation can be found in Chap. 19 of Hartmann (1998).

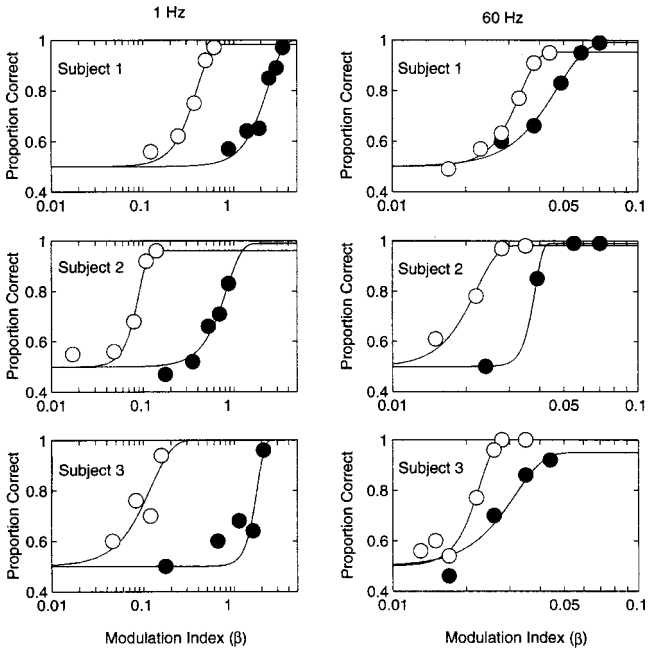

FIG. 1. Psychometric functions for three subjects detecting phase modulation in the dichotic and monaural conditions. Left-hand column: 1-Hz modulation; right-hand column: 60-Hz modulation. The proportion of intervals where the subject correctly identified the target interval is plotted against the modulation index (β; logarithmic axis). Each point is based on at least 100 observations. Filled symbols represent the monaural condition and open symbols represent the dichotic condition. The smooth line on each curve is the best fitting Weibull function, used to calculate threshold (see text for details). The reader should note the difference between the scales on the ordinate in the plots for the two modulation rates.

III. RESULTS

A. Experiment 1: The detection of monaural and dichotic phase modulation

Figure 1 shows psychometric functions for three subjects detecting the sinusoidal phase modulation of a 500-Hz carrier at the modulation rates of 1 Hz (left-hand column)

and 60 Hz (right-hand column). In all six panels, the proportion of correct responses is plotted as a function of modulation index (β), on semi-logarithmic axes. Each data point is based on at least 100 observations and the smooth curves through the data are the best-fitting Weibull functions.

For 1-Hz modulation (Fig. 1, left-hand column), in the monaural condition (solid circles), subjects reported that they perceived changes in the pitch of the signal at the modulation rate. At 1 Hz in the dichotic condition (open circles), they reported perceiving movement of a sound source. At the 1-Hz modulation rate, performance in the dichotic condition was about an order of magnitude better than in the monaural condition for all three subjects.

For 60-Hz modulation (Fig. 1, right-hand column; note the change of scale on the abscissa), the observers reported hearing a rough quality (Zwicker, 1952) when the modulation was present in both the monaural and dichotic conditions and no subjects reported hearing movement. Performance with dichotic stimuli was again better than with monaural stimuli, but the binaural advantage was reduced to a factor of 2.

Figure 2 shows thresholds in modulation index corresponding to 75% correct detection of monaural (solid circles) and dichotic (open circles) phase modulation, for modulation rates between 1 and 240 Hz. Error bars (where they exceed the size of the data point) represent the (nonparametric) estimates of the standard error of the threshold modulation index (Wichmann and Hill, 2000a, b). Figure 3 shows the ratio between dichotic and monaural thresholds, the dichotic advantage, for each of the three subjects. Performance in the dichotic condition changed very little with increasing modulation rate up to 20 Hz, but performance in the monaural condition improved dramatically over that range. Thresholds in the monaural condition are in accordance with previous work on FM detection (e.g., Zwicker, 1952; Schorer, 1986). It should be noted that FM thresholds are sometimes reported in Hz [i.e., as Δf; see Eq. (5)], or as the ratio of Δf to the carrier frequency, f_c (see, for example, Kay and Matthews, 1972; Moore and Glasberg, 1989). When plotted in that way, the relation between thresholds and modulation rate remains approximately constant. Our monaural thresholds are observed to decline simply because the units of depth when expressed as β are inversely determined by modulation rate.

The dichotic advantage became small at modulation rates above 40 or 60 Hz (most readily visible in Fig. 3). Although there were clear differences in detection performance with the monaural and dichotic stimuli at higher modulation rates, no subject reported hearing any movement in the dichotic stimulus once the modulation rate exceeded about 5 Hz.

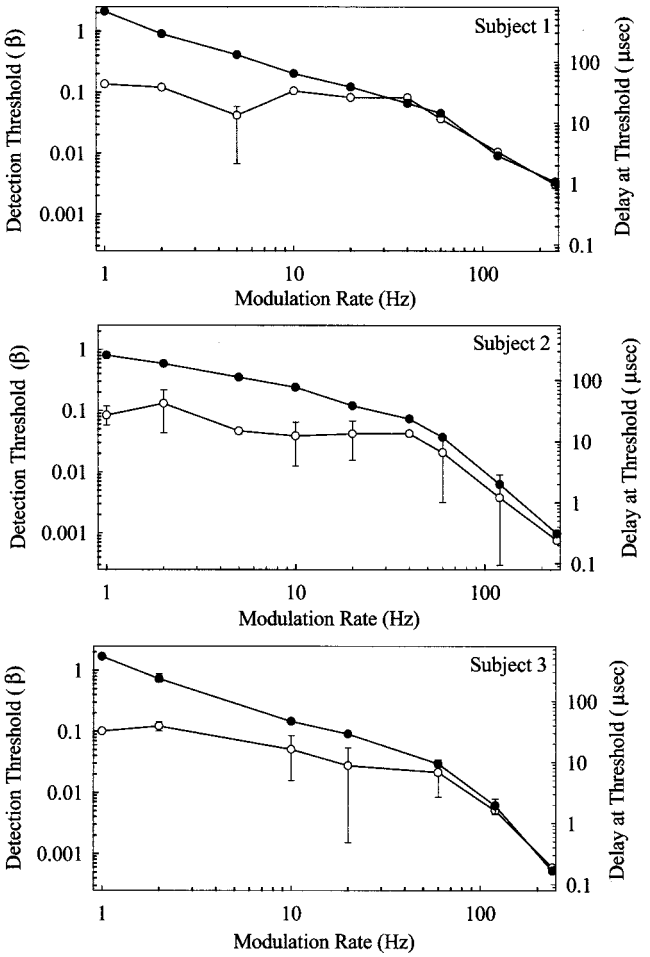

FIG. 2. Thresholds (modulation depth corresponding to 75% correct) for detection of phase modulation in the dichotic (open symbols) and monaural (filled symbols) conditions, as a function of modulation rate. Each plot shows data for one subject. Each point is based on at least 100 observations, and the error bars represent the standard error of the threshold (see text for details). The left-hand ordinate shows thresholds in modulation index (β); the right ordinate shows interaural delay in microseconds, applicable only in the dichotic condition.

B. Experiment 2: The effects of interaural level

The presence of a pure tone presented to the right ear (the reference tone) provides information that is clearly very useful to the binaural system in detecting phase modulation. The next experiment explored how the detectability of phase modulation in one ear depends on the level of the reference tone in the other. We used 2-Hz modulation with the level of the reference tone in the right ear attenuated by different amounts relative to the fixed level of the carrier in the left. Otherwise, the experimental conditions were the same as in the previous experiment.

Figure 4 shows the modulation depth corresponding to 75% correct responses as a function of the attenuation of the reference tone (in decibels) relative to the level of the carrier, which was 80 dB SPL. The error bars, when larger than the data points, represent the nonparametric estimates of the standard error of the threshold. The horizontal dashed line in each plot shows the 75% detection threshold for monaural phase modulation at 2 Hz for each subject. Each panel shows data for a different subject.

Subjects reported that an interaural level difference of more than about 10 dB led to the percept of the sound being localized entirely in the left ear and no perception of movement. In spite of this, there was little change in the detectability of the phase modulation until the reference tone was more than 40 dB below the level of the modulated carrier. Moreover, a dichotic advantage persisted, as can be seen by the difference between the dichotic values and the monaural value (indicated by the dashed horizontal line), even when

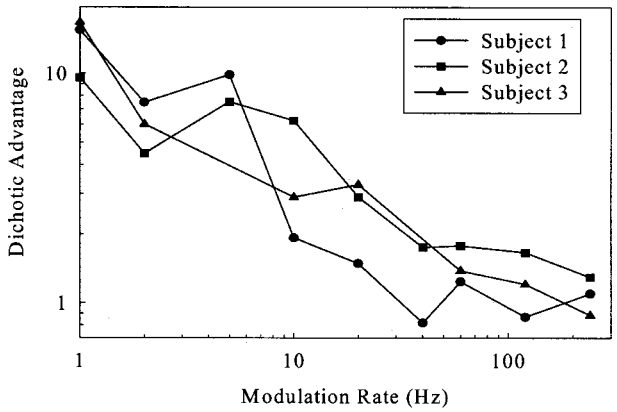

FIG. 3. The dichotic advantage is plotted as a function of modulation rate, with logarithmic ordinate and abscissa scales. Dichotic advantage is defined as the ratio between the monaural and binaural thresholds; a ratio exceeding unity indicates an advantage.

the reference tone was very nearly inaudible.

IV. DISCUSSION

The findings demonstrate that at low modulation frequencies, the detection of phase modulation in one ear is aided by the presence of a pure tone in the other. The observations confirm and extend those reported previously (Taylor *et al.*, 1971; Green *et al.*, 1976; Henning and Zwicker, 1984; Zwicker and Henning, 1985). The dichotic advantage is apparent for modulation frequencies up to 40 or 60 Hz and it is preserved to a great extent even when there is a large difference in level between the phase-modulated and the reference tones.

A. The effects of modulation rate

Although at low modulation rates subjects have a distinct advantage for detecting dichotic phase modulation compared to monaural detection, the dichotic advantage becomes progressively smaller for all subjects as the modulation rate increases, and disappears once it exceeds about 40–60 Hz. The modulation rate below which the dichotic advantage was found to be present in this study was higher than in the previous studies of Green *et al.* (1976), Henning and Zwicker (1984), and Zwicker and Henning (1985), despite the carrier frequency being the same in the present study as in the first study. The difference probably arises from the use of the 2I-2AFC paradigm in this study and the method of adjustments in the others.

One explanation of the observed decrease in the dichotic advantage as the modulation rate approaches 40–60 Hz is that the modulation rate has exceeded the subjects' critical modulation frequency (CMF) for a 500-Hz carrier; this has been reported to be approximately 60 Hz (Schorer, 1986). Zwicker (1952) was the first to postulate, from AM and FM detection experiments, that when the sidebands in the spectrum of a modulated tone lie outside the critical band, listeners can no longer make use of phase information contained in the spectrum of the tone. Thus detection thresholds for AM and FM are alike when the modulation rate exceeds half the critical bandwidth. At modulation rates below 60 Hz, our subjects were more sensitive to dichotic than monaural phase

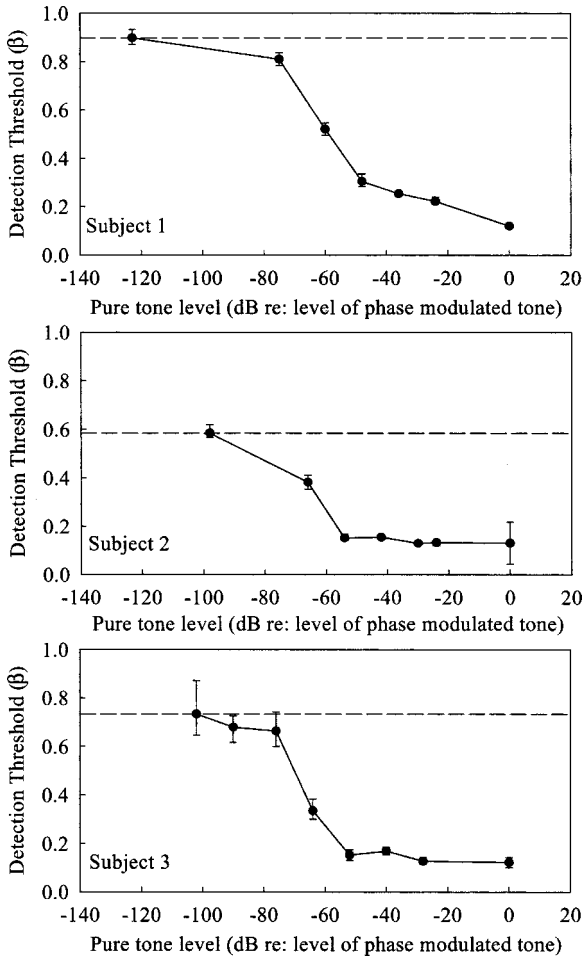

FIG. 4. Modulation depth corresponding to 75% correct detection from the dichotic condition is shown for three subjects, as a function of the level of the reference tone (in dB attenuation, relative to 80 dB SPL). The modulation rate was 2 Hz. Each panel presents data from a particular subject, and each observation is based on at least 100 observations. The horizontal dashed line shows the depth of modulation corresponding to 75% correct for each observer in the monaural condition from Fig. 2.

modulation, and so they could make use of the phase information contained in the spectra of the tones presented to each ear. However, when the modulation rate exceeds the CMF, the relevant spectral component of the modulated stimulus lies outside the critical band, the phase information is no longer available within one critical band, and the subjects appear to be unable to use it.

One issue that has frequently been addressed (Zwicker, 1952; Green, 1976; Moore, 1997) is the fact that the modulation of the stimulus frequency causes the stimulus to sweep over the frequency-tuning characteristics of the peripheral auditory filter. The consequence is that the effective input amplitude is also modulated, and this would generate an interaural amplitude modulation which the subject could use in addition. From the results of our second experiment it is clear that the level differences per se should not affect performance based on timing cues until the modulation index becomes very large. Interaction between an induced dynamic interaural-intensity cue and interaural-phase differences remains a possibility, although no dichotic advantage is obtained for detection of interaural amplitude modulation (IAM) over amplitude modulation (AM) detection (Witton

et al., 1998). Thus it appears that it is the interaural temporal cues that lead to the binaural advantage in the present study.

A second interpretation is that the binaural advantage decreases with increasing modulation rate because the segments of time spent in any given interaural phase condition decrease with increasing rate (Zwicker and Henning, 1985). This interpretation, however, is not easy to reconcile with the subjects' unchanging performance in the dichotic condition (the loss in binaural advantage arises principally from improvement in the monaural condition).

B. Effects of interaural level

Thresholds for detecting 2-Hz dichotic phase modulation are robust when there is a 40-dB interaural level difference, and the dichotic advantage persists even when the reference tone is almost inaudible. This suggests that the binaural system is able to make use of phase information when sounds are quiet. Phase-locked responding is certainly observed in primary auditory neurons at very low intensities (Johnson, 1980).

McFadden (1968) reported a similar phenomenon, from a series of experiments investigating binaural masking level differences (MLD). He measured the difference between noise-masked thresholds for a 400-Hz tone where the noise and signal were presented monaurally, and the condition where they were both binaural, but with an IPD of 180 degrees between the signal at each ear. The magnitude of the MLD was found not to decrease when the level of the noise was reduced by as much as 10 dB. A small MLD was obtained even when the interaural disparity in the noise was as great as 60 dB. Thus the effects of interaural level in this situation, where the phase difference enabling detection is static, are similar to those demonstrated in the present study with dynamic interaural phase.

Taylor *et al.* (1971) report relevant results with two fixed phases. They measured detection thresholds for a monaural sinusoidal burst masked by contralateral white noise, in the presence or absence of a contralateral cue. The cue was a sinusoid like the signal, but the cue was presented with a variety of phases and intensities relative to the signal. The phase of the cue sinusoid was an important factor in that some phases (''bad phases'') had a detrimental effect on detection, even compared to the condition with no cue. At 500 Hz, increasing the intensity of the cue in ''good phase'' (phases where the cue gave best performance) had little effect on detection, but it had a detrimental effect when the phase was ''bad.'' For the observers of Taylor *et al.*, the dichotic advantage disappeared with a 25-dB level difference. Unlike Taylor *et al.*, we did not use an unmodulated tone that was more intense than the carrier. Our stimuli, however, rotate through all interaural phases, both ''good'' and ''bad'' (to use the terms of Taylor *et al.*), at the modulation rate, and that may account for our observers preserving their binaural advantage at much larger level differences.

In the present study, when there was no interaural level difference, subjects reported a percept of sound movement for 2-Hz modulation in the dichotic condition. However, even when the tone is perceptually lateralized entirely in one ear, so that the subjects do not perceive the sound to move in the horizontal plane, thresholds for detecting the IPM remain the same. This observation suggests that perception of IPM at slow rates is not limited by the perception of motion, even though the percept is salient under certain conditions.

C. Neurophysiological parallels

Jeffress (1948) first postulated that interaural delay sensitivity was subserved by delay-line systems feeding arrays of coincidence detectors. Although the parallel with binaural cross-correlation does not appear to be valid (Gaskell, 1978; Henning, 1998), the physiological basis for the detection of IPDs has frequently been explored (Goldberg and Brown, 1969; Yin and Kuwada, 1983; Smith *et al.*, 1993). Sensitivity to static IPDs has been demonstrated in the medial nucleus of the superior olive (MSO) (e.g., Yin and Chan, 1990) and the inferior colliculus (e.g., Rose *et al.*, 1966). It has also been shown that dynamic interaural phase changes elicit very similar responses to static IPDs in the MSO (Spitzer and Semple, 1992). Similar evidence for the role of the MSO in humans has been reported by Griffiths *et al.*, 1994). However, although the responses of units in the gerbil MSO to dichotic phase modulation do not appear to differ from responses to static IPDs, neurons in the IC are reported as having special responses to dynamic phase changes (Spitzer and Semple, 1991, 1993).

Palmer *et al.* (1997) also measured responses to monaural and dichotic phase-modulation in IC units of the guinea pig using the stimulus we used in our psychophysical measurements. The response rate of low-frequency units was found to be modulated by presentation of both monaural and dichotic phase modulations. In the dichotic condition, the best phase of the IC units (the interaural phase difference at which maximum discharge occurs) was found to change linearly with the changing interaural phase of the stimulus. The amplitude of the peak discharge was found to decrease with increasing modulation rate, such that responses became insignificant for modulation rates above about 8–12 Hz.

The dichotic advantage observed in psychophysical studies (Fig. 3) was preserved up to at least 40 Hz, indicating that human subjects are still influenced by IPDs that are modulated at rates well above 12 Hz. Our listeners, however, reported hearing sound movement with interaural modulation rates of 1, 2, and 5 Hz, but not 10 Hz or above. Thus, although sound movement perception per se disappears at rates above 10 Hz, the advantage of interaural over monaural modulation detection persists to at least 40 Hz.

Palmer *et al.* (1997) also reported that the response to dichotic phase modulation was preserved in IC cells even when the level of the reference tone in the contralateral ear of the guinea pig was reduced by about 60 or 70 dB, well below the monaural and binaural (diotic) thresholds for the unit. The results are similar to those from primary auditory neurones reported by Johnson (1980), where, at least at their characteristic frequency, units retain a high index of phase locking until input levels are reduced to within a few tens of decibels of their absolute ''threshold.''

D. Is dichotic phase modulation detection sluggish?

Grantham and Wightman (1978) were the first to suggest that processing of IPM is sluggish. This suggestion was based on the observation that discrimination of IPM from FM deteriorated significantly with increasing modulation rate. Other work, based on measurements of the length of the binaural temporal window, i.e., the minimum binaural integration time, have supported the suggestion that binaural processing in general is sluggish. For example, measurements using binaural masking level difference (e.g., Bell, 1972; Kollmeier and Gilkey, 1990), gap detection (e.g., Akeroyd and Summerfield, 1999), and detection in notched noise (e.g., Culling and Summerfield, 1998) have demonstrated a binaural temporal window of 100 ms or more, an order of magnitude longer than the temporal window for monaural stimuli (Plack and Moore, 1990). Thus, it seems clear that binaural processing is sluggish, or restricted in temporal acuity, in many ways.

The data described here show that subjects are more sensitive to dichotic than monaural phase modulation at modulation rates of 40 Hz and below. This observation implies that the human auditory system is indeed sensitive in its response to dichotic phase modulation, at least when compared with its sensitivity to monaural phase changes. The detectability of monaural phase modulation (expressed in modulation index) increases as modulation rate is increased, so that the difference between dichotic and monaural performance decreases. But thresholds in the dichotic condition decrease very little with increasing rate, suggesting that the auditory system's capacity for processing this stimulus, as a function of the modulation index at threshold, is not affected adversely by the speed of the phase changes. Thus the results of the present study do not reflect any sluggishness in the processing of IPM. Indeed, binaural processing of IPM is more efficient than monaural processing of FM across a wide range of modulation rates.

Grantham (1986) showed that movement detection thresholds (although the movement was not cued by IPM) could also be described as sluggish as sensitivity was limited by the velocity of movement. Although we did not directly measure motion perception, the subjects observed that movement perception ceased when the modulation rate increased much above 5 Hz. Furthermore, neurophysiological responses to dichotic phase modulation in the IC of the guinea pig are not present above 8–12 Hz (Palmer *et al.*, 1997), and both observations suggest that the perception of movement might be sluggish. Thus were the subjects' task to depend on detecting movement, however, it seems clear that the maximum modulation rate for detection would be of the same order as that found in Grantham and Wightman's task.

V. SUMMARY

The findings described here show that subjects are an order of magnitude more sensitive to dichotic phase modulation than to monaural phase modulation. The dichotic advantage is greatest for 1-Hz modulation, and decreases with increasing rate, becoming small for 60-Hz modulation, principally because detectability in the monaural condition improves with modulation rate. This finding does not reflect the binaural sluggishness characteristic of sound movement detection. The advantage for detecting dichotic phase modulation also remains large in the presence of significant interaural level differences.

ACKNOWLEDGMENTS

This work was supported by the MRC and Rodin Remediation (CW).

[1]The maximum likelihood fitting procedure is described in two papers by Wichmann and Hill (2000a, b), available on the web at http://users.ox.ac.uk/~sruoxfor/psychofit/pages/papers.shtml, where software for the fitting routines is provided. The two-parameter Weibull function provides the basis for the fit and normally runs from 50% to 100% correct responses. Occasional lapses on the part of the observers can lead to large errors in the estimated slope of the function, particularly if they occur when the observers are performing close to the top of the function (Wichmann and Hill, 2000a, b). To avoid this problem, Wichmann and Hill introduce a third parameter, λ, called the lapse rate and constrained to be less than 6%. Thus the function fitted in Fig. 1 is given by

$$f(x) = 0.5 + (0.5 - \lambda)\left[1 - \exp\left(-\left(\frac{x}{\alpha}\right)^{\beta}\right)\right],$$

where x is the (non-negative) modulation index. Note: In this equation, β is used to represent the ''slope'' parameter of the Weibull function.

Akeroyd, M., and Summerfield, A. (**1999**). ''A binaural analogue of gap detection,'' J. Acoust. Soc. Am. **105**, 2807–2820.

Bell, D. (**1972**). ''Effect of fringe on masking-level difference when gating from uncorrelated to correlated noise,'' J. Acoust. Soc. Am. **52**, 525–529.

Chandler, D. W., and Grantham, D. W. (**1992**). ''Minimum audible movement angle in the horizontal plane as a function of stimulus frequency and bandwidth, source azimuth, and velocity,'' J. Acoust. Soc. Am. **91**, 1624–1636.

Culling, J., and Summerfield, A. (**1998**). ''Measurements of the binaural temporal window using a detection task,'' J. Acoust. Soc. Am. **103**, 3540–3553.

Gaskell, H. (**1978**). ''Some aspects of the localisation of transient sounds in man,'' D. Phil. Thesis, Oxford Univ.

Goldberg, J. M., and Brown, P. B. (**1969**). ''Response of binaural neurons of dog superior olivary complex to dichotic tonal stimuli: some physiological mechanisms of sound localization,'' J. Neurophysiol. **32**, 613–636.

Grantham, D. W. (**1986**). ''Detection and discrimination of simulated motion of auditory targets in the horizontal plane,'' J. Acoust. Soc. Am. **79**, 1939–1949.

Grantham, D. W., and Wightman, F. L. (**1978**). ''Detectability of varying interaural temporal differences,'' J. Acoust. Soc. Am. **63**, 511–523.

Green, G. G. R. (**1976**). ''Temporal aspects of audition,'' D. Phil. thesis, Oxford Univ.

Green, G. G. R., Heffer, J. S., and Ross, D. A. (**1976**). ''The detectability of apparent source movement effected by interaural phase modulation,'' J. Physiol. **260**, 49P.

Griffiths, T. D., Bench, C. J., and Frackowiack, R. S. J. (**1994**). ''Human corical areas selectively activated by apparent sound movement,'' Curr. Biol. **4**, 892–895.

Harris, J. D., and Sergeant, R. (**1971**). ''Monaural/binaural minimum audible angle for a moving sound source,'' J. Speech Hear. Res. **14**, 618–629.

Hartman, W. M. (**1998**). *Signals, Sound, and Sensation* (Springer Verlag, New York).

Henning, G. B. (**1988**). In *Basic Issues in Hearing*, edited by H. Duifhuis, J. W. Horst, and H. P. Wit (Academic, New York), pp. 141–142.

Henning, G. B., and Zwicker, E. (**1984**). ''Binaural masking level differences with tonal maskers,'' Hear. Res. **16**, 279–290.

Jeffress, L. A. (**1948**). ''A place theory of sound localization,'' J. Comp. Physiol. Psychol. **61**, 468–486.

Johnson, D. H. (**1980**). ''The relationship between spike rate and synchrony in responses of auditory nerve fibers to single tones,'' J. Acoust. Soc. Am. **68**, 1115–1122.

Kay, R. H., and Matthews, D. R. (**1972**). ''On the existence in human auditory pathways of channels selectively tuned to the modulation present in frequency-modulated tones,'' J. Physiol. **225**, 657–677.
Kollmeier, B., and Gilkey, R. H. (**1990**). ''Binarual forward and backward masking: Evidence for sluggishness in binaural detection,'' J. Acoust. Soc. Am. **87**, 1709–1719.
Licklider, J. C., Webster, J. C., and Hedlun, J. M. (**1950**). ''On the frequency limits of binaural beats,'' J. Acoust. Soc. Am. **22**, 468–473.
McFadden, D. (**1967**). ''Masking-level differences determined with and without interaural disparities in masker intensity,'' J. Acoust. Soc. Am. **44**, 212–223.
Moore, B. C. J. (**1997**). *An Introduction to the Psychology of Hearing*, 4th ed. (Academic, London).
Moore, B. C. J., and Glasberg, B. R. (**1989**). ''Mechanisms underlying the frequency discrimination of pulsed tones and the detection of frequency modulation,'' J. Acoust. Soc. Am. **86**, 1722–1732.
Palmer, A. R., Jiang, D., and McAlpine, D. (**1997**). ''Responses to sound motion: interaural amplitude and phase modulation in the inferior colliculus,'' paper presented at the 11th International Symposium on Hearing, Grantham, UK.
Plack, C. J., and Moore, B. C. J. (**1990**). ''Temporal window shape as a function of frequency and level,'' J. Acoust. Soc. Am. **87**, 2178–2187.
Poirier, P., Jiang, H., Lepore, F., and Guillemot, J.-P. (**1997**). ''Positional, directional and speed selectivities in the primary auditory cortex of the cat,'' Hear. Res. **113**, 1–13.
Rayleigh, Lord (**1907**). ''On our perception of sound direction,'' Philos. Mag. **13**, 214–232.
Reale, R. A., and Brugge, J. F. (**1990**). ''Auditory cortical neurons are sensitive to static and continuously changing interaural phase cues,'' J. Neurophysiol. **64**, 1247–1260.
Rose, J. E., Gross, N. B., Geisler, C. D., and Hind, J. E. (**1966**). ''Some neural mechanisms in the inferior colliculus of the cat which may be relevant to the localization of a sound source,'' J. Neurophysiol. **29**, 288–314.
Schorer, E. (**1986**). ''Critical modulation frequency based on the detection of AM versus FM tones,'' J. Acoust. Soc. Am. **79**, 1054–1057.
Smith, P. H., Joris, P. X., and Yin, T. C. T. (**1993**). ''Projections of physiologically characterized spherical bushy cell axons from the cochlear nucleus of the cat: evidence for delay lines to the medial superior olive,'' J. Comp. Neurol. **331**, 245–260.
Sovijärvi, A. R. A., and Hyvärinen, J. (**1974**). ''Auditory cortical neurons in the cat sensitive to the direction of sound source movement,'' Brain Res. **73**, 455–471.
Spitzer, M. W., and Semple, M. N. (**1991**). ''Interaural phase coding in auditory midbrain: Influence of dynamic stimulus features,'' Science **254**, 721–724.
Spitzer, M. W., and Semple, M. N. (**1992**). ''Responses to time-varying interaural phase disparity in gerbil superior olive: evidence for hierarchical processing,'' Soc. Neurosci. Abstr. **18**, 149.
Spitzer, M. W., and Semple, M. N. (**1993**). ''Responses of inferior colliculus neurons to time-varying interaural phase disparity: effects of shifting the locus of virtual motion,'' J. Neurophysiol. **69**, 1245–1263.
Stumpf, E., Toronchuk, J. M., and Cynader, M. S. (**1992**). ''Neurons in the cat primary auditory cortex sensitive to correlates of auditory motion in three dimensional space,'' Exp. Brain Res. **88**, 158–168.
Taylor, M. M., Clarke, D. P. J., and Smith, S. M. (**1971**). ''Monaural detection with contralateral cue (MDCC). II. Sinusoidal signals at a constant performance level,'' J. Acoust. Soc. Am. **49**, 1795–1804.
Toronchuk, J. M., Stumpf, E., and Cynader, M. S. (**1991**). ''Auditory cortex neurons sensitive to correlates of auditory motion: underlying mechanisms,'' Exp. Brain Res. **88**, 169–180.
Wagner, H., and Takahashi, T. (**1990**). ''Neurons in the midbrain of the Barn Owl are sensitive to the direction of apparent acoustic motion,'' Naturwissenschaften **77**, 439–442.
Wallach, H. (**1940**). ''The role of head movements and visual cues in sound localization,'' J. Exp. Psychol. **27**, 339–368.
Wichmann, F. A., and Hill, N. J. (**2000a**). ''The psychometric function I: fitting, sampling, and goodness-of-fit,'' available at http://users.ox.ac.uk/~sruoxfor/psychofit/pages/papers.shtml
Wichmann, F. A., and Hill, N. J. (**2000b**). ''The psychometric function II: bootstrap-based confidence intervals and sampling,'' available at http://users.ox.ac.uk/~sruoxfor/psychofit/pages/papers.shtml
Witton, C., Rees, A., Lavis, R., Griffiths, T. D., and Green, G. G. R. (**1998**). ''Detection and discrimination of apparent sound movement by human listeners,'' J. Physiol. **506P**, 85.
Yin, T. C. T., and Chan, J. C. K. (**1990**). ''Interaural time sensitivity in the medial superior olive of the cat,'' J. Neurophysiol. **64**, 465–488.
Yin, T. C. T., and Kuwada, S. (**1983**). ''Binaural interaction in low-frequency neurons in inferior colliculus of the cat. II. Effects of changing rate and direction of interaural phase,'' J. Neurophysiol. **50**, 1000–1019.
Zwicker, E. (**1952**). ''Die Grenzen der Hörbarkeit der Amplitudenmodulation und der Frequenzmodulation eines Tones,'' Acustica **2**, 125–133.
Zwicker, E., and Henning, G. B. (**1985**). ''The four factors leading to binaural masking level differences,'' Hear. Res. **19**, 29–47.

Localization of brief sounds: Effects of level and background noise

Ewan A. Macpherson[a] and John C. Middlebrooks
Kresge Hearing Research Institute, University of Michigan, 1301 East Ann Street, Ann Arbor, Michigan 48109-0506

(Received 8 November 1999; revised 3 May 2000; accepted 19 July 2000)

Listeners show systematic errors in vertical-plane localization of wide-band sounds when tested with brief-duration stimuli at high intensities, but long-duration sounds at any comfortable level do not produce such errors. Improvements in high-level sound localization associated with increased stimulus duration might result from temporal integration or from adaptation that might allow reliable processing of later portions of the stimulus. Free-field localization judgments were obtained for clicks and for 3- and 100-ms noise bursts presented at sensation levels from 30 to 55 dB. For the brief (clicks and 3-ms) stimuli, listeners showed compression of elevation judgments and increased rates and unusual patterns of front/back confusion at sensation levels higher than 40–45 dB. At lower sensation levels, brief sounds were localized accurately. The localization task was repeated using 3-ms noise burst targets in a background of spatially diffuse, wide-band noise intended to pre-adapt the system prior to the target onset. For high-level targets, the addition of background noise afforded mild release from the elevation compression effect. Finally, a train of identical, high-level, 3-ms bursts was found to be localized more accurately than a single burst. These results support the adaptation hypothesis.
[S0001-4966(00)05210-3]

PACS numbers: 43.66.Qp, 43.66.Ba [DWG]

I. INTRODUCTION

In general, human sound localization is reasonably accurate in azimuth and elevation when broad-spectrum sounds are presented at moderate sound levels and with durations on the order of 100 ms or greater (Oldfield and Parker, 1984; Wightman and Kistler, 1989; Makous and Middlebrookes, 1990; Carlile *et al.*, 1997). Two recent studies, however, have revealed some unusual aspects of the localization of brief sounds and suggest that the processing of spectral localization cues for sounds of short duration is degraded. In the present study we sought to extend and connect these findings.

In the first study, Hartmann and Rakerd (1993) presented noise bursts and clicks at low and high sound levels from one of three loudspeakers located behind, above, or in front of their listeners. They measured listeners' ability to identify the active loudspeaker. Identification accuracy was high and relatively unaffected by sound level for long-duration (880 ms) noise bursts. In contrast, accuracy for click stimuli decreased markedly as the sound level was increased. The authors termed this the *negative level effect* for clicks.

In a second study, Hofman and Van Opstal (1998) observed that the elevation component of localization judgments for frontally presented noise bursts became increasingly biased (or *compressed*) towards the horizontal plane as the duration of the stimulus was reduced from 500 to 3 ms. Elevation judgments maintained a high correlation with target elevation, but the ratio between the reported and actual target displacements from the horizontal plane was less than unity for brief stimuli. A similar compression occurred when silent gaps in trains of 3-ms noise bursts were increased from 0 to 77 ms. The authors interpreted these results as an indication that the auditory system derives a final estimate of elevation by integrating consecutive short-term estimates, and that a stimulus duration of at least 80 ms is required for an accurate final estimate. However, since their stimuli were presented at a relatively high sound pressure level (70 dB *re* 20 μPa), an alternative explanation is that this *elevation compression effect* is related to the negative level effect reported by Hartmann and Rakerd (1993).

Our aims in the present study were threefold. First, we wished to characterize more fully the localization by human listeners of brief, high-level sounds. By doing this we hoped to find an underlying pattern of responses that would account for both the negative level and elevation compression effects and, by extension, address general limitations of the auditory system in processing such sounds. In experiment I, we collected absolute judgments of sound source location for targets of long and short durations at low and high levels placed at many locations surrounding the listeners. This approach allowed us to expand on the work of Hartmann and Rakerd (1993), who reported identification error rates for three target locations but not the underlying distribution of localization responses, and on that of Hofman and Van Opstal (1998), in which listeners' responses were constrained to the ocular-motor range (approximately ± 30 degrees in azimuth and elevation), and in which sound intensity was held constant at a fairly high level. We also explored the possibility that the elevation compression reported in the latter study was caused by the inherent spectral irregularity of the brief Gaussian noise bursts used, which might have interfered with the extraction of pinna-based spectral cues. This was done by presenting both Gaussian noise and unvarying, flat-spectrum

[a]Electronic mail: emacpher@umich.edu

click stimuli. These stimulus types had similar bandwidths but different spectral and temporal irregularity and between-trial variability.

Second, in experiment II we tested the hypothesis that the elevation compression effect is due to an interaction of stimulus duration and level, rather than to short duration *per se*. If this is the case, then the negative level and elevation compression effects are likely different manifestations of a common failure of spectral cue processing for brief, loud sounds. Testing this hypothesis involved the localization of frontal, 3-ms noise bursts presented at sensation levels ranging between 30 and 55 dB.

Finally, we explored the possibility that peripheral adaptation influences the processing of spectral information in high-level stimuli. In experiment III, this was done by measuring elevation compression for brief, intense noise bursts presented in a background of wide-band noise of various intensities. This background noise was intended to pre-adapt the system prior to the target onset. In experiment IV, we examined the effect of increasing stimulus duration without adding independent spectral information. This was done by presenting stimuli comprised of repeated, identical, 3-ms noise bursts—a stimulus condition mentioned by Hofman and Van Opstal (1998).

II. EXPERIMENT I: EFFECTS OF LEVEL, DURATION, AND WAVEFORM

A. Methods

1. Subjects

Eighteen paid listeners (six female and twelve male, ages 18–36 years) were recruited from the student body of the University of Michigan and the staff of the Kresge Hearing Research Institute. Only three (including the first author, S18) had extensive listening experience in psychoacoustic experiments. All listeners had normal hearing as defined by standard audiometric testing. Five listeners (S18, S30, S51, S52, and S53) participated in experiment I. Four (including S18 and S51) participated in experiment II, six (including S18 and another from experiment II) in experiment III, and eight (including S18) in experiment IV.

2. Target stimulus types and locations

Stimuli were presented through one of two loudspeakers. The loudspeakers were calibrated by measuring their transfer functions using the Golay code excitation and deconvolution technique (Golay, 1961; Zhou *et al.*, 1992). The reciprocal of the transfer function of each loudspeaker was used to synthesize stimuli with one of two waveform types: Gaussian noise bursts and clicks. Both stimulus types were broadband, but differed in their variation from trial to trial. The noise bursts varied in waveform and spectral profile between trials, whereas the clicks had a frozen waveform and a flat spectrum.

The noise bursts had a bandwidth of 0.3–18 kHz with a roll-off of approximately 40 dB/oct below 1 kHz. A fresh Gaussian noise sample was generated on every trial. Clicks were synthesized by computing and windowing (to 3 ms) the inverse Fourier transform of the reciprocal of the measured transfer function of the appropriate loudspeaker. The resulting acoustic waveform had approximately 90% of its energy concentrated within 50 μs and was flat within ± 5 dB from 1 to 18 kHz. Using a similar transfer function inversion, the synthesis of the noise-burst stimuli incorporated a pre-equalization which effectively flattened the loudspeakers' transfer functions to within ± 1 dB across the stimulus bandwidth.

Noise-burst durations were either 100 or 3 ms including 1-ms raised-cosine onset and offset ramps. Levels were either *low* (25–35 dB above threshold) or *high* (50–60 dB above threshold). Given the listeners' measured thresholds (Sec. II A 4), the mean absolute sound pressure levels for the high-level 100- and 3-ms noise bursts were 62 and 71 dB, respectively.

We refer to the clicks and 3-ms noise bursts collectively as *short*, and 100-ms bursts as *long*. In the course of experiment I, clicks were presented once at low level and once at high level from each of 238 target locations. Noise bursts were presented twice (on separate trials) at each of the four combinations of level and duration (low-long, high-long, low-short, and high-short). Of the target locations, 190 lay in the half of auditory space lying between $+30$ degrees and -30 degrees of the vertical midline, and the remainder were positioned more laterally, within 40 degrees of the interaural axis (Fig. 1). Elevation ranged between -60 degrees and $+70$ degrees. This target distribution was intended to concentrate data collection at locations where the effects of incorrect spectral cue use would be most apparent, while encouraging the listeners to use the full range of lateral angle responses.

3. Apparatus

Stimuli were synthesized and presented at a sampling rate of 100 kHz using an array processor, digital-to-analog converters, and attenuators from Tucker-Davis Technologies (TDT). The signals fed a power amplifier (Adcom GFA-535II, modified for unity voltage gain) and were directed to the appropriate loudspeaker through a power multiplexer (TDT PM1). No explicit reconstruction filter was used, but the passband of the loudspeakers was sufficiently restricted to filter out any spectral artifacts, which would in any case have been inaudible, as they lay above the Nyquist frequency of 50 kHz. Stimuli were presented from one of two loudspeakers (Pioneer TS-879 two-way coaxial) mounted opposite each other on a 1.2-m-radius hoop. This hoop could be rotated about horizontal and vertical axes by computer-controlled stepper motors, thus allowing one or other of the loudspeakers to be positioned nearly anywhere around a centrally situated listener. The hoop was located in a large sound-attenuating anechoic chamber (2.6 m$\times$3.7 m$\times$3.2 m of usable space), the walls and ceiling of which were lined with glass-fiber wedges and the floor with sound-absorbing foam. All stimulus generation, hoop location, and data collection tasks were controlled by custom software written in C and MATLAB (The Mathworks, Inc.) running on a single Intel-based desk-top computer.

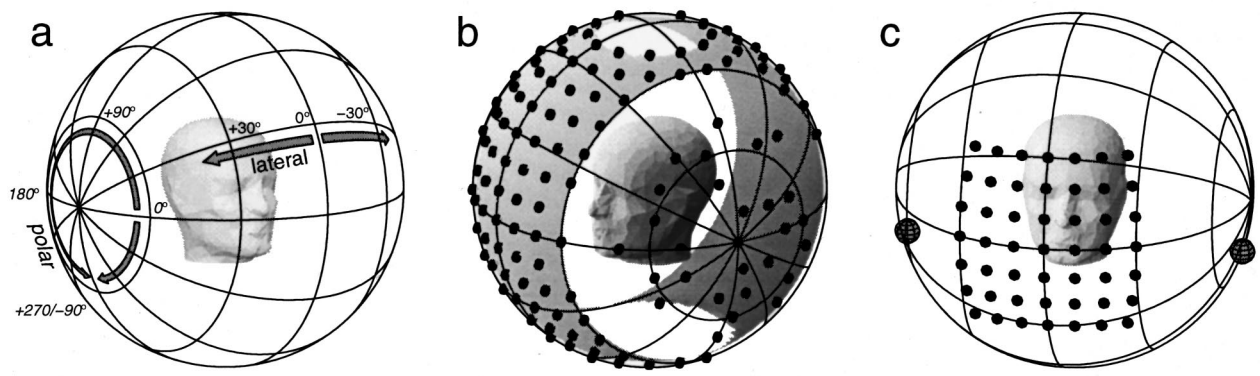

FIG. 1. Horizontal polar coordinate system and distributions of targets. (a) Lateral angle is the angle between the source and the median sagittal plane; positive values are to the listener's right. Polar, or circumaural, angle combines elevation and front/back position. −90 degrees: below; 0 degrees: front; +90 degrees: overhead; +180 degrees: rear. (b) In experiment I, 238 front, rear, and lateral target locations were distributed as shown with a concentration in the medial half of auditory space. Front and rear targets were equally numerous. (c) Experiments II and III used a restricted range of target locations in front of the listener. In Experiment III an antiphase background noise was delivered from two laterally positioned sources (gray spheres).

4. Detection thresholds

Prior to collecting localization data, detection thresholds for 100- and 3-ms Gaussian noise bursts and clicks were measured for each listener. Sounds were presented in the anechoic chamber from a loudspeaker at ear level directly in front of the listeners, who performed a two-interval, two-alternative, forced-choice task in which the signal level was controlled by a three-down, one-up adaptive tracking procedure (Levitt, 1971). Stimulus sensation levels were defined individually for each listener using these thresholds, and unless otherwise specified, all dB levels given in this paper refer to these sensation levels rather than absolute sound pressure level. Thresholds for the 3-ms noise bursts ranged between 14 and 18 dB and those for the 100-ms bursts between 3 and 10 dB ($re\ 20\ \mu$Pa). For the two listeners (S30 and S51) who had the highest thresholds for the short stimuli, it was not possible to present these sounds at the highest desired sensation levels (60 dB), due to the limited gain available in the stimulus delivery system. However, a sensation level of at least 55 dB was achievable in all cases.

5. Localization procedure

Localization trials were conducted in the darkened anechoic chamber. Each listener stood on a platform, the height of which was adjusted to position the head at the center of rotation of the loudspeaker hoop. Each wore a cap bearing a sensor which was part of a system (Polhemus FASTRAK) that allowed the orientation of the head to be measured. At the beginning of a block of trials, a *centering loudspeaker* situated at ear level outside the hoop in front of the listener emitted a series of noise bursts while an attached light-emitting diode (LED) flashed. This provided a visual and auditory reference for the frontal-horizontal direction. The listener oriented towards this speaker and depressed a response button to zero the head-tracking system.

Following this, a succession of localization trials was presented. First the hoop moved one of the loudspeakers to the target location. Then the centering loudspeaker began to produce a continuous, wide-band noise at a sound pressure level of approximately 40 dB. The listener oriented towards this sound, and depressed a button when ready to hear the target stimulus. The centering sound was turned off, and, following a random delay of 600–1200 ms, the stimulus was presented. Listeners indicated the apparent position of the target by turning the head and/or body so that the nose pointed in the desired direction. A second button press then triggered a reading of the head orientation and caused the program controlling the experiment to proceed to the next trial (Makous and Middlebrooks, 1990).

Listeners unfamiliar with the head-pointing task first completed a 10-min session of *head-training* in which they oriented to a visual target on the loudspeaker hoop. After each orienting response was recorded, the hoop was moved to position the target speaker at the response location, thus indicating the degree and direction of error. Auditory targets (250-ms wide-band noise bursts at a sensation level of 40 dB) were then introduced. All listeners completed one training session (60 trials) in which they oriented to auditory targets with the lights on in the anechoic chamber, two sessions with the lights off but with visual feedback from the target loudspeaker LED following each response, and then two or more sessions in the darkened chamber with no feedback. After each training session, the listeners were given verbal feedback about pervasive biases (typically undershoot in elevation) present in their orienting responses.

The test stimuli were presented in blocks of 100–120 trials. All trials in a block consisted of stimuli of similar duration (short or long) and level (low or high), but waveform types and locations were intermixed. In order to reduce cues to the target location based on the duration of motion of the hoop (which was clearly audible) the sequence of target locations within a block were sorted in such a way that the hoop always rotated by 60–120 degrees between trials. Each listener completed five blocks of trials for the long-low and long-high conditions and (due to the addition of the click waveform) seven blocks for the short-low and short-high. Each block of trials took approximately 15–20 min, and listeners typically completed two blocks per session separated by a rest period. Block types were interleaved throughout the course of the experiment. Prior to each session, listeners

completed 2–3 min of head-training (as described above) in preparation for the auditory localization task.

6. Data analysis

The negative level effect described by Hartmann and Rakerd (1993) manifested itself in the inability of listeners to correctly identify the source of an intense click as in front, overhead, or behind. It is likely that this effect resulted from misperception of the targets' elevation and front/back location. Hofman and Van Opstal (1998) found that the polar gain (slope of the target-response vertical angle function) decreased as the duration of their intense noise bursts was decreased, but that the variance in the responses was unaffected. In order to make a comparison with these two studies, the data from the present experiments were analyzed in terms of the gain and scatter of the lateral and polar angle response components and the rate of front/back reversals. Only responses for targets located within 30 degrees of the median plane were included in the analysis. Figure 2 shows how the analysis proceeded for a simulated data set.

First, the target and response locations, which were originally recorded in standard polar coordinates (azimuth and elevation), were converted to the horizontal polar coordinate system illustrated in Fig. 1. The *lateral* dimension represents angular displacement from the median sagittal plane, and *polar* (or *circumaural*; Shaw, 1982) angle represents rotation about the interaural axis, with locations on the horizontal plane in the frontal hemisphere having a polar angle of 0 degrees. This is a natural coordinate system for human localization data since perceived lateral angle is known to depend mainly on interaural cues such as low-frequency interaural time difference, whereas the perceived polar angle apparently is derived primarily from spectral information (Wightman and Kistler, 1992; Middlebrooks, 1992).

Next, regression lines were fit to the lateral and polar angle data in order to estimate the gain values. All lateral angle data showed a high correlation between target and response, and a simple least-squares, linear regression was used. This was not appropriate for the polar angle data in experiment I, which were frequently multi-modal (due to front/back reversals) with nontrivial numbers of outliers (Fig. 2).

To isolate the systematically biased and non-front/back reversed responses prior to computation of the polar angle gain, an *ad hoc* selective, iterative regression procedure was devised. Data for front- (polar angles from −90 degrees to +90 degrees and rear- (+90 degrees to +270 degrees) hemisphere targets were analyzed separately. To initialize the procedure, the data set was temporarily limited to trials in which the response fell in the correct (front or rear) hemisphere, and a regression line was fit to these points. Then all points lying farther from the line than a criterion distance, Δ, were eliminated and the regression recomputed using only the remaining data. This procedure was iterated (typically two to three times) until it converged. Points eliminated during one iteration were available for reselection in future iterations if the regression line moved closer to them. A value for Δ of 40 degrees was found empirically to work well in fitting the regression line to the main concentration of the response distributions while ignoring outliers and reversed responses. The front and rear polar gains were defined as the slopes of these regression lines. In experiments II and III, the targets and responses were restricted to a frontal region and a simple regression was used to compute the gain.

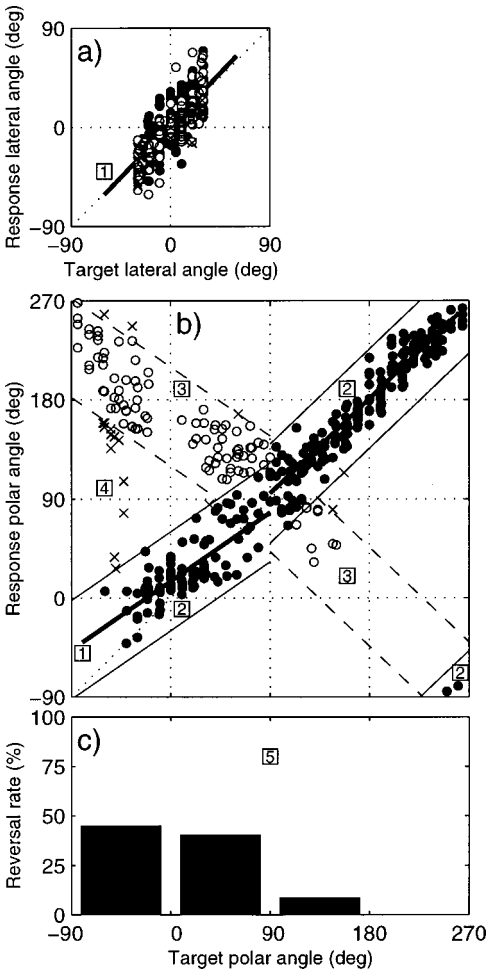

FIG. 2. Analysis procedure for localization response data: (a) lateral angle data, (b) polar angle data, and (c) front/back reversal rates. A simulated data set is presented as an example. (1) Regression lines were fit to the lateral and polar components of the target-response data (see text for details). Responses to front and rear targets were analyzed separately. Polar gain was defined as the slope of the regression line. (2) Responses within 45 degrees of the polar regression line were classed as *quasi-veridical* (filled circles, ●). Polar angle is circularly continuous, so responses in the upper left and lower right corners of the plot might be quasi-veridical. *Scatter* was defined as the standard deviation of the residuals of these data from the best-fit line. (3) Remaining responses within 45 degrees of the regression line once reflected into the opposite hemisphere were classed as *reversals* (open circles, ○). (4) The remainder were labeled *spurious* (×). (5) The proportion of reversal responses for targets in each quadrant was computed. Lateral angle responses are plotted with symbols representing the classification of the polar angle response.

Once the regression lines were found, each response was classified as *quasi-veridical*, *reversed*, or *spurious*. Quasi-veridical responses were defined as those lying within 45 degrees of the regression line. If the gain were close to 1, this region might extend into the opposite hemisphere for very high or very low target positions [Fig. 2(b)]. Reversed responses were those (not previously labeled quasi-veridical) lying within 45 degrees of the regression line once reflected

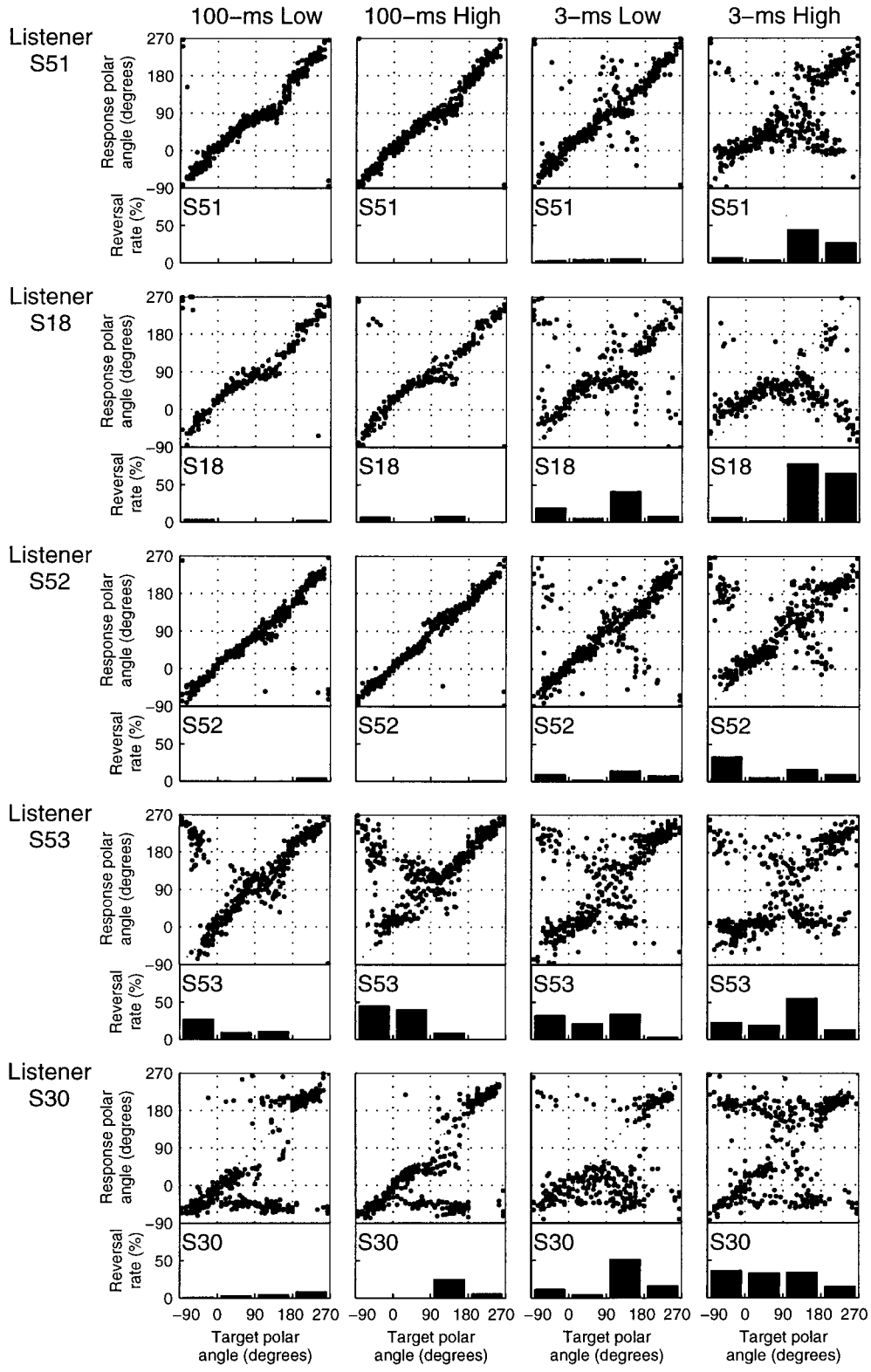

FIG. 3. Distribution of response polar angles and reversals to panoramic noise-burst stimuli. Each column of panels contains data for one noise-burst condition (100-ms low, 100-ms high, 3-ms low, and 3-ms high). Each row contains data for one listener. Click data are not shown. The histogram below each polar angle plot shows the reversal rate in each quadrant (front/down, front/up, rear/up, rear/down).

into the opposite hemisphere (region bounded by dashed lines). A later analysis of the data (Sec. II B 4) supports the legitimacy of this procedure. All remaining responses were classed as spurious. In Fig. 2(a), lateral angle responses are plotted with symbols corresponding to the classification of the response in the polar angle dimension.

Finally, using the regression lines and the response classification, values of scatter and reversal rate were computed. Polar angle scatter was calculated only for the quasi-veridical responses, and was defined as the standard deviation of the signed errors between the responses and the regression line. Reversal rates were defined as the percentage of responses classified as reversed for targets in each of four quadrants (front/down, front/up, rear/up, and rear/down). Reversal rates are shown in Figs. 2(c) and 3 in bar plots below the polar angle data.

B. Results

1. Polar angle response patterns: General observations

Examination of the panoramic localization data revealed that responses to the click stimuli were qualitatively similar to those to brief noise bursts. We concentrate here on the polar angle data for the noise bursts. The results for the clicks and the effect of waveform type are discussed in a later section (II B3), as is the lateral angle component of the responses (Sec. II B 5).

The polar angle components of listeners' responses in the four noise-burst conditions of experiment I are plotted in Fig. 3. Each row of panels shows the data for a single listener, and each column corresponds to a single stimulus condition. In the polar angle plots, veridical responses are those clustered near the positive diagonal, and reversed responses are those near the negative diagonal.

The 100-ms high-level condition provided the most stimulus energy per trial, and is the one most typical of other localization experiments using wide-band noise targets (Wightman and Kistler, 1989, for example) and of the baseline condition used by Hofman and Van Opstal (1998). It therefore provided the best insight into each listener's general localization ability, and, in particular, of the listeners' ability to process the spectral information necessary to estimate a target's polar angle.

The results for the 100-ms high-level condition (Fig. 3, second column) show that listeners S51, S18, and S52 are accurate localizers, with few reversed or spurious responses and little apparent compression in elevation judgments. Polar angle errors were highest for targets positioned above the listeners (near $+90$ degrees), a pattern which has been observed previously (Makous and Middlebrooks, 1990; Carlile *et al.*, 1997; Middlebrooks, 1999). Listener S53 produced accurate responses for targets in the rear hemisphere, but many responses to targets in the front were reversed to the rear. This is manifested as a concentration of points about the negative diagonal in the left half of the plot. A third pattern of responses was produced by listener S30, who responded accurately to most frontal and low-rear targets, but frequently pointed to a polar angle of approximately -45 degrees for targets in the upper hemisphere (polar angles between 0 degrees to 180 degrees) regardless of their true location. These data were excluded when regression lines were fit to S30's responses, but were included in calculations of scatter and reversal rates. We will refer to S51, S18, and S52 as *good* localizers, S53 as a *reverser*, and S30 as a *poor* localizer.

A comparison of the data for low- and high-level 100-ms targets (Fig. 3, columns 1 and 2) reveals no obvious effect of level, although listeners S53 and S30 did show a modest increase in reversal rates at the higher sound level. The largely unchanged performance is in agreement with the finding of Hartmann and Rakerd (1993) that there was no negative level effect for long noise-burst stimuli.

The 3-ms, low-level condition (Fig. 3, column 3) provided the lowest amount of stimulus energy per trial. The pattern of quasi-veridical responses appeared very similar to those for the 100-ms stimuli except perhaps for the poor listener, S30. For all listeners, there was an increase in scatter and the number of spurious responses and reversals in comparison to the 100-ms conditions. In general, however, the distribution of reversals across target quadrant was qualitatively similar to that observed for the 100-ms stimuli. That is, there was no substantial appearance of reversals in quadrants that had not exhibited them in either of the 100-ms conditions.

The 3-ms, high-level targets (Fig. 3, column 4) are those corresponding most closely to the high-level clicks used by Hartmann and Rakerd (1993) and to the shortest noise bursts used by Hofman and Van Opstal (1998). Hofman and Van Opstal observed compression of apparent elevation for frontal targets, while Hartmann and Rakerd found dramatic increases in error rates for identification of sources as front, overhead, or rear. The present results replicate the compression effect and demonstrate a distribution of polar angle errors which would account for Hartmann and Rakerd's results. Reduced polar angle gain can be clearly seen in the responses of listeners S51, S18, S52, and S53 as evidenced by the obviously shallow slopes of the main concentration of responses for targets in the front hemisphere. Reversal rates were higher in this stimulus condition than in any of the others, and for four of the five listeners (excepting S52), unusual patterns of reversals were observed. For example, listener S51 made no reversals from the rear-down quadrant in either of the long-duration conditions or in the 3-ms, low-level condition, but made a considerable number with the 3-ms, high-level targets. A similar pattern was observed for listeners S18 and S53. In addition, the poor localizer, S30, made many reversed responses for front-up and front-down targets, which had not occurred with the other types of stimuli.

2. Gain and scatter parameters

A quantitative summary of the polar angle results is provided in Fig. 4, in which polar angle gain and scatter parameters are plotted for the raw data of Fig. 3. For targets in the front [Figs. 4(a) and (b)], the three good localizers (solid lines) showed a consistent pattern of gain values; gains for the low- and high-level, 100-ms stimuli were approximately equal, gains for the 3-ms, low-level noise bursts were slightly reduced, and those for the 3-ms, high-level targets were substantially diminished. Apart from an exaggerated gain value for the 100-ms, low-level sounds, listener S53 showed approximately the same behavior. The results for S30 were anomalous in that the gain was substantially higher for the high-level, 3-ms stimuli than for the low-level ones. For S30, however, many of the targets that produced low-gain responses in the 3-ms, low-level condition produced reversals in the 3-ms, high-level condition, and, thus, were excluded from the gain computation. Four of the five listeners showed no effect of level but a small effect of duration on the scatter of front-target responses.

For targets in the rear [Figs. 4(c) and (d)], there appeared to be a decrease in gain associated with both high level (at both durations) and short duration (at both levels). The relative reduction in gain for 3-ms high-level stimuli presented from the rear was less than that observed for those

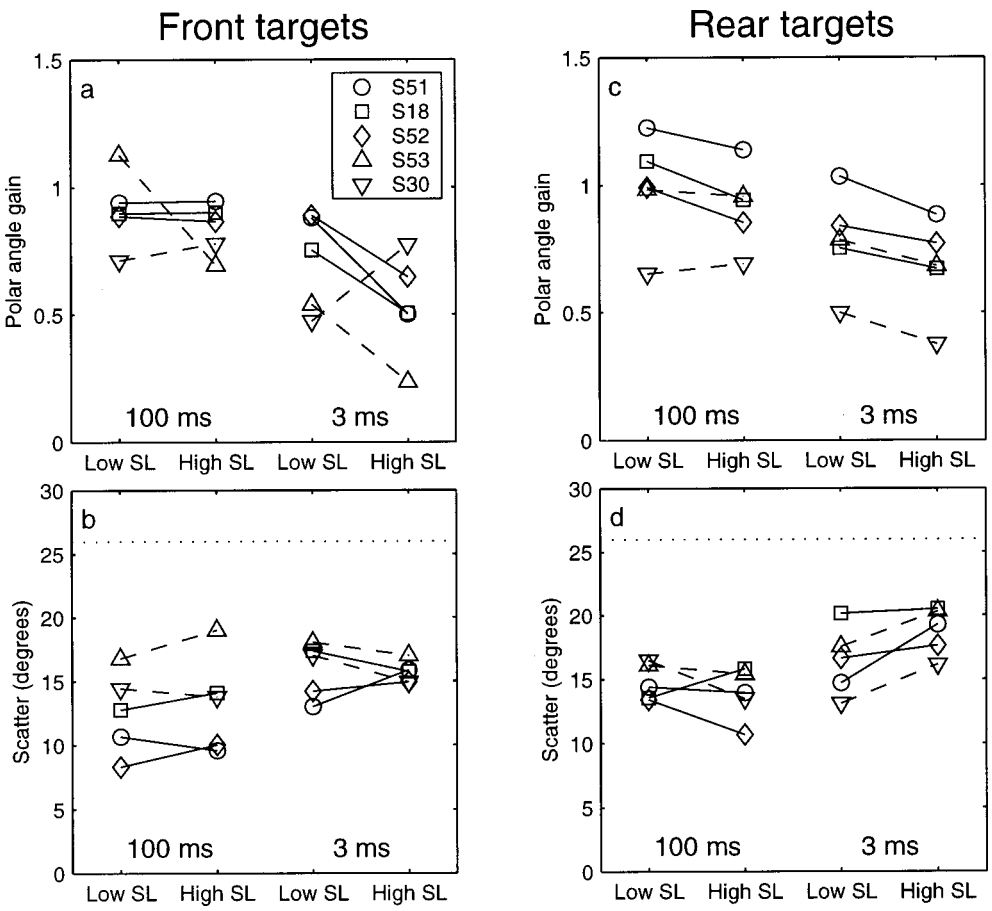

FIG. 4. Polar gain and scatter of responses to noise-burst targets. (a,b) Front-hemisphere targets. (c,d) Rear-hemisphere targets. The dotted line at approximately 26 degrees shows the scatter expected if responses were uniformly distributed throughout the quasi-veridical region rather than concentrated near the regression line.

presented from the front. Because the presentation levels for all stimuli were based on the detection threshold for a source directly ahead, on average rear targets had a lower absolute level at the eardrum (due to pinna shadowing), and this attenuation might have reduced the elevation compression effect.

Rear-target response scatter showed a trend similar to that for the front hemisphere targets, although the 3-ms, high-level sounds produced somewhat more scatter than the 3-ms low, which was not apparent in the front. On average, response scatter was slightly higher in the rear, which might be expected from the physical and memory demands of the head-pointing response task and from the fact that localization acuity is known to be poorer in the rear (Wightman and Kistler, 1989; Makous and Middlebrooks, 1990; Carlile *et al.*, 1997).

For all listeners but S30, rear gains were higher than those for front hemisphere targets even at the low level. The reason for this is unclear, since it is not obvious that poorer perceptual or response acuity in this hemisphere would necessarily lead to an exaggeration of head tilt.

Examination of the y-intercepts of the regression lines confirmed that the elevation compression was symmetrical for targets above and below the horizontal plane. That is, it was not due only to upwards bias of responses to lower-hemisphere targets or to downwards bias of responses to upper-hemisphere targets.

3. Effect of waveform type

A possible explanation for the elevation errors made by listeners presented with 3-ms stimuli in the Hofman and Van Opstal (1998) study is that irregularity in the spectra of the brief Gaussian noise bursts interfered with the extraction of accurate spectral cues from the stimuli. The magnitude spectrum of Gaussian noise has a Rayleigh distribution [the square root of the sum of squares of two normal deviates (Davenport and Root, 1958)]. Although flat on average, the spectra of individual noise bursts are irregular in detail and vary from trial to trial. The spectral irregularity for longer stimuli is finer grained and should be substantially eliminated by critical-band filtering and temporal integration. If the irregularity is the cause of degraded localization performance, one might expect that the flat-spectrum click stimuli used in the present study would allow more veridical polar angle judgments. In order to investigate this, responses to front-hemisphere targets were analyzed for equal numbers of the noise and click waveform types.

Clicks and 3-ms noise bursts elicited very similar gains at the low level, but for two of the good localizers (S51 and S18) high-level clicks produced substantially lower gain than noise bursts, although the overall pattern of responses was qualitatively similar. For S51, the Gaussian noise and click gains were 0.47 and 0.34, respectively, while for S18 the values were 0.55 and 0.30. We expected the opposite result if the polar gain compression observed by Hofman and Van Opstal were due to the random nature of their Gaussian stimuli.

4. Do reversed responses retain elevation information?

Evidence for the preservation of target elevation information in responses which fall in the wrong hemisphere can

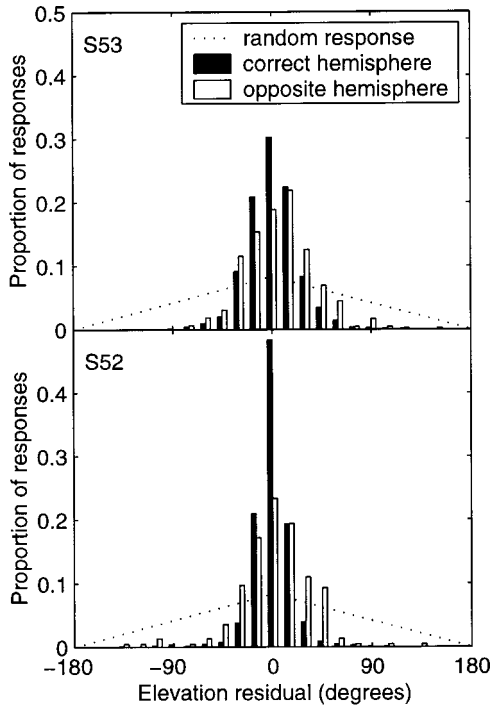

FIG. 5. Distribution of elevation residuals for correct- and opposite-hemisphere responses. Correct- and opposite-hemisphere distributions were normalized independently. Histograms show the distribution of the elevation component of the deviation of polar angles from the regression lines for all data plotted in Fig. 3. In the frontal hemisphere, elevation (ϕ) is equivalent to polar angle (β). In the rear, $\phi = 180° - \beta$.

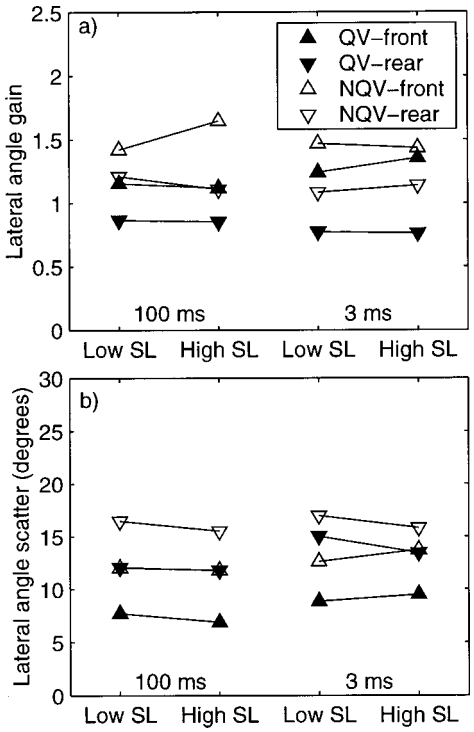

FIG. 6. Lateral angle gain (a) and scatter (b) of responses to noise-burst stimuli. QV: quasi-veridical; NQV: non-quasi-veridical (reversed and spurious). Values were computed for noise-burst stimuli and averaged across listeners. *Front* and *rear* refer to the hemisphere in which the *response* was made.

be seen in the tendency of most of these responses to cluster about the minor diagonal of the plots in Fig. 3. This is typical of the front/back confusions observed by others (Burger, 1958; Wightman and Kistler, 1989; Makous and Middlebrooks, 1990; Carlile *et al.*, 1997). If responses resulting in large polar angle errors did not retain any information about the target elevation, as suggested by Makous and Middlebrooks (1990), the results of the reversal rate computation described earlier would have little meaning.

In the front hemisphere on the median plane, elevation (ϕ) is equivalent to polar angle (β). In the rear, $\phi = 180 - \beta$. Consider a target at elevation ϕ_T, for which the linear regression predicts a mean response elevation of $\hat{\phi}_R$. For a particular response, ϕ_R, we define the *elevation residual* as $\phi_R - \hat{\phi}_R$. In Fig. 5, we plot histograms (with 15-degree bin-width) of the pooled distribution of elevation residuals for all noise-burst stimulus conditions for listeners S52 and S53. Responses falling in the same hemisphere (front or rear) as the target are plotted with filled bars, and those falling in the opposite hemisphere are plotted with open bars. All responses (quasi-veridical, reversed, and spurious) are included. The dotted line indicates the distribution of residuals which would be expected given a unity-gain regression line (i.e., $\hat{\phi}_R = \phi_T$) and a uniform distribution of response elevations uncorrelated with target location. Although the opposite-hemisphere judgments were somewhat more broadly distributed than those in the target hemisphere, they had a much lower error variance than would be expected by chance. This was true for the most accurate localizer (S52), the reverser (S53), and the other listeners (not shown). This result indicates that the majority of large-angle polar errors did retain target elevation information and thus that the computed polar gain and reversal rate values together captured most of the systematic deviations from veridicality in the listeners' responses.

5. Lateral angle responses

There was little apparent effect of stimulus duration or level on the gain parameter estimated from the lateral angle component of listeners' responses. Values computed for the noise bursts and averaged across listeners are plotted in Fig. 6. *Front* and *rear* refer to the hemisphere in which the response was made rather than to the target position. This was done because a response to the rear required the listener to turn his or her whole body, whereas a front hemisphere response could be made with neck motion only. Rearward responses were therefore likely less accurate due to the physical and memory demands of the task. There was no noteworthy effect of duration, level, or polar response category on the gains. The response location had the most consistent effect; gains for frontal responses were slightly higher than for the rear. Rear and nonveridical responses consistently showed more scatter.

III. EXPERIMENT II: EFFECTS OF LEVEL ON BRIEF NOISE BURSTS

The results from experiment I replicate the compression of apparent elevation observed by Hofman and Van Opstal (1998) and suggest that the compression was due to Hartmann and Rakerd's (1993) negative level effect for brief

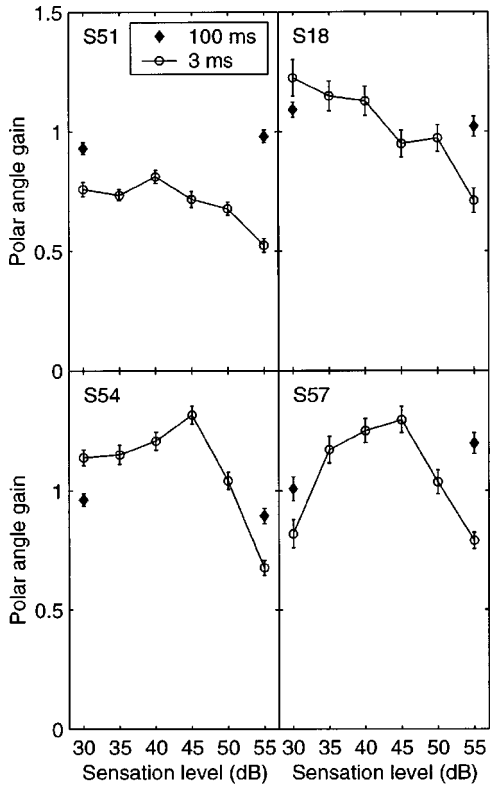

FIG. 7. Effect of level on polar angle gain for 3- and 100-ms Gaussian noise bursts. Each panel shows data for one listener. Open circles, 3-ms stimuli; Diamonds, 100-ms stimuli. Error bars show the standard error of the regression coefficient (polar angle gain).

stimuli (an interaction of level and duration) rather than to short duration alone. In experiment II we examined in detail the relationship between stimulus level and polar angle gain at the 3-ms stimulus duration. The results provide data complementary to those of Hofman and Van Opstal (their Fig. 8), who characterized the effects of duration at a single sound pressure level.

A. Methods

1. Subjects

Four listeners participated in experiment II. Two of these (S51 and the first author, S18) had previously participated in experiment I.

2. Stimuli and procedure

This experiment used the 3- and 100-ms Gaussian noise bursts previously described. The 3-ms bursts were presented at levels from 30 to 55 dB above threshold in 5-dB steps, while the 100-ms were presented at sensation levels of 30 and 55 dB only. The stimulus level was held constant within a block of trials. The target locations were limited to a region in front of the listener similar to that used by Hofman and Van Opstal (1998). Each block consisted of two separate presentations from each of the 49 combinations of the azimuth and elevation coordinates 0, ± 10, ± 20, and ± 30 degrees. The listeners were informed that all stimuli would be presented ''from the front.'' In each block, the order of presentation was shuffled, but no attempt was made to confound the hoop motion cue, as this would have seriously impaired the efficiency of data collection. At the beginning of each session, listeners completed 2–3 min of head-training as in experiment I, and in all other respects the procedure was the same as in that experiment. On each of two different days, one block of trials was run at each stimulus level. These data were combined for analysis.

B. Results

Figure 7 shows the polar angle gain obtained for 3-ms, Gaussian noise bursts presented at sensation levels between 30 and 55 dB (open circles) and for 100-ms bursts at 30 and 55 dB only (diamonds). Each panel shows the data for one of the four listeners. Error bars show the standard error of the regression coefficients and thus are indicative of the response scatter. The gains obtained at the lowest and highest levels in experiment II are not directly comparable to those from the low- and high-level conditions of experiment I since the range of stimulus locations was dissimilar, and this might have altered the listeners' response strategies (Perrett and Noble, 1995).

Examination of the data from each individual block confirmed that listeners' responses were quite repeatable. Across all listeners and conditions, the correlation between the gains obtained in the first and second blocks was 0.84 and the root-mean-squared difference in gains was 0.16. The anomalously low gain for S57 at 30 dB was due to differences between the data from the two runs in that condition, which yielded gains of 0.96 and 0.68 when analyzed separately.

No meaningful difference was observed between the two levels of the 100-ms stimuli, a result that replicated that of experiment I. In contrast, for the 3-ms stimuli, gain varied markedly with level. Three listeners achieved maximum gain for stimuli at 40 or 45 dB. For two of these (S54 and S57), the gain at the best level was substantially higher than that at 30 dB, whereas for the other (S51) it was not.

Despite individual differences, a marked decline in gain occurred at sensation levels above 40 or 45 dB for all four listeners. Averaged across listeners, the mean gains for the 100- and 3-ms stimuli did not differ significantly at the 30 dB level [$t(3)=0.06$, $p>0.45$], but at 55 dB the mean gain for the short noise bursts was significantly lower [$t(3)=3.40$, $p<0.05$]. The reductions in gain were not a statistical artifact of increased response scatter, as evidenced by the relatively constant size of the error bars. These results suggest that optimal spectral cue processing for the short duration stimuli occurred at a level approximately 40 dB above threshold.

IV. EXPERIMENT III: EFFECTS OF BACKGROUND NOISE

A. Motivation

Experiments I and II demonstrate that presentation of a brief sound at a sensation level greater than about 45 dB results in a compression of elevation judgements [i.e., the reduction in gain reported by Hofman and Van Opstal (1998)] and an increase in the rate of front/back confusions

[i.e., the negative level effect reported by Hartmann and Rakerd (1993)]. We entertained two hypotheses to account for those phenomena. The first, the *estimate-integration hypothesis* (or ''multiple-looks'' hypothesis), was suggested by Hofman and Van Opstal. Based on their data, they proposed a model in which the auditory system integrates spectral information over a duration of approximate 5 ms, from which a single, short-term elevation estimate is derived. Successive estimates of elevation are then integrated, with a stable composite estimate requiring a stimulus duration of approximately 80 ms.

The existence of the 5-ms spectral integration window is strongly supported by the results of the swept-tone experiments conducted by Hofman and Van Opstal (1998), and the reduced scatter for long versus short noise bursts at low level observed in the present study (Fig. 4) indicates that response accuracy can indeed be improved by extended observation. Nevertheless, our observation of fairly accurate localization of low-level brief sounds indicates that the 80-ms period of estimate integration is not always necessary. Additionally, accurate performance for high-level, long-duration sounds cannot result simply from the integration of elevation estimates based on the apparently distorted spectral information suggested by the responses to short, high-level stimuli.

We propose here a complementary *adaptation hypothesis*. We suppose that the degradation of localization of high-level brief sounds is due to some form of cochlear nonlinearity, which results in a distorted auditory nerve representation of high-level spectral cues. We further suppose that a stimulus duration of some tens of milliseconds permits the ear to adapt to a high-level sound, perhaps by the action of olivocochlear efferents on the cochlear amplifier. Such a mechanism would account for the success of listeners in localizing 100-ms high-level sounds by permitting extraction of accurate spectral information from later portions of the stimulus. It would also account for the elevation compression observed by Hofman and Van Opstal (1998) for trains of spaced, 3-ms noise bursts if the silent gaps in the stimulus affect the invocation or strength of the adaptive mechanism.

In experiment III, we compared these hypotheses by measuring localization of 3-ms sounds that were centered within 1000-ms spatially diffuse noise bursts. The estimate-integration hypothesis would predict that the diffuse noise would cause no improvement in localization and, most likely, would degrade localization by decreasing the signal-to-noise ratio. The adaptation hypothesis predicts the opposite result, that the 1000-ms diffuse sound would improve localization by activating the putative adaptive mechanism prior to the onset of the 3-ms target sound.

B. Methods

1. Subjects

Six listeners participated in experiment III. One of these (S54) had previously participated in experiment II, and one (the first author, S18) in both experiments I and II.

2. Stimuli and procedure

In this experiment the target sounds were 3-ms Gaussian noise bursts presented at levels 40 and 55 dB above the quiet threshold, which was determined as in experiment I. The locations were the 49 frontal ones used in experiment II. The target was presented either in quiet (as in experiments I and II) or 500 ms after the onset of a 1000-ms, wide-band background noise. This background noise consisted of a Gaussian noise waveform presented in anti-phase from two loudspeakers located 1.4 m to the left and right of the listener and 45 cm below ear level [Fig. 1(c)]. The transfer functions of these loudspeakers were not corrected. Antiphase noise was used in a attempt to produce a spatially diffuse sound (Blauert, 1997; Lipshitz, 1986). Listeners reported perceiving this sound either as diffuse or as originating from the rear.

Each block of 49 trials contained a single combination of stimulus and background noise levels. The 40-dB sensation level targets were presented either alone or simultaneously with the antiphase noise, which was attenuated by 30 or 20 dB below the level required to mask the target. The absolute level of the target was fixed at the level used in the quiet condition. Thus the masked sensation level for the targets in the background noise conditions was either 30 or 20 dB. Similarly, the 55-dB sensation level targets were presented in quiet and at 40, 30, and 20 dB above masked threshold. For each of these seven stimulus conditions, two 49-location blocks of trials were run and their data combined.

To determine the background noise level necessary to mask the 3-ms targets, a threshold was determined with a procedure similar to that used to measure detection thresholds described in experiment I. However, in this case the absolute signal level was held constant and the background noise level adjusted. It was not possible to obtain a masked threshold for the 55-dB stimulus directly because the required masker level was uncomfortably loud. Therefore, masking threshold levels for the 40- and 55-dB stimuli were estimated by adding offsets of -5 and $+10$ dB, respectively, to the value obtained for a 45-dB target.

The absolute level of the masking noise was estimated by measuring the signal level at one ear of a KEMAR manikin (Knowles Electronics) at the listening position in the anechoic chamber. For the 55-dB stimuli at a masked sensation level of 30 dB, the masker level was equivalent to that produced by a frontally presented broadband noise at a sound pressure level of 52–57 dB. The variation across listeners was due to differences in their quiet and masked detection thresholds for the 3-ms noise bursts.

C. Results

The polar angle gain of the responses in a variety of target- and background-noise-level conditions is plotted in Fig. 8 for six listeners. The abscissae are labeled by masked sensation level, so *larger* values indicate *lower* background noise levels. As in Fig. 7, error bars indicate the standard error of the regression coefficients. The results of experiment

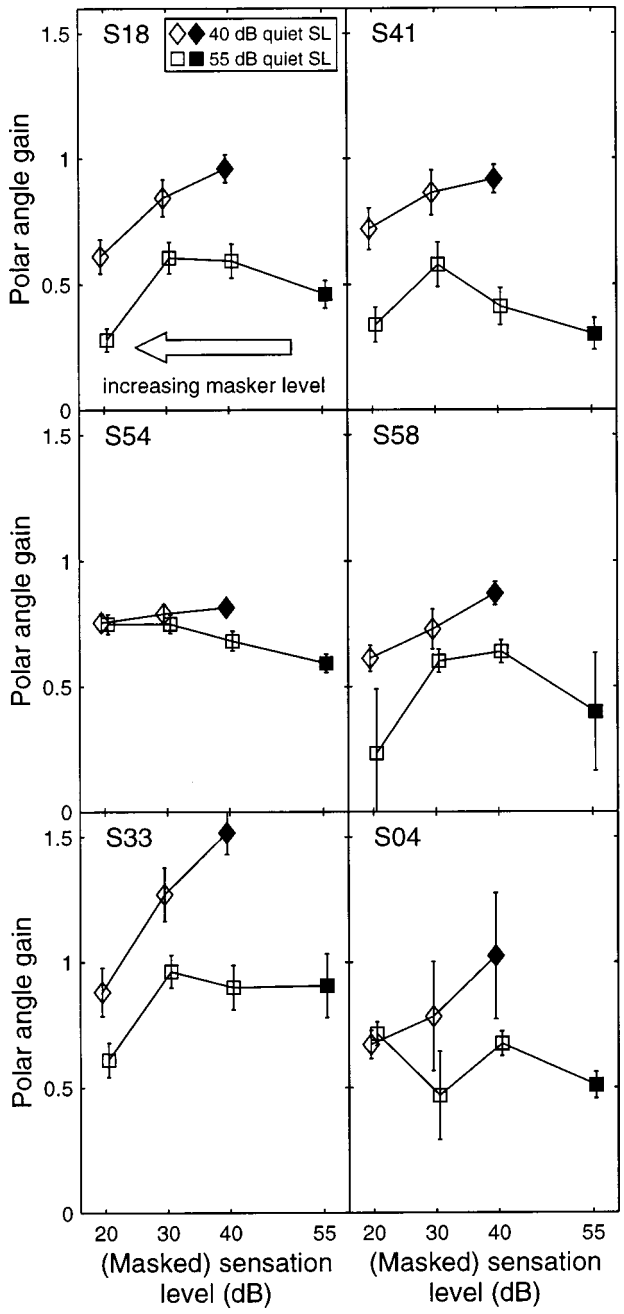

FIG. 8. Effect of background noise level on polar angle gain for 3-ms Gaussian noise bursts. Polar angle gains are shown for 40- (diamonds) and 55-dB (squares), 3-ms frontal targets presented in quiet (filled symbols) or 500 ms after the onset of a 1000-ms wide-band background noise (open symbols). Lower sensation levels indicate higher background noise levels. Error bars show the standard error of the regression coefficient (polar angle gain). For clarity, 40- and 55-dB points are slightly offset.

II indicated that the optimal target level was approximately 40 dB above threshold. For targets presented at this level (diamonds), the introduction of the background noise at a level 30 dB below that at which it masked the target (with the absolute level of the target held constant) resulted in decreased gain for all listeners. Further increases in the noise level caused additional compression.

In contrast, for 55-dB targets (squares), the introduction of background noise 40 dB below its masking level improved performance for five listeners and caused no decrement for the sixth (S33). A 10-dB increase in the noise level to produce a masked sensation level of 30 dB produced a further improvement in gain for four listeners (S18, S54, S41, and S33). A final increase to 20 dB below the masking level caused a precipitous decline in performance for four of the six listeners. The target was still clearly audible in this condition. As in experiment II, the error bars reveal that lower gain was not an artifact of increased response scatter, with the possible exception of listener S58. These results, although variable among listeners, are consistent with our hypothesis of an adaptive peripheral process necessary to extract spectral information from high-level sounds. A possible physiological mechanism is discussed in Sec. VI B 3.

V. EXPERIMENT IV: EFFECTS OF STIMULUS REPETITION

A. Motivation

Hofman and Van Opstal (1998) obtained similar, near-veridical, elevation responses for a concatenated train of *independent* 3-ms noise bursts and the 500-ms noise burst that served as their control stimulus. In contrast, they reported that performance was degraded when stimuli consisted of repeated *identical* 3-ms noise samples. In the framework of their model, the degraded performance with repeated identical samples of noise suggests that simply providing the system with access to multiple looks at the same brief, high-level stimulus is insufficient for accurate localization. In other words, the reduced gain obtained with single, 3-ms bursts is due not only to a failure to provide a stimulus of sufficient duration to allow the elevation estimate to stabilize over a period of 80 ms, but also to the fact that each individual estimate is based on distorted spectral cues.

According to our adaptation hypothesis, a stimulus composed of repeated 3-ms noise bursts should be localized near-veridically (like the low-level, short bursts in experiment I), since the adaptation process should allow accurate spectral information to be obtained from latter portions of the signal. As this prediction is at odds with the observation of Hofman and Van Opstal (1998), experiment IV was designed to characterize the vertical plane localization of a stimulus composed of repeated, identical, high-level, 3-ms noise bursts.

B. Subjects

Eight listeners participated in experiment IV, including the first author (S18) and seven others who had not participated in any of experiments I–III and who were unaware of the nature and outcome of those experiments. All met the audiometric criteria described in experiment I, and had received training and practice in the free-field localization task.

C. Stimuli and procedure

Three types of stimuli were presented. These were *single* 3-ms, Gaussian noise bursts at a sensation level of 55 dB; *concatenated*, independent, 3-ms bursts at the same absolute sound pressure level (approximately 70 dB *re* 20 μPa) with a total duration of 99 ms; and *repeated*, identical (i.e., frozen)

bursts with the same absolute level and total duration. Each block of trials consisted of a single presentation of one type of stimulus from each of 56 target locations. Half of these were in front of the listener with elevations and azimuths between −30 degrees and +30 degrees, and the remainder were positioned symmetrically in the rear. Data were obtained in the order concatenated, repeated, and single, thus any short-term practice effects should have reduced rather than enhanced the expected differences in polar angle gains. Listeners completed 5 min of head-training, following which all data for a single listener in the three conditions were collected in a single session.

D. Results

Polar angle gain and reversal rates were computed as previously described, and are plotted separately for each listener in Fig. 9. Although, as expected, all listeners produced high gain for the concatenated bursts and all but one (S66) had low gain for the single burst stimulus, the data do show marked individual differences. On the basis of the pattern of polar angle gains across stimulus conditions, listeners could be qualitatively divided into two groups. In the first group (S18, S77, S70, and S66), the gains for the repeated bursts were more similar to those for the concatenated bursts than to those for the single bursts. In the second group (S67, S76, S69, and S75), the gain for the repeated bursts was mid-way between those of the concatenated and single conditions.

Reversal rate patterns also varied between subjects. For four listeners (S18, S66, S67, and S76), reversal rates for the repeated bursts were similar to those for the concatenated, and lower than those for the single, suggesting that burst repetition was beneficial. For the remaining four, reversal rates for the single and repeated bursts were similar, indicating that repetition did not improve performance. These results do not provide a strong basis for choosing between the adaptation and estimate-integration hypotheses, but do give an indication of the range of variability in listeners' responses, and suggest that the result from one listener described by Hofman and Van Opstal (1998) might not be representative of listeners in general.

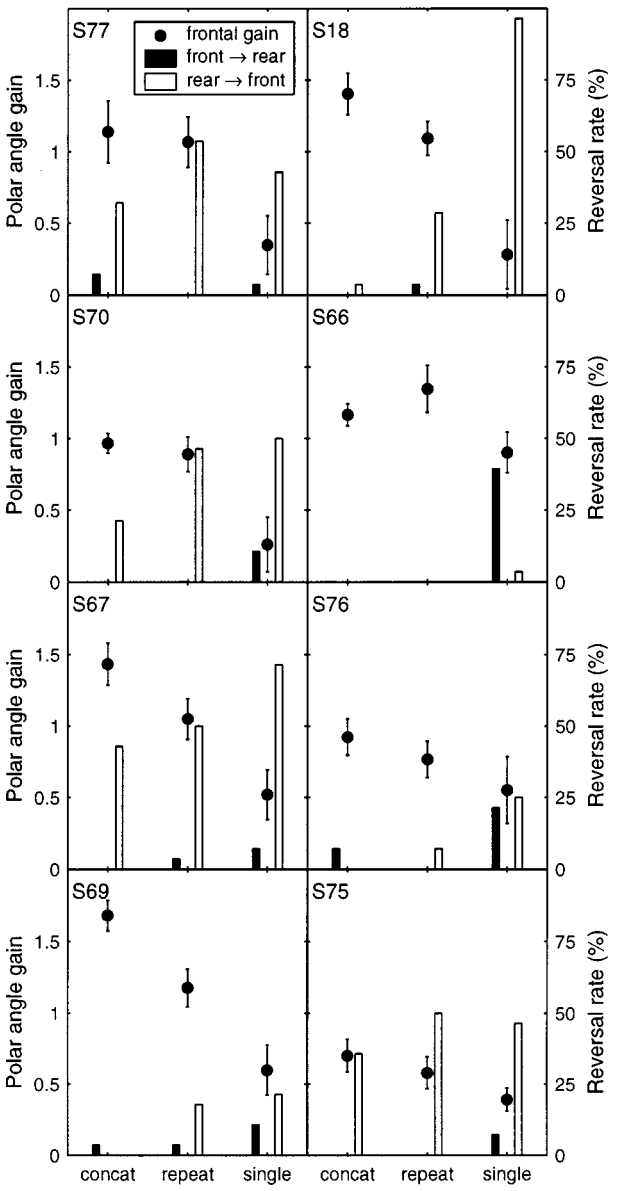

FIG. 9. Localization of concatenated, repeated, and single high-level noise bursts. Circles (●) show the polar angle gain for front-hemisphere targets. Error bars show the standard error of the regression coefficient (polar angle gain). Histograms show the front-to-rear (filled bars) and rear-to-front (open bars) reversal rates for each stimulus type.

VI. DISCUSSION

A. Overview of results

The results of experiments I and II demonstrate the following effects of level and duration on spectral-cue-based localization. *First*, there is little effect of level on the long (100-ms) stimuli in terms of polar gain, response variability, or reversal rate. In general, noise bursts of this duration at both levels are localized approximately veridically. *Second*, low-level, short noise bursts appear to be localized similarly to those of long duration, but with somewhat greater scatter and reversal rates, which might be expected given the low energy content of these stimuli. *Third*, localization responses to short, high-level stimuli are very different, and exhibit compression of polar gain and patterns of reversal not observed with the other stimulus types. Gaussian noise bursts and unvarying, flat-spectrum click stimuli all elicit the same types of responses. The results of experiment II indicate that the adverse effect of high level on the localization of brief sounds begins at levels approximately 40-45 dB above threshold.

The results of experiment III revealed a dissociation between the effects of background noise on 3-ms noise bursts presented at an optimal sensation level (40 dB) and at a level high enough to induce polar angle compression (55 dB). In the former case, the presence of increasing levels of background noise degraded listeners' performance and resulted in increasing amounts of polar gain compression. This might be expected since the addition of background noise must lower the signal-to-noise ratio. In contrast, the addition of moderate levels of background noise to the high-level stimuli resulted in a paradoxical improvement in performance—a partial release from the elevation compression effect. This is consistent with the notion that early portions of the stimulus can

engage an adaptive mechanism which allows accurate spectral information to be extracted from the target signal.

Whether our adaptation mechanism or some other accounts for accurate localization of long-duration high-level sounds, that mechanism is not completely effective at arbitrarily high input levels. A recent study (Rakerd *et al.*, 1998) revealed that even long-duration noise bursts are subject to a mild negative level effect at sound intensities significantly higher than those we employed here. Listeners were required to identify which of three loudspeakers, placed at elevations of -15 degrees, 0 degrees, and $+15$ degrees in the frontal midline, was the source of a 1-s, broadband noise. With the level of the noise roved between 60 and 72 dB (*re* 20 μPa), the percentage of correct responses was approximately 94%. When the level was increased to a range of 78-90 dB, performance dropped to 78% correct.

The release from polar angle compression observed for the high-level targets is the opposite of that expected if the background noise were localizable and interfering with the localization of the target. Studies of localization in multiple-source conditions have shown that when interference occurs, the perceived elevation of the target source tends to be pulled towards that of the distractor or masker (Good and Gilkey, 1994; Stellmack and Macpherson, 1995; Langendijk *et al.*, 1999). This would tend to reduce polar angle gain rather than increase it.

Although the addition of background noise improved localization accuracy for the 55-dB stimuli, the gains did not approach the near-veridical values obtained for 100-ms stimuli or for 3-ms stimuli at the optimal sensation level. This is understandable because the presence of any background noise must lower the signal-to-noise ratio even if it is beneficial in pre-adapting the system to the high-level target. If the adaptation hypothesis is correct, a long, high-level sound would act as a self-adaptor without compromising the signal-to-noise ratio.

In experiment IV, we looked for this self-adaptation in a 99-ms, high-level stimulus composed of a train of identical, 3-ms noise bursts. For four of eight listeners, polar angle gains for this repeated burst stimulus were similar to those for concatenated, fresh samples of noise, but for the others, the gains were intermediate between the concatenated and single burst values. Unfortunately, this result does not unequivocally support either the adaptation or estimate integration hypotheses. Although the spectral envelopes of the repeated noise bursts were statistically similar to those of single bursts, it should be noted that the repeated stimulus was in effect a harmonic tone complex with a fundamental of 333 Hz. This property would have generated a temporal pattern of auditory nerve activity quite different from that produced by the noise stimuli. Previous studies have shown that flat-spectrum 253-Hz (Stellmack and Macpherson, 1995) and 100-Hz (Good and Gilkey, 1996) tone harmonic complexes can be localized accurately in elevation.

B. Relation to previous results

1. Negative level and elevation compression effects

The results of experiment I provide a more detailed picture of the localization of brief, high-level sounds than have previous studies, but are consistent with the results of both Hartmann and Rakerd (1993) and Hofman and Van Opstal (1998). In particular, they reveal that the polar gain compression observed in the latter study is likely another manifestation of the negative level effect described in the former, and that it cannot be due simply to a failure of integration of spectrally based elevation estimates. This is the case because brief stimuli are more accurately localized at low levels than at high, even though the latter situation provides the observer with more signal energy.

In the present study, the high level for the 3-ms noise bursts was approximately the same as that used by Hofman and Van Opstal (1998), and similar compression of polar gain was observed for brief stimuli. However, it should be noted that in an earlier study using the eye-pointing response method (Frens and Van Opstal, 1995), elevation compression was observed for 3-, 5-, and 10-ms noise bursts at a sound pressure level of ''about 60 dB.'' This would correspond roughly to our 45-dB sensation level, but in experiment II we observed little or no compression at this level (Fig. 7). The two sets of eye-pointing data tend to support the estimate-integration hypothesis, since similar effects of duration were found at different signal levels. Alternatively, the discrepancy with our head-pointing responses at this 60-dB level might indicate that speeded oculomotor responses are driven by a less-detailed analysis of the stimulus. As discussed in Sec. VI B 2, response latencies for our listeners were an order of magnitude higher than those for the subjects in the eye-pointing studies and thus the final percept may have been the product of more refined processing. We view our methods as representative of those used in the bulk of previous localization research.

Although we did not measure full polar angle response patterns at fine increments in level, if it is assumed that the onset of anomalous front/back reversal patterns occurs at the same level as the onset of polar gain compression, then the results of experiment II agree with those of Hartmann and Rakerd (1993). In their Fig. 2, location identification errors for clicks increased dramatically above a sensation level of approximately 41 dB (sound pressure level 86 dB). In experiment II, we observed reductions of polar angle gain beginning at a similar sensation level (Fig. 7). However, the sensation levels we used in experiment II cannot be equated exactly with those used by Hartmann and Rakerd since their stimuli were presented in a wide-band background noise intended to mask speaker switching transients. The effect of background noise is a complex function of stimulus and noise levels as shown by the results of experiment III. Based on those results, we suggest that the presence of the background noise increased identification error rates for Hartmann and Rakerd's low-level stimuli and reduced error rates for the high-level sounds relative to quiet presentation.

In experiment II we did not measure polar angle gain at intermediate levels for the 100-ms stimulus. However, previous studies have shown that vertical plane localization for frontal, long-duration noise bursts is equally accurate across a wide range of intensities. Data are available for sensation levels of 20–30 dB (Roffler and Butler, 1968), 25–35 dB (present study, experiment I), 40–50 dB (Makous and

Middlebrooks, 1990), and 50–60 dB (present study), and for an absolute sound pressure level of 70 dB (Wightman and Kistler, 1989; Carlile *et al.*, 1997). Hartmann and Rakerd (1993) found no effect of level for long-duration noise bursts in their source identification experiment.

Listeners' inaccuracy in localizing brief, high-level noise bursts and clicks, the stereotypical nature of their errors, and their accurate localization in the lateral dimension suggest that the problem lies in the extraction of spectral cues for localization from these stimuli. That is, the central auditory system appears to receive from the periphery a distorted representation of the spectral profiles of these stimuli. The underlying pattern of (spectrum-dependent) polar angle responses for the low-level, short stimuli is more-or-less veridical, which suggests that the spectral representation might be noisy, but not distorted, in this case. One influence of increasing level on the transmission of spectral information is the well-known saturation of the rate-level functions of auditory nerve fibers. Sachs and Young (1979) showed that the distribution of firing rate across nerve fibers of different best frequencies provides a faithful representation of vowel spectra only at low levels. Presumably similar saturation occurs at the higher frequencies from which the necessary spectral cues for localization in the polar angle dimension are extracted. For example, Hartmann and Rakerd (1993) generalized their finding of a negative level effect for localization to the simple detection of pinnalike spectral filtering applied to clicks. Thus the negative level effect appears to result from a general deficit in spectral processing for brief, high-level stimuli, and is not peculiar to localization. It is perhaps noteworthy that the level at which polar gain compression was observed to begin in experiment II is similar to that at which the compressive nonlinearity of the basilar membrane is first observed [approximately 40 dB above threshold (Yates, 1990)].

2. Methodological differences

In this study, long and short stimuli were presented at equal sensation levels. Due to temporal integration of energy, longer stimuli are detectable at lower absolute levels than the brief noise bursts and clicks, and thus we considered the possibility that the lack of an elevation compression effect for high-level, long-duration stimuli is due to their lower absolute level. The results of Hofman and Van Opstal (1998) contradict this interpretation because all noise-burst stimuli in that study were presented at the same absolute sound pressure level (70 dB), which is approximately the same as that of the high-level, 3-ms noise bursts used in the present study. They did not observe compression of elevation for their 500-ms control stimulus presented at this level. Pilot data collected for the present study indicated an absence of elevation compression for the 100-ms stimuli at the same absolute level as the 3-ms noise bursts.

Direct comparison of the values of polar gain obtained in the present study with those of Hofman and Van Opstal (1998) should be done cautiously due to differences in the range of possible responses. The eye-pointing responses used in the earlier study were limited to the ocular-motor range over which the targets were distributed. In the present experiments II and III, the targets were similarly arrayed, but head-pointing responses outside this range could be made and were accepted. With the eye-pointing method it would be impossible to measure polar gains much greater than 1, such as those we observed in experiments II and IV. The latter are likely due to individual differences in head-pointing style rather than to highly nonveridical percepts. In addition, there is a tendency for psychophysical subjects to attempt to utilize the full possible response range, and this has been shown to affect localization responses (Perrett and Noble, 1995). This individual variability in gains is not a great problem since we restricted our analyses primarily to within-listener comparisons.

A final methodological difference concerns the timing of responses. The speeded eye-pointing technique employed by Hofman and Van Opstal (1998) yielded saccade onset latencies of 100–200 ms. Obviously the head and body movements required in the head-pointing response used in the present study precluded such short latencies. As is typical of most absolute localization studies, we did not require our subjects to respond as quickly as possible. Although the onset of head movement was not recorded, the delay between the stimulus offset and the final response was timed. This latency varied between 1 and 4 s, with a modal value of approximately 2 s.

3. Release from elevation compression—efferent activity?

The slow onset and noise activation of the adaptive process implicated by the results of experiment III are hallmarks of the olivocochlear efferent process. Although still not well understood, cochlear efferent activity seems to reduce the gain of the cochlear amplifier (Guinan, 1994, 1996), thus expanding the dynamic range of the auditory nerve (by avoiding saturation) and reducing signal masking in background noise (Winslow and Sachs, 1987). Buño (1978) has shown that the benefits of efferent activity can be produced by a contralateral noise signal, and therefore presumably by the binaural stimulation produced by a spatially presented source.

The range of signal-to-noise ratios over which the background noise was beneficial in experiment III was 10-20 dB. Although the experimental paradigm was much different, this is similar to the range of signal-to-noise ratios for which Dolan and Nuttall (1988) observed release from masking when electrically stimulating the crossed olivocochlear bundle in guinea pigs, and further supports the idea that efferent activity plays a role in the accurate spectral processing of long-duration, high-level sounds. It has also been suggested that olivocochlear antimasking should be most effective at mid-to-high frequencies (Stankovic and Guinan, 1999), where the primary spectral cues to sound location are found.

Hofman and Van Opstal (1998) observed a significant reduction in polar gain compression (relative to the 3-ms stimuli) for noise bursts as short as 10 or 20 ms and for 3-ms bursts presented in a train every 80 or 40 ms. These values are similar to the latencies observed for the olivocochlear reflex (Fex, 1962). Efferent activity is known to build up

with repeated presentation of a 50-ms noise burst (Liberman and Brown, 1986), but that buildup has not been investigated with stimuli similar to those employed by Hofman and Van Opstal.

The differences in performance between listeners in the background noise conditions might have been due to variability in detection thresholds for the target signals (either in quiet or in the presence of the background noise), differences in the noise level necessary to engage the putative adaptive process, or a combination of the two. Differences in thresholds caused the absolute level of the background noise used in each condition to vary between listeners over a 6-dB range. Also, the localization task in experiment III required the listeners to ignore the spatial attributes of the background noise and to focus attention on the frontally presented targets. Participants might have differed in their ability to do this.

C. Remaining questions

The results of experiments I and II provide a fairly thorough description of the negative level and elevation compression effects for brief stimuli over all of auditory space, but an explanation of the observed pattern of polar angle responses is still lacking. Specifically, what causes the increase in reversals and the compression of polar angle responses? We also consider the origin of the adaptive mechanism suggested by the results of experiment III.

1. Origin of reversals

Level-dependent reversals are more readily explained than polar gain compression if the primary mechanisms of spectral representation distortion are basilar membrane compression and auditory nerve saturation. While the exact spectral features which indicate front and rear positions are not known, the evidence suggests that primary front/back information is found in the spectrum above 5 kHz and that secondary cues lie below 2 kHz (Asano *et al.*, 1990). Blauert (1969/70) has suggested that front–rear discrimination is determined by the relative amounts of energy falling into particular frequency channels (''directional bands'') associated with each direction. If this is the case, peripheral compression and saturation would tend to reduce the amount by which the transduced energy ratio could vary and might bias listeners' judgments or increase uncertainty about front/back location. Compression might leave the frequencies of local spectral features relatively undisturbed and could account for the preservation of elevation information even when front/back position is disturbed.

2. Origin of the elevation compression effect

The shift of polar angle responses towards the horizontal plane is less easily explained by peripheral compression and saturation, which would tend to reduce the amplitude of spectral peaks and notches rather than shifting them to different frequencies. If spectral features are eliminated by saturation at high levels, the resulting distorted representation would best resemble a directional transfer function (DTF) from an overhead source and thus responses might be expected to be biased upwards. This result was not observed for sources above the median plane. A common feature of the DTFs of many human listeners is the tendency for local spectral features (such as notches) to move to higher frequencies as elevation increases (e.g., Middlebrooks, 1999). If some nonlinear process (such as filter broadening) did result in a shift of peak or notch center frequencies at high levels, it is difficult to imagine how center frequencies might be shifted downwards for DTF spectra corresponding to sources above the horizontal plane while being shifted upwards for sources below the horizontal. This situation would have to obtain if spectral cue processing follows a template-matching model (Middlebrooks, 1992; Zakarauskas and Cynader, 1993; Macpherson, 1997, 1998). It has been shown that the responses of points on the basilar membrane can exhibit spectral notches at high levels (Recio *et al.*, 1998), but this would not necessarily produce notches in the cochlear activation pattern itself.

There are at least four alternative hypotheses for the polar angle compression. First, level-induced distortion of the spectrum might impose a horizontal-plane-DTF-like character on the spectrum such that responses reflect a compromise between the conflicting veridical and spurious spectral cues. It is not obvious why a distorted cochlear representation should have this particular spectral character. Second, the polar angle of the response might be generated by integrating a spectrum-based location estimate away from the horizontal plane over the duration of the stimulus (Hofman and Van Opstal, 1998). This is an insufficient explanation because elevation compression does not occur for low-level, brief stimuli. Third, degraded spectral information might simply generate a default percept near the horizontal plane. This can be discounted since the observed gains were always much greater than 0. Finally, if the auditory image does not shift towards the horizontal, but simply broadens at high intensities, listeners might be less confident and therefore reluctant to make more extreme head-pointing responses. This might also apply to the eye-pointing method utilized by Hofman and Van Opstal. It seems likely that such uncertainty-related bias would be accompanied by an increase in response scatter, which we did not observe. Repeating the experiment with a verbal response method (Wightman and Kistler, 1989), would address this issue by eliminating the elevation-correlated motor component of the task.

To distinguish between these four hypotheses, it would be of great assistance to know how the peripheral representation of spectral features for brief stimuli varies with level. Detailed recordings of auditory nerve responses to appropriate DTF-filtered stimuli (May and Huang, 1997) would provide this information.

VII. CONCLUSIONS

In the present study we have shown in detail the deleterious effects on localization of high-level presentation of brief stimuli, and have expanded on and integrated previous work by Hartmann and Rakerd (1993) and Hofman and Van Opstal (1998). This phenomenon has practical implications, for example in the choice of signals in virtual auditory displays, and must also be taken into account when selecting stimuli for use in psychoacoustic or physiological investiga-

tions of sound localization or other auditory processes. The results are consistent with the hypothesis that for brief stimuli, high intensities result in distorted representations of spectral localization cues, and that peripheral adaptation, not temporal integration of short-term elevation estimates, is the essential mechanism allowing the accurate spectral processing of long-duration, high-level sounds. This result is relevant not simply to sound localization. Indeed, we propose that auditory localization tasks might provide a novel method of assaying the ability of the auditory system to process spectral information in general.

ACKNOWLEDGMENTS

The authors would like to thank David Dolan, Shigeto Furukawa, Li Xu, Brian Mickey, and Julie Arenberg for useful discussions; Wesley Grantham, Bill Noble, and two anonymous reviewers for constructive comments on an earlier draft; and Zekiye Onsan for invaluable technical assistance. This work was funded by NIH Grant Nos. R01DC00420 and T32DC00011.

Asano, F., Suzuki, Y., and Sone, T. (**1990**). ''Role of spectral cues in median plane localization,'' J. Acoust. Soc. Am. **88**, 159–168.

Blauert, J. (**1969/70**). ''Sound localization in the median plane,'' Acustica **22**, 205–213.

Blauert, J. (**1997**). *Spatial Hearing* (MIT, Cambridge, MA).

Buño, W. (**1978**). ''Auditory nerve fiber activity influenced by contralateral ear stimulation,'' Exp. Neurol. **59**, 62–74.

Burger, J. F. (**1958**). ''Front-back discrimination of the hearing system,'' Acustica **8**, 301–302.

Carlile, S., Leong, P., and Hyams, S. (**1997**). ''The nature and distribution of errors in sound localization by human listeners,'' Hear. Res. **114**, 179–196.

Davenport, Jr., W. B., and Root, W. L. (**1958**). *An Introduction to the Theory of Random Signals and Noise* (McGraw–Hill, New York).

Dolan, D. F., and Nuttall, A. L. (**1988**). ''Masked cochlear whole-nerve response intensity functions altered by electrical stimulation of the crossed olivocochlear bundle,'' J. Acoust. Soc. Am. **83**, 1081–1086.

Fex, J. (**1962**). ''Auditory activity in centrifugal and centripetal cochlear fibres in cat,'' Acta Physiol. Scand. **55**, 5–68.

Frens, M. A., and Van Opstal, A. J. (**1995**). ''A quantitative study of auditory-evoked saccadic eye movements in two dimensions,'' Exp. Brain Res. **107**, 103–117.

Golay, M. J. E. (**1961**). ''Complementary series,'' IRE Trans. Inf. Theory **7**, 82–87.

Good, M. D., and Gilkey, R. H. (**1994**). ''Auditory localization in noise. II. The effects of masker location,'' J. Acoust. Soc. Am. **95**, 2896.

Good, M. D., and Gilkey, R. H. (**1996**). ''Sound localization in noise: The effect of signal-to-noise ratio,'' J. Acoust. Soc. Am. **99**, 1108–1117.

Guinan, Jr., J. J. (**1994**). ''Effects of medial olivocochlear efferents on responses of auditory nerve fibers,'' J. Acoust. Soc. Am. **95**, 2812.

Guinan, Jr., J. J. (**1996**). ''The physiology of olivocochlear efferents,'' in *The Cochlea* (Springer-Verlag, New York), pp. 435–502.

Hartmann, W. M., and Rakerd, B. (**1993**). ''Auditory spectral discrimination and the localization of clicks in the sagittal plane,'' J. Acoust. Soc. Am. **94**, 2083–2092.

Hofman, P. M., and Opstal, J. V. (**1998**). ''Spectro-temporal factors in two-dimensional human sound localization,'' J. Acoust. Soc. Am. **103**, 2634–2648.

Langendijk, E. H. A., Wightman, F. L., and Kistler, D. J. (**1999**). ''Sound localization in the presence of one or two distracters,'' Abstr. ARO Midwinter Meeting **22**, 28.

Levitt, H. (**1971**). ''Transformed up-down methods in psychoacoustics,'' J. Acoust. Soc. Am. **49**, 467–477.

Liberman, M. C., and Brown, M. C. (**1986**). ''Physiology and anatomy of single olivocochlear neurons in the cat,'' Hear. Res. **24**, 17–36.

Lipshitz, S. P. (**1986**). ''Stereophonic microphone techniques ... are the purists wrong?,'' J. Audio Eng. Soc. **34**, 716–744.

Macpherson, E. A. (**1997**). ''A comparison of spectral correlation and local feature-matching models of pinna cue processing,'' J. Acoust. Soc. Am. **101**, 3104.

Macpherson, E. A. (**1998**). ''Spectral cue processing in the auditory localization of sounds with wideband non-flat spectra,'' Ph.D. thesis, University of Wisconsin—Madison.

Makous, J. C., and Middlebrooks, J. C. (**1990**). ''Two-dimensional sound localization by human listeners,'' J. Acoust. Soc. Am. **87**, 2188–2200.

May, B. J., and Huang, A. Y. (**1997**). ''Spectral cues for sound localization in cats: A model for discharge rate representations in the auditory nerve,'' J. Acoust. Soc. Am. **101**, 2705–2719.

Middlebrooks, J. C. (**1992**). ''Narrow-band sound localization related to external ear acoustics,'' J. Acoust. Soc. Am. **92**, 2607–2624.

Middlebrooks, J. C. (**1999**). ''Individual differences in external-ear transfer functions reduced by scaling in frequency,'' J. Acoust. Soc. Am. **106**, 1480–1492.

Oldfield, S. R., and Parker, S. P. A. (**1984**). ''Acuity of sound localisation: A topography of auditory space: I. Normal hearing conditions,'' Perception **13**, 581–600.

Perrett, S., and Noble, W. (**1995**). ''Available response choices affect localization of sound,'' Percept. Psychophys. **57**, 150–158.

Rakerd, B., Vander Velde, T., and Hartmann, W. (**1998**). ''Sound localization in the median sagittal plane by listeners with presbyacusis,'' J. Am. Acad. Aud. **9**, 466–479.

Recio, A., Rich, N. C., Narayan, S. S., and Ruggero, M. A. (**1998**). ''Basilar-membrane responses to clicks at the base of the chinchilla cochlea,'' J. Acoust. Soc. Am. **103**, 1972–1989.

Roffler, S. K., and Butler, R. A. (**1968**). ''Factors that influence the localization of sound in the vertical plane,'' J. Acoust. Soc. Am. **43**, 1255–1259.

Sachs, M. B., and Young, E. D. (**1979**). ''Encoding of steady-state vowels in the auditory nerve: Representation in terms of discharge rate,'' J. Acoust. Soc. Am. **66**, 470–479.

Shaw, E. A. G. (**1982**). ''External ear response and sound localization,'' in *Localization of Sound: Theory and Applications*, edited by R. W. Gatehouse (Amphora, Groton, CT), pp. 30–41.

Stankovic, K. M., and Guinan, Jr., J. J. (**1999**). ''Medial efferent effects on auditory-nerve responses to tail-frequency tones I: Rate reduction,'' J. Acoust. Soc. Am. **106**, 857–869.

Stellmack, M. A., and Macpherson, E. A. (**1995**). ''Localization of a virtual acoustic target in the presence of a distractor,'' J. Acoust. Soc. Am. **98**, 2906.

Wightman, F. L., and Kistler, D. J. (**1989**). ''Headphone simulation of free-field listening. II: Psychophysical validation,'' J. Acoust. Soc. Am. **85**, 868–878.

Wightman, F. L., and Kistler, D. J. (**1992**). ''The dominant role of low-frequency interaural time differences in sound localization,'' J. Acoust. Soc. Am. **91**, 1648–1661.

Winslow, R. L., and Sachs, M. B. (**1987**). ''Effect of electrical stimulation of the crossed olivocochlear bundle on auditory nerve response to tones in noise,'' J. Neurophysiol. **57**, 1002–1021.

Yates, G. K. (**1990**). ''Basilar membrane nonlinearity and its influence on auditory nerve rate-intensity functions,'' Hear. Res. **50**, 145–162.

Zakarauskas, P., and Cynader, M. S. (**1993**). ''A computational theory of spectral cue localization,'' J. Acoust. Soc. Am. **94**, 1323–1331.

Zhou, B., Green, D. M., and Middlebrooks, J. C. (**1992**). ''Characterization of external ear impulse responses using Golay codes,'' J. Acoust. Soc. Am. **92**, 1169–1171.

The meaning of the Kelly–Lochbaum acoustic-tube model

Hans Werner Strube[a)]
Drittes Physikalisches Institut, Universität Göttingen, Bürgerstrasse 42-44, D-37073 Göttingen, Germany

(Received 17 January 2000; accepted for publication 13 July 2000)

The scattering equations of the Kelly–Lochbaum segmented tube, including the time-varying extension by Strube, are originally based on the assumption of uniform spatial segments and stepwise time update of the acoustic impedances. Here, it is shown that the same equations can be derived without these assumptions for a nonuniform time-varying tube from the discretization of space and time derivatives by the bilinear z transform or by centered differences along the rotated coordinates $ct \pm x$. Moreover, the same equations also hold for a chain of lattice circuits (or equivalents) with appropriate parameters, if time derivatives are discretized by the bilinear z transform. These circuits can also be extended to simulate uniform segments of varying length. © *2000 Acoustical Society of America.* [S0001-4966(00)04310-1]

PACS numbers: 43.70.Bk, 43.72.Ja, 43.20.Wd [AL]

I. INTRODUCTION

For modeling acoustic wave transmission in the vocal tract, several approximations are usual. The basic assumption is essentially one-dimensional, plane wave propagation, since the diameter of the tract is small compared to the wavelength up to several kHz, which prevents propagation of higher modes. For digital simulation in a simple and efficient way, the nonuniform tube is usually replaced by a chain of uniform segments of equal length, as suggested by Kelly and Lochbaum (KL) (1962). Whereas realistic simulations require the modeling of acoustic losses, finite wall impedance, sources within the tract, termination by glottal and radiation impedances, our considerations will be restricted to the simplest approximation, the hard-walled, lossless tube as in the KL paper. Then, it is advantageous to describe the acoustic field not by pressure p and volume velocity q but by a pair of wave quantities, which are scattered at the segment boundaries. Figure 1 shows the signal flow graph. This is based on the fact that the general solution of the wave equation in a uniform tube is the sum of two oppositely traveling waves. Discretizing the time axis means considering pulse-like waves, with a fixed relation between sampling frequency f_s and segment length D. Although intuitively one might expect $f_s = c/D$ (which would indeed be possible), $f_s = c/2D$ was chosen by KL, where c is the speed of sound. Then, the delay by one segment has a z-transform representation $z^{-1/2}$. With this choice, the KL model is equivalent to a chain of ''unit elements'' coupled by ''two-port adaptors'' in the wave-digital-filter (WDF) terminology (Fettweis, 1971, 1986). Also, an equivalence (up to scaling factors) was found to the lattice filters occurring in linear-prediction theory (Atal and Hanauer, 1971; Wakita, 1973), where the $z^{-1/2}$ delay elements in the forward wave branch are moved into the backward branch, resulting in z^{-1} elements in this branch only. Similarly, KL already suggested z^{-1} elements in the forward branch only. But there is no need to combine pairs of $z^{-1/2}$ delays, because these can be implemented by computing the even and odd segments alternatingly.

In all these approaches the tube area function was constant in time. A generalization to the time-varying case was attempted by Maeda (1977), but postulated a continuity constraint not derived from the field equations. Another derivation based only on these equations was given by Strube (1982a, b), which led to time-variation effects with opposite sign as in Maeda's theory. A comparison of different assumptions was carried out by Liljencrants (1985), who found Maeda's approach more robust against temporal area undersampling but Strube's more appropriate for fast motion.

However, the spatial approximation by a piecewise uniform segmented tube was always an *a priori* assumption (in the time-varying case necessarily supplemented by a piecewise constant time dependence with update rate c/D). Even Maeda and Liljencrants did not mention the basic acoustic equations but started directly from the segmented tube (and some continuity postulates). Thus, one may ask what the meaning of this kind of discretization is from the view of known discretization paradigms from the theory of partial differential equations, without requiring the area function to be piecewise constant in space and time. Beside yielding a better fundamental insight, e.g., regarding the underlying approximation, this will lead to another approach to the time-varying case, consistent with Strube (1982a, b). It will also provide a better understanding of the meaning of the discrete wave quantities in relation to space–time samples of pressure and volume velocity and the role of the f_s choice.

Another old approach, still from the ''analog'' era, was a spatial discretization in the form of LC ladder circuits. The relation between LC-circuit models and the nonuniform tube will be clarified here, which requires a specific circuit type and time discretization. An interesting ''automatic'' consequence is a representation of locally varying length scale by a local first-order all-pass transformation, as previously suggested, e.g., by Välimäki and Karjalainen (1995).

The goal of this paper is not to introduce any new methods or more realistic representations of the vocal tract, but to demonstrate such previously ignored relationships between the mentioned well-known, simple methods.

[a)]Electronic mail: strube@physik3.gwdg.de

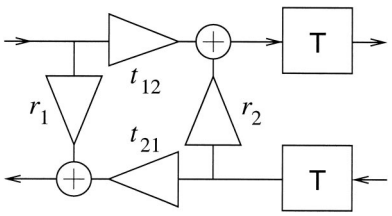

FIG. 1. Signal flow graph for one segment of the Kelly–Lochbaum model and its left boundary. Boxes T are delay elements. Triangles: r_i reflection coefficients, t_{ij} transmission coefficients. For pressure waves, $t_{12}=1+r_1$, $t_{21}=1+r_2$. In the time-invariant case, $r_2=-r_1$.

II. THE ACOUSTIC TUBE

Assume a lossless, hard-walled tube with approximately plane waves along the tube axis coordinate x. Let pressure $p(x,t)$, volume velocity $q(x,t)$, density $\rho(x,t)$ be ''small'' ac quantities, let $A(x,t)$ be the (possibly time-varying) area function, and speed of sound c and average density ρ_0 be constant. Then the linearized acoustic field equations read:

$$\rho_0\,\partial_t(q/A)=-\partial_x p, \tag{1}$$

$$\partial_t(\rho A)+\rho_0\,\partial_t A=-\rho_0\,\partial_x q, \tag{2}$$

$$p=c^2\rho. \tag{3}$$

Here, ∂_t, ∂_x are abbreviations for $\partial/\partial t$, $\partial/\partial x$. Whereas the three-dimensional form of these equations is found in any acoustics textbook, the time-varying one-dimensional form (Portnoff, 1973) has to be briefly explained. Equation (1) is the usual linearized Newton–Euler momentum equation, with q/A the particle velocity in the x direction, and Eq. (3) the usual state equation. Only the continuity equation (2) has a special one-dimensional form, since the one-dimensional mass density is $(\rho_0+\rho)A$, whose time derivative is the left-hand side of Eq. (2), and $\rho_0 q$ is the mass flow. The second term in Eq. (2) represents a flow source due to the motion of the tube walls. In practice, e.g., in the vocal tract, these usually move too slowly to generate audible sound; also, this merely results in an additive field component, so this term will henceforth be neglected. Then, Eqs. (2) and (3) can be combined into

$$\partial_t(pA)/\rho_0 c^2=-\partial_x q. \tag{4}$$

Obviously, the two field equations (1) and (4) are of a form analogous to those of a lossless electrical transmission line, if p is identified with voltage and q with current and

$$L'=\rho_0/A,\quad C'=A/\rho_0 c^2 \tag{5}$$

correspond to an inductance and capacitance density, respectively; cf. Flanagan (1965). These are not independent, since $L'C'=c^{-2}$ is constant. Thus, the tube may be completely described by the acoustic impedance (in electrical transmission lines called ''characteristic impedance,'' which has a different meaning in acoustics)

$$Z=\sqrt{L'/C'}=\rho_0 c/A; \tag{6}$$

then, $L'=Z/c$, $C'=1/Zc$. Equations (1) and (4) are rewritten as

$$-\partial_x p=\partial_t(L'q)=c^{-1}\partial_t(qZ), \tag{7a}$$

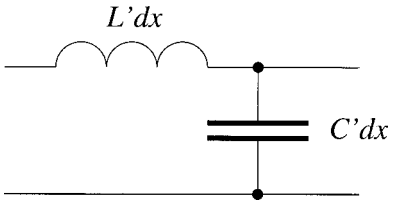

FIG. 2. Infinitesimal element of lossless transmission line.

$$-\partial_x q=\partial_t(C'p)=c^{-1}\partial_t(p/Z). \tag{7b}$$

This corresponds to an infinitesimal transmission-line element as in Fig. 2.

Alternatively, we can form unidirectional waves

$$p^+=(p+Zq)/2,\quad p^-=(p-Zq)/2, \tag{8}$$

and also combined space–time coordinates $ct\pm x$ parallel to the wave trajectories. Derivatives along these directions are $\partial_\pm=c^{-1}\partial_t\pm\partial_x$. By substituting $c^{-1}\partial_t=(\partial_++\partial_-)/2$, $\partial_x=(\partial_+-\partial_-)/2$ and combining terms according to Eq. (8), Eqs. (7) are transformed into

$$\partial_+ p^+-\partial_- p^-=0, \tag{9a}$$

$$\partial_+(p^+/Z)+\partial_-(p^-/Z)=0. \tag{9b}$$

From a solution of this, the original field quantities can be recovered by inverting Eq. (8) as

$$p=p^++p^-,\quad q=(p^+-p^-)/Z. \tag{10}$$

Note that we have used pressure waves here. In the literature, especially related to linear-prediction lattice filters, often volume-velocity waves are used instead. These are simply $q^\pm=p^\pm/Z=(p/Z\pm q)/2$. Because of invariance with respect to duality transformations $p\leftrightarrow q$, $Z\leftrightarrow 1/Z$, any equations for pressure waves can be converted into those for volume-velocity waves by substituting $p^+\to q^+$, $p^-\to -q^-$, $Z\to 1/Z$. Square-root-of-power waves ($p^\pm/\sqrt{Z}$) would also be possible, but they lead to more complicated scattering equations in the discrete case.

III. DISCRETIZATION

A. Derivation of KL-type scattering equations

Consider the approximation of a derivative [written here for a function of time $u(t)$ with derivative $\dot{u}(t)$] in the case of equispaced discretization with sampling frequency f_s, with $u_k:=u(k/f_s)$, k integer. The simplest approximation would be a first-order difference: $\dot{u}_k=f_s(u_k-u_{k-1})$. This is an asymmetric expression with a phase error, which can be removed by taking the symmetric second-order difference: $\dot{u}_k=f_s(u_{k+1}-u_{k-1})/2$. In z-transform notation, these two approximations correspond to the filters $f_s(1-z^{-1})$ and $f_s(z-z^{-1})/2$, respectively. Another symmetric second-order approach is the implicit expression $\dot{u}_k+\dot{u}_{k-1}=2f_s(u_k-u_{k-1})$. This is equivalent to the trapezoidal rule for numerical integration and corresponds to the filter $2f_s(1-z^{-1})/(1+z^{-1})$, the well-known ''bilinear z transform.''

With one space and one time dimension, the same or different discretization rules can be applied to space and time. Also, the grid of sampling points can have various

forms. We consider regular rectangular point lattices only, or the rhombic sublattice whose indices have an even sum. Moreover, the two field quantities and the acoustic impedances Z (or area values A) might be sampled at different points. Then, we can state the following:

The KL tube model, including the time-varying case, is equivalent to

(i) bilinear transformation of both space and time derivatives for p and q in Eqs. (7), but also to
(ii) mutually centered simple differences of p^+, p^- in Eqs. (9) along the diagonals of the sampling-lattice cells, with p, q, Z or p^+, p^-, Z all sampled at the same points of a rectangular lattice with sampling relation $f_s = c/D$.

The sampling points in this discretization correspond to the centers of the constant-Z space–time tiles of the KL model.

1. Proof. Let T be a time-shift operator delaying by one sampling interval (corresponding to z^{-1} in the z domain) and X an analogous space shift operator. Then, the bilinear transforms of Eqs. (7) in both space and time become

$$\frac{v}{c}(1+\mathsf{X})(1-\mathsf{T})(qZ)+(1+\mathsf{T})(1-\mathsf{X})p=0, \tag{11a}$$

$$\frac{v}{c}(1+\mathsf{X})(1-\mathsf{T})\left(\frac{p}{Z}\right)+(1+\mathsf{T})(1-\mathsf{X})q=0, \tag{11b}$$

where $v = f_s D$ is the ratio of the temporal and spatial sampling frequencies. This discretization was already used by Portnoff (1973), including the (here dropped) $\partial_t A$ term from Eq. (2). Choosing $v = c$, Eqs. (11) can be written

$$(1-\mathsf{XT})(p+Zq)-(\mathsf{X}-\mathsf{T})(p-Zq)=0, \tag{12a}$$

$$(1-\mathsf{XT})(p/Z+q)+(\mathsf{X}-\mathsf{T})(p/Z-q)=0, \tag{12b}$$

or, with unidirectionally traveling waves from Eq. (8),

$$(1-\mathsf{XT})p^+-(\mathsf{X}-\mathsf{T})p^-=0, \tag{13a}$$

$$(1-\mathsf{XT})(p^+/Z)+(\mathsf{X}-\mathsf{T})(p^-/Z)=0. \tag{13b}$$

This is obviously also obtained directly from Eqs. (9) by taking mutually centered differences along the wave trajectories.

With subscripts n for space and k for time samples, this reads explicitly

$$p^+_{n,k}-p^+_{n-1,k-1}-p^-_{n-1,k}+p^-_{n,k-1}=0, \tag{14a}$$

$$p^+_{n,k}Z^{-1}_{n,k}-p^+_{n-1,k-1}Z^{-1}_{n-1,k-1}+p^-_{n-1,k}Z^{-1}_{n-1,k}-p^-_{n,k-1}Z^{-1}_{n,k-1} =0. \tag{14b}$$

Given two of the four quantities $p^+_{n,k}$, $p^+_{n-1,k-1}$, $p^-_{n-1,k}$, $p^-_{n,k-1}$, the other two can be computed. For instance, if the initial values (time $k-1$) are given, this yields the scattering equations

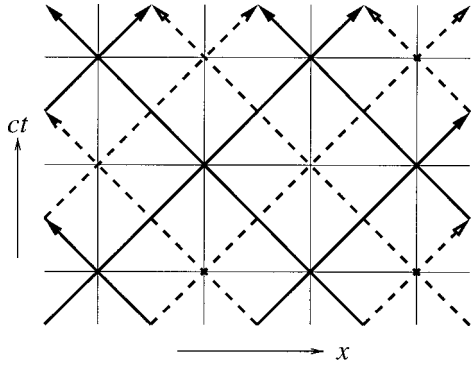

FIG. 3. Space–time diagram of pulse propagation in a KL network. Thin solid: boundaries of tiles of constant Z; solid: pulse-wave trajectories for $f_s = c/2D$; long dashed: additional trajectories if $f_s = c/D$.

$$p^-_{n-1,k}=\frac{Z^{-1}_{n-1,k-1}-Z^{-1}_{n,k}}{Z^{-1}_{n-1,k}+Z^{-1}_{n,k}}\,p^+_{n-1,k-1} + \frac{Z^{-1}_{n,k-1}+Z^{-1}_{n,k}}{Z^{-1}_{n-1,k}+Z^{-1}_{n,k}}\,p^-_{n,k-1}, \tag{15a}$$

$$p^+_{n,k}=\frac{Z^{-1}_{n-1,k}+Z^{-1}_{n-1,k-1}}{Z^{-1}_{n-1,k}+Z^{-1}_{n,k}}\,p^+_{n-1,k-1} -\frac{Z^{-1}_{n-1,k}-Z^{-1}_{n,k-1}}{Z^{-1}_{n-1,k}+Z^{-1}_{n,k}}\,p^-_{n,k-1}. \tag{15b}$$

These are formally equivalent to the equations for the scattering of short pulses at a spatiotemporal discontinuity, i.e., at the intersection of the boundary of two uniform transmission-line segments and the moment of Z change in the case of stepwise time-varying Z, as derived by this author before by an entirely different approach (Strube, 1982a, b), assuming an *a priori* given spatial segmentation and stepwise time variation. (There, the $p^\pm$ actually had to be interpreted as total pulse intensities, because the pulse shape, consisting of two halves passing ''before'' and ''after'' the spatiotemporal discontinuity, changed in the scattering.) In the time-invariant case, the familiar KL scattering equations are obtained. However, now the spatial segmentation and stepwise time variation have not been *assumed* but are an *a posteriori* interpretation of the results from two standard discretization methods.

B. Two choices of sampling frequency

Note that, when the sampling frequency $f_s = c/D$ is used, the pulse-wave trajectory lattice is composed of two sublattices (solid and long-dashed in Fig. 3) that do not interact, except possibly through boundary conditions. Thus, the temporal sampling frequency for the wave quantities can be reduced to $c/2D$, but then the time-sampling points for forward and backward waves, and for even- and odd-space sampling points, are interleaved. The field quantities p and q are then not recoverable at the original sampling points but can be artificially constructed at the segment boundaries un-

der a spatial continuity assumption [in the time-varying case, continuity in both space and time cannot be achieved (Strube, 1982b)]:

$$p_{n-1/2,k-1/2} = p^+_{n,k} + p^-_{n,k-1} = p^+_{n-1,k-1} + p^-_{n-1,k}, \tag{16a}$$

$$q_{n-1/2,k-1/2} = p^+_{n,k}/Z_{n,k} - p^-_{n,k-1}/Z_{n,k-1} = p^+_{n-1,k-1}/Z_{n-1,k-1} - p^-_{n-1,k}/Z_{n-1,k}. \tag{16b}$$

Thus, this case is not interpretable as a standard space–time discretization of an arbitrary $Z(x,t)$ but requires the *a priori* assumption of piecewise constant Z.

The two sampling frequencies also lead to different treatment of terminating impedances at the tube ends. If $f_s = c/2D$, these can only be attached to the end of a full segment, since only there are both p and q (or p^+ and p^-) defined. If $f_s = c/D$, however, we can choose to attach them to the end of a full or a half segment. In fact, the latter might be preferable, since it is the center of the segment where the field quantities can be recovered without *a priori* assumption of a segmented and stepwise time-varying tube. In both cases, the impedances can conveniently be implemented by WDF techniques, also based on (formal) wave quantities (Fettweis, 1971, 1986; Strube, 1982b).

C. Features and limitations

The approximation of derivatives in the discretization chosen is of second order only. As the frequency warping due to the bilinear transform is the same for spatial and temporal frequencies, no dispersion is introduced by the discretization, and the directions of the wave trajectories (characteristics) are preserved.

For the time-invariant case, stability is ensured since the discrete algorithm is an exact analogy to pulse propagation in an (idealized) segmented acoustic tube, a *passive* physical system. However, in the time-varying case, the solutions may become unstable. This should not be blamed on the discretization method but has physical reasons. The moving walls can pump energy into the system in the same way as in a parametric amplifier. When there are losses, e.g., due to terminating load impedances, this will not cause a practical problem. In vocal-tract simulations, the time-varying treatment is almost irrelevant except in modeling the glottal slit and possibly plosives.

What happens if damping terms are included in the field equations? The losses in an acoustic tube, expressed by a resistance density R' and a conductance density G' (Flanagan, 1965), actually have a square-root-of-frequency dependence and cannot be modeled by any finite-order discrete-time system. If one assumes the (unrealistic) case $R'/G' = Z^2$, a uniform tube would again have independent forward and backward waves, albeit exponentially decaying. Thus, in KL-type segmented tube models, losses are often crudely introduced by decay factors in the segmental waves. But, a formal derivation of a KL-type segmented-tube representation in a way analogous to the above no longer seems possible.

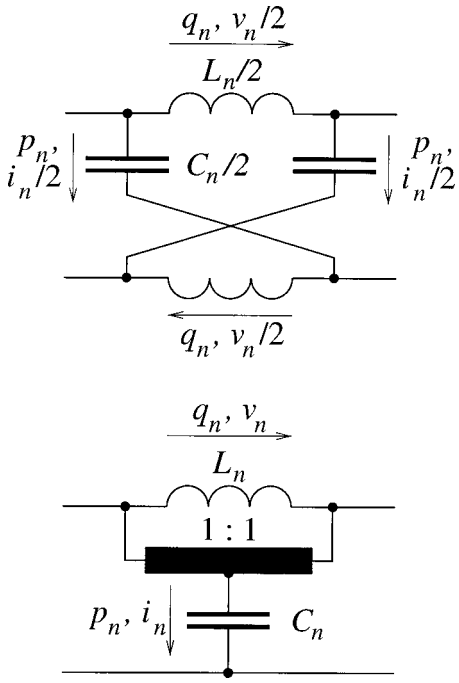

FIG. 4. Top: lattice circuit. Bottom: equivalent common-ground circuit; filled rectangle: ideal autotransformer. (The parallel connection of inductance and ideal autotransformer can be implemented as a single coil with center tap and fully coupled halves.)

IV. RELATION TO LC NETWORKS

A. Ladders, lattices, and the KL tube

The infinitesimal transmission-line element (Fig. 2) suggests an approximation of the nonuniform line by a chain of such elements of *finite* size, replacing dx by D. Let us keep the time axis continuous for the moment. Such LC ladder networks, which were frequently used in the analog era, correspond to a spatial discretization where the sampling points of p and C' are interleaved with those of q and L', and spatial derivatives become simple differences. This is very distinct from the KL model. Unlike a tube model, the LC ladder has low-pass characteristics and each segment circuit has a frequency-dependent characteristic impedance.

However, there is a another possibility, a chain of lattice (bridge) circuits [Fig. 4 (top)], which seems never to have been considered in vocal-tract simulations. Each segment circuit has a constant characteristic impedance and an all-pass behavior when terminated by this. To avoid the pairwise occurrence of ''half'' inductances and capacitances and the lack of a common ground, equivalent common-ground circuits with transformers may be used instead, for instance, Fig. 4 (bottom) (see textbooks on two-port theory, e.g., Klein, 1972).

Such a chain will be shown to yield the same discrete equations as the KL model if p_n are the voltages across the capacitances and q_n the currents through the inductances. And, it will offer an immediate generalization to local length-scale warping, corresponding to varying segment length D.

Let i_n be the currents through the C_n of the common-ground circuits or twice the currents through $C_n/2$ in the lattice circuits, likewise v_n the voltages across the L_n or

twice the voltages across the $L_n/2$; see Fig. 4. Let $p_{n-1/2}$, $q_{n-1/2}$ be the voltage and current at the left port of circuit n. Then, by looking at two adjacent circuits the following obviously holds:

$$p_n + v_n/2 = p_{n-1/2} = p_{n-1} - v_{n-1}/2, \tag{17a}$$

$$q_n + i_n/2 = q_{n-1/2} = q_{n-1} - i_{n-1}/2, \tag{17b}$$

$$i_n = \frac{d}{dt}(C_n p_n), \quad v_n = \frac{d}{dt}(L_n q_n), \tag{17c}$$

whence

$$\frac{1}{2}\left(\frac{d}{dt}(L_n q_n) + \frac{d}{dt}(L_{n-1} q_{n-1})\right) + p_n - p_{n-1} = 0, \tag{18a}$$

$$\frac{1}{2}\left(\frac{d}{dt}(C_n p_n) + \frac{d}{dt}(C_{n-1} p_{n-1})\right) + q_n - q_{n-1} = 0. \tag{18b}$$

This has the same appearance as a discretization of the spatial derivatives in Eqs. (7) by the bilinear z transform, with $L_n = Z_n D/c$, $C_n = D/(Z_n c)$. If time is now discretized with $f_s = (L_n C_n)^{-1/2} = c/D$ and the bilinear z transform applied to the time derivatives, we have the same situation that led to the scattering equations Eqs. (14), which are thus again obtained.

The time sampling of $p_{n-1/2}$, $q_{n-1/2}$ is at integer k as for p_n, q_n, unlike the half-integer k in Eqs. (16). Applying the (temporal) bilinear z transform to Eqs. (17) and expressing p_n, q_n by p_n^+, p_n^- according to Eq. (8) shows that $p_{n-1/2,k-1/2}$ from Eqs. (16) must be identified with $(p_{n-1/2,k} + p_{n-1/2,k-1})/2$, and correspondingly for q.

But where are the waves $p^\pm$ in the lattice chain? They can be made manifest when the time discretization of derivatives is done by the WDF method (Fettweis, 1986) instead of the bilinear z transform (both are essentially equivalent). The formal WDF wave quantities at the ports connected to the adjacent circuits are identifiable with the $p^\pm$ (for a full equality, the WDF waves must be averaged over two subsequent time samples to yield the $p^\pm$). In the WDF representation, the scattering of the waves at the boundaries between the circuits is described by the same two-port adaptor as in Fig. 1 (left half).

B. Application to local segment-length variation

An old problem is the continuous variation of the length of single segments in a sampled-data tube model. The difficulty arises from the strict proportionality between spatial and temporal sampling intervals. As the temporal sampling is usually fixed, one has to give up the simple forward/backward wave approach and interpolate in some way. Simple or sophisticated interpolation techniques have been described, e.g., Strube, 1975; Välimäki *et al.*, 1994. An especially simple and appealing method—not introducing losses or stability problems—is a replacemant of delays z^{-1} by all-pass filters $H_n(z)$ (Välimäki and Karjalainen, 1995), in the first-order case

$$H_n(z) = (z^{-1} - \alpha_n)/(1 - \alpha_n z^{-1}), \quad |\alpha_n| < 1. \tag{19}$$

Note that this is equal in form to but different in meaning from the usual all-pass transform used for frequency warping of whole transfer functions. Here it is applied to a single segment n in order to change the wave delay in the low-frequency limit. Expanding $H_n(\exp(i\omega/f_s))$ for small ω shows the delay to be $f_s^{-1}(1+\alpha_n)/(1-\alpha_n)$.

The first-order all-pass transform follows in a natural way from the lattice circuit if we choose $D_n = c\sqrt{L_n C_n}$ (now dependent on n) $\neq D = c/f_s$, but retain $Z_n = \sqrt{L_n/C_n}$.

From Fig. 4 we see

$$p_{n+1/2} - p_{n-1/2} = -v_n = -d(L_n q_n)/dt, \tag{20a}$$

$$q_{n+1/2} - q_{n-1/2} = -i_n = -d(C_n p_n)/dt. \tag{20b}$$

Assuming L_n and C_n time invariant, bilinear z transform of the time derivatives yields

$$(1+\mathsf{T})(p_{n+1/2} - p_{n-1/2}) + 2f_s L_n (1-\mathsf{T}) q_n = 0, \tag{21a}$$

$$(1+\mathsf{T})(q_{n+1/2} - q_{n-1/2}) + 2f_s C_n (1-\mathsf{T}) p_n = 0, \tag{21b}$$

where T is the time delay operator by $1/f_s$. Note that, from Eqs. (17), $p_n = (p_{n+1/2} + p_{n-1/2})/2$, $q_n = (q_{n+1/2} + q_{n-1/2})/2$, and let $\delta_n = D_n/D = f_s L_n/Z_n = f_s C_n Z_n$. Inserting all this, then forming the sum and difference of Eq. (21a) and Z_n times Eq. (21b), and combining p, q to $p^\pm$ according to Eq. (8) yields, after trivial but lengthy arithmetic,

$$(1+\mathsf{T})(p^+_{n+1/2} - p^+_{n-1/2}) + \delta_n (1-\mathsf{T})(p^+_{n+1/2} + p^+_{n-1/2}) = 0, \tag{22a}$$

$$(1+\mathsf{T})(p^-_{n+1/2} - p^-_{n-1/2}) - \delta_n (1-\mathsf{T})(p^-_{n+1/2} + p^-_{n-1/2}) = 0, \tag{22b}$$

or, going to the z domain ($\mathsf{T} \to z^{-1}$) and rearranging terms,

$$((\delta_n + 1) - (\delta_n - 1)z^{-1}) p^+_{n+1/2} = ((\delta_n + 1) - (\delta_n - 1)z^{-1}) p^+_{n-1/2}, \tag{23a}$$

$$((\delta_n + 1) - (\delta_n - 1)z^{-1}) p^-_{n-1/2} = ((\delta_n + 1) - (\delta_n - 1)z^{-1}) p^-_{n+1/2}. \tag{23b}$$

These are obviously two equal all-pass filters for the waves, $p^+_{n+1/2} = H_n p^+_{n-1/2}$, $p^-_{n-1/2} = H_n p^-_{n+1/2}$, H_n according to Eq. (19) with $\alpha_n = (\delta_n - 1)/(\delta_n + 1)$. (As for the notation, it is consistent only for a single circuit; $p^+_{n-1/2}$ of circuit n is not identical with $p^+_{(n-1)+1/2}$ of circuit $n-1$.)

There is one difficulty. All-pass filters have a delay-free path, since $(z^{-1} - \alpha_n)/(1 - \alpha_n z^{-1}) = -\alpha_n + (1 - \alpha_n^2) z^{-1}/(1 - \alpha_n z^{-1})$. If there were nonzero reflections (also delay-free) at the boundaries to the two neighboring segments, a delay-free loop would occur: forward all-pass→right reflection →backward all-pass→left reflection→ .... Such a loop is not allowed in realizable discrete-time systems. Thus, the segment must be connected at least on one side to an ordinary segment of equal impedance in order to avoid one of the two reflections. This is equivalent to the cascading of all-pass filters with ordinary delay elements as done by Välimäki and Karjalainen (1995).

V. CONCLUSION

It was shown that the scattering equations of the Kelly–Lochbaum segmented model for a nonuniform tube can be derived from a representation of space and time derivatives by the bilinear z transform or by mutually centered differences along the spatiotemporal wave trajectories. In the time-varying case, this yields the extension suggested by this author before. Unlike then, no *a priori* assumption of piecewise constancy of the acoustic impedance in space and time is used now. The sampling points for acoustic impedance, pressure, and volume velocity correspond to the centers of the uniform segments (or space–time tiles of constant Z). However, the present derivation requires the choice of $f_s = c/D$ rather than the usual $f_s = c/2D$. The latter would not allow the knowledge of pressure and volume velocity at the segment centers, only at the boundaries of assumed uniform segments.

The same equations can also be represented by a chain of lattice circuits (or their equivalents), with the time differentiation due to inductances and capacitances discretized either by the bilinear z transform or by the WDF method. The lattice circuits easily generalize to a representation of segments of varying length that is equivalent to a *local* first-order all-pass transform.

ACKNOWLEDGMENTS

I would like to thank one of the reviewers for valuable hints and for supplying a missing reference.

Atal, B. S., and Hanauer, S. L. (**1971**). ''Speech analysis and synthesis by linear prediction of the speech wave,'' J. Acoust. Soc. Am. **50**, 637–655.

Fettweis, A. (**1971**). ''Digital filters related to classical filter networks,'' Arch. Elektr. Uebertrag. **25**, 79–89.

Fettweis, A. (**1986**). ''Wave digital filters: theory and practice,'' Proc. IEEE **74**, 270–327.

Flanagan, J. L. (**1965**). *Speech Analysis, Synthesis and Perception* (Springer, Berlin).

Kelly, J. L., and Lochbaum, C. C. (**1962**). ''Speech synthesis,'' in *Proceedings of the Fourth International Congress on Acoustics*, Paper G42, pp. 1–4, reprinted in: *Speech Synthesis*, edited by J. L. Flanagan and L. R. Rabiner (Dowden, Hutchinson & Ross, Stroudsburg, 1973), pp. 127–130.

Klein, W. (**1972**). *Vierpoltheorie* (Bibliographisches Institut, Mannheim), p. 38.

Liljencrants, J. (**1985**). ''Speech Synthesis with a Reflection-Type Line Analog,'' doctoral dissertation, Royal Inst. Technol., Stockholm.

Maeda, S. (**1977**). ''On a simulation method of dynamically varying vocal tract: Reconsideration of the Kelly–Lochbaum model,'' in *Modèles Articulatoires et Phonétique—Articulatory Modeling and Phonetics*, edited by R. Carré, R. Descout, and M. Wajskop (G.A.L.F., Brussels/Grenoble/Lannion), pp. 281–288.

Portnoff, M. R. (**1973**). ''A quasi-one-dimensional digital simulation for the time-varying vocal tract,'' thesis, Massachusetts Institute of Technology, Department of Electrical Engineering.

Strube, H. W. (**1975**). ''Sampled-data representation of a nonuniform lossless tube of continuously variable length,'' J. Acoust. Soc. Am. **57**, 256–257.

Strube, H. W. (**1982a**). ''Time-varying wave digital filters and vocal-tract models,'' IEEE International Conference Acoustics, Speech, and Signal Processing (ICASSP 82), Paris, Paper S6.4, pp. 923–926.

Strube, H. W. (**1982b**). ''Time-varying wave digital filters for modeling analog systems,'' IEEE Trans. Acoust., Speech, Signal Process. **ASSP-30**, 864–868.

Välimäki, V., Karjalainen, M. and Kuisma, T. (**1994**). ''Articulatory speech synthesis based on fractional delay waveguide filters,'' IEEE International Conference on Acoustics, Speech, and Signal Processing (ICASSP 94), Vol. 1, pp. 585–588.

Välimäki, V., and Karjalainen, M. (**1995**). ''Implementation of fractional delay waveguide models using all-pass filters,'' IEEE International Conference Acoustics, Speech, and Signal Processing (ICASSP 95), Vol. 2, pp. 1524–1527.

Wakita, H. (**1973**). ''Direct estimation of the vocal tract shape by inverse filtering of acoustic speech waveforms,'' IEEE Trans. Audio Electroacoust. **AU-21**, 417–427.

Time-varying spectral change in the vowels of children and adults

Peter F. Assmann and William F. Katz
School of Human Development and Callier Center for Communication Disorders, The University of Texas at Dallas, Box 830688, Richardson, Texas 75083

(Received 30 August 1999; accepted for publication 23 June 2000)

Recent studies have shown that time-varying changes in formant pattern contribute to the phonetic specification of vowels. This variation could be especially important in children's vowels, because children have higher fundamental frequencies (f_0's) than adults, and formant-frequency estimation is generally less reliable when f_0 is high. To investigate the contribution of time-varying changes in formant pattern to the identification of children's vowels, three experiments were carried out with natural and synthesized versions of 12 American English vowels spoken by children (ages 7, 5, and 3 years) as well as adult males and females. Experiment 1 showed that (i) vowels generated with a cascade formant synthesizer (with hand-tracked formants) were less accurately identified than natural versions; and (ii) vowels synthesized with steady-state formant frequencies were harder to identify than those which preserved the natural variation in formant pattern over time. The decline in intelligibility was similar across talker groups, and there was no evidence that formant movement plays a greater role in children's vowels compared to adults. Experiment 2 replicated these findings using a semi-automatic formant-tracking algorithm. Experiment 3 showed that the effects of formant movement were the same for vowels synthesized with noise excitation (as in whispered speech) and pulsed excitation (as in voiced speech), although, on average, the whispered vowels were less accurately identified than their voiced counterparts. Taken together, the results indicate that the cues provided by changes in the formant frequencies over time contribute materially to the intelligibility of vowels produced by children and adults, but these time-varying formant frequency cues do not interact with properties of the voicing source.
[S0001-4966(00)01410-7]

PACS numbers: 43.71.An, 43.70.Ep, 43.71.Es [KRK]

I. INTRODUCTION

The perception of vowel quality is determined mainly by the formant pattern and its changes over time (Rosner and Pickering, 1994). Traditionally, vowels were described as static entities, analyzed in terms of a single, brief spectral sample taken from their central region or ''nucleus'' (e.g., Peterson and Barney, 1952). However, several sources of evidence now indicate that time-varying changes in the frequencies of the lowest three formants contribute to the perception of vowel quality, even in monophthongs (Di Benedetto, 1989; Fox, 1989; Hillenbrand and Gayvert, 1993; Hillenbrand *et al.*, 1995; Nábělek and Ovchinnikov, 1997; Nearey and Assmann, 1986; Nearey, 1989; Andruski and Nearey, 1992; Strange *et al.*, 1983; Strange, 1989; Pols and van Son, 1993; Zahorian and Jaghargi, 1991, 1993).

Hillenbrand (1995) and Hillenbrand and Nearey (1999) reported that vowels synthesized with ''flattened'' formant tracks (i.e., with the formant pattern held constant across the duration of the vowel) were identified less accurately than vowels for which the natural variations in formant frequencies were preserved. Their synthesized stimuli were modeled after a large sample of vowels produced by men, women, and children (ages 10–12 years). Formant flattening led to a 15% drop in mean identification accuracy, suggesting that formant movement plays an important role in the perceptual specification of American English vowels.

One reason for the detrimental effects of formant flattening may be that formant movement helps to disambiguate pairs of vowels whose spectral shapes are similar in their ''nucleus'' regions but differ in their off-glides [e.g., the vowels /ɪ/ and /e/ in American English (Nearey and Assmann, 1986)]. Formant-frequency changes could also provide evidence of the locations of ''merged'' formant peaks when pairs of formants approach one another in frequency. The likelihood of merged formants is greater when the fundamental frequency (f_0) is high and the spectrum envelope is sparsely ''sampled'' at the frequencies of the harmonics. Given the importance of the formant peaks for vowel identification, it might be predicted that vowels with high f_0's would be identified less accurately than those with low f_0's. This prediction has been confirmed in experiments with synthetic vowels (Ryalls and Lieberman, 1982; Diehl *et al.*, 1996).

An illustration of sparse spectral sampling is provided in Fig. 1, which shows the amplitude spectrum of the vowel /ɔ/ spoken by a 3-year old child. The left panel shows the amplitude spectrum of the onset portion of the vowel, along with the envelope of the spectrum estimated by linear predictive coding (LPC) analysis. The f_0 is about 262 Hz, and hence neither representation provides clear evidence of the second formant, located in the vicinity of 1050 Hz. This is a typical example of a pair of merged formants: only a single peak is evident in the region of *F*1 and *F*2.

In the right panel, the time variation in formant pattern is

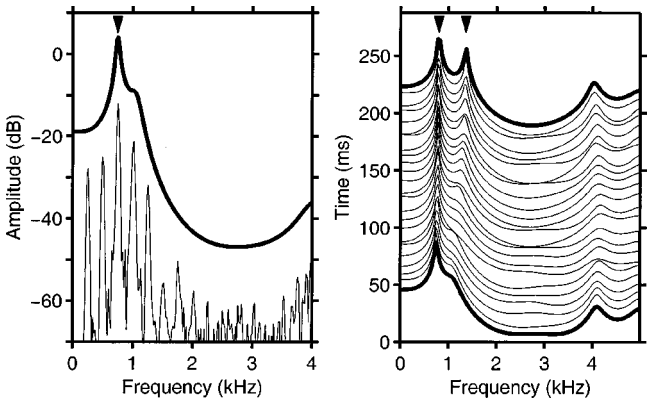

FIG. 1. Effects of time-varying changes in formant pattern on the resolution of formant peaks. The left panel shows the amplitude spectrum of a 45-ms segment from the onset portion of the vowel /ɔ/, spoken by a 3-year-old child. The dark trace is the spectrum envelope, estimated using autocorrelation LPC (10 coefficients, 512-point Hanning window, 10-kHz sample rate). The right panel shows a succession of LPC analyses obtained at 8-ms intervals throughout the vowel.

illustrated by a set of LPC spectra sampled at successive 8-ms intervals throughout the duration of the vowel. The envelope of the spectrum is more clearly defined, by extrapolation, when the vowel is sampled repeatedly at different time points. If formant movement is beneficial because it provides a basis for tracking merged formants, then these benefits should be greater for vowels with high f_0's because they contain a higher incidence of such mergers.

The relevance of the example in Fig. 1 depends on the ability of the auditory system to recover features of the spectral envelope (such as the frequencies of formant peaks or aspect of spectral shape) from the raw waveform. Psychophysical studies suggest that auditory frequency analysis is sufficiently selective at low frequencies to resolve the individual harmonic components of vowels in the frequency region below 1 kHz, even in adult male voices with low f_0's (Moore and Glasberg, 1987). Since the first formant peak does not necessarily coincide with any single harmonic, its frequency must be derived, possibly by interpolating across the peaks in the excitation pattern that correspond to the individual harmonics (Darwin and Gardner, 1985; Assmann and Nearey, 1987). When the f_0 is high (as in children's speech), the spectrum envelope is less clearly defined in the speech signal, further increasing the uncertainty in the formant estimation process (Dissard and Darwin, 2000) and, by inference, the likelihood of making identification errors. If a higher f_0 leads to poorer specification of formant peaks or other relevant aspects of spectral shape, then time-varying changes in formant-frequency ought to provide greater benefits for children's vowels than for adults' vowels.[1]

A corollary of this prediction is that time-varying changes in formant frequency should provide reduced benefits when f_0 is eliminated from the signal, as in whispered speech. Whispered speech retains the formant structure of voiced speech but not its harmonic fine structure. The broadband noise excitation of whispered speech generates a continuous spectrum, and potentially more accurate resolution of the formant peaks, provided the analysis window is sufficient in length to average out short-term fluctuations in the noise.[2] If formant peaks are more accurately represented in the auditory excitation patterns of whispered than voiced vowels, then whispered vowels might be expected to show reduced benefits of formant movement, compared to voiced vowels. However, whispered vowels are less intelligible than voiced vowels under some conditions (Tartter, 1991; Katz and Assmann, 2000). Voicing source manipulations therefore provide a basis for testing the generality of the perceptual benefits of time-varying changes in formant pattern, and may yield further insights into the mechanisms involved in vowel perception.

The present study had two main objectives: first, to determine whether time-varying changes in formant frequencies make a greater contribution to the identification of children's vowels than adults' vowels; second, to determine how the perceptual effects of formant movement generalize across changes in voicing source. Listening tests were carried out using natural and synthesized vowels, including conditions where the center frequencies of formants were held constant over the duration of the vowel (Hillenbrand, 1995). Vowels were synthesized using pulsed excitation (generating voiced vowels) and noise excitation (generating whispered vowels).

II. EXPERIMENT 1

Compared to adults, children's speech is more variable in f_0, formant frequencies, and durational properties (Eguchi and Hirsh, 1969; Kent, 1976; Smith *et al.*, 1995; Hillenbrand *et al.*, 1995; Lee *et al.*, 1999). Since the majority of earlier studies of children's speech have measured speech acoustics in older children, we included younger children of ages 7, 5, and 3 years in our sample.

A. Speech materials

Recordings were made of the 12 monophthongal vowels of American English in /hVd/ context: /i/ (heed); /ɪ/ (hid); /e/ (hayed); /ɛ/ (head); /æ/ (had); /ʌ/ (hud); /ɑ/ (hod); /ɔ/ (hawed); /ɝ/ (herd); /o/ (hoed); /ʊ/ (hood); /u/ (who'd).

B. Talkers

Ten men, 10 women, and 30 children (ages 7, 5, and 3) served as talkers. The majority of the adult talkers were longtime residents of the Dallas, Texas region, but 38% had lived in other cities during their childhood. All of the children were raised in the urban Dallas area.

C. Recording procedure

An audio cassette master tape with 6 repetitions of the 12 vowels in random sequence served as a prompt for the talkers. The adult talkers completed the set twice, for a total of 144 vowel tokens (12 vowels × 12 repetitions of each vowel). Each recording session lasted about 40 min. Recording sessions for the children took somewhat longer, and hence children completed only one set of 72 vowel tokens (12 vowels × 6 repetitions). Because children occasionally had difficulty producing target sounds following the first rep-

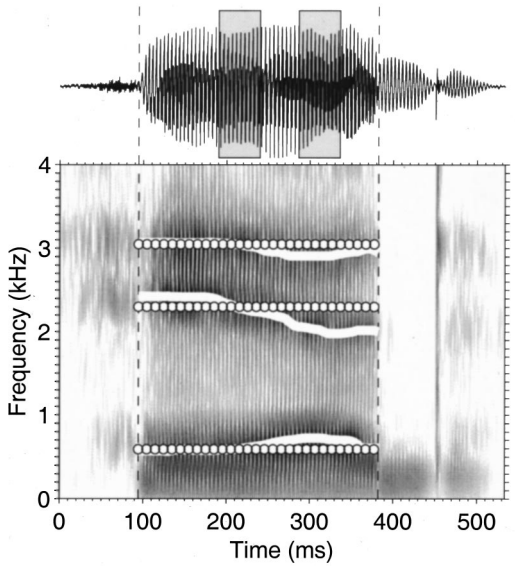

FIG. 2. The upper trace is the waveform of the syllable /hed/ spoken by an adult female. The shaded boxes indicate the first and second sample windows, starting at 33% and 66% of the distance from onset to offset of the vowel, respectively. The spectrogram shows the trajectories of *F*1, *F*2, and *F*3 frequencies with white lines. The unfilled circles show the ''flattened'' formants used in the FlatF condition of experiment 1.

etition of the audio tape, they were given additional chances to repeat target items following examples given by the examiner.

Recordings were made in a sound-treated room using a Shure SM-94 microphone and a portable audio DAT recorder, model AIWA HD-X3000. The digital waveforms were transferred to computer disk at a rate of 48 kHz and 16-bit resolution using a DAT-Link+ digital audio interface.

D. Acoustic analysis

A subset of 180 vowel tokens (12 vowels × 3 talkers × 5 talker groups) was used to extract parameters for synthesizing the stimuli in experiment 1. Selection was based on informal judgments of adequate pronunciation quality by the two authors. The waveforms were digitally low-pass filtered with an eighth-order elliptical filter (5.7 kHz, −115 dB/oct) and resampled at 12 kHz for subsequent analyses. The onsets and offsets of the vowels were determined by visual inspection, as illustrated by the dashed lines in Fig. 2. Vowel onset was defined as the beginning of the first pitch period of the voiced segment of the syllable. Vowel offset was defined as the end of the last pitch period before the stop closure created by the final /d/.

To obtain a parametric description of the vowels suitable for a formant-based synthesizer, estimates of fundamental frequency (f_0), amplitude of voicing (AV) and formant center frequencies (*F*1-*F*4) were obtained every 5 ms. Estimates of f_0 were made using an implementation of the Meddis and Hewitt (1991) pitch model. The amplitude of voicing (AV) was computed using a sliding rectangular root mean square (rms) window (25-ms frames, 5-ms overlap). Formant center frequencies were tracked using a custom MATLAB program (Assmann *et al.*, 1994). This program allows the user to identify the trajectories of the formants by visual inspection and superimpose their tracks on a spectrogram of the vowel using a mouse-based drawing tool. A synthesized version can then be generated and played back to compare with the spoken version, and the process can be repeated until a good match is found.

E. Statistical analysis of vowel formant frequencies

To analyze formant-frequency change, we adopted a version of the ''dual-target'' model described by Nearey and Assmann (1986). Vowel formant frequencies were measured using LPC analysis and a semi-automatic formant-tracking procedure, described in detail in Sec. III A below. Measurements were taken at two different time points in the vowel, illustrated by the shaded boxes in Fig. 2. The sample windows had their onsets at 33% and 66% of the vowel's duration, respectively. The goal was to include as much as possible of the formant movement within the vowel, while minimizing the neutralizing effects of the flanking consonants. Informal listening to gated versions of the vowels that spanned the two sample windows did not reveal a strong impression of the final /d/ for a majority of the tokens. Moreover, the formant trajectory defined by the two targets did not consistently point toward the same spectral locus (Delattre *et al.*, 1955; Sussman *et al.*, 1991) as might be expected if the second sample window were too close to the consonant closure. *F*1, *F*2, *F*3 frequencies and f_0 were estimated as the median of five successive measurements spaced 5-ms apart.

Table I lists the f_0 and formant-frequency estimates from the first sample window for the 12 vowels and 5 talker groups. These measurements served as the basis for the ''flattened formant'' stimuli of experiment 1. Means and standard errors are based on three talkers in each group. An analysis of variance (ANOVA) of vowel formant frequencies was carried out, covering the factors vowel (with 12 levels), group (with 5 levels), and sample (with two levels: first and second sample windows). As expected, there were significant main effects of vowel for *F*1 [$F_{(11,110)}=84.59$, $p<0.01$], *F*2 [$F_{(11,110)}=117.32$, $p<0.01$], and *F*3 [$F_{(11,110)}=30.85$, $p<0.01$]; and talker group for *F*1 [$F_{(4,10)}=12.18$, $p<0.01$], *F*2 [$F_{(4,10)}=52.08$, $p<0.05$], and *F*3 [$F_{(4,10)}=47.82$, $p<0.01$], but the interaction of talker group × vowel was not significant for any of the formants.

In addition to showing the expected pattern of higher formant frequencies in the vowels of young children, Table I shows that the standard errors are larger for several of the children's vowels, compared to those of adults, consistent with reports of greater variability in children's formant frequencies. However, it cannot be ruled out that this increased variability is due to formant measurement error associated with the higher f_0's of children's vowels, nor that this variability is irrelevant for vowel perception. These issues are addressed in experiments 1 and 2.

Of particular interest for the present study was the significant interaction of sample × vowel, indicating the presence of time variation in the frequencies of *F*1 [$F_{(11,110)}=12.65$, $p<0.01$] and *F*2 [$F_{(11,110)}=21.74$, $p<0.01$], but not *F*3 [$F_{(11,110)}=1.14$, $p=0.34$]. Figure 3 illustrates the pattern of formant movement for the male talkers. The mean *F*1 and *F*2 frequencies for the first and second time samples are

TABLE I. Means and standard errors (in parentheses) of vowel fundamental and formant frequencies (in Hz) from the first sample window, across the three talkers in each group. (See text for details.)

		/i/	/ɪ/	/e/	/ɛ/	/æ/	/ʌ/	/ɝ/	/ɑ/	/ɔ/	/o/	/ʊ/	/u/
Adult	*F*3	3003	2654	2557	2643	2580	2539	1686	2468	2564	2390	2364	2321
Males		(61)	(64)	(39)	(69)	(30)	(99)	(41)	(53)	(111)	(86)	(83)	(112)
	*F*2	2345	1974	1982	1855	1809	1455	1457	1214	1081	1182	1376	1373
		(146)	(86)	(74)	(96)	(26)	(14)	(71)	(12)	(17)	(28)	(105)	(139)
	*F*1	300	445	497	534	694	638	523	754	654	523	426	353
		(6)	(31)	(14)	(21)	(50)	(49)	(29)	(49)	(15)	(31)	(20)	(20)
	f_0	110	108	111	102	101	102	105	103	101	112	112	131
		(9)	(12)	(13)	(10)	(8)	(10)	(11)	(8)	(10)	(10)	(10)	(7)
Adult	*F*3	3256	2965	2990	2929	2875	2887	1870	2966	2947	2634	2734	2636
Females		(194)	(177)	(210)	(158)	(97)	(153)	(84)	(16)	(125)	(129)	(94)	(136)
	*F*2	2588	2161	2309	2144	2051	1751	1508	1273	1203	1470	1685	1755
		(164)	(142)	(126)	(104)	(90)	(55)	(62)	(92)	(48)	(69)	(77)	(157)
	*F*1	429	522	572	586	836	767	640	688	816	636	516	430
		(26)	(58)	(20)	(42)	(50)	(19)	(61)	(32)	(44)	(24)	(51)	(28)
	f_0	216	207	209	204	199	199	201	208	194	201	207	217
		(6)	(8)	(10)	(10)	(4)	(7)	(1)	(9)	(6)	(8)	(7)	(12)
Age 7	*F*3	3977	3896	3620	3713	3621	3443	2297	3083	3343	3252	3663	3162
		(161)	(226)	(42)	(244)	(318)	(160)	(97)	(189)	(178)	(87)	(177)	(303)
	*F*2	3402	2825	2822	2485	2324	1896	1776	1565	1494	1601	2031	1838
		(95)	(106)	(48)	(67)	(52)	(72)	(80)	(90)	(74)	(45)	(191)	(80)
	*F*1	358	583	590	799	1074	832	601	954	895	620	579	491
		(46)	(63)	(31)	(61)	(89)	(140)	(41)	(128)	(54)	(57)	(71)	(25)
	f_0	257	237	253	246	235	250	253	254	241	246	250	257
		(8)	(6)	(12)	(6)	(16)	(14)	(6)	(4)	(3)	(8)	(8)	(6)
Age 5	*F*3	4058	3954	3923	3922	4022	3742	2498	3136	3228	3133	3626	3809
		(83)	(95)	(56)	(106)	(130)	(159)	(131)	(246)	(249)	(312)	(167)	(90)
	*F*2	3535	2914	3050	2684	2505	1965	2019	1602	1502	1620	1919	1711
		(74)	(139)	(61)	(72)	(52)	(156)	(53)	(68)	(58)	(110)	(192)	(172)
	*F*1	472	571	580	871	1161	732	599	1066	850	647	526	471
		(81)	(47)	(25)	(102)	(52)	(77)	(52)	(87)	(144)	(20)	(20)	(69)
	f_0	280	269	269	263	240	258	251	251	241	254	270	273
		(13)	(11)	(8)	(8)	(3)	(6)	(13)	(7)	(3)	(4)	(11)	(15)
Age 3	*F*3	4061	4331	3721	4294	3961	3333	2661	3866	3382	3228	3899	2866
		(188)	(177)	(277)	(145)	(440)	(313)	(147)	(427)	(385)	(276)	(282)	(314)
	*F*2	3437	2740	2863	2639	2503	1965	1752	1656	1465	1636	1828	1891
		(67)	(62)	(72)	(13)	(170)	(58)	(94)	(109)	(202)	(84)	(205)	(216)
	*F*1	427	621	717	760	1256	789	726	1060	938	652	649	502
		(42)	(44)	(37)	(10)	(110)	(69)	(60)	(109)	(111)	(33)	(10)	(45)
	f_0	246	230	218	211	227	214	233	248	209	227	251	271
		(29)	(29)	(27)	(16)	(14)	(14)	(9)	(21)	(26)	(36)	(21)	(21)

shown by the origins and tails of the arrows. The direction and extent of formant-frequency movement is consistent with studies of other dialects of American English (e.g., Nearey and Assmann, 1986, for western Canada; Hillenbrand and Nearey, 1999, for western Michigan). The greatest formant movement is seen for the vowels /e/, /o/, /ɑ/, /ʌ/, /ʊ/, and /ɔ/, while /i/, /u/, /æ/, and /ɝ/ are relatively stationary. In general, the lax vowels /ɪ/, /ɛ/, and /æ/ tend to point toward the middle of the vowel space, consistent with the pattern found in other dialects of American English, although the magnitude of these changes is smaller for the north Texas vowels. This discrepancy may reflect dialect variation, or differences in the choice of time windows. Our first sample point was taken somewhat later, and the second sample somewhat earlier than in previous studies.[3]

The pattern of formant movement was similar across the five talker groups: neither the talker group × sample nor the talker group × sample × vowel interactions were significant for any of the formants. Hence children's vowels appear to display qualitatively similar patterns of vowel-inherent spectral change to those of adults.

F. Experimental conditions

The stimuli were natural and synthesized versions of the 12 vowels provided by the adult and child talkers. Stimuli were presented to adult listeners for identification in five conditions:

(1) *Natural*: The vowel portion of the syllable was extracted (as illustrated by the dashed lines in Fig. 2) and presented without further modification.
(2) *Full*: A synthesized version of the vowel was constructed using the acoustic parameters (f_0, AV, *F*1, *F*2, *F*3, *F*4, *F*5) derived from an analysis of the vowel portion of the /hVd/ syllables. Synthetic vowels were constructed using a frequency-domain version of the Klatt (1980) cascade formant synthesizer (Assmann *et al.*, 1994) with six formants at a sample rate of 24 kHz. The

center frequencies of the higher formants were fixed at 4500 Hz ($F5$) and 5500 Hz ($F6$) for the adult males, using the synthesizer defaults for an adult male voice suggested by Klatt (1980). The frequencies of $F5$ and $F6$ were scaled upwards by 20% for the adult females (5400 and 6600 Hz, respectively) and by 50% for the three groups of children (6750 and 8250 Hz). The bandwidths of the six formants were held constant ($B1$: 90; $B2$: 110; $B3$: 170; $B4$: 250; $B5$: 300; $B6$: 450 Hz). Stimuli were scaled to the maximum peak-to-peak amplitude afforded by the 16-bit quantization range. A 10.7-ms Kaiser window was used to shape the onset and offset of each stimulus to minimize transients.

(3) *FlatF1*: The center frequency of the first formant was held constant at the estimated $F1$ frequency from the first sample window (indicated by the first shaded box in Fig. 2). The remaining parameters displayed ''natural'' (i.e., measured) variations as a function of time.

(4) *FlatF2*: The center frequency of the second formant was held constant at the estimated $F2$ frequency from the first sample window.

(5) *FlatF*: The center frequencies of all formants and f_0 were held constant at their estimated frequencies from the first sample window.

G. Listeners

The listeners were nine adults who reported normal hearing and were native speakers of American English. All had completed an undergraduate course in phonetics. Most were long-term residents of the Dallas, Texas area.

H. Procedure

The stimuli were presented on-line at a sample rate of 24 kHz, low-pass filtered (10-kHz cutoff; Tucker-Davis Technologies FT5), attenuated (TDT PA4), amplified (TDT HB5), and presented diotically via headphones (Sennheiser HD-414) in a double-walled sound booth. Stimulus presentation levels ranged from 69 to 81 dB SPL (A weighting), with a mean of 74 dB. Stimuli representing the 12 vowels, 5 talker groups, and 5 synthesis conditions were interspersed in random order from trial to trial. Listeners were tested individually, and the experiment was self-paced. They responded to each stimulus by selecting 1 of 12 panels from a response box displayed on the computer screen. The panels were labeled with the orthographic representations of the /hVd/ words, and their corresponding phonetic symbols were superimposed on the screen with a plastic overlay.

Listeners began by completing three brief practice sets. In each set they heard vowels spoken by different talkers, one exemplifying each talker group, but using talkers who were not included in the main experiment. In the first set they listened to examples of 12 natural vowels without assigning vowel responses. In the second set they identified 36 vowels from the natural condition and received feedback indicating whether their responses were correct or incorrect. If their score was less than 85% correct (31/36) they were required to repeat the set until they reached this goal. In the third set they heard examples of 12 synthesized vowels from the full condition without assigning vowel responses. They next completed the main experiment, which included 1260 stimuli [12 vowels × 5 groups × 3 talkers per group × 7 conditions, i.e., the five conditions described above plus two additional conditions described elsewhere (Katz and Assmann, 2000)] in three blocks of 420 trials. Each block lasted about 40 min.

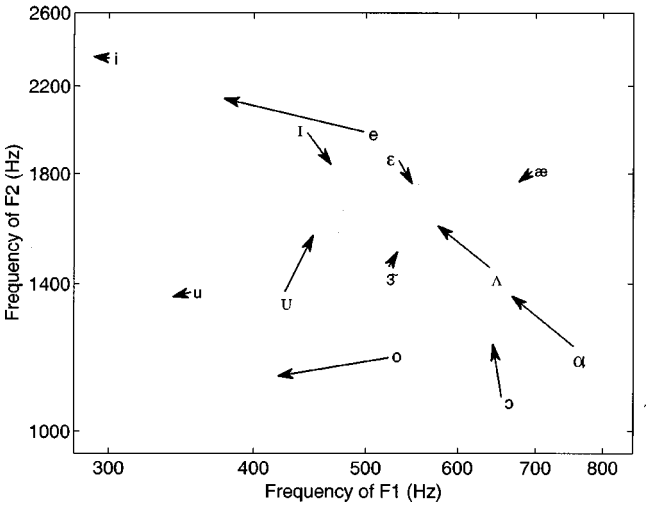

FIG. 3. Formant-frequency movement for the 12 vowels spoken by the adult males. The origin of each arrow shows the mean $F1$ and $F2$ frequencies across the three talkers for the first sample window (starting at 33% of the vowel duration), while the tail shows the second sample window (starting at 66% of the vowel duration).

I. Results and discussion

The identification data were analyzed with two main objectives: (i) to compare identification accuracy for natural and synthesized vowels spoken by adults and children, and (ii) to study the effects of ''flattening'' the formant trajectories on vowel identification for the five talker groups. A three-way analysis of variance (ANOVA) revealed significant main effects of talker group [$F_{(4,32)}=16.60$; $p<0.01$], condition [$F_{(4,32)}=138.00$, $p<0.01$], and vowel [$F_{(11,88)}=19.10$, $p<0.01$]. All interactions were significant: talker group × condition [$F_{(16,128)}=5.01$; $p<0.01$], condition × vowel [$F_{(44,352)}=17.50$; $p<0.01$], talker group × vowel [$F_{(44,352)}=17.50$; $p<0.01$], and talker group × condition × vowel [$F_{(176,1408)}=3.38$; $p<0.01$]. The key patterns in these data are described below.

1. Identification of natural and synthesized vowels

Identification accuracy was lower for the synthesized vowels (full condition) than for the spoken vowels (natural condition) after which they were patterned. Figure 4 shows this pattern across the five talker groups. The largest decline in accuracy was found for adult females (20%). The smallest decline was for the 3-year-old children (3%), whose natural recorded vowels were the least intelligible overall. The three-way interaction of talker group ×condition × vowel was analyzed with Scheffé tests to assess the drop in intelligibility from natural to full conditions. The analysis revealed significantly ($p<0.05$) lower accuracy in the full condition for

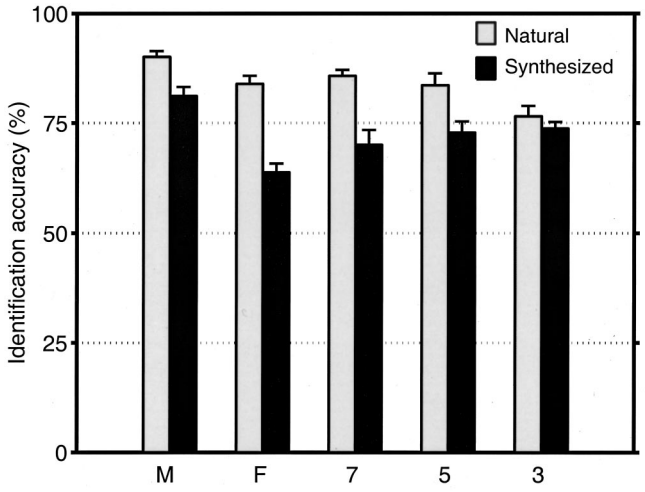

FIG. 4. Mean identification accuracy for the natural and full (synthesized) conditions for vowels spoken by adult males (M), adult females (F), and children (ages 7, 5, 3) in experiment 1. Error bars show the standard errors across the nine listeners.

the following talker group and vowel combinations: 3-year-olds: /o/; 5-year-olds: /e/, /u/; 7-year-olds: /ʊ/; adult females: /ɪ/, /æ/, /ʊ/; adult males: /ɝ/. In some of these cases, the lower intelligibility of the synthesized vowels can be attributed to difficulties in tracking closely spaced formants.

2. Effects of holding formant frequencies constant

Significantly lower identification accuracy was obtained when either *F*1, *F*2, or all formants plus f_0 were held constant. Figure 5 shows mean accuracy in the four synthesis conditions for the five talker groups. On average, eliminating the time variation in *F*1 resulted in a 6% drop in identification. Holding *F*2 constant lowered performance by about 5%, while removing the time variation from all formant frequencies plus f_0 lowered performance by about 12%. These patterns were broadly similar across talker groups, with two

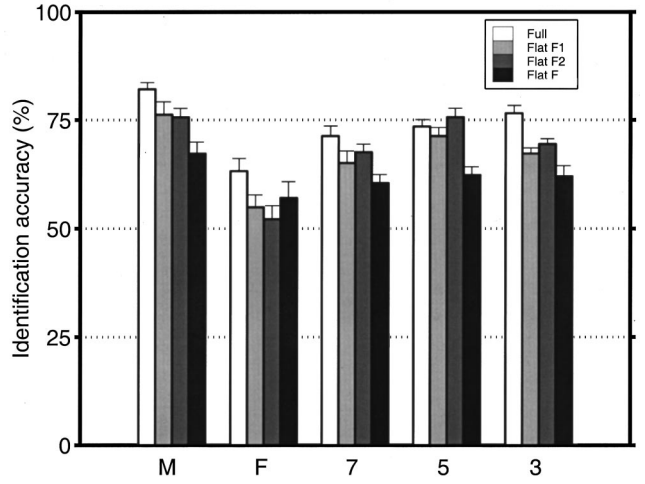

FIG. 5. Mean identification accuracy for vowels synthesized with time-varying formants (full condition) and with flattened formants (flat *F*1, flat *F*2, and FlatF conditions) spoken by adult males (M), adult females (F), and children (ages 7, 5, 3) in experiment 1. Error bars show the standard errors across the listeners.

exceptions. First, the 5-year-olds did not show a decline when *F*1 or *F*2 were held constant, although their scores were close to those of other talker groups when all formants and f_0 were held constant. Second, the adult females did not show a further decline when all formants and f_0 were held constant, compared to *F*1 and *F*2 alone. These differences merit further study with a larger sample of talkers. Overall, however, the results provided no support for the idea that time-varying changes in formant frequencies offer greater benefits for identifying vowels spoken by children.

Figure 6 shows that the effects of formant flattening were not evenly distributed across the vowels. The vowels /e/ and /o/, which are strongly diphthongized in American English, showed substantial declines, with more than a 65% drop from the full condition to FlatF condition. For both /e/ and /o/, holding *F*1 constant had a larger effect than holding *F*2 constant. Smaller declines were observed for /u/ and /ɔ/, while most of the remaining vowels showed little effect of formant flattening. Surprisingly, /ɑ/ showed an *increase* of more than 20% when all formants and f_0 were held constant. The reason may be related to dialect and/or formant-tracking errors: for this vowel, eliminating the time variation made it easier to identify.

The results in Fig. 6 are combined across the five talker groups, but the ANOVA also showed a significant three-way interaction of talker group × condition × vowel. Interpretation of the three-way interaction was complicated by performance near ceiling or floor in several conditions, but overall there were only minor deviations from the pattern in Fig. 6. In general, deviations from the pattern were least evident for those vowels showing the greatest effects of formant flattening (i.e., /e/ and /o/).

3. Relationship between f_0 and formant flattening

The results of experiment 1 failed to confirm the prediction that time-varying changes in formant frequencies would provide greater benefits for the vowels of children than adults. One interpretation is that these benefits are not related to spectral resolution, but arise for other reasons. Before accepting this conclusion, however, it is necessary to consider other differences between the vowels of children and adults that might contribute to formant resolution. For example, narrowing the bandwidth of a formant or increasing its distance from adjacent formants could lead to improved specification of its peak, counteracting the loss of resolution caused by the high f_0.

Formant bandwidths were held constant across the talker groups, ruling this out as a possible confound. Moreover, formant bandwidth estimates from natural speech generally suggest wider rather than narrower bandwidths with increasing formant-frequency above 500 Hz (Hawks and Miller, 1995), and formant bandwidths are estimated to be about 25% larger in women than in men (Fujimura and Lindqvist, 1971). A second factor is that children have smaller vocal tracts than adults, and hence the upward shift in their formant frequencies could lead to larger frequency distances between adjacent formants. However, a statistical analysis of formant distances (*F*3-*F*2 and *F*2-*F*1, with formant frequencies ex-

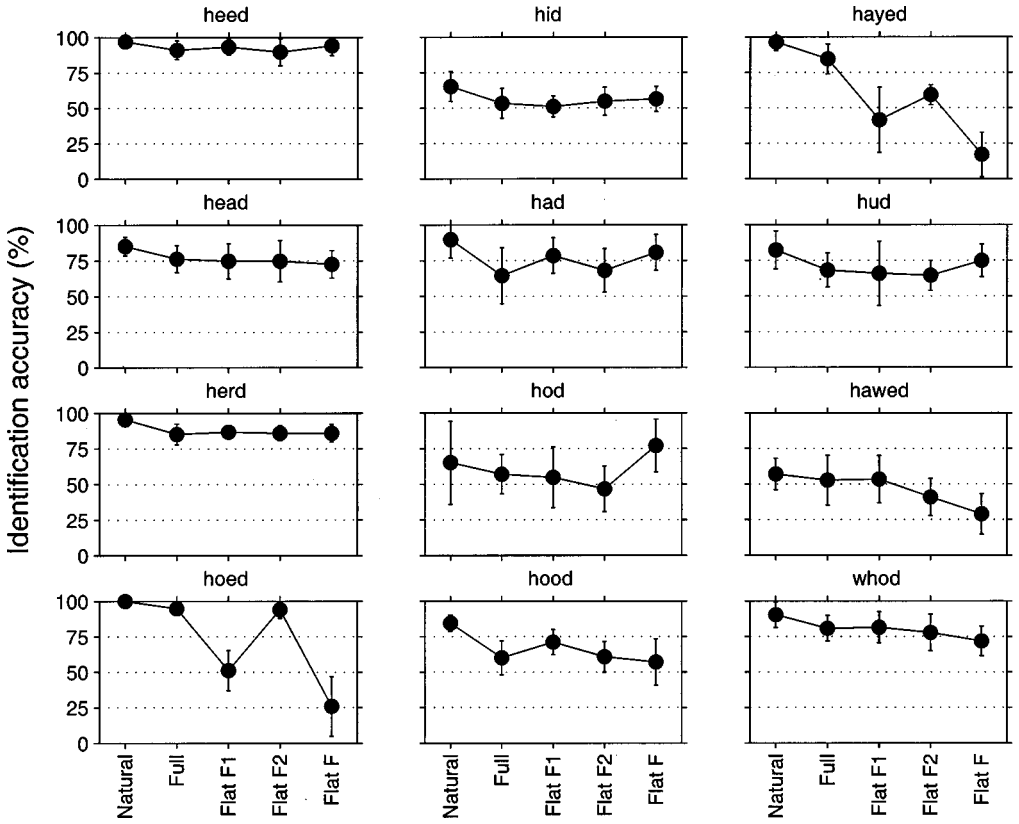

FIG. 6. Mean identification accuracy for the 12 natural vowels and synthesized versions, with time-varying formants (full condition) and with flattened formants (flat *F*1, flat *F*2, and FlatF conditions) in experiment 1. Error bars show the standard errors across the listeners.

pressed in log units), failed to reveal significant differences between child and adult talkers.

Although other differences between children's and adults' vowels cannot be ruled out, the results of experiment 1 suggest that the benefits of formant flattening are not enhanced in vowels with high f_0's. This conclusion is supported by an analysis of individual vowel tokens. The amount of benefit provided by spectral change was quantified in terms of the difference between scores in the full condition and in the FlatF condition. The correlation between difference scores and the vowel's f_0 was close to zero ($r=-0.06$; $N=180$). There was a weak relationship between f_0 and formant distance, for *F*2-*F*1 ($r=0.29$; $N=180$; $p<0.01$) and *F*3-*F*2 ($r=0.26$; $N=180$; $p<0.01$). A partial correlation analysis was performed to assess the relationship between f_0 and formant flattening when the effects of formant separation are partialled out. In both cases the correlation remained near zero, for *F*2-*F*1 ($r=0.05$; $N=180$) and *F*3-*F*2 ($r=-0.01$; $N=180$). These analyses support the conclusion that the effects of formant flattening do not depend on f_0.

III. EXPERIMENT 2

Because formants are relatively difficult to estimate in speech produced with high f_0 values, it is possible that some of the group-specific differences noted in experiment 1 (e.g., the large difference between natural vs full conditions for adult females and the small difference between natural versus full conditions for 3-year-old children) could have resulted, in part, from errors in estimating formant frequencies by hand. Experiment 2 therefore evaluated a synthesis strategy that relied on a semi-automatic formant-tracking procedure.

A. Method

Experimental conditions were identical to those used in experiment 1, except that the stimuli were generated from the same recorded /hVd/ words using a semi-automated formant-tracking procedure. The frequencies of the formants (*F*1, *F*2, *F*3) were estimated using a dynamic programming method which assigns raw formant-frequency ''candidates'' to ''tracks'' given a set of constraints on the proximity of adjacent formants and continuity over time. Formant candidates were obtained by autocorrelation LPC (12-kHz sample rate, 512-point Hanning window, 5-ms frame update rate, and 95% pre-emphasis). The order of the LPC analysis was adjusted to match the number of expected formants in the 0-6 kHz range, and the number of coefficients ranged from 8 to 14, depending on the talker. Formant candidates were obtained by solving for the roots of the predictor polynomial. A subsequent stage of post-processing was included to eliminate residual errors due to ''spurious'' formant-frequency candidates. Finally, median smoothing was applied to eliminate sudden changes in formant-frequency.

Stimulus presentation, testing procedures, response collection, and data analysis were the same as described for experiment 1.

B. Listeners

The listeners were ten adults who reported normal hearing and were native speakers of American English. Most of the listeners were long term residents of the Dallas, Texas area. All had completed an undergraduate course in phonetics. One of the listeners had participated in experiment 1.

C. Results

There was little effect of formant-frequency estimation method: on average, hand-tracked and auto-tracked vowels showed less than 1% difference in intelligibility. The largest improvement was a nearly 6% difference in the female auto-tracked vowels. The largest drop was a 5% difference for 3-year-olds. A three-way ANOVA revealed the same pattern as in experiment 1, with a significant interaction of talker group $\times$ condition $\times$ vowel [$F_{(176,1584)}=3.78$; $p<0.01$]. Qualitative inspection of individual vowel $\times$ talker group plots revealed an interaction similar to that found for experiment 1. Therefore, it appears that the perceptual consequences of the formant manipulations presented in experiment 1 do not depend on the formant-tracking method.

IV. EXPERIMENT 3

Experiments 1 and 2 showed that eliminating the time variation in formant frequencies from synthesized vowels led to a significant decline in intelligibility. However, no evidence was found of a link between the benefits of formant dynamics and f_0. A significant correlation would be predicted if formant movement helps to define poorly resolved formant peaks or other aspects of spectral shape when f_0 is high.

Research with natural speech has shown that whispered vowels are less intelligible than voiced vowels (Tartter, 1991). Tartter found that the increased error rate for whispered vowels was due in part to increased confusions among vowels adjacent in the vowel space defined by *F*1 and *F*2 frequencies. Formant movement can help to disambiguate such pairs of vowels, and hence formant flattening might be expected to lead to a greater reduction in identification accuracy for whispered compared to phonated vowels. On the other hand, if formant movement is beneficial because it helps to define formant peaks when f_0 is high, then replacing the voicing source with noise might be expected to yield reduced effects of formant flattening in whispered vowels compared to voiced vowels, particularly for children. Experiment 3 tested these two contrasting predictions by examining the interaction of formant flattening and the presence or absence of voicing.

A. Method

Vowels were synthesized using the auto-tracked formant measurements from experiment 2 and the cascade formant synthesis model (Klatt, 1980). Vowels were synthesized either with pulsed excitation (to produce ''voiced'' vowels, as in experiment 2) or noise excitation (generating ''unvoiced'' or whispered vowels). In addition, each was synthesized with time-varying formant frequencies (full condition) or with all formants and f_0 held constant across time (FlatF condition). A total of 720 vowels was generated (2 voicing states $\times$ 2 formant change conditions $\times$ 5 talker groups $\times$ 3 talkers/group $\times$ 12 vowels). Stimulus presentation, testing procedures, response collection, and data analysis were the same as described for experiment 1.

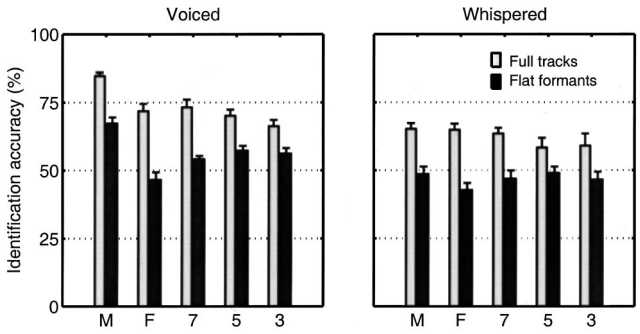

FIG. 7. Mean identification accuracy for the synthesized voiced and whispered vowels spoken by adult males (M), adult females (F), and three groups of children (ages 7, 5, 3) in experiment 3. Error bars show the standard errors across the eight listeners.

B. Listeners

Eight adults who reported normal hearing and were native speakers of American English served as listeners. Most were long-term residents of the Dallas, Texas area. All had completed an undergraduate course in phonetics. Two of the listeners had participated in experiment 1, and one in experiment 2.

C. Results

Elimination of time variation in the frequencies of the formants and f_0 lowered identification accuracy by 17% for the voiced vowels and 15% for the unvoiced (whispered) vowels, on average. This shows that time-varying changes in formant frequencies have similar effects for whispered and voiced vowels. In comparison, replacement of the voicing source with aperiodic noise lowered mean identification accuracy by 11%.

There was a significant interaction of formant flattening $\times$ talker group [$F_{(4,28)}=5.35$; $p<0.01$], and of voicing source $\times$ talker group [$F_{(4,28)}=4.73$; $p<0.01$], but the three-way interaction of formant flattening $\times$ voicing source $\times$ talker group was not significant. Figure 7 shows that the shift from voicing to whisper has the effect of eliminating the selective advantage of the vowels of adult males over the other four talker groups.

Holding the formant frequencies constant had a larger effect on the vowels of adult females (24% drop) compared to those of other talker groups (11%–18% drop), possibly because the vowels of the adult females were generally more susceptible to synthesis errors (Fig. 4). Figure 7 shows that

TABLE II. Means and standard errors (in parentheses) of vowel identification accuracy for the eight listeners in experiment 3. The data are pooled across the five talker groups. Full tracks refers to vowels synthesized with time-varying formant frequencies and f_0; flat formants refers to vowels synthesized with steady-state formant frequencies and f_0. Voiced vowels are synthesized with a pulsed voicing source; whispered vowels have broadband noise excitation.

	Full tracks		Flat formants	
	Voiced	Whispered	Voiced	Whispered
/i/	84.2 (5.2)	72.5 (4.8)	83.3 (4.9)	78.3 (4.7)
/ɪ/	74.2 (4.4)	68.3 (4.8)	40.0 (6.5)	60.8 (6.6)
/e/	95.0 (2.1)	75.8 (6.8)	25.0 (6.0)	3.3 (3.3)
/ɛ/	74.2 (3.7)	66.7 (4.7)	75.0 (4.8)	65.0 (3.5)
/æ/	73.3 (4.9)	37.5 (8.0)	71.7 (4.5)	44.2 (6.7)
/ʌ/	40.8 (5.7)	38.3 (5.3)	46.7 (5.2)	35.0 (4.1)
/ɝ/	94.2 (2.0)	84.2 (3.5)	85.0 (3.5)	69.2 (3.8)
/ɑ/	43.3 (6.8)	38.3 (7.5)	51.7 (5.7)	46.7 (4.9)
/ɔ/	55.8 (8.0)	45.0 (5.9)	38.3 (5.2)	38.3 (5.5)
/o/	94.2 (2.0)	85.8 (4.8)	31.7 (6.6)	11.7 (3.5)
/ʊ/	72.5 (6.0)	78.3 (5.0)	44.2 (8.2)	56.7 (7.5)
/u/	77.5 (4.2)	55.8 (5.5)	83.3 (2.8)	51.7 (4.3)
Mean	73.3 (5.2)	62.2 (4.8)	56.3 (4.9)	46.7 (4.7)

eliminating the time variation from the formant frequencies led to a substantial drop in accuracy for all talker groups, with similar reductions for whispered and voiced vowels.

The three-way interaction of formant flattening × voicing source × vowel was significant [$F_{(11,77)}=2.49$; $p<0.01$] and is shown in Table II. Consistent with the results of experiment 1, the largest effects of formant flattening were observed for the vowels /e/ and /o/. Effects of formant flattening were similar for the voiced and whispered versions of these vowels. Several other vowels (e.g., /ɪ/ and /ʊ/) also showed small declines when their formants were held constant.

Although most vowels showed some effect of shifting from a voiced to whispered source, the changes were not uniform across the vowels. The largest effects emerged for the vowels /u/ and /æ/, neither of which was affected substantially by the flattening of their formants. Some vowels, like /i/ and /ɛ/, showed little effect of either manipulation.

Overall, the results of experiment 3 showed that the formant flattening and voicing source manipulations did not interact. Moreover, their effects were not the same for different vowels and talker groups. The ANOVA showed significant interactions of formant flattening × talker group × vowel [$F_{(44,308)}=3.36$; $p<0.01$] and voicing source × talker group × vowel [$F_{(44,308)}=2.95$; $p<0.01$], but no systematic patterns emerged from an inspection of these interactions. The four-way interaction of formant flattening × voicing source × talker group × vowel was not significant. An interesting finding was that the vowels most affected by the change in voicing were hardly affected by the flattening of their formants. The reverse pattern did not appear to hold, since the vowels most affected by flattening their formants also showed a decline when the source changed from voicing to whisper.

The lower intelligibility of noise-excited (whispered) compared to pulse-excited (voiced) vowels was also found by Katz and Assmann (2000) using an experimental design similar to experiment 3. They showed that this effect does not arise simply because whispered speech contains less energy at low frequencies, compared to voiced speech (Stevens, 1999): a similar reduction in intelligibility was found with noise-excited vowels which preserved the spectral tilt characteristics of the voiced vowels. Katz and Assmann attributed the reduced intelligibility of whispered vowels to the elimination of harmonicity and/or periodicity.

V. GENERAL DISCUSSION

An acoustic analysis confirmed previous findings (Egushi and Hirsh, 1969; Lee *et al.*, 1999) that children's vowels have higher formant frequencies than those of adults, as well as greater variability across talkers. The increased variability can be attributed to limitations in motor control and the reduced flexibility that accompanies the early stages of neuromotor maturation. In contrast, comparisons of formant-frequency trajectories for individual vowels revealed similar patterns for children and adults. These data suggest that children can produce appropriate patterns of formant-frequency movement in a mature manner as early as age 3.[4]

Three important findings emerged from the perceptual experiments. First, we confirmed that the removal of time-varying changes in formant frequency from synthetic vowels produced lower identification accuracy. This finding replicated earlier work by Hillenbrand (1995) and Hillenbrand and Nearey (1999) for W. Michigan talkers. Our talkers were from the Dallas, Texas region, extending the results to another dialect of American English, and also to children as young as age 3.

Eliminating the time variation from all formants and f_0 resulted in a 12%–16% reduction in mean identification accuracy in experiments 1–3. In comparison, flattening just one formant ($F1$ or $F2$) led to a drop of nearly half that magnitude (6% and 5% reduction, respectively). The similar drop for $F1$ and $F2$ suggests that time-varying changes in each formant made roughly the same contribution to vowel identification. However, differences were noted for /e/ and /o/, where flattening $F1$ degraded performance more than flattening $F2$. This pattern is consistent with the extent of acoustic change in the $F1 \times F2$ space, and is compatible with the finding that $F1$ frequency is more discriminable than $F2$ (Kewley-Port and Watson, 1994). $F2$ flattening had little effect on /o/, but rather pronounced effects on /e/. The smaller contribution of $F2$ for the vowel /o/ might be part of its phonetic specification in the north Texas dialect of American English. The proximity of $F1$ and $F2$ frequencies for /o/ might also be a factor.

The second finding was that the synthesized vocalic portions of the syllables were less well identified than the natural versions, despite the fact that the formant transitions and f_0 variation were preserved. This finding, also reported by Hillenbrand and Nearey (1999), suggests that although formant-frequency variation is indisputably important for vowel quality, other signal properties that contribute to vowel identification are lost when vowels are synthesized in accordance with the cascade formant synthesis model described by Klatt (1980). We are currently investigating

sources of error in the synthesis procedure that might be responsible for differences between the natural and synthesized vowels. Candidates include inaccuracies in the voicing source model, errors in formant measurement, and distortions of spectral shape resulting from the use of the formant representation (Hillenbrand and Nearey, 1999).

The third finding is that formant-frequency flattening did not interact with manipulations of the voicing source. Its effects were similar for adults and children, and no evidence was found that time-varying changes in formant-frequency provided greater benefits for children's voices with high f_0. Flattening the trajectories of the formants led to similar reductions in identification accuracy for whispered and voiced vowels. Taken together, these results argue against the idea that time-varying changes in formant-frequency contribute by specifying the locations of formant peaks when f_0 is high.

Katz and Assmann (2000) tested a related hypothesis, that time variation in f_0 might help to trace out the spectrum envelope in vowels with high f_0. Hillenbrand and Gayvert (1993) had previously shown a small but reliable improvement when steady-state vowels were synthesized with a linear f_0 glide rather than constant f_0. However, using the same design as in experiment 1 of the current study, Katz and Assmann found no effect of replacing the natural time-varying changes in f_0 with steady-state f_0. Moreover, there was little evidence of a link between vowel identification accuracy and f_0, a result also reported by Hillenbrand and Nearey (1999). One explanation for the discrepancy between studies may be that time-varying changes in f_0 lead to higher identification accuracy only in the special case where vowels are synthesized with steady-state formant patterns, a condition not investigated in the present study. On the whole, these studies provided little evidence that time-varying changes in either f_0 or formant-frequency lead to improved resolution of spectral features such as formant peaks.

The finding that the benefits of time-varying changes in formant frequency do not interact with properties of the voicing source raises the following question: if formant movement does not help to specify the locations of formant peaks, how then do listeners overcome the problem of reduced spectral resolution when f_0 is high? The answer may be that the auditory representations of vowels with high f_0 are *not* subject to the degradation observed in their amplitude spectra. Accurate vowel identification may not require precise specification of the formant peaks, or there may be sufficient cues remaining in vowels with high f_0 to fill in the details lost by sparse sampling. Alternative models have been proposed that do not rely on formants, but instead use spectral shape parameters derived from principal components analysis or related methods (e.g., Bakkum *et al.*, 1995; Zahorian and Jaghargi, 1993). A question for future research is how these models would account for the effects of formant flattening and their independence of changes in voicing source. The auditory excitation patterns that generally serve as the input to spectral shape models assign greater weight to the low-frequency region of the spectrum, and are therefore likely to show increased, rather than reduced, dependence on f_0.

A second question concerns the basis for the beneficial effects of time-varying spectral change: if not by improving spectral resolution, how then does formant movement help? The answer may be that formant movement provides a basis for maintaining phonetic distinctiveness in crowded vowel systems such as English (Ladefoged and Maddieson, 1996). Several of our findings are consistent with this hypothesis. First, the effects of formant-frequency flattening were not uniform across the vowel set. Consistent with previous investigations demonstrating the perceptual salience of time-varying formant frequencies for American English vowels (e.g., Strange *et al.*, 1983; Nearey and Assmann, 1986; Hillenbrand, 1995), the largest decrements in identification were found for the vowels that showed the largest excursions in their formant trajectories, /e/ and /o/. Second, there was a tendency for neighboring vowels in the *F*1-*F*2 plane to display opposing patterns of formant movement (Nearey and Assmann, 1986). This can be seen by inspection of Fig. 3: vowels whose onsets are close together (such as /e/ and /ɛ/) tend to display vector movement in opposing directions. This suggests that formant movement provides greater benefits in crowded regions of the vowel space. If formant movement serves a contrast-enhancing function in vowel perception, then manipulations such as flattening the formants might be predicted to have reduced effects in languages with smaller vowel inventories.

ACKNOWLEDGMENTS

This research was supported by Grant No. 11423-590 from the Texas Advanced Research Program, awarded by the Texas Higher Education Coordinating Board. Portions of this research were reported at the 130th Meeting of the Acoustical Society of America in St. Louis, MO. The authors would like to thank Kathleen Jenouri, Matt Sommer, Elaine Teoh, Ginger Stickney, Debbie Moncrieff, Phillip Hamilton, and Charles Rees for their assistance in data collection and analysis, Terry Nearey for help in software development and thoughtful discussions, and Chris Darwin, Keith Kluender, and an anonymous reviewer for helpful comments on the manuscript.

[1]This prediction rests on the assumption that the detrimental effects of higher f_0 are not accompanied by other differences between the vowels of adults and children that lead to *improved* resolution of children's vowels compared to adults, such as narrower formant bandwidths or increased frequency separation between adjacent formants. This caveat is discussed in Sec. II I 3.

[2]The spectra of voiced vowels contain peaks at the frequencies of the harmonics when the temporal window is longer than the period of the fundamental. When f_0 is high, these peaks may be too sparse to allow for accurate formant estimation. However, the harmonic structure can be eliminated by performing a spectral analysis with a temporal window equal to or shorter than the duration of a single pitch period. An accurate representation of the vocal tract transfer function can be obtained from a pitch-synchronous analysis, but this approach requires precise estimates of f_0 (de Cheveigné and Kawahara, 1999).

[3]One of the reviewers raised the concern that the initial sample used to derive the formant parameters for the flattened-formant conditions was taken somewhat later in the vowel than in earlier studies, and therefore may have underestimated the formant movement in the vowels. Hillenbrand and Nearey (1999) used an analysis window centered at 20% and 80% of the duration of the vocalic nucleus. We repeated the acoustic analysis using their 20%–80% time window and obtained the same statistical results as reported in Sec. II D above, although several vowels did show increased

formant movement with more extreme time windows (particularly /ʌ/, /æ/, /e/, and /o/ in *F*1, and /ɔ/, /ɑ/, /ʊ/, and /ʌ/ in *F*2). The perceptual consequences of selecting a later sample are probably minor, however, as a subset of these vowels with reduced formant movement when measured with the 33%–66% time window (e.g., /ʌ/, /æ/, /ɑ/, /ʊ/) showed little decline in identification accuracy from the full to FlatF conditions of experiment 1 (see Fig. 6).

[4]This interpretation must be treated with caution because Lee *et al.* (1999) reported greater time-varying spectral change for children's vowels compared to those of adults. Our acoustic analyses provided little evidence of increased time variation in the formant trajectories of children's vowels. Differences in vowel set, elicitation procedure, and analysis method may be responsible for the discrepancy.

Andruski, J. E., and Nearey, T. M. (**1992**). ''On the sufficiency of compound target specification of isolated vowels and vowels in /bVb/ syllables,'' J. Acoust. Soc. Am. **91**, 390–410.

Assmann, P. F., and Nearey, T. M. (**1987**). ''Perception of front vowels: The role of harmonics in the first formant region,'' J. Acoust. Soc. Am. **81**, 520–534.

Assmann, P. F., Ballard, W., Bornstein, L., and Paschall, D. D. (**1994**). ''TrackDraw: A graphical interface for controlling the parameters of a speech synthesizer,'' Behav. Res. Methods Instrum. Comput. **26**, 431–436.

Bakkum, M. J., Plomp, R., and Pols, L. W. (**1995**). ''Objective analysis versus subjective assessment of vowels pronounced by deaf and normal-hearing children,'' J. Acoust. Soc. Am. **98**, 745–762.

Darwin, C. J., and Gardner, R. B. (**1985**). ''Which harmonics contribute to the estimation of first-formant frequency?'' Speech Commun. **4**, 231–235.

de Cheveigné, A., and Kawahara, H. (**1999**). ''Missing data model of vowel perception,'' J. Acoust. Soc. Am. **105**, 3497–3508.

Delattre, P. C., Liberman, A. M., and Cooper, F. S. (**1955**). ''Acoustic loci and transitional cues for consonants,'' J. Acoust. Soc. Am. **27**, 769–773.

Di Benedetto, M. G. (**1989**). ''Frequency and time variations of the first formant: Properties relevant to the perception of vowel height,'' J. Acoust. Soc. Am. **86**, 67–77.

Diehl, R. L., Lindblom, B., Hoemeke, K. A., and Fahey, R. P. (**1996**). ''On explaining certain male-female differences in the phonetic realization of vowel categories,'' J. Phonetics **24**, 187–208.

Dissard, P., and Darwin, C. J. (**2000**). ''Extracting spectral envelopes: formant frequency matching between sounds on different and modulated fundamental frequencies,'' J. Acoust. Soc. Am. **107**, 960–969.

Eguchi, S., and Hirsh, I. J. (**1969**). ''Development of speech sounds in children,'' Acta Oto-Laryngol. Suppl. **257**, 1–51.

Fox, R. A. (**1989**). ''Dynamic information in the identification and discrimination of vowels,'' Phonetica **46**, 97–116.

Fujimura, O., and Lindqvist, J. (**1971**). ''Sweep-tone measurements of vocal-tract characteristics,'' J. Acoust. Soc. Am. **49**, 541–558.

Hawks, J. W., and Miller, J. D. (**1995**). ''A formant bandwidth estimation procedure for vowel synthesis,'' J. Acoust. Soc. Am. **97**, 1343–1344.

Hillenbrand, J. (**1995**). ''Identification of vowels resynthesized from /hVd/ utterances: Effects of formant contour,'' J. Acoust. Soc. Am. **97**, 3245(A).

Hillenbrand, J., and Gayvert, R. T. (**1993**). ''Identification of steady-state vowels synthesized from the Peterson and Barney measurements,'' J. Acoust. Soc. Am. **94**, 668–674.

Hillenbrand, J., and Nearey, T. M. (**1999**). ''Identification of resynthesized /hVd/ utterances: Effects of formant contour,'' J. Acoust. Soc. Am. **105**, 3509–3523.

Hillenbrand, J., Getty, L. A., Clark, M. J., and Wheeler, K. (**1995**). ''Acoustic characteristics of American English vowels,'' J. Acoust. Soc. Am. **97**, 3099–3111.

Katz, W. F., and Assmann, P. F. (**2000**). ''Identification of children's and adult's vowels: Intrinsic fundamental frequency, presence of voicing, and voicing dynamics,'' submitted to J. Phonetics.

Kent, R. D. (**1976**). ''Anatomical and neuromuscular maturation of the speech mechanism: Evidence from acoustic study,'' J. Speech Hear. Res. **19**, 421–445.

Kewley-Port, D., and Watson, C. S. (**1994**). ''Formant-frequency discrimination for isolated English vowels,'' J. Acoust. Soc. Am. **95**, 485–496.

Klatt, D. H. (**1980**). ''Software for a cascade/parallel formant synthesizer,'' J. Acoust. Soc. Am. **67**, 971–995.

Ladefoged, P., and Maddieson, I. (**1996**). *The Sounds of the World's Languages* (Blackwell, London).

Lee, S., Potamianos, A., and Narayanan, S. (**1999**). ''Acoustics of children's speech: Developmental changes of temporal and spectral parameters,'' J. Acoust. Soc. Am. **105**, 1455–1468.

Meddis, R., and Hewitt, M. (**1991**). ''Virtual pitch and phase sensitivity of a computer model of the auditory periphery. I: Pitch identification,'' J. Acoust. Soc. Am. **89**, 2866–2882.

Moore, B. C. J., and Glasberg, B. R. (**1987**). ''Formulas describing frequency selectivity as a function of frequency and level, and their use in calculating excitation patterns,'' Hear. Res. **28**, 209–225.

Nábělek, A. K., and Ovchinnikov, A. (**1997**). ''Perception of nonlinear and linear formant trajectories,'' J. Acoust. Soc. Am. **101**, 488–497.

Nearey, T. M. (**1989**). ''Static, dynamic, and relational properties in vowel perception,'' J. Acoust. Soc. Am. **85**, 2088–2113.

Nearey, T. M., and Assmann, P. F. (**1986**). ''Modelling the role of inherent spectral change in vowel identification,'' J. Acoust. Soc. Am. **80**, 1297–1308.

Peterson and Barney. (**1952**). ''Control methods used in a study of vowels,'' J. Acoust. Soc. Am. **24**, 175–184.

Pols, L. C. W., and Van Son, R. J. J. H. (**1993**). ''Acoustics and perception of dynamic vowel segments,'' Speech Commun. **13**, 135–147.

Ryalls, J., and Lieberman, P. (**1982**). ''Fundamental frequency and vowel perception,'' J. Acoust. Soc. Am. **72**, 1631–1634.

Rosner, B. S., and Pickering, J. B. (**1994**). *Vowel Perception and Production* (Oxford University Press, New York).

Smith, B. L., Kenney, M. K., and Hussain, S. (**1995**). ''A longitudinal investigation of duration and temporal variability in children's speech production,'' J. Acoust. Soc. Am. **99**, 2344–2349.

Stevens, K. H. (**1999**). *Acoustic Phonetics* (M.I.T. Press, Cambridge, MA).

Strange, W. (**1989**). ''Evolving theories of vowel perception,'' J. Acoust. Soc. Am. **85**, 2081–2087.

Strange, W., Jenkins, J. J., and Johnson, T. L. (**1983**). ''Dynamic specification of coarticulated vowels,'' J. Acoust. Soc. Am. **74**, 695–705.

Sussman, H. M., McCaffrey, H. A. L., and Matthews, S. A. (**1991**). ''An investigation of locus equations as a source of relational invariance for stop place categorization, '' J. Acoust. Soc. Am. **90**, 1309–1325.

Tartter, V. C. (**1991**). ''Identifiability of vowels and speakers from whispered syllables,'' Percept. Psychophys. **49**, 365–372.

Zahorian, S. A., and Jaghargi, A. J. (**1991**). ''Speaker normalization of static and dynamic vowel spectral features,'' J. Acoust. Soc. Am. **90**, 67–75.

Zahorian, S. A., and Jaghargi, A. J. (**1993**). ''Spectral-shape features versus formants as acoustic correlates for vowels,'' J. Acoust. Soc. Am. **94**, 1966–1982.

Sources of listener disagreement in voice quality assessment

Jody Kreiman[a] and Bruce R. Gerratt
Division of Head and Neck Surgery, UCLA School of Medicine, 31-24 Rehabilitation Center, Los Angeles, California 90095-1794

(Received 10 April 2000; accepted for publication 23 June 2000)

Traditional interval or ordinal rating scale protocols appear to be poorly suited to measuring vocal quality. To investigate why this might be so, listeners were asked to classify pathological voices as having or not having different voice qualities. It was reasoned that this simple task would allow listeners to focus on the kind of quality a voice had, rather than how much of a quality it possessed, and thus might provide evidence for the validity of traditional vocal qualities. In experiment 1, listeners judged whether natural pathological voice samples were or were not primarily breathy and rough. Listener agreement in both tasks was above chance, but listeners agreed poorly that individual voices belonged in particular perceptual classes. To determine whether these results reflect listeners' difficulty agreeing about single perceptual attributes of complex stimuli, listeners in experiment 2 classified natural pathological voices and synthetic stimuli (varying in $f0$ only) as low pitched or not low pitched. If disagreements derive from difficulties dividing an auditory continuum consistently, then patterns of agreement should be similar for both kinds of stimuli. In fact, listener agreement was significantly better for the synthetic stimuli than for the natural voices. Difficulty isolating single perceptual dimensions of complex stimuli thus appears to be one reason why traditional unidimensional rating protocols are unsuited to measuring pathologic voice quality. Listeners did agree that a few aphonic voices were breathy, and that a few voices with prominent vocal fry and/or interharmonics were rough. These few cases of agreement may have occurred because the acoustic characteristics of the voices in question corresponded to the limiting case of the quality being judged. Values of $f0$ that generated listener agreement in experiment 2 were more extreme for natural than for synthetic stimuli, consistent with this interpretation. © *2000 Acoustical Society of America.* [S0001-4966(00)01310-2]

PACS numbers: 43.71.Bp, 43.71.Gv [KRK]

I. INTRODUCTION

Rating scale measures of vocal quality are often used clinically to evaluate pathological voices, and serve as a standard of comparison for acoustic measures of voice. Traditional rating protocols use unidimensional ordinal or interval scales, and require listeners to focus selectively on specific aspects of voice (e.g., breathiness or roughness) and assess the extent to which a voice has that particular quality. Although recent evidence (Kreiman and Gerratt, 1998) indicates that such protocols may be poorly suited to measuring vocal quality, it is unclear why difficulties arise. Multidimensional scaling data (e.g., Kreiman and Gerratt, 1996) suggest that fundamental problems exist with the validity of traditional voice quality scales. In that study, similarities among voices were not well predicted by traditional rating scales, or indeed by any set of static phonetic or linguistic-style ''features.'' Other studies (e.g., Kreiman *et al.*, 1993; Gerratt *et al.*, 1993; Kreiman and Gerratt, 1998) suggest that problems with traditional voice assessment protocols may be due to factors in addition to or instead of scale validity. For example, individual listeners are reasonably self-consistent in their judgments of specific aspects of vocal quality, but across listeners more than 60% (and as much as 78%) of the variance in ratings of voices may be due to factors other than differences among voices in the quality being rated (Kreiman and Gerratt, 1998). This discrepancy between test-retest and inter-rater reliability suggests that factors including stable long-term differences between raters in perceptual strategy, or short-term differences within and between listeners in attention to different aspects of the stimuli, may contribute to poor reliability of traditional voice rating protocols. (See Kreiman *et al.*, 1993, for a discussion of other hypothetical sources of variability in ratings of voice.)

Although existing data do not allow rater unreliability to be attributed unambiguously to any particular cause or causes, it is possible to use alternate measurement techniques to differentiate problems of scale validity from other sources of disagreements among raters. Binary classification systems for describing voice quality, in which voices are assigned to broad categories based on quality (a breathy voice; a strained voice) may offer such clues. Classification tasks differ from traditional scalar judgments in the level of measurement required and in the complexity of the judgment made, and we reasoned that these simplifications would allow listeners to focus on the *kind* of quality of a voice has, rather than how much of a quality it possesses. If traditional labels for voice quality have psychological reality, then listeners should agree that some voices unambiguously possess that quality (a breathy voice; a rough voice).

Classification systems for describing voice quality are

[a]Author to whom correspondence should be addressed; electronic mail: jkreiman@ucla.edu

very old, and underlie many modern studies of voice. Such systems have their basis in studies of oratory and elocution, with many common terms dating from the Romans. For example, in the first century BC Cicero (see Cicero, 1948) used the term ''asperam'' (''rough''), and in the second century AD Julius Pollux (see Pollux, 1706; cited by Austin, 1806) employed terms like ''aeneam'' (''brassy'') and ''raucam'' (''hoarse'') (Austin, 1806; Laver, 1980). Attempts at systematic classification of vocal quality began in the 19th century. For example, Rush (1859) distinguished four qualities of voice (''natural,'' ''falsette,'' ''whispering,'' and an ''improved'' quality labeled ''orotund''), and also described ''guttural vibration'' and ''tremulous movement.'' Goldbury and Russell (1844; cited by Gray, 1943) distinguished the qualities harsh, smooth, aspirated, pectoral, guttural, oral, orotund, and pure tone. (For interesting reviews see Plugge, 1942; Gray, 1943; Laver, 1980).

Despite early concerns that such labels for voice are at best metaphorical (Rush, 1859), these traditional classification systems for describing voice are readily discernible in contemporary descriptive usage. Although modern classification systems for measuring vocal quality have not to our knowledge been formally proposed, common usage and many studies assume that such systems are valid. Classification of voice qualities is especially prevalent in studies of speech synthesis, because attempts at synthesizing particular qualities (e.g., Wendahl, 1966; Klatt and Klatt, 1990; Childers and Lee, 1991; Lalwani and Childers, 1991) presuppose that perceptual classes for voice exist. Authors in such studies typically sort voices into groups based on perceptual criteria, and then investigate the synthesis strategies necessary to model that kind of phonation. Thus Childers and Lee (1991) selected examples of breathy, modal, fry, and falsetto phonation, and then examined the synthesis parameters necessary to reproduce each voice type. Gobl and Ni Chasaide (1992) modeled a single normal speaker who produced modal, breathy, whispery, tense, lax, and creaky voice, and Kasuya and Ando (1991) studied the synthesis of breathiness by selecting two ''breathy'' voices and copying them.

Other researchers (e.g., Martin *et al.*, 1995; Hillenbrand and Houde, 1996) have used a classification step as a precursor to gathering scalar rating of vocal quality. In these studies, voices were first sorted into classes corresponding to specific pathological voice ''types'' (i.e., qualities), and then were rated on the extent to which they possessed that quality. For example, Hillenbrand and Houde (1996) first selected a set of voices that ''appeared to depart from normal voice quality primarily in the direction of breathiness'' (p. 313), after which listeners rated the level of breathiness of those stimuli.

A few researchers have examined listeners' abilities to classify voices in the manner required by such studies. Colton and Estill (1981) asked normal speakers to produce samples of conversional speech, cry, twang, and operatic ring, which listeners then sorted into four classes with better than chance accuracy. Rammage *et al.* (1992) trained expert listeners with standard samples of several qualities (breathiness, strain/harshness, high pitch, low pitch, glottal attacks, phonation breaks, pitch breaks, and roughness/glottal fry). They then asked listeners to rate severity of dysphonia, to check off which features were present in each voice sample, and to indicate which of the checked features was dominant in the sample. Although no statistical analysis was undertaken, listeners reportedly agreed well about the overall severity of pathology, but not about the specific perceptual features present or dominant in each sample. Martin and colleagues (Martin *et al.*, 1995; Martin and Wolfe, 1996) asked listeners to sort voices into four groups (breathy, rough, hoarse, normal) after training with synthetic prototypes for each voice type. In both studies, about 60% of listeners agreed about the class in which about 60% of voices belonged; agreement was below 60% for the remaining voices. It is not clear from their discussion if agreement exceeded chance levels.

In the present study, we examined levels and patterns of listener agreement in a binary classification task for pathological voices. In particular, we attempted to determine whether listener disagreements were due to fundamental problems of scale validity, or to the manner in which quality has been measured. If listeners agree reliably in their classifications, the validity of traditional scales is supported, and disagreement in ordinal and interval rating scale protocols may be attributed to other factors, including limitations of the particular measurement techniques employed.

II. EXPERIMENT 1

A. Method

1. Stimuli

Stimuli were drawn from a previous study (Kreiman and Gerratt, 1996), where they are described in detail. Briefly, the voices of 80 male and 80 female speakers with vocal pathology were selected from a large library of samples recorded under identical conditions as part of a phonatory function analysis. Each speaker sustained the vowel /a/ for as long as possible. Voices were recorded using a microphone placed off-axis 5 cm away from the speaker's lips. Utterances were low-pass filtered at 8 kHz and digitized directly at 20 kHz with 12-bit resolution. A 2-s sample was excerpted from the middle of each utterance. Stimuli were equalized for peak intensity, and onsets and offsets were multiplied by 40-ms ramps to eliminate click artifacts.

Speakers ranged in age from 18–96 years, and represented a variety of diagnoses. Severity of pathology was rated on a 6-point equal-appearing interval scale by unanimous vote of the authors and an experienced speech-language pathologist. (Differences in rating were resolved by discussion.) Chi square analysis indicated that severity of pathology, diagnostic category, gender, and speakers' ages were statistically independent in these voice sets (Kreiman and Gerratt, 1996), reducing the likelihood that differences in quality are confounded with extraneous factors.

2. Listeners

A total of 19 expert listeners participated in these experiments. Eleven listeners provided two sets of quality judgments (one for breathiness and one for roughness), and 8 listeners made judgments of one quality only, for a total of 15 listeners/task. Each listener had a minimum of 3 years'

post-graduate experience evaluating and/or treating voice disorders. Listeners reported no history of hearing difficulties.

3. Procedure

At each session, listeners heard the 160 stimulus voices, along with 40 repeated trials (inserted at random into the sequence of trials), for a total of 200 trials/session. Testing took place in a double-walled IAC sound-attenuated booth. Stimuli were low-pass filtered at 8 kHz and presented in free field over high fidelity loudspeakers (Boston Acoustics AD40) at a comfortable listening level (approximately 80 dB SPL).

Judgments of breathiness and roughness were made at separate sessions. For each voice, listeners were instructed to decide whether or not its quality departed from normal primarily in the direction of breathiness (or roughness), and to respond either ''primarily breathy'' or ''not primarily breathy'' (or ''primarily rough''/''not primarily rough''). They were asked to disregard the severity of pathology or apparent type of voice disorder, and were allowed to replay each stimulus as often as necessary before making their judgment. When listeners participated in two sessions, these were separated by at least 1 week. Task order was randomized across listeners, and stimuli were rerandomized for every presentation. Each listening session lasted about 30 min.

B. Results

1. Test-retest agreement

For judgments of breathiness, test-retest agreement (the percentage of repeated voices placed in the same class both times they were presented) averaged 85.0% across listeners [standard deviation (s.d.)=6.81; range=72.5%–97.5%]. For judgments of roughness, test-retest agreement averaged 80.7% (s.d=6.97; range=70%–92.5%).

2. Classification responses

Listeners varied in how frequently they applied the labels ''primarily breathy'' and ''primarily rough'' to the stimuli. Across listeners, the number of ''rough'' responses ranged from 26–101/160 (mean=63.4; s.d.=20.3). The number of ''breathy'' responses ranged from 33–94/160 (mean=60.8, s.d.=15.4).

Despite differences in rates of responding, pairs of listeners agreed fairly well in their classification judgments. On average, two listeners agreed in their responses for 73.5% of voices in the breathiness task (s.d.=6.3%; range=58.1%–88.1% agreement), and for 69.5% of voices in the roughness task (s.d.=7.3%; range=49.4%–100%).

However, across all listeners, agreement levels were rather poor. The frequency with which listeners responded ''primarily breathy'' or ''primarily rough'' was calculated for each voice, and the distribution of these frequencies is shown in Fig. 1. In this figure, a value of 15 on the *x* axis (rightmost columns) indicates that all 15 listeners agreed a voice was primarily breathy or rough; a value of 0 indicates that all listeners agreed the voice was not primarily breathy or rough (i.e., 0 listeners classified the voice as breathy or rough). The relative height of the endpoints depends on the *a priori* distribution of voice qualities in the population, and thus cannot be interpreted directly. However, if listeners agree in their judgments that voices did or did not belong in a class, these functions should dip to zero between endpoints, because the center of the *x* axis represents maximum disagreement. Thus good listener agreement should result in a roughly U-shaped curve.

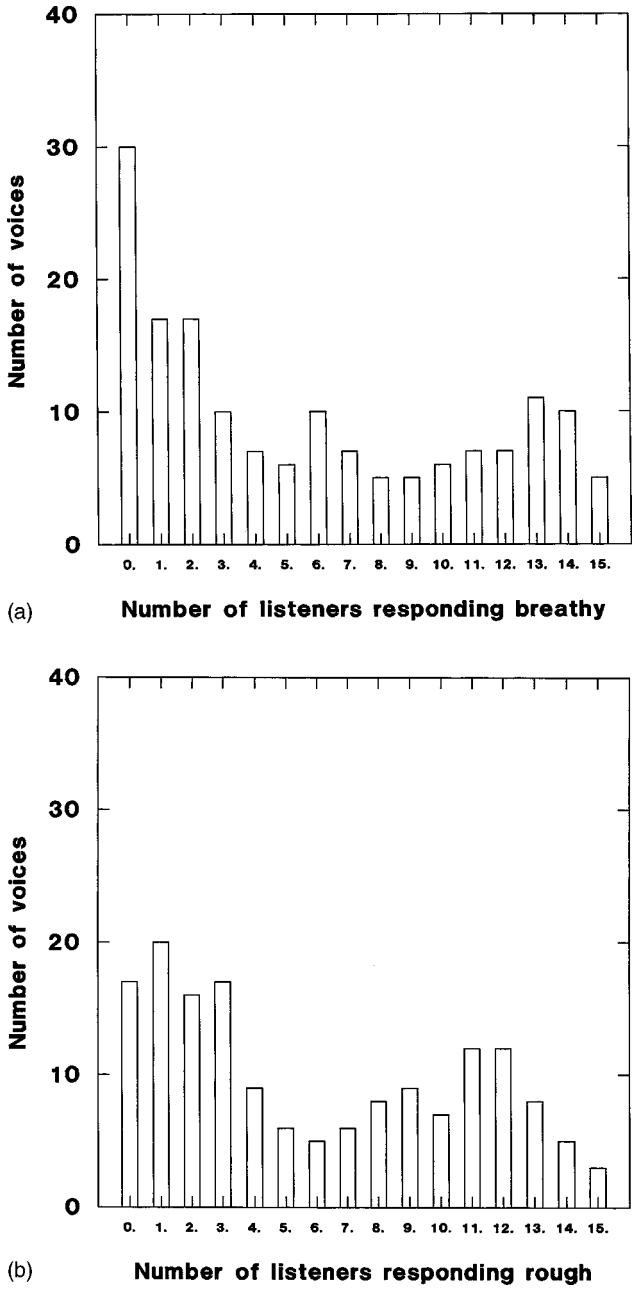

FIG. 1. Distribution of agreement levels for the two binary classification tasks. The *x* axis shows the number of listeners agreeing in their classification of a voice; the *y* axis shows the number of voices which received that level of agreement. Column totals sum to 160, the number of voice stimuli. (a) Breathiness judgments. (b) Roughness judgments.

This was not the case in the present data. Listeners agreed better that a voice was not primarily breathy or rough than they did that a voice belonged in a class, but otherwise levels of agreement were rather flat across the scale, and did not approach zero between endpoints. Further, listeners

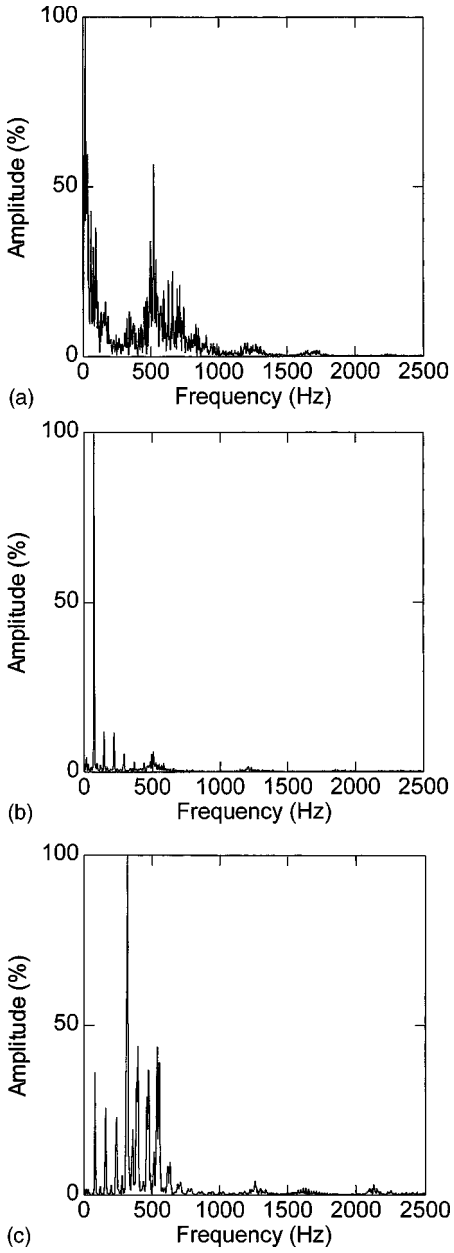

FIG. 2. Examples of linear FFT spectra for voices unanimously judged to be primarily breathy or primarily rough. Amplitude ranges from minimum to maximum, in percent. (a) A voice unanimously judged to be primarily breathy. (b) A voice unanimously judged to be primarily breathy. (c) A voice unanimously classified as primarily rough. Note the presence of interharmonics.

unanimously agreed that only 3/160 voices (1.9%) were primarily rough; only 5/160 voices (3.1%) were unanimously judged primarily breathy.

All five voices unanimously classified as ''primarily breathy'' were aphonic or near-aphonic, with limited harmonic structure above 700 Hz [Figs. 2(a), (b)]. The three voices unanimously classified as ''primarily rough'' were acoustically heterogeneous. All three were characterized by intermittent or continuous bifurcations and interharmonics; one had a very low $f0$, and one included prominent vocal fry [Fig. 2(c)]. The number of listeners responding ''rough'' was also significantly correlated with rated severity of vocal pathology ($r=0.70$, $p<0.05$), suggesting that roughness is also confounded with severity of pathology. The likelihood that a voice would be judged primarily breathy is also significantly correlated with severity in these data ($r=0.49$, $p<0.05$), but the correlation is significantly lower than for roughness ($t(157)=4.15$, $p<0.05$).

Statistical analysis of these data is complicated by the fact that there are no correct or incorrect answers. Voices cannot be placed *a priori* into perceptual classes, so the *a priori* proportions of breathy and rough voices in the population of pathological voices are unknown. For this reason, we used three different estimates of the frequency of ''primarily breathy'' and ''primarily rough'' voices in the overall population of voices to test the hypothesis that observed patterns of agreement were due to chance. The first estimate was the proportion of ''primarily *x*'' responses by the listener who responded ''primarily *x*'' least often; the second estimate was the proportion of responses by the listener with the largest number of ''primarily *x*'' responses; and the third estimate was the overall proportion of ''primarily breathy'' or ''primarily rough'' responses across the pooled group of listeners. The binomial probabilities of observing *N* agreements, *N*-1 agreements, *N*-2 agreements, and so on, were calculated (e.g., Hays, 1994, p. 140 ff.) for each of these three different estimates of the frequency of each quality in the population of speakers.[1]

Expected values (given the assumed proportion of ''breathy'' and ''not breathy'' voices in the sample and the assumption of random sampling from that population) are plotted with observed levels of agreement in Fig. 3. As this figure shows, observed agreement for both qualities is above the expected values at the margins of the figures, but below expected values in the middle of the figures. In other words, listeners agreed at above chance levels, and disagreed at below chance levels. Thus the hypothesis that results reflect random guessing can be rejected, for a range of assumed probabilities of ''primarily breathy'' and ''primarily rough'' voices.

C. Discussion

These results do not support the traditional assumption that pathological voices can be meaningfully assigned to broadly applicable perceptual classes. Although listeners agreed at better than chance levels, for most voices substantial disagreement existed as to whether or not that voice belonged in a given class. However, listeners did agree in their classification judgments for a few pathological stimuli, consistent with the venerable idea that commonly used categories like breathiness and roughness are real. We speculate that listeners agreed in their judgments of these particular voices because the stimuli correspond to acoustic or physiological extremes, which represent a limit of phonation and thus are perceptually stable across listeners. When voices do not approach such a phonatory limit, we speculate, listeners are unable to consistently isolate and assess single dimensions in highly variable perceptual contexts, so perceptual strategies diverge.

For example, all five voices unanimously classified as ''primarily breathy'' were aphonic or near-aphonic, as noted above. Aphonia is a well-defined physiological and acoustic

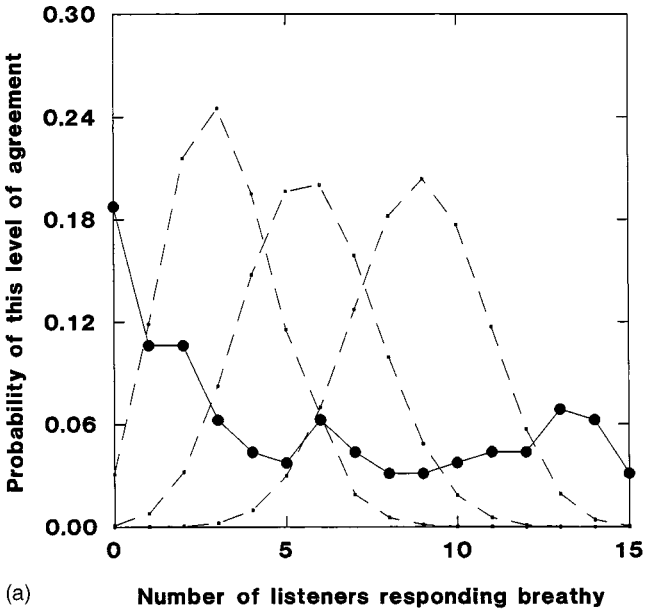

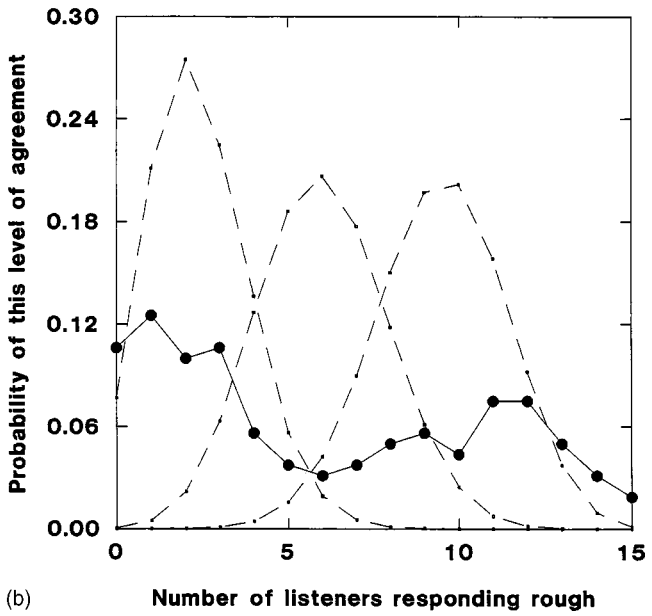

FIG. 3. Expected (dashed curves) and observed (solid curves) levels of listener agreement for the binary classification tasks. The *x* axis indicates the number of listeners agreeing in their classification of a voice; the *y* axis shows the probability of that many listeners agreeing, given the assumed likelihood of ''breathy'' or ''rough'' voices in the population. The leftmost dotted curve represents the most conservative assumption about this *a priori* probability; the rightmost curve represents the most liberal assumption. (a) Judgments of breathiness. (b) Judgments of roughness.

limit to phonation—the point at which the vocal folds cease to vibrate and the vocal tract is excited solely with turbulent noise—and thus constitutes the limiting case for breathiness as classically defined (e.g., Fairbanks, 1940). Because aphonia is the extreme case of breathiness, other aspects of vocal quality (for example, fundamental frequency, overall loudness, or the spectral characteristics of the turbulence noise) are perceptually irrelevant; the voice is breathy whatever values any other characteristics may assume. Thus the listeners' task is simplified; in essence, the voice loses degrees of freedom perceptually, so listeners lose opportunities to disagree. Note that the values of these other aspects may be relevant when other qualities (such as the roughness of the voice) are judged, so that a single voice can be placed in more than one perceptual class. Thus phonation that is ''perceptually stable'' with respect to one quality is not necessarily ''perceptually simple.''

In the case of roughness, vocal fry and bifurcated phonation are also well-defined physiologically and acoustically (e.g., Hollien *et al.*, 1966, 1977; Herzel *et al.*, 1991; Berry *et al.*, 1996; Omori *et al.*, 1997), and are well-distinguished perceptually from each other and from modal phonation (Hollien and Wendahl, 1968; Michel and Hollien, 1968; Omori *et al.*, 1997; see Gerratt and Kreiman, 2000, for review). Apparently these kinds of phonation are both associated with the label ''rough,'' which is also significantly confounded with overall severity of pathology. Variable attention by individual listeners to these different aspects of the voice signal may account for lower overall agreement that a voice was (and was not) ''primarily rough.''

One concern limits our interpretation of results from this study. Although disagreements among listeners may be related to listener difficulty in agreeing about single perceptual facets of complex voice stimuli, as argued above, findings may also be artifacts of the restrictive binary classification task used. Because the task required listeners to segment continuously varying vocal quality into two discrete classes, listeners' disagreements may reflect difficulties and differences in the placement of class boundaries. To investigate this possibility, we asked listeners to classify the natural voice stimuli used in experiment 1 according to their vocal pitch. Listeners were also asked to make similar judgments for a set of synthetic stimuli varying only in fundamental frequency. Pitch was selected as a stimulus dimension because it fulfills several criteria. First, problems regarding scale validity should not provoke disagreement among listeners, because the psychological reality of pitch is well established (see, e.g., Plomp, 1976, for review). Further, voice fundamental frequency has consistently emerged as perceptually important from studies of vocal quality (Kreiman *et al.*, 1990). Finally, the acoustic correlates of pitch are well understood, so synthesis is straightforward and accurate. If listener disagreements are related to inconsistent segmenting of a stimulus continuum, patterns and numbers of disagreements should be similar for the synthetic and natural voices, because pitch varies continuously in both cases. On the other hand, if disagreements are due to inconsistencies in how listeners isolate single dimensions in complex patterns, then agreement should be better for the synthetic stimuli than for the natural stimuli. In this view, the homogeneity of the synthetic stimuli promotes uniform perceptual strategies both within and across listeners, because only one variable changes within a fixed context across the stimulus set. Thus a consistent perceptual strategy can be adopted across listeners and applied for all the stimuli. With the natural voice samples, a single perceptual strategy is far less likely to emerge across listeners and voices, because pitch cues operate in perceptual contexts that vary widely from voice to voice. Consequently, the acoustic complexity of the pathologic voices hypothetically prevents listeners from converg-

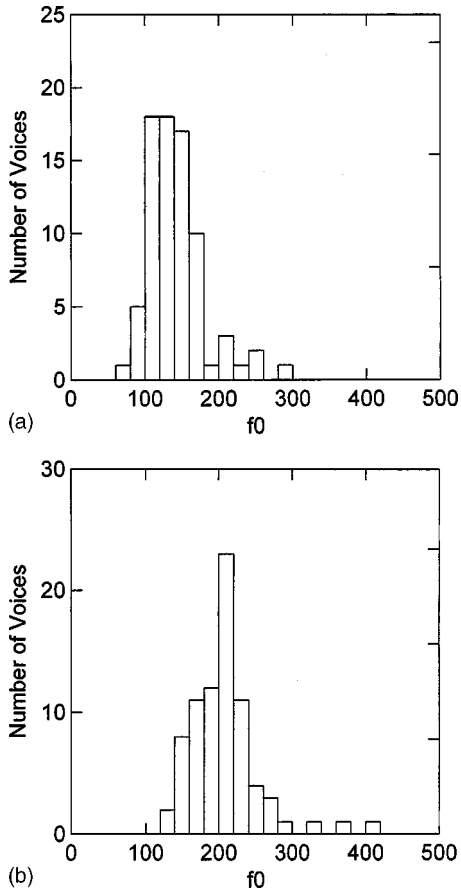

FIG. 4. Distributions of $f0$ values for the natural and synthetic voice stimuli. (a) Male voices. (b) Female voices.

ing on a single perceptual strategy and making the same judgments.

III. EXPERIMENT 2

A. Method

1. Stimuli

Two sets of stimuli were used in this experiment. The first included the 80 male and 80 female natural voice samples used in experiment 1. The second included synthetic male and female voices whose $f0$ values varied to match the distribution of mean $f0$ values for the natural stimuli (Fig. 4). Mean $f0$ values were measured from the center frequency of the lowest harmonic in a fast Fourier transform (FFT) spectrum calculated over the entire voice sample, and again with CSpeech software (Milenkovic, 1987; Milenkovic and Read, 1992). Values for voices with bifurcations or prominent amplitude modulations were rejected. The final set of synthetic voices included 77 male and 78 female tokens. Synthetic stimuli (2 s in duration) were created with a custom-designed formant synthesizer. Synthesizer parameters other $f0$ were modeled on natural tokens of /a/ spoken by normal male and female speakers (Table I), and were held constant across stimuli.

TABLE I. $f0$ and formant frequencies for the synthetic stimuli.

	Females	Males
$f0$ (Hz)	125–425	70–370
$F1$ (Hz)	850	800
$F2$ (Hz)	1400	1346
$F3$ (Hz)	2815	2500
$F4$ (Hz)	4299	3400
$F5$ (Hz)	···	4373

2. Listeners

Fifteen expert listeners participated in this experiment. Four had participated in experiment 1; however, the two experiments were separated by several months. Each listener had a minimum of 3 years' post-graduate experience evaluating and/or treating voice disorders. Listeners reported no history of hearing difficulties.

3. Procedure

For each stimulus, listeners were asked to decide whether the voice was low pitched or not low pitched, relative to average normal speakers of the appropriate gender. They were allowed to replay stimuli as often as necessary before making their decisions. Because $f0$ expectations differ for male and female voices, male and female stimuli were presented in separate blocks of trials, as were synthetic and natural stimuli. Thus each listener heard four blocks of stimuli: male natural voices, female natural voices, male synthetic voices, and female synthetic voices. Order of blocks was randomized across listeners, and stimuli within a block were rerandomized for each listener. Listeners were informed of the class of stimuli to be judged prior to hearing each block of trials.

To assess test-retest reliability, 20% of trials (selected at random) were repeated in each block of stimuli. Repeated trials were inserted at random into the sequence of trials. Other testing conditions were identical to those used in experiment 1. Listeners completed all four blocks of trials at a single session lasting about 1/2 hour.

B. Results

1. Test-retest agreement

For the natural stimuli, test-retest agreement was comparable to that observed in experiment 1, averaging 81.8% across listeners (s.d.=9.61; range=62%–95%). Listeners were significantly more self-consistent when classifying the synthetic stimuli [mean test-retest agreement=86.7%; s.d.=9.0; range=73.3%–100%; matched samples $t(14)=-2.21$, $p<0.05$].

2. Classification responses

As with judgments of breathiness and roughness, listeners varied in the number of voices they considered low pitched. For the natural stimuli, the number of ''low pitched'' responses was similar to the number of ''primarily breathy'' and ''primarily rough'' responses, ranging from 40–91 (out of 160 stimuli; mean=62.5, s.d.=15.3). Pairwise agreement among raters for judgments of the pitch of natural stimuli was also similar to agreement for breathiness and roughness. On average, two listeners agreed about 73.9% of

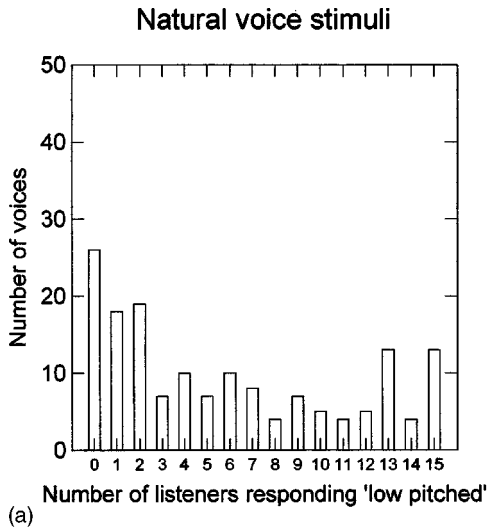

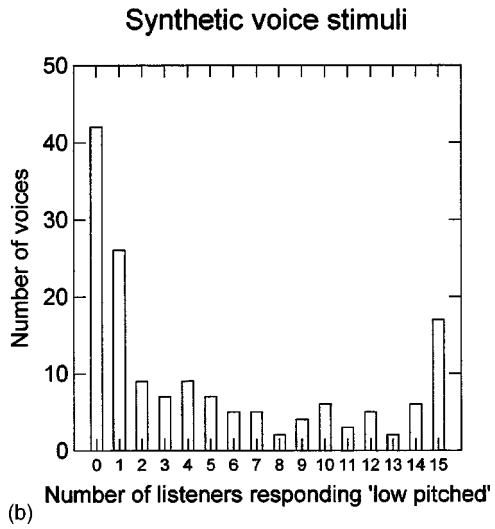

FIG. 5. Distribution of agreement levels for the pitch judgment tasks. The *x* axis shows the number of listeners agreeing in their classification of a voice; the *y* axis shows the number of voices which received that level of agreement. (a) Natural voice stimuli. Column totals sum to 160, the number of pathological voice stimuli. (b) Synthetic voice stimuli. Column totals sum to 155, the number of synthetic voice stimuli.

their pitch judgments (compared to 73.5% agreement in breathiness judgments, and 69.5% agreement in roughness judgments).

For the synthetic stimuli, the proportion of ''low pitched'' responses was lower than that for the natural stimuli (mean=51.5/155 stimuli; s.d.=18.3; range=29–84). However, pairwise agreement among listeners was significantly better for judgments of the synthetic stimuli [mean pairwise agreement=80.1%; s.d.=7.6; range=61.9%–92.3%; matched samples $t(103)=-7.85$, $p<0.05$].

Patterns of overall agreement for the two sets of pitch judgments are shown in Fig. 5. As in experiment 1, a value of 15 on the *x* axis (rightmost columns) indicates that all 15 listeners agreed a voice was low pitched; a value of 0 on the *x* axis indicates that all listeners agreed the voice was not low pitched (i.e., 0 listeners classified the voice as low pitched).

As this figure shows, listeners agreed substantially better for the synthetic than for the natural stimuli, even though $f0$ values were identical for the two sets of stimuli. Listeners unanimously agreed that 27.1% of synthetic stimuli were not low pitched, vs 16.2% of natural stimuli; and they agreed unanimously that 11.0% synthetic stimuli were low pitched, vs 8.1% of natural stimuli.

In addition, patterns of listener agreement and disagreement differed for the two tasks. For the natural stimuli, levels of agreement were rather flat across the figure, and did not approach zero between endpoints, indicating that for many voices listeners were divided as to whether or not that voice was low pitched. In contrast, for the majority of the synthetic stimuli (91/155) all or all but one of the listeners agreed in their judgments. Significant disagreement occurred for relatively few voices, resulting in the predicted U-shaped function. Thus the observed disagreements for the synthetic stimuli seem to represent primarily minor differences in the placement of boundaries between classes of stimuli.

To test the hypothesis that agreement rates were better for judgments of synthetic stimuli than for judgments of the breathiness, roughness, or pitch of natural stimuli, data were first transformed using the following procedure. Recall that classification responses for individual voices ranged from 0 (all raters agreed the voice did not belong in a class) to 15 (all raters agreed the voice did belong in the class). This scale was modified such that it ranged from perfect agreement to maximum disagreement among raters. That is, scores of 0 and 15 were converted to 100% agreement; scores of 1 and 14 were converted to 93.3% agreement (i.e., all but one rater agreed in their classification judgment); scores of 2 and 13 were converted to 86.7% agreement; and so on. Note that this new scale ranged from 100% agreement to 53.3% agreement, because a divided panel (7 votes vs 8 votes) represented the maximum possible disagreement among raters.

Because these data can assume only a small number of values, a Kruskal-Wallis one-way nonparametric analysis of variance (ANOVA) was used to compare transformed agreement rates for the four binary classification tasks (judgments of breathiness, roughness, pitch/natural stimuli, and pitch/synthetic stimuli). Tasks differed significantly in the levels of overall agreement observed (Kruskal-Wallis test statistic $=21.21$, $df=3$, $p<0.05$). *Post-hoc* comparisons indicated that listeners agreed significantly better ($p<0.05$, adjusted for multiple comparisons) in their judgments of the synthetic stimuli than they did in the other three tasks, for which agreement levels did not differ ($p>0.05$).

Figure 6 shows the likelihood of listener agreement plotted against $f0$ for the natural and synthetic stimuli. For the natural voices, pitch category is apparently ambiguous for fundamental frequencies below about 300 Hz for female voices (shown as filled circles in the figure), and below about 200 Hz for male voices (shown as stars). Voices with $f0$ above these values were unambiguously not low pitched; but voices with $f0$ below these values might or might not be considered low pitched. A different pattern emerged for the synthetic voices. For these stimuli, the likelihood of ''low pitched'' responses decreased smoothly across frequencies, and bottomed out at about 150 Hz for males and 250 Hz for females.

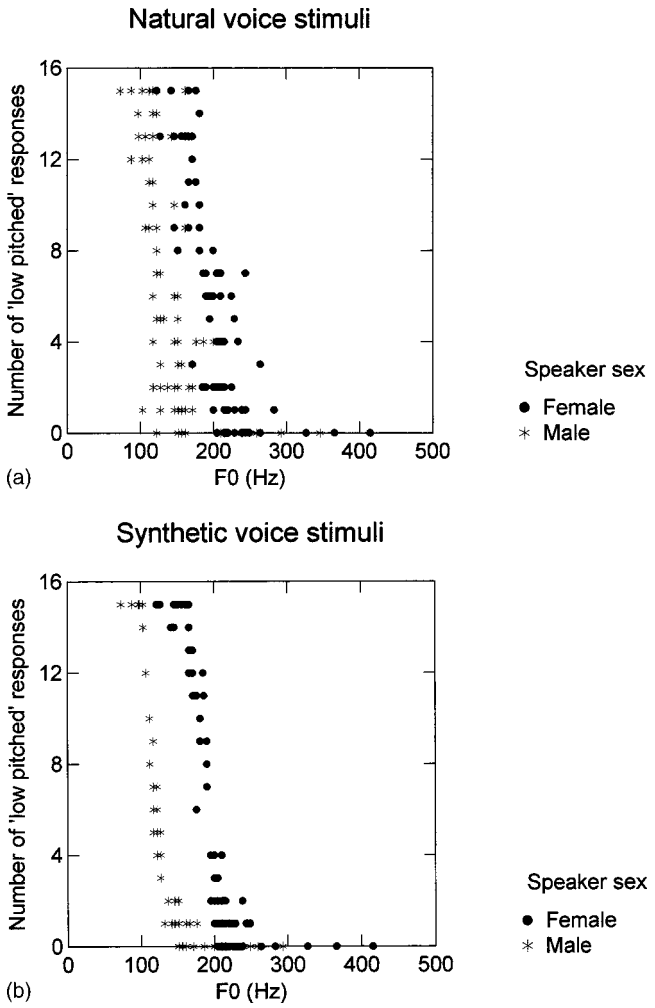

FIG. 6. The likelihood of listener agreement about the pitch of natural and synthetic stimuli, vs $f0$. Male stimuli are plotted with stars; female stimuli are plotted with filled circles. (a) Natural voice stimuli ($n=160$). (b) Synthetic voice stimuli ($n=155$). Note that many points overlap in this figure.

C. Discussion

These results indicate that the high levels of disagreement observed for judgments of natural stimuli were not due solely to difficulties segmenting a continuum or to some other task-related factor. Instead, they appear to be directly related to characteristics of the stimuli. Listener agreement about the pitch of the natural voices did not differ significantly from agreement about breathiness and roughness. However, both test-retest agreement and inter-rate agreement were significantly better when listeners classified the pitch of synthetic voice stimuli, which varied only in $f0$. Listener agreement for the synthetic voices was very well predicted by $f0$, as one would expect. Agreement increased sharply and smoothly as $f0$ departed from population mean values (about 130 Hz for male speakers and 220 Hz for females; e.g., Peterson and Barney, 1952). The relationship between $f0$ and pitch was more complicated for the natural voices. Although in general listener agreement varied with $f0$, listeners sometimes agreed about the pitch of voices whose $f0$ was near the population mean, and disagreed about voices for which $f0$ was substantially above or below average [Fig. 6(a)]. Further, the $f0$ values at which listeners no longer disagreed about vocal pitch were about 50 Hz higher for the natural than for the synthetic stimuli. Thus it appears that not only listener agreement levels, but also the amount of evidence listeners require to agree about the presence of a vocal quality, depend on stimulus complexity. These results are consistent with the hypothesis that listeners are unable to agree in their judgments of specific attributes of voice because they cannot consistently focus attention on individual quality dimensions of complex signals.

IV. GENERAL DISCUSSION

These results are consistent with the claim that unidimensional rating scale approaches are inappropriate for measuring pathological vocal quality. Even in a simple binary classification task, listeners were unable to agree with each other consistently about the breathiness, roughness, or pitch of natural pathological voice stimuli. However, agreement was significantly better for pitch judgments when stimuli were relatively simple synthetic vowels. This suggests that disagreements are not due to characteristics of the classification task, but instead are related to listeners' difficulty in isolating single dimensions of complex stimuli.

The notion that listeners agree about the quality of a few pathological voices because those voices correspond to physiological or acoustic extremes accounts well for the present data. If listeners agree in their judgments only when a voice is at or very near a phonatory limit, agreement will be uncommon, because such voices are relatively rare. This explanation also accounts for the fact that listeners agreed better about which voices were not breathy, rough, or low pitched than about which voices belonged in a particular class. As argued above, only a single, extreme, relatively uncommon vocal configuration will generate agreement that a voice belongs in a class. Agreement that a voice is not in a class requires that listeners agree that the voice does not correspond to one specific acoustic pattern, but does not require that they agree about the particular manner in which it deviates from that pattern. Such limited agreement is apparently relatively easy to achieve. Although this interpretation is speculative at present due to the small number of voices about which listeners agreed, the hypothesis that phonation near physiologic or acoustic limits is reliably perceived across listeners could be tested, using either natural or synthetic stimuli.

Because traditional dimensions for voice quality usually range from ''normal'' to ''severe,'' the present results might seem to imply that valid rating protocols could be constructed with reference to these extreme stimuli. For example, such voices could hypothetically be used to create sets of ''anchor stimuli'' varying in steps from normal to the extreme. Listeners could then judge quality with reference to these anchors, rather than by comparison to variable internal standards for a quality (e.g., Gerratt *et al.*, 1993). However, even if a few acoustically extreme voice stimuli are treated as ''cardinal'' in quality (Jones, 1922; Abercrombie, 1967), these voices are unlikely to provide a basis for creating a useful set of ordinal- or interval scale features for all voices. As voices depart from the extreme limits of phonation, no basis exists for weighing the many different facets of quality

that occur, and listeners are free to focus their attention in any way they like, leading to listener disagreement. In this way, the existence of a few ''cardinal'' voices does not imply that continuous features for the vast majority of voices can also be defined, or that other voices can be classified or ranked with reference to these extreme stimuli.

These results also suggest that perception of pathological qualities like breathiness and roughness may differ from the perception of phonemic breathiness and roughness in languages that distinguish phonation types, analogous to differences between the perception of (nonphonemic) pitch and (phonemic) tone (e.g., Gandour and Harshman, 1978; Gandour *et al.*, 1988). Vocal quality varies continuously in many dimensions, as phonetic quality does, but no formal system of contrasts (analogous to the phonology of a language) exists to divide this voice quality continuum into discrete classes. Linguistic sound categories (phonemes) can be established by reference to contrasts in meaning, but when judging voice quality, an infinite number of arrangements is possible, so ''mistake'' is undefined and listeners have an unrestricted choice of responses. (See Belkin *et al.*, 1997, for discussion of a similar problem with the description of odors.)

In conclusion, the data presented here suggest that traditional labels for vocal quality may be valid in a limited way, but that pathologic voice quality assessment using traditional perceptual labels is not generally useful. The particular pattern of observed listener disagreements appears to be related in part to difficulty isolating single perceptual dimensions of complex stimuli, and listener agreements may be accounted for by the relative perceptual stability of a small number of stimuli corresponding to well-defined acoustic or physiological extremes. This pattern of agreements and disagreements among listeners is consistent with problems that have arisen in the study of other sensory modalities (for example, taste and smell) that also lack category or featural structure, and for which no satisfactory, consensually accepted descriptive terminology exists (e.g., Belkin *et al.*, 1997), and possibly cannot exist in the absence of such structure. Measuring perceptual responses to such stimuli presents a considerable challenge.

ACKNOWLEDGMENTS

We thank James Hillenbrand and Thomas Baer for insightful and enormously helpful comments on an earlier version of this paper. This research was supported by Grant No. DC01797 from the National Institute on Deafness and Other Communication Disorders.

[1]With the number of listeners as N, the proportion of breathy (or rough) voices in the population as p, and q equal to $1-p$, the chance probability of N successes (N listeners responding ''breathy'' or ''rough''), $N-1$ successes, $N-2$ successes. . .0 successes, can be estimated using the formula $p(r \text{ successes}; N,p)=\binom{N}{r}p^r q^{N-r}$.

Abercrombie, D. (**1967**). *Elements of General Phonetics* (Aldine, Chicago).
Austin, G. (**1806**). *Chironomia* (Cadell and Davies, London). Reprinted by Southern Illinois University Press, Carbondale, IL, 1966.
Belkin, K., Martin, R., Kemp, S. E., and Gilbert, A. N. (**1997**). ''Auditory pitch as a perceptual analogue to odor quality,'' Psychol. Sci. **8**, 340–342.
Berry, D. A., Herzel, H., Titze, I. R., and Story, B. H. (**1996**). ''Bifurcations in excised larynx experiments,'' J. Voice **10**, 129–138.
Childers, D. G., and Lee, C. K. (**1991**). ''Vocal quality factors: Analysis, synthesis, and perception,'' J. Acoust. Soc. Am. **90**, 2394–2410.
Cicero (**1948**). *De Oratore*, translated by E. W. Sutton and H. Rackham (Harvard University Press, Cambridge, MA).
Colton, R., and Estill, J. (**1981**). ''Elements of voice quality: Perceptual, acoustic and physiologic aspects,'' in *Speech and Language: Advances in Basic Research and Practice*, edited by N. J. Lass (Academic, New York), Vol. 5, pp. 311–403.
Fairbanks, G. (**1940**). *Voice and Articulation Drillbook* (Harper, New York).
Gandour, J., and Harshman, R (**1978**). ''Crosslanguage differences in tone perception: A multidimensional scaling investigation,'' Lang. Speech **21**, 1–33.
Gandour, J., Petty, S. H., and Dardarananda, R. (**1988**). ''Perception and production of tone in aphasia,'' Brain Lang. **35**, 201–240.
Gerratt, B. R., and Kreiman, J. (**2000**). ''Toward a taxonomy of nonmodal phonation,'' J. Phonetics (in press).
Gerratt, B. R., Kreiman, J., Antonanzas-Barroso, N., and Berke, G. S. (**1993**). ''Comparing internal and external standards in voice quality judgments,'' J. Speech Hear. Res. **36**, 14–20.
Gobl, C., and Ni Chasaide, A. (**1992**). ''Acoustic characteristics of voice quality,'' Speech Commun. **11**, 481–490.
Goldbury, J., and Russell, W. (**1844**). *The American Common-School Reader and Speaker* (Tappan and Whitmore, Boston) (cited by Gray, 1943).
Gray, G. W. (**1943**). ''The 'voice qualities' in the history of elocution,'' Q. J. Speech **29**, 475–480.
Hays, W. L. (**1994**). *Statistics*, 5th ed. (Harcourt Brace, New York).
Herzel, H., Steinecke, I., Mende, W., and Wermke, K. (**1991**). ''Chaos and bifurcations during voiced speech,'' in *Complexity, Chaos, and Biological Evolution*, edited by I. Mosekilde and L. Mosekilde (Plenum, New York), pp. 41–50.
Hillenbrand, J., and Houde, R. A. (**1996**). ''Acoustic correlates of breathy vocal quality: Dysphonic voices and continuous speech,'' J. Speech Hear. Res. **39**, 311–321.
Hollien, H., Girard, G. T., and Coleman, R. F. (**1977**). ''Vocal fold vibratory patterns of pulse register phonation,'' Folia Phoniatr. **29**, 200–205.
Hollien, H., Moore, P., Wendahl, R. W., and Michel, J. (**1966**). ''On the nature of vocal fry,'' J. Speech Hear. Res. **9**, 245–247.
Hollien, H., and Wendahl, R. W. (**1968**). ''Perceptual study of vocal fry,'' J. Acoust. Soc. Am. **43**, 506–509.
Jones, D. (**1922**). *An Outline of English Phonetics*, 9th ed. (Cambridge University Press, Cambridge, 1972).
Kasuya, H., and Ando, Y. (**1991**). ''Acoustic analysis, synthesis, and perception of breathy voice,'' in *Vocal Fold Physiology: Acoustic, Perceptual, and Physiological Aspects of Voice Mechanisms*, edited by J. Gauffin and B. Hammarberg (Singular, San Diego), pp. 251–258.
Klatt, D. H., and Klatt, L. C. (**1990**). ''Analysis, synthesis, and perception of voice quality variations among female and male talkers,'' J. Acoust. Soc. Am. **87**, 820–857.
Kreiman, J., and Gerratt, B. R. (**1996**). ''The perceptual structure of pathologic voice quality,'' J. Acoust. Soc. Am. **100**, 1787–1795.
Kreiman, J., and Gerratt, B. R. (**1998**). ''Validity of rating scale measures of voice quality,'' J. Acoust. Soc. Am. **104**, 1598–1608.
Kreiman, J., Gerratt, B. R., Kempster, G., Erman, A., and Berke, G. S. (**1993**). ''Perceptual evaluation of voice quality: Review, tutorial, and a framework for future research,'' J. Speech Hear. Res. **36**, 21–40.
Kreiman, J., Gerratt, B. R., and Precoda, K. (**1990**). ''Listener experience and perception of voice quality,'' J. Speech Hear. Res. **33**, 103–115.
Lalwani, A. L., and Childers, D. G. (**1991**). ''Modeling vocal disorders via formant synthesis,'' Proc. ICASSP, pp. 505–508.
Laver, J. (**1980**). ''The analysis of vocal quality: From the classical period to the twentieth century,'' in *Towards a History of Phonetics*, edited by R. E. Asher and E. J. A. Henderson (Edingburgh University Press, Edinburgh), pp. 79–99.
Martin, D., Fitch, J., and Wolfe, V. (**1995**). ''Pathologic voice type and the acoustic prediction of severity,'' J. Speech Hear. Res. **38**, 765–771.
Martin, D., and Wolfe, V. (**1996**). ''Effects of perceptual training based upon synthesized voice signals,'' Percept. Mot. Skills **83**, 1291–1298.
Michel, J., and Hollien, H. (**1968**). ''Perceptual differentiation of vocal fry and harshness,'' J. Speech Hear. Res. **11**, 439–443.
Milenkovic, P. H. (**1987**). ''Least mean square measure of voice perturbation,'' J. Speech Hear. Res. **30**, 529–538.

Milenkovic, P., and Read, C. (**1992**). *CSpeech Version 4 User's Manual* (Paul Milenkovic, Madison, WI).
Omori, K., Kojima, H., Kakani, R., Slavit, D. H., and Blaugrund, S. M. (**1997**). ''Acoustic characteristics of rough voice: Subharmonics,'' J. Voice **11**, 40–47.
Peterson, G. E., and Barney, H. L. (**1952**). ''Control methods used in a study of the vowels,'' J. Acoust. Soc. Am. **24**, 175–184.
Plomp, R. (**1976**). *Aspects of Tone Sensation* (Academic, New York).
Plugge, D. E. (**1942**). '' 'Voice qualities' in oral interpretation,'' Q. J. Speech **28**, 442–444.
Pollux, J. (**1706**). *Onomasticon*, Amsterdam edition (cited by Austin, 1806).
Rammage, L. A., Peppard, R., and Bless, D. M. (**1992**). ''Aerodynamic, laryngoscopic, and perceptual-acoustic characteristics in dysphonic females with posterior glottal chinks: A retrospective study,'' J. Voice **6**, 64–78.
Rush, J. (**1859**). *The Philosophy of the Human Voice*, 5th ed. (J. B. Lippincott, Philadelphia).
Wendahl, R. W. (**1966**). ''Some parameters of auditory roughness,'' Folia Phoniatr. **18**, 26–32.

Effects of the salience of pitch and periodicity information on the intelligibility of four-channel vocoded speech: Implications for cochlear implants

Andrew Faulkner,[a] Stuart Rosen, and Clare Smith
Department of Phonetics and Linguistics, University College London, Wolfson House, 4 Stephenson Way, London NW1 2HE, United Kingdom

(Received 8 April 2000; accepted for publication 24 July 2000)

Recent simulations of continuous interleaved sampling (CIS) cochlear implant speech processors have used acoustic stimulation that provides only weak cues to pitch, periodicity, and aperiodicity, although these are regarded as important perceptual factors of speech. Four-channel vocoders simulating CIS processors have been constructed, in which the salience of speech-derived periodicity and pitch information was manipulated. The highest salience of pitch and periodicity was provided by an explicit encoding, using a pulse carrier following fundamental frequency for voiced speech, and a noise carrier during voiceless speech. Other processors included noise-excited vocoders with envelope cutoff frequencies of 32 and 400 Hz. The use of a pulse carrier following fundamental frequency gave substantially higher performance in identification of frequency glides than did vocoders using envelope-modulated noise carriers. The perception of consonant voicing information was improved by processors that preserved periodicity, and connected discourse tracking rates were slightly faster with noise carriers modulated by envelopes with a cutoff frequency of 400 Hz compared to 32 Hz. However, consonant and vowel identification, sentence intelligibility, and connected discourse tracking rates were generally similar through all of the processors. For these speech tasks, pitch and periodicity beyond the weak information available from 400 Hz envelope-modulated noise did not contribute substantially to performance. [S0001-4966(00)05810-0]

PACS numbers: 43.71.Ky, 43.71.Bp, 43.66.Ts [CWT]

I. INTRODUCTION

Pitch variation, and the presence of periodic and/or aperiodic excitation, are widely held to be important cues for the perception of speech. However, surprisingly little is known of their contribution to speech intelligibility except in what may be a special case, that of auditory signals that contain no spectral structure. With such signals, these factors contribute in several important ways. The timing of periodic and aperiodic excitation are dominant temporal cues to consonant identity (Faulkner and Rosen, 1999). Furthermore, for the audio-visual perception of connected speech, both voice pitch and the timing of voiced excitation provide distinct elements of complementary support to visual cues (Breeuwer and Plomp, 1986; Grant *et al.*, 1985; Risberg, 1974; Risberg and Lubker, 1978; Rosen, Fourcin, and Moore, 1981). Speech presented through a cochlear implant, or through a vocoder-like simulation of an implant speech processor, is represented by a relatively small number of spectral bands, each conveying temporal envelope information. It may be expected, then, that the temporal information that contributes to speech perception through such processing is similar to the temporal information that dominates perception from signals that convey no spectral information.

Vocoder-like speech-processing methods have been used in a number of recent studies that aim to simulate cochlear implant speech processors (Dorman, Loizou, and Rainey, 1997a, 1997b; Rosen, Faulkner, and Wilkinson, 1999; Shannon *et al.*, 1995; Shannon, Zeng, and Wygonski, 1998). These simulations represent the spectro-temporal information delivered to the auditory nerve by continuous interleaved sampling (CIS) processors (Wilson *et al.*, 1991). In a CIS implant, the signals presented along the electrode array represent amplitude envelopes extracted from a series of bandpass filters. These envelopes, typically smoothed to carry temporal information below 400 Hz, are imposed on biphasic pulse carriers that generally have a rate between 1 and 2 kHz.

The simulation studies performed so far have paid little attention to the nature of the temporal cues provided. Rather, the focus has been on the role of spectral resolution (Dorman, Loizou, and Rainey, 1997b; Shannon *et al.*, 1995) and the effects of shifts of the spectral envelope (Dorman *et al.*, 1997a; Rosen *et al.*, 1999; Shannon *et al.*, 1998). Here, we focus on the contributions to speech intelligibility that can be attributed to speech-related pitch information (i.e., variation in voice fundamental frequency) and to periodicity information (i.e., the presence of periodic laryngeal excitation or of aperiodic voiceless excitation).

Previous simulation studies have made use of either bandpass-filtered noise carriers, or a series of fixed-frequency sinusoidal carriers to deliver amplitude envelope information in selected frequency bands to the normal ear. Temporal cues to pitch variation, and to the simple presence of periodicity, are carried by the modulation of the pulse stimulation from a CIS processor as long as two conditions are met. The envelope smoothing filter must encompass the voice fundamental frequency range and the pulse stimulation

[a]Electronic mail: andyf@phon.ucl.ac.uk

rate must be sufficiently high to sample this frequency range adequately. Similarly, where vocoder simulations use sufficiently high envelope bandwidths to modulate noise carriers,[1] these too are capable of signaling pitch and periodicity for modulation rates up to a few hundred Hz (e.g., Pollack, 1969). However, the salience of the pitch of modulated noise is weak compared to that of harmonic sounds such as voiced speech, and it is important to establish the limitations that such simulations may have in respect to the transmission of pitch and periodicity. Little is known about the effects of the salience of periodicity in such simulations. Fu and Shannon (2000) report little effect of varying the envelope cutoff frequency between 16 and 400 Hz for English consonant materials with four-channel noise-excited vocoders. In Chinese, however, it has been shown that tonal cues carried by noise modulated by a 400-Hz bandwidth speech envelope can contribute to sentence-level speech perception using such simulations (Fu, Zeng, and Shannon, 1998).

A. Pitch and periodicity cues from a CIS cochlear implant processor

The representation of pitch variation and of speech periodicity for users of a CIS cochlear implant speech processor will depend not only on the extent to which the corresponding temporal information is contained in the extracted amplitude envelopes, but also on the extent to which the patient is able to process this information. This latter aspect is not well understood, although it is clear that there are very wide variations between patients. A study of periodic/aperiodic discrimination in single-channel implant users showed some patients to have good abilities in identifying periodic from aperiodic pulse stimulation, at least for stimuli of 200-ms duration (Fourcin *et al.*, 1979). However, except for one subject, the stimuli used in that study were directly periodic or aperiodic, not pulse carriers with periodic or aperiodic amplitude modulation. McDermott and McKay (1997) studied one individual implant patient under conditions comparable to CIS stimulation. Sinusoidal amplitude modulation of a 1200-Hz pulse train delivered to a single bipolar electrode pair allowed the discrimination of modulation rates differing by 3% to 4% around a 100-Hz rate. Around a 200-Hz rate, thresholds were between 4% and 27%, depending on the stimulation site. Other selected CIS implant processor users have also showed good ability in the pitch ranking of pulsatile stimulation that carries sinusoidal amplitude modulation up to modulation rates of 1 kHz (Wilson *et al.*, 1997). However, this last study gives rather limited information on pitch discrimination, since the ranked modulation rates differed in steps of 100 Hz.

B. Representation of pitch information in vocoder carriers

In normal hearing, pitch perception is thought to be based primarily on temporal cues derived from resolved lower-frequency harmonics, including the fundamental component, and also on periodicity cues in the temporal envelope in auditory filter channels driven by adjacent unresolved harmonics. Spectral details and overall spectral shape are also related to fundamental frequency, and are encoded by place within the limits of auditory frequency resolution. For quasi-periodic speech-like signals, a CIS implant processor would not be expected to deliver useful place-based spectral pitch cues within the voice fundamental frequency (Fx) range. The primary reason for this is that the channel bandpass filters are too wide to resolve individual harmonics of such fundamental frequencies.[2] In addition, the spectral shape of speech is constantly varying independently of fundamental frequency, so that spectral envelope is unlikely to be a reliable source of pitch information for speech. Hence, only envelope periodicity cues will be available to signal pitch for speech. The carrier in a CIS processor is a non-random high-rate pulse rather than the random noise typically used in simulations. For this reason, temporal modulation of the carrier related to Fx will be noise-free, and the neural responses to this stimulation are also likely to be strongly synchronized to the modulation (Wilson *et al.*, 1997).

This study introduces the use of frequency-controlled pulse carriers for voiced speech. Here, the carrier for voiced speech is a flat-spectrum pulse train whose period is controlled by voice fundamental frequency. The carrier is passed through a series of bandpass filters to control the frequency content of the different output bands. The use of such a carrier is not intended to represent the pulsatile stimulation of CIS, which cannot be accurately emulated in acoustic hearing. Rather, the intention is to achieve the highest possible pitch salience by providing a rich set of pitch cues both from individually resolved lower harmonics and from temporal envelope cues from the unresolvable higher harmonics. The noise carriers typical of most previous simulation studies necessarily lack harmonic content, and provide only temporal envelope cues to pitch. With noise carriers, the periodicity of the temporal envelope related to voice pitch will be noisy by virtue of the random nature of the carrier. Such random fluctuations in the carrier will be more significant in the lower vocoder bands, where the rate of the inherent envelope fluctuations of the filtered carrier is closer to the rate of the envelope fluctuations extracted from periodic speech. The random nature of noise carriers may well weaken pitch salience compared to that derived from CIS processors by those implant users who are able to fully process the temporal information carried by envelope-modulated pulse stimulation.

II. EXPERIMENTAL QUESTIONS

The studies reported here address two related issues, using a variety of segmental and connected speech tasks. Given that simulations of vocoder-like CIS speech processors deliver limited pitch and periodicity information, what impact does this have on speech intelligibility, and would more salient pitch and periodicity cues improve performance?

III. METHODS

A. Signal processing

Signal processing was implemented in real time, using the ALADDIN INTERACTIVE DSP WORKBENCH software (v1.02, AB Nyvalla DSP). It ran at a 16-kHz sample rate on a Loughborough Sound Images DSP card with a Texas Instru-

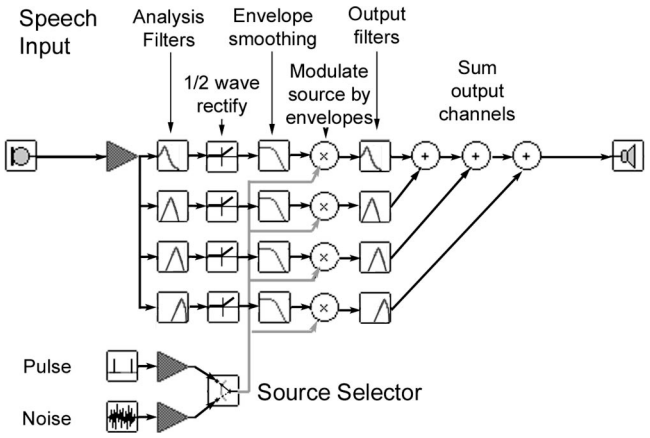

FIG. 1. Block diagram showing speech processing common to all processor simulations.

ments TMS320C31 processor. All processors used here had four channels, with the analysis and output filters being identical, so that the spectral representation was tonotopically accurate within the constraints of the limited spectral resolution. A block diagram of the common components of the processors is shown in Fig. 1. Each channel consisted of a series of blocks, comprising: a bandpass filter applied to the speech input; a rectifier and low-pass filter to extract the amplitude envelope from that spectral band; a multiplier that modulated a carrier signal by that envelope; a final bandpass filter, matching the analysis filter, shaped the spectrum of the modulated carrier signal.

The four analysis and output filter bands were based on equal basilar membrane distance (Greenwood, 1990). The filter slopes crossed at their −6-dB cutoff frequencies, these being 100, 392, 1005, 2294, and 5000 Hz. The bandpass analysis filters, and the corresponding output filters, were eighth-order elliptical IIR designs, with slopes in excess of 50 dB/octave, and stop bands at least 50 dB down on the passband. The amplitude envelope was extracted from each analysis filter output by half-wave rectification followed by a fourth-order elliptical low-pass filter, with a slope of about 48 dB/octave.

1. Speech-processing conditions

The various processing conditions are summarized in Table I. With one exception, the envelope extraction employed a 32-Hz low-pass filter, so that temporal information in the voice pitch and periodicity range was eliminated from the envelope. The salience of speech-derived pitch and periodicity was manipulated through the selection and control of the carrier signal. The fullest and most salient representation of pitch and periodicity was produced using processing similar to classic speech synthesizing vocoders (Dudley, 1939). Here, the carrier source during voiced speech was a pulse signal whose frequency followed that of the fundamental frequency of the speech input (*Fx*). The carrier source for voiceless speech was a random noise (symbolized as *Nx*). This condition is notated as *FxNx*. The pulse carrier was a monophasic pulse with a width of one sample (63 μS). Within the 8-kHz overall bandwidth of the processor, the spectral envelope of this pulse train and the noise source were both flat, and both source signals had the same rms level.

A processor similar to that used for condition *FxNx* differed only in using a fixed 150-Hz pulse rate rather than a speech-derived pulse rate. This processor preserved the contrast between periodic and purely aperiodic excitation, while discarding voice pitch variation. It is designated as condition *VxNx*.

A third processor discarded both periodicity and pitch information and was produced by using a fixed-frequency 150-Hz pulse source for all speech input. This condition was designated *Mpulses* (monotone pulses).

Two further processors employed a filtered white-noise carrier for all speech. These are similar to the processors used by Shannon *et al.* (1995). They differed from each other only in the low-pass cutoff frequency of the envelope filters, which was either 400 Hz in condition *Noise400*, or 32 Hz in condition *Noise32*. The 400-Hz envelope cutoff was expected to allow speech periodicity and pitch information to be preserved in the extracted envelope. However, the perceptual salience of this information was not expected to be as high as for condition *FxNx*. The use of a 32-Hz cutoff frequency together with the 48-dB/octave slope of the envelope filter was expected to eliminate virtually all pitch and periodicity cues in condition *Noise32*.

With the exception of processor *Noise400*, all processors represent the spectral envelope of the input signal essentially identically. The spectral envelope signaled by processor *Noise400* differs in the representation of spectral envelope changes at a more rapid rate (up to 400 rather than 32 Hz). The spectra resulting from a pulsatile carrier inevitably differ from those from noise carriers in that harmonics

TABLE I. Summary of processor conditions (see the text for details).

Processor	Voiced speech carrier	Voiceless speech carrier	Envelope low-pass cutoff (Hz)	Expected salience of pitch and periodicity
Noise400	Noise	Noise	400	Both weak
Noise32	Noise	Noise	32	Both nil
VxNx	150-Hz pulse train	Noise	32	High for periodicity, nil for pitch
FxNx	*Fx* pulse train	Noise	32	Both high
Mpulses	150-Hz pulse train	150-Hz pulse train	32	Both nil

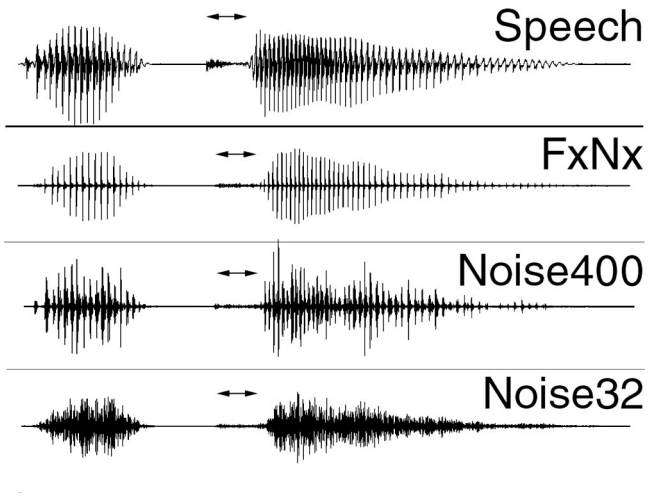

FIG. 2. Waveforms of speech input and output of band 3 from processors *FxNx*, *Noise400*, and *Noise32* for a male production of /ɑtɑ/. The arrows indicate the temporal extent of voiceless excitation in the input. The output of processor *VxNx* will differ from that of *FxNx* only in that, during voiced speech, the carrier-pulse rate is fixed at 150 Hz. The output from processor *Mpulses* will be similar to that from *Noise32*, except that the output is always periodic at a fixed rate of 150 Hz.

of the carrier are present. However, this spectral detail is unrelated to the spectral shape of the input signal. When the pulse rate is controlled by the speech fundamental frequency, this spectral detail is one source of pitch information.[3] Processors *Noise32* and *Mpulses* both eliminate temporal cues to the pitch and the periodicity of the input speech, and differ only in that the output is either always aperiodic or always periodic.

2. Voicing detection and source switching

All speech materials were accompanied by a laryngographic signal marking glottal closure. Before processing through the simulations, the raw laryngograph waveform was preprocessed to produce a single discrete pulse at each laryngeal closure. The processors took this pulse train as input in addition to the speech signal. A dc offset was added to the pulse input to ensure that it passed through zero, and a zero-crossing detector was employed to detect the pulse period. Alternate zero-crossings triggered the generation of a carrier pulse. A sample-and-hold with a 10-ms time constant was applied to the output of the zero-crossing detector and the output of this stage was used as a voicing detector. The voicing detector output, smoothed by a first-order 50-Hz low-pass filter, was used to switch between the pulse and a white-noise source. The input speech was delayed by 30 ms before the initial bandpass analysis filtering to allow accurate time alignment of the switching between the vocoder carrier signals with changing speech excitation.

B. Results of speech processing

Figure 2 shows the output of the third spectral channel of processors *FxNx*, *Noise400*, and *Noise32* for the intervocalic consonant /ɑtɑ/, together with the original speech. It illustrates the representation of fundamental frequency and periodicity in the various processed signals.

C. Speech perceptual tests

Auditory performance for segmental and connected-speech materials was measured using four standard procedures. The contributions of periodicity and pitch information conveyed by the different processors were measured by reference to performance with processor *Noise32*, which conveys neither periodicity nor pitch. With the exception of connected discourse tracking, no feedback was given.

1. Consonant identification

The consonant set contained 20 intervocalic consonants with the vowel /ɑ/. These comprised all the English consonants except for /ð,ʒ,h,ŋ/. Materials were from digital anechoic recordings presented at a 22.05-kHz sample rate and were from one female and one male talker, mixed in each test run. Both talkers had a standard Southern British English accent. Each run presented 40 consonants, with one consonant from each talker being selected at random from a set of six to ten tokens. Stimulus presentation was computer controlled. Subjects responded using the computer mouse to select one of 20 buttons on the computer screen that were orthographically labeled to represent each of the 20 consonants.

2. Vowel identification

17 b-vowel-d words from the same two talkers were used, again from digital anechoic recordings presented at a 22.05-kHz sample rate. Presentation was computer controlled. Each test run presented one token of each word from each of the two talkers, selected at random from a total set of six to ten tokens of each word from each talker. The vowel set contained ten monophthongs (in the words *bad, bard, bead, bed, bid, bird, bod, board, booed*, and *bud*) and seven diphthongs (in the words *bared, bayed, beard, bide, bode, boughed*, and *Boyd*). The spellings given here are those that appeared on the computer response buttons.

3. Sentence perception

BKB sentences from a different female talker with the same British accent were used, from an analog audio-visual recording on U-matic videotape (EPI Group, 1986; Foster *et al.*, 1993). Each test run used one list of 16 sentences with 50 scored key words per list.

4. Connected discourse tracking

Live voice connected discourse tracking (CDT: DeFilippo and Scott, 1978) was conducted by a third single female talker (author CS). In CDT, the talker wore laryngograph electrodes to provide a larynx period and voicing reference. Materials were taken from texts for students of English as a second language.

D. Pitch salience test

Pitch salience through each processor was examined by the use of tone glides. The stimuli were sawtooth waves, chosen as having a spectrum similar to that of voiced speech. Each was 500 ms in duration and had a linear fundamental frequency transition from start to end. Three fundamental

frequency ranges were included, centered around 155, 220, and 310 Hz. The start and end frequencies of the glides varied in six steps from a ratio of 1:0.5 to a ratio of 1:0.93. The test was again presented under computer control. On each trial, subjects heard a single glide, and were asked to categorize it as either ''rising'' or ''falling'' in pitch. They responded by clicking on one of two response buttons labeled with a rising or falling line. No feedback was provided. Each single administration of this test presented one rising and one falling tone at each start-to-end frequency ratio in each of the three frequency ranges, with 36 stimuli in total.

IV. PROCEDURE

Five subjects, screened for normal hearing up to 4 kHz, were recruited for the consonant, vowel, sentence, and tone glide tests. For each of these tests, six testing blocks were presented, in which each of the four tests was administered once through each of the five processors. The first two blocks were treated as practice. Because only 21 BKB lists were available, one identical BKB list was presented repeatedly for the first two practice blocks. In the final four blocks, a different BKB list was presented on every occasion.

CDT was run subsequently, with two subjects who had taken part in the earlier tests and an additional four subjects who were also screened for normal hearing. The CDT testing used only four of the five processors, with the *VxNx* processor being excluded. Each of the total of six testing sessions included 10 min of CDT with each of the four processors used. Each of these 10-min blocks was scored in two subunits of 5-min duration. Unprocessed speech was presented at the start of the first session to familiarize subjects with the task and to estimate ceiling performance rates. The order of use of the four processors was counterbalanced in a different order for each subject over the six sessions.

V. RESULTS

A. Frequency glides

Psychometric functions for labeling of glide direction as a function of start-to-end frequency ratio are shown in Fig. 3. For processor *FxNx*, performance for all the glide stimuli was at very high levels, as would be expected given the direct representation of the signal frequency in the carrier signal. Even with the smallest start-to-end frequency ratio of 1:0.93, scores were around 90% correct. Both modulated-noise processors allowed a limited identification of the direction of pitch glides. Performance with processor *Noise400* was above 75% correct for ratios of 1:0.66 and larger. Performance with processor *Noise32* was poorer than with *Noise400*, but better than that shown by the fixed-frequency pulse processors *Mpulses* and *VxNx*. For these, performance was close to chance as would be expected. The above-chance performance with processors *VxNx* and *Mpulses* at the largest frequency ratios, and the somewhat higher level of performance with *Noise32*, can only be attributed to spectral envelope differences that arise as harmonics of the input signal shift between processor bands, since the 32-Hz envelope bandwidth of these processors cannot encode fundamental frequency.

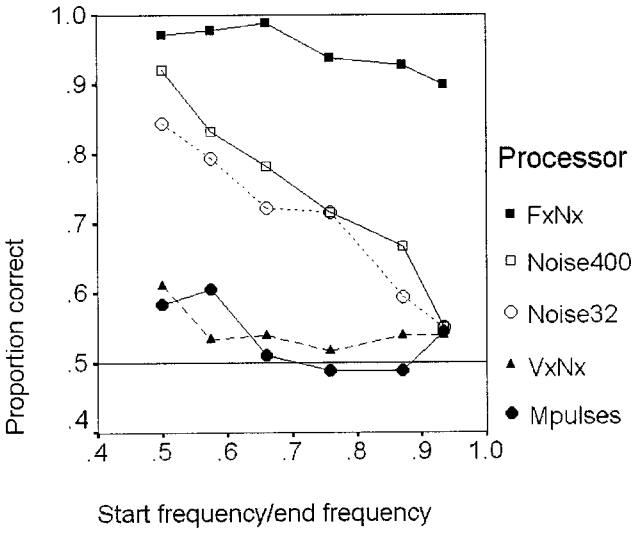

FIG. 3. Performance in labeling processed sawtooth wave frequency glides as a function of the ratio of the start and end frequencies (ignoring glide direction). Each point shows a mean score over four test sessions from 15 samples over the 3 frequency ranges and the 5 subjects. Chance performance is 50% correct.

Psychometric functions for the proportion of ''fall'' responses as a function of the log(base 10) of the start-to-end frequency ratio were estimated using a logistic regression applied to the group data. The resulting slope estimates and their 95%-confidence limits are shown in Fig. 4. The slope for processor *FxNx* is substantially steeper than that in all other conditions. The slope for the 400-Hz envelope bandwidth noise-carrier processor *Noise400* is slightly but significantly steeper than that for the *Noise32* processor. Slopes for the two fixed-period pulse processors *Mpulses* and *VxNx* are close to zero.

B. Vowel identification

Box and whisker plots of the group data with each processor are shown in Fig. 5. Scores were around 50% correct in all conditions. A repeated-measures analysis of variance

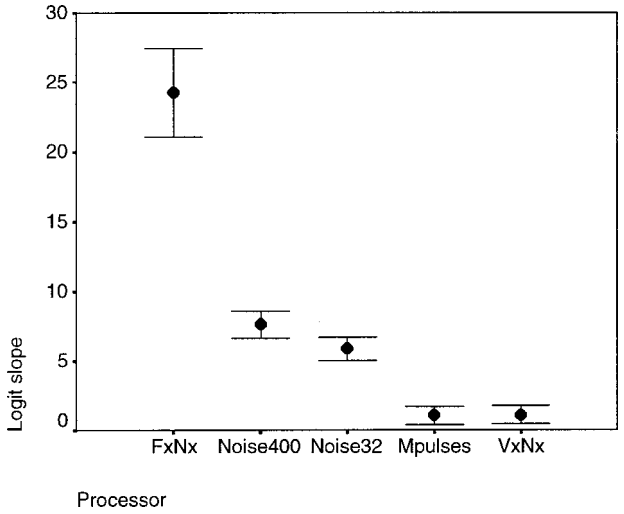

FIG. 4. Slopes of the psychometric functions estimated from a logistic regression of the proportion of ''fall'' responses as a function of the log(base 10) of the start-to-end frequency ratio. Error bars are 95%-confidence limits.

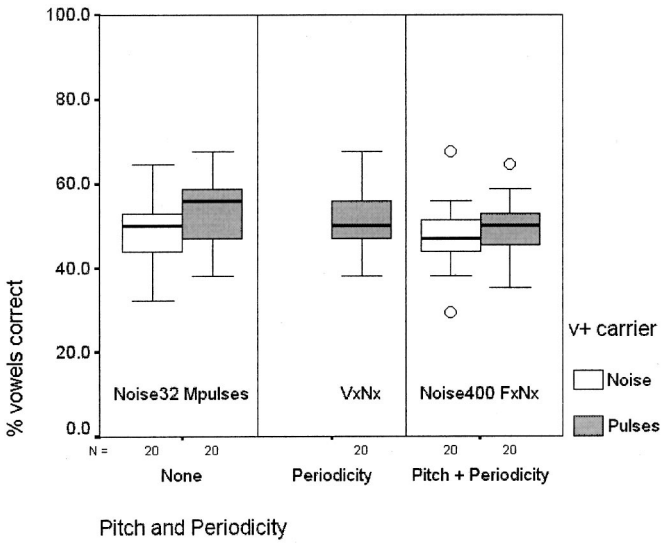

FIG. 5. Box and whisker plots showing percentage-correct vowel identification in the processor conditions. The legend ''v+ carrier'' indicates the carrier signal for voiced speech. Boxes represent the 25 to 75 percentile ranges of the data (over subjects, talker, and test run). In this and subsequent box and whisker plots, the bar within each box is the median. The whiskers show the range of scores excluding any outlying points that are more than 1.5 box widths from the box edge. Outliers are shown as open circles, or as asterisks for points more than 3 box widths from the box edge.

(ANOVA) was carried out on data from the last four test sessions, using factors of processor, talker, and test session. The only significant effect was that of test session [$F(3,12) = 14.34$, $p < 0.001$, power$=0.998$].[4] Although all processors delivered equivalent representations of the slowly changing spectral structure of vowels, processors that signaled voice fundamental frequency and hence speaker sex might have been expected to show higher performance. This was not, however, the case. Performance with these four-channel processors was comparable to that found for a processor similar to *Noise400* in a previous study using the same vowel set from the female talker only (Rosen *et al.*, 1999).

C. Intervocalic consonants

1. Overall accuracy

Group results are shown in Fig. 6. A repeated-measures ANOVA of overall accuracy was carried out using factors of processor, talker, and test session. Here, there was no effect of test session, nor were there any significant interactions between any factors. A significant effect of talker [$F(1,4) = 43.9$, $p = 0.003$, $\eta^2 = 0.916$, power$=0.997$][5] indicated higher scores for the female speech used here. There was a significant effect of processor [$F(4,16) = 5.66$, $p = 0.005$, power$=0.926$]. *A priori* contrasts comparing each processor to *Noise32* showed significantly higher scores for processor *Noise400* than for this reference condition ($p = 0.025$, $\eta^2 = 0.754$, power$=0.746$). Hence, the use of a 400-Hz rather than a 32-Hz envelope bandwidth to modulate purely noise carriers increased performance. No other processor differed significantly from the reference, nor were other pairwise differences significant according to Bonferroni-corrected *post hoc* tests.

2. Consonant feature information

A second series of ANOVAs was performed on information transfer measures (Miller and Nicely, 1955) computed from confusion matrices summed over the last four test sessions. A summary of these ANOVAs is presented in Table II. The data are displayed in Fig. 7.

A more salient representation of periodic and aperiodic excitation would be expected to lead to improved identification of manner and voicing features (Faulkner *et al.*, 1989; Faulkner and Rosen, 1999). *A priori* comparisons of voicing information transmission with the reference condition *Noise32* showed significant differences for all four of the

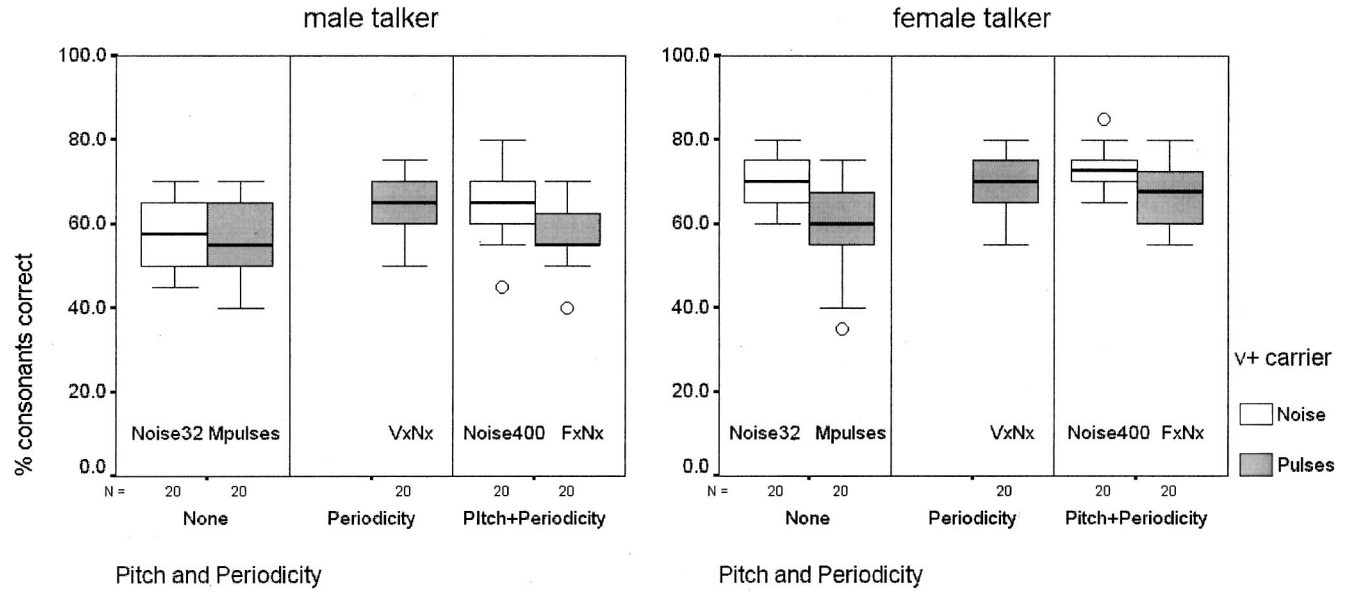

FIG. 6. Box and whisker plot showing percentage-correct consonant identification for each talker using the five processors. The box plots show the distribution of scores over subject and test run.

TABLE II. Summary of repeated-measures ANOVAs of consonant feature information transmission (interaction terms were always nonsignificant and are not shown).

Measure	Factor	*df*	*F*	*p*	η^2	Observed power
Voicing	Processor	1.22,4.88	19.10	0.007	0.827	0.948
	Talker	1,4	9.44	0.037	0.702	0.639
Place	Processor	4,16	8.27	0.001	0.674	0.988
	Talker	1,4	28.16	0.006	0.876	0.971
Manner	Processor	4,16	2.61	0.075	0.395	0.594
	Talker	1,4	11.96	0.026	0.749	0.735

other processors (see Table III). Scores were higher than the *Noise32* reference for processors *FxNx* and *VxNx* (both signaling periodicity information though the periodicity of the carrier), and for *Noise400*, (signaling periodicity information through higher rate envelope components). For processor *Mpulses*, voicing information scores were significantly lower than with the reference. Hence, all processors that represented the presence of speech periodicity, either by an explicit coding of periodicity and aperiodicity, or through the transmission of envelope modulations in the voice periodicity range, showed higher voicing transmission than the reference. The degree of voicing information provided by the

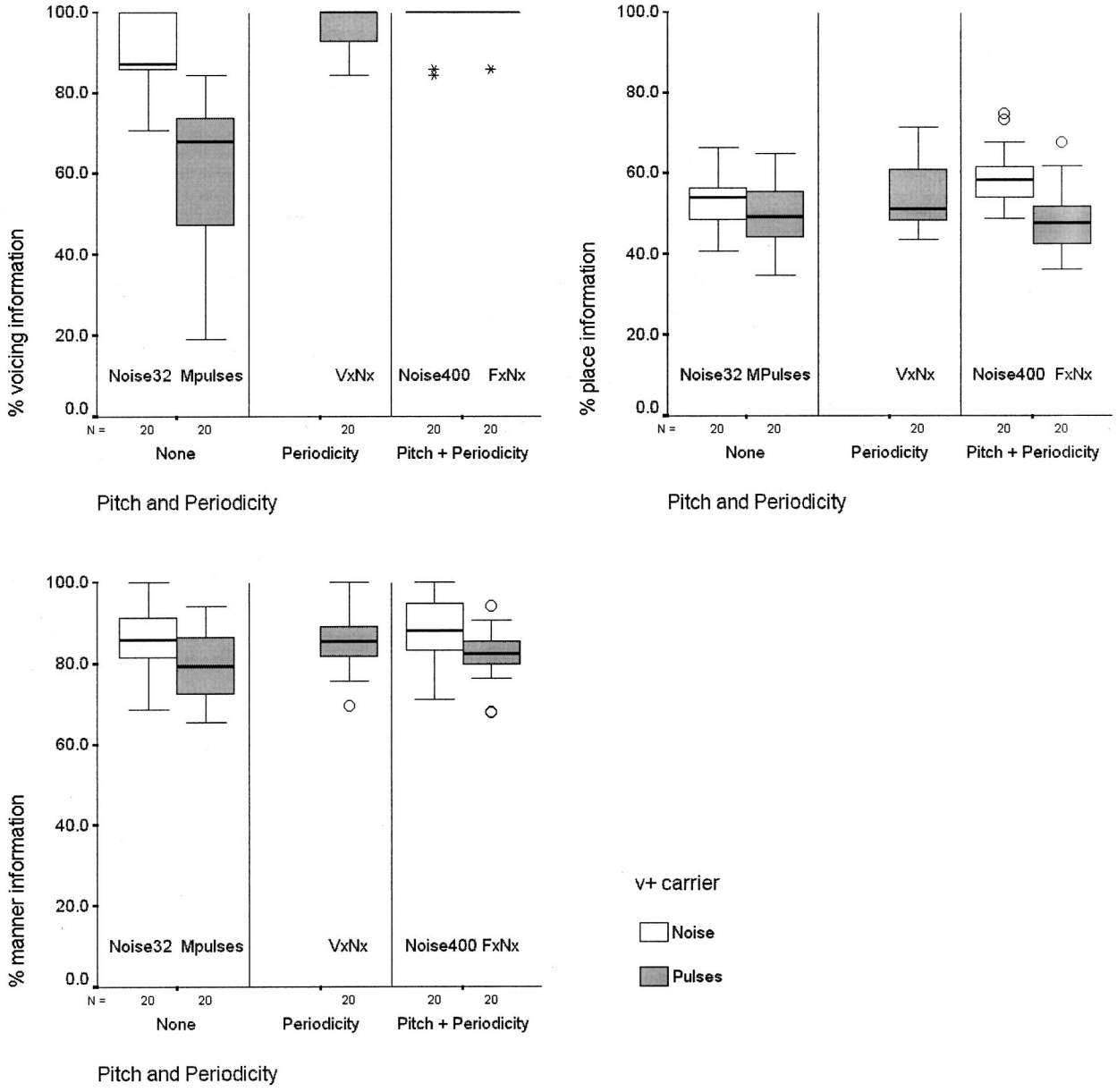

FIG. 7. Box and whisker plots of voicing, manner, and place information. The displayed data show the distribution of scores for each subject and talker.

TABLE III. Significant *a priori* contrasts against reference condition for consonant feature information. A + sign in the second column indicates scores higher than the reference, while − indicates lower scores.

Measure	Condition compared to *Noise32*	p	η^2	Observed power
Voicing	*FxNx*+	0.005	0.883	0.978
	Mpulses−	0.019	0.785	0.811
	Noise400+	0.027	0.745	0.727
	VxNx+	0.003	0.918	0.997
Place	*FxNx*−	0.008	0.854	0.944
	Noise400+	0.030	0.731	0.696

Noise32 reference is presumably based on dynamic spectral shape information. Processor *Mpulses* showed lower voicing information transmission than the *Noise32* reference while delivering identical dynamic spectral shape information carried by a constant and fixed-rate periodic carrier rather than by a noise carrier. This reduction of voicing information suggests that a carrier that is always periodic interferes with the use of spectral cues to this feature contrast.

For manner information there were no significant effects of processor, only an effect of talker, with higher scores for the female talker. This suggests that periodicity/aperiodicity is not a powerful cue for manner contrasts such as that between voiceless fricatives and voiced plosives or nasals, despite the difference in the excitation sources.

There were significant main effects of processor and talker for place information. An *a priori* comparison of processors against the *Noise32* reference showed two significant differences (Table III). Processor *Noise400* led to higher place information than the reference, while processor *FxNx* gave significantly lower scores. A Bonferroni-corrected paired comparison between processors showed only one significant pairwise difference in place information scores, this being between processors *Noise400* and *FxNx*. All processors except for *Noise400* presented equivalent spectro-

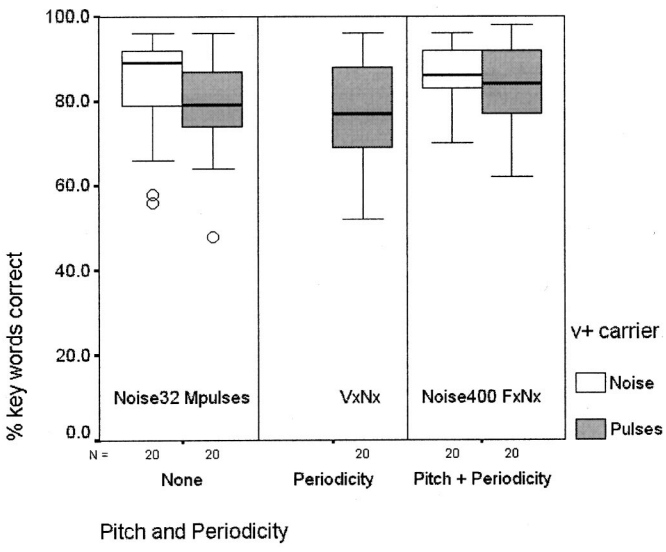

FIG. 8. Box and whisker plots of percentage of key words correctly identified from BKB sentences. Displayed data are the distribution of scores over subject and test session.

temporal information, while *Noise400* represented more rapid spectral envelope changes (resulting from the presence of envelope information above 32 and below 400 Hz) that were not present in the output of the other processors. This seems the most likely explanation for the higher place scores obtained through this processor. It is difficult to interpret the finding that place information with processor *FxNx* was lower by 7% than with the *Noise32* reference.

D. BKB sentences

Group scores using the key-word loose scoring method are shown in Fig. 8. Scores were similar in all conditions. Scores were rather high for a four-channel processor compared to another study that used the same materials and a processor similar to the *Noise400* condition (Rosen, Faulkner, and Wilkinson, 1999), and may be limited by ceiling effects. A repeated-measures ANOVA using factors of processor and test session was performed. There was no significant effect of test session. There was a significant main effect of processor [$F(0.128,0.009)=5.449$, $p=0.014$, power=0.825]. *A priori* contrasts showed no significant differences compared to the *Noise32* reference. Bonferroni-corrected paired comparisons between all five processors showed only one pairwise difference, this being between the highest-scoring processor *Noise400* and the lowest, *VxNx*.

E. Connected discourse tracking

Tracking rates through the four processors used for CDT (see Fig. 9) were all significantly lower than that with unprocessed speech (the *VxNx* processor was not used here). A repeated-measures ANOVA was applied to CDT rates over the last four 10-min testing blocks with each processor, excluding the unprocessed speech condition. This showed a significant effect of block [$F(1.96,9.78)=8.22$, $p=0.008$, power=0.875]. Block did not interact with any other factor. An *a priori* contrast with the reference processor *Noise32* showed that rates through processor *Noise400* were significantly higher than rates obtained from the reference ($p=0.003$, $\eta^2=0.845$, power=0.983). Only this pairwise difference between processors was significant in *posthoc* Bonferroni comparisons.

That the noise-carrier processors showed a significant effect of the envelope filter cutoff suggests that speech-derived pitch and periodicity cues may increase the ease and rate of speech communication. However, this explanation would also require that rates through processor *FxNx* (where the carrier conveys voice fundamental frequency) should exceed those through the fixed-pulse rate processor *Mpulses*. This, however, was not the case. It is concluded, therefore, that the difference between CDT rates through the *Noise400* and *Noise32* processors is due to the signaling of more rapid spectral changes by processor *Noise400* rather than to the presence of pitch and periodicity cues.

VI. DISCUSSION AND CONCLUSIONS

A. Salience of pitch and periodicity information across processors

Results from the frequency-glide labeling task confirm that processors differed in the salience of pitch information.

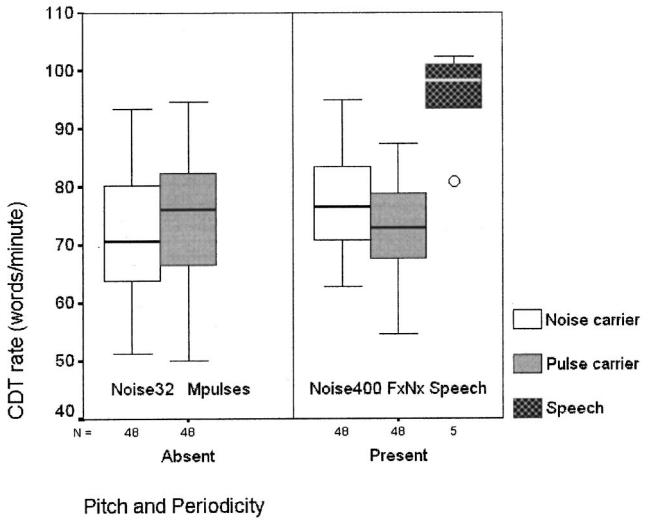

FIG. 9. Box and whisker plots of CDT rates (over subject and test session) for four processors and for unprocessed speech. The carrier used for voiced speech is indicated by box color. Data for speech are missing for one subject.

It can be assumed that temporal cues to speech periodicity/aperiodicity will have the same relative salience as those to voice pitch information across processors, since periodicity information necessarily resides in the same modulation frequency range as voice pitch.

The noise-carrier processors permitted relatively poor discrimination of pitch glide direction compared to a pulse train, as would be expected from previous studies of pitch percepts from amplitude-modulated noise. Even when the noise was modulated by an envelope having a 32-Hz envelope, discrimination of pitch glide direction was above chance performance. This is attributed to spectral envelope shifts that arise as harmonics of the input to the processor shift from one analysis band to the next. It seems unlikely, however, that with a signal such as speech, whose spectrum is constantly changing, there exist spectral shifts that are sufficiently well correlated with fundamental frequency to signal voice pitch change in the absence of more salient temporal cues or of resolved harmonic components.

Processors *Noise32*, and *Mpulses* differed only in the use of a noise compared to a pulsatile carrier, and apart from the random nature of the noise carrier, they conveyed identical spectral and temporal information, with temporal cues to pitch variation in the input signal being negligible. However, scores from processor *Mpulses* were significantly lower than from processor *Noise32* for the frequency-glide task. This suggests that a carrier with a strongly salient and constant pitch may in some way ''mask'' input-related pitch cues carried in the spectral information provided by the processor.

B. The role of pitch variation signaled by simulated processors

The processor with an *Fx*-controlled pulse rate never led to significantly higher speech scores than the noise-carrier processors carrying modulation up to 400 Hz. Despite the limited salience of informative pitch variation, we therefore conclude that 400 Hz envelope modulated noise carriers are adequate in this respect for the simulation of cochlear implant processors for speech intelligibility tasks such as those used here. Conversely, the limited sensitivity of any of the speech measures here to variations of pitch salience may signal the inadequacy of all of these measures for evaluating the availability to a listener of the full range of significant acoustic factors in speech perception.

Processors *FxNx* and *VxNx*, varying purely in the representation of informative pitch information, showed no significant differences in vowel, consonant, or sentence identification, indicating that with these tasks, pitch variation has no significance in the presence of spectral information. These two processors were not compared in CDT. However, there were no significant differences in CDT rate between the *FxNx* and *Mpulses* processors, indicating that neither pitch variation nor the periodic/aperiodic contrast contributed substantially in this task.

C. Consonant feature information from periodic and aperiodic carriers

The representation of periodicity and aperiodicity in the carrier signals does have a measurable effect on the transmission of consonant voicing. Compared to processor *Noise32*, consonant voicing information was significantly higher for processors that signaled the presence of periodicity in speech, whether through a change in the carrier's periodicity (*FxNx* and *VxNx*) or through noise-carrier modulations in the *Fx* range (*Noise400*). This outcome is consistent with a recently reported trend towards higher voicing information transmission in cochlear implant users as envelope bandwidths were increased from 40 to 320 and to 640 Hz (Fu and Shannon, 2000). Fu and Shannon also reported no effect of increasing the envelope bandwidth from 20 up to 640 Hz on overall or feature level consonant identification in simulations with normal listeners. However, the present data do show small but significant increases in both voicing information (8.4%) and overall consonant identification (4.7%) for a 400-Hz envelope bandwidth compared to one of 32 Hz. While the higher voicing transmission from processor *Noise400* could be due to relatively rapid between-channel level changes, the increased voicing information from processors *FxNx* and *VxNx* compared to *Noise32* can only be due to the encoding of periodicity, since these three processors all have the same 32-Hz envelope bandwidth.

Voicing information from processor *Mpulses*, where the carrier was always periodic, was significantly lower than from all the other processors. Since processor *Mpulses* differed from processor *Noise32* only in the use of a fixed-rate pulse carrier rather than noise, lower voicing scores from processor *Mpulses* must be attributable to the strong and constant periodic percept of the carrier, this being unrelated to the periodicity of the input. It appears that listeners do not readily associate this percept with voiceless speech. In contrast, it seems that the constant aperiodic percept from processor *Noise32* can be interpreted as representing voiced speech.[6] That this is possible may perhaps be based on our natural experience of whispered speech.

D. Results in relation to signals lacking spectral information

In the absence of spectral information, previous studies have shown that voice pitch information contributes substantially to the audio-visual perception of sentences and CDT (e.g., Rosen *et al.*, 1981; Waldstein and Boothroyd, 1994). When, as here, there is a limited degree of spectral information present, neither sentence perception nor CDT show clear evidence of a contribution of pitch information, despite the previous findings of strong effects of pitch information when spectral cues are absent.[7]

The auditory identification of consonants from spectrally invariant auditory signals also shows a substantial contribution from input-related periodicity or aperiodicity to contrasts of manner and voicing (Faulkner and Rosen, 1999). For voicing contrasts, the same effect of periodicity is evident here. For manner contrasts, however, there is no measurable contribution of periodicity information. It seems, then, that when limited spectral structure is present, spectral balance cues are sufficient to mark those manner of articulation differences that can also be signaled by temporal cues to speech periodicity/aperiodicity.

E. The role of pitch in speech communication

The present studies are likely to substantially underestimate the contribution of pitch information to communication, especially where paralinguistic cues (e.g., to talker identity or pragmatics) are important. Furthermore, envelope-based pitch cues have been shown to contribute to Chinese sentence perception through similar processors (Fu *et al.*, 1998). The most reasonable interpretation of our findings is not that factors such as voice pitch are unimportant. Rather, we would argue that the intelligibility measures used here lack sensitivity to important aspects of speech quality. Since the speech tests used here are, with the exception of CDT, essentially the same as those almost universally used in clinical research evaluating cochlear implant benefit, it may be that conventional speech-based measures of benefit are missing aspects of speech perception that are of real importance in speech communication. Intonation is widely held to be a major factor in the development of spoken language. Hence, the role of voice pitch information in cochlear implant speech processing should not be dismissed simply because it appears to have little impact on intelligibility for adult listeners. It is entirely possible that during speech development, intonation and other prosodic factors may play a much larger role in perceptual speech processing than in the mature adult.

Finally, we note that these simulation data suggest that the use of a fixed-rate carrier signals in the voice *Fx* range (here at 150 Hz) as carriers of multiband speech envelope information may be inappropriate in speech perceptual prostheses because of the inherent periodicity and fixed-pitch percepts produced by such carriers. Compared to aperiodic carriers, or carriers signaling speech-derived periodicity and aperiodicity, the identification of consonant voicing contrasts is significantly poorer. This difficulty may not arise with the higher pulse rates that are typically used in CIS processors, but it does seem likely to limit the effectiveness of cochlear implant speech processors that use fixed-pulse rates within the voice fundamental frequency range.

ACKNOWLEDGMENTS

Supported by a Wellcome Trust Summer Vacation Scholarship to Clare Smith (Ref. No. VS/98/UCL/001) and CEC TIDE project OSCAR (No. TP 1217). We are grateful to Chris Turner, Philip Loizou, and an anonymous reviewer for helpful comments on a previous version of this paper.

[1]The modulation of sinusoidal carriers by envelopes whose bandwidths extend into the voice fundamental frequency range leads to a rather complex acoustic stimulus, due to the presence of sidebands. This results in spectral cues to pitch even though the spectra are not harmonic.

[2]Data described by Dorman *et al.* (1996) do indicate weak spectrally based pitch percepts for one user of a CIS processor when the input signals were single sine waves. For sinusoidal stimuli, the spectral envelope as represented by the processor filter bank is correlated to input fundamental frequency.

[3]The amplitude modulation of pulsatile carriers inevitably affects spectral detail through the introduction of sidebands. Since the modulating bandwidth for such carriers was limited to 32 Hz, the spectrum at each harmonic component will be only slightly broadened. Such details are not expected to be perceptually significant.

[4]Here and elsewhere, F tests on factors with $df>1$ are based on Huynh–Feldt epsilon correction factors.

[5]η^2 indicates the eta-squared statistic that represents the proportion of variability in the dependent variable due to the independent variable.

[6]A related suggestion, that a fixed rate of pulsatile electrical stimulation within the voice fundamental frequency range may ''interfere'' with envelope perception, has recently been made (Fu and Shannon, 2000).

[7]It remains possible, although rather implausible, that a contribution of pitch variation to CDT performance occurs only with audio-visual presentation.

Breeuwer, M., and Plomp, R. (**1986**). ''Speech reading supplemented with auditorily presented speech parameters,'' J. Acoust. Soc. Am. **79**, 481–499.

DeFilippo, C. L., and Scott, B. L. (**1978**). ''A method for training and evaluation of the reception of ongoing speech,'' J. Acoust. Soc. Am. **63**, 1186–1192.

Dorman, M. F., Smith, L. M., Smith, M., and Parkin, J. L. (**1996**). ''Frequency discrimination and speech recognition by patients who use the Ineraid and continuous interleaved sampling cochlear-implant signal processors,'' J. Acoust. Soc. Am. **99**, 1174–1184.

Dorman, M. F., Loizou, P. C., and Rainey, D. (**1997a**). ''Simulating the effect of cochlear-implant electrode insertion depth on speech understanding,'' J. Acoust. Soc. Am. **102**, 2993–2996.

Dorman, M. F., Loizou, P. C., and Rainey, D. (**1997b**). ''Speech intelligibility as a function of the number of channels for signal processors using sine-wave and noise-band outputs,'' J. Acoust. Soc. Am. **102**, 2403–2411.

Dudley, H. (**1939**). ''The vocoder,'' Bell Lab. Rec. **17**, 122–126.

EPI Group (**1986**). *The BKB (Bamford-Kowal-Bench) Standard Sentence Lists* [Video recordings] (Department of Phonetics and Linguistics, University College London, London).

Faulkner, A., Potter, C., Ball, G., and Rosen, S. (**1989**). ''Audiovisual speech perception of intervocalic consonants with auditory voicing and voiced/voiceless speech pattern presentation,'' Speech, Hearing and Language, Work in progress, University College London, Department of Phonetics and Linguistics **3**, 85–106.

Faulkner, A., and Rosen, S. (**1999**). ''Contributions of temporal encodings of voicing, voicelessness, fundamental frequency and amplitude variation in audio-visual and auditory speech perception,'' J. Acoust. Soc. Am. **106**, 2063–2073.

Foster, J. R., Summerfield, A. Q., Marshall, D. H., Palmer, L., Ball, V., and

Rosen, S. (**1993**). ''Lip-reading the BKB sentence lists; corrections for list and practice effects,'' Br. J. Audiol. **27**, 233–246.
Fourcin, A. J., Rosen, S. M., Moore, B. C. J., Douek, E. E., Clarke, G. P., Dodson, H., and Bannister, L. H. (**1979**). ''External electrical stimulation of the cochlea: Clinical, psychophysical, speech-perceptual and histological findings,'' Br. J. Audiol. **13**, 85–107.
Fu, Q.-J., and Shannon, R. V. (**2000**). ''Effect of stimulation rate on phoneme recognition by Nucleus-22 cochlear implant listeners,'' J. Acoust. Soc. Am. **107**, 589–597.
Fu, Q.-J., Zeng, F.-G., and Shannon, R. V. (**1998**). ''Importance of tonal envelope cues in Chinese speech recognition,'' J. Acoust. Soc. Am. **104**, 505–510.
Grant, K. W., Ardell, L. H., Kuhl, P. K., and Sparks, D. W. (**1985**). ''The contribution of fundamental frequency, amplitude envelope and voicing duration cues to speechreading in normal-hearing subjects,'' J. Acoust. Soc. Am. **77**, 671–677.
Greenwood, D. D. (**1990**). ''A cochlear frequency-position function for several species—29 years later,'' J. Acoust. Soc. Am. **87**, 2592–2605.
McDermott, H. J., and McKay, C. M. (**1997**). ''Musical pitch perception with electrical stimulation of the cochlea,'' J. Acoust. Soc. Am. **101**, 1622–1631.
Miller, G. A., and Nicely, P. E. (**1955**). ''An analysis of perceptual confusions among some English consonants,'' J. Acoust. Soc. Am. **27**, 338–352.
Pollack, I. (**1969**). ''Periodicity pitch for white noise—fact or artefact,'' J. Acoust. Soc. Am. **45**, 237–238.
Risberg, A. (**1974**). ''The importance of prosodic speech elements for the lipreader,'' Paper presented at the Visual and Audio-Visual Perception of Speech, Sixth Danavox Symposium: Scandinavian Audiology, Supplementum 4.
Risberg, A., and Lubker, J. L. (**1978**). ''Prosody and speechreading,'' Report of STL-QPSR, Dept. of Linguistics, University of Stockholm, Stockholm, Sweden, **4**, pp. 1–16.
Rosen, S., Faulkner, A., and Wilkinson, L. (**1999**). ''Perceptual adaptation by normal listeners to upward shifts of spectral information in speech and its relevance for users of cochlear implants,'' J. Acoust. Soc. Am. **106**, 3629–3636.
Rosen, S., Fourcin, A. J., and Moore, B. C. J. (**1981**). ''Voice pitch as an aid to lipreading,'' Nature (London) **291**, 150–152.
Shannon, R. V., Zeng, F.-G., Kamath, V., Wygonski, J., and Ekelid, M. (**1995**). ''Speech recognition with primarily temporal cues,'' Science **270**, 303–304.
Shannon, R. V., Zeng, F.-G., and Wygonski, J. (**1998**). ''Speech recognition with altered spectral distribution of envelope cues,'' J. Acoust. Soc. Am. **104**, 2467–2476.
Waldstein, R. S., and Boothroyd, A. (**1994**). ''Speechreading enhancement using a sinusoidal substitute for voice fundamental frequency,'' Speech Commun. **14**, 303–312.
Wilson, B., Finley, C., Lawson, D., Wolford, R., Eddington, D., and Rabinowitz, W. (**1991**). ''Better speech recognition with cochlear implants,'' Nature (London) **352**, 2.
Wilson, B., Zerbi, M., Finley, C., Lawson, D., and van den Honert, C. (**1997**). Eighth Quarterly Progress Report, 1 May through 31 July 1997. NIH Project N01-DC-5-2103: Speech Processors for Auditory Prostheses: Research Triangle Institute.

Localization of multiple sound sources with two microphones[a)]

Chen Liu,[b)] Bruce C. Wheeler, William D. O'Brien, Jr., Robert C. Bilger, Charissa R. Lansing, and Albert S. Feng

Beckman Institute for Advanced Science and Technology, University of Illinois at Urbana-Champaign, Urbana, Illinois 61801

(Received 10 July 1998; revised 20 July 1999; revised 22 April 2000; accepted 28 June 2000)

This paper presents a two-microphone technique for localization of multiple sound sources. Its fundamental structure is adopted from a binaural signal-processing scheme employed in biological systems for the localization of sources using interaural time differences (ITD). The two input signals are transformed to the frequency domain and analyzed for coincidences along left/right-channel delay-line pairs. The coincidence information is enhanced by a nonlinear operation followed by a temporal integration. The azimuths of the sound sources are estimated by integrating the coincidence locations across the broadband of frequencies in speech signals (the ''direct'' method). Further improvement is achieved by using a novel ''stencil'' filter pattern recognition procedure. This includes coincidences due to phase delays of greater than 2π, which are generally regarded as ambiguous information. It is demonstrated that the stencil method can greatly enhance localization of lateral sources over the direct method. Also discussed and analyzed are two limitations involved in both methods, namely missed and artifactual sound sources. Anechoic chamber tests as well as computer simulation experiments showed that the signal-processing system generally worked well in detecting the spatial azimuths of four or six simultaneously competing sound sources. © *2000 Acoustical Society of America.* [S0001-4966(00)04110-2]

PACS numbers: 43.72.Ew, 43.66.Qp, 43.66.Ts [JLH]

I. INTRODUCTION

Localization of multiple sound sources is regarded as a challenging task, especially when the signals have overlapping spectra. Yet this capacity is important for the ability to extract signals in acoustically cluttered environments. A variety of signal-processing algorithms has been proposed to attack this problem, most of which revolve around the principle of creating a highly directional receiving system for enhanced detection of signals within a small sector of space, as used in different engineering applications (e.g., sonar systems). The dominant approach is the beamforming technique using an array of spatially distributed microphones (Flanagan *et al.*, 1985). A caveat of the microphone array system is that a relatively large array size and a large number of sensors are required in order to obtain a high degree of spatial selectivity. Furthermore, because one beamformer can only localize one source, multiple systems are necessary to localize different sources simultaneously.

An alternative to the array signal-processing approach is suggested by the neural computational mechanism in biological systems (Cherry, 1953; Bronkhorst and Plomp, 1992). It is well known that human beings as well as other living organisms can communicate effectively by sound in noisy and reverberant environments, in large part due to the advantage of directional hearing conferred by a binaural system (for a review, see Blauert, 1983). A binaural system can effectively compute interaural differences in time and intensity, thereby making it possible to accurately determine the directions of sound sources. Numerous binaural models have been advanced over the last half-century (see reviews by Colburn and Durlach, 1978; Colburn, 1996; and Stern and Trahiotis, 1995, 1997). Of these, the model by Jeffress (1948) has been validated anatomically and physiologically (Konishi *et al.*, 1988; Takahashi and Keller, 1994; Yin and Chan, 1990). Essentially, the Jeffress model involves the creation of a spatial map in the nervous system, i.e., the location of a sound in space is represented by the interaural time difference and the latter is determined by the location of signal coincidence along a dual delay-line neural network.

For the past two decades, the Jeffress model has been incorporated into auditory processors for localization of sound sources (e.g., Colburn, 1973, 1977; Blauert, 1980; Lindemann, 1986; Shamma *et al.*, 1989; Stern and Trahiotis, 1992; Gaik, 1993; Bodden, 1993; Banks, 1993). These processors produce satisfactory results for the localization of two sources but the performance degrades significantly when the signals are speech sounds and the number of sources is greater. In contrast, humans can localize as many as six concurrent sources, if not more (Bronkhorst and Plomp, 1992).

In this paper, we describe a two-microphone signal-processing system based on the Jeffress model capable of detecting and localizing a large number of sound sources in the ambient environment. Two major features of our system are utilization of: (1) a nonlinear procedure for determining the source locations, and (2) the intermicrophone time difference (ITD) information over the *entire* frequency broadband, including phase-ambiguous information at high frequencies. Anechoic chamber tests as well as computer simulation tests showed that four or six speakers could be satisfactorily detected and localized simultaneously. In the next section, we-

[a)]Portions of this paper were presented at the Hearing Aid Research & Development Conference, Bethesda, MD, Sept. 1997.

[b)]Present address: Motorola Labs, 55 Shuman Boulevard, Naperville, IL 60563.

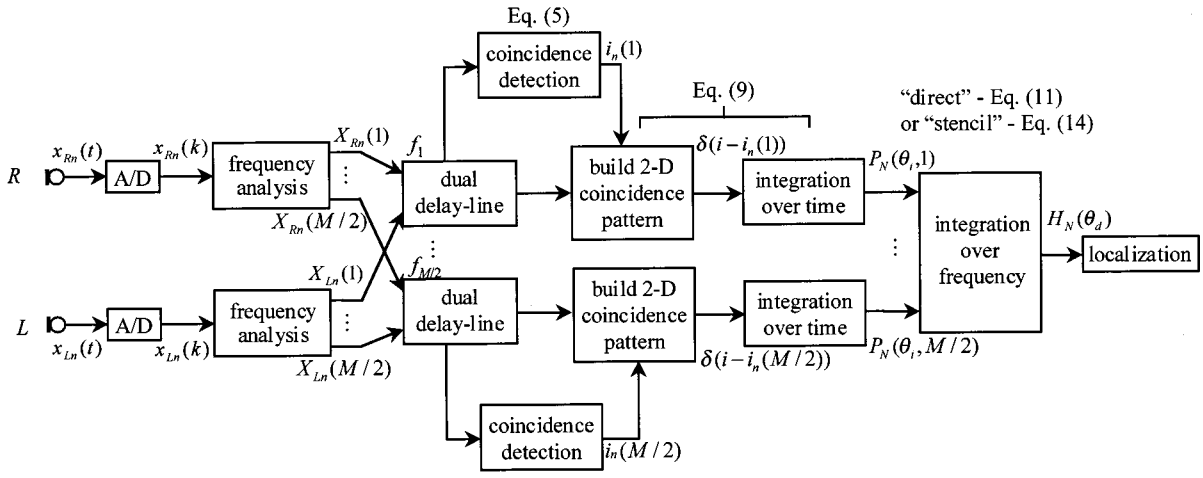

FIG. 1. Block diagram of the broadband localization system.

describe the dual delay-line structure as well as the coincidence detection method. In Sec. III, we describe a ''direct'' broadband computational scheme, operating in the frequency domain, for identifying the ITD information along the dual delay line. In Sec. IV, we describe how the performance of the ''direct'' method can be further improved by using a ''stencil'' filter that exploits both the unambiguous as well as the ambiguous ITD information (i.e., phase delays of greater than 2π). The results of experiments and discussions as well as analyses of limitations of the two methods are given in the final section.

II. NARROWBAND LOCALIZATION

A. Dual delay-line structure

The schematic diagram of the signal processing system is shown in Fig. 1. The system assumes two inputs, $x_{Ln}(t)$ and $x_{Rn}(t)$, supplied by two identical omnidirectional microphones. Signal processing is performed in the digital frequency domain, using separate A/D converters. Digitized signals are denoted by $x_{Ln}(k)$ and $x_{Rn}(k)$. The subscripts L and R represent the left and right channels, respectively, and the index n refers to the nth time frame of the short-term Fourier transform. Once digitized, the signals are decomposed using the short-term Fourier transform into $X_{Ln}(m)$ and $X_{Rn}(m)$, $m=1,...,M/2$; the corresponding discrete frequencies are $f_m=mf_s/M$, where f_s is the sampling rate.

A ''dual delay-line'' network (Jeffress, 1948) is used for determining the directions of sound sources. For each frequency, the complex signals $X_{Ln}(m)$ and $X_{Rn}(m)$ from the two channels are fed into a pair of delay lines consisting of an odd number of delay units (Fig. 2). The values τ_i $(i=1,...,I)$ of the time delays are assigned *a priori* such that the acoustic space in front of the two microphones is divided uniformly into I sectors in azimuth, and each sector is uniquely mapped to one specific location in the dual delay line. Thus, if we assume there is no acoustic shadowing effect between the two microphones, the value of the delay units may be derived from

$$\tau_i=\frac{\mathrm{ITD}_{\max}}{2}\sin\left(\frac{i-1}{I-1}\pi-\frac{\pi}{2}\right),\quad i=1,...,I, \tag{1}$$

where $\mathrm{ITD}_{\max}$, which equals D/c, is the maximum intermicrophone time difference, D is the distance between the two microphones, and c is the speed of sound. The two delay lines delay the signals received by the left and right microphones separately, with progressively longer delays as they propagate through the delay lines. The midpoint of the dual delay line therefore corresponds to an ITD of zero, i.e., to a source located in the midplane. In other words, for a source located directly ahead of the microphones, coincidence of

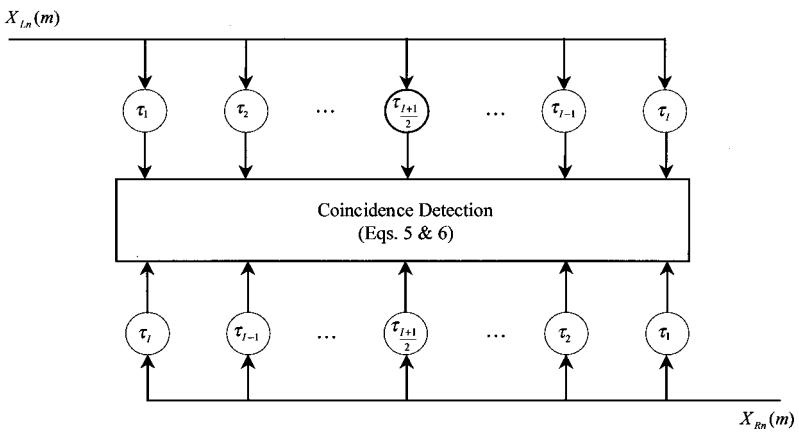

FIG. 2. The dual delay-line structure for narrow-band coincidence detection.

signals from the two microphones takes place in the middle of the dual delay line. A source located in the lateral sound field corresponds to nonzero ITD and thus will be represented on one side of the dual delay line. For example, when an acoustic signal emanates from an azimuth on the right side of the system, coincidence of signals will occur at a location on the left side of the dual delay line (i.e., the signals from the left and right microphones are in phase at this location). It is noted that to maintain symmetry in presenting the theory, Eq. (1) is given in the form of a noncausal structure, namely, the values of delay τ_i ($i=1,...,I$) can be negative. Shifting the input signals by $\mathrm{ITD}_{\max}/2$ makes the structure causal. If we replace the index i (namely, the location along the dual delay line) with the corresponding spatial azimuth θ_i (i.e., the signals in the two channels corresponding to a source at azimuth θ_i have a zero phase difference at location i in the dual delay line), Eq. (1) can be expressed as

$$\tau_i = -\frac{\mathrm{ITD}_{\max}}{2}\sin\theta_i, \tag{2}$$

where

$$\theta_i = \frac{\pi}{2} - \frac{i-1}{I-1}\pi, \quad i=1,...,I. \tag{3}$$

The intermicrophone time difference ITD_i of the source located at azimuth θ_i equals

$$\mathrm{ITD}_i = -(\tau_i - \tau_{I-i+1}) = -[\tau_i - (-\tau_i)] = -2\tau_i, \quad i=1,...,I, \tag{4}$$

where the relationship $\tau_{I-i+1} = -\tau_i$ follows from Eq. (1), and $\mathrm{ITD}_i > 0$ (or $\theta_i > 0$) corresponds to the situation when the source is on the right-hand side of the midline of the microphones. Due to the one-to-one mapping relationship, the parameters i, τ_i, θ_i, and ITD_i are used equivalently in this paper for representing the location in the dual delay line as well as the corresponding azimuth.

B. Coincidence detection

Perhaps the simplest method for finding coincidence locations is to find the point in the delay line at which there is a minimum in the magnitude of the difference between the two channel signals. It is analogous to the operational principle of a pressure-gradient receiver in biological systems (Feng and Shofner, 1981). We choose to find the minimum magnitude $\Delta X_n^{(i)}(m)$ of the difference between the frequency domain representations $X_{Ln}^{(i)}(m)$ and $X_{Rn}^{(i)}(m)$ at each discrete frequency m, yielding $M/2$ potentially different locations. If a spatially coherent source is present, all $M/2$ locations will be consistent across frequency. This operation is described in Eqs. (5)–(8). Thus,

$$i_n(m) = \arg\min_i [\Delta X_n^{(i)}(m)], \quad m=1,...,M/2, \tag{5}$$

where

$$\Delta X_n^{(i)}(m) = |X_{Ln}^{(i)}(m) - X_{Rn}^{(i)}(m)|, \quad i=1,...,I; \ \ m=1,...,M/2, \tag{6}$$

$$X_{Ln}^{(i)}(m) = X_{Ln}(m)\exp(-j2\pi f_m \tau_i), \quad i=1,...,I; \ \ m=1,...,M/2, \tag{7}$$

$$X_{Rn}^{(i)}(m) = X_{Rn}(m)\exp(-j2\pi f_m \tau_{I-i+1}), \quad i=1,...,I; \ \ m=1,...,M/2. \tag{8}$$

When the amplitudes of the two channel signals are identical, the value of $\Delta X_n^{(i)}(m)$ at the coincidence location is equal to zero. In practice, however, there is an intermicrophone intensity difference. Nonetheless, the two channel signals will still be in phase at the same point and the value of $\Delta X_n^{(i)}(m)$, although nonzero, is minimal at this point. Thus, the existence of the intermicrophone intensity difference does not affect the determination of the narrow-band coincidence location. Intensity equalization is unnecessary for the purpose of coincidence detection; its incorporation in fact will offset the space map on the delay line.

A number of methods are available for identifying the in-phase or coincidence point in the dual delay line. For example, Bodden (1993) used a cross-correlation method by computing a running integration on the 24 critical bands in the time domain. However, since our signals have already been transformed to the frequency domain it is computationally efficient to simply perform the subtractions in Eq. (6) and to look for minima using Eq. (5). On a frequency-by-frequency basis, the point of minimum magnitude of difference between two channels is the same as the point of minimum phase difference. As mentioned earlier, this calculation is robust against intermicrophone intensity differences. As described next, this technique gives us the ability to estimate azimuth by integrating the coincidence locations.

III. LOCALIZATION USING THE "PRIMARY" CONTOUR (THE "DIRECT" METHOD)

A. Spectral integration

Our coincidence detection method described in the preceding section can be viewed as a narrow-band operation because it is performed for each frequency. When there is one source and the signal $x_n(k)$ is broadband, the direction of the source estimated based on the frequency component f_m in the nth time frame corresponds to the coincidence location $i_n(m)$, which satisfies Eq. (5). However, where there are multiple sources emitting spectrally overlapping sounds, interactions between sources in the nth time frame may lead to coincidences corresponding to phantom sources (e.g., at the midpoint between two identical sources). To overcome this problem, we integrate coincidence locations over both time (described later) and frequency. Our strategy takes advantage of the following facts: (a) normal conversation includes a large number of pauses (Flanagan, 1972, p. 386) which provide opportunities for competing sounds to be detected, and (b) when several independent sources emit sounds simultaneously, usually one can find frequency bins which are dominated by one source. Banks (1993) implicitly used a similar assumption for localization of two sound sources.

The broadband coincidence detection developed here assumes that the intermicrophone time delay is independent of

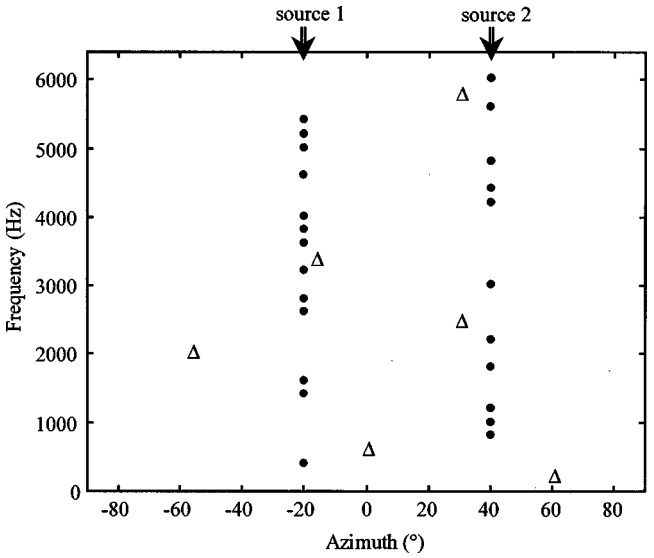

FIG. 3. A schematic depiction of the instantaneous 2D coincidence pattern illustrating the typical pattern of narrow-band coincidence detection and the effect of interaction between two sources using the direct method. Filled circles are data points showing correct localization. Data points associated with phantom detection are shown in open triangles. Note that the high-frequency ambiguity is neglected here.

frequency. When the two microphones are mounted on a structure where there is little diffraction, this assumption is satisfied. The importance of the consistency of the interaural timing information across frequency in the lateralization of broadband binaural stimuli was previously indicated and exploited in the model of Stern and Trahiotis (1992). However, if the diffraction is not negligible (such as due to head shadowing), the delay is not completely independent of frequency (Durlach and Colburn, 1978; Blauert, 1983). Therefore, care in this regard should be taken in implementation.

The logical basis for the ''direct'' broadband integration is illustrated in a schematic figure in Fig. 3, wherein the locations of coincidence are plotted against the signal frequency (y axis) and azimuth (x axis) for a two-source stimulus arrangement. The graph suggests that there are two sources plus some misidentified locations at frequencies where both sources have significant energy. Obviously, by integrating the coincidence pattern across frequency we are able to gain more robust and reliable estimates of the locations of real sources. Previously, Banks (1993) adopted an image processing technique for detecting short vertical straight segments, which, however, restricts the binaural information to a narrow spectral band of the signal. In contrast, our localization algorithm utilizes the ITD information throughout the entire spectral band. Localization based on broadband coincidence detection has also been demonstrated neurophysiologically in barn owls (Takahashi and Keller, 1994).

Our method accumulates the locations of coincidence, not the value of the function used to determine the minima. This is equivalent to applying a Kronecker delta function, $\delta(i-i_n(m))$, to $\Delta X_n^{(i)}(m)$ in Eq. (6) prior to the integration across frequency. This enhances the expression of coincidence location in the 2D pattern for each frequency f_m. An alternative way of representing the localization results with impulses can be formulated by incorporating an idea from Colburn's model (Colburn, 1977; Colburn *et al.*, 1990). In Colburn's localization model, the input signals are transformed into trains of impulses simulating the firing of neural spikes prior to coincidence detection.

B. Temporal integration

Integration over time is achieved by the use of a forgetting average of the instantaneous 2D coincidence patterns (such as the example in Fig. 3) acquired over the preceding set of time frames. When the signals are not correlated at each frequency, mutual interference between signals can be gradually attenuated by temporal integration. The interaction between sources as well as the effect of temporal integration will be illustrated with an example in the next section.

C. Algorithm

Our computational strategy, including both temporal and spectral integrations, is as follows:

(a) The instantaneous 2D coincidence patterns at each frequency f_m are integrated over time

$$P_N(\theta_i,m)=\sum_{n=1}^{N}\beta^{N-n}\delta(i-i_n(m)),$$

$$i=1,...,I;\quad m=1,...,M/2, \tag{9}$$

where β, restricted to be between 0 and 1, is a weighting coefficient which exponentially de-emphasizes (or forgets) the effect of previous coincidence results, $\delta(\cdot)$ is the Kronecker delta function, i represents the location in the dual delay line corresponding to spatial azimuth θ_i [Eq. (3)], and N refers to the current time frame. We chose β in the range of 0.85–0.99 for our tests. A smaller value of β takes insufficient advantage of spatial information in past coincidence patterns, while a larger value, by overemphasizing past patterns, may make the system less sensitive to source dynamics such as onset, offset, or movement. Thus, one can choose an optimum value for β, trading off localization enhancement for higher sensitivity to the source movement. We let $\beta=0.98$ in our following experiments, in which all the sources were stationary.

(b) The temporally integrated coincidence pattern $P_N(\theta_i,m)$ is then thresholded so as to eliminate the majority of spurious coincidence detections

$$P_N(\theta_i,m)=\begin{cases}P_N(\theta_i,m), & P_N(\theta_i,m)\geqslant\Gamma\\ 0, & \text{otherwise}\end{cases}. \tag{10}$$

Here Γ is set greater than or equal to zero. A greater value of Γ can remove phantom coincidences that last longer. In our tests, we set $\Gamma=1$, which removed the phantom coincidences lasting for one time frame only.

(c) In the ''direct'' method the temporally integrated and thresholded coincidence patterns are integrated over frequency

$$H_N(\theta_d)=\sum_m P_N(\theta_d,m),\quad d=1,...,I. \tag{11}$$

Formally, the integration is conducted along the primary contour (a vertical line for each azimuthal angle as suggested in Fig. 3). In the next section the contour is extended to account for phase ambiguity at high frequencies.

Ideally, the peaks in $H_N(\theta_d)$ occur at the azimuthal angles at which the sound sources are located. Other peaks may be due to noise or due to interaction of multiple sources. The former generally gives rise to peaks that are significantly higher than the latter after broadband integration. Hence, a simple clustering of the peaks of $H_N(\theta_d)$ by height into two groups can extract the peaks corresponding to the real sources. First, we derive the envelope of $H_N(\theta_d)$ by applying a low-pass filter on the function. Then, all the local minima of the envelope are located. The local maximum of $H_N(\theta_d)$ between each adjacent pair of minima is determined as a valid peak. (In our implementation the low-pass filter cutoff was defined as 1/32 with 1 corresponding to half the sample rate.) In comparison with the narrow-band localization, the broadband localization not only enhances the accuracy of localization, it also enables localization of multiple sources.

The low and high frequencies play complementary roles in the broadband localization. First, the estimation of coincidence locations is more accurate at high frequencies, which produces more consistent peaks in the 3D coincidence pattern, and eventually narrower and sharper peaks after spectral integration. The estimation error at low frequencies will result in a wide spread of response peaks, thereby producing broader and lower peaks after spectral integration. The reason for this estimation error will be discussed in detail in Sec. V B 1. Second, high-frequency components in speech (mostly from consonants) occupy a smaller proportion of time when compared to the low-frequency sounds (mostly from vowels) and hence are much less likely to coincide temporally in normal conversation. However, because lower-frequency sounds (vowels) occupy a larger proportion of time in conversation (Flanagan, 1972), a localization scheme based solely on high-frequency components may not work all the time. Hence, the broadband scheme confers the advantages of both the low- and high-frequency components, with the low-frequency information providing the estimate of source localization most of the time and the high-frequency information enhancing the accuracy of localization.

The energy information is removed prior to spectral integration [Eq. (9)]. Therefore, the height of a peak in $H_N(\theta_d)$ only indirectly reflects the energy of a sound; instead, it is influenced by factors such as the energy of the signal relative to the energy of the other signals in each frequency bin, and the number of frequency bins as well as the duration over which the signal is dominant. Since each frequency bin contributes equally in the broadband integration (in contrast to time-domain correlation algorithms), high-energy signals are less likely to mask low-energy signals, especially if they occupy distinct frequency bands during at least part of the integration time. However, the drawback is that very narrow-band and short-duration signals could be missed.

Our method has the potential to localize sound sources dynamically as they move in space, although we have not tested this capability. Movement trajectories could be estimated from the sets of locations computed at each time window, e.g., every 5 ms in our tests.

IV. LOCALIZATION WITH THE ''STENCIL'' FILTER

A. High-frequency ambiguity

In practice, when the entire band is exploited for localization, the 3D coincidence pattern is not as simple as the vertical straight traces shown in Fig. 3 because for high frequencies there is *no* one-to-one map of auditory space using time or phase cues. For mammals including humans, it has been postulated (Mills, 1972; Gourevitch, 1987) that localization of sound azimuth depends on two cues: interaural time differences at low frequencies, and interaural intensity differences at high frequencies. The primary argument is the fact that the interaural time difference is ambiguous for high-frequency sounds because the wavelengths are shorter than the separation between the two ears.

Figure 4(A) illustrates a theoretical broadband coincidence pattern $P_N(\theta_i, m)$ calculated by using the coincidence detection [Eqs. (5)–(8)], for an intermicrophone distance of 144 mm over the frequency range of 0–6400 Hz. The solid traces in Fig. 4(A) represent the coincidence points of a source at $-60°$ azimuth over frequency, the dotted traces the coincidence pattern for a source at 45° azimuth. The phase ambiguities at frequencies >1200 Hz are shown as the curved traces which shall be referred to as the ''secondary'' traces, to distinguish them from the vertical (or ''primary'') trace.

The existence of the ambiguous, secondary traces in $P_N(\theta_i, m)$ will generate artifactual peaks in $H_N(\theta_d)$. When there are several sources in the ambient environment, superposition of secondary traces from several sources produces a noisier $H_N(\theta_d)$. The artifact peaks, when far away from the peaks of any real sources, may result in a false detection of nonexistent sources, and, when close to the peaks of real sources, they may affect both the detection and estimation of the azimuths of real sources. We will give a detailed discussion and analysis in the experiment section.

B. Stencil filter corresponding to the uniform-azimuth dual delay line

The advantage of short, high-frequency consonants in sound localization (described in Sec. III C) is normally offset by high-frequency phase ambiguity. To reduce the ambiguity effect, a weighting scheme can be used to reduce the importance of the secondary traces relative to the primary traces (Stern *et al.*, 1988; Stern and Trahiotis, 1992). We have chosen to take a different approach to accounting for this issue. We have created a ''stencil'' filtering method, which takes full advantage of the information in the secondary traces. In essence, both the primary trace and the secondary traces are utilized in the directional estimation. In principle, this approach should help significantly in cases where one source is heavily masked spectrally by other sources and its primary traces are distorted by overlap from the secondary traces associated with other sources. A justification of this method is the fact that each sound azimuth is uniquely associated with a specific phase-coincidence trace pattern [see Fig. 4(A) for

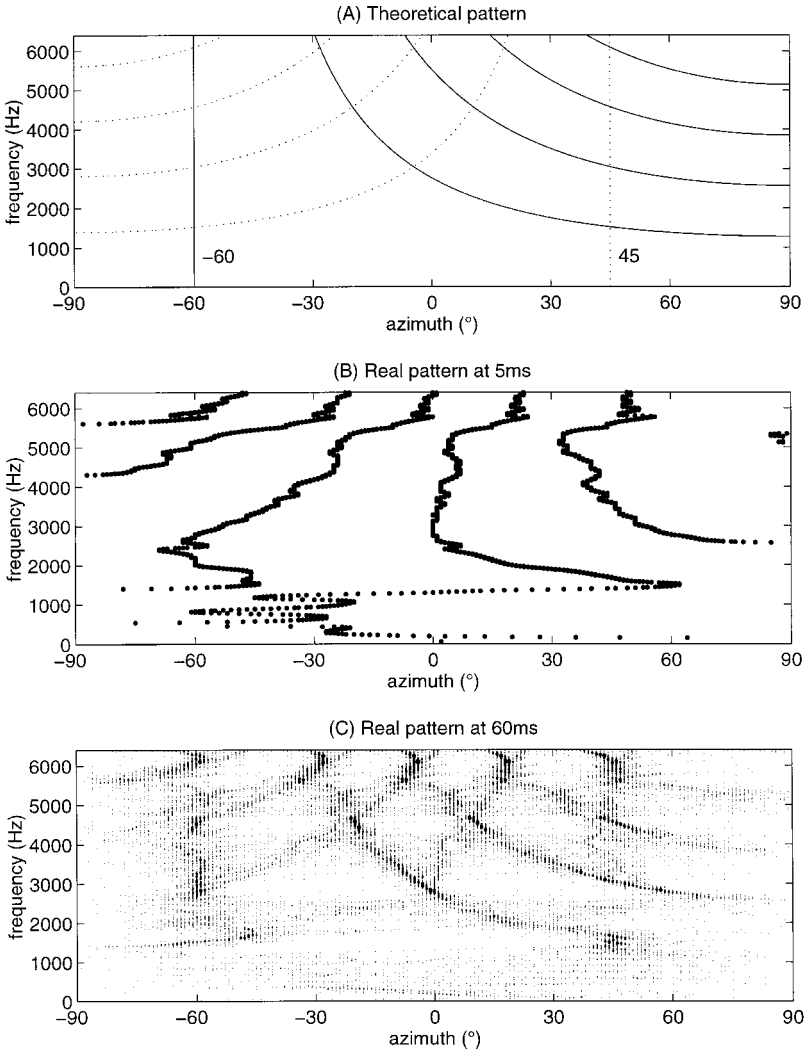

FIG. 4. (A) Primary (vertical traces) and secondary contours (curved traces) from theoretical broadband coincidence patterns associated with a source at −60° in azimuth and a source at 45° in azimuth. The solid lines are the pattern corresponding to −60° azimuth and the dotted lines to 45°. In (B) and (C) are shown the actual broadband coincidence patterns generated by two concurrent sources at −60° and 45° azimuths, at 5 ms (B) and 60 ms (C) after the onset. The temporal weighting factor β=0.98. The window length is 20 ms with consecutive windows overlapped by 15 ms.

coincidence patterns associated with −60° (solid lines) and 45° (dotted lines)]. For example, it is possible to construct a filter applied on $P_N(\theta_i,m)$, such that when deriving $H_N(\theta_d=-60°)$ we integrate the peaks not only along the primary trace (at $\theta_i=-60°$), but also along the secondary traces for −60°. Similarly, we can derive the $H_N(\theta_d)$ for *all* the azimuthal directions θ_d $(d=1,...,I)$. For each θ_d, the filter looks like a stencil window with a shape defined by the ideal pattern $P_N(\theta_i,m)$ $(i=1,...,I;m=1,...,M/2)$.

Below, the concepts of stencil filtering and temporal integration (deferred from Sec. III B) are illustrated using a real example [Figs. 4(B) and (C)]. In this example, a female talker was located at −60° azimuth and a male talker at 45° azimuth. They concurrently uttered a different word at identical average intensity. Figure 4(B) shows the broadband coincidence pattern for the first time frame (5 ms after onset). It can be seen that, due to the interaction between the two sources, the coincidence pattern was highly irregular and did not provide a good indication of the locations of the sources. After 60 ms, however, both sources were clearly revealed in the pattern [Fig. 4(C)].

Corresponding to the coincidence detection [Eqs. (5)–(8)], a mathematical expression of the stencil filter is

$$\sin\theta_i-\sin\theta_d=\frac{\gamma_{d,m}}{\mathrm{ITD}_{\max}f_m}, \tag{12}$$

where, as previously defined, θ_i represents the place along the dual delay line by using the corresponding spatial azimuth, and θ_d is the azimuthal direction for which the broadband integration is conducted. Please note that since Eq. (12) was derived based on the 3D coincidence trace pattern $P_N(\theta_i,m)$, it can be used both for characterizing the integration contours of the stencil filter, and for describing the 3D coincidence pattern of the sound sources. For differentiating the two uses, we refer to the former as the *integration contours* and the latter as *coincidence traces*. The parameter $\gamma_{d,m}$ is an integer, equal to the number of intersections of the integration contours with the horizontal line $f=f_m$. The range of $\gamma_{d,M/2}$ (M/2 is the highest digital frequency, and $f_{M/2}=f_s/2$) also equals the number of the integration contours associated with the direction θ_d in the 3D pattern $P_N(\theta_i,m)$. The primary contour corresponds to $\gamma_{d,m}=0$. For a specific azimuthal direction θ_d, the range of valid $\gamma_{m,d}$, or the number of the integration contours, is

$$-\mathrm{ITD}_{\max}f_m(1+\sin\theta_d)\leqslant\gamma_{d,m}\leqslant\mathrm{ITD}_{\max}f_m(1-\sin\theta_d). \tag{13}$$

See Appendix B for derivation of Eqs. (12) and (13).

By employing the stencil filter [Eq. (12)], the broadband integration procedure in Eq. (11) becomes

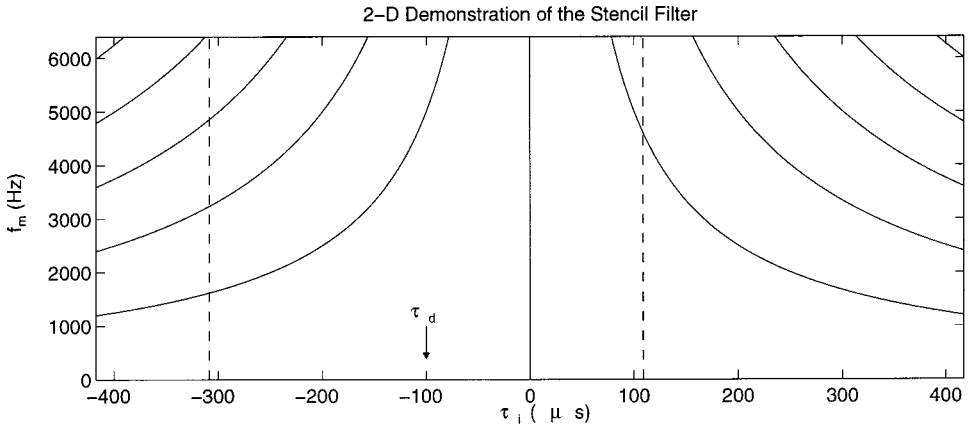

FIG. 5. Two-dimensional representation of the stencil filter corresponding to dual delay line with a uniform τ_i. The x axis represents location along the dual delay line by the corresponding delay unit τ_i in the left channel. Within the window defined by the two vertical dashed-line markers is shown the stencil pattern that is associated with the direction $\theta_d = 28.63°$ azimuth [the direction corresponds to location $\tau_d = -100\ \mu$s in dual delay line by using Eq. (2)].

$$H_N(\theta_d) = \frac{1}{A(\theta_d)} \sum_m P_N\left[\sin^{-1}\left(\sin\theta_d + \frac{\gamma_{d,m}}{\mathrm{ITD}_{\max} f_m}\right), m\right],$$
$$d = 1,...,I, \tag{14}$$

where $A(\theta_d)$ denotes the number of points involved in the summation. The normalization is used because the number of discrete points contained in the integration contours may vary with the targeted azimuth θ_d. It can be seen that the direct method [Eq. (11)] is a special case of the stencil method [Eq. (14)], i.e., when $\gamma_{d,m} = 0$. The block diagram of the whole system is given in Fig. 1.

C. Stencil filter corresponding to uniform time delay in a dual delay line

A disadvantage of the stencil pattern in Eq. (12) is that it varies with azimuth θ_d. Thus, in implementation, a large memory is required for storing the stencil filter patterns. This shortcoming can be overcome, but with a tradeoff. As shown in Eq. (2), both variables θ_i and τ_i are equivalent and represent the same position along the dual delay line. The difference between them is that θ_i indicates location in the dual delay line by virtue of its spatial azimuth θ_i, whereas τ_i denotes location by virtue of the value τ_i of the corresponding time-delay unit. The stencil pattern is simpler if it is expressed with τ_i. Namely,

$$\tau_d - \tau_i = \frac{\gamma_{d,m}}{2 f_m}, \tag{15}$$

where τ_d relates to θ_d through Eq. (2). For a specific τ_d, the range of valid $\gamma_{m,d}$ is

$$-(\mathrm{ITD}_{\max} - 2\tau_d) f_m \leqslant \gamma_{d,m} \leqslant (\mathrm{ITD}_{\max} + 2\tau_d) f_m,$$
$$\gamma_{d,m} \text{ is an integer.} \tag{16}$$

Obviously, changing the value of τ_d only shifts the coincidence pattern (or stencil pattern) along the τ_i axis but without changing its shape. A 2D display of the stencil filter function defined by Eqs. (15) and (16) ($0 \leqslant f_m \leqslant 6.4$ kHz and $\mathrm{ITD}_{\max} = 417.4\ \mu$s) is given in Fig. 5, in which the actual stencil pattern corresponding to a τ_d is within the region between the two dashed-line markers centered at τ_d (e.g., $\tau_d = -100\ \mu$s in Fig. 5). A caveat of Eq. (15) is that, because the scaling of the delay units τ_i is linearly uniform along the dual delay line, the partition of the frontal azimuth by the dual delay line is not uniform, with the regions close to the midplane having higher azimuthal resolution. Therefore, to obtain an equivalent resolution in azimuth, using a uniform τ_i would require a much larger number I of delay units than using a uniform θ_i (see Fig. 6).

V. EXPERIMENTS AND ANALYSES

A. Method

The signal-processing system was evaluated both in computer simulation and in acoustic tests using physical devices in an anechoic chamber. In computer simulation, we evaluated the performance of the system under two experimental conditions: one-talker and two-talker tests. In anechoic chamber tests, we evaluated its performance under the condition of four-talker tests. The speech materials consisted of spondaic words spoken by native speakers of American English. All the speech recordings were equalized in average intensity. Unless otherwise stated, the words in each experimental condition were temporally aligned, i.e., all the talkers started speaking at the same time; this represented a challenging listening condition. The intermicrophone distance was 144 mm. The speech material was presented in free field, and various azimuthal configurations were used for each experimental condition. No diffraction or shadowing effect existed between the two microphones, and the intermicrophone intensity difference was set to zero across all frequencies for the tests in the computer simulation.

The signals were low-pass filtered at 6 kHz and sampled at a 12.8-kHz rate with 16-bit quantization. In the short-term spectral analysis, a 20-ms segment of signal was weighted by a Hamming window, padded with zeros to 2048 points, and Fourier transformed with frequency resolution of about 6 Hz. Consecutive frames overlapped by 15 ms. The values of the time delay units τ_i ($i = 1,...,I$) in the dual delay line corresponded to a uniform azimuthal resolution of 0.5° (namely, $I = 361$). Both the direct and stencil methods were tested; the stencil method used a uniform-azimuth dual delay line [Eqs. (12) and (13)]. The value of the weighting factor β in the temporal integration [Eq. (9)] was 0.98. The threshold Γ [for cleaning the sporadic impulses in the 3D coincidence pattern in Eq. (10)] was 1.

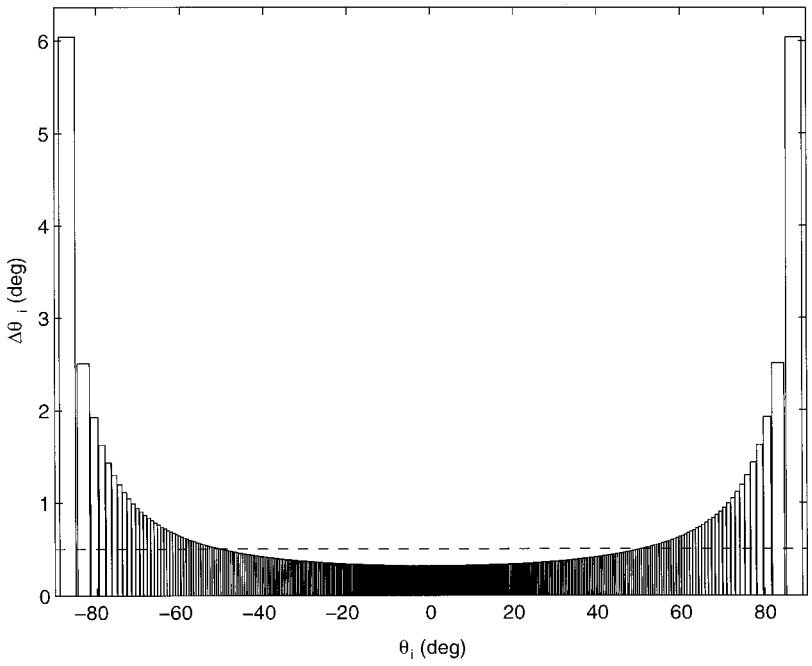

FIG. 6. The azimuthal resolution of dual delay line with a uniform τ_i. The x axis is azimuth. The y axis shows the interval of mapping azimuths between adjacent points in the dual delay line. As a reference, the horizontal dashed line indicates the resolution of dual delay line with a uniform θ_i having the same number of delay units ($I=361$).

B. Results and analyses

1. Acuity of localization in one-talker tests

The purpose of the one-talker computer-simulation tests was to evaluate the acuity of the localization peak of a single source in the absence of any interfering sound. Figure 7 shows the value of $H_N(\theta_d)$ at 30 ms (or $N=6$) after the beginning of a spondaic word ''pancake'' by a female speaker from several different azimuths. When the source was close to the 0° azimuth, $H_N(\theta_d)$ had a distinct and sharp peak corresponding to the source azimuth with both the direct and stencil methods. For a source positioned more laterally in the sound field, the peak was progressively lower and broader. The reason is that an estimation error, although very small, always exists in frequency analysis due to the finite length of the time window. In the current analysis, we employed a time window of 20 ms by characterizing speech as a quasistationary signal. The error is larger for low frequencies because fewer periods of sine waves are present in the time window for low frequencies than for high frequencies.

However, even for the same frequency, due to the nonlinear temporal resolution associated with the dual delay line with uniform azimuth, this estimation error has a varying effect on $H_N(\theta_d)$ along the dual delay line. This estimation error includes errors in the estimates of both amplitude and phase while the width of the peak in $H_N(\theta_d)$ is attributed to the error in the phase estimate. Because the intermicrophone time difference is a sine function of the azimuth θ_i [Eq. (2)], the difference $\Delta\tau_i$ (namely, $\tau_i-\tau_{i-1}$) between adjacent delay units is greater for i in the middle than toward the two ends of the dual delay line. For the dual delay line used in our tests, the maximum value of $\Delta\tau_i$ is 1821.2 ns (in the middle of the dual delay line) and the minimum value is 7.9465 ns (at the both ends of the dual delay line). Therefore, the same phase error in the frequency analysis may result in impulses deviating more in the 3D coincidence pattern $P_N(\theta_i,m)$ when the source is located laterally than when the source is close to the midline. Consequently, the direct broadband integration [Eq. (11)] produces a lower and broader peak in $H_N(\theta_d)$ for a more lateral θ_d.

It is noted that when i is close to the midpoint of the dual delay line, the value $\Delta\tau_i$ of delay resolution is larger than the phase error. Therefore, when a source is located laterally, its primary trace lies away from the midpoint, and is inherently low in spatial consistency, while one or more of its secondary traces are more consistent in the middle of the dual delay line. Consequently, the resultant peak of integration in $H_N(\theta_d)$ is more pronounced and sharper when using the stencil method (that performs integration along both the primary and secondary contours) than using the direct method (that performs integration along the primary contour only). This is evident as shown by comparing Figs. 7(E) and (F).

In principle, the low acuity in the lateral sound field will affect resolution of two closely adjacent sources located laterally, as will be shown in the next subsection. However, it is noted that this kind of resolution should be distinguished from the resolution of the dual delay line itself. In other words, increasing the number I of the delay units in a dual delay line provides a finer azimuthal partition and hence higher spatial precision, but the ability to resolve two adjacent sources is compromised by the low acuity, especially in the lateral field, due to the phase estimation error.

2. Interaction of sources in two-talker tests

We conducted a series of two-talker tests in the computer simulation to analyze the interactions between sources. We compared the performances of the direct and stencil methods, for talkers situated in different positions, and for sources having different relative intensities, and onset times. We also used the two-talker tests as an example to analyze the origin as well as the location of the artifacts that became problematic in localization of multiple sources with both

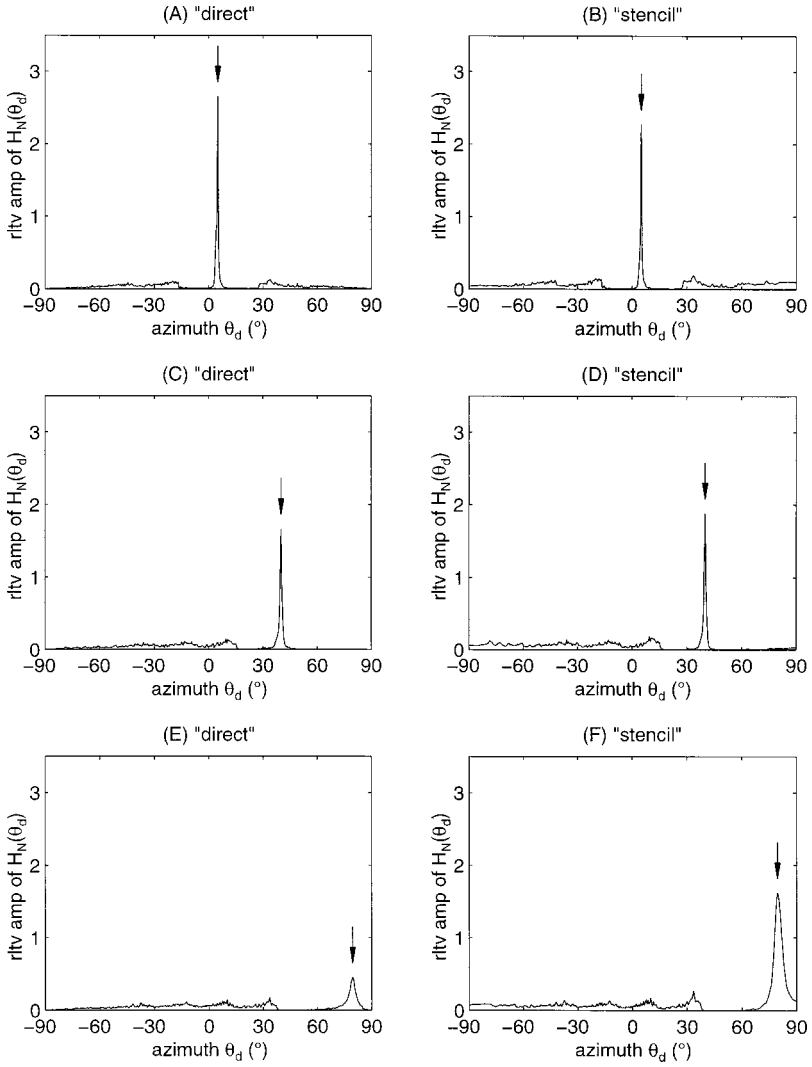

FIG. 7. Localization results $H_N(\theta_d)$ of one source (spondaic word ''pancake'' spoken by a female speaker) at different azimuths. The *x* axis is azimuth (θ_d) of the talker, and the *y* axis represents the relative amplitude of $H_N(\theta_d)$ taken at $N=6$ (or 30 ms) after onset of speech. Left panels (A), (C), (E) are results from the direct method, while right panels (B), (D), (F) are from the stencil method. The talker was located at 5° (A), (B), 40° (C), (D), or 80° (E), (F). The arrow in each panel indicates the real location. The localization peak is high, narrow, and sharp with both methods when the source is close to midline (A), (B), (C), (D). The acuity reduced in the lateral sound field with the direct method (E); the stencil filter restores considerable lateral acuity (F).

methods. For these tests, we used the speech materials from a male talker (M2 saying ''playground'') and a female talker (F1 saying ''pancake'').

a. Different spatial configurations. The nine configurations used in our tests are shown in Table I. The result from a typical configuration (Configuration #1: M2 at 0° and F1 at 40°) is shown in Fig. 8. Both methods gave accurate estimates of the locations of the two talkers with no significant difference between the two methods. Note that the localization computation was conducted once for each frame, i.e., every 5 ms, but the display of the $H_N(\theta_d)$ function in Fig. 8 (and all the 3D graphics in the experiment section) is shown once every 50 ms for clarity.

Configurations #2, #3, and #4 (see Table I) were designed to evaluate the system resolution for two closely adjacent sources (5° apart) at different azimuthal directions. The results given in Fig. 9 show that there was little difference in performance between the direct and stencil methods. Both methods could easily and clearly distinguish the two closely adjacent sources when they were in front of the microphones [Figs. 9(A)–(D)]; distinguishing the two sources became increasingly more difficult as the two sources were positioned more laterally [Figs. 9(E) and (F)]. As analyzed in the preceding subsection, this is due to the lower and broader peaks in $H_N(\theta_d)$ for sources located in the lateral sound field.

Configuration #5 represents a situation in which the two sources are far apart from each other (160° in this case) such that one source is at each lateral side. As mentioned in the preceding subsection, when sound sources were located laterally, the ambiguous secondary traces in $P_N(\theta_i, m)$ showed high spatial consistency. As a result, when using the direct integration, the secondary traces resulted in a number of artifact peaks in $H_N(\theta_d)$ which might be more prominent than the peaks resulting from integration along the primary contours corresponding to the real sources [Fig. 10(A)]. In con-

TABLE I. Configurations in the two-talker tests for analysis of the performance of the dual delay line.

Configuration index		1	2	3	4	5	6	7	8	9
Source	M2	0°	0°	40°	75°	−80°	−40°	0°	40°	−40°
Azimuth	F1	40°	5°	45°	80°	80°	80°	80°	80°	45°

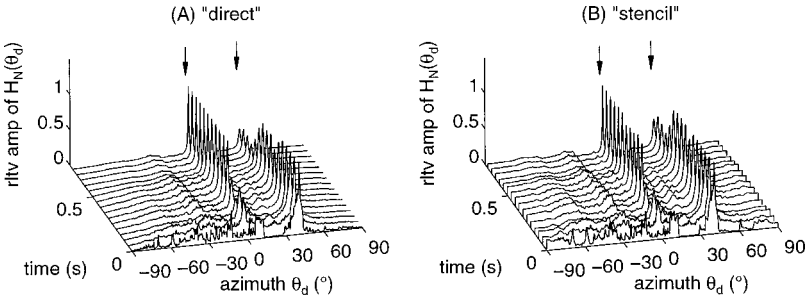

FIG. 8. Localization of two talkers using direct (A) and stencil (B) methods. Two talkers were located at 0° and 40° (indicated by arrows). The talkers spoke different words that had the same average intensity and were temporally aligned. The localization computation was conducted once every 5 ms, but the display is shown every 50 ms for clarity.

trast, the stencil method, which utilized both the primary and secondary traces for localization, enhanced the peaks of real sources. At the same time, the artifact peaks were dramatically suppressed, allowing reliable localization of the real sources [Fig. 10(B)].

Configurations #6, #7, and #8 illustrate another merit of using the stencil method. Similar to the one-talker tests, the localization peak was much lower and obscured as the source approached ±90° with the direct method. However, using the stencil filter amplified the height of the response peak of a lateral source [e.g., see the source at 80° in Figs. 10(C) and (D) for configuration #7].

b. Different relative rms intensities. Tests were conducted to examine the effect of relative intensity on localization. In particular, we sought to determine the ability of the algorithm to locate a weaker sound in the presence of a more intense interfering sound. The tests were conducted with three configurations (configurations #1, 2, and 9 in Table I) using three different relative intensities (the rms intensity of M2 was +5 dB, +10 dB, and +15 dB relative to F1). To determine whether the effect of intensity was independent of speaker and location, three more tests were conducted for configuration #9 where the rms intensity of M2 was −5 dB, −10 dB, and −15 dB relative to F1, respectively. Both the direct and stencil methods were tested for each situation. Results show that, with both methods, the two sources could be localized for an intensity difference of up to 10 dB (Fig. 11). The peak associated with the weaker source (at −40°) grew higher with time; this was attributed to the temporal integration [Eq. (9)]. For intensity difference greater than 10

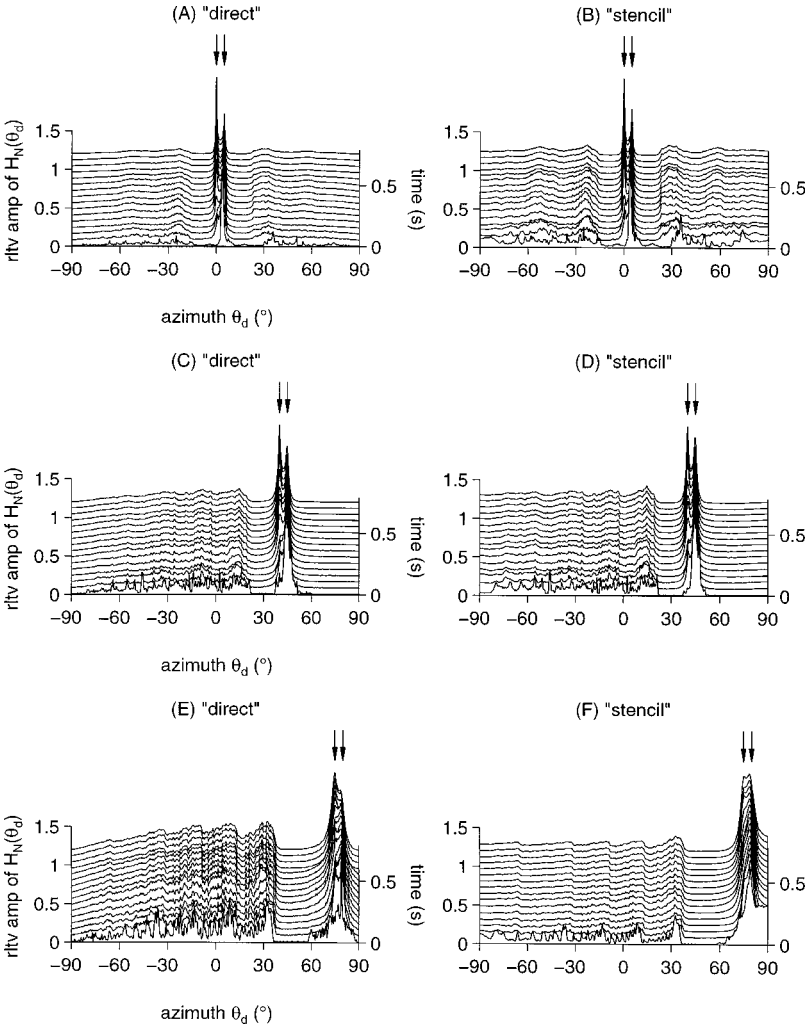

FIG. 9. Location of two closely adjacent talkers (separated by 5°) at various azimuths. The locations of the talkers were: 0° and 5° in (A), (B), 40° and 45° in (C), (D), 75° and 80° in (E), (F). The real locations of the talkers are indicated by arrows. The left column is from direct method; right column from stencil method. Resolution of the sources becomes difficult when they are located laterally (E), (F). The localization computation was conducted once every 5 ms, but the display is shown every 50 ms for clarity.

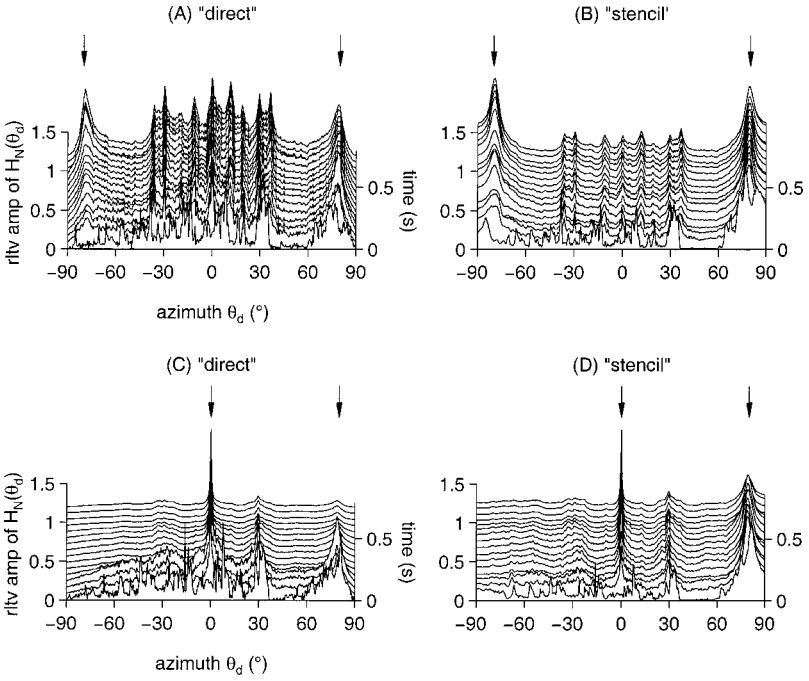

FIG. 10. Localization of two lateral sources. In the first case (A), (B), the two sources were located at −80° and 80° (shown by arrows). The artifactual peaks were very high with the direct method (A), whereas the stencil method (B) enhanced the height of the real peaks and suppressed the artifactual peaks. In the second case (C), (D), the talkers were located at 0° and 80°. The talker at 80° was poorly detected and localized by the direct method (C). The stencil method improved its localization (D). The localization computation was conducted once every 5 ms, but the display is shown every 50 ms for clarity.

dB, the weaker source could not be detected.

c. Different onset times. These tests were conducted to examine the dynamic performance of the algorithm when one sound source is present and a second source goes on or off. The words ''playground'' spoken by Talker M2 and ''pancake'' spoken by Talker F1 (approximately 750 and 670 ms in duration, respectively) were presented using the same three spatial configurations as in the preceding subsection. For each configuration, the speech signal from F1 was delayed relative to M2 by 97.7, 195.3, and 293.0 ms, respectively. Figure 12 illustrates the system performance for the case with 195.3-ms delay (M2 at −40° and F1 at 45°). Both the direct and stencil methods could respond to the onset and offset of each talker. The responses lagged behind the onset or offset by about 100 ms. The response lag was a side effect of temporal integration in Eq. (9), which although enhanced and stabilized localization of sound sources, produced an inertia in the response to the onset and offset of the sound.

d. Location of the artifacts. Some of the above two-talker tests revealed an artifact issue in $H_N(\theta_d)$, such as those shown in Fig. 10(A), introduced from the broadband integration operation. This phenomenon exists in both the direct and stencil methods. We illustrate the issues with an example using the direct method, although the analysis applies to the stencil method and to the situations involving more talkers. Since $H_N(\theta_d)$ is the result of broadband integration of the 3D coincidence pattern $P_N(\theta_i, m)$ along the principal contour [Eq. (11)], the artifact peaks are generated by integration of the coincidence peaks lying on the secondary traces contributed by some other source(s). This is a result of high-frequency ambiguity. These can also be seen in Fig. 7 for the one-talker case. However, this kind of peak is generally extremely low, compared to the peaks associated with real sources, in $H_N(\theta_d)$ after our broadband integration. Nonetheless, there are two general contributing factors to artifactual peaks (neither of which is sufficient for the occurrence of artifactual peaks).

(a) In the 3D coincidence pattern $P_N(\theta_i, m)$, the peaks of coincidence are more pronounced at the intersections of the secondary coincidence traces. In Appendix C we give an example showing the intersections between the coincidence patterns for two talkers from 80° and −80°, and how they produce the artifactual peaks in Fig. 10(A), after integration along the primary contours. This is the main contributor to the artifactual peaks in all our tests. However, often this problem does not exist; for instance, our solution of Eq. (C3) indicates that the secondary coincidence traces of two talkers have no intersections when they are less than 20° apart from each other, and this separation can increase up to 50° when the two talkers are in a lateral sound field on the same side. The number of intersections increases when the two talkers are farther away from each other, and the maximal number

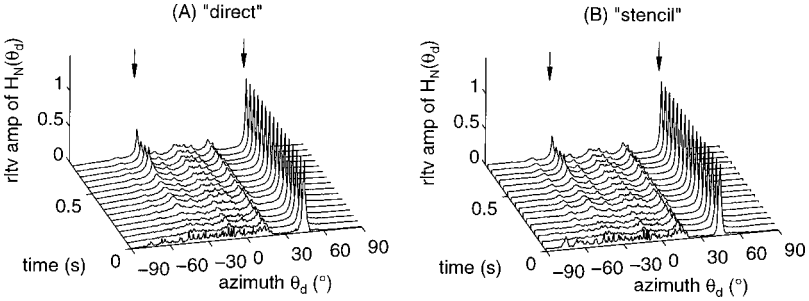

FIG. 11. Effects of relative intensity on localization: a weak talker at −40° and a stronger talker (10 dB higher in average intensity) at 45°. Both the direct (A) and stencil (B) methods can barely detect the weaker source. However, localization becomes easier as the weak source lasts longer. The localization computation was conducted once every 5 ms, but the display is shown every 50 ms for clarity.

of intersections under our experimental setup is ten.

(b) Another cause of the artifactual peak is high coincidence peaks at the high-frequency end of the secondary traces. (As discussed in Sec. IV B 1, due to increased phase estimation error, each secondary trace is high and narrow at the high frequency end and gradually becomes lower and broader toward the low-frequency end.) Sometimes these peaks are almost as conspicuous as the coincidence peaks in $H_N(\theta_d)$ associated with real sources [e.g., Fig. 7(E) and Fig. 9(E)], thereby making it difficult to distinguish which are real and which are artifacts. Yet another cause is when a sound has an unusually large amount of energy concentrated in selected frequencies. This sound will elicit prominent coincidence peaks at those frequencies in both the primary and secondary traces—the latter can produce artifactual peaks in $H_N(\theta_d)$. However, this situation is not applicable to a wideband signal like speech.

A single coincidence peak can lie only on one principal contour but on multiple secondary contours. Hence, each peak contributes to the calculation of $H_N(\theta_d)$ at multiple azimuths in the stencil integration method and could contribute to artifactual peaks in $H_N(\theta_d)$ at these azimuths. However, these artifactual peaks are generally of low magnitude and readily removed by thresholding methods.

The artifact issue is less important when there are only a few (e.g., less than four) talkers. In that case, the chance of generating artifactual peaks is small, and these peaks are generally so weak that most can be separated from the real peaks using thresholding methods. However, as the number of talkers increases, it becomes more difficult to reject artifacts.

3. Multitalker tests in an anechoic room

To determine the system performance in environments close to real-world situations, we carried out on-site acoustic tests where loudspeakers delivered prerecorded sound from multiple talkers. Spondaic words recorded from four talkers (two males and two females) were presented from an equal distance to the input microphones at equal average intensity in an anechoic room (the Frances Searle Hall at Northwestern University) under several configurations (see Table II). The four speech segments were presented simultaneously. The instantaneous response of our system initially showed many scattered response peaks due to random interaction between sources. Some of these indicated the locations of the sources and others were artifacts. Within 100–200 ms, the response peaks associated with the real sources remained or became more prominent but the scattered artifactual peaks were attenuated. The direct and stencil methods could generally determine the locations of three out of the four sources accurately during the first 50 ms. However, it usually took 200–300 ms for the system to determine the presence and locations of all four sources.

For the purpose of illustration, the result of one test (configuration #3 from Table II) is shown in detail in Fig. 13. Each slice of the 3D graphic at instant $n=N$ represents the integration result $H_N(\theta_d)$. The localization computation was conducted once every 5 ms, but the display is shown every 50 ms for clarity. Figure 13(A) shows the result of the direct method. The sources F1 at $-50°$ and M1 at 10° were easily detected. The presence of the source F2 at 45° was detected with an estimation error of 8° (indicated by the arrow with clear face color at 37°). The error was due to the influence of the nearby intersection of the coincidence patterns of the sources at 10° and $-80°$. An artifact source showed up at $-18°$ (indicated by arrow ⇓), which was caused by both the intersection of the coincidence patterns of the sources at 10° and $-50°$ and the intersection between sources at 10° and 45°. The source M2 at $-80°$ was completely missed by the direct method. In contrast, Fig. 13(B) shows that all four sources were successfully detected by the stencil method. The magnitude of the peak corresponding to F2 at 45° was enhanced due to incorporation of the secondary contours, although the estimation error remained large. The most significant improvement is that the lateral source M2 at $-80°$ becomes more conspicuous.

The results for the other tests are outlined in text.

(a) Configuration #1: Both the direct and stencil methods were able to detect three sources (0°, 20°, 75°). Both methods began to target the three sources correctly at the 30th ms. This correct detection stayed until the end. The peak at 75° was relatively low for the first 500 ms because the source energy was low, but was more pronounced for the last 400 ms. The direct method failed to identify the source at 75° for 60 ms at 290th ms. The source at 20° was localized with 3° error for the first 500 ms, but the error grew to 11° for the last 400 ms due to the increasingly stronger interaction between the sources at 0° and 75° that occurred near 20°. Both methods missed the $-75°$ source entirely. Both methods had two consistent artifact peaks, one at $-21°$ (due to strong ambiguous coincidence peaks of the 0° source at high frequencies) and one at $-54°$ (due to ambiguous coincidence peaks of the 20° source at high frequencies).

(b) Configuration #2: This result was the best among the five configurations tested. Both methods successfully detected all four sources for their entire duration. With both methods, the localization errors were smaller than 2° except that the 30° source had a localization error of 8° for the first 360 ms, perhaps due to the interaction between the 0° and 60° sources. The direct method had an artifactual peak at 2° for the last 400 ms due to ambiguous coincidence peaks of the $-45°$ source at high frequencies, while the stencil method did not have any artifacts.

(c) Configuration #4: Both methods localized the 5° source entirely and the 15° source after the first 230 ms. Both methods also detected the $-30°$ source but with an 8° error for the first 600 ms, due presumably to the interaction between the sources at 15° and $-60°$. The direct method detected the $-60°$ source entirely but with a 5° error. The stencil method detected the same source only for the first 850 ms but with a 2° error; then the $-60°$ peak was replaced by an artifact peak around $-72°$ for the last 600 ms, due to the interaction between sources at 15°, $-30°$, and $-60°$. Both methods had artifactual peaks at 31° (from interaction between sources $-60°$ and 5°) and 42° (from interaction between sources 15°, $-30°$, and $-60°$ and between sources $-30°$, and 5°), for the first 1.1 s (direct method) and first 850 ms (stencil method). The direct method also had an artifac-

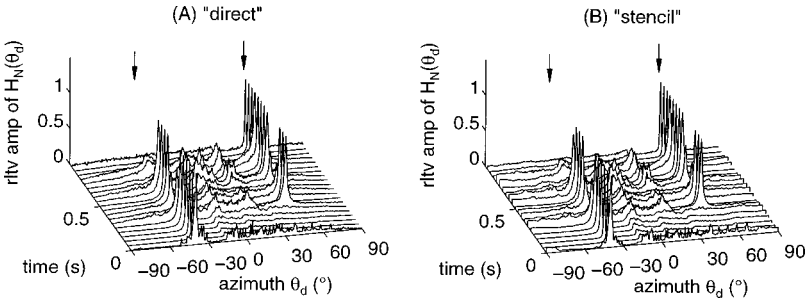

FIG. 12. Effects of different onset times on localization. The onset time of speech from source at 45° lagged behind that from source at −40° by 195 ms. Both the direct (A) and stencil (B) methods can respond to the onset and offset of the signals. The localization computation was conducted once every 5 ms, but the display is shown every 50 ms for clarity.

tual peak around −6° for the last 500 ms (from interaction between sources 15°, −30°, and −60°).

(d) Configuration #5: Both methods localized the sources at −70°, −25°, and 10° correctly, but missed the 80° source entirely. Both methods had artifactual peaks around 61° (due to the interaction between the sources at −70° and 25°) and −2° (due to the interaction between the sources at 25° and −25).

In summary, of the five configurations in four-talker tests, almost all the sources are successfully localized by the two methods with the following exceptions: they missed the −75° source entirely in configuration #1 and the 80° source entirely in configuration #5, and the direct method missed the −80° source entirely in configuration #3. There were on average 1–2 artifact peaks in each test.

One important issue related to the performance evaluation is how we define hits and misses. We evaluated the system performance using three criteria for hits (±2°, ±5°, or ±10°). Several results are notable: (a) The azimuth estimations were generally quite accurate (for more than 60% of our trials, the error was less than 2°). (b) The accuracy of azimuth estimations was highest for sources located near the midline, and the estimate was less accurate for sources located more laterally. (c) As the hit threshold was relaxed, more sources were detected and localized, but the errors increased. (d) There was no significant difference between the direct and stencil methods in terms of estimation accuracy. However, most of the lateral sources missed by the direct method could be reliably localized by the stencil method.

A further evaluation of misses is shown in Fig. 14. The evaluation was made over the period of 200–600 ms (i.e., the middle segment of test signals) when the localization was most stable. Three different hit criteria (±2°, ±5°, and ±10°) were used, and the hit/miss was determined once for each frame, i.e., every 5 ms. We note that the frequency of misses was very small for sources close to the midline. For sources located more laterally, however, the source detection degraded as the frequency of misses increased. As before, the criterion for hits also played a role in the result. As the threshold was relaxed, the number of misses decreased. When comparing the left and right columns, it can be seen that the stencil method is more effective in localizing the lateral sources. This result was consistent with our analysis with the one-talker and two-talker computer-simulation tests.

To evaluate whether the system performance was talker- and/or word dependent, we conducted four talker tests under the same experimental conditions in the anechoic chamber using a different group of spondaic words from a different group of talkers. These tests revealed that the system performance showed no systematic difference across talkers, or speech materials, in terms of source detection and localization accuracy. As before, the stencil method was superior in detecting and localizing the sources at the lateral side.

TABLE II. Summary of experimental setups for four-talker anechoic chamber tests.

Speaker		M1	M2	F1	F2
Word		*''armchair''*	*''playground''*	*''pancake''*	*''woodwork''*
Config. idx	1	−75°	0°	20°	75°
	2	30°	−45°	60°	−10°
	3	10°	−80°	−50°	45°
	4	−30°	15°	5°	−60°
	5	−25°	25°	−70°	80°

C. Discussion

1. Artifacts

In terms of sound localization, there were two kinds of artifacts: (i) classification artifacts, i.e., those response peaks that corresponded to a real source but were classified as artifacts due to the strict criterion for hits (e.g., the arrow with clear face color at 37° in Fig. 13), and (ii) phantom responses, i.e., the responses that did not correspond to real sources (e.g., arrow ⇓ at −18° in Fig. 13). In Sec. V B 2 d, we have given analyses about the origin and location of the artifacts in the situation of two talkers. The principle is easily extended to the situations with more talkers. For example, the artifact at −18° had a dual origin: the intersection between the coincidence patterns of the sources at 10° and −50° and the intersection between the sources at 10° and 45°.

Elimination of the artifacts can be accomplished by using a more sophisticated method for recognizing the 3D coincidence pattern $P_N(\theta_i, m)$. However, this generally comes with a price of more intensive computation. A modified stencil method is being pursued in our continuing research.

2. Maximal number of talkers

Due to the constraints of our experimental facility, evaluation of the system performance for more than four talkers was conducted only in the computer simulation. In the computer simulation, results from six-talker situations were not very different from results from four-talker situations. Specifically, of our 7 six-talker configurations, all the sources could be successfully localized (except that in two configurations the direct method missed a lateral source) and

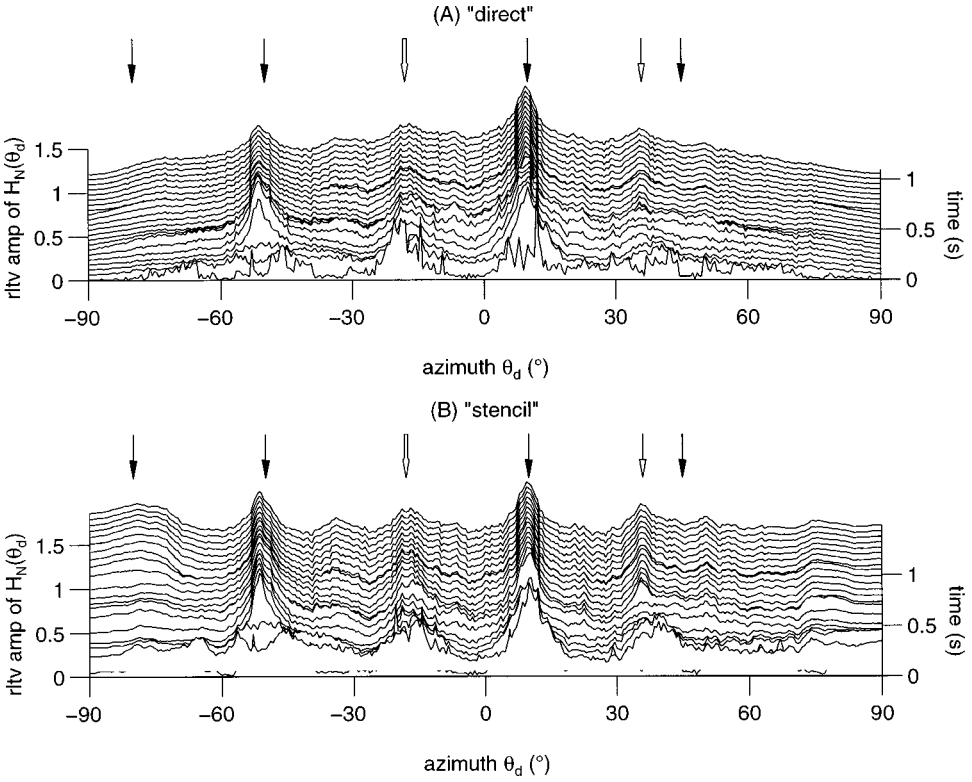

FIG. 13. Localization of four talkers (configuration #3 in Table II) in an anechoic chamber using the direct (A) and stencil (B) methods. The actual locations are shown by single tail, black face-color arrows. The single tail, clear face-color arrows (at 37°) indicate the estimated location of source F2 at 45°. The arrows ⇓ indicate the artifactual peaks that do not correspond to any of the real sources. The direct method missed the lateral source M2 at −80° (A), while the stencil method successfully localized all four sources (B). The localization computation was conducted once every 5 ms, but the display is shown every 50 ms for clarity.

there were at most 1–2 artifact peaks in a configuration (Liu *et al.*, 1997). In general, the performance in the more complex environment was slightly inferior to the results from the less complex environment. What, then, is the maximum number of talkers that can be localized by the system? This is difficult to determine because, in addition to the number of talkers, the system performance also depends on the relative time of occurrence, the spectrum, and intensity of concurrent phonemes, the number and duration of pauses in the speech, as well as the relative locations of the talkers in the auditory space. The limit of the system is mainly attributed to two kinds of problems. The first is related to the coincidence

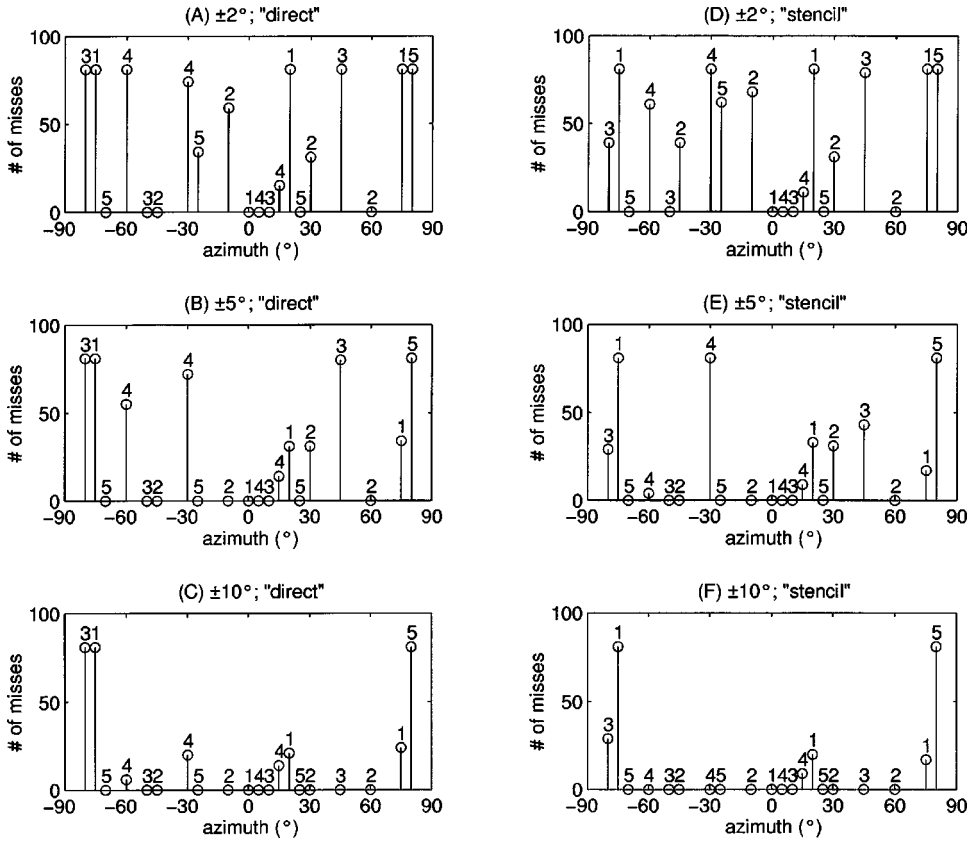

FIG. 14. Number of misses incurred in the four-talker anechoic chamber tests. The hit/miss was determined once for each frame (every 5 ms). The left panels (A), (B), (C) are from the direct method; the right panels (D), (E), (F) from the stencil method. The hit threshold was ±2°, ±5°, and ±10°, respectively, for each row. The number above each stem denotes the index of the test configuration. As the hit threshold is higher, the number of misses decreases. For both methods, the sources closer to the midline were more easily detected while lateral sources were more often missed. However, the stencil method can localize more sources than the direct method, especially when the hit threshold is large [compare (B) and (E), (C) and (F)].

detection step. When the duration of one source masked by others is longer, the spectrum of one source masked by others is wider, or the intensity of one source is lower relative to others, it is more difficult for the source to be detected in the narrow-band coincidence detection. The second is related to the recognition of the 3D coincidence pattern. When a source is located very laterally, when the number of sources is large, or when the sound duration is short, it is difficult for the source to be detected by temporal and broadband integration. All these factors are being studied for a deeper understanding of the method proposed.

3. Head-shadow effect

The present system was applied without any object between the two microphones. However, any diffraction from an object between the two microphones, such as the head-shadow effect, will complicate our theory. The diffraction will introduce both sound-pressure change and phase shift, as functions of size of the object, frequency, and the direction of incidence. It can be interpreted as filtering with the transfer function characteristic of the diffraction. Theoretically this effect can be removed by filtering with the reciprocal of the diffraction transfer function. This filter can be incorporated into the delay units of the dual delay line. Although it is possible to calculate the filter coefficients based on the shape of the object, we suggest that the values be measured empirically. However, the added filtering will likely degrade the computational performance of the system. How well the filtering will compensate for the deviation from ideal introduced by head-shadow diffraction is not known.

VI. SUMMARY AND CONCLUSION

In this research, we developed a signal-processing system for determining the spatial locations of multiple sound sources with two microphones. The system is based on a dual delay-line structure, which detects the intermicrophone time difference (which depends on the source azimuth) using a coincidence detection method. The direction information is mapped, in a nonlinear manner, from the dual delay line onto a 3D coincidence pattern. Both temporal integration and spectral integration are employed to take full advantage of the broad bandwidth such that the source azimuth can be estimated reliably in adverse noisy conditions. We also developed a novel stencil filter to enhance the localization of sound sources in lateral fields.

Results show that our broadband localization technique works well in complex auditory scenes involving four talkers in an anechoic space or six talkers in computer simulation. The limitations of the method require further investigation. Work in progress involves extending the results to real rooms over a range of reverberation times.

A number of problems remain to be addressed. First, because we do not have the elevation asymmetry, which in the case of humans results from the filtering effects of head, body, and pinna, the present version of the system cannot localize vertically. However, simple geometry argues that a second pair of microphones oriented vertically could identify elevation. Second, as shown in the experimental results, some artifacts in the localization need to be removed by a more sophisticated pattern recognition method. Third, the dual delay-line architecture, as well as parallel nature of computation is suited for very large-scale integrated (VLSI) implementation and miniaturization for eventual use. For instance, Mead *et al.* (1991) has reported a VLSI implementation of neural network architecture for a silicon cochlea. These problems are the focus of ongoing investigation. In our research, the overall goal is to not only localize the sources of speech sounds but also to selectively extract the speech from one (or more) talker(s). What is shown in this paper is the ability of the system to detect and locate the sources. In a separate paper, we shall describe how the system can extract the speech from one of the talkers with high fidelity.

ACKNOWLEDGMENTS

This research was supported by grants from the Beckman Institute at the University of Illinois at Urbana-Champaign, and the Mary Jane Neer Research Fund. The work was conducted while the first author (C.L.) was a Beckman Fellow. We thank Jiri Jonas for his enthusiasm for this project, Terry Takahashi for suggestions in the early phase of the research, Dean Garstecki for permission to use the anechoic chamber at Northwestern University, Susanne Aref for advice on data analysis, and Benjamin Grosser, John Prato, Youngmin Kim, and Huiming Zhang for assistance in some of the experiments. A number of staff members in the Beckman Institute voluntarily participated in the recording of speech materials used in the tests; their participation is appreciated. The facilities of the Visualization Laboratory at the Beckman Institute were employed in part of the experiments.

APPENDIX A

In order to illustrate the coincidence detection method, we consider a simplified dual delay line at frequency $\omega_m = 2\pi f_m$ (Fig. A1). Illustrated is a case where there are two sources: source 1 and source 2. It will be seen that the conclusion applies to cases involving more sources. Suppose that the coincidence locations of source 1 and source 2 are at $i_{\text{source 1}} = s$ and $i_{\text{source 2}} = g$ along the dual delay line, respectively, and that the in-phase signal source 1 at $i_{\text{source 1}} = s$ is $A_s \exp[j(\omega_m t + \phi_s)]$ and the in-phase signal source 2 at $i_{\text{source 2}} = g$ is $A_g \exp[j(\omega_m t + \phi_g)]$. Thus, at an arbitrary location i along the dual delay line, the signals from the left and right channels are, respectively,

$$X_L^{(i)}(m) = A_s \exp j[\omega_m(t + \tau_s - \tau_i) + \phi_s] + A_g \exp j[\omega_m(t + \tau_g - \tau_i) + \phi_g], \tag{A1}$$

and

$$X_R^{(i)}(m) = A_s \exp j[\omega_m(t + \tau_{I-s+1} - \tau_{I-i+1}) + \phi_s] + A_g \exp j[\omega_m(t + \tau_{I-g+1} - \tau_{I-i+1}) + \phi_g], \tag{A2}$$

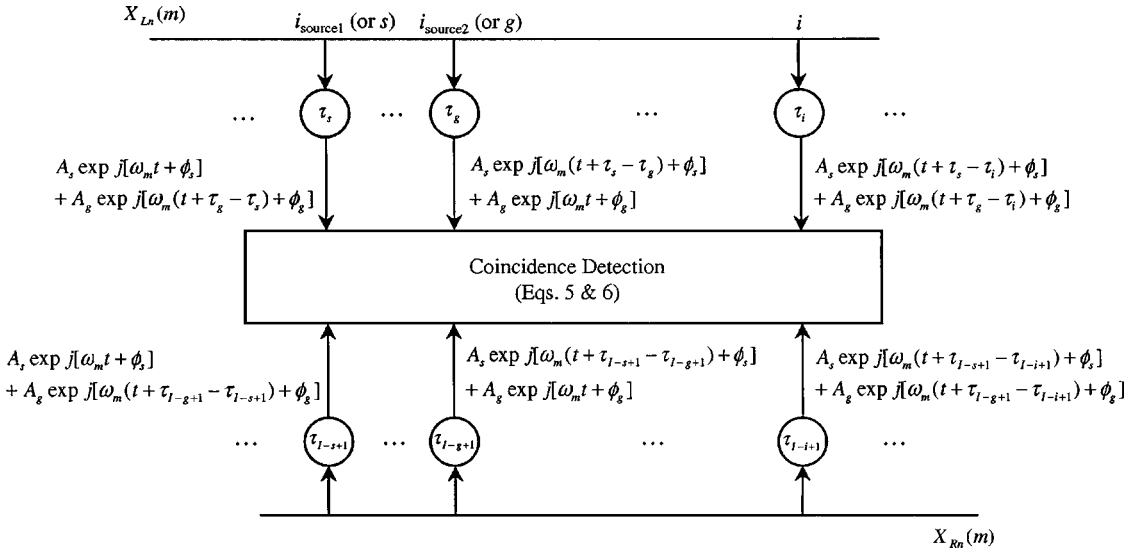

FIG. A1. The dual delay-line structure.

where τ_s, τ_{I-s+1}, τ_g, τ_{I-g+1}, τ_i, and τ_{I-i+1} are values of delay units at locations s, g, and i, in the left and right channels, respectively.

The coincidence detection calculates the value of $|X_L^{(i)}(m)-X_R^{(i)}(m)|$ [Eq. (6)]. After substituting Eqs. (A1) and (A2), we obtain the following:

$$|X_L^{(i)}(m)-X_R^{(i)}(m)|=2\Bigg\{A_s^2\sin^2\frac{\omega_m}{2}[(\tau_s-\tau_i)-(\tau_{I-s+1}-\tau_{I-i+1})]+A_g^2\sin^2\frac{\omega_m}{2}[(\tau_g-\tau_i)-(\tau_{I-g+1}-\tau_{I-i+1})]$$
$$+2A_sA_g\sin\frac{\omega_m}{2}[(\tau_s-\tau_i)-(\tau_{I-s+1}-\tau_{I-i+1})]\sin\frac{\omega_m}{2}[(\tau_g-\tau_i)-(\tau_{I-g+1}-\tau_{I-i+1})]\cos\kappa_{s,g}(m)\Bigg\}^{1/2}, \tag{A3}$$

where $\kappa_{s,g}(m)=(\omega_m/2)(\tau_s-\tau_g+\tau_{I-s+1}-\tau_{I-g+1})+(\phi_s-\phi_g)$ in the cross term.

Consider the relation between the values τ_i and τ_{I-i+1} of any paired delay units. By employing Eq. (1), we have

$$\tau_{I-i+1}=\frac{\text{ITD}_{\max}}{2}\sin\left[\frac{(I-i+1)-1}{I-1}\pi-\frac{\pi}{2}\right]$$
$$=-\frac{\text{ITD}_{\max}}{2}\sin\left(\frac{i-1}{I-1}\pi-\frac{\pi}{2}\right)=-\tau_i. \tag{A4}$$

Similarly, we have $\tau_{I-s+1}=-\tau_s$ and $\tau_{I-g+1}=-\tau_g$. Using these relations, Eq. (A3) can be further simplified such that

$$|X_L^{(i)}(m)-X_R^{(i)}(m)|$$
$$=2[A_s^2\sin^2\omega_m(\tau_s-\tau_i)+A_g^2\sin^2\omega_m(\tau_g-\tau_i)+2A_sA_g$$
$$\times\sin\omega_m(\tau_s-\tau_i)\sin\omega_m(\tau_g-\tau_i)\cos\kappa_{s,g}(m)]^{1/2}. \tag{A5}$$

It is easy to see that Eq. (A5) has the form

$$\text{term}(s-i)+\text{term}(g-i)+\text{cross term}. \tag{A6}$$

It is the first and second terms that indicate the directions of the two sources.

APPENDIX B

In order to obtain the expression of the stencil pattern, we focus on either of the first two terms in Eq. (A5). We use the subscript d to denote the source being focused. Referring to Eq. (5), the minimum point of $|\sin^2\omega_m(\tau_d-\tau_i)|$ should correspond to the direction of the source d, thus,

$$\arg\min_i|\sin^2\omega_m(\tau_d-\tau_i)|=\{i:\omega_m(\tau_d-\tau_i)=\gamma_{d,m}\pi,$$
$$\gamma_{d,m}\ \text{is an integer}\}. \tag{B1}$$

After substituting Eq. (2) for τ_d and τ_i into Eq. (B1) and considering that $\omega_m=2\pi f_m$, we can get the expression Eq. (12) of the stencil pattern. Considering $-1\leqslant\sin\theta_i\leqslant1$, the range of $\gamma_{d,m}$ in Eq. (13) can be derived from Eq. (12).

APPENDIX C

Let us calculate the intersections between the coincidence trace patterns of two sources. We assume the azimuths of the two sources are θ_d' and θ_d'', respectively. Since the coincidence pattern of each source is determined by Eq. (13), the intersections of the two patterns can be obtained by solving the following system:

TABLE CI. The calculated intersection points between the coincidence traces of the two sound sources located at 80° and −80°, respectively. The values in boldface are the intersections by the secondary traces.

$\gamma''_{d,m}$ \ $\gamma'_{d,m}$	0	1	2	3	4	5
−5	−80°	⋯	⋯	⋯	⋯	⋯
−4	−80°	**−36.2°**	⋯	⋯	⋯	⋯
−3	−80°	**−29.5°**	**−11.4°**	⋯	⋯	⋯
−2	−80°	**−19.2°**	**0°**	**11.4°**	⋯	⋯
−1	−80°	**0°**	**19.2°**	**29.5°**	**36.2°**	⋯
0	⋯	80°	80°	80°	80°	80°

$$\sin\theta'_i-\sin\theta'_d=\frac{\gamma'_{d,m}}{\mathrm{ITD}_{\max}f_m}$$
$$\sin\theta''_i-\sin\theta''_d=\frac{\gamma''_{d,m}}{\mathrm{ITD}_{\max}f_m}. \tag{C1}$$

The solution is

$$\sin\theta'_i=\sin\theta''_i=\frac{\gamma''_{d,m}\sin\theta'_d-\gamma'_{d,m}\sin\theta''_d}{\gamma''_{d,m}-\gamma'_{d,m}}$$
$$f_m=\frac{\gamma''_{d,m}-\gamma'_{d,m}}{\mathrm{ITD}_{\max}(\sin\theta'_d-\sin\theta''_d)}. \tag{C2}$$

The number of the intersection points is not only determined by the validity of Eq. (C2) but also the ranges of $\gamma'_{d,m}$ and $\gamma''_{d,m}$ [Eq. (13)]. Thus, the contraints are

$$-1\leqslant\frac{\gamma''_{d,m}\sin\theta'_d-\gamma'_{d,m}\sin\theta''_d}{\gamma''_{d,m}-\gamma'_{d,m}}\leqslant 1$$
$$0\leqslant\frac{\gamma''_{d,m}-\gamma'_{d,m}}{\mathrm{ITD}_{\max}(\sin\theta'_d-\sin\theta''_d)}\leqslant f_s/2$$
$$-\mathrm{ITD}_{\max}f_m(1+\sin\theta'_d)\leqslant\gamma'_{d,m}\leqslant\mathrm{ITD}_{\max}f_m(1-\sin\theta'_d)$$
$$-\mathrm{ITD}_{\max}f_m(1+\sin\theta''_d)\leqslant\gamma''_{d,m}\leqslant\mathrm{ITD}_{\max}f_m(1-\sin\theta''_d). \tag{C3}$$

The number of intersections can be obtained by numerically solving the above system.

We calculate for the intersections of the two sources in Fig. 10(A); thus $\theta'_d=-80°$ and $\theta''_d=80°$. The result is displayed in Table CI. There are 20 intersection points altogether between the coincidence traces of the two speakers, among which 10 intersections might contribute the artifacts at 9 different places through the direct integration.

Banks, D. (**1993**). ''Localisation and separation of simultaneous voices with two microphones,'' IEE Proc.-I Commun. Speech Vision **140**, 229–234.

Blauert, J. (**1980**). ''Modelling of interaural time and intensity difference discrimination,'' in *Psychophysical, Physiological and Behavioural Studies in Hearing: Proceedings of the 5th International Symposium on Hearing*, edited by G. V. D. Brink and F. A. Bilsen (Delft University Press, Delft, Noordwijkerhout, The Netherlands), pp. 421–424.

Blauert, J. (**1983**). *Spatial Hearing: The Psychophysics of Human Sound Localization*, translated by John S. Allen (The MIT Press, Cambridge, MA).

Bodden, M. (**1993**). ''Modeling human sound source localization and the cocktail-party-effect,'' Acta Acust. (China) **1**, 43–55.

Bronkhorst, A. W., and Plomp, R. (**1992**). ''Effect of multiple speechlike maskers on binaural speech recognition in normal and impaired hearing,'' J. Acoust. Soc. Am. **92**, 3132–3139.

Cherry, E. C. (**1953**). ''Some experiments on the recognition of speech, with one and with two ears,'' J. Acoust. Soc. Am. **25**, 975–979.

Colburn, H. S. (**1973**). ''Theory of binaural interaction based on auditory-nerve data. I. General strategy and preliminary results on interaural discrimination,'' J. Acoust. Soc. Am. **54**, 1458–1470.

Colburn, H. S. (**1977**). ''Theory of binaural interaction based on auditory-nerve data. II. Detection of tones in noise,'' J. Acoust. Soc. Am. **61**, 525–533.

Colburn, H. S. (**1996**). ''Computational models of binaural processing,'' in *Auditory Computation*, edited by H. L. Hawkins, T. A. McMullen, A. N. Popper, and R. R. Fay (Springer, New York), pp. 332–400.

Colburn, H. S., and Durlach, N. I. (**1978**). ''Models of binaural interaction,'' in *Handbook of Perception, IV: Hearing*, edited by E. C. Carterette and P. F. Morton (Academic, New York).

Colburn, H. S., Han, Y., and Culotta, C. P. (**1990**). ''Coincidence model of MSO responses,'' Hear. Res. **49**, 335–346.

Durlach, N. I., and Colburn, H. S. (**1978**). ''Binaural phenomena,'' in *Handbook of Perception, IV: Hearing*, edited by E. C. Carterette and P. F. Morton (Academic, New York).

Feng, A. S., and Shofner, W. P. (**1981**). ''Peripheral basis of sound localization in anurans: Acoustic properties of the frog's ear,'' Hear. Res. **5**, 201–216.

Flanagan, J. L., Johnston, J. D., Zahn, R., and Elko, G. W. (**1985**). ''Computer steered microphone arrays for sound transduction in large rooms,'' J. Acoust. Soc. Am. **78**, 1508–1518.

Flanagan, J. L. (**1972**). *Speech Analysis, Synthesis and Perception* (Springer, Berlin).

Gaik, W. (**1993**). ''Combined evaluation of interaural time and intensity differences: Psychoacoustic results and computer modeling,'' J. Acoust. Soc. Am. **94**, 98–110.

Gourevitch, G. (**1987**). ''Binaural hearing in land mammals,'' in *Directional Hearing*, edited by W. A. Yost and G. Gourevitch (Springer, New York), pp. 226–246.

Jeffress, L. A. (**1948**). ''A place theory of sound localization,'' J. Comp. Physiol. Psychol. **41**, 35–39.

Konishi, M., Takahashi, T., T., Wagner, H., Sullivan, W. E., and Carr, C. E. (**1988**). ''Neurophysiological and anatomical substrates of sound localization in the owl,'' in *Auditory Function: Neurobiological Bases of Hearing*, edited by M. E. Gerald, W. E. Gall, and W. M. Cowan (Wiley, New York), pp. 721–745.

Lindemann, W. (**1986**). ''Extension of a binaural cross-correlation model by contralateral inhibition. I. Simulation of lateralization for stationary signals,'' J. Acoust. Soc. Am. **80**, 1608–1622.

Liu, C., Feng, A. S., Wheeler, B., O'Brien, W. D., Bilger, R. C., and Lansing, C. (**1997**). ''A binaurally based auditory processor effectively extracts speech in the presence of multiple competing sounds,'' Hearing Aid Research and Development Conference, NIH, Bethesda, MD, Sept., 1997.

Mead, C. A., Arreguit, X., and Lazzaro, J. (**1991**). ''Analog VLSI model of binaural hearing,'' IEEE Trans. Neural Netw. **2**, 230–236.

Mills, A. W. (**1972**). ''Auditory localization,'' in *Foundations of Modern Auditory Theory*, edited by V. T. Jerry (Academic, New York), pp. 301–348.

Shamma, S. A., Shen, N., and Gopalaswamy, P. (**1989**). ''Stereausis: Binaural processing without neural delays,'' J. Acoust. Soc. Am. **86**, 989–1006.

Stern, R. M., and Trahiotis, C. (**1992**). ''The role of consistency of interaural time over frequency in binaural lateralization,'' in *Auditory Physiology and Perception, Proceedings of the 9th International Symposium on Hearing*, edited by Y. Cazals, L. Demany, and K. Horner (Pergamon, Oxford, Carcens, France), pp. 547–554.

Stern, R. M., and Trahiotis, C. (**1995**). ''Models of binaural interaction,'' in *Hearing*, edited by B. C. J. Moore (Academic, San Diego), pp. 347–386.
Stern, R. M., and Trahiotis, C. (**1997**). ''Models of binaural perception,'' in *Binaural and Spatial Hearing in Real and Virtual Environments*, edited by R. H. Gilkey and T. R. Anderson (Erlbaum, Mahwah, NJ), pp. 499–532.
Stern, R. M., Zeiberg, A. S., and Trahiotis, C. (**1988**). ''Lateralization of complex binaural stimuli: A weighted-image model,'' J. Acoust. Soc. Am. **84**, 156–165.
Takahashi, T. T., and Keller, C. H. (**1994**). ''Representation of multiple sound sources in the owl's auditory space map,'' J. Neurosci. **14**, 4780–4793.
Yin, T. C. T., and Chan, J. C. K. (**1990**). ''Interaural time sensitivity in medial superior olive of cat,'' J. Neurophysiol. **64**, 465–488.

Chinese dialect identification using segmental and prosodic features

Wen-Whei Chang and Wuei-He Tsai
Department of Communications Engineering, National Chiao-Tung University, Hsinchu, Taiwan, Republic of China

(Received 9 September 1999; revised 14 April 2000; accepted 29 June 2000)

Several approaches to Chinese dialect identification based on segmental and prosodic features of speech are described in this paper. When using segmental information only, the system performs phonotactic analysis after speech utterances have been tokenized into sequences of broad phonetic classes. The second scheme comprises prosodic models which are trained to capture tone sequence information for individual dialects. Also proposed is a novel approach that examines differences between Chinese dialects at broad phonetic and prosodic levels. These algorithms were evaluated via a multispeaker read-speech mode. Simulation results indicate that the combined use of segmental and prosodic features allows the proposed system to discriminate among three major Chinese dialects spoken in Taiwan with 93.0% accuracy. © *2000 Acoustical Society of America.* [S0001-4966(00)03410-X]

PACS numbers: 43.72.Ne [DOS]

I. INTRODUCTION

Automatic language identification (language ID) is an active research area with the goal of multilingual information access. A language-ID system takes test utterances as inputs and produces the identities of the languages being spoken as outputs. Previous work[1] suggests that the language characteristics are represented in the segmental and prosodic features of speech utterances. Segmental features can be acoustic–phonetic, which refers to the acoustic realizations of phonemes, or phonotactic, which refers to the rules governing combination of various phonemes in a language. Prosodic information is encoded in the pitch, amplitude, and duration variations that span across segments. Although language-discriminating information can be found at various levels, how to best combine them for reliable language ID is still an unsolved problem. A language-ID approach based only on phonotactics was applied by House and Neuburg[2] using a hidden Markov model (HMM) trained on phonetic transcriptions of text. Recent research demonstrates that further enhancement can be realized by additionally incorporating prosodic information[3] and acoustic–phonetic information.[3–5] In using these approaches, it is assumed that the acoustic structures of individual languages can be explored by segmenting speech into basic sound units such as phonemes. Languages can then be identified by computing features within and across segments that are likely to capture the relevant phonetic and prosodic aspects of these languages.

Until recently, research in Chinese language processing was almost exclusively aimed at voice dictation of Mandarin Chinese.[6] However, hundreds of Chinese dialects exist and may be linguistically divided into seven major groups, namely, Mandarin, Holo, Hakka, Wu, Yue, Xiang, and Gan.[7] There are minor differences within each group, but there are major differences of such magnitude between groups that the groups sound mutually unintelligible. The interconnections between the Chinese dialects are in fact as complicated as those among the family of Romance languages, such as French, Spanish, and Italian. This motivated our research into trying to devise a system for determining the identities of spoken Chinese dialects. During the initial stage of developing our dialect-ID system, special efforts were made to discriminate among three major Chinese dialects spoken in Taiwan, Mandarin, Holo, and Hakka. Porting a well-developed language-ID technique to the problem of Chinese dialect ID may present its own set of problems. This is because various Chinese dialects are more closely related than the Romance languages; they use the same grammar and written characters, and include many homonyms that share the same pronunciation. System design approaches that consider Chinese language characteristics are believed to be the key to providing better solutions to the dialect-ID problem.

II. THEORY

A. Overview

The key to solving the problem of Chinese dialect ID is the detection and exploitation of characteristic features that distinguish dialects from one another. From a linguistic standpoint, the greatest differences among Chinese dialects are in the area of phonology, the least in the area of grammar. Vocabulary differences fall between these extremes. A distinctive feature of the Chinese language is that all the characters are monosyllabic. Traditional descriptions of Chinese divide syllables into combinations of *initials* and *finals* rather than into individual phonemes. An *initial* is the consonant onset (C_1) of a syllable, while a *final* consists of a nucleus (U) and an ending (C_2), where C_2 is a consonant and U can be a vowel or diphthong. There are 22 *initials* and 38 *finals* in Mandarin, 18 *initials* and 75 *finals* in Holo, and 19 *initials* and 65 *finals* in Hakka. These *initials* and *finals* can be further decomposed into more basic sound units such as phonemes and broad phonetic classes (BPCs). Table I gives a list of phonetic elements of Chinese language. De-

TABLE I. Phonetic elements used in Chinese language.

	Broad phonetic classes	Phonemes
Syllable onset (C_1)	Stop (S)	[p] [t] [k] [ph] [th] [kh] [b] [g] [l]
	Fricative (F)	[f] [h] [s] [sh] [shi] [j] [v]
	Affricate (A)	[j] [ji] [ch] [chi] [tz] [ts]
	Nasal (N)	[m] [n] [ng]
Syllable nucleus (U)	Vowel or diphthong (V)	[a] [e] [i] [o] [u] [è] [ai] [ao] [au] [ei] [eu] [ia] [ie] [io] [iu] [oa] [oe] [oi] [ou] [ua] [ue] [ui] [uo] [iao] [uai]
Syllable ending (C_2)	Stop (S)	[p] [t] [k]
	Fricative (F)	[h]
	Nasal (N)	[m] [n] [ng]

pending on the manner of articulation, phonemes can be categorized into five BPCs including the stop (S), fricative (F), affricate (A), nasal (N), and vowel or diphthong (V). Hereafter, we use this five-character alphabet in referring to BPCs. In this study, we propose using BPCs rather than phonemes as the bases for dialect discrimination. This is mainly because BPCs are relatively invariant across Chinese dialects, eliminating the need for developing a standard phonemic transcription system appropriate for all dialects. Chinese dialects differ in the frequency of BPC occurrences and the order in which BPCs occur in syllables. Table II lists eligible BPC combinations used in individual dialects. It shows that an *initial* is composed of a single BPC while a *final* generally contains one or two BPCs.

TABLE II. Eligible combinations of broad phonetic classes in Chinese syllables (S: stop, F: fricative, A: affricate, N: nasal, V: vowel or diphthong).

Syllable					
Initial	*Final*		Dialect		
Onset	Nucleus	Ending	Mandarin	Holo	Hakka
S	V	S		√	√
F	V	S		√	√
A	V	S		√	√
N	V	S		√	√
	V	S		√	√
S	V	F		√	
F	V	F		√	
A	V	F		√	
N	V	F		√	
	V	F		√	
S	V	N	√	√	√
F	V	N	√	√	√
A	V	N	√	√	√
N	V	N	√	√	√
	V	N	√	√	√
S	V		√	√	√
F	V		√	√	√
A	V		√	√	√
N	V		√	√	√
	V		√	√	√
S		N		√	√
F		N		√	√
A		N		√	√
N		N		√	√
		N		√	√

Another important feature of Chinese language is the existence of lexical tones for syllables, which means syllables may have the same phonetic compositions, but different lexical meanings when spoken with different tones. Chinese is spoken with four basic tones, traditionally labeled *ping* (level), *shaang* (rising), *chiuh* (departing), and *ruh* (entering). The most distinctive feature of *ruh*-tone syllables is that they end in one of the three stops /p/, /t/, and /k/, and thus, are much shorter in duration. The other tones consist of syllables that end in vowels, fricatives, or nasals, and differ from one another in their pitch contours. Each of these four basic tones is further split into *yin* and *yang* categories according to whether the *initial* is voiced or unvoiced, thus giving rise to an eight-tone system for spoken Chinese. Pitch contours are generally affected by *initials* in this way: pronunciation of syllables with voiced *initials* begins at a lower pitch than that used for those with unvoiced *initials*. Table III shows the eight traditional tonal categories of Chinese language. It is important to note that only a few modern dialects preserve this eight-tone system intact; in many dialects two or more of these tonal categories have been merged. For example, Mandarin does not have a *ruh* tone and requires only four tones to cover pitch variations within syllables. Chinese dialects differ not only in the number of distinct tonal categories they use, but also in the acoustic realizations of similar tones. To illustrate this, we follow Chao's system[8] for tonal notation and represent pitch height on a 5-point scale, on which 1 is low, 2 half-low, 3 middle, 4 half-high, and 5 high. Using this notation, tones can be described by indicating their beginning and ending points; in a few cases tones have concave or convex contours making it necessary to include one turning point as well. For example, in Mandarin the *shaang* tone is associated with a tone value 214, and thus falls first from the half-low point to the low point and then rises to the half-high point. Details of the tones used in individual dialects, along with their tone values on the 5-point scale, are shown in Table IV.

B. Probabilistic framework

Designing a reliable dialect-ID scheme requires that stochastic models be used to summarize some of the most relevant aspects of language acoustics. As suggested by Hazen and Zue,[3] we formulated the problem using a segment-based probabilistic framework. Choosing an appropriate representation of acoustic information is the first step in applying statistical methods to solving the dialect-ID problem. The specific types of feature measurements considered here are pitch contour and mel-cepstrum. Pitch contour is tone related, whereas the mel-cepstrum is used for determining phonetic transcriptions of utterances. Speech signals are preprocessed to extract these features for every 40-ms Hamming-windowed frame with 10-ms frame shifts.

Consider a text consisting of a succession of J Chinese characters, each of which is pronounced as a single syllable. In describing syllable j, let t_j represent the lexical tone and let $\{w_{3j-2}, w_{3j-1}, w_{3j}\}$ represent a BPC triplet used to tokenize the syllable onset, nucleus, and ending. The underlying tone and BPC sequences of an utterance can thus be defined by $T=\{t_1, t_2, \ldots, t_J\}$ and $W=\{w_1, w_2, \ldots, w_{3J}\}$, re-

TABLE III. The eight traditional tonal categories of Chinese language.

	Tonal category			
Initial class	*ping*	*shaang*	*chiuh*	*ruh*
Unvoiced	*yinping* (upper level)	*yinshaang* (upper rising)	*yinchiuh* (upper departing)	*yinruh* (upper entering)
Voiced	*yangping* (lower level)	*yangshaang* (lower rising)	*yangchiuh* (lower departing)	*yangruh* (lower entering)

spectively. Notice that not all syllables have three phonemes and hence null frames may exist in the BPC sequence W. From a modeling perspective, speech signals can be considered as templates formed by concatenating sequences of acoustic segments. Each segment roughly represents a BPC and is characterized by variable-length vector sequences of two acoustic features: pitch and mel-cepstrum. Mel-cepstral features are measured frame by frame and are of the following form:

$$\mathbf{c}=\{c_{s(1)},\ldots,c_{s(2)-1},c_{s(2)},\ldots,c_{s(3)-1},\ldots,c_{s(3J)},\ldots,c_K\}, \quad (1)$$

where K is the number of frames in an utterance and $s(l)$ denotes the starting frame for segment l. Similarly, $\mathbf{p}=\{p_1,p_2,\ldots,p_K\}$ is the sequence of K vectors representing the pitch measurements of an utterance.

The first of the three dialect-ID experiments we conducted was based on sequential BPC statistics, the second on pitch contour, and the third on a combination of pitch and segmental features. We begin by presenting the formulation of a probabilistic framework employed in the third experiment. Speech signals were first processed to extract pitch and mel-cepstral features, and these feature measurements were used to train stochastic models for every dialect to be recognized. Dialects were then identified by matching test utterances with the stochastic model of each dialect and calculating the *a posteriori* probability $\Pr(L_i|W,T,\mathbf{c},\mathbf{p})$ of the measurements $\{\mathbf{c},\mathbf{p}\}$ and the sequences $\{W,T\}$ for each dialect L_i. According to the maximum-likelihood decision rule, the classifier should decide in favor of a dialect $\hat{L}$, satisfying

$$\hat{L}=\arg\max \log \Pr(L_i|W,T,\mathbf{c},\mathbf{p}). \quad (2)$$

Since language-discriminating information can be found at various levels, it is worth evaluating the relative contribution towards dialect ID that each source of information provides. To advance with this, it is more convenient to rewrite Eq. (2) as

$$\hat{L}=\arg\max_i\{\log \Pr(\mathbf{c}|\mathbf{p},W,T,L_i)+\log \Pr(\mathbf{p},T|W,L_i) + \log \Pr(W|L_i)\}, \quad (3)$$

where the *a priori* dialect probability $\Pr(L_i)$ is assumed to be uniform and hence ignored. When only access to the BPC sequence W and mel-cepstral features $\mathbf{c}$ are available, the dialect-ID process can be simplified as follows:

$$\hat{L}=\arg\max_i[\log \Pr(\mathbf{c}|W,L_i)+\log \Pr(W|L_i)]. \quad (4)$$

A two-step approach, BPC recognition followed by phonotactic analysis, has been shown to be effective for language ID[9] and hence was employed in experiment 1. During recognition, the front-end BPC recognizer decodes the mel-cepstral features $\mathbf{c}$ into a BPC sequence $\hat{W}$ using the following expression:

$$\hat{W}=\arg\max_W \log \Pr(\mathbf{c}|W,L_i). \quad (5)$$

After that, the phonotactic analysis component calculates the likelihood of BPC sequence $\hat{W}$ being produced in each of the dialects. The most likely language model is thereby identified, and the dialect $\hat{L}$ of that model is taken as the hypothetical dialect of the test utterance in the following form:

$$\hat{L}=\arg\max_i \log \Pr(\hat{W}|L_i). \quad (6)$$

The approach employed in experiment 2 incorporated only the prosodic information as represented by pitch contour $\mathbf{p}$ and the tone sequence T. This reduced dialect-ID processing to the following:

$$\hat{L}=\arg\max_i \log \Pr(\mathbf{p},T|L_i) = \arg\max_i[\log \Pr(\mathbf{p}|T,L_i)+\log \Pr(T|L_i)]. \quad (7)$$

Implicit in this equation is the assumption that the prosodic model $\Pr(\mathbf{p},T|L_i)$ can be expressed as the product of two separate models: the pitch model $\Pr(\mathbf{p}|T,L_i)$ and the tone model $\Pr(T|L_i)$. The pitch model accounts for the various realizations of Chinese tones that may occur across dialects, and the tone model accounts for the tone statistics within each dialect.

TABLE IV. Tonal categories used in Mandarin, Holo, and Hakka, along with their tone values on the 5-point scale of pitch height. (Underlining of a tonal value indicates that the tone in question is shorter than those which are not underlined.)

Tonal category		Dialect		
		Mandarin	Holo	Hakka
ping	*yin*	55	43	44
	yang	35	21	12
shaang	*yin*	214	51	31
	yang			
chiuh	*yin*	51	35	42
	yang		212	
ruh	*yin*		43	21
	yang		21	44

III. EXPERIMENT 1: BPC RECOGNITION FOLLOWED BY LANGUAGE MODELING

A. Introduction

The proposed approach was motivated by previous experiments[2] showing that languages can be distinguished solely by means of sequential BPC statistics. Our system consisted of BPC recognizers followed by phonotactically motivated language models, and included two subsystems. The first processed utterances using a bank of dialect-dependent acoustic models in parallel, and output phonetic elements associated with the most likely model. Given the mel-cepstral features $\mathbf{c}$, the most likely BPC sequence $\hat{W}=(\hat{w}_1,\hat{w}_2,\ldots,\hat{w}_{3J})$ was determined using Eq. (5). By assuming mel-cepstral measurements are statistically independent across segments, we were able to solve for the individually most likely BPC $\hat{w}_l$ for segment l as follows:

$$\hat{w}_l=\arg\max_{w_l}\log \Pr(\mathbf{c}^{(l)}|w_l,L_i),\quad 1\leqslant l\leqslant 3J, \tag{8}$$

where $\mathbf{c}^{(l)}=\{c_{s(l)},\ldots,c_{s(l+1)-1}\}$ represents the mel-cepstral measurements for segment l. The second subsystem calculated the likelihood that BPC sequence $\hat{W}$ would be produced in each of the dialects. The maximum-likelihood classifier hypothesized that $\hat{L}$ was the dialect of the test utterance using Eq. (6).

B. Method

1. Speech corpora

Eight male speakers, aged between 18 and 30, were employed to collect Chinese speech corpora that contained utterances spoken in three dialects, Mandarin, Holo, and Hakka. For this study we attempted to avoid the speaker bias by using speakers who are fluent in the three dialects studied. The first corpus, denoted as DB-1, was designed to provide a corpus of sentential utterances for the training and testing of language models. Our text materials consisted of 30 folk-tale passages in colloquial style. Each passage consisted of 26 to 32 syllables, and the texts were grouped by passages into sets of 20 and 10. The set with 20 passages was used for training, and the set with 10 passages was used for testing. All the speakers were asked to read the text three times, once in each of the three dialects. Each syllable was spoken almost as if isolated from the adjacent syllables, but without pauses and with syllables joined in a normal-feeling and fluent manner. The number of training utterances in DB-1 was 480 (20 passages$\times$8 speakers$\times$3 dialects), and the number of test utterances in DB-1 was 240 (10 passages$\times$8 speakers $\times$3 dialects). The second corpus, denoted as DB-2, contained two sets of monosyllabic utterances produced by each of the eight speakers, one for training and one for testing in our BPC recognition experiment. Each set consisted of one reading of all eligible syllables, including 408 Mandarin syllables, 808 Holo syllables, and 708 Hakka syllables. All of the utterances in the speech corpora were recorded in a relatively quite environment, and then sampled at 16 kHz with 16-bit precision.

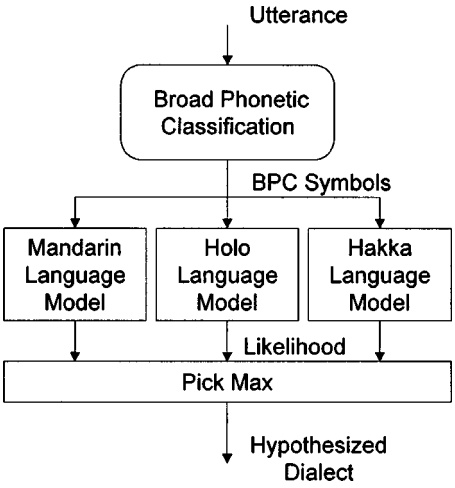

FIG. 1. Illustration of dialect-ID process which performs broad phonetic classification followed by phonotactic analysis.

2. Procedure

The basic idea was to perform phonotactic analysis after speech utterances had been tokenized into BPC sequences. A block diagram of the proposed dialect-ID system is shown in Fig. 1. In designing the BPC recognizer, we found the phonological structures of Chinese syllables could be used to advantage in broad phonetic segmentation of speech. As shown in Fig. 2, the BPC recognizer begins with *initial/final* segmentation in order to reduce the inventory size of allowable units of which Chinese syllables are composed. After

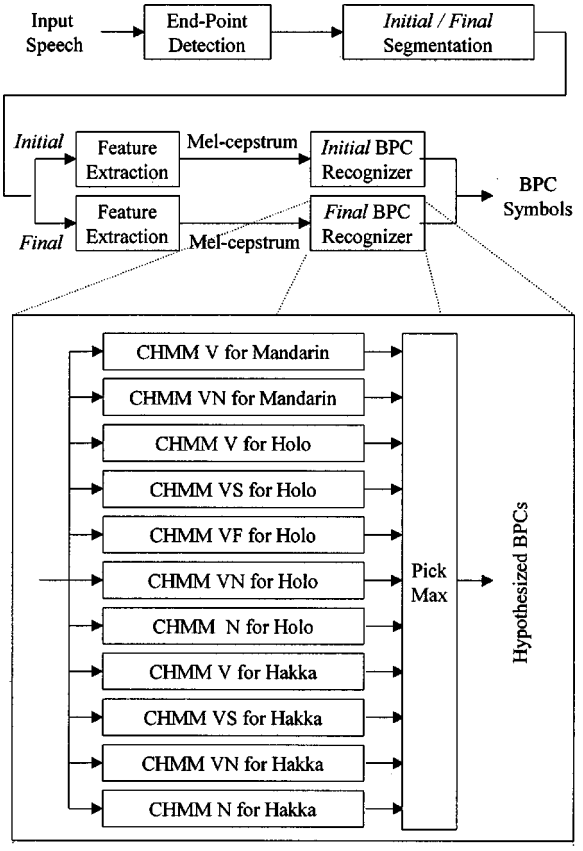

FIG. 2. Detailed description of broad phonetic classification (S: stop, F: fricative, A: affricate, N: nasal, V: vowel or diphthong).

TABLE V. Dialect-ID results based on sequential BPC statistics.

	Recognition		
Actual	Mandarin	Holo	Hakka
Mandarin	**0.50**	0.00	0.50
Holo	0.00	**0.80**	0.20
Hakka	0.10	0.00	**0.90**

that, speech utterances are converted from their digital waveform representations into streams of feature vectors consisting of the lowest ten coefficients of the mel-cepstrum. The temporal structures of these feature vectors are described using a segment-based continuous density hidden Markov model (CHMM) with a left-to-right topology. Each model has nine states and its state observation probability density is modeled as a mixture of 15 underlying Gaussian densities. The training set of the DB-2 corpus was used to estimate the model parameters according to the segmental *k*-means algorithm.[10] During recognition, we employ Viterbi decoding to find the optimal state sequence associated with observed acoustic features and then calculate the likelihood that test subsyllables were produced in each of the CHMMs. Finally, test subsyllables are tokenized as BPC patterns used to train the maximum-likelihood model.

Using the BPC recognizer as a front end, phonetic transcriptions of speech utterances are reduced to five-character alphabets and these samples are used to form language models that perform the dialect-ID task. Training and test utterances were chosen from the DB-1 corpus. In the training phase, a separate language model was created for each dialect by running the training utterances into the BPC recognizer and computing transition probabilities between successive BPCs. In our implementation, an ergodic five-state discrete observation HMM (DHMM) was used with parameters trained according to the Baum–Welch reestimation algorithm.[11] When an unknown utterance is received, the language model receives as its input the sequence of recognized BPCs and produces as output the likelihood of the dialects being spoken. Finally, the dialect of the language model that predicts the utterance with the highest likelihood is taken as the dialect of the test utterance.

C. Results and discussion

We first examined the performance of the CHMM-based BPC recognizer used as the front-end processor in this experiment. The top-choice accuracy achieved a recognition score of 81.4%, as compared with phonetically labeled data. Further analysis of our results showed that recognition errors occurred mainly in classification of fricative sounds as stops. Sequential statistics on these BPCs were then input to the language models that performed dialect ID. Table V shows a confusion matrix using the identification results for this experiment. The rows of the confusion matrix correspond to the dialects actually being spoken and the columns indicate the dialects identified. The classification accuracy of 73.3% indicates that BPC sequence information alone cannot provide sufficient cues for making accurate dialect-ID decisions. As the table shows, dialect-ID results have a bias towards identifying test utterances as Hakka. We speculate that this might be attributed to the difference in closeness between pairs of the three dialects. Support for such a speculation can be found in Cheng,[12] in which the correlation method was applied to phonological elements to quantify affinity among Chinese dialects. It was found that the highest degree of closeness among the three dialects studied was in the Mandarin–Hakka pair, the middle in the Holo–Hakka pair, and the least in the Mandarin–Holo pair. To elaborate further, we follow the method in Juang and Rabiner[13] and compute the probabilistic distance for measuring the dissimilarity between pairs of DHMM-based language models. Considering two HMMs specified by the parameter sets λ_1 and λ_2, the probabilistic distance measure is defined by

$$\mathcal{D}_s(\lambda_1,\lambda_2)=\frac{1}{2M}\left[\log\frac{\Pr(\mathcal{O}^{(2)}|\lambda_1)}{\Pr(\mathcal{O}^{(2)}|\lambda_2)}+\log\frac{\Pr(\mathcal{O}^{(1)}|\lambda_2)}{\Pr(\mathcal{O}^{(1)}|\lambda_1)}\right], \tag{9}$$

where $\mathcal{O}^{(j)}$ is the sequence of M observations generated by the model λ_j. It was found that as the distance measure increased, there was a corresponding improvement in dialect-ID accuracy. Our results showing the measured distances for pairwise dialect-ID tasks are plotted in Fig. 3. It is clear from this figure that the dialect-ID system using BPC sequence information was more successful when applied to distinguishing Mandarin from Holo. We also found that the system did not yield better performance with an increase in the number of states used in the language model, perhaps because Chinese-language phonologic pattern is predominantly an alternation of C_1, U, and C_2, making it particularly suited to a three-state language model.

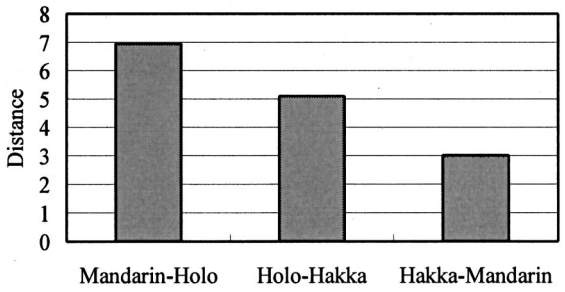

FIG. 3. The measured distances between language models for pairwise dialect ID.

IV. EXPERIMENT 2: PROSODIC MODELING

A. Introduction

Most current approaches to language ID make little or no use of prosodic measures, despite evidence showing that prosodic information is useful in human identification of languages. The main reason for this is the difficulty of finding an appropriate feature set that captures linguistically relevant prosodic information. Early approaches that incorporated a limited number of prosodic features did not produce satisfactory results.[14] Improved language-ID performance requires better modeling of prosody using a large set of feature measurements such as those proposed by Thyme-Gobbel and Hutchins.[15] They used a total of 220 features including av-

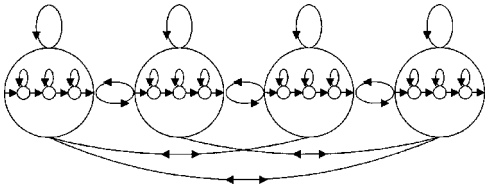

FIG. 4. Illustration of CHMM-based prosodic model used for Mandarin.

erages, deltas, standard deviations, and correlations of measures deduced from pitch contours, syllable durations, amplitudes, and rhythms. However, increasing the amount of detail in the models can be computationally costly. This problem can be alleviated in the dialect-ID task, mainly because the Chinese tonal system provides an efficient way to describe pitch contour dynamics. The goal of this experiment was to investigate whether Chinese dialects can be identified using only pitch measurements **p** and the tone sequence *T*. Accordingly, we sought to determine the most likely dialect $\hat{L}$ using Eq. (7).

B. Method

The utterances used to train and test the prosodic models were taken from the DB-1 corpus. Prosodic models designed to capture the tonal statistics of individual dialects were created using a composite HMM structure. The underlying hypothesis is that the tones in utterances are produced as probabilistic functions of ergodic Markov chains. Each state corresponds to one of the tonal categories and is built from an elementary three-state left-to-right HMM. Because at most, one turning point exists in standard pitch contours, it suffices to postulate that the pitch contour dynamics corresponding to various tones can be modeled by three states. Figure 4 shows the state transition diagram required to represent the Mandarin prosodic model. In our implementation, each elementary model was created using a CHMM with the observation probability density modeled as a mixture of five Gaussian densities per state. Observations were independent streams of pitch and differential pitch extracted from digitized speech using the simple inverse filter tracking (SIFT) algorithm.[16] In order to describe pitch contour dynamics, CHMM-based prosodic models for each of the target dialects were constructed using parameters trained with the segmental *k*-means algorithm. When a test utterance is received, the prosodic model takes the pitch measurements as input and produces the likelihood of the dialects being spoken as output. The dialect of the model most likely to have produced the test utterance observations is taken as the dialect of the test utterance.

C. Results and discussion

Table VI shows a confusion matrix using dialect-ID results for experiment 2. We can see in the table that pitch information alone allowed the system to identify three dialects with an accuracy score of 64.3%, indicating that prosodic features are highly useful in Chinese dialect ID. The success of this prosodic model arises from its ability to exploit not only differences among dialects that exist in tonal statistics, but also differences in the realizations of similar tones in those dialects. To elaborate further, we plotted the probabilistic distances that measured dissimilarities between pairs of CHMM-based prosodic models. The results, shown in Fig. 5, indicate that from a prosodic standpoint, differentiation between Mandarin and Hakka is easier than other pairwise dialect-ID tasks. While these results suggest that pitch-based prosodic features possess language-discriminating information, it may be overly ambitious to hope that a single prosodic model can be designed to capture all of the complexities of a dialect. Therefore, a system that considers segmental and prosodic information might be required to achieve a higher degree of dialect-ID accuracy.

TABLE VI. Dialect-ID performance of the pitch-based prosodic model.

	Recognition		
Actual	Mandarin	Holo	Hakka
Mandarin	**0.73**	0.12	0.15
Holo	0.30	**0.54**	0.16
Hakka	0.11	0.23	**0.66**

V. EXPERIMENT 3: SYSTEM INTEGRATION

A. Introduction

The approach employed in experiment 1, BPC recognition followed by language modeling, has been shown to be effective for language ID,[9,17] and may be considered as representing the state of the art. The main disadvantage of this approach is that the observations used in language modeling are not extracted directly from mel-cepstral coefficients, but rather from the imperfect outputs of the front-end BPC recognizer. To compensate for this shortcoming, we propose incorporating dialect-specific phonotactic constraints into the phonetic tokenization rather than applying these constraints after BPC recognition has been completed. Furthermore, we believe that prosody may provide many benefits as an enhancement to the state-of-the-art technique by acting as a secondary source of language-discriminating information. Although a similar approach to combining segmental features with prosodic modeling was presented by Hazen and Zue,[3] the basic design here is quite different due to the special characteristics of the Chinese language. It has long been recognized that there was no explicit model to describe prosodic information, especially for nontonal languages such as English. Therefore, Hazen and Zue[3] proposed a prosodic

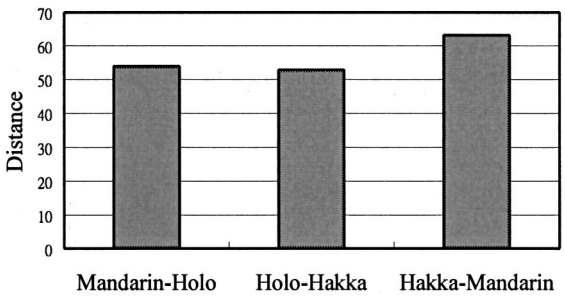

FIG. 5. The measured distances between prosodic models for pairwise dialect ID.

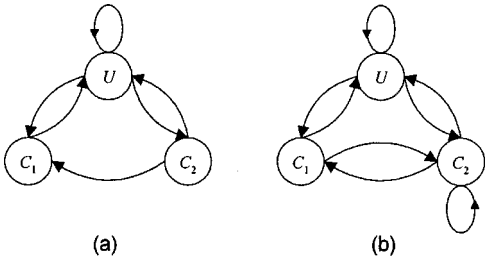

FIG. 6. State transition diagrams of composite models used for (a) Mandarin and (b) Holo and Hakka (C_1: syllable onset, U: syllable nucleus, C_2: syllable ending).

model that only captures simple statistical information about the fundamental frequency and segmental duration of an utterance. However, the prosodic modeling problem is not a serious obstacle in our dialect-ID system, mainly because Chinese-language prosodic units are annotated in the tone levels. For this experiment we attempted to determine the most likely dialect using Eq. (2), by combining segmental and prosodic information within a unified framework.

B. Method

The basic idea was to combine segmental and prosodic information to achieve a higher degree of dialect-ID accuracy. The first step toward realization was to use a three-state Markov chain to model the changing statistical characteristics present in BPC production. Each state corresponds to one acoustic segment, such as syllable onset (C_1), syllable nucleus (U), or syllable ending (C_2). The choice of model topology depended on the syllable types phonologically allowed in the target dialect. Holo and Hakka allow six syllable types, represented by U, C_1U, UC_2, C_1UC_2, C_1C_2, and C_2, while Mandarin allows only four syllable types, U, C_1U, UC_2, and C_1UC_2. Figure 6 shows the state transition diagrams required to model the individual dialects. This model has a composite structure; it is a large Markov chain in which each state is built from a bank of elementary left-to-right HMMs. Note that the final state of one elementary HMM is connected to the initial state of the following elementary HMM by a null transition.

In order to integrate prosodic features into the composite model, we propose using tonal BPCs rather than BPCs as the bases for dialect discrimination. Every tonal BPC can, in fact, be considered as a combination of two components: one of the possible tones plus one of the five possible BPCs. Since pitch is defined only for voiced speech, the pertinent tone-related portions of syllables are the nuclei from which distinctive pitch changes are perceived. Recognizing this, we needed only to superimpose distinct tonal notations onto the BPC equivalents of the syllable nuclei in order to obtain a set of BPC variants that shares the same BPCs but has distinct lexical tones. To illustrate this, details of the elementary HMMs required to model the Holo syllables are shown in Fig. 7, with V_j denoting the BPC symbol V associated with the tone j. In our implementation, each elementary model uses a three-state left-to-right CHMM with its observation probability density modeled as a mixture of five Gaussian densities per state. Observations are independent streams of

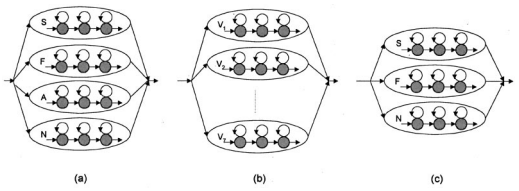

FIG. 7. Elementary HMMs required for modeling Holo (a) syllable onset, (b) syllable nucleus, and (c) syllable ending (S: stop, F: fricative, A: affricate, N: nasal, V: vowel or diphthong).

mel-cepstral coefficients and pitch measurements derived from digitized speech. By using mel-cepstral coefficients as parts of state observations, the stochastic acoustic–phonetic model can be directly incorporated into the dialect-ID process without forward decoding of underlying BPC sequences. This eliminates many of the errors made by the front-end BPC recognizer.

The dialect-ID system operates in two phases: training and recognition. The utterances used here were taken from the DB-1 corpus. In the training phase, a composite model was trained for every dialect to be recognized by running the segmental k-means algorithm. During recognition, the test utterance was classified by extracting feature vectors from digitized waveform and then calculating the likelihood that these feature vectors were produced in each of the three dialects. The dialect of the model most likely to have produced the test utterance was taken as the dialect of the test utterance. By allowing the system to use a composite model during the Viterbi decoding process, the most likely dialect was optimal with respect to some combination of segmental and prosodic information.

C. Results and discussion

Table VII lists a confusion matrix showing the dialect-ID results for the system that examined differences between dialects at broad-phonetic and prosodic levels. In it we see that compared with the first two experiments, the effectiveness of using an integrated segmental-prosodic model for dialect ID is clearly demonstrated. The top-choice accuracy was measured to obtain a recognition score of 93.0%. Among the reasons for this success, we find that the integration of acoustic–phonetic and phonotactic information by means of a composite HMM model increases phonological discrimination across dialects. It is also important to note that the language-discriminating power of the system can be improved by using tonal BPCs as the bases for its elementary HMMs.

TABLE VII. Dialect-ID performance of the integrated segmental-prosodic model.

	Recognition		
Actual	Mandarin	Holo	Hakka
Mandarin	**0.94**	0.03	0.03
Holo	0.00	**0.86**	0.14
Hakka	0.00	0.01	**0.99**

VI. SUMMARY

This paper presents several approaches that employ varying degrees of linguistic traits discriminate among three major Chinese dialects spoken in Taiwan. The first approach includes two subsystems, the first of which uses acoustic models to recognize broad-phonetic classes, and the second uses language models to identify target dialects. Simulation results indicate that while segmental features are useful in Chinese dialect ID, other sources of information are likely to help in distinguishing between dialects with greater accuracy. The importance of incorporating prosodic information is reflected in the observation that using only pitch contour dynamics allows the system to identify three dialects with 64.3% accuracy. Recognizing this, we studied the issue of how to best combine segmental and prosodic features within one system. Using a composite HMM for information integration, our proposed method demonstrates the promise of improving system performance by increasing its language-discriminating power. The main attraction of the proposed dialect-ID approach arises from its being tailored specifically to the Chinese language, and the ease with which it can be extended to identify other Chinese dialects as well.

Although fairly good performances were reported in these experiments, more work is needed to further validate the proposed dialect-ID system for a wider range of speech corpora. Specifically, it should include combined male and female speech. It should also include continuous speech that preserves tone sandhi[8] during recording even when the utterances are being stretched temporally for easy processing. When dealing with combined male and female speech, a promising approach is to first determine the speaker's gender and then to perform dialect identification using the models of selected gender. Automatic gender classification has been previously investigated using the difference of position of the first and second formants between male and female speakers.[18] In extending the current system for continuous speech, more sophisticated tone models are necessary because tone patterns of syllables in continuous speech are subject to various modifications by sandhi rules. In our view, this problem should be approached with the same modeling techniques as were used in tone recognition of continuous speech. Previous work[6] on Mandarin speech suggests that it suffices to describe the tone sandhi and coarticulation effects using a total of 23 context-dependent tone models. However, it is still unclear at this time how many such models will be required for accurate modeling the tone variations across syllables in Holo and Hakka.

ACKNOWLEDGMENTS

This research was supported by the National Science Council, Taiwan, ROC, under Grant No. NSC87-2213-E009-039. The authors are very grateful to the unknown reviewers and the associate editor, Dr. Douglas O'Shaughnessy, for their careful readings of this paper and their constructive suggestions.

[1] Y. K. Muthusamy, E. Barnard, and R. A. Cole, ''Reviewing automatic language identification,'' IEEE Signal Process. Mag. **4**, 33–41 (1994).
[2] A. S. House and E. P. Neuburg, ''Toward automatic identification of the language of an utterance. I. Preliminary methodological considerations,'' J. Acoust. Soc. Am. **62**, 708–713 (1977).
[3] T. J. Hazen and V. W. Zue, ''Segment-based automatic language identification,'' J. Acoust. Soc. Am. **101**, 2323–2331 (1997).
[4] M. A. Zissman, ''Comparison of four approaches to automatic language identification of telephone speech,'' IEEE Trans. Speech Audio Process. **SAP-4**, 31–44 (1996).
[5] L. F. Lamel and J. L. Gauvain, ''Language identification using phone-based acoustic likelihoods,'' in *Proceedings of the 1994 International Conference on Acoustics, Speech, and Signal Processing* (IEEE, Piscataway, NJ, 1994), pp. 293–296.
[6] L. S. Lee, ''Voice dictation of Mandarin Chinese,'' IEEE Signal Process. Mag. **14**, 63–101 (1997).
[7] S. R. Ramsey, *The Languages of China* (Princeton University Press, Princeton, NJ, 1987).
[8] Y. R. Chao, *A Grammar of Spoken Chinese* (University of California, Berkeley, CA, 1968).
[9] Y. K. Muthusamy, K. Berkling, T. Arai, R. A. Cole, and E. Barnard, ''A comparison of approaches to automatic language identification using telephone speech,'' in *Proceedings of 3rd European Conference on Speech Communication and Technology* (European Speech Communication Association, Grenoble, France, 1993), pp. 1307–1310.
[10] L. R. Rabiner, J. G. Wilpon, and B. H. Juang, ''A segmental *k*-means algorithm training procedure for connected word recognition,'' AT&T Tech. J. **65**, 21–32 (1986).
[11] L. E. Baum, T. Petrie, G. Soules, and N. Weiss, ''A maximization technique occurring in the statistical analysis of probabilistic functions of Markov chains,'' Ann. Math. Stat. **41**, 164–171 (1970).
[12] C. C. Cheng, ''Quantifying affinity among Chinese dialects,'' J. Chin. Linguist. **3**, 78–112 (1991).
[13] B. H. Juang and L. R. Rabiner, ''A probabilistic distance measure for hidden Markov models,'' AT&T Tech. J. **64**, 391–408 (1985).
[14] Y. K. Muthusamy, ''Segmental approach to automatic language identification,'' Ph.D. thesis, Oregon Graduate Institute of Science & Technology (1993).
[15] A. Thyme-Gobbel and S. E. Hutchins, ''On using prosodic cues in automatic language identification,'' in *Proceedings of the 1996 International Conference on Spoken Language Processing* (Philadelphia, PA, 1996), pp. 1768–1771.
[16] J. D. Markel, ''The SIFT algorithm for fundamental frequency estimation,'' IEEE Trans. Audio Electroacoust. **AU-20**, 367–377 (1972).
[17] T. J. Hazen and V. W. Zue, ''Automatic language identification using a segment based approach,'' in *Proceedings of the 3rd European Conference on Speech Communication and Technology* (European Speech Communication Assoc., Grenoble, France, 1993), pp. 1303–1306.
[18] R. Vergin, A. Farhat, and D. O'Shaughnessy, ''Robust gender-dependent acoustic–phonetic modelling in continuous speech recognition based on a new automatic male/female classification,'' in *Proceedings of the 1996 International Conference on Spoken Language Processing* (Philadelphia, PA, 1996), pp. 1081–1084.

Angular scatter ultrasound imaging of wavelength scale targets

James C. Lacefield[a] and Olaf T. von Ramm
Department of Biomedical Engineering and Center for Emerging Cardiovascular Technologies, Duke University, Durham, North Carolina 27708

(Received 28 August 1999; accepted for publication 20 July 2000)

A bistatic ultrasound imaging system is demonstrated that uses two 32-element linear phased array transducers oriented at an angle of 40 degrees to one another. The system simultaneously acquires and displays in real time one conventional backscatter image and one ''angular scatter'' image formed using side-scattered echoes from the same B-mode sector region. Experiments are presented that show differences in the magnitudes of backscatter and angular scatter signals acquired from three nylon monofilaments with diameters less than one wavelength and from soft tissue structures *in vivo*. The relative magnitudes of angular scatter signals from the monofilaments are qualitatively consistent with a theoretical analysis of acoustic scattering from elastic cylinders. Larger tissue features are more clearly defined in angular scatter images. This result is attributed to the orientation of specularly reflecting surfaces and the expected influence of scattering angle on the system's sensitivity to different scatterer spacings.
[S0001-4966(00)05410-2]

PACS numbers: 43.80.Ev, 43.80.Jz, 43.80.Vj [FD]

I. INTRODUCTION

A real-time ultrasound imaging system has been implemented using two linear phased array transducers.[1] One transducer, the backscatter array, transmits an ultrasonic pulse into the medium to be imaged and detects the returning echoes to form a B-mode image. The second transducer, the angular scatter array, is positioned at a 40-degree angle to the transmitting aperture and receives echoes scattered away from the transmit axis along the direction of the scattering angle, θ (Fig. 1). The system thus simultaneously acquires and displays one conventional backscatter image and one ''angular scatter'' image of the same region in real time.

The angular scatter system is analogous to bistatic radar and sonar technologies that have found specialized applications in those fields. One use for bistatic radar that is relevant to the present study is improved detection of targets such as ''stealth'' aircraft that scatter most strongly at angles away from backscatter.[2] This article reports experiments demonstrating progress toward similar applications in medical imaging. Signals acquired from discrete solid targets and angular scatter images of soft tissue structures are examined. Solid elastic targets with diameters on the order of one wavelength are considered because their scattering responses frequently include prominent peaks at the scattering angles formed by the experimental system. A theoretical model of acoustic scattering[3] is reviewed to illustrate the differences expected in backscatter and angular scatter signals from elastic cylinders of various diameters. Pulse-echo signals acquired from three nylon monofilaments with different diameters are compared qualitatively to model calculations. Sample *in vivo* images demonstrate that the use of a bistatic imaging geometry is feasible in a clinical setting and that contrast differences are observed between backscatter and angular scatter images of soft tissue. An explanation for the latter result is given using a k-space description of the imaging process.[4,5]

II. THEORY

A. Acoustic scattering from solid objects

The most commonly cited analytical model for scattering from a discrete target in a fluid medium is Faran's orthogonal function series solution to the wave equation at the boundary of the scatterer.[3] The model assumes an incident plane wave and uses the coordinate system shown in Fig. 2. Faran obtained an asymptotic solution for the scattered pressure observed at a distance, r, much larger than the radius of the scatterer, a. For the example of a cylindrical scatterer,

$$|p_s| = P\left(\frac{2}{\pi kr}\right)^{1/2}\left|\sum_{m=0}^{\infty} \varepsilon_m \sin\eta_m \exp(i\eta_m)\cos(m\theta)\right|, \qquad (1)$$

where P denotes the amplitude of the incident plane wave. The Neumann factor, ε_m, is a constant whose value is one when $m=0$ and two for all positive integer m. The parameter η_m denotes the phase angles of the various modes of the scattered wave. The phase angles are complicated functions of the density, longitudinal speed of sound, and Poisson's ratio of the scatterer, the density and longitudinal speed of sound of the surrounding fluid, and the product ka ($k=2\pi/\lambda$), which relates the radius of the target to the incident wavelength, λ.

The effect of cylinder radius on backscatter and angular scatter pressure magnitudes was studied by numerically evaluating Eq. (1) and plotting the results as functions of ka in Fig. 3. Scattering from nylon cylinders in water was analyzed for comparison with the experimental studies using nylon monofilaments that are reported later in this article. Nylon was modeled using published values[6] for its density ($\rho=1120$ kg/m^3), longitudinal speed of sound

[a]Current address: Department of Electrical and Computer Engineering, University of Rochester, Rochester, NY 14627.

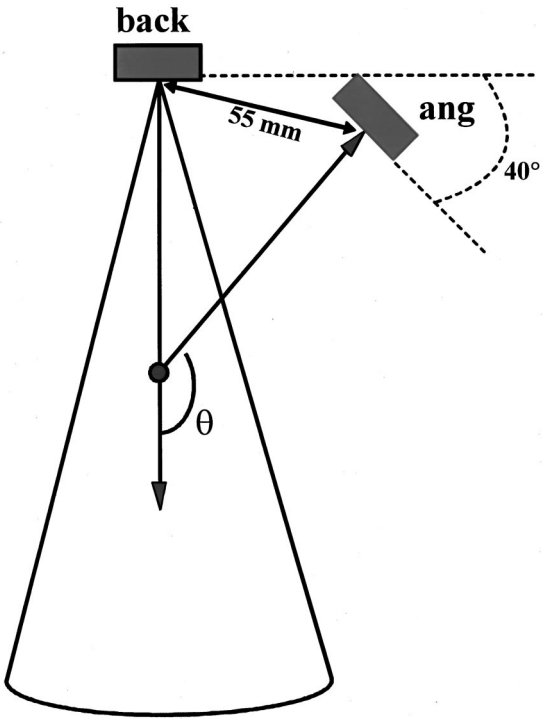

FIG. 1. Angular scatter imaging system geometry. The angular scatter array (ang) is positioned 55 mm away from the backscatter array (back) and rotated toward the backscatter array by 40 degrees. The instrument acquires B-mode images from within a sector region originating at the center of the backscatter array. The scattering angle, θ, at any point in the sector is defined by the angle between the transmit and receive directions, depicted by the arrows.

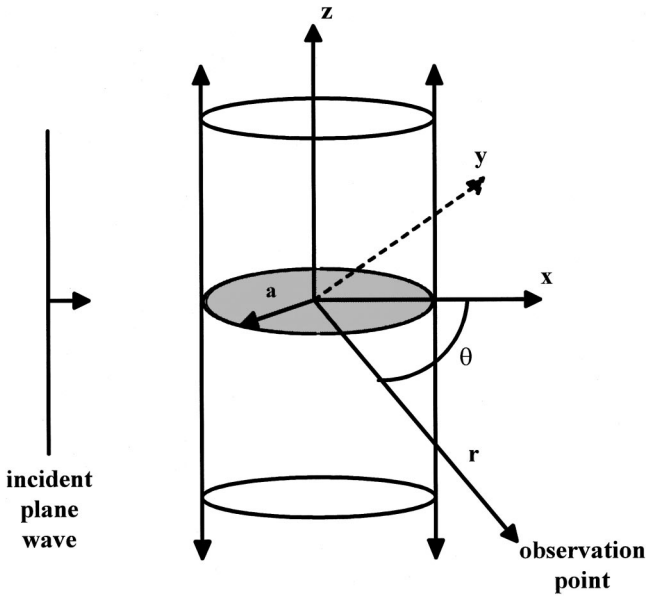

FIG. 2. Coordinate system for analysis of scattering from a cylinder with radius a. The cylinder is centered at the origin of the coordinate system and insonified by a plane wave propagating in the positive x direction. The scattered wave is observed at a position far from the origin specified by the vector $\mathbf{r}$ that subtends the scattering angle, θ, with the positive x axis.

($c=2600$ m/s), and Poisson's ratio ($\sigma=0.39$). The required material parameters for water are $\rho=1000$ kg/m^3 and $c=1480$ m/s. The backscatter and angular scatter curves were calculated by setting $\theta=180$ degrees and 135 degrees, respectively, where the former scattering angle represents the backscatter case and the latter angle occurs in the experimental system at the intersection of the normals to the transmit and angular scatter receive apertures. The vertical dotted lines on each graph mark the ka values 0.8, 1.9, and 2.7 that are produced at the center frequency of the system by the three monofilaments studied. Both curves in Fig. 3 are characterized by resonance peaks, which are typical features in the scattering responses of compressible solids.[7] The resonances occur at different values of ka in the backscatter and angular scatter echoes, which implies that elastic targets will appear with differing brightness levels in backscatter and angular scatter images, especially when $ka>1$.

B. K-space analysis of scattering experiments

The model reviewed above assumes a single frequency incident plane wave and measurement of the scattered pressure at a single point in the far field. These conditions correspond to sampling the scattered wave at a single spatial frequency, or a single point in k-space.[4,5] A realistic imaging system interrogates a medium over an extended region of k-space that is defined by the spatial Fourier transform of the radio frequency point-spread function. In this case, the measured data is equivalent to the spatial frequency spectrum of the acoustic inhomogeneities windowed by the k-space spread of the imaging system. With reference to Fig. 3, the experimental angular scatter signal from a discrete target will be averaged over a ka interval determined by the system bandwidth and will also be a combination of responses over a range of scattering angles due to the finite extent of the apertures. As a result of this averaging, quantitative analysis of measured data using a scattering model like the one reviewed earlier is very difficult.

The k-space description of the imaging process also sug-

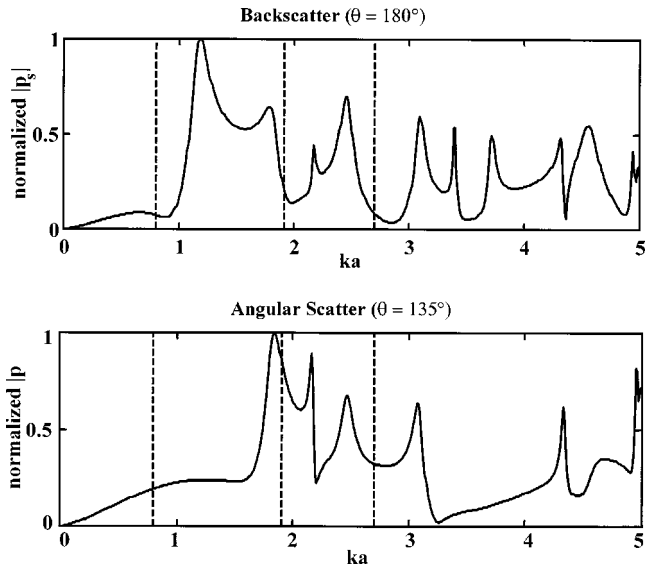

FIG. 3. Theoretical backscatter ($\theta=180$ degrees) and angular scatter ($\theta=135$ degrees) pressure magnitudes scattered from a nylon cylinder in water, plotted as functions of ka. The curves were generated by numerical evaluation of Eq. (1). The vertical lines indicate the ka values corresponding to the three monofilaments used in the measurements at the center frequency of the experimental system.

gests a means by which differences in backscatter and angular scatter signals from a diffusely scattering medium such as soft tissue can be related to scatterer size. The k-space spread of the system is centered at a spatial frequency magnitude equal to the magnitude of the reference scattering vector,[5]

$$|\mathbf{K_0}| = 2k \sin(\theta/2). \quad (2)$$

Equation (2) indicates that the system samples the medium at lower spatial frequencies as the scattering angle decreases from backscatter (θ=180 degrees). Therefore, an angular scatter system, compared to a backscatter system, will be more sensitive to tissue structures with larger characteristic scatterer spacings. The k-space spread of the system complicates this model, but this interpretation of Eq. (2) is valid provided the backscatter and angular scatter k-space windows are sufficiently nonoverlapping.

III. METHODS

A. Angular scatter system specifications

The angular scatter imaging system has been described in detail elsewhere,[1] but the transducer specifications and image format are reviewed here for reference during discussion of the experiments reported in this article. The system is comprised of two 32-element linear phased array apertures connected to the Duke University phased array scanner.[8] The arrays are positioned 55 mm apart from one another and angled toward one another by 40 degrees, as shown in Fig. 1. Both transducers have a 2.5-MHz center frequency and a −6-dB bandwidth of 0.9 MHz, but the backscatter aperture is 12 mm in length whereas the angular scatter aperture is 11 mm. These arrays were the most similar pair of transducers available for this study.

The angular scatter system operates in a manner similar to a conventional medical ultrasound scanner. The backscatter array transmits a steered, focused pulse into the medium and detects backscattered echoes using dynamic receive focusing. The angular scatter signal is acquired by steering the receive beam of the angular scatter array in real time to track the propagating pulse, a procedure known as receive pulse chasing. Each scan line includes 33 discrete receive foci covering the range interval from 40 to 130 mm relative to the transmit origin. The scattering angles subtended at the receive foci typically range from 105 degrees to 155 degrees. The array positions and scattering angles were selected by considering the influence of scattering angle on spatial resolution, the rate at which the angular scatter receive beam must be steered to effectively track the pulse, and the operating characteristics of the Duke scanner.

B. Measurement of pulse-echo signals from monofilament targets

The amplitude of backscatter and angular scatter echoes from nylon monofilaments in water were studied as a function of depth. The arrays were clamped in fixed positions and suspended in a water tank with the backscatter array parallel to the surface of the water. A monofilament was attached to an aluminum frame and suspended below the backscatter array with its long axis perpendicular to the scan plane. The frame was clamped to a three-axis positioning stage (Velmex, Inc., Bloomfield, NY) that was used to adjust the position of the monofilament. Envelope detected signals were acquired along the 0-degree azimuth direction (i.e., normal to the backscatter array) and displayed on a digital oscilloscope (model TDS 754A, Tektronix, Inc., Wilsonville, OR). Each signal represented a single scan line acquired using 33 receive foci positioned such that receive pulse chasing was performed over the range interval from 40 to 130 mm. Twenty-five acquisitions of each signal were averaged on the oscilloscope, and the measurement function of the oscilloscope was used to display the maximum voltage of the averaged signal with a precision of ±0.01 V. The maximum value of the signal envelope was studied as a measure of the brightness with which the target would appear in a B-mode image. Measurements were performed at 43 target positions from 36 to 120 mm range in 2-mm increments. The scattering angle varied from 115 degrees to 155 degrees over that range interval. The experiment was repeated for each of three monofilaments with diameters of 0.15, 0.36, and 0.51 mm (0.25λ, 0.61λ, and 0.86λ, respectively).

C. Acquisition of *in vivo* images

Backscatter and angular scatter images of the liver and kidney of a healthy male volunteer were acquired to demonstrate the feasibility of angular scatter imaging in a clinical setting and to allow qualitative comparisons of soft tissue images. The images were acquired in real time and videotaped, and then selected images were photographed. Some modifications were made to the imaging procedure described in Sec. III A to improve the appearance of the images. The size of the transmit aperture was doubled to 64 elements and 24 mm to increase the acoustic power output and decrease the transmit beam width. Logarithmic compression was applied to the received signals to allow data within a 30-dB magnitude range to be represented on a 20-dB dynamic range display. The display hardware that corrects geometric distortion in angular scatter images[9] was abandoned to eliminate noise introduced by its analog-to-digital and digital-to-analog converters. Partial, but imperfect, correction for geometric distortion was obtained by varying the deflection rate of the display's cathode ray beam line by line.

IV. RESULTS

A. Magnitudes of pulse-echo signals from monofilaments

The magnitudes of the backscatter signals from the three monofilaments are plotted as functions of range in Fig. 4, and the angular scatter data are plotted in Fig. 5. No error bars are shown on the graphs because the averaged signals were stable at the precision of the measurement (±0.01 V). The absolute magnitudes of the two signals are not directly comparable because the backscatter and angular scatter arrays were not matched, but qualitative comments can be made about the data. The backscatter signal amplitude decreased monotonically with increasing range above 50 mm. This observation is attributed to divergence of both the transmit beam and the scattered waves. In contrast, the angular

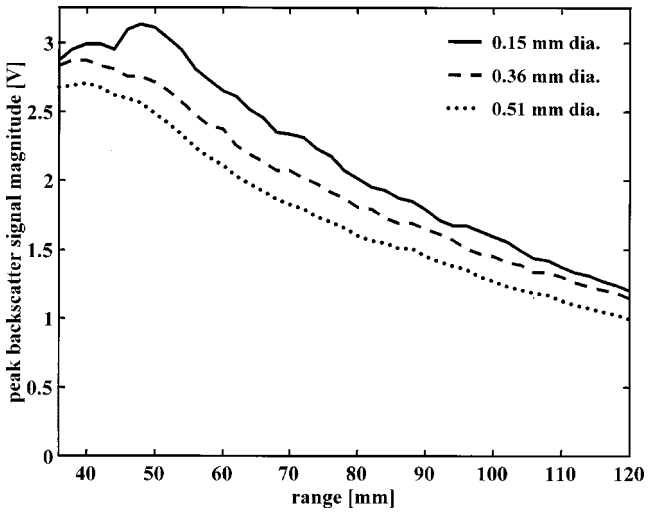

FIG. 4. Measured peak backscatter signal magnitudes as a function of range along the 0 degree azimuth direction for three monofilaments with diameters as indicated in the figure.

scatter data from the two larger targets each include a peak near the center of the scan line that coincided with the directivity peak of the receive array.[1] The angular scatter curves are less smooth than the backscatter curves because at each receive focus position the transmit pulse propagates across the lateral dimension of the angular scatter beam, which produces a fluctuation in sensitivity.

One noteworthy difference between the two signals can be demonstrated by comparing the data curves for the smallest monofilament to the curves for the larger targets. For both backscatter and angular scatter, the data curves for the 0.36- and 0.51-mm monofilaments have similar shapes, with the 0.36-mm data having slightly larger amplitude. However, the angular scatter signal from the 0.15-mm monofilament is significantly weaker than the other angular scatter signals, especially in the vicinity of the receiver directivity peak where

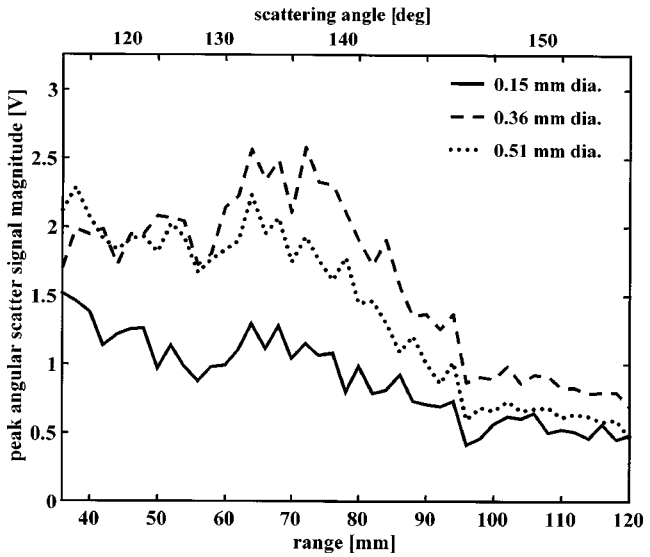

FIG. 5. Measured peak angular scatter signal magnitudes as a function of range along the 0 degree azimuth direction for three monofilaments with diameters as indicated in the figure. Scattering angles subtended at selected ranges are indicated along the top of the figure.

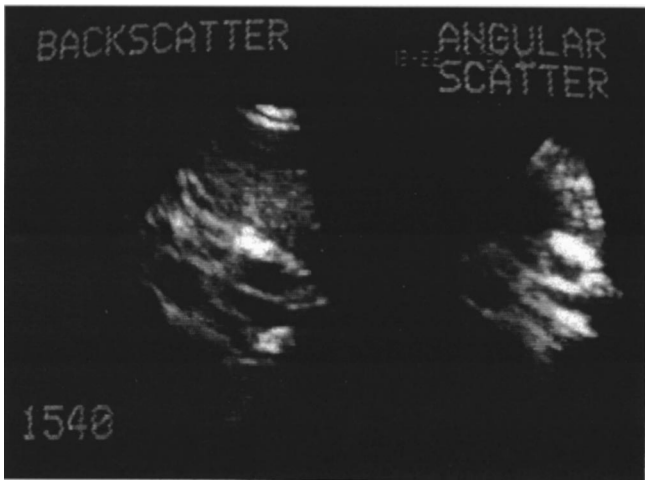

FIG. 6. Backscatter and angular scatter images showing cross sections of three abdominal blood vessels.

the 0.15-mm curve is noticeably flatter than the other curves. The 0.15-mm monofilament produced the largest backscatter amplitude, and the shape of the curve as a function of range is similar to the data curves obtained using the larger monofilaments.

B. Sample *in vivo* images

Transverse abdominal images showing some major blood vessels are presented in Fig. 6. The backscatter image is on the left side of the figure and the angular scatter image is on the right. The images are oriented as shown in Fig. 1 with the backscatter array directly above the sectors and the angular scatter array in the direction of the top right-hand corner of the images. The directivity of the angular scatter array is evident from the bright diagonal band through the center of the angular scatter image. The borders of the two large vessels in this region are much brighter in the angular scatter image than in the backscatter image. Some residual geometric distortion is apparent in the shape of the vessels in the angular scatter image. Similar comments apply to the transverse image of a kidney shown in Fig. 7. The speckle

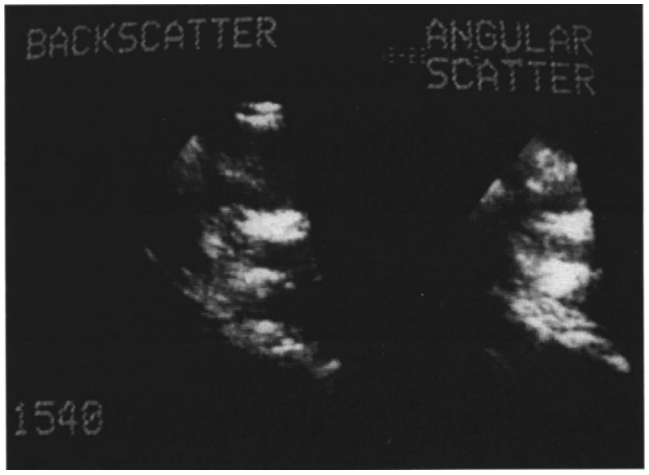

FIG. 7. Backscatter and angular scatter images showing transverse slices through the kidney.

pattern produced by the medulla of the kidney is significantly brighter in the angular scatter image.

V. DISCUSSION AND CONCLUSIONS

The purposes of the monofilament measurements summarized in Figs. 4 and 5 are to compare backscatter and angular scatter signals acquired from a simple target and to test if any differences between the two signals can be explained using the Faran scattering theory. Calcifications with diameters on the order of one wavelength are an example of elastic scatterers relevant to medical imaging that have been modeled using the Faran theory.[10,11] Calcified lesions will generally have more complicated geometries than the monofilaments, so conclusions drawn from the monofilament data may not be directly applicable to angular scatter detection of calcifications.

As discussed in Sec. III B, the broadband nature of the instrument makes comparisons between theoretical and measured scattering data difficult. For the example of the largest monofilament, the −6-dB frequencies of the system define a ka interval from 2.2 to 3.2 that includes two local minima and two local maxima of the theoretical backscatter curve. Therefore, local ka peaks are obscured by averaging over the system bandwidth, and the single-frequency Faran theory cannot be directly applied to the experimental data. The finite size of the apertures results in a range of scattering angles being subtended at any instant, so there is an averaging effect over those angles that is equivalent to the averaging over ka. Another complicating factor is that the angular scatter array has an unusually narrow directivity (the measured −3-dB width of the angular response is 20 degrees[1]), so the peaks in the angular scatter curves for the 0.36- and 0.51-mm monofilaments are strongly influenced by the receiver directivity. As a result, differences in the angular scatter signal magnitudes are largest around the directivity peak, which lies near the 135-degree scattering angle.

One point of agreement between the measurements and the analysis is that the amplitudes of the three angular scatter signals are in the order suggested by the theoretical curve (Fig. 3) sampled at the ka values of interest. In spite of the limitations summarized in the previous paragraph, this agreement seems physically meaningful. The effect of the instrument on the data may be approximated by visualizing a low-pass-filtered version of the theoretical angular scatter curve. It is reasonable to expect that such smoothing would produce a large peak near $ka=1.9$ (corresponding to the 0.36-mm monofilament), a slightly smaller peak near $ka=2.7$ (for the 0.51-mm monofilament), and a significantly lower scattered amplitude around $ka=0.8$ (for the 0.15-mm monofilament). That pattern is observed in the measured angular scatter data (Fig. 5), especially around the directivity peak where the receiver sensitivity is highest. A more thorough broadband analysis of the theoretical data following a method like that of Mast and Waag[5] is in principle possible, but it would be difficult to accurately account for the complicating factors listed above, so such computations are unlikely to enhance the qualitative comparisons made here.

The *in vivo* images are of interest for two reasons. First, they demonstrate the feasibility of using a bistatic imaging geometry in a clinical setting. One limitation of the two-array geometry is that a large acoustic window is necessary so both arrays can be kept in contact with the volunteer. Abdominal images were acquired so that requirement could be met. The second noteworthy observation is that larger anatomical structures are more clearly defined in the angular scatter images. Multiple factors contribute to that observation. For example, the surfaces of the abdominal blood vessels in Fig. 6 appear to be oriented appropriately to produce strong specular reflections in the direction of the angular scatter receiver. The importance of specular reflections in Fig. 6 is consistent with an earlier study[9] that attributed differences between backscatter and angular scatter images to a reduction of reverberation artifacts in the angular scatter images. A different comparison can be made for the kidney structure shown in Fig. 7, which is an example of a speckle target that has a brighter appearance in the angular scatter image. The relatively smaller magnitude of the reference scattering vector [Eq. (2)] in the angular scatter case implies that larger diffusely scattering structures should be highlighted in the angular scatter image compared to the backscatter image. One possible approach for future studies to corroborate this interpretation is to acquire images at other frequencies as an alternative means of changing the magnitude of the scattering vector.

The experiments reported here encourage further investigation of angular scatting imaging techniques for medical applications. Differences in backscatter and angular scatter signals have been demonstrated for discrete solid targets in the monofilament measurements and for specularly reflecting and diffusely scattering targets *in vivo*. It is especially noteworthy that those differences were discernable in real time images. Future efforts to identify applications where qualitative differences in the images are diagnostically significant are recommended to most effectively exploit the real time capability of the system.

ACKNOWLEDGMENTS

John Castellucci assisted with the acquisition of *in vivo* images. This project was supported by NSF/ERC Grant No. CDR-8622201 and NIH Grant No. HL-58104.

[1] J. C. Lacefield and O. T. von Ramm, ''Design and characterization of a real-time angular scatter ultrasound imaging system,'' IEEE Trans. Ultrason. Ferroelectr. Freq. Control **47**, 222–232 (2000).
[2] N. J. Willis, *Bistatic Radar*, 2nd ed. (Technology Service, Silver Spring, MD, 1995), Chap. 1.
[3] J. J. Faran, ''Sound scattering by solid cylinders and spheres,'' J. Acoust. Soc. Am. **23**, 405–418 (1951).
[4] R. M. Lerner and R. C. Waag, ''Wave space interpretation of scattered ultrasound,'' Ultrasound Med. Biol. **14**, 97–102 (1988).
[5] T. D. Mast and R. C. Waag, ''Wave space resolution in ultrasonic scattering measurements,'' J. Acoust. Soc. Am. **98**, 3050–3058 (1995).
[6] G. S. Kino, *Acoustic Waves: Devices, Imaging, and Analog Signal Processing* (Prentice-Hall, Englewood Cliffs, NJ, 1987), Appendix B.
[7] R. Hickling, ''Analysis of echoes from a solid elastic sphere in water,'' J. Acoust. Soc. Am. **34**, 1582–1592 (1962).

[8] O. T. von Ramm, S. W. Smith, and H. G. Pavy, Jr., ''High speed ultrasound volumetric imaging system—II: Parallel processing and display,'' IEEE Trans. Ultrason. Ferroelectr. Freq. Control **38**, 109–115 (1991).
[9] M. T. Robinson and O. T. von Ramm, ''Real-time angular scatter imaging system for improved tissue contrast in diagnostic ultrasound images,'' IEEE Trans. Ultrason. Ferroelectr. Freq. Control **41**, 44–52 (1994).
[10] L. Filipczynski, T. Kujawska, and G. Lypacewicz, ''Ultrasonic echo method in detection of breast calcifications: transient analysis,'' Arch. Acoust. **11**, 287–298 (1986).
[11] M. E. Anderson, M. S. C. Soo, and G. E. Trahey, ''Microcalcifications as elastic scatterers under ultrasound,'' IEEE Trans. Ultrason. Ferroelectr. Freq. Control **45**, 925–934 (1998).

Analysis of acoustic communication by ants

Robert Hickling[a)]
National Center for Physical Acoustics, University of Mississippi, University, Mississippi 38677

Richard L. Brown
Department of Entomology and Plant Pathology, Mississippi State University, Mississippi State, Mississippi 39762

(Received 14 April 2000; accepted for publication 21 June 2000)

An analysis is presented of acoustic communication by ants, based on near-field theory and on data obtained from the black imported fire ant *Solenopsis richteri* and other sources. Generally ant stridulatory sounds are barely audible, but they occur continuously in ant colonies. Because ants appear unresponsive to airborne sound, myrmecologists have concluded that stridulatory signals are transmitted through the substrate. However, transmission through the substrate is unlikely, for reasons given in the paper. Apparently ants communicate mainly through the air, and the acoustic receptors are hairlike sensilla on the antennae that respond to particle sound velocity. This may seem inconsistent with the fact that ants are unresponsive to airborne sound (on a scale of meters), but the inconsistency can be resolved if acoustic communication occurs within the near field, on a scale of about 100 mm. In the near field, the particle sound velocity is significantly enhanced and has a steep gradient. These features can be used to exclude extraneous sound, and to determine the direction and distance of a near-field source. Additionally, we observed that the tracheal air sacs of *S. richteri* can expand within the gaster, possibly amplifying the radiation of stridulatory sound. © *2000 Acoustical Society of America.* [S0001-4966(00)04210-7]

PACS numbers: 43.80.Ka, 43.64.Tk [WA]

INTRODUCTION

Many ant species, particularly those that live in the soil, communicate acoustically by stridulating.[1] Stridulation is the rubbing of one part of an insect's body against another to produce sound. The stridulatory organ of the black imported fire ant, *Solenopsis richteri*, described in the paper, is typical of ants. Amplified sounds of stridulation of *S. richteri* are provided on the internet.[2] Generally the sounds are barely audible. For *S. richteri*, they are just above a faint whisper, about 2 mPa or 40 dB (Ref. 20 μPa), at a distance of 100 mm.

The prevailing opinion among myrmecologists appears to be that acoustic communication is relatively unimportant compared to chemical communication.[3,4] In fact, it is believed[4] that ant communication evolved using chemicals, largely bypassing the use of sound. However, it is unlikely that acoustic communication is unimportant, in view of the number of species of ant that stridulate. Also it is unlikely that ants rely principally on chemical communication, because, in highly organized ant societies, it will frequently be necessary to update information. This cannot be done effectively with chemicals in the way that it can with sound.

The de-emphasizing of acoustic communication by myrmecologists appears to have resulted in some misunderstanding of the use of sound by ants, particularly with regard to the transmission and reception of stridulatory signals. It is easy to demonstrate by shouting at ants that they are unresponsive to airborne sound on a scale of a meter or more. This was shown painstakingly for eight species of ants almost a century ago, using a piano, a violin, and a Galton whistle, over a frequency range from 30 Hz to 60 kHz.[5] On the other hand, because of the presence of subgenual chordotonal organs in the legs,[4] ants are sensitive to vibrations in the substrate. From this, myrmecologists have concluded that stridulatory signals are transmitted through the substrate.[3,4]

But an examination of the substrate-transmission hypothesis raises doubts about its validity. We can clearly hear ant signals transmitted through the air. Most recordings of ant signals reported in the literature are of airborne sound measured with sound pressure microphones. Other reasons for questioning the substrate-transmission hypothesis are discussed in the paper. It would seem that the stridulatory signals are principally airborne. Of course, ants must still be unresponsive to airborne sound on a scale of a meter or more. It is one of the purposes of this paper to show, from basic near-field theory, that ants can communicate through the air in the near field, on a scale of about 100 mm, and yet be insensitive to ambient airborne sound on a larger scale.

The receptors of airborne sound in ants are most probably trichoid, or hairlike, sensilla on the antennae. *S. richteri* and other ant species have concentrations of trichoid sensilla on the apical segments of the antennae. Many kinds of insects detect sound through the motion induced in trichoid sensilla by the particle velocity of sound, or sound velocity.[6–8] But, because of the belief in substrate transmission, this does not appear to have been considered for ants.

The overall objective of this paper is to develop a coherent understanding of acoustic communication by ants, based on near-field theory,[9] and on data obtained both from our investigation of *S. richteri* and from the work of others.

[a)]Present address: Sonometrics Inc., 8306 Huntington Road, Huntington Woods, MI 48070.

Although the complete theory of the near field is not readily available in texts, it is well understood by entomologists that many species of insect sense sound velocity in the near field. What we have done is to show how ants can use the enhancement of sound velocity and the steep velocity gradient in the near field to improve the signal to noise ratio of stridulatory signals and to determine the location of small sources of sound.

S. richteri came to the United States from South America and is an example of an invasion insect which, when transplanted from its original habitat, can cause serious damage to animal and plant life. In the long run, the only way to control such insects is through basic research. Learning how they communicate acoustically is part of such research. First we provide some background information on *S. richteri*.

BACKGROUND ON IMPORTED FIRE ANTS

There are two species of imported fire ant, *S. richteri* and *S. invicta*. The word ''imported'' distinguishes these ants from fire ants indigenous to the United States. In the 1930s, *S. richteri* was introduced accidentally from South America at Mobile, AL, followed by the more resilient red fire ant, *S. invicta*.[10] From Mobile, *S. invicta* spread throughout the Southeastern United States from Florida to Texas. Recently they became established in New Mexico and California.[11] *S. richteri* seem to exist principally in northern Mississippi and Alabama and in southern Tennessee[10] and were conveniently located for our study. The results we obtain for *S. richteri* apply equally to *S. invicta*. The density of imported fire ants in the United States is often about five times greater than in their original habitat in South America, apparently because there are no natural enemies in the United States, such as *Pseudacteon* phorid flies.[11,12]

The problem with imported fire ants is their sting. Each ant can sting many times and concerted attacks can involve thousands of ants. The stings are usually lethal to other insects, nestling birds, and young mammals. With humans, the stings can be painful; allergic reactions and sometimes death can occur.[10]

THE STRIDULATORY ORGAN

As with many ant species, the stridulatory organ of *S. richteri* is located at the ''waist,'' i.e., at the junction of the postpetiole and the bulbous posterior portion of the abdomen, called the gaster (Fig. 1). It consists of a washboardlike set of ridges on the anterior dorsal surface of the gaster, together with a scraper on the rim of the postpetiole. When the gaster is moved up and down, the scraper is made to run back and forth over the file of ridges, generating squeaking sounds or chirps. The up and down movement of the gaster, sometimes called gaster flagging, is a visual indication of stridulation. The SEM (scanning electron micrograph) of the stridulatory organ of *S. richteri* in Fig. 2 shows the file of ridges on the gaster and the rim of the postpetiole containing the scraper. For *S. richteri*, the number of ridges is about 40 to 50. The frequency of the squeaking sounds appears to be determined largely by the rate of tooth impact of the scraper as it moves over the ridges.[13] LDV (Laser Doppler Vibrometer) studies of another ant species, *Atta sexdens*,[14] have shown that stridulatory sound is radiated principally by the surface of the gaster. Because the gaster is very small relative to the wavelength it seems unlikely that the sound is related to structural resonance. More probably it is caused by stick-slip[15] associated with frictional interaction between the scraper and the ridges.

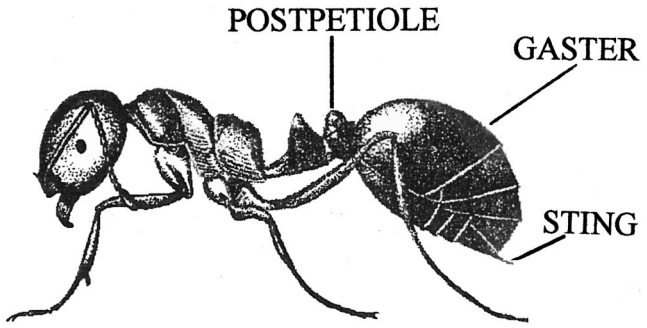

FIG. 1. Drawing of worker of imported fire ant, *Solenopsis richteri*. Typically, workers range in length from about 2 to 6 mm.

S. richteri is unusual in that larger workers have a transparent dorsal cuticle on the gaster. This permits microscope examination of the expansion and contraction of the tracheal air sacs inside the gaster that are part of the respiratory system. A major worker of *S. richteri* was embrittled by dipping in liquid nitrogen and a portion of the gaster broken off to reveal the expanded sacs lying side-by-side, as shown in Fig. 3. It is seen that the expanded sacs fill the anterior of the gaster. Since they appear to be in contact with the outer cuticle, it is reasonable to suppose that they could play a role in amplifying the sound generated by the stridulatory organ. Microscope observation shows that the air sacs of *S. richteri* do not always expand when the ant is stridulating. Further investigation is needed to determine if there is a connection between the expanded sacs and stridulatory sound.

STRIDULATORY SOUNDS

Examples of the stridulatory sounds of *S. richteri* were determined for different situations, as shown in Fig. 4. In this figure, the signals have an 8-s duration. Corresponding 24-s recordings of the signals are given on the internet.[2] The human ear can easily distinguish the sounds of stridulation from other sounds. Signal No. 1, in Fig. 4(a), is the sound generated by a large number of ants when a probe, fitted with a Bruel and Kjaer $\frac{1}{2}$-in. microphone, is pushed into an ant mound. As the ants pass close to the microphone, a variety of different signals can be heard above the background noise of stridulatory sound. Clearly these are not ''a monotonous series of chirps,'' as described in Ref. 3. The ants appear to be highly agitated and they rush out to attack the probe. As has been noted previously by Wheeler,[16] the rapidity of the response is probably due to acoustic communication, because the reaction to chemical communication would be slower.

The variety of stridulatory sounds in the alarm signal induced us to perform additional tests in the laboratory. Part of an ant mound, in a plastic container about 250 mm in diameter and 100 mm high, was placed in a double sound-

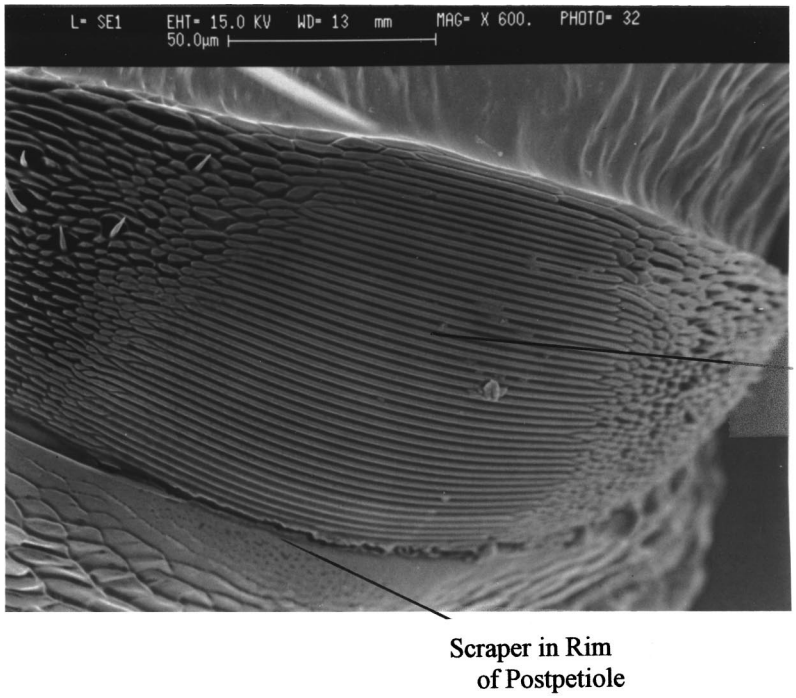

FIG. 2. Scanning electron micrograph of the stridulatory organ of *S. richteri* showing the washboardlike set of ridges on the anterior dorsal surface of the gaster and the rim of the postpetiole containing the scraper.

proof box[17] with windows. Inside the box, the plastic container rests on a custom sensor consisting of a sensitive, low-cost electret microphone in a stethoscope head. This sensor has a sensitivity comparable to a 1-in. Bruel and Kjaer condenser microphone, i.e., about 50 mV/Pa. It has been used extensively to detect and monitor larval activity in cotton bolls, fruit, nuts and grain.[17] For ant sounds, this method of monitoring is similar to listening to sounds in an adjoining room with one's ear pressed against the wall. Both the ear and the microphone in the stethoscope detect sound pressure. Much of the signal processing was performed, for frequencies up to 20 kHz, using a computerized speech-analysis system (Kay Elemetrics Model 4300).

Signal No. 2 in Fig. 4(b) shows the typical activity sounds of an undisturbed group of ants, punctuated briefly by chirps from an individual ant. The chirps occur at regular intervals. Their purpose is unclear, but they probably serve to indicate group or territorial awareness, one of the broad communication functions of social insects listed in Ref. 3. Signal No. 3 in Fig. 4(c) was generated by a single ant, during an attack on a caterpillar by a number of ants. This was the only type of stridulatory signal to occur during the attack. We also

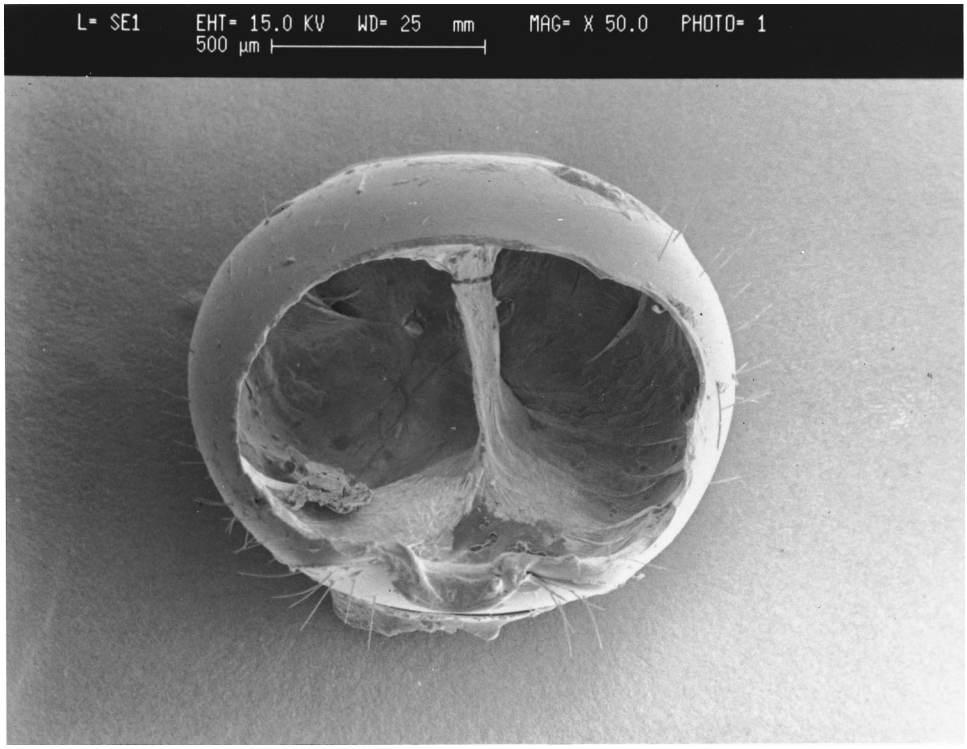

FIG. 3. Scanning electron micrograph of cryofractured gaster showing the expanded air sacs of a major worker of *S. richteri*.

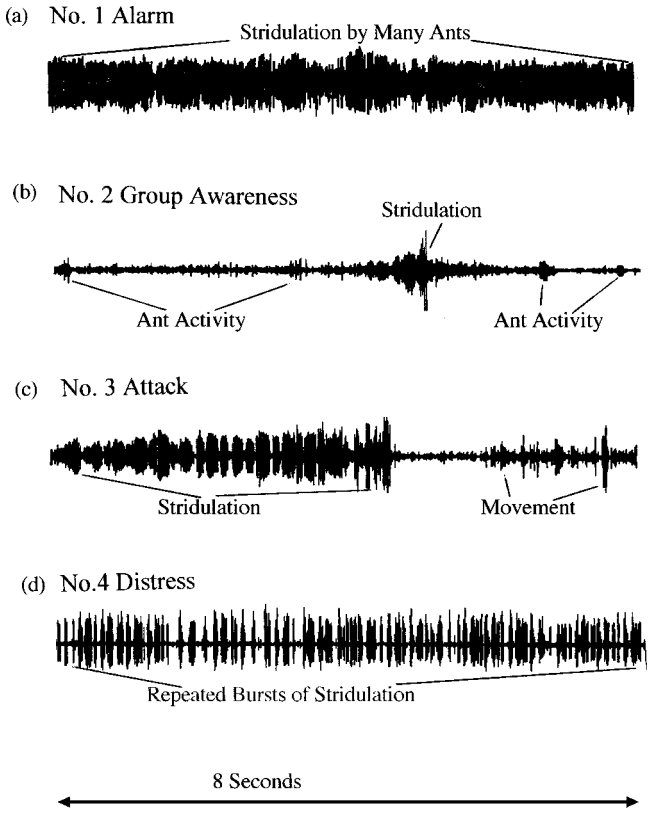

FIG. 4. Pressure-time traces of stridulatory signals of *S. richteri* (a) No. 1—Alarm signal due to insertion of microphone probe in mound; (b) No. 2—Sounds of normal activity with occasional stridulatory signal; (c) No. 3—Attack on caterpillar and (d) No. 4—Distress signal from ant with caught antenna.

recorded an attack on an earthworm, and struggles with other ants of the same species from a different colony. In these recordings, the stridulatory signals are the same as those in the attack on the caterpillar. The signal appears to come from a single ant. Whether this is always the same ant is unknown. The attack signal can also be heard among the stridulatory sounds in the alarm Signal No. 1.[2] Signal No. 4, in Fig. 4(d), was generated by a major worker with one of its antennae caught. This re-iterated type of distress signal was observed with both major and minor workers. In general the distress signal produced by majors is about 3 to 4 times louder than that of minors. Sometimes it is not as prolonged as in Fig. 4(d). There are other situations in which stridulation can occur, such as mating, moving the colony and in attacks by parasites, but these were not investigated.

One of the main differences between the signals in Fig. 4 is duration. Signal No. 1 lasts for about 10 min and then gradually dies away. Similarly signal No. 4 lasts for periods of minutes or more. Signals Nos. 2 and 3 are of much shorter duration. In addition, there appear to be other features that distinguish the signals from each other. The differences between the signals may indicate a kind of rudimentary language.

Since it was recorded with a B & K microphone with a flat response, the alarm Signal No. 1 was used to find the frequency spectrum of the sounds of *S. richteri*. The spectrum, shown in Fig. 5, was determined using MATLAB[18] with a digital filter to remove low-frequency ambient noise below

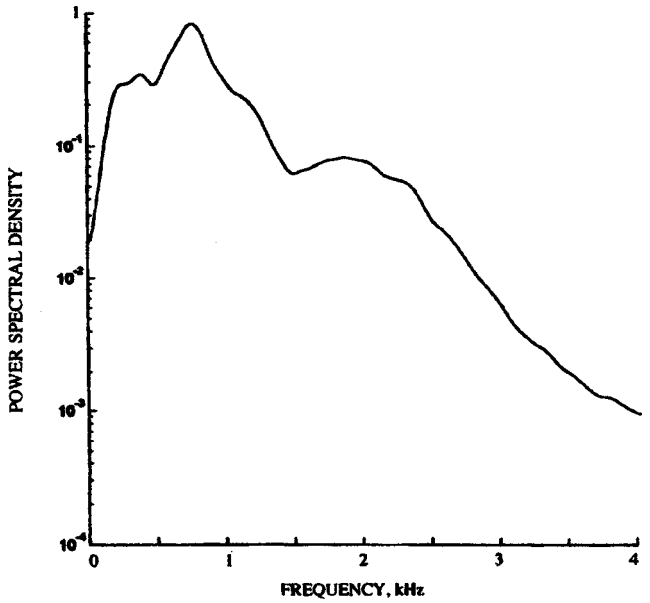

FIG. 5. Spectrum of alarm signal No.1 showing frequency content of stridulatory signals of *S. richteri*.

about 200 Hz. The peak of the spectrum is seen to occur around 700 Hz, with most of the spectral content below about 1.5 kHz. Stridulatory sound consists of unitary components, or syllables, associated with a single up-and-down movement of the gaster.[19] The ear can easily distinguish these, and they can be further identified from videos. Typically the duration of a component is less than three-tenths of a second.

TRANSMISSION OF STRIDULATORY SOUND

The sounds of *S. richteri* are audible even when the ants are located on foam rubber. Hence it is reasonable to suppose that stridulatory signals are transmitted through the air. However, since there is a strong belief among myrmecologists that the signals are transmitted through the substrate, it is necessary to review arguments underlying this belief to examine their validity.

Evidence in support of the substrate-transmission hypothesis is believed to be provided by a well-known feature of ant behavior, namely the rescue, by fellow ants, of an ant buried beneath a soil subsidence. The buried ant stridulates (and emits chemical signals) to attract its fellows, and, since the stridulatory signals pass through the soil, this is taken to indicate that the signals are structure-borne through the substrate.[3,4] However, it is important to recall that soil is a granular, not a continuous solid. Sound transmission in granular materials is a well-studied field,[20,21] and one of the principal means of transmission is through the air in the inter-granular passages. This has been demonstrated, for example, by the differences in transmission speed that occur when the same granular material is immersed in different gases.[22] Also there are many kinds of insects that live (and breathe) in the soil. It would seem likely, then, that the acoustic signals of a buried ant are transmitted mainly through the inter-granular air passages and not through the

solid matrix of the soil. Certainly chemical signals are transmitted this way.

Evidence in support of the substrate-transmission hypothesis is also believed to be provided by the observation that an ant can excite structure-borne vibration in a leaf. The leaf-cutting ant, *Atta cephalotes*, stridulates and excites vibrations with its mandibles, as it cuts the leaf, apparently to attract other members of the colony to that particular leaf.[23] Using an LDV system, the vibrations of the leaf were found to be measurable when the mandibles of the stridulating ant are in contact with the leaf, but barely detectable when only the tarsi or feet are in contact.[23] When an ant stridulates, its mandibles generally are not in contact with the substrate. Since soil is not a continuous, flexible solid like a leaf, the vibrations caused by a stridulating ant through the tarsi are probably not detectable in soil. There are no known reports of LDV measurements of stridulatory vibrations in the soil. The structure of an ant's body indicates that it is not designed to transmit vibrations from the stridulatory organ to the substrate, because vibrations pass through the ant's body along a highly attenuating path, through various joints to tarsi with a very small contact area.

As they move about, ants are likely to encounter a variety of substrate materials, such as soil, wood, leaves, animal tissue and manmade objects of various sorts. Since these can have very different vibration characteristics, it is unlikely that ants have the ability to adjust acoustic communication accordingly. It is much more likely that ants use an unchanging, uncomplicated transmission path, through the air.

RECEPTION OF STRIDULATORY SOUND BY ANTS

Since many types of insects use mechanosensory trichoid sensilla to detect airborne sound,[6–8,24–32] it is likely that ants do the same. Mechanosensory trichoid sensilla have membranous sockets and are free to move within a sound field. The sensilla are driven back and forth in the sound field by air-induced drag and virtual mass forces about the point of attachment.[30,31] They fire phasically in a one-to-one relation with direction during each cycle of oscillation. This sets an upper limit to the frequencies they can ''hear'' of about 1 or 2 kHz.[6–8,24–32] Trichoid sensilla occur on all parts of an ant's body. However, there are concentrations on the apical segments of the antennae, as shown in the SEMs of the antennae of S. *richteri* in Fig. 6. Similar concentrations occur with other ant species. For example, Dumpert counted 441 sensilla on the apical segments of *Lasius fuliginosus*.[33] Trichoid sensilla are used for olfactory, tactile and other forms of sensing, as well as for sound.

The segmented antenna of an ant is similar to that of some parasitic wasps and the honeybee in being elbowed between the long basal segment and the shorter terminal segments. The maneuverability provided at the antennal base and the elbowed joint allows the ant to hold the antenna straight, either laterally or anteriorly, or to hold the antenna with the basal segment forming a right angle with the terminal segments which may be directed anteriorly or ventrally.[3,4] The tips of the antennae can thus be aligned in any desired direction. This facilitates sensing the gradient of sound velocity in the near field. It allows the ant to orient the antennae and extend the tips to obtain maximum sensitivity to the sound-velocity gradient and thus to determine the direction and location of a sound source. The distance between the extended tips of the antennae of a worker of *S. richteri* is roughly between 2 and 5 mm.

During the past two decades, there has been a major interest in the response of trichoid sensilla to sound.[24–32] The sensilla are particularly receptive to signals in the near field where the sound velocity is greatly enhanced. Sound velocity is a vector, in contrast to sound pressure, the scalar quantity commonly measured in acoustics. Sound velocity microphones have been developed for insect acoustics.[34,35] Also there are laser Doppler methods,[36] which have been used to measure gaster vibration[15] and the motion of trichoid sensilla.[32] However, it is difficult to use these methods in the restricted space of the near field. Instead the enhanced sound velocities of the near field have been simulated by intense plane sound waves, or with some form of relatively slow airflow.[23–32] In these simulations, an important feature of the near field has been neglected, namely the steep gradient of the sound velocity. The significance of the gradient is examined later, in the section on the use of near-field acoustics by ants.

JUSTIFICATION OF THE MONOPOLE MODEL FOR ANT SOUNDS

The monopole model for ant sounds, given in the Appendix, shows how ants can use near-field sound for communication while excluding extraneous noise from further away. However it is necessary first to justify the model.

(a) *Frequency*. In the model, frequency has to be about a kilohertz or less because, when the frequency is greater than a few kilohertz, the near field is too small to include a sufficient number of ants for acoustic communication. Since the peak frequency in Fig. 6 occurs at about 700 Hz, *S. richteri* clearly meets this requirement. Similarly the peak frequency for other ant species is below a kilohertz, as, for example, for *A. sexdens*, in the spectrum in Fig. 3 of Ref. 14.

However, the stridulatory signals of the African ponerine ant *Megaponera foetens* (Fabr.),[37] and the leaf-cutting ant *Atta cephalotes* L.,[38] have been reported to be ultrasonic (above 20 kHz). If this is true, it presents a serious obstacle to use of the near field for acoustic communication. It is necessary, therefore, to examine these results carefully. The signal processing is the same in both papers. Stridulatory signals of airborne sound are given, but no spectral plots. By comparing the stridulatory signals with ultrasonic signals, say for a bat,[39] it is immediately seen that the stridulatory signals are not ultrasonic. Compared to the bat signals, the ant signals are significantly expanded in time, with respect to the peaks and zero crossings of the signals. Counting the peaks and zero crossings relative to the time scale provides an estimate of the center frequency of the signals.[39] This was found to be between 700 and 900 Hz, consistent with the peak frequency for *S. richteri* in Fig. 5. To be certain that there is no significant ultrasound in the signals, a more complete analysis was performed, digitizing the signals by hand and using MATLAB to generate a spectrum. Again this

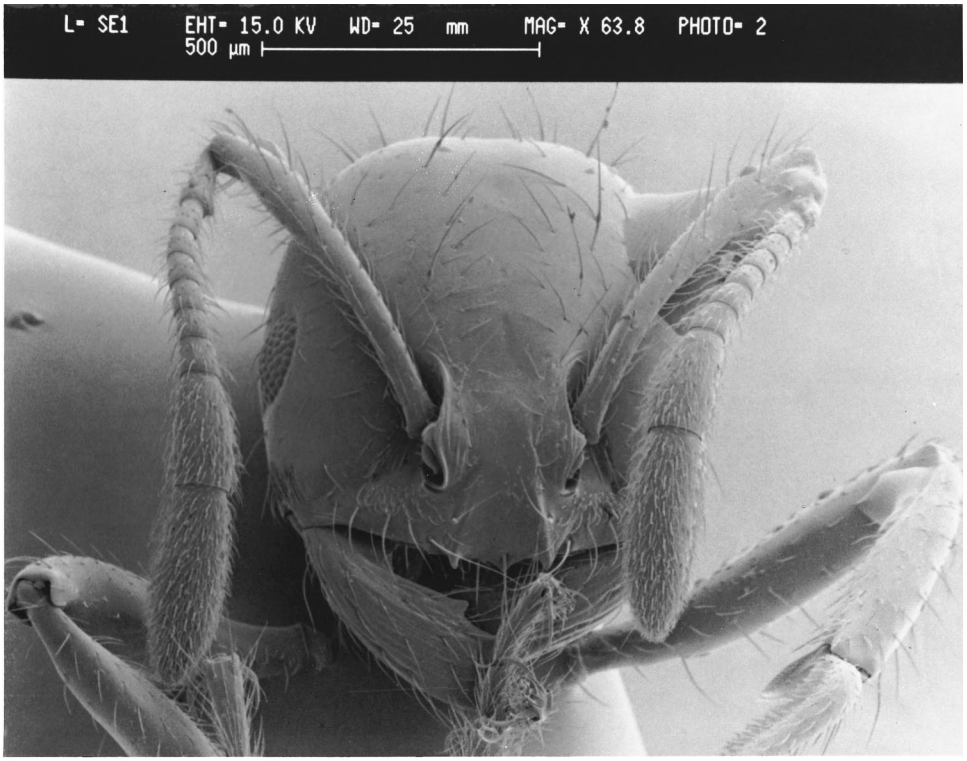

(a)

(b)

FIG. 6. Scanning electron micrographs of the antenna of a worker of *S. richteri* showing (a) trichoid sensilla on the elbowed antenna and (b) concentration of trichoid sensilla on the apical segments.

showed a peak between 700 and 900 Hz, similar to Fig. 5. The conclusion that the signals are mainly ultrasonic thus appears to be a mistake.

To further demonstrate the absence of ultrasound in ant signals, we investigated the signals of *S. richteri*. We inserted a $\frac{1}{4}$-in. B & K microphone (Model No. 4135) into a mound and analyzed the resulting sound using a Hewlett–Packard Model No. 35665A analyzer. This measurement system detects frequencies up to about 100 kHz. We found nothing significant above about 3 kHz.

In summary then, there appears to be no reason to believe that the frequency of ant signals occurs principally at

ultrasonic frequencies. Instead, the available evidence indicates that the frequency is mainly associated with tooth impact around and below 1 kHz, thus enabling ants to use the near field. It also follows that an ant is very small compared to the wavelength, which is another requirement of the monopole model.

(b) *Uniformity of Radiated Sound*. In the monopole model, it is assumed that the sound of the ant is radiated uniformly. To test the validity of this assumption, we used a Bruel & Kjaer $\frac{1}{2}$-in. microphone to measure the stridulatory sound from individual medium-sized workers of *S. richteri*, at different positions around the ant, at a radial distance of about 100 mm. The ants were restrained on a hard flat surface in an anechoic room and continuously emitted the distress signal No. 4. Because the signals varied with time, the sound field was never perfectly uniform. However, for all intents and purposes, it appeared to be uniform. We investigated the frequency range between 200 Hz and 1.6 kHz, looking in particular for the figure-eight pattern of a dipole, or for a pattern of null positions for a higher-order source. Nothing of this nature was found. The average overall rms sound pressure at 100 mm for *S. richteri* was found to be roughly 2 mPa (40 dB), or just above a whisper. This piece of data is used to further justify the model.

USE OF NEAR-FIELD SOUND BY ANTS

The sound velocity v corresponding to the sound pressure of 2 mPa for *S. richteri* measured at a distance of 100 mm, can be estimated using the simple formula for spherical waves relating pressure and velocity[40]

$$v = pF(kr)/\rho c, \tag{1}$$

where $F(kr) = kr/\sqrt{(1+(kr)^2)}$, p is the sound pressure and ρ and c are the density and speed of sound of air. Equation (1) can also be obtained from Eqs. (A1) and (A2) in the Appendix. From Eq. (A6) in the Appendix, $kr \sim 1$; hence v at 100 mm is 3.1×10^{-3} mm/s. From this it is possible to use the monopole model, at a frequency of 700 Hz, to extrapolate back to the velocity at the surface of the source (gaster), as shown in Fig. 7. We use 700 Hz because it is the frequency of the spectral peak in Fig. 5. Assuming the gaster of *S. richteri* to have a radius of about 1 mm, the extrapolated value of sound velocity at its surface is seen to be about 19 mm/s. The reasonableness of this result can be domonstrated by comparing with LDV measurements of the corresponding velocity at the surface of the gaster of *A. sexdens* at 1 kHz.[14] Measurements at four locations on the gaster (Table I in Ref. 14) were converted to ordinary units and arithmetically averaged, resulting in a value of 30 mm/s, which is compared to the extrapolated value of 19 mm/s for *S. richteri*. The comparison cannot be expected to show close agreement, but it is close enough to show that the monopole model provides a realistic representation of the enhancement and steep gradient of the sound velocity in the near field of an ant.

How the steep gradient of the sound velocity affects the response of trichoid sensilla has not been investigated. It is likely that the sensilla will respond more sensitively in the steep gradient than with plane waves. The study of such an effect is beyond the scope of this paper. What can be done here is to investigate the use of the two antennae of an ant to sense the steepness of the gradient, using relative differences in sound velocity between the antennae. We assume two separations of the tips of the antennae, 2 and 5 mm apart, and calculate the relative difference in sound velocity between the tips, using the data in the 700 Hz curve in Fig. 7. The difference in percent is plotted in Fig. 8, as a function of distance from the source. The figure shows how, by using the antennae to sense the relative difference in sound velocity, an ant can be sensitive to sound in the near field of a small source but insensitive to sound in the far field. In the near field, the difference is greater than 10%, which is a threshold often found by experimental psychologists to be the just noticeable difference in sensation between two sensors. For example, the threshold for detecting interaural sound-pressure differences in human hearing is 6%–10%.[41] On the other hand, in the far field, the relative difference in sound velocity

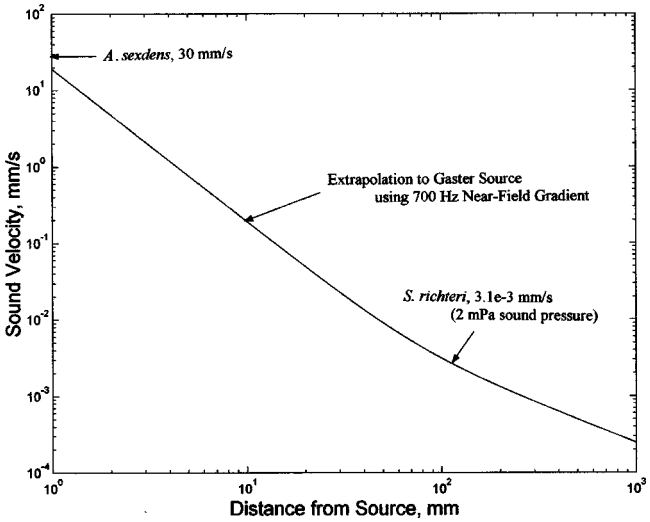

FIG. 7. Gradient of the sound velocity in the vicinity of a small spherical source of 1 mm radius, pulsating at a frequency of 700 Hz. This shows the extrapolation back to the source from a sound velocity of 4.4×10^{-3} mm/s at 100 mm for *S. richteri* (corresponding to a sound pressure of 2 mPa), compared to the velocity at the surface of the gaster for *A. sexdens* (Ref. 14).

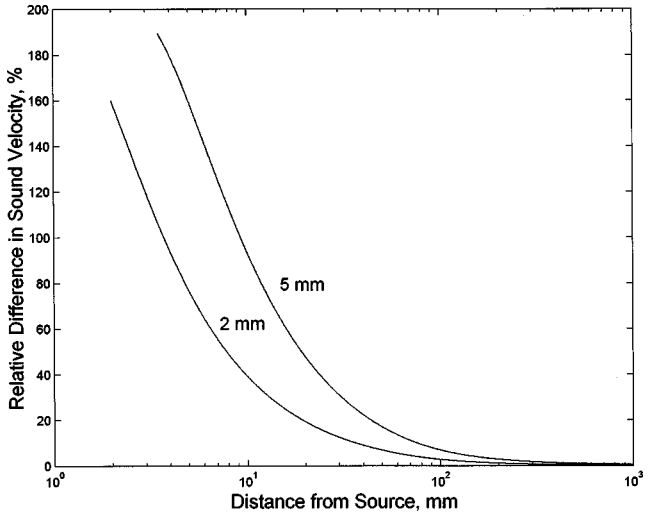

FIG. 8. Percent relative difference in sound velocity between the tips of the antennae of *S. richteri*, 2 and 5 mm apart, for the velocity gradient in Fig. 7.

is vanishingly small, well below the 10% threshold. The steep gradient thus creates a special condition, which enables an ant to sense signals from another ant, while shutting out extraneous noise interference.

In summary, the two features of the near field that can be used to improve the signal to noise ratio of ant signals are (a) the enhancement and (b) the steep gradient of the sound velocity. Since the stridulatory signals are quite distinctive, it is possible that ants may also use simple signal processing. The near field thus provides ants with an acoustical world of their own. It is conjectured that ants can extend the range of acoustic communication beyond the near field by relaying signals from one to another. Also it is conjectured that the larger ants of *S. richteri* play a greater role in acoustic communication than the smaller ants.

In Fig. 8 it is assumed that the tips of the antennae are in line with the small source. This orientation is the most sensitive for detecting relative differences in sound velocity. Because of the maneuverability of the antennae, an ant can always adjust its antennae to this position, thus determining the direction of the source. Figure 8 also shows there is a one-to-one relation between the relative difference in sound velocity and the distance to the source. This provides a means of determining the distance to the source, as well as its direction. Since ants appear to have poor vision[3,4] and often operate in the dark, this capability would be quite useful.

The monopole model in the Appendix is for a small pulsating spherical source in free space. However, in the environment of an ant, there are reflecting surfaces. If the ant is resting on a reflecting planar surface, the model continues to provide a realistic representation of the near field. But, inside a mound, the walls of tunnels and galleries form different kinds of reflecting surfaces, which require more complex modeling. The enhancement and steep gradient of the sound velocity still occur in the near field, however.

INTERACTION WITH PHORID FLIES

It is known that fire ants can detect phorid-fly parasites as they hover a few millimeters above the ants.[12] Presumably they detect the sound of the fly's wing beats. This provides an additional argument for believing that ants sense sound through the air. The frequency of the wing beats of the phorid fly has not been measured, so that the corresponding extent of its near field is not known.

CONCLUDING COMMENTS

That ants communicate through the air in the near field appears to be the only consistent way of explaining the facts relating to acoustic communication by ants. There is as yet no direct experimental proof that ants sense the relative difference in sound velocity between the antennae, but they are capable of it and, in view of the advantages it provides, it would be surprising if they did not. The near field of a small source with its enhancement and steep gradient of the sound velocity are major features in the acoustic environment of ants. In fact, it seems likely that the ants' stridulatory and acoustic sensing systems have evolved by making use of these features. As indicated in the Appendix, ants use lower frequencies to increase the range of the near field, even though this reduces the power of the radiated sound. Hence they have to rely on the features of the near field to improve the signal to noise ratio of their signals. It is likely that other insects make similar use of the near field.

ACKNOWLEDGMENTS

The authors are grateful to Peng Lee and Wei Wei at the National Center for Physical Acoustics for expert assistance with the acoustical experiments. William Monroe and others at the Electron Microscope Center at Mississippi State University provided assistance with microscopy. The Agricultural Research Service of the U.S. Department of Agriculture supported a major part of the work.

APPENDIX

The complete theory of a monopole, or simple source, is not generally available in texts. We use the theory given in Ref. 9. It is also available in some older texts, for example, Ref. 42.

A monopole radiates sound equally in all directions. It can be represented by a small sphere of radius a located at the origin, pulsating periodically with circular frequency $2\pi f = kc$, f being the frequency, k the wave number and c the speed of sound in the fluid medium. The pulsations of the monopole have a volume rate of fluid flow S. At a radial distance r in the surrounding acoustic field, the sound pressure p, and the radial sound velocity (particle velocity of sound) v are given respectively by

$$p = -\rho c^2 ika(a/r)G, \tag{A1}$$

$$v = -c(a/r)^2[ika(r/a) - 1]G, \tag{A2}$$

where $G = S\exp[ik(r-ct)]/(4\pi a^2 c)$ and i is the square root of -1. To draw conclusions from these equations for different frequencies, source sizes and fluid media, it is helpful to introduce nondimensionalization as follows:

$$S' = S/(4\pi a^2 c); \quad p' = p/(\rho c^2); \quad v' = v/c \text{ and } r' = r/a, \tag{A3}$$

together with the nondimensional frequency parameter ka. The amplitudes of p' and v' are then

$$|p'| = ka(1/r')S' \tag{A4}$$

and

$$|v'| = (1/r')^2[1 + (ka\, r')^2]^{1/2}S'. \tag{A5}$$

The sound velocity varies as $1/r'^2$ close to the source and as $1/r'$ further away. The region of $1/r'^2$ dependence is called the near field and the region of $1/r'$ dependence is called the far field. The near field gradually merges into the far field. Unlike sound velocity, sound pressure varies as $1/r'$ in both the near and far fields. Thus sound velocity characterizes the near field, not sound pressure. The near field consists of a nonpropagating reactive energy field, which forms a transition zone between the relatively high velocity of the radiating surface of the source and the much lower sound velocity of normal acoustic propagation in the far field.[9] The change

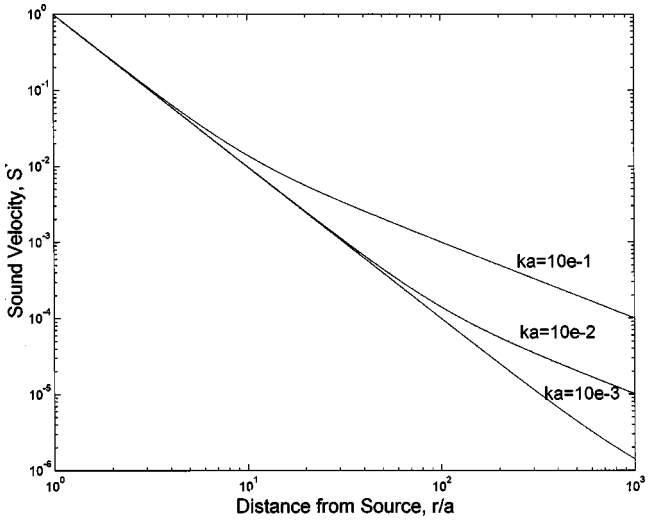

FIG. A1. Gradient of the sound velocity amplitude for different values of the nondimensional frequency *ka*, for a small pulsating sphere of radius a, showing the near and far fields, plotted as a function of the nondimensional distance *r/a* from the surface of the sphere.

in slope is illustrated in Fig. A1 where the amplitude of v' is plotted as a function of r' for different values of ka. From the figure, it is seen that the change occurs roughly when $kar' \sim 1$, or more simply when

$$kr \sim 1. \tag{A6}$$

This relation determines the extent of the near field, given the frequency of the sound and the nature of the fluid medium. The lower the frequency the greater the extent of the near field. For example, if the frequency is 700 Hz, the corresponding wavelength in air is about 0.5 m. From the relation $k = 2\pi/\lambda$, where λ is the wavelength, it follows that k is about 12.7 m^{-1}. From Eq. (A6) the radial extent of the near field is then approximately 80 mm.

The driving force DF at the surface of the small spherical source is given[9] by

$$\mathrm{DF} = -i4\pi a^2 \rho c^2 kaS' \exp[ik(r-ct)], \tag{A7}$$

which increases linearly with frequency. The radiated sound power RSP is

$$\mathrm{RSP} = \rho c 4\pi a^2 (ka)^2 S'^2, \tag{A8}$$

which increases as frequency squared. An ant can thus increase the power of the sound it radiates by increasing the frequency. However, this reduces the size of the near field and increases the driving force or effort expended by the ant. Apparently ants have opted for greater range with less effort and hence rely on the special features of the near field to improve the signal to noise ratio of stridulatory signals. In water ($c = 1500$ m/s), the extent of the near field is about four times greater than in air ($c = 344$ m/s).

[1] H. Markl, ''The evolution of stridulatory communication in ants,'' Proceedings of 7th Congress of the International Union for the Study of Social Insects, London, pp. 258–265 (1973).

[2] R. Hickling, ''Stridulation Sounds of *Solenopsis richteri* ,'' Recordings at Internet website: www.olemiss.edu/~hickling/ (The recordings last for 24 secs and are in wave-format.) (1998).

[3] B. Holldobler and E. O. Wilson, *The Ants* (The Belknap Press of Harvard University Press, Cambridge, MA, 1990), pp. 227–229, 255–259.

[4] B. Holldobler and E. O. Wilson, *Journey to the Ants* (The Belknap Press of Harvard University Press, Cambridge, MA, 1995), pp. 51–58.

[5] A. M. Fielde and G. H. Parker, ''The Reaction of Ants to Material Vibrations,'' Proc. Acad. Natural Sciences of Philadelphia, pp. 642–649, September (1904).

[6] R. F. Chapman, *The Insects: Structure and Function*, 4th ed. (Cambridge University Press, Cambridge, England, 1998), p. 615.

[7] A. W. Ewing, *Arthropod Bioacoustics: Neurobiology and Behavior* (Cornell University Press, Ithaca, NY, 1989), p. 60.

[8] H. C. Bennet-Clark, ''Insect hearing: Acoustics and transduction,'' *Insect Communication*, edited by T. Lewis (Academic, London, 1984), pp. 49–82.

[9] P. M. Morse and K. U. Ingard, *Theoretical Acoustics* (McGraw-Hill, New York, 1968), pp. 311–315.

[10] S. B. Vinson, ''Invasion of the red imported fire ant,'' Am. Entomologist **43**, 23–39 (1997).

[11] Agricultural Research Magazine, September issue, pages 2 and 5–8 (U.S. Department of Agriculture, 1999).

[12] S. D. Porter, R. K. Vander Meer, M. A. Pesquero, S. Campiolo and H. G. Fowler, ''Solenopsis (Hymenoptera: Formicidae) fire ant reactions to attacks of *Pseudacteon* flies (Diptera: Phoridae) in southeastern Brazil,'' Ann. Entomol. Soc. Am. **88**, 570–575 (1995).

[13] C. P. Haskins and E. V. Enzmann, ''Studies of certain sociological and physiological features in the formicidae,'' Ann. (N.Y.) Acad. Sci. **37**, 97–162 (1938).

[14] W. M. Masters, J. Tautz, N. H. Fletcher, and H. Markl, ''Body vibration and sound production in an insect (*Atta sexdens*) without specialized radiating structures,'' J. Comp. Physiol. A **150**, 235–243 (1983).

[15] M. T. Bengisu and A. Akay, ''Stick-slip oscillations: Dynamics of friction and surface roughness,'' J. Acoust. Soc. Am. **105**, 194–205 (1999).

[16] W. M. Wheeler, *Ants, Their Structure, Development and Behavior* (Columbia University Press, New York, 1910), pp. 512–515.

[17] R. Hickling, P. Lee, D. Velea, T. J. Dennehy, and A. I. Patin, ''Acoustic system for rapidly detecting and monitoring pink bollworm in cotton bolls,'' Proceedings of National Beltwide Cotton Conferences, San Antonio, TX, Jan. 4–8 (2000).

[18] ''MATLAB, The Language for Technical Computing,'' The Math Works Inc., Natick, MA (1999).

[19] H. G. Spangler, ''Ant stridulations and their synchronization with abdominal movement,'' Science **155**, 1687–1689 (1967).

[20] I. Tolstoy, Ed., *Acoustics, Elasticity and Thermodynamics of Porous Media, Twenty-One Papers by M. A. Biot* (Acoustical Society of America, Woodbury, NY, 1991).

[21] C. Zwicker and C. W. Kosten, *Sound Absorbing Materials* (Elsevier, New York, 1949).

[22] R. Hickling, W. Wei, and D. W. Hagstrum, ''Studies of sound transmission in various types of stored grain for acoustic detection of insects,'' Appl. Acoust. **50**, 263–278 (1997).

[23] F. Roces, J. Tautz, and B. Holldobler, ''Stridulation in leaf-cutting ants,'' Naturwissenschaften **80**, 521–524 (1993).

[24] J. Tautz, ''Reception of medium vibration by thoracal hairs of caterpillars of *Baranthra brassicae* L. (Lepidoptera, Noctuidae),'' J. Comp. Physiol. **118**, 13–31 (1977).

[25] N. H. Fletcher, ''Acoustical response of hair receptors in insects,'' J. Comp. Physiol. A **127**, 185–189 (1978).

[26] J. Tautz, ''Reception of particle oscillation in a medium—An unorthodox sensory capacity,'' Naturwissenschaften **66**, 452–461 (1979).

[27] J. Tautz and H. Markl, ''Caterpillars detect flying wasps by hairs sensitive to airborne vibration,'' Behav. Ecol. Sociobiol. **4**, 101–110 (1979).

[28] T. Shimozawa and M. Kanou, ''Varieties of filiform hairs: range fractionation by sensory afferents and cercal interneurons of a cricket,'' J. Comp. Physiol. A **155**, 485–493 (1984).

[29] G. Kamper and H. U. Kleindienst, ''Oscillation of cricket sensory hairs in a low-frequency sound field,'' J. Comp. Physiol. A **167**, 193–200 (1990).

[30] J. A. C. Humphrey, R. Devarakonda, I. Inglesias, and F. G. Barth, ''Dynamics of arthropod filiform hairs. I. Mathematical modelling of the hair and air motions,'' Philos. Trans. R. Soc. London, Ser. B **340**, 423–444 (1993).

[31] F. G. Barth, U. Wastl, J. A. C. Humphrey, and R. Devarakonda, ''Dynamics of arthropod filiform hairs II. Mechanical properties of spider trichobothria (*Cupiennius salei* Keys),'' Philos. Trans. R. Soc. London, Ser. B **340**, 445–461 (1993).

[32] T. Kumagai, T. Shimozawa, and Y. Baba, ''Mobilities of the cercal wind-

receptor hairs of the cricket, *Gryllus bimaculatus*,'' J. Comp. Physiol. A **183**, 7–21 (1998).
[33] K. Dumpert, ''Bau and verteilung der Sensillen auf der Antennengeissel von *Lasius fuliginosus* (Latr.) (Hymenoptera, Formicidae),'' Z. Morphol. Oekol. Tiere **73**, 95–116 (1972).
[34] H. C. Bennet-Clark, ''A particle velocity microphone for the song of small insects and other acoustic measurements,'' J. Exp. Biol. **108**, 459–463 (1984).
[35] A. Michelsen, W. F. Towne, W. H. Kirchner, and P. Kryger, ''The acoustic near field of a dancing honeybee,'' J. Comp. Physiol. A **161**, 633–643 (1987).
[36] R. J. Goldstein, Ed., *Fluid Mechanics Measurement* (Taylor & Francis, Philadelphia, 1996).
[37] B. Holdobler, U. Braun, W. Gronenberg, W. K. Kirschner, and C. Peeters, ''Trail Communication in the Ant *Magaponera foetens* (Fabr.) (Formicidae, Ponerinae),'' J. Insect Physiol. **40**, 585–593 (1994).
[38] H. Markl, ''Stridulation in leaf cutting ants,'' Science **149**, 1392–1393 (1965).
[39] D. R. Griffin, *Listening in the Dark: The Acoustic Orientation of Bats and Men* (Yale University Press, New Haven, 1958), p. 90.
[40] L. E. Kinsler, A. R. Frey, A. B. Coppens, and J. V. Sanders, *Fundamentals of Acoustics* (Wiley, New York, 1982), pp. 113–114.
[41] W. A. Yost, *Fundamentals of Hearing, An Introduction* (Academic, San Diego, CA, 1977), pp. 140–146.
[42] H. F. Olson, *Acoustical Engineering* (Princeton University Press, Van Nostrand, New York, 1957), pp. 30–35.

Behavioral responses of humpback whales (*Megaptera novaeangliae*) to full-scale ATOC signals

A. S. Frankel[a] and C. W. Clark[b]
Cornell Bioacoustics Research Program, 159 Sapsucker Woods Road, Ithaca, New York 14850

(Received 22 December 1999; accepted for publication 23 June 2000)

Loud (195 dB *re* 1 μPa at 1 m) 75-Hz signals were broadcast with an ATOC projector to measure ocean temperature. Respiratory and movement behaviors of humpback whales off North Kauai, Hawaii, were examined for potential changes in response to these transmissions and to vessels. Few vessel effects were observed, but there were fewer vessels operating during this study than in previous years. No overt responses to ATOC were observed for received levels of 98–109 dB *re* 1 μPa. An analysis of covariance, using the no-sound behavioral rate as a covariate to control for interpod variation, found that the distance and time between successive surfacings of humpbacks increased slightly with an increase in estimated received ATOC sound level. These responses are very similar to those observed in response to scaled-amplitude playbacks of ATOC signals [Frankel and Clark, Can. J. Zool. **76**, 521–535 (1998)]. These similar results were obtained with different sound projectors, in different years and locations, and at different ranges creating a different sound field. The repeatability of the findings for these two different studies indicates that these effects, while small, are robust. This suggests that at least for the ATOC signal, the received sound level is a good predictor of response. © *2000 Acoustical Society of America.* [S0001-4966(00)02610-2]

PACS numbers: 43.80.Ka, 43.80.Nd, 43.30.Sf [WA]

I. INTRODUCTION

Humpback whales show behavioral responses to several different human-made stimuli, including vessel, aircraft, active sonars (3.1–3.6 kHz), and possibly seismic exploration (summarized in Richardson *et al.*, 1995). In most of these cases, it is probable that the acoustic component of the stimulus provokes the response. This underlies the principal concern regarding the potential impact of the Acoustic Thermometry of Ocean Climate (ATOC) project on the marine mammals.

In 1993, the ATOC group proposed to measure the temperature of the ocean with an acoustic method (Munk, 1993). Water temperature is the dominant factor affecting the speed of sound in the ocean, so an accurate measurement of sound speed can be used to infer temperature across long distance paths. The ATOC project has used sound projectors located near the sound channel axis off Hawaii and California to transmit an *m*-sequence signal. The *m*-sequence is a sine wave with phase reversals that encode timing information (Au *et al.*, 1997). It has a 75-Hz center frequency and a broadband source level of 195 dB *re* 1 μPa at 1 m. These signals have been detected at various listening stations around the rim of the North Pacific Ocean. Accurate measurements of the travel times of the ATOC signals have resulted in water temperature measurements along the paths between the source and receivers (ATOC Consortium, 1998; Worcester *et al.*, 1999).

Soon after the announcement of the ATOC project in 1993, a Marine Mammal Research Program (MMRP) was established to study the effects of these proposed transmissions on the behavior and distribution of selected marine mammal species in both Hawaii and California. Study species were chosen based on their presumed ability to hear low-frequency signals, their likelihood of being exposed to the ATOC sound, and the feasibility of gathering enough data to draw conclusions. The humpback whale (*Megaptera novaeangliae*) was chosen as the focal species in Hawaii. Humpbacks are seasonally numerous, produce signals below and above the frequency of ATOC, and offer an extensive history of baseline data with well-developed research techniques.

In Hawaii, Frankel and Clark (submitted) found no changes in humpback distribution in response to ATOC transmissions during the 1998 season. There were indications of a response at the Californian study site, where humpback whales were found further, on average, from the source when the ATOC source was transmitting than during no-sound control portions (Calambokidis *et al.*, 1998).

Behavioral responses may be observed without producing changes in spatial distribution. Short-term behavioral changes caused by vessels have been reported by many authors (Baker and Herman, 1989; Bauer, 1986; Frankel and Clark, 1998). These short-term responses have not produced a major shift of whales away from areas of highest vessel density (Forestell *et al.*, 1991; Mobley *et al.*, 1999), although there is evidence that mother and calf pods in West Maui may have moved offshore in response to persistent vessel traffic (Glockner-Ferrari and Ferrari, 1985; Salden, 1988).

Humpback whale behavioral responses to playback of scaled-ATOC signals were examined in 1996 (Frankel and Clark, 1998). ATOC signals were transmitted with a broadband source level of 172 dB *re* 1 μPa at 1 m. Received levels at whales ranged from below ambient noise level (~105 dB) to as high as 130 dB *re* 1 μPa. Humpback

[a]Electronic mail: asf6@cornell.edu
[b]Electronic mail: cwc2@cornell.edu

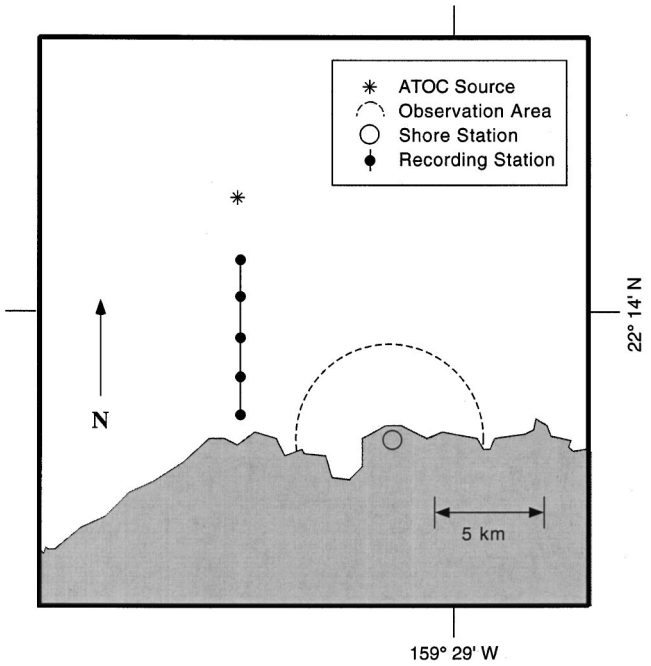

FIG. 1. Schematic for the 1998 study area on the North shore of Kauai, Hawaii is shown. The location of the shore station where observations were made is indicated with the square. The asterisk represents the location of the ATOC source. The observation area is indicated by the arc. The black dots show the position of the five recording stations used to measure the received level of the ATOC source.

whales showed no overt responses to these ATOC playbacks. However, statistical analysis found that both the dive duration and the distance traveled between successive surfacings increased with increasing received level of the ATOC playback signal.

Here we report on the results of behavioral observations conducted using the same methods of the previous study, but with the actual ATOC source replacing the playback speaker.

II. METHODS

A. Overview

The ATOC source was placed 14 km north of Kauai (22.35°N, 159.47°W) at a depth of 850 m, in the summer of 1997. Because low-frequency sound propagation in shallow water is complex and modeling results are unreliable, a transmission loss (TL) study was conducted to measure the received ATOC sound levels within the study area.

Behavioral observations were conducted from 9 February to 24 March 1998 from a shore station (see Fig. 1). Whale observers did not know when ATOC transmissions occurred. Experimental blocks had periodic transmissions while control blocks had none. Times of transmissions during the experimental blocks were varied to create an equal probability of transmission throughout the day. Behavioral observation and visual tracking followed the procedures described in Frankel and Clark (1998).

B. Transmission loss study

Received level (RL) data were collected from 30 October 1997 to 14 December 1997. RL data were collected from a vertical line array (VLA) of calibrated hydrophones using a TEAC RD-101T multichannel digital audio tape recorder. The VLA hydrophones were at depths of 10, 20, 40, and 80 m, encompassing the probable diving range of humpbacks. Ambient noise in the 60–90-Hz band was measured during times without transmissions. The power in the 60–90-Hz band was also measured during ATOC transmissions to determine transmission loss. Data were acquired to computer files using an advanced version of Cornell Canary software (Charif *et al.*, 1995) running on an Apple PowerMac 8100. Sound level measurements were made later using the PowerMeter, a Matlab program that automatically calculated the power in the 60–90-Hz band every second. The 25th percentile value of all of these 1-s measurements made on each transmission recording was returned as the received level measurement. The 25th percentile was chosen to reduce or eliminate the effect of artifacts such as transients and self-noise (e.g., recording vessel hull-slap and noise resulting from array movement through the water) (Frankel and Clark, 1998).

C. Experimental design

During the humpback research season, transmissions were scheduled to be more frequent during the prime observation period (0630 h to 1400 h). In order to insure that the observers remained blind to the experimental condition, the transmission schedule was structured such that there was a multi-day block of control days without transmissions (control) followed by a multi-day block with transmissions (ATOC). During an ATOC block, four ATOC signals were transmitted during daylight hours. Any single transmission consisted of a 5-min ramp-up at a steady rate of 6 dB/min from 165 to 195 dB *re* 1 μPa followed by 20 min at 195 dB. As shown in Fig. 2, transmissions were repeated at 2-h intervals over an 8-h period. The 2 h between transmissions allowed the collection of baseline behavioral data before a transmission.

In order to reduce the chances of an observer guessing whether the source was on or off, the start time of the first transmission occurring on each successive day of a four-day ATOC condition was delayed by 30 min. With this procedure, during any day in the four-day ATOC block, there would be a near-equal probability of a transmission at any time between 0630 and 1400 h Hawaiian Standard Time.

Two nighttime transmissions per day were added at 2000h and 0000h starting on 1 March 1998. This was done when autonomous bottom-mounted acoustic recorders (referred to as ''pop-ups'') were installed, allowing acoustic monitoring at night.

The behavioral analyses examined behavioral rates before, during, and after individual 25-min transmissions within an ATOC block. The null hypothesis tested was that none of the behavioral measures would show a change with respect to ATOC transmissions.

D. Behavioral observation

Behavioral data were collected from a focal pod of whales obtained using visual observation and theodolite

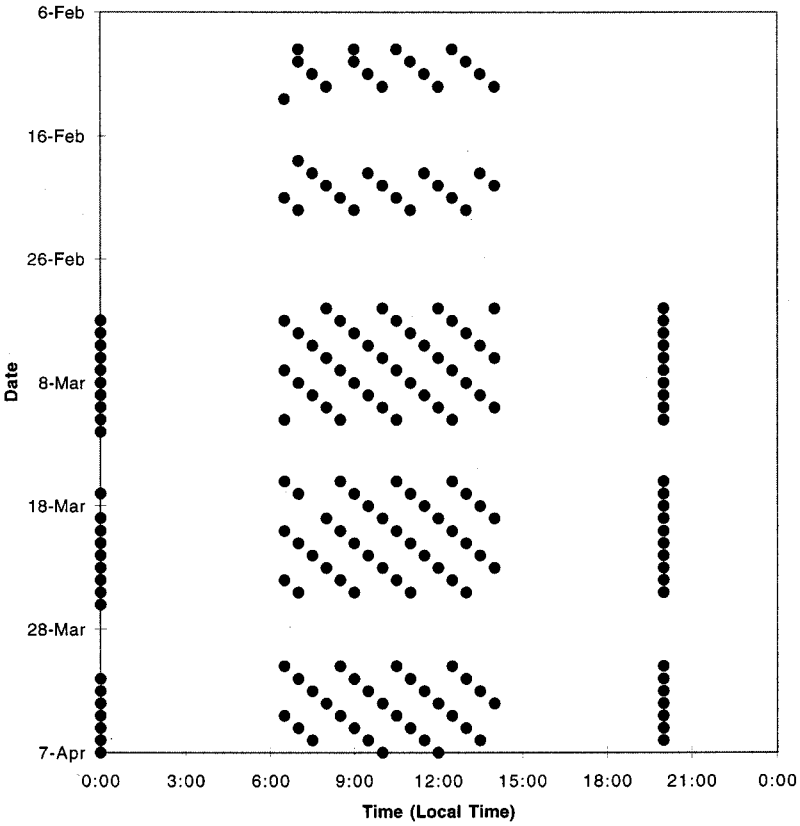

FIG. 2. The ATOC transmission schedule during the 1998 studying showing the pattern of five control and ATOC blocks. The first two transmission blocks included only transmissions during daytime hours. Once the pop-ups were deployed on 1 March 1998, two nighttime transmissions were added to the transmission schedule.

tracking following established MMRP protocols (Frankel and Clark, 1998). Focal pods were chosen on the basis of good sightability, and the likelihood that they would remain in view long enough for adequate data collection. Behavioral data were collected from the focal pod only, while all pods were tracked with the theodolite. Shore station observations documented behaviors of whales that were <5 km from shore, where most ($\sim$74%) of the humpbacks are found in the winter (Forsyth *et al.*, 1991). The shore station also documented vessel movement patterns with the same procedures used for whales. The shore station attempted to follow focal humpback pods for as long as possible in order to obtain observations of individual pods before, during, and after an ATOC transmission. Small pods and mother and calf pods were selected preferentially, due to their greater probability of responding to artificial stimuli.

E. Behaviors examined

Based on results from previous studies, the following seven behavioral variables were chosen for analysis. They are the following.

Measure	Unit
Whale speed (or segment speed)	(km/h)
Whale segment duration	(h)
Whale segment length	(km)
Blow rate	(blows/whale/hour)
Surface blow/rate	(blows/whale/surface time)
Surface time	(h)
Dive time	(h)

The first three measures describe movement and are derived from theodolite data. A segment is defined as the line between two successive surfacing locations. The last four measures describe respiratory and dive behavior, and are derived from focal pod observations. The sample sizes for the movement variables were greater than the sample sizes for behavioral measures since the theodolite operator could track multiple pods while the behavioral observer could follow only one pod at a time.

F. Analytical methods

To control for any distinctive behavior patterns of a pod, the analysis focused on potential changes in a pod's behavior between control and ATOC portions (before and during an individual transmission). An analysis of covariance (ANCOVA) test was used so that each pod served as its own control. With this method, the behavioral effects of pod size and calf presence are inherently accounted for in the overall model. The mean value of each behavior was calculated from data prior to and during the ATOC transmission. The control value of each behavior was used as the covariate in an analysis of covariance (ANCOVA) to control for interindividual variability. The effect of pod composition was included in the covariate. ATOC effects were represented as the estimated received ATOC level at the pod. The received level was estimated from the empirically determined transmission loss curve shown in Fig. 3, and the range of the pod from the ATOC source, as determined by theodolite. Descriptors of the nearest vessel present during the observation were included in the analysis in order to test for vessel effects. Frankel *et al.* (1996) found that the closest vessel had a

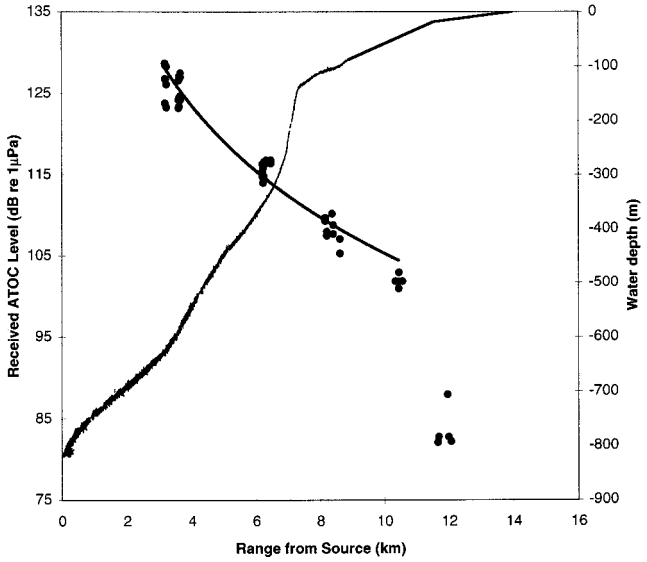

FIG. 3. The measured received sound level is shown as a function of range. Data from a single radial line of measurement stations are shown. These empirical data were used to estimate the received sound level at the whale for the behavioral analyses. The bathymetry underlying these measurements is shown. The sharp upslope rise with increasing range from the source probably contributes to the transition from the deep-water spherical spreading loss [TL=19.4* $\log_{10}$ (range)] to the observed TL=45.7* $\log_{10}$ (range) function ($R^2=0.95$).

greater statistical effect on whale behavior than more distant vessels. The parameters used to describe the vessels were separation between vessel and whale, vessel type (size), vessel speed, number of vessels present, vessel linearity index, and orientation of the vessel relative to the whale (Bowles *et al.*, 1994).

To reduce the number of vessel terms that had to be included in the model and the complexity of these related variables, a principal components analysis (PCA) was conducted on these six vessel descriptors. A standard correlation-based PCA was used. The principal components were included in the model as interaction terms with the vessel presence variable, so that observations made without vessels could also be included in the analysis. The collection of independent variables is referred to as the overall model.

III. RESULTS

A. Transmission loss study

Acoustic recordings were collected between 30 October and 14 December 1997. A total of 265 acoustic samples were taken at various ranges and along six radials. The data for the longest radial, extending south of the source, starting at 3.7 km from the source and ending 12 km south, are shown in Fig. 3. The transmission loss of 66–71 dB over the first 3.7 km indicates that transmission loss initially approximated spherical spreading loss [TL=19.4*$\log_{10}$(range)]. The transmission loss then transitioned to an estimated TL =45.7*$\log_{10}$(range). The dramatic increase in transmission loss is most probably a result of the effects of upslope propagation and destructive interference. This transmission loss function was used to estimate the received ATOC level at each pod, based on its distance from the source during transmissions.

It is important to note that the measured ATOC sound level (60–90 Hz) was less than 120 dB *re* 1 μPa at all locations within the 100 fathom contour. The mean ambient noise level in the 60–90-Hz band during the fall, prior to the arrival of humpback whales, was 96 dB *re* 1 μPa (N =24 798; s.d.=9.8, sample duration=1 s). Earlier work conducted off the Island of Hawaii during the winter season estimated ambient noise in the 60–90-Hz band at 105 dB *re* 1 μPa (Frankel and Clark, 1998). This winter value was likely elevated by the contributions from singing humpback whales.

B. Behavioral results

Behavioral data were collected between 9 February and 20 March 1998 when a total of 110 h were spent in 92 focal pod behavioral observation sessions. Observations containing control and ATOC portions were obtained for 65 pods.

Each whale behavior was tested separately with an ANCOVA. The covariate was the value of the behavior in the control portion. The estimated received sound level of the ATOC represented the ATOC effect. The first three vessel principal components were included in the ANCOVA models. The ANCOVA model for each whale behavior is presented and discussed separately.

1. Whale speed

The overall model was statistically significant. The covariate was extremely significant, indicating that the measures of the behavior during the control portion of the observation partially predicts the behavioral measure during the ATOC transmission. This also allows each pod to serve as its own control, as the unique variation of that pod's behavior is controlled for by the covariate. In this model, there was no measured effect of the ATOC transmission or vessels on the speed of whales.

2. Whale segment duration

The overall model was statistically significant, and is shown in Table I. The covariate was statistically significant. The estimated received level of the ATOC transmission had a statistically significant effect on segment duration. The parameter (regression) estimate for the estimated received sound level was 0.010, indicating that as the received sound level increased, the duration of time between successive surfacings increased as well. Figure 4 shows that over the RL range of 98–109 dB the segment duration values, adjusted for the effect of the covariate, increased as a function of the received sound level. There was no effect of vessels on this behavioral measure. The predicted effect of vessel presence was an increase in segment duration.

3. Whale segment length

The overall model was significant, and is shown in Table II. The covariate was again strongly significant. The estimated received level of the ATOC transmission 1 had a

TABLE I. Whale segment duration.

$R^2=0.431$ Source	DF	Sum of squares	Mean square	F value	Pr>F
Model	6	0.536 958 11	0.089 493 02	7.07	0.0001
Error	56	0.708 715 38	0.012 655 63		
Corrected total	62	1.245 673 49			

Factor	DF	Type I SS	Mean square	F value	Pr>F
Baseline behavior or covariate	1	0.431 681 79	0.431 681 79	34.11	0.0001
Estimated received level	1	0.055 750 00	0.055 750 00	4.41	0.0404
Vessel presence (VP)	1	0.017 877 38	0.017 877 38	1.41	0.2396
VP* Vessel PC1	1	0.002 242 03	0.002 242 03	0.18	0.6754
VP* Vessel PC2	1	0.029 261 58	0.029 261 58	2.31	0.1340
VP* Vessel PC3	1	0.000 145 32	0.000 145 32	0.01	0.9150

Parameter	Estimate	T for H0: Parameter=0	Pr>$\|T\|$	Standard error of estimate
Intercept	−1.035 362 537	−1.65	0.1054	0.629 123 78
Baseline behavior or covariate	0.747 597 121	4.69	0.0001	0.159 413 13
Estimated received level	0.010 651 831	1.69	0.0967	0.006 304 25
Vessel presence	0.062 539 695	1.74	0.0871	0.035 912 78
VP* Vessel PC1	−0.020 621 711	−1.14	0.2574	0.018 023 17
VP* Vessel PC2	−0.028 426 789	−1.52	0.1342	0.018 706 21
VP* Vessel PC3	−0.001 743 626	−0.11	0.9150	0.016 271 49

Note: The ANCOVA results for whale segment duration are shown. The estimated received level of the ATOC signal predicted that segment duration would increase with received sound level. Vessel presence was a near-significant predictor as well.

significant effect on segment length as well. The parameter (regression) estimate was 0.089. Figure 5 shows that over the RL range of 98–109 dB the adjusted segment length increased as received level of the ATOC signal increased. There was no statistically significant effect of vessels on this behavioral measure. Vessel presence and the first two vessel principal components, however, were close to being significant ($0.05<p\leqslant 0.10$). Vessel presence would lead to an increase in the segment length. The other two vessel principal components would predict smaller decreases in segment length. These two principal components were primarily combinations of the number of vessels, their linearity index, speed separation from the whale, and type. Increases in all of these tended toward decreasing segment length.

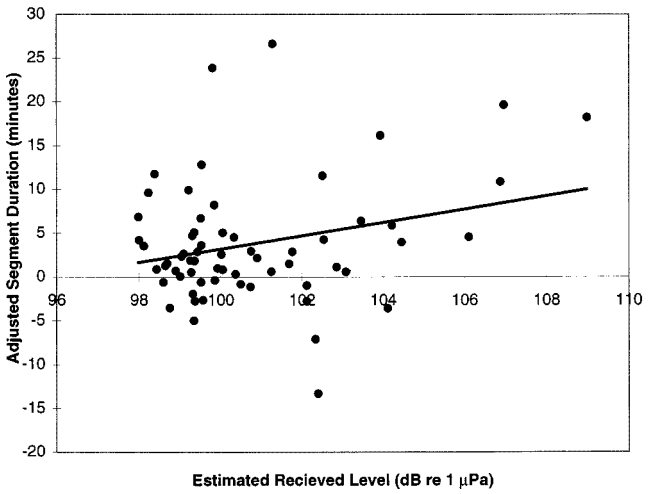

FIG. 4. Segment duration was first adjusted to remove the effect of the covariate (control portion segment duration). The adjusted durations were then plotted against estimated received ATOC sound level. The regression line shows the slight increase in segment duration as received ATOC sound level increases.

4. Blow rate

The overall model was not statistically significant, indicating that there were no measured effects of ATOC or vessels on blow rate.

5. Surface blow rate

The overall model was statistically significant [$F(4,14)=4.36$, $p=0.0268$]. There was no effect of ATOC sound level on blow rate; however, the presence of vessels affected the surface blow rate. The parameter estimate was -0.009, indicating a decrease in surface blow rate when vessels were present. The third principal component was nearly statistically significant ($p=0.067$). Its trend was also toward decreased surface blow rate. The third principal component essentially represents the relative orientation score. Therefore, the trend was for surface blow rate to decrease as whales and vessels were oriented toward each other.

6. Surface time

The overall model was statistically significant. None of the effects, other than the covariate, were significant, indicating that there was no measurable effect of ATOC or vessels on the amount of time whales spent at the surface.

7. Dive time

The overall model was not statistically significant, indicating that there were no measured effects of ATOC or vessels on dive time.

TABLE II. Whale segment length.

$R^2=0.441$ Source	DF	Sum of squares	Mean square	F value	Pr>F
Model	6	9.312 958 68	1.552 159 78	7.77	0.0001
Error	59	11.789 601 89	0.199 823 76		
Corrected total	65	21.102 560 57			

Factor	DF	Type I SS	Mean square	F value	Pr>F
Baseline behavior or covariate	1	4.703 723 00	4.703 723 00	23.54	0.0001
Estimated received level	1	3.342 953 24	3.342 953 24	16.73	0.0001
Vessel presence (VP)	1	0.319 296 02	0.319 296 02	1.60	0.2112
VP* Vessel PC1	1	0.150 407 89	0.150 407 89	0.75	0.3891
VP* Vessel PC2	1	0.410 021 33	0.410 021 33	2.05	0.1573
VP* Vessel PC3	1	0.386 557 20	0.386 557 20	1.93	0.1695

Parameter	Estimate	T for H0: Parameter=0	Pr>$\|T\|$	Standard error of estimate
Intercept	−8.613 514 169	−3.57	0.0007	2.414 127 79
Baseline behavior or covariate	0.293 449 973	1.91	0.0611	0.153 692 76
Estimated received level	0.089 222 893	3.69	0.0005	0.024 210 14
Vessel presence	0.282 921 564	1.98	0.0522	0.142 772 38
VP* Vessel PC1	−0.120 521 352	−1.72	0.0898	0.069 875 33
VP* Vessel PC2	−0.123 315 510	−1.67	0.1008	0.073 971 59
VP* Vessel PC3	−0.089 942 938	−1.39	0.1695	0.064 667 15

Note: The ANCOVA results for whale segment length are shown. The estimated received level of the ATOC signal predicted that segment duration would increase with received sound level. Vessel presence was a near-significant predictor as well.

C. Abundance of vessels

The number of vessels and the distances between whales and the nearest vessel were compared between 1994 and 1998. The mean number of vessels observed per session in 1994 was 1.66 (s.d.=1.62) and 1.11 (s.d.=1.19) in 1998. Furthermore, the mean separation distance increased from 3.09 km in 1994 to 8.04 km in 1998. The number of boats permitted to launch from the Hanalei River, the only wintertime harbor on the North Shore of Kauai, was reduced between 1994 and 1998 by changes in local regulations. On average, there were fewer vessels in 1998 and they were further away from the whales than in 1994.

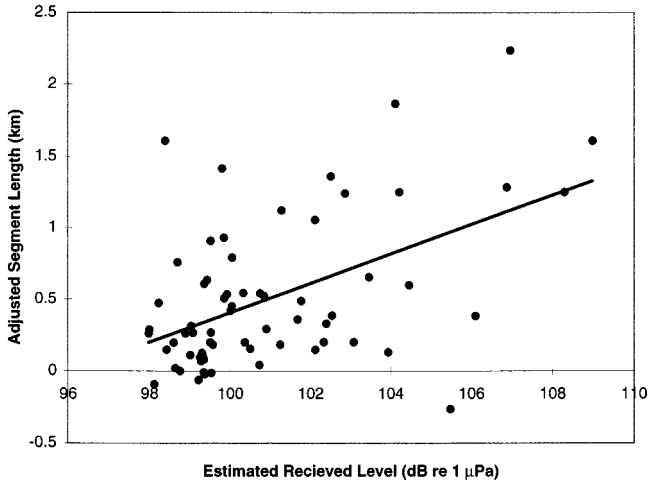

FIG. 5. Segment length was first adjusted to remove the effect of the covariate (control portion segment length). The adjusted lengths were then plotted against received ATOC sound level. The regression line shows the slight increase in segment length as estimated received ATOC sound level increases.

IV. DISCUSSION

The behaviors of humpback whales presented with full-scale (i.e., ''normal'') ATOC sounds were observed using the same methods as in a previous study that documented responses to scaled playbacks of ATOC sounds. In both the previous and current study, the ATOC signals were represented in the analysis as the estimated received sound level rather than a simple ''on/off'' variable.

The analysis of covariance revealed that both the time and the distance between successive surfacings increased with increasing estimated received sound level. This result is consistent with the results of the scaled-ATOC work conducted off the Island of Hawaii in 1996 (Frankel and Clark, 1998). Humpbacks exhibited similar responses to the same ATOC signal at similar received levels. These results indicate that ATOC transmissions produce subtle but repeatable, predictable short-term behavioral changes in humpback whales.

The striking similarity between the 1996 and 1998 responses addresses a long-standing issue regarding whale reactions to noise. Earlier work with gray whales found that 50% of the migrating population deflected from their course when the received level of industrial noise reached 116–124 dB re 1 μPa. Given the limitations in source level in the gray whale study (~162 dB re 1 μPa), the 50% avoidance occurred at ranges of ~100 m from the playback vessel. It was recently suggested that the whales responded more to

the proximity of the source than to the received level (Ellison and Weixel, 1994). The scaled ATOC playback experiment (Frankel and Clark, 1998) and the current study used two different sound sources with vastly different source levels (172 dB vs 195 dB *re* 1 μPa at 1 m). Both studies documented similar responses at similar received levels (98 to 130 dB), but at vastly different distances from the source (~100–2000 m vs 8–12 km). This indicates that for the ATOC signal, received level proved to be a better predictor of response than proximity. It is also important to note that the predictions of increased duration and length of movement segments are valid only to received levels of up to 130 dB *re* 1 μPa. Extrapolating to higher received levels is not reliable given the present results and could lead to significant prediction errors.

The conclusion that received level is a good predictor of response does not generalize to all species and signals. Playback of U.S. Navy low-frequency active sonar signals to gray whales evoked strong responses when the acoustic source was in their migratory path. When the source was moved offshore 2 km, there was no response to the signals, even though the received sound levels were comparable (Clark *et al.*, 1999). In this case, received level alone cannot explain the observed behavior.

The only behavior affected by vessels was surface blow rate, although other whale behaviors had near-significant vessel effects. When vessels were present the surface blow rate decreased slightly. During the ATOC playback experiment, surface blow rate was found to decrease as vessel size increased (Frankel and Clark, 1998). In that study, and in most other studies, a greater number of vessel effects were detected. The apparent reduction in vessel effect in 1998 may be explained by the drop in vessel traffic off Kauai from 1994 to 1998.

How comparable are the effects of vessel traffic and ATOC transmissions? The mean estimated received level of the ATOC transmissions at the location of all the focal pods in the analysis ranged from 98.0 to 109.0 dB (mean=101.4 dB; s.d.=2.58; $N=65$). This is less than or equal to typical vessel acoustic stimuli. Frankel and Clark (1998) found that, at higher traffic levels than those seen in the present study, the single vessel closest to the whale affected more behaviors than the ATOC playback stimulus. This suggests that the effects of ATOC signals are roughly comparable to that of low to moderate vessel activity. Both study sites experience much less vessel traffic than humpback habitats off Maui or O'ahu.

The presence of vessels and the occurrence of ATOC transmissions were found to produce short-term behavioral changes. The question needing to be addressed is that of biological significance and cumulative impact. Do these subtle short-term responses have any long-term implications? Humpback whales frequently encounter vessels throughout most of their range in Hawaii and major portions of their range in Alaska. Increased vessel traffic may be responsible for a shift in the distribution of mother and calf pods off Maui (Glockner-Ferrari and Ferrari, 1985; Salden, 1988). However, this effect was not seen when all pod types were considered (Forestell *et al.*, 1991).

During the 25 years that humpbacks have been studied in Hawaii, vessel traffic has steadily increased. There is now evidence that the population of humpbacks is increasing. A comparison of statewide aerial surveys conducted in 1976–1980, and repeated in 1990, found that sighting rates had increased throughout the state (Mobley *et al.*, 1999). The most recent population estimates based on photographic resightings reported a much higher population level than earlier estimates (Calambokidis *et al.*, 1997; Cerchio, 1998). Therefore, it seems that if vessel interactions do have some negative long-term effect, it is not sufficient to prevent the population from growing. ATOC transmissions will likely have even less long-term impact on the population than vessels because ATOC affects a much smaller fraction of the humpback habitat (approximately 157 km^2) than vessels. Furthermore, ATOC can affect behavior only on the wintering grounds whereas vessels may be present on the wintering and summering grounds as well as during migration.

The results of the research presented here and conducted earlier with humpback whales indicate that the hearing range of humpback whales encompasses the 75-Hz ATOC signal. However, whales within 12 km of the source show only subtle, short-term effects on their surface behaviors. They do not show any immediately obvious response to the ATOC signal at received levels <130 dB. They do not abandon their coastal habitat adjacent to the offshore ATOC source. They returned to that habitat in the year following a season of exposure to that source. We conclude that the present operation of the ATOC source off Kauai is not sufficient to cause biologically significant changes in behavior for the humpback population wintering off Hawaii. However, we emphasize that this conclusion cannot be generalized to the effects of cumulative impacts from multiple sources including ATOC, and a suite of other man-made sources such as local vessel traffic, commercial vessel traffic, oil and gas seismic surveys, and various sonars. Understanding cumulative impacts will require much broader knowledge of habitat use, behavioral ecology, underwater acoustics, and man-made noise in the ocean.

ACKNOWLEDGMENTS

We would like to thank a number of people for helping to make this research and this report possible. We would first like to thank the members of the 1994 and 1998 research teams, who collected the data used in this report. They are Vicki Beaver, Greg Campbell, Alison Craig, Janet Doherty, Megan Ferguson, Bridget Ferris, Christine Gabriele, Mia Griafalconi, Leila Hatch, Eric Howarth, Matt Irinaga, Gene Kent, Tom Kieckhefer, Tom Norris, Susan Reeve, Mari Smultea, Dave Weller, and Ann Zoidis. At the Cornell Laboratory of Ornithology, the support of Tom Calupca, Russ Charif, Brian Corzilius, Kathy Dunsmore, Melissa Fowler, Kurt Fristrup, Connie Gordon, Marguerite McCartney, and Harold Mills was invaluable. Peter Worcester and Susie Pike at the Scripps Institution of Oceanography were very helpful as were Bruce Howe, Jim Mercer, and Shirley Westlander of the Applied Physics Laboratory of the University of Washington. Special thanks to Robert C. Gisiner of the Office of Naval Research for helping to support this research. The

MMRP Advisory Board under the Chairmanship of W. John Richardson has provided many helpful comments and review throughout the years. Research was conducted under permits issued by the National Marine Fisheries Service (No. 970) and the State of Hawaii Permit (PRO98-06). The comments of two anonymous reviewers were appreciated and contributed to this manuscript. Funding was provided through the Advanced Research Projects Agency and this work relates to the Advanced Research Projects Agency Grant No. MDA972-93-1-0003 funded by the Strategic Environmental Research and Development Program (SERDP). The United States Government has a royalty-free license throughout the world in all copyrightable material herein. Additional funding was supplied through SERDP Grant No. 00014-97-1-0571.

ATOC Consortium (**1998**). ''Ocean Climate Change: Comparison of Acoustic Tomography, Satellite Altimetry, and Modeling,'' Science **281**, 1327–1332.

Au, W. W. L., Nachtigall, P. E., and Pawloski, J. A. (**1997**). ''The effects of the ATOC signal on dolphins and whales,'' J. Acoust. Soc. Am. **101**, 2973–2977.

Baker, C. S., and Herman, L. M. (**1989**). ''The behavioral responses of summering humpback whales to vessel traffic: Experimental and opportunistic observations,'' Kewalo Basin Marine Mammal Laboratory, Honolulu.

Bauer, G. B. (**1986**). ''The Behavior of Humpback Whales in Hawaii and Modifications of Behavior Induced by Human Interventions,'' dissertation, University of Hawaii at Manoa, Honolulu.

Bowles, A. E., Smultea, M., Würsig, B., DeMaster, D. P., and Palka, D. (**1994**). ''Relative abundance and behavior of marine mammals exposed to transmissions from the Heard Island Feasibility Test,'' J. Acoust. Soc. Am. **96**, 2469–2484.

Calambokidis, J., Chandler, T. E., Costa, D. P., Clark, C. W., and Whitehead, H. (**1998**). ''Effects of the ATOC Sound Source on the distribution of marine mammals observed from aerial surveys off Central California,'' in World Marine Mammal Science Conference, Monaco, p. 22.

Calambokidis, J., Steiger, G. H., Straley, J. M., II, T. J. Q., Herman, L. M., Cerchio, S., Salden, D. R., Yamaguchi, M., Sato, F., Urbán, J., Jacobsen, J., Ziegesar, O. v., Balcomb, K. C., Gabriele, C. M., Dalheim, M. E., Higashi, N., Uchida, S., Ford, J. K. B., Miyamura, Y., Guevara, P. L. d., Mizroch, S. A., Schlender, L., and Rasumssen, K. (**1997**). ''Abundance and population structure of humpback whales in the North Pacific basin,'' National Marine Fisheries Services, Southwest Fisheries Science Center, La Jolla, CA.

Cerchio, S. (**1998**). ''Estimates of humpback whale abundance off Kauai, 1989–1993: evaluating biases associated with sampling the Hawaiian Islands breeding assemblage,'' Mar. Ecol.: Prog. Ser. **175**, 23–34.

Charif, R. A., Mitchell, S., and Clark, C. W. (**1995**). ''Canary 1.2 User's Manual,'' 1.2.1/Ed (Cornell Laboratory of Ornithology, Ithaca, NY).

Clark, C. W., Tyack, P., and Ellison, W. T. (**1999**). ''Responses of Four Species of Whales to Sounds of SURTASS LFA Sonar Transmissions,'' Cornell University, Woods Hole Oceanographic Institution, Marine Acoustics, Inc.

Ellison, W. T., and Weixel, K. S. (**1994**). ''Considerations for designing underwater acoustical playback experiments,'' J. Acoust. Soc. Am. **96**, 3316.

Forestell, P. H., Brown, E. K., Herman, L. M., and Mobley, Jr., J. R. (**1991**). ''Near-shore distribution of humpback whales near Maui, Hawaii: 1976–1991,'' in Ninth Biennial Conference on the Biology of Marine Mammals, Chicago, IL, p. 23 (abstract).

Forsyth, N., Mobley, J. R., and Bauer, G. B. (**1991**). ''Depth preferences in 'Hawaiian' humpbacks,'' in Ninth Biennial Conference on the Biology of Marine Mammals, Chicago, IL, p. 24.

Frankel, A. S., and Clark, C. W. (**1998**). ''Results of low-frequency *m*-sequence noise playbacks to humpback whales in Hawaii,'' Can. J. Zool. **76**, 521–535.

Frankel, A. S., and Clark, C. W. (**submitted**). ''Factors affecting the distribution and abundance of humpback whales off the North Shore of Kauai,'' Mar. Mamm. Sci.

Frankel, A. S., Smultea, M. A., and Kieckhefer, T. R. (**1996**). ''Humpback Whale Behavior observed from Kauai shore stations 1994: Baseline Behavior and Vessel Effects,'' Cornell University.

Glockner-Ferrari, D. A., and Ferrari, M. J. (**1985**). ''Individual Identification, behavior, reproduction, and distribution of humpback whales, *Megaptera novaeangliae*, in Hawaii,'' Rep. No. MMC-83/06 NTIS PB85-200772, Marine Mammal Commission.

Mobley, J. R., Bauer, G. B., and Herman, L. M. (**1999**). ''Changes over a ten-year interval in the distribution and relative abundance of humpback whales (*Megaptera novaeangliae*) wintering in Hawaiian waters,'' Aq. Mamm. **25**, 63–72.

Munk, W. (**1993**). ''The sound of oceans warming,'' The Sciences September/October, 21–26.

Richardson, W. J., Greene, C. R., Malme, C. I., and Thompson, D. H. (**1995**). *Marine Mammals and Noise*, 1st ed. (Academic, San Diego).

Salden, D. R. (**1988**). ''Humpback whale encounter rates offshore of Maui, Hawaii,'' J. Wildl. Manage. **52**, 301–304.

Worcester, P. F., Cornuelle, B. D., Dzieciuch, M. A., Munk, W. H., Howe, B. M., Mercer, J. A., Spindel, R. C., Colosi, J. A., Metzger, K., Birdsall, T. G., and Baggeroer, A. B. (**1999**). ''A test of basin-scale acoustic thermometry using a large-aperture vertical array at 3250-km range in the eastern North Pacific Ocean,'' J. Acoust. Soc. Am. **105**, 3185–3201.

Sounds produced by Australian Irrawaddy dolphins, *Orcaella brevirostris*

Sofie M. Van Parijs,[a] Guido J. Parra, and Peter J. Corkeron
School of Tropical Environment Sciences and Geography, James Cook University, Townsville QLD 4811, Australia

(Received 24 March 2000; accepted for publication 26 June 2000)

Sounds produced by Irrawaddy dolphins, *Orcaella brevirostris*, were recorded in coastal waters off northern Australia. They exhibit a varied repertoire, consisting of broadband clicks, pulsed sounds and whistles. Broad-band clicks, ''creaks'' and ''buzz'' sounds were recorded during foraging, while ''squeaks'' were recorded only during socializing. Both whistle types were recorded during foraging and socializing. The sounds produced by Irrawaddy dolphins do not resemble those of their nearest taxonomic relative, the killer whale, *Orcinus orca*. Pulsed sounds appear to resemble those produced by *Sotalia* and nonwhistling delphinids (e.g., *Cephalorhynchus* spp.). Irrawaddy dolphins exhibit a vocal repertoire that could reflect the acoustic specialization of this species to its environment. © *2000 Acoustical Society of America.* [S0001-4966(00)02510-8]

PACS numbers: 43.80.Ka [WA]

I. INTRODUCTION

Delphinid cetaceans are well known for their impressive capacities to produce and perceive sounds (e.g., Caldwell *et al.*, 1990; Ford, 1991). Previous studies of delphinid sounds and related behavior have concentrated on the Delphinines, particularly bottlenose dolphins, *Tursiops* spp. (e.g., Janik and Slater, 1998; Sayigh *et al.*, 1999). Here, we describe the acoustic repertoire of Irrawaddy dolphins, *Orcaella brevirostris*, and relate sounds produced to specific behaviors.

Little is known of the biology of Irrawaddy dolphins. They occur in inshore coastal areas and some rivers from eastern India to northeastern Australia and through southeast Asia to Vietnam (Stacey and Arnold, 1999). There are two types of Irrawaddy dolphins (Arnold and Heinsohn, 1996; Stacey and Leatherwood, 1997), and the taxonomy of these two types remains unclear. There may be two species of *Orcaella* rather than one, separated either by ecotype (riverine/estuarine) or by geography (Asia/Indonesian/Philippines, or Australia/New Guinea)(Le Duc *et al.*, 1999). Nothing is known about the acoustic behavior of Irrawaddy dolphins in the wild. The only published report of recordings is from one captive study, which reported that Irrawaddy dolphins used single component sonar signals of about 60 kHz and that no audible whistles or pure tones were recorded (Kamminga *et al.*, 1983). These animals were of the riverine or southeast Asian form. Here we describe the sounds recorded from a free-ranging population of coastal Irrawaddy dolphins in Australia.

II. METHODS

This study was conducted between March 1999 and January 2000, in Cleveland Bay (19°15′S, 146°50′E) and Halifax Bay (18°50′S, 146°30′E), Queensland, Australia. Acoustic and behavioral observations of Irrawaddy dolphins were made over four days, 17 March 1999, 6 and 7 July 1999, and 20 January 2000 at two different sites from either a 4.5-m inflatable boat or a 12-m diesel boat.

Visual observations of group size, composition and predominant (over 50% of group members) surface behavior were made every 10-min. Group composition was determined by visual observations of body size, and categorized into adults, juveniles or calves (see Shane, 1990). A group was defined as either a solitary animal, or any aggregation of dolphins where a member of the aggregation was within 10 m of any other member in the first five minutes of observation (modified from Corkeron, 1997). Observed behaviors were divided into the categories traveling, socializing, foraging and milling, derived from Shane (1990) and Barrett-Lennard *et al.* (1996). Observations were made during calm weather (Beaufort sea states less than 3) and no rain.

Acoustic recordings of underwater sounds from Irrawaddy dolphins were made continuously throughout each sighting of a group. Recordings were made using a High Tech Inc. hydrophone (model HTI-96-MIN, sensitivity: −170 dB, frequency response: 5 Hz to 30 kHz ±1.0 dB, −165 dB *re*: 1 V/μPa) and a digital audio tape recorder, SONY TCD-D8 (frequency response: 20 Hz to 22 kHz ±1.0 dB). The acoustic recordings were digitized as spectrograms using BatSound analysis program (Pettersson Elektronik A.B., 1996). Sounds were divided into three acoustic categories: broadband clicks, pulsed sounds and narrow-band frequency-modulated sounds (whistles). Whistle types were defined according to variations in their spectral contours. Sounds were separated into three different quality categories: poor, medium and good—based on their spectrogram quality (fast Fourier transforms, *dt*: 10 ms, *df*: 102 Hz, FFT size: 512). Only medium and good signals, where all parameters of a spectral contour were distinctly measurable, were used for these analyses. Five parameters were measured for all whistles, total duration (seconds), start frequency (kHz), end frequency (kHz), minimum frequency (kHz) and maximum frequency (kHz). For all pulsed and broadband clicks, total

[a]Also at Norwegian Polar Institute, Norway; Electronic mail: sofie@npolar.no

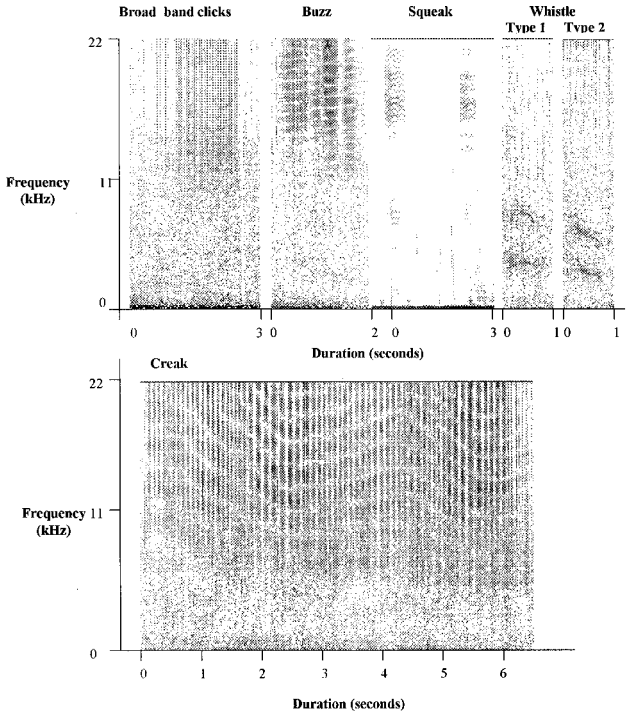

FIG. 1. Spectrogram representations of a broad-band click train, pulsed sounds comprising, the ''creak,'' ''buzz'' and ''squeak,'' and two whistle types recorded from Irrawaddy dolphins (fast Fourier transforms, sample rate 44.1 kHz, *dt*: 10 ms, *df*: 102 Hz, FFT size: 512). Each whistle type had either one or two harmonics. Note the frequency range of the recording equipment limits spectrogram representations of the sounds.

duration (seconds) and repetition rate, i.e., the number of clicks per second was measured. A behavior was assigned to each sound type as a result of the behavioral category determined in the relevant concurrent 10-min sample.

III. RESULTS

A total of 12 behavioral samples were recorded over a total of 115 min across 4 days over a 10-month period. Group sizes of between 4 and 11 individuals ($N=7$, mean=7 ± 1 SE) were observed during this study. Groups were composed of either adults only ($N=6$) or adults and two juveniles ($N=1$). We were unable to make recordings of traveling dolphins, and milling was not observed during this study. Foraging behavior was most commonly observed (nine samples), followed by socializing (three samples) ($N=12$).

A. Broadband clicks

Broadband clicks occurred as a series of clicks (Fig. 1), commonly referred to as ''click trains'' (Popper, 1980). Click trains ranged above 22 kHz in frequency and had a click rate of between 10 and 46 clicks/second (N of click trains=49). The duration of each click train varied widely, ranging from 0.5 to 11 s, with a mean duration around 3.6 ± 2.9 s.d. Click trains were recorded most frequently during foraging (94%), followed by socializing (6%).

B. Pulsed sounds

''Creak'' sounds consisted of clicks emitted at high repetition rates ranging between 44 and 82 clicks/second forming long pulsed sounds, with a mean duration of 4.1 ± 2.0 s.d. seconds and a frequency range above 22 kHz ($N=44$) (Fig. 1). ''Creaks'' were predominantly recorded during foraging (61%) and very infrequently during socializing (39%). ''Buzz'' sounds consisted of clicks emitted at high repetition rates ranging between 51 and 116 clicks/second forming short pulsed sounds, with a frequency range of above 22 kHz ($N=28$) (Fig. 1). The duration of each buzz ranged between 0.3 and 1.1 s and had a mean duration of around 0.6 ± 0.2 s.d. ''Buzz'' sounds were recorded during foraging (95%), and during socializing (5%). ''Squeak'' sounds were burst pulsed sounds with clearly defined structure (Fig. 1, $N=17$). They ranged from 0.1 to 0.3 s in duration with a mean of 0.2 ± 0.06 s.d. seconds. Their frequency range was above 22 kHz. ''Squeaks'' were only heard when Irrawaddy dolphins were engaged in social behavior (100%).

TABLE I. Descriptive statistics showing mean $\pm$sd and range for vocalization duration (seconds), minimum frequency (kHz), maximum frequency (kHz), start frequency (kHz) and end frequency (kHz) for Irrawaddy dolphin whistles.

Vocal type	Duration (s)	Min (kHz)	Max (kHz)	Start (kHz)	End (kHz)	*N*
Whistle1						
Mean $\pm$sd	0.2 ± 0.02	3.2 ± 1.2	4.2 ± 1.1	4.5 ± 2.6	4.1 ± 2.1	26
range	0.1–0.3	1.1–5.2	3–6	1.1–3.2	2–5.0	
Whistle2						
Mean $\pm$sd	0.3 ± 0.01	3.1 ± 1.4	4.2 ± 1.4	4.3 ± 1.7	3.0 ± 1.3	25
range	0.2–0.3	2.4–3.5	3.4–5.7	3.4–5.7	2.4–3.1	

C. Whistles

Whistles were narrow-band, frequency-modulated sounds (Popper, 1980). There were two different whistle types, categorized according to their spectral contours (Fig. 1). Each whistle type varied in frequency and duration (Table I). Each type had between one and two harmonics. Whistle types 1 and 2 were heard during both foraging (WH1=90%, WH2=84%) and socializing (WH1=10%, WH2=16%).

IV. DISCUSSION

This is the first description of the vocal repertoire of free-ranging Irrawaddy dolphins. Irrawaddy dolphins produce broadband clicks and at least three types of pulsed sounds and two types of whistles (Fig. 1). A previous study showed that captive Irrawaddy dolphins produced ultrasonic sounds (Kamminga *et al.*, 1983) but did not document any frequency-modulated or pure tone sounds from this species.

Click trains were produced mostly during foraging and to a lesser extent during socializing, results similar to those of delphinids with established echolocation capacities (e.g., Popper, 1980). Irrawaddy dolphins produce a range of pulsed sounds (Fig. 1). The ''creak'' and ''buzz'' sounds resemble the tonal ''cry'' sounds produced by all *Cephalorhynchus* spp. (e.g., Evans and Awbrey, 1984; Dziedic and Buffrenil, 1989; Dawson, 1991) as they are both formed by ''high pulse repetition rates of clicks'' characterized on spectro-

grams by a complicated harmonic structure. Clicks with high repetition rates have also been described in *Sotalia fluviatilis* (Da Silva and Best, 1994). As in Hector's dolphins (Dawson, 1991), ''cry'' type sounds in Irrawaddy dolphins are associated with both socializing and foraging contexts. In contrast, Irrawaddy dolphins' ''squeak'' sounds were only associated with social behavior. Squeaks were short burst-pulsed sounds resembling those produced by some delphinines (Herzing, 1996).

Irrawaddy dolphins (Fig. 1, Table I) produced at least two whistle types. All were short in duration, low in frequency (1 to 8 kHz) and simple in form compared with the elaborate whistle repertoires observed in other delphinid species (e.g., Caldwell *et al.*, 1990; Norris *et al.*, 1994). The two whistle types were associated with both foraging and socializing. Irrawaddy whistles resemble those reported in *Sotalia fluviatilis*, which produce simple, short (less than 0.5 s), rising or U-shaped whistles with dominant frequencies of 10–15 kHz (Da Silva and Best, 1994). *Sotalia* live in shallow, turbid habitats similar to Irrawaddy dolphins (Da Silva and Best, 1994). The apparent similarities in the vocal repertoires of these species suggest that ecology may exert a considerable influence on the evolution of sound production and type.

The phylogenetic position of *Orcaella* has been the subject of considerable debate (see Arnold and Heinsohn, 1996; Le Duc *et al.*, 1999). The most recent phylogeny of the Delphinidae suggests that Irrawaddy dolphins are most closely related to killer whales (LeDuc *et al.*, 1999). The vocal repertoire of Irrawaddy dolphins appears not to resemble that of killer whales. However, it is similar to those of the nonwhistling *Cephalorhynchus* spp. and to a Stenonine, *Sotalia*. The vocal repertoire of the Irrawaddy dolphin includes sounds resembling those produced by nonwhistling delphinid species but includes two simple whistles. The relative importance of phylogeny and ecology in the evolution of delphinids' vocal repertoire remains unstudied.

ACKNOWLEDGMENTS

Our thanks to the Queensland Marine Parks Service for help with data collection and Peter Arnold for providing references. This work was funded by the Natural Heritage Trust ''Coasts and Cleans Seas'' program. Fieldwork was carried out under permit from the Great Barrier Reef Marine Park Authority, and with ethical approval from James Cook University. We thank three anonymous referees for providing constructive comments on this manuscript.

Arnold, P. W., and Heinsohn, G. E. (**1996**). '' Phylogentic status of the Irrawaddy dolphins, *Orcaella brevirostris* (Owen in Gray): A cladistic analysis,'' Memoirs of the Queensland Museum **39**, 141–204.

Barrett-Lennard, L. G., Ford, J. K. B., and Heise, K. A. (**1996**). '' The mixed blessing of echolocation: differences in sonar use by fish-eating and mammal-eating killer whales,'' Anim. Behav. **51** (3), 553–565.

Caldwell, M. C., Caldwell, D. K., and Tyack, P. L. (**1990**). ''Review of the signature whistle hypothesis for the Atlantic bottlenose dolphin,'' in *The Bottlenose Dolphin*, edited by S. Leatherwood and R. R. Reeves (Academic, New York), pp. 199–234.

Corkeron, P. J. (**1997**). ''Bottlenose dolphins, *Tursiops truncatus*,in southeast Queensland waters: social structure and conservation biology,'' in *Marine Mammal Research in the Southern Hemisphere. Volume 1. Status, Ecology and Medicine*, edited by M. Hindell and C. Kemper (Surrey Beatty, Chipping Norton), pp. 1–10.

Da Silva, V. M., and Best, R. C. (**1994**). Tucuxi—*Sotalia fluviatilis* (Gervais, 1853), in *Handbook of Marine Mammals. Volume 5: The First Book of Dolphins*, edited by S. H. Ridgway and R. Harrison (Academic, New York).

Dawson, S. M. (**1991**). ''Click and communication: the behavioral and social contexts of Hector's dolphin vocalizations.'' Ethol. **88**, 265–276.

Dziedzic, A., and De Buffrenil, V. (**1989**). ''Acoustic signals of the Commerson's dolphin, *Cephalorhynchus commersonii*, in the Kerguelen Islands,'' J. Mammal. **70**, 449–452

Evans, W. E., and Awbrey, F. T. (**1984**). ''High frequency pulses of Commerson's dolphin and Dall's porpoise.'' Am. Zool. **24**, 2A.

Ford, I. (**1991**). ''Vocal traditions among resident killer whales (*Orcinus orca*) in coastal waters of British Columbia,'' Can. J. Zool. **69**, 1454–1481.

Herzing, D. L. (**1996**). ''Vocalizations and associated underwater behavior of free-ranging Atlantic spotted dolphins, *Stenella frontalis*, and bottlenose dolphins, *Tursiops truncatus*,'' Aquat. Mamm. **22**(2), 61–79.

Kamminga, C., Wiersma, H., and Dudok Van Heel, W. H. (**1983**). ''Investigations on cetacean sonar. VI. Sonar sounds from *Orcaella brevirostris*, of the Mahakam river, East Kalimantan, Indonesia; first description of acoustic behavior,'' Aquat. Mamm. **10**, 83–95.

Janik, V. M., and Slater, P. J. B. (**1998**). ''Context-specific use suggests that bottlenose dolphin signature whistles are cohesion calls,'' Anim. Behav. **56**(4), 829–838.

LeDuc, R. G., Perrin, W. F., and Dizon, A. E. (**1999**) ''Phylogenetic relationships among the delphinid cetaceans based on full cytochrome B sequences,'' Mar. Mamm. Sci. **15**(3), 619–648.

Norris, K. S., Wursig, B, Wells, R. S., and Wursig, M. (**1994**). *The Hawaiian Spinner Dolphin* (Univ. California, Berkeley).

Pettersson Elektronik A. B. (**1996**). Batsound. Tallbacksvagen 51, S-75645 Uppsala, Sweden.

Popper, A. N. (**1980**). ''Sound emission and detection by delphinids,'' in *Cetacean Behavior: Mechanisms and Functions*, edited by L. M. Herman (Wiley, New York), pp. 1–52.

Sayigh, L. S., Tyack, P. L., Wells, R. S., Solow, A. R., Scott, M. D., and Irvine, A. B. (**1999**). ''Individual recognition in wild bottnose dolphins: a field test using playback experiments,'' Anim. Behav. **57**(1), 41–50.

Shane, S. H. (**1990**). ''Behavior and ecology of the Bottlenose dolphin at Sanibel Island, Florida,'' in *The Bottlenose Dolphin*, edited by S. Leatherwood and R. R. Reeves (Academic), pp. 245–266.

Stacey, P. J., and Leatherwood, S. (**1997**). ''The Irrawaddy dolphin, *Orcaella brevirostris*: a summary of current knowledge and recommendations for conservation action,'' Asian Mar. Biol. **14**, 195–214.

Stacey, P. J., and Arnold, P. W. (**1999**). ''*Orcaella brevirostris*,'' Mamm. Sp. **616**, 1–8.

LETTERS TO THE EDITOR

This Letters section is for publishing (a) brief acoustical research or applied acoustical reports, (b) comments on articles or letters previously published in this Journal, and (c) a reply by the article author to criticism by the Letter author in (b). Extensive reports should be submitted as articles, not in a letter series. Letters are peer-reviewed on the same basis as articles, but usually require less review time before acceptance. Letters cannot exceed four printed pages (approximately 3000–4000 words) including figures, tables, references, and a required abstract of about 100 words.

Scattering of ultrasonic waves by void inclusions

E. Ruffino and P. P. Delsanto
INFM, Dipartimento di Fisica, Politecnico di Torino, Torino, Italy

(Received 8 June 1999; revised 17 December 1999; accepted 22 February 2000)

The Local Interaction Simulation Approach (LISA) has been applied to study the propagation of ultrasonic pulses in materials containing void inclusions. First the case of a single scatterer has been considered, with the conclusion that a void must be represented by at least four cells of the discretization lattice. Then the case of ultrasound propagation in a material with both a regular and random distribution of inclusions has been studied. Interesting interference effects have been obtained and it can be concluded that in both cases LISA allows reliable and efficient simulations to be performed. © *2000 Acoustical Society of America.* [S0001-4966(00)00706-2]

PACS numbers: 43.20.Fn, 43.20.Gp, 43.20.Px [ANN]

INTRODUCTION

Ultrasonic waves yield a very useful tool for a nondestructive evaluation of specimens with multiple embedded void (or other) inclusions.[1–4] From the theoretical point of view, however, the problem of multiple scattering from the inclusions is, except in elementary cases, very difficult. Several analytical methods have been proposed, also in view of a comparison with experimental results.[5,6] Among them, Twersky's formalism[7–9] and effective medium theory[10] may be used when the wavelength is much greater than the size of the scatterers, while the parabolic approximation[11] is valid in the opposite case, i.e., for a wavelength much smaller than the size of the scatterers. In the framework of the Resonance Scattering Theory, Überall *et al.*[12,13] have extended the treatment of single-scattering resonances into a multiple scattering formalism, which allows one to treat the much more difficult and interesting case in which the wavelength and the scatterers are of the same order of amplitude.

These analytical techniques are, of course, the tool of choice, whenever the specifications of the problem allow their use in view of a closed form solution, i.e., when the geometry of the specimen and the boundary conditions are elementary, the distribution of inclusions regular, the incident wave a continuous wave. In all other cases it is advantageous or even necessary to resort to numerical techniques.

In the present contribution we utilize the Local Interaction Simulation Approach (LISA),[14–16] which has been applied to study a variety of problems of diffusion, growth, absorption and desorption, nondestructive evaluation, solitons generation and even biophysics and biomedicine. The method LISA is briefly discussed in Sec. I.

Although the problem of ultrasound diffusion from a single scatterer has been thoroughly investigated in the literature,[12,13,17,18] a LISA analysis can be useful for a better understanding of the scattering from an arbitrary voids distribution. Such a study is carried on in Sec. II. Finally, in Secs. III and IV, several examples of problems of scattering from a regular and, respectively, random distribution of void inclusions are considered.

I. THE METHOD

As mentioned in the Introduction, the method used for the numerical calculations is the Local Interaction Simulation Approach (LISA). LISA resembles finite difference equations (FDE), inasmuch as it employs a space and time discretization to reduce the problem to a set of iterative equations (IE). The main difference is that with FDE's one first aims to transform the problem under study into a set of Partial Differential equations (PDE) in the framework of a continuous model; then one discretizes the PDE's by means of the well known FD formalism[19,20] in order to obtain the IE's, taking care that convergence and stability criteria be satisfied. By contrast, with LISA one aims from the beginning at a discrete model, from which the IE's can be directly obtained. All kinds of local features may be incorporated into the discrete model in a heuristic way, bypassing the PDE's. The local nature of the approach allows one to treat a problem concerning a complex heterogeneous medium with the same ease as if it were homogeneous, since each partition of it is considered independently.

In the present contribution we restrict ourselves for simplicity to consider two-dimensional (2D) media, i.e., media with translational symmetry with respect to a given direction, along which we align the *z*-axis. We then assume that it is a

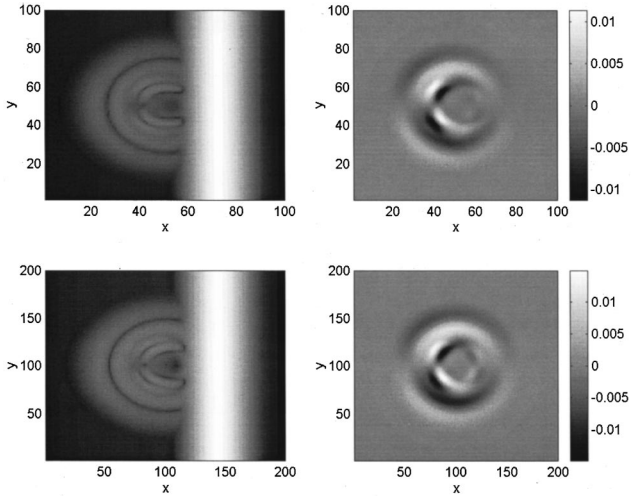

FIG. 1. Snapshots of a longitudinal plane wave, Gaussian in time, traveling from the left to the right in a homogeneous rectangular specimen with a void inclusion in its center. Upper plots: $\varepsilon\times\varepsilon$ flaw. Lower plots: $2\varepsilon\times 2\varepsilon$ flaw. Left plots: total amplitude. Right plots: mode-converted shear components and corresponding grayness scale.

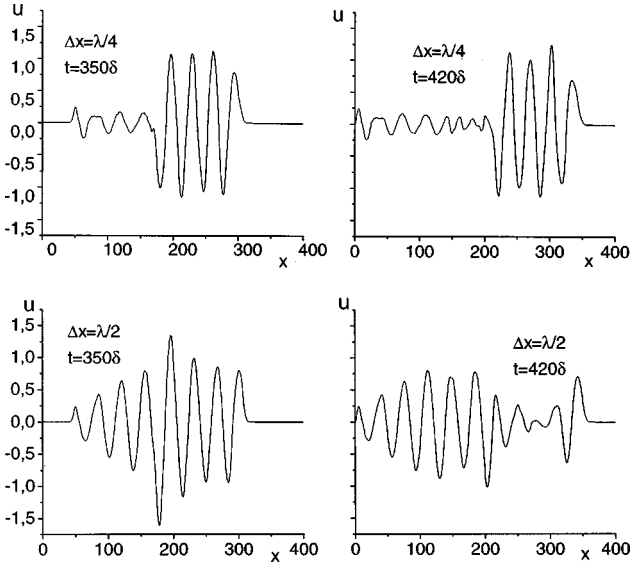

FIG. 2. Longitudinal components of the displacement along a horizontal cut in the case of a multiple sine wave incident upon a specimen with a regular distribution of voids.

rectangular plate and divide it into tiny ''cells'' of size $\varepsilon\times\varepsilon$, with the x- and y-axes parallel to its sides. The IE's for the displacement vector $w_{ij}^{(t)}$ at the time t of a generic grid-point (i,j) at the intersection of four cells of density ρ_k and Lamè constants $\lambda_k,\mu_k,(k=1,4)$, respectively, are[21]

$$w_{ij}^{(t+1)}=2w_{ij}^{(t)}-w_{ij}^{(t-1)}+\frac{\delta^2}{\overline{\rho}\varepsilon^2}\sum_{i',j'}\sum_{k}M_{i'j'}^{(k)}(w_{i'j'}^{(t)}-w_{ij}^{(t)}),\qquad(1)$$

where δ is the time discretization step, (i',j') represent the eight ''nearest neighbors'' of (i,j), i.e., $(i\pm1,j\pm1)$, $(i\pm1,j)$, and $(i,j\pm1)$, $\overline{\rho}$ is the average density among the four cells and

$$\begin{pmatrix}0 & \psi_k^{(+)}\\ \psi_k^{(+)} & 0\end{pmatrix}\quad\text{for } i'=i\pm1,\quad j'=j\pm1,$$

$$M_{i'j'}^{(k)}=\begin{pmatrix}\frac{1}{2}\sigma_k & -\psi_k^{(-)}\\ \psi_k^{(-)} & \frac{1}{2}\mu_k\end{pmatrix}\quad\text{for } i'=i\pm1,\quad j'=j,\qquad(2)$$

$$\begin{pmatrix}\frac{1}{2}\mu_k & \psi_k^{(-)}\\ -\psi_k^{(-)} & \frac{1}{2}\sigma_k\end{pmatrix}\quad\text{for } i'=i,\quad j'=j\pm1,$$

where

$$\psi_k^{(\pm)}=(-1)^{k+1}\frac{(\lambda_k\pm\mu_k)}{4},\quad \sigma_k=\lambda_k+2\mu_k.\qquad(3)$$

II. SCATTERING FROM A SINGLE VOID INCLUSION

We consider here a homogeneous, isotropic specimen, with a void inclusion in its center. We assume that the specimen is two dimensional and rectangular with sides $I\varepsilon\times J\varepsilon$. A longitudinal plane wave, Gaussian in time, is injected from the left side, normal to it, at the time $t=0$. The values $\lambda=4.4$, $\mu=2.09$ and $\rho=1.2$ a.u. are used for the Lamè constants and density of the material, respectively; ε is chosen equal to 1 and δ is fixed according to the stability condition $\delta=\varepsilon\sqrt{\rho/(\lambda+3\mu)}$.[14] Correspondingly, the longitudinal and shear phase velocities are given by 2.67 and 1.32 a.u., respectively.

Figure 1 shows a snapshot of the wave at the time $t=220\delta$, i.e., shortly after the wave has overrun the flaw. The left plots represent the total amplitude A of the pulse, while the right plots display its y-component, which at this time almost coincides with the shear component. These plots are reported in order to emphasize the mode conversion caused by the void. In the left plots we observe a white stripe representing the ''transmitted'' wave, which propagates almost undisturbed, since the flaw is very small. On the left of the stripe we notice a complex pattern, due to the scattering from the void, with an outer ring representing the longitudinal reflected wave front encompassing various mode-converted shear and longitudinal waves. In the right plots we observe the antisymmetric nature of the shear component (with respect to the x-axis), which comes as a consequence of the antisymmetric coupling terms in Eq. (1).

In Fig. 1 the upper plots refer to a 100×100 grid with a 1×1 void (in units of ε) and a pulse described by means of $N=30$ node points, while the lower plots relate to a 200×200 grid with a 2×2 void and $N=60$ node points. The node points are distributed at equal distances for one third along the half maximum width σ and for the other two thirds along the two tails of the Gaussian. It would seem that, except for a lower level of accuracy, which gives a fuzzier look to the upper plots, the two cases should be completely equivalent. This is not, however, the case. In fact, a closer inspection of Eq. (1) reveals that one cell empty inclusions do not represent real voids, since $\overline{\rho}$ does not vanish if the voids consist of a single cell. Real voids must be represented by empty inclusions of size at least 2×2, as in the bottom plots. The upper ones correspond in the reality to the case of a partially filled void.

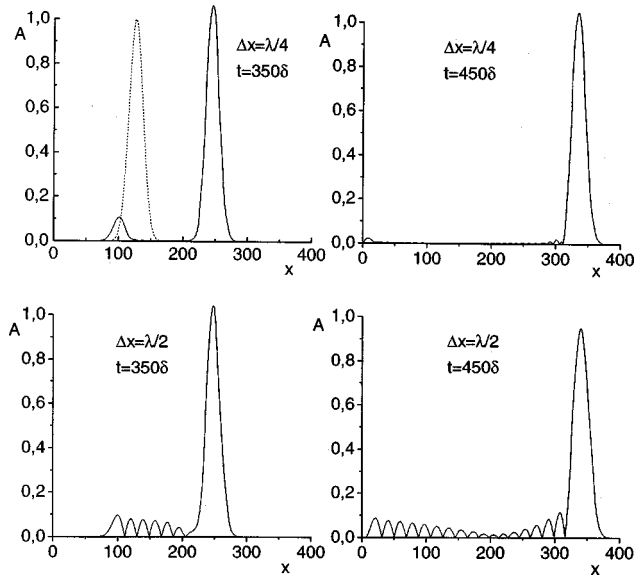

FIG. 3. Total amplitude of the displacement along a horizontal cut in the case of a Gaussian pulse (represented by a dashed line in the upper left plot) incident upon a specimen with regular distribution of voids.

III. SCATTERING FROM A REGULAR DISTRIBUTION OF VOID INCLUSIONS

We consider now a regular distribution of voids (described by 2×2 squares) and assume that they are distributed in the region between $x_1=200\varepsilon$ and $x_2=324\varepsilon$, with a spacing $\Delta y=3\varepsilon$ and

(i) $\Delta x=\lambda/4$,
(ii) $\Delta x=\lambda/2$,

where $\lambda=36\varepsilon$ is the wavelength of the incident wave.

Figure 2 shows the longitudinal component of the displacement along a horizontal cut through the center of the specimen in the case of an incident multiple (4 periods) sine wave. The upper plots correspond to $\Delta x=\lambda/4$, which is the condition for destructive interference. At $t=350\delta$ the wave has already entered completely the voids region and, as expected, the transmitted pulse has endured little change. In fact, little energy has gone into the reflected wave, due to the destructive interference between the various components reflected from each column of voids. The effect is reversed in the lower plots, which correspond to the condition of constructive interference: $\Delta x=\lambda/2$. In this case much of the energy goes to the reflected pulse, while the transmitted pulse undergoes a severe degradation. In both cases the pattern becomes better established at later times, since the interference is then more complete, as it can be seen from the right plots, which correspond to the time $t=420\delta$.

Figure 3 shows that interference effects may be obtained also in the case of Gaussian pulses. In this case we define the ''wavelength'' as $\lambda=n\varepsilon$, where n is the number of gridpoints which describe numerically the source pulse (assumed to be negligible elsewhere). In our case $n=72$. The upper plots of Fig. 3 refer to the destructive interference condition. In fact we observe, especially at the time $t=450\delta$, that the reflected pulse almost vanishes. The bottom plots refer to the constructive interference condition, with an effect which

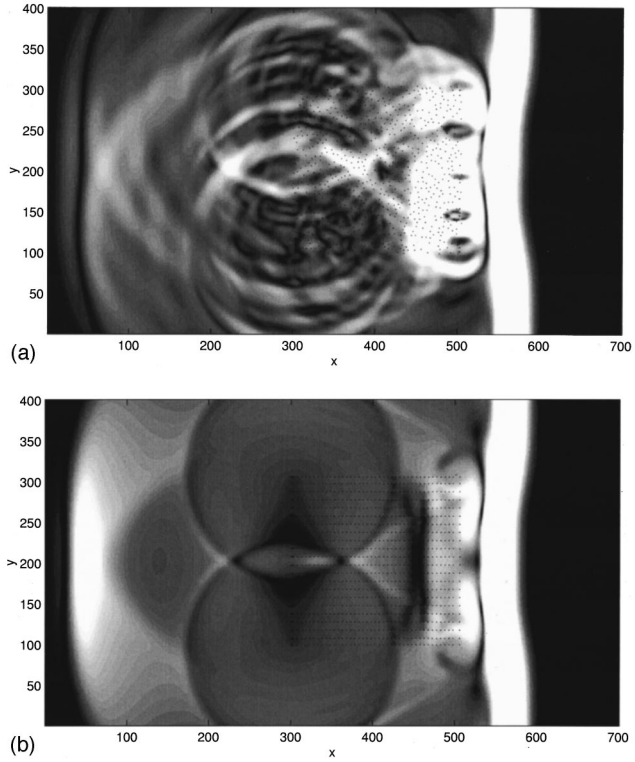

FIG. 4. Snapshots of the amplitude of an ultrasonic pulse propagating in a specimen with (a) a random distribution; (b) a uniform distribution of voids (represented by small dots).

again is more conspicuous as time progresses. In addition, the left top plot shows that the transmitted pulse is higher than the incident one (dotted line). This interesting result can be explained by using conservation of energy.[22] As the wave moves from a higher to a lower stiffness area (where voids are present), the amount of material deformation needed to store the energy increases and with it the wave amplitude.

IV. SCATTERING FROM A RANDOM DISTRIBUTION OF VOID INCLUSIONS

The procedure illustrated in the previous sections is particularly useful in the case of irregular distributions of voids, since then analytical methods become hopelessly intricate. By contrast, numerical simulations performed by means of LISA are not more exacting than in the case of regular or even homogeneous specimens, except for the size of the grid, which obviously must increase with the number (or complexity) of the discontinuities. Thus for our calculations we have adopted a lattice of 700×400 cells to describe the specimen, which is assumed to be homogeneous but for a region $(300<i<500,\ 100<j<300)$, with a high density (10%) of randomly distributed voids (2×2). The longitudinal source wave (plane in the y-direction) is assumed to have a Gaussian profile (in the x-direction) specified by $N=40$ node points.

In Fig. 4 snapshots of the total amplitude of the pulse in the case of a random distribution of voids are compared with the case of uniform distribution. The time is in both cases $t=800\delta$, i.e., after the pulse has completely crossed the voids region. In both cases we observe, on the right side, a large

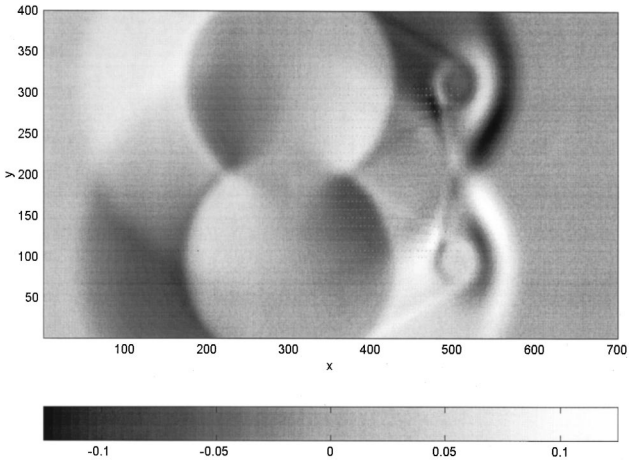

FIG. 5. Snapshot of the shear component of the pulse corresponding to case (b) of Fig. 4.

stripe corresponding to the longitudinal transmitted pulse (rather deformed with respect to the incident pulse) and, on the left, an interference pattern due to the reflected and mode-converted pulse components, originated by the multiple scattering. The interference pattern is similar in both cases, but much clearer and well resolved in Fig. 4(b). It is expected that a significant difference remains between the two cases, since a periodic arrangement, being crystal-like, yields some degree of anisotropy, which is of course absent in a random distribution. However, the difference tends to disappear when a void's density increases beyond a given threshold (even if in this case the model would represent perhaps more a cavity with solid particles than a solid with voids).

Analyzing in more detail the plots of Fig. 4, we find to the very left of Fig. 4(b) a strong (white) longitudinal reflected pulse, which is symmetric with respect to the horizontal center line ($y=200\varepsilon$). Next we observe that an interference pattern in the shape of an ''8'' is generated, due to the diffraction from the void inclusions lattice. This pattern includes both longitudinal (symmetric) and shear (antisymmetric) components, as shown in Fig. 5, where the latter are plotted. A grayness scale is included in Fig. 5, in order to clarify the antisymmetric nature of the shear pulse. A strong ''creeping'' longitudinal wave is then observed along the right side of the void's region [see Fig. 4(b)], while two shear ''eyes'' are generated at the two right corners (see Fig. 5). Finally, the stripe corresponding to the transmitted pulse displays local variations (energy losses) and an overall bending to the left, due to the slowing down effect of the void inclusions.

Similar effects may also be noticed in Fig. 4(a), although the patterns are much more confused, due to the randomness of the voids distribution, e.g., we observe that, instead of a single well defined figure ''8'' pattern, several less resolved similar patterns emerge. Likewise, the ''creeping'' pulses of Fig. 4(b) give rise to a blotchy whitish region around the right side of the voids region in Fig. 4(a).

V. CONCLUSIONS

We have studied the application of the Local Interaction Simulation Approach (LISA) to the investigation of the ultrasonic wave propagation in materials with void inclusions.

First we have considered the problem of ultrasound diffusion from a single scatterer, in order to better understand the scattering mechanism. We have found that at least four empty ''cells''are needed for a realistic description of void inclusions by means of LISA. Then we have analyzed some instances with both regular and random distributions of voids, finding interesting interference and mode conversion patterns in the reflected waves. We have also shown that the interference pattern is rather confused when only a (relatively) small number of flaws is assumed (plots not shown for brevity), but it becomes well resolved and clear when the number of voids is strongly increased.

As a conclusion, the LISA method appears to be quite adequate to study the scattering of ultrasonic waves even if the number of inclusions is very high and their distribution quite irregular. The method is also very efficient since, in a parallel processing environment, the computer time required on a large grid is not more than a few minutes. These simulations may have a great practical interest in the field of quantitative nondestructive evaluation, both for the characterization of structural materials, at the macroscopic level, and for the study of mesoscopic nonclassical nonlinearity, whose relevance has been recently demonstrated in several materials.[23]

ACKNOWLEDGMENTS

This work was supported by the INFM Parallel Computing Initiative. We also wish to thank Professor Herbert Überall for helpful discussions.

[1] N. Phan-Thien and S. Kim, *Microstructure in Elastic Media. Principle and Computational Methods* (Oxford University Press, New York, 1994).
[2] M. Ciarletta and D. Iesan, *Nonclassical Elastic Solids* (Wiley, New York, 1993).
[3] P. A. Martin, ''Scattering of elastic waves by inclusions with thin interface layers,'' Methoden Verfahren Math. Phys. **37**, 161–168 (1991).
[4] Y. M. Chen, ''Determination of shapes, size and material composition of large inclusions in elastic media from scattered waves,'' in *Inverse Problems in Engineering Mechanics* (Springer, Berlin, 1993), p. 377.
[5] M. de Billy and G. Quentin, ''Scattering by cylindrical targets using very short ultrasonic pulses and Fourier analysis,'' in *Acoustic Resonance Scattering*, edited by H. Überall (Gordon & Breach Science, New York, 1989).
[6] X. L. Bao and H. Überall, ''Experimental study of acoustic resonances of elastic spheres and hemispherically endcapped cylinders,'' in *Acoustic Resonance Scattering*, edited by H. Überall (Gordon & Breach Science, New York, 1989).
[7] V. Twersky, ''Coherent scalar field in pair-correlate random distributions of aligned scatterers,'' J. Math. Phys. **18**, 2468 (1977).
[8] V. Twersky, ''Coherent electromagnetic waves in pair-correlated random distributions of aligned scatterers,'' J. Math. Phys. **19**, 215 (1978).
[9] V. Twersky, ''Acoustic bulk parameters in distributions of pair-correlated scatterers,'' J. Acoust. Soc. Am. **64**, 1710 (1978).
[10] A. H. Nayfeh, *Wave Propagation in Layered Anisotropic Media* (Elsevier, Amsterdam, 1995).
[11] A. Ishimaru, *Wave Propagating and Scattering in Random Media* (Academic, New York, 1978).
[12] Y. Guo and H. Überall, ''Radar depolarization in the ground based system due to chaff,'' J. Electromagn. Waves Appl. **7**, 197 (1993).
[13] Y. Guo and H. Überall, ''The resonance effect of a wire in response to transient waves,'' J. Electromagn. Waves Appl. **8**, 355 (1994).

[14] P. P. Delsanto *et al.*, ''Simulation of ultrasonic pulse propagation in complex media,'' in *New Perspectives on Problems in Classical and Quantum Physics*, edited by P. P. Delsanto and A. Saenz (Gordon & Breach, New York, 1998), p. 51.
[15] R. S. Schechter, H. H. Chaskelis, R. B. Mignogna, and P. P. Delsanto, ''Real-time parallel computation and visualization of ultrasonic pulses in solids using the connection machine,'' Science **265**, 1188–1192 (1994).
[16] P. P. Delsanto *et al.*, ''Connection machine simulation of ultrasonic wave propagation in materials. I: The one-dimensional case,'' Wave Motion **16**, 65 (1992); , **20**, 295 (1994); , **26**, 329–339 (1997).
[17] L. E. Kinsler, A. Frey, A. C. Coppens, and J. V. Sanders, *Fundamentals of Acoustics* (Wiley, New York, 1982).
[18] J. D. Achenbach, *Wave Propagation in Elastic Solids* (North-Holland, Amsterdam, 1973).
[19] N. Bellomo and L. Preziosi, *Modelling Mathematical Methods and Scientific Computation* (CRC, Boca Raton, FL, 1995).
[20] J. C. Strickwerda, *Finite Difference Schemes and Partial Differential Equations* (Wadsworth-Brooks, 1989).
[21] P. P. Delsanto and M. Scalerandi, ''A spring model for the simulation of the propagation of ultrasonic pulses through imperfect contact interfaces,'' J. Acoust. Soc. Am. **104**, 2584–2591 (1998).
[22] J. S. McIntyre *et al.*, ''Wave propagation in a composite with wavy reinforced fibres,'' in *Review of Progress in Quantitative Nondestructive Evaluation* edited by D. O. Thompson and D. E. Chimenti (Plenum, New York, 1995), Vol. 14.
[23] R. A. Guyer and P. A. Johnson, ''Nonlinear mesoscopic elasticity: Evidence for a new class of materials,'' Phys. Today (April), 30–36 (1999).

Optical measurement of the speed of sound in air over the temperature range 300–650 K

Roger C. Hart
ICASE, NASA Langley Research Center, Hampton, Virginia 23681-2199

R. Jeffrey Balla and G. C. Herring
AMDB, NASA Langley Research Center, Hampton, Virginia 23681-2199

(Received 14 September 1999; accepted for publication 3 July 2000)

Using laser-induced thermal acoustics (LITA), the speed of sound in room air (1 atm) is measured over the temperature range 300–650 K. Since the LITA apparatus maintains a fixed sound wavelength as temperature is varied, this temperature range simultaneously corresponds to a sound frequency range of 10–15 MHz. The data are compared to a published model and typically agree within 0.1%–0.4% at each of 21 temperatures. © *2000 Acoustical Society of America.* [S0001-4966(00)02910-6]

PACS numbers: 43.28.Bj, 43.20.Hq [LCS]

The speed of sound in air near room temperature has been intensely studied over a range of various parameters such as frequency, humidity, and pressure. This body of work, stretching back three centuries, has been reviewed by Wong.[1] Most of this work was conducted in the audio (20–20 000 Hz) or hundreds-of-kHz frequency range. Less frequently, work was carried out in the MHz range. At room temperature, sound speed models for air[1] and pure gases[2] agree with measurement to 0.03% or better. However, previous work on the speed of sound in air is limited to temperatures of ~300 K and below. In this letter we present measurements of the speed of sound (10–15 MHz) in air at 1 atm over the 300–650 K temperature range and compare these data with theoretical values. This letter is an outgrowth of our earlier work[3] in developing remote diagnostics for flow temperature in wind tunnels.

We compare our experimental data to a model synthesized by Zuckerwar.[4] The speed of sound is written in the standard Laplacian form with corrections for various gas-phase phenomena. Thus

$$V_{\text{sound}}=[(\gamma_0 RT/M)(1+C_1)(1+C_2)(1+C_3)]^{0.5}, \quad (1)$$

where γ_0 is the ratio of specific heats, R is the universal gas constant, T is the temperature, and M is the molecular mass. C_1 is a correction for the temperature variation of γ_0, C_2 is a correction for virial (nonideal gas) effects, and C_3 is a combined correction for the vibrational, rotational, and translational (classical thermal and viscous) relaxations. For our experimental conditions, C_1, C_2, and C_3 are each $\leqslant 0.05$. Additional details of these corrections are described in Refs. 3 and 4.

The experimental method is laser-induced thermal acoustics[5] (LITA). Detailed descriptions of the LITA apparatus, procedure, and data analysis are given in Ref. 3. Sound waves are produced by crossing two high-peak-power pulsed laser beams (532 nm) at ~1 deg, forming interference fringes at the crossing inside an oven. Two counterpropagating ultrasonic sound wave packets are launched by electrostriction. The propagation of these two acoustic waves is monitored by probing them with a long-duration laser pulse (750 nm) that is Bragg diffracted into a fast optical detector. This probe signal decays as the wave packets propagate out of the sample volume (defined by the probe beam) and as the waves are attenuated through relaxation. In principle, speed of sound can be determined from the wavelength (derived from beam crossing angle) and frequency of the temporal modulation of the signal. This modulation arises from the beating of two individual diffracted light beams (one from each sound wave packet) that are Doppler shifted relative to each other. Since we cannot measure our 1-deg crossing angle to 0.1% accuracy geometrically, we effectively measure it with another LITA apparatus. We simultaneously generate a second LITA signal with the same crossing angle in a reference cell at known temperature of ~295 K. The sound speed in the oven is then determined from the ratio of the LITA frequencies observed in the oven, f^{LITA}, and reference cell, f^{ref}, and the known sound speed V^{ref} in the reference cell. Oven temperatures were read with a precision of 0.2 K with a thermocouple, which had been calibrated by comparison with a precision NIST-traceable Pt thermometer. Allowing for small temperature gradients in the oven, we estimate an absolute uncertainty in the measurement of the oven temperature of 0.33% (±1 K at 300 K, growing to ±2 K at 600 K). The small day-to-day variations in atmospheric pressure produce negligible changes in the speed of sound, relative to the accuracy that we achieve here.

The results of our experiment are summarized in Table I. Quantities associated with a single laser shot use subscript *i*, quantities averaged over a single run (100 shots in ~2 min) use subscript *j*, and all quantities without a subscript *i* or *j* are averaged over a temperature bin of 3–15 runs. A total of 107 100-shot runs were made, of which more than 9500 shots yielded usable data. The data shown have been binned into 21 temperatures, the width of the bins varying from 0 K (all runs at the same temperature) to 5.0 K. The reason for consolidating the 107 runs into 21 temperature bins is to reduce the length of Table I. For each good shot of

TABLE I. Summary of model and measurements for the speed of sound in air from 300 to 650 K using LITA.

T (K)	N	N_r	H (%)	f^{LITA} (MHz)	V^{LITA} (m/s)	V^{mod} (m/s)	ΔV (m/s)	σ_m (m/s)	$\sigma_{\Delta V}$ (m/s)
296.9	1432	15	34	10.18	347.5	346.2	1.1	0.018	0.51
303.8	445	6	33	10.21	350.7	350.2	0.73	0.032	0.75
313.0	282	3	46	10.55	354.2	355.7	−1.5	0.043	0.081
321.1	294	3	29	10.51	360.3	360.0	0.31	0.034	0.035
346.0	292	3	30	10.92	374.6	373.7	0.92	0.036	0.095
374.7	288	3	25	11.29	388.7	388.9	−0.20	0.054	0.066
381.3	282	3	27	11.48	392.8	392.3	0.46	0.042	0.15
408.4	277	3	43	12.28	407.6	406.3	1.2	0.060	0.25
415.2	591	6	31	11.95	409.6	409.5	0.30	0.033	0.14
431.7	299	3	45	12.39	415.8	417.8	−2.0	0.053	0.23
443.1	297	3	26	12.31	423.6	423.0	0.61	0.054	0.14
467.8	660	7	34	12.75	434.7	434.8	−0.12	0.041	0.81
482.6	497	6	32	12.84	440.3	441.6	−1.1	0.05	0.28
499.3	903	10	32	13.17	449.2	449.3	−0.03	0.038	0.84
520.6	776	9	40	13.57	458.0	458.9	−1.0	0.043	1.34
528.4	496	6	34	13.54	461.5	462.2	−0.58	0.053	0.38
551.4	257	3	36	13.87	472.7	472.3	0.45	0.071	0.13
570.2	188	3	41	14.25	481.0	480.5	0.5	0.12	0.18
603.1	274	3	43	14.67	492.7	494.3	−1.6	0.10	0.31
631.3	257	3	41	14.99	504.5	505.7	−1.3	0.10	0.41
653.2	498	6	41	15.29	514.7	514.6	0.24	0.089	1.13

each run, the oven sound speed $V_i^{\mathrm{LITA}}=V_i^{\mathrm{ref}}(f_i^{\mathrm{LITA}}/f_i^{\mathrm{ref}})$ was determined, and for each run, an unweighted average V_j^{LITA} was found. Using the observed oven temperature, humidity, and the unweighted average of measured sound frequency f_j^{LITA} for each run, we calculated V_j^{mod} from the model.

In Table I, N_r is the number of runs and N is the total number of shots used in each bin. The average temperature T, relative humidity H, and model velocity V^{mod} for each bin were calculated as the average of per run values weighted by the number of good shots in each run, e.g., $T=\Sigma(N_jT_j)/\Sigma N_j$. Average values of f^{LITA} and V^{LITA} were weighted with the per run standard deviations of the mean σ_j. The quantity σ_m was calculated from the per run standard deviations of the mean σ_j weighted by N_j according to $\sigma_m=[\Sigma(N_j(N_j-1)\sigma_j^2)/\Sigma(N_j(N_j-1))]^{1/2}$; thus σ_m is the standard deviation of the mean of the distribution if all the runs in a bin are normalized to have the same mean value. The average of the differences $\Delta V_j=V_j^{\mathrm{LITA}}-V_j^{\mathrm{mod}}$, weighted by per run standard deviations, is denoted by ΔV, while the standard deviation of the ΔV_j, again weighted by per run standard deviations, is denoted by $\sigma_{\Delta V}$.

Comparison of the σ_m and $\sigma_{\Delta V}$ allows evaluation of the short ($\leqslant$10 min) and long-term ($\geqslant$1 day) repeatability of the method. All bins containing three runs comprise data taken over a 10-min period; here $\sigma_{\Delta V}$ is only a few times σ_m (average value=2.7 for $N_r=3$). Bins containing more than three runs contain data from more than one day and show substantially higher values of $\sigma_{\Delta V}/\sigma_m$ ($\sim$30 for the $N_r=15$ bin). Clearly our implementation of the reference cell technique does not provide long-term stability comparable to the short-term precision. The uncertainty due to temperature and the statistical uncertainty σ_m are comparable, and adding them in quadrature results in the total uncertainties (1σ) shown as error bars in Fig. 1. Our measurements are in complete agreement with the model, and significantly smaller uncertainties will be necessary to find deviations from the model.

Our results lead us to believe that this noninvasive method for generating and detecting free-field ultrasonic waves is promising for future work in gas-phase acoustics. The statistics of our sound speed measurements can be improved by averaging more laser shots. In addition, improvements in future LITA apparatus and ovens are possible. Thus we anticipate that LITA can be used for characterization of the speed of sound for a variety of gases, frequencies, and temperatures with improved uncertainties compared to those we have achieved here.

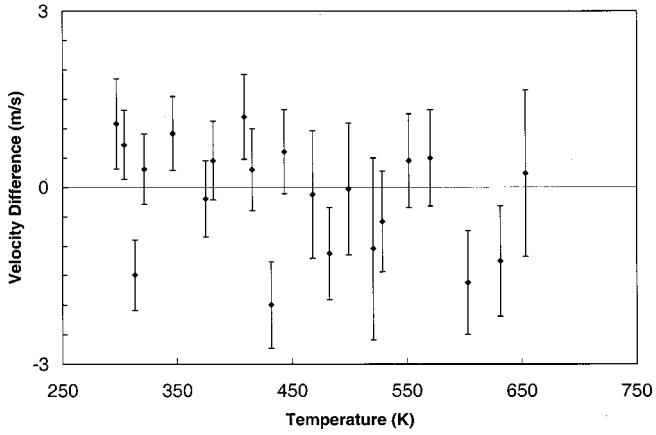

FIG. 1. Velocity difference (ΔV from Table I) between measurements and the model as a function of temperature. Uncertainties due to temperature uncertainties and sound velocity uncertainties (σ_m from Table I) were added in quadrature to obtain the total 1σ uncertainties, indicated by the error bars.

ACKNOWLEDGMENT

We gratefully thank A. Zuckerwar for helpful discussions.

[1] G. S. K. Wong, ''Speed of sound in standard air,'' J. Acoust. Soc. Am. **79**, 1359–1366 (1986).
[2] A. J. Zuckerwar, ''Speed of sound in real gases. II. Comparison with experiment,'' J. Acoust. Soc. Am. **100**, 2747 (1996).
[3] R. C. Hart, R. J. Balla, and G. C. Herring, ''Nonresonant referenced laser induced thermal acoustics thermometry in air,'' Appl. Opt. **38**, 577–584 (1999).
[4] A. J. Zuckerwar, ''Speed of sound in real gases. I. Theory,'' J. Acoust. Soc. Am. **100**, 2747 (1996).
[5] E. B. Cummings, H. G. Hornung, M. S. Brown, and P. A. DeBarber, ''Measurement of gas-phase sound speed and thermal diffusivity over a broad pressure range using laser-induced thermal acoustics,'' Opt. Lett. **20**, 1577–1579 (1995).

Phase and group velocities of fast and slow compressional waves in trabecular bone

Frédéric Padilla and Pascal Laugier
Laboratoire d'Imagerie Paramétrique—CNRS UMR 7623, Université Paris 6—Pierre et Marie Curie, 15 rue de l'Ecole de Médecine, 75006 Paris, France

(Received 18 February 2000; accepted for publication 16 June 2000)

This Letter is an extension to a multilayer model of porous bone first proposed by Hughes *et al.* [Ultrasound Med. Biol. **25**, 811–821 (1999)]. Both slow and fast compressional waves propagate when the acoustic wave propagation is parallel to the trabecular alignment. However, a slow wave disappears at high refraction angles. To explain this phenomenon, the multilayer model is extended to compute group velocity surface and arrival times with an angle. Two major effects are highlighted as the refraction angle increases. First, the energy of the slow wave is refracted from the phase propagation direction. Second, the signals of fast and slow waves overlap. As a consequence, the slow wave may not be observed for a refraction angle greater than 40°, which is in agreement with previous experimental data published by Hughes *et al.* and others. © *2000 Acoustical Society of America.* [S0001-4966(00)04109-6]

PACS numbers: 43.80.Ev, 43.80.Jz, 43.80.Qf [FD]

I. INTRODUCTION

Ultrasound propagation through trabecular bone is a major issue in medical ultrasound. A number of studies have demonstrated that ultrasonic velocity and attenuation represent a promising means of evaluating the skeletal status in osteoporosis.[1–4] Most of the current clinical devices are based on measurements at the calcaneus (heel bone).[5,6] The calcaneus is mainly composed of trabecular (or spongy) bone, which is a very porous medium. The solid porous frame is made of small plates or rods (trabeculas) that are interconnected. This trabecular network is highly anisotropic and heterogeneous.

The propagation of two types of compressional waves (a slow and a fast wave) has been reported independently by several authors.[7,8] However, the presence of the slow wave depends on the orientation between the beam axis and the direction of main orientation of the bone trabecular network. Both the fast and the slow waves propagate through trabecular bone when the acoustic wave propagation is parallel to the trabecular alignment. The slow wave tends to disappear at high angles to the trabecular alignment.[1,8]

A multilayer model has been applied to porous bone to compare theory against experiment for the measured phase velocity by Hughes *et al.*[7] and for the slowness surface by Hubbuck *et al.*,[9] for both slow and fast compressional waves. This Letter is an extension to these previous works, making use of their theory and data, and the data of Hosokawa and Otani,[8] to present two explanations why the previous authors did not observe two compressional waves at certain angles.

This multilayer model was originally developed by Schoenberg[10] to describe propagation through alternating fluid and solid layers. It was first used for bone by Hughes *et al.* and, as shown by these authors, it predicts the existence of two compressional waves. This is a very interesting alternative to Biot's model for propagation in porous media,[11,12] which was usually used to describe propagation in trabecular bone[13] before the work of Hughes *et al.* The first model of Biot was developed for isotropic media and predicts the existence of two compressional waves. Its difficulty is that it requires the knowledge of several parameters, including elastic and structural parameters. While these parameters can be estimated in isotropic media such as sands or glass beads, it may be quite difficult to measure these quantities in bone that is highly anisotropic and heterogeneous. Some of these parameters, however, have been estimated for bones by Hosokawa and Otani,[8] Williams,[14] or Mc Kelvie and Palmer,[15] but only for two propagation directions: parallel and orthogonal to the axis of main orientation of the bone trabecular network. Biot has developed as well a model for anisotropic media,[16] but it is even more difficult to use than the first one. The multilayer used by Hughes *et al.* is also a very interesting way to study anisotropy in porous bone.

We present in this Letter an analysis of an extension to

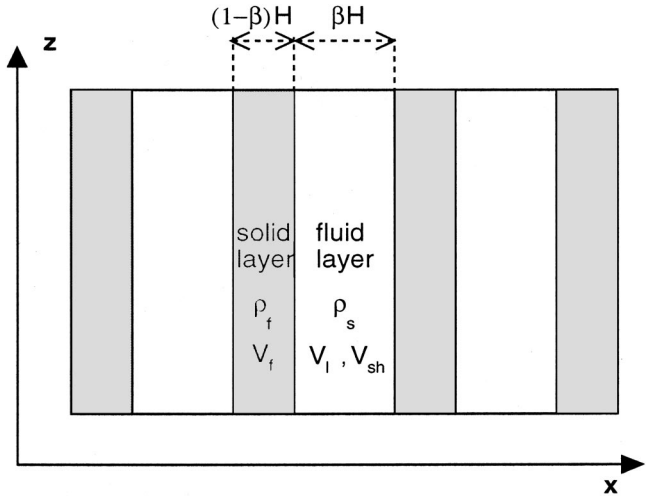

FIG. 1. Schematic representation of bone as a multilayer (alternating fluid and solid layers). Spatial period is H, thickness of fluid layers is βH, thickness of solid layers is $(1-\beta)H$. The **x** coordinate is perpendicular to the layers; the **z** axis is parallel to them.

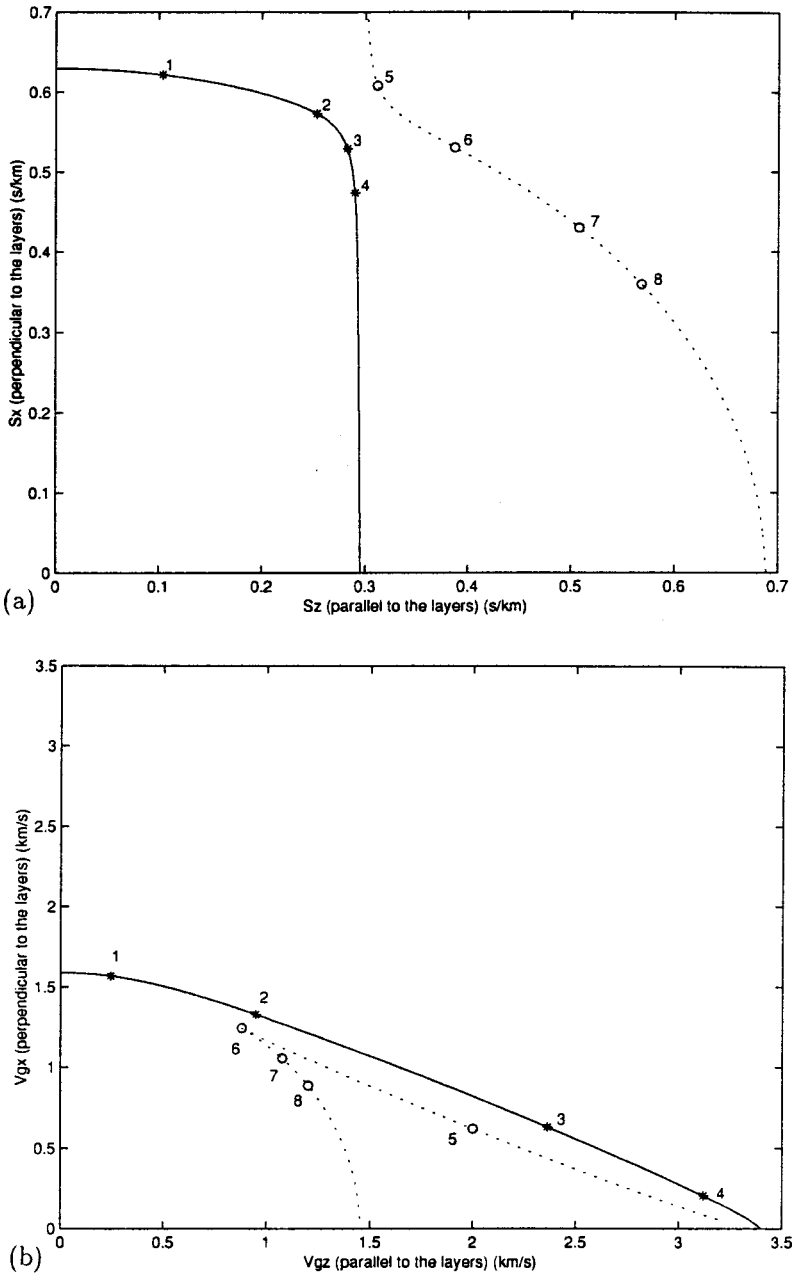

FIG. 2. Phase slowness surface (a) and group velocity surface (b) for the fast wave (solid lines) and the slow wave (dashed lines). Curves have been computed using Eqs. (2) and (3) of Ref. 7 for (a), and Eq. (34) of Ref. 10 for (b). The points 1–8 describe phase propagation directions on curve (a) and the corresponding energy propagation directions on curve (b).

the multilayer model of trabecular bone, in order to interpret the observation of a slow wave with an angle. Two main effects are presented. The first is derived from an analysis of the energy refraction, and the second is derived from studying the arrival times of fast and slow compressional waves with an angle.

II. THEORETICAL RESULTS

Schoenberg[10] derived a model for propagation of waves in a multilayer of alternating fluid and solid layers shown in Fig. 1. In the low-frequency approximation of the Schoenberg multilayer model (i.e., when the wavelength is large compared to the thickness of the layers), the phase propagation is described in terms of the slowness vector, which has the same orientation as the phase velocity vector and the inverse amplitude. Hughes *et al.*[7] proposed a multilayer model of bone to which they applied the theory of Schoenberg: The alignment of the layers is supposed to represent the main orientation of the bone trabecular network. They restricted their study to phase slowness and velocity only, using Eqs. (2) and (3) of Ref. 7 to compute the components of the slowness vector S_z parallel to the layers and S_x normal to the layers.

In the current Letter, we make use of Eq. (34) of Ref. 10 to compute group velocity, for the first time for the multilayer model of bone. We assume that group and energy velocities are identical.

Phase slowness surfaces (originally plotted by Hubbuck *et al.*[9]) and group velocities surfaces have been plotted in Fig. 2. The values of the parameters describing the trabecular bone are summarized in Table I. As previously reported by the theoretical predictions of Hughes *et al.*[7] and Hubbuck *et al.*,[9] and observed in trabecular bone specimen,[7,9,8] from these curves, one may deduce that two waves may propagate parallel to the trabecular network, and that the phase velocity

TABLE I. Values of parameters describing the trabecular bone taken from Refs. 8 and 7.

Parameter	Value
Density of bone ρ_s	1960 kg/m^3
Density of fluid (marrow) ρ_f	990 kg/m^3
Solid compressional speed V_s	3200 m/s
Solid shear speed V_{sh}	1800 m/s
Fluid compressional speed V_f	1500 m/s
Porosity β	0,65

of the fast wave is smaller in the direction perpendicular to the main orientation of the bone network than in the direction parallel to it.

The first novel result of this Letter concerns the energy refraction. Figure 2 clearly shows that the phase and energy of both waves do not propagate in the same direction This is a characteristic of an anisotropic medium. Some points on the phase slowness surface, and their corresponding points on the group velocity surface have been marked out. It may then be noticed that energy of the slow wave cannot propagate in the perpendicular direction to the network. More precisely, group velocity of a slow wave cannot propagate with a refraction angle greater than $\theta_r = \theta_6 \approx 55°$; cf. point 6 in Fig. 2 (here $\theta_r = 0°$ corresponds to ultrasound propagation parallel to the layers). In particular, this means that no signal of the slow wave may be received when the sound beam is perpendicular to the trabecular network. However, the disappearance of the slow wave has been observed experimentally for $\theta_r \approx 45°$ by Hughes *et al.*[1] and for $\theta_r \approx 40°$ by Hosokawa and Otani.[8] This suggests that energy refraction is not the only mechanism responsible for the disappearance of the slow wave with an angle.

We have identified another effect that contributes to this phenomenon: the overlap of signals associated to fast and slow waves. In order to demonstrate it, as we know the phase velocity of both waves, we calculate the arrival time for both waves. In fact, we calculate the time difference between the time of flight for a straight propagation in water and the time of flight in the presence of the sample. From Fig. 3, this time

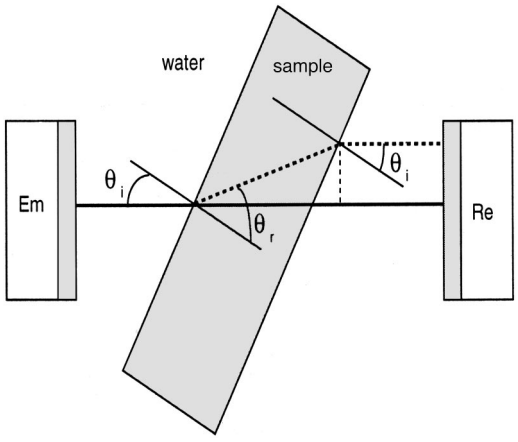

FIG. 3. Ray propagation between the emitter (Em) and receiver (Re) in water (bold lines) and in the presence of the sample (bold dashed lines). θ_i is the incidence angle in the fluid, θ_r is the refraction angle in the sample. $\theta_r = 0°$ corresponds to propagation parallel to the layers, and $\theta_r = 90°$ corresponds to propagation perpendicular to the layers.

difference Δt may be expressed as the difference between time to propagate AB with velocity V_f in the fluid and time to propagate AB' with velocity $V_\varphi(\theta_r)$ in the bone:

$$\Delta t = \frac{d}{\cos\theta_r}\left[\frac{1}{V_\varphi(\theta_r)} - \frac{\cos(\theta_r - \theta_i)}{V_f}\right], \tag{1}$$

where θ_i is the incidence angle in the fluid, θ_r is the refraction angle in the sample, d is the thickness of the sample (approximately 1 cm in Refs. 7 and 8), and $V_\varphi(\theta_r)$ is the phase velocity in the sample in the direction θ_r. To compute Eq. (1), we have employed Eq. (2) of Ref. 7 and Descartes–Snell law, which may be expressed as $V_f \sin\theta_i = V_\varphi(\theta_r)\sin\theta_r$. Note that Eq. (1) was checked by computing absolute arrival times for both slow and fast waves. Our theoretical predictions were found to be of the same order of magnitude as the experimental values of Hughes *et al.*[7] and Hosokawa and Otani.[8]

The time difference Δt between the arrival times for both fast and slow compressional waves was plotted in Fig. 4 as a function of the refraction angle θ_r. It may be observed that the difference of arrival times of the two waves is below 2 μs as soon as θ_r is greater than 40°. This corresponds approximately to a pulse duration for the experimental frequencies (approximately 1 MHz). It is also expected that the two signals should become indistinguishable as soon as θ_r exceeds 40°.

It should also be interesting in future works to study the effect of the energy refraction on the amplitude of the transmitted signal: as the group velocity of the slow wave is refracted, less signal school is received for this wave.

III. COMPARISON WITH EXPERIMENTAL RESULTS

Several experimental results on trabecular bones have been reported. However, it seems that only Hughes *et al.*[7] and Hosokawa and Otani[8] have published experimental results documenting the propagation as a function of the angle.

We have demonstrated that group velocity of the slow wave would be totally refracted in the sample as soon as $\theta_r \approx \theta_6 \approx 55°$ (cf. Fig. 2). However, the slow wave was observed only for refraction angles below 40°–45°: this is due to the overlap of the two signals. The pulse duration for Hughes *et al.* was approximately 4 μs (central frequency close to 1 MHz), and for Hosokawa approximately 2 μs (central frequency close to 1 MHz). We have shown with Fig. 4 that for θ_i greater than 40°, the time difference between arrival times of slow and fast waves is lower than 2 μs. So, for a refraction angle greater than 40°, the two signals become indistinguishable.

IV. CONCLUSION

The multilayer model gives relevant information to interpret anisotropic propagation in porous bones. This model, first applied to bone by Hughes *et al.*,[7] allow us to explain why the slow wave is not observed under certain angles of propagation in trabecular bone.

Our prediction of the angle at which the slow wave ceases to propagate, based on our use of a group velocity surface, and our analysis of the angle at which a fast and

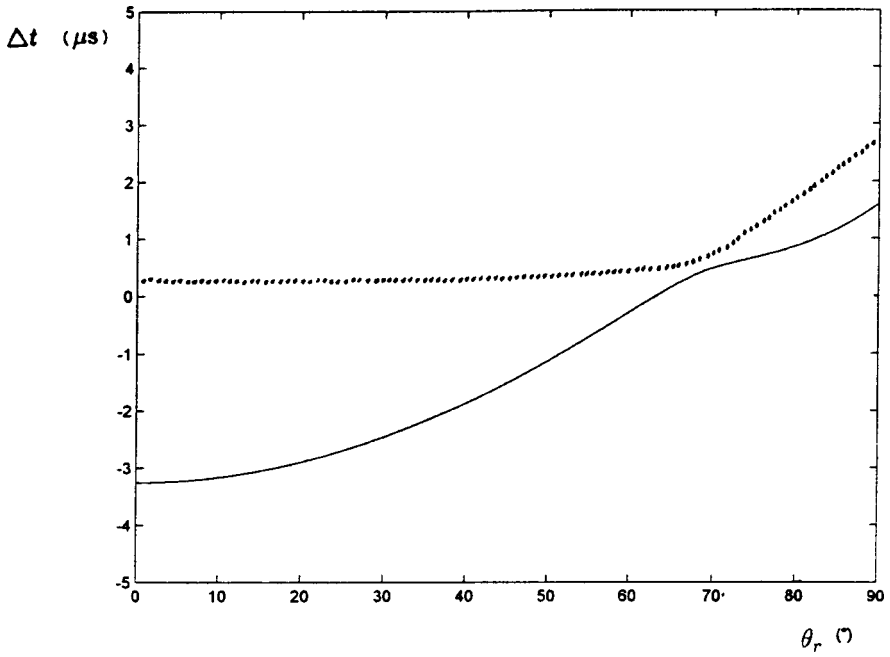

FIG. 4. The time difference as a function of the refraction angle θ_r. Δt is calculated as the time difference between the time of flight for a straight propagation in water and the time of flight in the presence of the sample for the fast wave (solid lines) and the slow wave (dashed lines).

slow wave may overlap, gives reasonable agreement with the cutoff angles recorded by other groups. While one of the reasons proposed is a relatively minor technical issue, the other involves a novel development of the multilayer model for the application to bone.

It seems also that attention should be focused in future works on the fast wave properties. In a clinical measurement configuration, the beam axis is perpendicular to the main orientation of trabecular network, and information is also conveyed only by the fast wave signal. The multilayer model may be useful in providing insight into the influence of structural anisotropy on quantitative ultrasound.

[1] D. Hans, P. Dargent-Moline, A. M. Schott *et al.*, ''Ultrasonographic heel measurements to predict hip fracture in elderly women: the epidos prospective study,'' Lancet **348**, 511–514 (1996).

[2] D. C. Bauer, C. C. Glüer, J. A. Cauley, T. M. Vogt, K. E. Ensrud, and H. K. Genant, ''Broadband ultrasound attenuation predicts fractures strongly and independently of densitiometry in older women,'' Arch. Int. Med. **157**, 629–634 (1997).

[3] P. W. Thomson, J. Taylor, R. Oliver, and A. Fisher, ''Quantitative ultrasound of the heel predicts wrist and osteoporosis-related fractures in women age 45–75 years,'' J. Clin. Densitometry **1**, 219–225 (1998).

[4] E. W. Gregg, A. M. Kriska, L. M. Salamone, M. M. Roberts, S. J. Anderson, and R. E. Ferrell, ''The epedemiology of quantitative ultrasound: a review of the relationships with bone mass, osteoporosis and fracture risk,'' Osteoporosis Int. **7**, 89–99 (1997).

[5] C. F. Njeh, D. Hans, T. Fuerst, C. C. Glüer, and H. K. Genant, *Quantitative Ultrasound: Assessment of Osteoporosis and Bone Status* (Martin Dunitz, London, 1999).

[6] P. Laugier, B. Fournier, and G. Berger, ''Ultrasound parametric imaging of the calcaneus: in vivo results with a new device,'' Calcif. Tissue Int. **58**, 326–331 (1996).

[7] E. R. Hughes, T. G. Leighton, G. W. Petley, and P. R. White, ''Ultrasonic propagation in cancellous bone: a new stratified model,'' Ultrasound Med. Biol. **25**, 811–821 (1999).

[8] A. Hosokawa and T. Otani, ''Acoustic anisotropy in bovine cancellous bone,'' J. Acoust. Soc. Am. **103**, 2718–2722 (1998).

[9] E. R. Hubbuck, T. G. Leighton, P. R. White, and G. W. Petley, ''A stratified model of ultrasonic propagation in cancellous bone,'' J. Acoust. Soc. Am. **103**, 3039 (A) (1998).

[10] M. Schoenberg, ''Wave propagation in alternating solid and fluid layers,'' Wave Motion **6**, 303–321 (1984).

[11] M. A. Biot, ''Theory of propagation of elastic waves in a fluid-saturated porous solid. I Low-frequency range,'' J. Acoust. Soc. Am. **28**, 168–178 (1956).

[12] M. A. Biot, ''Theory of propagation of elastic waves in a fluid-saturated porous solid. II Higher frequency range,'' J. Acoust. Soc. Am. **28**, 178–191 (1956).

[13] T. J. Haire and C. M. Langton, ''Biot theory: A review of its application to ultrasound propagation through cancellous bone,'' Bone (N.Y.) **24**, 291–295 (1999).

[14] J. L. Williams, ''Ultrasonic wave propagation in cancellous and cortical bone: Prediction of some experimental results by Biot's theory,'' J. Acoust. Soc. Am. **91**, 1106–1112 (1992).

[15] M. L. Mc Kelvie and S. B. Palmer, ''The interaction of ultrasound with cancellous bone,'' Phys. Med. Biol. **36**, 1331–1340 (1991).

[16] M. A. Biot, ''Theory of deformation of a porous anisotropic solid,'' J. Appl. Phys. **27**, 459–467 (1956).